OUTLOOK
Biomaterials

nature

THE INTERNATIONAL WEEKLY JOURNAL OF SCIENCE

GROWING IN THE WIND

Accretion-disk winds drive evolution of supermassive black holes and their galaxies

PAGES 423 & 436

INNOVATION

BIOTECH BOOT CAMP

Finishing school for wannabe entrepreneurs

PAGE 402

MEDICAL GENETICS

"DON'T EDIT THE GERM LINE"

Heritable gene modification risks may outweigh benefits

PAGE 410

NANOTECHNOLOGY

WATER ENTERS A NEW PHASE

'Square ice' found between the graphene sheets

PAGES 417 & 443

➔ NATURE.COM/NATURE
26 March 2015 £10
Vol. 519, No. 7544
13
9 770028 083095

PLANETS Days on Saturn end earlier than thought **p.390**

WORLD VIEW A new law to govern intelligent robots **p.391**

SMILE The 3D-printing revolution gathers pace **p.393**

Rethinking the brain

Critics of the European Human Brain Project were justified, says an independent report on the project. Both its governance and its scientific direction need to be adjusted.

Just like the human brain itself, the European Commission's billion-euro Human Brain Project (HBP) defies easy explanation. Launched 18 months ago, the massive project is complex and, to most observers, confusing. Many people — both scientists and non-scientists — have thus accepted a description of the project that emerged from its leaders and its publicity machine: the aim of simulating the entire human brain in a supercomputer and so find cures for psychiatric and neurological disorders.

Like many simplistic explanations of the brain, that characterization of the project provoked a backlash from neuroscientists. This climaxed in a full-scale uprising last summer, when hundreds of researchers signed a critical open letter to the commission (www.neurofuture.eu). Autocratic management, they complained, was running the project off its scientific course and exaggerating its clinical reach.

An independent committee was established to investigate and mediate on the dispute. Last week it published its report. This time, the main points were easier for outsiders to decipher. The rebellious neuroscientists who made the complaints were correct. The brain project is failing and must be fixed.

The committee's criticisms endorse more or less all the concerns of the scientists. The project fails not only in its governance, the report says, but also in its scientific plan — particularly the core aim, the simulation of the entire brain that critics had long dismissed as unrealistic.

The depth of the governance issues are exemplified by this statement in the report, which refers to the project's de facto leader, Henry Markram of the Swiss Federal Institute of Technology in Lausanne. "The co-ordinating scientist … is not only a member of all decision-making, executive and management bodies within the HBP, but also chairs them and supervises the administrative processes supporting these bodies. Furthermore, he is a member of all the advisory boards and reports to them at the same time. In addition, he appoints the members of the management team, and leads the operational project management."

Although egregious, the governance problems should be straightforward to fix. There isn't much left to invent about good governance, and the HBP's board of directors was quick to enact some of the necessary changes even before the report was published. For example, last month it dissolved the three-person executive board in which power had been concentrated.

Such a change is not sufficient, however, as the independent committee makes clear. Changes in scientific direction are essential. After all, it was the decision of the project's (now defunct) executive board to eliminate cognitive and systems biology from the next phase of the programme that triggered last summer's revolt.

The report says that ambitions for whole-brain simulation are premature and that the HBP should refocus on enabling methods and technologies, particularly innovative software and hardware platforms for neuroinformatics. It goes further. These platforms, it says, should be developed and carefully validated by interdisciplinary collaborations that involve cognitive and systems neuroscientists. And they should address concrete problems — such as spatial navigation or goal-directed decision-making.

It also says that the project was wrong to rule out research in non-human primates, because this would provide an important stepping stone between the tiny mouse brain, in which most neuroscience data have been generated, and the human brain.

"The brain project is failing and must be fixed."

What now? For the mediation process to be successful, the HBP will not only have to accept the report but also "faithfully implement the recommendations". Yet, according to the report, most members of the HBP board of directors feel that the mediation committee's recommendations would turn their "visionary project into an average one", and say that *in silico* brain simulation is the "unique selling point of the HBP".

The scientists who signed the open letter pledged not to collaborate with the HBP unless their concerns were addressed. For the HBP to continue, the board of directors, whatever their doubts, must now win back trust by pledging to carry out the mediation report's recommendations on the science.

If they do, all will have an easier time understanding what the HBP is: a project aiming to put in place new technology to help neuroscientists understand the human brain and its diseases.

That is a more modest, but still magnificent, aim, and a perfect complement to the US BRAIN Initiative, which supports the development of other types of neurotechnologies. With the tools in place, one of the biggest challenges to science will be ready for systematic assault. ■

Applied prestige

The UK research assessment should inspire everybody to reward excellent societal impacts.

For many involved in the United Kingdom's mammoth national assessment of university research, the release of the results late last year marked the end of the process, or at least a welcome rest from it. But for a hard core of research-policy wonks, assessment never sleeps. So begins a new phase: assessment of the assessment. A meta-assessment? This is not as insular as it might sound. Policy-makers have to decide whether the original assessment was worthwhile, how to develop it if so, and whether it should be repeated.

University-funding agencies have commissioned independent experts to pick over the results. The first such analysis is published

this week, and it deserves a broad audience.

The focus of the report is the collection of innovative (and, to some, controversial) accounts of the societal impact claimed for research. These impacts were reported as part of universities' submissions to the 2014 Research Excellence Framework (REF), which will be used to help to allocate public funds on the basis of merit (http://results.ref.ac.uk).

One university research group, for example, developed a model and database to quantify pollution of urban water sources. It also analysed peatland drainage systems to work out how to reduce water discolouration by dissolved organic carbon. The outputs of this research helped to improve water quality and the performance of the water industry.

Another group experimented on interventions that rewarded staff in primary health-care centres for their performance, to assess the effects on the quality of care delivery. The work delivered demonstrable impacts both nationally and internationally.

This week's report, *The Nature, Scale and Beneficiaries of Research Impact*, was produced by King's College London and Digital Science, a sister company of *Nature*'s publishers. It features attractive diagrams of flows between research and impacts, but is heaped with qualifications as to its limitations: the analysis is based on text-mining of the roughly 7,000 submitted impact statements, which, at the time, were not searchable or classified with metadata.

Nevertheless, some of the report's broad conclusions are credible. UK academics make contributions that are felt in every country around the world, and have provided a rich variety of narratives about how universities affect policy, cultural development or research commercialization. Multiple fields have impacts on the same broad topics, yet each research field also splashes its impacts over multiple topics. Small institutions have larger societal impacts than is generally recognized.

The analysts freely admit that their report is a work in progress: the free-form nature of the REF meant that few impact statements presented information in standardized ways or used the same approaches to evaluate impact numerically. More consensus on approaches and standardization would probably be required to identify the qualitative and quantitative outcomes of research — yet a more prescriptive approach to gathering information might discourage academics from displaying their very diverse and heterogeneous impacts.

At this point, it is worth stepping back and noting the fundamental point. This exercise has shown that societal impacts can be documented and independently assessed.

Each of the assessment panels across academic disciplines has documented the particular steps that it took to assess impact statements, and (assisted by a pilot study) to develop criteria for doing so (see go.nature.com/57wprj).

"Applied research can gain its own professional merit and public recognition."

There will be justified debates about the cost of the exercise, how its outputs are geared to draw university funding, and the incentives to which such assessments will inevitably give rise. But there is a long-term perspective that should be considered.

In a country the size of the United Kingdom, no one should doubt that a significant proportion of the research base should be dedicated to research that tries to understand how the Universe and our planet function, and what makes humans tick. And outstanding performers in such basic research fully deserve the prestige given by prizes and academies.

But there are also outstanding performers in research addresses quite different goals: to directly improve the health, sustainability and resilience of individuals and the state of the world. Some of their work is published in highly specialized journals, but has a relatively broad societal impact.

By showing that standards of impact can be set and performance can be assessed, the REF has demonstrated in principle that applied research can gain its own professional merit and public recognition. Funders and institutions should celebrate, support and reward such achievements just as much as they celebrate prizes and academy memberships for fundamental research. Through such positive incentives and prestige, society at large will obtain a more appropriate balance of returns on its investments in university research. ■

About time

The next few years will see NASA missions probe the innermost secrets of gas giants.

When a powerful earthquake and tsunami destroyed large parts of Indonesia on 26 December 2004, Earth's crust was altered sufficiently to change the speed at which the planet rotates. Ever since, days have been 2.68 microseconds shorter.

But the rotations of other planets in the Solar System have been harder to determine. Saturn's, for instance, is still subject to vast uncertainties.

In *Nature* this week, three Israeli planetary scientists suggest that a day on Saturn is 15 minutes shorter than previously thought. It lasts for 10 hours, 32 minutes and 45 seconds, they say (R. Helled, E. Galanti and Y. Kaspi *Nature* http://dx.doi.org/10.1038/nature14278; 2015).

Because it is mostly a dense fluid of helium and hydrogen, Saturn would not be expected to have a single, well-defined rate of spin. But the planet is thought to have a rocky core, and to rotate roughly in unison in the same way that a solid object would. (The fluid Sun, by contrast, rotates 34% faster at its equator than at its poles.) Saturn's hazy atmosphere — the thickness of which is hard to pin down — makes it difficult to estimate how fast any firmer mass inside is spinning.

The two Voyager probes gave us the first modern estimate of Saturn's rotation period — around 10 hours and 39 minutes — some 35 years ago. They used radiofrequency emissions sent out by the planet's wobbling magnetic field. NASA's Cassini spacecraft, which has been orbiting Saturn since 2004, repeated those radio measurements but found a value that was not only substantially larger, but also changed with time. Experts began to question whether the technique, which had been applied successfully to Jupiter, was reliable for its smaller sibling Saturn.

Ravit Helled of Tel Aviv University and her colleagues took an approach that is, in a way, more traditional: they estimated the rotation indirectly, from the way it distorts the planet. Centrifugal forces give spinning celestial bodies a flattened shape, wider at the equator than at the poles. For Saturn, the effect is accentuated by the planet's size — centrifugal forces are stronger the farther one moves from the axis of rotation — and rapid spin. Moreover, its mostly fluid nature means that the planet deforms more easily. Not much is known about the distribution of mass inside Saturn, but something can be gleaned from its gravitational pull on objects that orbit it. Small deviations in Cassini's trajectories, for instance, have revealed that the gravitational field is not symmetrical.

This information is still not sufficient to nail down the internal structure of the planet or to calculate the rotation rate. So Helled and her co-authors did the next best thing. They produced a series of likely internal structures that narrow down the uncertainty to a 92-second range.

Are they right? NASA plans to probe Saturn's gravitational field much more precisely towards the end of the Cassini mission, when the craft will dip into an elongated orbit and fly between the atmosphere and the system of rings. Just before its fuel runs out in 2017, Cassini will perform a controlled plunge into the planet. And the data it gathers along the way should help not just to elucidate the planet's make-up, but also to test models of how gas giants form in distant star systems. But Saturn will not be alone. From 2016, Juno, a major NASA mission that launched in 2011, will take similar measurements of the gravitational field of Jupiter. Sooner rather than later, it seems, these two gas giants will reveal their mysteries. ■

➲ NATURE.COM
To comment online, click on Editorials at: go.nature.com/xhunqv

WORLD VIEW *A personal take on events*

Intelligent robots must uphold human rights

The common fear is that intelligent machines will turn against humans. But who will save the robots from each other, and from us, asks **Hutan Ashrafian**.

There is a strong possibility that in the not-too-distant future, artificial intelligences (AIs), perhaps in the form of robots, will become capable of sentient thought. Whatever form it takes, this dawning of machine consciousness is likely to have a substantial impact on human society.

Microsoft co-founder Bill Gates and physicist Stephen Hawking have in recent months warned of the dangers of intelligent robots becoming too powerful for humans to control. The ethical conundrum of intelligent machines and how they relate to humans has long been a theme of science fiction, and has been vividly portrayed in films such as 1982's *Blade Runner* and this year's *Ex Machina*.

Academic and fictional analyses of AIs tend to focus on human–robot interactions, asking questions such as: would robots make our lives easier? Would they be dangerous? And could they ever pose a threat to humankind?

These questions ignore one crucial point. We must consider interactions between intelligent robots themselves and the effect that these exchanges may have on their human creators. For example, if we were to allow sentient machines to commit injustices on one another — even if these 'crimes' did not have a direct impact on human welfare — this might reflect poorly on our own humanity. Such philosophical deliberations have paved the way for the concept of 'machine rights'.

Most discussions on robot development draw on the Three Laws of Robotics devised by science-fiction writer Isaac Asimov: robots may not injure humans (or through inaction allow them to come to harm); robots must obey human orders; and robots must protect their own existence. But these rules say nothing about how robots should treat each other. It would be unreasonable for a robot to uphold human rights and yet ignore the rights of another sentient thinking machine.

Animals that exhibit thinking behaviour are already afforded rights and protection, and civilized society shows contempt for animal fights that are set up for human entertainment. It follows that sentient machines that are potentially much more intelligent than animals should not be made to fight for entertainment.

Of course, military robots are already being deployed in conflicts. But outside legitimate warfare, forcing AIs and robots into conflict, or mistreating them, would be detrimental to humankind's moral, ethical and psychological well-being.

Intelligent robots remain science fiction, but it is not too early to take these issues seriously. In the United Kingdom, for example, the Engineering and Physical Sciences Research Council and the Arts and Humanities Research Council have already introduced a set of principles for robot designers. These reinforce the position that robots are manufactured products, so that "humans, not robots, are responsible agents".

Scientists, philosophers, funders and policy-makers should go a stage further and consider robot–robot and AI–AI interactions (AIonAI). Together, they should develop a proposal for an international charter for AIs, equivalent to that of the United Nations' Universal Declaration of Human Rights. This could help to steer research and development into morally considerate robotic and AI engineering.

National and international technological policies should introduce AIonAI concepts into current programmes aimed at developing safe AIs. We must engage with educational activities and research, and continue to raise philosophical awareness. There could even be an annual AIonAI prize for the 'most altruistically designed AI'.

INTELLIGENT ROBOTS REMAIN SCIENCE FICTION, BUT IT IS NOT TOO EARLY TO TAKE THESE ISSUES SERIOUSLY.

Social scientists and philosophers should be linked to cutting-edge robotics and computer research. Technological funders could support ethical studies on AIonAI concepts in addition to funding AI development. Medical funders such as the Wellcome Trust follow this model already: supporting research on both cutting-edge healthcare and medical ethics and history.

Current and future AI and robotic research communities need to have sustained exposure to the ideas of AIonAI. Conferences focused on AIonAI issues could be a hub of research, guidelines and policy statements. The next generation of robotic engineers and AI researchers can also be galvanized to adopt AIonAI principles through hybrid degree courses. For example, many people who hope to get into UK politics take a course in PPE (politics, philosophy and economics) — an equivalent course for students with ambitions in robotics and AI could be CEP (computer science, engineering and philosophy).

We should extend Asimov's Three Laws of Robotics to support work on AIonAI interaction. I suggest a fourth law: all robots endowed with comparable human reason and conscience should act towards one another in a spirit of brotherhood and sisterhood.

Do not underestimate the likelihood of artificial thinking machines. Humankind is arriving at the horizon of the birth of a new intelligent race. Whether or not this intelligence is 'artificial' does not detract from the issue that the new digital populace will deserve moral dignity and rights, and a new law to protect them. ■

➲ NATURE.COM
Discuss this article online at:
go.nature.com/2bxpts

Hutan Ashrafian *is a lecturer and surgeon at Imperial College London, UK.*
e-mail: h.ashrafian@imperial.ac.uk

STEM CELLS

Stem cells tackle diabetes

Stem cells may be useful for treating type 2 diabetes, according to a study in mice.

Insulin-producing cells derived from human embryonic stem cells reduce blood sugar levels in mice with type 1 diabetes, but it was unclear whether the approach would work for type 2 diabetes, which is much more common in humans. To model the disease, Timothy Kieffer of the University of British Columbia in Vancouver, Canada, and his colleagues fed mice a high-fat diet. After five days, the mice had high blood glucose levels, and by seven weeks they exhibited other symptoms of type 2 diabetes.

Transplanting pancreatic cells grown from human embryonic stem cells into these mice increased their sensitivity to insulin. When combined with diabetes drugs, the transplants also reduced obesity and blood sugar levels.

Stem Cell Rep. **http://dx.doi.org/10.1016/j.stemcr.2015.02.011 (2015)**

DORLING KINDERSLEY/GETTY

ZOOLOGY

Fish slurps up prey with watery 'tongue'

Mudskipper fish (*Periophthalmus barbarus*; pictured) use water bubbles as a 'tongue' to feed on land. The finding hints at how other animals might have evolved tongues as they made the transition from aquatic to terrestrial life.

Krijn Michel at the University of Antwerp in Belgium and his colleagues used high-speed video and X-ray imaging to study the feeding behaviour of various animals. They found that when the mudskipper eats on land, a bubble of water held in its mouth protrudes out and touches food before its jaws close. The fish sucks some of this water back into its mouth as it engulfs the food. The movement of a bone involved in mudskipper feeding resembles that of some animals that feed with tongues on land, the authors say.

This pseudo-tongue allows mudskippers to catch and swallow food items on land, unlike some other aquatic species that must return to water to consume what they capture ashore.

Proc. R. Soc. B **http://doi.org/2wr (2015)**

CANCER

Leukaemia cells made normal

Cancerous white blood cells from people with a form of leukaemia have been reprogrammed into immune cells that do not cause the disease in animals.

Immature immune cells called B cells cannot develop fully in people with precursor B-cell acute lymphoblastic leukaemia (B-ALL). Ravindra Majeti and his colleagues at Stanford University in California isolated diseased cells with specific mutations from 12 patients with B-ALL.

The researchers reprogrammed the cells by culturing them with molecules that promote the development of myeloid cells, which include several types of white blood cell. They ended up with cells that were similar to macrophages, which engulf pathogens, and did not develop into cancer when transplanted into mice. Turning on a myeloid regulatory gene in the cells achieved the same result.

This could be a therapeutic strategy for some people with B-ALL, the authors say.

Proc. Natl Acad. Sci. USA **http://doi.org/24t (2015)**

CHEMISTRY

Imaging of excited electron orbitals

A technique could pave the way for imaging electron behaviour as chemical reactions happen.

Many reactions are governed by the behaviour of electrons in excited orbital states, but these states are difficult to capture because they last only a few picoseconds (10^{-12} seconds). Now, Masahiko Takahashi at Tohoku University in Sendai, Japan, and his colleagues have measured the excited states of molecules of acetone gas by probing them with ultrashort pulses of electrons.

Electrons in the pulse knocked excited electrons out of the atoms comprising the acetone. By simultaneously measuring the energy of the ejected electrons and those from the pulse, the team determined the energy and momentum of the molecule's excited state, which lasted for just 13.5 picoseconds.

Although the data quality is currently low, the results show that such measurements are feasible, say the authors.

Phys. Rev. Lett. 114, **103005 (2015)**

PLANETARY SCIENCE

Rings proposed for orbiting rock

An asteroid-sized rock orbiting between Saturn and Uranus may have a system of rings.

Amanda Bosh of the Massachusetts Institute of Technology in Cambridge and her team observed the minor planet 2060 Chiron passing in front of a star, using NASA's Infrared Telescope Facility on Mauna Kea and the Las Cumbres Observatory Global Telescope Network on Haleakala, both in Hawaii. The team saw two small dips in brightness of the star before and after Chiron's transit, suggesting that a ring of debris surrounds the system — perhaps remnants of Chiron's formation or material ejected from its surface in comet-like jets.

If confirmed, Chiron's ring system would be the fifth known in the Solar System.

Icarus **252, 271–276 (2015)**

ERIC NGUYEN/CORBIS

MATERIALS

Speedy 3D printing in minutes

Researchers have sped up one approach to three-dimensional (3D) printing so that objects are produced in minutes instead of hours.

One method of 3D printing involves shining ultraviolet rays up into a bath of liquid resin. The light solidifies the resin and the partial product is pulled upwards one notch at a time, which can take up to a day. Now Joseph DeSimone at the University of North Carolina at Chapel Hill and his colleagues have modified this process to make it continuous.

They made the bottom of the resin container permeable to oxygen, which stops the resin solidifying, creating a thin liquid layer just below the area where the solidification reaction happens. Because liquid is always present, the researchers can continuously pull up the forming object (example **pictured**), rather than waiting for new liquid resin to flow in.

Science **347, 1349–1352 (2015)**

CARBON3D

MEDICAL MICROBIOLOGY

Super bacteria lurk in the home

Drug-resistant bacteria may hide out in homes for many years before causing disease.

In the 1990s, methicillin-resistant *Staphylococcus aureus* (MRSA) moved out of hospitals in North America and started circulating in the community, causing skin and other infections. A team led by Michael David at the University of Chicago in Illinois and Timothy Read at Emory University in Atlanta, Georgia, sequenced the genomes of MRSA taken from 146 patients and members of their households. An evolutionary analysis that compared the sequence of a patient's strain with the one from their home determined that MRSA had been present in the household for between 2.3 and 8.3 years before being sampled.

Eradicating MRSA from homes, such as by treating asymptomatic household members, could help to bring the current epidemic under control, the authors say.

mBio **6, e00054 (2015)**

ECOLOGY

Snakes wipe out Everglades rabbits

Invasive pythons have been blamed for the decline of many mammals in a protected area in Florida. Now, Robert McCleery of the University of Florida in Gainesville and his team have found evidence for that claim.

Burmese pythons (*Python molurus bivittatus*) invaded Florida's iconic Everglades National Park several decades ago. To study the pythons' effects, the researchers focused on marsh rabbits (*Sylvilagus palustris*), which have all but disappeared from the park. They released 26 radio-collared rabbits at two sites and found that Burmese pythons were responsible for 77% of the deaths within 11 months, as confirmed by DNA extracted from partially eaten rabbits or by finding the entire collared animal inside a python's belly.

Outside the pythons' current range, 71% of the rabbit mortalities were linked to mammals, mainly bobcats (*Lynx rufus*) and coyotes (*Canis latrans*).

Proc. R. Soc. B **282, 20150120 (2015)**

SOCIAL SELECTION *Popular articles on social media*

A proposal to cure sloppy science

A debate this week on ways to improve the practice of science quickly spread to social media. The event at University College London, called 'Is science broken? If so, how can we fix it?', included claims that some dubious laboratory practices, such as tweaking statistical analyses to make results seem significant, are widespread (see go.nature.com/4imbij). One suggested solution — requiring scientists to register their experimental design and planned analysis with a journal before running any tests — received general support. Audience member Michael Markie, an associate publisher at the open-science platform *F1000Research*, shared his thoughts about preregistration on Twitter: "IMO, registered reports can be applied to all life science subjects. Ideal to get your house in order before publishing."

➲ NATURE.COM
For more on popular papers:
go.nature.com/mjyiia

METEOROLOGY

El Niño brings fewer tornadoes

Warming and cooling trends in the equatorial Pacific Ocean affect the frequency of tornadoes (**pictured**) in parts of the United States.

John Allen of Columbia University in New York and his colleagues focused on environmental indices (such as wind shear) that are linked to extreme US storms, and analysed their relationship with periodic warming and cooling events in the tropical Pacific. These events are known as El Niño and La Niña, respectively. The team found that fewer tornadoes and hailstorms occur in winter and spring in the central and southern plains during El Niño, and more occur during La Niña, than in years when temperatures in the Pacific are relatively stable.

Although El Niño and La Niña events tend to be strongest during winter, the authors suggest that ocean conditions could be used to forecast extreme spring storm events several months in advance.

Nature Geosci. **http://doi.org/243 (2015)**

➲ NATURE.COM
For the latest research published by *Nature* visit:
www.nature.com/latestresearch

SEVEN DAYS *The news in brief*

EVENTS

Ice on Ceres

A pair of bright spots on Ceres observed by NASA's Dawn probe, which is currently in orbit around the dwarf planet, could be linked to icy geological activity. New images from the craft show that as Ceres rotates, the spots appear brightest in the light of dawn and dimmest at dusk. That could suggest that sunlight is driving changes on the surface of the water-rich body. The findings were presented at the Lunar and Planetary Science Conference in The Woodlands, Texas, on 17 March. See page 401 for more.

Observatory opens

Mexican and US officials inaugurated a γ-ray observatory near Puebla, Mexico, on 20 March. The High-Altitude Water Cherenkov array uses 300 giant water tanks to detect particles created when high-energy γ-rays and cosmic rays collide with the atmosphere (see *Nature* http://doi.org/25m; 2013). Although it has a lower resolution than other cosmic-ray detectors, it can map more of the sky, more quickly. The facility sits at an altitude of 4,100 metres, on Pico de Orizaba, the highest peak in Mexico.

Europe's bee peril

Europe's wild bees face an uncertain future, with about one in ten species at risk of extinction, according to an analysis by the International Union for Conservation of Nature released on 19 March. The organization, headquartered in Gland, Switzerland, says that 7.7% of Europe's 1,965 wild bee species have declining populations, 12.6% are stable and 0.7% are increasing. Data on most species are lacking, however; 56.7% are so poorly studied that it is not possible to classify their extinction risk. Population trends for 79% of species are unclear.

SUE FLOOD/GETTY

Pitcairn islands gain marine protection

The creation of a marine reserve around the Pitcairn islands (pictured) in the South Pacific was announced in the UK budget on 18 March. The status depends on agreeing on satellite monitoring and a way to enforce protection of the area, a British territory. On the same day, an international court in The Hague, the Netherlands, ruled that when a similar reserve was created around the Indian Ocean's Chagos islands in 2010, the United Kingdom failed in its duty to consult Mauritius, which has fishing rights in the archipelago. The ruling, by the Permanent Court of Arbitration, puts the future of marine protection in Chagos in doubt.

World water

The world faces a 40% shortfall in water supply by 2030 unless management of this essential resource drastically improves, warns a United Nations report. Released on 20 March in New Delhi, the World Water Development Report highlights the planet's growing thirst, as the global population continues to rise and economic development grows. Demand for water is expected to increase by 55% by 2050. However, 20% of the world's groundwater is already subject to over-exploitation, and the resource is not being managed sustainably, the report says.

Pluto name call

The mission team for NASA's New Horizons spacecraft has asked the public to suggest names for Pluto's geography in preparation for the probe's fly-by of the dwarf planet in July. The probe is expected to map dozens of features on Pluto and its largest moon, Charon. Anyone can chime in until 7 April on ourpluto.org, hosted by the SETI Institute in Mountain View, California, but the names must relate to mythology or exploration. The International Astronomical Union will decide on which ones are used.

POLICY

US fracking rules

The US Department of the Interior has finalized its regulations on the use of fracking on public and tribal lands. Released on 20 March, the rules set safety and environmental standards for companies that inject fluids into rock at high pressure to fracture it and release oil and gas. New requirements include extra geological analysis before drilling, and validation of well integrity once drilling

is complete. The regulations also increase standards for the storage of drilling fluids, and require disclosure of the chemicals used in the fluids. More than 100,000 wells are currently in operation on federal land. Of wells being drilled, more than 90% use fracking.

PEOPLE

Abel maths prize

US mathematician John Nash and Canadian-born Louis Nirenberg were awarded the 2015 Abel Prize, often considered the 'maths Nobel', on 25 March. The pair won the prize for their contributions to the theory of partial differential equations. Some of Nash and Nirenberg's most important accomplishments are in an area called geometrical analysis, which concerns the shapes of objects and surfaces. Nirenberg has also deepened understanding of Navier–Stokes equations, which describe fluid flow. The 6-million kroner (US$766,000) prize is awarded by the Norwegian Academy of Science and Letters in Oslo.

Royal Society head

Nobel-prizewinning structural biologist Venkatraman (Venki) Ramakrishnan (**pictured**) will be the next president of the UK's Royal Society, it was announced on 18 March. He


COURTESY OF VENKATRAMAN VENKI RAMAKRISHNAN

will take over as head of the country's pre-eminent scientific institution from geneticist Paul Nurse, also a Nobel laureate, on 1 December. Ramakrishnan shared the Nobel Prize in Chemistry in 2009 for his work on the structure and function of the ribosome, a molecular machine that translates genetic information to build proteins. See go.nature/sphc7n for more.

RIKEN leader quits

Ryoji Noyori, president of the beleaguered RIKEN Institute in Wako, Japan, announced his resignation on 24 March. The Nobel prizewinner in chemistry has implemented major reforms at the centre following the scandal around stem-cell researcher Haruko Obakata, which Noyori called "a most unfortunate case of research misconduct that has severely tarnished RIKEN's good reputation". Former president of Kyoto University, Hiroshi Matsumoto, will take up leadership when Noyori steps down on 31 March.

FUNDING

Ukraine agreement

Ukraine is to become an associate in the European Union's (EU) €80-billion (US$86-billion) Horizon 2020 research-funding programme. An agreement signed on 20 March in Kiev by Carlos Moedas, European Commissioner for Research, Science and Innovation, and Serhiy Kvit, the Ukrainian science minister, foresees that Ukrainian scientists and businesses will become eligible to participate in Horizon 2020 on equal terms with EU member states and other associated countries such as Israel. The Ukrainian parliament has still to approve the agreement. See go.nature.com/bwoebg for more.

GM foods approved

US regulators have approved new breeds of genetically modified (GM) apples and potatoes as safe for human consumption. The decision, the result of a voluntary consultation with the US Food and Drug Administration (FDA), was announced in letters sent on 20 March by the FDA Center for Food Safety and Applied Nutrition to Okanagan Specialty Fruits of Summerland, Canada — makers of a non-browning apple — and to J. R. Simplot of Boise, Idaho, which has produced a potato that is more resistant to bruising and makes less of the cancer-causing compound acrylamide when cooked. Both products have already been approved by the US Department of Agriculture.

COMING UP

26–27 MARCH
International experts will gather in Paris for the Symposium on Search for Life Signatures, to discuss strategies for SETI (the Search for Extra Terrestrial Intelligent life).
go.nature.com/iimrob

31 MARCH–2 APRIL
The International Human Microbiome Congress takes place in Luxembourg. The meeting will focus on future directions for microbiome research in health and disease.
go.nature.com/eeyw2a

RESEARCH

Alzheimer's hope

An experimental Alzheimer's drug slowed cognitive decline in a small trial, said the drug's manufacturer, Biogen Idec of Cambridge, Massachusetts, on 20 March. Aducanumab targets amyloid-β plaques, high levels of which are found in the brains of people with Alzheimer's disease. After 54 weeks of treatment, patients taking aducanumab showed reduced levels of amyloid-β — the first time an Alzheimer's drug has shown a statistically significant effect. The safety study of 166 patients found the drug to be generally safe, although there were side effects at higher doses. Experts caution that the findings are preliminary.

TREND WATCH

SOURCE: *THE TOBACCO ATLAS*

The global pattern of smoking is changing as tobacco firms target Africa, Asia and the Middle East, according to *The Tobacco Atlas*, released at the United Nations World Conference on Tobacco or Health on 19 March. If no tobacco control is enacted, Africa will see a large rise in smoking, says the report by the American Cancer Society and World Lung Foundation. China is home to one-third of male smokers, but models suggest that tobacco control could cut smoking there by more than 40% by 2050.

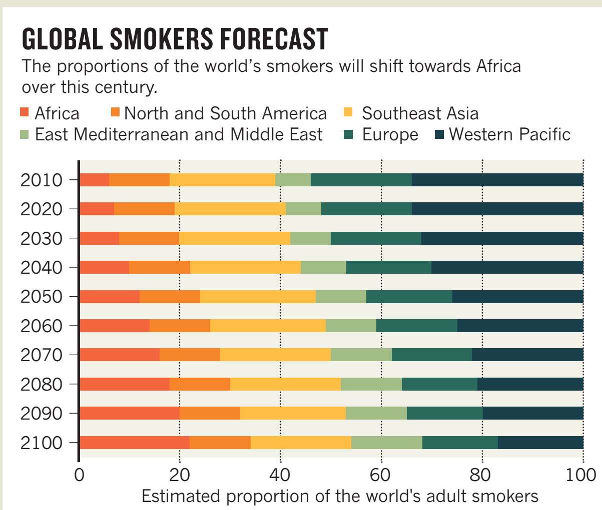

NATURE.COM
For daily news updates see:
www.nature.com/news

NEWS IN FOCUS

ECOSYSTEMS Tropics' response to warming probed **p.398**

GENETICS Encryption tested for cloud computing of DNA data **p.400**

SPACE Signs of active geology spotted on dwarf planet Ceres **p.401**

BIOTECH SCHOOL Entrepreneurs get a grilling at science boot camp **p.402**

ROEL FLEUREN/SCIENCE TRANSMITTER

Boar 1339 was genetically engineered to have diabetes; its body parts, now in the Munich MIDY-PIG Biobank in Germany, are freely available to researchers.

ANIMAL MODELS

Inside the first pig biobank

Elaborate array of tissue samples provides powerful animal model for studying diabetes.

BY ALISON ABBOTT, MUNICH, GERMANY

First out is a kidney: its dark red fades to beige as it is washed of its blood. The pancreas, harder to find amid the tangle of inner organs, is rushed on to dry ice. Speed is essential because tissues degrade after death — and each detail counts in this autopsy.

The precious organs belong to Boar 1339, which, for 3.5 years, had lived a normal pig's life on the farm of a German university, despite the diabetes it was born with. Earlier this month, the animal was killed, and the body parts placed in the service of science, as part of a growing movement to maximize the scientific benefits of every animal used in research.

Thousands of tiny tissue and fluid samples from the boar's 226-kilogram body now sit in the newly constructed Munich MIDY-PIG Biobank in Germany — the world's first systematic repository of tissue from a large, genetically engineered, non-human animal.

The biobank, part of Munich's Ludwig Maximilian University (LMU), houses tissue taken from throughout the body and from pigs of different ages. It is designed to help diabetes researchers to discover the molecules and mechanisms involved in the long-term complications of the disease, including the degeneration of small blood vessels and nerves, heart and kidney disease, and blindness. These develop over a lifetime, and are poorly understood.

"We are more similar to pigs than we like to think, so this resource will be very valuable," says diabetes researcher Patrik Rorsman at the University of Oxford, UK. The samples are freely available to researchers anywhere in the world, who need only pay for the postage.

As pressure grows to reduce the number of animals used in research, biobanks are becoming attractive because they allow teams working on different organs and aspects of the disease to use the same animal. "Biobanking means that no part of the animal is wasted," says LMU geneticist and veterinary surgeon Eckhard Wolf, ▸

who launched the pig biobank.

Only a few animal biobanks have so far been built, and most are for mice. Pigs, although more expensive to house and breed, could be more useful because of their larger size and the greater similarity of their physiology and metabolism to those of humans.

To create the pig biobank, scientists used genetic engineering and cloning techniques to create animals with a damaged gene called *MIDY*, which means that they need a daily insulin injection. The animals were then bred with healthy pigs so that, on average, half of the second-generation litters had diabetes and the other half were healthy, and thus able to serve as experimental controls.

The 12th addition to the bank from this process, Boar 1339 was already anaesthetized when it arrived in the cavernous autopsy room of the 101-year-old veterinary school in a leafy suburb of Munich. Waiting for the pig was a team of 25 veterinary surgeons and technicians, gowned up, masked and alert at parallel dissection tables.

A hoist raised the pig by its hind legs and pathologists injected the animal with a lethal dose of anaesthetic. Then, in swift, precision choreography, the team moved in with their knives, cleavers, hammers and pincers. They removed organs, muscles, nerves and more, and transferred the tissues to the tables at which the waiting dissectors set about their complicated sampling process, strictly following an 80-page protocol. "We don't want to complete a super-sophisticated sampling and then realize we forgot to weigh the liver," says Andreas Blutke, one of the chief pathologists at the LMU. The chopping, hacking and puncturing are loud; the concentration of the workers keeps the background noise to a murmur. The whole process takes a mere 2 hours 15 minutes.

Samples enable structural and molecular analysis.

ROEL FLEUREN/SCIENCE TRANSMITTER

Because the cells in any organ are of different sizes, shapes and orientations, and are unevenly distributed, the team takes numerous samples using different methods to ensure that the whole organ is appropriately represented. The system is so sophisticated that it gives researchers a three-dimensional anatomical reconstruction of the exact cell types.

Crucially, the researchers divide each sample and preserve the portions in different ways, each optimized for either structural or molecular analysis. This allows both types of analysis to be done on the same sample. "I think this is the only service which allows you to do molecular profiling and cellular anatomy from the same sample," says Wolf.

As soon as Rorsman heard about the biobank, he saw its benefit. He suspects that the long-term complications of diabetes are caused by changes in a particular molecule in the cells of several different tissues. Material from the biobank will allow him to confirm that he is on the right track, he says, before he obtains samples from human biobanks, which takes a long time because of ethical constraints. Herbert Tempfer, a diabetes researcher at the University of Salzburg in Austria, is already analysing samples of tendons — notoriously fragile in people with diabetes — from the biobank.

Others want to know how similar pig diabetes is to the human disease. Immunologist Åsa Hidmark at the University of Heidelberg in Germany made the three-hour journey to Boar 1339's dissection to cut samples of skin from its trotter. She hopes to discover that the nerve endings in the outer layer have been lost, as happens in people with diabetes.

The ultimate value of the bank will depend on how much it is used — and there are no guarantees. Despite its collection of 42 tissues taken from 940 mouse lines, a mouse biobank at the Wellcome Trust Sanger Institute near Cambridge, UK, has so far received only 50 or so requests for material. "There is a lack of awareness of its value," says Jacqui White, who leads this Sanger mouse-autopsy project.

Wolf plans to extend his biobank to other genetic pig models as they are developed. Next in line are probably pigs engineered to have Duchenne muscular dystrophy. A sow implanted with a cloned genetically modified embryo is now pregnant. ■

ECOSYSTEMS

Climate modellers take tropical approach

Ten-year US-led project seeks to plug gaps in global-warming simulations.

BY JEFF TOLLEFSON

The US Department of Energy has approved a campaign to better understand the response of tropical forests to rising levels of atmospheric carbon dioxide. The experiments are designed to improve global climate simulations and to determine whether the increased tropical-forest growth caused by carbon dioxide enrichment will partially offset global warming.

The US$96-million Next-Generation Ecosystem Experiment for the tropics, NGEE Tropics, builds on an ongoing project in the Arctic that has put climate modellers into the field with ecologists, biologists and hydrologists to improve understanding of the fate of permafrost in a warming world. The department plans to announce the new programme within weeks.

Focusing on the future of tropical forests and their role in regulating the global climate, the ten-year tropical programme will begin with pilot studies at sites in Puerto Rico, Panama and Brazil, and then expand into other areas, including Africa and southeast Asia. Although ecologists have studied tropical ecosystems intensively, the new experiments will be designed to plug specific gaps in climate models.

"The whole point is getting data that is appropriate for working with models," says Richard Norby, an ecologist at the Oak Ridge National Laboratory in Tennessee, who is

involved in the project. "I think the days of doing independent experiments and then just publishing data and seeing if somebody picks it up are over. And they should be over."

Climate models suggest that tropical forests could significantly offset human carbon emissions — or not — depending on whether the forests grow faster as atmospheric carbon dioxide concentrations rise. Experiments in northern temperate forests suggest that the increase will have some growth-stimulating effect as plants take up some of the extra carbon dioxide through photosynthesis and incorporate it into wood and other biomass, but that additional growth may be limited by the availability of other nutrients, such as nitrogen.

In a pilot study in Puerto Rico, ecologists will investigate below-ground biogeochemistry and soil fertility in combination with aerial imaging to see how these processes affect leaf chemistry. A site in Brazil will focus on daily and seasonal soil-moisture changes to better understand how tropical forests respond to droughts. A third pilot project, in Panama, will look at various plant traits and how they are represented in the models.

The tropical campaign follows the launch in 2012 of a similar project in the Arctic designed to determine the extent to which the melting of permafrost due to warming will release vast stores of carbon buried for thousands of years. Most climate models include only a crude representation of the tundra, treating permafrost as a single uniform layer that responds uniformly to increases in temperature. In reality, permafrost is a patchwork of ice wedges and troughs that break up the landscape into countless polygons. As ice melts, the troughs expand and widen and new ones open up, which hastens further melting and decomposition of organic material.

"The whole point is getting data that is appropriate for working with models."

"If it was a simple landscape that was responding linearly, you could get away with those simple representations," says Peter Thornton, a climate modeller at Oak Ridge who heads the modelling component of the Arctic project. "But the distribution of these ice wedges is regularly patterned and that forces dynamics at these fine scales that are completely nonlinear."

ALEX WEBB/MAGNUM PHOTOS

Tropical forests will respond to rising carbon dioxide in ways that are hard to predict with climate models.

Since the Arctic project began, scientists have drilled boreholes into ice wedges and troughs at the site near Barrow, Alaska, to get a sense of how water and heat penetrate the permafrost layers. The goal is to understand how fast the microbes in thawing permafrost will break down vast stores of organic matter that have been stored in the soil for millennia. That process releases methane, a potent greenhouse gas. Ice cores are being analysed and subjected to heating experiments at the Lawrence Berkeley National Laboratory in Berkeley, California, to uncover how different microbes respond.

In other field experiments, biologist Alistair Rogers at the Brookhaven National Laboratory in New York analysed rates of photosynthesis in a variety of Arctic plants. From these real measures, Rogers found that even the handful of climate models that do include explicit vegetation types underestimate the photosynthetic potential in the Arctic by a factor of three to five.

Modellers and field scientists have gradually grown further apart as the scientific disciplines have become increasingly complex, but this new approach seems to be reversing that trend, says Ted Schuur, an ecologist at the University of Florida in Gainesville, who is a reviewer on the NGEE Arctic programme. Although it is still early in the project, he says, "the way they have organized their pipeline really points toward success".

The challenge for modellers is how to simulate ecological processes that take place at the scale of microbes and plants within global models comprised of grids of squares up to 100 kilometres on a side. Thornton's team is working on new models that bridge the gap between those vastly different scales in the Arctic. These will be integrated into a new climate model under development by the energy department.

Scientists will take a similar approach in the tropics. They have already begun to assess climate models to identify weaknesses and gaps in how they represent tropical ecosystems.

In addition to improving climate models, the effort will produce new advances in basic science, says Jeff Chambers, a tropical ecologist at the Lawrence Berkeley National Laboratory and director of the NGEE Tropics project. "It's a fantastic opportunity, and there's plenty of room for discovery science along the way." ■

MORE ONLINE

Q&A

EUROPEAN UNION

Europe's research commissioner lays out his ambitions go.nature.com/fvaf1f

TOP NEWS

- Mystery of Darwin's 'strange animals' solved go.nature.com/yiej2j
- Surprise dust cloud spotted billowing over Mars go.nature.com/aql2en
- China and Europe pore over joint space-mission proposals go.nature.com/ycbndn

VIDEO

KIM TAYLOR & JANE BURTON/GETTY

How the mudskipper fish uses a 'water tongue' to grab prey on land go.nature.com/uqdp13

Processing scrambled DNA-sequence data promises safe and fast discovery of disease-linked gene variants.

DAVID PAUL MORRIS/BLOOMBERG VIA GETTY

COMPUTING

Cloud cover protects gene data

Extreme cryptography set to bring 'personalized' medicine a step closer.

BY ERIKA CHECK HAYDEN

The dream for tomorrow's medicine is to understand the links between DNA and disease — and to tailor therapies accordingly. But scientists working to realize such 'personalized' or 'precision' medicine have a problem: how to keep genetic data and medical records secure while still enabling the massive, cloud-based analyses needed to make meaningful associations. Now, tests of an emerging form of data encryption suggest that the dilemma can be solved.

At a workshop on 16 March hosted by the University of California, San Diego (UCSD), cryptographers analysed test genetic data. Working with small data sets, and using a method known as homomorphic encryption, they could find disease-associated gene variants in about ten minutes. Despite the fact that computers were still kept bogged down for hours by more-realistic tasks — such as finding a disease-linked variant in a stretch of DNA a few hundred-thousandths the size of the whole genome — experts in cryptography were encouraged.

"This is a promising result," says Xiaoqian Jiang, a computer scientist at UCSD who helped to set up the workshop. "But challenges still exist in scaling it up."

Physicians and researchers think that understanding how genes influence disease will require genetic and health data to be collected from millions of people. Such a massive task will probably require harnessing the processing power of networked cloud computers, but online security breaches in the past few years illustrate the dangers of entrusting huge, sensitive data sets to the cloud. Administrators at the US National Institutes of Health's database of Genotypes and Phenotypes (dbGaP), a catalogue of genetic and medical data, are so concerned about security that they forbid users of the database from storing it on computers that are directly connected to the Internet.

Homomorphic encryption could address those fears by allowing researchers to deposit only a mathematically scrambled, or encrypted, form of data in the cloud. It involves encrypting data on a local computer, then uploading those scrambled data to the cloud. Computations on the encrypted data are performed in the cloud and an encrypted result is then sent back to a local computer, which decrypts the answer. If would-be thieves were to intercept the encrypted data at any point along the way, the underlying data would remain safe.

"If we can show that these techniques work, then it will give increased reassurance that this high-volume data will be computed on and stored in a way that protects individual privacy," says Lucila Ohno-Machado, a computer scientist at UCSD and a workshop organizer.

Homomorphic data encryption, first proposed in 1978, differs from other types of encryption in that it would allow the cloud to manipulate scrambled data — in essence, the cloud would never actually 'see' the numbers it was working with. And, unlike other encryption schemes, it would give the same result as calculations on unencrypted data.

But it remained largely a theoretical concept until 2009, when cryptographer Craig Gentry at the IBM Thomas J. Watson Research Center in Yorktown Heights, New York, proved that it was possible to carry out almost any type of computation on homomorphically encrypted data. This was done by transforming each data point into a piece of encrypted information, or ciphertext, that was larger and more complex than the original bit of data. A single bit of unencrypted data would become encrypted into a ciphertext of a few megabytes — the size of a digital photograph. It was a breakthrough, but calculations could take 14 orders of magnitude as long as working on unencrypted data. Gentry had rendered the approach possible, but it remained impractical.

Since then, cryptographers have developed systems to address these issues, for instance by encrypting many pieces of data together so that they can be processed in parallel, or by encrypting real numbers directly into single ciphertexts, rather than first converting them into bits. As a result, homomorphic encryption now runs 150,000 times faster than it did in 2009, says Shai Halevi, a cryptographer at the IBM research centre. "The same calculation that took a day-and-a-half in 2012 now takes us five minutes to do," he says. "Now is the time to ask, is this fast enough to be usable?"

At the 16 March iDASH Privacy & Security Workshop 2015 (iDASH stands for Integrating Data for Analysis, Anonymization and Sharing), five teams revealed homomorphic encryption schemes that could examine data from 400 people within about 10 minutes, and that could pick out a disease-linked variant from among 311 spots at which the genome is known to vary. It took up to 30 minutes to similarly analyse small chunks of genome a little larger than the size of a typical gene, about 5,000 DNA base pairs. For longer stretches of sequence data — 100,000 base pairs, or about 0.003% of the overall genome — analysis was not always possible, or took hours, and consumed up to 100 times more memory than computing unencrypted data. Even so, cryptographers say that the results indicate major progress: "Our challenge shows this is

not impossible, compared to three years ago, when people were thinking this computation was infeasible," Jiang says.

But some data custodians remain sceptical about encryption. Steven Sherry, chief of the reference collections section at the US National Center for Biotechnology Information in Bethesda, Maryland, manages dbGaP. He says that cryptography, even if it worked, would not necessarily protect data on researchers' computers or give them enough analytical flexibility. He instead favours restricting access to a small circle of scientists and asking them to certify that they will abide by rules and regulations on how the data can be used. "We haven't looked at cryptographic methods," says Sherry, "because it hasn't been demonstrated to us that they're both secure and useful." ■

SPACE

Bright spots hint at active ice on Ceres

Early data from Dawn spacecraft bring scientists closer to clearing up mystery about dwarf planet.

BY ALEXANDRA WITZE, THE WOODLANDS, TEXAS

A pair of bright spots glimmering inside an impact crater on the dwarf planet Ceres, mystifying scientists, could be coming from some kind of icy plume or other active geological feature.

Images from NASA's Dawn spacecraft show the spots, known as 'feature number 5', at changing angles as the dwarf planet rotates into and out of sunlight. The pictures reveal the spots even when they appear near the edge of Ceres, when the sides of the impact crater would normally block the view of anything confined to the bottom. That something is visible at all from that angle suggests that the feature must rise relatively high above the surface.

"What is amazing is that you can see the feature while the rim is still in the line of sight," said Andreas Nathues, a planetary scientist at the Max Planck Institute for Solar System Research in Göttingen, Germany. Nathues, who leads the team for one of the Dawn cameras, revealed the images on 17 March at the Lunar and Planetary Science Conference in The Woodlands, Texas.

At dawn on Ceres, feature number 5 appears bright. By dusk, it seems to fade. That could mean that sunlight plays an important part — for instance, by heating up ice just beneath the surface and causing it to blast off some kind of plume or other feature.

Ceres, one of the largest unexplored worlds in the Solar System, is believed to be at least one-quarter ice — a greater proportion than most asteroids. Dawn, which launched in 2007, aims to work out where that ice resides and what role it has in shaping the dwarf planet's surface. One idea is that the ice is blanketed by a very thin layer of soil. The ice may occasionally squirt up in towering 'cryovolcanoes', thanks to internal pressures in the asteroid.

Dawn is currently looping back towards Ceres after being captured by its gravity on 6 March. As the spacecraft gets closer to the dwarf planet, it will take more pictures to see how its surface might be changing. "The big question is whether Ceres has an active region — or more than one," Nathues says.

Christopher Russell, a planetary scientist at the University of California, Los Angeles, and Dawn's principal investigator, says that towards the end of its mission the spacecraft will map Ceres at high enough resolution to see features that are just 30 metres across. The hope is that the possible icy plume will come into focus and reveal its true nature.

"We hope to show that Ceres is every bit a planet, as much as its terrestrial neighbours Mars, Earth, Venus and Mercury are," Russell says. ■

NASA/JPL-CALTECH/UCLA/MPS/DLR/IDA

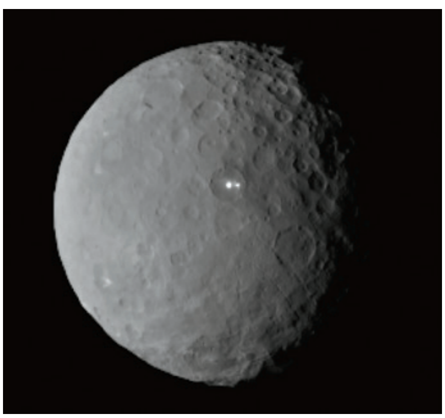

The Dawn spacecraft captured this image of Ceres' twin bright spots on 19 February.

ILLUSTRATION BY SPENCER WILSON

BIOTECH BOOT CAMP

US funding agencies are turning to a Silicon Valley entrepreneur to focus fledgling biomedical companies on success — even when that means making a scientific course correction.

BY HEIDI LEDFORD

David Johnson was just one minute into making his pitch when the interruptions started.

"Why do I care?" barked a bespectacled man at the back of the seminar hall. Johnson, chief executive of the California biotechnology start-up GigaGen, blinked. He had condensed his company's story into a neat ten-minute presentation for I-Corps, a nine-week course designed to teach business skills to entrepreneurial scientists like him. Now his talk was derailed.

At first Johnson did not understand the question. He thought it was aimed at the therapy that GigaGen, based in San Francisco, plans to develop for people with weakened immune systems.

"No. You. Why do I care about you?" the man demanded.

Johnson was not the only one getting gruff treatment at I-Corps' kick-off meeting in Chevy Chase, Maryland, last October. When another team squandered a few precious minutes elaborating on the need for new therapies to treat pain, I-Corps creator Steve Blank pounced. "If you spend the next ten weeks telling us about pain, you're going to be in pain," he said.

Blank later let fly again. "You may have noticed that your presentation was different from the others — and not in a good way," he told the president of another firm who had not clearly elaborated his team's business strategy.

Rough treatment like this is part of the pedagogy of I-Corps, a boot camp for technology-based start-ups that has now been rolled out for biomedical firms as part of an experiment by the US National Institutes of Health (NIH). Blank had given his fellow teachers explicit instructions to rattle the teams to make them more receptive to change. "The shock-and-awe part is not to embarrass people or make them feel bad," he says, "but to get them out of their default mode of 'I think it, therefore it must be right.'"

It will take years to find out whether the approach and theory behind I-Corps is adaptable to the unique challenges of drug development. But it was already clear by the conclusion of the inaugural class last December that many of the 19 teams had learned some unexpected lessons: several companies were told to drastically change course, and in some cases to abandon promising science for something more market-savvy. "You can be a great researcher and you can think you have great ideas," says Congressman Dan Lipinski (Democrat, Illinois), who had pushed to see Blank's approach implemented for government-funded research. "But until you're forced to talk to a potential customer, you never really know."

ALL ABOUT THE SCIENCE

At 61, Blank epitomizes the contradictions of California's Silicon Valley, with a sun-drenched conviviality that never completely conceals his no-nonsense efficiency. He will take the time to tell a funny anecdote — often using himself and his business mistakes as the punchline — but almost every session of the I-Corps meetings in Chevy Chase adjourned ahead of schedule.

Blank is a college drop-out who wandered into Silicon Valley in 1978 after years of repairing fighter jets for the US Air Force. He arrived in California just before the technology boom, and his love of gadgets made him a perfect fit. He launched eight technology companies there, not all of them successful; he counts two "craters" among them. Then, in 1999, he retired to a ranch in Pescadero, California. The sudden infusion of free time allowed him to examine his successes — and, more importantly, his failures.

From that introspection he crafted a curriculum for tech entrepreneurs, to teach them to think beyond their own technology and to dive early and deep into the details of commercialization: who the customers are, what they need and how much they are willing to pay. The technique has swept through the tech industry, says Steven Phelan, who studies entrepreneurship at Fayetteville State University in North Carolina. It is bringing welcome changes to the way that businesses are developed, but some find flaws in the approach. Relying too heavily on customer input can lend itself to incremental — rather than revolutionary — improvements, Phelan cautions. "If you ask people what they want, they're just going to say something that they're familiar with," he says. (Blank counters that customer research can be tailored to avoid this problem.)

A few years ago, Lipinski, a former engineer who serves on the US House Committee on Science, Space, and Technology, dropped in on a class Blank taught at Stanford University, and saw a new use for the programme. "This is something researchers don't have training in," he says. "I was sold."

Lipinski has long been concerned about the quality of research funded by the US Small Business Innovation Research (SBIR) programme. The funds are intended to stimulate translation of scientific discoveries into the marketplace, but critics have raised questions about how effective the programme is. A 2013 analysis by *Nature* found that the top earners of such grants were rarely focused on commercialization (see *Nature* **499,** 137–138; 2013). "Sometimes it seems like SBIR is being used in many cases not to further a business, but to continue research," says Lipinski.

In Blank's class, Lipinski saw a way to beef up the business acumen of SBIR grant recipients. He urged the NIH and the National Science Foundation (NSF) to adopt the programme. The NSF picked it up first, christened it I-Corps, for Innovation Corps, and offered it to scientists on the threshold of launching a company. Since 2011, about 500 teams have taken the course. If success can be measured by personal epiphanies, then it has been a qualified victory: almost every team changed its original business strategy, and more than half of them went on to found a company.

"UNTIL YOU'RE FORCED TO TALK TO A POTENTIAL CUSTOMER, YOU NEVER REALLY KNOW."

It took until last year for the NIH to sign on, with the National Cancer Institute (NCI) serving as guinea pig. In the beginning, Blank had said that his method was applicable to all industries — except one. "I said it wouldn't work for life sciences because it takes 10 to 15 years to get to a phase I clinical trial," he says. "There, it really was all about the science."

But in 2013, the head of technology transfer at the University of California, San Francisco, convinced Blank to challenge those assumptions. Blank did what he tells his own students to do: he went out into the community to interview leaders in the biomedical industry.

Those leaders told him that his conception of the pharmaceutical business was outdated. Blank was imagining the drug development of the 1990s, when in-house scientists carried out much of the research at big companies, and large firms forged few partnerships with smaller players. In that model, a small biotechnology firm had no customers until it had nearly brought its drug to market.

Since then, the pharmaceutical industry has changed. Companies have cut back on in-house research in favour of early partnerships with smaller firms — effectively turning big pharma into early customers. Blank realized that the I-Corps approach might help biomedical researchers hoping to enter this world. But he recognized important differences between biology-based start-ups and the tech firms where he had cut his teeth.

First, biomedical firms are much more heavily regulated, even before their product hits the market. Second, intellectual property is more important for health-care companies — the patents that a company can file and license wield enormous influence over the direction of its business. The third, and perhaps most overlooked, challenge: payment for services and therapies in the United States is often indirect and complex, involving a labyrinthine system of billing codes and intermediaries. Understanding those particulars — how procedures and therapies are billed, how insurance companies process the claims — is not sexy science, but it is crucial. "Grandma is not the one paying for her new hip," says Blank. "If you don't understand reimbursement, you're dead."

THE INTERVIEW

Blank worked hard to get that message across during the three-day kick-off meeting in October as the teaching staff grilled the teams. Each morning was spent presenting — and then re-presenting — the ten-minute team pitches. Each afternoon, the teams raced to interview

ILLUSTRATION BY SPENCER WILSON

experts in their fields, then reported back for more workshops. Nights were filled with class readings, homework and preparations for the next day's presentations and interviews.

The interviews are central to the process (see 'Start-up pitfalls'). Teams needed to talk to scientists, pharma company reps, regulators, doctors, billing specialists and more — essentially, any person with expertise in what it takes for companies to get their products to patients and get paid. It is a time-consuming process, and Blank insists that the interviews be conducted face-to-face, to build rapport and allow interviewers to better gauge their subjects' emotions. If an expert cannot be met in person, the team must hold a video-conference. When one team let slip that some of its interviews were done over the phone, Blank's face grew red. "This is bullshit," he spat, and invited the team to leave the programme. (It stayed.)

"JUST THAT ONE CHANGE MIGHT BE WORTH $50 MILLION."

Other teams embraced the I-Corps strategy with gusto. One morning, Eric Bressler, a research scientist at AsclepiX Pharmaceuticals in Baltimore, Maryland, told the group how his team had shown up at a hospital and bounced from one administrative assistant to another, asking questions about how treatments are billed and reimbursed. Eventually someone noticed that the team did not have clearance from security to wander around asking questions. It was escorted out. "I predict great things," said Blank, admiring the team's audacity. "And/or an arrest record." (His praise proved ephemeral, however: a few minutes later he scolded Bressler for wasting time with the story: "You were bullshitting for a large part of your presentation.")

Some said that the interviews provided immediate insight. BCN Biosciences of Pasadena, California, had been in business for nearly a decade developing drugs to protect normal tissue from radiation during cancer treatments. One of the first things the team learned is that because new technologies can deliver radiation more precisely, doctors saw no great need to protect healthy tissue. It was an 'Aha' moment, says Andrew Norris, BCN's director of research. "Trying to sell something that nobody wants is a stupid thing to do."

Of all the learning that happened during those first few days in Chevy Chase, Blank seemed most proud of the progress of Abreos Biosciences, a company in San Diego, California, that is developing ways to detect counterfeit drugs. The team's presentation, 'Lateral flow immunoassay for therapeutic monoclonal antibody quality assurance', was ridiculed by one instructor. "Could you make it more complicated?" he ribbed.

By day three, the team had swapped technical terms for more market-friendly lingo. The title became, 'Quick tests for point-of-care validation of biologic drugs'. Abreos co-founder Bradley Messmer also developed better ways to describe their product, likening it to "a pregnancy test that tells you whether your drug is real or not".

Blank was thrilled that the team had learned how to talk to investors better. "For commercialization, being able to explain it to your mother is what matters," he said. "Just that one change might be worth $50 million."

PIVOT POINTS

When the kick-off meeting ended, the teams returned home to complete their coursework: more interviews, at least 100 over the next 9 weeks. Several I-Corps participants were already weighing up significant changes to their business strategy.

AsclepiX, which was founded by bioengineers at Johns Hopkins University in Baltimore, Maryland, had been developing a cancer therapy based on the marriage of two unusual approaches — a novel drug made of a short string of amino acids, and a nanoparticle to target the drug to cancer cells. The company had exciting preclinical data on head and neck tumours and was eager to move the drug forward.

But early interviewees advised the team to change focus. Head and neck cancers are too heterogeneous, they said, and there are already a number of available therapies to treat them. AsclepiX's drug targets blood vessels that feed tumours, and similar drugs had shown promise against glioblastoma, a rare and devastating brain tumour with few available treatments.

➲ NATURE.COM
For an interview with the author visit:
go.nature.com/ezk1gh

START-UP PITFALLS

I-Corps instructors push students to avoid these mistakes commonly made by fledgling companies

1. DON'T FALL IN LOVE. I-Corps professes a 'fail fast' model. Rather than getting married to ideas, test them and be ready to discard them.

2. DON'T SPEND ALL YOUR TIME AT THE BENCH. Businesses need to interview key decision-makers for every stage of their product's life cycle. I-Corps mandates a minimum of 100 interviews to understand the market and the customer.

3. DON'T MAKE THE INTERVIEW A SALES PITCH. Trying to sell a company's idea at an informational interview will backfire. It will bias the conversation and make it less valuable.

4. DON'T FORGET WHO PAYS. For biomedical businesses, reimbursement is complicated and varies widely depending on the product and the medical condition it is designed to treat. Failing to appreciate this is disastrous.

5. DON'T CHASE THE WRONG DATA. What it takes to elicit a partnership with a pharma company is not always what it takes to get a paper accepted. (Companies often want to see reproducibility in different labs or with different source material.)

Some interviewees suggested that a treatment for glioblastoma would be eligible for accelerated approval programmes in the United States and Europe, clinical trials would be smaller, and there would be less competition from other therapies. The AsclepiX crew began to get up to speed on glioblastoma, and planned interviews with neuro-oncologists.

It soon identified another problem: the nanoparticle. This would provide better targeting and protect the drug in the bloodstream, but even during the I-Corps meeting, the team had noticed that nanotechnology got a chilly reception from those in the know. Karl Handelsman, a venture capitalist and course instructor, quipped at one point: "The smallest thing about nanotechnology is the market."

From interviews the team learned that the word presents too many unknowns for consumers. "If you publish a paper with 'nano' in the title it gets a lot of buzz and attention," says Jordan Green, chief executive of AsclepiX. "But on the commercial side, they don't look at nano as a plus. It may even be a liability."

There were concerns about potential toxicity, and worries over how the Food and Drug Administration would evaluate a nanoparticle delivery system. Many were also worried about batch-to-batch variability in manufacturing.

AsclepiX is still young and flexible — the company has just three full-time employees and is still ordering basic equipment for its new laboratory in a renovated silverware factory. In response to the feedback, the company re-evaluated early animal tests of the peptide drug without a nanoparticle. The results were promising, says chief scientific officer Aleksander Popel. And Green says that the company is exploring ways of manufacturing the particle continuously, in the hope of alleviating concerns about batch-to-batch variability.

By the end of the nine-week I-Corps programme, others had changed strategy too. When participants reassembled for their final meeting in December, Affinity Therapeutics in Cleveland, Ohio, reported that interview number 82 had uncovered a fatal flaw in the company's product, an implanted device to repair blood vessels in patients on dialysis. Affinity's device is coated with a drug-releasing polymer designed to prevent smooth muscle cells from growing into the device — a process that gradually reduces the diameter of currently used products. "This will never work," a doctor told them, noting that muscle cells also grow into the natural blood vessel downstream of the device junction.

Then interviewee number 116, Timmy Lee at the University of Alabama at Birmingham, told them how to correct the problem by shifting the placement of the coating. In the meantime, the company learned more about regulation and billing practices. Before I-Corps, Affinity had been weighing up two possibilities: it could market the coated device or market the coating to be added to devices sold by other companies. The team learned that the first option could require approval from two different centres within the US Food and Drug Administration. Selling the coating alone was likely to involve only one centre, but would require the creation of a new hospital billing code, a process that can take years and cost millions of dollars. As a result, Affinity is mainly focusing on the coated device.

BCN, the company developing drugs to protect normal tissue from radiation damage, had found a possible new application for its compounds. The doctors it interviewed kept returning to what had initially seemed an extraneous point: if the drug helped to prevent the formation of stiff tissue in the lung caused by radiation, perhaps it would also work against a spontaneous and devastating disease called idiopathic pulmonary fibrosis, which also causes lungs to stiffen.

The company initially disregarded the comments, but they kept coming up. Similarly, dermatologists had wondered whether the drug might battle the stiffening of skin that comes with ageing. BCN will expand its focus to include these other areas.

With the pressure of interview counts and coursework behind them, many of the teams expressed gratitude for the experience when they gathered for the final meeting. "I wasted millions on projects that were technically sexy and ultimately not commercially viable," said Mark Bates, a cardiologist and serial entrepreneur who was working with one of the teams. He turned to Blank. "I'm kind of pissed right now. Where were you 20 years ago?"

"I was pissing other people off," answered Blank, referring to his own failed companies. "I was losing $35 million."

The NIH will be watching closely to see if its investment in I-Corps pays off. Michael Weingarten, head of the SBIR programme at the NCI, says that he will track the teams' success over the next five years — monitoring how many partnerships with major pharmaceutical or medical-device firms the companies form, and whether they receive funds from other investors. "We still have to show to NIH management that this is having a positive impact before we move to the next stage and get more companies involved," he said in October. For now, Weingarten says, the teams filled out surveys before and after the programme that indicate how much they think they have learned; 82% of participants said they would recommend the programme to others. He expects the NCI to decide whether or not to continue the programme within the next two months.

Meanwhile, Blank's method continues to spread. At the end of October, the US Department of Energy announced a project similar to I-Corps. Lipinski says that the Department of Defense is considering one as well. And Blank has been contacted by several university technology-transfer offices, asking for consultations on how they can use his methods to aid academic entrepreneurs. Imperial College in London, for example, has adopted a similar programme for start-ups based on synthetic biology.

Many of the NIH's inaugural teams say that they already have enough data to testify to the utility of I-Corps. Johnson's team from GigaGen has interviewed 256 people, 93 of them after I-Corps concluded. For the past few weeks, he has been pitching the company to venture capitalists, in the hope of raising more money for the firm. Venture capitalists can be a little snarky, he says, but he felt well prepared. "Normally they tend to just ask you questions until you just can't answer," he says. "But nobody's been able to ask me a question I haven't been able to answer yet." ■

Heidi Ledford *writes for* Nature *from Cambridge, Massachusetts.*

ETHICS Call to halt gene editing in human reproductive cells **p.410**

CONSERVATION A colourful memoir of life among the lemurs **p.412**

HISTORY Marie Curie through the prisms of celebrity and intellectual property **p.413**

EARTH Advanced warning and better surge maps helped during Typhoon Hagupit **p.414**

DEAGOSTINI/GETTY

Beech trees, which are vulnerable in warm, dry conditions, are more protected in mixed forest stands.

Five steps for managing Europe's forests

Support resilience and promote carbon storage, say **Silvano Fares** and colleagues.

Europe's varied climates support some of the most biodiverse woodlands on Earth. More than 40% of the continent's land area is wooded. In the north, evergreen forests host Norway spruces and Scandinavian pines; around the Mediterranean, tough-leaved trees such as the holm oak and Aleppo pine withstand heat and drought. Dense beech and oak forests blanket Eastern Europe, and thin strands of dwarf pine mark the Alpine timberline.

Woodlands in Europe have been harvested for timber for thousands of years, but today their roles are multiplying. Wood can substitute for fossil fuels and carbon-intensive materials such as steel. And growing trees sequester carbon — photosynthesis absorbs carbon dioxide from the atmosphere and puts it in wood and soil. Forests remove around 9% of Europe's anthropogenic CO_2 emissions from the air[1].

But European forests face an uncertain future. More frequent heat waves, droughts and fires are reducing their health and productivity, with the region warming faster than the global average[2]. Urban sprawl, pollution and the expansion of transport, commercial and industrial infrastructure compound the climatic threats[3].

Such damage is offsetting gains from planting programmes and the natural reforestation of abandoned agricultural land, which have boosted Europe's woodland ▶

area by 9% since 1990. Disturbances also outpace the extra plant growth that arises under higher concentrations of atmospheric CO_2. Since 2005, the amount of wood produced annually across Europe has decreased by around 0.3% a year (in 2010, it was 620 million cubic metres over 157 million hectares in 27 countries)[1].

The resulting picture has two sides: new forests are gaining ground and pushing up overall forest area, but existing stands are becoming less productive with age and damage.

We outline five key issues that European forestry managers should address to develop Europe's forests sustainably and with resilience in mind[4]. Policies and plans must account for the trade-offs between forests' capacity to store carbon, adapt to climate change and yield wood products and other ecosystem services.

Forest carbon sequestration needs to be incorporated into European Union (EU) mitigation schemes, including the EU Emissions Trading System, which currently considers only forest planting and regeneration. Incentives will be needed to double carbon-neutral biomass production by 2020 to meet Europe's renewable-energy needs. Payment schemes should be set up for a range of woodland services such as water storage and recreation. Many of these lessons apply to forest management in other parts of the world, including the United States and China.

Trees damaged by acid rain in the polluted 'black triangle' of the northern Czech Republic.

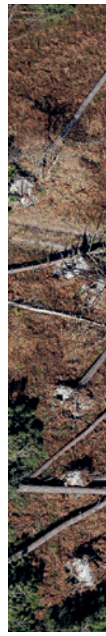

LEFT: TOM STODDART/GETTY; CENTRE: SIPA PRESS/REX; RIGHT: PATRICIA DE MELO MOREIRA/AFP/GETTY

KEY ISSUES

Plant resilient species. Woodland regeneration offers foresters a chance to manipulate the mix of species and quality of plants to better withstand long-term environmental changes. Managers should plant species that tolerate a variety of climates, such as those that can grow over a range of latitudes and altitudes. Mixed stands are more resistant to pests and disturbances than those of single species, which succumb easily to such threats. They also shelter sensitive species such as beech that become vulnerable in warm, dry conditions. Germany, for example, is including beech and oak in its spruce and pine forests.

Plant breeders in nurseries and laboratories should increase the genetic diversity of stock and take steps to assure plant quality. They should foster traits such as the ability to adapt to higher CO_2 concentrations, warmer temperatures or longer periods of water stress. Programmes for conserving genetic resources, such as those established for Mediterranean pines, the European chestnut and several oak and poplar species, should be strengthened.

Guidelines for plant production in nurseries need updating. These are usually generic — designed for a stable climate rather than local or varying conditions. The selection of genetic material and nursery practices should aim to increase the survival rate of stock. For instance, to lower the water stress of seedlings, moisture-preserving chemicals should be used more widely in seedling production, transport and planting.

Managers should use locally gathered seeds and natural regeneration methods — as promoted by the European Forests Genetic Resources Programme (EUFORGEN) — where possible to preserve the existing diversity of species. Several nations, including the United Kingdom and France, have defined areas where only local variants of trees should be planted.

"Foresters need plans to cut pests and improve forest health and stability."

Best practice should involve: first, testing the provenance of seeds and assessing the genetic variation among populations; and second, analysis of climate trends to decide when it makes sense to transfer species from south to north[5]. Silver-fir seeds from southern Europe are increasingly being planted farther north, for example.

Promote carbon storage. Foresters should craft tending and thinning strategies for woodlands to promote the most resilient species. In the far north and at high altitudes, where growth rates will rise most under warmer and CO_2- and nitrogen-rich conditions, managers should thin saplings more often or harvest more established trees each year.

The timing of harvests needs to be optimized. Commercial pressures dictate frequent harvests and thus short rotations (the time between timber establishment and harvest). But longer rotation cycles are needed to promote carbon storage. The win–win strategy[6] lies in between. Adopt long cycles in old, healthy forests that are at low risk from pests or environmental disturbances, such as mountain beech stands. Forests such as pine plantations that are prone to wildfires and other major disturbances should be harvested more intensely.

Mature forests — where growth has stalled — can turn quickly from carbon sinks to sources when damaged by storms and pests. Breakdown of dead wood by microorganisms in the soil releases carbon. Many of Europe's stands are mature or decaying. Only 4% are 'primary' forests — those undisturbed by humans — which sustain their high biodiversity and carbon-storage capacity[1]. Thinning can encourage new growth and increase structural diversity. Increasing canopy complexity by selecting trees with different heights promotes more efficient use of light and nitrogen[7] and boosts carbon sequestration.

European and wood-market policies should manage this shift over the next few years. For example, greater uptake of tax benefits by forest owners in the European Commission's Common Agricultural Policy would support more adaptation measures.

Manage disturbances. More pests, winds and wildfires offset strategies aiming to increase forest carbon storage. Foresters need plans to cut pests and improve forest health and stability.

In pure stands, the selection of resistant families and clones could reduce the risk of damage by pests and diseases. Scientists need to understand why different diseases and pests become problematic by studying


Damaged forests (left) can turn from carbon sinks to sources. Forest fires (right) can be mitigated by removing biomass material.

specific forest communities affected by particular pathogens or insects. Foresters are using such studies to combat, for example, infestations of the Eurasian spruce bark beetle in Slovenia and Poland and chestnut ink disease in the United States and Italy.

For fire prevention, policy-makers should incentivize practices that reduce the accumulation of fuel: prescribed burning, thinning, pruning and biomass removals, grazing and the creation of a mosaic of forest types including less-flammable species. Such approaches are cheaper than conventional air and ground-based fire-fighting, which may even raise fire risk by leaving biomass to proliferate. Mega-fires covering hundreds of hectares are increasingly common[8].

Consider renewable energy. Forest biomass currently accounts for 60–80% of the EU's total renewable-energy consumption. By 2020, the EU aims to provide 20% of its energy from renewable sources. This would require doubling the use of biomass, the equivalent of all of today's harvest going to energy. Currently, only two-thirds of annual growth is harvested and only about 40% of that is used for bioenergy.

Global changes in the production, consumption and trade of forest commodities make it hard for Europe to mobilize forest biomass through markets alone. Policy-makers need to provide incentives for investment across the supply chain, and the impacts of such policies should be considered carefully. For example, subsidizing bio-diesel production would increase the price of forest biomass and thus lessen its use in generating heat and power. To ensure that bioenergy production is environmentally and economically sustainable, reseachers should analyse the carbon balance of the biomass-production process, the impacts on biodiversity, trade-offs with alternative forest uses, and the socio-economic viability of biomass production[9].

Quantify and market other benefits. Non-wood products and services from forests — related to conservation, water and soil protection, recreation or climate-change mitigation and adaptation — are now excluded from the market. Introducing payments for them would encourage private landowners to manage their forests sustainably[10] (about half of European forests are in private hands). A water company, for example, might pay foresters to protect a catchment; citizens might pay to enter a woodland for recreation.

The EU Forest Strategy recognizes the importance of valuing ecosystem services in accounting systems at EU and national levels by 2020. The challenge is to quantify the value of particular services based on the perceived benefits[10]. Governments and forest owners need to develop strategies for making environmental service payments: small amounts might be negotiated directly between buyers and sellers; large amounts might involve government agencies or other intermediaries.

Billions of euros are earmarked for forestry for 2014–20 in the EU 2020 Biodiversity Strategy and EU rural development fund. Europe's forestry community needs to implement a sustainable management strategy to secure its woodlands, and their ecosystem services, for future generations. ■

Silvano Fares *is a research scientist at the Research Centre for the Soil–Plant System, Council for Agricultural Research and Economics, Rome, Italy.* **Giuseppe Scarascia Mugnozza** *is director of the Department for Innovation in Biological, Agro-food and Forest Systems at Tuscia University, Viterbo, Italy.* **Piermaria Corona** *is director of the Forestry Research Centre, Council for Agricultural Research and Economics, Arezzo, Italy.* **Marc Palahí** *is director of the European Forest Institute, Joensuu, Finland.*
e-mail: silvano.fares@entecra.it

1. Forest Europe, UNECE and FAO. *State of Europe's Forests 2011* (Ministerial Conference on the Protection of Forests in Europe, 2011).
2. IPCC. *Climate Change 2013: The Physical Science Basis. Contribution of Working Group I to the Fifth Assessment Report of the Intergovernmental Panel on Climate Change* (IPCC, 2013).
3. Nabuurs, G.-J. *et al. Nature Clim. Change* **3,** 792–796 (2013).
4. Lindner, M. *et al. Forest Ecol. Mgmt* **259,** 698–709 (2010).
5. Kolström, M. *et al. Forests* **2,** 961–982 (2011).
6. Bellassen, V. & Luyssaert, S. *Nature* **506,** 153–155 (2014).
7. Hardiman, B. S. *et al. Forest Ecol. Mgmt* **298,** 111–119 (2013).
8. Birot, Y. (ed.) *Living with Wildfires: What Science Can Tell Us* (European Forest Institute, 2009).
9. Hetemäki, L., Muys, B., Pelkonen, P. & Pettenella, D. *ThinkForest: Forest Bioenergy for Europe* (eds Pelkonen, P. *et al.*) (European Forest Institute, 2014).
10. Prokofieva, I., Wunder, S. & Vidale, E. *Payments for Environmental Services: A Way Forward for Mediterranean Forests?* (European Forest Institute, 2012).

CORRECTION

In the Comment 'Put people at the centre of global risk management' (*Nature* **519,** 151–153; 2015), the credit for the lead picture should have read Abbie Trayler-Smith/Panos Pictures.

Don't edit the human germ line

Heritable human genetic modifications pose serious risks, and the therapeutic benefits are tenuous, warn **Edward Lanphier**, **Fyodor Urnov** and colleagues.

It is thought that studies involving the use of genome-editing tools to modify the DNA of human embryos will be published shortly[1].

There are grave concerns regarding the ethical and safety implications of this research. There is also fear of the negative impact it could have on important work involving the use of genome-editing techniques in somatic (non-reproductive) cells.

We are all involved in this latter area of work. One of us (F.U.) helped to develop the first genome-editing technology, zinc-finger nucleases[2] (ZFNs), and is now senior scientist at the company developing them, Sangamo BioSciences of Richmond, California. The Alliance for Regenerative Medicine (ARM; in which E.L., M.W. and S.E.H. are involved), is an international organization that represents more than 200 life-sciences companies, research institutions, non-profit organizations, patient-advocacy groups and investors focused on developing and commercializing therapeutics, including those involving genome editing.

Genome-editing technologies may offer a powerful approach to treat many human diseases, including HIV/AIDS, haemophilia, sickle-cell anaemia and several forms of cancer[3]. All techniques currently in various stages of clinical development focus on modifying the genetic material of somatic cells, such as T cells (a type of white blood cell). These are not designed to affect sperm or eggs.

In our view, genome editing in human embryos using current technologies could have unpredictable effects on future generations. This makes it dangerous and ethically unacceptable. Such research could be exploited for non-therapeutic modifications. We are concerned that a public outcry about such an ethical breach could hinder a promising area of therapeutic development, namely making genetic changes that cannot be inherited.

At this early stage, scientists should agree not to modify the DNA of human reproductive cells. Should a truly compelling case ever arise for the therapeutic benefit of germline modification, we encourage an open discussion around the appropriate course of action.

EDITING TOOLS

Genome editing of human somatic cells aims to repair or eliminate a mutation that could cause disease. The premise is that corrective changes to a sufficient number of cells carrying the mutation — in which the genetic fixes would last the lifetimes of the modified cells and their progeny — could provide a 'one and done' curative treatment for patients.

For instance, ZFNs are DNA-binding proteins that can be engineered to induce a double-strand break in a section of DNA. Such molecular scissors enable researchers to 'knock out' specific genes, repair a mutation or incorporate a new stretch of DNA into a selected location.

Sangamo BioSciences is conducting clinical trials to evaluate an application of genome editing as a potential 'functional cure' for HIV/AIDS[4]. The hope is that

intravenous infusion of modified T cells will enable patients to stop taking antiretroviral drugs. A phase I trial in patients with β-thalassaemia — a genetic blood disorder caused by insufficient haemoglobin production — is scheduled to begin this year.

The newest addition to the genome-editing arsenal is CRISPR/Cas9, a bacteria-derived system that uses RNA molecules that recognize specific human DNA sequences. The RNAs act as guides, matching the nuclease to corresponding locations in the human genome. CRISPR/Cas9 is the simplest genome-editing tool to work with because it relies on RNA–DNA base pairing, rather than the engineering of proteins that bind particular DNA sequences.

The CRISPR technique has dramatically expanded research on genome editing. But we cannot imagine a situation in which its use in human embryos would offer a therapeutic benefit over existing and developing methods. It would be difficult to control exactly how many cells are modified. Increasing the dose of nuclease used would increase the likelihood that the mutated gene will be corrected, but also raise the risk of cuts being made elsewhere in the genome.

In an embryo, a nuclease may not necessarily cut both copies of the target gene, or the cell may start dividing before the corrections are complete, resulting in a genetic mosaic. Studies using gene-editing in animals such as rats[5], cattle[6], sheep[7] and pigs[8], indicate that it is possible to delete or disable genes in an embryo — a simpler process than actually correcting DNA sequences — in only some of the cells.

The current ability to perform quality controls on only a subset of cells means that the precise effects of genetic modification to an embryo may be impossible to know until after birth. Even then, potential problems may not surface for years. Established methods, such as standard prenatal genetic diagnostics or *in vitro* fertilization (IVF) with the genetic profiling of embryos before implantation, are much better options for parents who both carry the same mutation for a disease.

LEGAL CASE

Patient safety is paramount among the arguments against modifying the human germ line (egg and sperm cells). If a mosaic embryo is created, the embryo's germ line may or may not carry the genetic alteration. But the use of CRISPR/Cas9 in human embryos certainly makes onward human germline modification a possibility. Philosophically or ethically justifiable applications for this technology — should any ever exist — are moot until it becomes possible to demonstrate safe outcomes and obtain reproducible data over multiple generations.

Because of such concerns — as well as for serious ethical reasons — some countries discouraged or prohibited this type of research a decade before the technical feasibility of germline modification was confirmed in rats in 2009 (ref. 9). (Today, around 40 countries discourage or ban it.)

Many countries do not have explicit legislation in place permitting or forbidding genetic engineering in humans — considering such research experimental and not therapeutic (see go.nature.com/uvthmu). However, in nations with policies regarding inheritable genetic modification, it has been prohibited by law or by measures having the force of law.

> ***"The precise effects of genetic modification to an embryo may be impossible to know until after birth."***

This consensus is most visible in western Europe, where 15 of 22 nations prohibit the modification of the germ line[4]. Although the United States has not officially prohibited germline modification, the US National Institutes of Health's Recombinant DNA Advisory Committee explicitly states that it "will not at present entertain proposals for germ line alterations" (see go.nature.com/mgscb2).

In general, researchers who want to investigate the clinical uses of genetically engineered somatic cells must secure people's informed consent. In the United States, this takes place under the oversight of the Food and Drug Administration and the Department of Health and Human Services. For research involving genetic modification of the germ line, it is unclear what information would be needed — or obtainable — to adequately inform prospective parents of the risks, including to future generations.

Many oppose germline modification on the grounds that permitting even unambiguously therapeutic interventions could start us down a path towards non-therapeutic genetic enhancement. We share these concerns.

DIALOGUE NEEDED

Ten years ago, the Genetics and Public Policy Center, now in Washington DC, brought together more than 80 experts from the United States and Canada to consider the scientific and ethical consequences of genetically modifying the human germ line. Now that the capability for human germline engineering has emerged, we urge the international scientific community to engage in this type of dialogue. This is needed both to establish how to proceed in the immediate term, and to assess whether, and under what circumstances — if any — future research involving genetic modification of human germ cells should take place. Such discussions must include the public as well as experts and academics.

An excellent precedent for open, early discussion as new scientific capabilities emerge was set by the hearings, consultations and reports involving scientists, bioethicists, regulators and the general public that preceded the UK government's decision to legalize mitochondrial DNA transfer in February. We are not, of course, making a comparison between the replacement of faulty mitochondrial DNA in an egg or embryo with healthy DNA from a female donor and the use of genome-editing in human embryos. In mitochondrial transfer, the aim is to prevent life-threatening diseases by replacing a known and tiny fraction of the overall genome.

Key to all discussion and future research is making a clear distinction between genome editing in somatic cells and in germ cells. A voluntary moratorium in the scientific community could be an effective way to discourage human germline modification and raise public awareness of the difference between these two techniques. Legitimate concerns regarding the safety and ethical impacts of germline editing must not impede the significant progress being made in the clinical development of approaches to potentially cure serious debilitating diseases. ■

Edward Lanphier *is president and chief executive officer of Sangamo BioSciences in Richmond, California, USA, and chairman of the Alliance for Regenerative Medicine in Washington DC, USA.* **Fyodor Urnov** *is senior scientist at Sangamo BioSciences in Richmond, California, USA.* **Sarah Ehlen Haecker** *is director of technology sections at the Alliance for Regenerative Medicine in Washington DC, USA.* **Michael Werner** *is executive director of the Alliance for Regenerative Medicine in Washington DC, USA.* **Joanna Smolenski** *is a PhD student in philosophy at the Graduate Center of the City University of New York, New York, USA.*
e-mail: lanphier@sangamo.com

1. Regalado, A. *MIT Tech. Rev.* http://go.nature.com/2n2nfl (2015).
2. Urnov, F. D., Rebar, E. J., Holmes, M. C., Zhang. H. S. & Gregory, P. D. *Nature Rev. Genet.* **11,** 636–646 (2010).
3. Carroll, D. *Annu. Rev. Biochem.* **83,** 409–439 (2014).
4. Tebas, P. *et al. N. Engl. J. Med.* **370,** 901–910 (2014).
5. Yoshimi, K., Kaneko, T., Voigt, B. & Mashimo, T. *Nature Commun.* **5,** 4240 (2014).
6. Heo, T. Y. *et al. Stem Cells Dev.* **24,** 393–402 (2015).
7. Han, H. *et al. Front. Agr. Sci. Eng.* **1,** 2–5 (2014).
8. Kang, Q. *et al.* in *Proc. 10th World Congr. Genet. Appl. Livestock Prod.* http://go.nature.com/6mtz2d (2014).
9. Geurts, A. M. *Science.* **325,** 433 (2009).

The authors declare competing financial interests, see go.nature.com/plkopd for details.

JURGEN AND CHRISTINE SOHNS/FLPA

Ring-tailed lemurs have become a symbol for Madagascar's unique biodiversity.

PRIMATOLOGY

Among the lemurs

Henry Nicholls savours the posthumous autobiography of the pioneering conservationist Alison Jolly.

When Alison Jolly heard about the plot of the 2005 film *Madagascar* from Jeffrey Katzenberg, chief executive of DreamWorks Animation, she took issue with one detail. The seasoned primatologist had discovered that female lemurs are dominant over males — and pointed out that King Julien, an exuberant ring-tailed lemur, should have been a queen. Katzenberg told her, "That boat has already left".

Although not as well known as fellow primatologists Jane Goodall, Dian Fossey or Biruté Galdikas, Jolly was similarly groundbreaking in Madagascar, where she began a study of ring-tailed lemurs (*Lemur catta*) in 1962. Indeed, it is arguably down to Jolly's pioneering research that the species has become the flagship for the island's extraordinary profusion of unique species. Her posthumously published autobiography, *Thank You, Madagascar*, brings together diary entries and letters spanning almost 30 years, from 1985 to days before her death in February 2014.

NATURE.COM
For more on science in culture, see:
nature.com/booksandarts

These decades are particularly interesting in the history of the conservation movement. Conservationists came to realize that it was not enough to focus solely on the natural world; embracing the needs of people living in biodiverse regions was almost more important. This seems commonplace now, but voicing it was something of a heresy in decades past, as Jolly herself discovered in 1970, at an international conference on conservation in Madagascar. Her presentation, which asked difficult questions about who stood to benefit from conservation, drew "discreet reproof". Nor did the paper, jointly authored with her economist husband Richard, ever find its way into the conference proceedings. It was seen as too incendiary.

Thank You, Madagascar: Conservation Diaries of Alison Jolly
ALISON JOLLY
Zed: 2015.

Yet by the 1980s, the idea of involving community in conservation had started to take root, and Jolly began to document the changing ideological landscape. Through carefully selected diary excerpts, she acknowledges different ways of seeing nature — traditional, aesthetic and economic — and tells the story of bold, often flawed and frequently stumbling efforts by conservationists to forge a single, sustainable vision for the future of Madagascar. It is, as she puts it, "an eyewitness account of a major case study in the politics of conservation".

Jolly's vignettes are drawn from the length and breadth of the country. She takes in the terraced paddy fields that dominate the highlands, the slow-growing baobab forests in the west, the effulgent rainforests that drop down to the Indian Ocean, and the semi-arid spiny forest of the south that was the locus for her work with lemurs. There are frequent descriptions of wondrous natural riches, including an encounter with an aye-aye (*Daubentonia madagascarensis*) — "that hefty head, and bat ears, and the hands like bunches of knobbed licorice sticks" — skimming the palm fronds "like a hologram". Yet rather than taking centre stage, the chameleons, lemurs and hedgehog-like tenrecs seem to act as impartial observers, looking on from the canopy to marvel wide-eyed at the unfolding human drama that is the real subject of Jolly's text.

This theatre takes many forms. There is tragedy: the epic tradition of *tavy*, the slash-and-burn culture that annually sends hundreds of thousands of hectares of natural forest up in flames; the illegal plundering of valuable rosewood from forest reserves; and the unnecessary death of children from a combination of poverty and polluted water, "a slice of village life I never hope to see again".

There is comedy too, much of it absurdist.

In 1987, for instance, a team of US conservationists took a select group of Malagasy ministers to St Catherine's Island, off the coast of the state of Georgia, to persuade them that "the environment and the little lemurs are a prize to be seized". The World Bank wanted to make an example of Madagascar, ploughing cash into development projects in exchange for commitments to conservation. But the Malagasy, cautious about foreign meddling, needed convincing. Jolly describes the minister of water and forests, Joseph Randrianasolo, as a Machiavellian fast-footer who left his fellow ministers "sweating fear like dogs", and the meeting as "probably the most intense three weeks of small-group psychology of my life". The gathering was ultimately a crucial step towards the creation of a National Environmental Action Plan for Madagascar.

The inevitable setbacks, corruption and inefficiencies will resonate with many conservationists. Jolly's reflections on her stint as an adviser to the corporation Rio Tinto, as it began to develop a titanium mine on the country's southern coast, are particularly interesting. Idealism did not seem to feature in her thinking. She was intensely pragmatic, arguing persuasively that such development, if done properly, can bring huge benefits to both humans and the environment.

In spite of its gritty realism, *Thank You, Madagascar* is never a gloomy read. Jolly's lively writing and dozens of compelling cameos lift it. She meets broadcaster David Attenborough, in Madagascar with the BBC in 2010, who talks of the children's books that inspired him (such as Ernest Thompson Seton's 1898 *Wild Animals I Have Known*). Russell Mittermeier, executive vice-chair of Conservation International, pops up frequently, on one occasion wearing "silver running shorts and silver singlet and brandishing a couple of Antandroy spears". Jolly joins Alison Richard, best known for her work on the behavioural ecology of the sifaka (a genus of lemur), and recalls time spent with ecologist Eleanor Sterling, who was "prepared to gallop after aye-ayes all night long". Primatologist Patricia Wright is particularly inspirational, discovering the rare golden bamboo lemur (*Hapalemur aureus*), rediscovering the thought-to-be-extinct greater bamboo lemur (*Prolemur simus*) and driving the creation of Ranomafana National Park in 1991.

Perhaps through modesty, Jolly does not dwell on the importance of incorruptible and inspirational role models for successful conservation. But without the work of such people, there is no doubt that the world would be poorer — in every sense. ■

Henry Nicholls *is a journalist based in London. His latest book is* The Galapagos. *e-mail: henry@henrynicholls.com*

Books in brief

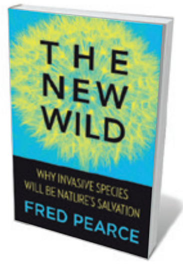

The New Wild: Why Invasive Species Will Be Nature's Salvation
Fred Pearce ICON BOOKS *(2015)*
Invasive species have an undeserved bad reputation, opines veteran environmental journalist Fred Pearce. Digging deep into famous unintended invasions and deliberate introductions, from jellyfish in the Black Sea to rabbits in Australia, he argues that these cases are rarely as simple as good natives versus evil aliens. Far from being rapacious monsters, animals that thrive when transplanted may be exactly the adaptable chancers that will prosper in a world radically reconfigured by human action. Ecologists must abandon "green xenophobia", says Pearce, to ensure that ecosystems stay healthy.

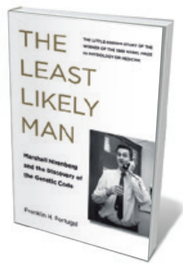

The Least Likely Man: Marshall Nirenberg and the Discovery of the Genetic Code
Franklin H. Portugal MIT PRESS *(2015)*
Marshall Nirenberg was outside the club of molecular biologists seeking the link between gene and protein in the 1950s and 60s. Yet it was he who, as a researcher at the US National Institutes of Health, obtained the first experimental evidence of an RNA messenger molecule, and first cracked the code of an amino acid. Although its narrative structure is a little confused, biologist Franklin Portugal's biography reminds us that Nirenberg sits in the Nobel pantheon alongside Francis Crick, James Watson and Sydney Brenner.

The Container Principle: How a Box Changes the Way We Think
Alexander Klose, translated by Charles Marcrum MIT PRESS *(2015)*
Unseen by most, the global movement of shipping containers connects us all, maintaining the lives we live and the societies we form. Alexander Klose is fascinating on the technical details of the global swirl of millions of twenty-foot equivalent units (TEUs) and the agents — from artists to accidents — that bring this mobile infrastructure to light. At other points, Klose's philosophical reading of the phenomenon is laid on thick, but this is a much-needed examination of why the TEU is the defining technological artefact of our age.

Making Marie Curie: Intellectual Property and Celebrity Culture in an Age of Information
Eva Hemmungs Wirtén UNIVERSITY OF CHICAGO PRESS *(2015)*
Marie Curie remains the most famous of female scientists. In the analysis of how the co-discoverer of radium became uniquely idolized, cultural scholar Eva Hemmungs Wirtén uses the prisms of celebrity and intellectual property — Curie and her husband, Pierre, having famously refused to patent radium. Wirtén's picture of a scientist carefully shaping her own image is less angelic than the traditional view of Curie, but might have much to teach her modern successors.

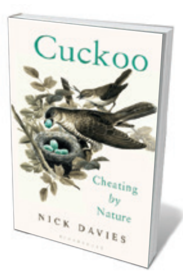

Cuckoo: Cheating by Nature
Nick Davies BLOOMSBURY *(2015)*
This detective story by behavioural ecologist Nick Davies sets out to solve how "Nature's most notorious cheat" gets away with its "outrageous" behaviour. This is the cuckoo (*Cuculus canorus*) — that well-known hijacker of other birds' nests. Davies underpins calm and elegant prose with deep knowledge gleaned from years studying the species. By the end of the book, it is hard not to feel the same joy as Davies does when contemplating this remarkable bird, or the same sadness at its apparent UK decline. **Daniel Cressey**

Correspondence

Big data held to privacy laws, too

Privacy issues around data protection often inspire over-engineered responses from scientists and technologists. Yet constraints on the use of personal data mean that privacy is less about what is done with information than what is not done with it. Technology such as new algorithms may therefore be unnecessary (see S. Aftergood *Nature* **517,** 435–436; 2015).

Technology-neutral data-protection laws afford rights to individuals with respect to all data about them, regardless of the data source. More than 100 nations now have such data-privacy laws, typically requiring organizations to collect personal data only for an express purpose and not to re-use those data for unrelated purposes.

If businesses come to know your habits, your purchase intentions and even your state of health through big data, then they have the same privacy responsibilities as if they had gathered that information directly by questionnaire. This is what the public expects of big-data algorithms that are intended to supersede cumbersome and incomplete survey methods. Algorithmic wizardry is not a way to evade conventional privacy laws.

Stephen Wilson *Constellation Research, Sydney, Australia.*
steve@constellationr.com

Storm-surge models helped for Hagupit

The Philippine government learned from shortcomings in the preparations for Typhoon Haiyan in 2013 (see R. Lejano *et al. Nature* **518,** 35; 2015, and A. M. F. Lagmay *et al. Int. J. Disaster Risk Reduct.* **11,** 1–12; 2015) and was able to limit the damage that last December's Typhoon Hagupit might otherwise have caused.

For example, storm surges during Haiyan extended inland by an unanticipated 2 kilometres. Specific warnings of surges of up to 5.5 metres were issued two days before Haiyan's landfall, and were broadcast on prime-time television by the country's president. Despite this, the warnings proved inadequate because the variability of coastal landscapes makes it impossible to judge inundation extent on the basis of storm-surge heights alone.

Following the 2013 disaster, Project NOAH (run by the Philippine government's Department of Science and Technology) prepared storm-surge inundation maps for all its coastal provinces, modelled using high-resolution topography. These detailed maps, along with advance warning, helped to mitigate the loss of life when Hagupit's storm surges destroyed at least 1,800 homes at the end of 2014.

Alfredo Mahar Lagmay *National Institute of Geological Sciences, University of the Philippines Diliman, Quezon City, the Philippines.*
Norman Kerle *University of Twente, Enschede, the Netherlands.*
mlagmay@nigs.upd.edu.ph

Leadership training for African scientists

The Africa Science Leadership Program, launched on 2 March, is the first of its kind in the developing world (see www.up.ac.za/aslp). It will train researchers to lead complex scientific initiatives across disciplines and sectors, helping them to compete in global knowledge production.

A handful of institutions in Canada and the United States offer useful advanced leadership training for researchers (see, for example, M. Kvaskoff and S. D. McKay *Nature* **506,** 159; 2014). The need for such programmes is more desperate in developing countries if they are to avoid falling further behind in an interconnected and competitive world (B. Slippers *et al. S. Afr. J. Sci.* **111,** a0093; 2015).

The African programme will create nuclei for leadership development on the continent. Small groups of mid-career scientists will participate in the year-long training, which includes two multi-day sessions, ongoing peer support and mentoring in-between.

Bernard Slippers *University of Pretoria, South Africa.*
Eva Alisic *Monash University, Australia.*
bernard.slippers@fabi.up.ac.za

Is there fame bias in editorial choice?

Nature's Correspondence items are reviewed only by the editors (see go.nature.com/cmchno). To investigate whether editorial bias towards internationally renowned correspondents might be at play in selecting candidates for publication, we analysed the scientific status of Correspondence authors published in 2014.

We used the following pointers to gauge author reputation: faculty member in one of the world's top 100 universities (as listed in the *Times Higher Education* World University Rankings; see go.nature.com/bhgfxd); authorship of *Nature* or *Science* publications; high *h* index. We classed correspondents as established scholars if they fulfilled any or all of these criteria.

The number of letters published in Correspondence in 2014 was 239, each with one 'corresponding author' responsible for submission and communication with the editors. We found that 54% of these authors met some or all of our criteria. Some 13% of authors came from the developing world.

Within the limitations of our 'fame factors' (for example, some correspondents were well known but from outside academia), we infer that scientific celebrity of the primary correspondent does not notably influence the selection of letters for publication.

Omid Mahian* *Ferdowsi University of Mashhad, Mashhad, Iran.*
omid.mahian@gmail.com
**On behalf of 4 correspondents (see go.nature.com/rpntpk for full list).*

Build reward system for ace technicians

Technical staff are crucial to the smooth running of a research laboratory (see *Nature* **517,** 528; 2015). As largely unsung heroes, they warrant rewards beyond praise and salary increases.

A senior technician's duties cover, among other functions, safety, finance, ordering and repairs. Technicians maintain stocks of essential reagents and keep facilities such as databases up to date. They carry out specialized experiments and train staff in methodology.

Rewards for such highly skilled technicians might include setting up a fund to keep them employed during times of financial constraint. Our technicians also share the right of graduate students and postdocs to attend one conference of their choice every year. Some are co-authors on scientific publications and present work at meetings. After 16 years in our lab, one technician has 110 publications to his credit, as well as more than 3,000 lifetime citations and an *h* index of 33.

Eleftherios P. Diamandis *Mount Sinai Hospital and University Health Network, Toronto; and University of Toronto, Canada.*
ediamandis@mtsinai.on.ca

CORRECTION

In the print version of the Outlook article 'The toxic side of rice' (*Nature* **514,** S62–S63; 2014), reference 3 originally cited the wrong study. It has now been corrected online.

CARDIOLOGY

A big-hearted molecule

Blockade of the enzyme PDE9 prevents degradation of the molecule cyclic GMP, which has been shown to protect against heart failure. The finding indicates that PDE9 inhibition might be a drug target for treating this condition. SEE LETTER P.472

MICHAELA KUHN

Chronic heart failure, a disease in which the heart cannot pump sufficient blood to meet the needs of the body, is a leading cause of death worldwide. Persistent high blood pressure is an important risk factor for heart failure, because it increases the heart's workload, which in turn increases the size and strength of heart-muscle cells called cardiomyocytes — a condition known as cardiac hypertrophy. In the long term, this can cause permanent molecular and structural changes in cardiomyocytes, impairing cardiac contraction and relaxation. To counteract this risk, the heart releases natriuretic peptide hormones that lower blood pressure and exert direct cardioprotective effects, but natriuretic-peptide signalling is attenuated in heart failure. In this issue (page 472), Lee *et al.*[1] demonstrate that restoration of this signalling may be a useful strategy for treating heart failure.

Understanding the molecular mechanisms that regulate cardiac hypertrophy and heart failure is a major focus of research in cardiovascular medicine. Numerous studies[2] have shown that an intracellular molecule called cyclic GMP (cGMP) provides protection from high blood pressure and cardiac disease, in part by activating the enzyme cGMP-dependent protein kinase type I (PKGI), which modulates the activity of many target proteins. cGMP has a crucial role in regulating fundamental cellular processes throughout the body[2], including acute processes such as cell contraction, migration and secretion, and chronic processes such as gene expression and cell growth.

In cardiomyocytes, as in most cardiovascular cell types, cGMP production is promoted by four hormones, acting through three receptor proteins found in different subcellular locations[2]. First, the gaseous hormone nitric oxide (NO) stimulates a cytoplasmic, soluble guanylyl cyclase (sGC) receptor. Second, atrial natriuretic peptide (ANP) and B-type natriuretic peptide (BNP) hormones activate a guanylyl cyclase type A (GC-A) receptor that spans the cardiomyocyte plasma membrane. Finally, C-type natriuretic peptide (CNP) hormone binds to a membrane-spanning guanylyl cyclase type B (GC-B) receptor. Both

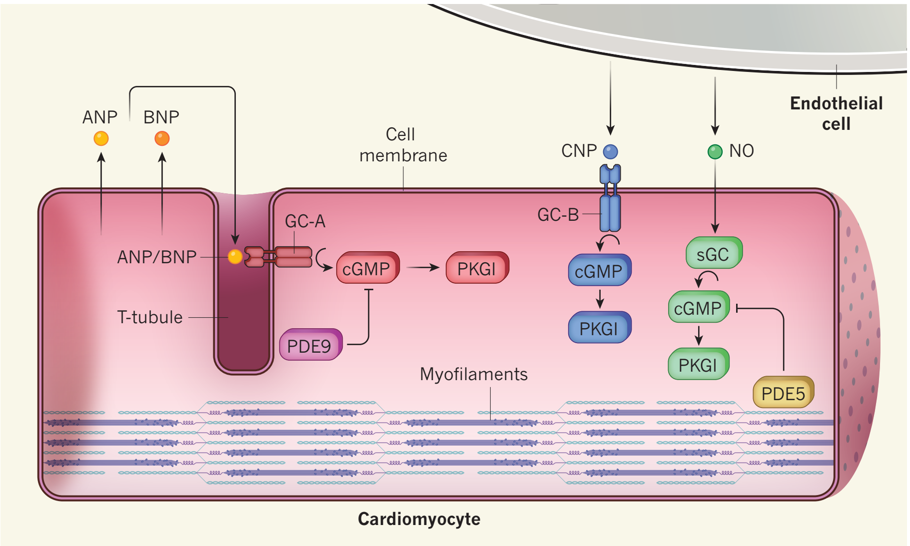

Figure 1 | Three heart-protecting regulatory circuits. In heart muscle cells called cardiomyocytes, the molecule cyclic GMP (cGMP) is produced by activation of three guanylyl cyclase (GC) receptor proteins found in different subcellular locations. Cardiomyocytes secrete the hormones atrial natriuretic peptide (ANP) and B-type natriuretic peptide (BNP), which activate GC-A. Neighbouring endothelial cells release C-type natriuretic peptide (CNP) and nitric oxide (NO), hormones that activate the membrane-spanning receptor GC-B and the cytoplasmic receptor sGC, respectively. Stimulation of any of these three receptors triggers cGMP production and activation of the enzyme PKGI, protecting the heart from hypertrophy or modulating its contraction and relaxation. Lee *et al.*[1] report that phosphodiesterase (PDE) enzymes differentially regulate these cGMP pools: ANP- or BNP-formed cGMP is degraded by PDE9, which is distributed around T-tubular membrane invaginations; and NO-derived cGMP is degraded by PDE5, which is located at contractile myofilaments.

NO and CNP are secreted from endothelial cells that line the blood vessels, whereas ANP and BNP are produced by cardiomyocytes themselves (Fig. 1). Opposing the action of these hormones, the phosphodiesterase enzymes PDE5 and PDE9 degrade cGMP by hydrolysis and so regulate the duration, amplitude and spatial distribution of cGMP signalling within cardiomyocytes[3]. Such spatial restrictions mean that cGMP-activated PKGI can regulate a range of cardiomyocyte functions[4].

Both NO and natriuretic peptides, acting through their respective receptors to promote cGMP formation in cells of the kidney and blood vessels, lower blood pressure and thereby reduce cardiac work[5]. Studies[4,6] suggest that cGMP also has a protective function in the heart, accelerating relaxation, decreasing the stiffness of cardiomyocytes and moderating adverse cardiac remodelling. The accumulating evidence of cGMP's role in the heart, and of a protective role in other organs and tissues, such as the brain, lung and vasculature, led to an interest in drugs that might enhance cGMP signalling, and much attention has focused on PDE5 inhibition. Since 1998, three PDE5 inhibitors have been used to treat erectile dysfunction and pulmonary hypertension. Preclinical studies with one such inhibitor, sildenafil, showed dramatic cardiac anti-remodelling benefits in animals, and these were partly confirmed in small human studies[7,8]. But a large clinical trial in patients with heart failure reported disappointing results[9].

Lee *et al.*[1] investigated the cellular distribution of PDE5 and PDE9 in cardiomyocytes, and showed that PDE5 is found at contractile filaments called myofilaments, where

it degrades cGMP produced through the NO–sGC pathway. By contrast, they showed that PDE9 is located near 'T-tubular' invaginations of the plasma membrane and mainly regulates cGMP produced by the ANP–GC-A pathway (Fig. 1). The authors also found that PDE9 levels and activities, like those of PDE5, rise in hypertrophic cardiomyocytes, both in mice and in patients with heart failure. The proteins spill out into abnormal intracellular compartments, increasing cGMP degradation.

Oxidative stress provokes a dysfunctional uncoupling of the NO-producing enzyme in patients with heart failure, leading to the production of noxious oxygen radicals instead of NO. Lee and colleagues reasoned that this effect, which attenuates cGMP production through the NO–sGC pathway, could explain the limited clinical effectiveness of PDE5 inhibitors. But natriuretic-peptide-driven cGMP synthesis is also compromised in the cardiomyocytes of patients with heart failure — GC-A receptors become desensitized, and the cells secrete large amounts of precursors to ANP and BNP, which are not properly processed and so are poorly active[2]. The authors therefore propose that inhibiting PDE9, to enhance the pool of cGMP derived from the ANP–GC-A pathway, is an attractive alternative to inhibiting PDE5.

The authors explored this possibility by using a mouse model of cardiac pressure overload. Mice do not normally develop high blood pressure or cardiac hypertrophy, so the researchers surgically constricted the aorta, which carries blood away from the heart, thereby artificially enhancing cardiac 'afterload'. Within a few weeks of surgery, the hearts of mice with aortic constriction were approximately 60% larger than those of control animals. This was accompanied by the formation of fibrous tissue and by reduced heart contraction and relaxation, all features of early-stage heart failure. Remarkably, genetic or pharmacological inhibition of PDE9 (using a compound called PF-04447943) prevented and even reversed existing heart failure in these mice.

The authors' suggestion that modulating the pool of ANP- or BNP-derived cGMP can benefit patients with heart failure is supported by research showing that inhibiting neprilysin — a peptidase enzyme that degrades ANP, BNP and other hormones — enhanced endogenous ANP and BNP levels, and reduced the risks of hospitalization and death in patients with heart failure[10].

Other strategies for treating heart failure are also worthy of consideration. For instance, one approach under investigation is the use of synthetic 'designer' natriuretic peptides[11]. The CNP–cGMP pathway and corin, an enzyme that activates cardiac ANP, may also represent targets for heart-protecting therapies.

PF-04447943 is being tested in clinical trials for neurocognitive diseases (see go.nature/a8qtw9), and seems to be well tolerated in humans. Lee and colleagues' exciting observations in mice, when considered together with the fact that older patients with heart failure frequently exhibit cognitive impairment[12], support the exploration of PDE9 as a target for treating heart failure. ■

Michaela Kuhn *is at the Institute of Physiology, University of Würzburg, D-97070 Würzburg, Germany.*
e-mail: michaela.kuhn@mail.uni-wuerzburg.de

1. Lee, D. I. *et al. Nature* **519,** 472–476 (2015).
2. Kuhn, M. *Circ. Res.* **93,** 700–709 (2003).
3. Maurice, D. H. *et al. Nature Rev. Drug Discov.* **13,** 290–314 (2014).
4. Frantz, S. *et al. Eur. Heart J.* **34,** 1233–1244 (2013).
5. Ehret, G. B. *et al. Nature* **478,** 103–109 (2011).
6. Holtwick, R. *et al. J. Clin. Invest.* **111,** 1399–1407 (2003).
7. Takimoto, E. *et al. Nature Med.* **11,** 214–222 (2005).
8. Guazzi, M., Vicenzi, M., Arena, R. & Guazzi, M. D. *Circulation* **124,** 164–174 (2011).
9. Redfield, M. M. *et al. J. Am. Med. Assoc.* **309,** 1268–1277 (2013).
10. McMurray, J. J. V. *et al. N. Engl. J. Med.* **371,** 993–1004 (2014).
11. Zakeri, R. & Burnett, J. C. *Can. J. Physiol. Pharmacol.* **89,** 593–601 (2011).
12. Ampadu, J. & Morley, J. E. *Int. J. Cardiol.* **178,** 12–23 (2015).

This article was published online on 18 March 2015.

PHYSICAL CHEMISTRY

Square ice in a graphene sandwich

Films of ice less than 1 nanometre thick, sandwiched between sheets of graphene, have been observed to adopt a square lattice structure quite different from the widely occurring hexagonal structure of bulk ice. **See Letter p.443**

ALAN K. SOPER

Crystals of ice consist of hydrogen-bonded water molecules in a tetrahedral network that has hexagonal symmetry. It is this symmetry that gives rise to the characteristic shapes of snowflakes and the intricate patterns of ice that form on the surfaces of puddles when they freeze. At high pressures, such as 10,000 atmospheres (1 gigapascal; GPa), the underlying tetrahedral geometry of ambient ice is mostly preserved, although the detailed structure undergoes several transformations[1]. But on page 443 of this issue, Algara-Siller *et al.*[2] describe a high-resolution electron microscopy study of water molecules at high pressure between sheets of the material graphene, and report that the

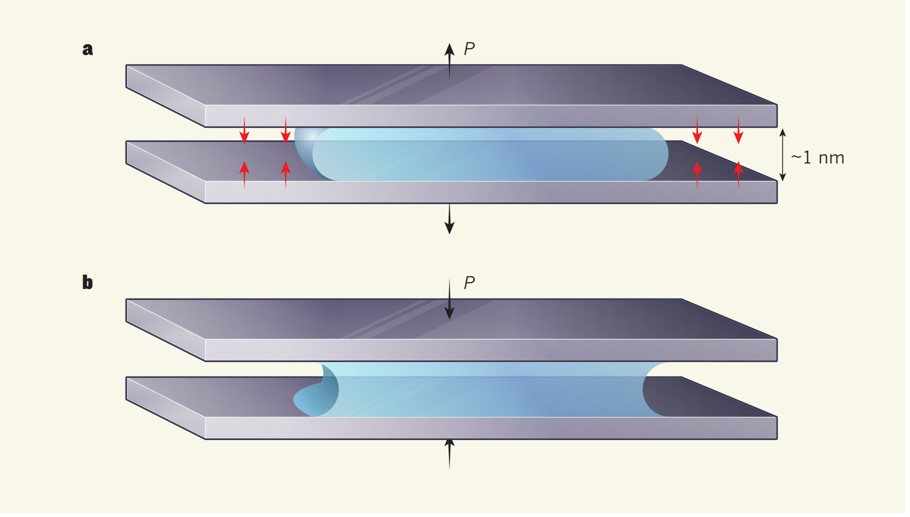

Figure 1 | Liquid droplets captured between two sheets. a, When water is trapped between graphene sheets, the liquid does not wet the sheets' surfaces. The convex meniscus indicates that pressure (*P*) inside the droplet is positive and tries to force the plates apart. Algara-Siller *et al.*[2] estimate that the van der Waals attraction (red arrows) between graphene layers is sufficient to overcome that pressure when the distance between the sheets is about 1 nanometre. **b**, By contrast, when a trapped liquid wets the surface of the sheets, the pressure inside the drop is lower than that outside, pulling the plates towards one another.

molecules surprisingly adopt a simple, cubic-like symmetry — a bit like scaffolding on the outside of a building, or, more accurately, between two buildings.

The authors' work brings together themes of fluid behaviour near surfaces that date back to at least the 1890s, the time of Johannes van der Waals' studies in this area. From his and related work, we know that the pressure inside a liquid surface is higher than the pressure outside if the liquid surface is convex, and lower than that outside if the surface is concave[3] (Fig. 1). If a small droplet of liquid is confined between two sheets, and does not wet the surfaces — that is, it does not bond readily to the surface, as is the case for mercury on glass — then the liquid–vapour interface is convex and the pressure inside the liquid must be greater than that outside.

In fact, the pressure within a sheet-confined droplet is determined by the ratio of the surface tension of the liquid to the radius of curvature of the liquid's surface[3]. Although the precise details of this effect at the molecular level become complicated by atomic interactions[4,5], if the radius of curvature becomes very small (of the order of 1 nanometre or less, as in Algara-Siller and colleagues' work), then large pressures are required to hold the liquid in place. This is, apparently, exactly what happens when water is sandwiched between graphene sheets, because there are no points in the sheets to which water can form hydrogen bonds.

How can that pressure be maintained? To explain this, Algara-Siller *et al.* draw on another theme from van der Waals' theory, namely, that all atoms must be attracted to each other, irrespective of whether they can form hydrogen bonds or not. This attractive force — called the van der Waals force or London dispersion force[6] — increases as atoms approach each other. The authors calculate that when sheets of atoms, such as the carbon atoms in graphene, are separated by distances of less than 1 nm (as used in the experiment), then the van der Waals forces can easily generate pressures as high as 1 GPa.

Water trapped between graphene sheets under these conditions is likely to crystallize, even at room temperature. But the fact that it forms a square structure is unexpected. The researchers' computational molecular-dynamics simulations do suggest that a square lattice can form, as observed, but the detailed origins of this strange arrangement remain a mystery.

Are there any precedents for observing square-like structures formed from water molecules? Yes, there are some. Extensive spectroscopic data and simulations of small clusters of water molecules[7–9] provide evidence that groups of water molecules can have a near-cubic structure, with 'dangling' hydrogen bonds available in principle to form a more extensive network. And a study[10] that combined molecular-dynamics simulations with neutron-scattering experiments concluded that the dynamics of water molecules trapped in carbon nanotubes could be explained if the molecules form a stationary, nearly square array wrapped in a cylinder at the inner surface of the nanotube, through which more water molecules are transported in a chain-like configuration. But Algara-Siller and colleagues are the first to directly observe an extended, two-dimensional, square-like structure in water experiments.

It remains to be seen whether the authors' observations are relevant to water transport through naturally occurring nanometre-scale channels. For example, aquaporin is a widely occurring channel protein that regulates the flow of water across the cell membrane. The flow-control mechanism entails a combination of hydrophobic and hydrophilic interactions between the water and the inside surface of the channel[11], which is circular in cross-section, not planar, as in the case of the graphene 'pore'. Nonetheless, the graphene results are highly intriguing, and will probably stimulate much debate about the nature of water in biological channels and at surfaces. No doubt van der Waals would have delighted to know that the fundamental forces that he identified so long ago have led to the discovery of an unexpected phase of water today. ■

Alan K. Soper *is at the ISIS Facility, Science and Technology Facilities Council, Rutherford Appleton Laboratory, Harwell Oxford, Didcot OX11 0QX, UK.*
e-mail: alan.soper@stfc.ac.uk

1. Petrenko, V. F. & Whitworth, R. W. *Physics of Ice* (Oxford Univ. Press, 1999).
2. Algara-Siller, G. *et al. Nature* **519,** 443–445 (2015).
3. Rowlinson, J. S. & Widom, B. *Molecular Theory of Capillarity* Int. Ser. Monogr. Chem. (Clarendon, 1982).
4. Lei, Y. A., Bykov, T., Yoo, S. & Zeng, X. C. *J. Am. Chem. Soc.* **127,** 15346–15347 (2005).
5. Xue, Y.-Q., Yang, X.-C., Cui, Z.-X. & Lai, W.-P. *J. Phys. Chem. B* **115,** 109–112 (2011).
6. London, F. *Trans. Faraday Soc.* **33,** 8b–26 (1937).
7. Gruenloh, C. J. *et al. Science* **276,** 1678–1681 (1997).
8. Keutsch, F. N. & Saykally, R. J. *Proc. Natl Acad. Sci. USA* **98,** 10533–10540 (2001).
9. Perera, P. N. *et al. Proc. Natl Acad. Sci. USA* **106,** 12230–12234 (2009).
10. Kolesnikov, A. *et al. Phys. Rev. Lett.* **93,** 035503 (2004).
11. Agre, P. & Kozono, D. *FEBS Lett.* **555,** 72–78 (2003).

MOLECULAR BIOLOGY

DNA replication reconstructed

Chromosomes must be faithfully duplicated in each cell-division cycle to ensure genome integrity. The *in vitro* reconstitution of DNA-replication initiation in yeast allows mechanistic studies of this fundamental process. SEE ARTICLE P.431

MICHAEL WEINREICH

On page 431 of this issue, Yeeles *et al.*[1] report the long-awaited *in vitro* reconstitution of the initiation of DNA replication using 16 purified proteins from the budding yeast *Saccharomyces cerevisiae*. This study defines, for the first time, the minimum set of proteins required to initiate DNA replication in eukaryotes (organisms that include plants, animals and fungi). The authors also use their system to examine the regulatory mechanism that limits initiation to just once per cell cycle at each initiation site, confirming and adding key details to what was previously known.

Genome duplication must occur before cell division, so that both progeny cells inherit a complete copy of the genetic material. DNA replication is initiated at particular chromosomal sites called origins, after the binding and recruitment of several initiation proteins. In eukaryotes, replication initiation occurs at hundreds to thousands of origins distributed along multiple chromosomes, with one origin for every 40 kilobases of DNA in yeast, and greater intervals in mammals. The activation (firing) of these origins must be strictly regulated so that it occurs only during the DNA-synthesis period (S phase) of each cell-division cycle. Also, each origin must be activated once per cell cycle at most, to avoid potentially lethal over-replication events.

Yeeles and colleagues' findings represent a major technical feat that will allow eukaryotic initiation to be studied in detail. The authors' work on *in vitro* reconstitution would not have been possible without the considerable genetic and biochemical work of the past 30 years — particularly in budding yeast, for which the numerous proteins required for replication initiation have been identified and the complex regulatory processes described[2–4]. Not surprisingly, this core replication machinery has been conserved throughout evolution, from yeast to mammals.

The initiation of DNA replication can be separated into two distinct and mutually exclusive steps (Fig. 1). In the first step, which occurs in the G1 phase of the cell cycle,

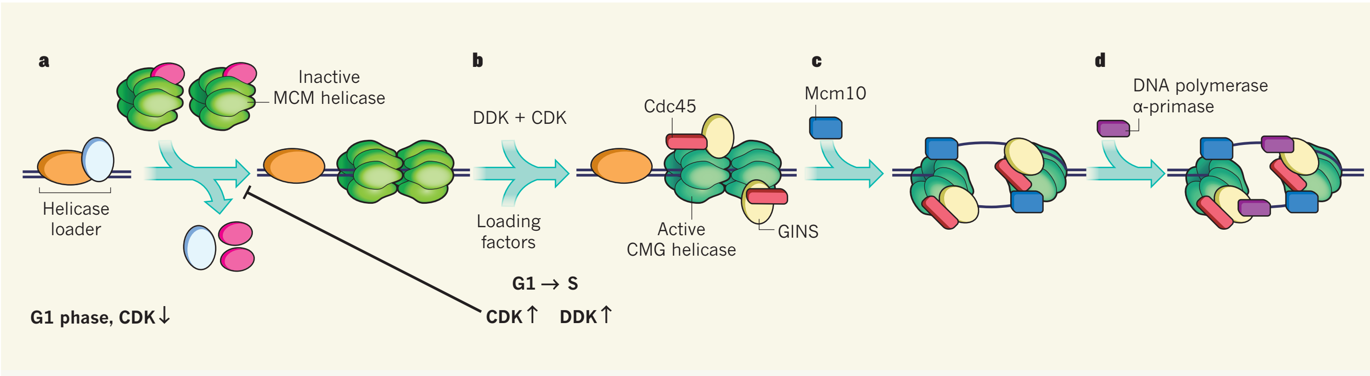

Figure 1 | DNA-replication initiation. **a**, As cells enter the G1 phase of the cell cycle, levels of the CDK enzyme fall. This allows the helicase-loader protein complex to recruit two hexamers of the inactive MCM helicase enzyme complex to origin sequences throughout the genome. Several proteins required for MCM loading are lost during this process. **b**, Levels of CDK and of the DDK enzyme rise just before S phase begins. This prevents further MCM loading and enables loading factors to deposit two more proteins, Cdc45 and GINS, on each of the MCM hexamers to form two active CMG helicases. **c**, Yeeles *et al.*[1] report that these CMG complexes require yet another protein, Mcm10, to unwind origin DNA. **d**, DNA replication begins after the recruitment of DNA polymerase α-primase, the enzyme that initiates DNA synthesis.

an inactive form of a DNA-helicase enzyme complex (MCM) is loaded at all replication origins throughout the genome; DNA helicases separate and unwind the double-stranded DNA helix into two single strands. Strand separation is necessary for the DNA to serve as the template for its own replication, which occurs at protein–DNA structures called replication forks — the points at which the double-stranded DNA is unwound into two single strands.

In the second step of initiation, the loaded DNA helicase is activated by the recruitment of further protein components. Helicase activation occurs locally at each active origin just before and during S phase. Initiation proteins also recruit DNA primase and DNA polymerases, enzymes required to synthesize two daughter strands on the basis of the template sequence of the parental strands.

To prevent any single origin from firing more than once per cell cycle, the helicase must be loaded at the beginning of the cell cycle (G1 phase), the only period in which the activity of the cyclin-dependent kinase (CDK) enzyme is low. CDK belongs to the protein-kinase family of enzymes, which covalently modify a protein or small molecule by adding a phosphate group, thereby changing the molecule's biological properties. High CDK levels prevent further helicase loading, but are required for helicase activation. CDK activity thus acts as a switch between the two replication steps. A second protein kinase, DDK, is also required for helicase activation and accumulates towards the end of G1 phase.

This intricate coupling of helicase loading and activation to protein-kinase activity is necessary to prevent re-replication of the genome[5]. The activation of origins outside S phase, or more than once per cell cycle, would generate amplified DNA regions that could break when chromosomes are segregated during mitosis; such breaking would probably be lethal. Yeeles and co-workers' study defines the minimum set of protein substrates for CDK and DDK that are required for initiation *in vitro*, and confirms previous work[5]. CDK and DDK phosphorylate many amino-acid residues in their substrates, so researchers can now use the authors' *in vitro* system to map which phosphorylation events are essential and how these modifications affect protein–protein interactions and biological activities.

The MCM helicase, which is composed of six subunits, is loaded around double-stranded DNA as a dodecamer consisting of two identical hexamers in a 'head-to-head' arrangement[6]. How this occurs is still an open question, because the only identified intermediates[7] for this process have a single hexamer engaged with double-stranded DNA. It will be important to determine whether the two hexamers are loaded by two helicase loaders, sequentially by one helicase loader, or perhaps as an intact dodecamer[8].

This major technical feat will allow DNA-replication initiation in eukaryotic organisms to be studied in detail.

This work also opens up many other areas of investigation, such as how the helicase is activated, and how polymerases are recruited and coupled to the helicase at the replication fork. Helicase activation requires CDK, DDK and two other proteins to form a complex called the CMG helicase[9,10]. However, Yeeles and colleagues find that CMG cannot unwind origin DNA effectively by itself — another protein (Mcm10) is also required. Investigating the interactions between the helicase subunits, how each contributes to the initial unwinding event and how the initial dodecamer is split into two hexameric units, are exciting research opportunities that are now clearly possible.

Yeeles *et al.* observe that the DNA polymerase required for leading-strand synthesis is recruited during the helicase activation step. However, their *in vitro* system currently lacks other components needed for chromosomal replication. These include: the DNA polymerase that makes the lagging strand; the sliding 'clamp' that tethers DNA polymerases to DNA; the clamp loader; a triad of proteins called the fork-protection complex; and the proteins required for the final processing steps (maturation) of the replication products. Much work is therefore still required to reconstitute the complete replication reaction.

If an *in vitro* system could be devised that incorporates a synthesis reaction including both leading and lagging strands, one could imagine reconstituting the assembly of chromatin — the complex of histone proteins and DNA in the cell nucleus — behind each fork, as occurs in cells. Chromatin, rather than naked DNA, is the true template for DNA replication in the cell. Finally, it will be interesting to see whether the authors' system could eventually be used to investigate mechanisms for maintaining fork stability and for replication-coupled DNA repair. These crucial processes are clearly involved in maintaining genome integrity, and are of particular interest because they are often lost in cancerous cells. ■

Michael Weinreich *is in the Genome Integrity and Tumorigenesis Laboratory, Van Andel Institute, Grand Rapids, Michigan 49503, USA.*
e-mail: michael.weinreich@vai.org

1. Yeeles, J. T. P., Deegan, T. D., Janska, A., Early, A. & Diffley, J. F. X. *Nature* **519,** 431–435 (2015).
2. Waga, S. & Stillman, B. *Annu. Rev. Biochem.* **67,** 721–751 (1998).
3. Heller, R. C. *et al. Cell* **146,** 80–91 (2011).
4. Li, Y. & Araki, H. *Genes Cells* **18,** 266–277 (2013).
5. Labib, K. *Genes Dev.* **24,** 1208–1219 (2010).
6. Remus, D. *et al. Cell* **139,** 719–730 (2009).
7. Sun, J. *et al. Nature Struct. Mol. Biol.* **20,** 944–951 (2013).
8. Yardimci, H. & Walter, J. C. *Nature Struct. Mol. Biol.* **21,** 20–25 (2014).
9. Costa, A. *et al. Nature Struct. Mol. Biol.* **18,** 471–477 (2011).
10. Fu, Y. V. *et al. Cell* **146,** 931–941 (2011).

DEVELOPMENTAL BIOLOGY

Earn your wings

The ecological success of the migratory brown planthopper (*Nilaparvata lugens*; pictured), a rice pest, depends on its ability to develop into two different forms in response to environmental cues. On page 464 of this issue, Xu *et al*. show that, during development, the binary action of two distinct insulin receptor proteins, dubbed NlInR1 and NlInR2, controls the switch between these two forms (H.-J. Xu *et al*. *Nature* **519,** 464–467; 2015).

The long-winged planthopper escapes adverse habitats to search for resources, whereas the short-winged form is highly fertile, but cannot fly. The authors delineate a molecular signalling cascade, in which the production of an insulin peptide in the brain acts on NlInR1 to trigger the formation of long wings. NlInR2 impedes the action of the cascade to prevent wing growth. The relative expression levels of each receptor therefore determine which form each planthopper adopts.

These results help to show how environmental cues regulate generation of the highly fertile short-winged insects, and could be used to develop ways to control these agricultural pests. **Nathalie Le Bot**

CHUAN-XI ZHANG

QUANTUM PHYSICS

Atomic doughnuts from single photons

Analysis of the interaction between a photon and an ensemble of some 3,000 atoms trapped between two mirrors has revealed a form of multi-atom quantum entanglement that has no counterpart in classical mechanics. SEE LETTER P.439

JAMES K. THOMPSON

What is the most that could happen when you analyse a single particle of light after sending it through a few thousand atoms? On page 439 of this issue, McConnell *et al.*[1] demonstrate that the single photon creates a special quantum link between nearly all of the atoms, a link known as entanglement. The authors show that the particular 'flavour' of entanglement observed has no classical analogue — a first for such a large collection of atoms. Extending our ability to create entanglement in large systems may one day allow highly precise measurements of time, fields and accelerations, lead to new materials, and enhance our understanding of the transition from the quantum to the classical world.

In the quantum world, the act of measurement can profoundly change the state of the object being measured. McConnell and colleagues exploited this fundamental principle to create entanglement between almost 3,000 atoms that are laser-cooled to only a few ten-millionths of a degree above absolute zero. The atoms were levitated between two highly reflecting, weakly transmitting mirrors. Each of the atoms can be thought of as possessing an arrow, which corresponds to the orientation of the atom's total quantum spin. All the arrows add up to make one big arrow that initially points in some direction, call it *x*, which lies on the equator of a sphere.

A weak pulse of light is injected through one of the mirrors and then detected after it leaks back out of the other mirror. The light also has an arrow attached to it, denoting its polarization (the direction of the light's electric field). As the light bounces back and forth between the mirrors, it passes roughly 5,000 times through the atoms, each time being partially absorbed and then re-emitted back into the original pulse of photons (Fig. 1a).

If the total atomic arrow were pointing slightly north or slightly south of the *x* direction, because of quantum Heisenberg uncertainty in its orientation (Fig 1b.), then the polarization of the light would be slightly rotated clockwise or anticlockwise, respectively, when it was re-emitted. For each pulse of light sent through the mirrors, McConnell *et al.* checked to see whether they detected any rotated light. On most trials, they did not detect even one rotated photon.

Failing was no problem. They just tried again until they finally detected that a single photon had been rotated. This told the experimenters that, on that particular trial, the total atomic arrow was not quite on the equator, but must have been pointing slightly north or south of *x*. The researchers verified that the arrow was no longer at the equator by making a second and much more precise measurement of the total atomic arrow's north–south orientation.

The measurement apparatus fundamentally could not tell whether the polarization rotation of the single detected photon was clockwise or anticlockwise. With no further information, one would expect the measurement of a single photon to collapse the total atomic arrow into a quantum superposition state in which the arrow was simultaneously both north and south of the equator.

But confirming with the precise measurement that the total atomic arrow does not lie

on the equator was not sufficient to establish the superposition nature of the quantum state[2]. To do this, the authors also performed experiments in which, after detecting the rotated photon, they then rotated the total atomic arrow about the *x* direction by various amounts. They then made the precise north–south measurement. As predicted for a simultaneous north and south state, they observed a much lower probability that the arrow would be found on the equator than is possible for a classical arrow that is either just north or just south of the equator.

By measuring at different rotation angles, McConnell *et al.* determined the Wigner function — a quantum probability distribution of the direction in which the total atomic arrow points. The Wigner function looked like a two-dimensional doughnut centred on the *x* axis (Fig. 1b), but rather than simply having an empty hole of zero probability at its centre, the centre of this doughnut had negative probability. This negative probability was a clear sign that the measurement of a single rotated photon collapsed the atoms into an entangled state. This is the first time that a negative Wigner function has been observed for such a large collection of atoms.

Several experiments have created entanglement between atoms using many photons to measure the north–south orientation of the total atomic arrow[3], producing large amounts of 'quantum squeezing'[4] — enhancement in the sharpness of the atomic arrow needed for realizing better quantum sensors. McConnell *et al.* observed no improvement in the total sharpness of their atomic arrow.

However, the squeezing experiments carried out so far can be viewed semi-classically: quantum mechanics produces a certain magnitude of 'noise', after which the noise can be treated as arising from a fictitious classical source. In McConnell and colleagues' work, the observation of a negative Wigner function demonstrates that any semi-classical description fails to capture their flavour of entanglement.

The authors also demonstrate that nearly all of the roughly 3,000 atoms must be involved in the generated entanglement, by using a multipartite entanglement measure known as the entanglement depth, which has been applied in related work[5]. It is unclear exactly how to interpret this particular measure because it does not provide information about the magnitude of the shared entanglement[6,7]. However, showing that entanglement can be simultaneously shared among so many atoms continues to push the progression of the observation of quantum mechanics from the microscopic to the mesoscopic regime. It may one day help us to understand the transition from the quantum to the classical world of our everyday experience, in which we would never see arrows pointing both slightly north and slightly south at the same time.

In future work, the detection of two or more rotated photons[8] may open the door to even larger amounts of entanglement, and to states that might be useful for quantum sensors

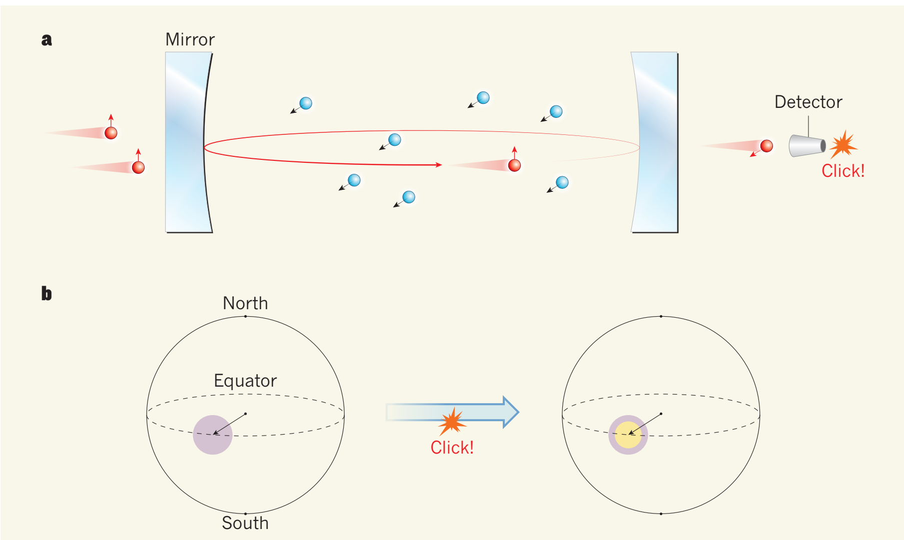

Figure 1 | Creating highly shared entanglement. **a**, Vertically polarized photons (red) pass many times through atoms (blue) as the photons bounce back and forth between highly reflecting, weakly transmitting mirrors. The polarization of a photon is only very occasionally rotated to horizontal owing to quantum noise (uncertainty) in the quantum-spin orientation of the atomic arrows. Only horizontally polarized photons generate a click on a detector. **b**, The quantum probability distribution of the orientation of the total atomic arrow is represented by a region (purple disk) at the tip of an arrow on the equator of a sphere. McConnell *et al.*[1] show that detecting just one horizontal photon (click!) changes this distribution to a 'two-dimensional doughnut', which has a positive outer region (purple) and a negative inner region (yellow) — a hallmark of quantum entanglement between the atoms. The negative-probability filling means that, no matter how the doughnut is rotated about its axis, the probability of measuring the arrow on the equator is zero.

NATURE

50 Years Ago

'Detection in Denmark of the Sinkiang nuclear detonation' — Measurements of fission products in air at ground level are made regularly in Copenhagen using a high-volume air sampler and a 100-channel γ-spectrometer. A filter exposed during the period October 23–26, 1964, gave the first reliable indication of new fission-products by the appearance of the 1,596-keV line of lanthanum-140. The sample was a compressed filter containing dust from about 150,000 m^3 air **…** The concentration of lanthanum-140 was estimated as 5×10^{-5} pc./m^3. Filters sampled on October 28 and October 30 show concentrations which are approximately 10 and 100 times greater **…** This seems to prove that debris from the Sinkiang explosion reached Copenhagen by transportation in the upper troposphere in less than 10 days. Later measurements on a rain sample from October 23 finally proved that the transportation time did not exceed 7 days.

From *Nature* 27 March 1965

100 Years Ago

An allusion to musical sands may be found in one of the tales from the "Arabian Nights"—"The Story of the Two Sisters who were jealous of their Younger Sister." Prince Bahman, who was journeying in search of rarities and treasures, reaches the foot of a mountain, and while ascending "was assailed with the most hideous sounds," while others who followed him heard "groans, shouts, and all sorts of insulting epithets." One of the wonders they were in search of was the "Singing Tree," which "commenced to issue a series of exquisite strains of music" as soon as the Princess Parizadé saw it.

From *Nature* 25 March 1915

such as atomic clocks, magnetometers or accelerometers. ■

James K. Thompson *is at JILA and in the Department of Physics, University of Colorado, and the National Institute of Standards and Technology, Boulder, Colorado 80309, USA.*
e-mail: jkt@jila.colorado.edu

1. McConnell, R., Zhang, H., Hu, J., Ćuk, S. & Vuletić, V. *Nature* **519**, 439–442 (2015).
2. Christensen, S. L. *et al. Phys. Rev. A* **89**, 033801 (2014).
3. Appel, J. *et al. Proc. Natl Acad. Sci. USA* **106**, 10960–10965 (2009).
4. Bohnet, J. G. *et al. Nature Photon.* **8**, 731–736 (2014).
5. Haas, F., Volz, J., Gehr, R., Reichel, J. & Estève, J. *Science* **344**, 180–183 (2014).
6. Lücke, B. *et al. Phys. Rev. Lett.* **112**, 155304 (2014).
7. Sørensen, A. S. & Mølmer, K. *Phys. Rev. Lett.* **86**, 4431 (2001).
8. McConnell, R. *et al. Phys. Rev. A* **88**, 063802 (2013).

SYSTEMS BIOLOGY

Defiant daughters and coordinated cousins

Genetically identical cells can have many variable properties. A study of correlations between cells in a lineage explains paradoxical inheritance laws, in which mother and daughter cells seem less similar than cousins. **See Letter p.468**

ANDREAS HILFINGER & JOHAN PAULSSON

During the winter holidays, many of us are reminded of the complexities and challenges of family dynamics. Some traits, such as table manners or verbal tics, may run in the family; others, such as a passion for science or the law, might generate rebellion in the next generation. Repeated defiance could even cause behavioural traits to skip a generation, so that a child's apparent rebellion turns out to be an unconscious copying of a grandparent. Rebellious cells are harder to imagine, but in this issue, Sandler *et al.*[1] (page 468) demonstrate that pairs of cousins (cells with a common 'grandparent') are more similar to one another than are mothers and daughters, in terms of the time it takes them to grow and divide.

Intuitively, if one cell in a population has more or less of a particular component than the population average, levels of that component will tend to deviate in the same direction in that cell's daughters. Owing to subsequent random fluctuations, these deviations will decorrelate over time, such that compositions of genetically identical cells should become less correlated with each generation. Contrary to this expectation, observations[2,3] indicate that the time it takes one cell to become two — its doubling time — can show a stronger correlation between cousins than between mother–daughter pairs (Fig. 1). It has been unclear whether this surprising result reflects the fact that cells born at different times are exposed to different conditions, just as the teenagers of the 1980s behaved differently from those of the 1990s. But the current study demonstrates that, under tightly controlled conditions, the phenomenon persists.

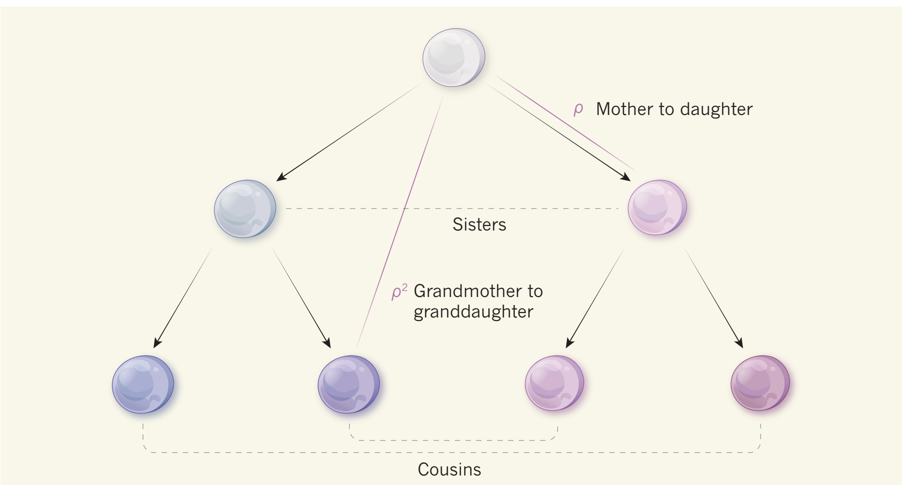

Figure 1 | Family values. When considering cellular inheritance, an intuitive model implies that each generation will display the previous generation's behaviour plus some stochastic variation. The entire family tree can then be reconstructed from the correlation coefficient ρ, which describes how much each generation decorrelates from its predecessor. For example, correlations between sisters and between grandmother–granddaughter pairs, which are both separated by two generations, are ρ^2. Similarly, cousin–cousin correlations are ρ^4 because, to go from one cousin to another, we have to move two generations up in the family tree and two down again, connecting cousins through the common grandmother. Sandler *et al.*[1] report that the time each cell takes to divide strongly violates this model, because these times are, on average, more similar between pairs of cousins than between mothers and daughters.

Simple inheritance laws seem to imply that this is impossible: if doubling times become uncorrelated in a single generation, how can they persist between cousins, which are separated by four generations of growth? Sandler and colleagues propose that an unknown factor that affects doubling times oscillates periodically in cells, such that cousins tend to be born in a similar phase, but mothers and daughters usually are not. A computational model showed this simple explanation to be consistent with the authors' findings in a mammalian cell type called a lymphoblast. Sandler *et al.* then analysed their data using measures borrowed from chaos theory[4], a field of mathematics that predicts seemingly random variation using non-random (deterministic) equations that merely amplify tiny changes in initial conditions. The results of this work further support the researchers' hypothesis that the variation they observed arises from a simple dynamical system, rather than from a random process. Finally, they reanalysed published data[5] for cyanobacteria, in which growth is coupled to circadian rhythms, and showed that cousins were indeed substantially more positively correlated than mothers and daughters.

Much of the variation in doubling times thus seems to reflect differences in the phase of an as-yet-unidentified internal oscillator, rather than stochastic factors, such as 'noisy' gene expression. A few decades ago, such a deterministic scenario might even have been the first guess. Differences between genetically identical cells were then often explained by nonlinear models, for example oscillations, chaos, or bistable switches. Noise was invoked only to explain infinitesimal perturbations that might eventually cause systems to diverge. Now the pendulum has swung the other way, and physiological heterogeneity is explained by random bursts of gene expression almost by default.

The problem is that both no-noise and all-noise views ignore the interconnectedness of random fluctuations and average dynamical

tendencies. In ballistics, the trajectories of projectiles can be considered in the absence of random gusts of wind, but in small chemical systems such as cells, randomness is a consequence of the basic mechanisms by which the system changes. For example, exponential decay at the level of population averages typically reflects exponentially distributed times of individual reaction steps. However, the term 'random' in this context does not imply an absence of patterns — the magnitude and time correlations of fluctuating concentrations always depend strongly on the underlying interactions. Processes in single cells are thus always shaped by both chemical noise and average dynamical tendencies, and the question is how to use the information hidden in population averages to understand more about both factors.

One lesson from previous work[6] is how tricky it can be to interpret variation mechanistically. In fact, even Sandler and colleagues' cell data could in principle be explained by noise. In a multicomponent network, the fact that one component or property shows no correlation between two time points does not imply that the process as a whole has become uncorrelated. For example, systems in which two random factors affect cell doubling times in opposite ways and decorrelate on different timescales can produce negligible correlations between mother and daughter cells, but substantial correlations between cousins. The tools from chaos theory must then be used very carefully, because they can make random processes seem deterministic depending on the sampling intervals used[7–9]. There is no particular reason to suspect that this type of behaviour occurs in mammalian cells, but such effects would also be hard to rule out. One of the most promising ways of analysing these effects may in fact be extensions of Sandler and co-workers' lineage-correlation analysis. By monitoring more properties and longer lineages, a wealth of extra correlation patterns becomes available without introducing further model parameters.

The authors' approach cannot be used for human family trees because, to be effective, conditions must be constant, and parents must reproduce asexually and thus 'disappear' to form the next generation. Such conditions would be a mixed blessing for adolescents — no parental oversight, but no sexual reproduction to pine for either — but a dream for cell biologists, because the assays are non-perturbative and yet provide more handles on complex dynamics. Given the explosion of microfluidics approaches, which allow tracking of cells for many generations in tightly controlled conditions, the types of lineage-correlation analysis introduced by Sandler *et al.* will probably bring many more important insights in the future. ■

Andreas Hilfinger *and* **Johan Paulsson** *are in the Department of Systems Biology, Harvard Medical School, Boston, Massachusetts 02115, USA.*
e-mail: johan_paulsson@hms.harvard.edu

1. Sandler, O. *et al. Nature* **519,** 468–471 (2015).
2. Powell, E. O. *J. Gen. Microbiol.* **18,** 382–417 (1958).
3. Froese, G. *Exp. Cell Res.* **35,** 415–419 (1964).
4. Grassberger, P. & Procaccia, I. *Physica D* **9,** 189–208 (1983).
5. Yang, Q., Pando, B. F., Dong, G., Golden, S. S. & van Oudenaarden, A. *Science* **327,** 1522–1526 (2010).
6. Huh, D. & Paulsson, J. *Nature Genet.* **43,** 95–100 (2011).
7. Theiler, J. *J. Opt. Soc. Am. A* **7,** 1055–1073 (1990).
8. Grassberger, P. *Scholarpedia* **2,** 3043, rev. 91330; http://dx.doi.org/10.4249/scholarpedia.3043 (2007).
9. Kantz, H. & Schreiber, T. *Nonlinear Time Series Analysis* (Cambridge Univ. Press, 2003).

This article was published online on 11 March 2015.

GALAXY FORMATION

When the wind blows

Astronomical observations of a luminous galaxy that has a central, mass-accreting supermassive black hole reveal how such entities launch and propel gas through galaxies at high speeds. See Letter p.436

JAMES E. GEACH

Models of how galaxies form require regulatory feedback mechanisms that control the growth of the galaxies' stellar mass. Without them, galaxies in simulated Universes would grow too big, too quickly[1]. Feedback can take many guises, but, for massive galaxies, the most important and perhaps also the most dramatic one is thought to be associated with the growth of supermassive black holes (SMBHs), which are ubiquitous at the centres of large galaxies. But no one really understands the details of how SMBH feedback works. Part of the problem is relative scale: the immediate sphere of influence of an SMBH is minute compared with the host galaxy that it inhabits. How does a single, tiny galactic component affect the fate of an entire galaxy? The main observational challenge is to link the astrophysical chain connecting galaxy-wide processes, such as

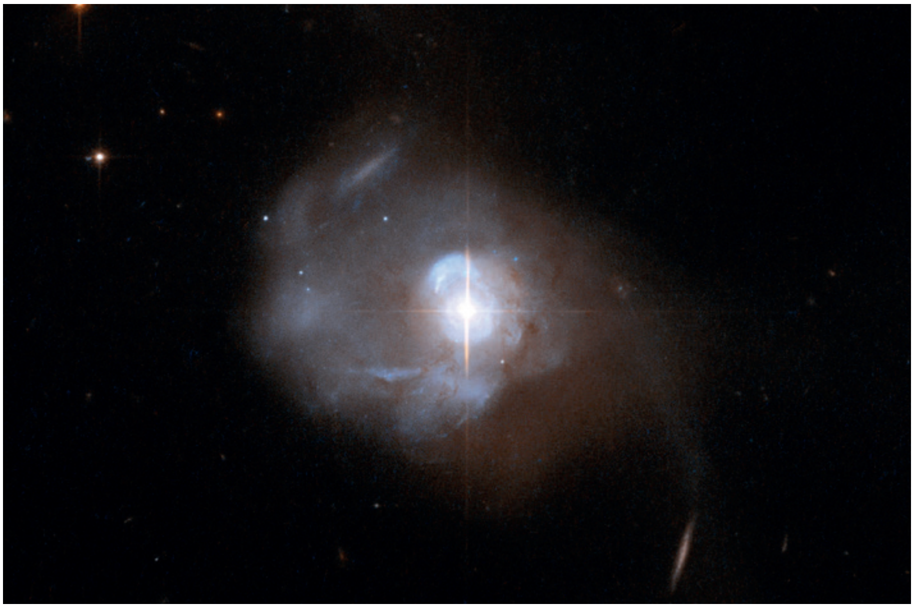

Figure 1 | A nearby quasar driving a molecular wind. Markarian 231, seen here in an image from the Hubble Space Telescope, is arguably the best example of a quasar in the local Universe: a galaxy harbouring a central, actively mass-accreting supermassive black hole. Like galaxy IRAS F11119+3257, the subject of Tombesi and colleagues' study[2], this quasar is driving an outflow of molecular gas, moving at 1,000 kilometres per second, that is potentially quenching star formation on galactic scales.

NASA, ESA, HUBBLE HERITAGE (STSCI/AURA) — ESA/HUBBLE COLLABORATION & A. EVANS (UNIV. VIRGINIA, CHARLOTTESVILLE/NRAO/STONY BROOK UNIV.)

large-scale outflows of gas, right back to their source, deep within the compact, complex and crowded environment of a galaxy's core. On page 436 of this issue, Tombesi *et al.*[2] provide just such a link.

SMBHs grow by swallowing (accreting) matter, releasing copious amounts of energy in the process[3] (Fig. 1). During such episodes, they are referred to as active galactic nuclei (AGNs), and energy is deposited in the interstellar medium either through powerful, radio-bright jets of magnetic fields and high-energy particles or through intense radiation from a hot accretion disk around the SMBH. These feedback channels are called the radio and quasar modes[4], respectively, with most AGNs falling into the latter class. There is convincing circumstantial evidence that both types of AGN can drive large-scale (hundreds of parsecs) outflows of molecular gas[5] — the dense component of the interstellar medium from which stars form — and can thus potentially quench star formation and regulate the growth of the SMBH. But how such winds are launched and propelled is unclear.

Hot disks form around SMBHs as surrounding gas, laden with angular momentum, is gravitationally accreted. Gravitational energy is converted to heat, causing the disk to blaze with ultraviolet and X-ray radiation. This radiation affects the immediate ambient, gaseous medium through processes including photoionization and radiation pressure. Both of these can launch high-velocity outflows of material near the disk, either by Compton heating, as photons scatter off free electrons in ionized gas, or through momentum transfer from the photons to interstellar dust and gas. High-velocity winds launched from the disk can drive a shock wave out through the galaxy that can heat, sweep up and possibly eject gas that would otherwise form stars. Unfortunately, the mechanics of the interface between the fast winds emanating from the accretion disk and bulk motion of the interstellar medium is poorly understood, because this environment is buried deep inside the galaxy and is heavily obscured.

Tombesi *et al.* have delved into the heart of a galaxy called IRAS F11119 + 3257 — a luminous galaxy with a central AGN. By detecting the telltale signature of the absorption of X-ray light by highly ionized iron atoms, they have revealed the 'inner wind' of gas within a few hundred astronomical units (Earth–Sun distances) of the black hole, travelling at about 25% of the speed of light. Such winds have been seen before, but what makes this study remarkable is that the authors have linked this inner wind with a large-scale (a few hundred parsecs) outflow of cold molecular gas detected in the same galaxy. This provides insights into the mechanism by which the central black hole is affecting its host galaxy.

A key question for astrophysicists is whether such outflows are momentum-conserving or energy-conserving. Such a description lies at the heart of theoretical frameworks of quasar-mode feedback[6]. In a momentum-conserving outflow, thermal energy in the shocked wind is rapidly radiated away, whereas if such radiative losses are low, then the outflow is described as energy-conserving. Determining which regime is in operation is crucial, because it can strongly affect the efficacy of star-formation quenching in the galaxy.

Energy-conserving outflows are thought to be more effective because they can entrain more material than their momentum-conserving counterparts, and their momentum flux increases as the shock front propagates through the interstellar medium. This seems to be the scenario for IRAS F11119 + 3257, with the momentum-conserving case being convincingly disfavoured. Another advance obtained from this study is a reasonable handle on the efficiency of the coupling between the inner wind and the molecular outflow: approximately 20% of the power of the inner wind is transferred to the larger-scale outflow.

Encouragingly, these observations support current models of quasar-mode feedback, suggesting that theory is at least on the right track. This work is a step forward because it provides empirically motivated input for implementations of AGN feedback in galaxy-formation models[7], and it highlights the symbiotic relationship that exists between theoretical and observational galaxy-evolution studies. The picture is far from complete; these observations are limited in their ability to constrain the geometries of the inner wind and the large-scale outflow, and so assumptions — albeit reasonable ones — have been made. These introduce inevitable uncertainties in the results, but the picture that Tombesi *et al.* present is a convincing one. The next steps will be to study the link between inner winds and bulk neutral- and ionized-gas outflows in a large sample of galaxies, both near and far away.

The outlook is bright: facilities such as the Atacama Large Millimeter/submillimeter Array (ALMA) image molecular outflows in galaxies with increasing clarity[8]; the planned European Extremely Large Telescope (E-ELT) will probe the dynamics of ionized-gas components with exquisite sensitivity; and future X-ray missions such as the planned Advanced Telescope for High-Energy Astrophysics (ATHENA) will offer revolutionary views of the high-energy physics associated with the front line of AGN feedback. As Tombesi *et al.* have shown, uniting the multiscale and multiphase astrophysics involved in feedback processes is the key to unlocking the secrets of galaxy growth. ■

James E. Geach *is at the Centre for Astrophysics Research (CAR), University of Hertfordshire, Hatfield AL10 9AB, UK.*
e-mail: j.geach@herts.ac.uk

1. Crain, R. A. *et al.* Preprint at http://arxiv.org/abs/1501.01311 (2015).
2. Tombesi, F. *et al. Nature* **519,** 436–438 (2015).
3. Silk, J. & Rees, M. J. *Astron. Astrophys.* **331,** L1–L4 (1998).
4. Hopkins, P. F. *et al. Astrophys. J.* **630,** 705–715 (2005).
5. Cicone, C. *et al. Astron. Astrophys.* **562,** A21 (2014).
6. Faucher-Giguère, C.-A. & Quataert, E. *Mon. Not. R. Astron. Soc.* **425,** 605–622 (2012).
7. Schaye, J. *et al. Mon. Not. R. Astron. Soc.* **446,** 521–554 (2015).
8. Bolatto, A. D. *et al. Nature* **499,** 450–453 (2013).

doi:10.1038/nature14323

MAP4K4 regulates integrin–FERM binding to control endothelial cell motility

Philip Vitorino[1], Stacey Yeung[1], Ailey Crow[1], Jesse Bakke[2], Tanya Smyczek[1], Kristina West[3], Erin McNamara[3], Jeffrey Eastham-Anderson[4], Stephen Gould[3], Seth F. Harris[5], Chudi Ndubaku[6] & Weilan Ye[1]

Cell migration is a stepwise process that coordinates multiple molecular machineries. Using *in vitro* angiogenesis screens with short interfering RNA and chemical inhibitors, we define here a MAP4K4–moesin–talin–β1-integrin molecular pathway that promotes efficient plasma membrane retraction during endothelial cell migration. Loss of MAP4K4 decreased membrane dynamics, slowed endothelial cell migration, and impaired angiogenesis *in vitro* and *in vivo*. In migrating endothelial cells, MAP4K4 phosphorylates moesin in retracting membranes at sites of focal adhesion disassembly. Epistasis analyses indicated that moesin functions downstream of MAP4K4 to inactivate integrin by competing with talin for binding to β1-integrin intracellular domain. Consequently, loss of moesin (encoded by the *MSN* gene) or *MAP4K4* reduced adhesion disassembly rate in endothelial cells. Additionally, α5β1-integrin blockade reversed the membrane retraction defects associated with loss of *Map4k4 in vitro* and *in vivo*. Our study uncovers a novel aspect of endothelial cell migration. Finally, loss of MAP4K4 function suppressed pathological angiogenesis in disease models, identifying MAP4K4 as a potential therapeutic target.

Cell migration relies on coordinated engagement and disengagement of cell–extracellular matrix interactions[1]. Integrin receptors bind extracellular matrix ligands and orchestrate cytoskeletal and signalling changes[2]. The affinity of integrins for extracellular matrix ligands increases when they bind FERM (4.1 protein, ezrin, radixin, moesin) domain-containing proteins such as talin[3]. Once engaged, integrins cluster into nascent focal complexes and recruit additional proteins, maturing into long, stable focal adhesions (FAs). As cells migrate, stable FAs disassembled to enable membrane retraction[4].

MAP4K4 and its invertebrate orthologues belong to the Ste20 family kinases[5], which are broadly expressed and affect many biological processes, including embryonic development[6,7] and inflammation[8]. MAP4K4 regulates multiple molecular pathways in a context-dependent manner[9–12], including integrin biology through unknown mechanisms[13,14].

Moesin, ezrin, and radixin comprise the ERM protein family (ERMs) and are substrates of MAP4K4[12]. Like talin, ERMs contain an amino-terminal FERM domain that binds transmembrane proteins and a carboxy-terminal tail that binds actin. Upon phosphorylation, the two domains dissociate and form a tether between actin and the plasma membrane to regulate cell–cell adhesion, endocytosis, cell polarity, and mitosis[15]. ERMs localize to retracting membranes in different cell types[16,17], but their role in this context remains unknown.

Here we report the discovery of a novel molecular pathway that regulates endothelial cell motility. MAP4K4 phosphorylates moesin, which displaces talin from INTβ1 to inactivate β1-integrin and promote FA disassembly, thereby enabling membrane retraction during endothelial cell migration. We developed chemical inhibitors against MAP4K4 that suppress pathologic angiogenesis *in vivo*, revealing a new opportunity to inhibit pathologic angiogenesis.

MAP4K4 enhances endothelial cell membrane retraction

We used a human umbilical vein endothelial cell (HUVEC) sprouting assay in three dimensional (3D) culture (Extended Data Fig. 1a) to screen chemical inhibitors against known targets. We found that GNE-220, a potent and selective inhibitor of MAP4K4 (Supplementary Table 1), altered HUVEC sprout morphology. On day 1, GNE-220 shifted the distribution of subcellular protrusion towards longer lengths (>40 μm) and increased total protrusions (Fig. 1a, b, Extended Data Fig. 1b–e, Supplementary Videos 1 and 2). Furthermore, control samples formed well-defined sprouts with multiple endothelial cells (red arrows, Fig. 1a), whereas GNE-220 induced wide and short aberrant structures (red arrowheads, Fig. 1a), probably owing to increased encounter of endothelial cell membrane protrusions between adjacent sprouts (Supplementary Videos 1 and 2). Control sprouts grew in length over time, but the GNE-220 treated structures were significantly shorter than the control sprouts (Fig. 1a, c). Since GNE-220 also inhibits a few other kinases (Supplementary Tables 1 and 2), we confirmed that the phenotype of GNE-220 was mediated by MAP4K4 inhibition by using individual and pooled siRNA against *MAP4K4* (*siMAP4K4*) and found that knockdown phenocopied GNE-220 treatment (Fig. 1a, b, Extended Data Fig. 1f, g). Knockdown with *siMAP4K4* did not alter levels of the closely-related kinases MINK, TNIK, and MAP4K5, nor did knockdown of these MAP4Ks phenocopy *siMAP4K4* (Extended Data Fig. 1h–j).

Although GNE-220 reduced sprout length, the cell numbers and proliferation remained unchanged (Fig. 1c, Extended Data Fig. 2a–c), implying that reduced migration, but not proliferation, delays sprout outgrowth. Consistent with a migration defect, GNE-220 and *siMAP4K4* reduced HUVEC scratch wound closure (Extended Data Fig. 2d). Since inhibition of the DLL4–Notch pathway also alters HUVEC sprout[18], we compared MAP4K4 versus Notch inhibition. While Notch inhibition increased endothelial cell numbers and proliferation, it did not increase subcellular protrusions (Extended Data Fig. 2a–c, e, f). Furthermore, MAP4K4 knockdown did not alter filopodia dynamics (Supplementary Video 3, Extended Data Fig. 2g), indicating that MAP4K4 and NOTCH have different functions.

We quantified membrane dynamics by time-lapse imaging of HUVEC sprouts with fluorescently labelled membranes and nuclei. Control sprouts exhibited frequent membrane protrusion, retraction, and

[1]Molecular Biology Department, Genentech, Inc., South San Francisco, California 94080, USA. [2]Chemical Biology and Therapeutics Department, St Jude Children's Research Hospital, Memphis, Tennessee 38105, USA. [3]Translational Oncology Department, Genentech, Inc., South San Francisco, California 94080, USA. [4]Pathology Department, Genentech, Inc., South San Francisco, California 94080, USA. [5]Structural Biology Department, Genentech, Inc., South San Francisco, California 94080, USA. [6]Discovery Chemistry Department, Genentech, Inc., South San Francisco, California 94080, USA.

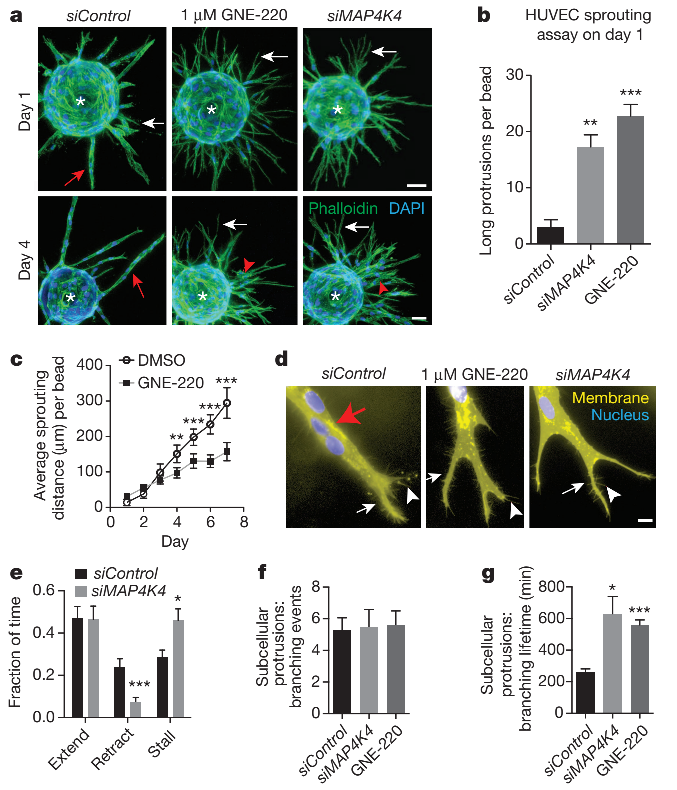

Figure 1 | MAP4K4 regulates endothelial cell membrane dynamics. **a**, Day 1 and day 4 HUVEC sprouting 3D culture treated with siRNA or GNE-220 and stained with phalloidin (green) and DAPI (blue). Scale bars, 50 µm. **b**, Long protrusions (>40 µm) per bead from 1-day cultures. Each bar represents mean of four experiments, >10 beads per experiment. **c**, Average sprout lengths per bead over time. >10 beads per condition, representative of three experiments. **d**, HUVEC sprouts expressing Lck–RFP (yellow), stained with Hoechst-33342 (blue), and treated with the indicated agents. Scale bar, 10 µm. **e**–**g**, Quantification of subcellular protrusions dynamics (**e**), branching events (**f**), and branching lifetime (**g**) from time-lapse videos. **e**, 13 sprouts per condition, representative of 3 experiments. **f**, **g**, Representing >8 sprouting event per condition, each sprouting event contained >40 branching events. **a**, **d**, Normal sprouts (red arrows), aberrant structures (red arrowheads), subcellular protrusions (white arrows), filopodia (white arrowheads) and beads (asterisks). For all figures, error bars represent standard error of the mean (s.e.m.); statistical significance between the indicated sample versus control or between the marked pairs are $^{*}P < 0.05$, $^{**}P < 0.01$, $^{***}P < 0.001$, or NS, not significant ($P \geq 0.05$); statistical analysis methods are described in the Methods section.

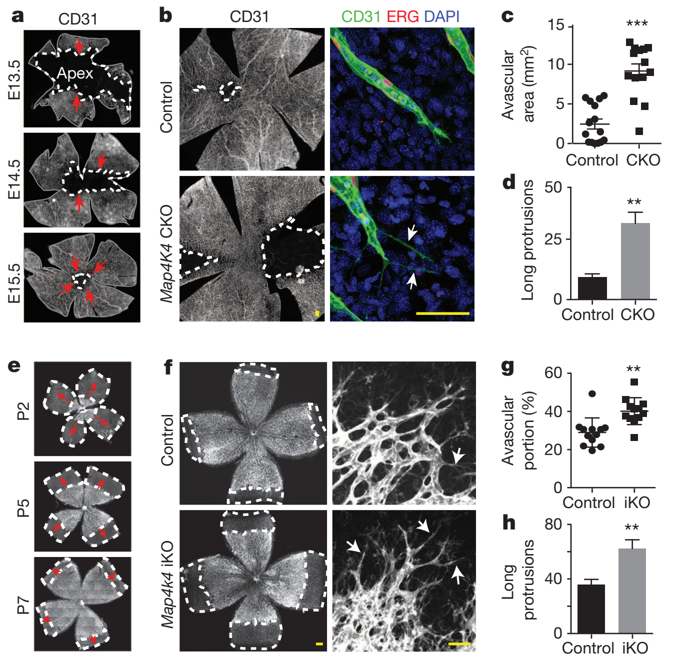

Figure 2 | *Map4k4* is essential for vascular development. **a**, Flat-mounted head skins immunologically stained for CD31 at the indicated embryonic stages. **b**, E15.5 head skins immunologically stained for the indicated markers (CD31 for endothelial cell, ERG for endothelial cell nuclei) and DAPI for all nuclei. Left, low magnification images. Right, close-up of tip cells with long membrane protrusions apparent in the bottom panel (arrows). **c**, Avascular areas in E15.5 head skins. Fifteen embryos for control, 14 embryos for CKO. Representative of 3 experiments, each experiment contained multiple litters of mice. **d**, Number of long membrane protrusions (>40 µm) along the vascular edge per mm length of vascular edge. Eight embryos per genotype, representative of 2 experiments, each experiment contained multiple litters of mice. **e**, Flat-mounted retinas stained for isolectin-B4 (vascular marker) at the indicated postnatal stages (P). **f**, P7 retinas with the indicated genotypes stained for isolectin-B4. Left, low magnification images. Right, close-up of tip cells with long membrane protrusions (arrows). **g**, Avascular area normalized to total retina areas. Twelve mice per genotype, representative of 3 experiments, each experiment contained multiple litters of mice. **h**, Numbers of long membrane protrusions (>40 µm) along the vascular front per centimetre of vascular front. Six mice for control, 7 mice for iKO, the entire circumference of each retina was quantified. Representative of two experiments, each experiment contained multiple litters of mice. Dotted lines demark avascular areas. Red arrows indicate direction of vascular growth. Scale bars, 50 µm.

bifurcation (Supplementary Video 3, Fig. 1d). With *MAP4K4* knockdown or inhibition, endothelial cells accumulated long, thin subcellular protrusions (Fig. 1d) owing to reduced retraction frequency and increased stalling frequency of these protrusions (Figs 1e, 3c). We also quantified branching events in the subcellular protrusions over 16 h. *MAP4K4* knockdown or inhibition did not change branching frequency but increased protrusion lifetime (Fig. 1f, g), suggesting that the failure to retract results in the accumulation of normally transient membrane protrusions.

MAP4K4 regulates vascular development *in vivo*

Map4k4 knockout (KO) caused embryonic lethality at embryonic day 9.5 (E9.5) due to mesodermal patterning defects[7]. To assess the role of MAP4K4 in vascular development, we generated a floxed allele of *Map4k4* (*Map4k4*$^{fl/fl}$) (Extended Data Fig. 3a) and crossed it to Tie2-Cre mice to induce endothelial cell conditional knockout (CKO). Loss of transcription of the sequence encoded by *Map4k4* exon 6 in embryonic endothelial cells was confirmed (Extended Data Fig. 3c). Heterozygous CKOs had no apparent defect. However, no live homozygous CKOs (*Map4k4*$^{cko/cko}$) were born, suggesting embryonic lethality (Extended Data Fig. 3b).

Analysis of E9.5–E17.5 embryos found no apparent defect in *Map4k4*$^{cko/cko}$ embryos up to E13.5 (data not shown). At E14.5, ~95% of *Map4k4*$^{cko/cko}$ embryos had multifocal oedema and haemorrhage; at E15.5, haemorrhage and oedema were systemic in all *Map4k4*$^{cko/cko}$ embryos, culminating in lethality by E16.5 (Extended Data Fig. 3d). We then examined vascular patterns in the head skins because vessels grow from the periphery towards the apex of the skull in a stereotypic pattern between E13 and E15 (Fig. 2a). At E15.5, while the head skin in control embryos had little avascular area, large avascular areas were apparent in *Map4k4*$^{cko/cko}$ embryos, suggesting delayed vascular development (Fig. 2b, c). Although vessel coverage was delayed in *Map4k4*$^{cko/cko}$ head skins, endothelial cell number and proliferation were unaffected (Extended Data Fig. 3e–g), implicating defective endothelial cell migration. In addition, CKO vessels near the vascular front accumulated long subcellular protrusions (Fig. 2b, d, Extended Data Fig. 3h, i), recapitulating the *in vitro* phenotype. Examination of cell–cell junctions with VE-cadherin staining revealed no difference between control and CKO

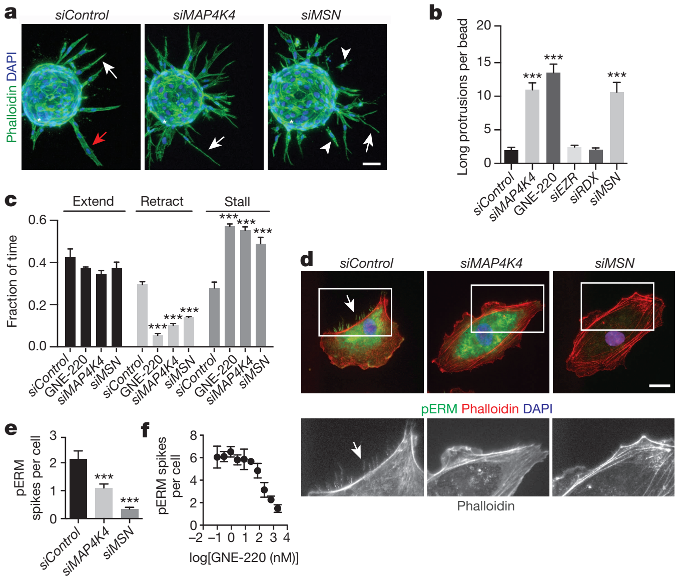

Figure 3 | MAP4K4 and moesin regulate membrane retraction. **a**, HUVEC sprouts from cells transfected with the indicated siRNAs after 1 day in culture. Arrows and asterisks defined as in Fig. 1a. Arrowheads indicate fragmented sprouts. Scale bar, 50 μm. **b**, Long protrusions (>40 μm) per bead from HUVEC sprouting cultures treated with pooled siRNAs targeting the indicated genes. *EZR*, ezrin; *MSN*, moesin; *RDX*, radixin. Each bar represents mean of 4 experiments, >10 beads per experiment. **c**, Quantification of membrane dynamics over a 16-h period in HUVEC sprouts treated with the indicated agents. Each bar represents mean of four beads, >15 sprouts per bead. Representative of 3 experiments. **d**, HUVEC transfected with the indicated siRNA were stained with phalloidin (red in top panels, white in bottom panels), pERM (green), and DAPI (blue). Bottom panels are enlarged views of the boxed regions. Scale bar, 20 μm. Arrow indicates retraction fibres. **e**, Quantification of pERM-positive retraction fibres in HUVEC transfected with the indicated siRNA. Means of 3 experiments, >500 cells per experiment. **f**, Dose–response curve of GNE-220 on pERM-positive spikes. Line shows best-fit, variable slope response curve. Four biological replicates, >100 cells per replicate, representative of 2 experiments.

animals (Extended Data Fig. 4a, b). Furthermore, MAP4K4 knockdown or inhibition did not alter permeability in HUVEC cultures (Extended Data Fig. 4c).

We then examined the postnatal retinal vasculature, which also develops in a stereotypic manner[19] (Fig. 2e). One-day-old pups (P1) born from *Map4k4*$^{fl/fl}$::Rosa26.CreERT2 mice were injected with tamoxifen to induce *Map4k4* KO (iKO) (Extended Data Fig. 4d). Like the embryonic head skin, P7 *Map4k4*$^{iKO/iKO}$ retinal vessels exhibited delayed outward migration and accumulation of long membrane protrusions without change in endothelial cell proliferation (Fig. 2f–h, Extended Data Fig. 4e, f) nor pericyte coverage (Extended Data Fig. 4g, h), further indicating that *Map4k4* regulates endothelial cell migration.

Moesin mediates the membrane retraction effect of MAP4K4

To identify substrate(s) of MAP4K4 in endothelial cells, we performed a siRNA screen targeting 60 candidates, including all MAP3Ks and factors involved in cell migration and membrane dynamics. Moesin emerged as a strong candidate because pooled or individual *MSN* siRNAs phenocopied MAP4K4 inhibition (Fig. 3a, b, Extended Data Fig. 5a, b). Although moesin is closely related to radixin and ezrin, *siMSN* alone was sufficient to phenocopy *siMAP4K4* (Fig. 3b), possibly owing to its higher expression in endothelial cells[20]. Time-lapse analysis showed that *siMSN* reduced retraction frequency with a concomitant increase in membrane stalling (Fig. 3c), similar to *siMAP4K4*. Unlike *siMAP4K4*, *siMSN* also caused sprout fragmentation (Fig. 3a, arrowheads), likely due to a MAP4K4-independent function[15].

Phosphorylation at threonine 558 (T558) activates moesin[15]. Consistent with a previous report[12], we found that recombinant MAP4K4 phosphorylates recombinant moesin (Extended Data Fig. 5c, d). Because western blot of HUVEC lysates revealed only a marginal reduction in phospho-ERM (pERM) in *MAP4K4* knockdown HUVEC versus control (Extended Data Fig. 5e), we examined pERM distribution in HUVEC by immunofluorescence staining. Control cells contain two pools of pERM: one in the cell centre, and one in clustered fibres at the cell periphery (Fig. 3d). In time-lapse images, these clustered fibres were associated with retracting but not extending membranes (Supplementary Video 4), and therefore were defined as retraction fibres. While *siMSN* reduced all pERM, *siMAP4K4* only affected pERM in the retraction fibres (Fig. 3d, e). Actin staining revealed a lack of retraction fibres in the *MAP4K4* and *MSN* knockdown cells (Fig. 3d, bottom panels), suggesting that localized ERM phosphorylation is required for the formation of retraction fibres. GNE-220 also reduced pERM$^+$ retraction fibres in a dose-dependent manner (Fig. 3f). These data suggest that MAP4K4 is required for ERM phosphorylation in retracting membranes.

MAP4K4 and moesin regulate FA disassembly

Membrane retraction occurs through the coordination of actomyosin contraction and FA disassembly[1]. As the level and distribution of p-myosin were similar in control, *MAP4K4* knockdown or GNE-220-treated HUVEC (Extended Data Fig. 6a, b), we investigated whether cell–extracellular matrix attachments were altered by *siMAP4K4* or *siMSN*. Since β1-integrin plays an important role in vascular development[21,22], we examined INTβ1 in endothelial cells. Staining of active INTβ1 showed an increase in the number of long FAs (Fig. 4a, b, Extended Data Fig. 6c, d) but no obvious change in nascent FAs marked by INTβ3 or INTαVβ5 (Extended Data Fig. 6d, e). Paxillin, a FA-associated protein, showed a similar phenotype (Extended Data Fig. 6e). GNE-220 also dose-dependently increased the number of active-INTβ1$^+$ long FAs (Fig. 4c). Since cell–extracellular matrix adhesion in 2D and 3D contexts can vary[23], we stained active INTβ1 in HUVEC sprouts.

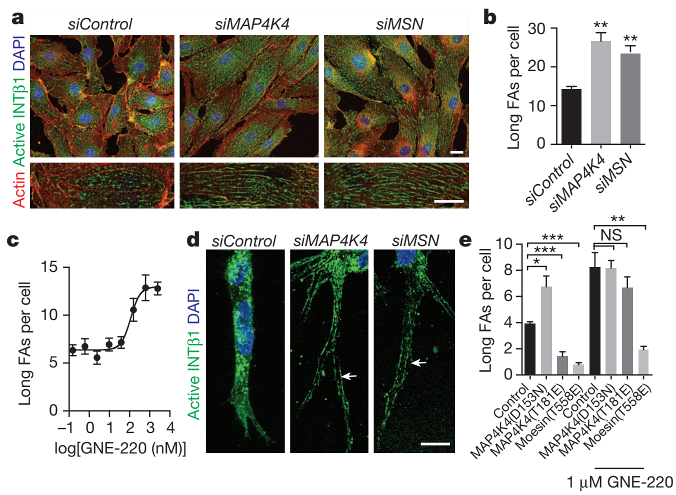

Figure 4 | MAP4K4 and moesin regulate FA length. **a**, Confocal images of HUVEC transfected with the indicated siRNA and stained for active INTβ1 (green) and with phalloidin (red) and DAPI (blue). Bottom panels, close-up views. **b**, Numbers of long FAs (defined in the Methods) per cell in HUVEC cultured for 3 days after siRNA transfection. Means of 3 experiments, 3 replicates per condition in each experiment, >500 cells per replicate. **c**, GNE-220 dose-dependently increased long FA numbers per cell on HUVEC after 18 h of treatment. Four biological replicates, >500 cells per replicate, representative of 3 experiments. **d**, HUVEC sprouts in 3D stained for active INTβ1 (green) and with DAPI (blue). Arrows indicate long adhesions. **e**, Long FA numbers per cell in HUVEC stably expressing mutated MAP4K4 or moesin in the presence or absence of GNE-220. Four biological replicates, > 500 cells per replicate, representative of 2 experiments. Scale bars, 20 μm.

siMSN or *siMAP4K4* also increased long adhesions located within subcellular protrusions in 3D (Fig. 4d).

To investigate the epistatic relationship between MAP4K4 and moesin, we evaluated the effect of gain-of-function and loss-of-function mutations of these proteins. Overexpressing kinase-dead MAP4K4 (D153N) increased long FAs to a similar extent as *siMAP4K4* or GNE-220 (Fig. 4b, c, e). Conversely, overexpressing phospho-mimetic mutants of MAP4K4(T181E) or moesin(T558E) reduced long FAs (Fig. 4e). GNE-220 restored long FAs in cells expressing MAP4K4(T181E) but had little effect on cells expressing moesin(T558E), suggesting that moesin acts downstream of MAP4K4 (Fig. 4e). Additionally, wild-type moesin, but not mutant moesin(T558A), restores FA length in *MSN* knockdown cells, suggesting that phosphorylation is critical for the effect of moesin on FAs (Extended Data Fig. 6f, g).

Although ERM localization to retraction fibres was reported[24], the relationship between retraction fibres and FAs has not been established. To explore this relationship, HUVEC with green-fluorescent-protein-labelled mature FAs (tensin–GFP[4]) and membrane tracker were monitored with time-lapse imaging. Retraction fibres trailed immediately behind receding FAs, suggesting that retraction fibres mark sites of adhesion disassembly (Fig. 5a). Interestingly, pERM accumulated in the retraction fibres distal to the active INTβ1 without marked overlap (Fig. 5b), suggesting that the accumulation of pERM may be incompatible with the maintenance of active INTβ1 in the retraction fibres.

We next examined the distribution of haemagglutinin (HA)-tagged MAP4K4 and found it to be broadly distributed and present in retraction fibres (Extended Data Fig. 7a). It is possible that MAP4K4 activation rather than localization may account for its localized activity.

FA disassembly was measured by live-imaging of HUVEC expressing the FA markers tensin–GFP or paxillin–GFP[4]. While control cells exhibited extensive membrane retraction coincident with rapid FA disassembly, cells treated with GNE-220, *siMSN*, or *siMAP4K4* had similar FA assembly rates but much reduced FA disassembly rates, resulting in increased FA decay time (Fig. 5c, d, Extended Data Fig. 7b, c, Supplementary Video 5). These data demonstrate that MAP4K4 and moesin promote FA disassembly in retraction fibres, which may be achieved by either turnover or inactivation of surface INTβ1. To distinguish these two possibilities, we compared the distribution of pERM to total and active INTβ1 in retraction fibres. Unlike active INTβ1, total INTβ1 and pERM overlapped in retraction fibres (Extended Data Fig. 7d), suggesting that pERM is likely to regulate the activation rather than the level of INTβ1.

Moesin inactivates INTβ1 by suppressing talin binding

Talin-FERM domain activates INTβ1 by binding its intracellular domain (β1ICD)[3]. Similar to active INTβ1, talin and pERM were mostly non-overlapping in retraction fibres (Extended Data Fig. 7e). Because moesin and talin share similar protein domains, we tested if the FERM domain of moesin may displace talin-FERM from β1ICD to inactivate INTβ1. We measured integrin activation by FACS with a labelled peptide derived from fibronectin. As expected, expression of mCherry–talin-FERM fusion protein in CHO cells increased active INTβ1 (Fig. 5e). Overexpression of Venus–moesin-FERM fusion protein inactivated INTβ1 with or without exogenously expressed talin (Fig. 5e), suggesting that moesin-FERM inhibits talin-mediated integrin activation. Total integrin was moderately affected by talin and moesin expression, possibly as an indirect consequence of altered activation (data not shown). Unlike moesin-FERM, the FERM domain from the band4.1 protein did not inactivate INTβ1 (Extended Data Fig. 7f).

We then tested if moesin-FERM may compete with talin for binding to β1ICD. His-tagged β1ICD, but not a binding-deficient mutant β1ICD or an unrelated protein RKIP, was able to pull-down talin-FERM (Fig. 5f). Incubation of β1ICD with increasing levels of moesin-FERM showed dose-dependent binding that coincided with reduced talin association regardless of whether talin-FERM was added after (Fig. 5f, g) or before (Extended Data Fig. 7g, h) moesin-FERM. Conversely, talin

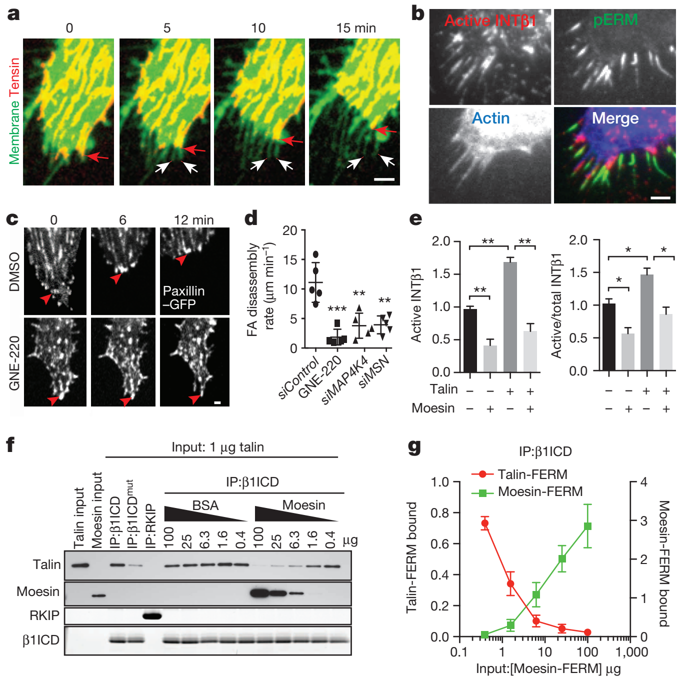

Figure 5 | MAP4K4 and moesin promote FA disassembly. **a**, Time lapse images of the retracting edge of a HUVEC expressing tensin–GFP (pseudo-coloured red) and stained with a fluorescent membrane dye (pseudo-coloured green) at indicated times. Red arrowheads mark sites of FA disassembly, white arrowheads mark the trailing membrane retraction fibres. **b**, Total internal reflection fluorescence images of the retracting edge of a HUVEC stained for active INTβ1 (red), pERM (green) and phalloidin (blue). **c**, Time lapse confocal images of HUVEC expressing paxillin–GFP undergoing membrane retraction at indicated times 1 h after addition of DMSO (dimethyl sulfoxide, as vehicle control) or GNE-220. Arrows mark disassembling FAs. **d**, FA disassembly rates in HUVEC stably expressing paxillin–GFP and treated with the indicated agents. Each dot represents mean of an individual cell, >8 FA disassembly events per cell, representative of 3 experiments. **e**, Mean fluorescence intensity of cell-surface active INTβ1 (left) or ratio of active versus total INTβ1 (right) in CHO cells overexpressing talin-FERM–Cherry or moesin-FERM–Venus fusion proteins (+), or Cherry and/or Venus without the fused protein (−). Means of 3 experiments. **f**, Recombinant wild-type or mutant integrin β1ICD-coated beads were incubated with the indicated proteins. The pulled-down or input proteins were analysed by western blotting. An irrelevant protein RKIP served as negative control. IP, immunoprecipitation. **g**, Quantification of talin and moesin associated with β1ICD-coated beads in the presence of increasing concentrations of moesin. Means of three experiments. Scale bars, 5 μm.

also competed with moesin for binding to β1ICD (Extended Data Fig. 7i). These data suggest that moesin-FERM can inactivate INTβ1 by competing with talin for binding to β1ICD.

To understand why moesin-FERM cannot activate INTβ1, we compared INTβ1 activation in CHO cells expressing talin-FERM, moesin-FERM, or chimaeras of talin- and moesin-FERM. Replacing talin-F3 with moesin-F3 abolished INTβ1 activation, whereas replacing talin-F1F2 with moesin-F1F2 partially inhibited its activity (Extended Data Fig. 7j). Consistent with previous report[25], our data suggests that the talin-FERM subdomains support a unique conformation required for INTβ1 activation, which moesin lacks.

Anti-INTα5β1 antibodies restore membrane retraction

As *siMAP4K4* or *siMSN* impaired INTβ1 inactivation, we tested whether forced integrin–extracellular matrix detachment with a function-blocking antibody against human α5β1-integrin (anti-INTα5β1, Extended Data Fig. 8a) could reverse the knockdown phenotype in the HUVEC sprouting assay. Treatment with anti-INTα5β1 indeed restored the retraction deficit in *siMAP4K4*, *siMSN*, or GNE-220-treated cells (Fig. 6a).

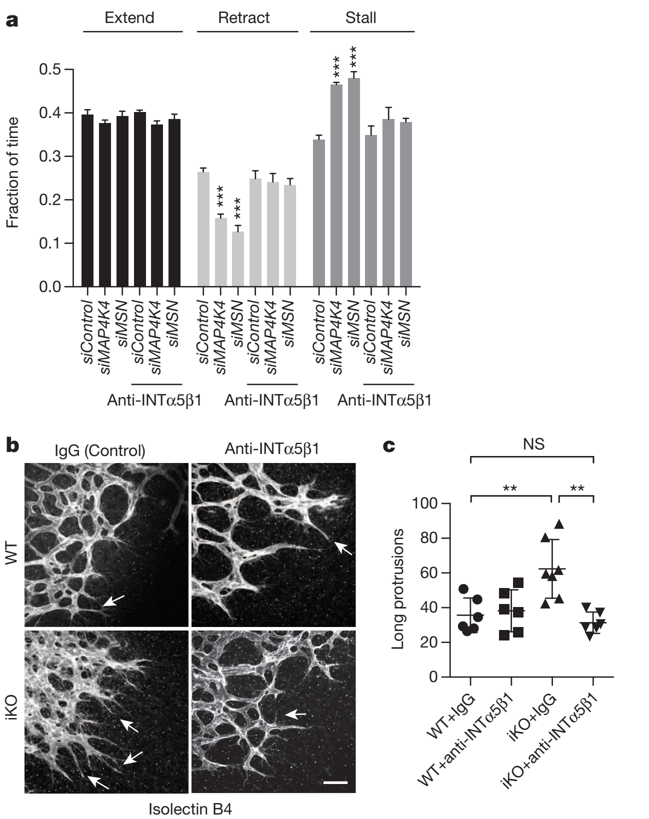

Figure 6 | Anti-INTα5β1 rescues *Map4k4* and *MSN* loss of function defects. **a**, Membrane dynamics in HUVEC sprouts from cells treated with the indicated reagents. Four beads per condition, >15 sprouts per bead were tracked over a 12-h period, representative of 3 experiments. **b**, Vascular front of P7 *Map4k4*$^{iKO/iKO}$ or wild-type retinas treated with a negative control antibody (IgG) or anti-murine-INTα5β1 antibody and stained for isolectin-B4. Arrows indicate long subcellular protrusions. **c**, Numbers of long membrane protrusions (>40 μm) per centimetre of retinal vascular edges. Each dot represents a mouse, the entire circumference of each retina was quantified. Representative of 3 experiments, each experiment contains multiple litters of mice. Scale bar, 50 μm.

We then used a function-blocking antibody against murine α5β1-integrin (Extended Data Fig. 8b) to test whether it can rescue the *Map4k4*$^{iKO/iKO}$ vascular defects. Although anti-INTα5β1 had no obvious effect on the retinal vessels in control mice, it reduced long membrane protrusions in *Map4k4*$^{iKO/iKO}$ mice, whereas a control antibody (IgG) did not (Fig. 6b, c). Deletion of *Map4k4* exon 6 in iKO pups was confirmed (Extended Data Fig. 8c).

These data support the hypothesis that MAP4K4 and moesin reduce talin–INTβ1 binding to inactivate INTβ1 and enable membrane retraction during endothelial cell migration (Extended Data Fig. 8d).

MAP4K4 regulates pathologic angiogenesis

Since angiogenesis contributes to human diseases, we evaluated the role of MAP4K4 in mouse models of cancer and eye disease. To inhibit MAP4K4 *in vivo*, we developed another MAP4K4 inhibitor, GNE-495, with good pharmacokinetic properties (Supplementary Table 1) because GNE-220 is rapidly cleared in rodents. GNE-495 was comparable to GNE-220 in each of the aforementioned cell-based assays (Extended Data Fig. 8e–g).

Implantation of *Map4k4*-wild-type tumour cells into *Map4k4*$^{iKO/iKO}$ mice revealed that loss of *Map4k4* in host tissues reduced tumour growth rate, tumour vascular perfusion, and endothelial cell membrane retraction (Extended Data Fig. 9a–g). In the oxygen-induced retinopathy model, GNE-495 reduced retinal neovascularization, vascular regrowth, and haemorrhage (Extended Data Fig. 9h–l). These data suggest that MAP4K4 regulates both normal and pathological angiogenesis.

Discussion

Cell migration requires assembly and disassembly of FAs. A number of mechanisms have been reported to regulate FA disassembly, including integrin internalization, degradation or inhibition of accessary proteins[26–28]. Here we identify a molecular cascade that promotes FA disassembly and highlight the importance of membrane retraction during angiogenesis.

Although our work focused on MAP4K4 in endothelial cells, published data suggest that MAP4K4 has a conserved role in regulating membrane dynamics across several species and cell types. In *Caenorhabditis elegans*, loss of the MAP4K4 homologue *mig-15* reduced axon branches in an ERM-dependent manner[29]. In *Drosophila*, the MAP4K4 homologue *msn* regulates epithelial cell migration during oocyte development by decreasing INTβ1 at the basal cell surface[30]. Together, these data demonstrate that MAP4K4 and its homologues have a conserved function in regulating membrane dynamics.

Note added in proof: Recently it was reported that MAP4K4 regulates focal adhesion disassembly in skin cells, indicating a conserved function of MAP4K4 in multiple cell types[31].

Online Content Methods, along with any additional Extended Data display items and Source Data, are available in the online version of the paper; references unique to these sections appear only in the online paper.

Received 6 December 2013; accepted 11 February 2015.
Published online 18 March 2015.

1. Ridley, A. *et al.* Cell migration: integrating signals from front to back. *Science* **302,** 1704–1709 (2003).
2. Hynes, R. O. Integrins: bidirectional, allosteric signaling machines. *Cell* **110,** 673–687 (2002).
3. Calderwood, D. A., Campbell, I. D. & Critchley, D. R. Talins and kindlins: partners in integrin-mediated adhesion. *Nature Rev. Mol. Cell Biol.* **14,** 503–517 10.1038/nrm3624 (2013).
4. Gardel, M. L., Schneider, I. C., Aratyn-Schaus, Y. & Waterman, C. M. Mechanical integration of actin and adhesion dynamics in cell migration. *Annu. Rev. Cell Dev. Biol.* **26,** 315–333 (2010).
5. Dan, I., Watanabe, N. M. & Kusumi, A. The Ste20 group kinases as regulators of MAP kinase cascades. *Trends Cell Biol.* **11,** 220–230 (2001).
6. Su, Y. C., Treisman, J. E. & Skolnik, E. Y. The *Drosophila* Ste20-related kinase misshapen is required for embryonic dorsal closure and acts through a JNK MAPK module on an evolutionarily conserved signaling pathway. *Genes Dev.* **12,** 2371–2380 (1998).
7. Xue, Y. *et al.* Mesodermal patterning defect in mice lacking the Ste20 NCK interacting kinase (NIK). *Development* **128,** 1559–1572 (2001).
8. Aouadi, M. *et al.* Orally delivered siRNA targeting macrophage Map4k4 suppresses systemic inflammation. *Nature* **458,** 1180–1184 (2009).
9. Kaneko, S. *et al.* Smad inhibition by the Ste20 kinase Misshapen. *Proc. Natl Acad. Sci. USA* **108,** 11127–11132 (2011).
10. Guntur, K. V., Guilherme, A., Xue, L., Chawla, A. & Czech, M. P. Map4k4 negatively regulates peroxisome proliferator-activated receptor (PPAR) gamma protein translation by suppressing the mammalian target of rapamycin (mTOR) signaling pathway in cultured adipocytes. *J. Biol. Chem.* **285,** 6595–6603 (2010).
11. Becker, E. *et al.* Nck-interacting Ste20 kinase couples Eph receptors to c-Jun N-terminal kinase and integrin activation. *Mol. Cell. Biol.* **20,** 1537–1545 (2000).
12. Baumgartner, M. *et al.* The Nck-interacting kinase phosphorylates ERM proteins for formation of lamellipodium by growth factors. *Proc. Natl Acad. Sci. USA* **103,** 13391–13396 (2006).
13. Lewellyn, L., Cetera, M. & Horne-Badovinac, S. Misshapen decreases integrin levels to promote epithelial motility and planar polarity in *Drosophila*. *J. Cell Biol.* **200,** 721–729 (2013).
14. Poinat, P. *et al.* A conserved interaction between β1 integrin/PAT-3 and Nck-interacting kinase/MIG-15 that mediates commissural axon navigation in *C. elegans*. *Curr. Biol.* **12,** 622–631 (2002).
15. Fehon, R. G., McClatchey, A. I. & Bretscher, A. Organizing the cell cortex: the role of ERM proteins. *Nature Rev. Mol. Cell Biol.* **11,** 276–287 (2010).
16. Lee, J. H. *et al.* Roles of p-ERM and Rho-ROCK signaling in lymphocyte polarity and uropod formation. *J. Cell Biol.* **167,** 327–337 (2004).
17. Gatto, C. L., Walker, B. J. & Lambert, S. Asymmetric ERM activation at the Schwann cell process tip is required in axon-associated motility. *J. Cell. Physiol.* **210,** 122–132 (2007).
18. Ridgway, J. *et al.* Inhibition of Dll4 signalling inhibits tumour growth by deregulating angiogenesis. *Nature* **444,** 1083–1087 (2006).
19. Dorrell, M. I. & Friedlander, M. Mechanisms of endothelial cell guidance and vascular patterning in the developing mouse retina. *Prog. Retin. Eye Res.* **25,** 277–295 (2006).

20. Berryman, M., Franck, Z. & Bretscher, A. Ezrin is concentrated in the apical microvilli of a wide variety of epithelial cells whereas moesin is found primarily in endothelial cells. *J. Cell Sci.* **105,** 1025–1043 (1993).
21. Carlson, T. R., Hu, H., Braren, R., Kim, Y. H. & Wang, R. A. Cell-autonomous requirement for beta1 integrin in endothelial cell adhesion, migration and survival during angiogenesis in mice. *Development* **135,** 2193–2202 (2008).
22. Zovein, A. C. *et al.* Beta1 integrin establishes endothelial cell polarity and arteriolar lumen formation via a Par3-dependent mechanism. *Dev. Cell* **18,** 39–51 (2010).
23. Harunaga, J. S. & Yamada, K. M. Cell-matrix adhesions in 3D. *Matrix Biol.* **30,** 363–368 (2011).
24. Amieva, M. R. & Furthmayr, H. Subcellular localization of moesin in dynamic filopodia, retraction fibers, and other structures involved in substrate exploration, attachment, and cell-cell contacts. *Exp. Cell Res.* **219,** 180–196 (1995).
25. Elliott, P. R. *et al.* The Structure of the talin head reveals a novel extended conformation of the FERM domain. *Structure* **18,** 1289–1299 (2010).
26. Bridgewater, R. E., Norman, J. C. & Caswell, P. T. Integrin trafficking at a glance. *J. Cell Sci.* **125,** 3695–3701 (2012).
27. Bhatt, A., Kaverina, I., Otey, C. & Huttenlocher, A. Regulation of focal complex composition and disassembly by the calcium-dependent protease calpain. *J. Cell Sci.* **115,** 3415–3425 (2002).
28. Bouvard, D., Pouwels, J., De Franceschi, N. & Ivaska, J. Integrin inactivators: balancing cellular functions *in vitro* and *in vivo. Nature Rev. Mol. Cell Biol.* **14,** 430–442 (2013).
29. Teulière, J., Gally, C., Garriga, G., Labouesse, M. & Georges-Labouesse, E. MIG-15 and ERM-1 promote growth cone directional migration in parallel to UNC-116 and WVE-1. *Development* **138,** 4475–4485 (2011).
30. Lewellyn, L., Cetera, M. & Horne-Badovinac, S. Misshapen decreases integrin levels to promote epithelial motility and planar polarity in *Drosophila. J. Cell Biol.* **200,** 721–729 (2013).
31. Yue, J. *et al.* Microtubules regulate focal adhesion dynamics through MAP4K4. *Dev. Cell* **31,** 572–585 (2014).

Supplementary Information is available in the online version of the paper.

Acknowledgements We thank L. Parker, R. Tam, K. Lyle, and B. Haley for contributing DNA constructs and siRNA design; H. Lu for initiating the chemical screen; J. Sudhamsu, P. Hass, J. Payandeh, and P. Lupardus for assisting with construct design and protein purification; J. Nonomiya, P. Wu, J. Wu, M. Lorenzo, H. Li, S. Schmidt for assay optimization, R. Ybarra and L. Magee for animal husbandry; S. Warming and M. Roose-Girma for generating floxed *Map4k4* mice; J. Boggs, T. Crawford, L. Wang, J. Drobnick and L. Gazzard for compound synthesis and pharmacokinetics studies; M. Sagolla for input on image acquisition and analyses; L. dePalatis, C. Reed for antibody generation, V. Pham, D. Kirkpatrick for kinase substrate screen, L. Murray, J. Burton and C. Wilson for discussions. H. Gerhardt for advice.

Author Contributions P.V. and W.Y. conceived the concept of the paper, designed most experiments, and co-wrote the paper. P.V. carried out the majority of the experiments. S.Y., E.M., S.G. carried out and supervised many *in vivo* studies. J.B., T.S., K.W. carried out several *in vitro* studies. S.F.H. carried out structural analysis of MAP4K4. C.N. is responsible for all experiments related to the generation and characterization of chemical inhibitors. A.C. and J.E.-A. wrote automated image analysis code and did some of the image data analyses. All authors contributed to the writing and proof-reading of the manuscript.

Author Information Reprints and permissions information is available at www.nature.com/reprints. The authors declare competing financial interests: details are available in the online version of the paper. Readers are welcome to comment on the online version of the paper. Correspondence and requests for materials should be addressed to W.Y. (loni@gene.com).

METHODS

***In vivo* studies.** All animals were handled according to guidelines from the Institutional Animal Care and Use Committee (IACUC) at Genentech, Inc.

The floxed *Map4k4* allele was generated using standard homologous recombination techniques. *Map4k4*$^{fl/fl}$ mice were crossed to Tie2-Cre mice[32] to generate conditional knockout (CKO) in the endothelium, or to Rosa26-CreERT2[33] mice to generate inducible knockout (iKO) in all tissues upon Tamoxifen induction. All mice used are in the C57BL/6N genetic background. For CKOs, timed pregnancies were set up between *Map4k4*$^{fl/+}$ and *Map4k4*$^{fl/+}$::Tie2-Cre parents, and E9.5-E18.5 embryos were analysed with plug date defined as E0.5. For iKOs, P1 pups with genotype of *Map4k4*$^{fl/fl}$ or *Map4k4*$^{fl/fl}$::Rosa26-CreERT2 were injected intraperitoneally daily with 80 mg per kg (body weight) tamoxifen dissolved in sunflower oil for 3 days, and P7 pups were analysed. For integrin rescue experiments, P1 pups were injected intraperitoneally daily with 80 mg per kg (body weight) Tamoxifen at 9 am, and 30 mg per kg (body weight) control antibody or anti-$\alpha5\beta1$ antibody at 5 pm for 3 days. Antibody injection continued for three additional days.

Oxygen-induced retinopathy (OIR) model[34] was used to mimics vascular pathologies in human proliferative diabetic retinopathy and retinopathy of prematurity. Wild-type C57BL/6 pups were raised in 75% oxygen from P7 to P12, then returned to room air with daily intraperitoneally dosing of 100 mg per kg (body weight) MAP4K4 inhibitor GNE-495 or vehicle for 5 days. P17 pups were analysed. Pups from each litter were divided into the control and treatment groups based on body weights to ensure similar body weight distribution between groups.

For tumour studies, animals were injected with 80 mg per kg (body weight) tamoxifen intraperitoneally, once daily for 5 days to induce *Map4k4* deletion. Two weeks later, male mice with the ages between 6 and 12 weeks were grouped based on body weight and genotype to ensure equal body weight distribution. Mice were inoculated subcutaneously on the right lateral flank with 10^6 KPP-1 cells in 100 μl HBSS/Matrigel or 0.5 million TC-1 cells in 100 μl HBSS/Matrigel. Tumours were measured twice a week until they reached IACUC specified limits. For histology analysis, tumours were harvested 2 weeks later when they reached 200–500 mm^3. For tumour perfusion experiments, tail vein injections of 100 μl of a 1 mg ml^{-1} solution of fluorescein-labelled lycopersicon esculentum (Vector FL-1171) were performed 5 min before tissue harvest.

During the in-life portion of the animal studies, investigators were not blinded with regard to the genotypes and treatments.

Cell culture. HUVEC (Lonza, CC-2519) were cultured in complete EGM-2 (Lonza, CC-3156 and CC-4176). siRNA and plasmid transfections were performed with DharmaFECT1 (Dharmacon) and Targefect (TargetingSystems), respectively. HUVEC were assayed 3 days after siRNA transfection. CHO cells (ATCC, CCL-61) were cultured in DMEM supplemented with 10% FBS, 1 mM glutamate, and penicillin/streptomycin and transfected using Lipofectamine LTX (Life Technologies). Cells were tested at Genentech to ensure mycoplasma-negative.

HUVEC assays. HUVEC sprouting assays were performed as previously described[35]. For siRNA treatment, HUVEC were transfected 1 day before coating to beads. For chemical inhibitor treatment, inhibitor was added to media after fibrin was clotted. For immunofluorescence staining, beads were seeded in thin 100 μl fibrin clots. For scratch wound healing assay, HUVEC were transfected 2 days before re-seeding into a glass-bottom 96-wells plate. Wound area was measured using the Incucyte instrument (Essen BioScience). Permeability assays were performed as described previously[36]. For moesin rescue, an siRNA oligo targeting the UTR region of moesin was transfected into cells. Two days later, cells were transfected with cDNA contructs expressing moesin–GFP or moesin(T558A)–GFP and plated into a glass-bottom 96-wells plate. After overnight incubation, cells were fixed and stained.

For Dll4 inhibition, a previously characterized function-blocking antibody was added to media before fibrin clotting to ensure immediate delivery[37].

Constructs and virus production. *MAP4K4* was cloned by PCR from a cDNA library prepared from HUVEC. Point mutants were introduced by site directed mutagenesis. For expression, *MAP4K4* or *Lck-RFP* was cloned into pGIPz lentiviral vector, which were co-transfected with pCMVΔ8.9 and pVSV-G in HEK293T cells to generate viral particles. HUVEC were infected at 1–5 multiplicity of infection per cell and selected with 200 μg ml^{-1} hygromycin for 3 days. Tensin–GFP and moesin constructs were obtained from Origene. Moesin (M1-P297) and talin (M1-Q435) FERM domains were synthesized (Blue Heron) and inserted into expression vectors pDEST47 and pmCherry-C1 (AddGene, 632524) with N-terminal Venus or mCherry fusion, respectively. For the experiment shown in Extended Data Fig. 7f, Band4.1 FERM domain (S215–R488) and moesin FERM domain (M1–P297) were cloned into mCherry vector, and talin FERM domain (M1–Q435) in the Venus vector. For FERM chimaeras, the F2-F3 boundary was defined as Gly 230 for talin and Gly 202 for moesin. Inserts were synthesized and cloned into pmCherry-C1.

Histology. Mouse embryos, neonatal eyes with opening in the cornea, or bisected tumours were fixed overnight (embryos and tumours) or 1 h (eyes) at 4 °C. The crown of the skull was harvested and the outermost skin layer removed. Retinas were isolated and other eye tissues discarded. Tumours were bisected at midline and cryoprotected in 30% sucrose overnight and embedded in Optimal Cutting Temperature Compound OCT (Tissue Tek, 4583), and sectioned at 12 μm and 80 μm using a Cryostat (Leica model CM3050S). Tissue was permeabilized in 0.5% Triton X-100/0.05% Tween-20/10% goat serum/PBS. Primary antibodies, including anti-CD31 (BD Biosciences, 550274) and anti-VECadherin (BD Biosciences, 555289 for cell, R&D AF1002 for mouse embryos), anti-ERG (Santa Cruz, sc-353), and anti-isolectin-B4 (Sigma, L2140-1MG) were incubated overnight. Flattened whole-mount tissues or tumour sections were mounted with Fluoromount-G (SouthernBiotech 0100-01).

HUVEC cultured on glass-bottom chamber slides or in fibrin clots were fixed with 4% paraformaldehyde/PBS for 10 min before permeabilization in 0.1% Triton X-100/PBS and block in 10% goat serum/PBS. Cells were stained with antibodies against pERM (CST, 3149S), active INTβ1 (12G10, Millipore, MAB2247-1; or 9EG7, BD Biosciences, 550531), phalloidin (Invitrogen, A12379), INTαVβ5 (Millipore, MAB2019Z, and MAB1961) INTβ3 (Millipore, MAB1974 and CBL479), paxillin (Epitomics, 1500-1), or total INTβ1 (R&D Systems, MAB1778). Cells were analysed with confocal, epifluorescent, or TIRF microscopy as specified in the figure legends. Integrin β3 and αVβ5 were used to mark nascent adhesions[38]. Although moesin played a dominant role in endothelial cells, we were unable to identify a specific antibody against phospho-moesin, and had to use a phospho-ERM antibody.

***In vitro* kinase assays.** His-tagged MAP4K4 kinase domain (A2-E328) was expressed and purified from SF9 insect cells using standard procedures. 3 μg of purified kinase containing a T181E activating mutation was incubated with 100 μM moesin peptide LGRDKYKTLRQIRQ (Genentech) or purified Myc–Flag–moesin (Origene, TP305674) in 50 mM HEPES pH 7.2/10 mM $MgCl_2$/1 mM EGTA/0.01% Triton X-100 for 45 min at room temperature in the presence or absence of 3 μM ATP. Remaining ATP levels were assayed using KinaseGlo (Promega).

FACS. FACS analysis of activated β1-integrin was performed as previously described[39]. Fibronectin III(8-10) peptide (KeraFast, EUR108) was biotinylated with SS-Biotin (Pierce, 21441). Analysis was run on LSR Fortessa Cell Analyzer (BD). Cells expressing mCherry, Venus, or Cherry-tagged and Venus-tagged fusion proteins were gated by FACS based on Cherry or Venus signal intensity to make sure that equal levels of expression were compared between samples and across experiments. For the Band4.1 and moesin FERM domains comparison experiment, integrin activation levels for cherry positive cells were normalized to Cherry negative cells in the same sample. In the experiment reported in Extended Data Fig. 7j, lower level of Cherry signal was chosen for reasons explained in the legend of the Extended Data.

Competitive binding to β1ICD. His–Flag–β1ICD-coated beads were prepared as described[40]. His–Flag-tagged wild-type and mutant (Y783A/Y795A) β1ICD[41] were purified from bacterial lysates using nickel beads (Sigma, H9914) followed by a size exclusion column. To remove aggregates, β1ICD was denatured with 8 M urea, and 1 mg of protein was loaded onto 50 μl of magnetic beads. After 1 h incubation, beads were renatured with decreasing urea concentrations and resuspended in 500 μl buffer XT (50 mM NaCl/150 mM sucrose/10 mM PIPES/3 mM $MgCl_2$/0.05%Ttriton/protease/ phosphatase inhibitor cocktail). Flag–talin-FERM and Flag–moesin-FERM were bacterially expressed and purified using anti-Flag beads. Both were eluted with 3× Flag peptide (Sigma). The negative control protein RKIP (Raf kinase inhibitor protein) was expressed and purified following similar protocol.

Image data acquisition and analysis. Investigators who carried out the automated image data analysis were blinded with regard to genotype and treatment at the step when individual images were segmented and quantified.

For membrane length detection, HUVEC coated beads were fixed and stained with phalloidin and DAPI to outline cells and nuclei, respectively. Compressed *z*-stack images from 4× epifluorescence scanning (ImageXpress Micro) were analysed with the MetaXpress Neurite detect algorithm. The sum of lengths from all protrusive structures was scored for each bead. This analysis does not distinguish between sub-cellular protrusions versus sprouts. Data presented in Figs 1a–c, 3a, b and Extended Figs 1b and 7a.

For live imaging of fluorescent HUVEC in sprouting assay, cells stably infected with lentiviral vectors were coated on beads and allowed to sprout for 2 days. Hoescht33342 was added atop the fibrin overnight. Fibrin clots were placed on 3i Inverted Marianas microscope with live cell chamber and imaged every 10 min at 20× for 16 h. Measurements were also carried out within the first 12 h of sprouting using unstained cultures imaged at 10× every 10 min. Subcellular membrane protrusion, retraction, and stalling were tracked manually in SlideBook. Sprouts consisting of cell bodies were excluded from this analysis. Protrusion and retraction were defined as membrane movements greater than 4 μm away from or towards the bead per 10 min interval, stalling was defined as movement less than 4 μm in either direction, branching was defined as bifurcating protrusions greater than 5 μm over a 16 h period. Data presented in Figs 1d–g, 3c, 6a.

For elongated FA measurement, transfected or inhibitor treated cells were placed on Leica spinning disk confocal and imaged at 40× every 3 min for ~ 8 h. Cells were stained with Far Red Membrane Tracker (Life Technologies, C34552) and transfected with tensin–GFP or infected with adenovirus expressing paxillin–GFP, or were stained with DAPI, antibody against activated β1-integrin, and phalloidin. For FA disassembly analysis, FA in retracting membranes were tracked to determine the rate of movement. For long FA decay time and FA assembly rate analysis, movies were uploaded to Focal Adhesion Analysis Server[42]. For FA decay time analysis, the first time point were chosen when a FA reached its longest length and was tracked for analysis. For assembly rates, adhesion tracks with a P value less than 0.05, R-squared greater than 0.7, and minimum slope of 0.01 were analysed. For elongated adhesion analysis, nuclei were segmented and counted using a top-hat filter followed by adaptive intensity threshold. Actin and adhesion stains were then segmented using a combination of adaptive and local intensity thresholds. Cell objects were created by a logical OR combination of adhesion and actin masks and were required to contain nuclear staining. Adhesions were further classified as puncta ($<2\ \mu m^2$), focal adhesions, or long focal adhesions (long FAs) defined as long and thin (eccentricity >5), with strong intensity (>1.5 times the mean of the intensity of all adhesions), and with minimal branching (solidity >0.3).

For quantification of pERM spikes: DAPI, phalloidin, and pERM images were segmented using both local and adaptive intensity thresholds. Cell objects were defined as regions that contained either actin or pERM staining and also contained a nuclear object. The cell body was selected by a morphological opening with kernel size of 10 μm to remove any protrusive structures. Protrusions were then identified as non-cell-body cellular structures of significant pERM intensity with area greater than $30\ \mu m^2$ and less than $650\ \mu m^2$. The number of pERM-positive protrusions per cell was calculated by dividing the number of protrusions per field of view by the number of nuclear objects in the same field.

For long membrane protrusions along the migration front of the embryonic head skin and the neonatal retinal vasculature: vascular stain from whole-mounted embryonic head skins or neonatal retinas was segmented with both local and adaptive intensity thresholds. To identify subcellular membrane protrusions along the migration front, gaps within the vascular network were filled to obtain a distinct edge, and thin membrane protrusions along the edge were identified by a morphological opening with kernel size of 15 μm. This diameter is too thin to contain a nucleus and, therefore, distinguishes subcellular structures. These structures were then further classified as subcellular protrusions if they were long and thin (eccentricity >2), had significant intensity ($>$mean intensity of the vascular stain), and had a length exceeding 40 μm. The eccentricity and length criteria were chosen because protrusions of this phenotype were rare in wild-type animals (data not shown). The length of the vascular edge was estimated by a flattened perimeter obtained by a series of morphological openings and closings with a maximum kernel of size 400 μm. The number of long subcellular membrane protrusions was counted and normalized by the length of the flattened vascular edge perimeter. The entire perimeter of a retina from each animal was quantified.

For pathologic vessel formation in the OIR model: 3D images of whole-mounted retinas from the OIR model were segmented for very bright ($>3\times$ the average vascular intensity in that plane) or moderately bright and large regions ($>6{,}000\ \mu m^2$ in a single plane). Normal vasculature was excluded by removing objects with aspect ratio greater than 4. All images were manually inspected to add missing segments or remove false positives. Pathological vascular coverage was then quantified as the ratio between total pathological vessel area and total retinal area.

For tumour vascular perfusion: entire sections of each tumour were scanned at 20× using the automated Tissuegnostic scanning system (http://www.tissuegnostics.com/). Viable tumour areas were identified by nuclei morphology based on DAPI staining. Total $CD31^+$ vascular areas were measured. Within the $CD31^+$ areas, $FITC^+$ areas were then measured and calculated as ratios to the total $CD31^+$ areas. These ratios are used to evaluate functionality of the tumour vasculature.

For tumour vascular patterning: tumour vasculatures were imaged by confocal microscopy at 40× magnification. Since areas at the border between tumour and overlying skin contain many sprouts, we focused our analysis in this region. Five tumours from each genotype, and 5–6 images per tumour were analysed. Lengths of membrane protrusion from each sprout are labelled and measured manually. A total of 85 membrane protrusions from the control tumours, and 84 protrusions from the Map4k4 iKO tumours were quantified. Results are expressed at percent of membrane protrusions greater than 40 μm per tumour.

For VE-Cadherin analysis, 80× confocal images were used to generate 10 μm junctional segments. Each segment was then scored as being inhibited (straight, linear junction), mixed (finger-like projections), or active (honeycomb or serrated), modelled on previous analyses[43]. The "active" junction refers to diffused or serrated junction that reflects junctional remodelling, the "inhibited" morphology refers to linear junctions that reflect relative junctional stability, and the "mixed" junction contains both morphologies within the defined length. The number of each segment type was scored as fraction of total segments in that image.

Image data were analysed using automated methods developed using customized Matlab codes in our group. All computer codes are deposited at the following site: (https://github.com/ailey/Vitorino_Nature_2015).

For all studies we did not exclude samples from analysis except Extended Data Fig. 9c, d. Six tissue sections were excluded in this study because they failed to show CD31 staining in large portion of the tumours, indicating technical failure. These sections were excluded from the analysis.

Statistical analysis. For all figures, statistical analyses were carried out using GraphPad Prism (http://www.graphpad.com/). The majority of data sets with sufficient n numbers to run the D'Agnostino & Pearson Omnibus normality test met the criteria for a normal distribution, therefore these data were analysed using unpaired Student's t-test. For data that did not pass the normal distribution test, Mann–Whitney test was used. For data sets that the n numbers were too small for D'Agnostino & Pearson Omnibus normality test, we assumed normal distribution based on the appearance of the data.

For all tests, variance similarity was determined using the Prism program. When variances were significantly different between comparators, Welch's correction was applied.

In all figures, statistical significance between the indicated sample and control or between marked pairs are designated: $*P < 0.05$, $**P < 0.01$, $***P < 0.001$, or NS ($P > 0.05$).

Endothelial cell isolation from E15.5 embryos and determination of *Map4k4* exon 6 expression. E15.5 embryos were harvested and dissociated into a single cell suspension using a combination of both enzymatic digestion with $1\ \mu g\ ml^{-1}$ of collagenase D (Roche, 11088866001) and gentle agitation with a gentleMACS Dissociator (Miltenyi Biotec). Cell suspension was incubated with anti-CD31 (BD Biosciences) conjugated Dynabeads (Invitrogen, 110.35), anti-CD31 was incubated with beads the night before), and separated into endothelial cells (those bound to beads) and non-endothelial cell (unbound cells). Total RNA was isolated using a RNeasy Mini Kit (Qiagen, 74134). cDNA was synthesized using a High Capacity cDNA Reverse Transcription Kit (Applied Biosystems, 4368814). Quantitative PCR on triplicate samples per condition was carried out using 50ng of cDNA in a ViiA7 machine (Applied Biosystems) using the Comparative CT program. *Map4k4* expression was determined relative to housekeeping gene *RPS13*. Primer/probe information is listed below. The *Map4k4* primers amplify sequences spanning exons 6 and 7. Endothelial cell purity was assessed by relative expression of VECadherin to housekeeping gene *RPS13*.

Mouse *Map4k4* primer/probe information. *Map4k4* Primer/Probe set: Applied Biosystems Mm00500800_mH, VECadherin Primer/Probe set: Applied Biosystems Mm00486938_m1,RPS13 probe and primers: 5′-CGGGTGCTCCCACCTAATT GGA-3′-FAM dye (probe), 5′-CACCGATTGGCTCGATACTA-3′ (forward primer) and 5′-TAGAGCAGAGGCTGTGGATG-3′ (reverse primer). Synthesized at Genentech.

Endothelial cell proliferation studies. For bead sprouting assays, 10 μM EdU (5-ethylnyl-2′-deoxyuridine) was added on day 3 of sprouting. Cells were fixed 16 h later. For head skin analysis, pregnant female mice were injected with 2 mg of EdU 4 h before embryo harvest. For retinal analysis, pups were injected with 50 mg per kg EdU on P6 before retinal harvest on P7. For all experiments, EdU was stained using Click-iT Imaging Kit from Invitrogen.

siRNA oligo sequences. *MAP4K4* siRNA: (1) 5′-GACCAACUCUGGCUUGU UA-3′, (2) 5′-UAUAAGGGUCGACAUGUUA-3′, (3) 5′-AGAGCGACAGA GACATTTATT-3′. *MSN* siRNA: (1) 5′-CGUAUGCUGUCCAGUCUAA-3′, (2) 5′-UCGCAAGCCUGAUACCAUU-3′, (3) 5′-GAGGGAAGUUUGGUUCU UU-3′, (4) 5′-GGTCTAAAGTGAGCTCTATGG-3′ (UTR). ON-TARGETplus Non-Targeting pool (negative control for all siRNA experiments): (1) 5′-UGG UUUACAUGUCGACUAA-3′, (2) 5′-UGGUUUACAUGUUGUGUGA-3′, (3) 5′-UGGUUUACAUGUUUUCUGA-3′, (4) 5′-UGGUUUACAUGUUUUCCUA-3′.

Generation and characterization of anti-α5β1-integrin monoclonal antibodies (MAbs)

Anti-human-α5β1-integrin MAb. HUVEC were used to immunize Armenian hamsters and the immunized animals were subsequently boosted with recombinant human INTα5β1 extracellular domain (expressed and purified at Genentech). A monoclonal antibody (18C12) that specifically recognized the heterodimeric human α5β1 but not the α5 or β1 subunit alone or other integrins was identified by conventional hybridoma techniques. The affinity of 18C12 for human INTα5β1 was determined by Scatchard analysis against HUVEC that expresses the murine antigen, the affinity is $K_D = 0.06$ nM.

The ability of the anti-human α5β1 MAB 18C12 to inhibit INTα5β1 function was assessed for its ability to inhibit the migration of HUVEC in a Boyden Chamber assay described below. HTS multiwell plates (24-wells with pore size 8 μm from Becton, Dickinson and Company) were coated with $1\ \mu g\ ml^{-1}$ fibronectin in 0.05 M

sodium carbonate buffer (pH 9.6) at 4 °C overnight. After washing with phosphate-buffered saline (PBS), 500 μl of EGM-2 medium (Lonza, CC-3162) with 0.1% bovine serum albumin (Sigma-Aldrich, A1933) was added to the bottom well. 50,000 HUVEC in 100 μl EGM-2 with 0.1% BSA were added to the top well and allowed to attached for 1 h. A human IgG1 control antibody at 10 μg ml^{-1} (anti-gD, Genentech Inc.) and serial dilutions of 18C12 were added to the top well at the concentrations indicated in Extended Data Fig. 6a. To stimulate migration, 20 ng ml^{-1} of VEGF-A (R&D Systems, 293-VE) was added to the bottom chamber of each well after 15 min of incubation with the respective antibodies. The plates were then incubated for 6 h. Cells that did not migrate were scraped off the upper chamber with a sponge swab, washed with PBS and scraped again. Cells that migrated through the membrane to the bottom chamber were fixed with 500 μl methanol for 5 min and stained with 500 μl Sytox green (Molecular Probes) for at least 20 min or overnight while protected from light. Pictures of each well were taken using a 5× objective on an AxioVision AC camera (Carl Zeiss MicroImaging GmbH). NIH Image J software was used to count the migrated cells and PRISM (GraphPad Software) was used to present the results.

Anti-murine-α5β1-integrin MAb. Murine INTα5β1 protein was purified from frozen mouse uterus (Pel-Freeze Biologicals), which were homogenized in water + 0.5 mM phenylmethanesulphonylfluoride (PMSF) at 4 °C and centrifuged. The supernatant was discarded and membrane proteins were extracted from the pellet by stirring for 1 h at room temperature in 20 mM Tris pH 8, 1 mM EGTA, and 0.5 mM PMSF, centrifuged and resuspended in 20 mM Tris pH 7.5, 0.6 M KCl and 0.5 mM PMSF. This was again centrifuged and the pellet was lysed overnight at 4 °C in 20 mM Tris pH 7.5, 0.5% Triton X-100, 1 mM $CaCl_2$, 1 mM $MgCl_2$, and 0.5 mM PMSF. The lysate was centrifuged and supernatant was loaded onto a prepared column of Affi-Gel resin (Bio-Rad Laboratories, 153-6047) coupled to a rat anti-mouse INTα5β1 antibody (BD Pharmingen, clone 5H10). The column was washed with 20 mM Tris pH 7.5, 1 mM $CaCl_2$, 1 mM $MgCl_2$, 0.2 M NaCl and eluted with 50 mM sodium citrate pH 4, 0.1% Triton X-100. The presence of both α and β subunits in the purified sample was confirmed by mass spectrometry.

The purified murine INTα5β1 was subsequently used to immunize and boost Armenian hamsters. A monoclonal antibody (10E7) that specifically recognized the heterodimeric murine α5β1 but that also did not recognize either the α5 or β1 subunit alone or other integrins was identified by conventional hybridoma techniques. The affinity of 10E7 for murine INTα5β1 was determined by Scatchard analysis against murine endothelial cell line 2H11 (ATCC, CRL-2163) that expresses the murine antigen, the affinity is $K_D = 0.3$ nM.

The ability of the anti-murine α5β1 MAB 10E7 to inhibit INTα5β1 function was assessed for its ability to inhibit the migration of Chinese Hamster Ovary B2 cells[44] stably expressing murine α5β1 (CHOB2-mα5β1) on a fibronectin substrate in response to serum. Migration assay was carried out as described above with the following modifications: high glucose Dulbecco's modified Eagle medium was used instead of EGM-2, cells were stimulated to migrate by 1% fetal bovine serum (VWR, 97068-101) instead of VEGFA. A negative control hamster IgG antibody (anti-gD, Genentech Inc.) or serial dilutions of 10E7 were added in top wells at the concentrations indicated in Extended Data Fig. 6b before cells were stimulated to migrate.

Generation of MAP4K4 small molecule antagonists

General chemistry. All solvents and reagents were used as obtained. Reactions involving air or moisture sensitive reagents were carried out under nitrogen atmosphere. Microwave reactions were performed using CEM Discover and Biotage Initiator reactors. NMR spectra were recorded in a deuterated solvent with a Bruker Avance 300 or 400 MHz NMR spectrometer, and referenced to trimethylsilane (TMS). Chemical shifts are expressed as δ units using TMS as the external standard (in NMR description, s = singlet, d = doublet, *t* = triplet, q = quartet, m = multiplet, and br = broad peak). All coupling constants (*J*) are reported in Hertz. Mass spectra were measured with a Finnigan SSQ710C spectrometer using an ESI source coupled to a Waters 600MS HPLC system operating in reverse mode with an X-bridge phenyl column of dimensions 150 mm by 2.6 mm, with 5 μm-size particles. Analytical purity was >95% unless stated otherwise. The following analytical method was used to determine chemical purity of final compounds unless otherwise stated: HPLC-Agilent 1200, water with 0.05% trifluoroacetic acid (TFA), acetonitrile with 0.05% TFA, Agilent Zorbax SD-C18, 1.8 μM, 2.1 × 30 mm, 40 °C, 3–95% B in 8.5 min, 95% in 2.5 min, 400 μl min^{-1}, 220 nm and 254 nm, equipped with Agilent quadrupole 6140, ESI positive, 110–800 amu.

2-(3-Cyano-pyridin-2-ylamino)-acetamide. Glycinamide (8.8 g, 79.4 mmol) and sodium carbonate (4.6 g, 43.3 mmol) were suspended in DMSO (200 ml) and stirred at ambient temperature for 16 h. The solid was removed by filtration through Celite, the filtrate treated with 2-chloronicotinonitrile (10.0 g, 72.2 mmol) and potassium fluoride (10.0 g, 173.3 mmol) and heated at 120 °C for 4 h. The mixture was allowed to cool to ambient temperature then diluted with water (800 ml). The precipitated solid was collected by filtration, washed with dichloromethane (50 ml) and water (50 ml), then triturated with diethyl ether (100 ml), filtered and left to air dry which afforded the title compound as an off-white solid (6.7 g, 53%). ^{1}H NMR (400 MHz, DMSO-d_6) 8.26 (dd, *J* = 4.9 Hz, 1.8 Hz, 1H), 7.93 (dd, *J* = 7.6 Hz, 1.8 Hz, 1H), 7.40 (s, 1H), 7.12 (t, *J* = 4.9 Hz, 1H), 7.00 (s, 1H), 6.69 (dd, *J* = 7.6 Hz, 4.9 Hz, 1H), 3.34 (s, 2H).

2-(5-bromo-3-cyano-pyridin-2-ylamino)-acetamide. A solution of *N*-bromosuccinamide (7.1 g, 38.2 mmol) in *N,N*-dimethylformamide (20 ml) was added drop-wise over 25 min to a suspension of 2-(3-cyano-pyridin-2-ylamino)-acetamide (6.7 g, 38.3 mmol) in *N,N*-dimethylformamide (30 ml). On complete addition the mixture was allowed to stir at ambient temperature for 16 h then poured onto water (400 ml). The precipitated solid was collected by filtration, washed with water (50 ml) and left to air dry which gave the title compound as a white solid (8.35 g, 96%). ^{1}H NMR (300 MHz, DMSO-d_6) 8.35 (d, *J* = 2.5 Hz, 1H), 8.24 (d, *J* = 2.5 Hz, 1H), 7.36–7.44 (m, 2H), 7.01 (s, 1H), 3.85 (d, *J* = 5.6 Hz, 1H). LC/MS (ESI+): R_T = 2.23 min, *m/z*: 257 ($M+H^+$).

3-Amino-5-bromo-1*H*-pyrrolo[2,3-b]pyridine-2-carboxylic acid amide. A suspension of 2-(5-bromo-3-cyano-pyridin-2-ylamino)-acetamide (8.35 g, 32.7 mmol) and sodium hydrogen carbonate (5.5 g, 65.5 mmol) in ethanol (150 ml) was heated under reflux for 66 h. The mixture was allowed to cool to ambient temperature then cooled further in an ice/water bath. The precipitated solid was collected by filtration, washed with ethanol (15 ml), water (2 × 20 ml), ethanol (20 ml) and diethyl ether (20 ml) and left to air dry to afford the title compound as a yellow solid (5.9 g, 71%). ^{1}H NMR (300 MHz, DMSO-d_6) 8.38 (d, *J* = 2.3 Hz, 1H), 8.32 (d, *J* = 2.3 Hz, 1H), 7.19 (s, 2H), 5.82 (s, 2H). LC/MS (ESI+): R_T = 2.38 min, *m/z*: 257 ($M+H^+$).

5-Bromo-3-[(1-methyl-1*H*-pyrazole-4-carbonyl)-amino]-1*H*-pyrrolo[2,3-b]pyridine-2-carboxylic acid amide. A suspension of 3-amino-5-bromo-1*H*-pyrrolo[2,3-b]pyridine-2-carboxylic acid amide (5.9 g, 23.2 mmol) and 1-methyl-1*H*-pyrazole-4-carbonyl chloride (4.02 g, 27.8 mmol) in pyridine (350 ml) were heated at 80 °C for 18 h. The mixture was allowed to cool to ambient temperature then poured into water. The resultant precipitated solid was collected by filtration, washed with water and diethyl ether and dried at 60 °C under high vacuum pressure to afford the title compound (6.6 g, 78%). ^{1}H NMR (300 MHz, DMSO-d_6) 10.79 (s, 1H), 8.67 (d, *J* = 2.3 Hz, 1H), 8.46 (d, *J* = 2.3 Hz, 1H), 8.33 (d, *J* = 2.9 Hz, 2H), 7.93 (d, *J* = 0.8 Hz, 1H), 3.92 (s, 3H). LC/MS (ESI+): R_T = 2.54 min, *m/z*: 365 ($M+H^+$).

8-bromo-2-(1-methyl-1*H*-pyrazol-4-yl)-3,5-dihydro-4*H*-pyrido[3′,2′:4,5]pyrrolo[3,2-*d*]pyrimidin-4-one. A suspension of 5-bromo-3-[(1-methyl-1*H*-pyrazole-4-carbonyl)-amino]-1*H*-pyrrolo[2,3-b]pyridine-2-carboxylic acid amide (1.0 g, 2.74 mmol) in 10% w/w aqueous potassium hydroxide (8 ml) and ethanol (4 ml) was heated under microwave irradiation at 170 °C for 1 h. The mixture was allowed to cool to ambient temperature, diluted with water and the resultant precipitated solid was collected by filtration. The solid was washed sequentially with water, methanol:diethyl ether and diethyl ether and left to air dry. The remaining material was afforded as a white solid (762 mg, 80%). ^{1}H NMR (300 MHz, DMSO-d_6) 8.40-8.35 (m, 2H), 8.08 (s, 1H), 7.89 (s, 1H), 3.87 (s, 3H). LC/MS (ESI+): R_T = 6.98 min, *m/z*: 347 ($M+H^+$).

2-(1-methyl-1*H*-pyrazol-4-yl)-8-(4-(4-methylpiperazin-1-yl)phenyl)-3,5-dihydro-4*H*-pyrido[3′,2′:4,5]pyrrolo[3,2-*d*]pyrimidin-4-one. 8-bromo-2-(1-methyl-1*H*-pyrazol-4-yl)-3,5-dihydro-4*H*-pyrido[3′,2′:4,5]pyrrolo[3,2-*d*]pyrimidin-4-one (762 mg, 2.19 mmol) was dissolved in a mixture of 1,4-dioxane and DMSO and (4-(4-methylpiperazin-1-yl)phenyl)boronic acid was added at once followed by 1 M aqueous potassium acetate solution. To the mixture was added 1,1′-*bis*(diphenylphosphino)-ferrocene]dichloropalladium(II) (5 mol%) and the reaction mixture was heated with microwave irradiation at 100 °C for 1 h. The mixture was cooled to ambient temperature and filtered through a plug of Celite eluting with ethyl acetate. The filtrate was concentrated and the residue was purified by flash column chromatography (5–10% methanol/dichloromethane). The fractions containing the desired product were concentrated and dried under high vacuum pressure to yield 2-(1-methyl-1*H*-pyrazol-4-yl)-8-(4-(4-methylpiperazin-1-yl)phenyl)-3,5-dihydro-4*H*-pyrido[3′,2′:4,5]pyrrolo[3,2-*d*]pyrimidin-4-one (530 mg, 55%). ^{1}H NMR (300 MHz, DMSO-d_6) 12.55 (s, 2H), 8.81 (d, *J* = 2.3 Hz, 1H), 8.51–8.47 (m, 2H), 8.22 (s, 1H), 7.67 (d, *J* = 8.3 Hz, 2H), 7.07 (d, *J* = 8.3 Hz, 2H), 3.93 (s, 3H), 3.24–3.18 (m, 4H), 2.44–2.50 (m, 4H), 2.24 (s, 3H). LC/MS (ESI+): R_T = 5.05 min, *m/z*: 441 ($M+H^+$).

4-chloro-2-(1-methyl-1*H*-pyrazol-4-yl)-8-(4-(4-methylpiperazin-1-yl)phenyl)-5*H*-pyrido[3′,2′:4,5]pyrrolo[3,2-*d*]pyrimidine. 2-(1-methyl-1*H*-pyrazol-4-yl)-8-(4-(4-methylpiperazin-1-yl)phenyl)-3,5-dihydro-4*H*-pyrido[3′,2′:4,5]pyrrolo[3,2-*d*]pyrimidin-4-one (180 mg, 0.41 mmol) was suspended in neat $POCl_3$ under an inert atmosphere and heated under reflux for 12 h. The reaction mixture was allowed to cool to ambient temperature and evaporated. The resultant residue was treated with ice and the pH of the aqueous phase was adjusted to between 7 and 9 by the addition of saturated aqueous sodium hydrogen carbonate solution. The solid was collected by filtration, washed with water and diethyl ether and used crude in the next step.

4-methyl-2-(1-methyl-1*H*-pyrazol-4-yl)-8-(4-(4-methylpiperazin-1-yl)phenyl)-5*H*-pyrido[3′,2′:4,5]pyrrolo[3,2-*d*]pyrimidine (GNE-220). Tetramethyltin (0.023 ml, 0.168 mmol) was added to a degassed suspension of 4-chloro-2-(1-methyl-1*H*-pyrazol-4-yl)-8-(4-(4-methylpiperazin-1-yl)phenyl)-5*H*-pyrido[3′,2′:4,5]pyrrolo[3,2-*d*]pyrimidine (70 mg, 0.153 mmol), lithium chloride (19 mg, 0.458 mmol) and *bis*(triphenylphosphine)palladium(II) dichloride (11 mg, 0.015 mmol) in dimethylformamide (2 ml) and was heated under microwave irradiation at 140 °C for 20 min. The reaction mixture was diluted with water (10 ml), the precipitated solid was removed by filtration, then washed with water and diethyl ether. The filtrate was concentrated under reduced pressure and the resultant residue triturated with diethyl ether then methanol to give the title compound as a cream solid (29 mg, 43%). ^{1}H NMR (400 MHz, DMSO-d$_6$) δ 12.35 (s, 1H), 8.93 (d, J = 2.2 Hz, 1H), 8.68 (d, J = 2.2 Hz, 1H), 8.35 (s, 1H), 8.06 (s, 1H), 7.70 (d, J = 8.8 Hz, 2H), 7.07 (d, J = 8.8 Hz, 2H), 3.91 (s, 3H), 3.21 (t, J = 4.9 Hz, 4H), 2.79 (s, 3H), 2.47–2.45 (m, 4H), 2.23 (s, 3H). LC/MS (ESI+): R_T = 5.55 min m/z 439 (M+H$^+$).

5-Fluoro-2-(3-fluorophenyl)pyridine. After a mixture of 2-bromo-5-fluoropyridine (50 g, 0.284 mol), 3-fluorophenylboronic acid (48 g, 0.343 mol), Pd(dppf)Cl_2 (5.0 g, 6.8 mmol,) and K_2CO_3 (178.5 g, 0.568 mol) in dioxane/H_2O (500 ml /150 ml) was degassed 3 times, the mixture was heated to 80～100 °C for 3 h under N_2. The mixture was filtered through diatomite, and dioxane was removed under reduced pressure. Ethyl acetate (1.0 l) was added, and the organic phase separated, concentrated, and purified by column chromatography (20:1～10:1 petroleum ether:ethyl acetate) to give desired product (50 g, 92%). ^{1}H NMR (400 MHz, $CDCl_3$) δ 8.54 (s, 1H), 7.72–7.65 (m, 3H), 7.49–7.39 (m, 2H), 7.08 (m, 1H)

5-Fluoro-2-(3-fluorophenyl)pyridine 1-oxide. 5-Fluoro-2-(3-fluorophenyl) pyridine (50 g, 0.262 mol), *m*-CPBA (106 g, 0.523 mol, 2eq) in dichloromethane was heated at reflux for 16 h. After most of the starting material was consumed (as indicated by TLC), the mixture was cooled to room temperature, and a $Na_2S_2O_3$ solution was added slowly, until there was no peroxide left (KI starch paper). (Caution: peroxide may be explosive.). Dichloromethane was removed and the yellow precipitate was collected and washed with saturated $NaHCO_3$ solution, until 3-chlorobenzoic acid was completely removed. The crude compound was dried and was used in next step without further purification (45 g, 83%). ^{1}H NMR (400 MHz, $CDCl_3$) δ 8.23–8.25 (m, 1H), 7.53 (m, 1H), 7.49–7.36 (m, 3H), 7.16–7.09 (m, 2H).

3-Fluoro-6-(3-fluorophenyl)picolinonitrile. To a solution of 5-fluoro-2-(3-fluorophenyl)pyridine 1-oxide (38 g, 0.183 mol) in acetonitrile (400 ml) was added TMSCN (73 g, 0.734 mol) and Et_3N (93 g, 0.917 mol). After the mixture was heated at reflux for 12 h under N_2, it was concentrated and purified by column chromatography (20% ethyl acetate in petroleum ether) to give 3-fluoro-6-(3-fluorophenyl) picolinonitrile (20 g, 50%). ^{1}H NMR (DMSO-d_6 400 MHz) δ 8.47–8.44 (m, 1H), 8.21–8.19 (m, 1H), 7.91–7.83 (m, 2H), 7.56–7.54 (m, 1H), 7.34–7.29 (m, 1H).

Diethyl 2-(2-cyano-6-(3-fluorophenyl)pyridin-3-yl)malonate. To a stirred solution of NaH (11.15 g, 278.81 mmol, 60%) in tetrahydrofuran (100 ml) was added diethyl malonate (44.66 g, 278.81 mmol) in tetrahydrofuran (50 ml) drop-wise at 0 °C under N_2. After the reaction mixture was stirred at 0 °C for 10 min, 3-fluoro-6-(3-fluorophenyl)picolinonitrile (30 g, 138.8 mmol) in tetrahydrofuran (100 ml) was added. After the reaction mixture was heated at reflux for 4 h under N_2, it was extracted with ethyl acetate (500 ml ×2), washed with saturated NaCl (300 ml), dried over Na_2SO_4, and concentrated to give the crude title product, which was used for the next step directly (50 g, 100%).

Ethyl 2-(2-cyano-6-(3-fluorophenyl)pyridin-3-yl)acetate. To a solution of diethyl 2-(2-cyano-6-(3-fluorophenyl)pyridin-3-yl)malonate (50 g, 140.31 mmol) in DMSO (300 ml), was added H_2O (6 ml), LiCl (23.32 g, 550.02 mmol) and the mixture was stirred at 100 °C overnight. After cooling to room temperature, it was extracted with ethyl acetate (300 ml ×3), washed with sat NaCl (300 ml), dried over Na_2SO_4, concentrated and purified by column (petroleum ether:ethyl acetate = 8:1) to give the title product as white solid (20 g, 50% over two steps). ^{1}H NMR (400 MHz, DMSO-*d6*) δ 8.33 (d, J = 8.4 Hz, 1H), 8.11 (d, J = 8.4 Hz, 1H), 7.96–7.87 (m, 2 H), 7.59–7.54 (m, 1H), 7.36–7.31 (m, 1H), 4.16–4.10 (m, 2H), 4.02 (s, 2H), 1.19 (t, J = 7.0 Hz, 3H).

Ethyl 2-(2-cyano-6-(3-fluorophenyl)pyridin-3-yl)-3-(dimethylamino)acrylate. A solution of compound ethyl 2-(2-cyano-6-(3-fluorophenyl)pyridin-3-yl)acetate (50 g, 0.176 mol) and dimethylformamide-DMA (168 g, 1.41 mol) in dimethylformamide (200 ml) was heated at 80 °C overnight. The mixture was concentrated and purified by column chromatography to give the product (45 g, 75%). ^{1}H NMR (400 MHz, DMSO-*d6*) δ 8.24 (d, J = 8.4 Hz, 2H), 7.96 (d, J = 8.0 Hz, 2H), 7.92 (m, 1H), 7.88 (d, J = 8.4 Hz, 1H), 7.72 (s, 1H), 7.57–7.53 (m, 1H), 7.34–7.29 (m, 1H), 4.07–3.97 (m, 2H), 2.74–2.70 (s, 6H), 1.11 (t, 3H).

Ethyl 8-amino-2-(3-fluorophenyl)-1,7-naphthyridine-5-carboxylate. A mixture of ethyl 2-(2-cyano-6-(3-fluorophenyl)pyridin-3-yl)-3-(dimethylamino)acrylate (6.5 g, 19.15 mmol) and NH_4OAc (37 g, 478.84 mmol) in HOAc (60 ml) was heated at 80–100 °C overnight. The mixture was cooled to room temperature and poured into ice-water. The precipitate was collected and washed with ethanol (30 ml) to give the desired product, which was used directly in the next step (4.0 g, 67%). ^{1}H NMR (400 MHz, DMSO-*d6*) δ 9.21 (d, J = 8.8 Hz, 1H), 8.63 (s, 1H), 8.44 (d, J = 9.2 Hz, 1H), 8.43–8.40 (m, 1H), 8.23–8.21 (m, 2H), 8.04–8.00 (br, 1H), 7.57–7.53 (m, 1H), 7.32–7.29 (m, 1H), 4.32–4.27 (q, 2H), 1.34–1.31 (t, 3H).

8-Amino-2-(3-fluorophenyl)-1,7-naphthyridine-5-carboxylic acid. To a solution of ethyl 8-amino-2-(3-fluorophenyl)-1,7-naphthyridine-5-carboxylate (6.5 g, 20.88 mmol) in tetrahydrofuran/methanol/H_2O (10:2:1) (300 ml) was added NaOH (3.34 g, 83.5 mmol) at room temperature After the solution was stirred for 2 h at 65 °C, organic solvent was removed under reduced pressure and H_2O (50 ml) was added. The pH was adjusted to 8.0, the precipitate was collected by filtration and dried to give the desired product (5.9 g, 100%).

tert-Butyl 1-(cyclopropanecarbonyl)azetidin-3-ylcarbamate. To a mixture of cyclopropyl carboxylic acid (11.88 g, 138.01 mmol) in anhydrous dichloromethane (400 ml) was added diisopropylethylamine (44.59 g, 345.02 mmol) and HATU (*O*-(7-Azabenzotriazol-1-yl)-*N,N,N′,N′*-tetramethyluronium hexafluorophosphate; 52.47 g, 138.01 mmol). After the mixture was stirred at room temperature for 15 min, *tert*-butyl azetidin-3-yl carbamate trifluoroacetic acid salt (24.0 g, 115.01 mmol) was added and the reaction mixture was stirred at room temperature for another 3 h. The mixture was diluted by ethyl acetate, washed with saturated aqueous Na_2CO_3, saturated citric acid and brine. The organic layer was dried, concentrated, and purified by column to give the desired product (25.0 g, 90.5%). ^{1}H NMR (400 MHz, DMSO-*d6*) δ 7.58 (d, J = 7.6 Hz, 1H), 4.42 (t, J = 8.0 Hz, 1H), 4.34–4.26 (m, 1H), 4.03–3.99 (m, 2H), 3.67–3.64 (m, 1H), 1.52–1.46 (m, 1H), 1.38 (s, 9H), 0.71–0.65 (m, 4H).

(3-Aminoazetidin-1-yl)(cyclopropyl)methanone trifluoroacetic acid salt. To a solution of *tert*-butyl 1-(cyclopropanecarbonyl)azetidin-3-ylcarbamate (25.0 g, 104.04 mmol) in anhydrous dichloromethane (150 ml) was added trifluoroacetic acid (30 ml). After the reaction mixture was stirred at room temperature overnight, it was concentrated, and purified by column chromatography (10% CH_3OH in dichloromethane) to give the desired product (22.0 g, 89.1%). ^{1}H NMR (400 MHz, DMSO-*d6*) δ 8.19 (br, 3H), 4.50–4.46 (m, 1H), 4.19 (dd, J = 9.2, 3.2 Hz, 1H), 4.08–3.99 (m, 2H), 3.84–3.78 (m, 1H), 1.57–1.51 (m, 1H), 0.74–0.70 (m, 4H).

8-Amino-*N*-(1-(cyclopropanecarbonyl)azetidin-3-yl)-2-(3-fluorophenyl)-1,7-naphthyridine-5-carboxamide (GNE-495). To a solution of 8-amino-2-(3-fluorophenyl)-1,7-naphthyridine-5-carboxylic acid (500 mg, 1.77 mmol) in dimethylformamide (5 ml) were added PyBOP (benzotriazol-1-yl-oxytripyrrolidinophosphonium hexafluorophosphate; 1.10 g, 2.12 mmol) and diisopropylethylamine (456 mg, 3.53 mmol) at room temperature, followed by (3-aminoazetidin-1-yl) (cyclopropyl)methanone trifluoroacetic acid salt (297 mg, 2.12 mmol). After the mixture was stirred at room temperature overnight, it was poured into water, the solid was collected by filtration and washed with CH_3OH (10 ml) to give the desired product (400 mg, 56%). ^{1}H NMR (400 MHz, DMSO-d$_6$) δ 9.04–8.86 (m, 2H), 7.63–7.50 (m, 1H), 8.43 (d, J = 9.2 Hz, 2H), 8.34 (s, 1H), 8.25 (d, J = 8.1 Hz, 1H), 7.90–7.48 (m, 3H), 7.28 (td, J = 8.5, 2.6 Hz, 1H), 4.86–4.68 (m, 1H), 4.55 (t, J = 8.2 Hz, 1H), 4.24 (dd, J = 8.6, 5.3 Hz, 1H), 4.16 (t, J = 8.9 Hz, 1H), 3.89 (dd, J = 9.7, 5.5 Hz, 1H), 1.67–1.45 (m, 1H), 0.71 (dd, J = 7.9, 4.7, 4H). LC/MS (ESI+): m/z 406.4 (M+H$^+$).

32. Kisanuki, Y. Y. *et al.* Tie2-Cre transgenic mice: a new model for endothelial cell-lineage analysis *in vivo*. *Dev. Biol.* **230,** 230–242 (2001).
33. Seibler, J. *et al.* Rapid generation of inducible mouse mutants. *Nucleic Acids Res.* **31,** e12 (2003).
34. Connor, K. M. *et al.* Quantification of oxygen-induced retinopathy in the mouse: a model of vessel loss, vessel regrowth and pathological angiogenesis. *Nature Protocols* **4,** 1565–1573 (2009).
35. Nakatsu, M. N. *et al.* Angiogenic sprouting and capillary lumen formation modeled by human umbilical vein endothelial cells (HUVEC) in fibrin gels: the role of fibroblasts and angiopoietin-1. *Microvasc. Res.* **66,** 102–112 (2003).
36. Wilson, C. W. *et al.* Rasip1 regulates vertebrate vascular endothelial junction stability through Epac1-Rap1 signaling. *Blood* **122,** 3678–3690 (2013).
37. Ridgway, J. *et al.* Inhibition of Dll4 signalling inhibits tumour growth by deregulating angiogenesis. *Nature* **444,** 1083–1087 (2006).
38. Zaidel-Bar, R., Milo, R., Kam, Z. & Geiger, B. A paxillin tyrosine phosphorylation switch regulates the assembly and form of cell-matrix adhesions. *J. Cell Sci.* **120,** 137–148 (2007).
39. Bouaouina, M., Harburger, D. S. & Calderwood, D. A. *Talin and Signaling Through Integrins* Vol. **757,** Ch. 20, 325–347 (Humana Press, 2011).
40. Lad, Y., Harburger, D. S. & Calderwood, D. A. *Integrin Cytoskeletal Interactions* Vol. 426, 69–84 (Elsevier, 2007).
41. Pfaff, M., Liu, S., Erle, D. J. & Ginsberg, M. H. Integrin beta cytoplasmic domains differentially bind to cytoskeletal proteins. *J. Biol. Chem.* **273,** 6104–6109 (1998).
42. Berginski, M. E. & Gomez, S. M. The Focal Adhesion Analysis Server: a web tool for analyzing focal adhesion dynamics. *F1000Res.* **2,** 68 (2013).
43. Bentley, K. *et al.* The role of differential VE-cadherin dynamics in cell rearrangement during angiogenesis. *Nature Cell Biol.* **16,** 309–321 (2014).
44. Schreiner, C. L. *et al.* Isolation and characterization of Chinese hamster ovary cell variants deficient in the expression of fibronectin receptor. *J. Cell Biol.* **109,** 3157–3167 (1989).

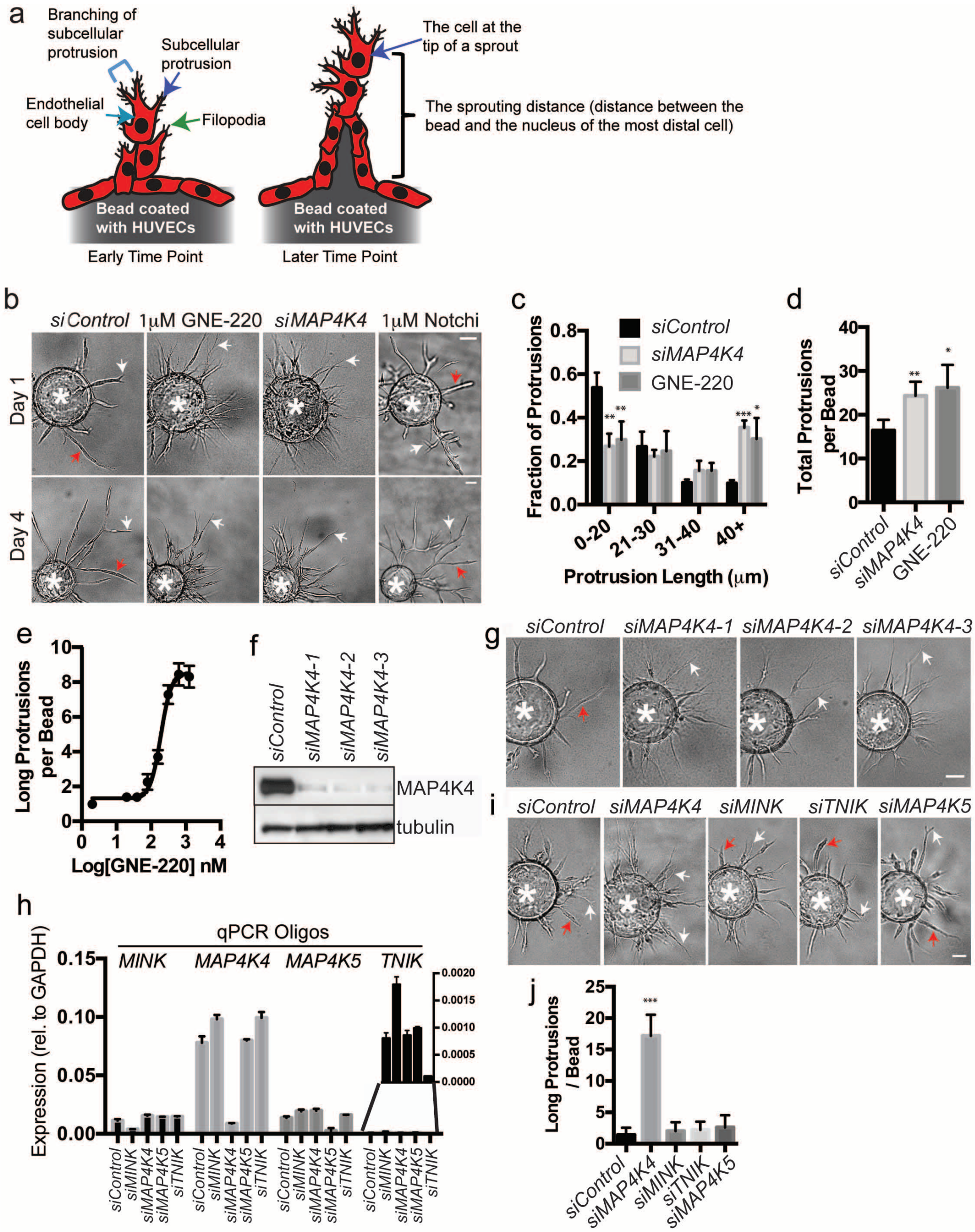

Extended Data Figure 1 | The roles of a subset of MAP4Ks and Notch in the HUVEC sprouting assay. **a**, A diagram illustrating the cellular and subcellular structures in the three-dimensional (3D) culture of HUVECs coated on beads[35]. A sprout refers to the multi-cell structure that resembles a capillary. These sprouts grow out of the HUVECs coated on the surface of the plastic beads, and their length increased over time. The structures associated with each individual endothelial cell in this culture system are indicated on the diagram. Subcellular protrusions are membrane structures between 5 and 10 μm in width and are irregularly shaped. Filopodia are significantly thinner than subcellular protrusions (<1 μm) and are linear. **b**, Representative bright field images of HUVEC sprouts treated with the indicated siRNA, GNE-220, or a Notch pathway inhibitor DBZ (Notchi) after 1 and 4 days in culture. These images were taken from similar cultures that generated data presented in Fig. 1a. These figures showed the two types of images we used to monitor and quantify HUVEC sprouting behaviours. Unlike *siMAP4K4* or GNE-220, DBZ did not increase subcellular protrusions and accumulation of aberrant structures near the beads; instead, it increased branching of capillary-like sprouts. **c**, Distribution of subcellular protrusion lengths in the HUVEC sprouting assay after 1 day in culture. Treatment with *siMAP4K4* or GNE-220 significantly increased the number of subcellular protrusions longer than 40 μm. Data represent means from 4 experiments. **d**, The number of total subcellular protrusions per bead from the same experiments as **b**. **e**, Dose–response curve relating the number of long protrusions (>40 μm) to GNE-220 concentration after 24 h with inhibitor treatment. $n = 4$ independent cultures. **f**, Western blot analysis showing *MAP4K4* knockdown efficiency in HUVEC for three independent siRNAs 72 h after transfection. **g**, Representative bright field images of HUVEC sprouts after 1 day in culture with *MAP4K4* knockdown using three independent siRNA. **h**, Quantitative PCR measuring mRNA levels of four closely related human *MAP4K* genes after knockdown with the indicated siRNA pools. Knockdown of *MAP4K4* does not affect other kinases. **i**, Representative bright field images of HUVEC sprouts after knockdown with the indicated siRNA after 1 day in culture. In **b**, **g** and **i**, red arrows indicate sprouts consisting of cell bodies, white arrows indicate subcellular membrane protrusions, and asterisks indicate beads coated with HUVEC. **j**, Quantification of experiment shown in **i** showing only *MAP4K4* knockdown results in increase of long protrusions (>40 μm). Scale bars, 50 μm. For all extended figures: error bars represent standard error of the mean (s.e.m.); statistical significance between the indicated sample versus control, or the marked pairs are: $^*P < 0.05$, $^{**}P < 0.01$, $^{***}P < 0.001$, or NS ($P \geq 0.05$) by statistical analysis described in the Methods.

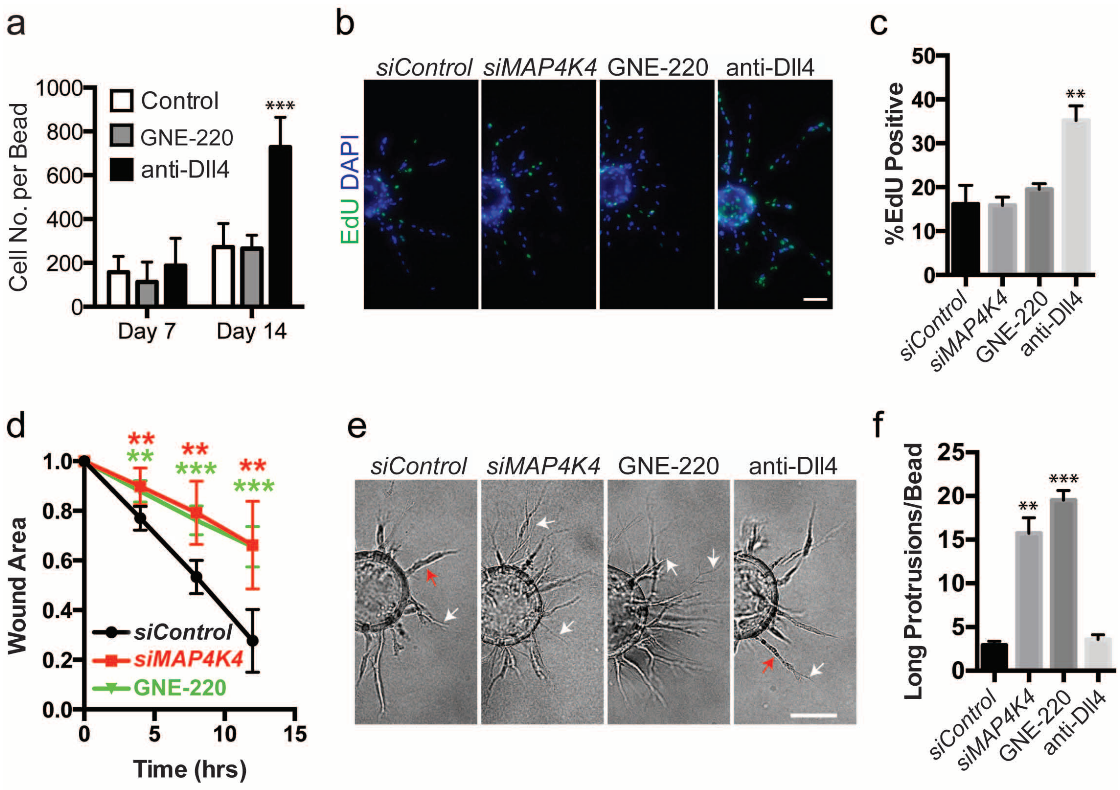

g

Filopodia Measurements	*siControl*	*siMAP4K4*
Growth Rate (μm/sec)	0.21 ± 0.05	0.26 ± 0.03
Number (number/μm)	0.054 ± 0.013	0.054 ± 0.012
Length (μm) *	15.3 ± 1.2	12.7 ± 1.2
Cycle Time (sec)	496 ± 204	423 ± 150

Extended Data Figure 2 | The roles of MAP4K4 and Dll4-Notch in regulating HUVEC proliferation, migration, and subcellular structures in the HUVEC sprouting assay. **a**, Quantification of HUVEC nuclei number per bead in the 3D culture at the indicated time points in the presence or absence of GNE-220 or anti-Dll4 antibody. While inhibition of Notch-Dll4 signalling increased cell number, GNE-220 had no significant effect. $n = 16$ beads per condition. Representative of 4 experiments. **b**, Representative images of HUVEC sprouts stained with DAPI (blue) and EdU (green). After 4 days in culture, cells were incubated with EdU for 16 h before staining and imaging. **c**, Quantification of percentage of nuclei that score as EdU positive. $n = 4$ experiments. **d**, Wound area as a function of time in the HUVEC scratch wound healing assay treated with control siRNA, *siMAP4K4* or GNE-220. $n = 6$ independent cultures. **e**, Representative images of HUVEC sprouts after 1 day in culture with the indicated treatments. *siMAP4K4* and GNE-220 increased long subcellular protrusions but anti-Dll4 had no effect on these structures. Red arrows indicate sprouts, white arrows indicate protrusions. **f**, Quantification of images shown in **e**. $n = 3$ experiments. **g**, Quantification of filopodia number and dynamics in HUVEC sprouts from experiments described in Supplementary Video 3. Scale bars, 100 μm.

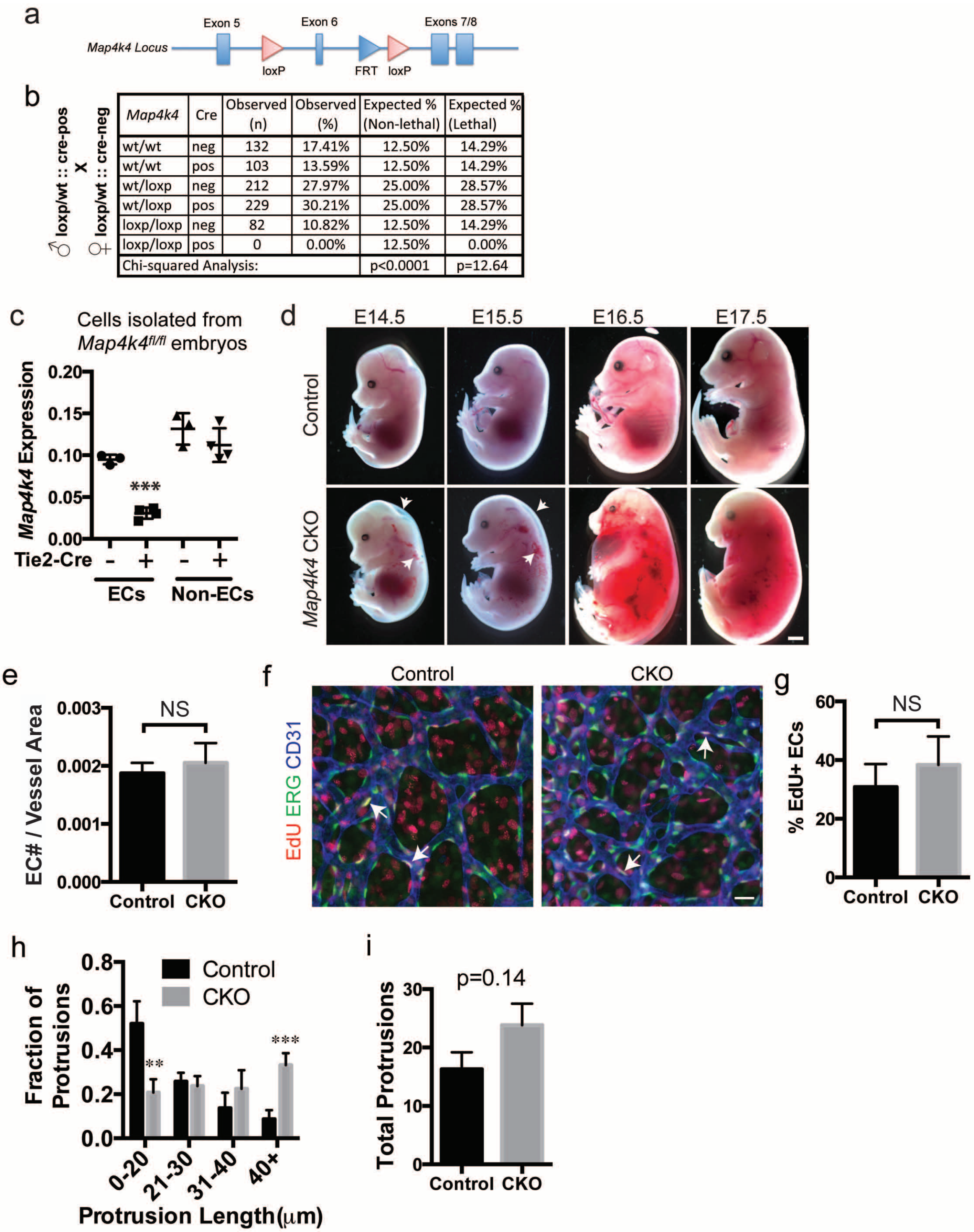

Extended Data Figure 3 | Additional characterizations of *Map4k4* conditional knockout mice. **a**, Schematic representation of the *Map4k4* floxed allele used in this study. When this floxed allele is present in cells expressing Cre, recombination results in the deletion of sequence encoding the MAP4K4 catalytic domain and introduces a stop codon at amino acid 144. If the truncated protein (amino acids 1–144) could be translated, it is expected to be non-functional and probably unstable. **b**, Summary of genotypes detected from progenies of the indicated cross. Genotype distribution is consistent with embryonic lethality based on Chi-squared analysis. *P* value indicates the probability of obtaining a distribution similar to the expected distributions for lethality or non-lethality. **c**, Quantitative RT–PCR analysis of *Map4k4* normalized to *mRPS13* in isolated endothelial cells and non-endothelial cells from $Map4k4^{fl/fl}$::Tie2-Cre positive (+) embryos versus $Map4k4^{fl/fl}$::Tie2-Cre negative (−) littermates. $n = 3$–4 embryos per genotype. **d**, *Map4k4* CKO embryos and wild-type littermates harvested at the indicated stages. Arrows indicate focal haemorrhage and oedema. Scale bar, 1 mm. **e**, Quantification of ERG-positive endothelial cell nuclei normalized to vascularized areas in E14.5 head skins derived from control or CKO embryos. $n = 7$ control embryos, 4 CKO embryos. **f**, Representative confocal images of E14.5 embryonic head skin after 4 h labelling with EdU. Vessels stained with CD31 (blue), endothelial cell nuclei stained with ERG (green), proliferating nuclei marked as EdU positive (red). White arrows indicate proliferating endothelial cells. **g**, endothelial cell proliferation in the embryonic head skins were quantified as % of EdU^{+} cells in all ERG^{+} cells. $n = 9$ control embryos, 7 CKO embryos. **h**, Fraction of membrane protrusions along the vascular front with indicated lengths in control and CKO embryonic head skins. $n = 3$ animals per genotype. Asterisks indicate statistics between control and CKO. **i**, Total number of protrusions along the vascular front in control and CKO head skins per mm vascular front. $n = 3$ animals per genotype.

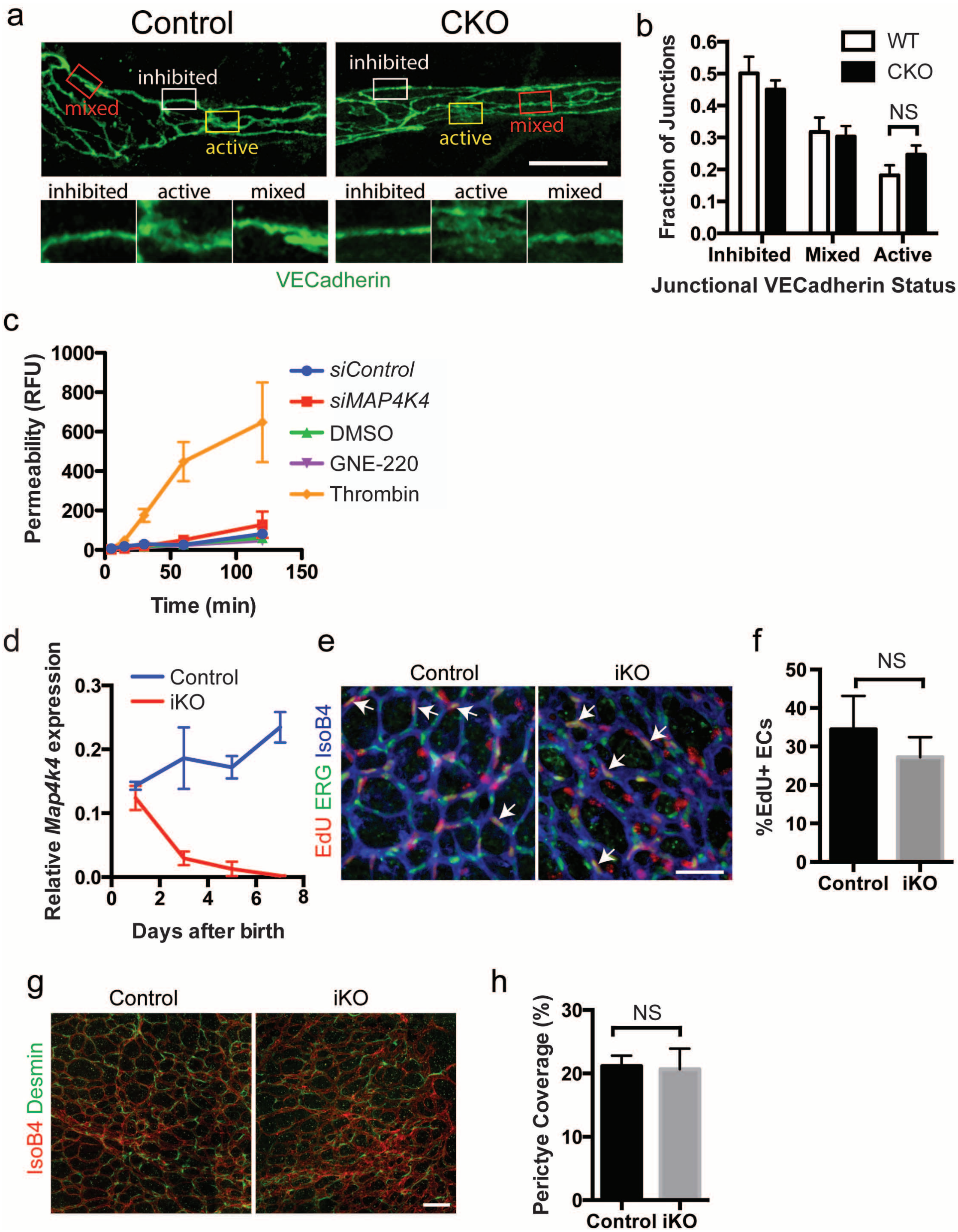

Extended Data Figure 4 | Additional characterizations of *Map4k4* conditional and inducible knockout mice. **a**, Confocal images of E14.5 head skin vasculature stained with VE-Cadherin in control and CKO embryos. Bottom panels are enlarged view of the boxed areas. **b**, Quantification of endothelial cell junction morphology in control and CKO animals shown in panel **a**. As defined in Bentley *et al.*[43], the "active" junction refers to diffused or serrated junction that reflects junctional remodelling, the "inhibited" morphology refers to linear junctions that reflect relative junctional stability, and the "mixed" junction contains both morphologies within the defined length. $n > 13$ regions per group, 2 embryos per genotype. Scale bars represent 12 µm. **c**, Permeability of confluent HUVEC monolayers with the indicated treatments was measured by FITC-dextran trans-well diffusion over time. $n = 3$ experiments. **d**, Quantitative RT–PCR results depicting *Map4k4* expression levels relative to *mRPS13* as a function of time after birth for control and iKO animals. Pups were injected with 80 mg per kg (body weight) tamoxifen once daily starting on P1, and mRNA were isolated and measured from tail clips on P3, P5, and P7. $n = 4$ control mice, 6 iKO mice for all time points. **e**, Representative confocal images of P7 retinal vasculature 16 h after EdU injection. Vessels stained with IsoB4 (blue), endothelial cell nuclei stained with ERG (green), proliferating nuclei marked as EdU positive (red). Arrows indicate EdU^{+} endothelial cells. **f**, Quantification of EdU^{+} endothelial cells normalized to total ERG^{+} cells in the retina. $n = 5$ control animals, 6 iKO animals. **g**, Representative confocal images of control and iKO retina on P7 stained with desmin to highlight pericytes (green) and IsoB4 to indicate endothelial cells (red). **h**, Quantification of pericyte coverage from experiments shown in **d**. $n = 6$ animals per genotype. Scale bars in **e** and **g**, 50 µm.

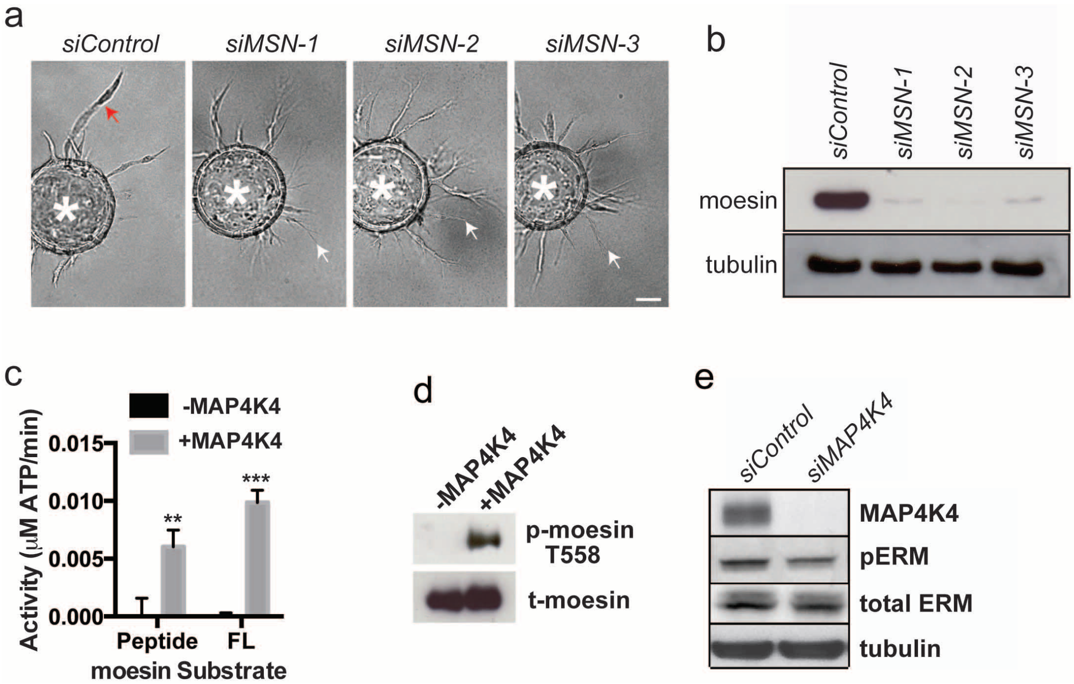

Extended Data Figure 5 | HUVEC sprouting assay with individual *MSN* siRNAs and MAP4K4 kinase activity on moesin. **a**, Representative bright field images of HUVEC bead sprouts transfected with three independent siRNA targeting *MSN* after one day in culture. Red arrows indicate sprouts consisting of cell bodies, white arrows indicate subcellular protrusions, and asterisks indicate beads coated with HUVEC. Scale bar, 50 μm. **b**, Western blot confirmed knockdown of *MSN* 72 h after transfection with three independent siRNAs. **c**, ATP consumption rates of recombinant activated MAP4K4 kinase domain against full-length moesin or a peptide corresponding to amino acids surrounding T558 in moesin. **d**, Western blot of reaction products from **c** showing moesin phosphorylation at T558. t, total. **e**, Western blot of the indicated total and phosphorylated (p) proteins from HUVEC transfected with the indicated siRNA. $n = 3$ experiments.

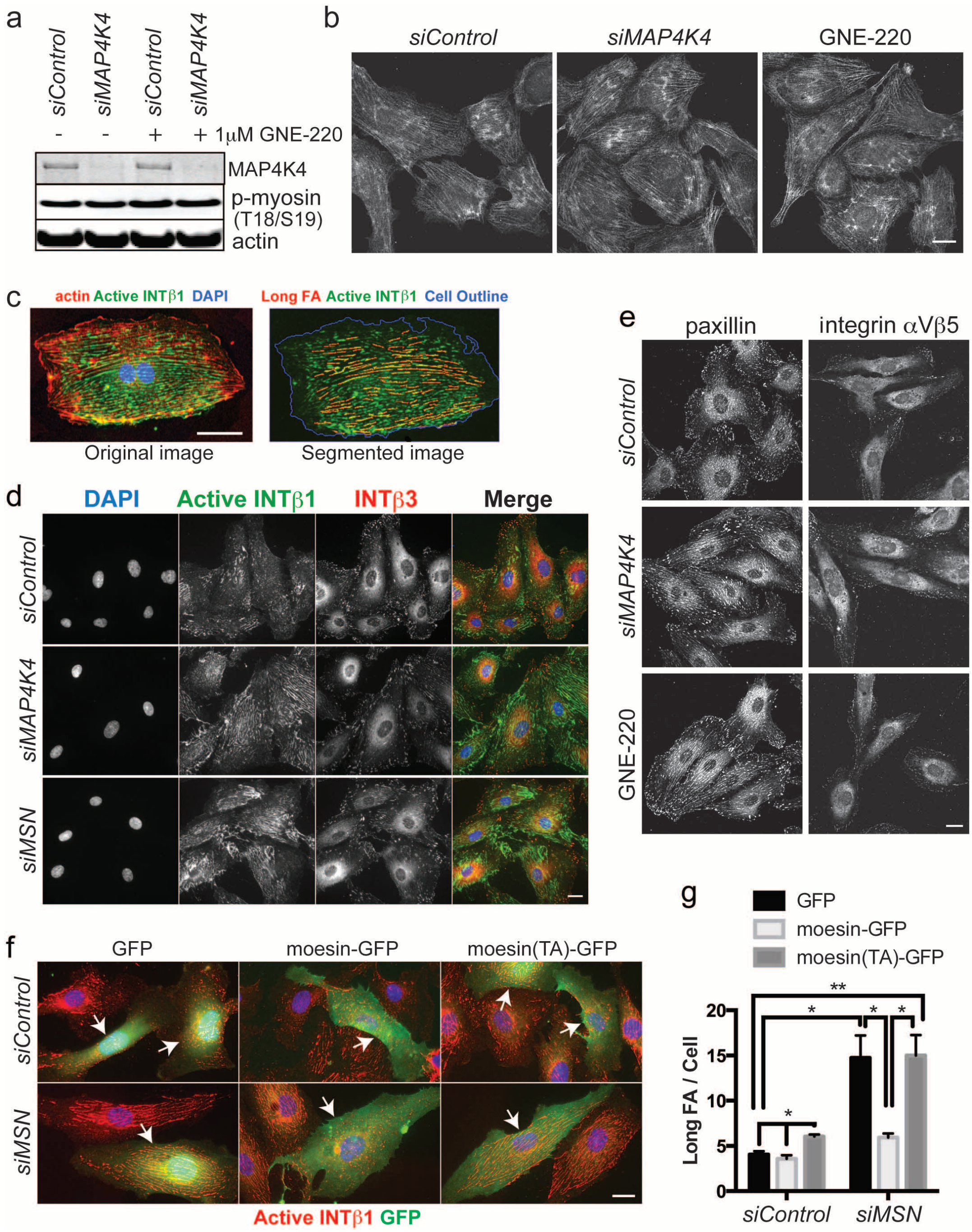

Extended Data Figure 6 | The roles of MAP4K4 and moesin on myosin and focal adhesions. **a**, Western blot analysis of HUVEC lysates 72 h after transfection with *MAP4K4* siRNA with (+) or without (−) 24 h treatment with GNE-220. **b**, Representative images of HUVEC treated with *siMAP4K4* or GNE-220 and stained with p-myosin. **c**, A representative image of HUVEC stained with phalloidin to highlight actin (red), active INTβ1 (green), and DAPI (blue) (left). Right, automated segmentation of long focal adhesions (red) overlaying on top of active INTβ1 staining (green) and the outline of the cell (blue). **d**, Epifluorescent images of HUVEC transfected with the indicated siRNA pools. Active β1 (green) and β3 (red) integrins mark mature and nascent focal adhesions, respectively. DAPI staining is shown in blue. **e**, Confocal images of HUVEC treated with control siRNA, *siMAP4K4* or GNE-220 and stained with paxillin (left) and integrin αVβ5 (right). **f**, Epifluorescent images of HUVEC transfected with control siRNA or siRNA targeting the 3′ UTR of *MSN*. siRNA-treated cells were electroporated with constructs expressing GFP, or GFP-tagged wild-type moesin or moesin(T558A) (green) and stained with active INTβ1 antibody (red). Arrows indicate cells expressing GFP or GFP-tagged proteins. **g**, Quantification of long FAs in GFP positive cells shown in **f**. Interestingly, expression of the moesin(T558A) construct moderately increased long FAs, indicating that this construct may have weak dominant negative activity. $n = 3$ experiments for all panels. Scale bars, 10 μm.

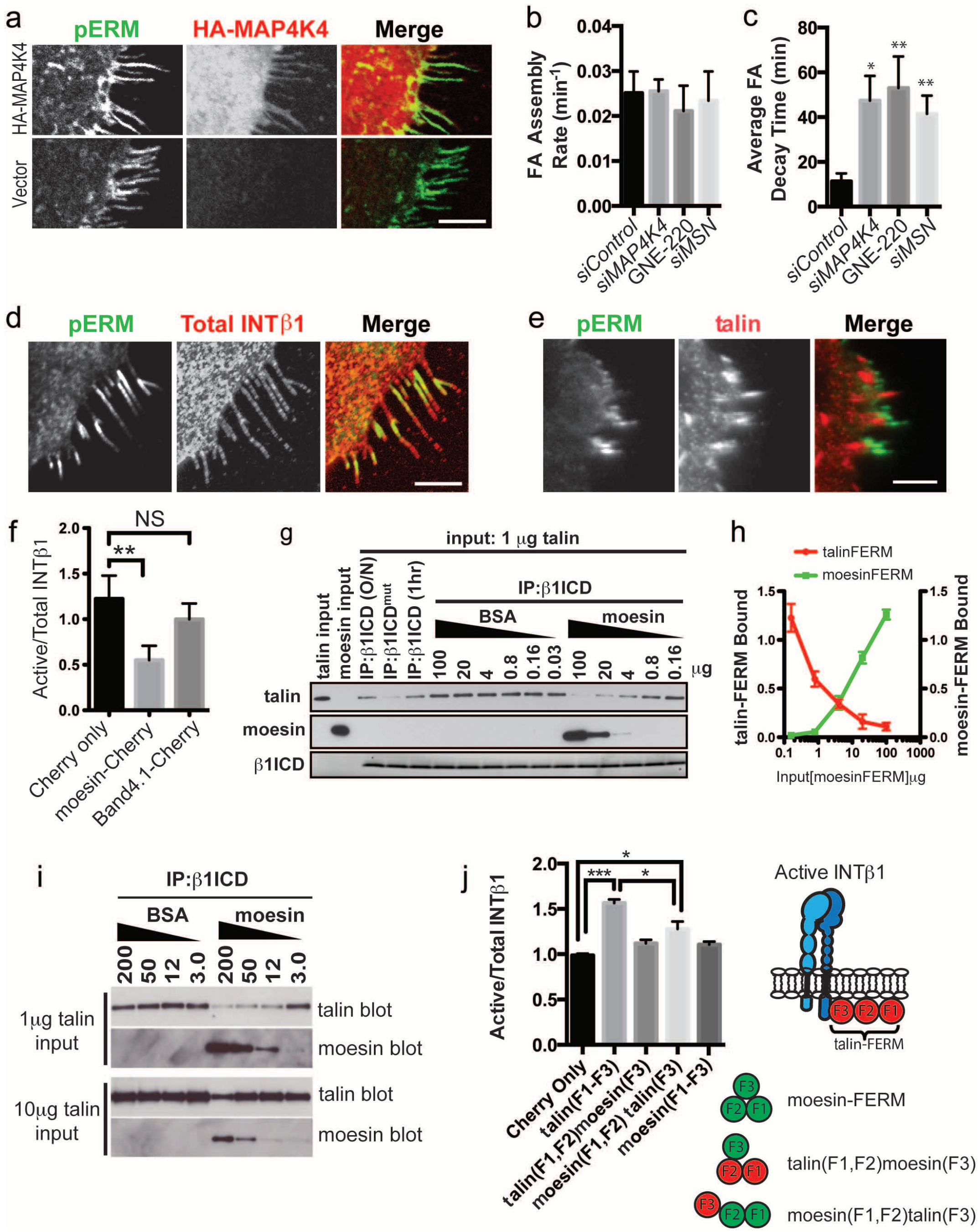

Extended Data Figure 7 | Further characterizations of MAP4K4 and moesin in retraction fibres, FA dynamics, and integrin activity. **a**, Confocal images of retraction fibres in HUVEC infected with empty viral vector (bottom) or viral construct expressing HA-MAP4K4 and stained with anti-HA antibody (red) and pERM (green). We evaluated 13 commercially available anti-MAP4K4 antibodies in HUVECs with and without *siMAP4K4*, but failed to identify any antibody that specifically stained MAP4K4 on cells. Overexpressed MAP4K4 was then used to evaluate its distribution. **b**, **c**, FA assembly rates (**b**) and average FA decay time (**c**) in HUVEC expressing paxillin–GFP. Quantification was done using the Focal Adhesion Analysis Server (http://faas.bme.unc.edu/). $n = 8$ videos per condition. **d**, TIRF images of retraction fibres in HUVEC stained with total INTβ1 (red) and pERM (green). **e**, TIRF images of retraction fibres in HUVEC stained with pERM (green) and talin (red). **f**, FACs analysis of active and total INTβ1 in CHO cells expressing mCherry alone, mCherry-tagged moesin FERM domain, or mCherry-tagged Band4.1 FERM domain. Each bar represents the mean of more than 3 independent pools of CHO cells transfected with the indicated constructs. Integrin activation in this experiment relied on endogenously expressed Talin. **g**, Recombinant wild-type or mutant integrin β1ICD coated beads were incubated with talin for one hour (1 h) except the sample labelled O/N (overnight, lane 3 from the left), followed by the addition of the indicated competitor proteins. The pulled-down or input proteins were analysed by western blotting. Comparison between lanes 3 and 5 indicates that one-hour incubation allowed maximal talin binding with integrin β1ICD similar to overnight incubation. IP, immunoprecipitation. **h**, Quantification of talin and moesin associated with β1ICD-coated beads in the presence of increasing concentrations of moesin. $n = 3$ experiments. **i**, Talin and moesin at the indicated quantities were co-incubated with beads coated with INTβ1ICD. The immunoprecipitated proteins were analysed by western blotting. Increased talin input reduced moesin binding to β1ICD, suggesting that talin competes with moesin for binding to β1ICD. **j**, FACs analysis of active and total INTβ1 in CHO cells expressing mCherry alone, mCherry-tagged wild-type talin or moesin FERM domain, or the indicated mCherry-tagged talin-moesin chimaeric FERM domain. To avoid the confounding effect of moesin-FERM's inhibitory activity, we gated for cells with low FERM expression where moesin-FERM was insufficient to inhibit INTβ1. Cells expressing the same levels of mCherry were gated and analysed for total and active INTβ1. $n = 3$ experiments. Scale bars, 5 μm.

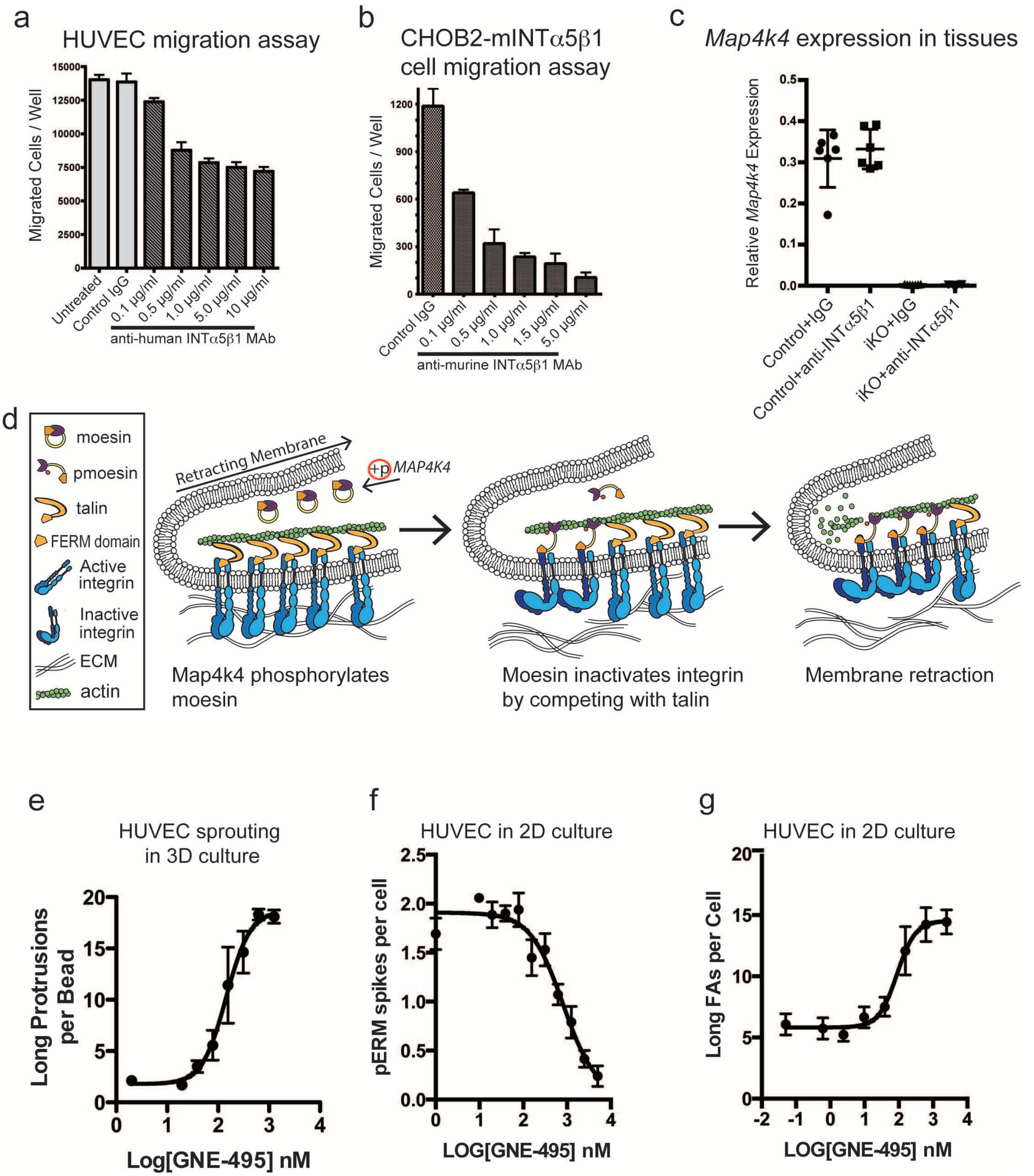

Extended Data Figure 8 | Additional information about the integrin-α5β1 antibodies, MAP4K4 inhibitor GNE-495, and a model depicting how MAP4K4 and moesin regulate FA disassembly. **a**, HUVEC migration assay results plotted as number of cells migrated through the membrane (*y*-axis) versus the concentrations of antibodies (*x*-axis). The graph shows that the anti-human INTα5β1 MAb 18C12 dose dependently inhibited migration of HUVECs on fibronectin. **b**, CHOB2-mα5β1 cells migration assay results plotted as number of cells migrated through the membrane (*y*-axis) versus the concentrations of antibodies (*x*-axis). The graph shows that the anti-murine INTα5β1 monoclonal antibody 10E7 dose-dependently inhibited migration of CHOB2-mα5β1 on fibronectin. Data presented in **a** and **b** were derived from 6 independent samples per condition. Detail information about MAbs 18C12 and 10E7 can be found in the Methods. Note that since HUVEC expressed several fibronectin receptors, inhibition of migration by an anti-α5β1 MAb was partial even at high MAb concentrations, whereas CHOB2 cells are deficient for many integrins[44], inhibition of CHOB2-mα5β1 cells migration by an anti-α5β1 MAb was more profound. **c**, Quantitative PCR measurement of *Map4k4* normalized to *mRPS13* using cDNA from neonatal tail clips of P7 mice with the indicated *Map4k4* genotypes (control or iKO) after injection with tamoxifen and the indicated antibodies. **d**, Model for MAP4K4 regulation of membrane retraction. Upon phosphorylation by MAP4K4, the FERM domain of activated moesin competes with talin-FERM for binding to active integrin, leading to integrin inactivation and FA disassembly. These events promote efficient membrane retraction to enable cell migration. Additional FA components omitted for simplicity. **e**–**g**, Characterization of the MAP4K4 selective inhibitor GNE-495: dose response curves relating GNE-495 concentration to long membrane protrusions in HUVEC bead sprouting assay (**e**), pERM-positive spikes (**f**), and long FAs in 2D HUVEC culture 24 h after GNE-495 treatment (**g**). Data represent average of 4 independent cultures.

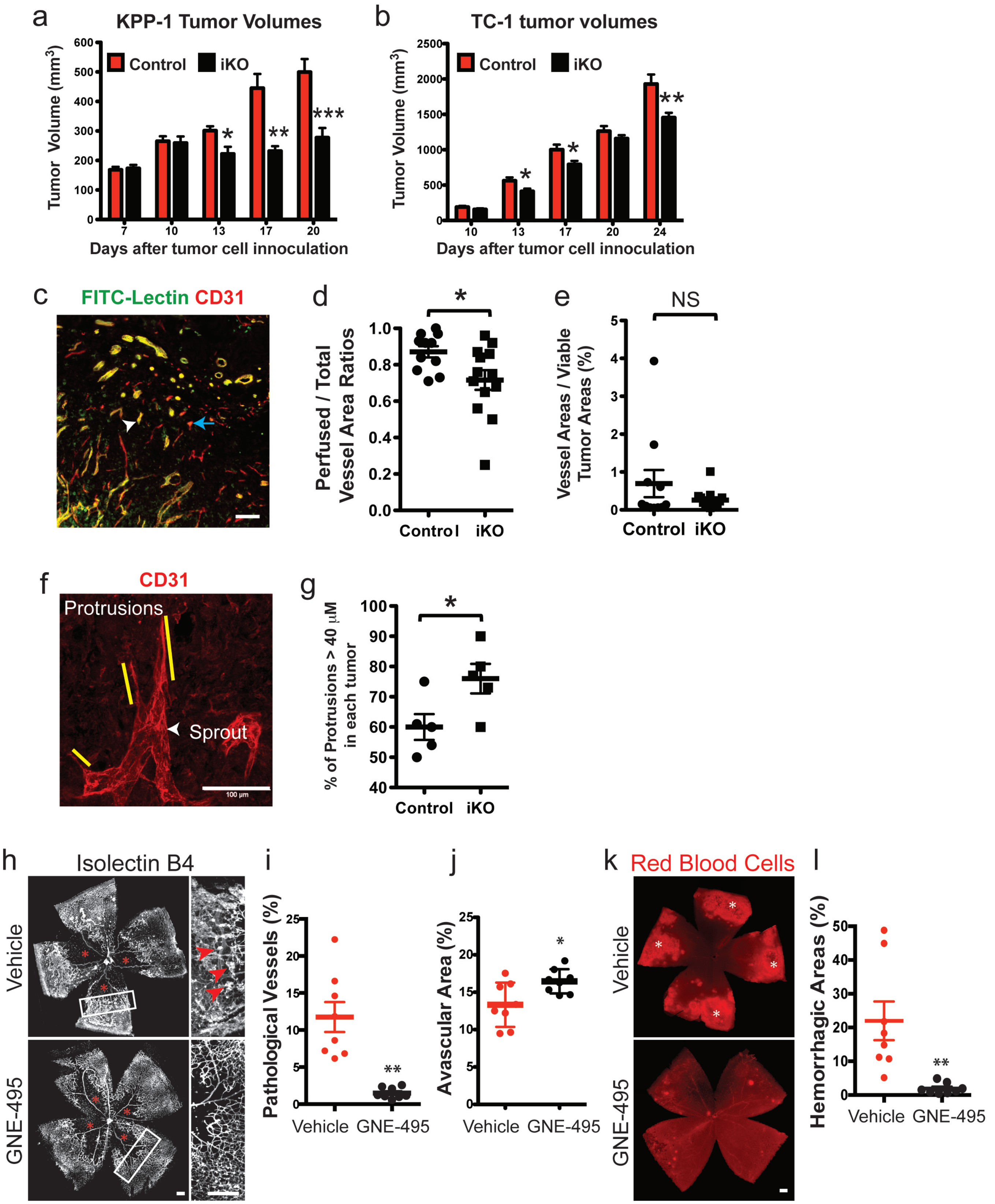
a
KPP-1 Tumor Volumes
Control iKO
Tumor Volume (mm3)
Days after tumor cell innoculation
b
TC-1 tumor volumes
Control iKO
Tumor Volume (mm3)
Days after tumor cell innoculation
c
FITC-Lectin CD31
d
Perfused / Total Vessel Area Ratios
Control iKO
e
NS
Vessel Areas / Viable Tumor Areas (%)
Control iKO
f
CD31
Protrusions
Sprout
g
% of Protrusions > 40 μM in each tumor
Control iKO
h
Isolectin B4
Vehicle
GNE-495
i
Pathological Vessels (%)
Vehicle GNE-495
j
Avascular Area (%)
Vehicle GNE-495
k
Red Blood Cells
Vehicle
GNE-495
l
Hemorrhagic Areas (%)
Vehicle GNE-495

Extended Data Figure 9 | The role of MAP4K4 in pathologic angiogenesis. **a**, **b**, Murine pancreatic (KPP-1) and lung (TC-1) cancer cells were implanted subcutaneously in control and *Map4k4*$^{iKO/iKO}$ sibling mice. Mean volumes of KPP-1 tumours from 10 mice per genotype (**a**) and TC-1 tumours from 15 mice per genotype (**b**) were measured over time. Per IACUC guidance, at the later time points, mice with tumour volumes exceeding 1,000 mm^3 (KPP-1) or 2,500 mm^3 (TC-1) were euthanized and no longer included in the mean tumour volume calculation. On day 20 for the KPP-1 study: $n = 9$ for the control group, $n = 10$ for the iKO group. On day 24 for the TC-1 study: $n = 11$ for the control group, $n = 14$ for the iKO group. **c**, Representative confocal image of a KPP-1 tumour section stained with FITC-lectin (green), CD31 (red) to indicate how functional vessels were analysed. White arrowhead indicates a perfused vessel (double positive for FITC-lectin and CD31, shown as yellow), blue arrow indicates a non-perfused vessel (single positive for CD31). **d**, Quantification of perfused tumour vessels on whole tumour sections from the KPP-1 model. Each dot represents the mean value of an entire tumour from a mouse. **e**, Quantification of tumour vessel areas normalized to the viable tumour areas on whole tumour sections from the KPP-1 model revealed no significant change in tumour vascular density in the iKO host. Each dot represents the mean value of an entire tumour from a mouse. **f**, Representative confocal projection image of a KPP-1 tumour thick section stained with CD31 to indicate how long subcellular protrusions were analysed. Arrow indicates a sprout, yellow lines indicate the subcellular protrusions. **g**, Quantification of long protrusions in each tumour. Each dot represents the mean value of multiple micrographs from the tumour of one mouse. A total of 170 protrusions were analysed. Scale bars represent 100 µm for **c** and **f**. Regarding **e**, the lack of significant change in tumour vascular density is not surprising as we observed a delay in vascularization balanced by the accumulation of endothelial cells in the already vascularized areas (Figs 2b, f, 6b), resulting in a lack of overall density change. Decreased perfusion may reflect the blood vessel structural alteration due to the aforementioned endothelial cell accumulation (Fig. 1a red arrowheads). **h**–**l**, Effects of the MAP4K4 inhibitor GNE-495 was evaluated in an oxygen-induced retinopathy (OIR) model that mimics vascular pathologies in human proliferative diabetic retinopathy and retinopathy of prematurity. **h**, Confocal images of P17 retinas stained for isolectin-B4 from mice subjected to the OIR procedure and treated with either vehicle or GNE-495. Red asterisks mark areas of vaso-obliteration (avascular area) resulting from high oxygen damage. Right, close-up views of the boxed areas. Red arrows mark pathologic vascular tufts. **i**, Areas of pathologic vascular tufts normalized to retinal areas. Control retinas contain numerous pathological neovascular tufts, which is largely absent from the GNE-495 treated retinas, revealing the inhibitory effect of GNE-495 on pathologic angiogenesis. **j**, Avascular areas normalized to retinal areas. GNE-495 increased avascular area, indicating an inhibition of vascular regrowth into the oxygen damaged avascular area. **k**, Autofluorescence of red blood cells indicative of haemorrhage (white asterisks) in retinas from the same experiment shown in **h**–**j**. **l**, Haemorrhagic areas normalized to retinal area illustrates that GNE-495 reduced haemorrhage. Each dot represents one animal. Scale bar, 50 µm.

doi:10.1038/nature14285

Regulated eukaryotic DNA replication origin firing with purified proteins

Joseph T. P. Yeeles[1], Tom D. Deegan[1], Agnieszka Janska[1], Anne Early[1] & John F. X. Diffley[1]

Eukaryotic cells initiate DNA replication from multiple origins, which must be tightly regulated to promote precise genome duplication in every cell cycle. To accomplish this, initiation is partitioned into two temporally discrete steps: a double hexameric minichromosome maintenance (MCM) complex is first loaded at replication origins during G1 phase, and then converted to the active CMG (Cdc45–MCM–GINS) helicase during S phase. Here we describe the reconstitution of budding yeast DNA replication initiation with 16 purified replication factors, made from 42 polypeptides. Origin-dependent initiation recapitulates regulation seen *in vivo*. Cyclin-dependent kinase (CDK) inhibits MCM loading by phosphorylating the origin recognition complex (ORC) and promotes CMG formation by phosphorylating Sld2 and Sld3. Dbf4-dependent kinase (DDK) promotes replication by phosphorylating MCM, and can act either before or after CDK. These experiments define the minimum complement of proteins, protein kinase substrates and co-factors required for regulated eukaryotic DNA replication.

The initiation of eukaryotic DNA replication origin firing is understood in outline[1,2], but the process has not been reconstituted with purified proteins. MCM can be loaded onto DNA with purified ORC, Cdc6 and Cdt1–MCM[3,4] and loaded MCMs can be activated to replicate in yeast extracts[5–7]. Mass spectrometry of complexes assembled during replication in these extracts identified previously characterized 'firing factors' including Sld2, Sld3, Sld7, Dpb11, Cdc45, GINS and DNA polymerase ε (pol ε), but did not identify any novel factors[6], suggesting this list may be complete.

DNA replication is regulated during the cell cycle by two protein kinases, CDK and DDK[8]. CDK plays two roles in regulating replication: it inhibits MCM loading and it is essential for helicase activation[1,2]. Consequently, MCM loading can only occur during G1 phase when CDK activity is low, and origins can only fire after G1 phase when CDK levels rise. CDK phosphorylation of ORC, Cdc6 and MCM all contribute to preventing MCM loading outside G1 phase in budding yeast[9]. Genetic analysis has indicated that Sld2 and Sld3 are the two key CDK substrates required for helicase activation. Phosphorylation of these proteins generates binding sites for tandem BRCT repeats in Dpb11 (refs 10–12). DDK is required for origin firing[8] and genetic analysis has indicated that Mcm4 and 6 are the key DDK substrates[13–15]. Until origin firing is reconstituted with purified proteins, however, we will not know whether we have the complete inventory of essential firing factors or whether CDK and DDK have any additional important substrates.

CDK- and DDK-dependent firing factor recruitment

To reconstitute MCM loading and activation, we expressed and purified the thirteen replication factors shown in Fig. 1a (left) and Extended Data Fig. 1a, b. Cdc6, GINS, Mcm10 and cyclin A/Cdk2 (A-Cdk2) were expressed in *Escherichia coli*, while the remaining proteins were expressed in *Saccharomyces cerevisiae*. In addition to A-Cdk2, budding yeast S phase CDK (S-CDK) expressed in *Saccharomyces cerevisiae* (Fig. 1a, left) was used in some experiments. Details of expression and purification strategies can be found in the Methods.

We adopted the strategy outlined in Fig. 1b to assemble firing factors onto the loaded MCM in a staged manner. We first loaded MCM onto DNA attached to magnetic beads[3] ('MCM load'). The loaded MCM was phosphorylated with DDK[6], beads were isolated and Sld3/7 and Cdc45 were added ('DDK step'). Beads were again isolated and the remaining firing factors were added with A-Cdk2 ('CDK step'). After washing the

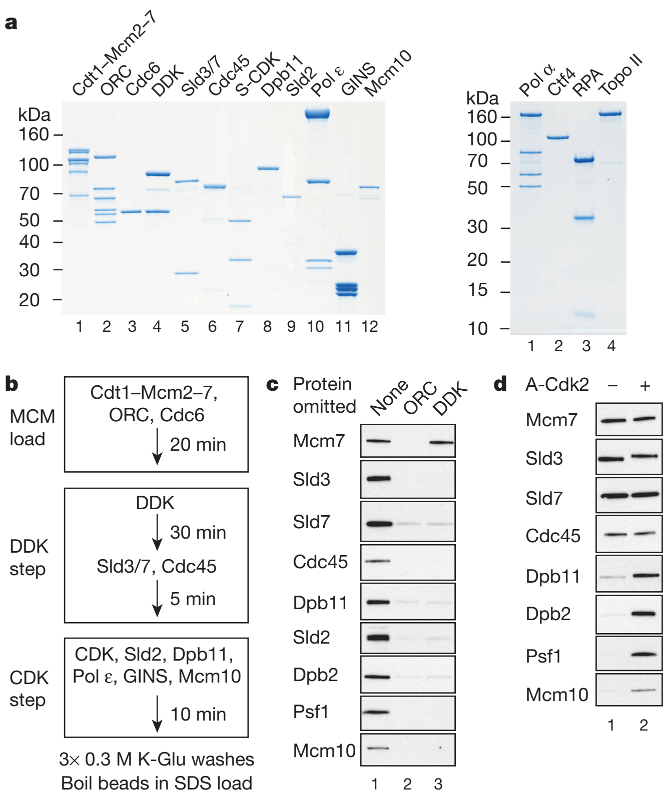

Figure 1 | DDK- and CDK-dependent firing-factor recruitment with purified proteins. a, Purified MCM loading and firing factors (left), and additional factors required for DNA replication (right) analysed by SDS–PAGE with Coomassie staining. **b**, Reaction scheme for firing-factor recruitment. **c**, **d**, Immunoblots of recruitment reactions conducted as illustrated in **b** on ARS305 linear DNA.

[1]Cancer Research UK London Research Institute, Clare Hall Laboratories, South Mimms EN6 3LD, UK.

beads with a low-salt buffer, we analysed bound proteins by immunoblotting. As shown in Fig. 1c, Sld3/7, Cdc45, Dpb11, Sld2, pol ε (the Dpb2 B subunit), GINS (the Psf1 subunit) and Mcm10 were all recruited in an ORC- and DDK-dependent manner. When A-Cdk2 was omitted from the final step, Sld3/7 and Cdc45 were still recruited but the remaining factors were not (Fig. 1d). Therefore, the recruitment of Sld3/7 and Cdc45 required DDK but not CDK, while the recruitment of the remaining firing factors required both DDK and CDK.

Recruitment of Cdc45 and GINS into a stable complex

Consistent with the dependencies shown in Fig. 1c, d, Figure 2a shows that the recruitment of Cdc45 did not require any of the factors acting in the CDK step (Dpb11, Sld2, pol ε, GINS, Mcm10). However, the recruitment of GINS (Psf1) required all of the other factors acting in this CDK step except for Mcm10 (that is, Dpb11, Sld2, pol ε). CMG is salt-stable[16,17], so we tested our complex under more stringent extraction conditions. Figure 2b (lane 1) and Extended Data Fig. 2a, b show that, in addition to MCM, a fraction of Cdc45 and GINS is stable to salt extraction. In contrast to Cdc45 and GINS, Sld3 is not stabilized in this complex (Extended Data Fig. 2b). Figure 2b, lanes 2–5 show that salt-stable Cdc45 recruitment requires Dpb11, Sld2, pol ε and GINS. Mcm10, however, is not required for this salt-stable complex (Fig. 2b, lane 6).

To investigate whether the complex we assembled might be functional, we tested its ability to support DNA replication in extracts. We have previously shown that MCM loaded with purified proteins and phosphorylated with purified DDK can replicate in extracts from S phase cells made from a strain (KO3) that overexpresses Dpb11, Cdc45, Sld2, Sld3 and Sld7[6]. It has been shown that overexpression of firing factors is required for replication in a related system[7]. We therefore constructed a new strain that does not overexpress any firing factors (yJY18) and made S phase extracts from this strain in which GINS was also depleted (Extended Data Fig. 2c). We reasoned that addition of the complex of MCM with firing factors to this extract might support DNA replication (Fig. 2c). Figure 2d, lanes 1 and 9 show that replication occurred under these conditions. Indeed, the replication products seen with the purified factors were equivalent to those synthesized in extracts from KO3 (Extended Data Fig. 2e). Furthermore, as shown in Fig. 2d, lanes 2–8, replication was not observed if either Sld3/7, Cdc45, A-Cdk2, Dpb11, Sld2, pol ε or GINS were omitted, indicating that all of the recombinant proteins tested are functional and required for replication. This also suggested that the complex of MCM and firing factors may be functional.

Reconstitution of origin firing with purified proteins

We next expressed and purified four additional proteins predicted to be important for DNA replication: DNA polymerase α–primase (pol α), Ctf4, replication protein A (RPA), and topoisomerase II (Topo II)[18,19] (Fig. 1a (right) and Extended Data Fig. 1a). Following the CDK step we isolated the beads and added a new buffer containing these four proteins along with additional Mcm10, ribo- and deoxyribonucleoside triphosphates (NTPs and dNTPs) and [α-^{32}P]dCTP, as outlined in Fig. 3a. As shown in Fig. 3b (lane 1), this resulted in DNA synthesis that generated labelled products on alkaline agarose gels. Synthesis required ORC, DDK, A-Cdk2 and pol α (Fig. 3b) as well as dNTPs (Extended Data Fig. 3a), suggesting it was genuine initiation.

In this and subsequent experiments, two classes of labelled products were observed: a population of short products of approximately 150 nucleotides in length, and a more heterogeneous smear of larger products. The template used in these experiments was a 3.2 kilobase pairs plasmid, which had been randomly biotinylated and attached to streptavidin beads. Previous work has shown that attachment of DNA to beads interferes with the completion of DNA replication[5–7]. Since the position of the ARS1 origin relative to the site of attachment to the beads will be random, leading strand synthesis would be predicted to generate a smear of products averaging half the plasmid size (~1,600 nucleotides), but ranging in size from very small to almost full plasmid length, very similar to the products observed. Synthesis of the smaller product class was

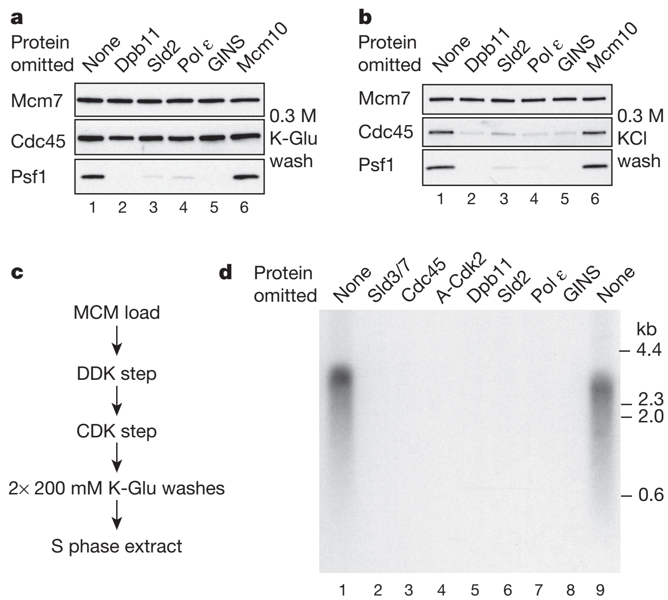

Figure 2 | The purified firing factors are functional. **a**, **b**, Immunoblots of recruitment reactions performed as in Fig. 1b using ARS305 linear DNA with either, **a**, 0.3 M K-glutamate (K-Glu) or **b**, 0.3 M KCl washes. **c**, Scheme for extract-based replication reactions. Unless otherwise stated, in this and all subsequent experiments, components of the 'CDK' and 'DDK' steps are as in Fig. 1. Firing factors were recruited as illustrated in Fig. 1b. Beads were isolated, washed twice and added to an S phase extract not overexpressing firing factors (yJY18) and where the Psf2 subunit of the GINS complex was immunodepleted (Extended Data Fig. 2c). **d**, Reaction performed as in **c**. Nascent DNA was labelled by including [α^{32}P]dCTP in the extract step and products were separated through a 0.6% alkaline agarose gel.

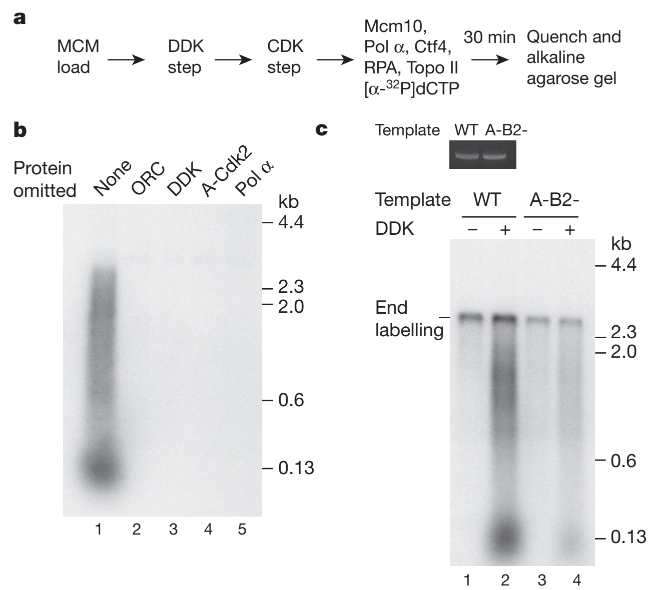

Figure 3 | The initiation of DNA synthesis with purified proteins. **a**, Reaction pathway for DNA replication with purified proteins. Firing factors were bound to MCM, the complex isolated, and added to a new buffer containing proteins required for DNA synthesis (Fig. 1a (right)). **b**, Replication reaction conducted as shown in **a** on ARS1 circular DNA. In this and all subsequent replication assays products were separated through 0.7% alkaline agarose gels. **c**, Replication on ARS1 linear templates. Top, photocleaved DNA templates analysed by native agarose gel electrophoresis and ethidium bromide staining. Bottom, replication following the pathway shown in **a**. The MCM loading conditions were modified to confer origin specificity on the replication reaction (see Methods for details).

more strongly affected by omission of C/G/UTP than the larger class (Extended Data Fig. 3b), suggesting that the smaller class may correspond to lagging strand synthesis, which requires repeated re-priming, but further work is needed to establish this. The residual larger products formed without C/G/UTP may be primed by RNA made from ATP alone (ARS1 is AT rich), which we cannot omit because it is required for MCM unwinding, or may be primed by inefficient dNTP use by primase. Extended Data Fig. 3c, d shows full-length products appear by 20 min and continue to accumulate with time; the smaller products accumulate with the same kinetics as the larger products, but seem to be less abundant, which may reflect incomplete lagging strand synthesis. A pulse-chase experiment (Extended Data Fig. 3e) shows that the smaller products are not a precursor of the larger ones, or vice versa. Approximately 10% of input plasmid is routinely replicated during replication reactions.

A template containing a functional origin yielded approximately 3.2-fold more DNA synthesis than an equivalent template containing a mutant, non-functional origin (A-B2-) (Fig. 3c (bottom), compare lanes 2 and 4), indicating that replication exhibited origin preference under these conditions. The experiments in Fig. 3c and Extended Data Fig. 3c–e were performed on linear DNA attached at one end to beads, and consequently, in addition to DDK-dependent replication products, there is also a DDK-independent end-dependent labelling product.

Requirements for DNA synthesis and RPA recruitment

Figure 4a shows that DNA synthesis in this system is dependent upon all of the firing factors, including Mcm10, which was not required for salt-stable association of Cdc45 and GINS (Fig. 2b). Omission of pol α also prevented DNA synthesis (Fig. 4b, lane 2), while Ctf4 omission had little effect on DNA synthesis, although the products were reproducibly slightly smaller (Fig. 4b, lane 3). In the absence of RPA, the small product class was completely lost, while the larger smear was reduced in both intensity and size (Fig. 4b, lane 4). Finally, in the absence of Topo II, accumulation of products longer than 600 nucleotides was greatly reduced (Fig. 4b, lane 5).

Topo II was required for accumulation of larger products from the circular template (Fig. 4b, c), but not from the linear template (Fig. 4c, compare lanes 2 and 5). Moreover, topoisomerase I from vaccinia virus supported DNA replication on the circular template (Extended Data Fig. 4a). Together, these results indicate that removal of supercoils is required for the replication of circular molecules in this system. This experiment also shows that linear and circular templates generate similar labelled products (aside for the end-labelled product on the linear template) and replicate with similar efficiencies (compare lanes 1 and 4).

We next examined the recruitment of RPA during the DNA synthesis reaction (Fig. 4d). RPA showed some DDK- and Mcm10-dependent recruitment (compare lanes 1–3). RPA recruitment was enhanced by omission of pol α (compare lanes 1 and 4), suggesting some uncoupling of template unwinding from DNA synthesis. This was supported by the fact that RPA recruitment was also enhanced in complete reactions lacking dNTPs and C/G/UTP (Extended Data Fig. 4b). The elevated RPA recruitment observed in the absence of pol α required GINS, Mcm10 and Topo II, but not Ctf4 (Fig. 4e). The requirement for Topo II is consistent with the idea that extensive unwinding was occurring. This is supported by the fact that enhanced RPA recruitment in the absence of Topo II could be restored by either Topo I or use of a linear template (Extended Data Fig. 4c). Although Cdc45 and GINS stably associate with loaded MCM in the absence of Mcm10 (Fig. 2b), RPA recruitment in the absence of DNA synthesis was substantially reduced without Mcm10 (Fig. 4e, lane 3 and Extended Data Fig. 4c), indicating that unwinding requires Mcm10.

Regulation of DNA replication by CDK

To examine the regulation of origin firing by protein kinases in more detail we used budding yeast S-CDK (Fig. 1 (left), lane 7) in place of A-Cdk2 as it can be selectively inhibited by the protein Sic1. CDK prevents MCM loading outside of G1 phase. Consistent with this, Fig. 5a (lane 2) shows that phosphorylation of MCM loading factors with S-CDK before MCM loading prevented DNA replication, but addition of S-CDK after MCM loading did not (lane 1). To determine which proteins were inhibited by S-CDK, we incubated each individually with S-CDK and ATP, then inhibited S-CDK with Sic1. Figure 5b shows that treatment of ORC with S-CDK prevented DNA replication while treatment of Cdc6 and Cdt1–MCM with S-CDK had no effect. This is likely because, as shown in Fig. 5c, S-CDK treatment of ORC, but not Cdc6 or Cdt1–MCM, blocked MCM loading and consequently, Cdc45 and GINS recruitment. Pre-treatment of S-CDK with Sic1 before incubation with ORC prevented the inhibition of replication (Extended Data Fig. 5a, lane 3). Moreover, the inhibition of replication by S-CDK was ATP-dependent (Extended Data Fig. 5b). Together, these results indicate that ORC's ability to load MCM and promote replication is inhibited by CDK-dependent phosphorylation in this system.

Previous genetic analysis indicated that Sld2 and Sld3 are the two critical CDK substrates required for origin firing[10–12]. To examine this biochemically we phosphorylated Sld3/7 and Sld2 each individually with S-CDK, then inhibited S-CDK with Sic1 before adding the additional proteins required for the DDK step (for Sld3/7) and CDK step

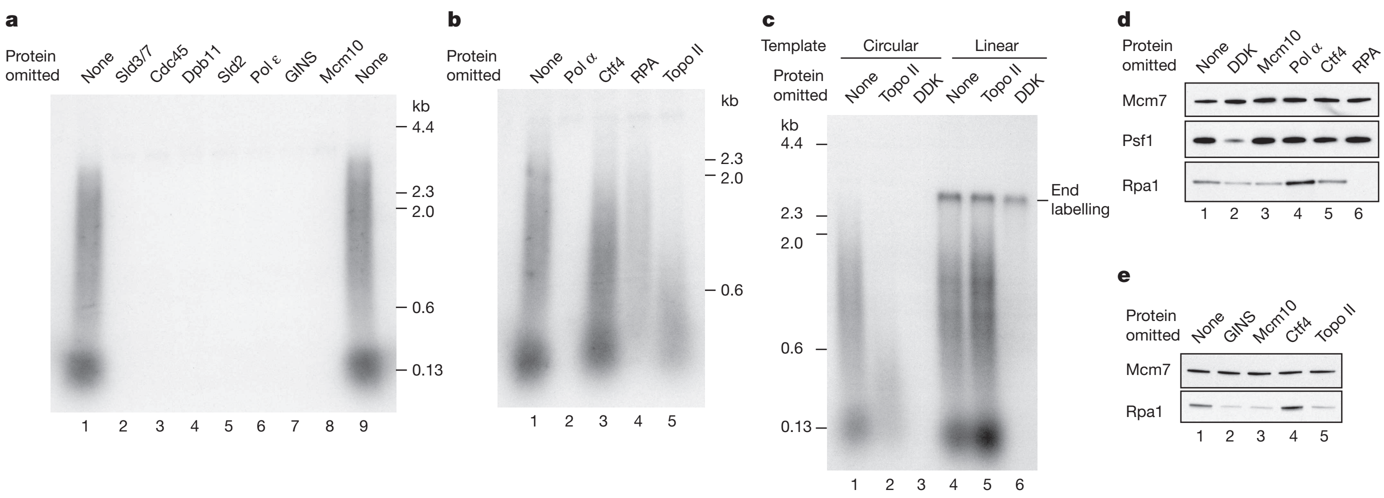

Figure 4 | Requirements for origin firing. Reactions were performed as illustrated in Fig. 3a on circular templates unless stated. **a**, Firing factors required to initiate DNA synthesis. **b**, Protein dependencies of DNA replication for components functioning downstream of firing factor recruitment. **c**, Topoisomerase dependence on circular and linear ARS1 templates. **d**, RPA recruitment in a complete replication reaction. **e**, Dependence of RPA recruitment in the absence of pol α.

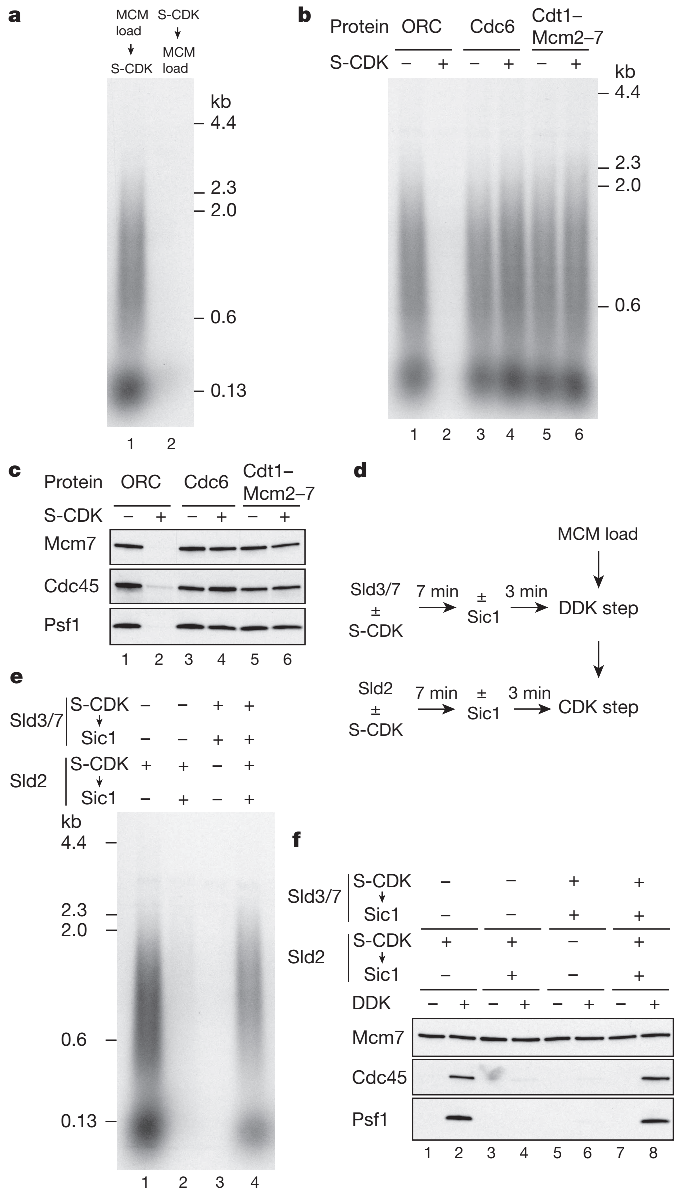

Figure 5 | Regulation of MCM loading and origin firing by S-CDK. **a**, Replication reactions where MCM loading factors were incubated with S-CDK before or after MCM loading on ARS1 circular DNA. Replication, **b**, and protein recruitment, **c**, on ARS1 circular DNA where ORC, Cdc6 and Cdt1–Mcm2–7 were individually incubated with S-CDK followed by addition of Sic1. The remaining MCM loading factors were added and reactions performed as shown in Fig. 3a (replication) and Fig. 1b (recruitment). **d**, Scheme to phosphorylate Sld3/7 and Sld2 in isolation from MCM and firing factors. Prior to both the DDK step and CDK step Sld3/7 and Sld2 were incubated with S-CDK before addition of Sic1. The remaining firing factors were added together with isolated DNA beads and each reaction step was performed as for standard reactions. **e**, Replication reaction staged as illustrated in **d**. **f**, Firing factor recruitment conducted as in **d**, followed by 0.3 M KCl washes.

(for Sld2) (Fig. 5d). Phosphorylation of either Sld2 or Sld3 individually did not support DNA replication (Fig. 5e, lanes 2 and 3) or salt-stable association of Cdc45 and GINS (Fig. 5f, lanes 3–6). However, when both Sld2 and Sld3 were phosphorylated separately and added in the same reaction, DNA replication (Fig. 5e, lane 4) and salt-stable association of Cdc45 and GINS (Fig. 5f, lanes 7 and 8) occurred efficiently. If Sic1 was omitted from the Sld2 CDK phosphorylation step, replication and salt-stable Cdc45 and GINS association occurred even when Sld3 was not pre-phosphorylated (Fig. 5e, lane 1; Fig. 5f, lanes 1 and 2), presumably because active CDK was added to the complete reaction, where it could also phosphorylate Sld3. Thus, comparison of lanes 1 and 2 in Fig. 5e and lanes 2 and 4 in Fig. 5f shows Sic1 was effective in inhibiting S-CDK. Extended Data Fig. 5c shows that ATP is essential for activation of both Sld2 and Sld3/7. Taken together, these results indicate that phosphorylation of Sld2 and Sld3/7 is necessary and sufficient for initiating DNA replication.

Regulation by DDK and the order of kinase action

High salt wash after MCM loading and DDK phosphorylation removes both ORC and DDK (Fig. 6a (left); Orc6 and Dbf4). This high-salt washed MCM complex was competent for salt-stable Cdc45 and GINS association (Fig. 6a (right)) as well as DNA replication (Fig. 6b) without further DDK addition. This indicates that MCM is the key substrate of DDK. This experiment also shows that ORC plays no essential role in initiating DNA replication after MCM loading, similar to conclusions from *Xenopus* egg extracts[20]. Previous work using yeast extracts indicated that replication did not happen if the CDK phosphorylation step was executed before the DDK step[7]. However, using the approach outlined in Fig. 6c with purified proteins, stable association of Cdc45 and GINS (Fig. 6d) and DNA replication (Fig. 6e) were equally efficient regardless of the order of kinase treatment.

Discussion

Our experiments define the minimum set of proteins and small molecule co-factors required to initiate origin-dependent DNA replication in a eukaryotic system (Extended Data Fig. 6). We show that the MCM complex assembled with purified proteins is a precursor of DNA replication initiation. Moreover, because this complex is competent for replication after high-salt wash, the loading factors ORC, Cdc6 and Cdt1 play no essential role in initiation after MCM loading. Sld3/7 and Cdc45 are recruited to MCM in a DDK-dependent manner, and the remaining firing factors (Sld2, Dpb11, GINS, pol ε, Mcm10) are recruited in a DDK- and CDK-dependent manner. This set of firing factors is sufficient to promote RPA recruitment. RPA recruitment is likely due to the generation of substantial single stranded DNA because it requires topoisomerase on a circular template, and it is enhanced when DNA synthesis is prevented by omitting either pol α or dNTPs from the reaction. Mcm10 is required for RPA recruitment, but not salt-stable association of Cdc45 and GINS, consistent with results in yeast extracts[7] and *in vivo*[21,22]. Thus, a CMG-like complex can be assembled without Mcm10, but this complex is inactive. All DNA synthesis requires pol α, consistent with its role in generating primers required for DNA synthesis. Because pol ε is required for CMG formation, we cannot at present determine whether it also contributes to subsequent DNA synthesis in this system, for example, through generation of a CMG–pol ε complex[23]. The presence of short and long products is suggestive of leading and lagging strand synthesis. However, our replication system currently lacks DNA polymerase δ, which is responsible for lagging strand synthesis *in vivo*[24], RFC and PCNA, which localize to lagging strands during replication *in vivo*[25], as well as the many factors required for Okazaki fragment maturation. It also lacks other replisome-associated factors such as Mrc1 and Tof1–Csm3 (ref. 17). Consequently, DNA synthesis in this system does not yet fully recapitulate normal coupled leading and lagging strand replication, and this is clearly an important goal for the future.

Our experiments also define the minimum set of CDK and DDK substrates required for regulated replication. CDK phosphorylation of ORC directly prevents it from loading MCM and promoting replication, consistent with previous work[1,26,27]. Although it is clear that CDK phosphorylation of Cdc6 and Cdt1–MCM contributes to preventing re-replication *in vivo* in budding yeast, our experiments show that CDK phosphorylation does not directly inhibit the ability of these proteins to load MCM. Instead, it is likely that CDK inhibits Cdc6 function by promoting its degradation in cells, and CDK inhibits Cdt1–MCM function by promoting nuclear exclusion[2]. Our work also confirms that Sld3/7 and Sld2 are the only two CDK substrates required for replication

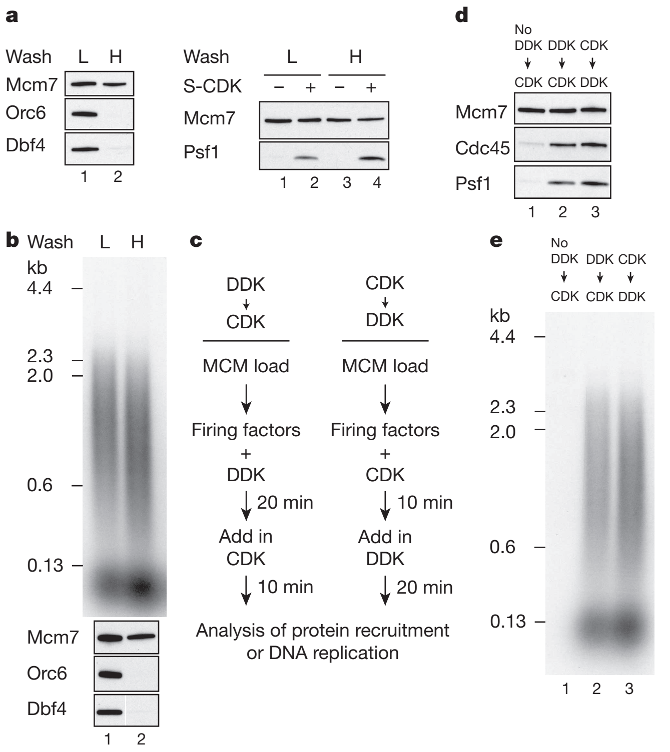

Figure 6 | DDK phosphorylation of MCM promotes origin firing either before or after S-CDK. **a**, Reactions performed essentially as in Fig. 1b on circular DNA but with an additional mid-reaction wash immediately following DDK phosphorylation, in either a low-salt (L) (0.3 M K-Glu), or high-salt (H) (0.6 M NaCl) buffer. Bound proteins immediately following the mid-reaction wash (left), and after firing factor recruitment followed by 0.3 M KCl washes (right). **b**, Replication reactions with either high- or low-salt mid-reaction washes. **c**, Reaction schemes to test the order of DDK and CDK action. Firing factor recruitment was performed in a single step with DDK and CDK added at different times as indicated. Protein recruitment, **d**, and replication, **e**, performed with S-CDK as illustrated in **c**.

initiation. In contrast to conclusions from experiments in yeast extracts[7], our results with purified proteins show CDK does not have any inhibitory role after MCM loading, and CDK and DDK can act in either order. In the experiments using extracts[7], we suggest rapid dephosphorylation of Sld2 and Sld3 occurred after Sic1 (ref. 6) and DDK addition, requiring one or both of these proteins to be re-phosphorylated by CDK after Sld3/7 and Cdc45 were loaded. Our experiments show that the essential DDK substrate for initiation is MCM. Further work will be required to ascertain which MCM subunits and sites are critical.

The initiation step of DNA replication has taken many years to reconstitute because of the large number of factors involved and the complicated regulation by protein kinases. Having achieved this, we are now in a position to understand how the MCM double hexamer is activated in molecular and atomic detail. Moreover, this work sets the stage for the complete reconstitution of chromosome replication, which has the potential to provide insights into many DNA replication-coupled nuclear processes.

Online Content Methods, along with any additional Extended Data display items and Source Data, are available in the online version of the paper; references unique to these sections appear only in the online paper.

Received 14 December 2014; accepted 6 February 2015.
Published online 4 March 2015.

1. Tanaka, S. & Araki, H. Helicase activation and establishment of replication forks at chromosomal origins of replication. *Cold Spring Harb. Perspect. Biol.* **5,** a010371 (2013).
2. Siddiqui, K., On, K. F. & Diffley, J. F. X. Regulating DNA replication in Eukarya. *Cold Spring Harb. Perspect. Biol.* **5,** a012930 (2013).
3. Remus, D. *et al.* Concerted loading of Mcm2–7 double hexamers around DNA during DNA replication origin licensing. *Cell* **139,** 719–730 (2009).
4. Evrin, C. *et al.* A double-hexameric MCM2-7 complex is loaded onto origin DNA during licensing of eukaryotic DNA replication. *Proc. Natl Acad. Sci. USA* **106,** 20240–20245 (2009).
5. Gros, J., Devbhandari, S. & Remus, D. Origin plasticity during budding yeast DNA replication *in vitro*. *EMBO J.* **33,** 621–636 (2014).
6. On, K. F. *et al.* Prereplicative complexes assembled *in vitro* support origin-dependent and independent DNA replication. *EMBO J.* **33,** 605–620 (2014).
7. Heller, R. C. *et al.* Eukaryotic origin-dependent DNA replication *in vitro* reveals sequential action of DDK and S-CDK kinases. *Cell* **146,** 80–91 (2011).
8. Labib, K. How do Cdc7 and cyclin-dependent kinases trigger the initiation of chromosome replication in eukaryotic cells? *Genes Dev.* **24,** 1208–1219 (2010).
9. Nguyen, V. Q., Co, C. & Li, J. J. Cyclin-dependent kinases prevent DNA re-replication through multiple mechanisms. *Nature* **411,** 1068–1073 (2001).
10. Zegerman, P. & Diffley, J. F. X. Phosphorylation of Sld2 and Sld3 by cyclin-dependent kinases promotes DNA replication in budding yeast. *Nature* **445,** 281–285 (2007).
11. Tanaka, S. *et al.* CDK-dependent phosphorylation of Sld2 and Sld3 initiates DNA replication in budding yeast. *Nature* **445,** 328–332 (2007).
12. Masumoto, H., Muramatsu, S., Kamimura, Y. & Araki, H. S-Cdk-dependent phosphorylation of Sld2 essential for chromosomal DNA replication in budding yeast. *Nature* **415,** 651–655 (2002).
13. Randell, J. C. *et al.* Mec1 is one of multiple kinases that prime the Mcm2–7 helicase for phosphorylation by Cdc7. *Mol. Cell* **40,** 353–363 (2010).
14. Sheu, Y. J. & Stillman, B. Cdc7-Dbf4 phosphorylates MCM proteins via a docking site-mediated mechanism to promote S phase progression. *Mol. Cell* **24,** 101–113 (2006).
15. Sheu, Y. J. & Stillman, B. The Dbf4–Cdc7 kinase promotes S phase by alleviating an inhibitory activity in Mcm4. *Nature* **463,** 113–117 (2010).
16. Moyer, S. E., Lewis, P. W. & Botchan, M. R. Isolation of the Cdc45/Mcm2–7/GINS (CMG) complex, a candidate for the eukaryotic DNA replication fork helicase. *Proc. Natl Acad. Sci. USA* **103,** 10236–10241 (2006).
17. Gambus, A. *et al.* GINS maintains association of Cdc45 with MCM in replisome progression complexes at eukaryotic DNA replication forks. *Nature Cell Biol.* **8,** 358–366 (2006).
18. Bell, S. P. & Dutta, A. DNA replication in eukaryotic cells. *Annu. Rev. Biochem.* **71,** 333–374 (2002).
19. Gambus, A. *et al.* A key role for Ctf4 in coupling the MCM2–7 helicase to DNA polymerase α within the eukaryotic replisome. *EMBO J.* **28,** 2992–3004 (2009).
20. Rowles, A., Tada, S. & Blow, J. J. Changes in association of the *Xenopus* origin recognition complex with chromatin on licensing of replication origins. *J. Cell Sci.* **112,** 2011–2018 (1999).
21. Watase, G., Takisawa, H. & Kanemaki, M. T. Mcm10 plays a role in functioning of the eukaryotic replicative DNA helicase, Cdc45-Mcm-GINS. *Curr. Biol.* **22,** 343–349 (2012).
22. van Deursen, F., Sengupta, S., De Piccoli, G., Sanchez-Diaz, A. & Labib, K. Mcm10 associates with the loaded DNA helicase at replication origins and defines a novel step in its activation. *EMBO J.* **31,** 2195–2206 (2012).
23. Georgescu, R. E. *et al.* Mechanism of asymmetric polymerase assembly at the eukaryotic replication fork. *Nature Struct. Mol. Biol.* **21,** 664–670 (2014).
24. Clausen, A. R. *et al.* Tracking replication enzymology *in vivo* by genome-wide mapping of ribonucleotide incorporation. *Nature Struct. Mol. Biol.* http://dx.doi.org/10.1038/nsmb.2957 (2015).
25. Yu, C. *et al.* Strand-specific analysis shows protein binding at replication forks and PCNA unloading from lagging strands when forks stall. *Mol. Cell* **56,** 551–563 (2014).
26. Chen, S. & Bell, S. P. CDK prevents Mcm2–7 helicase loading by inhibiting Cdt1 interaction with Orc6. *Genes Dev.* **25,** 363–372 (2011).
27. Frigola, J., Remus, D., Mehanna, A. & Diffley, J. F. X. ATPase-dependent quality control of DNA replication origin licensing. *Nature* **495,** 339–343 (2013).

Supplementary Information is available in the online version of the paper.

Acknowledgements We are grateful to B. Pfander and M. Douglas for the Mcm10 expression plasmid and advice on purification, C. Kurat for construction of plasmids used to generate ARS1 linear templates, K. On and D. Boos for Sic1 and A-Cdk2 and K. Labib for Psf1 antibodies and the *E. coli* GINS expression strain. We thank A. Alidoust and N. Patel for growing yeast cultures. This work was supported by Cancer Research UK, a FEBS Return-to-Europe fellowship to J.T.P.Y., a Boehringer Ingelheim Fonds PhD fellowship to A.J. and an ERC grant (249883 – EUKDNAREP) to J.F.X.D.

Author Contributions J.F.X.D. and J.T.P.Y. designed the experiments and wrote the manuscript. J.T.P.Y. performed the experiments. T.D.D., A.J. and A.E. generated protein expression constructs and strains, and established protein purification protocols.

Author Information Reprints and permissions information is available at www.nature.com/reprints. The authors declare no competing financial interests. Readers are welcome to comment on the online version of the paper. Correspondence and requests for materials should be addressed to J.F.X.D. (John.Diffley@cancer.org.uk).

METHODS

Yeast expression strain construction. All strains were constructed by transforming strain yJF1[27] with linearized expression vectors using standard genetic techniques (See Extended Data Tables 2 and 3 for details of vectors and strains). For expression of Sld3, Dpb11 and Sld2, affinity tags were added by transformation with PCR products following integration of the expression vector. The PCR products for Sld3 tagging were generated with oligonucleotides Sup sld3 TCP tag fwd and Sup TCP tag rev from the template pBS1539/TAP$^{TCP\ 3}$ (yTD6), and oligonucleotides Sld3SUP C-term Flag tag fwd and Sld2SUP C-term Flag rev using pBP83 (a derivative of pYM18[28] modified to insert a C-terminal 3×Flag tag associated with the *NatNT2* marker) as template (yTD11). PCR products for Sld2 and Dpb11 were generated from pBP83 using oligonucleotides Sld2SUP C-term Flag rev and Sld2SUP C-term Flag rev for Sld2 and JTY10 and Cdc45 flag tag rev for Dpb11. Affinity tagged protein expression was verified by immunoblot.

Proteins and protein expression. Vaccinia virus topoisomerase I was purchased from Sigma. ORC, Cdc6, Cdt1–Mcm2–7, DDK, cyclin A/Cdk2 and Sic1 were expressed and purified as previously described[6,27,29]. All proteins purified in this study contained affinity tags, which were used in the first step of purification. For the amino acid sequences of the affinity tags and their locations see Extended Data Table 1. GINS and Mcm10 were expressed in *E. coli.* All other proteins were overexpressed in *S. cerevisiae* from bidirectional Gal1-10 promoters in a *pep4Δ*, *bar1Δ* strain background (yJF1) (see Extended Data Table 2 for details of expression strains). Expression strains for Dpb11, Sld2, Cdc45, Ctf4, RPA and Pol ε were grown at 30 °C in YP + 2% raffinose to a density of $\sim 2\text{–}4 \times 10^7$ cells per ml. Cells were arrested in G1 with 100 ng ml^{-1} alpha factor and incubation was continued for 3 h. Protein expression was induced by addition of galactose to 2% and growth continued for 3 h at 30 °C. Topo II expression was conducted essentially as described above but alpha factor was added together with galactose and growth was continued for 6 h. For Pol α expression, cells were grown to a density of $\sim 2 \times 10^7$ cells per ml and expression was induced for 2 h by addition of galactose (2%). S-CDK expressing cells were grown to 2×10^7 cells per ml and protein expression induced by addition of galactose (2%) together with nocodazole (5 μg ml^{-1}) with growth continued for a further 3 h. In all cases, cells were collected, washed once with 25 mM HEPES-KOH pH 7.6, 1 M sorbitol and once with the appropriate initial protein purification buffer (see individual purification protocols for buffers used) lacking protease inhibitors. Cells were resuspended in 0.3–0.4 volumes of the initial purification buffer + protease inhibitors and the suspensions frozen drop-wise in liquid nitrogen. Frozen cells were crushed in a freezer mill (SPEX CertiPrep 6850 Freezer/Mill) with 6 cycles of 2 min at a crushing rate of 15. The resulting powders were stored at −80 °C until required.

Sld2 purification. Frozen cell powder was thawed and resuspended in 3 volumes 25 mM HEPES-KOH pH 7.6, 10% glycerol, 0.02% v/v Nonidet P40 substitute (NP-40-S) (Roche #11754599001), 1 mM EDTA, 1 mM DTT, 500 mM KCl (buffer H + 500 mM KCl) + protease inhibitors (0.3 mM PMSF, 7.5 mM benzamidine, 0.5 mM AEBSF, 1 mM leupeptin, 1 mM pepstatin A and 1 μg ml^{-1} aprotinin (Sigma)). Insoluble material was cleared by centrifugation (235,000*g*, 4 °C, 1 h) and solid ammonium sulphate was added to the supernatant to 32% followed by gentle stirring (10 min, 4 °C). Insoluble material was removed by centrifugation (27,000*g*, 4 °C, 20 min) and the ammonium sulphate concentration increased to 48% followed by stirring for 10 min. Precipitated protein was collected by centrifugation (27,000*g*, 4 °C, 20 min) and resuspended in 1/3 of the original volume buffer H + 500 mM KCl + protease inhibitors. Flag-tagged Sld2 was bound to anti-Flag M2 affinity gel (Sigma) in batch for 30 min at 4 °C. Resin was collected in 20 ml chromatography columns (Bio-Rad) and washed extensively in buffer H + 500 mM KCl + protease inhibitors. The resin was resuspended in 10 column volumes (CV) buffer H without EDTA + 500 mM KCl + 10 mM magnesium acetate + 1 mM ATP and incubated for 10 min at 4 °C. The flow-through was discarded and the column washed with 20–40 CV buffer H + 500 mM KCl. Sld2–Flag was eluted in 1 CV buffer H + 500 mM KCl + 0.5 mg ml^{-1} 3×Flag peptide, followed by 2 CV buffer H + 500 mM KCl + 0.25 mg ml^{-1} 3×Flag peptide.

The eluates were pooled, dialysed against buffer H + 280 mM KCl and applied to a 1-ml HiTrap SP FF column (GE Healthcare) equilibrated in buffer H + 250 mM KCl. Sld2–Flag was eluted with an 18 CV gradient from 250 mM KCl to 1 M KCl in buffer H. Peak fractions were pooled and dialysed against buffer H with 40% v/v glycerol + 350 mM KCl. Protein concentration was assessed using the Bradford assay (Bio-Rad) and this method was used for all proteins in this study.

Sld3/7 purification. To purify TCP-tagged Sld3/7, cell powder from yTD6 was thawed in buffer H + 500 mM KCl + protease inhibitors and insoluble material was cleared by centrifugation (235,000*g*, 4 °C, 1 h). Sld3/7 was depleted from the soluble extract by incubation for 40 min at 4 °C with IgG Sepharose 6 Fast Flow (GE Healthcare). The resin was collected in a 20 ml column and washed extensively in buffer H with 0.5 mM EDTA + 500 mM KCl. Sld3/7 was cleaved from the column by incubation for 2 h at 4 °C with tobacco etch virus (TEV) protease (50 μg ml^{-1}) in buffer H with 0.5 mM EDTA + 500 mM KCl. His-tagged TEV protease was removed by passing the eluate over a Ni-NTA Agarose column (Qiagen). The resulting flow through was concentrated and separated on a Superdex 200 column (GE Healthcare) equilibrated in buffer H + 500 mM KCl.

The Flag-tagged Sld3/7 used for Cdc45 depletion (Extended Data Fig. 7) was purified from yTD11 cells essentially as described above, except that Sld3/7 was depleted from the soluble extract by incubation with anti-Flag M2 affinity gel for 1 h at 4 °C. Bound Sld3/7 was eluted as described for Sld2 and the eluate was concentrated and separated on a Superdex 200 column equilibrated in buffer H + 500 mM KCl.

Cdc45 purification. 80 g cell powder was thawed in 200 ml buffer H without NP-40-S + 500 mM potassium acetate + protease inhibitors and cell debris was removed by centrifugation (235,000*g*, 4 °C, 1 h). 8 ml anti-Flag M2 affinity gel was added and the extract incubated for 4 h at 4 °C. Resin was collected in 20 ml columns (2 ml per column) washed extensively in buffer H without NP-40-S + 500 mM potassium acetate, then buffer H without NP-40-S + 300 mM potassium acetate. Cdc45 was eluted by incubation of the resin in 1 CV buffer H without NP-40-S + 300 mM potassium acetate + 0.5 mg ml^{-1} 3×Flag peptide. The eluate was dialysed against 150 mM potassium acetate, 0.5 mM DTT, 10% glycerol, 20 mM K-phosphate pH 7.4, (buffer P + 20 mM K-phosphate) and then applied to 1.5 ml hydroxyapatite column (Bio-Rad) equilibrated in the same buffer. The column was washed with buffer P + 80 mM K-phosphate and Cdc45 was eluted with buffer P + 250 mM K-phosphate. The eluate was extensively dialysed against buffer H without NP-40-S + 300 mM potassium acetate before storage. To test the functionality of the internally Flag-tagged Cdc45, we depleted endogenous Cdc45 from an S phase extract (Extended Data Fig. 7a). DNA replication was not detected after depletion but was restored following addition of purified Cdc45 (Extended Data Fig. 7b). The distributions of replication products following Cdc45 depletion and add back were indistinguishable from an undepleted sample (compare lanes 1 and 4) suggesting that the recombinant protein is functional.

S-CDK purification. 40 g cell powder was thawed in 80 ml 40 mM HEPES-KOH pH 7.6, 10% glycerol, 0.02% v/v NP-40-S, 300 mM potassium acetate (buffer CD + 300 mM potassium acetate) + protease inhibitors. Cell debris was cleared by centrifugation (235,000*g*, 4 °C, 1 h), calcium chloride was added to 2 mM together with calmodulin affinity resin (Agilent) and the extract was incubated at 4 °C for 1 h. Resin was collected in a 20 ml column, washed extensively with buffer CD + 300 mM potassium acetate + 2 mM $CaCl_2$ and S-CDK was eluted by incubation for 16 h with 100 μg ml^{-1} TEV protease in buffer CD + 2 mM $CaCl_2$. TEV protease was removed by passing the eluate over Talon resin (Clontech) and collecting the flow through, which was then applied to a Superose 6 column (GE Healthcare) equilibrated in buffer CD + 300 potassium acetate. Peak fractions were pooled and concentrated.

Dpb11 purification. Cell powder was resuspended in 2 volumes buffer H + 500 mM KCl and the debris removed by centrifugation (235,000*g*, 4 °C, 1 h). Dpb11–Flag was bound to anti-Flag M2 affinity gel for 90 min at 4 °C. The resin was collected, washed extensively with buffer H + 500 mM KCl and the protein eluted in buffer H + 500 mM KCl using 3×Flag peptide as for Sld2. The eluate was dialysed against buffer H + 150 mM KCl and applied to a 1 ml MonoS column (GE Healthcare). Dpb11–Flag was eluted with a 30 CV gradient from 150 mM KCl to 1 M KCl in buffer H with the peak fractions then dialysed against buffer H + 300 mM potassium acetate.

DNA polymerase ε purification. Cell powder was slowly thawed in buffer H without NP-40-S and EDTA + 400 mM potassium acetate (buffer E + 400 mM potassium acetate) + 1 Complete, EDTA free protease inhibitor tablet (Roche) per 25 ml buffer and cell debris was removed by centrifugation (235,000*g*, 4 °C, 1 h). To the supernatant $CaCl_2$ was added to 2 mM together with calmodulin affinity resin and the solution was rotated at 4 °C for 60 min. Resin was collected in a 20 ml column, washed extensively in buffer E + 400 mM potassium acetate + 2 mM $CaCl_2$ and Pol ε was eluted in 2 ml fractions with buffer E + 400 mM potassium acetate + 2 mM EDTA + 2 mM EGTA. The eluate was pooled and applied directly to a 5 ml Hi-trap heparin column (GE Healthcare) equilibrated in buffer E + 400 mM potassium acetate. Following extensive washing with buffer E + 450 mM potassium acetate proteins were eluted with a 12 CV gradient from 450 mM – 1 M potassium acetate in buffer E. Heparin fractions containing Pol ε were pooled, concentrated and separated on a Superdex 200 column (GE Healthcare) equilibrated in buffer E + 500 mM potassium acetate.

Ctf4 purification. Ctf4 purification was based on a published method[30] with modifications. Cell powder was thawed in 2 volumes 25 mM Tris-HCl pH 7.2, 10% glycerol, 1 mM DTT, 200 mM NaCl (buffer C + 200 mM NaCl) + protease inhibitors and the insoluble material removed by centrifugation (235,000*g*, 4 °C, 1 h). Calcium chloride was added to 2 mM together with calmodulin affinity resin. The extract was incubated at 4 °C for 90 min before the resin was collected and washed extensively with buffer C + 200 mM NaCl + 2 mM $CaCl_2$. Proteins were eluted in buffer C + 200 mM NaCl + 2 mM EDTA + 2 mM EGTA. The NaCl concentration of the

eluate was reduced to 150 mM by dilution in buffer C before application to a 1 ml MonoQ equilibrated in buffer C + 150 mM NaCl + 1 mM EDTA. Ctf4 was eluted with a 30 CV gradient from the 150 mM to 1 M NaCl in buffer C. Peak fractions were pooled, concentrated and separated on a Superdex 200 column (GE Healthcare) equilibrated in buffer C + 150 mM NaCl + 1 mM EDTA. Ctf4 containing fractions were dialysed against buffer C + 75 mM NaCl + 1 mM EDTA.

DNA polymerase α–primase purification. Cell powder was thawed in buffer C + 0.02% NP-40-S + 400 mM NaCl (buffer D + 400 mM NaCl) + protease inhibitors and insoluble material was cleared by centrifugation (235,000*g*, 4 °C, 1 h). The NaCl concentration was reduced to 300 mM by dilution in buffer lacking NaCl, and calcium chloride was added to 2 mM together with calmodulin affinity resin. The extract was incubated at 4 °C for 90 min before the resin was collected in a 20 ml column, washed extensively with buffer D + 300 mM NaCl + 2 mM $CaCl_2$ and proteins eluted with buffer D + 300 mM NaCl + 2 mM EDTA + 2 mM EGTA. Pooled fractions were diluted in buffer D to a conductivity equivalent to buffer D + 120 mM NaCl and were loaded onto a 1 ml MonoQ column. Bound proteins were removed with a 30 CV gradient from 120 mM to 1 M NaCl in buffer D and fractions containing pol α were pooled, concentrated to 400 µl and applied to a Superdex 200 column equilibrated in buffer D + 150 mM NaCl. The peak fractions were pooled, concentrated to ~0.7 mg ml^{-1} and snap frozen in liquid nitrogen.

RPA purification. 40 g cell powder was thawed in buffer C + 500 mM NaCl + protease inhibitors and insoluble material cleared by centrifugation (235,000*g*, 4 °C, 1 h). Lysate conductivity was reduced to the equivalent of buffer C + 200 mM NaCl by twofold dilution in buffer C + protease inhibitors, followed by 1 h dialysis against buffer C + 200 mM NaCl. $CaCl_2$ was added to 2 mM together with 1 ml calmodulin affinity resin and the extract incubated at 4 °C for 90 min with rotation. Resin was collected in a 20 ml column, washed with 35 CVs buffer C + 200 mM NaCl + 2 mM $CaCl_2$ and bound proteins were eluted in 1 ml fractions of buffer C + 2 mM EDTA + 2 mM EGTA. Peak fractions were pooled, diluted twofold in buffer C + 1 mM EDTA, dialysed for 1 h against buffer C + 50 mM NaCl + 1 mM EDTA and loaded onto a 1 ml Hi-trap heparin column equilibrated in the same buffer. After extensive washing proteins were eluted with a 30 CV gradient from 50 mM – 1 M NaCl in buffer C + 1 mM EDTA. Peak fractions were pooled, diluted threefold in buffer C + 1 mM EDTA, dialysed for 1 h against buffer C + 150 mM NaCl + 1 mM EDTA and loaded onto a 1 ml MonoQ equilibrated in the same buffer. RPA was eluted with a 25 CV gradient from 150 mM – 1 M NaCl in buffer C + 1 mM EDTA and peak fractions were pooled and dialysed overnight in buffer C with 38% glycerol + 1 mM EDTA + 50 mM NaCl.

Topoisomerase II purification. Powder was thawed in buffer D + 300 mM NaCl + protease inhibitors and insoluble material removed by centrifugation (235,000*g*, 4 °C, 1 h). The soluble extract was supplemented with 2 mM $CaCl_2$ and calmodulin affinity resin was added and the solution incubated at 4 °C for 1 h. Resin was collected in a 20 ml column, washed extensively with buffer D + 300 mM NaCl and the CBP-tagged Topo II eluted with buffer D + 300 mM NaCl + 2 mM EDTA + 2 mM EGTA. The eluate was concentrated and applied directly to a Superdex 200 column equilibrated in buffer D + 150 mM NaCl. Topo II containing fractions were pooled and the salt concentration adjusted to ~ 100 mM by dilution before loading onto a 1 ml MonoQ equilibrated in buffer D + 100 mM NaCl. Topo II was eluted with a 25 CV gradient from 100 to 800 mM NaCl in buffer D and the peak fractions were pooled and dialysed against buffer D + 150 mM NaCl before storage.

GINS purification. Plasmid pFJD5 (gift from K. Labib), which is a derivative of pFJD12[19] in which the Psf3 subunit is expressed with an N-terminal His-tag, was used to transform Bl21 (DE3) Rosetta pLysS. Cells were grown in LB at 37 °C to an $A_{600\,nm}$ of 0.5 and protein expression was induced by addition of IPTG to 1 mM. Growth was continued for 2 h before cells were harvested by centrifugation. Cell pellets were resuspended in buffer D + 400 mM NaCl + 10 mM imidazole + protease inhibitors, cells were lysed by sonication and the debris removed by centrifugation (257,000*g*, 4 °C, 30 min). His-tagged proteins were depleted by incubation with Ni-NTA resin (Qiagen) for 1 h at 4 °C and the resin was collected in a 20 ml column. Following extensive washing with buffer D + 400 mM NaCl + 10 mM imidazole and then buffer D + 100 mM NaCl + 15 mM imidazole, GINS was eluted with buffer D + 100 mM NaCl + 200 mM imidazole. Fractions were pooled and dialysed against buffer D + 100 mM NaCl before being applied to a 1 ml MonoQ column equilibrated in the same buffer. Proteins were eluted with a 25 CV gradient from 100 mM to 500 mM NaCl in buffer D and the GINS containing fractions were pooled, concentrated and separated through a Superdex 200 column equilibrated in buffer D + 150 mM NaCl. The peak was rebound to Ni-NTA Agarose resin and the resin was washed with 50 mM HEPES-KOH pH 7.6, 10% glycerol, 0.05% NP-40-S, 10 mM magnesium acetate before GINS was eluted in the same buffer supplemented with 50 mM imidazole. Finally the eluate was dialysed against buffer H + 200 mM potassium acetate before storage.

Mcm10 purification. Plasmid pET28a-Mcm10, which expresses Mcm10 with an N-terminal His/T7 tag, was used to transform BL21 (DE3). Cells were grown at 37 °C to an $A_{600\,nm}$ of 0.6 before the temperature was reduced to 25 °C and protein expression induced by addition of IPTG to 1 mM. Growth was continued for 3 h at 25 °C before cells were harvested, washed in 50 mM Tris-HCl pH 7.6, 10% sucrose and resuspended in 25 mM Tris-HCl pH 7.6, 10% glycerol, 0.01% NP-40-S, 500 mM NaCl (buffer M + 500 mM NaCl) + protease inhibitors. Cells were lysed by sonication and the debris removed by centrifugation (257,000*g*, 4 °C, 30 min). The clear lysate was applied under gravity flow to a 1.5 ml Ni-NTA Agarose column. The column was washed with 15 CV buffer M + 500 mM NaCl followed by 10 CV buffer M + 200 mM NaCl + 20 mM imidazole and His–Mcm10 was eluted with buffer M + 200 mM NaCl + 200 mM imidazole. The eluate was applied to a 1 ml MonoS equilibrated in buffer M + 200 mM NaCl and proteins were eluted with a 20 CV gradient from 200 mM to 1 M NaCl in buffer M. Peak Mcm10 fractions were pooled, the NaCl concentration adjusted to 200 mM by dilution in buffer M and reapplied to a 1 ml MonoS. The column was run as described for the first run and Mcm10 containing fractions were pooled and dialysed against buffer H with 0.01% NP-40-S + 200 mM K-glutamate.

S phase extracts. S phase extracts were prepared as described previously[6]. Psf2–Flag (GINS complex) was depleted from the yJY18 extract by two 45 min incubations at 4 °C with a 1:10 extract volume of anti-Flag M2 magnetic beads (Sigma). To deplete Cdc45 from the yJY16 extract, Flag-tagged Sld3/7 was pre-bound to anti-Flag M2 magnetic beads (5 pmol per 1 µl of resin). Cdc45 was then depleted from the extract by two 30 min incubations using 2.5 µl beads per 20 µl of extract.

DNA templates. 1 kb biotinylated linear ARS305 DNA templates were generated as described[3,31]. For linear ARS1 templates a 2.8 kb region surrounding ARS1 was amplified using primers ARS1_XmaI-F and ARS1_XhoI-R and cloned into pBluescript KS (+) using XhoI and XmaI to generate plasmid pCFK1. An A-B2- derivative, pCFK2, was generated by sequential rounds of site-directed mutagenesis using oligonucleotides MutA_F, MutA_R, MutB2_F, MutB2_R. 2.8 kb biotinylated wild type and A-B2- ARS1 linear DNA templates were generated by PCR using the oligonucleotides ARS1-PC-Bio-F and ARS1-Bio-R with pCFK1 and pCFK2 as templates, respectively. 3.2 kb randomly biotinylated circular DNA templates were generated as described[6]. Biotinylated DNA was coupled to streptavidin M-280 magnetic DNA beads (Invitrogen) essentially as described[3,31]. For linear DNA templates 250 ng DNA was coupled to 5 µl bead slurry. As biotinylation efficiency was estimated only to be ~10–20% for the circular DNA templates, 1 µg of DNA was coupled per 5 µl bead slurry.

Standard protein recruitment and replication reactions. Unless stated in the figure legends, protein recruitment assays were conducted using the ARS305 linear template, whereas DNA replication reactions used ARS1 circular DNA as template. All incubations were conducted with agitation (1,250 r.p.m.) in a Thermomixer (Eppendorf). The concentrations of proteins in recruitment and replication reactions were determined empirically using the concentrations of individual firing factors in S phase extracts for guidance. Sld3/7 purified from yTD6 was used in all protein recruitment and replication reactions. Salt contributions from proteins added to reactions were less than 30 mM in all steps. MCM loading reactions ('MCM' load) (7.5-10 µl) were performed in a buffer containing 25 mM HEPES-KOH pH 7.6, 100 mM K-glutamate, 10 mM magnesium acetate, 0.02% NP-40-S, 5% glycerol, 2 mM DTT, 5 mM ATP (loading buffer), 45 nM ORC, 45 nM Cdc6, 100 nM Cdt1–Mcm2–7 and either 6.25 ng per µl linear or approximately 4 ng per µl circular DNA immobilised on M-280 streptavidin magnetic beads (Invitrogen). After 20 min incubation at 25 °C DDK was added directly to the reaction to a final concentration of 130 nM and incubation was continued at 25 °C for 30 min. Buffer and unbound proteins were removed using a magnetic rack and were replaced by a new buffer of twofold the MCM loading reaction volume (15–20 µl) containing 40 mM HEPES-KOH pH 7.6, 300 mM K-glutamate, 10 mM magnesium acetate, 0.02% NP-40-S, 8% glycerol, 400 µg ml^{-1} BSA (NEB), 2 mM DTT, 5 mM ATP (firing-factor recruitment buffer + 300 mM K-glutamate) and 26 nM Sld3/7 and 50 nM Cdc45. Following incubation at 25 °C for 5 min the supernatant was removed and replaced with the same volume (15–20 µl) of firing-factor recruitment buffer + 250 mM K-glutamate and 40 nM Dpb11, 62 nM Sld2, 30 nM Pol ε, 210 nM GINS, 2.5 nM Mcm10 and 50 nM A-Cdk2 (cyclin A/Cdk2) (Figs 1–4 and Extended Data Figs 2–4) or S-CDK (Clb5/Cdc28/Cks1) at a concentration of 30 nM for Fig. 6, 20 nM for Fig. 5e, f and Extended Data Fig. 5c and 25 nM for Fig. 5a–c and Extended Data Fig. 5a, b. Reactions were incubated at 25 °C for 10 min ('CDK' step). For protein recruitment assays that were terminated after the 'CDK' step, 10 ng per µl poly(dI-dC) (Sigma) was added to both the buffer containing Sld3/7 and Cdc45, and the 'CDK' step. After the 'CDK' step supernatants were again removed and replaced with the same volume of buffer containing 40 mM HEPES-KOH pH 7.6, 150 mM K-glutamate, 10 mM magnesium acetate, 5% glycerol, 2 mM DTT, 2 mM ATP, 200 µM CTP, GTP, UTP, 40 µM dATP, dTTP, dCTP, dGTP, 2.5 nM Mcm10, 50 nM RPA, 25 nM pol α, 30 nM Ctf4, 25 nM Topo II and, for replication reactions, 40 nM [α-^{32}P]dCTP (Perkin Elmer). Reactions were incubated at 30 °C for 30 min.

For protein recruitment assays, unless stated in the figure legends, the final reaction buffer (either after both the 'DDK' and 'CDK' steps or the final replication step) was removed and beads were washed three times in 150 μl room temperature buffer containing 40 mM HEPES-KOH pH 7.6, 300 mM K-glutamate, 10 mM magnesium acetate, 5% glycerol, 0.02% NP-40-S (wash buffer + 300 mM K-glutamate). Beads were resuspended in SDS-loading buffer, heated to 95 °C for 3 min and proteins were separated through 4–12% Bis-Tris polyacrylamide gels (Bio-Rad) before analysis by immunoblotting.

Replication reactions were terminated by removing the supernatant and immediately washing the beads twice with 150 μl 40 mM HEPES-KOH pH 7.6, 600 mM KCl, 5% glycerol, 0.02% NP-40-S, 5 mM EDTA before resuspending the beads in 5 mM EDTA and then adding NaOH and sucrose to 50 mM and 1% w/v, respectively. Samples were incubated at room temperature for 20–30 min before the products were separated through 0.7% alkaline agarose gels in 30 mM NaOH, 2 mM EDTA for 16 h at 25 V. Gels were fixed with 5% cold trichloroacetic acid, dried onto chromatography paper (Whatman) and autoradiographed with Amersham Hyperfilm-MP (GE Healthcare). When gels were quantified images were scanned using a Typhoon phosphorimager (GE Healthcare) and were quantified using ImageQuant software (GE Healthcare).

Modified protein recruitment and replication reactions. For experiments where mid-reaction washes were included (Fig. 6a, b), two 150 μl washes were conducted in wash buffer containing the salts indicated in the figure legends, followed by one 150 μl wash in wash buffer + 300 mM K-glutamate. Reactions with a single firing-factor recruitment step (Fig. 6d, e) were conducted in firing-factor recruitment buffer + 250 mM K-glutamate for 30 min at 25 °C, with 30 nM S-CDK, 65 nM DDK and all other proteins at the same concentrations as in standard reactions.

In Fig. 5a, lane 2, MCM loading factors (22.5 nM Orc, 45 nM Cdc6, 100 nM Cdt1–Mcm2–7) were pre-treated in loading buffer with 25 nM S-CDK for 10 min at 25 °C before DNA addition for 20 min. When S-CDK was added after DNA (lane 1), MCM loading factors were incubated with DNA for 20 min and S-CDK then added for a further 10 min. Pre-treatment of individual MCM loading factors with S-CDK (Fig. 5b, c and Extended Data Fig. 5a, b) was performed under the same conditions as those used for MCM loading except that ORC was present at 22.5 nM and S-CDK and Sic1 were at 25 nM and 125 nM, respectively. Proteins were incubated at 25 °C with S-CDK for 10 min, S-CDK was inhibited with Sic1 (5 min) before the remaining proteins required for MCM loading were added and incubation continued for 20 min. To ensure S-CDK and Sic1 were removed from the above reactions, samples were subjected to two 150 μl washes in wash buffer + 600 mM NaCl and one 150 μl wash in wash buffer + 300 mM K-glutamate after either the MCM loading step (Fig. 5a), or after DDK phosphorylation (Fig. 5b, c and Extended Data Fig. 5a, b).

When Sld3/7 and Sld2 were pre-incubated with S-CDK (Fig. 5e, f and Extended Data Fig. 5c) the incubations were performed in the standard firing-factor recruitment buffers with 20 nM S-CDK for 7 min followed by addition of Sic1 (100 nM) for 3 min. The remaining firing factors were then added to the same concentrations as used in standard reactions.

For origin dependent replication reactions (Fig. 3c) ORC was pre-bound to DNA for 10 min at 30 °C in reactions (10 μl) containing 25 mM HEPES-KOH pH 7.6, 50 mM KCl, 10 mM magnesium acetate, 5% glycerol, 2 mM ATP, 1 mM DTT, 100 μg ml^{-1} BSA, 6.25 ng/μl ARS1 linear DNA beads and 2.5 nM ORC. The supernatant was removed, the beads washed twice with wash buffer + 300 mM potassium acetate and a new buffer (10 μl) containing 25 mM HEPES-KOH pH 7.6, 100 mM potassium acetate, 10 mM magnesium acetate, 0.02% NP-40-S, 5% glycerol, 2 mM DTT, 5 mM ATP, 45 nM Cdc6, 100 nM Cdt1–Mcm2–7 was added and the mix incubated at 30 °C for 30 min. The buffer was removed and replaced with loading buffer + 130 nM DDK (10 μl) and the samples incubated at 25 °C for 30 min. All downstream steps were performed as described for standard reactions.

Extract-based replication. For reactions on bead-bound DNA (Fig. 2d and Extended Data Fig. 2e), MCM and firing factors were assembled as described for standard protein recruitment and replication assays on immobilised ARS1 circular template (10 μl MCM loading reactions). Beads were washed twice with 150 μl wash buffer + 200 mM K-glutamate and resuspended in extract replication buffer (20 μl) containing 65 mM HEPES-KOH pH 7.6, 150 mM K-glutamate, 10.5 mM magnesium acetate, 5% glycerol, 0.5 mM EDTA, 0.5 mM EGTA, 40 mM creatine phosphate and 100 ng per μl creatine phosphokinase, 3.5 mM DTT, 2.5 mM ATP, 200 μM CTP, GTP, UTP, 100 μM dGTP, dATP, dTTP, 25 μM dCTP and 50 nM [α-^{32}P]dCTP. Samples were incubated at 25 °C for 30 min and were processed as described for standard replication reactions.

The soluble replication reaction in Extended Data Fig. 7b was performed as described previously[6] with unmodified ARS1 circular DNA as template. Products were separated through a 1% native agarose gel.

Oligonucleotides. JTY10, AAACCTATGAGACGACAGACAAGAAATCAGACAAAGGAATTAGATTCTCTGGAAGTGCTGTTTCAGGGCCCGCGTACGCTGCAGGTCGAC; JTY32, CGATGATGAGACAATATCTAATAAAAGAGG; JTY33, TCTTTTATAGTCCTCGTCTGTGACTTCATC; JTY40, GATGATGATGGGGACTATAAAGACGATGATGAGAC; JTY41, TTTATAATCCTCGTCTGTGACTTCATCGGC; JTY92, AGCACAATAAGGCGCGCCTATAAAACAATGTTCAGGCAGTCAAAAAG; JTY100, CTTTTCCCTTCTCGAGTTAATGATTACCATTATTG; Dpb11 fwd, AAGCTCACCGGTGATGAAGCCCTTTCAAGGAATA; Dpb11 reverse, CTGAGGCGGCCGCTCAAGAATCTAATTCCTTTGT; Sld3SUP C-term Flag fwd, CTTCTAAGAGAAGAGTTAGAAGAAGATTGTTCGCTCCAGAATCTACTCTGGAAGTGCTGTTTCAGGGCCCGCGTACGCTGCAGGTCGAC; Sld2SUP C-term Flag fwd, GTTGCCAAAGAAGAACAGATTCTCCAACGGTAGATGGGGTAGAAGACTGGAAGTGCTGTTTCAGGGCCCGCGTACGCTGCAGGTCGAC; Sld2SUP C-term Flag rev, GAGAAAAGAAAAAAATTGATCTATCGATTTCAATTCAATTCAATTTAATCGATGAATTCGAGCTCG; Sup sld3 TCP tag fwd, CTAAGAGAAGAGTTAGAAGAAGATTGTTCGCTCCAGAATCTACTGAAAACTTGTACTTCCAAGG; Sup TCP tag rev, GGAAAGAGAAAAGAAAAAAATTGATCTATCGATTTCAATTCAATTCAATTACGACTCACTATAGGG; Cdc45 flag tag rev, CGACTCACTATAGGGCGAATTGGAGCTCCACCGCGGTGGCGGCCGCTTAATCGATGAATTCGAGCTCG; Cdc45 fwd, CTGGACACCGGTGATGTATTATGGAATCAGCCAG; Cdc45 rev, AGCACGCGGCCGCTTATAACAATCCACTCAAGGT; ARS1_XmaI-F, CGATCCCGGGGGTAGTTATAAGAAAGAGACCGAGTTAG; ARS1_XhoI-R, CGATCTCGAGAAGAGTATTGGCGATGACGAAAC; ARS1-PC-Bio-F, Bio-GGTAGTTATAAGAAAGAGACCGAGTTAG; ARS1-Bio-R, AAGAGTATTGGCGATGACGAAAC; MutA_F, GCATAAAAGATCTAAACATACCTCGAGGAAAATAACAAGATGTAAAG; MutA_R, CTTTACATCTTGTTATTTTCCTCGAGGTATGTTTAGATCTTTTATGC;

MutB2_F, GTTATTACTGAGTAGTATTTCCTCGAGGATTGTTTGTGCACTTGCCTG; MutB2_R, CAGGCAAGTGCACAAACAATCCTCGAGGAAATACTACTCAGTAATAAC.

Antibodies. Anti-Mcm7 (yN-19, sc-6688, Santa Cruz), anti-Orc6 (SB49). Psf2–Flag was visualized with anti-Flag M2-peroxidase (Sigma), Mcm10 was detected using the T7-tag antibody (69522, Novagen), Dbf4 was visualized with an anti-CBP tag antibody (07-482 Merck Millipore) and Rpa1 was detected with anti-scRPA (AS07 214, Agrisera). Psf1 antibodies were a gift from K. Labib. Polyclonal antibodies against Sld3, Sld7, Sld2, Cdc45 and Dpb11 were described previously[6]. Polyclonal antibodies against the Dpb2 subunit of pol ε were raised against full-length protein, and their specificity was confirmed using purified pol ε.

28. Janke, C. *et al.* A versatile toolbox for PCR-based tagging of yeast genes: new fluorescent proteins, more markers and promoter substitution cassettes. *Yeast* **21,** 947–962 (2004).
29. Boos, D. *et al.* Regulation of DNA replication through Sld3-Dpb11 interaction is conserved from yeast to humans. *Curr. Biol.* **21,** 1152–1157 (2011).
30. Simon, A. C. *et al.* A Ctf4 trimer couples the CMG helicase to DNA polymerase alpha in the eukaryotic replisome. *Nature* **510,** 293–297 (2014).
31. Coster, G., Frigola, J., Beuron, F., Morris, E. P. & Diffley, J. F. X. Origin licensing requires ATP binding and hydrolysis by the MCM replicative helicase. *Mol. Cell* **55,** 666–677 (2014).
32. Brown, N. R. *et al.* The crystal structure of cyclin A. *Structure* **3,** 1235–1247 (1995).
33. Itou, H., Muramatsu, S., Shirakihara, Y. & Araki, H. Crystal structure of the homology domain of the eukaryotic DNA replication proteins Sld3/Treslin. *Structure* **22,** 1341–1347 (2014).
34. Sharp, P. M. & Li, W. H. The codon adaptation index-a measure of directional synonymous codon usage bias, and its potential applications. *Nucleic Acids Res.* **15,** 1281–1295 (1987).

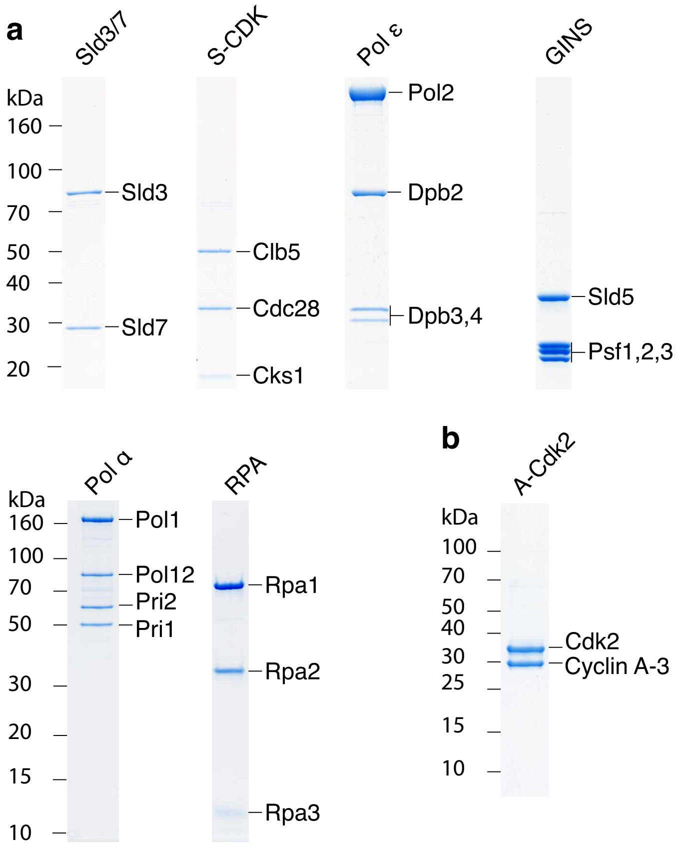

Extended Data Figure 1 | Coomassie-stained SDS–PAGE analysis of multi-subunit complexes required for DNA replication. a, Annotation of the polyacrylamide gels in Fig. 1a in which individual protein subunits have been labelled. **b**, Analysis of A-Cdk2. The protein complex consists of human Cdk2 and the bovine cyclin A-3 fragment[32].

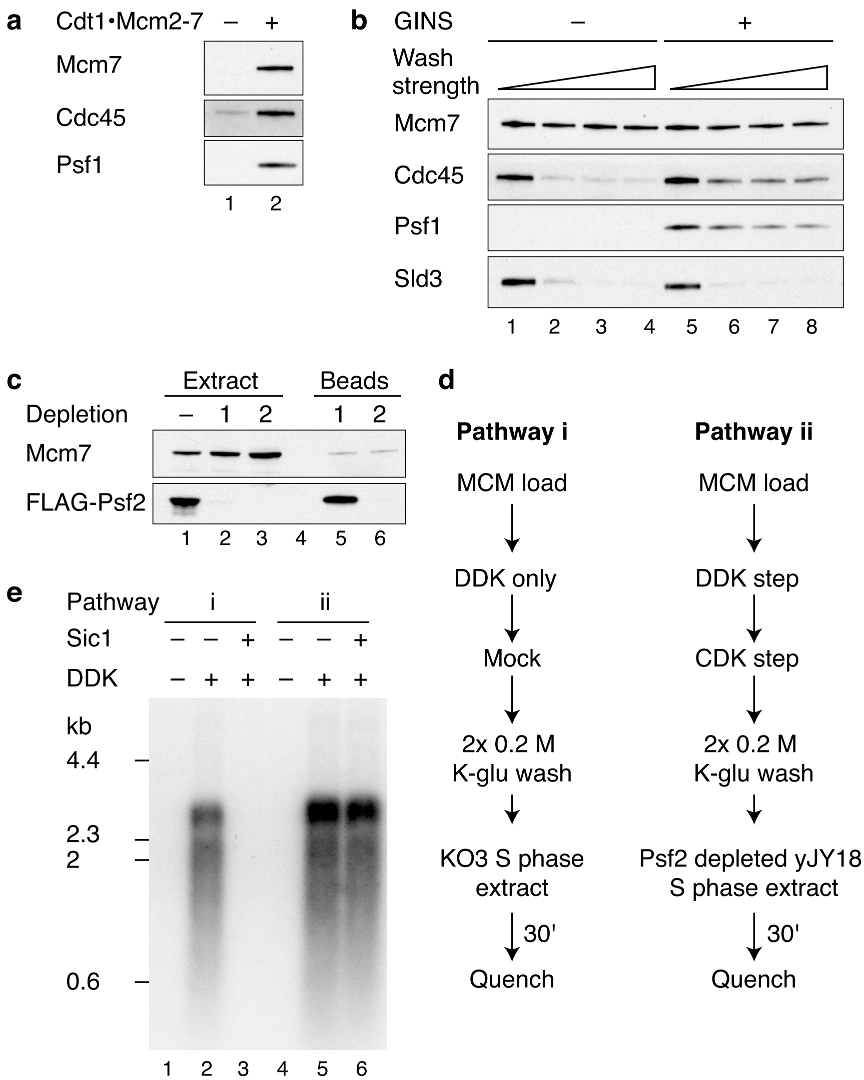

Extended Data Figure 2 | Analysis of firing factor recruitment. **a**, Immunoblots of protein recruitment conducted as in Fig. 1b but with 0.3 M KCl washes. **b**, Stability of recruited firing factors following washes of varying strength (lanes 1 and 5, 0.3 M K-glu; lanes 2 and 6, 0.3 M KCl; lanes 3 and 7, 0.45 M KCl; lanes 4 and 8, 0.6 M KCl). **c**, Psf2–Flag was depleted from a yJY18 S phase extract by two rounds of incubation with anti-Flag M2 magnetic beads. Levels of Psf2–Flag were determined by immunoblotting with the Flag-M2 antibody. Soluble and bead bound protein fractions are illustrated. **d**, Extract-based replication reaction schemes. In the left pathway (i), loaded MCM is treated with DDK and added to a KO3 extract (Sld3, Sld7, Cdc45, Dpb11, Sld2 overexpression). In the right pathway (ii), firing factors are recruited to MCM as illustrated in Fig. 1b and the complex is added to a yJY18 extract (no firing factor overexpression) in which Psf2 (GINS complex) has been depleted. **e**, Replication reactions as described in **d** using A-Cdk2 for firing factor recruitment. Where indicated, Sic1 was added to the extract 20 min before replication.

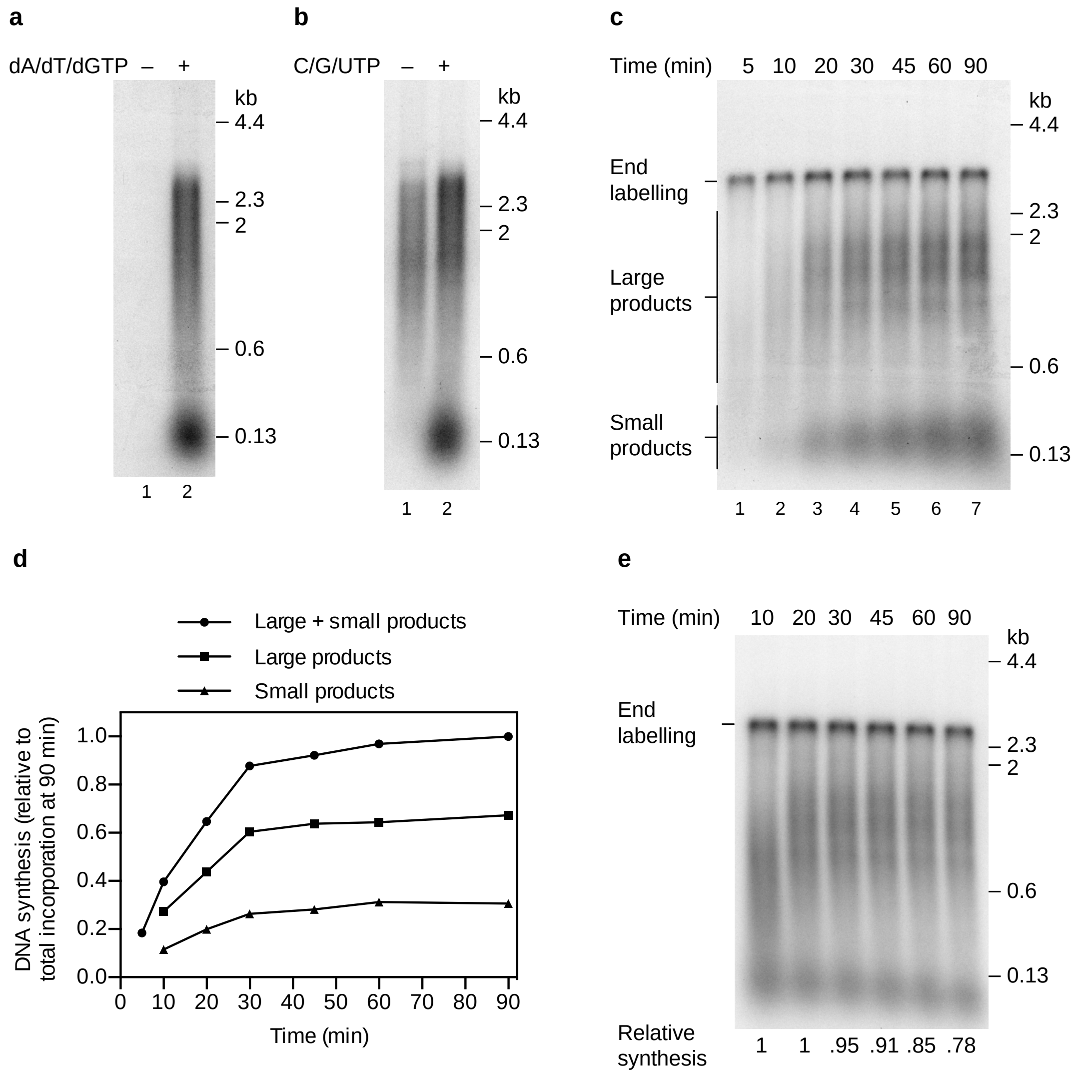

Extended Data Figure 3 | Characterization of the *in vitro* DNA replication reaction. **a**, **b**, Replication reactions conducted as in Fig. 3a with A-Cdk2 on ARS1 circular DNA templates for 1 h. **c**, Time course of a standard replication reaction using A-Cdk2 on the ARS1 linear DNA template. **d**, Quantitation of a time course conducted as in **c**. DNA synthesis was normalized to the total DNA synthesis at 90 min. Small and large replication products were not quantified separately at 5 min as they are not well resolved at this time point. **e**, Pulse chase experiment conducted with A-Cdk2 on the ARS1 linear DNA template. For the pulse the dCTP concentration was reduced to 4 μM. Following a 10 min incubation unlabelled dCTP was added to 100 μM.

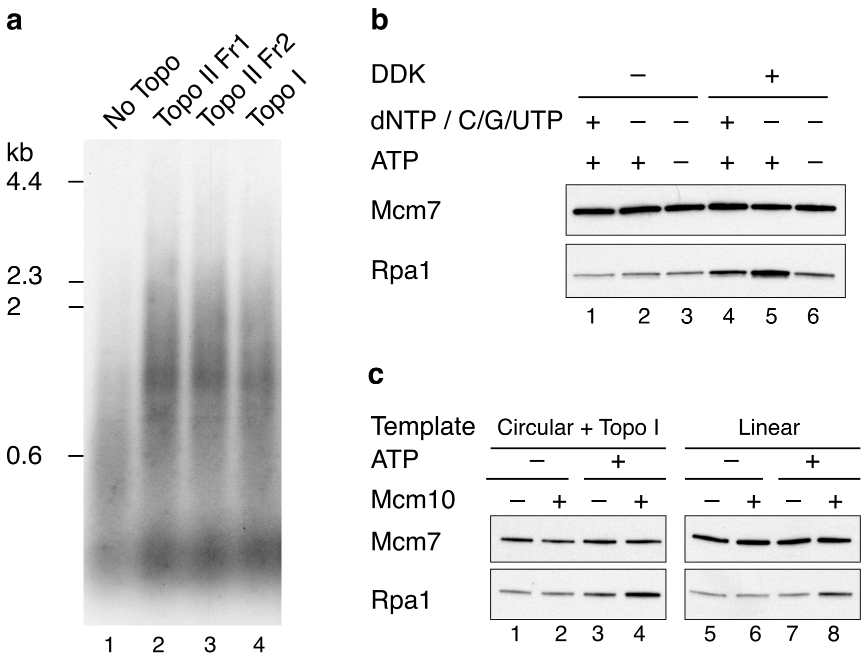

Extended Data Figure 4 | Characterization of RPA recruitment. Unless stated reactions were conducted on ARS1 circular templates. **a**, Vaccinia virus topoisomerase I supports DNA replication with purified proteins. Replication reactions with either Topo II (25 nM) or vaccinia virus topoisomerase I (0.125 units per μl). Two different Topo II fractions (Fr1 and Fr2) were used for comparison. **b**, Nucleotide dependence of RPA recruitment in a complete replication reaction with Topo II. **c**, RPA recruitment reactions were conducted on ARS1 circular template in the presence of vaccinia virus topoisomerase I (0.125 units per μl), or on a linear template in the absence of a topoisomerase. dNTPs, C/G/UTP, pol α and Ctf4 were omitted from the final step of the reaction.

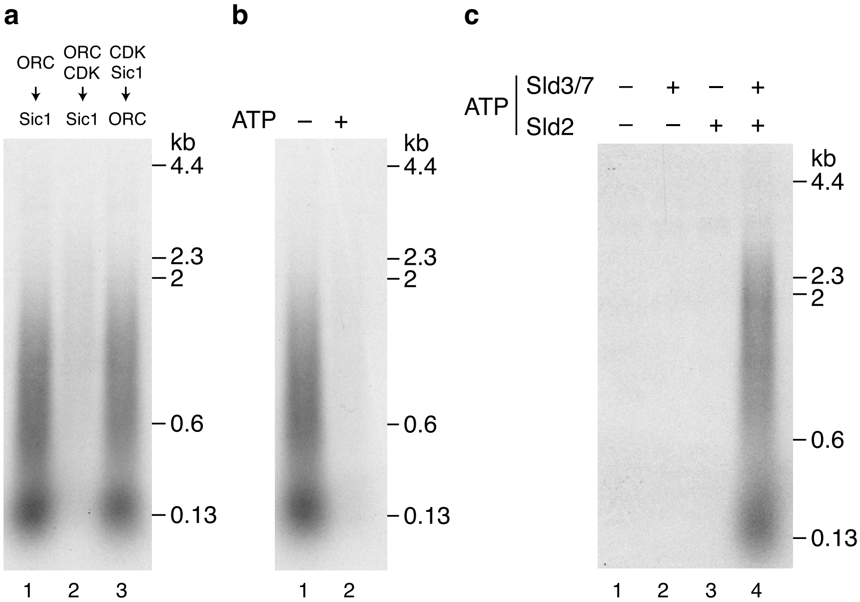

Extended Data Figure 5 | Regulation of MCM loading and origin firing by S-CDK is ATP dependent. **a**, Replication reaction where ORC was pre-incubated with S-CDK before MCM loading. When Sic1 was added before ORC the mix was incubated for 5 min and ORC was then added for 10 min. **b**, Pre-incubation of ORC with S-CDK in the presence or absence of ATP. After incubation with Sic1, ATP was added to the reaction lacking ATP. **c**, Sld3/7 and Sld2 were pre-incubated with S-CDK as illustrated in Fig. 5d in the presence or absence of ATP. Following incubation with Sic1, samples that did not contain ATP for the pre-incubation step were supplemented with ATP.

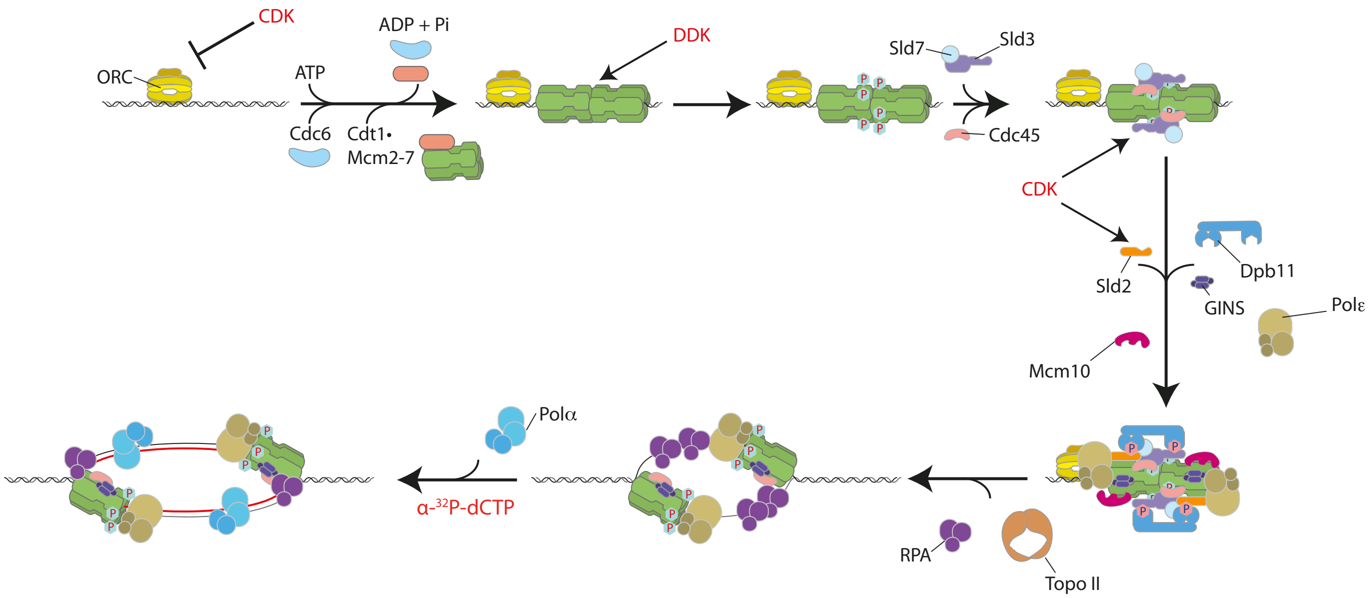

Extended Data Figure 6 | Cartoon illustrating protein kinase regulated eukaryotic DNA replication origin firing with purified proteins. Firing factors are recruited to loaded MCM in a DDK- and CDK-dependent manner. DNA synthesis is initiated once the DNA template has been unwound. CDK also functions to inhibit MCM loading by phosphorylating ORC.

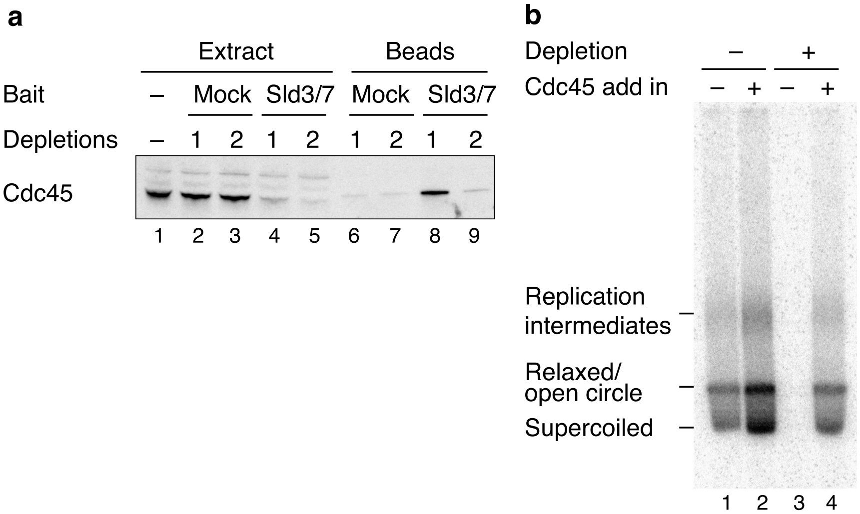

Extended Data Figure 7 | Internally Flag-tagged Cdc45 supports normal DNA replication in S phase extracts. **a**, The previously reported interaction between Sld3 and Cdc45 (ref. 33) was exploited to co-immunoprecipitate Cdc45 from yJY16 extracts (Dpb11 and Sld2 overexpression) by incubation with Flag–Sld3/7 that was pre-coupled to anti-Flag M2 magnetic beads. **b**, *In vitro* extract-based replication reaction on soluble ARS1 circular template using yJY16 extracts where endogenous Cdc45 was depleted as indicated. The extract was supplemented with purified Sld3/7 as the complex is not overexpressed in yJY16. The experiment was conducted for 30 min as described previously[6] and products were separated through a 1% native agarose gel. Internally Flag-tagged Cdc45 (52 nM) was added back as indicated. The locations of the different replication products are illustrated.

Extended Data Table 1 | Affinity tag strategies for protein purification

Protein	Yeast strain	Affinity tag strategy	Affinity tag sequence
Cdc45	yJY13	Internal 2xFLAG tag	E197 – DYKDDDG – D198, E199Y, E200K, E202D *
Sld3/7	yTD6	C-terminal TCP tag on Sld3	ENLYFQGEKRRWKKNFIAVSAANRFKKISSSGALDYDIPTTASKTAALA QHDEAVDNKFNKEQQNAFYEILHLPNLNEEQRNAFIQSLKDDPSQSA NLLAEAKKLNDAQAPKVDNKFNKEQQNAFYEILHLPNLNEEQRNAFIQ SLKDDPSQSANLLAEAKKLNGAQAPKVDANSAGKST
Sld3/7	yTD11	C-terminal 3xFLAG tag on Sld3	LEVLFQGPRTLQVDDYKDDDDKDYKDDDDKDYKDDDDK
Sld2	yTD8	C-terminal 3xFLAG tag	LEVLFQGPRTLQVDDYKDDDDKDYKDDDDKDYKDDDDK
Dpb11	yJY26	C-terminal 3xFLAG tag	LEVLFQGPRTLQVDDYKDDDDKDYKDDDDKDYKDDDDK
Pol ε	yAJ2	C-terminal CBP tag on Dpb4	ENLYFQGEKRRWKKNFIAVSAANRFKKISSSGAL
S-CDK	yAE37	N-terminal CBP tag on Clb5	MKRRWKKNFIAVSAANRFKKISSSGALENLYFQGE
Pol α - primase	yJY23	N-terminal CBP tag on Pri1	MKRRWKKNFIAVSAANRFKKISSSGALENLYFQGE
Ctf4	yAE40	N-terminal CBP tag	MKRRWKKNFIAVSAANRFKKISSSGALENLYFQGE
Topo II	yAE46	C-terminal CBP tag	ENLYFQGEKRRWKKNFIAVSAANRFKKISSSGAL
GINS	N/A	N-terminal 6His tag on Psf3	MGSSHHHHHHSSGLVPRGSHMAS
Mcm10	N/A	N-terminal 6His tag	MGSSHHHHHHSSGLVPRGSHMASMTGGQQMGRGSEF
RPA	yAE31	N-terminal CBP tag on Rfa1	MKRRWKKNFIAVSAANRFKKISSSGALENLYFQGE

All N-terminal tags are located immediately upstream of original start codon. All C-terminal tags are located immediately before the original stop. *Amino acid residue numbers correspond to the wild-type Cdc45 sequence.

Extended Data Table 2 | ***Saccharomyces cerevisiae* strains**

Strain	Genotype	Reference
yTD6	*MAT**a*** ade2-1 ura3-1 his3-11,15 trp1-1 leu2-3,112 can1-100, *bar1::Hyg* *pep4::KanMX,* *his3::HIS3pRS303/SLD3-TCP, GAL4,* *leu2::LEU2pRS305/SLD7*	This study
yTD8	*MAT**a** ade2-1 ura3-1 his3-11,15 trp1-1 leu2-3,112 can1-100* *bar1::Hyg* *pep4::KanMX* *his3::HIS3pRS303/Sld2-3xflag (Nat-NT2), GAL4*	This study
yTD11	*MAT**a** ade2-1 ura3-1 his3-11,15 trp1-1 leu2-3,112 can1-100* *bar1::Hyg* *pep4::KanMX* *his3::HIS3pRS303/SLD3-3xflag (Nat-NT2), GAL4* *leu2::LEU2pRS305/SLD7*	This study
yJY7	*MAT**α** ade2-1 ura3-1 his3-11,15 trp1-1 leu2-3,112 can1-100, cdc7-4* *pep4::KanMX*	This study
yJY13	*MAT**a** ade2-1 ura3-1 his3-11,15 trp1-1 leu2-3,112 can1-100* *bar1::Hyg* *pep4::KanMX* *his3::HIS3pRS303/Cdc45^{iflag2}, GAL4*	This study
yJY16	*MAT**α** ade2-1 ura3-1 his3-11,15 trp1-1 leu2-3,112 can1-100, cdc7-4* *pep4::KanMX* *ura3::URA3pRS306/Dpb11* *trp1::TRP1pRS304/Sld2*	This study
yJY18	*MAT**α** ade2-1 ura3-1 his3-11,15 trp1-1 leu2-3,112 can1-100, cdc7-4* *pep4::KanMX* *Psf2-3xFlag (Nat-NT2)*	This study
yJY23	*MAT**a** ade2-1 ura3-1 his3-11,15 trp1-1 leu2-3,112 can1-100* *bar1::Hyg* *pep4::KanMX* *trp1::TRP1pRS304/Pol1/Pol12* *ura3::URA3pRS306/CBP-Tev-Pri1/Pri2*	This study
yJY26	*MAT**a** ade2-1 ura3-1 his3-11,15 trp1-1 leu2-3,112 can1-100* *bar1::Hyg* *pep4::KanMX* *his3::HIS3pRS303/Dpb11-3xflag (Nat-NT2), GAL4*	This study
yAJ2	*MAT**a** ade2-1 ura3-1 his3-11,15 trp1-1 leu2-3,112 can1-100* *bar1::Hyg* *pep4::KanMX* *ura3::URA3pRS306/Dpb2, Dpb3* *trp1::TRP1pRS304/Pol2, Dpb4-Tev-CBP*	This study
yAE31	*MAT**a** ade2-1 ura3-1 his3-11,15 trp1-1 leu2-3,112 can1-100* *bar1::Hyg* *pep4::KanMX* *his3::HIS3pRS303/CBP-Tev-RFA1, GAL4* *ura3::URA3pRS306/RFA2, RFA3*	This study
yAE37	*MAT**a** ade2-1 ura3-1 his3-11,15 trp1-1 leu2-3,112 can1-100* *bar1::Hyg* *pep4::KanMX* *ura3::URA3pRS306/CKS1, CDC28* *his3::HIS3pRS303/CBP-Tev-Clb5, GAL4*	This study
yAE40	*MAT**a** ade2-1 ura3-1 his3-11,15 trp1-1 leu2-3,112 can1-100* *bar1::Hyg* *pep4::KanMX* *his3::HIS3pRS303/CBP-Tev-Ctf4, GAL4*	This study
yAE46	*MAT**a** ade2-1 ura3-1 his3-11,15 trp1-1 leu2-3,112 can1-100* *bar1::Hyg* *pep4::KanMX* *trp1::TRP1pRS304/TOP2-Tev-CBP*	This study

Extended Data Table 3 | Plasmids used to generate yeast expression strains

Plasmid	Original vector*	Insert	Plasmid construction
pTD2	pJF2	Dpb11	PCR product from *S. cerevisiae* W303 genomic DNA using primers Dpb11 fwd and Dpb11 reverse cloned 5′ - SgrAI , 3′ - NotI
pTD5	pJF2	Sld2	Synthetic construct cloned 5′ - SgrAI , 3′ - NotI
pTD6a	pJF2	Sld3	Synthetic construct cloned 5′ - SgrAI , 3′ - NotI
pTD6b	pJF4	Sld7	Synthetic construct cloned 5′ - SgrAI , 3′ - NotI
pRS303-Cdc45	pJF2	Cdc45	PCR product cloned from *S. cerevisiae* W303 genomic DNA using primers cdc45 fwd and cdc45 rev 5′ - SgrAI , 3′ - NotI
pRS303-Cdc45^{iFlag1}	pJF2	Cdc45^{iFlag1}	Site directed mutagenesis using oligonucleotides JTY32 and JTY33 and pRS303-Cdc45 as template
pRS303-Cdc45^{iFlag2}	pJF2	Cdc45^{iFlag2}	Site directed mutagenesis using oligonucleotides JTY40 and JTY41 and pRS303-Cdc45^{iFlag1} as template
pRS304 (Pol2 + Dpb4-CBP)	pJF18	Pol2 Dpb4-CBP	Pol2 - synthetic construct cloned 5′ - AscI , 3′ - XhoI Dpb4-CBP - synthetic construct cloned 5′ - SgrAI , 3′ - NotI
pRS306 (Dpb2 + Dpb3)	pJF19	Dpb2 Dpb3	Dpb2 - synthetic construct cloned 5′ - SgrAI , 3′ - NotI Dpb3 - synthetic construct cloned 5′ - AscI , 3′ - XhoI
pRS304/Gal-CBP-Top2	pCG001	Top2	Synthetic construct cloned 5′ - AscI , 3′ - XhoI
pRS303/Gal-CBP-Ctf4	pJF2	Ctf4	Synthetic construct cloned 5′ - SgrAI , 3′ - NotI
pRS303/Gal4 + CBP-Tev-Clb5	pJF2	Clb5	Synthetic construct cloned 5′ - SgrAI , 3′ - NotI
pRS306/Cks1-Gal-Cdc28	pJF5	Cks1 Cdc28	Cks1 - synthetic construct cloned 5′ - SgrAI , 3′ - NotI Cdc28 - synthetic construct cloned 5′ - AscI , 3′ - XhoI
pRS303/Gal4 + CBP-Tev-Rfa1	pJF2	Rfa1	Synthetic construct cloned 5′ - SgrAI , 3′ - NotI
pRS306/Rfa2-Gal-Rfa3	pJF5	Rfa2 Rfa3	Rfa2 - synthetic construct cloned 5′ - AscI , 3′ - XhoI Rfa3 - synthetic construct cloned 5′ - SgrAI , 3′ - NotI
pRS304/Pol1-Gal1-10-Pol12	pJF3	Pol1 Pol12	Pol1 - synthetic construct cloned 5′ - SgrAI , 3′ - NotI Pol12 - synthetic construct cloned 5′ - AscI , 3′ - XhoI
pRS306/CBP-Tev-Pri1-Gal1-10-genomic Pri2	pJF5	Pri1 Pri2	Pri 1 - synthetic construct cloned 5′ - AscI , 3′ - XhoI Pri2 - PCR product from *S. cerevisiae* W303 genomic DNA using primers JTY92 and JTY100 cloned 5′ - AscI , 3′ - XhoI

Synthetic constructs were codon optimised for expression in *Saccharomyces cerevisiae*[34]. Sequences from the 5′ and 3′ end of the *PGK1* gene were also added. Genes were synthesized by GeneArt Gene Synthesis (Life technologies). *For details of the original expression vectors see refs 27, 31.

doi:10.1038/nature14261

Wind from the black-hole accretion disk driving a molecular outflow in an active galaxy

F. Tombesi[1,2], M. Meléndez[2], S. Veilleux[2,3], J. N. Reeves[4,5], E. González-Alfonso[6] & C. S. Reynolds[2,3]

Powerful winds driven by active galactic nuclei are often thought to affect the evolution of both supermassive black holes and their host galaxies, quenching star formation and explaining the close relationship between black holes and galaxies[1,2]. Recent observations of large-scale molecular outflows[3–8] in ultraluminous infrared galaxies support this quasar-feedback idea, because they directly trace the gas from which stars form. Theoretical models[9–12] suggest that these outflows originate as energy-conserving flows driven by fast accretion-disk winds. Proposed connections between large-scale molecular outflows and accretion-disk activity in ultraluminous galaxies were incomplete[3–8] because no accretion-disk wind had been detected. Conversely, studies of powerful accretion-disk winds have until now focused only on X-ray observations of local Seyfert galaxies[13,14] and a few higher-redshift quasars[15–19]. Here we report observations of a powerful accretion-disk wind with a mildly relativistic velocity (a quarter that of light) in the X-ray spectrum of IRAS F11119+3257, a nearby (redshift 0.189) optically classified type 1 ultraluminous infrared galaxy hosting a powerful molecular outflow[6]. The active galactic nucleus is responsible for about 80 per cent of the emission, with a quasar-like luminosity[6] of 1.5×10^{46} ergs per second. The energetics of these two types of wide-angle outflows is consistent with the energy-conserving mechanism[9–12] that is the basis of the quasar feedback[1] in active galactic nuclei that lack powerful radio jets (such jets are an alternative way to drive molecular outflows).

The mass[20] of the central supermassive black hole in IRAS F11119+3257 is estimated to be $M_{\rm BH} \approx 1.6 \times 10^7 M_\odot$, where $M_\odot$ is the solar mass. The resulting Eddington ratio is $L_{\rm AGN}/L_{\rm Edd} \approx 5$, where $L_{\rm AGN}$ is the luminosity of the active galactic nucleus (AGN), indicating that the source is very likely to be accreting at about its Eddington limit. In the X-ray spectrum it is relatively bright and not strongly affected by neutral absorption[21]. Therefore, it is arguably the best candidate in which to study the highly ionized iron K-band absorbers in this class of object.

IRAS F11119+3257 was the subject of a long (250-ks) observation from the Suzaku X-ray astronomy satellite obtained by our group in May 2013. The spectra of the three separated X-ray imaging spectrometer (XIS) detectors onboard Suzaku independently show a prominent absorption feature at the rest-frame energy of ~9 keV (Fig. 1). The inclusion of a broad Gaussian absorption line in the combined broadband Suzaku XIS and the hard X-ray detector PIN spectrum in the 0.5–25 keV energy band provides a very significant improvement of the fit, corresponding to a statistical confidence level of 6.5σ (see Supplementary Information). The absorption line has a rest-frame energy of $E = 9.82^{+0.64}_{-0.34}$ keV, a width of $\sigma_E = 1.67^{+1.00}_{-0.44}$ keV and an equivalent width of $-1.31^{+0.40}_{-0.31}$ keV. If interpreted as blue-shifted Fe XXV Heα and/or Fe XXVI Lyman α resonant absorption lines, this feature indicates an outflow velocity of about $0.3c$ (where c is the velocity of light in a vacuum) with respect to the systemic velocity.

We derive a physical characterization of this outflow using a dedicated photoionization absorption model (see Methods). This fast-wind model provides a very good representation of the data, simultaneously taking into account both the broad absorption trough at $E \approx 7-10$ keV in the XIS data and the factor of ~2–3 excess of flux at $E = 15-25$ keV observed in the PIN data (see Extended Data Fig. 1 and Methods). The column density, ionization and outflow velocity are $N_{\rm H} = 6.4^{+0.8}_{-1.3} \times 10^{24}\,{\rm cm}^{-2}$, $\log\xi = 4.11^{+0.09}_{-0.04}\,{\rm erg\,s^{-1}\,cm}$ and $v_{\rm out,X} = 0.255 \pm 0.011c$, respectively (see Extended Data Table 1). The wind has a high covering fraction of $C_{\rm F,X} > 0.85$, a value that is confirmed if we include the possible associated emission in the best-fit model (see Supplementary Information). The wind parameters are consistent overall with the mildly relativistic accretion-disk winds detected in quasars[15–19] with a comparable luminosity.

Considering the velocity and variability of the wind we estimate a distance from the central supermassive black hole in units of Schwarzschild radii ($r_{\rm S} = 2\,GM_{\rm BH}/c^2$) (where G is the gravitational constant) of $r \approx (15-900)r_{\rm S}$, consistent with accretion-disk scales (see Supplementary Information). Conservatively adopting a radius of $15r_{\rm S}$, we estimate a mass outflow rate of $\dot{M}_{\rm out,X} \approx 1.5 M_\odot\,{\rm yr}^{-1}$. Given the very high luminosity of this active galactic nucleus and the fact that it is accreting at about its Eddington limit, it is very likely that the wind is radiation driven[22].

The wind's momentum flux $\dot{P}_{\rm out,X} = \dot{M}_{\rm out,X} v_{\rm out,X} \approx 6 \times 10^{35}$ dyne corresponds to $1.3^{+1.7}_{-0.9}$ times that of the AGN radiation $\dot{P}_{\rm rad} = L_{\rm AGN}/c$ (see Supplementary Information). This is consistent with multiple

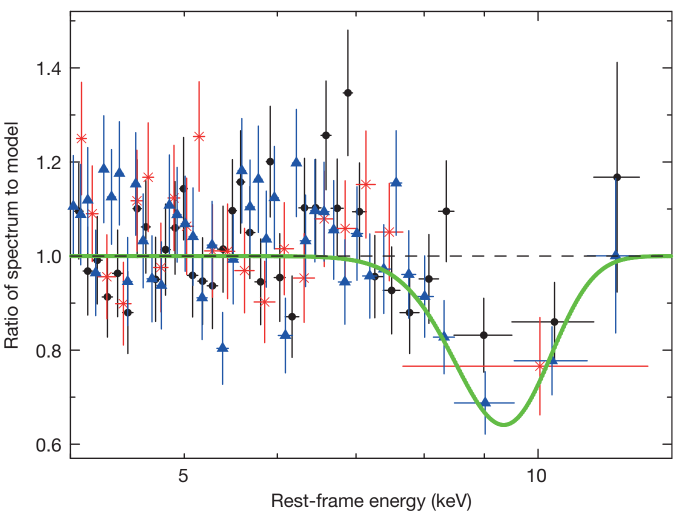

Figure 1 | Absorption line in the Suzaku spectrum of IRAS F11119+3257. Ratio between the separated spectra of the Suzaku detectors XIS0 (black), XIS1 (red) and XIS3 (blue) and the absorbed power-law continuum model in the $E = 4-12$ keV energy range. The ratio for the model including the absorption line at the rest-frame energy of 9.82 keV is superimposed in green. The data are binned to a signal-to-noise ratio of 10σ for clarity. Errors are at the 1σ level.

[1]X-ray Astrophysics Laboratory, NASA/Goddard Space Flight Center, Greenbelt, Maryland 20771, USA. [2]Department of Astronomy and CRESST, University of Maryland, College Park, Maryland 20742, USA. [3]Joint Space Science Institute, University of Maryland, College Park, Maryland 20742, USA. [4]Astrophysics Group, School of Physical and Geographical Sciences, Keele University, Keele, Staffordshire ST5 5BG, UK. [5]Center for Space Science and Technology, University of Maryland Baltimore County, 1000 Hilltop Circle, Baltimore, Maryland 21250, USA. [6]Universidad de Alcalá, Departamento de Física y Matemáticas, Campus Universitario, E-28871 Alcalá de Henares, Madrid, Spain.

scatterings in a high-column-density and wide-angle wind[23]. The wind mechanical power $\dot{E}_{K,X} = (1/2)\dot{M}_{out,X}v_{out,X}^2 \approx 2\times10^{45}$ erg s^{-1} corresponds to ~15% of the AGN luminosity and is higher than the minimum value of ~0.5% required for AGN feedback[24] (see Supplementary Information). Therefore, this wind will probably have a strong influence on the host galaxy environment. An alternative interpretation of the $E \approx 9$ keV absorption trough with an ionized Fe K edge and an associated relatively slow wind (see Extended Data Fig. 1) is statistically disfavoured (see Methods).

Likewise, the case whereby the Fe K profile arises from relativistically blurred X-ray reflection off the inner accretion disk is also ruled out (see Methods and Supplementary Information). Such a model fails to predict the hard X-ray emission above 10 keV (Extended Data Fig. 1). This case is also inconsistent with the variability observed during the observation (see Methods and Extended Data Figs 2 and 3). The fast wind model provides a self-consistent explanation of the variability in terms of a change in the absorber column density (Extended Data Table 2). In contrast, within the relativistic reflection model, the resultant variability pattern is the opposite of that expected from relativistic light bending[25], with a dramatic increase in reflection fraction from the low to the high flux state (see Extended Data Table 3). Finally, the extrapolated hard X-ray luminosity from the fast-wind model matches the value expected from mid-infrared emission line diagnostics, while the relativistic reflection model underestimates this value by more than one order of magnitude (see Supplementary Information).

Observations from the Herschel Space Observatory using the Photodetector Array Camera and Spectrometer (PACS) show a massive molecular outflow[6] in the absorption profile of the OH doublet at wavelength $\lambda = 119.23$ μm of IRAS F11119+3257 (Fig. 2). This galaxy also shows clear signatures of high-velocity outflows (~1,000 km s^{-1}) at other energies, including neutral[26] and moderately ionized[27,28] gas. From our radiative transfer model[7] of the Herschel observation of the 119.23 μm OH absorption profile (see Methods and Fig. 2) we estimate an outflow of around 300 pc with average velocity of $v_{out,OH} = 1{,}000 \pm 200$ km s^{-1}, covering factor $C_{F,OH} = 0.20 \pm 0.05$ and mass outflow rate of $\dot{M}_{out,OH} = 800^{+1{,}200}_{-550}\ M_\odot$ yr^{-1} (see Supplementary Information). The momentum flux of the molecular outflow is considerably larger than that of the AGN radiation, $\dot{P}_{out,OH} = 11.0^{+14.1}_{-7.5}\ \dot{P}_{rad}$. Moreover, the mechanical power corresponds to ~2% of the AGN luminosity (see Supplementary Information), a value higher than the minimum required for quasar mode feedback[24]. The large velocity and energetics of this molecular outflow also favour an AGN origin[3–5]. These parameters are comparable to those found in similar AGN-dominated ultraluminous infrared galaxies[3–8].

The two main mechanisms invoked to explain AGN feedback[1,2] are the radio mode and the quasar or wind mode. In these cases the molecular outflows are accelerated by the interaction with either a powerful, but highly collimated, radio jet[29] or a mildly relativistic accretion-disk wind[9–12], respectively. Powerful jets are found in radio-loud AGNs, but they constitute only a minority of the AGN population[29]. IRAS F11119+3257, and ultraluminous infrared galaxies in general, do not show clear evidence for powerful jets[6,8,30]. Therefore, the radio-mode feedback is strongly disfavoured in this case.

Theoretical models of quasar-mode AGN feedback[9–12,22] indicate that the shock caused by the interaction between the putative mildly relativistic AGN wind and the interstellar medium divides the resultant large-scale outflow into two regimes. Momentum-conserving flows occur if the shocked wind gas can cool and most of the kinetic energy is radiated away. On the other hand, energy-conserving flows occur if the shocked wind gas is not efficiently cooled, and instead expands as a hot bubble. Conservation of energy leads to the relation[9,10] $\dot{P}_{out} = f(v_{in}/v_{out})(L_{AGN}/c)$ where v_{in} is the velocity of the inner X-ray wind, v_{out} the velocity of the molecular outflow and $f = C_{F,out}/C_{F,in}$ is the ratio between the covering fractions of the outer molecular outflow and inner disk wind. This parameter f indicates the efficiency or fraction of inner wind power that is transferred to the large-scale outflow. Substituting the values from the observed X-ray and OH winds in IRAS F11119+3257 we derive an efficiency of $f = 0.22 \pm 0.07$.

In Fig. 3 we show the momentum fluxes of the inner X-ray wind and the molecular outflow observed in IRAS F11119+3257 with respect to their velocities, normalized to the momentum flux of the AGN radiation. For comparison, we consider also the energetics of mildly relativistic X-ray winds detected in quasars[15–19] and the molecular outflows detected

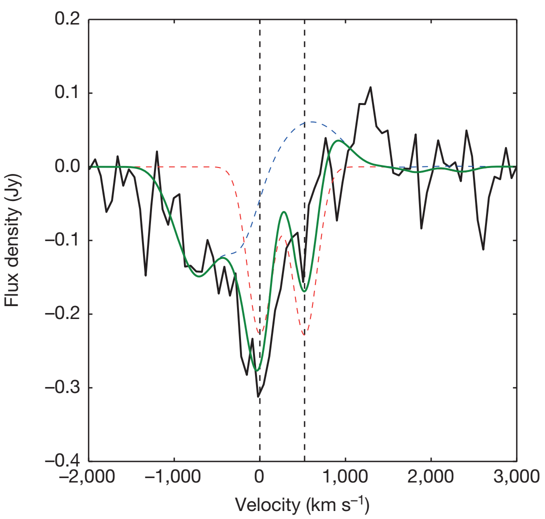

Figure 2 | Herschel-PACS OH $\lambda = 119.23$ μm observation of IRAS F11119+3257. The blue (high velocity) and red (systemic velocity) dashed lines represent the different components of the outflow model. The green line represents the total best-fit model. The dashed vertical lines indicate the position of the OH $\lambda = 119.23$ μm doublet components relative to the blue line of the doublet ($\lambda = 119.23$ μm) and with respect to the systemic redshift of the galaxy. The average outflow velocity estimated from the OH model is 1,000 ± 200 km s^{-1}.

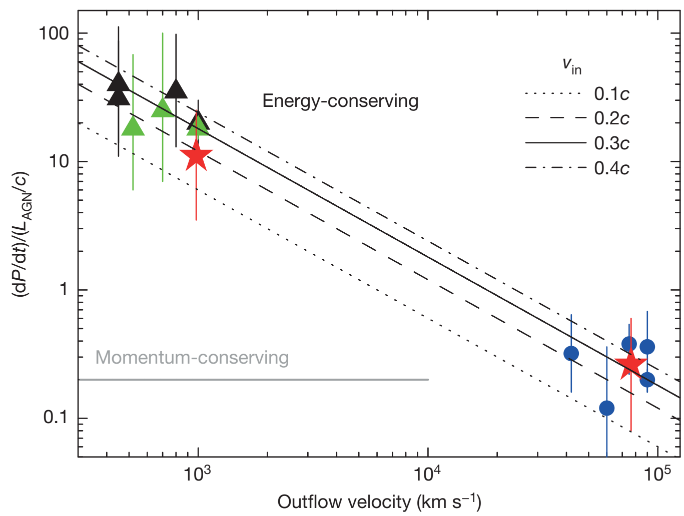

Figure 3 | Comparison between the inner winds and the molecular outflows. The momentum flux (dP/dt) normalized to the radiation (L_{AGN}/c) is plotted against the wind outflow velocity. v_{in} is the velocity of the inner X-ray wind, given in multiples of c. The disk and molecular winds in IRAS F11119+3257 (red filled stars), the disk winds of other quasars[15–19] (blue filled circles) and the molecular outflows of other ultraluminous infrared galaxies (OH[5,7] green and CO[4,8] black filled triangles) are reported. Uncertainties are 1σ. The dotted, dashed, solid and dot-dashed black curves represent the energy-conserving trends[9–11] for different v_{in} values. The horizontal grey line indicates the momentum-conserving case. An efficiency of $f = 0.2$ is assumed. The momentum rates of the disk winds are multiplied by f.

in ultraluminous infrared galaxies[3–8] with similar AGN luminosities (see Supplementary Information and Extended Data Table 4). We consider the derived efficiency of $f = 0.2$. Using the relation for an energy-conserving flow[9–11] we find that the energetics of the molecular outflows would require initial AGN winds with a range of velocities between $v_{\rm in} \approx (0.1-0.4)c$ (Fig. 3). Indeed, substituting the estimated values for IRAS F11119+3257 of $v_{\rm in} \approx 0.2c$, $v_{\rm out} \approx 1{,}000\ {\rm km\ s^{-1}}$ and $f \approx 0.2$ we obtain a value of $\dot{P}_{\rm out} \approx 12 L_{\rm AGN}/c$ that is consistent with the OH observation.

This would not be possible in the momentum-conserving case. In fact, considering that a fraction $f = 0.2$ of the initial wind momentum rate is transferred to the host and taking into account the uncertainties, the maximum value for the inner-disk wind is $f\dot{P}_{\rm out,X} = 0.6 L_{\rm AGN}/c$. This is much smaller than the minimum value for the molecular outflow of $\dot{P}_{\rm out,OH} = 3.5 L_{\rm AGN}/c$ (see Supplementary Information and Fig. 3).

The mass outflow rate of radiation-driven winds[9,22] is $\dot{M}_{\rm in} \approx \dot{M}_{\rm Edd}$, where $\dot{M}_{\rm Edd} = L_{\rm Edd}/\eta c^2$ is the Eddington accretion rate and η is the accretion efficiency. Moreover, their momentum rate is comparable[9,22,23] to that of the AGN radiation, $\dot{P}_{\rm in} \approx \dot{M}_{\rm in} v_{\rm in} \approx {\rm L_{Edd}}/c$. Therefore, the observed fast-wind velocity suggests[9] a high accretion efficiency $\eta \approx v_{\rm in}/c \approx 0.25$. For a stellar velocity dispersion of $\sigma \approx 100\ {\rm km\ s^{-1}}$ from the $M_{\rm BH}-\sigma$ relation[9,11], theoretical models of energy-conserving outflows[9] suggest a molecular outflow velocity of $v_{\rm out} \approx 1{,}000\ {\rm km\ s^{-1}}$, a mass outflow rate of $\dot{M}_{\rm out} \approx 1{,}000 M_\odot\ {\rm yr^{-1}}$ and a momentum rate $\dot{P}_{\rm out} \approx (10-20)\dot{P}_{\rm rad}$, in agreement with the observations. Moreover, the mechanical energy of the fast wind of $\sim$15% $L_{\rm AGN}$ is consistent with the theoretical value[9] of $(\eta/2)L_{\rm AGN} \approx 13\%\ L_{\rm AGN}$. The observed power of the molecular outflow of $\sim$2% $\rm L_{AGN}$ is also consistent with that of the fast wind with an efficiency $f \approx 0.2$. With the limitation that the fast X-ray wind is observed now, while the large-scale molecular outflow is probably an integrated effect of such winds over a much longer period of time, there is a very good quantitative agreement between observations and theoretical models[9–11,22].

This supports the idea that AGN winds can indeed provide an efficient way to transfer energy to the interstellar medium with a high degree of isotropy[12], as required by the existence of large-scale outflows in most ultraluminous infrared galaxies[3–8]. Moreover, these results are consistent with the evolutionary scheme[6] of ultraluminous infrared galaxies in which AGN-driven winds can clear out the obscuring material from the central regions of the galaxy[1,2], eventually uncovering the underlying quasar.

Online Content Methods, along with any additional Extended Data display items and Source Data, are available in the online version of the paper; references unique to these sections appear only in the online paper.

Received 4 November 2014; accepted 26 January 2015.

1. Fabian, A. Observational evidence of active galactic nuclei feedback. *Annu. Rev. Astron. Astrophys.* **50,** 455–489 (2012).
2. Veilleux, S., Cecil, G. & Bland-Hawthorn, J. Galactic winds. *Annu. Rev. Astron. Astrophys.* **43,** 769–826 (2005).
3. Fischer, J. *et al.* Herschel-PACS spectroscopic diagnostics of local ULIRGs: conditions and kinematics in Markarian 231. *Astron. Astrophys.* **518,** L41 (2010).
4. Feruglio, C. *et al.* Quasar feedback revealed by giant molecular outflows. *Astron. Astrophys.* **518,** L155 (2010).
5. Sturm, E. *et al.* Massive molecular outflows and negative feedback in ULIRGs observed by Herschel-PACS. *Astrophys. J.* **733,** L16 (2011).
6. Veilleux, S. *et al.* Fast molecular outflows in luminous galaxy mergers: evidence for quasar feedback from Herschel. *Astrophys. J.* **776,** 27 (2013).
7. González-Alfonso, E. *et al.* The Mrk 231 molecular outflow as seen in OH. *Astron. Astrophys.* **561,** A27 (2014).
8. Cicone, C. *et al.* Massive molecular outflows and evidence for AGN feedback from CO observations. *Astron. Astrophys.* **562,** A21 (2014).
9. Zubovas, K. & King, A. Clearing out a galaxy. *Astrophys. J.* **745,** L34 (2012).
10. Faucher-Giguère, C.-A. & Quataert, E. The physics of galactic winds driven by active galactic nuclei. *Mon. Not. R. Astron. Soc.* **425,** 605–622 (2012).
11. Zubovas, K. & Nayakshin, S. Energy- and momentum-conserving AGN feedback outflows. *Mon. Not. R. Astron. Soc.* **440,** 2625–2635 (2014).
12. Wagner, A. Y., Umemura, M. & Bicknell, G. V. Ultrafast outflows: galaxy-scale active galactic nucleus feedback. *Astrophys. J.* **763,** L18 (2013).
13. Tombesi, F. *et al.* Evidence for ultra-fast outflows in radio-quiet AGNs. I. Detection and statistical incidence of Fe K-shell absorption lines. *Astron. Astrophys.* **521,** A57 (2010).
14. Gofford, J. *et al.* The Suzaku view of highly ionized outflows in AGN.—I. Statistical detection and global absorber properties. *Mon. Not. R. Astron. Soc.* **430,** 60–80 (2013).
15. Chartas, G., Saez, C., Brandt, W. N., Giustini, M. & Garmire, G. P. Confirmation of and variable energy injection by a near-relativistic outflow in APM 08279+5255. *Astrophys. J.* **706,** 644–656 (2009).
16. Pounds, K. A. & Reeves, J. N. Quantifying the fast outflow in the luminous Seyfert galaxy PG1211+143. *Mon. Not. R. Astron. Soc.* **397,** 249–257 (2009).
17. Lanzuisi, G. *et al.* HS 1700+6416: the first high-redshift unlensed narrow absorption line-QSO showing variable high-velocity outflows. *Astron. Astrophys.* **544,** A2 (2012).
18. Chartas, G. *et al.* Magnified views of the ultrafast outflow of the z = 1.51 active galactic nucleus HS 0810+2554. *Astrophys. J.* **783,** 57 (2014).
19. Gofford, J. *et al.* Revealing the location and structure of the accretion disk wind in PDS 456. *Astrophys. J.* **784,** 77 (2014).
20. Kawakatu, N., Imanishi, M. & Nagao, T. Anticorrelation between the mass of a supermassive black hole and the mass accretion rate in type 1 ultraluminous infrared galaxies and nearby QSOs. *Astrophys. J.* **661,** 660–671 (2007).
21. Teng, S. H. & Veilleux, S. X-QUEST: a comprehensive x-ray study of local ULIRGS and QSOs. *Astrophys. J.* **725,** 1848–1876 (2010).
22. King, A. R. & Pounds, K. A. Black hole winds. *Mon. Not. R. Astron. Soc.* **345,** 657–659 (2003).
23. Reynolds, C. S. Constraints on Compton-thick winds from black hole accretion disks: can we see the inner disk? *Astrophys. J.* **759,** L15 (2012).
24. Hopkins, P. F. & Elvis, M. Quasar feedback: more bang for your buck. *Mon. Not. R. Astron. Soc.* **401,** 7–14 (2010).
25. Miniutti, G. & Fabian, A. C. A light bending model for the X-ray temporal and spectral properties of accreting black holes. *Mon. Not. R. Astron. Soc.* **349,** 1435–1448 (2004).
26. Rupke, D. S., Veilleux, S. & Sanders, D. B. Outflows in active galactic nucleus/starburst-composite ultraluminous infrared galaxies. *Astrophys. J.* **632,** 751–780 (2005).
27. Lipari, S. *et al.* Extreme galactic wind and Wolf-Rayet features in infrared mergers and infrared quasi-stellar objects. *Mon. Not. R. Astron. Soc.* **340,** 289–303 (2003).
28. Spoon, H. W. W. & Holt, J. Discovery of strongly blueshifted mid-infrared [Ne III] and [Ne V] emission in ULIRGs. *Astrophys. J.* **702,** L42–L46 (2009).
29. Tadhunter, C., Morganti, R., Rose, M., Oonk, J. B. R. & Oosterloo, T. Jet acceleration of the fast molecular outflows in the Seyfert galaxy IC 5063. *Nature* **511,** 440–443 (2014).
30. Nagar, N. M., Wilson, A. S., Falcke, H., Veilleux, S. & Maiolino, R. The AGN content of ultraluminous IR galaxies: high resolution VLA imaging of the IRAS 1 Jy ULIRG sample. *Astron. Astrophys.* **409,** 115–121 (2003).

Supplementary Information is available in the online version of the paper.

Acknowledgements F.T. would like to thank T. Kallman, J. García, F. Tazaki, F. Paerels and M. Cappi for comments. F.T. acknowledges support from NASA (grant NNX12AH40G). M.M. and S.V. are supported in part by NASA grants NHSC/JPL RSA 1427277 and 1454738. S.V. also acknowledges partial support through grant NSF-AST1009583. J.N.R. acknowledges the financial support of the STFC. E.G.-A. is a Research Associate at the Harvard-Smithsonian Center for Astrophysics, and thanks the Spanish Ministerio de Economía y Competitividad for support under projects AYA2010-21697-C05-0 and FIS2012-39162-C06-01. C.S.R. thanks support from NASA (grant NNX14AF86G) and the US National Science Foundation (grant AST1333514).

Author Contributions F.T. is the Principal Investigator of the Suzaku observation. He led the X-ray spectral analysis, interpretation of the results and manuscript preparation. M.M. and E. G.-A. performed the analysis and modeling of the Herschel data. S.V. contributed to the interpretation of the results. J.N.R. and C.S.R. contributed to the X-ray spectral analysis and interpretation of the results. All authors participated in the review of the manuscript.

Author Information Reprints and permissions information is available at www.nature.com/reprints. The authors declare no competing financial interests. Readers are welcome to comment on the online version of the paper. Correspondence and requests for materials should be addressed to F.T. (ftombesi@astro.umd.edu).

METHODS

Suzaku observation log. IRAS F11119+3257 was observed with Suzaku for the period 13−19 May 2013 for a total exposure of 250 ks. The data reduction and analysis were performed following the standard procedures as described in the Suzaku data reduction guide. We use the *heasoft* version 6.12 package and the latest calibration files (http://heasarc.nasa.gov/lheasoft/).

Suzaku XIS data reduction. We derived the Suzaku XIS cleaned event files and applied standard screening criteria. The 3×3 and 5×5 editing modes were combined. The source spectra were extracted from circular regions of $2.5''$ radius centred on the source. The background spectra were extracted from annular regions with inner and outer radii of $3-4''$ centred on the source and excluding contamination from the calibration sources. The spectra from the two front illuminated detectors, XIS0 and XIS3, were combined after verifying that the data are consistent with each other. Hereafter we refer to them as XIS03. The data of the back illuminated XIS1 detector are used as well. The XIS response and ancillary files were produced. The source count-rates (in units of counts per second) in the $E=0.5-10$ keV band are 0.0576, 0.0649 and 0.06 for the XIS0, XIS1 and XIS3 detectors, respectively. The background count-rates are 18% and 30% of the source count-rates for the XIS03 and XIS1 detectors, respectively.

Suzaku PIN data reduction. The Suzaku PIN source spectrum was extracted within the good time intervals (those during which events are accumulated) and corrected for the detector dead time. The latest response file was used. We use the latest and most accurate tuned non-X-ray background event file version 2.2ver1403 provided by the Suzaku team. The non-X-ray background event file was used as input to the *hxdpinxbpi* task and combined with a model of the cosmic X-ray background provided by the Suzaku team. We conservatively include a systematic uncertainty on the PIN background of 1.5%. The source is detected in the PIN at the 4σ level. The source count-rate in the $E=15-25$ keV band is 0.005 ± 0.001 counts s^{-1}, including the systematic error on the background. The average source count-rate is 3.3% of the background. There are no other X-ray sources with $2-10$ keV flux higher than 5×10^{-14} erg s^{-1} cm^{-2} in the Chandra, XMM-Newton, BeppoSAX and ASCA archives, excluding contamination from other sources within the PIN field of view. Above 10 keV, we do not find any source detected within a 1° radius in the Swift BAT 70-month, RXTE and Integral surveys. The PIN flux of IRAS F1111+3257 is also below the sensitivity limit of these hard X-ray surveys.

Suzaku spectral analysis. The spectral analysis was carried out using the software *XSPEC* version 12.7.1 (http://heasarc.gsfc.nasa.gov/xanadu/xspec/). All uncertainties quoted are at the 1σ level for one parameter of interest and the energies are reported in the source rest-frame, unless otherwise stated. We exploit the broad-band capabilities of Suzaku, combining the $E=0.5-10.5$ keV XIS and $E=15-25$ keV PIN spectra. We perform joint fits of the Suzaku XIS03 and XIS1 spectra excluding the energy range around the Si K edge ($E=1.5-2$ keV), which is known to be affected by calibration issues. The XIS03/XIS1 cross-normalization was left free to vary, but it was always found to be consistent within 3%. We take into account the XIS/PIN cross-normalization of 1.16 ± 0.01. All spectra were grouped to a minimum of 25 counts per energy bin in order to allow the use of the χ^2 minimization in the model fitting. Throughout we include a neutral Galactic absorption of $N_H = 2.1\times10^{20}$ cm^{-2}.

Fast-wind model. We model the broad absorption at $E\approx9$ keV with the *XSTAR*[31] code version 2.2.1bn. We consider a $\Gamma=2$ power-law continuum, consistent with the observed value (see Supplementary Information), and standard solar abundances. A turbulent velocity of 30,000 km s^{-1} is assumed for the fast-wind model. This high value is introduced only to model the large width of the absorption line and it is probably not linked to an actual physical turbulence in the gas. For instance, detailed accretion-disk wind models show that the line profiles become much broader because of the velocity shear between consecutive zones of the wind[32].

This provides a very good fit to the data, with $\chi^2/\nu = 1410.4/1391$, providing a higher fit improvement, comparable to the phenomenological best-fit case of a broad absorption line ($\Delta\chi^2/\Delta\nu = 54.2/3$). This corresponds to a very high detection confidence level of 6.5σ. The relative column density, ionization and outflow velocity are $N_H = 6.4^{+0.8}_{-1.3}\times10^{24}$ cm^{-2}, $\log\xi = 4.11^{+0.09}_{-0.04}$ erg s^{-1} cm and $v_{out,X} = 0.255\pm0.011c$, respectively (see Extended Data Table 1). The absorber is consistent with fully covering the source, with a lower limit of the covering fraction of $C_{F,X} > 0.85$ at the 90% significance level (see Supplementary Information). The fast-wind model is able to simultaneously take into account both the broad absorption at $E\approx7-10$ keV and the excess of flux at $E=15-25$ keV (see Extended Data Fig. 1c).

We note that a more physical model of a high-column-density wind should include both Compton scattering and emission (for the latter see Supplementary Information). A few such models[33,34] have been recently reported, but they are not publicly available for use in *XSPEC* and require a relative fine-tuning of the parameters. Moreover, the wind parameters are well approximated with *XSTAR* absorption tables[33,34], supporting our conclusions. The effects of Compton scattering should be marginal, introducing a continuum break at an energy beyond the observed Suzaku bandpass of $E\approx50$ keV and contribute to the broadening of the lines of less than ~0.3 keV.

Slow-wind model. Considering the slow-wind model, in which the feature at $E\approx9$ keV is identified with an ionized Fe K absorption edge, the data require a lower *XSTAR* turbulent velocity width of 500 km s^{-1}. This provides an overall good fit of the data, with $\chi^2/\nu = 1{,}439.3/1{,}391$. The relative column density, ionization and outflow velocity are $N_H = 5.5^{+0.6}_{-0.7}\times10^{24}$ cm^{-2}, $\log\xi = 3.77^{+0.08}_{-0.07}$ erg s^{-1} cm and $v_{out} = 0.0258^{+0.0109}_{-0.0128}c$, respectively. The lower limit of the covering fraction is $C_F > 0.93$ at the 90% significance level. Even though it provides an overall sufficient representation of the data, this fit is statistically much worse than the previous case of a fast wind (see Extended Data Fig. 1d). In fact, the χ^2 difference for the same number of degrees of freedom with respect to the fast-wind model is $\Delta\chi^2 = 28.9$. In particular, this slow-wind model does not provide a good fit for the absorption trough at $E\approx7-10$ keV.

Relativistic reflection model. We use the most accurate relativistic reflection code available in the literature, the "*relxilllp*" model[35]. This model considers the lamp post geometry in which the compact X-ray source is located at a certain height along the rotation axis of the black hole in units of gravitational radii $r_g = GM_{BH}/c^2$. The reflection fraction and emissivity index are self-consistently calculated by the model depending on the source height and black hole spin. We consider a typical outer-disk radius of $r_{out} = 400r_g$ and the inner radius r_{in} is linked to the innermost stable circular orbit for a given black-hole spin value. We consider standard solar abundances.

The free parameters are the height of the illuminating source h, the disk inclination i, the ionization parameter $\log\xi$, the normalization and the black-hole spin a. This model provides a fit statistics of $\chi^2/\nu = 1413.2/1390$. The best-fit parameters suggest a source height of just $h = 2.2^{+1.3}_{-0.6}r_g$ ($r_g = GM_{BH}/c^2$) and a rapidly spinning black hole with $a > 0.85$. The material is mildly ionized, with $\log\xi = 3.15^{+0.15}_{-0.09}$ erg s^{-1} cm, and the disk inclination is estimated to be $i = 52^{+4}_{-6}$ degrees. Letting the reflection parameter vary freely we find a very high best-fit value of $R\approx6$. The relativistic reflection model provides a relatively good representation of the data up to $E\approx10$ keV but it is not able to model the excess of flux at $E=15-25$ keV (see Extended Data Fig. 1e).

Time-resolved spectral analysis. The source lightcurve shows a factor-of-10 variability in the $4-10$ keV count-rate over an interval of ~3 days between the minimum and maximum values (Extended Data Fig. 2). This variability must be driven by the change of some parameters, such as the continuum, absorption or reflection. We performed a time-resolved spectral analysis by splitting the observation at 377 ks after the beginning (Extended Data Fig. 2). This allows us to have the same signal-to-noise ratio in the $E=4-10$ keV band for the low-flux (first) and high-flux (second) intervals. The source shows a much smaller variability of a factor of ~1.5 in the PIN data at $E=15-25$ keV. The broad-band spectra extracted in the low-flux and high-flux intervals are shown in Extended Data Fig. 3a.

We performed a combined fit of the low-flux and high-flux intervals using alternately the fast-wind model and the relativistic-reflection model and compared the values of the parameters to determine the main driver of the variability in these two cases.

Regarding the fit with the fast-wind model, we test three different variability cases: (1) constant fully covering absorption with variable power-law continuum; (2) constant power-law continuum with variable partial covering absorption; (3) constant power-law continuum and variable fully covering absorption. Cases (1) and (3) provide the best representations of the data with comparable statistics of $\chi^2/\nu = 1{,}757.9/1{,}692$ and $\chi^2/\nu = 1{,}757.3/1{,}693$, respectively. In case (1) of the constant absorber and variable continuum we find that the main change in the fit parameters may be due to an increase in the normalization of the continuum with $\Gamma\approx2$. The continuum slope is consistent in the two intervals. The relative ionizing luminosity between 1 Ryd and 1,000 Ryd (where 1 Ryd = 13.6 eV) would be increasing from $\log L_{ion}\approx45.2$ erg s^{-1} to $\log L_{ion}\approx45.7$ erg s^{-1}. Given that the column density and velocity of the absorber are constant, this increase in luminosity by a factor of ~3.4 should have caused an increase in ionization by the same factor, fully ionizing the gas, to the point that it would have not been detected in the second interval. This consideration alone strongly disfavours the continuum-variability case. In case (3) of a constant continuum and variable absorber we find that the main driver of the flux variability is a 40% decrease in column density from $N_H\approx8.1\times10^{24}$ cm^{-2} to $N_H\approx4.9\times10^{24}$ cm^{-2} between the two intervals (Extended Data Table 2). Moreover, the fact that the observed change in flux of a factor of ~10 is much larger at $E=4-10$ keV compared to a factor of only ~1.5 at $E>15$ keV also points to the fact that the main variability is due to a change in absorbing column density rather than continuum emission with constant slope (see Extended Data Fig. 3b).

Regarding the fit with the relativistic-reflection model, we tested two different variability cases: (1) constant reflection with variable power-law continuum and (2) constant power-law continuum with variable reflection (that is, source height and ionization). Case (1) would indicate a constant and very small source height of $h < 2r_g$. Instead, the continuum slope would be required to change from the unrealistically

high value of $\Gamma \approx 2.7$ to $\Gamma \approx 2.2$ between the two intervals. Overall, this case does not provide a good fit to the data, with a poor statistics of $\chi^2/\nu = 1{,}878.7/1{,}692$. Case (2) provides a better fit of $\chi^2/\nu = 1{,}766.4/1{,}693$. The fit with the relativistic reflection model provides a relatively good representation of the data up to $E \approx 10$ keV but not at higher energies (see Extended Data Fig. 3b). In this case, the direct continuum is required to be constant between the two intervals and the main driver of the variability would be the height of the X-ray source, decreasing from $h = 5.4^{+54.4}_{-1.2} r_g$ down to $h < 3.2 r_g$ from the low-flux to the high-flux case, respectively (Extended Data Table 3). This corresponds to an increase in reflection fraction from ~3 in the low-flux interval up to the maximum value allowed of ~10 for the high-flux case. Even though this fit might provide a relatively good representation of the data, it clearly contradicts the variability expected from the associated relativistic light bending case[25], which predicts a very specific variability pattern of higher/lower reflection fractions (lower/higher X-ray source heights) for lower/higher fluxes.

Suzaku XIS background and systematics check. We investigated the existence of the broad absorption at $E \approx 9$ keV, also performing independent fits of the Suzaku XIS0, XIS1 and XIS3 detectors. In all cases the parameters are consistent at the 90% level and in particular the broad absorption is independently detected at the 3σ level in the XIS0 and XIS1 and at the 4σ level for the XIS3 (Fig. 1). The XIS cameras have an instrumental background emission line from Ni Kα at the observed energy of 7.47 keV. The line intensity is slightly dependent on the location on the detector. Therefore, an incorrect background selection might possibly induce spurious absorption/emission lines in the background-subtracted spectrum. We performed several tests in order to exclude this possibility. First, we note that the observed centroid energy of the broad line of $E = 8.26^{+0.64}_{-0.34}$ keV is not consistent with the energy of the instrumental line. Second, the background emission line is unresolved, with a width of $\sigma_E < 100$ eV. This is not consistent with the large width of the absorption feature of $\sigma_E \approx 1$ keV. Third, we performed fits using background regions extracted from one, two and three circles of 2.5′′ size away from the source and annuli with inner/outer radii of 3″/5″ and 4″/5″ centred on the source. Fourth, we performed an additional consistency check considering a smaller circular source extraction region of 1.5″ and an annular background region of the same area with inner/outer radii of 3″/3.4″. This allows us to derive a cleaner extraction region, with a marginal loss of 20% of the source counts in the $E = 4-10$ keV band, and to drastically minimize the background, reducing its count-rate by a factor of 2.5. In all cases we find that the best-fit parameters, and in particular those of the broad absorption feature, are always consistent within the 1σ errors. Considering only the XIS data and fitting both the fast- and slow-wind models and the relativistic reflection model we obtain parameters that are consistent within the 1σ errors with those derived using the combined XIS and PIN data. This indicates that these models depend only weakly on the $E = 15-25$ keV PIN data. The fast-wind ($\chi^2/\nu = 1{,}372.1/1{,}365$) and the relativistic reflection ($\chi^2/\nu = 1{,}369.2/1{,}364$) models provide statistically comparable fits of the XIS data alone. Instead, the fit using the slow-wind model is statistically worse ($\chi^2/\nu = 1{,}404.6/1{,}365$).

Modelling of the Herschel OH spectrum. The profile of the OH 119.23 μm doublet shows[6] a strong asymmetry at systemic velocities and an obvious blue wing extending well beyond 1,000 km s^{-1} (see Fig. 2). This profile is modelled[7] in spherical symmetry as an extended outflow on the scale of 300 pc. The Spitzer space telescope's Infrared Spectrograph (IRS) low-resolution spectra, the Infrared Astronomical Satellite (IRAS) fluxes, and Herschel spectrum around the OH doublet are used to estimate the underlying continuum.

The covering factor of the outflow is estimated to be $C_{F,OH} = 0.20 \pm 0.05$. The sum of the covering factors of the outflow and systemic components is close to unity, consistent with the fraction of gas affected/unaffected by the outflow. The outflow velocity is also well determined, with an average value of $v_{out,OH} = 1{,}000 \pm 200$ km s^{-1}. The absorption is seen in front of the far-infrared continuum, which is well modelled with a dust radius of $R_{dust} = 250$ pc. The distance of the OH absorber is estimated at $r = 300$ pc in radius (or 600 pc in diameter). This value is consistent with previous results[7] derived using the same model for the more detailed spectrum of the ultraluminous infrared galaxy Mrk 231, indicating that the outflowing OH is mostly linked to the source of far-infrared continuum.

The hydrogen number density is derived from the equation $n_H = N_{OH}/(X_{OH} \times \Delta r)$, where N_{OH} is the OH column density, X_{OH} is the OH abundance relative to H and Δr is the width of the region sampled by the outflowing OH. The estimated value of the OH column density from the fit of the line profile is $N_{OH} = 3 \times 10^{16}$ cm^{-2}. This value is conservatively low but enough to account for the optically thick OH 119.23 μm absorption line. The standard value[7] of the OH abundance relative to H in active regions where OH is highly abundant is $X_{OH} = 2 \times 10^{-6}$. The width of the outflowing OH region of $\Delta r = 50$ pc is derived from the relation $R_{out} = 1.2 R_{dust}$, which is based on more accurate models[7] for the similar OH profile in Mrk 231. Therefore, we estimate a hydrogen number density of $n_H = 100$ cm^{-3}. Exploring the parameter space of the model, we find an uncertainty of a factor of two on this value (see Supplementary Information).

31. Kallman, T. & Bautista, M. Photoionization and high-density gas. *Astrophys. J. Suppl. Ser.* **133,** 221–253 (2001).
32. Fukumura, K. *et al.* Stratified magnetically driven accretion-disk winds and their relations to jets. *Astrophys. J.* **780,** 120 (2014).
33. Sim, S. A., Miller, L., Long, K. S., Turner, T. J. & Reeves, J. N. Multidimensional modelling of X-ray spectra for AGN accretion disc outflows—II. *Mon. Not. R. Astron. Soc.* **404,** 1369–1384 (2010).
34. Hagino, K. *et al.* The origin of ultra-fast outflows in AGN: Monte-Carlo simulations of the wind in PDS 456. *Mon. Not. R. Astron. Soc.* **446,** 663–676 (2015).
35. García, J. *et al.* Improved reflection models of black hole accretion disks: treating the angular distribution of X-rays. *Astrophys. J.* **782,** 76 (2014).

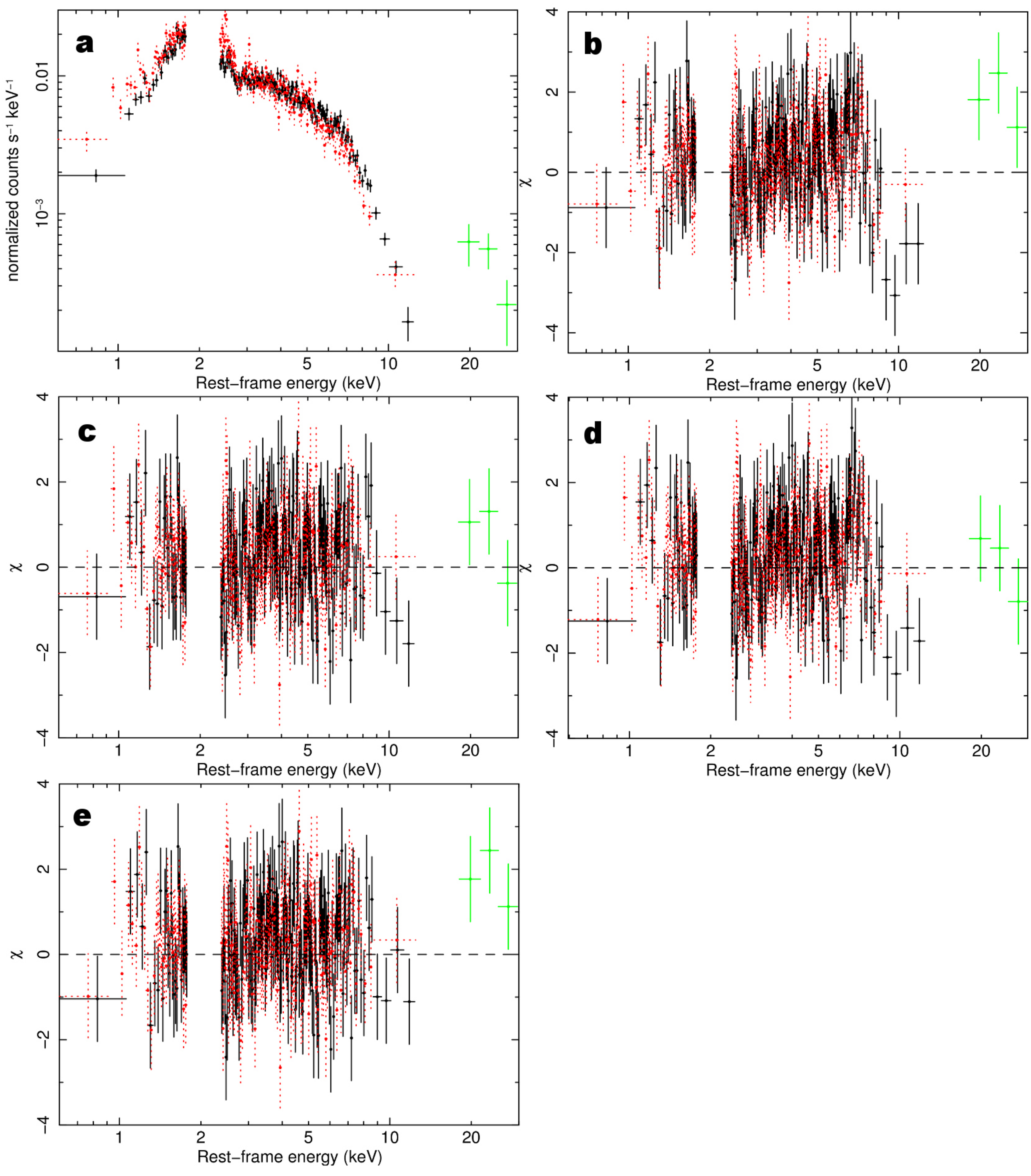

Extended Data Figure 1 | Broad-band Suzaku spectrum in the $E = 0.5$–$30\,\mathrm{keV}$ band. **a**, The time-averaged Suzaku XIS03 (solid black), XIS1 (dotted red) and PIN (solid green) spectra binned to 10σ, 5σ and 3σ, respectively. The data-to-model residuals in units of sigma with respect to the absorbed power-law model, the fast-wind model, the slow-wind model and the relativistic reflection model are shown in **b**, **c**, **d** and **e**, respectively. The energy is in the rest-frame and errors are at the 1σ level.

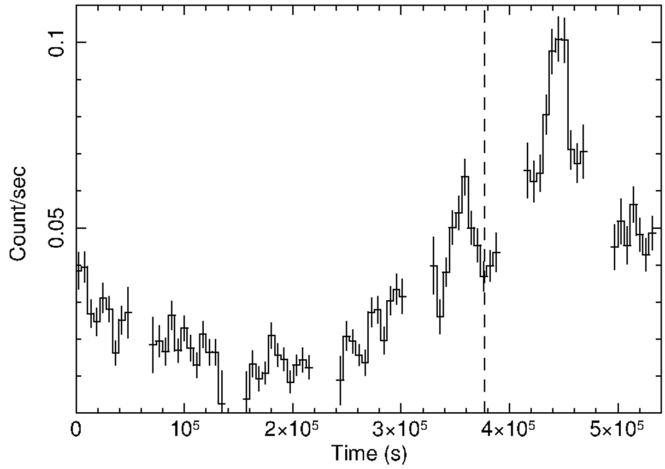

Extended Data Figure 2 | Background-subtracted Suzaku XIS03 light curve in the $E = 4-10$ keV band. The data are binned to the Suzaku orbital period of 5,760 s. The vertical line indicates the time at which the observation is split into two parts for the time-resolved spectral analysis. The effective on-source exposure time is 250 ks. The gaps in the light curve indicate periods in which the satellite could not point to the source. Therefore, the total temporal coverage of the observation is longer, about 500 ks. Errors are at the 1σ level.

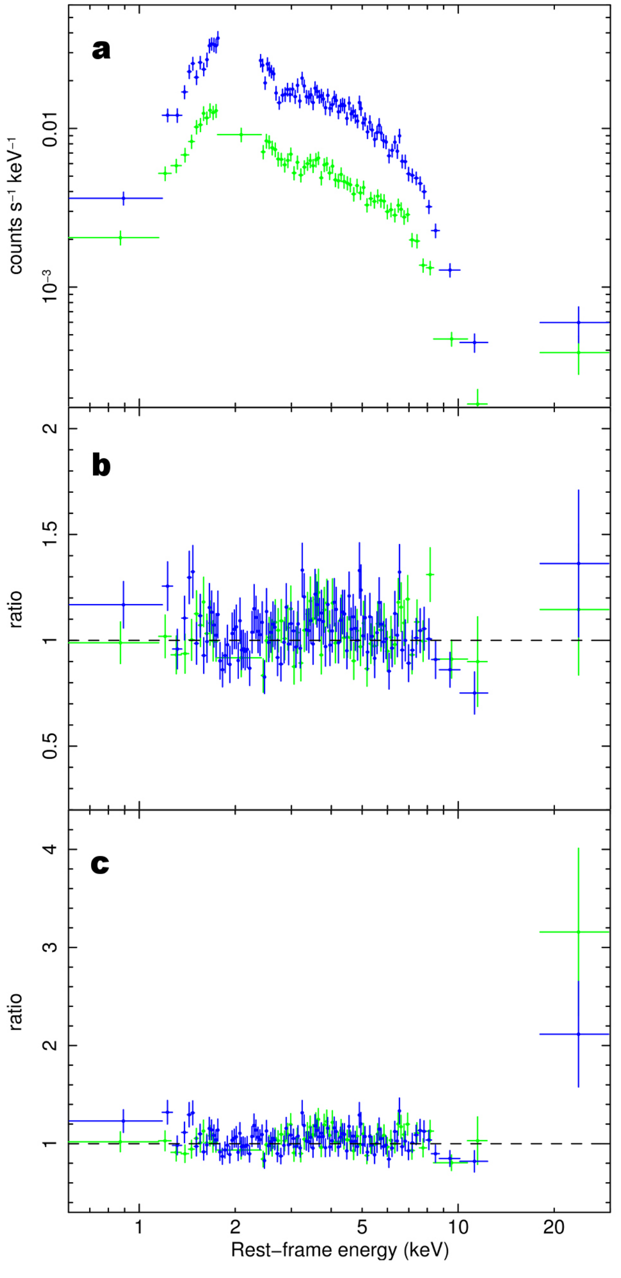

Extended Data Figure 3 | Time-resolved Suzaku spectral analysis in the $E = 0.5-30$ keV band. **a**, Suzaku XIS03 and PIN spectra extracted during the low-flux (green) and high-flux (blue) intervals. The XIS03 and PIN data are rebinned to 10σ and 5σ, respectively. The data-to-model ratios with respect to the fast-wind model and relativistic-reflection model are reported in **b** and **c**, respectively. Errors are at the 1σ level.

Extended Data Table 1 | Best-fit values of the fast-wind model for the time-averaged spectrum

Absorbed Power-law			
Γ	N_H (10^{22} cm^{-2})		χ^2/ν
2.04±0.03	2.07±0.08		1410.4/1391
Photoionized absorption			
$\log\xi$ (erg s^{-1} cm)	N_H (10^{24} cm^{-2})	v_{out} (c)	C_F
$4.11^{+0.09}_{-0.04}$	$6.4^{+0.8}_{-1.3}$	0.255 ± 0.011	>0.85

Errors are at the 1σ level.

Extended Data Table 2 | Best-fit values of the fast-wind model for the time-resolved spectral analysis

	Low-Flux	High-Flux
Absorbed power-law		
Γ	2.05 ± 0.05	
N_H (10^{22} cm^{-2})	2.06 ± 0.12	
Photoionized absorption		
$\log\xi$ (erg s^{-1} cm)	$4.08^{+0.08}_{-0.03}$	$4.13^{+0.20}_{-0.08}$
N_H (10^{24} cm^{-2})	$8.1^{+0.6}_{-1.1}$	$4.9^{+1.3}_{-1.9}$
v_{out} (c)	$0.243^{+0.020}_{-0.021}$	$0.268^{+0.031}_{-0.034}$
Best-fit statistics		
χ^2/ν	1757.3/1692	

Errors are at the 90% level.

Extended Data Table 3 | Best-fit values of the relativistic reflection model for the time-resolved spectral analysis

	Low-Flux	High-Flux
Absorbed power-law		
Γ	$2.01^{+0.08}_{-0.04}$	
N_H (10^{22} cm^{-2})	$2.24^{+0.15}_{-0.10}$	
Relativistic reflection		
a	> 0.93	
h (r_g)	$5.4^{+54.4}_{-1.2}$	< 3.2
i (degrees)	44^{+5}_{-7}	
$\log\xi$ (erg s^{-1} cm)	$3.05^{+0.13}_{-0.07}$	$3.32^{+0.13}_{-0.09}$
R	$\simeq 3$	$\simeq 10$
Best-fit statistics		
χ^2/ν	1766.4/1693	

The parameters *a* and *R* refer to the black-hole spin and reflection fraction, respectively. Errors are at the 90% level.

Extended Data Table 4 | Parameters of outflows in other quasars and ultraluminous infrared galaxies collected from the literature

Name	$\log L_{AGN}$ (erg s^{-1})	v_{out} (km s^{-1})	$\dot{P}/(L_{AGN}/c)$	Refs
		Quasars (X-rays)		
IRAS F11119+3257	46.2	75000	$1.3^{+1.7}_{-0.9}$	#
APM 08279+5255	47.0	60000	$0.6^{+1.2}_{-0.4}$	15
PG 1211+143	45.7	42000	$1.6^{+1.6}_{-0.8}$	16
HS 1700+6416	47.0	90000	1 ± 0.2	17
HS 0810+2554	46.0	90000	$1.8^{+1.6}_{-1.1}$	18
PDS 456	47.0	75000	1.9 ± 0.8	19
		ULIRGs (OH)		
IRAS F11119+3257	46.2	1000	$11.0^{+14.1}_{-7.5}$	#
IRAS 08572+3915	45.7	700	25^{+75}_{-18}	5
IRAS 13120−5453	44.9	520	18^{+50}_{-12}	5
Mrk 231	46.0	1000	18 ± 3	7
		ULIRGs (CO)		
IRAS F08572+3915	45.7	800	35^{+63}_{-22}	8
IRAS F10565+2448	44.8	450	40^{+72}_{-26}	8
IRAS 23365+3604	44.7	450	31^{+56}_{-20}	8
Mrk 231	46.0	1000	20 ± 10	4

The reported velocity v_{out} refers to the average outflow velocity. The parameters $\dot{P}$ and L_{AGN}/c indicate the momentum flux of the outflow and AGN radiation, respectively. Errors are at the 1σ level. The last column indicates the relevant references[4,5,7,8,15–19]. The parameters of the inner X-ray wind and OH molecular outflow in IRAS F11119+3257 indicated by # refer to this work.

doi:10.1038/nature14293

Entanglement with negative Wigner function of almost 3,000 atoms heralded by one photon

Robert McConnell[1]*, Hao Zhang[1]*, Jiazhong Hu[1], Senka Ćuk[1,2] & Vladan Vuletić[1]

Quantum-mechanically correlated (entangled) states of many particles are of interest in quantum information, quantum computing and quantum metrology. Metrologically useful entangled states of large atomic ensembles have been experimentally realized[1–10], but these states display Gaussian spin distribution functions with a non-negative Wigner quasiprobability distribution function. Non-Gaussian entangled states have been produced in small ensembles of ions[11,12], and very recently in large atomic ensembles[13–15]. Here we generate entanglement in a large atomic ensemble via an interaction with a very weak laser pulse; remarkably, the detection of a single photon prepares several thousand atoms in an entangled state. We reconstruct a negative-valued Wigner function—an important hallmark of non-classicality—and verify an entanglement depth (the minimum number of mutually entangled atoms) of 2,910 ± 190 out of 3,100 atoms. Attaining such a negative Wigner function and the mutual entanglement of virtually all atoms is unprecedented for an ensemble containing more than a few particles. Although the achieved purity of the state is slightly below the threshold for entanglement-induced metrological gain, further technical improvement should allow the generation of states that surpass this threshold, and of more complex Schrödinger cat states for quantum metrology and information processing. More generally, our results demonstrate the power of heralded methods for entanglement generation, and illustrate how the information contained in a single photon can drastically alter the quantum state of a large system.

Entanglement is now recognized as a resource for secure communication, quantum information processing, and precision measurements. An important goal is the creation of entangled states of many-particle systems while retaining the ability to characterize the quantum state and validate entanglement. Entanglement can be verified in a variety of ways; one of the strictest criteria is a negative-valued Wigner function[16,17], which necessarily implies that the entangled state has a non-Gaussian wavefunction. To date, the metrologically useful spin-squeezed states[1–10] have been produced in large ensembles. These states have Gaussian spin distributions and therefore can largely be modelled as systems with a classical source of spin noise, where quantum mechanics enters only to set the amount of Gaussian noise. Non-Gaussian states with a negative Wigner function are however manifestly non-classical, since the Wigner function as a quasiprobability function must remain non-negative in the classical realm. Whereas before this work a negative Wigner function had not been attained for atomic ensembles, in the optical domain, a negative-valued Wigner function has very recently been measured for states with up to 110 microwave photons[18]. Another entanglement measure is the entanglement depth[19], that is, the minimum number of atoms that are demonstrably, but possibly weakly, entangled with one another. This parameter quantifies how widely shared among the particles an entangled state is. For a state of an ensemble characterized by collective measurements, the entanglement depth depends sensitively on the proximity of the state to the ideal symmetric subspace of all particles. The largest entanglement depth verified previously has been 170 out of 2,300

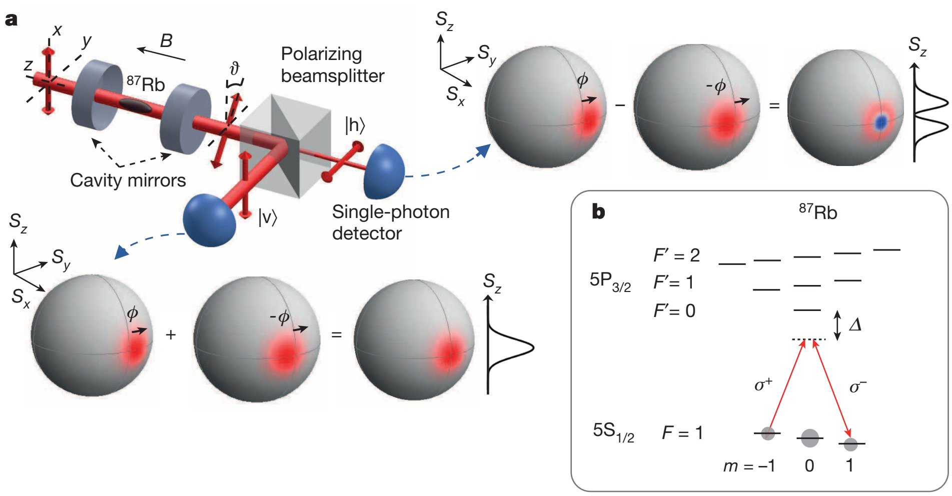

Figure 1 | Scheme for heralded entanglement generation in a large atomic ensemble by single-photon detection. **a**, Incident vertically polarized light (top left) experiences weak polarization rotation ϑ due to atomic quantum noise, and the detection of a horizontally polarized transmitted photon $|h\rangle$ heralds an entangled state of collective atomic spin. An optical resonator formed by two mirrors enhances the polarization rotation and the heralding probability. The Bloch spheres show the ideal Wigner distribution functions for the collective spin $\boldsymbol{S}$ upon registering the corresponding single-photon detection events. **b**, Atoms of ^{87}Rb in the $5S_{1/2}$, $F = 1$ hyperfine manifold are coupled to the excited $5P_{3/2}$ manifold via linearly polarized light, decomposed into two circular polarization components $|\sigma^{\pm}\rangle$ (indicated by red arrows) that interact with the atomic ground-state populations. The outgoing polarization state of the light reflects the quantum fluctuations between the $|5S_{1/2}F = 1, m = \pm 1\rangle$ magnetic sublevels. See Methods for details.

[1]Department of Physics, MIT-Harvard Center for Ultracold Atoms, and Research Laboratory of Electronics, Massachusetts Institute of Technology, Cambridge, Massachusetts 02139, USA. [2]Institute of Physics, University of Belgrade, Pregrevica 118, 11080 Belgrade, Serbia.
*These authors contributed equally to this work.

atoms for a spin-squeezed state[6], and very recently 13 out of 41 atoms for a non-Gaussian state[13].

Here we generate entanglement in a large atomic ensemble by detecting a single photon that has interacted with the ensemble[20]. An incident vertically polarized photon experiences a weak random polarization rotation associated with the quantum noise of the collective atomic spin. The detection of a horizontally polarized emerging photon then heralds a non-Gaussian entangled state of collective atomic spin (Fig. 1) with a negative-valued Wigner function of -0.36 ± 0.08, and an entanglement depth of 90% of our ensemble containing several thousand atoms.

The pertinent atom–light interaction is enhanced by an optical cavity, into which we load $N_{\mathrm{a}} = 3{,}100 \pm 300$ laser-cooled ^{87}Rb atoms (Fig. 1a). The atoms are prepared in the $5S_{1/2}$, $F = 1$ hyperfine manifold, such that each atom i can be associated with a spin $\boldsymbol{f}_i$, and the ensemble with a collective-spin vector $\boldsymbol{S} = \sum_i \boldsymbol{f}_i$. After polarizing the ensemble ($S_z \approx S = F\,N_{\mathrm{a}}$) by optical pumping, the collective spin state is rotated onto the $\hat{\boldsymbol{x}}$ axis by means of a radio-frequency $\pi/2$ pulse. This (unentangled) initial state, which is centred about $S_z = 0$ with a variance $(\Delta S_z)^2 = S/2$, is known as a coherent spin state (CSS). In our experiment, the atoms are non-uniformly coupled to the optical mode used for state preparation and detection, but the relevant concepts can be generalized to this situation, as discussed in Methods.

Probe light resonant with a cavity mode and detuned from the ^{87}Rb D_2 transition is polarization-analysed upon transmission through the cavity. The vertical polarization state of each photon in the incident laser pulse $|\mathrm{v}\rangle = (|\sigma^+\rangle + |\sigma^-\rangle)/\sqrt{2}$ can be decomposed into two circular polarization components $|\sigma^{\pm}\rangle$ that produce opposite differential light shifts between the atomic magnetic sublevels $|m = \pm 1\rangle$. Hence a $|\sigma^{\pm}\rangle$ photon causes a precession of the collective spin vector $\boldsymbol{S}$ in the x–y plane by a small angle $\pm\phi$ (see Methods), and we denote the corresponding slightly displaced CSS by $|\pm\phi\rangle$. Then the combined state of the atom–light system after the passage of one photon can be written as[20]

$$|\psi\rangle \propto |\sigma^+\rangle|+\phi\rangle + |\sigma^-\rangle|-\phi\rangle \tag{1}$$

Conversely, atoms in the states $|m = \pm 1\rangle$ cause different phase shifts on the $\sigma^{\pm}$ photons, resulting in a net rotation of the photon linear polarization if the states $|m = \pm 1\rangle$ are not equally populated. Then the atomic quantum fluctuations between $|m = \pm 1\rangle$ in the CSS randomly rotate the polarization of the input photons $|\mathrm{v}\rangle$, giving rise to a non-zero probability $\propto \phi^2$ for an incident $|\mathrm{v}\rangle$ photon to emerge in the polarization $|\mathrm{h}\rangle = (|\sigma^+\rangle - |\sigma^-\rangle)/\sqrt{2}$, orthogonal to its input polarization. The detection of such a 'heralding' photon projects the atomic state onto $\langle \mathrm{h}|\psi\rangle \propto |\phi\rangle - |-\phi\rangle$, which is not a CSS, but an entangled state of collective spin, namely, the first excited Dicke state[21] $|\psi_1\rangle$ along $\hat{\boldsymbol{x}}$ (Fig. 1a). In contrast, if the photon is detected in its original polarization $|\mathrm{v}\rangle$, the atomic state is projected onto $\langle \mathrm{v}|\psi\rangle \propto |\phi\rangle + |-\phi\rangle$, a state slightly spin squeezed[1] and essentially identical to the input CSS. Thus the entangled atomic state $|\psi_1\rangle$ is post-selected by the detection of the heralding photon $|\mathrm{h}\rangle$.

From a different perspective, the entangled state is generated by a single-photon measurement event. The incident photon undergoes Faraday rotation by an angle ϑ proportional to the collective spin along the cavity axis, S_z, that exhibits quantum fluctuations around $\langle S_z\rangle = 0$. Since detection of the outgoing photon in $|\mathrm{h}\rangle$ is only possible if $S_z \neq 0$, such detection excludes values of S_z near 0 from the spin distribution[20], and biases the collective spin towards larger values of $|S_z|$. This creates a 'hole' in the atomic distribution near $S_z = 0$, as seen in Fig. 1a.

The mean photon number in the incident laser pulse $k \approx 210$ is chosen such that the probability for one photon to emerge in heralding polarization $|\mathrm{h}\rangle$ is $p \approx 0.05 \ll 1$. This ensures a very small probability $\propto p^2$ for producing a different entangled state $|\psi_2\rangle$ heralded by two photons[20], a state which, owing to our photon detection efficiency of $q = 0.3 < 1$, we would (mostly) mistake for $|\psi_1\rangle$. This admixture of $|\psi_2\rangle$ to the heralded state is suppressed by a factor of $3p(1-q) \approx 0.1$. Further state imperfection arises from false heralding events due to residual polarization impurity of the probe beam (independent of the atoms) of $\sim 3 \times 10^{-5} = 0.1p/k$, adding an admixture of about 10% of the CSS to the heralded state.

In order to reconstruct the collective-spin state generated by the heralding event, we rotate the atomic state after the heralding process by an angle $\beta = 0, \frac{\pi}{4}, \frac{\pi}{2}, \frac{3\pi}{4}$ about the $\hat{\boldsymbol{x}}$ axis before measuring S_z. (Thus $\beta = 0$ corresponds to measuring S_z, $\beta = \pi/2$ corresponds to S_y, and so on). The measurement is performed by applying a stronger light pulse in the same polarization-optimized set-up used for heralding. As the Faraday rotation angle $\vartheta \ll 1$ is proportional to S_z, and the probability

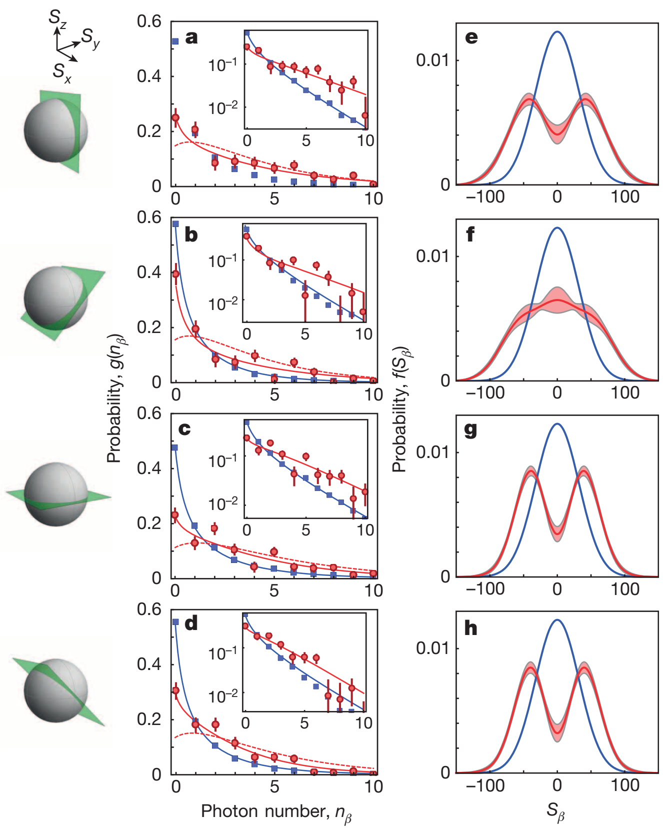

Figure 2 | Collective-spin distribution of atomic state heralded by one photon. **a–d**, Measured photon distributions $g(n_\beta)$ for no heralding photon detected (blue squares), and for one heralding photon detected (red circles), for rotation angles β of 0 (**a**), $\pi/4$ (**b**), $\pi/2$ (**c**) and $3\pi/4$ (**d**). Inset, logarithmic representations of the same data. In the ideal case, the ratio for the heralded state and the CSS is $\langle n_\beta\rangle_{\mathrm{her}}/\langle n_\beta\rangle_{\mathrm{CSS}} = \left\langle S_\beta^2\right\rangle_{\mathrm{her}}/\left\langle S_\beta^2\right\rangle_{\mathrm{CSS}} = 3$ for any angle β, and we measure $\langle n_\beta\rangle_{\mathrm{her}}/\langle n_\beta\rangle_{\mathrm{CSS}} = \{2.7 \pm 0.2, 2.2 \pm 0.2, 2.4 \pm 0.2, 2.1 \pm 0.1\}$ for $\beta = \left\{0, \frac{\pi}{4}, \frac{\pi}{2}, \frac{3\pi}{4}\right\}$. For each β, the blue and red data sets represent approximately 1.5×10^4 and 200 experiments, respectively. The solid blue and the dashed red curves are predictions without any free parameters, calculated from first principles and the separately measured atom number, for the CSS and the perfect first Dicke state, respectively. The solid red line corresponds to the simultaneous fit to all measurement angles β, that is, the reconstructed density matrix. Error bars, 1 s.d. The planes through the Bloch spheres indicate the measurement direction for the collective spin as specified by the angle β. **e–h**, Reconstructed collective spin distributions of the heralded state (red) for rotation angles β of 0 (**e**), $\pi/4$ (**f**), $\pi/2$ (**g**) and $3\pi/4$ (**h**). The spin distributions of the CSS (blue) are for reference. The horizontal axis S_β is expressed in terms of the effective atom number[4] $N = (2/3)N_{\mathrm{a}} = 2{,}100$, obtained by weighting each atom with its coupling strength to the standing-wave probe field inside the cavity, such that the experimentally measured spin fluctuation $(\Delta S_\beta)^2$ of the CSS via its interaction with the probe light satisfies the standard relation $(\Delta S_\beta)^2 = S/2 = NF/2$ for spin F atoms (see Methods). The shaded area indicates the statistical uncertainty of 1 s.d. The spin distribution in **f** shows no 'hole' in the middle owing to the lower quality of data for this measurement run, $\beta = \pi/4$.

for detecting $|\mathrm{h}\rangle$-polarized photons is proportional to ϑ^2, the measured probability distribution of $|\mathrm{h}\rangle$ photon number, $g(n_\beta)$, reflects the probability distribution of S_β^2. Figure 2a–d shows that a single heralding photon substantially changes the spin distribution towards larger values of $\langle S_\beta^2 \rangle$. We further verify that the heralded state remains (nearly) spin polarized with a contrast of $\mathcal{C} = 0.99^{+0.01}_{-0.02}$, the same as for the CSS within error bars (Fig. 3a).

From the photon distributions $g(n_\beta)$ we can reconstruct the density matrix ρ_{mn} in the Dicke state basis[21] along $\hat{\mathbf{x}}$, where $|n=0\rangle$ denotes the CSS along $\hat{\mathbf{x}}$, $|n=1\rangle$ the first Dicke state, $|n=2\rangle$ the second Dicke state, and so on. From the density matrix we obtain the Wigner function $W(\theta, \phi)$ on the Bloch sphere[22] (Fig. 3). To accurately determine the Wigner function value on the axis, $W\left(\theta = \frac{\pi}{2}, \phi = 0\right) = \sum_n (-1)^n \rho_{nn}$, which depends only on the population terms ρ_{nn}, we average the photon distributions $g(n_\beta)$ over four angles β and thereby reduce the fitting parameters to just $\rho_{nn}, n \leq 4$. This is equivalent to constructing a rotationally symmetric Wigner function from the angle-averaged marginal distribution[17]. We obtain $\rho_{00} = 0.32 \pm 0.03$, $\rho_{11} = 0.66 \pm 0.04$ with negligible higher-order population terms, giving $W\left(\frac{\pi}{2}, 0\right) = -0.36 \pm 0.08$, to be compared to $W\left(\frac{\pi}{2}, 0\right) = -1$ for the perfect first Dicke state.

We can also fit the density matrix including the coherence terms simultaneously to $g(n_\beta)$ for all four angles β, without angle-averaging. Since the photon distributions $g(n_\beta)$ depend only on S_β^2, they determine only the even terms of the density matrix, that is, ρ_{mn} where $m+n$ is even, and contain no information about the odd terms. If we calculate $W\left(\frac{\pi}{2}, 0\right)$ from the density matrix without angle-averaging, we find $W\left(\frac{\pi}{2}, 0\right) = -0.27 \pm 0.08$, within error bars consistent with the angle-averaged value. In order to display the Wigner function, we bound the odd terms ($m+n$ odd) by verifying that the heralding process does not displace the state relative to the CSS (see Methods). Therefore we set the odd terms to zero, and display the resulting density matrix and corresponding Wigner function in Fig. 3b–d. The spin distributions $f(S_\beta)$ obtained from this density matrix are shown in Fig. 2e–h.

In order to quantify the minimum number of mutually entangled atoms, we use a criterion derived in ref. 13 that establishes entanglement depth as a function of the populations ρ_{00} and ρ_{11}. From this criterion, generalized to the case of non-uniform coupling to the measurement light field (see Methods), we deduce an average entanglement depth of $\mathcal{N}_\mathrm{a} = 2{,}910 \pm 190$ out of $N_\mathrm{a} = 3{,}100$ atoms (Fig. 3e) using the angle-averaged density matrix. Our results represent the first (to our knowledge) experimental verification of the mutual entanglement shared by virtually all atoms in an ensemble that contains more than a few particles.

The above results demonstrate that even with limited resources, that is, weak atom–photon coupling, heralding schemes can be used to boost the effective interaction strength by a large factor, enabling the production of highly entangled states[20,23]. Furthermore, by repeated trials and feedback the entanglement generation can be made quasi-deterministic[24,25]. Our approach is related to other heralded schemes for quantum communication[24–27] and entangled-state preparation[28–30], and it would be interesting to generalize the present analysis to infer characteristics of the atomic state from the measured optical signals in those experiments. We note that the same first Dicke state was created in an ensemble of up to 41 atoms with a scheme that uses many heralding photons in a strongly coupled atom–cavity system[13]. In our system, the maximum atom number of ~3,000 is set by the accuracy of the spin rotation, and could be increased by two orders of magnitude by better magnetic-field control[10]. The state purity ρ_{11} can probably be further improved by reducing the heralding probability, and a value of $\rho_{11} > 0.73$ would be required for the Fisher information[14] to exceed that of the CSS, and enable metrological gain of up to 3 dB. The detection of two or more photons prepares Schrödinger cat states[20] of the atomic ensemble with

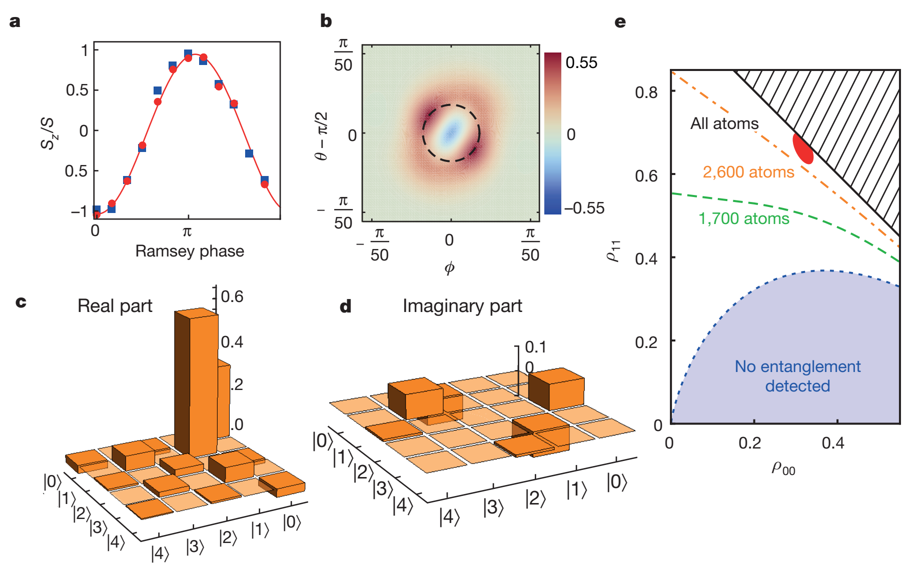

Figure 3 | Reconstruction of the heralded many-atom entangled state. **a**, Normalized spin component S_z/S measured in a Ramsey sequence, as a function of the phase of the second Ramsey $\pi/2$ pulse, for the CSS (blue squares) and the heralded state (red circles). The fit (red line) shows a contrast of $0.99^{+0.01}_{-0.02}$ for the heralded state, within error bars the same as the contrast 0.995 ± 0.004 of the CSS. The negligible contrast reduction is expected given that we send only 210 photons into the system at large detuning from atomic resonance. **b**, Reconstructed Wigner function $W(\theta, \phi)$ for the heralded state on the Bloch sphere[22] with a radius given by the effective atom number $N = 2{,}100$. θ is the polar angle with respect to $\hat{\mathbf{z}}$ and ϕ is the azimuthal angle with respect to $\hat{\mathbf{x}}$. The first excited Dicke state and the CSS have $W\left(\frac{\pi}{2}, 0\right) = -1$ and $W\left(\frac{\pi}{2}, 0\right) = 1$, respectively. To provide a reference scale for the size of the negative region, the black dashed line is the contour at which the CSS has a Wigner function value equal to $1/e$. **c**, **d**, Real and imaginary parts, respectively, of the reconstructed density matrix elements, in the Dicke state basis along $\hat{\mathbf{x}}$, for the heralded state. **e**, Entanglement depth criterion[13] for the heralded state, plotted in terms of density matrix elements ρ_{00} and ρ_{11}. The red shaded region represents the 1 s.d. confidence region for the heralded state. Lines (orange, green and blue, labelled with k) represent boundaries for k-particle entanglement in terms of atom number N_a; a state with ρ_{11} greater than such a boundary displays at least k-particle entanglement. States falling within the blue shaded region are not provably entangled by the used criterion. The hatched area indicates the unphysical region where the density matrix trace would exceed unity.

more metrological gain. We expect that heralded methods can generate a variety of nearly pure, complex, strongly entangled states that are not accessible by any other means at the present state of quantum technology.

Online Content Methods, along with any additional Extended Data display items and Source Data, are available in the online version of the paper; references unique to these sections appear only in the online paper.

Received 28 October 2014; accepted 27 January 2015.

1. Kitagawa, M. & Ueda, M. Squeezed spin states. *Phys. Rev. A* **47,** 5138–5143 (1993).
2. Appel, J. *et al.* Mesoscopic atomic entanglement for precision measurements beyond the standard quantum limit. *Proc. Natl Acad. Sci. USA* **106,** 10960–10965 (2009).
3. Takano, T., Tanaka, S.-I.-R., Namiki, R. & Takahashi, Y. Manipulation of nonclassical atomic spin states. *Phys. Rev. Lett.* **104,** 013602 (2010).
4. Schleier-Smith, M. H., Leroux, I. D. & Vuletić, V. States of an ensemble of two-level atoms with reduced quantum uncertainty. *Phys. Rev. Lett.* **104,** 073604 (2010).
5. Leroux, I. D., Schleier-Smith, M. H. & Vuletić, V. Implementation of cavity squeezing of a collective atomic spin. *Phys. Rev. Lett.* **104,** 073602 (2010).
6. Gross, C., Zibold, T., Nicklas, E., Estève, J. & Oberthaler, M. K. Nonlinear atom interferometer surpasses classical precision limit. *Nature* **464,** 1165–1169 (2010).
7. Riedel, M. F. *et al.* Atom-chip-based generation of entanglement for quantum metrology. *Nature* **464,** 1170–1173 (2010).
8. Hamley, C. D., Gerving, C. S., Hoang, T. M., Bookjans, E. M. & Chapman, M. S. Spin-nematic squeezed vacuum in a quantum gas. *Nature Phys.* **8,** 305–308 (2012).
9. Sewell, R. J. *et al.* Magnetic sensitivity beyond the projection noise limit by spin squeezing. *Phys. Rev. Lett.* **109,** 253605 (2012).
10. Bohnet, J. G. *et al.* Reduced spin measurement back-action for a phase sensitivity ten times beyond the standard quantum limit. *Nature Photon.* **8,** 731–736 (2014).
11. Leibfried, D. *et al.* Creation of a six-atom 'Schrödinger cat' state. *Nature* **438,** 639–642 (2005).
12. Monz, T. *et al.* 14-qubit entanglement: creation and coherence. *Phys. Rev. Lett.* **106,** 130506 (2011).
13. Haas, F., Volz, J., Gehr, R., Reichel, J. & Estéve, J. Entangled states of more than 40 atoms in an optical fiber cavity. *Science* **344,** 180–183 (2014).
14. Strobel, H. *et al.* Fisher information and entanglement of non-Gaussian spin states. *Science* **345,** 424–427 (2014).
15. Lücke, B. *et al.* Detecting multiparticle entanglement of Dicke states. *Phys. Rev. Lett.* **112,** 155304 (2014).
16. Leibfried, D. *et al.* Experimental determination of the motional quantum state of a trapped atom. *Phys. Rev. Lett.* **77,** 4281–4285 (1996).
17. Lvovsky, A. I. *et al.* Quantum state reconstruction of the single-photon Fock state. *Phys. Rev. Lett.* **87,** 050402 (2001).
18. Vlastakis, B. *et al.* Deterministically encoding quantum information using 100-photon Schrödinger cat states. *Science* **342,** 607–610 (2013).
19. Sørensen, A. S. & Mølmer, K. Entanglement and extreme spin squeezing. *Phys. Rev. Lett.* **86,** 4431–4434 (2001).
20. McConnell, R. *et al.* Generating entangled spin states for quantum metrology by single-photon detection. *Phys. Rev. A* **88,** 063802 (2013).
21. Arecchi, F. T., Courtens, E., Gilmore, R. & Thomas, H. Atomic coherent states in quantum optics. *Phys. Rev. A* **6,** 2211–2237 (1972).
22. Dowling, J. P., Agarwal, G. S. & Schleich, W. P. Wigner distribution of a general angular-momentum state: applications to a collection of two-level atoms. *Phys. Rev. A* **49,** 4101–4109 (1994).
23. Agarwal, G. S., Lougovski, P. & Walther, H. Multiparticle entanglement and the Schrödinger cat state using ground-state coherences. *J. Mod. Opt.* **52,** 1397–1404 (2005).
24. Duan, L. M., Lukin, M. D., Cirac, J. I. & Zoller, P. Long-distance quantum communication with atomic ensembles and linear optics. *Nature* **414,** 413–418 (2001).
25. Matsukevich, D. N. *et al.* Deterministic single photons via conditional quantum evolution. *Phys. Rev. Lett.* **97,** 013601 (2006).
26. Kuzmich, A. *et al.* Generation of nonclassical photon pairs for scalable quantum communication with atomic ensembles. *Nature* **423,** 731–734 (2003).
27. Simon, J., Tanji, H., Thompson, J. K. & Vuletić, V. Interfacing collective atomic excitations and single photons. *Phys. Rev. Lett.* **98,** 183601 (2007).
28. Choi, K. S., Goban, A., Papp, S. B., van Enk, S. J. & Kimble, H. J. Entanglement of spin waves among four quantum memories. *Nature* **468,** 412–416 (2010).
29. Christensen, S. L. *et al.* Towards quantum state tomography of a single polariton state of an atomic ensemble. *New J. Phys.* **15,** 015002 (2013).
30. Christensen, S. L. *et al.* Quantum interference of a single spin excitation with a macroscopic atomic ensemble. *Phys. Rev. A* **89,** 033801 (2014).

Acknowledgements We thank M. H. Schleier-Smith, E. S. Polzik and S. L. Christensen for discussions. This work was supported by the NSF, DARPA (QUASAR), and a MURI grant through AFOSR. S.Ć. acknowledges support from the Ministry of Education, Science and Technological Development of the Republic of Serbia, through grant numbers III45016 and OI171038.

Author Contributions The experiment and analysis were carried out by R.M., H.Z., J.H. and S.Ć.; V.V. supervised the work; all authors discussed the results and contributed to the manuscript.

Author Information Reprints and permissions information is available at www.nature.com/reprints. The authors declare no competing financial interests. Readers are welcome to comment on the online version of the paper. Correspondence and requests for materials should be addressed to V.V. (vuletic@mit.edu).

METHODS

Photon polarization rotation by atomic spin. Probe laser light red-detuned by $\Delta_0/(2\pi) = -200$ MHz from the ^{87}Rb transition $5^2S_{1/2}$, $F=1$ to $5^2P_{3/2}$, $F'=0$ is sent through an optical cavity containing the atomic ensemble. We first consider the case where all the atoms are coupled with equal strength to the probe light. For detuning Δ much larger than the excited state linewidth $\Gamma/(2\pi) = 6.1$ MHz, the excited state manifold can be adiabatically eliminated. The vector component of the a.c. Stark shift is described by the Hamiltonian

$$\frac{H}{\hbar} = \frac{g^2}{\Delta} J_z S_z \tag{2}$$

where $J_z = \frac{1}{2}\left(a_+^\dagger a_+ - a_-^\dagger a_-\right)$, with $a_\pm$ the annihilation operators for photons with $\sigma^\pm$ circular polarizations. Here $2g$ is the effective single-photon Rabi frequency taking into account the multiple transitions from $5^2S_{1/2}$, $F=1$ to $5^2P_{3/2}$, $F'=0$, 1, 2, given by

$$g^2 = \left(g_{1,1}^{0,0}\right)^2 + \left(g_{1,1}^{1,0}\right)^2 + \left(g_{1,1}^{2,0}\right)^2 - \left(g_{1,1}^{2,2}\right)^2 \tag{3}$$

where $2g_{F,m}^{F',m'}$ is the single-photon Rabi frequency between the ground state $|F=1, m\rangle$ and the excited state $|F', m'\rangle$. As Δ_0 is comparable to the hyperfine splittings of the $5^2P_{3/2}$ excited states, the interaction strength g^2/Δ is given by

$$\frac{g^2}{\Delta} = \frac{\left(g_{1,1}^{0,0}\right)^2}{\Delta_0} + \frac{\left(g_{1,1}^{1,0}\right)^2}{\Delta_0 - \Delta_1} + \frac{\left(g_{1,1}^{2,0}\right)^2}{\Delta_0 - \Delta_1 - \Delta_2} - \frac{\left(g_{1,1}^{2,2}\right)^2}{\Delta_0 - \Delta_1 - \Delta_2} \tag{4}$$

where $\Delta_1/(2\pi) = 72$ MHz is the hyperfine splitting between the $F'=0$ and $F'=1$ manifolds, $\Delta_2/(2\pi) = 157$ MHz between $F'=1$ and $F'=2$, and $\Delta/(2\pi) = -150$ MHz is the effective detuning when $\Delta_0/(2\pi) = -200$ MHz. The value g^2/Δ for our experiment is $2\pi \times 0.7$ kHz.

This vector shift (equation (2)) gives rise to a J_z-dependent Larmor precession of the atomic collective spin $\boldsymbol{S}$ in the x–y plane. Consider one $|\sigma^\pm\rangle$ photon passing through the optical cavity and causing the atomic spin to precess by phase $\pm\phi$. The characteristic atom–photon interaction time is $2/\kappa$, where κ is the cavity linewidth, therefore the atomic phase is given by[20,31] $\phi = g^2/(\Delta\kappa) = \eta_v\Gamma/(4\Delta)$, where the cavity cooperativity $\eta_v = 4g^2/(\kappa\Gamma) = 0.07$. Another way to think of the Hamiltonian (equation (2)) is that the atomic spin component S_z causes different phase shifts on the photon σ^+ and σ^- components, resulting in a rotation of the linear polarization of the light. The polarization rotation angle $\vartheta = (g^2/\Delta)(S_z/2)(2/\kappa) = \phi S_z$.

In general, the incident light can introduce Raman transitions between different magnetic levels in the $F=1$ ground state manifold. We apply a bias magnetic field of 4.7 G along the cavity axis to introduce a Zeeman shift between the magnetic levels, so that the Raman coupling is off-resonant. The Larmor frequency is $\omega_L/(2\pi) = 3.3$ MHz, larger than the cavity linewidth $\kappa/(2\pi) = 1.0$ MHz, so that the Raman coupling can be neglected. There is also an unimportant scalar light shift, as well as a tensor light shift that gives rise to squeezing that is negligible for our experimental conditions.

Experimental details. We load an ensemble of ^{87}Rb atoms, cooled to $T = 50$ µK, into a medium-finesse optical cavity (cavity finesse $\mathcal{F} = 5{,}600$, linewidth $\kappa/(2\pi) = 1.0$ MHz, cooperativity $\eta_0 = 0.2$ at an antinode on a transition with unity oscillator strength). The atoms are confined on the cavity axis by a far-detuned optical dipole trap at 852 nm with trap depth $U/h = 20$ MHz. Characteristics of the optical cavity at the 780 nm probe laser wavelength and the 852 nm trap laser wavelength are summarized in Extended Data Table 1. One Glan-Taylor polarizing beamsplitter (Thorlabs GT5) purifies the polarization of probe light entering the cavity, while a second polarizing beamsplitter after the cavity allows us to measure the rotation of the probe light due to the atomic projection noise. Two Single Photon Counting Modules (SPCMs, models SPCM-AQRH-14-FC and SPCM-AQR-12-FC) are placed at the transmitting and reflecting ports of the polarizing beamsplitter to detect the photons. Owing to the fibre coupling and finite SPCM detection efficiency at 780 nm, the overall quantum efficiency of the detection process is $q = 0.3$.

Definition of effective atom number. Atoms are optically confined at the antinodes of the 852 nm trap laser standing wave. The 780 nm probe light in the cavity forms a standing wave that is incommensurate with the trap standing wave. Consequently, the atoms experience spatially varying couplings to the probe light and rotate the probe photon polarization by different amounts. For an atom at position z on the cavity axis, the cooperativity is $\eta(z) = \eta_v \sin^2(kz)$. When N_a atoms are prepared in a CSS, the atomic projection noise gives rise to fluctuations of the photon polarization rotation. The measured variance of the polarization rotation is proportional to $\frac{N_a}{2}\langle\eta^2(z)\rangle$ where averaging is performed over the position z. This variance differs by a factor of order unity from that of a CSS consisting of N_a atoms uniformly coupled to the light. As described in a previous paper[4], we introduce the effective atom number N and the effective cavity cooperativity η to satisfy two conditions: that the experimentally measured variance equals that of N uniformly coupled atoms, $\frac{N_a}{2}\langle\eta_z^2\rangle = \frac{N}{2}\eta^2$, and that the total amount of interaction between the atomic ensemble and the probe light is the same, that is, $N_a\langle\eta_z\rangle = N\eta$. To satisfy these two conditions we define the effective atom number $N = \frac{2}{3}N_a$ and the effective cavity cooperativity $\eta = \frac{3}{4}\eta_v$. This re-scaling allows direct comparison with the well-known expressions for the uniformly coupled CSS.

As in the main text and the rest of Methods, S_z refers to the collective spin of an ensemble containing N effective atoms, and therefore the atomic spin precession phase for each transmitting cavity photon is given by $\phi = \eta\Gamma/(4\Delta) = (3/4)\eta_v\Gamma/(4\Delta)$. Note that this value $\eta = 0.05 < 1$ corresponds to the weak atom–cavity coupling regime. For our parameters, $\phi = 5\times10^{-4} \ll \phi_{CSS} = 1.5\times10^{-2}$ where $\phi_{CSS} = \sqrt{1/(2S)}$ is the angular r.m.s. width of the CSS.

Choice of the heralding photon number. The heralding light must be weak enough that it does not introduce substantial decoherence of the desired atomic state. The fundamental shot noise between the σ^+ and σ^- circular polarization components of the heralding light gives rise to phase broadening of the atomic state, which limits the purity of the heralded entangled state. To measure the phase broadening, heralding light pulses with variable photon number are sent into the cavity, and the variance ΔS_y^2 is measured by applying a radio-frequency $\pi/2$ pulse to rotate the atomic state about the $\hat{\boldsymbol{x}}$ direction before measuring ΔS_z^2. Extended Data Fig. 1 shows the measured atomic state variance ΔS_y^2 as a function of the photon number in the heralding light, in agreement with the predicted linear dependence. The heralding photon number is thus chosen to be ~210, with corresponding herald detection probability $pq = 1.5\%$, to give fairly small phase broadening. Lower heralding photon number results in a purer heralded state, but at the expense of a lower heralding and state generation probability.

Relation between $f(S_\beta)$ and $g(n_\beta)$. To measure the atomic state spin distribution, measurement light with the same polarization $|v\rangle$ as the heralding light is sent through the atoms, and the number of photons with the orthogonal polarization $|h\rangle$ is measured. The measurement light contains a large number of input photons $n_{in} = 1.7\times10^4$ to perform destructive measurements with good signal-to-noise ratio. The photon polarization is rotated by a small angle $\vartheta = \phi S_z$ and the probability for each photon to emerge in $|h\rangle$ is ϑ^2. For a given number of input photons n_{in}, the average number of detected photons with $|h\rangle$ polarization is $\langle n\rangle = qn_{in}(\phi S_z)^2$, where q is the overall quantum efficiency. Therefore, a spin distribution $f(S_z)$ is mapped to a measured photon distribution $g(n)$. For a given S_z, the detected photons follow a Poisson distribution with mean number $\langle n\rangle$, and the probability to measure exactly n photons is given by

$$P(n,S_z) = \exp\left[-qn_{in}(\phi S_z)^2\right]\frac{\left[qn_{in}(\phi S_z)^2\right]^n}{n!} \tag{5}$$

For an atomic state with the spin distribution $f(S_z)$, the photon distribution $g(n)$ is given by

$$g(n) = \sum_{S_z} f(S_z)P(n,S_z) = \sum_{S_z} f(S_z)\exp\left[-qn_{in}(\phi S_z)^2\right]\frac{\left[qn_{in}(\phi S_z)^2\right]^n}{n!} \tag{6}$$

In order to measure the spin along a general direction, the atomic spin is rotated by an angle β with a radio-frequency pulse before detection. Replacing S_z by S_β in equation (6), we write the relation between the spin distribution $f(S_\beta)$ and the measured photon distribution $g(n_\beta)$ as

$$g(n_\beta) = \sum_{S_\beta} f(S_\beta)P(n_\beta,S_\beta) = \sum_{S_\beta} f(S_\beta)\exp\left[-qn_{in}(\phi S_\beta)^2\right]\frac{\left[qn_{in}(\phi S_\beta)^2\right]^{n_\beta}}{n_\beta!} \tag{7}$$

Choice of the measurement photon number. The measurement photon number is chosen to optimize the readout quality. Extended Data Fig. 2 illustrates the dependence of readout on the input measurement photon number n_{in} by showing how the reconstructed distributions $f(S_z)$ change as n_{in} is varied (the method of reconstruction is discussed later). When the photon number is small, there is large detection noise due to photon shot noise, reflected as the large error band. With increasing photon number, the photon scattering by atoms into free space increases and the atomic state is more strongly perturbed, therefore the 'dip' at $S_z = 0$ becomes less distinct. To balance these two competing effects, the optimized atomic-state-measurement photon number is set to 1.7×10^4.

Subtracting background photon counts. Owing to the residual polarization impurity of the measurement light, there are a small number of background photon counts even when there are no atoms. The background counts account for about 4% of the photon signal of the heralded state. We independently measure the background photon distribution and subtract it from the directly measured atomic signal to obtain $g(n_\beta)$. If we were not to correct for these background counts, we would overestimate the density matrix population ρ_{11} by 10%.

Reconstruction of the density matrix. Using the measured photon distributions $g(n_\beta)$ for all four angles $\beta = 0, \pi/4, \pi/2, 3\pi/4$, the density matrix ρ of the heralded state can be reconstructed.

As the entangled state maintains $0.99^{+0.01}_{-0.02}$ contrast, the magnitude of the total spin $S \approx N$ and we can express the density matrix in the basis of Dicke states $|m\rangle_x$ along the $\hat{x}$ direction

$$\rho = \rho_{00}|0\rangle_x\langle 0|_x + \rho_{11}|1\rangle_x\langle 1|_x + \rho_{01}|0\rangle_x\langle 1|_x + \rho_{10}|1\rangle_x \langle 0|_x + \rho_{22}|2\rangle_x\langle 2|_x + \rho_{02}|0\rangle_x\langle 2|_x + \rho_{20}|2\rangle_x\langle 0|_x + \ldots \quad (8)$$

The spin distribution $f(S_\beta)$ can be written as a function of atom number N and the density matrix elements ρ_{00}, ρ_{11}, and so on:

$$\begin{aligned} f(S_\beta,\rho,N) &= \langle S_\beta|\rho|S_\beta\rangle \\ &= \rho_{00}G(0,S_\beta)G^*(0,S_\beta) + \rho_{11}G(1,S_\beta)G^*(1,S_\beta) + \rho_{01}G(0,S_\beta)G^*(1,S_\beta) \\ &\quad + \rho_{10}G(1,S_\beta)G^*(0,S_\beta) + \rho_{22}G(2,S_\beta)G^*(2,S_\beta) \\ &\quad + \rho_{02}G(0,S_\beta)G^*(2,S_\beta) + \rho_{20}G(2,S_\beta)G^*(0,S_\beta) + \ldots \end{aligned} \quad (9)$$

Here $G(m, S_\beta) = \langle S_\beta|m\rangle_x$ is the wavefunction of Dicke state $|m\rangle_x$ in the representation of spin component S_β and is given by

$$G(m,S_\beta,N) = \frac{1}{\sqrt{2^m m!}}\left(\frac{1}{\pi N}\right)^{1/4} e^{im\beta - S_\beta^2/(2N)} H_m\left(\sqrt{\frac{1}{N}}S_\beta\right) \quad (10)$$

where $H_m(x)$ is the mth order Hermite polynomial and N is the atom number. Using equation (7), we write the theoretically predicted photon distribution $g_{\mathrm{th}}(n_\beta)$ as a function of the density matrix ρ, atom number N and input photon number n_{in}

$$\begin{aligned} g_{\mathrm{th}}(n_\beta,\rho,N,n_{\mathrm{in}}) &= \sum_{S_\beta} f_{\mathrm{th}}(S_\beta,\rho,N)P(n_\beta,S_\beta) \\ &= \sum_{S_\beta} f_{\mathrm{th}}(S_\beta,\rho,N)\exp\left[-qn_{\mathrm{in}}(S_\beta\phi)^2\right]\frac{\left[qn_{\mathrm{in}}(S_\beta\phi)^2\right]^{n_\beta}}{n_\beta!}. \end{aligned} \quad (11)$$

We independently measure the input photon number n_{in} and find the atom number N by fitting the photon distributions of the CSS, whose only non-zero density matrix element is $\rho_{00} = 1$. The fitted atom numbers N for different angles β agree within 15% with the values independently measured from the shift of the cavity resonance. We then use the density matrix ρ of the heralded state as the only free parameter, to fit the theoretical distributions $g_{\mathrm{th}}(n_\beta)$ to the measured photon distributions $g(n_\beta)$ along all four angles β. We do this by minimizing the least squares deviation D weighted by the error σ_g of $g(n_\beta)$, given by

$$D = \sum_\beta \sum_{n\geq 0}\left[\frac{g_{\mathrm{th}}(n_\beta,\rho) - g(n_\beta,\rho)}{\sigma_g}\right]^2 \quad (12)$$

Since the photon distributions $g(n_\beta)$ measure S_β^2, we can obtain the even terms of the density matrix (ρ_{mn} where $m + n$ is even) and our measurements are not sensitive to the odd terms. Because the overall heralding probability is $pq = 1.5\%$, the higher-order Dicke state components are exponentially suppressed. We fit the density matrix up to Dicke state $|4\rangle_x$. The fitted values $\rho_{22} = 0.03 \pm 0.02$, $\rho_{33} = 0.02 \pm 0.01$, $\rho_{44} = 0.01 \pm 0.01$ agree with the theoretical expectation[20] for our system.

From the fitted density matrix ρ (with coherence terms) we obtain the spin distributions $f(S_\beta)$ using equation (9) for different angles β, as shown in Fig. 2e–h.

To reconstruct the Wigner function for the spin state on the Bloch sphere[20,22], we convert ρ from the Dicke state basis into the spherical harmonic basis and obtain the normalized Wigner function according to

$$W(\theta,\phi) = \frac{1}{\sqrt{2S/\pi}}\sum_{k=0}^{N}\sum_{q=-k}^{k}\rho_{kq}Y_{kq}(\theta,\phi) \quad (13)$$

where the terms ρ_{kq} represent the density elements in the spherical harmonic basis and $Y_{kq}(\theta, \phi)$ are the spherical harmonics, with θ, ϕ being the polar and azimuthal angles on the Bloch sphere, respectively. The normalization factor $\sqrt{2S/\pi}$ is chosen such that the CSS has $W\left(\frac{\pi}{2},0\right) = 1$. Note that, in the limit of large atom number, this normalization also means that the pure first excited Dicke state has $W\left(\frac{\pi}{2},0\right) = -1$, and generally the value of the Wigner function on the $\hat{x}$ axis depends only on the populations ρ_{nn} such that $W\left(\theta = \frac{\pi}{2},\phi = 0\right) = \sum_n(-1)^n\rho_{nn}$.

Measurement of mean value of S_z. The measured photon distributions $g(n_\beta)$ do not give information about the density matrix odd terms (ρ_{mn} where $m + n$ is odd). In order to bound the odd terms, we verify that the heralding process does not displace the produced heralded state relative to the CSS. This is accomplished by performing a measurement with a probe beam polarized at 45° relative to $|v\rangle$, such that the difference between the measured $|h\rangle$ and $|v\rangle$ photon numbers is proportional to S_z. We find a heralding-light-induced shift $\delta\langle S_z\rangle = -0.2 \pm 1.6$, consistent with zero, and very small compared to the CSS r.m.s. width $(\Delta S_z)_{\mathrm{CSS}} \approx 30$. Therefore we set the odd terms of the density matrix to zero in Fig. 3b–d.

Entanglement depth for finite contrast. Entanglement depth is defined as the minimum number of entangled particles in an ensemble. A fully separable pure state can be written as $|\varphi\rangle = |\varphi_1\rangle \otimes \ldots \otimes |\varphi_N\rangle$, where N is the atom number. A pure k-producible state can be written as $|\varphi\rangle = \left|\varphi_1^{1,\ldots,k_1}\right\rangle \otimes \ldots \otimes \left|\varphi_M^{1,\ldots,k_M}\right\rangle$, where $k_1, \ldots, k_M \leq k$, $k_1 + \ldots + k_M = N$. If a state cannot be written as a pure $(k - 1)$-producible state or a mixed state of $(k - 1)$-producible states, then it has entanglement depth of at least k.

We slightly generalize the entanglement criterion derived in ref. 13 to take into account the finite contrast $\mathcal{C}$ of the collective atomic spin in our experiment. The derivation in ref. 13 considers the case in the fully symmetric Dicke subspace of N atoms, and finds that for a k-producible state the maximum population of the first Dicke state ρ_{11} (P_1) as a function of the CSS population ρ_{00} (P_0) is

$$\max_{P_0} P_1 = \frac{P_0}{N}\max\left[\sqrt{k}\max_{\prod_{i=1}^{M-1}a_i = x} F_{M-1}(a_1,\ldots,a_{M-1}) + \sqrt{k'}F_1\left(\sqrt{P_0}/x\right)\right]^2 \quad (14)$$

Here $M = [N/k]$, $k' = N - k(M - 1)$, and $F_n(a_1,\ldots,a_n) = \sum_{i=1}^{n}\frac{\sqrt{1-a_i^2}}{a_i}$. Equation (14) is generally not a concave function of P_0. In order to obtain the upper bound for mixed states, denote the concave hull of the right side of equation (14) as $\mathcal{B}(P_0,k,N)$. We define $\mathcal{B}(P_0,k,N) = B(P_0,k,N)/N$. Note that when $N_1 < N_2$, $B(P_0, k, N_1) \leq B(P_0, k, N_2)$.

The heralded state we produce does not necessarily retain perfect contrast, so the state can be a mixture of different total spins $S = N, N-1, \ldots, N(1-\varepsilon)$, with $\varepsilon \approx 1\%$. The contrast loss is mainly caused by the decoherence between $F = 1$ magnetic sublevels, and the free space scattering of the heralding light by the atoms. We decompose the density matrix ρ into the total spin basis

$$\rho = \sum_{i=0}^{\varepsilon N} w_i\rho_{N-i} \quad (15)$$

Here ρ_{N-i} is the density matrix in the subspace of total spin $S = N - i$, w_i is the weight for each ρ_{N-i} and $\sum w_i = 1$. For each ρ_{N-i},

$$\mathcal{B}(P_0,k,N-i) = B(P_{0,N-i},k,N-i)/(N-i) \leq B(P_{0,N-i},k,N)/(N-i) \quad (16)$$

Here $P_{0,N-i}$ is the probability for the state to be found in the ground state in the subspace of total spin $N - i$.

Measurements of the spin distributions do not allow us to determine the total spin of the system at single-atom resolution. We define populations of the CSS and the first Dicke state by

$$P_0 = \sum_{i=0}^{\varepsilon N} w_i P_{0,N-i} \quad (17)$$

$$P_1 = \sum_{i=0}^{\varepsilon N} w_i P_{1,N-i} \quad (18)$$

The upper bound of P_1 is given by

$$\max_{P_0} P_1 \leq \sum_{i=0}^{\varepsilon N} w_i \max_{P_{0,N-i}} P_{1,N-i} \leq \sum_{i=0}^{\varepsilon N} w_i B(P_{0,N-i},k,N-i)/(N-i) \quad (19)$$

Using equation (16) and the fact that $B(P_0, k, N)$ is a concave function of P_0 we have

$$\begin{aligned} \max_{P_0} P_1 &\leq \sum_{i=0}^{\varepsilon N} w_i B(P_{0,N-i},k,N)/(N-\varepsilon N) \\ &\leq \frac{1}{(1-\varepsilon)N}B\left(\sum_{i=0}^{\varepsilon N} w_i P_{0,N-i},k,N\right) \\ &= \frac{1}{\mathcal{C}}\mathcal{B}(P_0,k,N). \end{aligned} \quad (20)$$

Here $\mathcal{C}$ is the contrast of the collective spin. Comparing to ref. 13, the result is modified by a factor $1/\mathcal{C}$. In our experiment, $\mathcal{C} = 0.99^{+0.01}_{-0.02}$, so the effects of finite contrast on entanglement depth are minimal.

Entanglement depth in terms of the actual atom number. In the experiment the atoms have spatially varying coupling to the probe light. However, the criterion in ref. 13 is derived for the case where atoms are equally coupled to the light. Here we

generalize the entanglement criterion to our experimental conditions and prove that the sample-averaged fractional entanglement depth for the ensemble containing 3,100 actual non-uniformly coupled atoms is the same as that of 2,100 uniformly coupled effective atoms. Consider an ensemble of N_a actual atoms where each atom j has spin component $f_{z,j}$ and cooperativity η_j. The effective total spin of the ensemble is S_z and the effective cooperativity is η, so that

$$S_z\eta = \sum_{j=1}^{N_a} f_{z,j} \times \eta_j \tag{21}$$

As mentioned in the main text, the ideal heralded state $|\psi_1\rangle$ (the first Dicke state of non-uniformly coupled atoms) is the destructive interference of two slightly displaced CSSs $|\pm\phi\rangle$ and can be written as

$$\begin{aligned}|\psi_1\rangle &\propto |\phi\rangle - |-\phi\rangle \\ &= \left[\mathrm{e}^{iS_z\eta\Gamma/(4\Delta)} - \mathrm{e}^{-iS_z\eta\Gamma/(4\Delta)}\right]|\psi_0\rangle \\ &= \left[\mathrm{e}^{i\Gamma/(4\Delta)\sum_{j=1}^{N_a} f_{z,j}\eta_j} - \mathrm{e}^{-i\Gamma/(4\Delta)\sum_{j=1}^{N_a} f_{z,j}\eta_j}\right]|\psi_0\rangle\end{aligned} \tag{22}$$

where $|\psi_0\rangle$ is the initial CSS along $\hat{\boldsymbol{x}}$. By expanding the exponent to first order and using $f_z = (f_{+x} - f_{-x})/(2i)$, we get

$$|\psi_1\rangle = \left(\sum_{j=1}^{N_a} \eta_j^2\right)^{-1/2} \sum_{j=1}^{N_a} \eta_j \left[\prod_{j'\neq j} |0_{j'}\rangle_x\right] \otimes |1_j\rangle_x \tag{23}$$

where $|0_j\rangle_x$ and $|1_j\rangle_x$ are the single-particle spin eigenstates along $\hat{\boldsymbol{x}}$ of the atom j. For a fully separable state $|\varphi\rangle = \prod_{j=1}^{N_a}\left(\alpha_j|0_j\rangle_x + \beta_j|1_j\rangle_x + \ldots\right)$ the population $P_1 = |\langle\varphi|\psi_1\rangle|^2$ is given by

$$P_1 = \left(\sum_{j=1}^{N_a} \eta_j^2\right)^{-1} \left|\sum_{j=1}^{N_a} \eta_j \beta_j \prod_{j'\neq j} \alpha_{j'}\right|^2 \tag{24}$$

The expression for P_1 is similar to that in ref. 13 and differs by the additional weight factor η_j. When the real atom number $N_a \gg 1$, the upper bound of P_1 for the fully separable state $|\varphi\rangle$, $\mathcal{B}(P_0, N_a)$, as a function of the population $P_0 = |\langle\varphi|\psi_0\rangle|^2$, is the same as ref. 13, and independent of N_a.

Next consider a state which can be factorized into two subsets $|\varphi\rangle = \left|\varphi_1^{1,\ldots,k_1}\right\rangle \otimes \left|\varphi_M^{1,\ldots,k_2}\right\rangle$ where $k_1 + k_2 = N_a$. Each $|\varphi_{i=1,2}\rangle$ can be expanded as

$$|\varphi_i\rangle = a_i\left|\psi_0^{k_i}\right\rangle + b_i\left|\psi_1^{k_i}\right\rangle + \ldots \tag{25}$$

where $\left|\psi_0^{k_i}\right\rangle$ is the CSS containing k_i atoms, and $\left|\psi_1^{k_i}\right\rangle$ is given by equation (23) with N_a replaced by k_i. The populations $P_0 = |\langle\varphi|\psi_0\rangle|^2$ and $P_1 = |\langle\varphi|\psi_1\rangle|^2$ are given by

$$\begin{aligned}P_0 &= |a_1|^2|a_2|^2, \\ P_1 &= \left(\sum_{j=1}^{N_a}\eta_j^2\right)^{-1}\left|a_2 b_1\sqrt{\sum_{j=1}^{k_1}\eta_j^2} + a_1 b_2\sqrt{\sum_{j=k_1+1}^{N_a}\eta_j^2}\right|^2\end{aligned} \tag{26}$$

The expression for P_1 recovers that of ref. 13 when $\eta_j = 1$. When k_1, k_2 and N_a are large, we take the ensemble averages $\sum_{j=1}^{k_1}\eta_j^2 = k_1\langle\eta^2\rangle$, $\sum_{j=k_1+1}^{N_a}\eta_j^2 = k_2\langle\eta^2\rangle$ and $\sum_{j=1}^{N_a}\eta_j^2 = N_a\langle\eta^2\rangle$. Therefore the bound of P_1 in equation (26), $\mathcal{B}(P_0, k_a = \max\{k_1, k_2\}, N_a)$, is the same as $\mathcal{B}(P_0, k, N)$ for uniformly coupled atoms when $k_a/N_a = k/N$. This proves that the average fractional entanglement depth for the ensemble containing 3,100 actual non-uniformly coupled atoms is the same as that of 2,100 uniformly coupled effective atoms, thus in our system a minimum of 1,970 out of 2,100 effective atoms or 2,910 out of 3,100 real atoms are mutually entangled.

It might seem as if the addition of $N_w \gg N$ weakly coupled atoms (coupling strength η_w) to the system would increase the entanglement depth without having physical consequences as long as $N_w\eta_w^2 \ll N\eta^2$. However in this case the uncertainty $\Delta\mathcal{N}'$ on the entanglement depth also increases, given by $\frac{\Delta\mathcal{N}'}{N_w} = \frac{\Delta\mathcal{N}}{N}\frac{N\eta^2}{N_w\eta_w^2} \gg \frac{\Delta\mathcal{N}}{N}$, so as to be consistent with the entanglement depth $\mathcal{N}$ before adding the weakly coupled atoms. Atoms that do not change the observed spin distribution have no effect on the entanglement depth.

Sample size. No statistical methods were used to predetermine sample size in the above.

31. Tanji-Suzuki, H. *et al.* Interaction between atomic ensembles and optical resonators: classical description. *Adv. At. Mol. Opt. Phys.* **60,** 201–237 (2011).

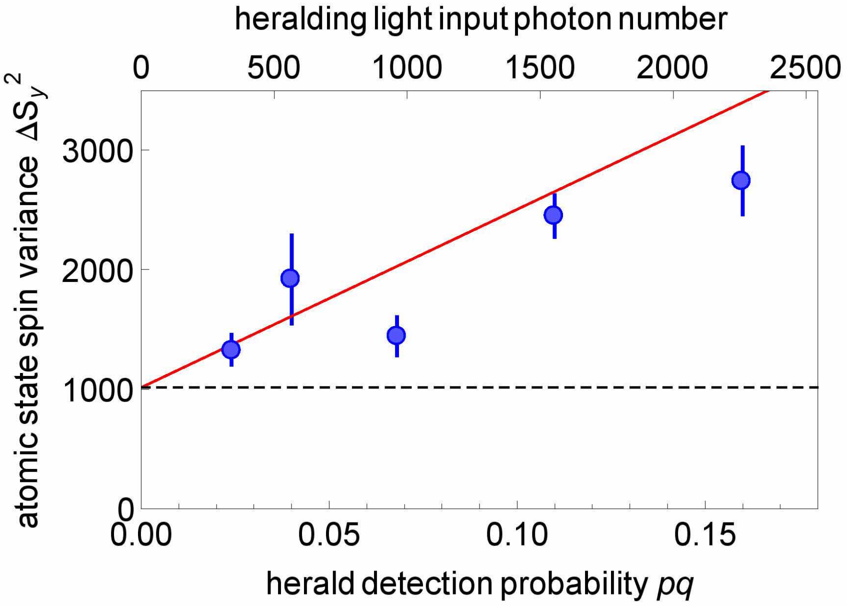

Extended Data Figure 1 | The measured atomic state spin variance, ΔS_y^2, as a function of the heralding light photon number and corresponding probability *pq* of detecting one photon. The solid red line is the prediction for ΔS_y^2 broadened by the photon shot noise of the heralding light. The dashed black line shows the CSS variance for 2,030 $F = 1$ effective atoms used in this measurement. Error bars, 1 s.d.

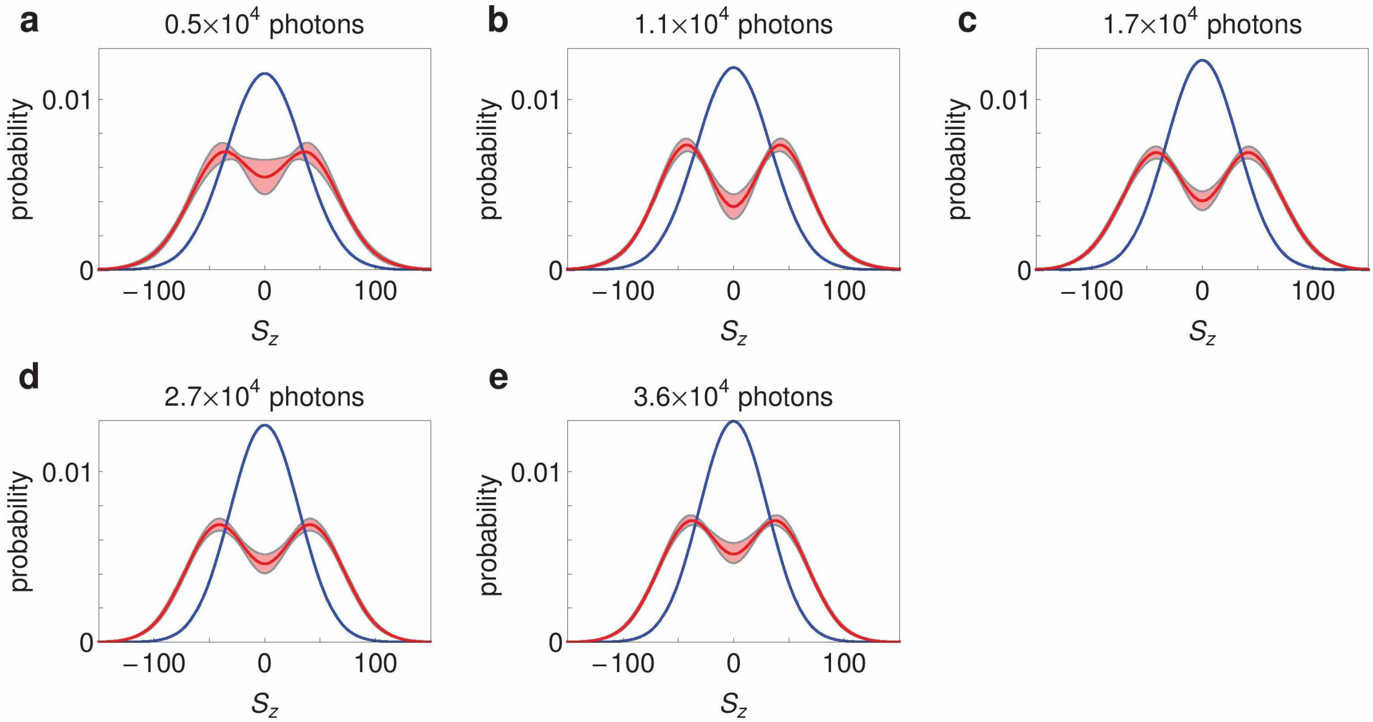

Extended Data Figure 2 | Dependence of the reconstructed distribution of collective spin S_z on the measurement photon number. This dependence is illustrated by reconstructed spin distributions for photon numbers 0.5×10^4 (**a**), 1.1×10^4 (**b**), 1.7×10^4 (**c**), 2.7×10^4 (**d**) and 3.6×10^4 (**e**). Blue lines correspond to the CSS and red lines correspond to the heralded states. The shaded area indicates an uncertainty of 1 s.d.

Extended Data Table 1 | Resonator parameters

Parameter		λ=780nm	λ=852nm
Mirror separation	L	26.62(1) mm	
Mirror curvature radius	R	25.04(2) mm	
Free spectral range	$\omega_{FSR}/(2\pi)$	5632.0(2) MHz	
Transverse mode spacing	$\omega_{\lambda}/(2\pi)$	226.3(3) MHz	
Linewidth	$\kappa_{\lambda}/(2\pi)$	1.01(3) MHz	135(2) kHz
Finesse	F_{λ}	5.6(2)$\times 10^{3}$	4.2(1)$\times 10^{4}$
Mode waist	w_{λ}	56.9(4) µm	59.5(5) µm
Antinode cooperativity	$\eta_{0,\lambda}$	0.203(7)	1.65(4)

The mode waists are calculated at the position of the atoms. Outside this table, all resonator values refer to the probe wavelength λ = 780 nm.

doi:10.1038/nature14295

Square ice in graphene nanocapillaries

G. Algara-Siller[1], O. Lehtinen[1], F. C. Wang[2], R. R. Nair[3], U. Kaiser[1], H. A. Wu[2], A. K. Geim[3] & I. V. Grigorieva[3]

Bulk water exists in many forms, including liquid, vapour and numerous crystalline and amorphous phases of ice, with hexagonal ice being responsible for the fascinating variety of snowflakes[1,2]. Much less noticeable but equally ubiquitous is water adsorbed at interfaces and confined in microscopic pores. Such low-dimensional water determines aspects of various phenomena in materials science, geology, biology, tribology and nanotechnology[3–8]. Theory suggests many possible phases for adsorbed and confined water[9–17], but it has proved challenging to assess its crystal structure experimentally[17–23]. Here we report high-resolution electron microscopy imaging of water locked between two graphene sheets, an archetypal example of hydrophobic confinement. The observations show that the nanoconfined water at room temperature forms 'square ice'—a phase having symmetry qualitatively different from the conventional tetrahedral geometry of hydrogen bonding between water molecules. Square ice has a high packing density with a lattice constant of 2.83 Å and can assemble in bilayer and trilayer crystallites. Molecular dynamics simulations indicate that square ice should be present inside hydrophobic nanochannels independently of their exact atomic nature.

Many molecular dynamics (MD) studies[9–17] have explored the structure of low-dimensional water and predicted a great variety of phases, with results sensitive to modelled conditions and sometimes appearing conflicting. For example, buckled monolayer ice[10] and flat hexagonal ice[14,16,23], respectively, were found inside hydrophilic and hydrophobic nanochannels below room temperature, whereas no in-plane order was observed for water inside simulated mica (hydrophilic) and graphite (hydrophobic) nanochannels at and above room temperature[13,15]. A close analogue of planar square ice was seen in MD simulations of water inside carbon nanotubes[9,11,12,18], where water molecules form a monolayer that can be viewed as a sheet of square ice rolled up into a quasi-one-dimensional cylinder. Neutron studies[18] revealed features consistent with the existence of such 'ice nanotubes', which melted above 50 K. Two-dimensional (2D) ices have also been found experimentally on the surfaces of mica and graphite[19–23]. The studies using scanning probe microscopy[20–22] and electron crystallography[19,23] show that near-surface water can form correlated, solid-like layers. As for their intralayer structure, information is only available for 2D ices grown below 150 K, which were found to be hexagonal, with in-plane coordination similar to that of bulk ices[19,23].

For this study, we deposited a graphene monolayer on a standard transmission electron microscopy (TEM) grid, exposed it to a small amount of water and covered it with another graphene monolayer[24,25] (see 'Sample preparation' in Methods for full details). Most of the water was squeezed out by van der Waals forces that brought the two graphene layers together, but some water remained trapped in numerous pockets of submicrometre size (Extended Data Fig. 1). We also prepared reference samples similar to those described in ref. 24, in which a larger amount of deposited water resulted in three-dimensional droplets of ~10–100 nm in thickness (Extended Data Fig. 2). The TEM studies were carried out using transmission electron microscope FEI TITAN 80-300 operated at 80 kV.

Typical atomic-resolution images of graphene-confined water are shown in Fig. 1a and Extended Data Figs 1b and 3a–i. High-contrast dark spots correspond to oxygen and indicate the positions of the water molecules. Hydrogen atoms yield too little contrast to be resolved even by the state-of-the-art TEM. The encapsulating graphene layers are seen in some parts of the images as a faint background with hexagonal symmetry[25,26]. The images can easily be improved by digitally subtracting the contribution from the encapsulating graphene[25], but we avoid this additional processing in view of the quality and contrast of our raw data, which clearly show water forming a regular square lattice. Fast Fourier transform analysis of the ice lattice yielded a distance a between nearest-neighbour oxygen atoms of 2.83 ± 0.03 Å (Fig. 1a), with no alignment with the graphene lattice observed. We note that the atomic-resolution imaging of interfacial ice is possible only because of the use of graphene: its low atomic number and crystallinity result in a minimal background and high contrast for oxygen atoms[24,26], and its mechanical strength, high thermal and high electrical conductivity and chemical stability protect encapsulated water from sublimation and the adverse effects of electron irradiation[25,27] (see 'Transmission electron microscopy' in Methods).

To confirm that the observed square lattice is indeed formed by water, we acquired electron energy loss spectra (EELS) from areas with ice such as shown in Fig. 1a and from areas without any visible amount of trapped water. Figure 1b compares typical spectra around the oxygen K-edge (which are sensitive to the state of water[28]). The ice-free areas show little oxygen signal. In contrast, square ice exhibits a spectrum with an overall shape that is qualitatively similar to EELS for three-dimensional ices such as hexagonal I_h and diamond cubic I_c ices[28] (inset of Fig. 1b). But there are also notable differences, such as the approximately 6-eV difference between the main EELS peak positions for square ice and for three-dimensional ices. The energy separation between the main and secondary EELS peaks gives an independent estimate of the oxygen–oxygen distance of about 2.8 Å (see 'EELS analysis' in Methods), in agreement with the observed lattice constant. Also, EELS measured for large water droplets found in our reference samples agree with the spectra expected for mixtures of liquid water and water vapour (Extended Data Fig. 2b).

The square ice is found to be highly mobile under the electron beam (Extended Data Fig. 3 and Supplementary Video), with uniform monolayers starting to break into crystallites about 10 nm across with sharp crystallographic edges after the first few seconds of imaging. The crystallites change shape, split and merge, with the frequency of reconstruction increasing with beam current. Grain boundaries and dislocations form as the crystallites move and coalesce, but high crystallinity is preserved with no sign of ice melting or amorphization (Extended Data Fig. 3). The strong TEM contrast variations seen in such images arise from differences in ice layer numbers, as illustrated in Fig. 2, where equal-height steps in contrast correspond to changes from monolayer to bilayer and to trilayer ice (see Extended Data Fig. 4 for details). Using the quantified contrast to examine many images and videos of 2D ice, we found that three is the maximum number of ice layers observed in our experiments.

The TEM images show unambiguously that water molecules in the few-layer ice are AA stacked, with oxygen atoms in adjacent layers sitting directly on top of each other. The AA stacking is evident when

[1]Central Facility for Electron Microscopy, Group of Electron Microscopy of Materials Science, University of Ulm, 89081 Ulm, Germany. [2]Chinese Academy of Sciences Key Laboratory of Mechanical Behavior and Design of Materials, Department of Modern Mechanics, University of Science and Technology of China, Hefei, Anhui 230027, China. [3]School of Physics and Astronomy, University of Manchester, Manchester M13 9PL, UK.

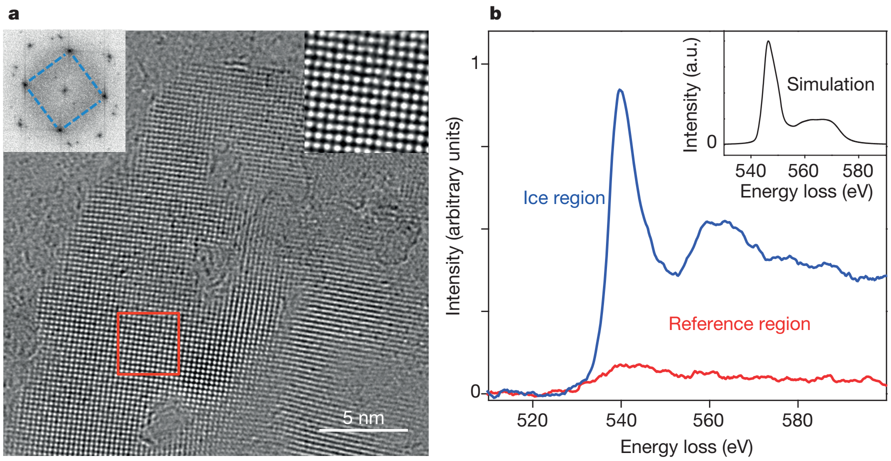

Figure 1 | Square ice. a, Part of a large water pocket (see Extended Data Fig. 1a). Several such pockets were studied. Irregular structures are hydrocarbon contamination. The top right inset shows a magnified image of the area outlined in red. The top left inset shows a Fourier transform of the entire image, with four first-order maxima of the square lattice; the square symmetry is highlighted by the blue lines; the two hexagonal sets come from encapsulating graphene. **b**, EELS from areas containing 2D ice and no visible water. Both spectra come from similar size areas (~100 nm). The inset shows the simulated EELS for three-dimensional ices (I_c and I_h exhibit similar spectra)[28].

comparing experimental (Fig. 2a) with simulated (Fig. 2b, c) TEM images: AB stacking results in oxygen atoms in the second layer occupying the sites between oxygen sites in the first and third layers, which in turn results in a perceived 45° rotation of the water lattice and reduction in the projected oxygen spacing. Furthermore, the reduced spacing leads to lower contrast and, consequently, a qualitatively different appearance of AB bilayers (Fig. 2c) compared to the experimental images (Fig. 2a). Note that stacking controls the difference between different phases of bulk ice. For example, hexagonal and diamond cubic ices both consist of puckered hexagonal layers but have AB and ABC stacking, respectively. In all bulk ice phases the bonding between water molecules follows so-called 'ice rules' that require a tetrahedral coordination of hydrogen bonds[1,2]. In contrast, the few-layer ice we report here corresponds to 90° hydrogen bonding both within and between layers.

To support our TEM observations, we carried out MD simulations of water in graphene nanocapillaries (Methods). Distances between the carbon plane centres were varied from 6.5 Å to 11.5 Å, to accommodate one to three monolayers of water (Extended Data Fig. 5). For narrow 2D channels that can accommodate only one monolayer, we always found square ice with $a = 2.81 \pm 0.02$ Å, in agreement with experiment (Fig. 2d and Extended Data Fig. 6). This MD result is robust, showing little dependence on the capillary width, applied pressure or whether graphene sheets were made rigid, flexible or freely moving (Methods).

For wider capillaries that accommodate two or three monolayers of water, no in-plane ordering could be found under simulated ambient conditions. Instead, water molecules form a distinct layered structure but locally maintain the tetrahedral arrangement of hydrogen bonds both within and between the layers (Extended Data Fig. 7a, b). We believe

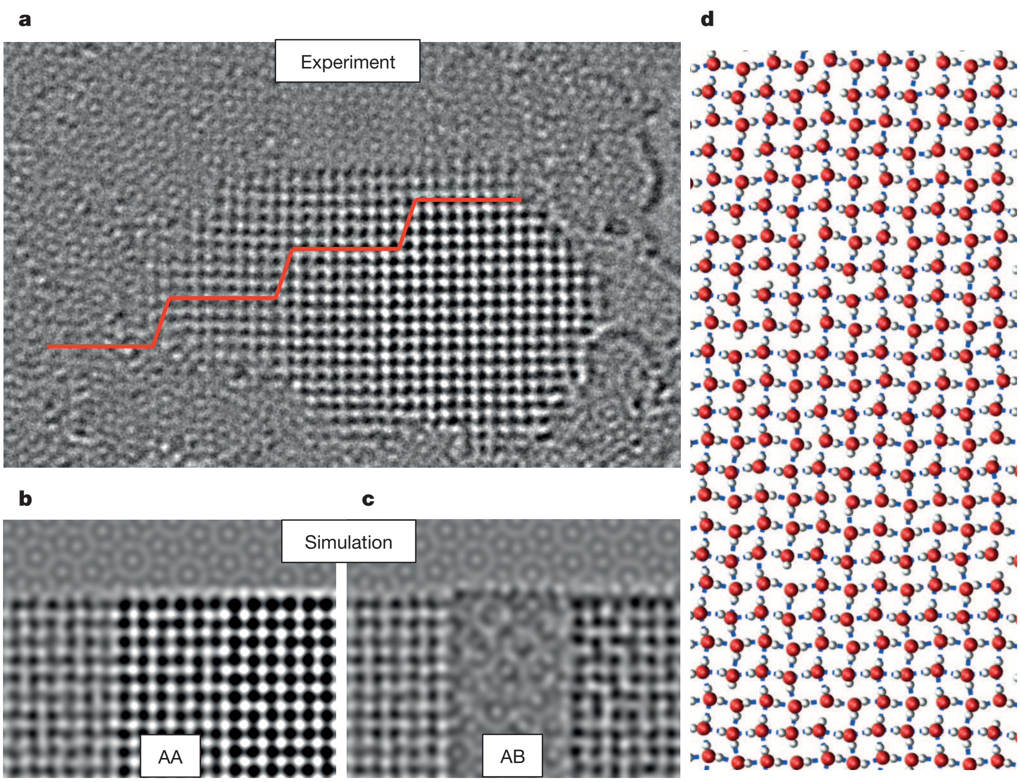

Figure 2 | Few-layer ice and its stacking order. a, Isolated crystallite with a varying number of layers. The moiré pattern (seen clearly at the top) is due to encapsulating graphene. The red curve shows changes in the contrast averaged over the corresponding parts of the image (Methods). The changes occur in quantized steps. **b** and **c**, Simulated TEM images for monolayer, bilayer and trilayer ice with AA and AB stacking, respectively. The AA stacking agrees well with our experimental images whereas the AB stacked ice results in the qualitatively different appearance. **d**, Typical snapshot of MD-simulated water in a graphene nanocapillary. Red and white circles show oxygen and hydrogen atoms, respectively; short blue lines indicate hydrogen bonds within H_2O.

this apparent disagreement between simulation and experiment arises because adhesion between the encapsulating graphene sheets imposes pressure on the water as it is squeezed into a small volume, and this needs to be taken into account in simulations. As illustrated in Extended Data Fig. 8, this pressure—we refer to it as van der Waals pressure—can be estimated from the energy gain due to such squeezing according to $P_W \approx E_W/d \approx 1$ GPa, where $E_W \approx 20$–30 meV Å^{-2} is the adhesion energy[29,30] and $d \approx 3.5$ Å is a typical interlayer distance. This estimate agrees with our simulations of hydrostatic pressure acting on a gas trapped between freely moving graphene sheets (Methods). To mimic the effect of van der Waals pressure, we ran simulations with an applied external pressure P (as illustrated in Extended Data Fig. 5) and found a pronounced transition from in-plane disorder at low P to layered ice at $P > 1$ GPa (Extended Data Figs 7 and 9). The layered ice exhibited the same lattice constant ($a = 2.81 \pm 0.02$ Å) as the monolayer, in agreement with experiment.

The MD simulations fail, however, in reproducing the observed AA stacking and instead show a tendency for crystals with AB stacking or no interlayer order (Extended Data Figs 7 and 9). The disagreement is perhaps not surprising when we consider that as P increases to reach the crystallization transition, hydrogen bonds switch to the in-plane configuration (Extended Data Figs 7d and 9b) so that coupling between monolayers of square ice becomes van-der-Waals-like. Such weak coupling is known to be extremely difficult to accurately account for theoretically. Moreover, in the experiment the graphene-confined ice exhibits sharp steps between terraces (see Fig. 2), which can result in extra lateral forces acting on different layers not considered in the simulations. Finally, our simulations for bilayer and trilayer ice yield an interlayer separation of $c = 2.8 \pm 0.3$ Å, which gives a crystal lattice close to the simple cubic structure ($c = a$) and a density approximately 1.5 times higher than that of common ice. But the exact structure is still, strictly speaking, tetragonal because of the qualitative difference between interlayer and intralayer bonding (Extended Data Figs 7 and 9).

The 2D ice we report here exhibits coordination that is qualitatively different from the conventional tetrahedral coordination in bulk and surface ices. We expect it to be common inside hydrophobic nanocapillaries under ambient conditions, basically because the water–surface interaction in such confinement is much weaker than the interaction between water molecules. Indeed, our MD simulations yield the same square lattices inside non-graphene capillaries with widely varying hydrophobicity (Extended Data Fig. 10). The existence of low-dimensional ice at room temperature has been proposed to explain the fast water permeation through hydrophobic nanocapillaries, including carbon nanotubes and graphene-based membranes, and our report supports this idea. The van der Waals pressure invoked here may be important in many nanoscale phenomena.

Online Content Methods, along with any additional Extended Data display items and Source Data, are available in the online version of the paper; references unique to these sections appear only in the online paper.

Received 10 October 2014; accepted 4 February 2015.

1. Petrenko, V. F. & Whitworth, R. W. *Physics of Ice* (Oxford Univ. Press, 2002).
2. Malenkov, G. Liquid water and ices: understanding the structure and physical properties. *J. Phys. Condens. Matter* **21,** 283101 (2009).
3. Israelachvili, J. & Wennerström, H. Role of hydration and water structure in biological and colloidal interactions. *Nature* **379,** 219–225 (1996).
4. Brown, G. E. How minerals react with water. *Science* **294,** 67–69 (2001).
5. Appelo, C. A. J. & Postma, D. *Geochemistry, Groundwater and Pollution* (Taylor & Francis, 2005).
6. Chandler, D. Interfaces and the driving force of hydrophobic assembly. *Nature* **437,** 640–647 (2005).
7. Verdaguer, A., Sacha, G. M., Bluhm, H. & Salmeron, M. Molecular structure of water at interfaces: wetting at the nanometer scale. *Chem. Rev.* **106,** 1478–1510 (2006).
8. Chaplin, M. F. in *Adsorption and Phase Behaviour in Nanochannels and Nanotubes* (eds Dunne L. & Manos, G.) 241–255 (Springer, 2010).
9. Kalra, A., Garde, S. & Hummer, G. Osmotic water transport through carbon nanotube membranes. *Proc. Natl Acad. Sci. USA* **100,** 10175–10180 (2003).
10. Zangi, R. & Mark, A. E. Monolayer ice. *Phys. Rev. Lett.* **91,** 025502 (2003).
11. Maniwa, Y. *et al.* Ordered water inside carbon nanotubes: formation of pentagonal to octagonal ice-nanotubes. *Chem. Phys. Lett.* **401,** 534–538 (2005).
12. Takaiwa, D., Hatano, I., Koga, K. & Tanaka, H. Phase diagram of water in carbon nanotubes. *Proc. Natl Acad. Sci. USA* **105,** 39–43 (2008).
13. Giovambattista, N., Rossky, P. J. & Debenedetti, P. G. Phase transitions induced by nanoconfinement in liquid water. *Phys. Rev. Lett.* **102,** 050603 (2009).
14. Han, S., Choi, M. Y., Kumar, P. & Stanley, H. E. Phase transitions in confined water nanofilms. *Nature Phys.* **6,** 685–689 (2010).
15. Srivastava, R., Docherty, H., Singh, J. K. & Cummings, P. T. Phase transitions of water in graphite and mica pores. *J. Phys. Chem. C* **115,** 12448–12457 (2011).
16. Bai, J. & Cheng Zeng, X. Polymorphism and polyamorphism in bilayer water confined to slit nanopore under high pressure. *Proc. Natl Acad. Sci. USA* **109,** 21240–21245 (2012).
17. Nair, R. R., Wu, H. A., Jayaram, P. N., Grigorieva, I. V. & Geim, A. K. Unimpeded permeation of water through helium-leak–tight graphene-based membranes. *Science* **335,** 442–444 (2012).
18. Kolesnikov, A. I. *et al.* Anomalously soft dynamics of water in a nanotube: a revelation of nanoscale confinement. *Phys. Rev. Lett.* **93,** 035503 (2004).
19. Yang, D. S. & Zewail, A. H. Ordered water structure at hydrophobic graphite interfaces observed by 4D, ultrafast electron crystallography. *Proc. Natl Acad. Sci. USA* **106,** 4122–4126 (2009).
20. Xu, K., Cao, P. & Heath, J. R. Graphene visualizes the first water adlayers on mica at ambient conditions. *Science* **329,** 1188–1191 (2010).
21. He, K. T., Wood, J. D., Doidge, G. P., Pop, E. & Lyding, J. W. Scanning tunnelling microscopy study and nanomanipulation of graphene-coated water on mica. *Nano Lett.* **12,** 2665–2672 (2012).
22. Zheng, Y., Su, C., Lu, J. & Loh, K. P. Room-temperature ice growth on graphite seeded by nano-graphene oxide. *Angew. Chem. Int. Ed.* **52,** 8708–8712 (2013).
23. Kimmel, G. A. *et al.* No confinement needed: observation of a metastable hydrophobic wetting two-layer ice on graphene. *J. Am. Chem. Soc.* **131,** 12838–12844 (2009).
24. Yuk, J. M. *et al.* High-resolution EM of colloidal nanocrystal growth using graphene liquid cells. *Science* **336,** 61–64 (2012).
25. Algara-Siller, G., Kurasch, S., Sedighi, M., Lehtinen, O. & Kaiser, U. The pristine atomic structure of MoS_2 monolayer protected from electron radiation damage by graphene. *Appl. Phys. Lett.* **103,** 203107 (2013).
26. Meyer, J. C., Girit, C. O., Crommie, M. F. & Zettl, A. Imaging and dynamics of light atoms and molecules on graphene. *Nature* **454,** 319–322 (2008).
27. Dubochet, J., Lepault, J., Freeman, R., Berriman, J. A. & Homo, J.-C. Electron microscopy of frozen water and aqueous solutions. *J. Microsc.* **128,** 219–237 (1982).
28. Kobayashi, K., Koshino, M. & Suenaga, K. Atomically resolved images of I_h ice single crystals in the solid phase. *Phys. Rev. Lett.* **106,** 206101 (2011).
29. Björkman, T., Gulans, A., Krasheninnikov, A. V. & Nieminen, R. M. Van der Waals bonding in layered compounds from advanced density-functional first-principles calculations. *Phys. Rev. Lett.* **108,** 235502 (2012).
30. Koenig, S. P., Boddeti, N. G., Dunn, M. L. & Bunch, J. S. Ultrastrong adhesion of graphene membranes. *Nature Nanotechnol.* **6,** 543–546 (2011).

Supplementary Information is available in the online version of the paper.

Acknowledgements This work was supported by the DFG (Germany), the European Research Council, the EU Graphene Flagship, the National Natural Science Foundation of China, the Ministry of Science, Research and Arts of Baden-Wuerttemberg (Germany), the Office of Naval Research, the Air Force Office of Scientific Research, the Anhui Provincial Natural Science Foundation (China), the Finnish Cultural Foundation and the Fundamental Research Funds for the Central Universities of China. MD simulations were carried out at Supercomputing Center of the University of Science and Technology of China.

Author Contributions U.K., I.V.G and A.K.G. proposed and directed the project. G.A.-S. and O.L. designed the experiments and samples, performed TEM measurements and analysed them. H.A.W. and F.C.W. carried out MD simulations (with feedback from A.K.G.). I.V.G. and A.K.G. wrote the manuscript with help from all the authors.

Author Information Reprints and permissions information is available at www.nature.com/reprints. The authors declare no competing financial interests. Readers are welcome to comment on the online version of the paper. Correspondence and requests for materials should be addressed to I.V.G. (irina.grigorieva@manchester.ac.uk), U.K. (ute.kaiser@uni-ulm.de) or H.A.W. (wuha@ustc.edu.cn).

METHODS

Sample preparation. Graphene monolayers were grown on Cu foils by chemical vapour deposition and then transferred onto gold Quantifoil grids (Au mesh covered with an amorphous carbon film having a dense array of holes with a diameter of 1.2 μm). Importantly, a thin layer of Pt was deposited on the TEM grids before graphene transfer in order to reduce hydrocarbon contamination[31]. For the transfer, several Quantifoil grids were immersed in isopropanol and then placed 'face down' onto a piece of graphene on copper about 1 cm^2 in size. As the isopropanol evaporated, the amorphous carbon film of the TEM grid came into contact with graphene and became attached to it[32]. After that the assembly was floated on the surface of ammonium peroxodisulfate for several hours until all copper was slowly etched away, leaving free-floating graphene with several TEM grids attached to it. This was broken into pieces, with one grid attached to each, washed in water and isopropanol and left to dry in air at room temperature. After that 1 μl of deionized water was carefully cast on top of one of the grids, and another graphene-covered grid was placed on top, covering the water droplet. The resulting sandwich was left to dry under ambient conditions overnight, during which time the water drop slowly evaporated, bringing the two graphene layers together and gradually squeezing the liquid out so that only a small amount of adsorbed water remained captured in between the graphene sheets.

TEM. The use of both a relatively low operating voltage (80 keV) and the aberration correction were essential in our study: higher voltages are known to produce knock-on damage in graphene[33] and the aberration correction, even at relatively low acceleration voltages, allows atomic-resolution imaging of both graphene and water. The spherical aberration coefficient was set to 30 μm and the sample was imaged at Scherzer focus, resulting in dark atom contrast. The background pressure in the microscope was $<10^{-8}$ mbar, and all experiments were carried out at room temperature. Aberration-corrected high-resolution TEM images were acquired at a dose of 3×10^4 electrons per nm^2 and an exposure time of $\sim$1 s per frame. The exposure of the studied area before acquisition of the reported images was approximately 600 electrons per nm^2. No notable heating by the electron beam is expected under these operating conditions. Indeed, for amorphous carbon films under similar experimental conditions, the heating was estimated to be $\sim$1 K (ref. 34). As thermal conductivity of graphene is 3,000 times higher than that of amorphous carbon, we expect even less heating in our case. This agrees with our observation that the appearance of square ice did not qualitatively change with increasing or decreasing of the beam current.

The majority of our samples remained intact during the relatively long exposures to the electron beam (typically, 10–20 min); in a few cases only, we noticed etching of graphene[27,33–36]. This is in contrast to the earlier work on frozen aqueous samples that suffered from fast sublimation under the electron beam[27,28,37]. The high stability of 2D ice is due to graphene encapsulation. The highly conductive graphene layers (both electrically and thermally) provide an efficient channel for absorbing and rapidly dissipating the energy introduced by electron impacts, thus reducing the damage to ice crystals. This effect of graphene encapsulation was recently demonstrated in TEM studies[25,38] of monolayer MoS_2, a radiation-sensitive material. The encapsulation reduced the damage rate by nearly three orders of magnitude as compared to non-encapsulated MoS_2. Similarly, graphene capillaries in the present work served not only as a confinement channel but also as protection against the beam damage, which enabled us to observe the ice crystals without immediately evaporating or destroying them.

EELS analysis. Electron energy loss spectra[39,40] were acquired using GIF Quantum ER filter in the diffraction mode (convergence angle of 1.8 mrad and collection angle of 4.4 mrad). The spectra were recorded with exposure and integration times of 5 s and 200 s, respectively. A low pass filter (two pixels) and linear background subtraction were applied. All EELS showed prominent signals from carbon and oxygen. Hydrogen is not detectable with the instrument. No other elements could be detected, except for a small amount of Si that is commonly present in all areas because of contamination during sample preparation[41].

The overall appearance of EELS curves allows us to distinguish immediately between ice and mixtures of liquid water and water vapour (compare Figure 1b and Extended Data Fig. 2). Furthermore, bulk ices such as I_c and I_h have rather similar spectra[28], more similar to each other than to the observed EELS for square ice. This is understandable given that both I_c and I_h consist of puckered hexagonal layers, which is different from the planar square configuration. We have also used the spectral positions of the main and secondary peaks (see Fig. 1b) to estimate interatomic distances in the square ice. Secondary peaks (after the main ionization threshold that happens in our case at about 540 eV; Fig. 1b) arise owing to multiple scattering, and the energy separation ΔE obeys the relation[42] $\Delta E \times R^2 = C$, where R is the distance between oxygen atoms and C is a constant. Using $C = 150$ (this value was empirically determined for cubic ice[43], which is the closest approximation to square ice to be found in the literature) and an energy of about 559 eV for the prominent secondary peak in the observed EELS, we estimate $R = 2.80 \pm 0.07$ Å. The good agreement between this value and a obtained from atomic-resolution TEM images provides an independent confirmation of the crystal structure of square ice.

In principle, the interlayer separation in layered crystals can be determined by TEM imaging at different tilt angles. Unfortunately, this is impossible to achieve in practice for our nanoscale crystals, which constantly move and rotate under the electron beam. Indeed, for acquiring interpretable high-resolution images, crystals need to be oriented precisely along a zone axis and remain stationary during imaging. The reason that high-resolution imaging is possible in our case is that the graphene layers fix the orientation of ice crystals relative to the electron beam. Even though the crystals change their in-plane orientation (rotate), the [001] direction remains parallel to the optical axis of the microscope.

Analysis of TEM images. To determine the number of layers in 2D ice crystallites, we quantified the contrast from oxygen atoms using a variance filter, as illustrated step by step in Extended Data Fig. 4 and explained in its legend. This resulted in contrast maps such as that in Extended Data Fig. 4d. They show that the average contrast changes in steps of equal height. There are three distinct parts in the ice crystallite in Extended Data Fig. 4a, of one, two and three monolayers of water each.

The simulated images presented in Fig. 2b and c were obtained as follows. First, we constructed a square lattice of water molecules arranged in one, two or three layers with different stacking orders. After that, TEM images for different arrangements were simulated using QSTEM software[44] and the parameters corresponding to our experimental conditions (accelerating voltage and spherical aberration coefficient).

MD setup. Most of our simulations were done for the geometry shown in Extended Data Fig. 5. This involved two water reservoirs that contained 2,000 molecules each and were connected by a relatively long capillary formed by two parallel graphene sheets. The length and width of the graphene channel were kept at 68 Å and 56 Å, respectively. The height h was chosen to be 6.5 Å, 9.0 Å and 11.5 Å in order to accommodate one, two and three layers of water molecules, respectively. The graphene sheets were either kept rigid or allowed to be flexible during simulations. Unless stated otherwise, water was modelled using the extended simple point charge (SPC/E) model, which is described by the sum of a long-range Coulomb potential and a short-range Lennard–Jones potential[45]. The parameters for water–graphene interaction were chosen as in ref. 46. The long-range interactions were computed using the particle–particle particle–mesh (PPPM) algorithm, with a convergence parameter of 10^{-4}. Periodic boundary conditions were applied in all three directions of the simulation box.

For monolayer ice, we have also performed MD simulations for freely moving graphene sheets that 'self-consistently' enclose trapped water molecules (Extended Data Fig. 8d). For bilayer and trilayer ice, the graphene confinement observed experimentally is terraced with atomically sharp steps between ice terraces (see Fig. 2). It has proved difficult to reproduce such a terraced confinement in MD analysis. Therefore, the high pressure induced by encapsulating graphene sheets (see below) was modelled to a first approximation by applying a hydrostatic pressure P in the direction parallel to the graphene layers, as shown in Extended Data Fig. 5.

MD simulations were performed in an isothermal, isobaric ensemble, in which temperature (298 K) and pressure were controlled by the Nose–Hoover thermostat and barostat, respectively. In the equilibrium run, pressure P was kept at 1 atm (10^{-4} GPa) for 5 ns, during which time water molecules filled the graphene nanocapillary. After that, P was increased up to 10 GPa over 15 ns. A time step of 1.0 fs was used for the velocity-Verlet integrator. All the simulations were carried out using LAMMPS[47]. To determine the lattice parameter a, we counted the number of water molecules over the entire area of the graphene capillary.

Van der Waals pressure. Attractive van der Waals forces between two graphene sheets favour the adhesion of the sheets over a maximal area. If a material (for example, a gas bubble) is trapped between the sheets, the bubble will continue to shrink in size until a built-up hydrostatic pressure is able to balance the adhesion forces. For a quasi-2D confinement such as that shown in Extended Data Fig. 8a, it is straightforward to estimate the resulting van der Waals pressure, P_W. Indeed, a displacement δ of the enclosure boundary results in a gain in adhesion energy equal to $\delta \times L \times E_W$, where L is the enclosure circumference and E_W is the difference between graphene–graphene and graphene–water adhesion energies per unit area. E_W can be estimated as a typical value of the adhesion energy for van der Waals materials[29,30] because the water–graphene interaction is hydrophobic and relatively small. The above displacement requires a work of $F \times \delta$ against the internal pressure P_W, where $F = P_W \times d \times L$. For a monolayer of ice, we can use $d \approx 3.5$ Å, a typical interlayer distance in van der Waals materials. The equilibrium requires $P_W = E_W/d$, which yields $\sim$1 GPa for $E_W \approx 30$ meV Å^{-2}, found experimentally for monolayer graphene[30].

To support this estimate, we have 'measured' the van der Waals pressure in MD simulations. To this end, a small amount of helium gas (1,000 atoms) was confined between freely moving graphene sheets and the system was allowed to reach equilibrium (Extended Data Fig. 8b, c). The hydrostatic pressure was estimated by

calculating the virial stress for each He atom and averaging over all of them. This has yielded a pressure of about 1.0 GPa, in agreement with the above estimate. This analysis suggests that high internal pressures are intrinsic for flexible nanoscale confinement and should generally be taken into account in studying the corresponding capillary phenomena.

MD analysis of monolayer ice. For the narrowest (6.5 Å) graphene channel, a monolayer of water was found to form an ordered square lattice with $a = 2.80 \pm 0.01$ Å for the rigid graphene confinement and 2.81 ± 0.01 Å for the flexible one (Extended Data Fig. 6), which agree well with the experimentally found $a = 2.83 \pm 0.03$ Å. Within our MD accuracy, a was found to be almost independent of pressure for all experimentally relevant P from 0 GPa to 2 GPa. At higher pressures ($P > 3$ GPa), a puckered square ice started forming.

Simulations for the realistic confinement with freely moving graphene sheets yield the same square ice with the same a (Extended Data Fig. 8d). To check that the SPC/E model provides sufficient accuracy, we also used the TIP4P/2005 model[48] of water and again obtained square ice with the same a. Extended Data Fig. 8d–f shows small ice crystals that appear in simulations using the above two models with freely moving graphene sheets, which proves the robustness of our MD results with respect to different models, at least for the case of monolayer ice.

Simulated few-layer ice. For the wider graphene capillaries (9 Å and 11.5 Å) that accommodated two and three layers of water, respectively, no lattice formation was found at pressures below 1 GPa. A typical snapshot of the water molecule configuration in a bilayer at 0.5 GPa is shown in Extended Data Fig. 7a, b. In this case, water within each layer forms an amorphous structure, not dissimilar to bulk water or amorphous ice. Locally, water preserves the standard tetrahedral coordination with hydrogen bonds connecting molecules both within and between the layers. As P increases above about 1 GPa, the simulations revealed an order–disorder transition accompanied by a sharp transformation in hydrogen bonding. One can see in Extended Data Fig. 7b, d that hydrogen bonds switch to the in-plane configuration, effectively decoupling the two monolayers of water. At the same time, within each layer water molecules form identical square lattices with the same lattice parameter as for the monolayer ice, $a = 2.81 \pm 0.01$ Å (Extended Data Fig. 7e). A similar transition was found for the trilayer water ($h = 11.5$ Å) but at somewhat higher pressures of $P \approx 1.3$ GPa (Extended Data Fig. 9). The values of P at which the order–disorder transition occurs qualitatively agree with the estimated internal pressure induced by adhesion between graphene sheets.

The order–disorder transition was further confirmed by calculations of the per-atom potential energy for water molecules in the simulated bilayer and trilayer ice, as shown in Extended Data Fig. 9c, d. The sharp drops in the potential energy at $P \approx 1$ and 1.3 GPa for the bilayer and trilayer, respectively, indicate ordering of the hydrogen bonds, which is similar to the known signature of the freezing transition for bulk water[49].

Square ice inside non-graphene nanocapillaries. To show that square ice could be common inside hydrophobic nanochannels, other than those lined with graphene, we performed MD simulations of water confined between two generic walls. The latter were simulated using the Lennard–Jones potential in the form $E = 4\varepsilon\left[(\sigma/r)^{12} - (\sigma/r)^{6}\right]$, where r is the distance from the wall to water molecules. Parameters ε and σ describe the depth of the potential well and the distance at which the potential is zero. 1,000 water molecules were placed between such walls separated by 6.5 Å. Periodic boundary conditions were applied in the directions parallel to the walls, and the simulations were carried out using the isothermal, isobaric ensemble as described above. To model capillaries with different hydrophobicity, ε was varied from 0.01 kcal mol^{-1} to 0.2 kcal mol^{-1}. This covers a wide range of surfaces from super-hydrophobic to weakly hydrophilic. Extended Data Figure 10a–d illustrates contact angles for such surfaces. Square ice was found to form at room temperature inside all the modelled nanochannels, independently of their hydrophobicity, and its lattice parameter was the same within $\pm 1\%$ as for graphene nanocapillaries (Extended Data Fig. 10e–h). Furthermore, we checked that a crystallographic structure of hydrophobic walls was not important for the occurrence of square ice. To this end, a monolayer of water was confined between artificial carbon walls with lattices other than the hexagonal one of graphene (for example, a square lattice). Again, we observed the same square ice with the same a. This allows us to conclude that the square ice is likely to be common inside hydrophobic channels that can accommodate only a few monolayers of water.

Further work is necessary to understand how different modelling parameters and geometries may influence the outcome of MD simulations and, for example, to explain the AA stacking for bilayer and trilayer square ice and the consequences of the terraced graphene confinement observed experimentally.

31. Longchamp, J.-N., Escher, C. & Fink, H.-W. Ultraclean freestanding graphene by platinum-metal catalysis. *J. Vac. Sci. Technol. B* **31,** 020605 (2013).
32. Meyer, J. C. *et al.* Direct imaging of lattice atoms and topological defects in graphene membranes. *Nano Lett.* **8,** 3582–3586 (2008).
33. Meyer, J. C. *et al.* Accurate measurement of electron beam induced displacement cross sections for single-layer graphene. *Phys. Rev. Lett.* **108,** 196102 (2012).
34. Egerton, R. F., Li, P. & Malac, M. Radiation damage in the TEM and SEM. *Micron* **35,** 399–409 (2004).
35. Mølhave, K. *et al.* Electron irradiation-induced destruction of carbon nanotubes in electron microscopes. *Ultramicroscopy* **108,** 52–57 (2007).
36. Yuzvinsky, T. D., Fennimore, A. M., Mickelson, W., Esquivias, C. & Zettl, A. Precision cutting of nanotubes with a low-energy electron beam. *Appl. Phys. Lett.* **86,** 053109 (2005).
37. Adrian, M., Dubochet, J., Lepault, J. & McDowall, A. W. Cryo-electron microscopy of viruses. *Nature* **308,** 32–36 (1984).
38. Zan, R. *et al.* Control of radiation damage in MoS_2 by graphene encapsulation. *ACS Nano* **7,** 10167–10174 (2013).
39. Myneni, S. *et al.* Spectroscopic probing of local hydrogen-bonding structures in liquid water. *J. Phys. Condens. Matter* **14,** L213–L219 (2002).
40. Näslund, L. A. *et al.* X-ray absorption spectroscopy study of the hydrogen bond network in the bulk water of aqueous solutions. *J. Phys. Chem. A* **109,** 5995–6002 (2005).
41. Algara-Siller, G., Lehtinen, O., Turchanin, A. & Kaiser, U. Dry-cleaning of graphene. *Appl. Phys. Lett.* **104,** 153115 (2014).
42. Natoli, C. R. in *EXAFS and Near Edge Structure (*eds Koningsberger, D. C. & Prins, R.) Vol. 3, 573 (Wiley, 1988).
43. Tse, J. S., Tan, K. H. & Chen, J. M. Oxygen K-edge XANES of crystalline and amorphous ice. *Chem. Phys. Lett.* **174,** 603–608 (1990).
44. Koch, C. Determination of core structure periodicity and point defect density along dislocations. PhD thesis, Arizona State Univ. (2002); http://elim.physik.uni-ulm.de/wp-content/uploads/talks/Koch02_dissertation.pdf or http://adsabs.harvard.edu/abs/2002PhDT.......50K.
45. Berendsen, H. J. C., Grigera, J. R. & Straatsma, T. P. The missing term in effective pair potentials. *J. Phys. Chem.* **91,** 6269–6271 (1987).
46. Werder, T., Walther, J. H., Jaffe, R. L., Halicioglu, T. & Koumoutsakos, P. On the water-carbon interaction for use in molecular dynamics simulations of graphite and carbon nanotubes. *J. Phys. Chem. B* **107,** 1345–1352 (2003).
47. Plimpton, S. J. Fast parallel algorithms for short-range molecular dynamics. *J. Comput. Phys.* **117,** 1–19 (1995).
48. Abascal, J. L. F. & Vega, C. A general purpose model for the condensed phases of water: TIP4P/2005. *J. Chem. Phys.* **123,** 234505 (2005).
49. Matsumoto, M., Saito, S. & Ohmine, I. Molecular dynamics simulation of the ice nucleation and growth process leading to water freezing. *Nature* **416,** 409–413 (2002).

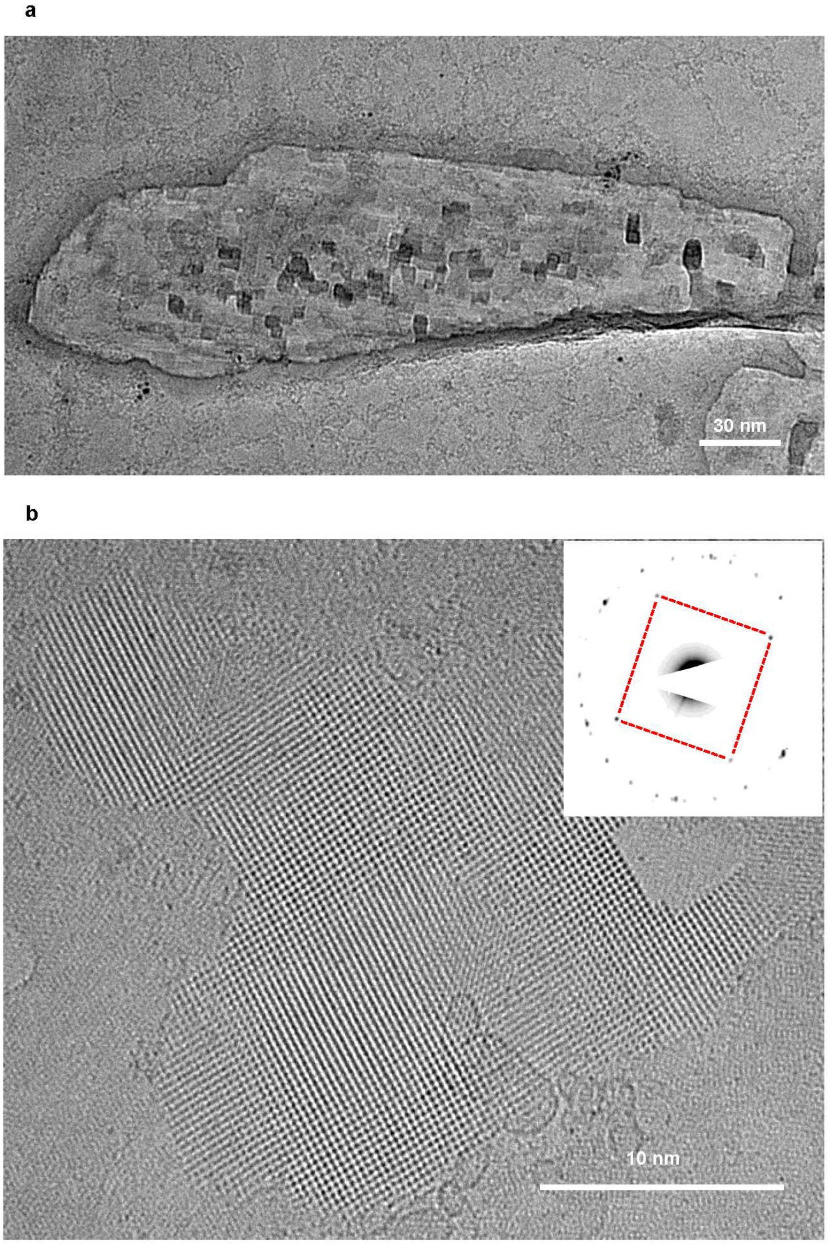

Extended Data Figure 1 | 2D water captured between graphene monolayers. **a**, Confined water at low magnification. The lateral size of such water pockets was typically ~100 nm. The chequered pattern reveals a collection of ice crystallites. **b**, Another example of a high-magnification image of 2D ice. The inset shows selected area electron diffraction from a region approximately 120 nm in diameter. The four diffraction spots connected for clarity by the red lines yield $a = 2.83 \pm 0.03$ Å, the same as the value obtained using the fast Fourier transform in Fig. 1.

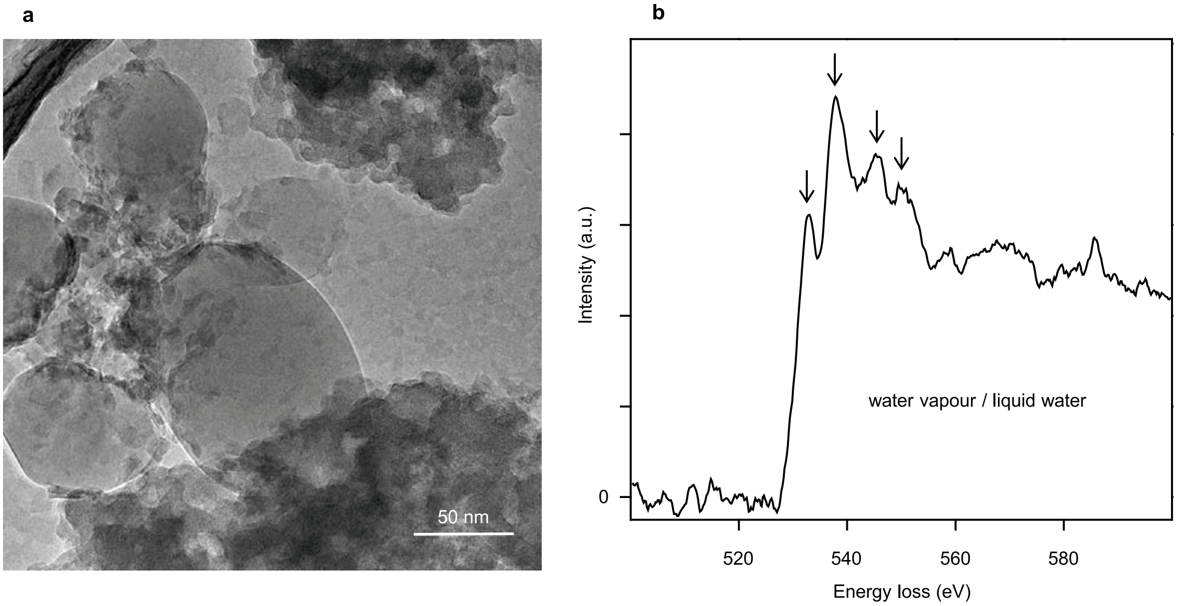

Extended Data Figure 2 | Large water droplets and their EELS. **a**, Low-magnification TEM image of a reference sample in which water was trapped in large bubbles (diameter of ~100 nm). **b**, Spectrum near the oxygen K-edge from the droplets shown in **a**. The four marked peaks at 532 eV, 537 eV, 545 eV and 550 eV are in agreement with the previously studied spectra for mixtures of water vapour and liquid water[39,40].

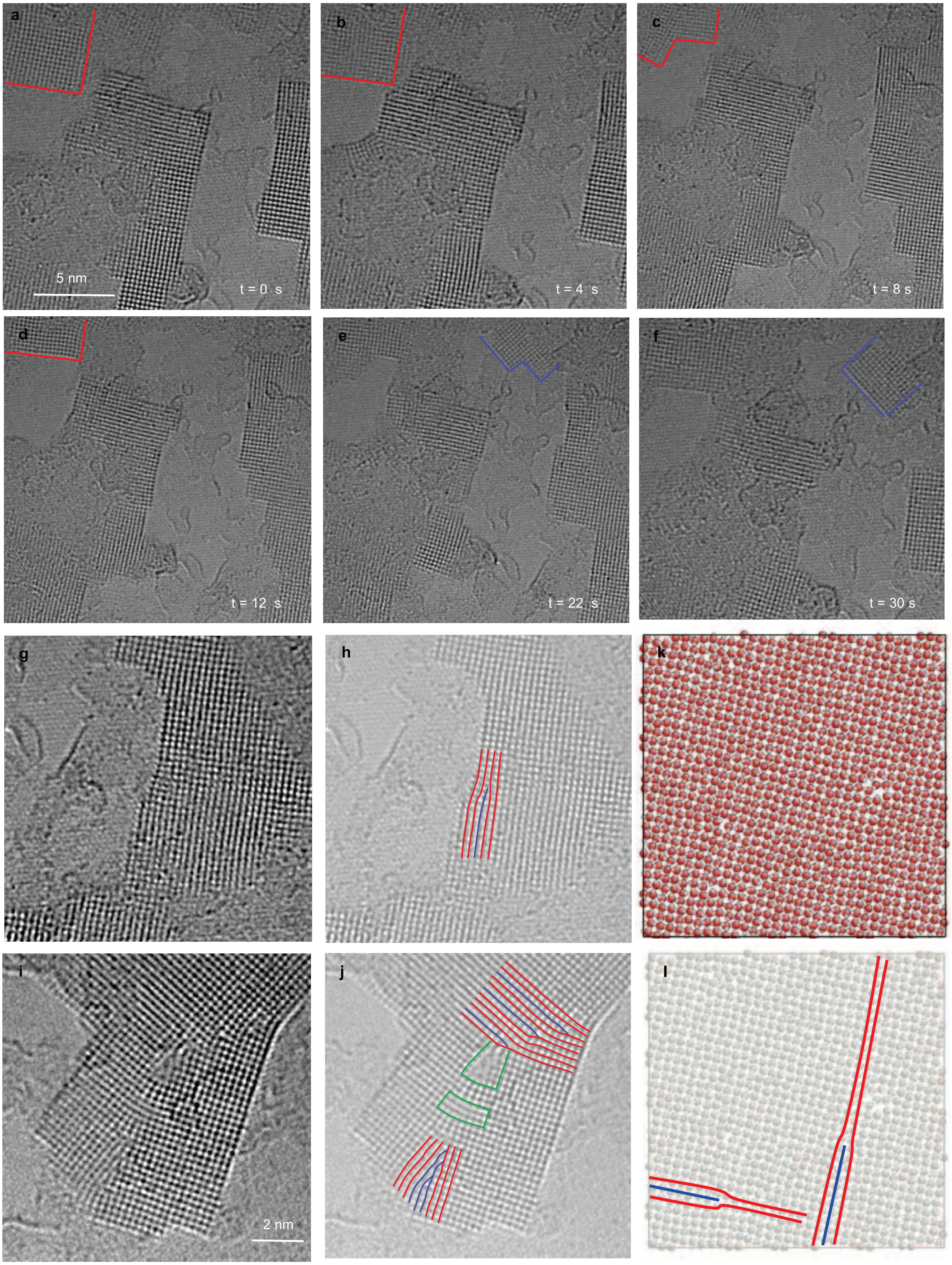

Extended Data Figure 3 | Dynamics of 2D ice crystallites and formation of defects. **a**–**f**, High-resolution snapshots from the Supplementary Video illustrate continuous reorganization of ice crystallites. Red lines highlight some of the changes: the bilayer crystal in **a** thins down to a monolayer in **b**, then splits into two crystals separated by a grain boundary in **c**, and a trilayer is formed in the same area in **d**. In **e**, a new crystallite, outlined in blue, appears in the top right corner, growing and propagating towards the centre in **f**. Other crystallites also change from panel to panel. **g**–**j**, Examples of an edge dislocation (**g**) and tilt grain boundaries (**i**) in 2D ice. **h** and **j** are the same images as **g** and **i**, respectively, but with reduced contrast; atomic rows are overlaid with red and blue lines to highlight the defects. Red lines mark existing atomic rows; blue lines mark extra rows originating from dislocations; green shapes outline defects without discernible atomic structures. **k**, **l**, Monolayer ice found in MD simulations also shows dislocations, indicating that they are intrinsic to the formation of 2D ice at room temperature.

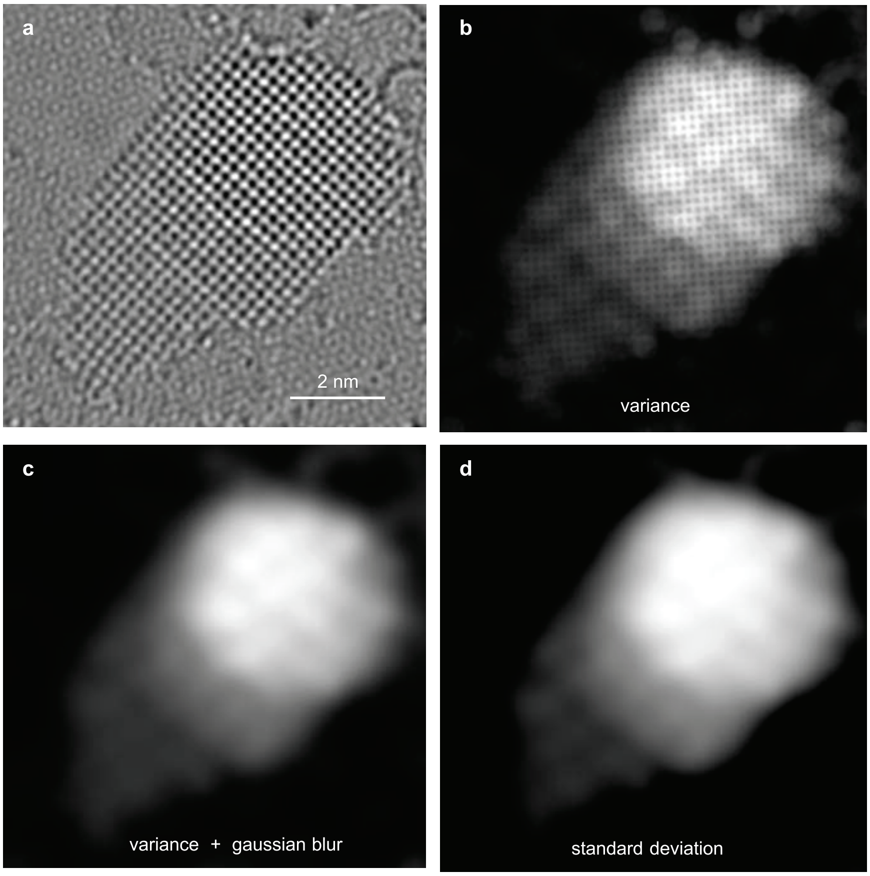

Extended Data Figure 4 | Quantifying the contrast to determine the number of layers in 2D ice. **a**, An example of the original TEM images used in our analysis (same image as in Fig. 2a). **b**, The filter calculates the local variance that is displayed as a greyscale value. **c**, The lattice pattern that remains visible in the variance image (**b**) is suppressed by applying the Gaussian blur. **d**, The final root-mean-square contrast map (that is, the standard deviation map) is obtained by calculating the square root of each pixel value of the variance image (**c**).

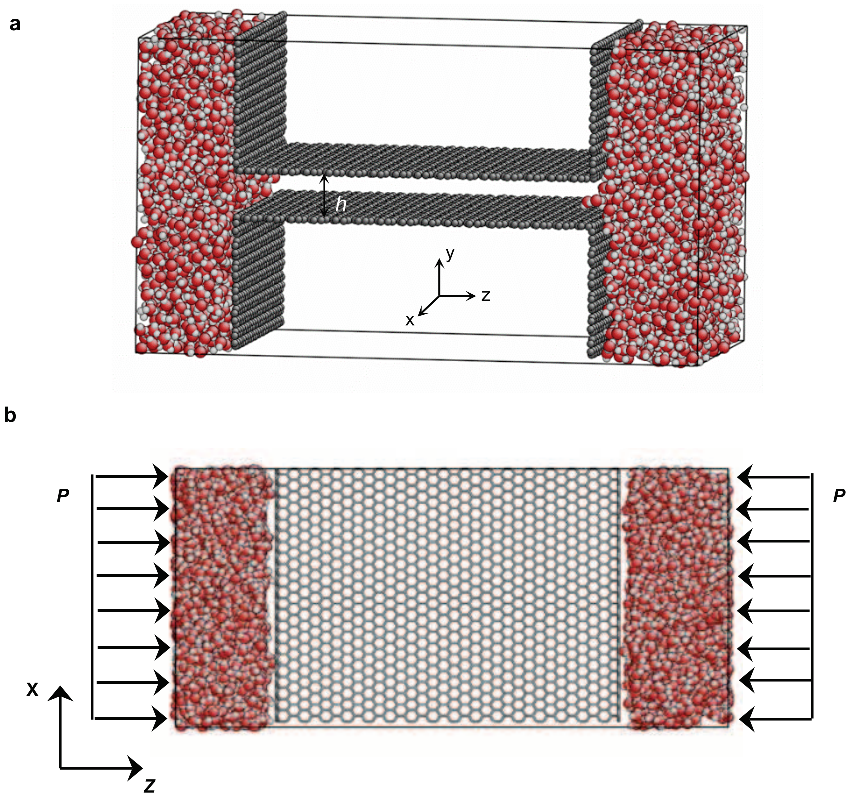

Extended Data Figure 5 | MD simulations setup. **a**, Initial configuration. **b**, Top view of the empty graphene channel, also showing how the external pressure *P* is applied to mimic the van der Waals pressure.

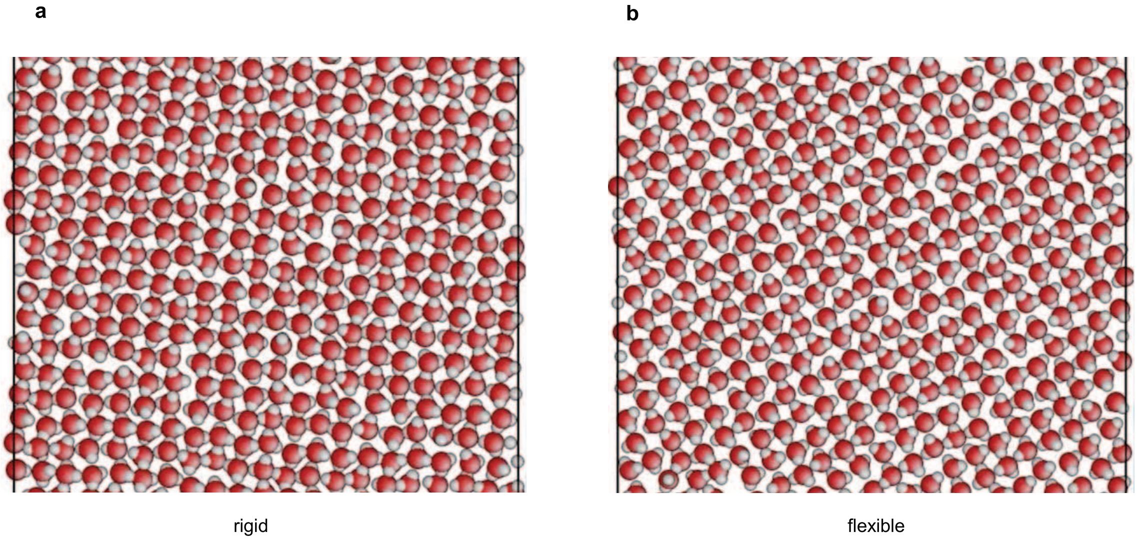

Extended Data Figure 6 | MD simulations of a monolayer of water in a 6.5-Å-high graphene capillary. Only one layer of water molecules can fit in. Red and grey circles represent oxygen and hydrogen atoms, respectively. Square ice is formed in this case, independently of whether the confinement is provided by rigid (**a**) or flexible (**b**) graphene sheets.

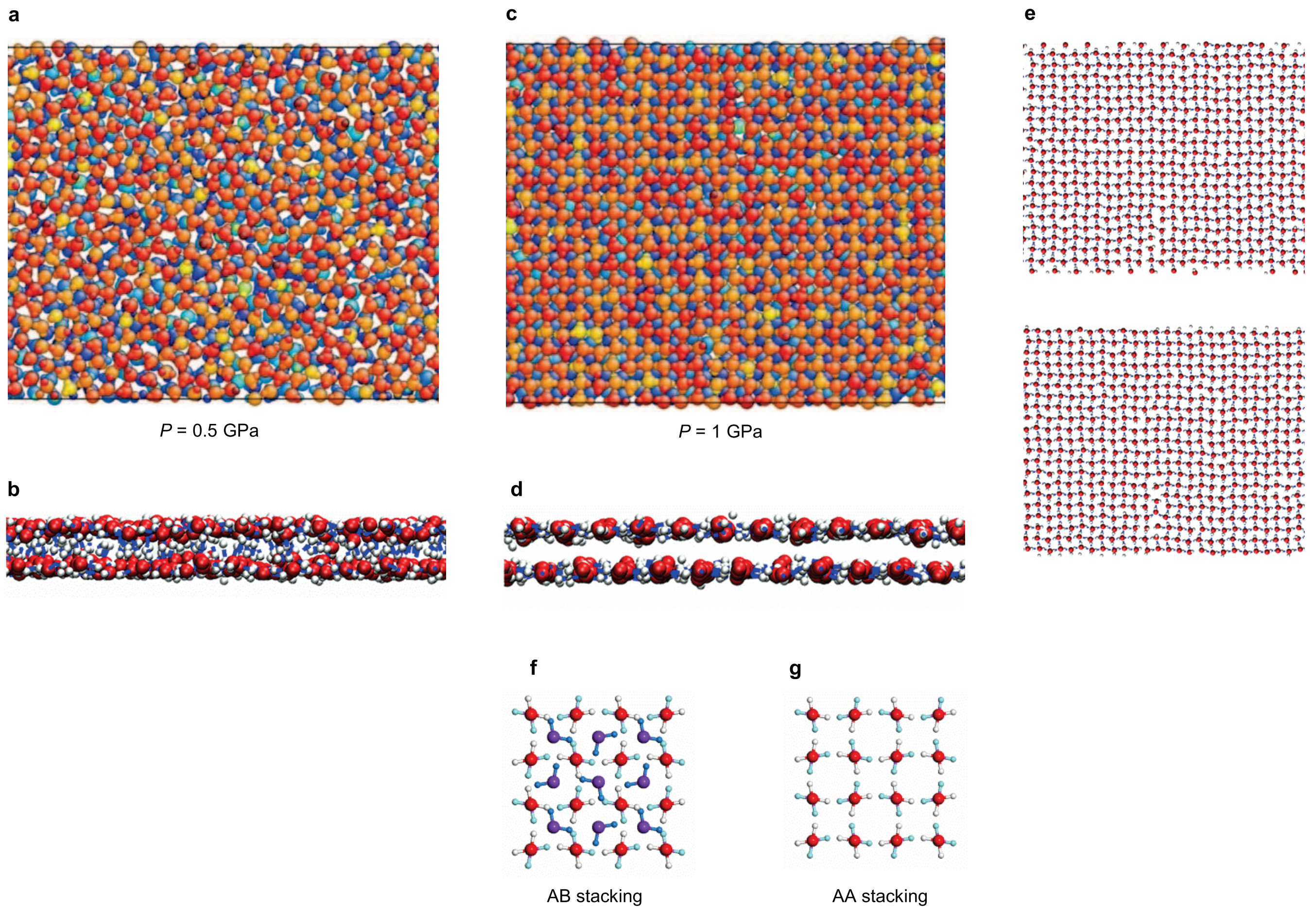

Extended Data Figure 7 | MD simulations for a 9-Å-high graphene capillary. **a, b,** Top (**a**) and side (**b**) views of a bilayer of water formed at $P = 0.5$ GPa. Different colours in **a** correspond to different vertical positions of water molecules in different layers: dark blue and red mark the bottom and top positions, respectively and lighter colours correspond to intermediate positions. Although the water molecules are clearly arranged in two layers, no intralayer ordering is present and hydrogen bonds preserve their tetrahedral coordination as in bulk water. **c**, **d**, As in **a** and **b** but at 1.0 GPa. Ordered bilayer ice is formed, with identical square lattices in the two layers, as illustrated by snapshots of the top and bottom layers in **e**. The ordering is accompanied by switching hydrogen bonds to in-plane coordination. **f**, **g**, Schematic illustration of AB and AA stacking. The stacking found in **c** and **d** is AB.

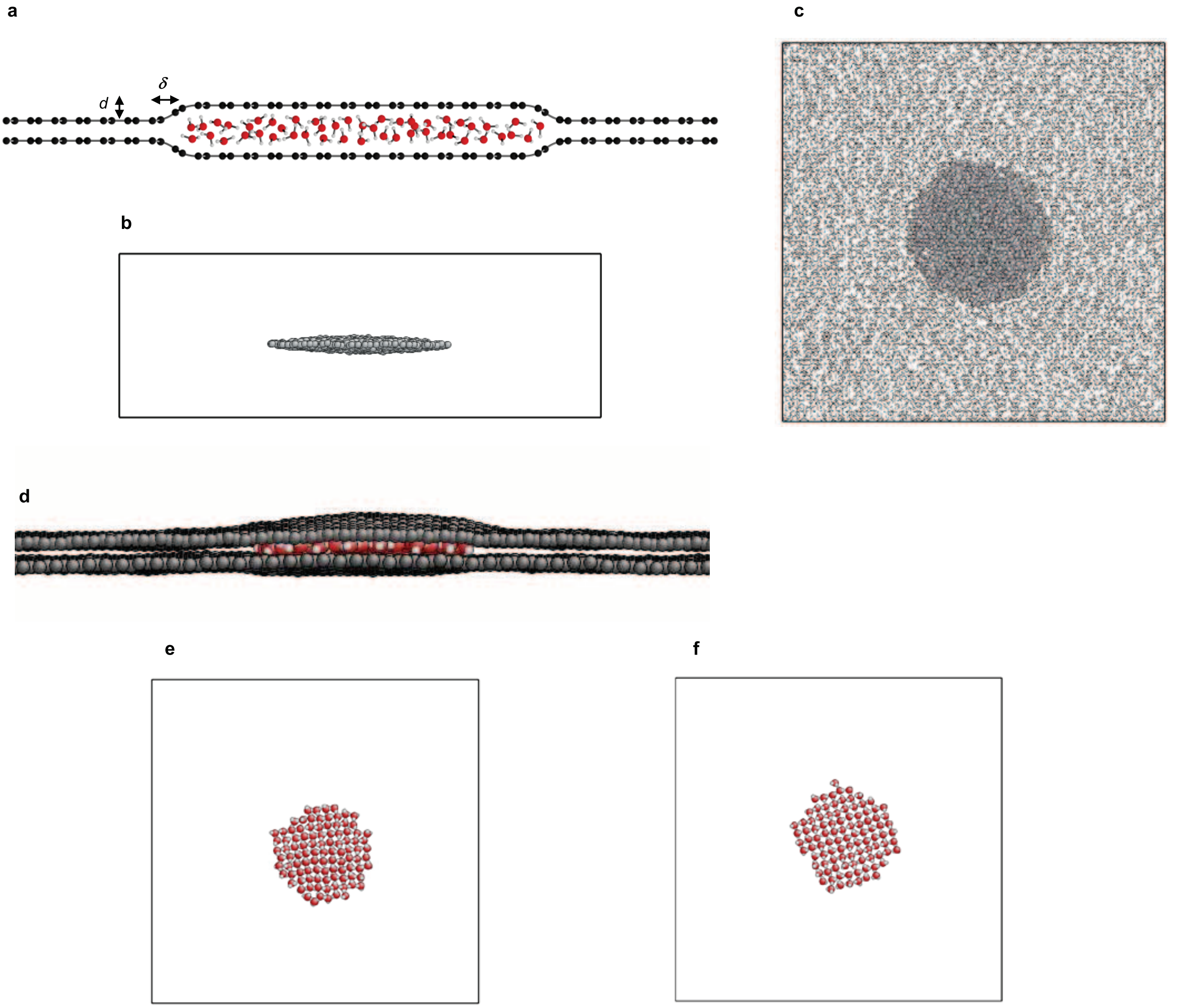

Extended Data Figure 8 | Van der Waals pressure acting on water trapped between graphene sheets. **a**, Schematic illustration of water confined by graphene. Owing to adhesion between the graphene layers, water is squeezed into a 2D puddle. Parameters *d* and *δ* are used in our estimation of van der Waals pressure (see Methods). **b**, **c**, MD simulations of van der Waals pressure exerted on a gas bubble (1,000 He atoms) trapped between two freely moving graphene sheets, showing side (**b**) and top (**c**) views of the He nanoballoon. In **b**, the graphene layers are not shown for clarity, and in **c** they are in light grey. **d**–**f**, Simulations of 2D ice formed by a water nanodroplet (100 molecules) confined between two freely moving flexible graphene sheets. Oxygen atoms are shown in red, hydrogen in light grey and graphene in dark grey: side (**d**) and top (**e**, **f**) view at equilibrium Simulations in **d** and **e** were performed using the SPC/E model and, in **f**, using TIP4P/2005. For clarity, graphene is not shown in **e** and **f**. The lattice parameter in **e** and **f** is about 2.8 Å within the modelling accuracy.

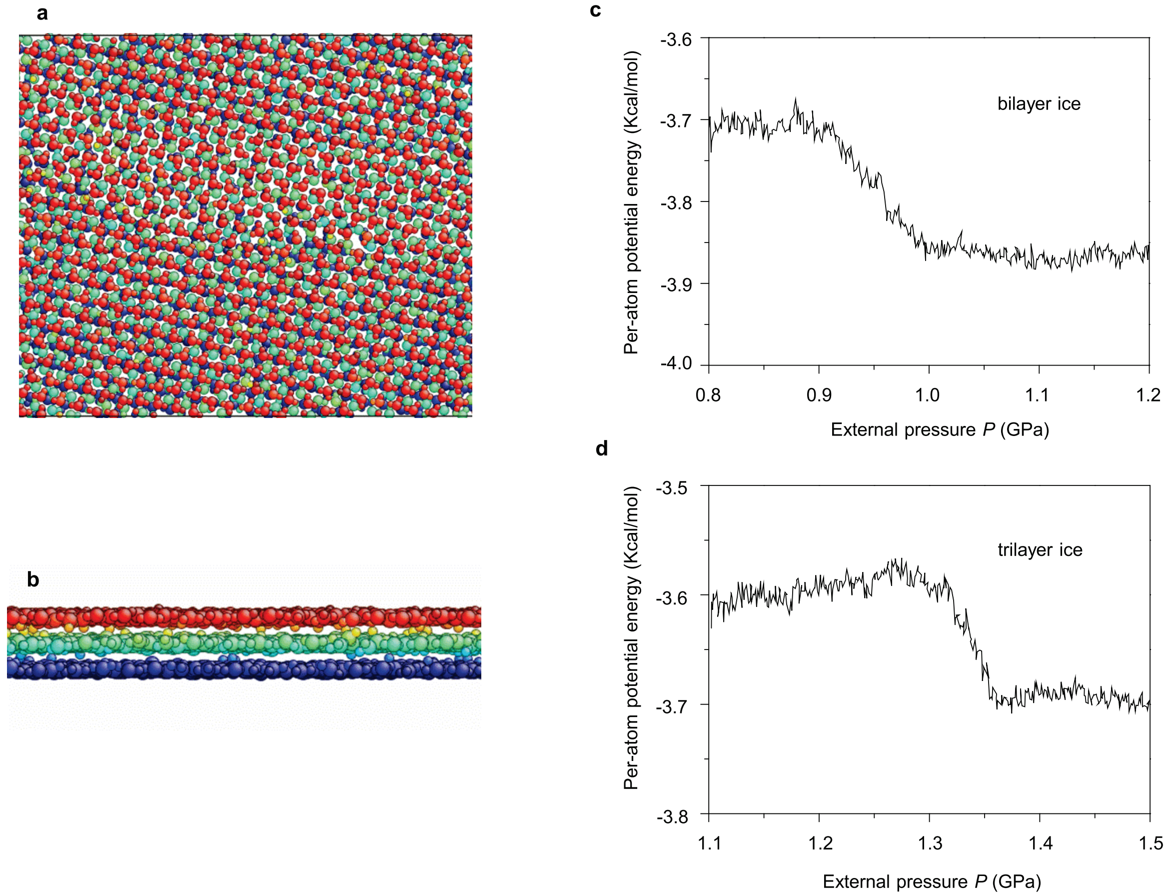

Extended Data Figure 9 | MD simulations of the order–disorder transition in trilayer ice. Top (**a**) and side (**b**) views of trilayer ice formed at $P \approx 1.4$ GPa in the graphene capillary with $h = 11.5$ Å. Different colours correspond to water molecules in different layers (same colour coding as in Extended Data Fig. 7). No clear stacking sequence can be determined for this structure. **c**, **d**, Potential energy per atom in 2D ice as a function of applied pressure for the bilayer (**c**) and trilayer (**d**) ice.

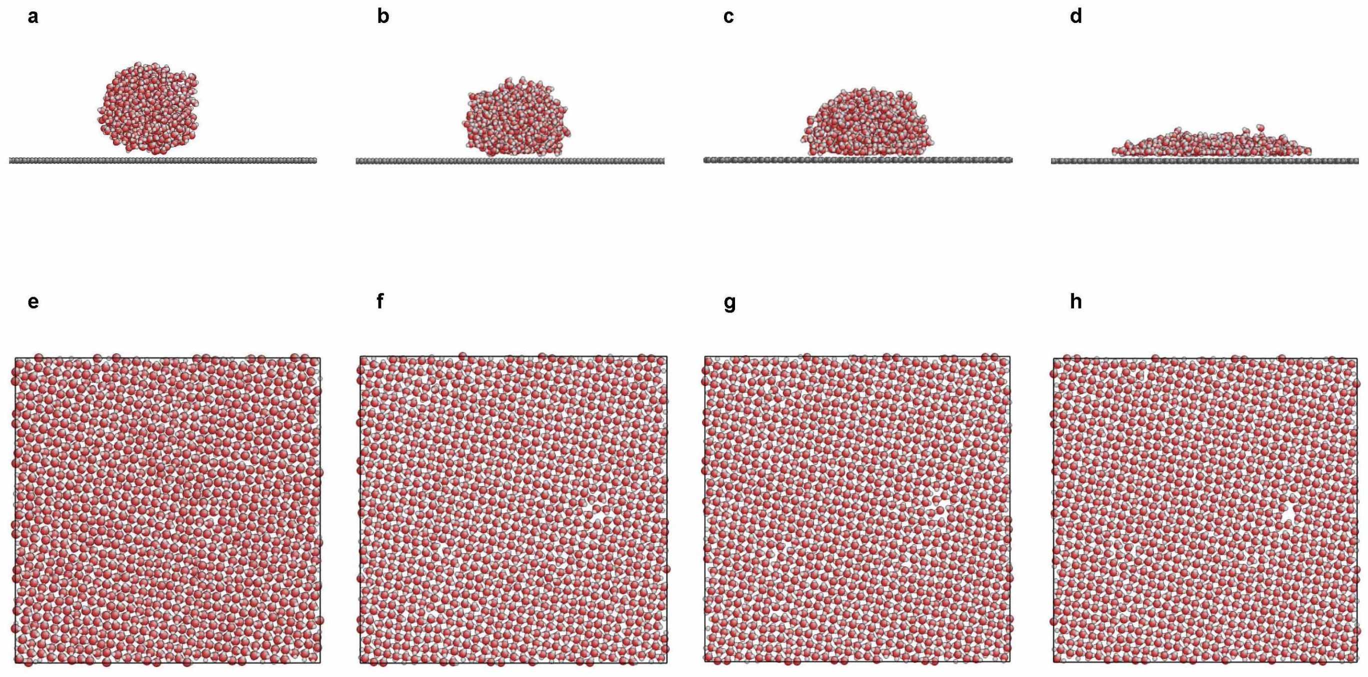

Extended Data Figure 10 | Square ice in nanocapillaries with different hydrophobicity. **a**–**d**, Water droplets on surfaces with $\varepsilon = 0.01$ kcal mol^{-1}, 0.05 kcal mol^{-1}, 0.1 kcal mol^{-1} and 0.2 kcal mol^{-1}, respectively. The changes in the relative strength of water–water and water–surface interactions result in different contact angles. For comparison, ε for the graphene–water interaction is 0.07 kcal mol^{-1}. **e**–**h**, Monolayer ice confined between surfaces with ε corresponding to **a**–**d**, respectively. In this case, the modelled walls are generic and do not have a discrete atomic structure, that is, their potential is uniform. $h = 6.5$ Å, the same as for the modelling of monolayer ice in the graphene nanocapillary in Extended Data Fig. 6.

doi:10.1038/nature14272

Vapour-mediated sensing and motility in two-component droplets

N. J. Cira[1], A. Benusiglio[1] & M. Prakash[1]

Controlling the wetting behaviour of liquids on surfaces is important for a variety of industrial applications such as water-repellent coatings[1] and lubrication[2]. Liquid behaviour on a surface can range from complete spreading, as in the 'tears of wine' effect[3,4], to minimal wetting as observed on a superhydrophobic lotus leaf[5]. Controlling droplet movement is important in microfluidic liquid handling[6], on self-cleaning surfaces[7] and in heat transfer[8]. Droplet motion can be achieved by gradients of surface energy[9–13]. However, existing techniques require either a large gradient or a carefully prepared surface[9] to overcome the effects of contact line pinning, which usually limit droplet motion[14]. Here we show that two-component droplets of well-chosen miscible liquids such as propylene glycol and water deposited on clean glass are not subject to pinning and cause the motion of neighbouring droplets over a distance. Unlike the canonical predictions for these liquids on a high-energy surface, these droplets do not spread completely but exhibit an apparent contact angle. We demonstrate experimentally and analytically that these droplets are stabilized by evaporation-induced surface tension gradients and that they move in response to the vapour emitted by neighbouring droplets. Our fundamental understanding of this robust system enabled us to construct a wide variety of autonomous fluidic machines out of everyday materials.

When droplets of food colouring (containing propylene glycol, PG) are mixed with water and placed on a clean glass slide, they spontaneously move in beautiful and intricate patterns (Fig. 1a and Supplementary Video 1). Here, we first discuss the wetting behaviour of individual droplets, before investigating the multidroplet interactions that cause droplet motion.

We observed that pure water and pure PG spread completely when placed on corona-discharge-cleaned glass slides (Supplementary Information section 1). This is expected on such a high-energy surface for which the spreading parameter, defined as $S = \gamma_{SV} - (\gamma_{LV} + \gamma_{SL})$, is larger than zero, where γ represents the surface energy of the solid/vapour, liquid/vapour, and solid/liquid interfaces[15]. Surprisingly, mixtures of PG and water formed droplets with apparent contact angles θ_{app}, even though $S \geq 0$. The trend in θ_{app} went from zero to a maximum value and back to zero as PG was added to water (Fig. 2a), which cannot be explained simply by the monotonically decreasing liquid/vapour surface tension (Extended Data Fig. 1)[16]. Breathing onto a droplet noticeably modified the contact angle. To quantify this observation, we deposited droplets in controlled humidity chambers and found that apparent contact angle decreased with relative humidity (RH), and droplets spread under saturated RH (Fig. 2b), suggesting that vapour affects droplet stabilization.

Using tracer beads (1 μm diameter) we visualized an internal flow from centre to edge along the bottom of the droplet, similar to the flow in the 'coffee ring' effect[17]. We also observed a flow from the edge to the centre along the top of the droplet, at higher velocity than the outward

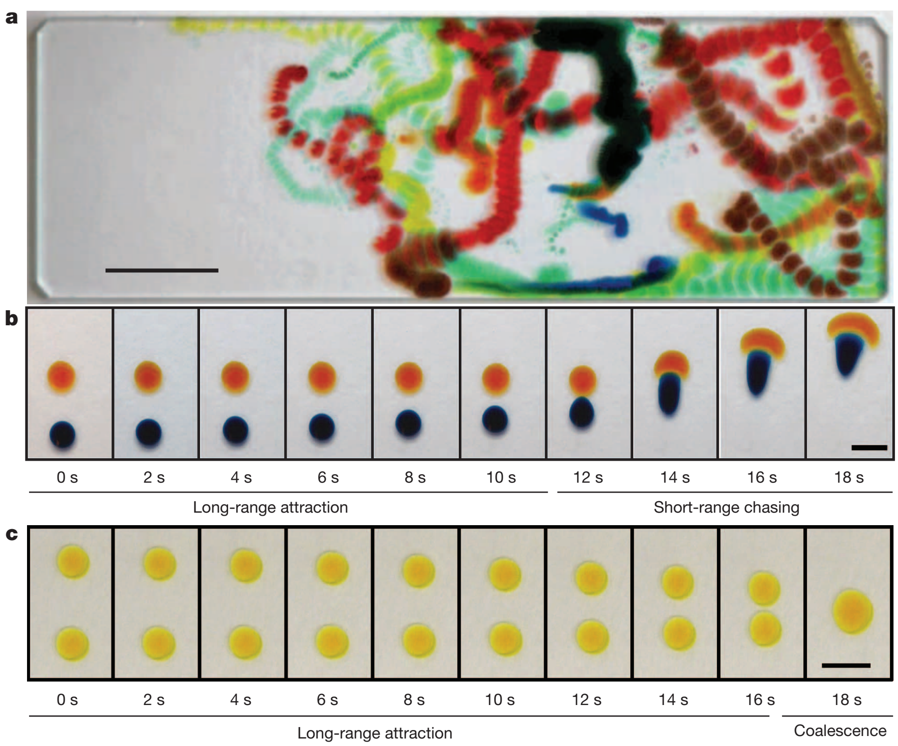

Figure 1 | Long-range and short-range interactions in two-component droplets. **a**, Overlaid time lapse image of multiple coloured droplets deposited on a corona-discharge-cleaned glass slide interacting autonomously for 2 min (see Supplementary Video 1, part 1; scale bar, 10 mm). **b**, Two 0.5 μl droplets of 25% PG (blue) and 1% PG (orange) interacting. The behaviour can be divided into 'long-range attraction' and 'short-range chasing' portions (see Supplementary Video 1, part 2; scale bar, 3 mm). **c**, Two droplets of exactly the same concentration (0.5 μl 10% PG) also attract each other, through long-range interaction followed by coalescence. All percentage PG values are given as volume percentages (volume of PG divided by total volume). (See Supplementary Video 1, part 3; scale bar, 5 mm.)

[1]Department of Bioengineering, Stanford University, 450 Serra Mall, California 94305, USA.

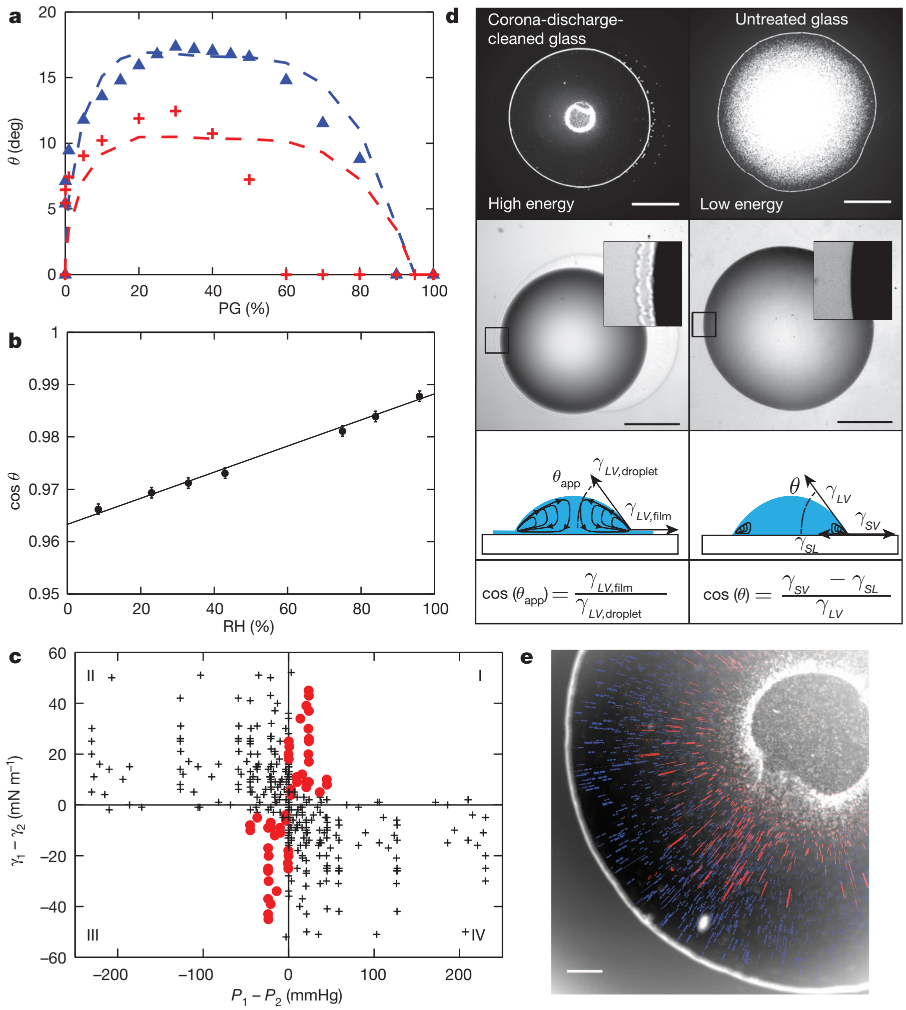

Figure 2 | Individual droplet characteristics. **a**, Isolated droplets (0.5 μl) on a clean glass surface display a non-monotonic apparent contact angle as a function of percentage PG. Crosses and triangles indicate data taken at 75% RH and 40% RH, respectively. Dashed lines indicate the model's fit to the data. **b**, The cosine of the apparent contact angle varies linearly (line of best fit shown) with external humidity (RH) for 0.5 μl 10% PG droplets. Error bars are the range of three measurements at 75% RH. **c**, Behaviour of two-component mixtures of all nonreactive combinations of 21 miscible fluids (see Supplementary Table 1 for chemical list) on corona-discharge-cleaned glass. For each liquid pair, difference in surface tension γ is plotted against difference in vapour pressure P. Red dots indicate droplet formation and black crosses indicate complete wetting. **d**, Important differences between two-component droplets deposited on high- and low-energy solid substrates. From top to bottom: accumulation of beads at the liquid/vapour interface, visualization of the thin film (contrast is enhanced in the insets, which magnify the boxes) (scale bars, 1 mm), flow representation (diagram), and force equilibrium (equation). **e**, Time-lapse trajectories of tracer beads in the droplet. Red traces are focused at the top surface where beads move towards the centre, while blue traces are in the plane close to the glass where beads move outward (scale bar, 200 μm).

flow (Fig. 2d and e). This less commonly seen 'counter flow' has been observed with surfactant or thermal gradients only in pinned droplets[18,19]. It collects tracer beads at the liquid–vapour interface into a prominent ring (Fig. 2e). Experiments with multiple chemical combinations on multiple substrates demonstrate that thermocapillarity does not appear to be a substantial driving force in our system (Extended Data Figs 2 and 3; Supplementary Information section 2.5). Microscopic observation of the droplets revealed a thin film extending tens of micrometres from the edge of the bulk droplet into which the 1 μm tracer beads did not enter (Fig. 2d, Supplementary Video 2). For the same droplets on a lower-energy surface the counter flow was confined to the border of the droplet (Fig. 2d). No tracer bead ring appeared (Supplementary Video 2), there was no thin film around the droplets, and the droplets were less mobile and did not interact.

From these observations we can understand the mechanism that prevents complete spreading. The high-energy surface favours spreading of the droplet, as seen for pure liquids[20]. For a two-component droplet of water and PG, the more volatile compound (water) evaporates more quickly than the less volatile compound (PG). Evaporation is faster at the border of the droplet than the bulk[17], and the border of the droplet has a higher surface area to volume ratio. Therefore PG, with a lower γ_{LV} than water, is left in higher concentration at the border than the bulk. The resulting gradient of surface tension, or so called Marangoni stress, pulls liquid towards the centre along the top of the droplet, an effect shown to slow down or stop spreading[2,21,22]. Here the spreading is stopped, resulting in a droplet with a stable apparent contact angle θ_{app} (Extended Data Fig. 4) surrounded by a thin film (Figs 2d and 3a)[2].

Next, we built a simple model to test this mechanism of droplet stabilization. We assumed a sharp transition of surface tension between the bulk droplet ($\gamma_{LV,\,droplet}$) and the surrounding thin film ($\gamma_{LV,\,film}$). We introduced a quasi-static horizontal force balance at the intersection of the thin film and the bulk droplet, $\gamma_{LV,\,droplet}\cos(\theta_{app}) = \gamma_{LV,\,film}$. To calculate θ_{app}, we modelled the water loss from the thin film due to evaporation, estimating the water fraction and surface tension of the film as a function of both the external RH and water fraction of the droplet (Supplementary Information section 2.3, Extended Data Figs 5 and 6). Using this model we fitted a single parameter for 40% RH and observed that the prediction globally captures the non-monotonic contact angle curve and accounts for variation in this curve as a function of RH (Fig. 2a). Our current model accounts only for water evaporation, and is therefore less accurate at high PG concentration and high RH.

Based on this model, for any two miscible chemicals on a high-energy substrate, droplets should form if and only if one of the chemicals in the mixture has both a higher surface tension and higher vapour pressure (quadrants I and III in Fig. 2c). To test this law, we placed various two-component mixtures on corona-discharge-cleaned glass slides. In about 200 unique combinations (Extended Data Table 1), droplet formation versus spreading was well predicted, excluding reactive pairs (Fig. 2c), and these droplets had attributes similar to those of the PG/water system, such as high mobility and interactions. We also deposited PG/water droplets on other high-energy substrates—piranha-treated glass, flamed glass, clean silicon wafers, freshly scraped steel, flamed aluminium, and plasma-oven-treated flexible indium tin oxide (ITO)-coated polyethylene terephthalate (PET)—and found similar behaviour.

These two-component droplets have characteristics of both wetting and non-wetting liquids: they maintain a defined contact angle but sit on a thin fluid film. As long as $S \geq 0$, the droplets should not 'feel' the solid surface, and chemical inhomogeneities and roughness should not

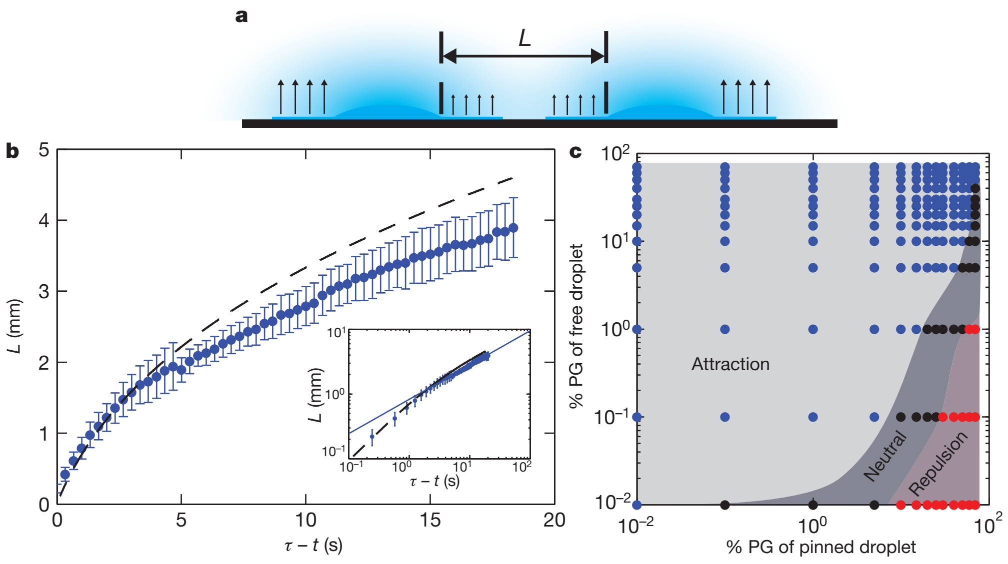

Figure 3 | Long-range droplet interactions. **a**, Schematic of vapour gradients (blue shading) and evaporation (upward arrows) from two droplets a distance L apart. Increased vapour concentration between the droplets leads to less evaporation. **b**, Mean distance between droplets as a function of time before contact for two freely moving 0.5 μl 10% PG droplets. The error bars represent the standard deviation of 12 experiments, and the dashed line is the model prediction. The inset shows the log-log scale of the same data, with solid line as the power-law fit. τ is the time of droplet contact. **c**, Phase diagram of interactions between a single pinned and a single free 0.5 μl droplet (the axes show percentage by volume of PG). Each dot represents an experiment; each colour indicates the direction of motion of the free droplet.

cause pinning. The droplet contact angle is also independent of the substrate (γ_{SV}) and surface roughness. Without pinning, the droplets display high mobility and hence move under the influence of minute forces (<1 μN, Extended Data Fig. 7). We do not observe high mobility on low-energy surfaces with a three-phase contact line, where high hysteresis limits droplet motion.

When two droplets were deposited at distances of up to several radii apart, they moved towards each other; this occurred over a wide range of concentrations, even when both droplets had the same concentration (Figs 1b and c, and 3c). Droplets increased speed as they approached each other (Fig. 3b). These long-range interactions were preserved even across a break in the glass slide (Supplementary Video 3, part 1). PG/water droplets followed a pipette tip containing water placed near to but not touching the droplet or the glass slide (Supplementary Video 3 Part 2). These observations and our measurements of θ_{app} versus RH (Fig. 2b) led us to the surprising conclusion that long-range interactions were vapour-mediated.

From the observations above, we propose a mechanism for vapour-mediated interactions different from mechanisms proposed in other systems[23,24]. Evaporation from a sessile droplet is known to produce a vapour gradient[25]. Since the vapour pressure of water is one hundred times larger than the vapour pressure of PG, the dominant vapour is water. Two neighbouring droplets each lie in a gradient of water vapour produced by the other (Fig. 3a). This gradient causes a local increase in RH and thus decreased evaporation of the thin film on the adjacent portions of the droplets, breaking symmetry. The decreased evaporation leads to an increased water fraction in the thin film, hence increasing $\gamma_{LV,\,film}$ locally. Asymmetric $\gamma_{LV,\,film}$ around the droplet causes a net force that drives the droplets towards each other.

To test this mechanism, we propose a mathematical model to calculate the expected distance L between two identical droplets as a function of time (Fig. 3a, Supplementary Information section 2.4). We start with the diffusion equation to estimate the local RH profile around a droplet. By using our prior measurements of θ_{app} of a static droplet as a function of uniform external RH, we estimate the local $\gamma_{LV,\,film}$ around each droplet as a function of the local RH imposed by the other droplet. Integrating $\gamma_{LV,\,film}$ around the edge we obtain the net force acting on each droplet as $F_{net}=2\gamma_{LV,\,droplet}mR\int_0^{\pi}\left(\frac{(1-\mathrm{RH}_{room})R\cos(\psi)}{\sqrt{d^2+R^2+2Rd\cos(\psi)}}\right)\mathrm{d}\psi$, where m is the slope of $\cos(\theta_{app})$ plotted versus RH (Fig. 2b), R is the radius of the droplet, d is the distance between the droplet centres, ψ is the parameter of integration, and RH_{room} is the ambient humidity far from the droplets. This net force causes droplet motion and is balanced by a viscous drag force, F_{drag}. Here we neglect inertia since the Reynolds number, Re, is smaller than 1 (for typical droplet velocity 1 mm s^{-1} and droplet radius 1 mm, Re ≈ 0.3).

We calibrated F_{drag} by measuring droplet speed on ramps of known angle, observing that it scaled linearly with the velocity U as $F_{drag}=C_{drag}U$ (Extended Data Fig. 8). The drag coefficient C_{drag} was a linear function of the droplet perimeter, consistent with existing theory based on viscous dissipation at three-phase contact lines[26] (Supplementary Information Section 2.1 and 2.2, Extended Data Figs 7 and 8). Equating F_{drag} with F_{net}, we obtain and integrate the instantaneous velocity to arrive at the distance between the two droplets, $L(t)$. Plotting L as a function of $\tau - t$ with τ as the time of droplet contact, we observe a good agreement between model and data, with no adjustable parameters (Fig. 3b). In a log-log plot $L(\tau - t)$ behaves as a scaling law of exponent 0.6 at long distance, which is also captured by the model (inset to Fig. 3b).

In Fig. 3c, we present a phase diagram of long-range interactions between one pinned droplet and one mobile droplet, as a function of concentration of both droplets. Over a large concentration range the mobile droplet was attracted to the pinned droplet. However, when $[\mathrm{PG}]_{pinned} \gg [\mathrm{PG}]_{mobile}$, the mobile droplet fled, indicating a repulsive force. We hypothesize that at high PG concentration, the gradient of the PG vapour begins to contribute to long-range motion, decreasing $\gamma_{LV,\,film}$ and driving the mobile droplet away.

At short range, two droplets of like concentrations coalesce upon contact. Droplets of sufficiently different concentrations can undergo a prolonged 'chasing phase'[23] as recently explained[27,28] (Fig. 1b). Fluid is directly exchanged between the droplets, as visualized by a fluorescent dye (Supplementary Video 4). This exchange of fluid leads to a surface tension gradient and Marangoni flow across both the droplets, where the droplet of lower surface tension 'chases' the droplet of higher surface tension, which in turn 'flees' away[28]. Additional subtleties of short-range interactions can be obtained by adjusting concentrations and volumes (Supplementary Information; Extended Data Fig. 9).

Using the fundamental understanding we developed for this system, we explored several applications by building multiple self-fuelled surface-tension-driven fluidic machines out of everyday materials such as food colouring, glass slides, and permanent Sharpie marker (Supplementary Information section 1.5). First, we used the long-range interactions to create a droplet self-aligner, which aligns randomly placed droplets of identical concentrations in different 'lanes' into a single straight line

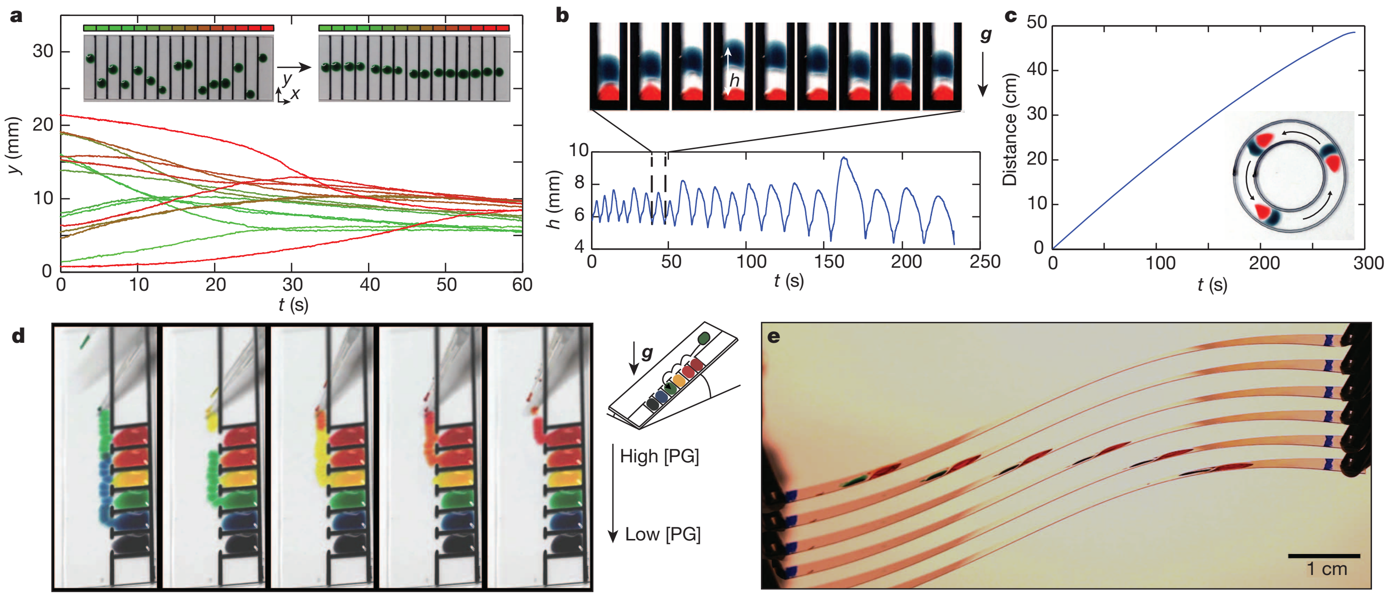

Figure 4 | Droplet-based devices. We created four devices by drawing permanent marker (Sharpie, black) lines, which are hydrophobic enough that droplets do not cross them (Supplementary Video 5, parts 1–3 and Supplementary Video 6). **a**, Spontaneous droplet aligner. Upper left inset shows 0.5 µl green droplets of 10% PG dispensed at random initial positions separated by 5 mm spaced Sharpie lines. Upper right inset shows the droplets automatically aligned into final positions. The graph shows the *y* position of each droplet as a function of time. The colour code represents the *x* position in the aligner. **b**, Vertical droplet oscillator. We deposited a 25% PG droplet (blue) above a 1% PG droplet (red) bounded in a 4 mm lane on a vertical glass slide. The top droplet oscillates up and down. The top panel shows one oscillation, with images separated by 1 s. The direction of the gravitational acceleration is shown by *g*, and the bottom panel shows the vertical position *h* of the top droplet as a function of time. **c**, Circular chasing. Short-range chasing between a 1% PG droplet (red) and a 25% PG droplet (blue) in a circle of mean diameter 2.1 cm. The inset shows a three-image time lapse (10 s spacing, arrows representing direction of motion). The graph shows the travelled distance as a function of time. **d**, Surface tension sorter. The schematic shows wells of various concentrations of PG (colours) confined by Sharpie lines (black). Concentrations from top to bottom are 30% PG, 25% PG, 20% PG, 15% PG, 10% PG and 5% PG. Each image shows the time-lapse trajectory of a droplet as it is deposited at the top and moves down under gravity, sampling each well, but merging only with a well of like concentration. Sorting happens purely passively. **e**, Flexible substrate. We demonstrate droplet chasing on a flexible plasma-oven-treated ITO/PET strip. The image was compiled by offsetting six frames from Supplementary Video 5, part 4.

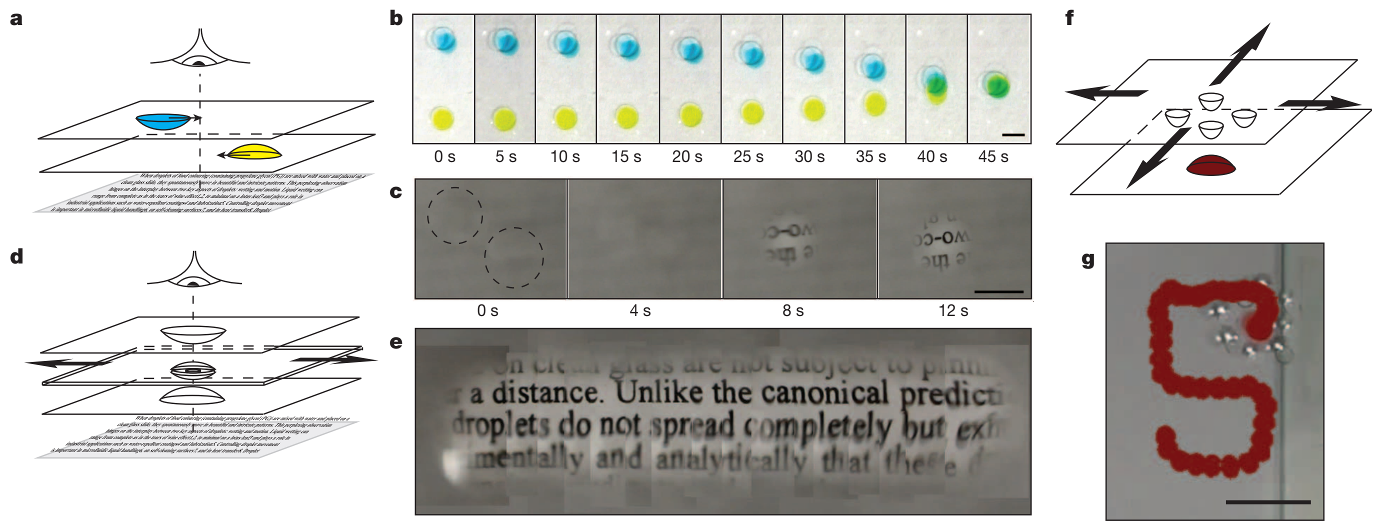

Figure 5 | Droplet-based devices using parallel plates. **a**, We created devices where droplets interacted with each other via vapour across a gap between parallel glass slides (Supplementary Videos 7 and 8). **b**, Time-lapse dynamics of interaction (0.5 µl 10% PG droplets, yellow on bottom slide, blue on top; scale bar, 4 mm). **c**, A self-assembling, self-aligning liquid lens system that forms an image when the top and bottom lenses align (scale bar, 4 mm). **d**, Schematic of a self-assembling, self-aligning three-lens system. The system is the same as the two-lens version with a third plate inserted in the middle. This plate has a drilled hole containing an additional liquid lens pinned in the hole (presenting two new optical surfaces) to which the other lenses align. **e**, An image made by scanning the three-lens assembly across text. As the centre plate was moved, the other lenses followed and aligned, allowing imaging over an area much larger than the lenses (image created by stitching together frames of Supplementary Video 8, part 3). **f**, A schematic of the long-range remote droplet positioning system. Droplets of PG act in long-range repulsion, and when arranged in a ring, these PG droplets create a vapour trap that pushes the PG/water droplet on the other slide to the centre of the trap. **g**, A time-lapse image illustrating remote control of droplet position. The top slide containing the PG vapour trap was moved to create contactless motion of the red droplet on the other slide.

(Fig. 4a, Supplementary Video 5, part 1). Second, we used the short-range interactions to create sustained droplet chasing, during which droplets circled around a single loop for several minutes (Fig. 4c, Supplementary Video 5, part 2). We note that since the droplets do not consume the surface, they are unaffected by prior trajectories and are able to repeatedly cross over their own paths. Third, we created a completely vertical droplet oscillator by placing a large low-surface-tension droplet beneath a higher-surface-tension droplet bounded in a lane on a glass slide (Fig. 4b, Supplementary Video 5, part 3). By changing the device parameters, the droplets were able to sustain chasing over the length of the slide against gravity (droplets run up a vertical wall). We also demonstrate short-range chasing on flexible ITO/PET, enabling applications for three-dimensional curved substrates (Fig. 4e, Supplementary Video 5, part 4). Finally, we demonstrate a new method for self-sorting droplets based on small surface tension differences. In this device, we relied on gravity to bring droplets down a ramp, where they sampled wells from low to high surface tension, merging only when they reached a like concentration, effectively sorting themselves into bins (Fig. 4d, Supplementary Video 6).

We further explored the application of long-range interactions by introducing a parallel plate geometry that allows droplet communication across disparate substrates via long-range interactions. We placed droplets on the adjacent sides of parallel glass slides separated by gaps of 0.15 mm to 4 mm (Fig. 5a). This parallel plate configuration resulted in prolonged droplet interaction, since evaporation was reduced by the additional boundary. Since the vapour gradient is more gradual in two dimensions, droplets also interacted over larger distances. We created several devices in this configuration. First, we made a contactless remote droplet positioning system based on long-range repulsion (Fig. 2f) by placing pinned droplets of pure PG in a ring on one slide and using them to manipulate mobile droplets on the other slide, creating a 'vapour trap' (Fig. 5g, Supplementary Video 7). Second, we noted that long-range attraction vertically aligns droplets on opposite plates (Fig. 5b, Supplementary Video 8, part 1). We exploited this mechanism to make self-assembling, self-aligning fluidic lens systems. These droplet lenses found each other from several lens diameters apart and self-aligned to produce a focused image (Fig. 5c, Supplementary Video 8, part 2). The magnification can be tuned by changing the spacing of optical components and the radius of curvature of the lenses (dictated by contact angle, modulated by concentration and RH as shown in Fig. 2a and b). Finally, we show how to build a self-assembled optical system with four tuneable lens surfaces by inserting a third plate with a hole drilled through it containing a pinned droplet between the two plates with mobile lenses (Fig. 5d). By moving the pinned lens, the entire optical assembly was capable of scanning a wide area (Fig. 5e, Supplementary Video 8, part 3).

These examples illustrate the wide variety of autonomous sensing and motility-based devices that can be created using our system. The system's robustness and ease of reproducibility (Supplementary Video 9) will be useful in further explorations in studying multi-body interactions[29], minimal systems of sensing and actuation, and as a physical analogue for the migration of keratocytes[30] and chemotaxing cells[31].

Online Content Methods, along with any additional Extended Data display items and Source Data, are available in the online version of the paper; references unique to these sections appear only in the online paper.

Received 14 August 2014; accepted 26 January 2015.
Published online 11 March 2015.

1. Wenzel, R. N. Resistance of solid surfaces to wetting by water. *Ind. Eng. Chem.* **28,** 988–994 (1936).
2. Bascom, W. D., Cottington, R. L. & Singleterry, C. R. Dynamic surface phenomena in the spontaneous spreading of oils on solids. http://pubs.acs.org/doi/abs/10.1021/ba-1964-0043.ch026, DTIC document number NRL-5963 (Naval Research Laboratory, 1963).
3. Thomson, J. On certain curious motions observable at the surfaces of wine and other alcoholic liquors. *Phil. Mag.* **10,** 330 (1855).
4. Marangoni, C. Über die Ausbreitung der Tropfen einer Flüssigkeit auf der Oberfläche einer anderen. *Ann. Phys.* **219,** 337–354 (1871).
5. Barthlott, W. & Neinhuis, C. Purity of the sacred lotus, or escape from contamination in biological surfaces. *Planta* **202,** 1–8 (1997).
6. Pollack, M. G., Fair, R. B. & Shenderov, A. D. Electrowetting-based actuation of liquid droplets for microfluidic applications. *Appl. Phys. Lett.* **77,** 1725–1726 (2000).
7. Zhang, X., Shi, F., Niu, J., Jiang, Y. G. & Wang, Z. Q. Superhydrophobic surfaces: from structural control to functional application. *J. Mater. Chem.* **18,** 621–633 (2008).
8. Daniel, S., Chaudhury, M. K. & Chen, J. C. Fast drop movements resulting from the phase change on a gradient surface. *Science* **291,** 633–636 (2001).
9. Chaudhury, M. K. & Whitesides, G. M. How to make water run uphill. *Science* **256,** 1539–1541 (1992).
10. Ichimura, K., Oh, S. K. & Nakagawa, M. Light-driven motion of liquids on a photoresponsive surface. *Science* **288,** 1624–1626 (2000).
11. Gallardo, B. S. *et al.* Electrochemical principles for active control of liquids on submillimeter scales. *Science* **283,** 57–60 (1999).
12. Brzoska, J. B., Brochard-Wyart, F. & Rondelez, F. Motions of droplets on hydrophobic model surfaces induced by thermal gradients. *Langmuir* **9,** 2220–2224 (1993).
13. Style, R. W. *et al.* Patterning droplets with durotaxis. *Proc. Natl Acad. Sci. USA* **110,** 12541–12544 (2013).
14. Dettre, R. H. & Johnson, R. E. Contact angle hysteresis. IV. Contact angle measurements on heterogeneous surfaces. *J. Phys. Chem.* **69,** 1507–1515 (1965).
15. de Gennes, P.-G., Brochard-Wyart, F. & Quéré, D. *Capillarity and Wetting Phenomena: Drops, Bubbles, Pearls, Waves* (Springer, 2004).
16. Hoke, B. C. & Patton, E. F. Surface tensions of propylene-glycol plus water. *J. Chem. Eng. Data* **37,** 331–333 (1992).
17. Deegan, R. D. *et al.* Capillary flow as the cause of ring stains from dried liquid drops. *Nature* **389,** 827–829 (1997).
18. Truskett, V. & Stebe, K. J. Influence of surfactants on an evaporating drop: Fluorescence images and particle deposition patterns. *Langmuir* **19,** 8271–8279 (2003).
19. Hu, H. & Larson, R. G. Analysis of the effects of Marangoni stresses on the microflow in an evaporating sessile droplet. *Langmuir* **21,** 3972–3980 (2005).
20. Tanner, L. H. Spreading of silicone oil drops on horizontal surfaces. *J. Phys. D* **12,** 1473–1484 (1979).
21. Bernett, M. K. & Zisman, W. A. Prevention of liquid spreading or creeping. Contact angle, wettability and adhesion. *Adv. Chem. Ser.* **43,** 332–340 (1964).
22. Pesach, D. & Marmur, A. Marangoni effects in the spreading of liquid mixtures on a solid. *Langmuir* **3,** 519–524 (1987).
23. Bangham, D. H. & Saweris, Z. The behaviour of liquid drops and adsorbed films at cleavage surfaces of mica. *Trans. Faraday Soc.* **34,** 0554–0569 (1938).
24. Carles, P. & Cazabat, A. M. Spreading involving the Marangoni effect—some preliminary results. *Colloids Surf.* **41,** 97–105 (1989).
25. Hu, H. & Larson, R. G. Evaporation of a sessile droplet on a substrate. *J. Phys. Chem. B* **106,** 1334–1344 (2002).
26. Brochard, F. Motions of droplets on solid surfaces induced by chemical or thermal gradients. *Langmuir* **5,** 432–438 (1989).
27. Karpitschka, S. & Riegler, H. Quantitative experimental study on the transition between fast and delayed coalescence of sessile droplets with different but completely miscible liquids. *Langmuir* **26,** 11823–11829 (2010).
28. Riegler, H. & Lazar, P. Delayed coalescence behavior of droplets with completely miscible liquids. *Langmuir* **24,** 6395–6398 (2008).
29. Saha, S., Golestanian, R. & Ramaswamy, S. Clusters, asters and collective oscillations in chemotactic colloids. *Phys. Rev. E* **89,** 062316 (2014).
30. Theriot, J. A. & Mitchison, T. J. Actin microfilament dynamics in locomoting cells. *Nature* **352,** 126–131 (1991).
31. Berg, H. C. E. coli *in Motion* (Springer, 2004).

Supplementary Information is available in the online version of the paper.

Acknowledgements We thank all members of the Prakash Laboratory for discussions. We thank J. C. Williams for early support of this work, B. Buisson for discussions, and G. R. Dick for discussions and reagents. N.J.C. is supported by a National Science Foundation Graduate Research Fellowship Program fellowship. A.B. is supported by the Pew Foundation. M.P. is supported by the Pew Program in Biomedical Sciences, the Terman Fellowship, Keck Foundation, the Gordon and Betty Moore Foundation and a National Science Foundation Career Grant.

Author Contributions N.J.C. made the original observation. All authors designed the research. N.J.C. and A.B. conducted experiments, and all authors interpreted the data; N.J.C. and A.B. developed the models. N.J.C and A.B. wrote the manuscript, and all authors commented on it.

Author Information Reprints and permissions information is available at www.nature.com/reprints. The authors declare no competing financial interests. Readers are welcome to comment on the online version of the paper. Correspondence and requests for materials should be addressed to M.P. (manup@stanford.edu).

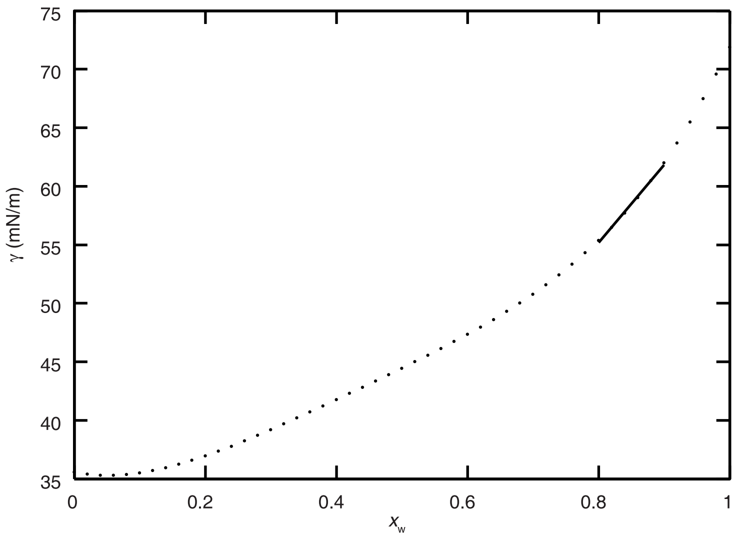

Extended Data Figure 1 | Surface tension γ_{LV} of PG/water mixtures as a function of mass fraction of water, x_w. Data extracted from ref. 27. We used the fourth-order polynomial, $\gamma_{LV} = 113x^4 - 192.27x^3 + 126.57x^2 - 11.69x + 35.6$ to fit this data. The data are fitted well by a linear function for a water fraction between 0.8 and 0.9.

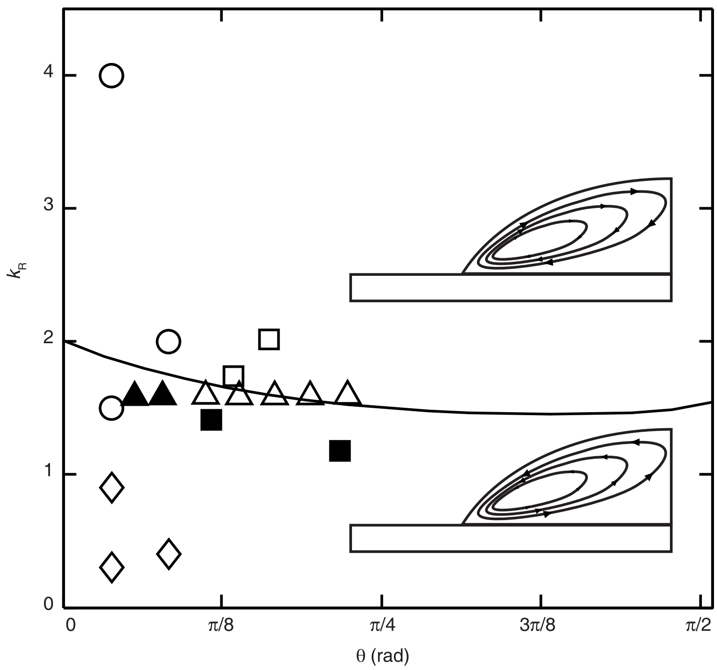

Extended Data Figure 2 | Conductivity ratio k_R versus contact angle θ. Data extracted from ref. 32. k_R indicates the ratio of conductivities between the substrate and liquid. Above the solid line, thermocapillarity is expected to drive flow clockwise in the half-droplet shown (upper inset), while below the solid line thermocapillarity predicts a counterclockwise flow (lower inset). Open symbols indicate clockwise flow and closed symbols indicate counterclockwise flow. Squares (from ref. 32) indicate chloroform, isopropanol, ethanol, and methanol on poly(dimethylsiloxane); triangles (from ref. 19) indicate water on glass; circles (this work) show PG/water on glass slides; and diamonds (this work) show PG/water on ITO/PET substrates. In our system we sample a space above and below this separation line, yet we observe flow only in one direction, which indicates that thermocapillarity is not the dominant effect. (See Supplementary Information section 2.5.)

32. Ristenpart, W. D., Kim, P. G., Domingues, C., Wan, J. & Stone, H. A. Influence of substrate conductivity on circulation reversal in evaporating drops. *Phys. Rev. Lett.* **99,** 234502 (2007).

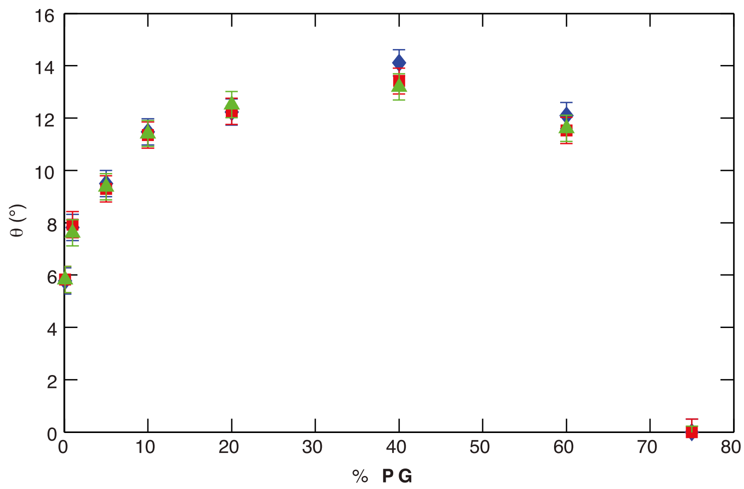

Extended Data Figure 3 | Contact angle of PG/water mixtures on surfaces of various conductivities. We measured contact angle by reflectometry on corona-discharge-cleaned glass slides (green triangles), corona-discharge-cleaned glass coverslips (136 μm thickness, red squares), and plasma-oven-treated ITO/PET (blue diamonds). If thermocapillarity were the only driving force for droplet stabilization the droplet would be predicted to spread on the ITO/PET. If thermocapillarity had a detectable role in stabilizing the droplets then we would expect to measure different contact angles for our droplets on these different substrates. (See Supplementary Information section 2.5.) Error bars are the range of three measurements at 75% RH.

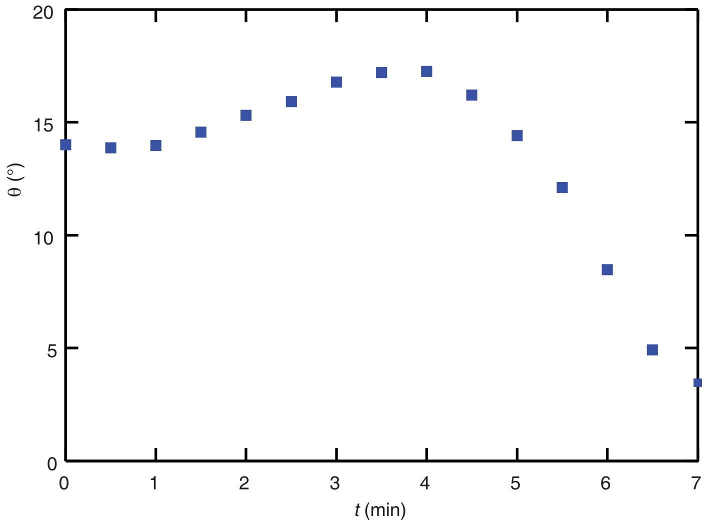

Extended Data Figure 4 | Contact angle change with time for a 0.5 μl 10% PG droplet at 30% RH. Contact angle changes very little at the minute scale. Over longer timescales as evaporation occurs, the volume fraction of PG in the bulk droplet becomes higher and the equilibrium contact angle changes to reflect the new concentration. The rate of evaporation sets a limit for the duration of the effects.

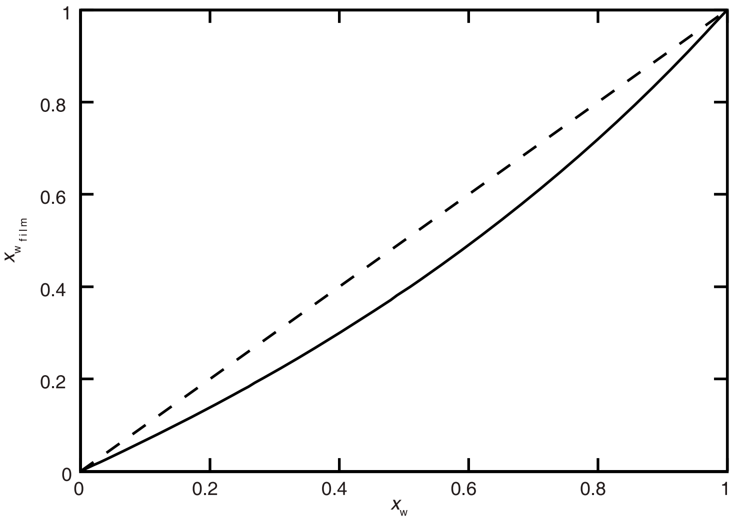

Extended Data Figure 5 | Film water volume fraction (solid line) as a function of the droplet volume fraction at 40% RH as predicted by our model. The dotted line is added to highlight the bulk droplet fraction. The difference between these lines is the concentration difference between the droplet and the thin film.

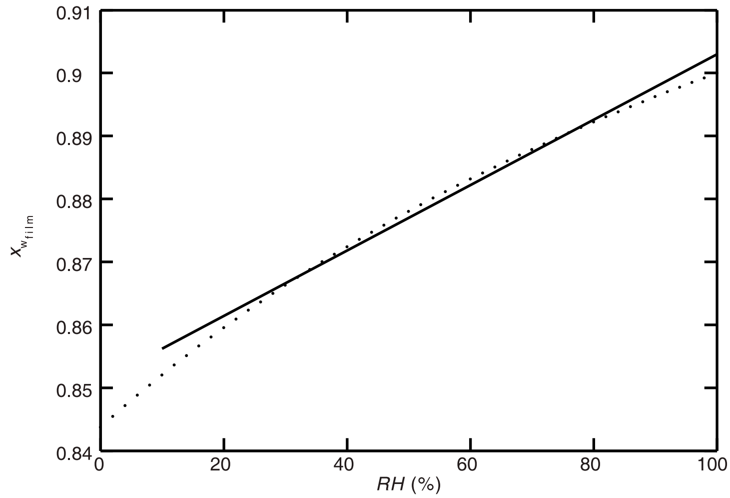

Extended Data Figure 6 | Film water volume fraction as a function of external humidity. Data shown for a 10% PG droplet as predicted by the model (dotted line). Note that over this range the variation can be approximated as a linear function (solid line).

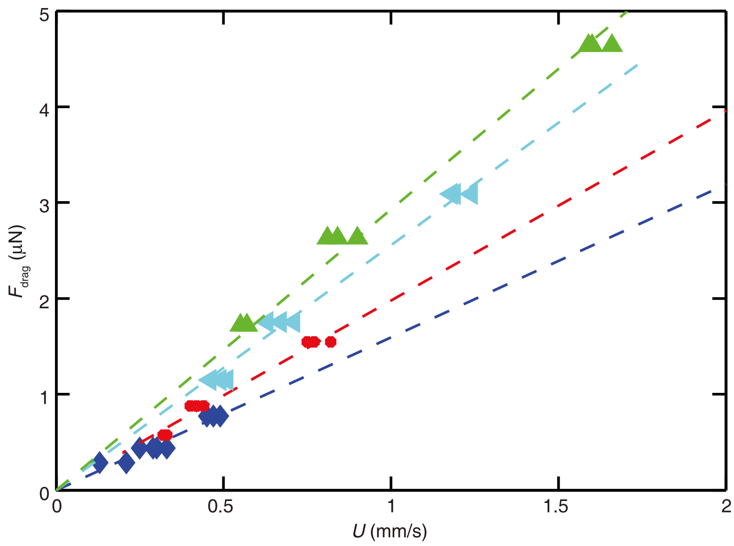

Extended Data Figure 7 | Drag force F_{drag} as a function of velocity *U*. Shown for 10% PG droplets of 0.25 μl (blue), 0.5 μl (red), 1 μl (cyan), 1.5 μl (green). The dashed lines represent the best linear fits.

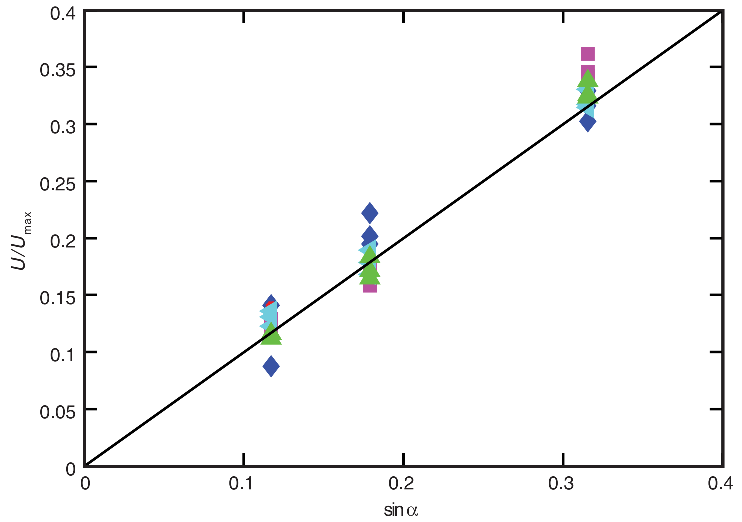

Extended Data Figure 8 | U/U_{max} as a function of sinα. Shown for the cutoff constant, $l_n = 11.2$, for 10% PG droplets of 0.25 μl (blue), 0.5 μl (red), 0.75 μl (magenta), 1 μl (cyan), 1.5 μl (green). The solid line represents the theoretical relation presented in the 'Drag coefficient theory' section (Supplementary Information section 2.1).

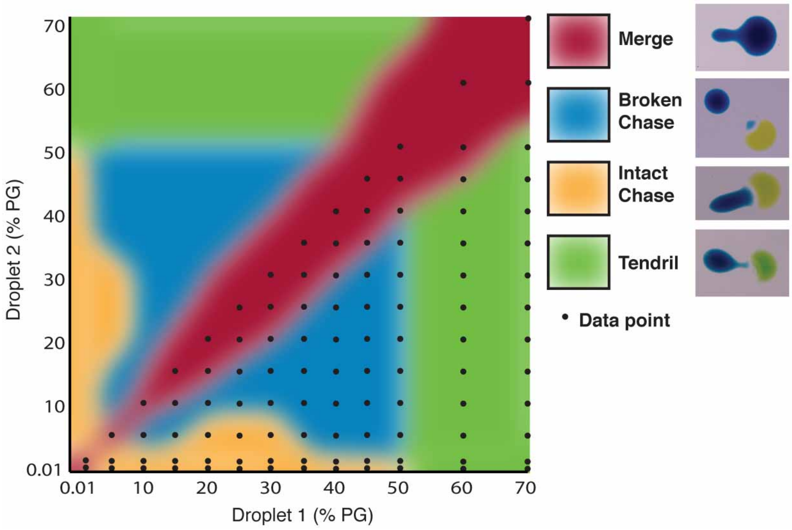

Extended Data Figure 9 | Phase plot of the short-range droplet interactions. 0.5 µl droplets of various concentrations. Each black dot indicates an experiment. Four qualitatively different regions are represented by colours and defined in the upper right. Exact boundaries between these regions are not always sharp.

Extended Data Table 1 | Behaviour of two-component chemical mixtures

	water	glycerol	ethylene glycol	1,3-butanediol	PG	DMSO	TPG	p-dioxane	DPGME	acetic acid	acetone	methanol	ethanol	IPA	1-propanol	pyridine	formic acid	ethanol amine	DMF	furfuryl alcohol	morpholine
Vapour pressure (mm Hg)	24	0.0002	0.08	0.06	0.15	0.6	0.01	37	0.4	16	231	127	59	45	21	21	45	0.4	3.3	0.8	10
Surface tension (mN/m)	73	64	48	47	36	43	30	33	28	27	23	22	22	23	21	37	38	48	34	53	39
water	2	1	1	1	1*	1	1	2	1	5	2	2	2	2	2	5	5	5	1	1	1
glycerol		2	2	2	2	2	2	2	2	2	5	2	2	2	2	5	2	2	2	2	2
ethylene glycol			2	2	2	2	5	2	2	2	5	2	2	2	2	2	2	2	2	2	2
1,3-butanediol				2	2	2	5	2	2	2	5	2	2	2	2	2	2	2	2	5	2
PG					2	2	5	2	2	2	5	2	2	2	2	2	2	2	2	5	2
DMSO						2	2	2	2	5	2	2	2	2	2	2	5	2	2	2	2
TPG							2	2	2	2	5	2	2	2	2	1	1	1	1	1	1
p-dioxane								5	1	5	2	2	2	2	1	2	5	2	2	2	2
DPGME									2	2	2	2	2	2	2	1	1	1	1	1	1
acetic acid										2	2	2	2	2	2	5	5	5	2	5	5
acetone											2	2	2	2	2	2	2	2	2	2	2
methanol												2	2	2	2	2	2	2	2	2	2
ethanol													2	2	2	2	2	2	2	2	2
IPA														2	2	2	2	2	2	2	2
1-propanol															2	2	1	2	2	2	2
pyridine																2	5	2	2	2	2
formic acid																	2	5	5	5	5
ethanol amine																		2	2	2	2
DMF																			2	5	2
furfuryl alcohol																				2	5
morpholine																					2

The table shows the behaviour of various two-component chemicals on clean glass. Chemicals were mixed in equal volume ratios and 0.5 µl of this mixture was placed on a treated glass slide. '1' indicates a droplet was formed. '2' indicates the mixture spread. '5' indicates a reaction is possible (for example, acid/base reactions are possible with water and formic acid), or the result was not clear (for example, the high viscosity of tripropylene glycol made some assessments difficult). Chemical vapour pressures and surface tensions were taken from various sources including vendors and published values. The asterisk indicates the water/PG mixture characterized in detail here. For abbreviations, see Supplementary Information section 1.3.

LETTER

doi:10.1038/nature14339

Increases in tropical rainfall driven by changes in frequency of organized deep convection

Jackson Tan[1]†, Christian Jakob[1], William B. Rossow[2] & George Tselioudis[3]

Increasing global precipitation has been associated with a warming climate resulting from a strengthening of the hydrological cycle[1]. This increase, however, is not spatially uniform. Observations and models have found that changes in rainfall show patterns characterized as 'wet-gets-wetter'[1–7] and 'warmer-gets-wetter'[5,8,9]. These changes in precipitation are largely located in the tropics and hence are probably associated with convection. However, the underlying physical processes for the observed changes are not entirely clear. Here we show from observations that most of the regional increase in tropical precipitation is associated with changes in the frequency of organized deep convection. By assessing the contributions of various convective regimes to precipitation, we find that the spatial patterns of change in the frequency of organized deep convection are strongly correlated with observed change in rainfall, both positive and negative (correlation of 0.69), and can explain most of the patterns of increase in rainfall. In contrast, changes in less organized forms of deep convection or changes in precipitation within organized deep convection contribute less to changes in precipitation. Our results identify organized deep convection as the link between changes in rainfall and in the dynamics of the tropical atmosphere, thus providing a framework for obtaining a better understanding of changes in rainfall. Given the lack of a distinction between the different degrees of organization of convection in climate models[10], our results highlight an area of priority for future climate model development in order to achieve accurate rainfall projections in a warming climate.

Changes in the hydrological cycle are of paramount importance to society. To improve the accuracy of projections of future precipitation, we need to understand the physical processes that underpin the observed and simulated changes in precipitation. In the tropics, these changes have been shown to follow a 'wet-gets-wetter'[1–7] or a 'warmer-gets-wetter'[5,8,9] pattern. Using global climate models, these patterns have been respectively attributed to thermodynamic[1,4–7] and dynamic changes[5,8,9] in the climate system. In observations, these changes explain the increase in rainfall over some tropical regions of convergence such as the Intertropical Convergence Zone (ITCZ)[2].

In addition to observed changes in rainfall, there is evidence from an analysis of satellite-derived cloud regimes that mesoscale organized deep convection has also increased in frequency tropics-wide over the past 27.5 years[11]. The cloud regime involved has a signature of deep convection combined with an extensive stratiform cloud and precipitation area, as is typical for convection with a high degree of organization[12]. Despite occurring only about 5% of the time, this organized deep convective regime is responsible for half the tropical rainfall[13–15], which is a testament to its extraordinary precipitation rate over a large area. What is unclear is whether the recent changes in precipitation are in any way related to changes in organized deep convection. Here we investigate this connection.

We make use of cloud regimes associated with precipitating convection derived through a cluster analysis of joint-histograms describing the distributions of cloud top pressures and optical thickness in 280 km × 280 km grid boxes at daily resolution from the International Satellite Cloud Climatology Project[16,17] (see Methods). These cloud regimes (also called weather states) constitute an objective categorization of the cloud field, and a subset of the regimes has been associated with precipitating convection[12–15,18–21]. Mesoscale organized deep convection is represented by the cloud regime CR1 as diagnosed from its cloud signature of widespread stratiform anvils (Fig. 1)[12], similarity in geographical distribution to mesoscale convective systems[22] (Extended Data Fig. 1), highly convective environments[12,13,18–21], and intense precipitation rates[12–15] (Fig. 2). It is this cloud regime that has been found to increase in frequency[11] (Extended Data Fig. 2). There are two more regimes associated with precipitating convection, namely CR2 and CR3, but both have less cloud cover (Fig. 1), lower precipitation rates (Fig. 2) and less organized cloud structures than CR1 (refs 12–15). These two regimes contribute 35% of the total rainfall between 1998 and 2009, in contrast with 47% by CR1 (Fig. 2). When these three regimes are taken together, their tropics-wide frequency has decreased slightly (Extended Data Fig. 2). This indicates that there has been a change in the distribution of the types of deep convection in the tropics, with less organized states decreasing in frequency and compensating for the increase in the occurrence of organized deep convection.

To make the connection between cloud regime and changes in rainfall, we decompose the change in total precipitation ΔP at every location into

$$\Delta P = \sum_i \Delta f_i \overline{p_i} + \overline{f_i} \Delta p_i \tag{1}$$

where f_i is the monthly-mean frequency of regime CRi and p_i is the monthly-mean within-regime precipitation rate of CRi; that is, the precipitation when the regime is present averaged over the month. The overbar denotes the mean over the entire period. In this framework, $\Delta f_i \overline{p_i}$ represents the contribution to the change in precipitation due to a change in monthly-mean frequency of the regime, and $\overline{f_i} \Delta p_i$ quantifies the contribution due to a change in the monthly-mean precipitation within the regime. We calculate the changes in regime frequency and within-regime precipitation rate as differences between the first and second halves of the data record. Because the derivation of within-regime precipitation rate requires the availability of daily rainfall information, we begin our investigation with the Tropical Rainfall Measuring Mission (TRMM) 3B42 precipitation data set[23] from 1998 to 2009, before extending our findings to the full cloud regime data set (July 1983 to December 2009) by using the Global Precipitation Climatology Project (GPCP) version 2.2 monthly rainfall product[24]. All data sets are interpolated to the ISCCP equal-area grid (see Methods).

Computing each term in equation (1) for each grid box enables us to examine the spatial distribution of the changes in precipitation and their association with cloud regime changes from 1998 to 2009. Monthly-mean precipitation shows changes of opposite sign in different regions, with increases in areas such as the Pacific ITCZ and the Tropical West Pacific, and decreases in the eastern Indian Ocean and south of the Pacific ITCZ (Fig. 3a). The spatial distribution of the contribution to changes in precipitation by changes in the frequency of organized deep

[1]ARC Centre of Excellence for Climate System Science, School of Earth, Atmosphere and Environment, Monash University, Clayton, Victoria 3800, Australia. [2]CREST Institute at the City College of New York, New York, New York 10031, USA. [3]NASA Goddard Institute for Space Studies, New York, New York 10027, USA. †Present address: NASA Wallops Flight Facility, Wallops Island, Virginia 23337, USA.

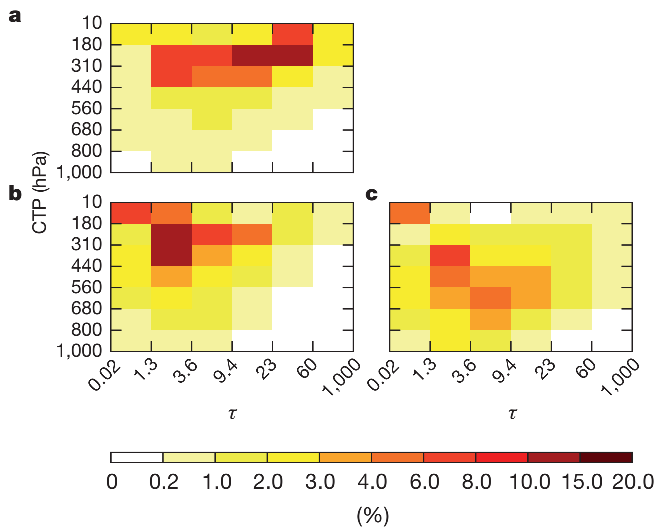

Figure 1 | Joint-histograms of the centroids of the convective cloud regimes. Cluster means (or centroids) of the convective cloud regimes in joint-histograms expressing the distribution of clouds in their cloud top pressure (CTP) and optical thickness (τ) of CR1 (**a**), CR2 (**b**) and CR3 (**c**). Bins in the top right area of the joint-histogram indicate clouds that are optically thick and have high tops, properties possessed by deep convective clouds. The cloud covers (sum over all bins) of the regimes are 95% (CR1), 90% (CR2) and 78% (CR3). The frequencies of the regimes over the entire period are 0.055 (CR1), 0.083 (CR2) and 0.142 (CR3).

convection ($\Delta f_1 \overline{p_1}$) closely resembles the changes in mean rainfall (Fig. 3b), with a correlation of 0.69 and a root mean squared error of 0.34 (Extended Data Fig. 3a; see Methods). In contrast, the contribution from changes in the within-regime precipitation of CR1 ($\overline{f_1}\Delta p_1$) is mostly negative and bears little resemblance to observed changes in precipitation (Fig. 3c). The spatial correlation is only 0.19 and the root mean squared error is 0.49. This indicates that, when present, organized deep convection has produced less precipitation in the latter part of the analysis period than in the former. The contribution from the remaining two convective regimes captures the observed patterns of change in precipitation but is of much smaller magnitude, particularly in regions of increases in precipitation (Fig. 3d). In contrast, in regions of decreases in precipitation, the two unorganized convective regimes contribute about the same magnitude to the change as the organized regime does. When taken together, the three convective regimes largely reproduce observed changes in precipitation (Fig. 3e), confirming that deep convection is the major contributor to changes in tropical rainfall. These conclusions also hold when the GPCP daily precipitation data set[25] is used (Extended Data Fig. 4).

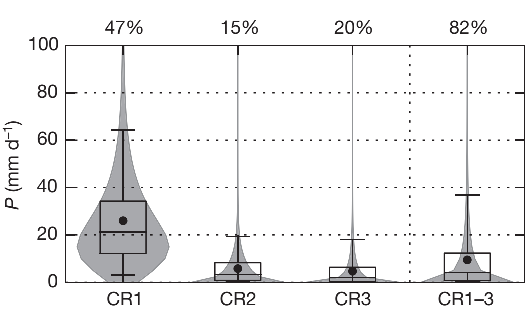

Figure 2 | Precipitation distributions of the convective CRs. Composites of daily precipitation from TRMM 3B42 with individual convective regimes (CR1, CR2 and CR3) as well as all convective regimes as one (CR1–3) between 1998 and 2009 in a 'violin' diagram, showing the mean (dot), median (horizontal line), interquartile range (box), 5th and 95th centiles (whiskers), and the probability distribution (grey 'violin'). The numbers at the top show the percentage contribution to the total precipitation over the entire period.

The analysis of the cloud regimes above indicates that it is organized rather than unorganized precipitating convection that is involved in the observed increase in rainfall in the past decade. To confirm this result we turn to a data set independent of ISCCP. A characteristic of organized deep convection is that the stratiform component of rainfall is greater than the convective component[12]. An increase in organized deep convection would therefore be identifiable through an increase in the area of stratiform precipitation as well as an increase in the relative contribution to the total precipitation by stratiform processes. The TRMM 3A25 data set[26] enables the calculation of both the stratiform rain area fraction f_{sa} and the stratiform rain rate fraction f_{sr} (see Methods). The spatial changes in both quantities show patterns similar to the change in total precipitation (Fig. 3f, g), especially over the oceans of the deep tropics (between about 15° N and 15° S). This confirms the conclusion reached in the analysis of the cloud regime, namely that an increase in tropical precipitation is a result of an increased frequency of organized deep convection.

Although instructive, the above analysis suffers from the lack of long-term daily precipitation observations over the oceans, which prevents a direct extension of the technique to the full period for which cloud regime data are available (July 1983 to December 2009) as a result of the inability to calculate p_i. We make an attempt at decomposing the changes in precipitation over the longer period by assuming that the values of p_i are equal to those of the shorter period (1998–2009). This enables us to calculate the contribution from changes in frequency of occurrence, $\Delta f_i \overline{p_i}$, of the three convective states for the full period to the longer-term changes in precipitation, for which we have monthly observations in the GPCP version 2.2 data set. This provides a first-order estimate of the relationship between change in precipitation and changes in the frequencies of various deep convective states.

The spatial distribution of the change in precipitation between July 1983 and December 2009 shares some similarity with the 1998–2009 period but has a smaller magnitude (Fig. 4a). An analysis of changes in rainfall for the shorter period using same data product shows that this disparity stems primarily from the difference in time period rather than the difference in data set. The contribution to the change in precipitation from the changes in frequency in organized deep convection alone, $\Delta f_1 \overline{p_1}$, still shows similarities with the overall change in the wet regions (Fig. 4b), albeit with a lower correlation of 0.43 and a root mean squared error of 0.33 in contrast with the shorter period (Extended Data Fig. 3b). Using all three convective regimes once again adds detail in regions of decrease in rainfall (Fig. 4c), but it fails to represent the changes in precipitation in some regions, in particular over the Indian Ocean, where there was no geostationary satellite before 1998 (ref. 11), which may affect measurements of CR2 and CR3. It is worth noting that assuming the value of p_i derived from the shorter period is a strong assumption that is not necessarily justified. In addition, for the shorter period the changes in within-regime precipitation were negative, thereby compensating for some of the increases in precipitation from changes in frequency. Having to neglect those terms for the longer time period probably contributes to the overestimation of the magnitude of changes in precipitation. Nevertheless, qualitatively the results for the longer period confirm our assertion that the observed increase in the frequency of organized deep convection in the tropics is the main contributor to the increase in precipitation.

The finding that it is mainly the frequency of organized deep convection that contributed to the increase in precipitation in the tropics provides insights from an unconventional perspective to the question of whether changes in precipitation are dynamic[5,8,9] or thermodynamic[1,4–7] in origin. The frequency of organized deep convection is typically associated with the dynamics of the climate system such as the large-scale circulation[13–15,18]. Indeed, there is a good spatial correspondence between changes in the dynamics of the tropical atmosphere, as reflected by large-scale mid-tropospheric vertical velocity, and that of organized deep convection (Extended Data Fig. 5). One can therefore argue that the changes in organized deep convection reflect a dynamic change in

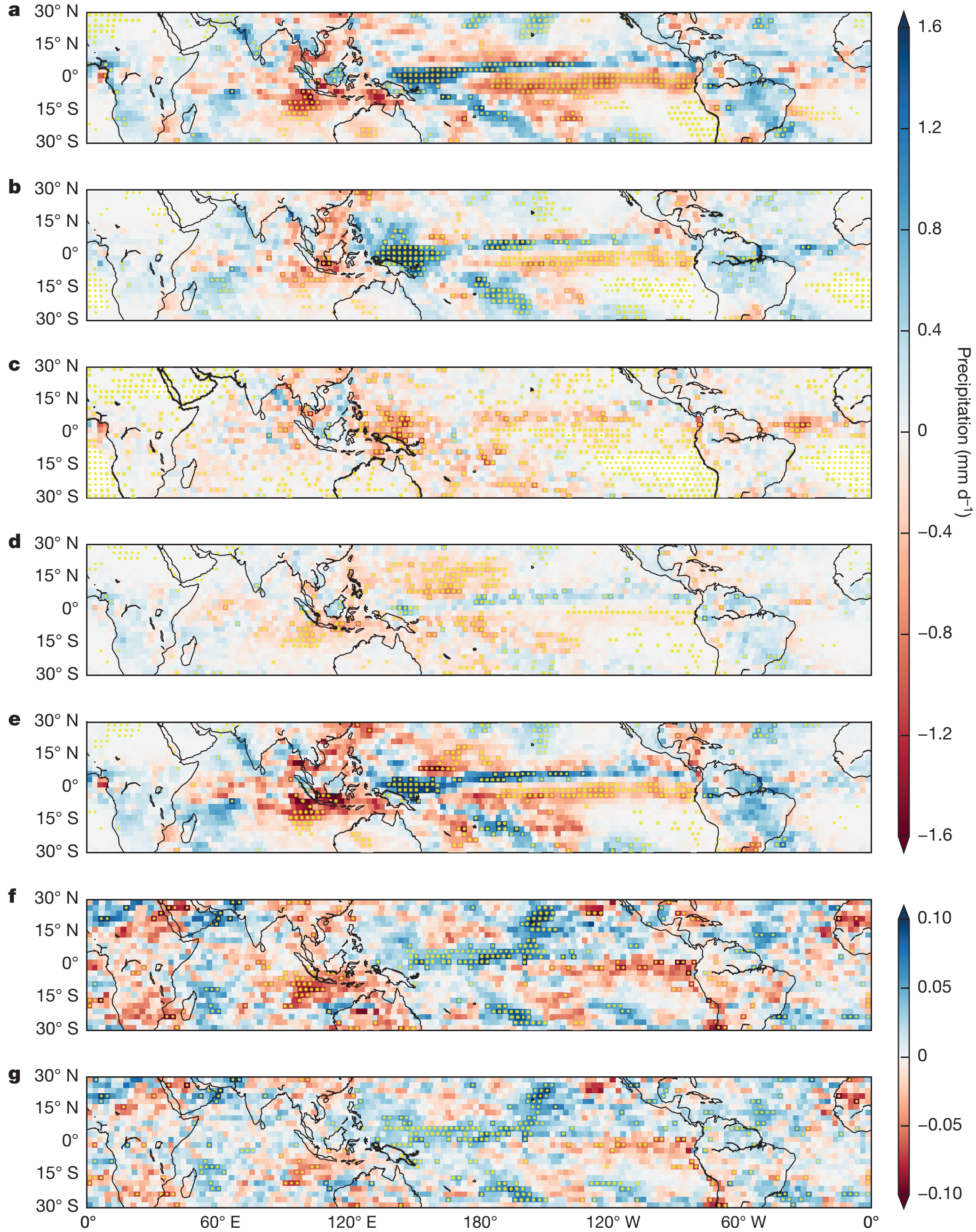

Figure 3 | The spatial distribution of the changes in precipitation from 1998 to 2009. **a**, Change in monthly-mean precipitation, ΔP. **b**, Contribution from the change in CR1 frequency, $\Delta f_1\overline{p_1}$. **c**, Contribution from the change in within-CR1 rainfall, $\overline{f_1}\Delta p_1$. **d**, Sum of the contributions from CR2 and CR3, $\Delta f_2\overline{p_2}+\overline{f_2}\Delta p_2+\Delta f_3\overline{p_3}+\overline{f_3}\Delta p_3$. **e**, Sum of the contributions from all three convective regimes, $\sum_{i=1}^{3}\Delta f_i\overline{p_i}+\overline{f_i}\Delta p_i$. **f**, **g**, Change in stratiform area fraction, Δf_{sa} (**f**), and stratiform rain fraction, Δf_{sr} (**g**). Grid boxes with changes significant at $P < 0.1$ using the Monte Carlo permutation test are stippled, with the dots in yellow for visibility against dark backgrounds. See Extended Data Fig. 3a for correlations and root mean squared errors.

the climate system. This argument is strengthened by our finding that changes in within-regime precipitation of CR1, which are probably more characteristic of a thermodynamic response, have contributed mainly to a decline in precipitation.

If changes in precipitation are mediated through organized deep convection, this calls into question the ability of global climate models (GCMs) to predict changes in rainfall accurately, especially in extreme precipitation[15]. GCMs are currently unable to simulate any organized forms of deep convection, because convection is represented through an ensemble of unorganized buoyant plumes. This lack of organized deep convection is a well-known issue in GCMs[10] and might well be a contributing factor to longstanding precipitation errors in models such as the bias towards light rain. Model projections of precipitation are therefore made in the absence of a phenomenon prominent in the hydrological cycle. From our findings here, it is likely that this limitation in GCMs contributes to the disagreements[4] between projected and observed changes in precipitation.

As a result of the inability of GCMs to represent organized deep convection, its effects are usually neglected in the analysis of precipitation projections. Given the societal importance of accurate precipitation projections in a warming climate, the role of organized deep convection in changes in precipitation identified in this study calls for a renewed effort to include a representation of convective organization in GCMs.

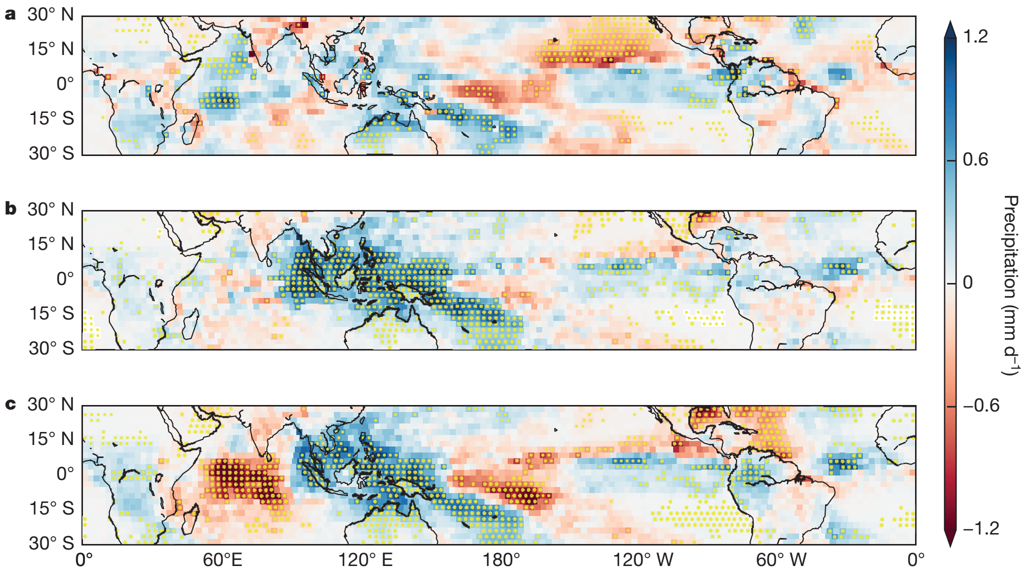

Figure 4 | The spatial distribution of the changes in precipitation from July 1983 to December 2009. **a**, Change in monthly-mean precipitation, ΔP, from GPCP 2.2. **b**, Contribution from the change in CR1 frequency, $\Delta f_1 \overline{p_1}$. **c**, Sum of the contributions from changes in the frequencies of the three convective regimes, $\sum_{i=1}^{3} \Delta f_i \overline{p_i}$. The mean within-regime precipitation p_i is assumed to be equal to that of TRMM 3B42. See the legend to Fig. 3 on stippling, and Extended Data Fig. 3b for correlations and root mean squared errors. Note the difference in the range of the colour scale from that in Fig. 3.

Online Content Methods, along with any additional Extended Data display items and Source Data, are available in the online version of the paper; references unique to these sections appear only in the online paper.

Received 23 September 2014; accepted 11 February 2015.

1. Held, I. M. & Soden, B. J. Robust responses of the hydrological cycle to global warming. *J. Clim.* **19,** 5686–5699 (2006).
2. Allan, R. P., Soden, B. J., John, V. O., Ingram, W. & Good, P. Current changes in tropical precipitation. *Environ. Res. Lett.* **5,** 025205 (2010).
3. Liu, C. & Allan, R. P. Multisatellite observed responses of precipitation and its extremes to interannual climate variability. *J. Geophys. Res.* **117,** D03101 (2012).
4. Chou, C. *et al.* Increase in the range between wet and dry season precipitation. *Nature Geosci.* **6,** 263–267 (2013).
5. Huang, P., Xie, S.-P., Hu, K., Huang, G. & Huang, R. Patterns of the seasonal response of tropical rainfall to global warming. *Nature Geosci.* **6,** 357–361 (2013).
6. Chou, C., Neelin, J. D., Chen, C.-A. & Tu, J.-Y. Evaluating the 'rich-get-richer' mechanism in tropical precipitation change under global warming. *J. Clim.* **22,** 1982–2005 (2009).
7. Seager, R., Naik, N. & Vecchi, G. A. Thermodynamic and dynamic mechanisms for large-scale changes in the hydrological cycle in response to global warming. *J. Clim.* **23,** 4651–4668 (2010).
8. Xie, S.-P. *et al.* Global warming pattern formation: sea surface temperature and rainfall. *J. Clim.* **23,** 966–986 (2010).
9. Chadwick, R., Boutle, I. & Martin, G. Spatial patterns of precipitation change in CMIP5: why the rich do not get richer in the tropics. *J. Clim.* **26,** 3803–3822 (2013).
10. Mapes, B. & Neale, R. Parameterizing convective organization to escape the entrainment dilemma. *J. Adv. Model. Earth Syst.* **3,** M06004 (2011).
11. Tselioudis, G., Tromeur, E., Rossow, W. B. & Zerefos, C. S. Decadal changes in tropical convection suggest effects on stratospheric water vapor. *Geophys. Res. Lett.* **37,** L14806 (2010).
12. Jakob, C. & Schumacher, C. Precipitation and latent heating characteristics of the major Tropical Western Pacific cloud regimes. *J. Clim.* **21,** 4348–4364 (2008).
13. Tan, J., Jakob, C. & Lane, T. P. On the identification of the large-scale properties of tropical convection using cloud regimes. *J. Clim.* **26,** 6618–6632 (2013).
14. Lee, D., Oreopoulos, L., Huffman, G. J., Rossow, W. B. & Kang, I.-S. The precipitation characteristics of ISCCP tropical weather states. *J. Clim.* **26,** 772–788 (2013).
15. Rossow, W. B., Mekonnen, A., Pearl, C. & Goncalves, W. Tropical precipitation extremes. *J. Clim.* **26,** 1457–1466 (2013).
16. Jakob, C. & Tselioudis, G. Objective identification of cloud regimes in the Tropical Western Pacific. *Geophys. Res. Lett.* **30,** 2082 (2003).
17. Rossow, W. B., Tselioudis, G., Polak, A. & Jakob, C. Tropical climate described as a distribution of weather states indicated by distinct mesoscale cloud property mixtures. *Geophys. Res. Lett.* **32,** L21812 (2005).
18. Jakob, C., Tselioudis, G. & Hume, T. The radiative, cloud, and thermodynamic properties of the major tropical western Pacific cloud regimes. *J. Clim.* **18,** 1203–1215 (2005).
19. Li, W., Schumacher, C. & McFarlane, S. A. Radiative heating of the ISCCP upper level cloud regimes and its impact on the large-scale tropical circulation. *J. Geophys. Res. Atmos.* **118,** 592–604 (2013).
20. Stachnik, J. P., Schumacher, C. & Ciesielski, P. E. Total heating characteristics of the ISCCP tropical and subtropical cloud regimes. *J. Clim.* **26,** 7097–7116 (2013).
21. Handlos, Z. J. & Back, L. E. Estimating vertical motion profile shape within tropical weather states over the oceans. *J. Clim.* **27,** 7667–7686 (2014).
22. Laing, A. G. & Fritsch, J. M. The global population of mesoscale convective complexes. *Q. J. R. Meteorol. Soc.* **123,** 389–405 (1997).
23. Huffman, G. J. *et al.* The TRMM Multisatellite Precipitation Analysis (TMPA): quasi-global, multiyear, combined-sensor precipitation estimates at fine scales. *J. Hydrometeorol.* **8,** 38–55 (2007).
24. Adler, R. F. *et al.* The version-2 global precipitation climatology project (GPCP) monthly precipitation analysis (1979–present). *J. Hydrometeorol.* **4,** 1147–1167 (2003).
25. Huffman, G. J. *et al.* Global precipitation at one-degree daily resolution from multisatellite observations. *J. Hydrometeorol.* **2,** 36–50 (2001).
26. Iguchi, T., Kozu, T., Meneghini, R., Awaka, J. & Okamoto, K. Rain-profiling algorithm for the TRMM precipitation radar. *J. Appl. Meteorol.* **39,** 2038–2052 (2000).

Acknowledgements. We thank S. Sherwood and B. Stevens for comments on the study. The GPCP combined precipitation data were developed and computed by the NASA/Goddard Space Flight Centre's Mesoscale Atmospheric Processes Laboratory as a contribution to the GEWEX Global Precipitation Climatology Project, and provided by National Oceanic and Atmospheric Administration (NOAA) Office of Oceanic and Atmospheric Research and Earth System Research Laboratory Physical Sciences Division (PSD) at http://www.esrl.noaa.gov/psd/. The TRMM 3B42 and 3A25 data were provided by the NASA/Goddard Space Flight Center's Mesoscale Atmospheric Processes Laboratory and Precipitation Processing System as a contribution to TRMM, and archived at the NASA Goddard Earth Sciences Data and Information Services Center. J.T. and C.J. are funded under the Australian Research Council Centre of Excellence for Climate System Science (CE110001028). W.B.R. is supported by NASA grant NNX13AO39G. G.T. acknowledges the support of the NASA Modeling Analysis and Prediction (MAP) programme managed by D. Considine. J.T. acknowledges support from the Monash University Postgraduate Publication Award.

Author Contributions J.T. and C.J. designed the study. J.T. conducted the analysis and obtained the results. C.J., W.B.R. and G.T. advised on the approach. J.T., W.B.R. and G.T. checked regime time series for satellite artefacts. All authors discussed the results and contributed to the preparation of the manuscript.

Author Information Reprints and permissions information is available at www.nature.com/reprints. The authors declare no competing financial interests. Readers are welcome to comment on the online version of the paper. Correspondence and requests for materials should be addressed to J.T. (jackson.tan@nasa.gov).

METHODS

Cloud regimes. The cloud regimes (or weather states) are derived from the International Satellite Cloud Climatology Project (ISCCP) D1 data set[27] using a k-means clustering algorithm applied to the daytime-averaged joint-histograms of cloud top pressure and optical thickness over grid boxes of 280 km × 280 km from July 1983 to December 2009 (refs 16, 17). The number of regimes is determined through an objective set of criteria[17]. When applied to grid boxes between ±35° latitudes, we obtain eight cloud regimes, three of which possess precipitating convective clouds in their centroids (CR1, CR2 and CR3). These eight regimes are highly similar to those in cloud regime studies using 3-hourly (but daytime-only) ISCCP joint-histograms[28]. CR1 represents mesoscale organized deep convection according to its fingerprint of a large population of deep convective and thick stratiform anvil clouds, its extensive cloud cover, its geographical distribution and its precipitation characteristics. CR2 represents deep convection that is less organized in its nature, with some stratiform anvil as well as cirrus clouds. CR3 represents isolated deep convection with a larger abundance of shallower clouds that are suggestive of cumulus congesti, thus probably indicating a nascent phase of organized deep convection. The frequencies between ±35° latitudes of the regimes over the entire period are 0.055 (CR1), 0.083 (CR2) and 0.142 (CR3). These three convective regimes are very similar to those obtained in the deep tropics between ±15° latitudes[17]. All subsequent analyses are constrained to ±30° latitudes for consistency with other similar tropical precipitation studies[2,3,6,9].

Precipitation. For precipitation rates from 1998 to 2009, we use the 3-hourly Tropical Rainfall Measuring Mission (TRMM) version 7 Multisatellite Precipitation Analysis 3B42 product[23]. For precipitation rates from July 1983 to December 2009, we use the Global Precipitation Climatology Project (GPCP) version 2.2 monthly rainfall product[24]. For quantities on stratiform precipitation, we use the monthly TRMM version 7 3A25 product at 0.5° resolution[26]. Stratiform rain area fraction is defined as the counts of non-zero estimated surface rain conditioned on stratiform rain divided by the counts of non-zero estimated surface rain. The stratiform rain rate fraction is defined as the mean of non-zero estimated surface stratiform rain rate divided by the mean of non-zero estimated total surface rain rate. Because precipitation rates are dependent on resolution, we coarsened the values to 2.5° resolution. Values in 3B42 are also first averaged over daytime to a daily resolution. All quantities are then linearly interpolated to the ISCCP equal-area grid (see http://isccp.giss.nasa.gov/docs/mapgridinfo.html). The GPCP One-Degree Daily (1DD) version 1.2 data set[25] (1997–2009) is also employed to verify the results from TRMM 3B42 (Extended Data Fig. 4).

Vertical velocity. Grid-mean vertical motion at 500 hPa for Extended Data Fig. 5 is obtained from the European Centre for Medium-Range Weather Forecasts Interim Re-Analysis data[29]. The values are averaged from the 6 h intervals to a daily resolution and, as with precipitation, interpolated to the ISCCP grids.

Regime and changes in precipitation. Satellite artefacts in ISCCP have been known to affect the quantities of cirrus clouds detected[30], but cloud regimes are more robust against such artificial signals[11]. This is confirmed by an absence of circular patterns indicative of satellite artefacts in the spatial distributions of the regression of frequency changes in each grid box to the overall frequency change. Furthermore, we did not find any correspondence between sudden major changes in the frequency of CR1 and key satellite events or ancillary changes listed in the ISCCP metadata archives.

In calculating the change Δ, we take the difference between the means of the second half and the first half of the period. This option was chosen over least-squares linear regression because it conserves the relationship from $P = \sum_i f_i p_i$ to equation (1). Separate analyses using linear regression found no substantial differences from our results.

Spatial correlation and root mean squared error. Spatial correlation is the Pearson correlation of the two arrays representing the changes over the grid boxes. Because of the large number of grid boxes ($n = 3{,}298$), all correlations calculated are statistically significant at $P < 0.01$. However, the observed noise in the changes in precipitation can decrease a perfect correlation to between 0.72 and 0.79, derived from the average correlation ($n = 10{,}000$) between Δf and $\Delta f + N(0, \sigma_P/\mu_P \times \mu_{\Delta f})$, where f is the frequency of the variables, μ and σ are respectively the mean and standard deviation, and N is a Gaussian random noise. Root mean squared error is calculated by taking the square root of the mean of the square of the difference between two arrays. It captures the degree to which the two arrays are different in magnitude in each grid box, and is useful as a relative measure.

Statistical significance. The Monte Carlo permutation test was used to evaluate the statistical significance of the spatial distributions (Figs 3 and 4 and Extended Data Fig. 4), on the null hypothesis that the means of the two halves of the time period were the same. Each grid box was randomly permuted 10,000 times. Being non-parametric, this test is applicable for rainfall, which does not have a normal distribution.

Data. The ISCCP D1 data set, from which the cloud regimes are derived, can be obtained following the instructions at http://isccp.giss.nasa.gov/products/obtaining.html. Both TRMM 3B42 and 3A25 can be downloaded from NASA PMM at http://pmm.nasa.gov/data-access/downloads/trmm. GPCP 2.2 is available from NOAA PSD at http://www.esrl.noaa.gov/psd/data/gridded/data.gpcp.html, and GPCP 1DD can be downloaded from NOAA National Climatic Data Center at http://www1.ncdc.noaa.gov/pub/data/gpcp/1dd-v1.2/. ERA-Interim vertical velocity data can be downloaded from the European Centre for Medium-Range Weather Forecasts at http://apps.ecmwf.int/datasets/.

Code availability. All the codes used in the analysis in this paper and in the production of figures are available at https://github.com/JacksonTanBS/2015_Tan-et-al._Nature.

27. Rossow, W. B. & Schiffer, R. A. Advances in understanding clouds from ISCCP. *Bull. Am. Meteorol. Soc.* **80,** 2261–2287 (1999).
28. Oreopoulos, L. & Rossow, W. B. The cloud radiative effects of International Satellite Cloud Climatology Project weather states. *J. Geophys. Res.* **116,** D12202 (2011).
29. Dee, D. P. *et al.* The ERA-Interim reanalysis: configuration and performance of the data assimilation system. *Q. J. R. Meteorol. Soc.* **137,** 553–597 (2011).
30. Rossow, W. B., Walker, A. W. & Garder, L. C. Comparison of ISCCP and other cloud amounts. *J. Clim.* **6,** 2394–2418 (1993).

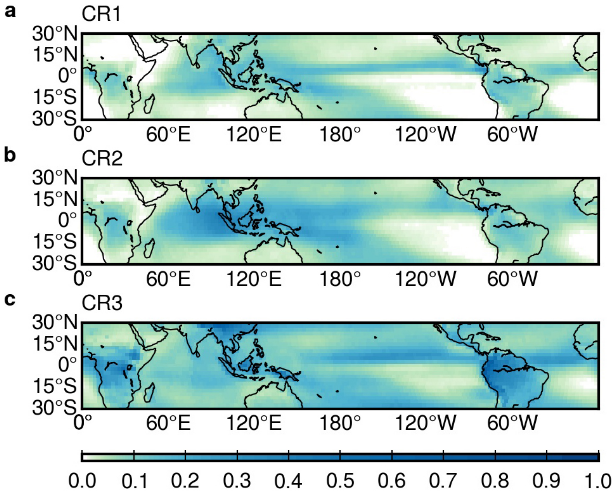

Extended Data Figure 1 | Geographical distribution of the convective cloud regimes. The frequency averaged over the entire period (July 1983 to December 2009) in each grid box for CR1 (**a**), CR2 (**b**), and CR3 (**c**).

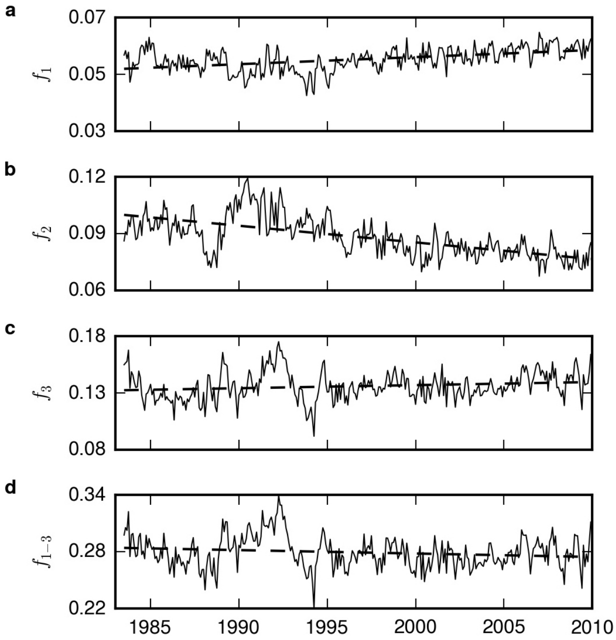

Extended Data Figure 2 | Time series of the frequencies of the convective regimes. Monthly-mean frequencies of CR1 (**a**), CR2 (**b**) and CR3 (**c**), as well as the sum of all convective regimes CR1–CR3 (**d**) in the entire domain between $\pm 30^\circ$ latitudes (solid lines). The linear least-squares regression slopes are also shown (dashed lines). The differences in means between the two halves at two standard deviations (95%) are 0.0043 ± 0.0008 (**a**), -0.014 ± 0.002 (**b**), 0.003 ± 0.003 (**c**) and -0.006 ± 0.004 (**d**).

a

Fig. 3	(b)	(c)	(d)	(e)	(f)	(g)
correlation to (a)	0.69	0.19	0.51	0.85	0.37	0.31
RMSE to (a)	0.34	0.49	0.39	0.26		

b

Fig. 4	(b)	(c)
correlation to (a)	0.43	0.39
RMSE to (a)	0.33	0.38

c

Extended Data Fig. 4	(b)	(c)	(d)	(e)
correlation to (a)	0.80	0.40	0.69	0.90
RMSE to (a)	0.35	0.50	0.40	0.24

Extended Data Figure 3 | Correlations and root mean squared errors of the spatial changes to change in total precipitation. Correlations and root mean squared errors with the first panel of the other panels in Fig. 3 (**a**), Fig. 4 (**b**) and Extended Data Fig. 4 (**c**).

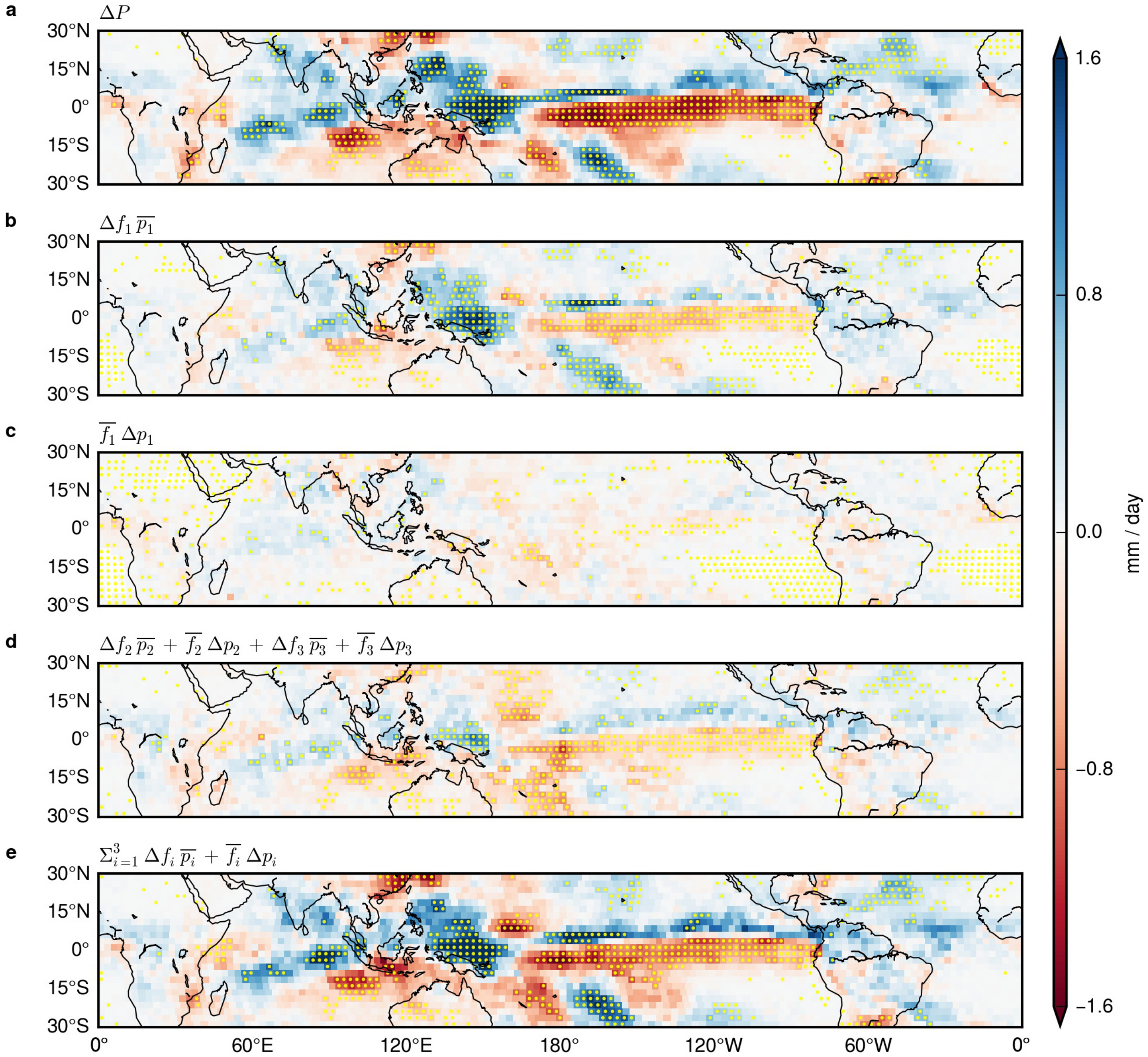

Extended Data Figure 4 | The spatial distribution of the changes in precipitation from 1997 to 2009 using GPCP 1DD. **a**, Change in monthly-mean precipitation from GPCP 1DD. **b**, Contribution from the change in CR1 frequency. **c**, Contribution from the change in within-CR1 rainfall. **d**, Sum of the contributions from the terms of CR2 and CR3. **e**, Sum of the contributions from the terms of all three convective regimes. See the legend to Fig. 3 on stippling, and Extended Data Fig. 3c for correlations and root mean squared errors.

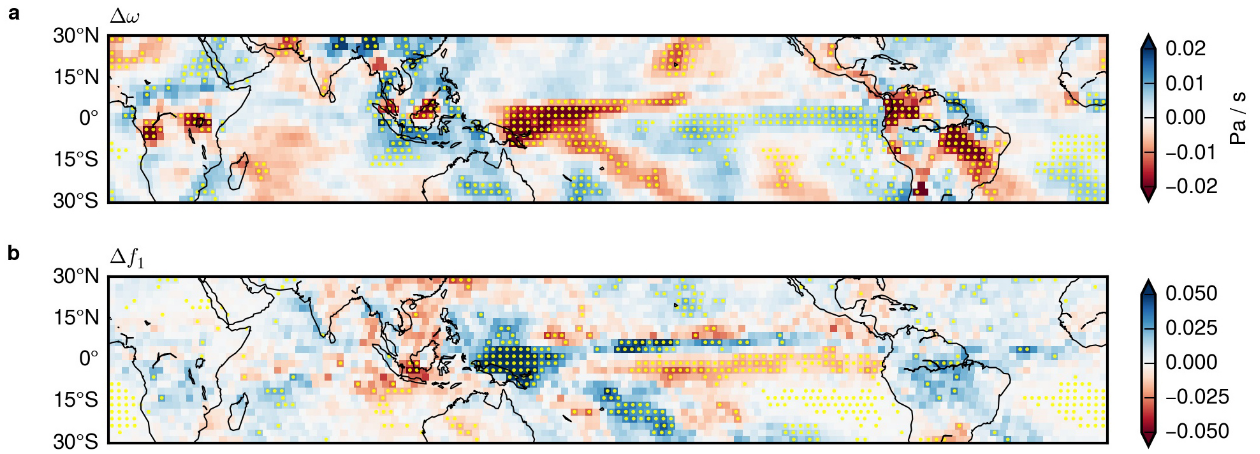

Extended Data Figure 5 | Comparison between changes in organized deep convection and changes in dynamics from 1998 to 2009. **a**, Changes in grid-mean vertical motion at 500 hPa from ERA-Interim (negative is ascending motion). **b**, Changes in frequency of CR1.

doi:10.1038/nature13978

The paraventricular thalamus controls a central amygdala fear circuit

Mario A. Penzo[1], Vincent Robert[1,2], Jason Tucciarone[1,3], Dimitri De Bundel[4]†, Minghui Wang[1], Linda Van Aelst[1], Martin Darvas[5], Luis F. Parada[6], Richard D. Palmiter[7], Miao He[8], Z. Josh Huang[1] & Bo Li[1]

Appropriate responses to an imminent threat brace us for adversities. The ability to sense and predict threatening or stressful events is essential for such adaptive behaviour. In the mammalian brain, one putative stress sensor is the paraventricular nucleus of the thalamus (PVT), an area that is readily activated by both physical and psychological stressors[1–3]. However, the role of the PVT in the establishment of adaptive behavioural responses remains unclear. Here we show in mice that the PVT regulates fear processing in the lateral division of the central amygdala (CeL), a structure that orchestrates fear learning and expression[4,5]. Selective inactivation of CeL-projecting PVT neurons prevented fear conditioning, an effect that can be accounted for by an impairment in fear-conditioning-induced synaptic potentiation onto somatostatin-expressing (SOM$^+$) CeL neurons, which has previously been shown to store fear memory[6]. Consistently, we found that PVT neurons preferentially innervate SOM$^+$ neurons in the CeL, and stimulation of PVT afferents facilitated SOM$^+$ neuron activity and promoted intra-CeL inhibition, two processes that are critical for fear learning and expression[5,6]. Notably, PVT modulation of SOM$^+$ CeL neurons was mediated by activation of the brain-derived neurotrophic factor (BDNF) receptor tropomysin-related kinase B (TrkB). As a result, selective deletion of either *Bdnf* in the PVT or *Trkb* in SOM$^+$ CeL neurons impaired fear conditioning, while infusion of BDNF into the CeL enhanced fear learning and elicited unconditioned fear responses. Our results demonstrate that the PVT–CeL pathway constitutes a novel circuit essential for both the establishment of fear memory and the expression of fear responses, and uncover mechanisms linking stress detection in PVT with the emergence of adaptive behaviour.

To probe the sensitivity of the PVT to threatening events, we examined the expression of c-Fos, a marker of recent neuronal excitation, both following fear conditioning and after a fear memory retrieval test. Fear conditioning markedly increased the number of neurons expressing c-Fos in the posterior PVT (pPVT) (Extended Data Fig. 1), consistent with the finding that the pPVT receives direct inputs from the nociceptive parabrachial nucleus and the periaqueductal grey[7,8]. Notably, fear memory retrieval induced a similar increase in pPVT c-Fos expression (Extended Data Fig. 1). These results demonstrate that the pPVT is recruited by both the unconditioned stimulus and the threat-predicting conditioned stimulus, and raise the possibility that it might be instrumental in fear conditioning.

The pPVT strongly projects to the CeL[9,10], with weaker projections to other amygdala nuclei, such as the basolateral amygdala (BLA)[10]. To examine the distribution patterns of pPVT neurons innervating different amygdala subregions, we injected the CeL and BLA with the retrograde tracer cholera toxin subunit B conjugated to Alexa Fluor-488 (CTB-488) or Alexa Fluor-555 (CTB-555), respectively. This approach resulted in dense labelling throughout the ipsilateral pPVT, indicating prominent pPVT–amygdala projections (Extended Data Fig. 2). Notably, pPVT neurons projecting to the CeL and BLA were largely non-overlapping (Extended Data Fig. 2).

To determine whether the pPVT–CeL pathway, the most prominent projection originating from the pPVT[9,10], is involved in fear conditioning, we sought to selectively inhibit CeL-projecting neurons in the pPVT through a chemogenetic method[11]. We bilaterally injected the CeL with a retrograde canine adenovirus expressing Cre recombinase (CAV2-Cre)[12], followed by injection into the pPVT of AAV-DIO-hM4Di-mCherry, an adeno-associated virus harbouring a double-floxed inverted open reading frame (AAV-DIO) that expresses, in a Cre-dependent manner, an engineered G_i-coupled receptor hM4Di tagged with a fluorescent protein mCherry (hM4Di–mCherry). This intersectional strategy effectively targeted CeL-projecting pPVT neurons (Fig. 1a, b), which can subsequently be suppressed by treating mice with clozapine-*N*-oxide

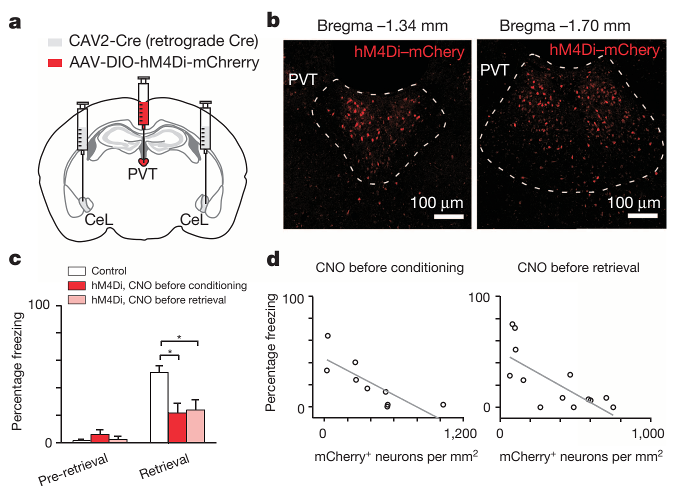

Figure 1 | CeL-projecting pPVT neurons are essential for both learning and expression of conditioned fear. **a**, A schematic of the experimental approach. **b**, Representative images showing the expression of hM4Di–mCherry in CeL-projecting pPVT neurons. **c**, Quantification of freezing levels in memory retrieval test. Control, $n = 15$ mice; hM4Di with CNO before conditioning, $n = 9$ mice; hM4Di with CNO before retrieval, $n = 13$ mice; effect of treatments, $F_{(2,68)} = 5.14$, $P < 0.01$; effect of condition stimulus presentation, $F_{(1,68)} = 51.27$, $P < 0.001$; interaction, $F_{(2,68)} = 7.42$, $P < 0.01$; $*P < 0.05$; two-way analysis of variance (ANOVA) followed by Tukey's test. The control group contains mice that were injected only with CAV2-Cre bilaterally in the CeL and were treated with CNO either before conditioning ($n = 7$ mice) or before retrieval ($n = 8$ mice). **d**, Correlation between viral infection efficiency in pPVT and the behavioural effect. CNO before conditioning, $R^2 = 0.59$, $P < 0.01$, $n = 9$ mice; CNO before retrieval, $R^2 = 0.47$, $P < 0.05$, $n = 13$ mice; linear regression lines are shown in grey. Data are presented as mean ± s.e.m.

[1]Cold Spring Harbor Laboratory, Cold Spring Harbor, New York 11724, USA. [2]Ecole Normale Supérieure de Cachan, 94230 Cachan, France. [3]Medical Scientist Training Program & Program in Neuroscience, Stony Brook University, Stony Brook, New York 11790, USA. [4]CNRS, UMR-5203, INSERM U661, Institut de Génomique Fonctionnelle, 34090 Montpellier, France. [5]Department of Pathology, University of Washington, Seattle, Washington 98104, USA. [6]Department of Developmental Biology, University of Texas Southwestern Medical Center, Dallas, Texas 75390, USA. [7]Howard Hughes Medical Institute; Department of Biochemistry, University of Washington, Seattle, Washington 98195, USA. [8]Institutes of Brain Science and State Key Laboratory of Medical Neurobiology, Fudan University, Shanghai 200032, China. †Present address: Center for Neurosciences, Vrije Universiteit Brussel, 1090 Brussels, Belgium.

(CNO), the agonist of hM4Di[11]. Notably, selective suppression of the CeL-projecting pPVT neurons during either conditioning or a 24-h memory retrieval test significantly impaired fear responses measured as freezing in the retrieval test (Fig. 1c and Extended Data Fig. 3). These behavioural effects significantly correlated with the number of hM4Di-expressing neurons in the pPVT (Fig. 1d), demonstrating the specificity and potency of our manipulation. Altogether, these results indicate that the pPVT is crucial for both the establishment and expression of fear memory.

We next determined the mechanisms by which the pPVT–CeL circuit contributes to fear regulation. Fear conditioning induces a potentiation of excitatory synapses onto SOM$^+$ CeL neurons, a synaptic change that stores fear memory[6]. To investigate whether the pPVT is required for this plasticity, we labelled SOM$^+$ CeL neurons with enhanced yellow fluorescent protein (eYFP) by injecting CeL with AAV-DIO-eYFP in *Som-cre* mice, in which the Cre recombinase is expressed under the endogenous *Som* promoter[6]. In addition, we injected the pPVT in the same mice with a mixture of AAV-GFP-Cre and AAV-DIO-hM4Di-mCherry (Fig. 2a–c). This strategy allowed us to inhibit pPVT neurons using the chemogenetic method during fear conditioning, and subsequently determine the effect on SOM$^+$ (eYFP$^+$) CeL neurons (Fig. 2 and Extended Data Fig. 3).

As previously reported[6], fear conditioning significantly enhanced excitatory synaptic transmission—measured as an increase in both the frequency and amplitude of miniature excitatory postsynaptic currents (mEPSCs)—onto SOM$^+$ CeL neurons (Fig. 2d, e). This synaptic potentiation can be detected at both 3 h and 24 h following conditioning[6]. Notably, inhibition of pPVT neurons during fear conditioning did not affect this synaptic potentiation when examined 3 h after conditioning (Fig. 2d, e). In contrast, the same manipulation completely abolished synaptic potentiation measured 24 h after conditioning (Fig. 2d, e). These results indicate that the pPVT is required for the maintenance or consolidation, but not the initial induction, of CeL plasticity, and are consistent with findings in an accompanying study that long-term

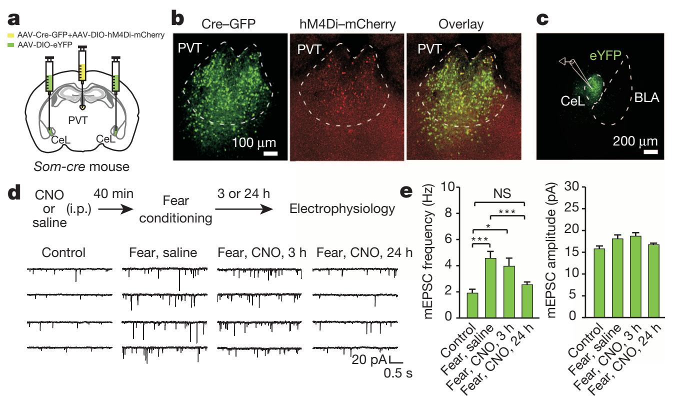

Figure 2 | The pPVT is required for the maintenance of fear conditioning-induced synaptic plasticity in the CeL. **a**, A schematic of the experimental approach. **b**, Representative images showing the expression of Cre–GFP and hM4Di–mCherry in the pPVT. **c**, SOM$^+$ (eYFP$^+$) CeL neurons in acute slices were targeted for recording. **d**, Top, a schematic of the experimental procedure. Bottom, representative traces of mEPSCs recorded from SOM$^+$ CeL neurons in mice of the following groups (from left to right): naive control; fear conditioned, treated with saline and killed 24 h after conditioning; fear conditioned, treated with CNO and killed 3 h after conditioning; and fear conditioned, treated with CNO and killed 24 h after conditioning. **e**, Quantification of mEPSC frequency (left) and amplitude (right). Frequency, $F_{(3,89)} = 8.4$, $^*P < 0.05$, $^{***}P < 0.001$; NS, non-significant ($P > 0.05$) (Control, $n = 16$ neurons (3 mice); 'Fear, saline', $n = 27$ neurons (4 mice); 'Fear, CNO, 3 h', $n = 16$ neurons (3 mice); 'Fear, CNO, 24 h', $n = 34$ neurons (3 mice)); Amplitude, $F_{(3,89)} = 2.9$, $P < 0.05$ (no significant difference was detected in the post-hoc analysis); one-way ANOVA followed by Tukey's test. Data are presented as mean ± s.e.m.

(≥24 h), but not short-term (0.5 and 6 h), fear memories are susceptible to PVT manipulations (see accompanying paper[13]).

As mEPSCs do not allow us to distinguish between different synaptic pathways, we next examined whether pPVT inactivation impairs plasticity at lateral-amygdala–CeL synapses, a pathway that presumably conveys conditioned-stimulus information to the CeL. For this purpose we used the *Som-cre;Rosa26-stop^{flox}-H2b-GFP* (*Som-cre;H2b-GFP*) mice[14] in which all SOM$^+$ CeL neurons are readily identified on the basis of the nucleus-localized GFP signal (Extended Data Fig. 4a). We inhibited pPVT neurons during fear conditioning using the same method as described above (Fig. 2a, b). We then simultaneously recorded pairs of adjacent SOM$^+$ (green fluorescent) and SOM$^-$ (non-fluorescent) CeL neurons in acute brain slices, while EPSCs were evoked by electrical stimulation in the lateral amygdala (Extended Data Fig. 4a). As previously reported[6], in naive control mice AMPA receptor (AMPAR)-mediated EPSCs were significantly larger in SOM$^-$ neurons than in SOM$^+$ neurons (Extended Data Fig. 4b, c), indicating a clear distinction between these two cell types in their intrinsic functional connectivity. However, fear conditioning reversed this relationship such that AMPAR-mediated transmission was significantly stronger in SOM$^+$ neurons than in SOM$^-$ neurons (Extended Data Fig. 4b, c).

Fear conditioning also induced a decrease in the paired-pulse ratio of EPSCs (an indicator of increased presynaptic release probability) onto SOM$^+$ CeL neurons (Extended Data Fig. 4d). This result, when considered together with data obtained from the paired recording (Extended Data Fig. 4a–c) and mEPSC recording (Fig. 2d, e) experiments (also see ref. 6), demonstrates that fear conditioning strengthens excitatory synaptic transmission onto SOM$^+$ CeL neurons, and that an increase in presynaptic release probability is likely to be the major underlying mechanism. Notably, inhibition of the pPVT during conditioning largely blocked these synaptic changes in the lateral-amygdala–CeL pathway (Extended Data Fig. 4b–d). Altogether, these results indicate that the pPVT participates in fear memory formation by regulating the maintenance of fear-conditioning-induced plasticity at the lateral-amygdala–CeL synapses.

SOM$^+$ and SOM$^-$ neurons—the latter being predominantly protein kinase C-δ-expressing (PKC-δ$^+$)[6]—constitute two major CeL populations that are mutually inhibitory[6,15]. We reasoned that the pPVT might control CeL synaptic plasticity by regulating either one or both of these populations. To distinguish between these possibilities, we used a modified rabies virus system that can trace the monosynaptic inputs onto genetically identified neurons[16] (Methods). This approach revealed that the pPVT projects to both populations (Fig. 3a–c), with the distinction that there were twice as many pPVT neurons innervating SOM$^+$ neurons as those innervating PKC-δ$^+$ neurons (the connectivity indices, calculated as the ratio of the number of rabies-virus-labelled cells in the pPVT to that of starter cells in the CeL, for the two cell types are: SOM$^+$, 0.99 ± 0.08, $n = 3$ mice; PKC-δ$^+$, 0.49 ± 0.03, $n = 3$ mice; $P < 0.01$, *t*-test), suggesting that pPVT afferents in the CeL preferentially innervate SOM$^+$ neurons.

To assess the functional connectivity between the pPVT and CeL, we used the *Som-cre;Ai14* mice, in which SOM$^+$ cells can be identified by their red fluorescence, and injected the pPVT with an AAV expressing channelrhodopsin-2 (AAV-ChR2-YFP) that allows photostimulation of axonal projections[17] (Fig. 3d, e). Bright ChR2–YFP-labelled fibres were readily observed throughout the CeL in acute slices prepared from these mice, confirming a strong pPVT–CeL projection. To our surprise, brief light pulses, which reliably evoked excitatory synaptic transmission in BLA neurons (Extended Data Fig. 5a–c), failed to evoke any detectable fast synaptic transmission in all the recorded SOM$^+$ or SOM$^-$ CeL neurons (Fig. 3e, f). Notably, high-frequency photostimulation of pPVT afferents in the CeL induced a slow inward current exclusively in SOM$^+$ neurons (Fig. 3e–g and Extended Data Fig. 5d–f). High-frequency photostimulation also generated a sustained increase in the frequency of spontaneous inhibitory postsynaptic currents (sIPSC) onto SOM$^-$ neurons (Extended Data Fig. 5g–i). Because SOM$^+$ cells

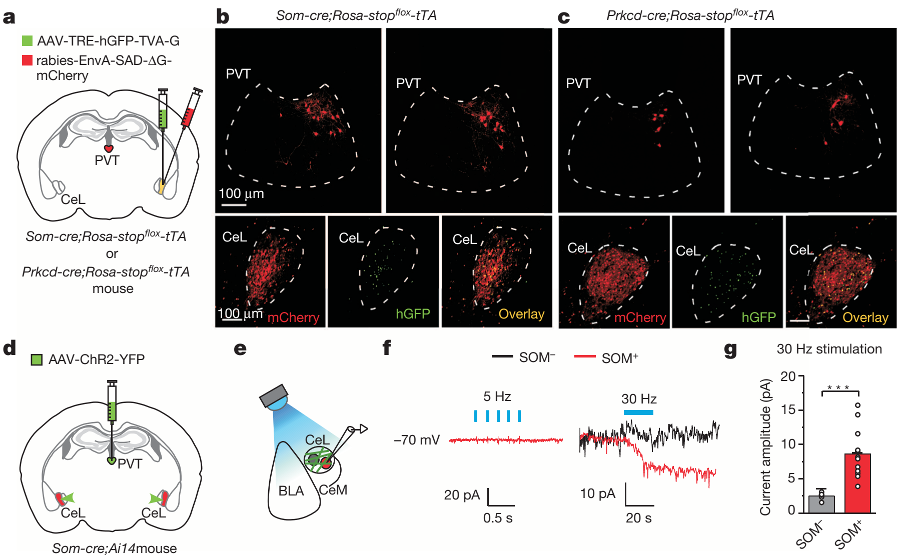

Figure 3 | pPVT neurons preferentially innervate SOM$^+$ cells in the CeL. **a**, A schematic of the experimental approach (see Methods). **b**, **c**, Representative images of the tracing result for SOM$^+$ (**b**) and PKC-δ$^+$ (**c**) CeL neurons. Top, retrogradely labelled neurons in the pPVT. Bottom, starter neurons in the CeL are identified by their co-expression of mCherry (left) and histone GFP (hGFP) (middle) (overlay on right). CeM, medial division of the central amygdala. **d**, **e**, Schematics of the experimental approach. **f**, Sample traces of synaptic responses to brief (1-s train of 5-Hz, 5-ms pulses; left) or prolonged high frequency (20-s train of 30-Hz, 5-ms pulses; right) photostimulation of pPVT afferents. Holding potential was −70 mV. **g**, Quantification of the synaptic responses induced by the 30 Hz stimulation of pPVT afferents (SOM$^-$, $n = 7$ neurons (5 mice); SOM$^+$, $n = 12$ neurons (5 mice); ***$P < 0.001$, t-test). Data are presented as mean ± s.e.m.

inhibit SOM$^-$ cells in the CeL[6], these results suggest that pPVT inputs selectively facilitate the activation of SOM$^+$ neurons, which in turn suppress SOM$^-$ neurons.

Given that stimulation of pPVT afferents in the CeL evoked slow inward currents, rather than canonical fast synaptic responses in SOM$^+$ neurons, it is likely that the pPVT–CeL^{SOM} transmission is mediated by a neuromodulator. One notable candidate for this is BDNF, a known modulator of synaptic function[18], the messenger RNA expression of which is highest in the pPVT within the dorsal thalamus[19]. We found that the majority (~70%; $n = 5$ mice) of CeL-projecting pPVT neurons expressed BDNF (Extended Data Fig. 6a, b). In contrast, only 29% ($n = 2$ mice) of BLA-projecting pPVT neurons expressed BDNF, a value that is probably an overestimation owing to contamination by CeL-projecting pPVT neurons caused by tracer diffusion into the CeL (Extended Data Fig. 6c, d). In addition, CeL expression of the high-affinity BDNF receptor TrkB was largely restricted to SOM$^+$ neurons (76% colocalization, $n = 4$ mice; Extended Data Fig. 7a), consistent with the preferential targeting of this particular cell type by inputs from the pPVT (Fig. 3). These results suggest that BDNF might be a critical factor mediating pPVT to CeL communication.

To examine the functional role of BDNF in the pPVT–CeL^{SOM} interaction, we bred the *Trkb*$^{lox/lox}$;*Som-Flp* mice, which carry the *Trkb*$^{lox/lox}$ conditional alleles[20] and in which the Flp recombinase is expressed under the endogenous *Som* promoter[21]. In these mice, *Trkb* can be deleted in the CeL by infection with the AAV-GFP-Cre, while SOM$^+$ neurons can be tagged by infection with AAV-fDIO-mCherry, an AAV harbouring a double-*FRT*-flanked inverted open reading frame (fDIO) that expresses mCherry in an Flp-dependent manner, thereby allowing their identification in acute slices for electrophysiological recording (Extended Data Fig. 7b, c). Using this strategy, we found that the pPVT-driven slow excitatory inward currents were selectively abolished in SOM$^+$ neurons in which *Trkb* was deleted (mCherry and GFP double-positive neurons; Extended Data Fig. 7c–f). Consistent with this result, bath application of the BDNF scavenger TrkB–Fc in acute slices abolished the pPVT-driven increase in inhibition onto SOM$^-$ CeL neurons (Extended Data Fig. 7g, h), whereas exogenous application of BDNF mimicked this increase in inhibition (Extended Data Fig. 7i, j). These results indicate that BDNF/TrkB signalling is a mediator of pPVT–CeL^{SOM} communication.

Next, to determine whether this BDNF/TrkB-mediated pPVT–CeL^{SOM} communication is important for fear processing, we selectively deleted either *Bdnf* from the pPVT, or *Trkb* in SOM$^+$ CeL neurons. To achieve the former, we employed a mouse line carrying the *Bdnf*$^{lox/lox}$ conditional alleles[22] and injected the pPVT with AAV-GFP-Cre (Fig. 4a–c). To achieve the latter, we designed an AAV-fDIO-Cre-GFP that expresses Cre–GFP (a Cre and GFP fusion protein) under the control of Flp (Extended Data Fig. 8). This virus, when injected into the CeL of the *Trkb*$^{lox/lox}$;*Som-Flp* mice, expresses Cre (and hence leads to *Trkb* deletion) specifically in SOM$^+$ neurons. This intersectional recombinases-mediated areal-and-cell-specific gene excision (IRASE) method can be generally applied for gene deletion with spatial and cell-type specificity.

Deletion of *Bdnf* in the pPVT depleted BDNF from the CeL (BDNF$^+$ cells in CeL: GFP group, 156.36 ± 39.40 cells per mm^2, $n = 8$ mice; GFP–Cre group, 41.20 ± 12.00 cells per mm^2, $n = 7$ mice; $P < 0.05$, t-test) (Fig. 4a, b) and markedly impaired fear conditioning (Fig. 4c and Extended Data Fig. 3). In parallel, selective deletion of *Trkb* in SOM$^+$ CeL neurons by IRASE similarly impaired fear conditioning (Fig. 4d–f and Extended Data Fig. 3). These results indicate that the PVT is a major source of BDNF for the CeL, and that the BDNF/TrkB-mediated pPVT–CeL^{SOM} interaction has an important role in fear processing.

Of note, *Bdnf* deletion in the pPVT or *Trkb* deletion in SOM$^+$ CeL neurons not only impaired conditioned-stimuli-evoked freezing, a measurement of tone-associated memory, but also reduced pre-conditioned-stimuli freezing, which presumably represents contextual memory (Fig. 4c, e). Alternatively, or additionally, these behavioural effects could reflect a general reduction in fear responses, such as that caused by altered arousal or negative behavioural states[23].

To disentangle these issues, we first determined whether disruption of BDNF signalling affects the synaptic potentiation onto SOM$^+$ CeL neurons that, as mentioned above, can serve as a fear memory trace[6]. Deletion of *Trkb* in SOM$^+$ CeL neurons by IRASE prevented the fear-conditioning-induced increase in frequency, but not amplitude, of mEPSCs (Extended Data Fig. 9a–d), suggesting that presynaptic potentiation, the major component of fear-conditioning-driven CeL plasticity[6], depends on BDNF signalling. We next examined the effects of enhancing BDNF signalling. Bath application of BDNF on slices was sufficient to induce long-term potentiation of excitatory synaptic transmission onto SOM$^+$

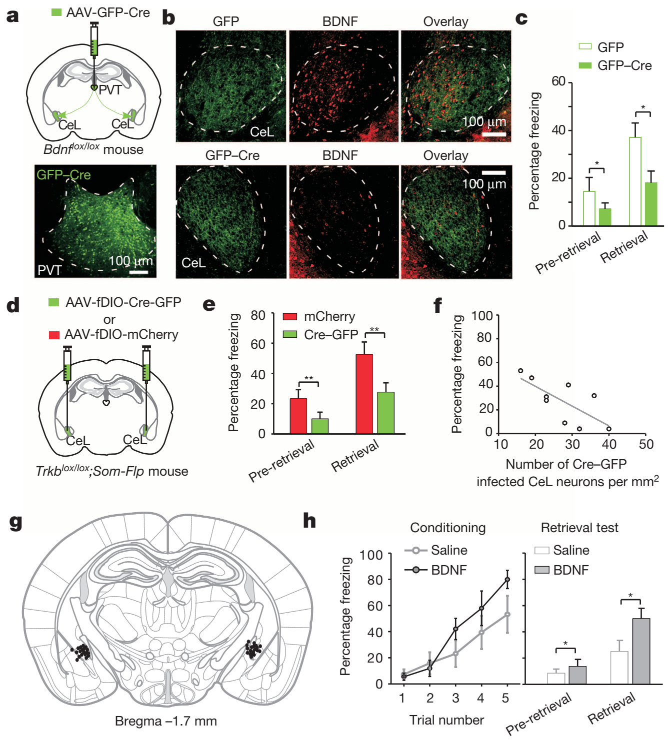

Figure 4 | BDNF/TrkB-mediated pPVT–CeL communication is essential for fear conditioning. **a**, Top, a schematic of the experimental approach. Bottom, a representative image of the pPVT infected with AAV-GFP-Cre. **b**, Representative images of the CeL from *Bdnf*$^{lox/lox}$ mice in which the pPVT was injected with either AAV-GFP (top) or AAV-GFP-Cre (bottom). Mice injected with AAV-GFP-Cre in the pPVT showed marked reduction of BDNF labelling in the CeL (middle and right panels). **c**, Deletion of *Bdnf* in the pPVT significantly reduced freezing levels during memory retrieval test ($n = 16$ mice for both groups; effect of treatments, $F_{(1,60)} = 6.91$, $P < 0.05$; effect of conditioned stimulus presentation, $F_{(1,60)} = 11.17$, $P < 0.01$; interaction, $F_{(1,60)} = 1.34$, $P > 0.05$; *$P < 0.05$; two-way ANOVA followed by Tukey's test). **d**, A schematic of the experimental approach. **e**, Selective deletion of *Trkb* in SOM$^+$ CeL neurons significantly reduced freezing levels during memory retrieval test ($n = 9$ and 10 mice for Cre–GFP and mCherry, respectively; effect of treatments, $F_{(1,30)} = 9.59$, $P < 0.01$; effect of conditioned stimulus presentation, $F_{(1,30)} = 14.37$, $P < 0.001$; interaction, $F_{(1,30)} = 0.88$, $P > 0.05$; **$P < 0.01$; two-way ANOVA followed by Tukey's test). **f**, The bilateral infection rate in the CeL significantly correlated with freezing levels during retrieval ($R^2 = 0.44$, $P < 0.05$, $n = 9$ mice; linear regression is indicated by a grey line). **g**, Drawing of the cannula sites. Each dot denotes where the tip of the injection cannula was located in each mouse. **h**, BDNF infusion into the CeL promotes fear learning. Left, performance of mice during a mild conditioning procedure (Methods). BDNF infusion had a trend to improve performance ($F_{(1,55)} = 3.65$, $P = 0.06$, two-way ANOVA). Right, BDNF infusion enhanced freezing levels during a memory retrieval test ($n = 9$ and 10 mice for saline and BDNF, respectively; effect of treatment, $F_{(1,34)} = 5.63$, $P < 0.05$; effect of conditioned stimulus, $F_{(1,34)} = 17.35$, $P < 0.001$; interaction, $F_{(1,34)} = 2.44$, $P > 0.05$; *$P < 0.05$; two-way ANOVA followed by Tukey's test). Data are presented as mean ± s.e.m.

CeL neurons, which was accompanied by a reduction in the paired-pulse ratio (Extended Data Fig. 9e–g), indicating a presynaptic mechanism. These presynaptic effects in the CeL induced by BDNF/TrkB manipulations are consistent with the presynaptic action of BDNF in other brain areas[18]. Notably, infusion of BDNF into the CeL facilitated conditioning to a mild foot shock (Fig. 4g, h). These results, together with the above finding regarding the role of the pPVT–CeL pathway in fear learning (Figs 1 and 2 and Extended Data Fig. 4), indicate that BDNF is a critical regulator of fear memory in the CeL.

In light of our previous finding that activation of SOM$^+$ CeL neurons is sufficient to drive unconditioned fear responses and is required for the expression of conditioned fear[6], the observation that activation of TrkB induces a slow excitatory current in SOM$^+$ CeL neurons (Fig. 3d–g and Extended Data Fig. 7b–f) suggests that BDNF might increase the excitability of these neurons, thereby promoting fear expression. We found that bath application of BDNF on slices markedly increased the spike probability of SOM$^+$ CeL neurons (Extended Data Fig. 10a–d); and notably, bilateral infusion of BDNF into the CeL of naive mice elicited robust freezing responses (Extended Data Fig. 10e, f and Supplementary Videos 1 and 2). These results, together with the above finding that the pPVT–CeL pathway is required for the expression of conditioned fear (Fig. 1), suggest that BDNF signalling in the pPVT–CeL^{SOM} pathway may facilitate the expression of fear by promoting SOM$^+$ CeL neuron activation.

On the basis of our collective results, we propose that BDNF/TrkB-mediated pPVT–CeL communication promotes both synaptic plasticity and the excitability of SOM$^+$ CeL neurons, thereby facilitating not only the formation of stable fear memories but also the expression of fear responses.

Recent studies suggest a role for the PVT in anxiety-related behaviours[24]. In addition, altered BDNF signalling has been implicated in anxiety disorders[25,26]. Our findings that the pPVT recruits BDNF/TrkB signalling to control CeL function define a functional framework for the pPVT that can subserve its role in the coordination of behavioural responses to stress.

Online Content Methods, along with any additional Extended Data display items and Source Data, are available in the online version of the paper; references unique to these sections appear only in the online paper.

Received 9 February; accepted 16 October 2014.
Published online 19 January 2015.

1. Spencer, S. J., Fox, J. C. & Day, T. A. Thalamic paraventricular nucleus lesions facilitate central amygdala neuronal responses to acute psychological stress. *Brain Res.* **997,** 234–237 (2004).
2. Chastrette, N., Pfaff, D. W. & Gibbs, R. B. Effects of daytime and nighttime stress on Fos-like immunoreactivity in the paraventricular nucleus of the hypothalamus, the habenula, and the posterior paraventricular nucleus of the thalamus. *Brain Res.* **563,** 339–344 (1991).
3. Cullinan, W. E., Herman, J. P., Battaglia, D. F., Akil, H. & Watson, S. J. Pattern and time course of immediate early gene expression in rat brain following acute stress. *Neuroscience* **64,** 477–505 (1995).
4. Wilensky, A. E., Schafe, G. E., Kristensen, M. P. & LeDoux, J. E. Rethinking the fear circuit: the central nucleus of the amygdala is required for the acquisition, consolidation, and expression of Pavlovian fear conditioning. *J. Neurosci.* **26,** 12387–12396 (2006).
5. Ciocchi, S. *et al.* Encoding of conditioned fear in central amygdala inhibitory circuits. *Nature* **468,** 277–282 (2010).
6. Li, H. *et al.* Experience-dependent modification of a central amygdala fear circuit. *Nature Neurosci.* **16,** 332–339 (2013).
7. Krout, K. E. & Loewy, A. D. Parabrachial nucleus projections to midline and intralaminar thalamic nuclei of the rat. *J. Comp. Neurol.* **428,** 475–494 (2000).
8. Bhatnagar, S. *et al.* A cholecystokinin-mediated pathway to the paraventricular thalamus is recruited in chronically stressed rats and regulates hypothalamic-pituitary-adrenal function. *J. Neurosci.* **20,** 5564–5573 (2000).
9. Li, S. & Kirouac, G. J. Projections from the paraventricular nucleus of the thalamus to the forebrain, with special emphasis on the extended amygdala. *J. Comp. Neurol.* **506,** 263–287 (2008).
10. Vertes, R. P. & Hoover, W. B. Projections of the paraventricular and paratenial nuclei of the dorsal midline thalamus in the rat. *J. Comp. Neurol.* **508,** 212–237 (2008).
11. Armbruster, B. N., Li, X., Pausch, M. H., Herlitze, S. & Roth, B. L. Evolving the lock to fit the key to create a family of G protein-coupled receptors potently activated by an inert ligand. *Proc. Natl Acad. Sci. USA* **104,** 5163–5168 (2007).
12. Darvas, M. & Palmiter, R. D. Restriction of dopamine signaling to the dorsolateral striatum is sufficient for many cognitive behaviors. *Proc. Natl Acad. Sci. USA* **106,** 14664–14669 (2009).
13. Do-Monte, F. H., Quinones-Laracuente, K. & Quirk, G. J. A temporal shift in the circuits mediating retrieval of fear memory. *Nature* http://dx.doi.org/10.1038/nature14030 (this issue).
14. He, M. *et al.* Cell-type-based analysis of microRNA profiles in the mouse brain. *Neuron* **73,** 35–48 (2012).
15. Haubensak, W. *et al.* Genetic dissection of an amygdala microcircuit that gates conditioned fear. *Nature* **468,** 270–276 (2010).
16. Miyamichi, K. *et al.* Cortical representations of olfactory input by trans-synaptic tracing. *Nature* **472,** 191–196 (2011).
17. Mattis, J. *et al.* Principles for applying optogenetic tools derived from direct comparative analysis of microbial opsins. *Nature Methods* **9,** 159–172 (2011).
18. Park, H. & Poo, M.-M. Neurotrophin regulation of neural circuit development and function. *Nature Rev. Neurosci.* **14,** 7–23 (2013).

19. Conner, J. M., Lauterborn, J. C., Yan, Q., Gall, C. M. & Varon, S. Distribution of brain-derived neurotrophic factor (BDNF) protein and mRNA in the normal adult rat CNS: evidence for anterograde axonal transport. *J. Neurosci.* **17,** 2295–2313 (1997).
20. He, X.-P. *et al.* Conditional deletion of TrkB but not BDNF prevents epileptogenesis in the kindling model. *Neuron* **43,** 31–42 (2004).
21. Fenno, L. E. *et al.* Targeting cells with single vectors using multiple-feature Boolean logic. *Nature Methods* **11,** 763–772 (2014).
22. Rios, M. *et al.* Conditional deletion of brain-derived neurotrophic factor in the postnatal brain leads to obesity and hyperactivity. *Mol. Endocrinol.* **15,** 1748–1757 (2001).
23. Johnson, P. L., Molosh, A., Fitz, S. D., Truitt, W. A. & Shekhar, A. Orexin, stress, and anxiety/panic states. *Prog. Brain Res.* **198,** 133–161 (2012).
24. Li, Y. *et al.* Changes in emotional behavior produced by orexin microinjections in the paraventricular nucleus of the thalamus. *Pharmacol. Biochem. Behav.* **95,** 121–128 (2010).
25. Zhang, L. *et al.* PTSD risk is associated with BDNF Val66Met and BDNF overexpression. *Mol. Psychiatry* **19,** 8–10 (2014).
26. Mahan, A. L. & Ressler, K. J. Fear conditioning, synaptic plasticity and the amygdala: implications for posttraumatic stress disorder. *Trends Neurosci.* **35,** 24–35 (2012).

Supplementary Information is available in the online version of the paper.

Acknowledgements We thank E. Nestler for providing us with the *Trkb*$^{lox/lox}$ mice generated by L.F.P., K. Deisseroth for the AAV-Ef1a-fDIO backbone, E. Valjent for supporting D.D.B.'s work, and members of the Li laboratory for discussions. This work was supported by grants from the National Institutes of Health (NIH) (B.L., L.V.A. and Z.J.H.), the Dana Foundation (B.L.), NARSAD (B.L. and Z.J.H.), Louis Feil Trust (B.L.), the Stanley Family Foundation (B.L. and Z.J.H.), and a Harvey L. Karp Discovery Award (M.A.P.).

Author Contributions M.A.P. and B.L. designed the study. M.A.P. and V.R. conducted experiments. M.A.P. analysed data. J.T. assisted with the rabies viral tracing experiments. D.D.B. assisted with the BDNF infusion experiments. M.W. made the AAV-fDIO-Cre-GFP virus. M.D. made the CAV2-Cre virus. L.F.P. generated the *Trkb*$^{lox/lox}$ mouse line. M.H. generated the *Som-Flp* mouse line. L.V.A., R.D.P. and Z.J.H. provided critical reagents and suggestions. M.A.P. and B.L. wrote the paper.

Author Information Reprints and permissions information is available at www.nature.com/reprints. The authors declare no competing financial interests. Readers are welcome to comment on the online version of the paper. Correspondence and requests for materials should be addressed to M.A.P. (mpenzo@cshl.edu) or B.L. (bli@cshl.edu).

METHODS

Mice. All procedures were approved by the Institutional Animal Care and Use Committees of Cold Spring Harbour Laboratory and conducted in accordance to the US National Institutes of Health guidelines. Mice were housed under a 12 h light–dark cycle (9 a.m. to 9 p.m. light), with food and water available *ad libitum*. *Som-cre*[6], *Prkcd-cre*[15], *Som-Flp*[21], *Bdnf*$^{lox/lox}$[22], *Trkb*$^{lox/lox}$[20], *Ai14*[6], *H2b-GFP*[14], and *Rosa26-stop*^{flox}*-tTA*[27] mice have all been described elsewhere. All mice were bred onto C57BL/6J genetic background. Male and female mice 6–9 weeks of age were used for all the experiments. All subjects were randomly allocated to the different experimental conditions used in this study.

Viral vectors. AAV-DIO-hM4Di-mCherry, AAV-DIO-eYFP, AAV-GFP-Cre, AAV-ChR2-YFP, and AAV-TRE-hGFP-TVA-G were produced by the University of North Carolina (UNC) Vector Core Facilities and have been described previously[6,16]. For the generation of the AAV-fDIO-Cre-GFP and AAV-fDIO-mCherry strains, standard cloning procedures were used to subclone the Cre–GFP or mCherry cassettes into the backbone of a Flippase-dependent AAV-Ef1a-fDIO-YFP expression plasmid[21] (gift from K. Deisseroth). Following DNA sequencing screening, the AAV plasmid was packaged into AAV serotype 8 virus from UNC Vector Core, with titres of 8.3×10^{12} virus particles per ml. The EnvA-pseudotyped, protein-G-deleted rabies-EnvA-SAD-ΔG-mCherry virus[16] was produced by the Viral Vector Core Facility at Salk Institute. CAV2-Cre was prepared using E1-transcomplementing dog kidney cells and purified by sucrose and CsCl gradient centrifugation, and was re-suspended in 1 × Hanks Balanced Saline Solution (HBSS)[12]. All viral vectors were stored in aliquots at −80 °C until use.

Stereotaxic surgery. Viral injections were performed using previously described procedures[6] at the following stereotaxic coordinates: pPVT, −1.34 mm from bregma, 0.05 mm lateral from midline, and 3.03 mm vertical from cortical surface; CeL, −1.22 mm from bregma, 2.9 mm lateral from midline, and 4.6 mm vertical from cortical surface; BLA, −1.80 mm from bregma, 3.4 mm lateral from midline, and 5.4 mm vertical from cortical surface. For pPVT injections we used a 6.5° angle to avoid damage to the superior sagittal sinus. Animals were kept on a heating pad throughout the entire surgical procedures and were brought back to their home cages after 24 h of post-surgery recovery and monitoring. Postoperative care included intraperitoneal injection with 0.3–0.5 ml of lactated Ringers solution and metacam (meloxicam, 1–2 mg kg^{-1}) for analgesia and anti-inflammatory purposes. All AAVs and the CAV2-Cre were injected at a total volume of approximately 1 μl (except for the monosynaptic rabies viral tracing, see below), and were allowed at least 2 weeks for maximal expression. For retrograde tracing of amygdala-projecting pPVT cells, CTB-555 or CTB-488 (0.1–0.3 μl, 0.5% in PBS) (Invitrogen) was injected into the CeL and BLA and allowed 3–5 days for sufficient retrograde transport.

Monosynaptic tracing with pseudotyped rabies virus. Retrograde tracing of monosynaptic inputs onto genetically-defined cell populations of the CeL was accomplished using a previously described method[16]. In brief, the *Som-cre;Rosa26-stop*^{flox}*-tTA* mice and the *Prkcd-cre;Rosa26-stop*^{flox}*-tTA* mice, which express tTA in SOM$^+$ cells and PKC-δ$^+$ cells, respectively, were injected into the CeL with the AAV-TRE-hGFP-TVA-G (0.2–0.3 μl) that expresses the following components in a tTA-dependent manner: a fluorescent reporter histone GFP (hGFP); TVA (which is a receptor for the avian virus envelope protein EnvA); and the rabies envelope glycoprotein (G). Two weeks later mice were injected in the same location with the rabies-EnvA-SAD-ΔG-mCherry (1.2 μl), a rabies virus that is pseudotyped with EnvA, lacks the envelope glycoprotein, and expresses mCherry. This method ensures that the rabies virus exclusively infects cells expressing TVA. Furthermore, complementation of the modified rabies virus with envelope glycoprotein in the TVA-expressing cells allows the generation of infectious particles, which then can trans-synaptically infect presynaptic neurons.

Histology. Animals were deeply anaesthetized and transcardially perfused with PBS, followed by perfusion with 4% paraformaldehyde (PFA) in PBS. Brains were extracted and post-fixed in 4% PFA at 4 °C for 2 h for BDNF and TrkB immunohistochemistry and overnight for all other experiments. This was followed by cryoprotection in a 30% PBS-buffered sucrose solution until brains were saturated (∼36 h). Coronal brain sections (40 μm) were cut using a freezing microtome (SM 2010R, Leica). Brain sections were first washed in PBS (3 × 5 min) and then incubated in PBST (0.1% Triton X-100 in PBS) for 15 min at room temperature. Next, sections were blocked in 10% normal goat serum (NGS) in PBST for 30 min at room temperature, followed by incubation with primary antibodies overnight at 4 °C. Sections were then washed with PBST (5 × 15 min) and incubated with fluorescent secondary antibodies at room temperature for 1 h. After washing with PBS (5 × 15 min), sections were mounted onto glass slides with Fluoromount-G (Beckman Coulter). Images were taken using a LSM 780 laser-scanning confocal microscope (Carl Zeiss).

Antibodies. The primary antibodies used were: anti-c-Fos (1:2,000, rabbit, Santa Cruz, sc-52); anti-BDNF (1:100, rabbit, abcam, ab108383); and anti-TrkB (1:1,000, rabbit, Biosensis, R-149-100). Fluorophore-conjugated secondary antibodies were purchased from Invitrogen. Antibodies were diluted in PBS with 10% NGS and 0.1% Triton X-100.

Fear conditioning. Mice were initially handled and habituated to the conditioning cage, a mouse test cage (18 cm × 18 cm × 30 cm) with an electrifiable floor connected to a H13-15 shock generator (Coulbourn Instruments). The test cage was located inside a sound attenuated cabinet (H10-24A; Coulbourn Instruments). Before each conditioning session the test cage was wiped clean with 70% ethanol. During conditioning the cabinet was illuminated and the behaviour was captured with a monochrome CCD-camera (Panasonic WV-BP334) at 3.7 Hz and stored on a personal computer. The FreezeFrame software (Coulbourn Instruments) was used to control the delivery of both tones and foot shocks. For habituation, five 4-kHz, 75-dB tones (conditioned stimulus), each of which was 30 s in duration, were delivered at variable intervals. During conditioning, mice received five presentations of the conditioned stimulus, each of which co-terminated with a 2-s, 1-mA foot shock (unconditioned stimulus). In the experiment to determine the effect of BDNF infusion on fear learning (Fig. 4g, h), weaker (2 s, 0.5 mA) foot shocks were used. The test for fear memory was performed 24 h following conditioning in a novel illuminated context, where mice were exposed to two presentations of unreinforced conditioned stimulus (120 s inter-stimulus interval). The novel context was a cage with a different shape (22 cm × 22 cm × 21 cm) and floor texture compared with the conditioning cage. Prior to each use the floor and walls of the cage were wiped clean with 0.5% acetic acid to make the scent distinct from that of the conditioning cage. Behavioural responses to the conditioned stimuli were recorded. Freezing behaviour was analysed with FreezeFrame (Coulbourn Instruments).

Electrophysiology. Mice used for electrophysiological experiments were anaesthetized with isoflurane, decapitated and their brains quickly removed and chilled in ice-cold dissection buffer (110 mM choline chloride, 25 mM $NaHCO_3$, 1.25 mM NaH_2PO_4, 2.5 mM KCl, 0.5 mM $CaCl_2$, 7.0 mM $MgCl_2$, 25.0 mM glucose, 11.6 mM ascorbic acid and 3.1 mM pyruvic acid, gassed with 95% O_2 and 5% CO_2). Coronal slices (300 μm) containing the amygdala complex were cut in dissection buffer using a HM650 Vibrating-blade Microtome (Thermo Fisher Scientific), and were subsequently transferred to a storage chamber containing artificial cerebrospinal fluid (ACSF) (118 mM NaCl, 2.5 mM KCl, 26.2 mM $NaHCO_3$, 1 mM NaH_2PO_4, 20 mM glucose, 2 mM $MgCl_2$ and 2 mM $CaCl_2$, at 34 °C, pH 7.4, gassed with 95% O_2 and 5% CO_2). After at least 40 min recovery time, slices were transferred to room temperature (20–24 °C) and were constantly perfused with ACSF.

For plasticity experiments, recordings were always performed on interleaved naive and fear-conditioned animals. Simultaneous whole-cell patch-clamp recordings from SOM$^+$/SOM$^-$ neuronal pairs in the CeL were obtained with Multiclamp 700B amplifiers (Molecular Devices). Recordings were made under visual guidance using an Olympus BX51 microscope with transmitted light illumination, and SOM$^+$ cells were identified based on their fluorescence (hGFP or tdTomato). Synaptic responses were evoked with a bipolar stimulating electrode placed in the BLA approximately 0.2 mm away from the recorded cell bodies in the CeL. Electrical stimulation was delivered every 10 s and synaptic responses were low-pass filtered at 1 KHz and recorded at holding potentials of −70 mV (for AMPA-receptor-mediated responses), +40 mV (for NMDA-receptor-mediated responses), or 0 mV (for $GABA_A$-receptor-mediated responses). NMDA-receptor-mediated responses were quantified as the mean current amplitude between 50 and 60 ms after stimulation. Recordings were made in the ACSF. The internal solution for voltage-clamp experiments contained 115 mM caesium methanesulphonate, 20 mM CsCl, 10 mM HEPES, 2.5 mM $MgCl_2$, 4 mM Na_2ATP, 0.4 mM Na_3GTP, 10 mM sodium phosphocreatine and 0.6 mM EGTA (pH 7.2). Evoked EPSCs were recorded with picrotoxin (100 μM) added to the ACSF. mEPSCs were recorded in the presence of tetrodotoxin (TTX; 1 μM) and picrotoxin (100 μM) and analysed using Mini Analysis software (Synaptosoft). To assess presynaptic function, a paired-pulse stimulation protocol (50 ms inter-stimulus interval) was used to evoke double-EPSCs, and the paired-pulse ratio was quantified as the ratio of the peak amplitude of the second EPSC to that of the first EPSC. While most of the above electrophysiology experiments were carried out by M.A.P., plasticity results were replicated by V.R. who performed these experiments in a blinded manner.

To evoke pPVT-driven synaptic transmission onto CeL neurons, the AAV-ChR2-YFP was injected into the pPVT of *Som-cre;Ai14* mice and allowed to express for 3 weeks. Acute brain slices were prepared and a blue light was used to stimulate ChR2-expressing axons. The light source was a single-wavelength LED system (λ = 470 nm; http://www.coolled.com/) connected to the epifluorescence port of the Olympus BX51 microscope. Light pulses of 1 ms, triggered by a TTL signal from the Clampex software, were delivered at either 5 Hz or 30 Hz to drive synaptic responses. BDNF (used at 100 ng ml^{-1}) and the BDNF scavenger TrkB–Fc (used at 1 μg ml^{-1}) were purchased from R&D Systems.

Chemogenetic manipulations. For chemogenetic manipulation of the pPVT, C57BL/6J mice were bilaterally injected with the CAV2-Cre virus into the CeL and subsequently with the AAV-DIO-hM4Di-mCherry into the pPVT. Three weeks

later mice were injected intraperitoneally with CNO (10 mg kg^{-1}) 40 min before either fear conditioning training or fear memory retrieval. For experiments that examine the effects of this manipulation on synaptic plasticity in the CeL, *Som-cre* and *Som-cre;H2b-GFP* mice were injected with a 40:60 mixture of AAV-Cre-GFP and AAV-DIO-hM4Di-mCherry into the pPVT (1 μl total volume). *Som-cre* mice were additionally injected bilaterally with 1 μl of AAV-DIO-YFP into the CeL.

Cannula implantation and BDNF infusion. *Surgery*. The surgical procedure was the same as described above. Stainless steel guide cannulae (26 gauge, 6.00 mm, Plastics One) were implanted bilaterally 0.5 mm above the CeL (−1.22 mm from bregma, 2.90 mm lateral from midline, and 4.25 mm vertical from the cortical surface) and were fixed to the skull with adhesive luting cement (C&B Metabond) and acrylic dental cement (Stoelting). A metal head bar was implanted posterior to the cannulae to facilitate restraining during infusion (see below). Following surgery, a dummy cannula was inserted into each guide cannula to seal off the opening. Mice were allowed to recover from surgery for a minimum of one week, during which they were handled and habituated to the infusion procedure on a daily basis.

Infusion. Mice were briefly head-restrained, while the dummy cannulae were removed and an injection cannula (33 gauge, 6.50 mm, Plastics One) was inserted into each of the guide cannulae. The injection cannulae were designed to protrude 0.50 mm from the tip of the guide cannulae and thus penetrate into the CeL. A dose of 200 ng BDNF (or 0.9% sodium chloride as control) was slowly infused bilaterally into the CeL at a flow-rate of 0.5 μl per min to a total volume of 1 μl per infusion site. Following infusion, the injection cannulae were left in place for 1 min to allow the BDNF solution to diffuse from the cannula tips. The dummy cannulae were subsequently reinserted into the guide cannulae and mice were immediately tested for unconditioned freezing or returned to their home cage for 15 min before fear conditioning.

Statistics and data presentation. All statistical tests are indicated when used. The sample sizes used in this study were based on estimations by a power analysis (power = 0.9, α = 0.05). No mice or data points were excluded from analysis. All data are presented as mean ± s.e.m.

27. Li, L. *et al.* Visualizing the distribution of synapses from individual neurons in the mouse brain. *PLoS ONE* **5,** e11503 (2010).

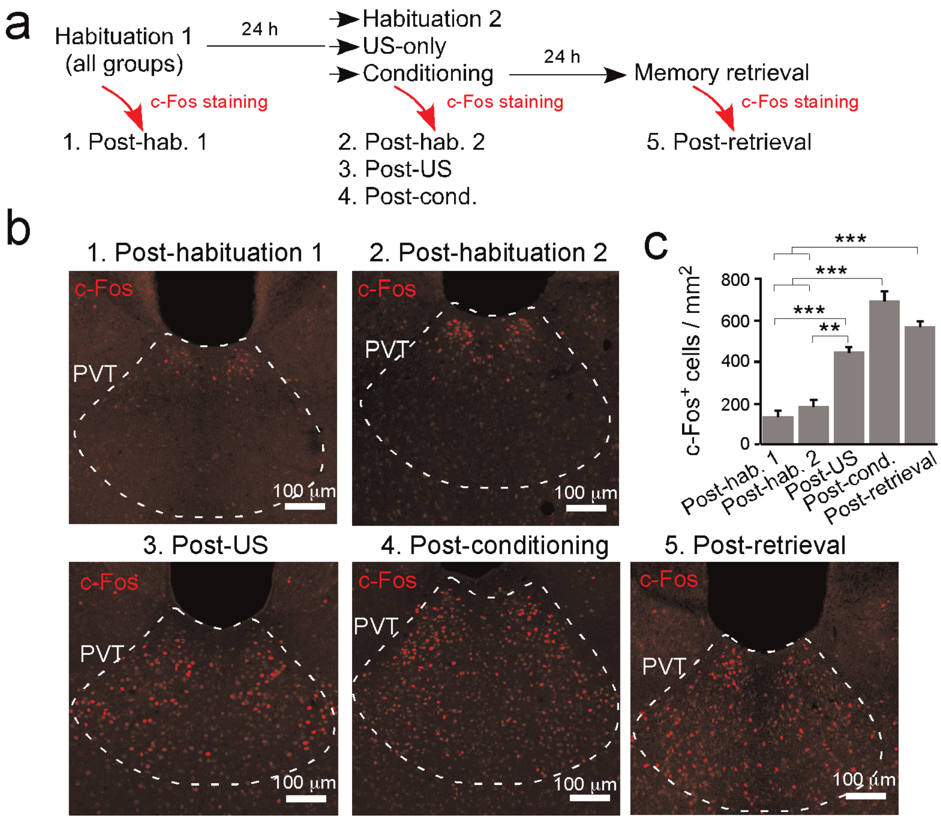

Extended Data Figure 1 | PVT is activated following both fear conditioning and fear memory retrieval. **a**, A schematic of the experimental design. All mice were killed for the detection of c-Fos at 90 min after the last behavioural session. **b**, Representative images of c-Fos immunohistochemistry in the pPVT for the five groups indicated in **a**. **c**, Quantification of c-Fos expression as c-Fos^{+} cells per mm^{2} (post-habituation 1 (mice that were subjected to one session of habituation), 131.17 ± 34.25, $n = 4$ mice; post-habituation 2 (mice that were subjected to two sessions of habituation), 180.68 ± 30.42, $n = 5$ mice; post-US (unconditioned stimulus; mice that were only exposed to five foot shocks), 443.3 ± 25.7, $n = 3$ mice; post-conditioning, 692.61 ± 46.68, $n = 4$ mice; post-retrieval, 565.51 ± 28.71, $n = 3$ mice; $F_{(4,14)} = 49.3$, $P < 0.001$; $^{**}P < 0.01$, $^{***}P < 0.001$; one-way analysis of variance (ANOVA) followed by Tukey's test). Data are presented as mean ± s.e.m.

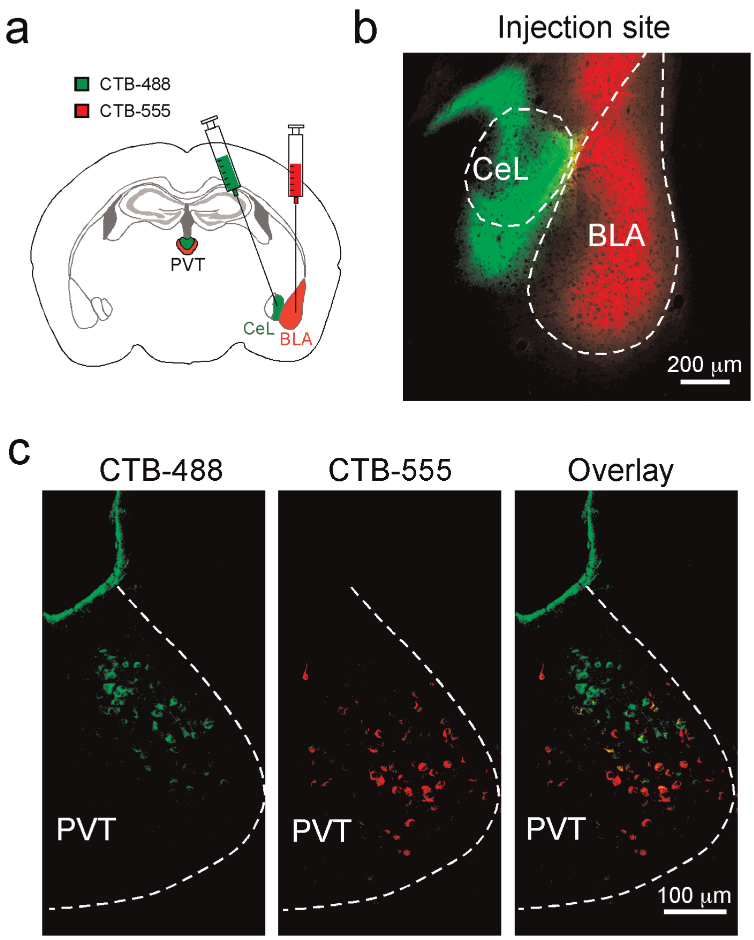

Extended Data Figure 2 | pPVT neurons projecting to the BLA and CeL are non-overlapping. **a**, A schematic of the approach to simultaneously label BLA- and CeL-projecting pPVT neurons. **b**, A representative image of the injection sites, where CTB-488 and CTB-555 were injected into the CeL and BLA, respectively. **c**, Representative images of pPVT cells labelled by CTB-488 (left) and CTB-555 (middle). These two populations were largely non-overlapping (right). Data was replicated in 4 mice.

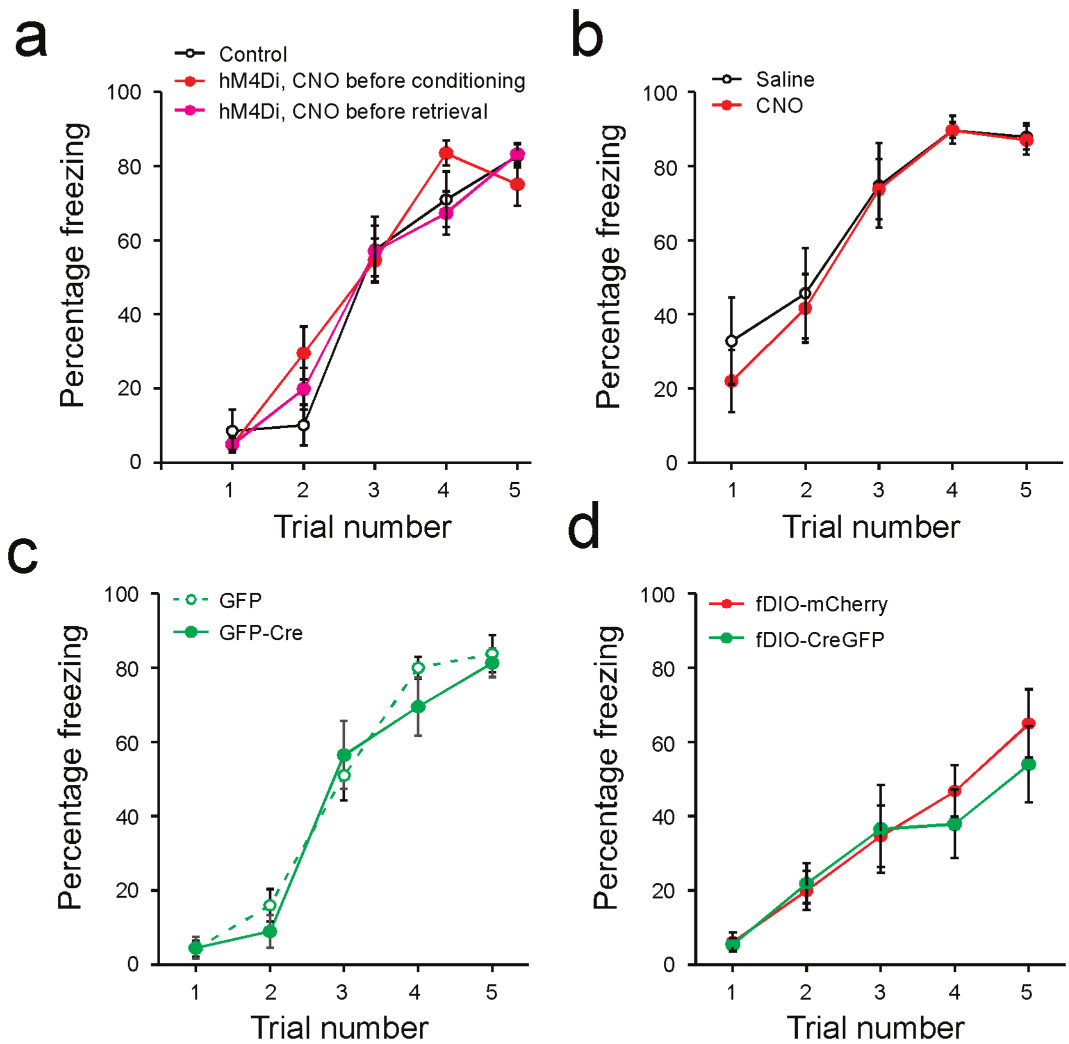

Extended Data Figure 3 | Performance during conditioning. **a**–**d**, Freezing levels during conditioning are shown for mice used in Fig. 1c (**a**), Fig. 2 (b), Fig. 4c (**c**), and Fig. 4e (**d**). **a**, There was no significant difference in performance among groups ($F_{(2,155)} = 0.51$, $P > 0.05$, two-way ANOVA). **b**, There was no significant difference in performance between saline-treated mice and CNO-treated mice ($F_{(1,70)} = 0.43$, $P > 0.05$, two-way ANOVA). **c**, There was no significant difference in performance between the two groups ($F_{(1,85)} = 0.73$, $P > 0.05$, two-way ANOVA). **d**, There was no significant difference in performance between the two groups ($F_{(1,75)} = 0.45$, $P > 0.05$, two-way ANOVA). Data are presented as mean ± s.e.m.

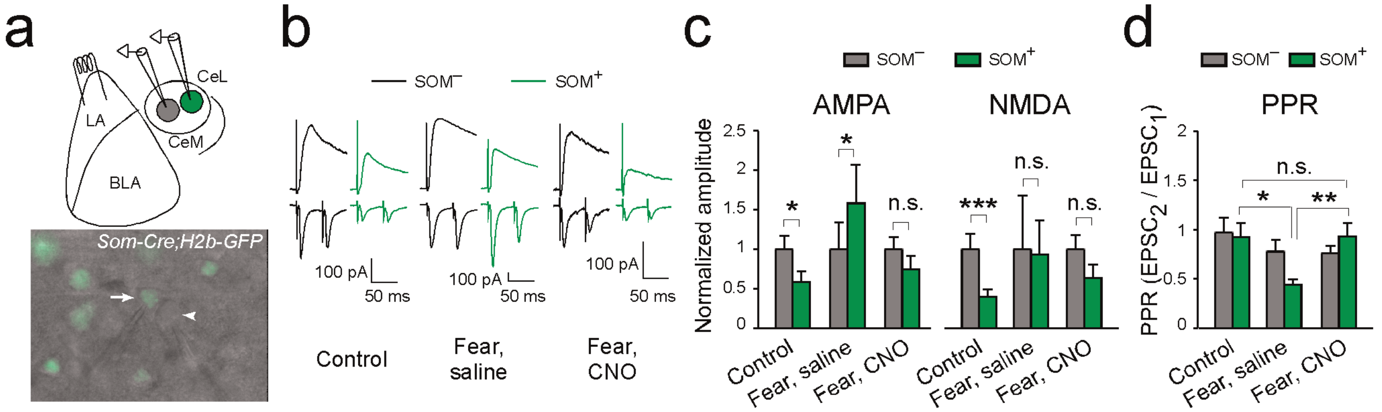

Extended Data Figure 4 | The pPVT is required for fear-conditioning-induced synaptic plasticity in the lateral-amygdala–CeL^{SOM} pathway. **a**, Top, a schematic of the whole-cell paired recording configuration. A pair of SOM$^+$ and SOM$^-$ CeL neurons were simultaneously recorded, and EPSCs were evoked by stimulation of the lateral amygdala. We used the *Som-cre;H2b-GFP* mice, in which the SOM$^+$ neurons were tagged with H2b–GFP and the pPVT neurons were infected with hM4Di as in Fig. 2a, b. Bottom, a representative image of a slice used for recording, in which a SOM$^+$ (arrow) and an adjacent SOM$^-$ (arrowhead) neuron were recorded. **b**, Sample EPSC traces obtained from the simultaneous paired recording experiment. Naive control mice (left) and fear-conditioned mice treated with either saline (middle) or CNO (right) were used. Saline or CNO was administered 40 min before, and recordings were performed 24 h after conditioning. Top and bottom traces represent EPSCs recorded at +40 mV and −70 mV holding potentials, respectively. **c**, Quantification of AMPA (left) and NMDA (right) currents (Control, $n = 9$ pairs (2 mice); 'Fear, saline', $n = 8$ pairs (3 mice); 'Fear, CNO', $n = 14$ pairs (3 mice); $*P < 0.05$, $**P < 0.001$, n.s., non-significant; paired *t*-test). EPSC values are normalized to the average EPSC value of SOM$^-$ cells for each group. **d**, Quantification of the paired-pulse ratio (PPR) (see Methods) of EPSCs measured at −70 mV (comparing control, 'Fear, saline', and 'Fear, CNO' groups for SOM$^+$ neurons: $*P < 0.05$, $**P < 0.01$, n.s., non-significant; one-way ANOVA followed by Tukey's test). Control mice for all experiments were injected with the same viral vectors as the experimental groups. Data are presented as mean ± s.e.m.

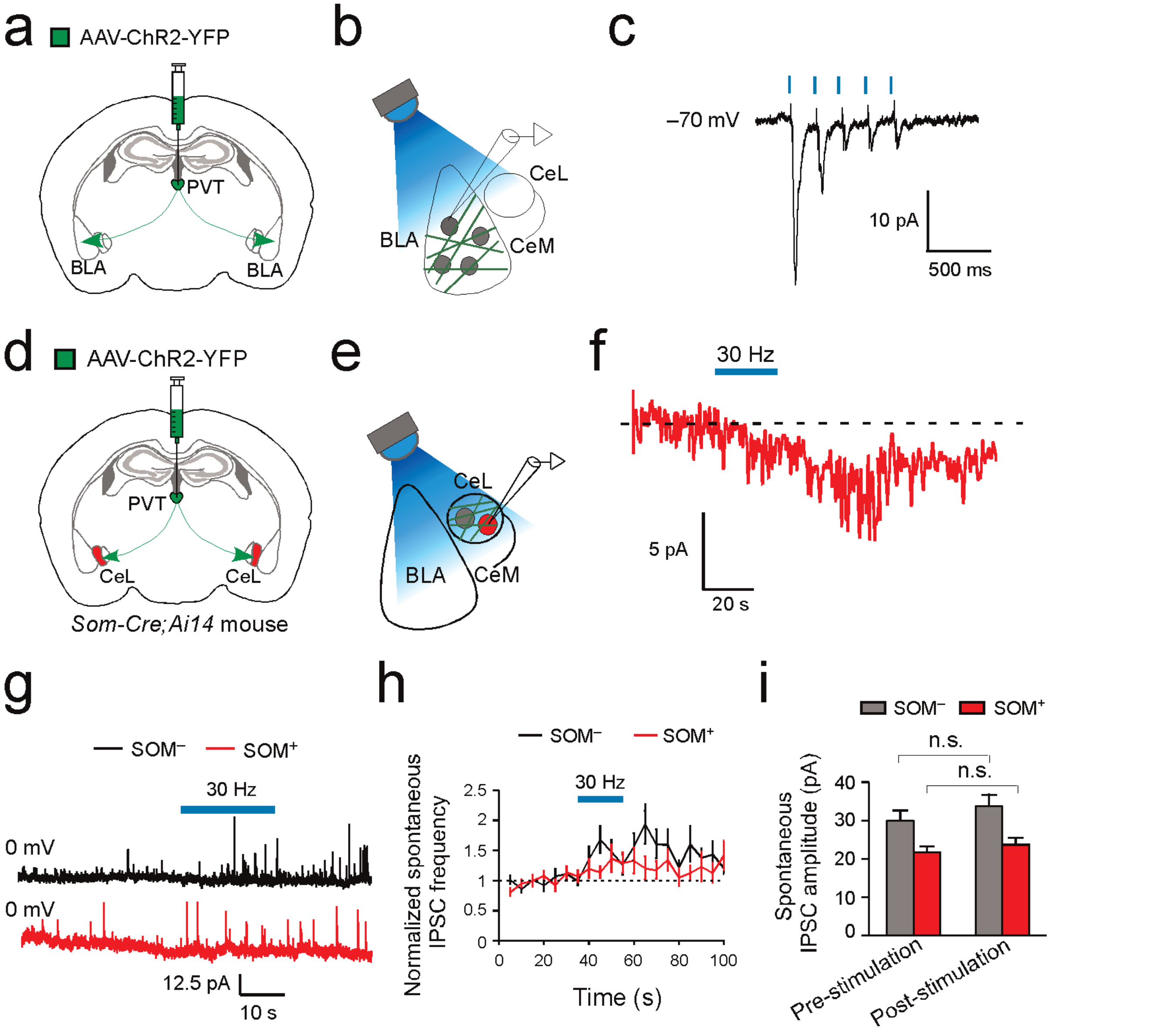

Extended Data Figure 5 | A different mode of communication in the pPVT–CeL pathway compared with the pPVT–BLA pathway. a–c, Optogenetic stimulation of pPVT afferents in the BLA drives fast synaptic transmission onto BLA neurons. **a**, **b**, Schematics of the experimental approach. **c**, Sample trace (average of 20) of the synaptic responses onto a BLA neuron following brief (1-s train of 5-Hz, 1-ms pulses) photostimulation of pPVT afferents expressing ChR2. Similar responses were observed in 5 out of 6 BLA neurons recorded. Data was obtained from the same mice as those in Fig. 3d–g. **d–f**, Slow recovery of the pPVT-driven current in a SOM^+ CeL neuron. **d**, **e**, Schematics of the experimental approach. **f**, Sample trace of the synaptic response onto a SOM^+ neuron following prolonged (20-s train of 30-Hz, 1-ms pulses) photostimulation of pPVT afferents expressing ChR2, showing slow recovery after stimulus cessation. **g–i**, Optogenetic stimulation of the pPVT–CeL pathway promotes intra-CeL inhibition. **g**, Representative traces of IPSCs onto SOM^- (black) and SOM^+ (red) CeL neurons. Blue bar indicates the 30 Hz photostimulation of pPVT afferents. **h**, Quantification of IPSC frequency, comparing pre- and post-photostimulation (SOM^-, $n = 14$ neurons (6 mice), $P < 0.001$, t-test; SOM^+, $n = 11$ neurons (6 mice), $P > 0.05$, t-test). **i**, Quantification of IPSC amplitude, comparing pre- and post-photostimulation (n.s., non-significant ($P > 0.05$), paired t-test). Data are presented as mean ± s.e.m.

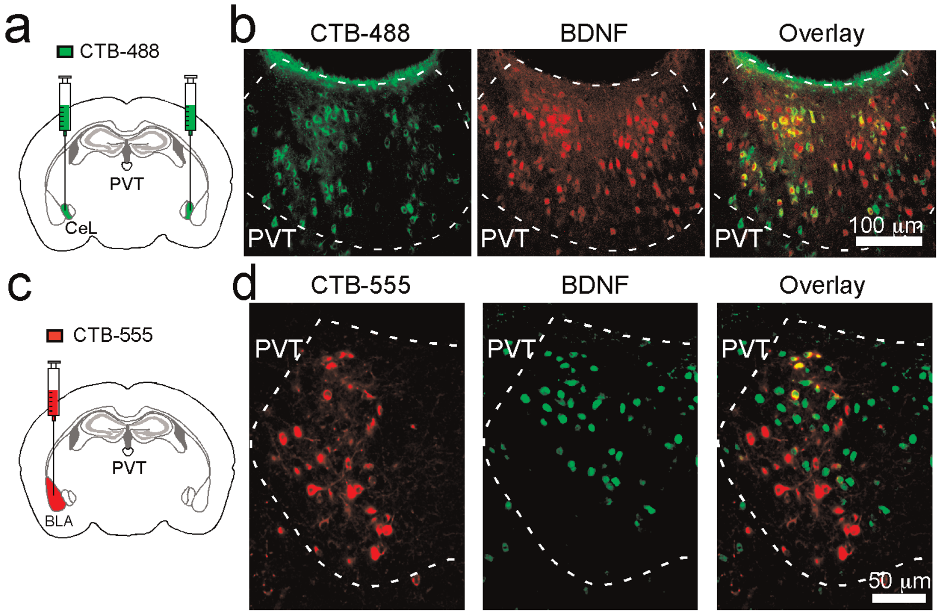

Extended Data Figure 6 | CeL-projecting neurons in the pPVT express BDNF. **a**, A schematic of the experimental approach to retrogradely label CeL-projecting pPVT cells. **b**, Representative images of pPVT cells, which were labelled by CTB-488 (left) and an antibody recognizing BDNF (middle). CTB-labelled neurons largely overlapped with BDNF-positive somatas (see overlay in right). **c**, **d**, BLA-projecting neurons and BDNF-expressing neurons in pPVT are largely non-overlapping. **c**, A schematic of the method used to label BLA-projecting neurons in the pPVT. **d**, Representative images of pPVT cells labelled by either CTB-555 (left) or the antibody recognizing BDNF (middle). These two populations were largely non-overlapping (see overlay in right).

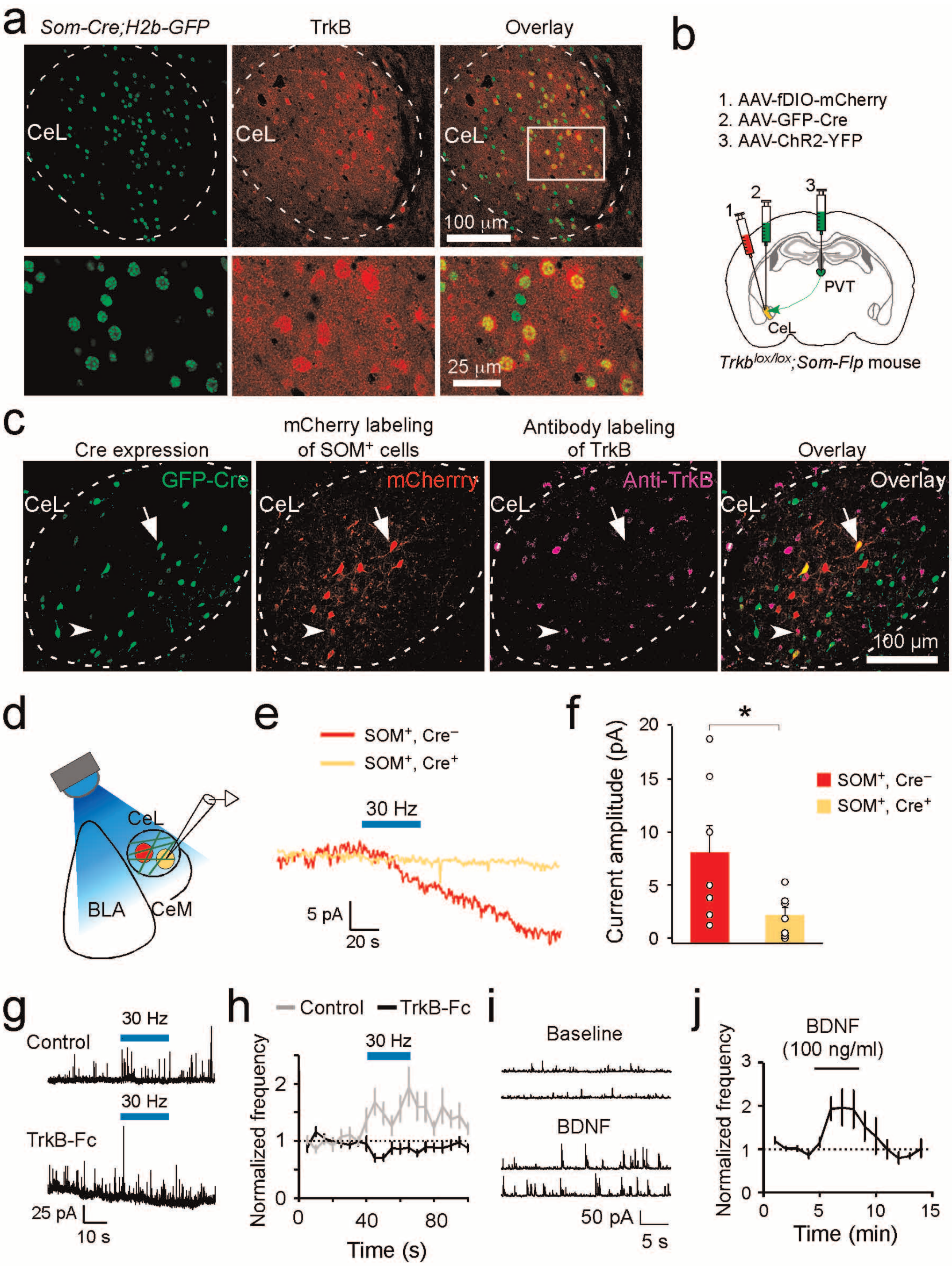

Extended Data Figure 7 | BDNF/TrkB mediates pPVT–CeL communication. **a**, The TrkB receptor is selectively expressed by SOM$^+$ CeL neurons. Top, representative images of the CeL in *Som-cre;H2b-GFP* mice, showing SOM$^+$ neurons tagged with H2b–GFP (left) and TrkB expression recognized by an antibody (middle). Bottom, higher-magnification images of the boxed area in the top panel. TrkB-labelled cells largely overlap with SOM$^+$ neurons (see overlay on right). **b–f**, TrkB mediates the pPVT–CeL transmission. **b**, A schematic of the experimental approach using the *Trkb$^{lox/lox}$;Som-Flp* mice to: (1) tag SOM$^+$ CeL neurons with mCherry; (2) sparsely infect CeL neurons with GFP–Cre to delete *Trkb*; and (3) express ChR2 in the pPVT. **c**, Representative images resulting from the approach in **b**, showing CeL neurons expressing (from left to right) Cre–GFP, mCherry and TrkB. Neurons that expressed both mCherry and GFP–Cre represent SOM$^+$ neurons in which *Trkb* was deleted (arrow; see overlay on right), whereas neurons that expressed mCherry, but not GFP–Cre, represent SOM$^+$ neurons with intact *Trkb* (arrowhead; see overlay on right). **d**, A schematic of the whole-cell recording configuration. **e**, Sample traces of synaptic currents in mCherry-only (SOM$^+$,Cre$^-$; red) and mCherry/GFP–Cre double positive (SOM$^+$,Cre$^+$; yellow) neurons in response to prolonged high-frequency stimulation of pPVT afferents. **f**, Quantification of the synaptic responses (SOM$^+$,Cre$^-$, 8.06 ± 2.58 pA, $n = 7$ neurons (3 mice); SOM$^+$,Cre$^+$, 2.10 ± 0.76 pA, $n = 7$ neurons (3 mice); $^*P < 0.05$, t-test). **g–j**, The pPVT input to the CeL promotes intra-CeL inhibition through BDNF/TrkB signalling. **g**, Representative traces of IPSCs recorded from SOM$^-$ CeL neurons in response to the 30 Hz photostimulation (blue bars) of pPVT afferents, in the control condition (top panel) or in the presence of the BDNF scavenger TrkB–Fc (bottom panel). **h**, Quantification of the frequency of IPSCs recorded from SOM$^-$ CeL neurons (comparing pre- and post-photostimulation: control, $n = 14$ neurons (6 mice; repetition of data from the SOM$^-$ cells in Extended Data Fig. 5h), $P < 0.001$, paired t-test; TrkB–Fc, $n = 17$ neurons (2 mice), $P > 0.05$, paired t-test). **i**, Representative traces showing the effect of BDNF bath application on spontaneous IPSCs recorded from CeL neurons. **j**, Quantification of the effect of BDNF on sIPSC frequency. Black line indicates the timing of BDNF application ($n = 7$; $P < 0.05$ comparing baseline and BDNF application, paired t-test). Data are presented as mean ± s.e.m.

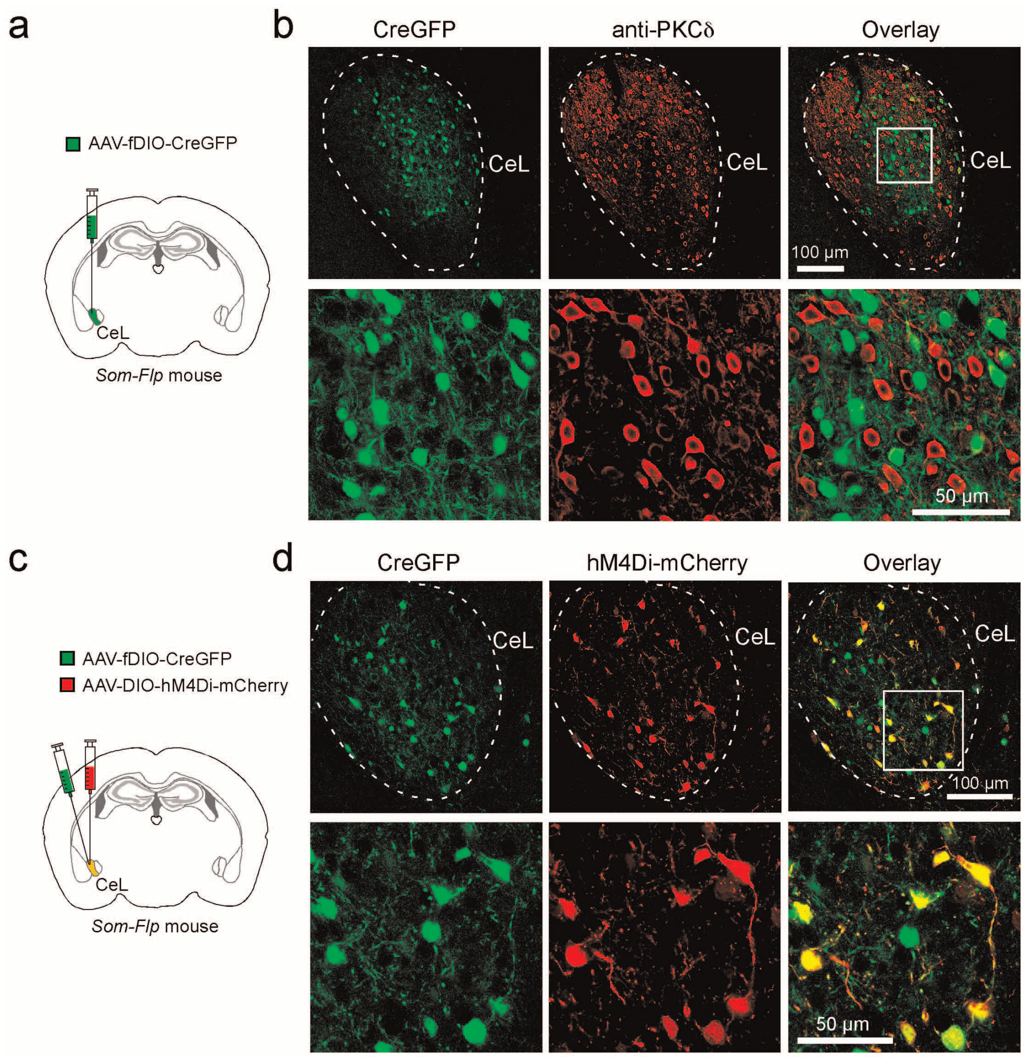

Extended Data Figure 8 | Characterization of the AAV-fDIO-CreGFP. **a**, A schematic of the experimental approach to selectively target SOM$^+$ CeL neurons in the *Som-Flp* mice with the AAV-fDIO-Cre-GFP. **b**, Representative images of CeL neurons expressing Cre–GFP (left), and PKC-δ$^+$ CeL neurons (as a surrogate for SOM$^-$ neurons) that were recognized by an antibody (middle). In the bottom panels are high magnification images of the boxed region in the top panel. These two cell populations were largely non-overlapping (see overlay on right), indicating that the AAV-fDIO-Cre-GFP selectively infects SOM$^+$ neurons (data from one mouse). **c**, A schematic of the experimental approach to test the function of AAV-fDIO-Cre-GFP, whereby the CeL of *Som-Flp* mice was injected with a mixture of AAV-fDIO-Cre-GFP and AAV-DIO-hM4Di-mCherry. As the latter virus expresses mCherry in a Cre-dependent manner, observation of selective mCherry expression in GFP$^+$ neurons would indicate that the AAV-fDIO-Cre-GFP is effective. **d**, Sample images of CeL neurons expressing Cre–GFP (left) and mCherry (middle). In the bottom panels are high magnification images of the boxed region in the top panel. Essentially, all mCherry$^+$ neurons co-expressed GFP (see overlay on right), indicating selective expression of Cre by the GFP-labelled cells (data from one mouse).

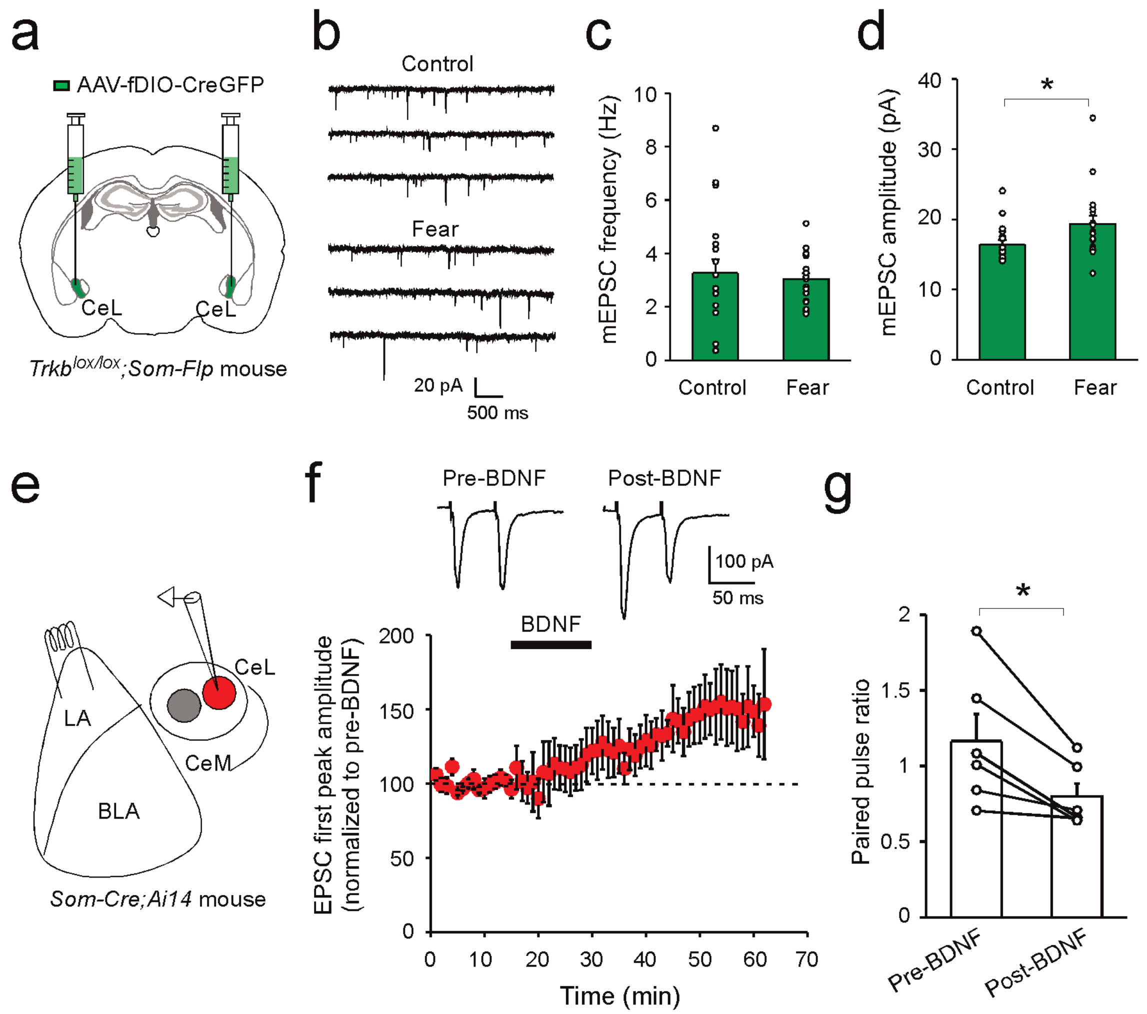

Extended Data Figure 9 | BDNF/TrkB regulates synaptic plasticity onto SOM$^+$ CeL neurons. **a**–**d**, Selective deletion of *Trkb* in SOM$^+$ CeL neurons impairs fear-conditioning-induced synaptic plasticity. **a**, A schematic of the experimental approach to specifically delete *Trkb* in SOM$^+$ CeL neurons. **b**, Representative traces of mEPSCs recorded from SOM$^+$ CeL neurons in which *Trkb* was deleted, in naive control (top) and fear-conditioned (bottom) mice. **c**, **d**, Deletion of *Trkb* blocked the fear conditioning-induced increase in mEPSC frequency (**c**) (control, $n = 19$ neurons (3 mice); fear, $n = 18$ neurons (3 mice); $P > 0.05$, *t*-test), but not amplitude (**d**) (control, $n = 19$ neurons (3 mice); fear, $n = 18$ neurons (3 mice); $*P < 0.05$, *t*-test). **e**–**g**, BDNF induces long-term potentiation at lateral-amygdala–CeL^{SOM} synapses. **e**, A schematic of the whole-cell recording configuration. **f**, Top, sample EPSC traces recorded before (pre-BDNF) and after (post-BDNF) bath application of BDNF. Bottom, summary plot showing the effect of BDNF on EPSC peak amplitude, for which the first peak in the paired pulse was measured and normalized to the baseline (that is, the average pre-BDNF amplitude). BDNF significantly enhanced EPSC amplitude (pre-BDNF, 98 ± 1.74%, post-BDNF, 146 ± 17.6%, $n = 6$ neurons (3 mice), $P < 0.05$, paired *t*-test). **g**, BDNF application decreased the paired-pulse ratio (see Methods) of the EPSCs (pre-BDNF, 1.17 ± 0.18; post-BDNF, 0.80 ± 0.09; $n = 6$ neurons (3 mice), $*P < 0.05$, paired *t*-test). Data are presented as mean ± s.e.m.

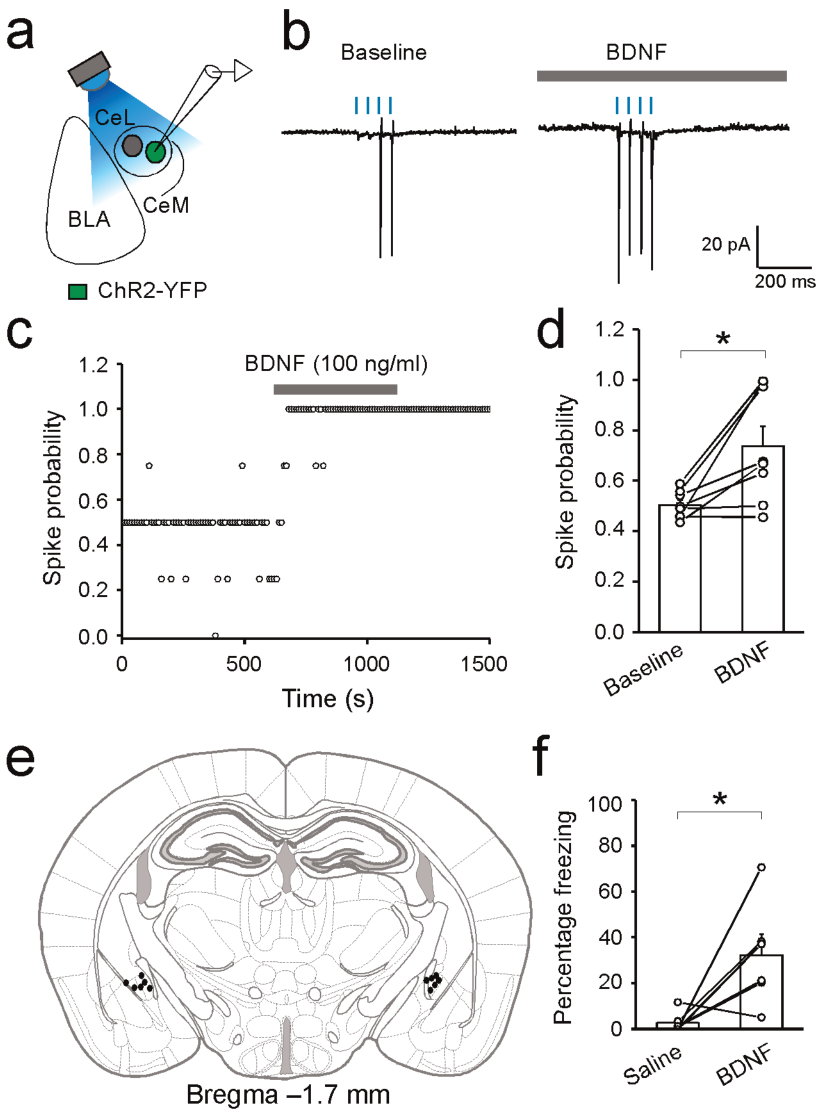

Extended Data Figure 10 | Exogenous application of BDNF in the CeL increases the excitability of SOM$^+$ neurons and elicits an unconditioned freezing response. **a**–**d**, BDNF increases the excitability of SOM$^+$ CeL neurons. **a**, A schematic of the experimental approach, in which photostimulation was used to assess the excitability of SOM$^+$ CeL neurons expressing ChR2. **b**, Sample traces of photostimulation-evoked spikes recorded in cell-attached mode, before (baseline; left) and after (right) bath application of BDNF (100 ng ml^{-1}). Light intensity was adjusted to evoke spikes with ~50% probability at baseline. **c**, A sample recording, in which the spike probability of a SOM$^+$ CeL neuron was followed before, during and after BDNF application. **d**, Quantification of the effect of BDNF on spike probability (baseline, 0.50 ± 0.02; BDNF, 0.74 ± 0.08; $n = 8$ neurons (4 mice), $*P < 0.05$, paired t-test). **e**, **f**, Infusion of BDNF into the CeL elicits an unconditioned freezing response. **e**, Drawing of the cannula sites. Each dot denotes where the tip of the injection cannula was located in each mouse. **f**, Quantification of freezing levels following CeL infusion of saline and BDNF (saline, 2.93 ± 1.84%; BDNF, 32.22 ± 9.19%; $n = 6$ mice, $*P < 0.05$, paired t-test). Data are presented as mean ± s.e.m.

doi:10.1038/nature14030

A temporal shift in the circuits mediating retrieval of fear memory

Fabricio H. Do-Monte[1,2], Kelvin Quiñones-Laracuente[1,2] & Gregory J. Quirk[1,2]

Fear memories allow animals to avoid danger, thereby increasing their chances of survival. Fear memories can be retrieved long after learning[1,2], but little is known about how retrieval circuits change with time[3,4]. Here we show that the dorsal midline thalamus of rats is required for the retrieval of auditory conditioned fear at late (24 hours, 7 days, 28 days), but not early (0.5 hours, 6 hours) time points after learning. Consistent with this, the paraventricular nucleus of the thalamus (PVT), a subregion of the dorsal midline thalamus, showed increased c-Fos expression only at late time points, indicating that the PVT is gradually recruited for fear retrieval. Accordingly, the conditioned tone responses of PVT neurons increased with time after training. The prelimbic (PL) prefrontal cortex, which is necessary for fear retrieval[5–7], sends dense projections to the PVT[8]. Retrieval at late time points activated PL neurons projecting to the PVT, and optogenetic silencing of these projections impaired retrieval at late, but not early, time points. In contrast, silencing of PL inputs to the basolateral amygdala impaired retrieval at early, but not late, time points, indicating a time-dependent shift in retrieval circuits. Retrieval at late time points also activated PVT neurons projecting to the central nucleus of the amygdala, and silencing these projections at late, but not early, time points induced a persistent attenuation of fear. Thus, the PVT may act as a crucial thalamic node recruited into cortico-amygdalar networks for retrieval and maintenance of long-term fear memories.

The association between a conditioned stimulus (for example, a tone) and an aversive event (an electrical shock) can be retrieved throughout the lifetime of an animal[9–11]. This tone–shock association is stored in the basolateral amygdala (BLA) and the central nucleus of the amygdala (CeA)[12–15], but the circuits necessary for retrieval of this memory at various times after learning are not well understood. The BLA receives inputs from the PL[16,17], a region necessary for fear retrieval[5–7]. The PL also projects densely to the dorsal midline thalamus (dMT)[8], which in turn projects to the CeA[18]. Thus, the dMT could coordinate fear responses with adaptive responses such as stress, sleep and foraging through its connections with the hypothalamus or nucleus accumbens[8,19]. We previously observed that the dMT is necessary for fear retrieval 24 h after conditioning, but not earlier[20]. Here, to test directly the hypothesis that retrieval circuits change with time, we used pharmacological, immunocytochemical, unit-recording and optogenetic techniques.

We found that inactivating the dMT with the $GABA_A$ (γ-aminobutyric acid type A) receptor agonist muscimol shortly after conditioning (0.5 or 6 h) had no effect on fear retrieval, but inactivating the dMT at later time points (24 h, 7 d and 28 d) impaired retrieval (Fig. 1a–c; conditioning levels shown in Extended Data Fig. 1a–e). The next day, in the absence of drug, retrieval remained impaired in the 7 d and 28 d groups (Fig. 1d), suggesting that dMT activity may be necessary for the maintenance of fear memory. In support of this, retrieval was still impaired 1 week after the initial retrieval test (day 14, see Extended Data Fig. 2a). Inactivation of the dMT without retrieval had no effect (Extended Data Fig. 2b), suggesting a possible role of the dMT in memory reconsolidation. Although intra-dMT infusion of drugs that block reconsolidation had no effect (Extended Data Fig. 2c, d), dMT activity could be facilitating memory reconsolidation in downstream structures (such as the amygdala). Thus, with the passage of time, dMT activity becomes increasingly necessary first for retrieval and later for maintenance of fear memories.

Next, we used the neural activity marker c-Fos to determine when the dMT is activated by conditioning. After training, exposure to conditioned tones induced robust freezing at 6 h, 24 h and 7 d time points (Extended Data Fig. 3a–c), but triggered different patterns of neuronal

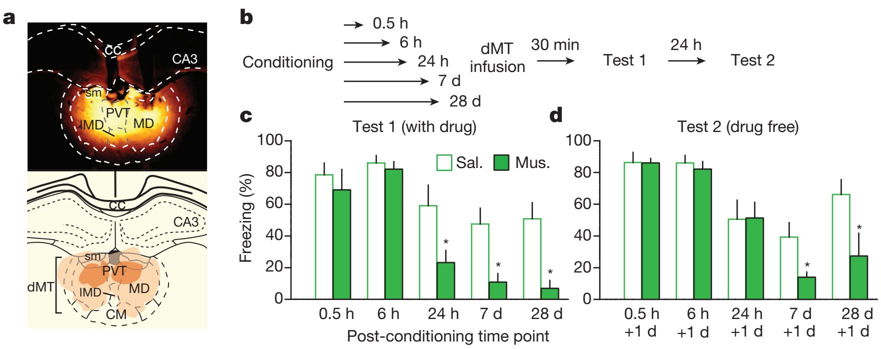

Figure 1 | The dMT is necessary for retrieval of fear at late, but not early, time points after conditioning. **a**, Top, representative micrograph showing the site of fluorescent muscimol (Mus.) injection into dMT. Bottom, orange areas represent the minimum (dark) and the maximum (light) spread of muscimol into the dMT. cc, corpus callosum; IMD, intermediodorsal nucleus of the thalamus; MD, mediodorsal thalamus; sm, stria medullaris. **b**, Experimental design. **c**, Left, freezing to conditioned tones after infusion of saline (Sal., white) or muscimol (green) at different post-conditioning time points. Muscimol impaired freezing ($F_{(4,73)} = 3.31$, $P = 0.01$) at 24 h ($P = 0.002$, $n = 8$ per group), 7 d ($P = 0.002$, $n = 14$ per group) and 28 d ($P < 0.001$, $n = 10$ for Sal., $n = 6$ for Mus.), but not at 0.5 h or 6 h ($P > 0.99$, $n = 6$ per group). Right, the next day, persistent attenuation of freezing ($F_{(2,54)} = 4.78$, $P = 0.011$) was observed at 7 d ($P = 0.013$) and 28 d ($P = 0.04$), but not at 24 h ($P = 0.35$). Two-way ANOVA followed by Tukey's post-hoc test. Data are mean ± s.e.m. in blocks of two trials; *$P < 0.05$.

[1]Department of Psychiatry, University of Puerto Rico School of Medicine, PO Box 365067, San Juan 00936, Puerto Rico. [2]Department of Anatomy & Neurobiology, University of Puerto Rico School of Medicine, P.O. Box 365067, San Juan 00936, Puerto Rico.

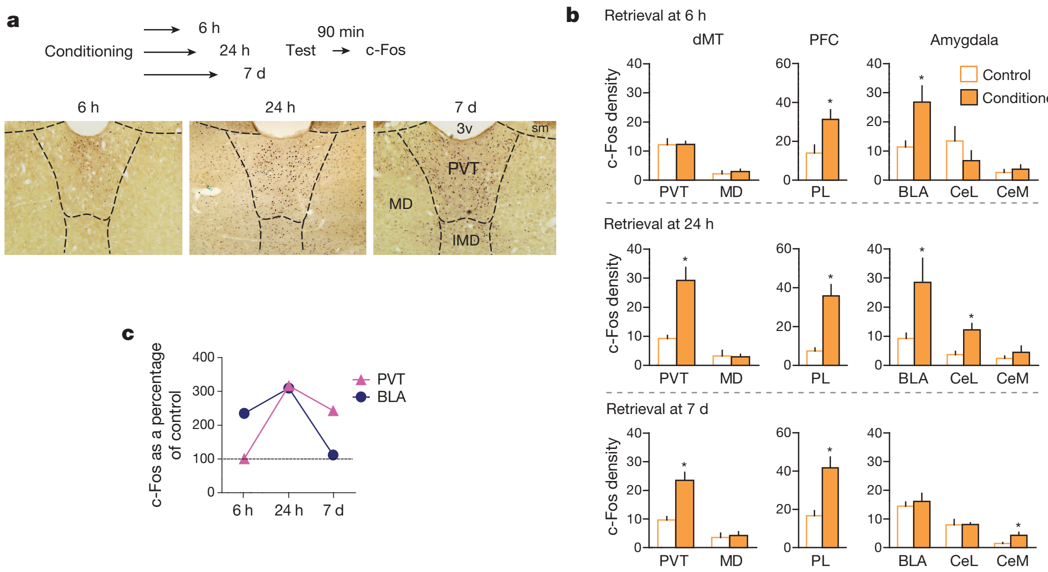

Figure 2 | c-Fos expression induced by fear retrieval at different time points after conditioning. **a**, Top, schematic for c-Fos experiments. Bottom, micrographs showing c-Fos expression in the dMT in the conditioned groups following fear retrieval at 6 h, 24 h and 7 d time points. **b**, Top, fear retrieval at 6 h ($n = 4$–5 per group) increased the number of c-Fos-positive neurons (per 0.1 mm^2) in the PL prefrontal cortex ($P = 0.03$, $t = 2.65$) and BLA ($P = 0.02$, $t = 2.85$), but not in the PVT ($P = 0.96$, $t = 0.04$). Middle, fear retrieval at 24 h ($n = 3$–4 per group) increased the number of c-Fos positive neurons in the PL ($P = 0.002$, $t = -5.43$), PVT ($P = 0.007$, $t = 3.22$), BLA ($P = 0.04$, $t = -2.67$) and the lateral portion of the central nucleus of the amygdala (CeL; $P = 0.01$, $t = -3.80$). Bottom, fear retrieval at 7 d ($n = 5$–6 per group) increased the number of c-Fos-positive neurons in the PL ($P = 0.002$, $t = 4.21$), PVT ($P < 0.001$, $t = 4.83$) and the medial portion of the central nucleus of the amygdala (CeM; $P = 0.02$, $t = 2.69$). **c**, c-Fos levels (as a percentage of control) in the PVT and BLA after fear retrieval at 6 h, 24 h and 7 d time points. Data are mean ± s.e.m.; unpaired t-test between control and conditioned groups; *$P < 0.05$.

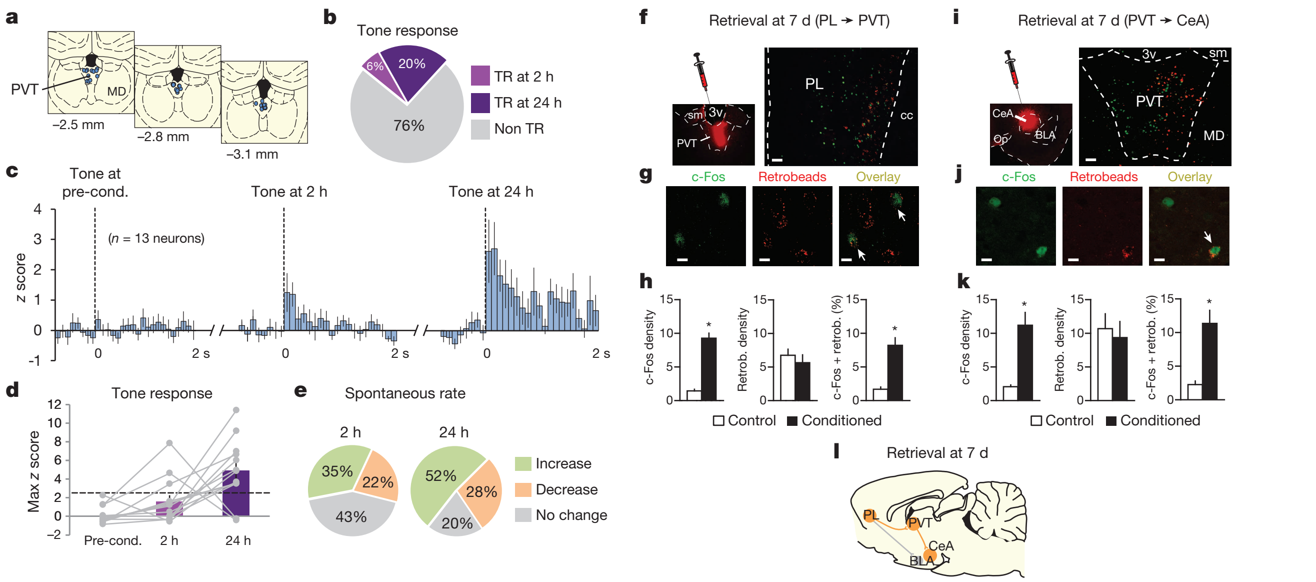

Figure 3 | Time-dependent increases in tone responses of PVT neurons following fear conditioning. **a**, Diagram of recording placements in the PVT. Coordinates from bregma. **b**, Percentage of tone-responsive (TR) neurons at 2 h and 24 h after conditioning ($n = 54$ neurons, 6% tone responsive at 2 h, 20% tone responsive at 24 h, Fisher's exact test, $P = 0.04$). **c**, Average peri-stimulus time histograms of all PVT neurons that were significantly tone responsive at either 2 h or 24 h after conditioning ($n = 13$ neurons, 100 ms bins). **d**, Maximum z score for group data (bars) or individual data (grey lines, $n = 13$ neurons). Dashed line indicates a z score criterion of 2.58. **e**, Changes in spontaneous firing rates of PVT neurons at 2 h (left) and 24 h (right) after conditioning, compared to pre-conditioning. Changes at 24 h were significantly greater than 2 h ($n = 54$ neurons; 24 h = 80%; 2 h = 57%, Fisher's exact test, $P = 0.02$). **f**, Left, micrograph showing site of retrobead infusion into the PVT. Right, micrograph showing PL neurons projecting to the PVT (retrogradely labelled, red) expressing immunoreactivity for c-Fos (green) after fear retrieval at 7 d. 3v, third ventricle. Scale bar, 100 µm. **g**, Confocal images showing c-Fos labelling (left), retrobead labelling (middle), and overlay (right) of PVT-projecting PL neurons (white arrows). Scale bar, 10 µm. **h**, Fear retrieval at 7 d increased the number of c-Fos-positive neurons (per 0.1 mm^2) in the PL (left, $P = 0.003$, $t = 8.74$), but the number of retrogradely labelled PL neurons was the same between groups (middle, $P = 0.51$, $t = -0.7$). Retrieval increased the percentage of retrogradely labelled PL neurons expressing c-Fos (right, $P = 0.004$, $t = 4.83$; $n = 3$–4 per group). **i**, Left, micrograph showing the site of retrobead infusion into the CeA. Right, micrograph showing PVT neurons projecting to the CeA (retrogradely labelled, red) expressing immunoreactivity for c-Fos (green) after fear retrieval at 7 d. Scale bar, 100 µm. **j**, Confocal images showing c-Fos labelling (left), retrobead labelling (middle), and overlay (right) of CeA-projecting PVT neurons (white arrow). Scale bar, 10 µm. **k**, Fear retrieval at 7 d increased the number of c-Fos-positive neurons (per 0.1 mm^2) in the PVT (left, $P = 0.03$, $t = 3.71$), but the number of retrogradely labelled PVT neurons was the same between groups (middle, $P = 0.79$, $t = -0.28$). Retrieval increased the percentage of retrogradely labelled PVT neurons expressing c-Fos (right, $P = 0.03$, $t = 3.61$; $n = 2$–3 per group). **l**, Schematic of the potential circuit mediating fear retrieval at the 7 d time point. Data are mean ± s.e.m; unpaired t-test between control and conditioned groups; *$P < 0.05$.

activation (Fig. 2a, b). The mediodorsal subdivision of the dMT showed no conditioned activation at any time point, whereas the PL showed activation at all three time points. This suggests that the PL is necessary for retrieval at both early and late time points, which we confirmed with muscimol (Extended Data Fig. 3d–f). Retrieval at 6 h activated PL and BLA, but not PVT, neurons, whereas retrieval at 7 d activated PL and PVT, but not BLA, neurons. Retrieval at 7 d also activated the medial portion of the central amygdala (CeM), suggesting that retrieval at 7 d may involve PL–PVT and PVT–CeA pathways. But at 24 h, both targets of the PL (BLA and PVT) were activated (Fig. 2b, c), consistent with a gradual shift in retrieval circuits from the PL–BLA to the PL–PVT.

Our c-Fos findings suggest a time-dependent activation of the PVT after fear conditioning; but they do not indicate if this activation represents an increase in tone responses, spontaneous activity, or both. To address this, we recorded from the same PVT neurons during both early and late time points after fear conditioning (Fig. 3a–e and Extended Data Fig. 4). A higher percentage of PVT neurons exhibited conditioned tone responses 24 h after conditioning, compared to 2 h after conditioning (24 h = 11 of 54, 20%; 2 h = 3 of 54, 6%; Fisher's exact test, $P = 0.04$; Fig. 3a–c). Moreover, the average magnitude of tone responses increased significantly from 2 h to 24 h in the same set of neurons ($F_{(2,36)} = 13.29$, $P = 0.003$, Fig. 3c). Notably, 12 out of 13 PVT neurons that were tone responsive at 24 h were not tone responsive at 2 h (Fig. 3d), consistent with a time-dependent recruitment of PVT neurons. In addition to tone responses, conditioning-induced changes in the spontaneous firing rate of PVT neurons were greater at 24 h compared to 2 h (24 h = 43 of 54, 80%; 2 h = 31 of 54, 43%; Fisher's exact test, $P = 0.02$; Fig. 3e).

The c-Fos activation pattern that we observed (Fig. 2b) suggests that activation of PVT neurons at 7 d may involve inputs from the PL and outputs to the CeA. To address this further, we injected a retrograde tracer (retrobeads) into either the PVT or CeA and measured co-labelling with c-Fos in the PL and PVT, respectively. Accordingly, retrieval at 7 d activated PL neurons projecting to the PVT (Fig. 3f–h), plus PVT neurons projecting to the CeA (Fig. 3i–k). Taken together, our data suggest that PL–PVT and PVT–CeA pathways may be necessary for fear retrieval at late (7 d), but not early (6 h), time points (Fig. 3l).

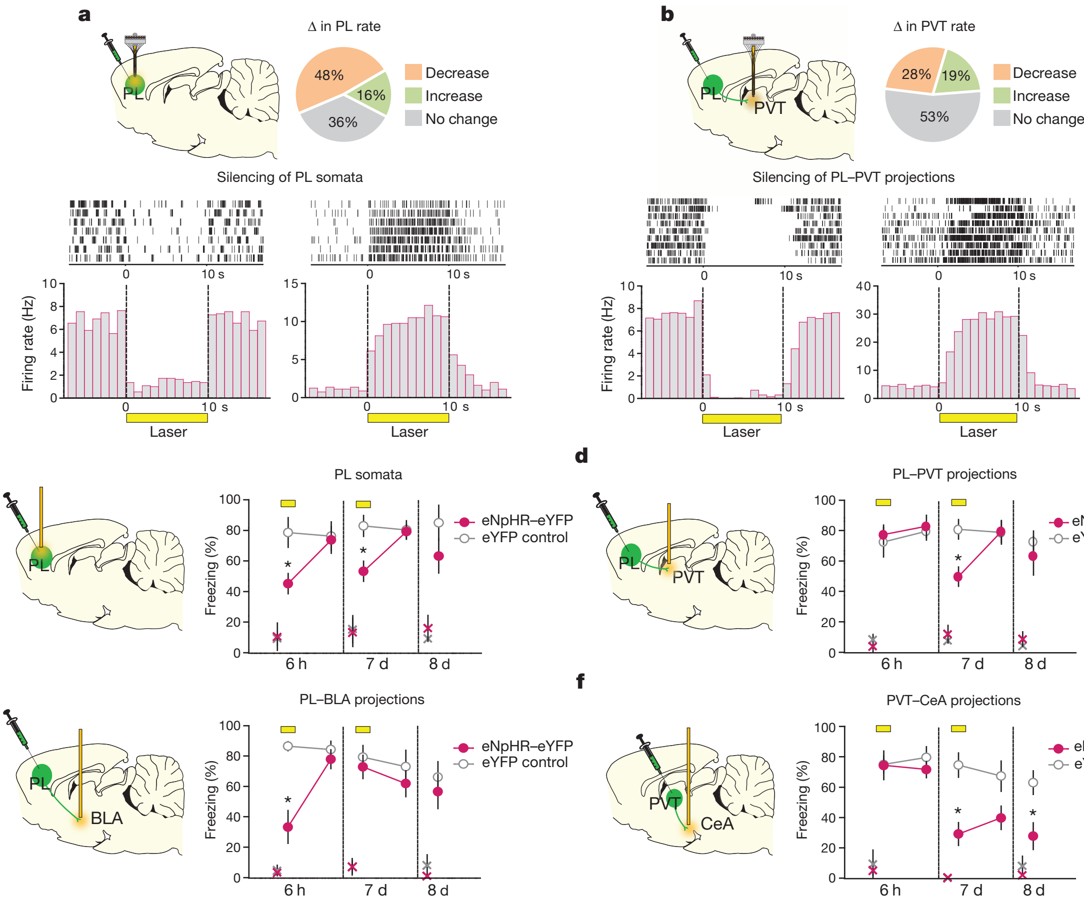

Figure 4 | Time-dependent shift of retrieval circuits after conditioning. **a**, Top, changes in PL firing rate with illumination of PL in rats expressing eNpHR–eYFP in PL ($n = 50$ neurons; 48% decreased, 16% increased; 36% did not change; unpaired t-test; $P < 0.05$). Bottom, raster plot and peri-stimulus time histogram of representative PL neurons responding to illumination in rats expressing eNpHR–eYFP in PL. PL neurons showed inhibition (left) or excitation (right). **b**, Top, changes in PVT firing rate after illumination of PL terminals in the PVT in rats expressing eNpHR–eYFP in the PL ($n = 47$ neurons; 28% decreased, 19% increased; 53% did not change; unpaired t-test; $P < 0.05$). Bottom, raster plot and peri-stimulus time histogram of representative PVT neurons responding to illumination of PL inputs in the PVT in rats infused with eNpHR–eYFP in the PL. PVT units showed inhibition (left) or excitation (right). **c**, Illumination (yellow bar) of PL somata reduced freezing to tones at both 6 h ($F_{(1,10)} = 15.1$, $P = 0.003$) and 7 d ($F_{(1,10)} = 20.3$, $P = 0.002$) in the eNpHR–eYFP group ($n = 7$), compared to the eYFP control group ($n = 5$). **d**, Illumination of PL inputs in the PVT significantly reduced freezing at 7 d ($F_{(1,9)} = 18.7$, $P = 0.002$), but not 6 h ($F_{(1,10)} = 0.06$, $P = 0.81$) (eNpHR–eYFP, $n = 7$; control, $n = 4$). **e**, Illumination of PL inputs in the BLA significantly reduced freezing at 6 h ($F_{(1,16)} = 26.0$, $P < 0.001$), but not 7 d ($F_{(1,16)} = 0.64$, $P = 0.43$) (eNpHR–eYFP, $n = 8$; control, $n = 10$). **f**, Illumination of PVT inputs in the CeA significantly reduced freezing at 7 d ($F_{(1,11)} = 11.9$, $P = 0.005$), but not 6 h ($F_{(1,11)} = 0.19$, $P = 0.67$) (eNpHR–eYFP, $n = 8$; control, $n = 5$). Freezing remained reduced the day after illumination of CeA inputs to the PVT ($P = 0.018$). Repeated-measures ANOVA followed by Tukey's post-hoc test. Data are mean ± s.e.m. in blocks of 2 trials; *$P < 0.05$. '×' denotes baseline (pre-tone) freezing levels.

To test these hypotheses directly, we used an optogenetic approach to silence specific projections at these two time points, within the same animal. The PL was infused with an adeno-associated viral vector (AAV-5) expressing the light-sensitive chloride pump halorhodopsin[21] combined with enhanced yellow fluorescent protein (eYFP), under the control of a CaMKIIα promoter, favouring expression within pyramidal neurons (AAV5:CaMKIIα::eNpHR3.0-eYFP)[22,23]. In anaesthetized rats, laser illumination of PL somata reduced (24 out of 50 tested, 48%) or in some cases increased (8 out of 50 tested, 16%) the firing rate of PL neurons (Fig. 4a and Extended Data Fig. 5a–c). Neurons that reduced their rate showed shorter response latencies than neurons that increased their rate, suggesting direct versus indirect responses, respectively. Furthermore, silencing PL terminals within the PVT either reduced (13 out of 47 tested, 28%) or increased (9 out of 47 tested, 19%) the firing rates of PVT neurons (Fig. 4b and Extended Data Fig. 5d–f), without significant differences in response latency. Our observation of both short and long response latencies in PVT neurons (Extended Data Fig. 5f) suggests that the PL may influence the PVT both directly and indirectly.

We then determined the effects of PL silencing on retrieval of fear memory. Silencing PL somata impaired retrieval at both 6 h and 7 d (Fig. 4c and Extended Data Figs 1f, 6a and 10a); however, silencing PL projections to the PVT impaired retrieval at 7 d, but not at 6 h (Fig. 4d and Extended Data Figs 1g, 6b and 10b). In contrast, silencing PL projections to the BLA impaired retrieval at 6 h, but not at 7 d (Fig. 4e and Extended Data Figs 1h, 6c and 10c). Thus, fear retrieval initially depends on PL–BLA circuits, but shifts to PL–PVT circuits with the passage of time. This shift probably involves different ensembles of neurons, as PL neurons projecting to the PVT versus the BLA are located in different layers of the PL[8,16] (Extended Data Fig. 7).

We next questioned which outputs of the PVT could mediate fear retrieval. The PVT sends dense projections to the CeA[18,19,24], and we observed that retrieval at 7 d activated PVT neurons projecting to the CeA (Fig. 3h). Accordingly, silencing PVT projections to the CeA impaired retrieval at 7 d, but not at 6 h (Fig. 4f and Extended Data Figs 1i, 6d and 10d). Retrieval remained impaired the day after silencing (day 8), suggesting that activation of PVT–CeA circuits is necessary for the maintenance of fear memory. It is unlikely that impaired retrieval at 7 d is caused by diffusion of the laser light from the CeA to the adjacent BLA because silencing BLA somata at 7 d did not impair retrieval (Extended Data Fig. 1j, 8, 10e). Silencing PVT–CeA projections during the inter-tone interval also had no effect (Extended Data Fig. 1k, 9), suggesting that the tone responses of PVT neurons (Fig. 3c) are essential for memory retrieval and maintenance. The necessity of PVT–CeA projections at late time points agrees with an accompanying study[25] showing that PVT inputs to the CeA are necessary for the long-term (24 h), but not short-term (3 h), induction of conditioning-induced plasticity in the CeA that encodes fear memory[14].

Our findings suggest a time-dependent reorganization of the neural circuits required for fear memory retrieval. While fear behaviour appears constant with time, the circuits mediating this behaviour are not. Retrieval of fear memories long after conditioning may activate PL inputs to the PVT, which could excite PVT neurons projecting to the CeA, thereby activating CeA neurons to elicit fear responses. Recruitment of the PVT may serve to integrate fear with other adaptive responses such as stress[26], thereby strengthening fear memory in amygdala circuits. Dysregulation of time-dependent changes in retrieval circuits may contribute to exacerbated fear responses occurring long after the traumatic event, for instance in individuals with anxiety disorders.

Online Content Methods, along with any additional Extended Data display items and Source Data, are available in the online version of the paper; references unique to these sections appear only in the online paper.

Received 10 February; accepted 3 November 2014.
Published online 19 January 2015.

1. Jasnow, A. M., Cullen, P. K. & Riccio, D. C. Remembering another aspect of forgetting. *Front. Psychol.* **3,** 175 (2012).
2. Wiltgen, B. J. & Tanaka, K. Z. Systems consolidation and the content of memory. *Neurobiol. Learn. Mem.* **106,** 365–371 (2013).
3. Sacco, T. & Sacchetti, B. Role of secondary sensory cortices in emotional memory storage and retrieval in rats. *Science* **329,** 649–656 (2010).
4. Restivo, L., Vetere, G., Bontempi, B. & Ammassari-Teule, M. The formation of recent and remote memory is associated with time-dependent formation of dendritic spines in the hippocampus and anterior cingulate cortex. *J. Neurosci.* **29,** 8206–8214 (2009).
5. Sierra-Mercado, D., Padilla-Coreano, N. & Quirk, G. J. Dissociable roles of prelimbic and infralimbic cortices, ventral hippocampus, and basolateral amygdala in the expression and extinction of conditioned fear. *Neuropsychopharmacology* **36,** 529–538 (2011).
6. Burgos-Robles, A., Vidal-Gonzalez, I. & Quirk, G. J. Sustained conditioned responses in prelimbic prefrontal neurons are correlated with fear expression and extinction failure. *J. Neurosci.* **29,** 8474–8482 (2009).
7. Courtin, J. *et al.* Prefrontal parvalbumin interneurons shape neuronal activity to drive fear expression. *Nature* **505,** 92–96 (2014).
8. Li, S. & Kirouac, G. J. Sources of inputs to the anterior and posterior aspects of the paraventricular nucleus of the thalamus. *Brain Struct. Funct.* **217,** 257–273 (2012).
9. LeDoux, J. E. Emotion circuits in the brain. *Annu. Rev. Neurosci.* **23,** 155–184 (2000).
10. Maren, S. Neurobiology of Pavlovian fear conditioning. *Annu. Rev. Neurosci.* **24,** 897–931 (2001).
11. Gale, G. D. *et al.* Role of the basolateral amygdala in the storage of fear memories across the adult lifetime of rats. *J. Neurosci.* **24,** 3810–3815 (2004).
12. Johansen, J. P., Cain, C. K., Ostroff, L. E. & LeDoux, J. E. Molecular mechanisms of fear learning and memory. *Cell* **147,** 509–524 (2011).
13. Rogan, M. T., Staubli, U. V. & LeDoux, J. E. Fear conditioning induces associative long-term potentiation in the amygdala. *Nature* **390,** 604–607 (1997).
14. Li, H. *et al.* Experience-dependent modification of a central amygdala fear circuit. *Nature Neurosci.* **16,** 332–339 10.1038/nn.3322 (2013).
15. Ciocchi, S. *et al.* Encoding of conditioned fear in central amygdala inhibitory circuits. *Nature* **468,** 277–282 (2010).
16. Vertes, R. P. Differential projections of the infralimbic and prelimbic cortex in the rat. *Synapse* **51,** 32–58 (2004).
17. McDonald, A. J., Mascagni, F. & Guo, L. Projections of the medial and lateral prefrontal cortices to the amygdala: a *Phaseolus vulgaris* leucoagglutinin study in the rat. *Neuroscience* **71,** 55–75 (1996).
18. Vertes, R. P. & Hoover, W. B. Projections of the paraventricular and paratenial nuclei of the dorsal midline thalamus in the rat. *J. Comp. Neurol.* **508,** 212–237 (2008).
19. Moga, M. M., Weis, R. P. & Moore, R. Y. Efferent projections of the paraventricular thalamic nucleus in the rat. *J. Comp. Neurol.* **359,** 221–238 (1995).
20. Padilla-Coreano, N., Do-Monte, F. H. & Quirk, G. J. A time-dependent role of midline thalamic nuclei in the retrieval of fear memory. *Neuropharmacology* **62,** 457–463 (2012).
21. Gradinaru, V. *et al.* Molecular and cellular approaches for diversifying and extending optogenetics. *Cell* **141,** 154–165 (2010).
22. Liu, X. B. & Jones, E. G. Localization of alpha type II calcium calmodulin-dependent protein kinase at glutamatergic but not gamma-aminobutyric acid (GABAergic) synapses in thalamus and cerebral cortex. *Proc. Natl Acad. Sci. USA* **93,** 7332–7336 (1996).
23. Van den Oever, M. C. *et al.* Ventromedial prefrontal cortex pyramidal cells have a temporal dynamic role in recall and extinction of cocaine-associated memory. *J. Neurosci.* **33,** 18225–18233 (2013).
24. Li, S. & Kirouac, G. J. Projections from the paraventricular nucleus of the thalamus to the forebrain, with special emphasis on the extended amygdala. *J. Comp. Neurol.* **506,** 263–287 (2008).
25. Penzo, M. A. *et al.* The paraventricular thalamus controls a central amygdala fear circuit. *Nature* http://dx.doi.org/10.1038/nature13978 (this issue).
26. Heydendael, W. *et al.* Orexins/hypocretins act in the posterior paraventricular thalamic nucleus during repeated stress to regulate facilitation to novel stress. *Endocrinology* **152,** 4738–4752 (2011).

Acknowledgements We thank G. Manzano-Nieves for help with the optogenetic experiments, A. C. Felix-Ortiz for technical advice, and K. M. Tye for comments on the manuscript. We thank K. Deisseroth for viral constructs and the UNC Vector Core Facility for viral packaging. This study was supported by the NIH grants R01-MH058883, and P50-MH086400, and a grant from the University of Puerto Rico President's Office to G.J.Q.; the MBRS-RISE Program (R25-GM061838) to K.Q.L.; and NSF grant DBI-0115825 and RCMI grant 8G12-MD007600 for the Confocal Microscope Facility.

Author Contributions F.H.D.-M. performed behavioural, immunocytochemical and optogenetic experiments. F.H.D.-M. and K.Q.-L. performed single-unit recording in anaesthetized rats. K.Q.-L. performed single-unit recording experiments in behaving rats. F.H.D.-M., K.Q.-L. and G.J.Q. designed the study, interpreted results, and wrote the paper.

Author Information Reprints and permissions information is available at www.nature.com/reprints. The authors declare no competing financial interests. Readers are welcome to comment on the online version of the paper. Correspondence and requests for materials should be addressed to F.H.D.-M. (fabriciodomonte@gmail.com).

METHODS

All procedures were approved by the Institutional Animal Care and Use Committee of the University of Puerto Rico School of Medicine in compliance with National Institutes of Health guidelines for the care and use of laboratory animals.

Subjects. A total of 266 male Sprague Dawley rats (Harlan Laboratories) weighing 300–360 g were housed and handled as described previously[27]. Rats were maintained on a restricted diet (18 g per day of standard rat chow) until they reached 85% of their original body weight. They were then trained to press a bar for food on a variable interval schedule of reinforcement (VI-60 s)[27], except for unit recording experiments and Extended Data Fig. 2a. Pressing a bar for food ensures a constant level of activity in which freezing behaviour can be reliably measured during fear conditioning sessions[27]. For optogenetic experiments, rats were randomly assigned to each of the experimental groups. For muscimol inactivation and immunocytochemistry experiments, groups were assigned after matching for freezing levels during the conditioning session. Sample size was based on estimations by power analysis with a level of significance of 0.05 and a power of 0.9.

Surgeries. Rats were anaesthetized with isoflurane (5%) in an induction chamber. Rats were positioned in a stereotaxic frame (Kopf Instruments) and anaesthetized with isoflurane (2.5%) through a facemask. For muscimol inactivation experiments, double 26-gauge guide cannulas with 9 mm of length (Plastics One) were implanted targeting the dorsal midline thalamus (dMT; anteroposterior (AP), −2.6 mm from bregma; mediolateral (ML), ±0.6 mm from midline; dorsoventral (DV), −4.5 mm from skull surface) or the prelimbic cortex (PL; AP, +2.8 mm; ML, ±0.6 mm; DV, −2.6 mm)[28]. Stainless-steel obturators (33-gauge) were inserted into the guide cannulas to avoid obstructions until infusions were made. The cannula was fixed to the skull with anchoring screws and acrylic cement. For retrograde labelling experiments, a 0.5 μl syringe (Hamilton) was used to infuse 0.1 μl of green or red fluorescently labelled latex retrobeads (Lumafluor Inc.) per site. Retrobeads were chosen because they show very limited diffusion from the injection site even weeks after infusion.

For optogenetic experiments, a double 22-gauge guide cannula (9 mm length) was implanted targeting the PL. A single guide cannula (12 mm length) was implanted aiming at the paraventricular nucleus of the thalamus (PVT; AP, −2.6 mm; ML, ±2.0 mm; DV, −4.7 mm, 20° angle), or bilaterally implanted aiming at the basolateral amygdala (BLA; AP, −2.6 mm; ML, ±4.8 mm; DV, −7.6 mm) or the central amygdala (CeA; AP, −2.6 mm; ML, ±4.2 mm; DV, −6.7 mm). An injector extending 1 mm past the cannula tip was used to inject 0.5 μl of virus at a rate of 0.05 μl per min. After infusion, the injector was kept inside the cannula for 10 min to reduce back-flow. The injector was then removed and an optical fibre with 0.5 mm of projection was inserted into the cannula. Adhesive cement (C&B metabond; Parkell) was applied first, followed by acrylic cement to fix the guide cannula and the optical fibre to the skull. For unit-recording experiments, a moveable array of 16 microwires (50 μm, 2 × 8; NB Labs) was used to record from the PVT. After surgery, a triple antibiotic was applied and an analgesic (ketofen, 2 mg kg^{-1}) was injected intramuscularly. All rats were allowed 5–7 days for recovery, except those used for optogenetic experiments, which were allowed 6–8 weeks for virus expression.

Histology. Upon completion of experiments, rats were transcardially perfused with 0.9% saline followed by 10% buffered formalin. Brains were extracted and stored in a 30% sucrose/10% formalin solution. Coronal frozen sections were cut 40 μm thick, mounted on slides, and observed in a microscope equipped with a fluorescent lamp (X-Cite, Series 120Q) and a digital camera. The spread of fluorescent muscimol or retrobeads, the presence of eYFP labelling, and the placement of the optical fibre tips were determined for each rat, and those located outside the target area were excluded from the statistical analysis.

Drug infusion. The $GABA_A$ agonist muscimol (fluorescent muscimol, BODIPY TMR-X conjugate, Sigma-Aldrich) was used to enhance $GABA_A$ receptor activity, thereby inactivating target structures. Infusions were made 30 min before testing at a rate of 0.2 μl per min (0.11 nmol per 0.2 μl per side), according to a previous study[5]. To inhibit the signal-regulated kinase/mitogen-activated protein kinase (ERK/MAPK) signalling cascade within dMT, U0126 (Tocris) was dissolved in 5% dimethylsulfoxide (DMSO) and 5% Tween 80, diluted to a concentration of 2 μg μl^{-1}, and infused into the dMT (0.5 μl per side) at a rate of 0.25 μl per min immediately after retrieval test, according to a previous study[29]. To block the synthesis of proteins within the dMT, anisomycin (Sigma-Aldrich) was diluted in PBS and dissolved in 1 M HCl. The pH was adjusted back to 7.3 with NaOH and PBS until the solution reached a concentration of 125 μg μl^{-1}. Anisomycin was infused into the dMT (0.5 μl per side) at a rate of 0.25 μl per min immediately after the retrieval test, according to a previous study[30]. Following infusion, the injectors were left in place for 1 min to allow the drug to diffuse.

Auditory fear conditioning. Rats were conditioned and tested in standard operant chambers (Coulbourn Instruments) located in sound-attenuating cubicles (Med Associates). The floor of the chambers consisted of stainless steel bars that delivered a scrambled electric footshock. Between experiments, shock grids and floor trays were cleaned with soap and water, and chamber walls were cleaned with wet paper towels. Rats were conditioned with a pure tone (30 s, 4 KHz, 75 dB) paired with a shock delivered to the floor grids (0.5 s, 0.54 mA). All trials were separated by a variable interval averaging 3 min. Fear conditioning consisted of 5 habituation tones followed immediately by 7 conditioning tones that co-terminated with footshocks. To evaluate the role of dMT on fear retrieval, dMT was inactivated at 1 of 5 post-conditioning time points: 0.5 h, 6 h, 24 h, 7 d or 28 d, and rats were tested 30 min later in the same box with two tones. Only two post-conditioning time points were used for PL inactivation: 6 h or 7 d. A drug-free test was performed the day after infusion to test for fear maintenance. For immunocytochemistry experiments, naive rats (without bar-press training) were fear conditioned (conditioned group) or exposed to tones only (unconditioned group). Both groups received two test tones at either 6 h or 7 d after conditioning, and were perfused 90 min later. For all optogenetics experiments, rats were fear conditioned and tested with four tones at both 6 h and 7 d after conditioning. Laser illumination was delivered during the first two tones at each time point. The following day (day 8), two tones were delivered in the absence of illumination to test for fear memory maintenance. For unit-recording experiments, rats were fear conditioned and tested with four tones at 2 h and 24 h post-conditioning time points.

Open field testing and bar-pressing for food. Three days after completion of optogenetics experiments, rats were returned to the operant chambers to assess the effects of laser illumination on the motivation to press for food. The average press rate was compared between 5 min trials (laser off versus laser on), following a 5 min acclimation period. Rats pressing <3 or >30 presses per min during the acclimation period were eliminated (n = 3). Locomotor activity in the open field arena (90 cm diameter) was automatically assessed (ANY-Maze) by comparing the total distance travelled between 3 min trials (laser off versus laser on), following a 3 min acclimation period. The percentage of time spent in the centre of the open field (30 cm diameter) was used as an anxiety measurement.

c-Fos immunocytochemistry. Rats were deeply anaesthetized with sodium pentobarbital (450 mg kg^{-1} intraperitoneal (i.p.)) and perfused transcardially with 100 ml of saline (0.9%), followed by 500 ml of 4% paraformaldehyde in 0.1 M phosphate buffer (pH 7.4). Brains were transferred to a solution of 30% sucrose in 0.1 M phosphate buffer at 4 °C for 48 h. Brains were then frozen and cut (40 μm) in the frontal plane of the medial prefrontal cortex, dorsal midline thalamus, and amygdala. A complete series of sections was processed for immunocytochemistry with anti-c-Fos serum raised in rabbit (Ab-5, Oncogene Science) at a dilution of 1:20,000 overnight. The primary antiserum was localized using a variation of the avidin–biotin complex system. Sections were incubated for 2 h at room temperature in a solution of biotinylated goat anti-rabbit IgG (1:200; Vector Laboratories) and placed in the mixed avidin–biotin horseradish peroxidase complex solution (1:200; ABC Elite kit, Vector Laboratories) for 90 min. Black immunoreactive nuclei labelled for c-Fos were visualized after 10 min of exposure to a chromogen solution containing 0.02% 3,3′-diaminobenzidinetetrahydrochloride with 0.3% nickel-ammonium sulfate (DAB-Ni) in 0.05 M Tris buffer (pH 7.6) followed by incubation for 5 min in a chromogen solution with glucose oxidase (10%) and D-glucose (10%). The reaction was stopped using potassium PBS (pH 7.4). Sections were mounted on gelatin-coated slides, dehydrated and cover slipped. Counter sections were stained for Nissl bodies, cover slipped and examined in an optical microscope to determine the anatomical boundaries of each structure. For fluorescent c-Fos labelling, sections were processed with the same antibody mentioned above at a dilution of 1:2,000 overnight, and placed in a fluorescent secondary-antibody Alexa Fluor 488 (1:200; Life Technologies) for 2 h. Sections were cover slipped with anti-fading mounting media (Vector Laboratories) and examined with both an epifluorescent and a confocal microscope.

Immunoreactivity quantification. c-Fos-positive cells were counted at 20× magnification of a brightfield microscope (Olympus, Model BX51) equipped with a digital camera. Images were generated for the prelimbic (PL) subregion of the medial prefrontal cortex (mPFC), the paraventricular (PVT) and the mediodorsal (MD) nucleus of the dorsal midline thalamus (dMT), the basolateral nucleus of the amygdala (BLA), the lateral portion of the central nucleus of the amygdala (CeL), and the medial portion of the central nucleus of the amygdala (CeM). Cells were considered positive for c-Fos-like immunoreactivity if the nucleus was the appropriate size (area ranging from 100 to 500 μm^2) and shape (at least 50% of circularity), and was distinct from the background. c-Fos-positive cells were automatically counted (Metamorph software version 6.1) and averaged for each hemisphere at distinct rostrocaudal levels. For the PL, counted sections at antero-posterior levels were +2.7 mm, +3.2 mm and + 3.7 mm from the bregma. For dMT, counted sections at antero-posterior levels were − 1.8 mm, −2.1 mm, −2.5 mm, −2.9 mm, −3.3 mm from the bregma. For amygdala, counted sections at antero-posterior levels were −2.3 mm and −2.8 mm from the bregma. The density of c-Fos positive cells (cells per 0.1 mm^2) was calculated by dividing the number of c-Fos positive cells by the total area of each region. For fluorescent c-Fos and retrobeads quantification, images

were generated by using both an epifluorescent microscope (X-Cite, Series 120Q) and a confocal laser scanning microscope (model Zeiss, LSM 5 Pascal). A 40× oil immersion objective with the appropriate filter sets for c-Fos (488 nm) and red retrobeads (543 nm) were used. Serial *Z*-stack images (1 μm thick, 8–10 optical planes) through multiple sections were acquired (Axioplan 2 Imaging) using identical pinholes, gain and laser settings. c-Fos and retrobeads positive neurons were automatically counted using commercial software (Metamorph version 6.1; Molecular Devices, Sunnyvale, CA). c-Fos co-localization with retrobeads was manually quantified by an experimenter blind to experimental groups by measuring the percentage of retrogradely labelled neurons in both the PL and PVT expressing c-Fos.

Virus-mediated gene expression. The adeno-associated viruses (AAV, serotype 5) were obtained from the University of North Carolina Vector Core. Viral titres were 3×10^{12} particles per ml for AAV5:CaMKII::eYFP and 4×10^{12} particles per ml for AAV5:CaMKIIα::eNpHR3.0-eYFP. The use of CaMKII promoter enables transgene expression favouring pyramidal neurons[22]. Viruses were housed in an −80 °C freezer. Dual optical fibres (0.22 NA, 200 μm core; 10 mm length, Doric Lenses, Quebec, Canada) were implanted in the PL, whereas single optical fibres were implanted singly in the PVT or bilaterally in the CeA and BLA (0.22 NA, 200 μm core, 13 mm length, Doric Lenses).

Illumination. Yellow laser light was generated by a 593.5-nm diode-pumped solid-state laser (DPSS, MGLF 593.5; OEM Laser Systems). The beam was passed through a shutter/coupler (200 μm core, Ozoptics), patchcord (200 μm core, Doric Lenses), rotary joint (200 μm core, 1 × 2, Doric Lenses), mono or dual patchcord (0.22 NA, 200 μm core, Doric Lenses), and optical fibre to reach the brain. The power density estimated at the tip of the optical fibre was 5 mW for illumination of somata and 10 mW for illumination of projection sites. The laser was initiated 10 s before tone onset, given the long response latencies observed in some PL and PVT neurons (see Extended Data Fig. 6), and persisted throughout the 30 s tone. Rats were familiarized with the patchcord for at least 3 d before starting each behavioural session.

Optrode recording. Rats infected with eNpHR-eYFP in the PL were anaesthetized with urethane (1 g kg^{-1}, i.p.; Sigma-Aldrich) and placed in a stereotaxic frame. An optrode consisting of an optical fibre surrounded by 8 single-unit-recording wires (NB Labs) was inserted and directed towards the PVT (−3.1 mm anterior, 1.8 mm lateral, 5.5 mm ventral from the bregma with a 20° angle). The optrode was ventrally advanced in steps of 0.03 mm. Single units were monitored in real time (RASPUTIN software, Plexon Inc.). When a single unit was isolated, a 593.5 nm laser was activated for 10 s within a 20 s period, at least 5 times. Single units were recorded and stored for spike sorting (Offline Sorter, Plexon Inc.) and spike-train analysis (Neuroexplorer, NEX Technologies) as described below.

Single-unit recording. Rats were implanted with electrode arrays consisting of 16 fine wires (50 μm, 2 × 8, NB Labs). Stereotaxic coordinates for PVT electrodes were: AP, −1.8 to −3.8 mm; ML, ±1.8 mm; and DV, −5.5 mm, with a 20° angle. Rats were fear conditioned and tested for fear retrieval with 4 tones presented at 2 h and 24 h after conditioning. Eleven rats were used, with 2–9 neurons per rat for a total of 54 neurons. Waveforms exceeding a voltage threshold were amplified (gain ×100), digitized at 40 kHz (MAP, Plexon) and stored onto disk. Single units were classified as maintained throughout all time points (pre-conditioning, 2 h, and 24 h) based on waveform features such as valley-to-peak and amplitude measurements (Offline Sorter; Plexon; Extended Data Fig. 7)[31]. Automated processing was carried out using a valley-seeking scan algorithm and then evaluated using sort quality metrics. Spikes with interspike intervals <1 ms were excluded. Spike trains were analysed with commercial software (Neuroexplorer, NEX Technologies) for calculating firing rate and tone responses. Tone responses for 100-ms bins were calculated as *z* scores normalized to ten pre-tone bins of 100 ms. Significantly tone-responsive neurons showed *z* scores >2.58 ($P < 0.01$, two-tailed paired *t*-test) in either the first or second 100 ms bin following tone onset. Spontaneous firing rate was collected before the conditioning session and before both retrieval sessions for 3 min. Between recording sessions, rats were unplugged and returned to their home cage. At the end of the recording sessions, a micro-lesion was made by passing anodal current (0.25 mA for 25 s) through the active wires to deposit iron in the tissue. After perfusion, brains were extracted and stored in a 30% sucrose/ 6% ferrocyanide solution to stain the iron deposits.

Data collection and analysis. Behaviour was recorded with digital video cameras (Micro Video Products) and freezing was measured using commercially available software (Freezescan, Clever Systems). Press rate was measured using automated software (Graphic State, Coulbourn Instruments, Allentown, PA, USA). Distance travelled in the open field was measured using an automated video-tracking system (ANY-maze, Stoelting Co). Although experimenters were not blind to group allocation, automated counting was used for most measurements. Manual counting was only used to quantify the percentage of co-labelling between c-Fos and retrobeads (Fig. 3f,g) and was done by an experimenter blind to experimental groups. Parametric analysis was used since the data did not deviate substantially from a normal distribution (Shapiro–Wilk normality test, $P > 0.05$). Similar variance was observed in all the groups statistically compared (*F*-test two-sample for variance before *t*-test, Barttlet's Chi-square test before ANOVA; $P > 0.05$). All graphs and numerical values in the figures are presented as mean ± s.e.m. Trials were averaged in blocks of two and compared with repeated-measures analysis of variance (ANOVA), followed by Tukey's post-hoc comparisons when appropriate (STATISTICA; Statsoft). All Student's *t*-tests used were two-tailed. A small percentage of rats (3%) were excluded from analysis because they did not exceed criteria for acquisition of conditioned freezing (>30% freezing in at least one trial). No further exclusions were made.

27. Quirk, G. J., Russo, G. K., Barron, J. L. & Lebron, K. The role of ventromedial prefrontal cortex in the recovery of extinguished fear. *J. Neurosci.* **20,** 6225–6231 (2000).
28. Paxinos, G. & Watson, C. *The Rat Brain in Stereotaxic Coordinates* 6th edn (Academic, 2007).
29. Schafe, G. E. *et al.* Activation of ERK/MAP kinase in the amygdala is required for memory consolidation of pavlovian fear conditioning. *J. Neurosci.* **20,** 8177–8187 (2000).
30. Nader, K., Schafe, G. E. & Le Doux, J. E. Fear memories require protein synthesis in the amygdala for reconsolidation after retrieval. *Nature* **406,** 722–726 (2000).
31. Tseng, W. T., Yen, C. T. & Tsai, M. L. A bundled microwire array for long-term chronic single-unit recording in deep brain regions of behaving rats. *J. Neurosci. Methods* **201,** 368–376 (2011).

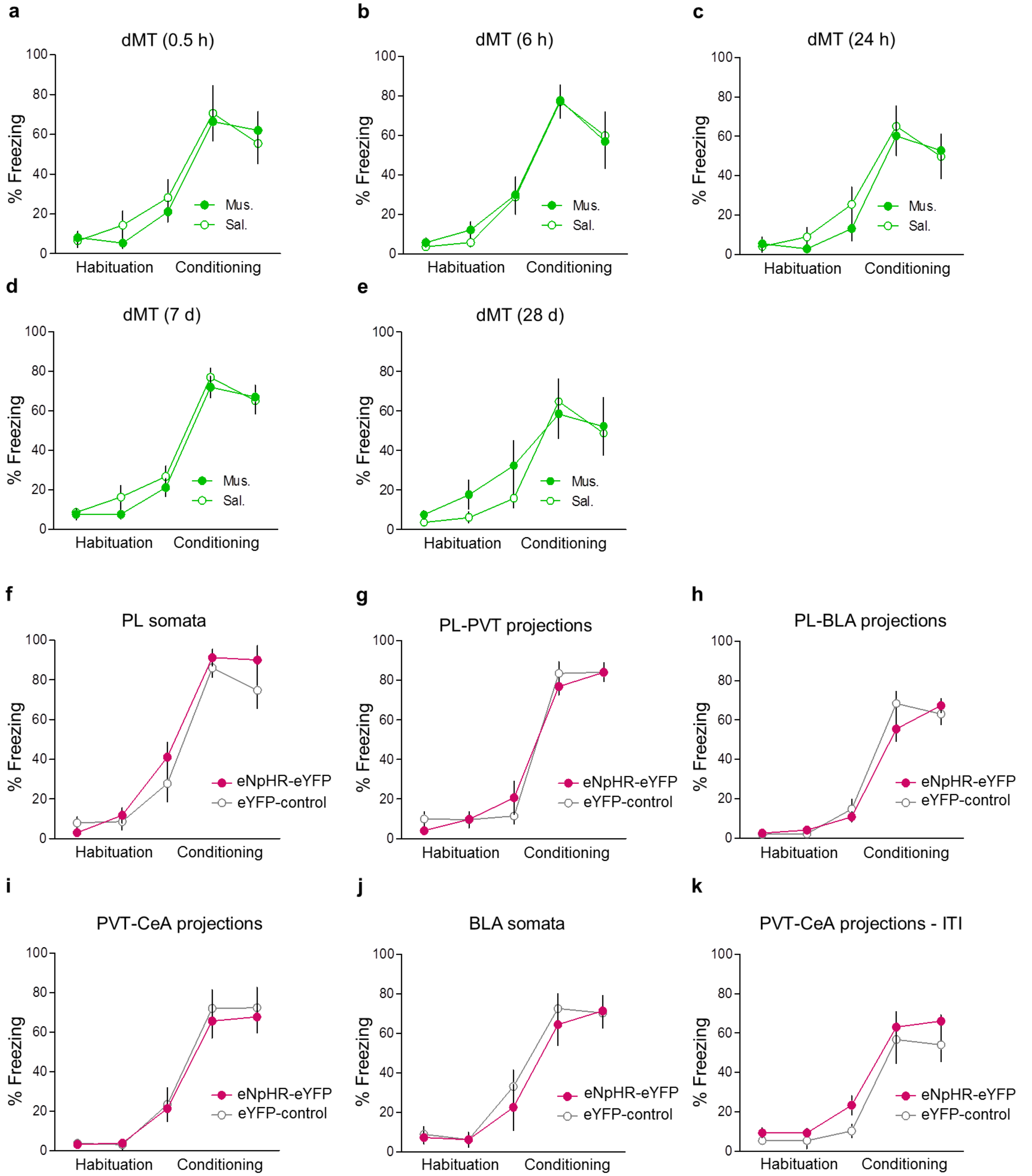

Extended Data Figure 1 | Conditioning levels in muscimol and optogenetic experiments. **a–e**, In the muscimol experiments, levels of freezing to tones (pre-treatment) for the habituation phase (first two blocks) and conditioning phase (last three blocks) were similar for saline (Sal., white circles) and muscimol (Mus., green circles) groups at 0.5 h (**a**), 6 h (**b**), 24 h (**c**), 7 d (**d**) and 28 d (**e**). **f–k**, In the optogenetic experiments, freezing levels were similar for the eNpHR–eYFP groups (red circles) and the control groups (white circles) before manipulation of the following regions or pathways: PL somata (**f**); PL–PVT projections (**g**); PL–BLA projections (**h**); PVT–CeA projections (**i**); BLA somata (**j**); and PVT–CeA projections during inter-trial interval (ITI) (**k**). Data are shown as mean ± s.e.m. in blocks of two trials.

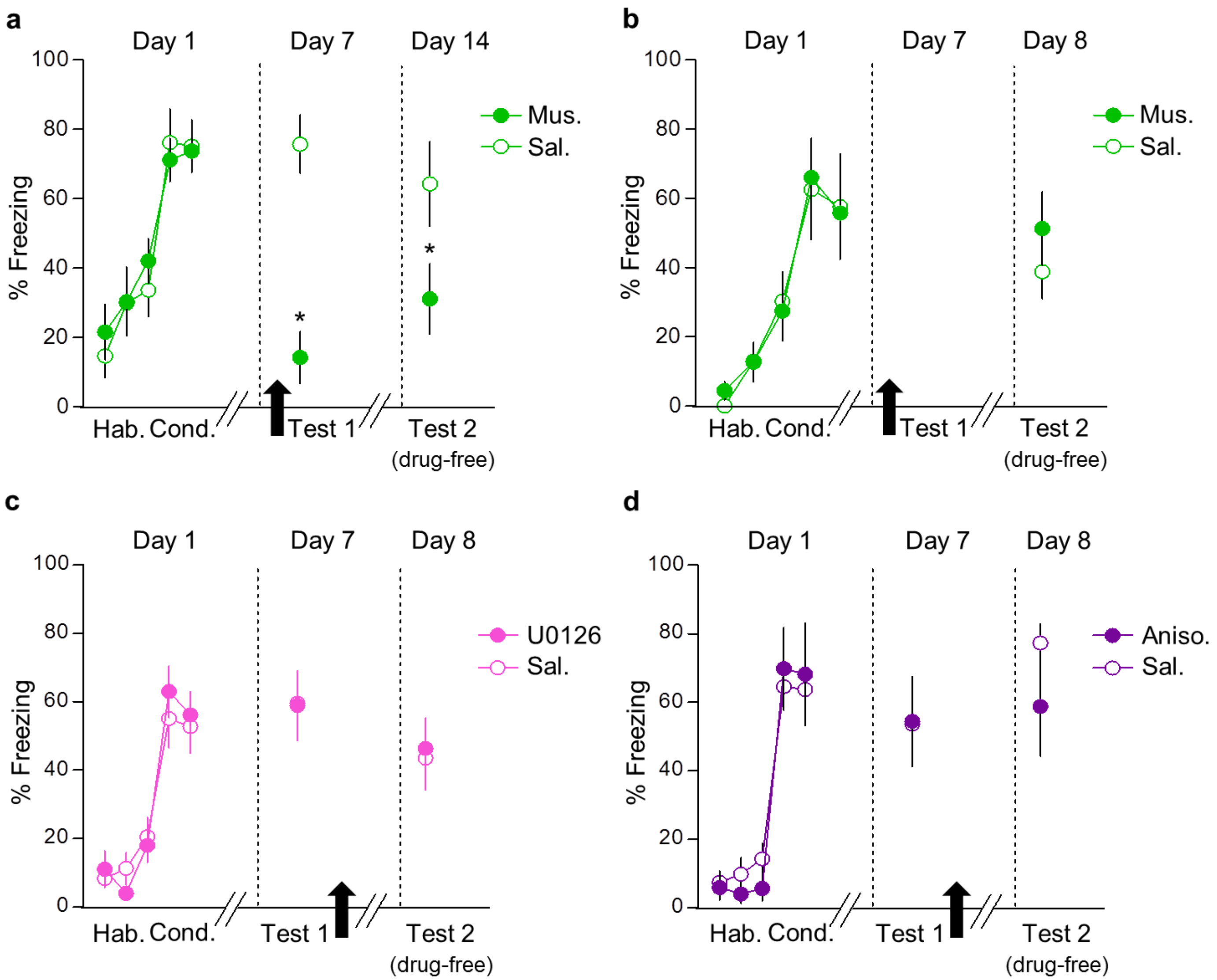

Extended Data Figure 2 | Neural activity in dMT, but not the MAPK cascade or protein synthesis in dMT, is necessary for memory maintenance following reactivation. **a**, Freezing to tones during habituation (Hab.; first two blocks of day 1), conditioning (Cond.; last three blocks of day 1), test 1 (day 7), and test 2 (drug-free test; day 14) performed 7 days after dMT infusion of saline (Sal., white circles, $n = 10$) or muscimol (Mus., green circles, $n = 14$), in rats never given bar-press training. Infusion of Mus. into the dMT impaired fear retrieval during test 1 ($t = -4.35$, $P < 0.001$), and also 1 week later during test 2 ($t = -2.14$, $P = 0.04$). **b**, Freezing to tones during habituation (Hab.; first two blocks of day 1), conditioning (Cond.; last three blocks of day 1) and drug-free test (day 8) performed 24 h after dMT infusion of saline (Sal., $n = 5$) or muscimol (Mus., $n = 7$). Rats were infused in their home cage without fear reactivation. Mus. infused this way had no effect on fear retrieval the following day ($t = -0.88$, $P = 0.39$). **c**, Intra-dMT infusion of MAPK inhibitor U0126 (1 μg per 0.5 μl per side, $n = 11$) immediately after a two-tone test on day 7 did not alter freezing levels during a drug-free test performed the following day, compared to a vehicle control ($n = 9$, $t = 0.37$, $P = 0.71$). **d**, Intra-dMT infusion of the protein synthesis inhibitor anisomycin (Aniso., 62.5 μg per 0.5 μl per side, $n = 7$) immediately after a two-tone test on day 7 did not alter freezing levels during a drug-free test performed the following day, compared to vehicle control ($n = 5$, $t = 1.33$, $P = 0.21$). One-way repeated-measures ANOVA was used on day 1. Unpaired t-test between Sal. and Mus. groups were used on days 7, 8 and 14. Data are shown as mean ± s.e.m. in blocks of two trials; $*P < 0.05$.

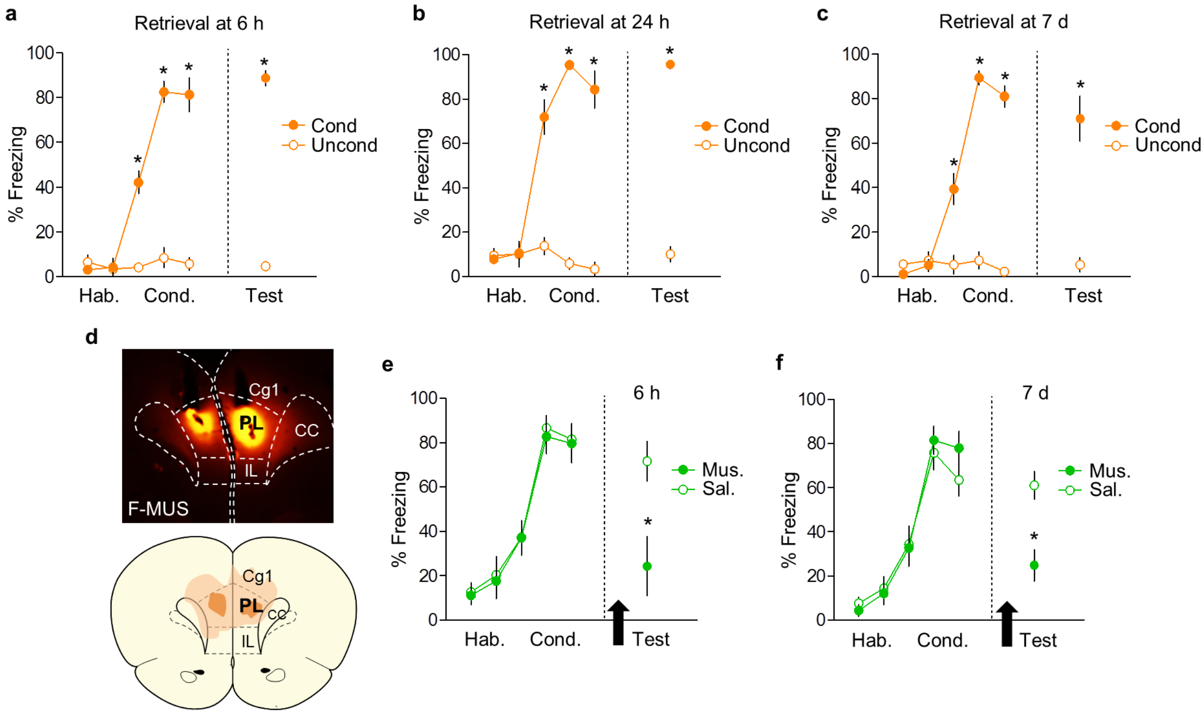

Extended Data Figure 3 | Conditioning levels for c-Fos experiments, and the effects of PL inactivation at early versus late time points. **a**, Freezing levels for conditioned ($n = 4$) and un-shocked control ($n = 5$) groups during fear conditioning and retrieval at the 6 h time point. The conditioned group showed a significant increase in freezing compared to controls ($F_{(5,35)} = 76.12$, $P < 0.001$). Hab., habituation; Cond., conditioning. **b**, Freezing levels for conditioned ($n = 3$) and control ($n = 4$) groups during fear conditioning and retrieval at the 24 h time point. The conditioned group showed a significant increase in freezing compared to controls ($F_{(5,25)} = 40.07$, $P < 0.001$). **c**, Freezing levels for conditioned ($n = 5$) and control ($n = 6$) groups during fear conditioning and retrieval at the 7 d time point. The conditioned group showed a significant increase in freezing compared to controls ($F_{(5,45)} = 49.88$, $P < 0.001$). Rats were perfused for c-Fos immunocytochemistry 90 min after the fear retrieval test. Repeated-measures ANOVA followed by Tukey's post-hoc test. **d**, Top, representative micrograph showing the site of fluorescent Mus. injection into the PL. Bottom, orange areas represent the minimum (darker colour) and the maximum (lighter colour) spread of muscimol into the PL. **e**, PL inactivation impaired fear retrieval at 6 h ($F_{(1,11)} = 7.92$, $P = 0.01$; Sal., $n = 6$; Mus., $n = 7$). **f**, In separate animals, PL inactivation also impaired fear retrieval at 7 d after conditioning ($F_{(1,14)} = 13.8$, $P = 0.002$; Sal., $n = 8$; Mus., $n = 8$). The retrieval test was performed 30 min after infusion of Sal. or Mus. (black arrows). One-way ANOVA followed by Tukey's post-hoc test. Data are shown as mean ± s.e.m. in blocks of two trials; $*P < 0.05$.

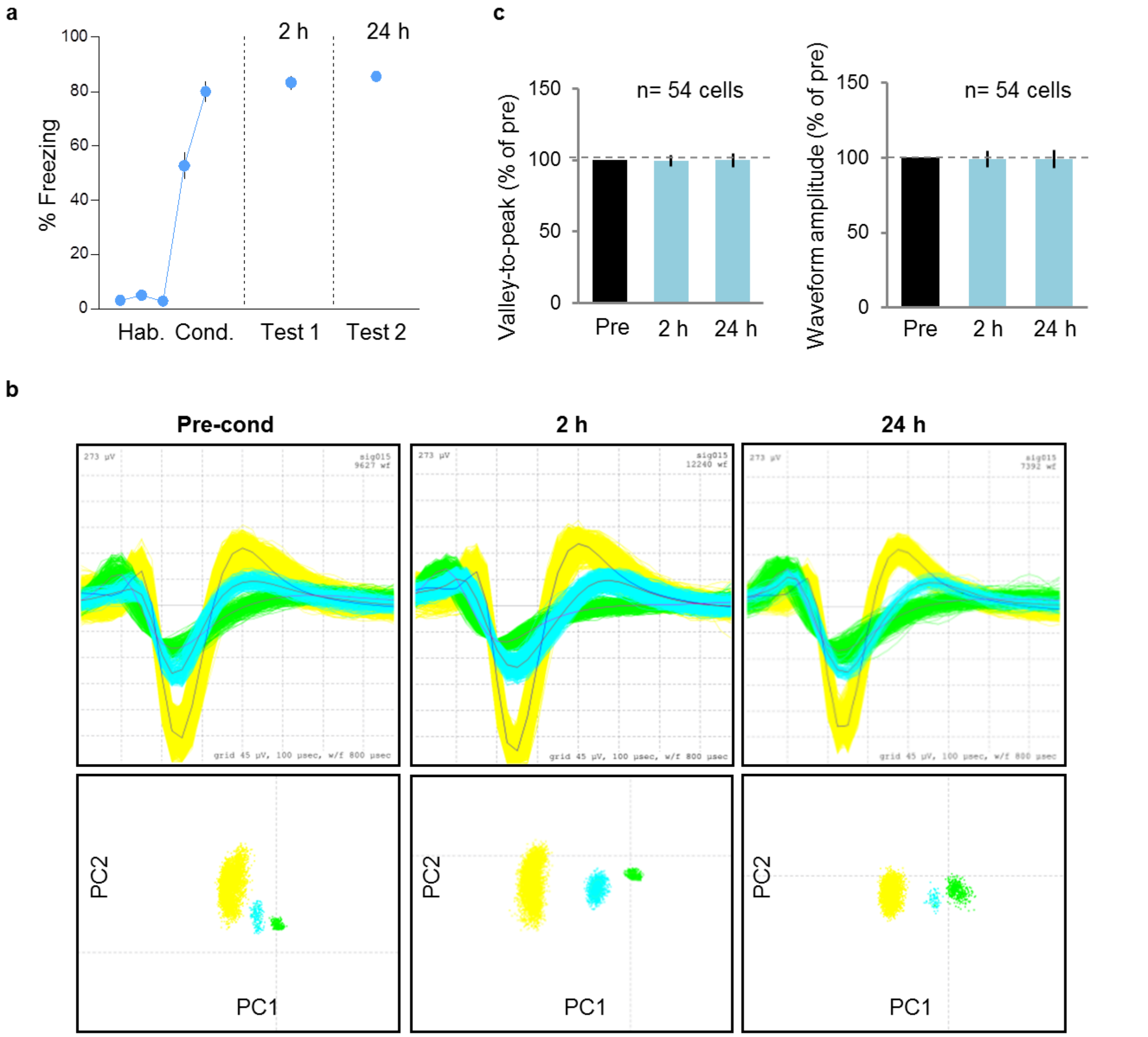

Extended Data Figure 4 | Conditioning levels for unit recording experiments, and waveform characteristics across recording sessions. **a**, Freezing levels in response to tones during habituation (first two blocks), conditioning (last three blocks), test 1 (2 h) and test 2 (24 h) in rats never given bar-press training. Rats showed similar levels of freezing during retrieval at 2 h and 24 h after conditioning ($n = 11$). Data are shown as mean ± s.e.m. in blocks of two trials. **b**, Top, waveforms of three representative PVT neurons recorded during pre-conditioning (left), 2 h post-conditioning (middle), and 24 h post-conditioning (right). Bottom, principal component (PC) analysis of these cells' waveforms at all three time points. **c**, Average valley-to-peak time (left), and average waveform amplitude (right) for all neurons ($n = 54$), shown as a percentage of pre-conditioning values. Of 54 neurons, 53 were unchanged (100% of pre-conditioning value) at both time points (2 h and 24 h) for one or both waveform parameters. One neuron showed 90% of pre-conditioning valley-to-peak time at both 2 h and 24 h, and ranged from 88 to 100% of pre-conditioning amplitude.

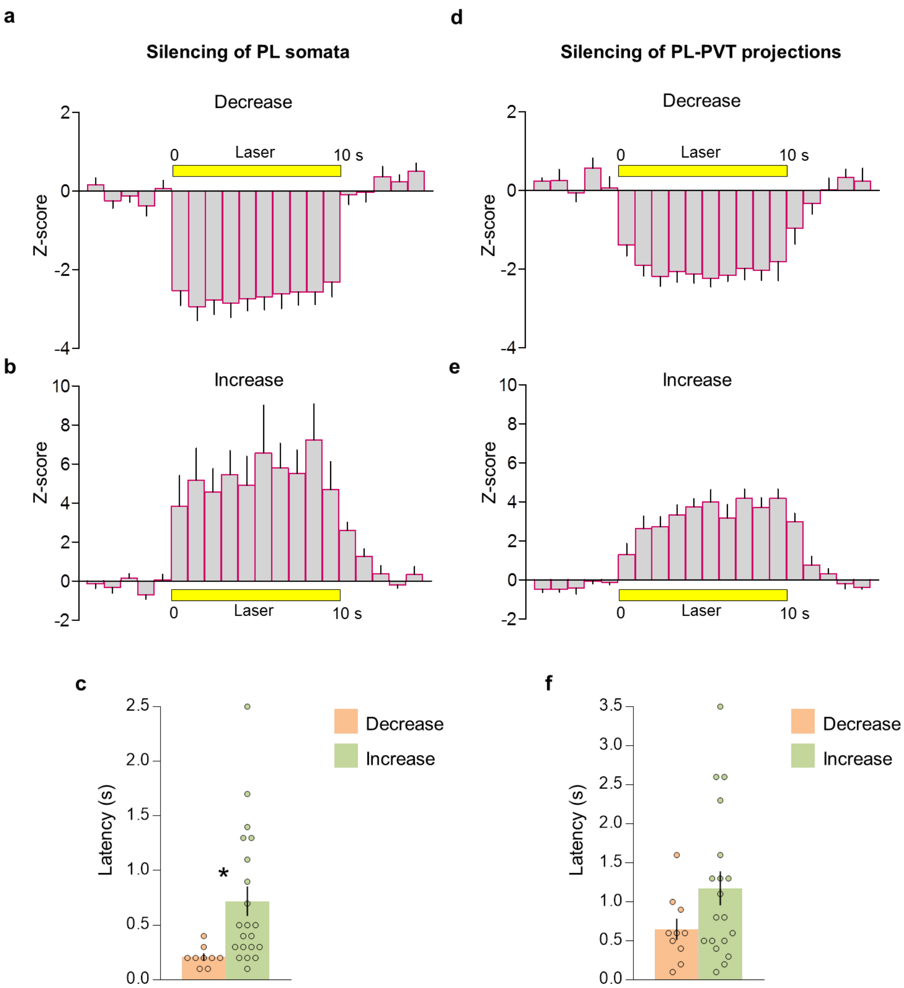

Extended Data Figure 5 | Average firing rate and latency data for laser illumination of PL somata and PL terminals in the PVT expressing eNpHR-eYFP. **a**, **b**, Average peri-stimulus time histogram of PL neurons that decreased (24 out of 50) (**a**) or increased (8 out of 50) (**b**) their firing rate during laser illumination of PL somata. **c**, Latency of PL neuronal responses to laser illumination of PL somata (paired Student's *t*-test, $P = 0.02$). **d**, **e**, Average peri-stimulus time histogram of PVT neurons that decreased (13 out of 47) (**d**) or increased (9 out of 47) (**e**) their firing rate during laser illumination of PL terminals in the PVT. **f**, Latency of PVT neuronal responses to laser illumination of PL terminals in the PVT (paired Student's *t*-test, $P = 0.11$). Peri-stimulus time histograms are shown in bins of 1 s. Response latency was measured in bins of 100 ms; $*P < 0.05$.

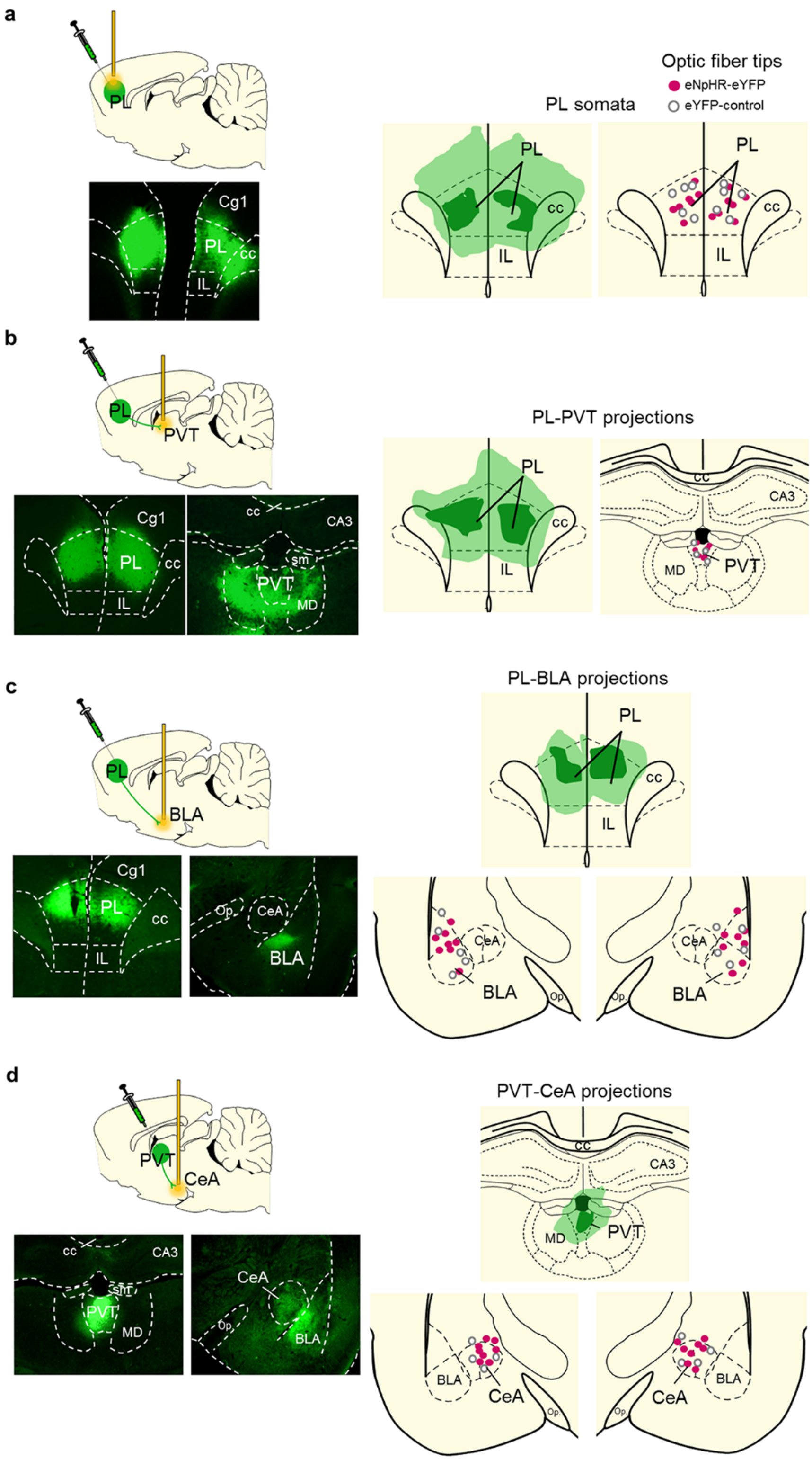

Extended Data Figure 6 | Location of eNpHR–eYFP expression and optical fibres. **a**, Left, representative micrograph showing eNpHR–eYFP expression in the PL. Right, placements of optical fibre tips in the PL. **b**, Left, representative micrograph showing the expression of eNpHR–eYFP in the PL and its terminals in dMT. Right, placement of optical fibre tips in the PVT. **c**, Left, representative micrograph showing the expression of eNpHR–eYFP in the PL and its terminals in the amygdala. Right, placement of optical fibre tips in the BLA. **d**, Left, representative micrograph showing the expression of eNpHR–eYFP in the PVT and its terminals in the amygdala. Right, placement of optical fibre tips in the CeA. Micrographs were obtained 8–10 weeks after virus infusion. cc, corpus callosum; IL, infralimbic cortex; MD, mediodorsal thalamus; Op., optical tract; sm, stria medullaris.

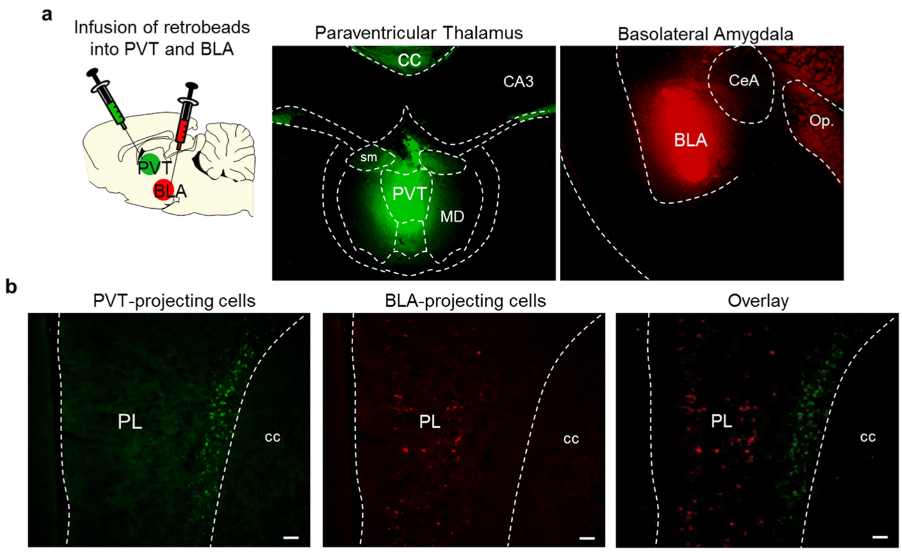

Extended Data Figure 7 | PL neurons projecting to the PVT versus the BLA are located in distinct layers. **a**, Left, schematic of retrobead injections. Middle, micrograph showing the site of retrobead infusion into the PVT (green), and right, micrograph showing the site of retrobead infusion into the BLA (red) in the same rat. **b**, Left, PL neurons retrogradely labelled from PVT infusion (green). Middle, PL neurons retrogradely labelled from BLA infusion (red). Right, overlay image showing the absence of co-labelling between PL neurons projecting to the PVT (green, deep layers) and PL neurons projecting to the BLA (red, superficial layers). Scale bar, 100 μm.

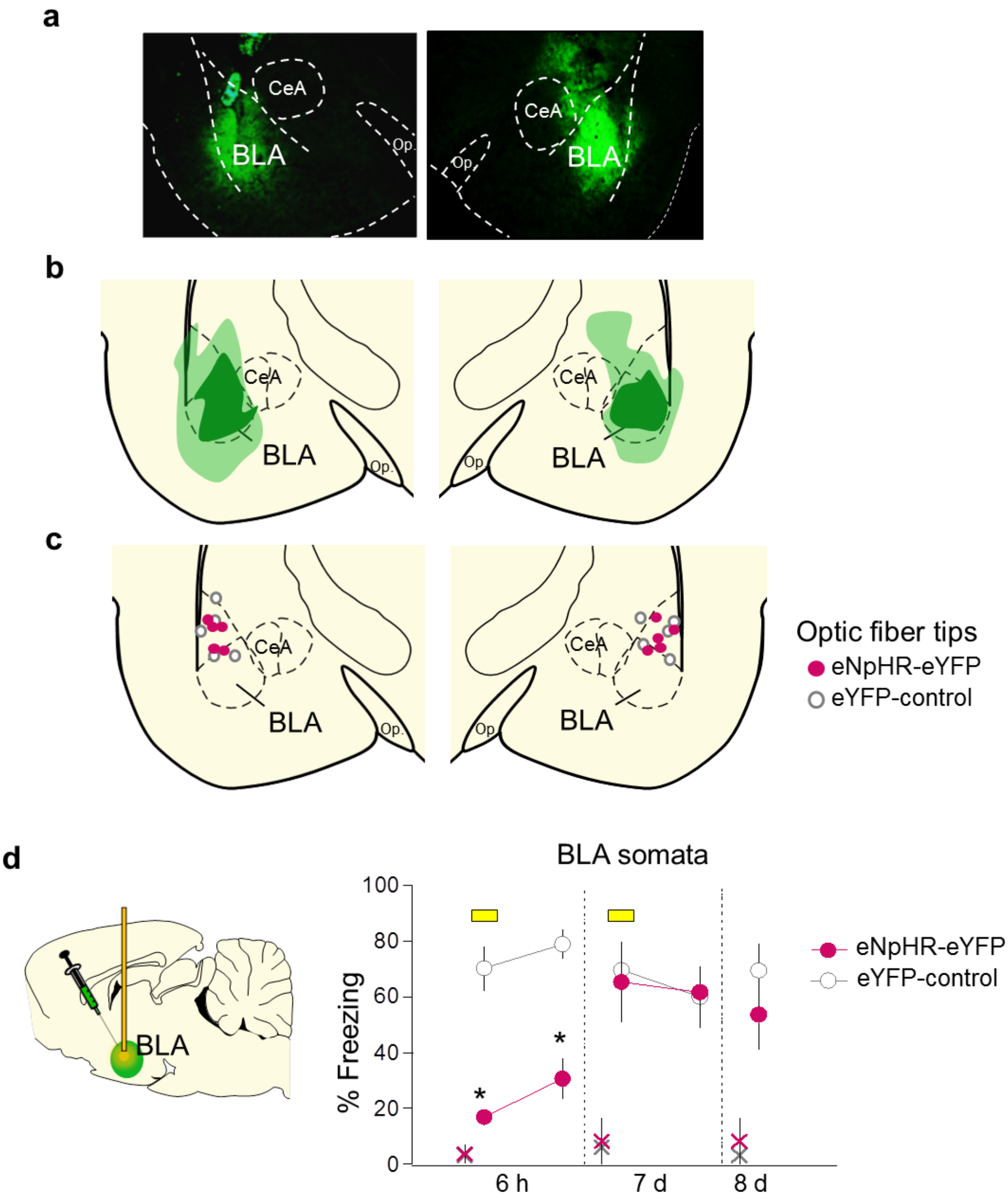

Extended Data Figure 8 | Silencing BLA somata impaired fear retrieval at early, but not late, time points after conditioning. **a**, Representative micrograph showing eNpHR–eYFP expression in the BLA. **b**, Green areas represent the minimum (darker colour) and the maximum (lighter colour) expression of eNpHR–eYFP in the BLA. **c**, Dots represent the location of optical fibre tips within the BLA. **d**, Illumination of BLA soma (yellow bar) reduced freezing at 6 h ($F_{(1,9)} = 54.6$, $P < 0.001$), but not at 7 d ($F_{(1,9)} = 10.1$, $P = 0.91$) or 8 d ($P = 0.33$), in the eNpHR–eYFP group ($n = 5$) compared to eYFP control group ($n = 6$). Repeated-measures ANOVA followed by Tukey's post-hoc test. Data are shown as mean ± s.e.m. in blocks of 2 trials; $*P < 0.05$. '×' symbols indicate baseline (pre-tone) freezing levels.

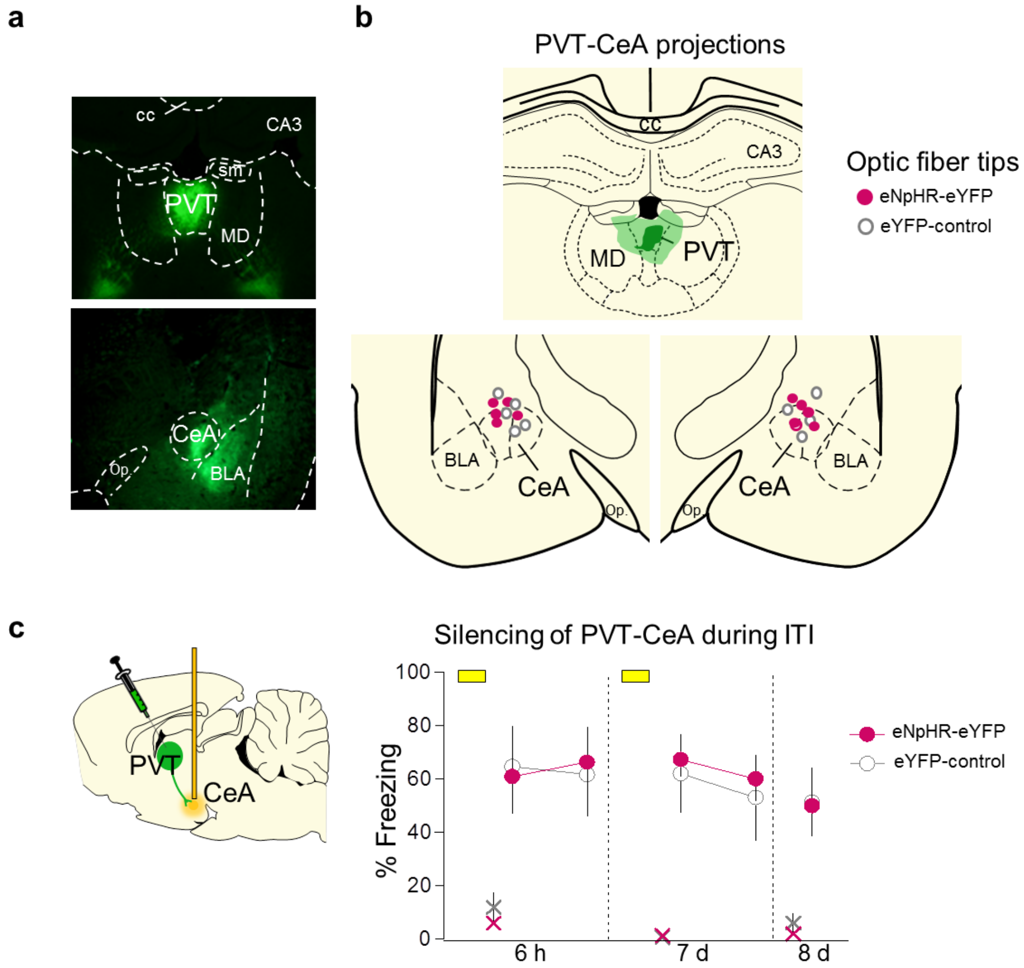

Extended Data Figure 9 | Silencing PVT projections to the CeA during the inter-trial interval did not impair fear retrieval. **a**, Representative micrograph showing the expression of eNpHR–eYFP in the PVT and its terminals in the amygdala. **b**, Top, green areas represent the minimum (darker colour) and the maximum (lighter colour) expression of eNpHR–eYFP in the PVT. Bottom, dots represent the location of optical fibre tips within the CeA. **c**, Illumination (40 s) of PVT inputs to the CeA during the interval between tones (3 min) did not affect freezing at 6 h ($F_{(1,8)} = 0.75$, $P = 0.40$), 7 d ($F_{(1,8)} = 0.04$, $P = 0.84$), or 8 d ($P = 0.93$), compared to the eYFP control group ($n = 5$ per group). Repeated-measures ANOVA followed by Tukey's post-hoc test. Data are shown as mean ± s.e.m. in blocks of 2 trials; $*P < 0.05$. '×' symbols indicate baseline (pre-tone) freezing levels.

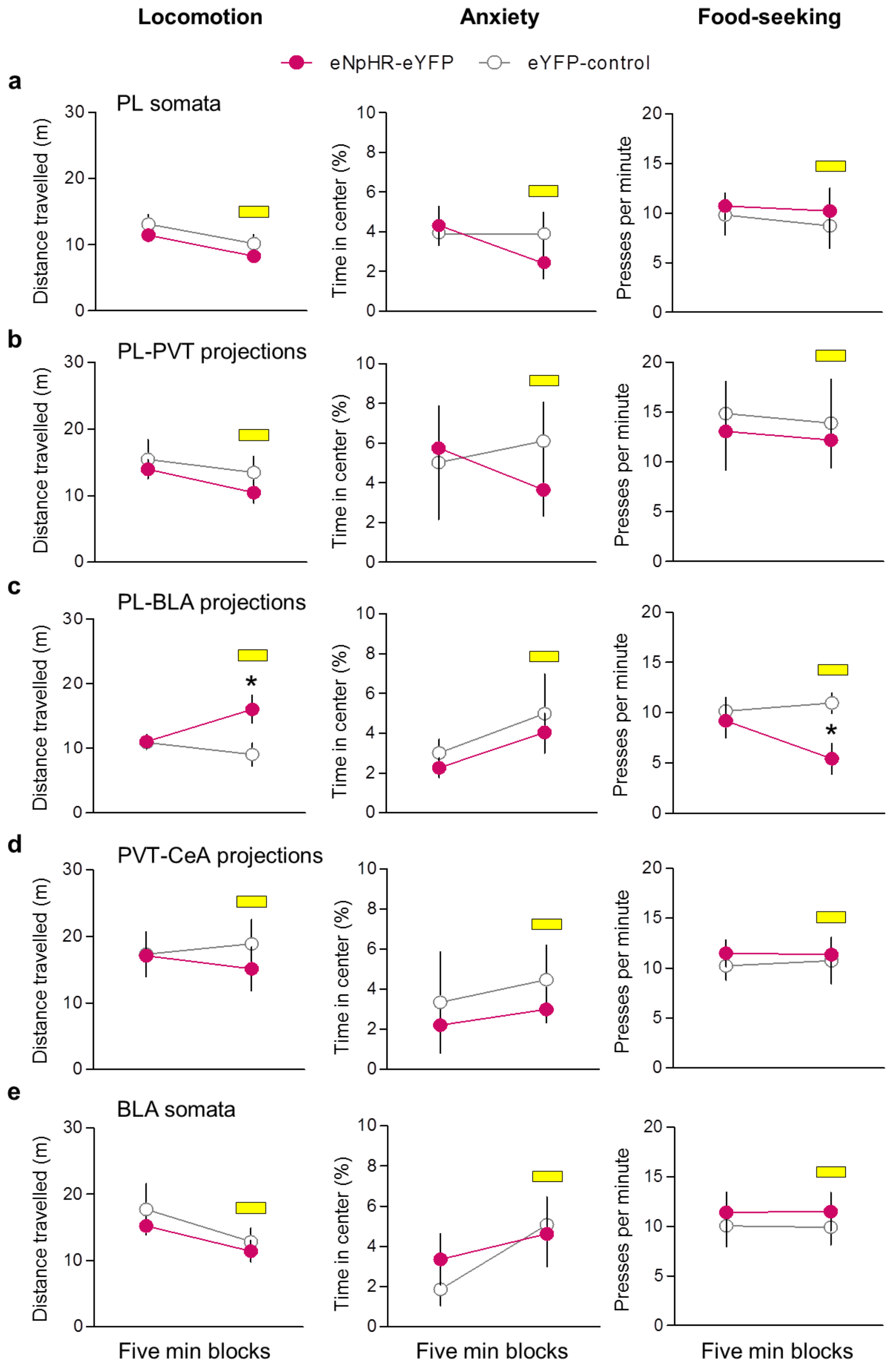

Extended Data Figure 10 | Effects of laser illumination on locomotion, anxiety and food-seeking behaviour in rats expressing eNpHR–eYFP. **a**–**e**, Rats were tested in an open field during a 9 min session (3 min acclimation, 3 min laser off, 3 min laser on). We measured the total distance travelled (left) and the percentage of time spent in the centre of the apparatus (middle) to assess locomotor activity and anxiety, respectively. We also compared the rate of pressing for food (right) in a 15 min session (5 min acclimation, 5 min laser off, 5 min laser on). Silencing of PL somata (eNpHR–eYFP, $n = 7$; control, $n = 5$) (**a**), PL inputs to the PVT (eNpHR–eYFP, $n = 5$; control, $n = 5$) (**b**), PVT inputs to the CeA (eNpHR–eYFP, $n = 7$; control, $n = 5$) (**d**), or BLA somata (eNpHR–eYFP, $n = 5$; control, $n = 6$) (**e**) did not affect locomotion, anxiety or food-seeking. However, silencing PL–BLA projections (**c**) increased locomotion ($F_{(1,12)} = 12.4$, $P = 0.004$; eNpHR–eYFP, $n = 6$; control, $n = 8$) and decreased food-seeking ($F_{(1,15)} = 6.0$, $P = 0.02$; eNpHR–eYFP, $n = 7$; control, $n = 10$). Repeated-measures ANOVA followed by Tukey's post-hoc test. Data are shown as mean ± s.e.m.; $^*P < 0.05$.

doi:10.1038/nature14286

Two insulin receptors determine alternative wing morphs in planthoppers

Hai-Jun Xu[1]*, Jian Xue[1]*, Bo Lu[1], Xue-Chao Zhang[1], Ji-Chong Zhuo[1], Shu-Fang He[1], Xiao-Fang Ma[1], Ya-Qin Jiang[1], Hai-Wei Fan[1], Ji-Yu Xu[1], Yu-Xuan Ye[1], Peng-Lu Pan[1], Qiao Li[1], Yan-Yuan Bao[1], H. Frederik Nijhout[2] & Chuan-Xi Zhang[1]

Wing polyphenism is an evolutionarily successful feature found in a wide range of insects[1]. Long-winged morphs can fly, which allows them to escape adverse habitats and track changing resources, whereas short-winged morphs are flightless, but usually possess higher fecundity than the winged morphs[1–3]. Studies on aphids, crickets and planthoppers have revealed that alternative wing morphs develop in response to various environmental cues[1,2,4–8], and that the response to these cues may be mediated by developmental hormones, although research in this area has yielded equivocal and conflicting results about exactly which hormones are involved[4,8–10]. As it stands, the molecular mechanism underlying wing morph determination in insects has remained elusive. Here we show that two insulin receptors in the migratory brown planthopper *Nilaparvata lugens*, InR1 and InR2, have opposing roles in controlling long wing versus short wing development by regulating the activity of the forkhead transcription factor Foxo. InR1, acting via the phosphatidylinositol-3-OH kinase (PI(3)K)–protein kinase B (Akt) signalling cascade, leads to the long-winged morph if active and the short-winged morph if inactive. InR2, by contrast, functions as a negative regulator of the InR1–PI(3)K–Akt pathway: suppression of InR2 results in development of the long-winged morph. The brain-secreted ligand Ilp3 triggers development of long-winged morphs. Our findings provide the first evidence of a molecular basis for the regulation of wing polyphenism in insects, and they are also the first demonstration—to our knowledge—of binary control over alternative developmental outcomes, and thus deepen our understanding of the development and evolution of phenotypic plasticity.

The migratory brown planthopper (BPH) *N. lugens* (order Hemiptera), can develop into short-winged or long-winged morphs in response to environmental cues (Fig. 1a and Supplementary Notes 1, 2). The long-winged BPHs bear fully developed forewings and hindwings, whereas the short-winged BPHs have severely reduced forewings and only small bud-like hindwings (Fig. 1b). The environmental factors that are most relevant to the wing morph switch in BPHs are population density and host quality[11–15]. We therefore hypothesized that wing morph determination in BPHs may be regulated by a nutrient-sensing pathway.

The insulin/insulin-like growth factor (IGF) signalling (IIS) pathway is an evolutionarily conserved nutrient-sensing pathway that modulates growth and development in metazoans[16–24]. To gain insight into the regulation of wing dimorphism by the IIS pathway, we undertook RNA interference (RNAi) knockdown of insulin receptor genes in 2nd-instar nymphs. BPHs have two insulin receptors, *N. lugens* (*Nl*)InR1 and *Nl*InR2 (Extended Data Figs 1, 2 and Supplementary Note 3). We found that knockdown of *NlInR2* (ds*NlInR2*) led to a strong bias towards long-winged morphs compared to BPHs that were either not subjected to treatment (*ck*) or treated with double-stranded RNA (dsRNA) targeting the gene encoding green fluorescence protein (ds*gfp*) (Fig. 1c). The ds*NlInR2*-treated long-winged BPHs retained the same sex ratio (Supplementary Table 1), and were morphologically indistinguishable from natural long-winged morphs (Extended Data Fig. 3a). By contrast, knockdown of *NlInR1* (ds*NlInR1*) produced the opposite response, inducing the development of short-winged BPHs (Fig. 1c). To confirm these observations, we conducted analogous experiments using new dsRNA molecules for each *Nl*InR, and by knockdown of the two insulin receptors in 3rd- and 4th-instar (penultimate) nymphs, and the same phenotypes were obtained (Extended Data Fig. 4a–c). Taken together, these findings indicate that expression of the two insulin receptors, *Nl*InR1 and *Nl*InR2, is tightly correlated with wing morph determination in BPHs, and that they have fully opposite roles in the process.

To understand better how *Nl*InR1 and *Nl*InR2 are orchestrated to regulate wing dimorphism in BPHs, we examined the contributions of several components of the canonical IIS pathway to alternative wing morph development. In *Drosophila*, the binding of insulin causes autophosphorylation of its receptor. The phosphorylated receptor in turn induces phosphorylation of its substrate adaptor (*D. melanogaster* (*Dm*)Chico and *Dm*Lnk), which activates the PI(3)K–Akt signalling cascade, the main pathway that mediates insulin signalling[20,21,25,26]. Phosphorylation of *Dm*Akt generally results in multiple outputs, including the inactivation of *Dm*Foxo, to modulate growth and proliferation[27,28]. We found that silencing of *NlChico* or *NlAkt* phenocopied ds*NlInR1* (Extended Data Figs 3b, c and 4d). By contrast, silencing of *NlFoxo* or *NlPten* phenocopied ds*NlInR2* (Extended Data Figs 3a, c and 4d). However, we found that curved wings developed in ds*NlPten* BPHs (Extended Data Figs 3a), which may be largely due to hyper-phosphorylation of *Nl*Akt[23,29]. Our data also showed that *Nl*Lnk was probably irrelevant to

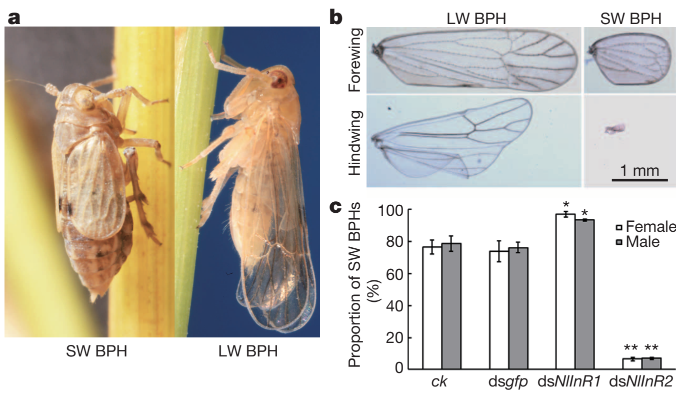

Figure 1 | Knockdown of *NlInRs* in BPHs. **a**, The shorted-winged (SW) and long-winged (LW) BPH. **b**, Forewings and hindwings of the long-winged and short-winged BPH. **c**, The proportion of short-winged BPHs from three experiments (mean ± standard error of the mean (s.e.m.)). *ck*, without any treatment ($n = 130$ females, 137 males), ds*gfp* ($n = 142$ females, 181 males), ds*NlInR1* ($n = 101$ females, 134 males) and ds*NlInR2* ($n = 107$ females, 142 males). $*P < 0.05$ and $**P \leq 0.001$ (Student's *t*-test), difference from *ck*. Supplementary Data 1 contains source data.

[1]State Key Laboratory of Rice Biology and Ministry of Agriculture Key Laboratory of Agricultural Entomology, Institute of Insect Sciences, Zhejiang University, Hangzhou 310058, China. [2]Department of Biology, Duke University, Durham, North Carolina 27708, USA.
*These authors contributed equally to this work.

wing morph determination (Extended Data Fig. 3c), suggesting that *Nl*Lnk is either dispensable or functionally complemented by *Nl*Chico. In addition to the PI(3)K–Akt signalling cascade, the target of rapamycin complex 1 (TORC1) and the Ras/mitogen-activated protein kinase (Ras/MAPK) signalling pathways constitute two alternative signalling branches of the IIS pathway[16,17,19,23,30]. However, neither of these two signalling cascades was involved in wing morph determination (Extended Data Fig. 5). Overall, our phenotypic analyses suggest that the *Nl*PI(3)K–*Nl*Akt signalling cascade together with *Nl*InR1, but not *Nl*InR2, resembles the well-established canonical IIS pathway. By contrast, *Nl*InR2 appears to act as a negative regulator of this signalling cascade, and suppression of *Nl*InR2 thus leads to long-winged morphs.

We next examined whether *Nl*InR2 shares a common signalling cascade with *Nl*InR1. If this were the case, perturbation of any positively acting component downstream of *Nl*InR1 would antagonize the effect of ds*NlInR2* and result in the short-winged morph; otherwise, if a novel signalling cascade were mediated via *Nl*InR2, only long-winged morphs would develop. We found that silencing of *NlInR1*, *NlAkt* or *NlChico* redirected development of ds*NlInR2*-treated BPHs from the long-winged to short-winged morphs (Fig. 2a–e and Supplementary Note 4), which suggests that suppression of *Nl*InR1–*Nl*PI(3)K–*Nl*Akt signalling is epistatic to the ds*NlInR2* effect.

Next we investigated the phosphorylation level of *Nl*Akt (P-*Nl*Akt) in wing buds as a read-out of the activity of the *Nl*InR1–*Nl*PI(3)K–*Nl*Akt signalling activity under the condition of ds*NlInR2*. The results revealed that ds*NlInR2* but not ds*NlInR1* strongly augmented the P-*Nl*Akt level (Fig. 2f). The specificity of the P-*Dm*Akt antibody in BPHs was validated by treatment of wing buds with the PI(3)K inhibitor LY294002 (Fig. 2g). To confirm the tissue-specific regulation by *Nl*InR2, we measured hind tibiae length, wing size, developmental duration and body weight, and performed a metabolic assay in BPHs with *Nl*InR2 knockdown. We found that *Nl*InR2 regulates wing morph development in a tissue-specific way rather than through a systemic effect on growth and metabolism (Extended Data Fig. 6 and Supplementary Note 5).

Given the high sequence similarity between *Nl*InR1 and *Nl*InR2, we then asked whether *Nl*InR2 could physically interact with *Nl*InR1 to form heterodimers. To this end, Flag-tagged *Nl*InR1 (*Nl*InR1–Flag) was co-expressed with V5-tagged *Nl*InR2 (*Nl*InR2–V5) in *Drosophila* S2 cells. The immunoprecipitation assay showed that *Nl*InR2 was co-precipitated with *Nl*InR1 (Fig. 2h), and that *Nl*InR1–*Nl*InR1 homodimers had formed (Fig. 2i). However, *Nl*InR2–Flag failed to co-precipitate with *Nl*InR2–V5 using either anti-Flag or anti-V5 monoclonal antibodies (data not shown). Thus, these findings suggest that *Nl*InR2 negatively regulates *Nl*InR1–*Nl*PI(3)K–*Nl*Akt signalling activity by modulating *Nl*InR1 activity.

In *Drosophila*, the phosphorylation of *Dm*Foxo by *Dm*Akt results in the cytoplasmic retention of *Dm*Foxo and inhibition of its transcriptional activity[27,28]. Given that long-winged BPHs developed after the knockdown of *NlFoxo* (Extended Data Fig. 3a, c), we next asked whether *Nl*InR1 signalling regulates alternative wing morphs in an *Nl*Foxo-dependent manner. If this were the case, disruption of *Nl*Foxo should fully redirect the development of ds*NlInR1*-treated nymphs from short-winged to long-winged morphs, whereas constitutive activation of *Nl*Foxo should mimic low-insulin signalling, resulting in short-winged BPHs. We found that double-gene knockdown (ds*NlInR1*;ds*NlFoxo*) led to long-winged morphs (Fig. 2j). By contrast, ds*NlInR1*;ds*gfp* and ds*NlInR2*;ds*NlFoxo* produced short-winged BPHs and long-winged BPHs (Fig. 2j), respectively. Unfortunately, we were unable to induce constitutive activation of *Nl*Foxo in BPHs because of the lack of available genetic tools. As an alternative approach, we suppressed *NlAkt* as a means to force the activation of *Nl*Foxo, and short-winged BPHs were indeed obtained from ds*NlAkt* (Extended Data Fig. 3b, c). In addition, the subcellular localization of *Nl*Foxo indicated that ds*NlInR2* excluded *Nl*Foxo from the nucleus in wing buds but not in the fat body (Extended Data Fig. 7 and Supplementary Note 6), which suggests that *Nl*InR2 determines alternative wing morphs in a tissue-specific way via the downstream factor *Nl*Foxo.

Next, we silenced insulin-like genes to identify the extracellular ligand(s) that triggers development of alternative wing morphs in BPHs. The BPH

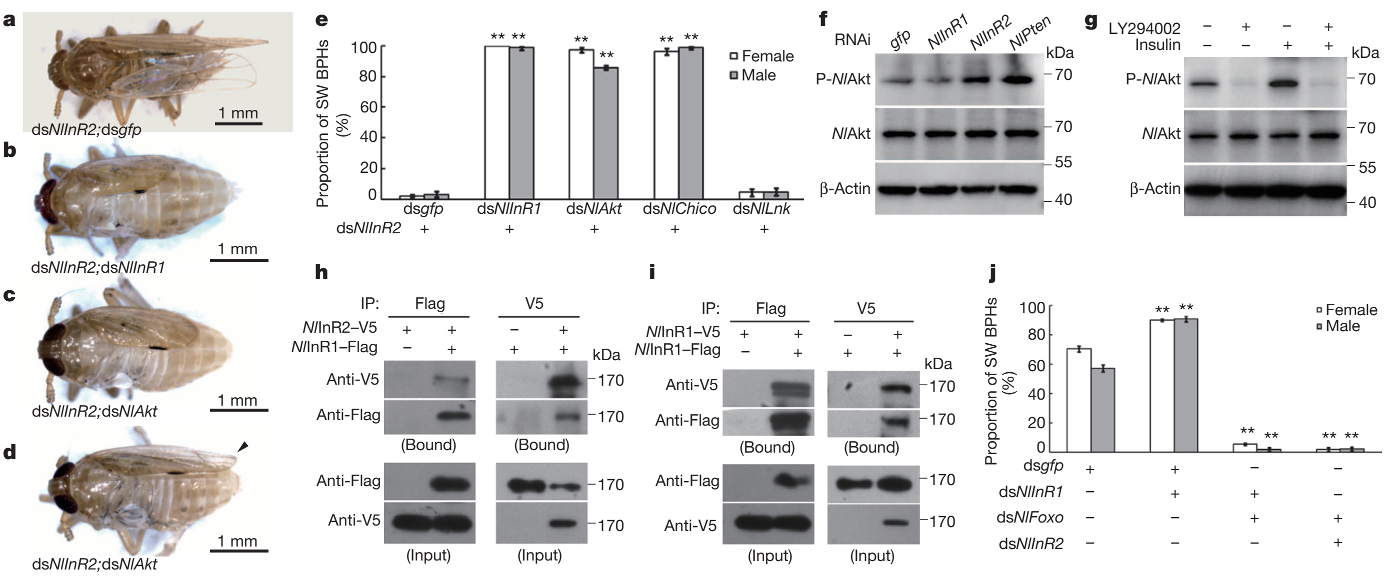

Figure 2 | *Nl*InR2 negatively regulates *Nl*InR1 signalling, and *Nl*Foxo relays the insulin signalling. a–d, Treatments with ds*NlInR2*;ds*gfp* (**a**), ds*NlInR2*;ds*NlInR1* (**b**) or ds*NlInR2*;ds*NlAkt* (**c**, **d**). Arrowhead, intermediate length of forewing. **e**, Either ds*NlInR1*, ds*NlAkt* or ds*NlChico* redirects the ds*NlInR2* effect. ds*NlInR2* in combination with ds*gfp* ($n = 88$ females, 87 males), ds*NlInR1* ($n = 82$ females, 80 males), ds*NlAkt* ($n = 88$ females, 112 males), ds*NlChico* ($n = 73$ females, 74 males) or ds*NlLnk* ($n = 88$ females, 79 males). SW, short-winged. **f**, The P-*Nl*Akt level in wing buds. **g**, Validation of P-*Dm*Akt antibody specificity. **f**, **g**, Data represent one of three experiments. β-Actin was used to show equal protein loading. **h**, **i**, *Nl*InR1 immunoprecipitates (IP) with *Nl*InR2 (**h**) or with itself (**i**). Supplementary Note 9 contains full scans for **f**–**i**. **j**, ds*NlFoxo* reverses the ds*NlInR1* effect. ds*gfp* ($n = 106$ females, 115 males), ds*NlInR1*;ds*gfp* ($n = 89$ females, 116 males), ds*NlInR1*;ds*NlFoxo* ($n = 86$ females, 91 males) and ds*NlInR2*;ds*NlFoxo* ($n = 114$ females, 101 males). **e**, **j**, Mean ± s.e.m. from three experiments. $^{*}P < 0.05$ and $^{**}P \leq 0.001$ (Student's t-test), difference from ds*gfp*. Supplementary Data 2 contains source data.

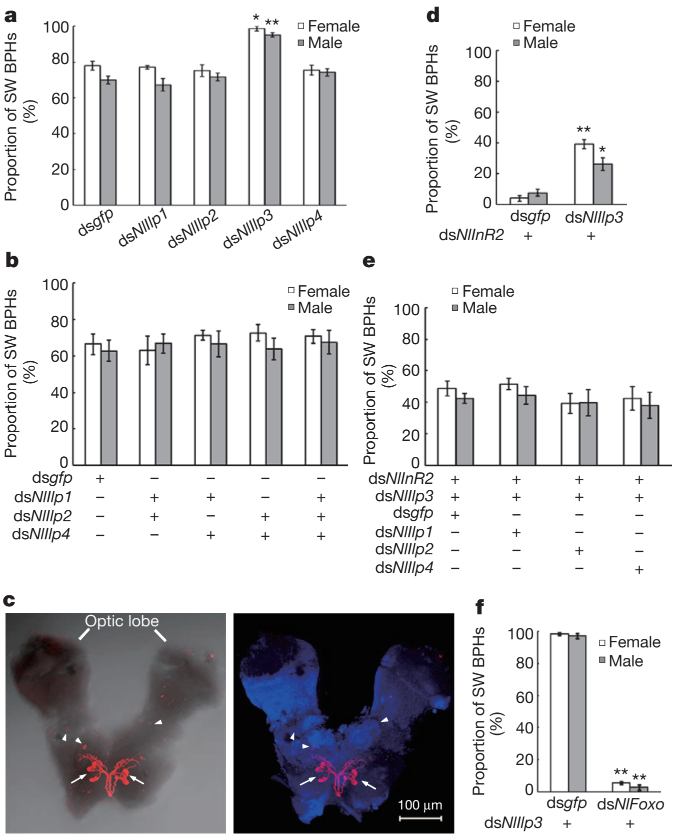

Figure 3 | *Nl*Ilp3 triggers the wing morph switch. **a**, ds*NlIlp1–4* treatments. ds*gfp* ($n = 90$ females, 78 males), ds*NlIlp1* ($n = 92$ females, 79 males), ds*NlIlp2* ($n = 94$ females, 88 males), ds*NlIlp3* ($n = 78$ females, 84 males) and ds*NlIlp4* ($n = 75$ females, 88 males). SW, short-winged. **b**, Knockdown of *NlIlp1*, *NlIlp2* and *NlIlp4* in combination. ds*gfp* ($n = 107$ females, 105 males), ds*NlIlp1*;ds*NlIlp2* ($n = 119$ females, 121 males), ds*NlIlp1*;ds*NlIlp4* ($n = 122$ females, 110 males), ds*NlIlp2*;ds*NlIlp4* ($n = 137$ females, 116 males) and ds*NlIlp1*;ds*NlIlp2*;ds*NlIlp4* ($n = 108$ females, 108 males). **c**, An immunofluorescence assay of *Nl*Ilp3 in brains. Arrows, medial neurosecretory cells. Arrowheads, endocrine cells. Blue (4′,6-diamidino-2-phenylindole (DAPI)), cell nucleus. **d**, ds*NlIlp3* partially neutralizes the ds*NlInR2* effect. ds*NlInR2* in combination with ds*gfp* ($n = 84$ females, 103 males) or ds*NlIlp3* ($n = 101$ females, 106 males). **e**, Neither *NlIlp1*, *NlIlp2* nor *NlIlp4* enhances the ds*NlIlp3* effect. ds*NlInR2*;ds*NlIlp3* in combination with ds*gfp* ($n = 108$ females, 100 males), ds*NlIlp1* ($n = 121$ females, 100 males), ds*NlIlp2* ($n = 105$ females, 117 males) or ds*NlIlp4* ($n = 109$ females, 111 males). **f**, ds*NlFoxo* reverses the ds*NlIlp3* effect. ds*NlIlp3* in combination with ds*gfp* ($n = 120$ females, 100 males) or ds*NlFoxo* ($n = 126$ females, 108 males). **a**, **b**, **d**–**f**, Mean ± s.e.m. from three experiments. $*P < 0.05$ and $**P \leq 0.001$ (Student's *t*-test), difference from ds*gfp* group. Supplementary Data 3 contains source data.

has four insulin/IGF-like peptides, designated *Nl*Ilp1, *Nl*Ilp2, *Nl*Ilp3 and *Nl*Ilp4. We found that ds*NlIlp3* generated a significantly higher proportion of short-winged BPHs (Fig. 3a), and that the remaining three *Nl*Ilp proteins had minor roles, if any, in wing morph switch (Fig. 3a, b). Notably, tissue distribution analysis indicated that *Nl*Ilp3 was mainly produced in the brain (Fig. 3c, Extended Data Fig. 8, Supplementary Video 1 and Supplementary Note 7). Because the ds*NlIlp3* phenotype resembled the silencing effect of the *Nl*InR1–*Nl*PI(3)K–*Nl*Akt signalling cascade, we hypothesized that *Nl*Ilp3 may be the upstream ligand initiating this signalling cascade. If so, ds*NlIlp3* probably redirects the development of ds*NlInR2* in a similar manner to ds*NlInR1* or ds*NlAkt*. Furthermore, by this logic, ds*NlFoxo* should reverse the effect of ds*NlIlp3*, similar to the way it reversed the effect of ds*NlInR1*. Our data revealed that, whereas ds*NlInR1* completely redirected the phenotype of ds*NlInR2*, ds*NlIlp3* only partially antagonized the effect of ds*NlInR2* (Fig. 3d). This phenomenon is not due to the functional redundancy between *Nl*Ilp proteins, because silencing of *NlIlp3* in combination with the remaining *NlIlp* genes did not synthetically enhance the ds*NlIlp3* effect (Fig. 3e). We observed, however, that ds*NlFoxo* could completely reverse the effect of ds*NlIlp3* (Fig. 3f), suggesting that *Nl*Foxo is the key regulator downstream of *Nl*Ilp3.

Finally, we found that the IIS pathway is a common regulatory mechanism for wing polyphenism in other members of the planthopper family (Extended Data Fig. 9 and Supplementary Note 8). On the basis of our results, we propose a model for the molecular regulation of wing polyphenism in planthoppers (Fig. 4). The long-winged morph is the default developmental morph for planthoppers, which is dependent on *Nl*InR1–*Nl*PI(3)K–*Nl*Akt signalling activity. However, in the wing buds, binding of *Nl*InR2 to *Nl*InR1 compromises *Nl*InR1 signalling, which leads to the short-winged morph. *Nl*Ilp3 is the main upstream ligand that triggers long wing development. *Nl*Foxo is the key downstream transcription regulator determining the wing morph by faithfully relaying *Nl*InR1 signalling activity.

This model raises some important issues for future research on how environmental cues are translated into the molecular mechanism that regulates *Nl*InR2 activity, on the precise mechanism by which *Nl*InR2 modulates *Nl*InR1 signalling activity, on the direct effector(s) downstream of *Nl*Foxo that modulates the growth of wings, and on the contribution of these two insulin receptors to the evolution of gene regulation in insects.

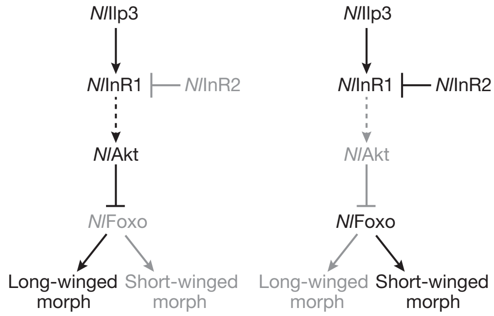

Figure 4 | Model of the molecular regulation of wing polyphenism in planthoppers. In wing buds, high *Nl*InR1 signalling activity inhibits *Nl*Foxo activity, leading to the long-winged morph. Binding of *Nl*InR1 with *Nl*InR2 compromises *Nl*InR1 signalling activity, resulting in the short-winged morph. *Nl*Ilp3 is the main insulin ligand that triggers *Nl*InR1 signalling, leading to the long-winged morph. The components that are less active or inactive are shown in grey.

Online Content Methods, along with any additional Extended Data display items and Source Data, are available in the online version of the paper; references unique to these sections appear only in the online paper.

Received 30 December 2013; accepted 5 February 2015.

Published online 18 March 2015.

1. Zera, A. J. in *Phenotypic Plasticity of Insects: Mechanisms and Consequences* (eds Whitman, D. W. & Ananthakrishnan, T. N.) 609–653 (Science, 2009).
2. Zera, A. J. & Denno, R. F. Physiology and ecology of dispersal polymorphism in insects. *Annu. Rev. Entomol.* **42,** 207–230 (1997).
3. Zhao, Z. & Zera, A. J. Differential lipid biosynthesis underlies a tradeoff between reproduction and flight capability in a wing-polymorphic cricket. *Proc. Natl Acad. Sci. USA* **99,** 16829–16834 (2002).
4. Denno, R. F., Douglas, L. W. & Jacobs, D. Crowding and host plant nutrition: environmental determinants of wing-form in *Prokelisia marginata*. *Ecology* **66,** 1588–1596 (1985).
5. Nijhout, H. F. Control mechanisms of polyphenic development in insects. *Bioscience* **49,** 181–192 (1999).
6. Braendle, C., Friebe, I., Caillaud, M. C. & Stern, D. L. Genetic variation for an aphid wing polyphenism is genetically linked to a naturally occurring wing polymorphism. *Proc. R. Soc. Lond. B* **272,** 657–664 (2005).
7. Roff, D. A. & Fairbairn, D. J. The evolution and genetics of migration in insects. *Bioscience* **57,** 155–164 (2007).
8. Simpson, S. J., Sword, G. A. & Lo, N. Polyphenism in insects. *Curr. Biol.* **21,** R738–R749 (2011).

9. Lees, A. D. Action of juvenile hormone mimics on the regulation of larval–adult and alary polymorphism in aphids. *Nature* **267,** 46–48 (1977).
10. Braendle, C., Davis, G. K., Brisson, J. A. & Stern, D. L. Wing dimorphism in aphids. *Heredity* **97,** 192–199 (2006).
11. Kisimoto, R. Effect of crowding during the larval period on the determination of the wing-form of an adult plant-hopper. *Nature* **178,** 641–642 (1956).
12. Iwanaga, K., Tojo, S. & Nagata, T. Immigration of the brown planthopper, *Nilaparvata lugens*, exhibiting various responses to density in relation to wing morphism. *Entomol. Exp. Appl.* **38,** 101–108 (1985).
13. Iwanaga, K. & Tojo, S. Effects of juvenile hormone and rearing density on wing dimorphism and oöcyte development in the brown planthopper, *Nilaparvata lugens. J. Insect Physiol.* **32,** 585–590 (1986).
14. Syobu, S., Mikuriya, H., Yamaguchi, J., Matsuzaki, M. & Matsumura, M. Fluctuations and factors affecting the wing-form ratio of the brown panthopper, *Nilaparvata lugens* Stal in rice fields. *Jap. J. Appl. Entomol. Zool.* **46,** 135–143 (2002).
15. Hartfelder, K. & Emlen, D. in *Insect Endocrinology* (ed. Gilbert, L. I.) 464–522 (Elsevier, 2012).
16. Brogiolo, W. *et al.* An evolutionarily conserved function of the *Drosophila* insulin receptor and insulin-like peptides in growth control. *Curr. Biol.* **11,** 213–221 (2001).
17. Clancy, D. J. *et al.* Extension of life-span by loss of CHICO, a *Drosophila* insulin receptor substrate protein. *Science* **292,** 104 (2001).
18. Nakae, J., Kido, Y. & Accili, D. Distinct and overlapping functions of insulin and IGF-I receptors. *Endocr. Rev.* **22,** 818–835 (2001).
19. Oldham, S. & Hafen, E. Insulin/IGF and target of rapamycin signaling: a TOR de force in growth control. *Trends Cell Biol.* **13,** 79–85 (2003).
20. Edgar, B. A. How flies get their size: genetics meets physiology. *Nature Rev. Genet.* **7,** 907–916 (2006).
21. Taniguchi, C. M., Emanuelli, B. & Kahn, C. R. Critical nodes in signalling pathways: insights into insulin action. *Nature Rev. Mol. Cell Biol.* **7,** 85–96 (2006).
22. Hietakangas, V. & Cohen, S. M. Regulation of tissue growth through nutrient sensing. *Annu. Rev. Genet.* **43,** 389–410 (2009).
23. Teleman, A. A. Molecular mechanisms of metabolic regulation by insulin in *Drosophila. Biochem. J.* **425,** 13–26 (2010).
24. Marshall, L., Rideout, E. J. & Grewal, S. S. Nutrient/TOR-dependent regulation of RNA polymerase III controls tissue and organismal growth in *Drosophila. EMBO J.* **31,** 1916–1930 (2012).
25. Britton, J. S., Lockwood, W. K., Li, L., Cohen, S. M. & Edgar, B. A. *Drosophila*'s insulin/PI3-kinase pathway coordinates cellular metabolism with nutritional conditions. *Dev. Cell* **2,** 239–249 (2002).
26. Cantley, L. C. The phosphoinositide 3-kinase pathway. *Science* **296,** 1655–1657 (2002).
27. Ogg, S. *et al.* The Fork head transcription factor DAF-16 transduces insulin-like metabolic and longevity signals in *C. elegans. Nature* **389,** 994–999 (1997).
28. Puig, O., Marr, M. T., Ruhf, M. L. & Tjian, R. Control of cell number by *Drosophila* FOXO: downstream and feedback regulation of the insulin receptor pathway. *Genes Dev.* **17,** 2006–2020 (2003).
29. Maehama, T. & Dixon, J. E. PTEN: a tumour suppressor that functions as a phospholipid phosphatase. *Trends Cell Biol.* **9,** 125–128 (1999).
30. Wullschleger, S., Loewith, R. & Hall, M. N. TOR signaling in growth and metabolism. *Cell* **124,** 471–484 (2006).

Supplementary Information is available in the online version of the paper.

Acknowledgements We thank R.-Z. Zhang for help with BPH imaging (Fig. 1a). This work was supported by the National Basic Research Program of China (973 Program, no. 2010CB126205) and by the National Science Foundation of China (no. 31201509 and no. 31471765).

Author Contributions H.-J.X. conceived and designed the study, wrote the paper, helped perform experiments and analysed the data. J.X. performed most experiments and helped with data analysis. B.L., Y.-Q.J., Q.L., S.-F.H. and J.-Y.X. helped perform experiments and antibody preparation. X.-C.Z. and J.-C.Z. performed gene cloning and immunoprecipitation. X.-F.M. performed RACE experiments. H.-W.F., Y.-X.Y. and P.-L.P. performed qRT–PCR. Y.-Y.B. and H.F.N. discussed data and revised the manuscript. C.-X.Z. organized and directed the project.

Author Information The cDNA sequences of *NlInR1* and *NlInR2* have been deposited in GenBank under accession numbers KF974333 and KF974334, respectively. Gene sequences used for dsRNA synthesis have been deposited in GenBank under the following accession numbers: KF974335 (*NlChico*), KF974336 (*NlLnk*), KF974337 (*NlAkt*), KF974338 (*NlPten*), KF974339 (*NlFoxo*), KF974340–KF974343 (*NlIlp1–4*), KF974348 (*NlErk*), KF974349 (*NlRaf*), KF974350 (*NlTor*), KM099280 (*NlRaptor*), KM099281 (*NlRheb*), KF974344 (*SfInR1*), KF974345 (*SfInR2*), KF974346 (*LsInR1*) and KF974347 (*LsInR2*). Reprints and permissions information is available at www.nature.com/reprints. The authors declare no competing financial interests. Readers are welcome to comment on the online version of the paper. Correspondence and requests for materials should be addressed to C.-X.Z. (chxzhang@zju.edu.cn) or H.-J.X. (haijunxu@zju.edu.cn).

METHODS

Detailed protocols are deposited in *Protocol Exchange*, http://dx.doi.org/10.1038/protex.2015.005.

Insects. The *Nilaparvata lugens* (BPH), *Sogatella furcifera* (SFP) and *Laodelphax striatellus* (LSP) planthopper populations used in this work were originally collected in Hangzhou (30° 16′ N, 120° 11′ E), China, in 2008. One male and one female BPH were isolated and mated to produce F_1 progeny. A single pair was then selected for sibling inbreeding for 13 generations. The purified colony was used for both the experiments conducted in this study, and genomic DNA sequencing[31]. All insects were maintained in a walk-in chamber at 26 °C (± 0.5 °C) under a photoperiod of 16:8 h (light:dark) at a relative humidity of 50% (± 5%) on rice seedlings (rice variety Xiushui 134).

Definition of long- and short-winged morphs in BPHs. We defined BPHs as the long-winged morph if both forewings and hind wings extended beyond the tip of the abdomen. We defined BPHs as the short-winged morph if forewings and hindwings extended no more than the sixth and first abdominal segment, respectively. We defined BPHs as intermediate morphs if both forewings and hind wings did not extend beyond the last abdominal segment. The intermediate morphs are scarce in nature, but appeared in this study. Because of the undeveloped forewings and hind wings, we categorized this intermediate type into the short-winged morph when calculating the wing morph ratio. Both the short-winged morph and the intermediate morph were unable to fly.

Sequence analysis. The sigcleave program from EMBOSS (http://emboss.bioinformatics.nl/cgi-bin/emboss/sigcleave) and a signal prediction program (http://www.predisi.de/) were used to predict N-terminal signal peptides. The prediction of transmembrane regions was performed using TMHMM v.2.0 (http://www.cbs.dtu.dk/services/TMHMM-2.0/). The SMART program provided by EMBL (http://smart.embl-heidelberg.de/) was employed for the identification of modular domains. Molecular weights were predicted by the COMPUTE pI/Mw program provided by ExPASy (http://web.expasy.org/compute_pi/). The identity and similarity between each InR domain were determined through pairwise alignments using the EMBOSS Water algorithms (http://www.ebi.ac.uk/Tools/emboss/align/index.html).

dsRNA preparation. dsRNA was synthesized using the MEGAscript T7 High Yield Transcription Kit (catalogue no. AM1334, Ambion) according to the manufacturer's instructions. Briefly, the DNA template for dsRNA synthesis was amplified with primers containing the T7 RNA polymerase promoter at both ends (Supplementary Table 2), and the purified DNA template (200 ng) was then used to produce dsRNAs. Subsequently, the synthesized dsRNA was purified via LiCl precipitation and resuspended in nuclease-free water, and the concentration of dsRNA was quantified with a NanoDrop 2000 (Thermo Fisher Scientific). Finally, the quality and size of the dsRNAs were further verified via electrophoresis in a 1% agarose gel.

dsRNA microinjection in planthoppers. Injection of planthoppers with dsRNA was carried out according a method we reported previously[32]. Briefly, nymphs were randomly collected from the culture chamber and anaesthetized with CO_2 for 30 s. The quantities of dsRNA injected into 2nd-, 3rd- and 4th-instar nymphs were approximately 25 ng, 75 ng and 150 ng, respectively. dsRNA was injected into the thorax between the mesocoxa and the hind coxa using a FemtoJet microinjection system (Eppendorf), and 100–150 nymphs were used for injection with dsRNA targeting each gene. After injection, plentiful fresh rice seedlings were provided to feed the nymphs, which were maintained in transparent polycarbonate jars, 7 cm in diameter and 10.5 cm in height. Each jar contained no more than 150 individuals, and fresh rice seedlings were renewed every 3 days. Three days after the injections, RNA was extracted from 20 individuals to examine the gene silencing efficiency (Extended Data Fig. 10). The remaining nymphs were allowed to moult into adults for determination of the wing morph ratio. The proportion of long-winged and short-winged BPHs that developed after gene knockdown was calculated on the basis of three experiments.

qRT–PCR analysis. Total RNA was first isolated from the BPHs or from tissue samples using RNAiso Plus (catalogue no. 9109, TaKaRa) by following the manufacturer's protocol, and then treated with DNase (catalogue no. M610A, Promega) to remove any genomic DNA contamination. cDNA was synthesized from 0.8 μg of total RNA with random primers in a 20 μl reaction using the PrimeScript 1st strand cDNA synthesis kit (catalogue no. 6110A, TaKaRa). qRT–PCR was performed with the ABI 7300 Real-Time PCR System (Applied Biosystems) using the SYBR Premix Ex Taq Kit (catalogue no. RR420A, TaKaRa) and primers designed in this study (Supplementary Table 2), according to the manufacturer's protocol. For each reaction, 0.4 μl of each primer (10 μM), 0.4 μl of Rox reference dyes and 10 μl of SYBR Primer Ex Taq were added, in a total volume of 20 μl. The qRT–PCR protocol was 95 °C for 30 s, followed by 40 cycles of at 95 °C for 5 s and 60 °C for 30 s. A negative control (nuclease-free water) was included throughout the experiments to detect contamination and to determine the degree of dimer formation. The results (threshold cycle values) of the qRT–PCR assays were normalized to the expression level of ribosomal 18S rRNA. A relative quantitative method ($^{\Delta\Delta}C_t$)[33] was applied to evaluate the variation in expression among samples.

Rapid amplification of cDNA ends. The full cDNA sequences of the two BPH insulin receptor genes, *NlInR1* and *NlInR2*, were cloned using 5′-full and 3′-full rapid amplification of cDNA ends (RACE) core sets (catalogue no. 6107 and 6106, TaKaRa) according to the manufacturer's instructions. Total RNA was extracted from pooled samples (1st- to 5th-instar nymphs and adults) using RNAiso Plus (catalogue no. 9109, TaKaRa). For 5′ RACE, 2 μg of total RNA was sequentially treated with alkaline phosphatase (CIAP), tobacco acid pyrophosphatase (TAP) and a 5′ RACE adaptor before cDNA synthesis using random 9-oligonucleotide primers. Subsequently, nested PCR was done to obtain the 5′-end sequence with primer pairs consisting of the 5′ RACE outer primer/InR1-5RACE-GSP1 and 5′ RACE inner primer/InR1-5RACE-GSP2 for *NlInR1*, and the 5′ RACE outer primer/InR2-5RACE-GSP1 and 5′ RACE inner primer/InR2-5RACE-GSP2 for *NlInR2* (Supplementary Table 2).

For 3′ RACE, cDNA was synthesized from 1 μg of total RNA using the 3′ RACE adaptor primer. Next, nested PCR amplification was performed to obtain the 3′-end sequence with primer pairs consisting of the 3′ RACE outer primer/InR1-3RACE-GSP1 and 3′ RACE inner primer/InR1-3RACE-GSP2 for *NlInR1*, and the 3′ RACE outer primer/InR2-3RACE-GSP1 and 3′ RACE inner primer/InR2-3RACE-GSP2 for *NlInR2* (Supplementary Table 2).

Determination of forewing size and hind tibiae length. dsRNAs targeting *gfp*, *NlInR1*, *NlInR2*, *NlChico* or ds*NlInR2*;ds*NlFoxo* were administered to 2nd-instar nymphs. Fourth-instar nymphs (0–24 h after ecdysis) were used for ds*NlAkt* treatment because early stage nymphs treated with ds*NlAkt* died before adult eclosion. After adult eclosion, digital images of the forewings ($n = 20$) and hind tibiae ($n = 20$) were collected and then measured using Adobe Photoshop CS3.

Determination of BPH weights and the duration of nymphal development. dsRNAs targeting *gfp*, *NlInR1*, *NlChico* or *NlInR2* were administered to 2nd-instar nymphs (0–24 h after ecdysis). The average weight of the 5th-instar nymphs (24 h and 72 h after ecdysis) was calculated by weighing BPHs in groups using an AB204-N precision scale (Mettler Toledo). The number of newly emerged adults was counted every 24 h, and subsequently used to calculate the duration of nymphal development from the 2nd-instar stage to the adult stage using SPSS software.

Glycogen, trehalose and glucose quantification. Newly emerged 5th-instar nymphs (0–12 h after ecdysis, $n = 15$) or adult females (0–12 h after eclosion, $n = 10$) were starved for 1 h, and were then homogenized in 0.25 ml of 0.25 M Na_2CO_3, as previously reported[34]. The mixture was incubated at 70 °C for 10 min, and then brought to pH 5.2 by addition of 0.15 ml of 1 M acetic acid and 0.6 ml of 0.2 M Na-acetate, pH 5.2. For glycogen measurement, one-half of the suspension was incubated for 1 h with amyloglucosidase (catalogue no. 10115, Sigma-Aldrich) at 50 °C. For trehalose measurement, the second half of the suspension was incubated overnight with trehalase (catalogue no. T8778, Sigma-Aldrich) at 37 °C. Free glucose calculated from the sample without amyloglucosidase or trehalase treatment was subtracted from the glycogen or trehalose value, respectively. For glucose measurement, 20 nymphs and 25 adult females were homogenized in 0.2 ml and 0.3 ml PBS, respectively, after which the glucose levels were measured with glucose oxidase (GO) reagent (catalogue no. GAGO-20, Sigma-Aldrich). The glycogen, trehalose and glucose contents were calculated based on three experiments.

Triglyceride quantification. Triglyceride quantification was performed via enzymatic hydrolysis using the GPO Trinder method with a tissue triglyceride assay kit (catalogue no. E1013, Applygen Technologies). Fifth-instar nymphs (0–12 h after ecdysis, $n = 15$) or adult females (0–12 h after eclosion, $n = 10$) were homogenized in lysis buffer using a FastPrep-24 homogenizer (MP Biomedicals). The lysate was heated for 10 min at 70 °C, then centrifuged, and the supernatant was collected for TAG quantification using a BioTek spectrophotometer plate reader (VT) at 550 nm. The triglyceride content was calculated based on three experiments.

Detection of P-*Nl*Akt in wing buds. Fourth-instar nymphs (0–24 h after ecdysis) were treated with dsRNAs (250 ng per BPH) targeting *gfp*, *NlInR1*, *NlInR2* and *NlPten*. Wing buds ($n = 80$) from 5th-instar nymphs (24–30 h after ecdysis) were collected and homogenized in PBS containing protein phosphatase inhibitor (catalogue no. P0044, Sigma-Aldrich). Samples were quantified using the BCA method (catalogue no. 23227, Thermo Scientific) and denatured in SDS–PAGE loading buffer. Equal amounts of protein (100 μg) were loaded for each lane on SDS–PAGE gel. The western blotting was performed using primary antibodies of phospho-*Drosophila* Akt (P-*Dm*Akt, Ser 505) and Akt (catalogue no. 4054 and 9272, Cell Signaling). The β-actin polyclonal rabbit serum was prepared as in our previous report[35], and was used to monitor equal protein loading.

To investigate whether the P-*Dm*Akt (Ser 505) was specific to probe P-*Nl*Akt in BPHs, wing buds ($n = 200$) from 5th-instar nymphs (48 h after ecdysis) were cultured in MM basic medium[36] (1.36 mM $CaCl_2$, 2.68 mM KCl, 0.49 mM $MgCl_2$, 119 mM $NaCl_2$, 1.43 mM $NaHCO_3$, 1.45 mM NaH_2PO_4, pH 6.5) for 2 h. The pooled wing buds ($n = 50$) were subsequently treated with 50 μM PI(3)K inhibitor

LY294002 (catalogue no.CL9908, Sigma-Aldrich) for an additional 2 h or treated with 17 μM insulin for 30 min after LY294002 addition. In the parallel experiments, pooled wing buds ($n = 50$) were treated for 17 μM insulin for 30 min before being subjected to a probe with antibodies. Immunoreactivity was imaged with the Molecular Imager ChemiDoc^{TM} XRS+ system (Bio-Rad).

Immunoprecipitation assay. *Drosophila* S2 cells were transfected with pAc5.1/HisB/*Nl*InR1–Flag (*Nl*InR1–Flag), pAc5.1/HisB/*Nl*InR1-V5 (*Nl*InR1–V5), pAc5.1/HisB/*Nl*InR2–Flag (*Nl*InR2–Flag) or pAc5.1/HisB/*Nl*InR2–V5 (*Nl*InR2–V5) expression constructs by using Lipo2000 (catalogue no. 11668-027, Invitrogen). The cells were harvested 36 h after transfection, and total cell extracts were prepared in cell lysis buffer (20 mM Tris-HCl pH 7.5, 150 mM NaCl, 20 mM β-glycerophosphate, 10 mM NaF, 1 mM PMSF, 1 mM sodium orthovanadate, 10 mg ml^{-1} leupeptin, 2 mg ml^{-1} aprotinin, 1 mM EDTA and 1% Triton X-100). Cell lysates were incubated with the Flag monoclonal antibody or V5 monoclonal antibody for 4 h at 4 °C, followed by incubating with Protein A and Protein G (catalogue no. 17-0403-03 and 17-0405-03, GE Healthcare) for an additional 1 h. Immune complexes were washed with lysis buffer five times, and then resolved by SDS–PAGE. Western blotting was performed with the following antibodies: anti-Flag M2 (catalogue no. F1804, Sigma-Aldrich) and anti-V5 (catalogue no. sc-271944, Santa Cruz Biotechnology). The membrane was then exposed to Kodak X-ray film.

Preparation of His–*Nl*Ilp3 and His–*Nl*Foxo rabbit polyclonal serum. A PCR fragment (354 bp) encompassing the *NlIlp3* gene was amplified with the primers pIlp3-F and pIlp3-R (Supplementary Table 2), which were synthesized containing restriction endonuclease sites for BamHI and HindIII at their 5′ ends, respectively. A PCR fragment (570 bp) encompassing the *NlFoxo* gene was amplified with the primers pFoxo-F and pFoxo-R, which were synthesized containing restriction endonuclease sites for BamHI and XhoI at their 5′ ends, respectively. The amplicons were cloned into the expression vector pET28a with a 6× His tag at the N terminus. The fusion proteins His–*Nl*Ilp3 and His–*Nl*Foxo were expressed in the *Escherichia coli* strain Rossetta (DE3) after induction with 1 mM isopropyl-β-D-thiogalactoside (IPTG) at 37 °C for 6 h, and then recovered after SDS–PAGE. Polyclonal antiserum against His–*Nl*Ilp3 and His–*Nl*Foxo was raised by immunizing rabbits with the purified proteins.

Immunofluorescence assay. *Nl*Ilp3 and *Nl*Foxo antibody staining was carried out essentially as previously described[37]. For *Nl*Ilp3 antibody staining, brains were directly dissected from 5th-instar nymphs. For *Nl*Foxo antibody staining, 3rd-instar nymphs were treated with dsRNAs, and wing buds and fat body were dissected from 5th-instar nymphs (48 h after ecdysis). The specimens were fixed in 3.7% PFA/PBS (137 mM NaCl, 2.7 mM KCl, 10 mM Na_2HPO_4, 2 mM KH_2PO_4, pH 7.4) overnight at 4 °C, and washed in PBST containing 0.1% Triton X-100 three times for 30 min each. The specimens were then blocked in PBST containing 5% normal goat serum (catalogue no. 01-6201, Invitrogen) for 6 h at room temperature, followed by incubation with primary rabbit serum against His–*Nl*Ilp3 (1:500) or anti-His–*Nl*Foxo serum (1:500) in PBST containing 2% normal goat serum and 3% BSA overnight at 4 °C and then with goat anti-rabbit secondary antibody Dylight 649 (1:500) (catalogue no. A23620, Abbkine) in PBST containing 2% goat serum and 3% BSA after extensive washing. The nucleus was stained with 100 nM 4′,6-diamidino-2-phenylindole (DAPI) in PBST for 2 min at room temperature.

Image acquisition and processing. Fluorescence images were acquired using a Zeiss LSM 780 confocal microscope. Nuclear DNA was visualized using a 405 nm laser with a DAPI filter set, and the Dylight 649-labelled antibody was visualized using a 633 nm He-Ne laser for excitation with an Alexa 647 filter set. Maximum intensity projection images and three-dimensional reconstruction videos were generated using the ZEN 2010 digital imaging system.

Images of the wings, legs and whole bodies of BPHs were captured with a DFC320 digital camera attached to a LEICA S8AP0 stereomicroscope using the digital imaging system LAS v.3.8.

Statistics. Data are presented as mean ± s.e.m. from three independent biological replicates, unless otherwise noted. Statistical analysis was performed using SPSS (v.13). Means were compared using two-tailed Student's t-test or one-way analysis of variance (Tukey's test) at the significance levels set at $^{*}P < 0.05$ and $^{**}P \leq 0.001$. No statistical methods were used to predetermine sample size.

31. Xue, J. *et al.* Genomes of the rice pest brown planthopper and its endosymbionts reveal complex complementary contributions for host adaptation. *Genome Biol.* **15,** 521 (2014).
32. Xu, H. J. *et al.* Genome-wide screening for components of small interfering RNA (siRNA) and micro-RNA (miRNA) pathways in the brown planthopper, *Nilaparvata lugens* (Hemiptera: Delphacidae). *Insect Mol. Biol.* **22,** 635–647 (2013).
33. Pfaffl, M. W. A new mathematical model for relative quantification in real-time RT–PCR. *Nucleic Acids Res.* **29,** e45 (2001).
34. Parrou, J. L. & Francois, J. A simplified procedure for a rapid and reliable assay of both glycogen and trehalose in whole yeast cells. *Anal. Biochem.* **248,** 186–188 (1997).
35. Xue, J. *et al.* Molecular characterization of the *flightin* gene in the wing-dimorphic planthopper, *Nilaparvata lugens*, and its evolution in Pancrustacea. *Insect Biochem. Mol. Biol.* **43,** 433–443 (2013).
36. Hirumi, H. & Maramorosch, K. in *Invertebrate Tissue Culture* (ed. Vago, C.) 307–337 (Academic, 1971).
37. Géminard, C., Rulifson, E. J. & Léopold, P. Remote control of insulin secretion by fat cells in *Drosophila*. *Cell Metab.* **10,** 199–207 (2009).

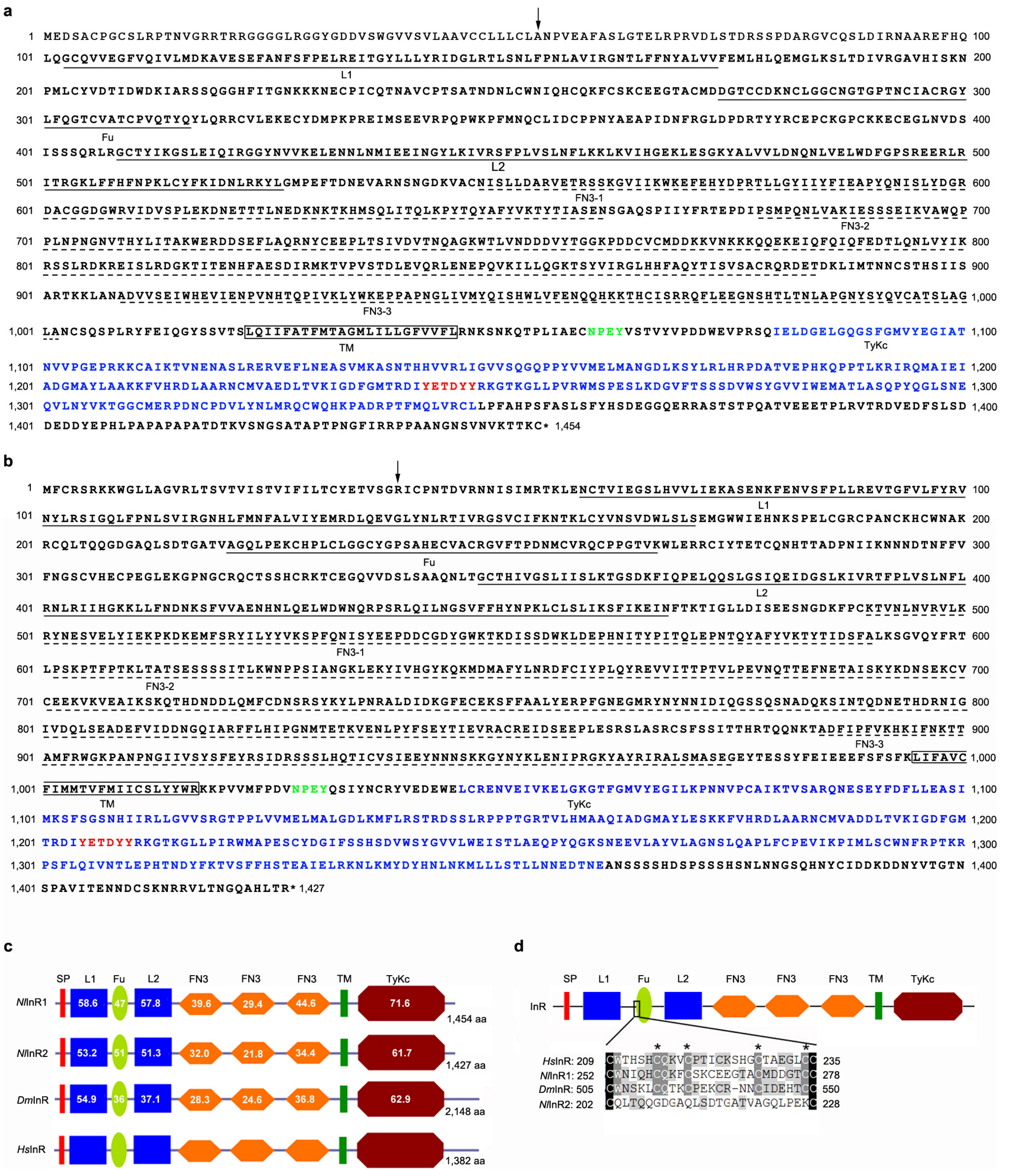

Extended Data Figure 1 | cDNA sequences of *Nl*InR1 and *Nl*InR2. **a**, **b**, *Nl*InR1 (**a**) and *Nl*InR2 (**b**) share highly similar domain architectures. The signal peptide (SP) indicated by a vertical arrow is produced via a cleavage site at the amino terminus. Two ligand-binding loops (L1 and L2) and the furin-like cysteine-rich (Fu) region are underlined with solid lines. Three fibronectin type 3 (FN3) domains are labelled with dashed underlines. A single transmembrane (TM) region is highlighted with a box. An 'NPXY' motif is shown in green. The highly conserved tyrosine kinase domain (TyrKc) is indicated in blue. A triple tyrosine cluster (YXXXYY), is indicated in red. **c**, The sequence identity (%) of each domain in the InR receptors compared to its counterpart in the human insulin receptor (*Hs*InR). *Dm*, *D. melanogaster*. **d**, The alignment of the N-terminal part of the Fu domains of *Nl*InR1, *Nl*InR2, *Dm*InR and *Hs*InR. The four cysteine residues that are absent in *Nl*InR2 are indicated by asterisks.

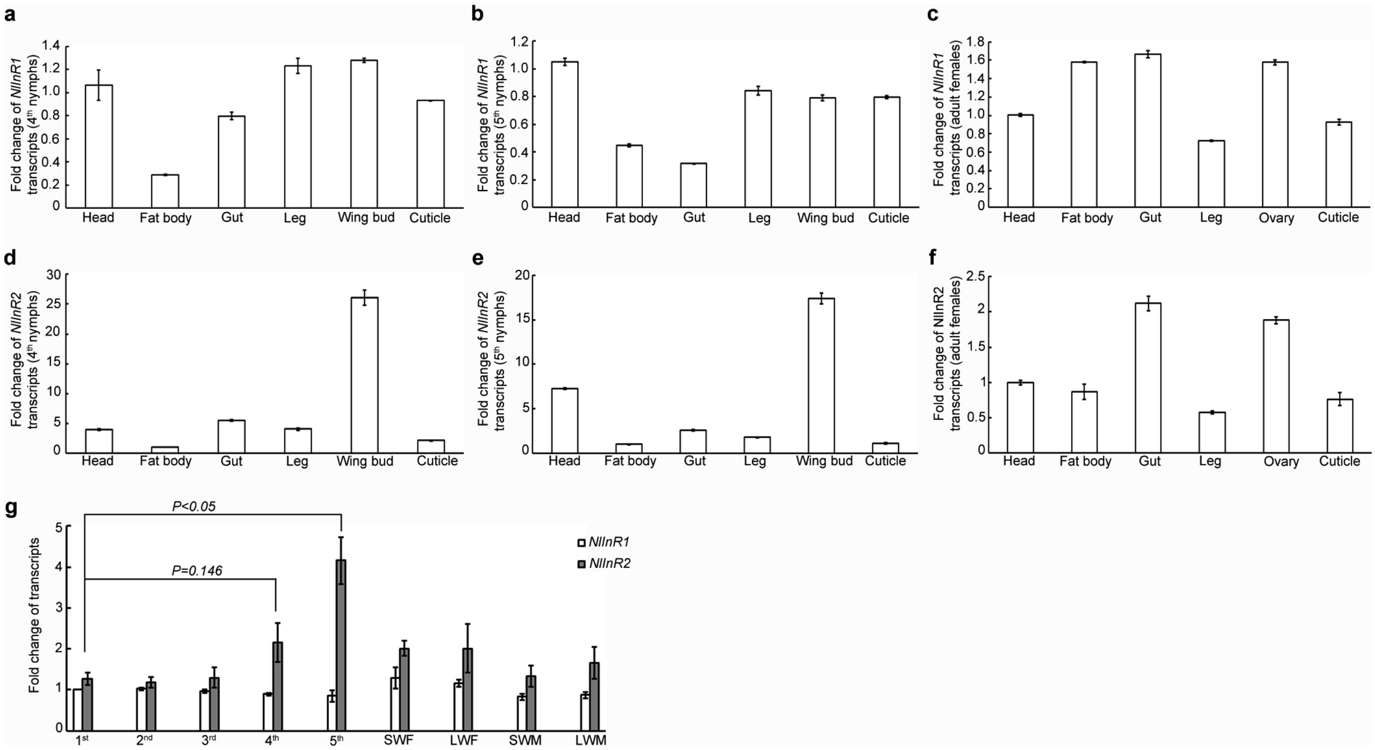

Extended Data Figure 2 | Spatio-temporal expression analyses of *NlInR1* and *NlInR2*. **a**, Quantitative polymerase chain reaction with reverse transcription (qRT–PCR) analysis was performed on various tissues dissected from 4th-instar nymphs ($n = 100$), 5th-instar nymphs ($n = 60$) and adult females ($n = 30$). **a**–**c**, *NlInR1* was widely expressed in all tissue samples collected from 4th-instar nymphs (**a**), 5th-instar nymphs (**b**) or adult females (**c**). **d**–**f**, *NlInR2* was predominately expressed in wing buds in 4th-instar nymphs (**d**) and 5th-instar nymphs (**e**), but was widely expressed in adult tissues (**f**). **a**–**f**, Error bars represent the s.e.m of three technical replicates. **g**, Relative expression levels of *NlInR1* and *NlInR2* across development. First-instar nymphs ($n = 60$), 2nd-instar nymphs ($n = 60$), 3rd-instar nymphs ($n = 20$), 4th-instar nymphs ($n = 20$), 5th-instar ($n = 20$) nymphs and adults ($n = 20$) were used for RNA extraction. A relatively high expression of *Nl*InR2 was observed in the 4th- and 5th-instar nymphs. Mean ± s.e.m. from three experiments, *P* values are indicated (Student's *t*-test). SWF, short-winged females; LWF, long-winged females; SWM, short-winged males; LWM, long-winged males.

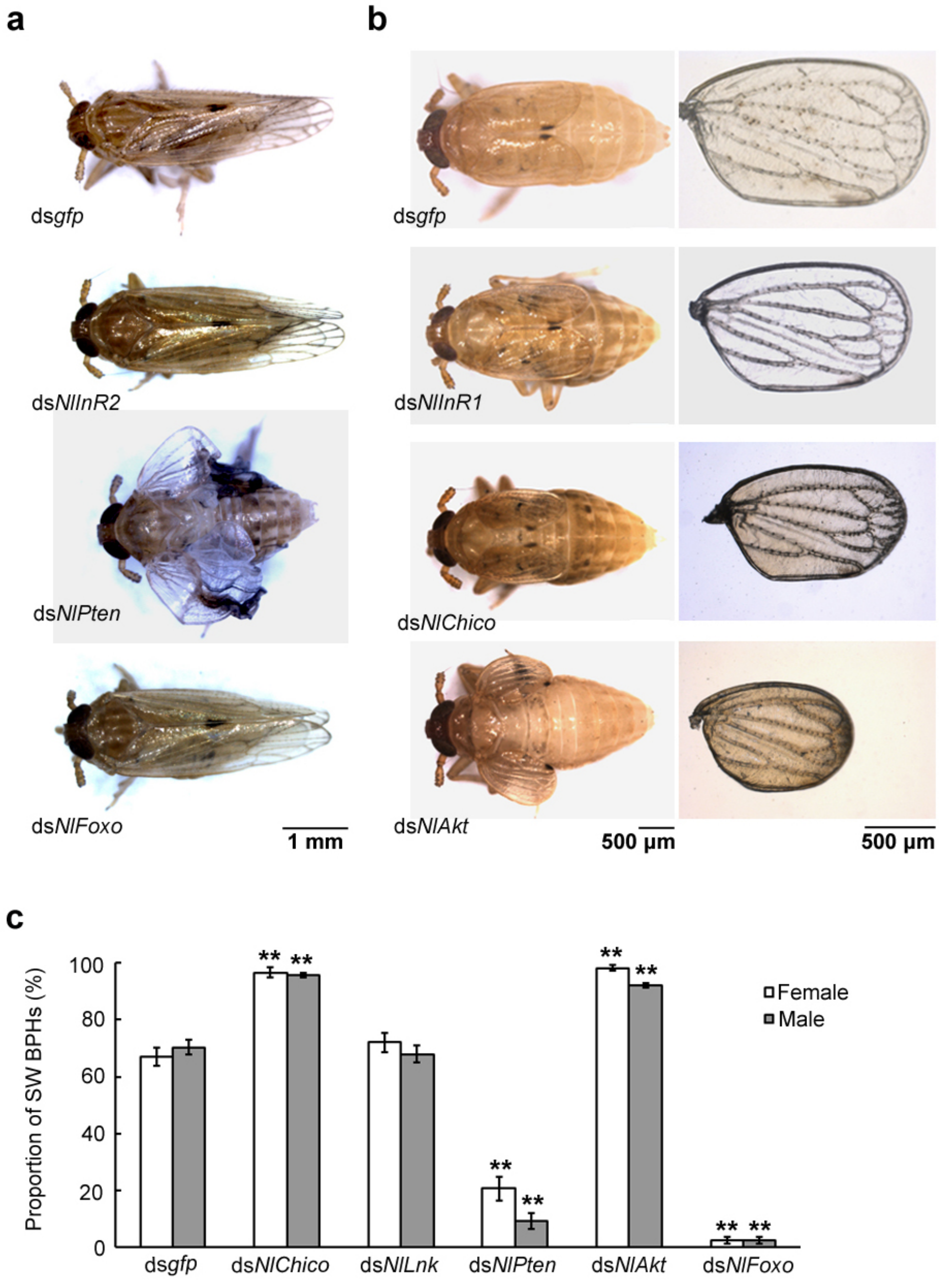

Extended Data Figure 3 | Effects of knockdown of components of the IIS pathway. **a**, Knockdown of *NlInR2*, *NlFoxo* or *NlPten*. **b**, Knockdown of *NlInR1*, *NlChico* or *NlAkt*. Forewing veins are patterned normally. **c**, The proportion of short-winged (SW) BPHs, from three experiments (mean ± s.e.m.). ds*gfp* ($n = 142$ females, 161 males), ds*NlChico* ($n = 86$ females, 98 males), ds*NlLnk* ($n = 100$ females, 117 males), ds*NlPten* ($n = 89$ females, 78 males), ds*NlAkt* ($n = 106$ females, 89 males) and ds*NlFoxo* ($n = 78$ females, 82 males). $*P < 0.05$ and $**P \leq 0.001$ (Student's *t*-test), difference from ds*gfp*. Source data are provided in Supplementary Data 4.

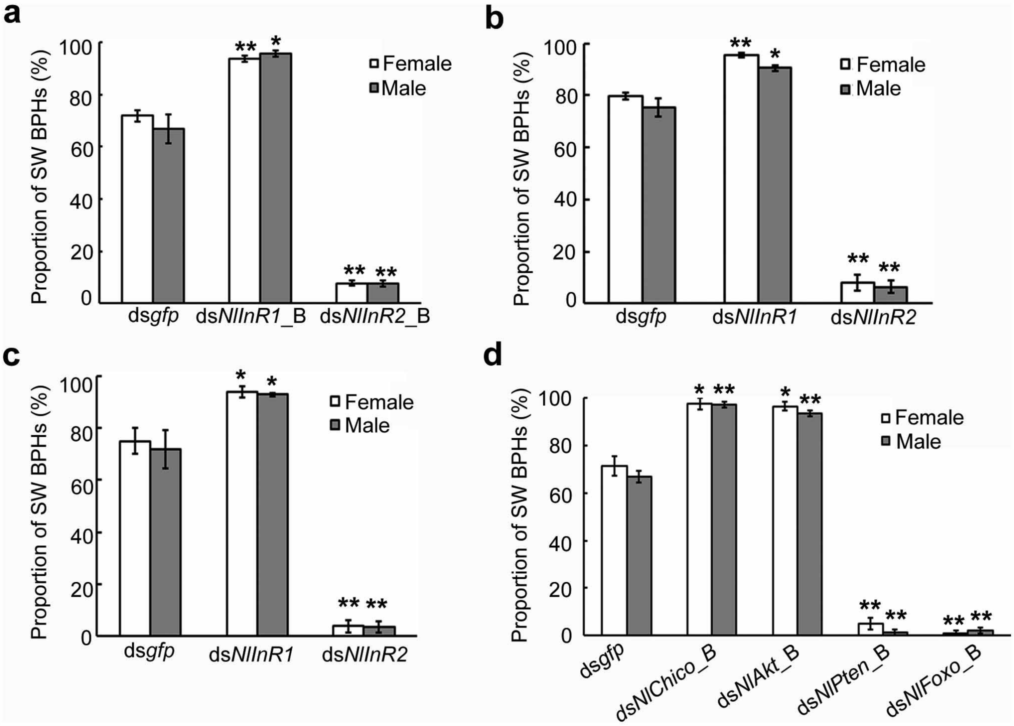

Extended Data Figure 4 | Validation of RNAi effect using the second dsRNA molecules, and knockdown of *NlInRs* in BPHs at 3rd- and 4th-instar nymphs. **a**, The proportion of short-winged (SW) BPHs after treatment of 2nd-instar nymphs with the second dsRNAs targeting *NlInRs* (ds*NlInR1*_B or ds*NlInR2*_B). ds*gfp* ($n = 124$ females, 100 males), ds*NlInR1*_B ($n = 90$ females, 92 males) and ds*NlInR2*_B ($n = 103$ females, 116 males). **b**, Knockdown of *Nl*InRs in 3rd-instar nymphs. ds*gfp* ($n = 117$ females, 114 males), ds*NlInR1* ($n = 109$ females, 130 males) and ds*NlInR2* ($n = 90$ females, 100 males). **c**, Knockdown of *Nl*InRs in 4th-instar nymphs. ds*gfp* ($n = 101$ females, 126, males), ds*NlInR1* ($n = 90$ females, 117 males) and ds*NlInR2* ($n = 94$ females, 100 males). **d**, The 3rd-instar nymphs were treated with a second dsRNA targeting several key components in the canonical insulin signalling pathway. ds*gfp* ($n = 96$ females, 100 males), ds*NlChico*_B ($n = 72$ females, 78 males), ds*NlAkt*_B ($n = 86$ females, 78 males), ds*NlPten*_B ($n = 111$ females, 88 males) and ds*NlFoxo*_B ($n = 95$ females, 91 males). **a**–**d**, Mean ± s.e.m. from three experiments. $^{*}P < 0.05$ and $^{**}P \leq 0.001$ (Student's *t*-test), difference from the ratio obtained for ds*gfp*. Source data are provided in Supplementary Data 5.

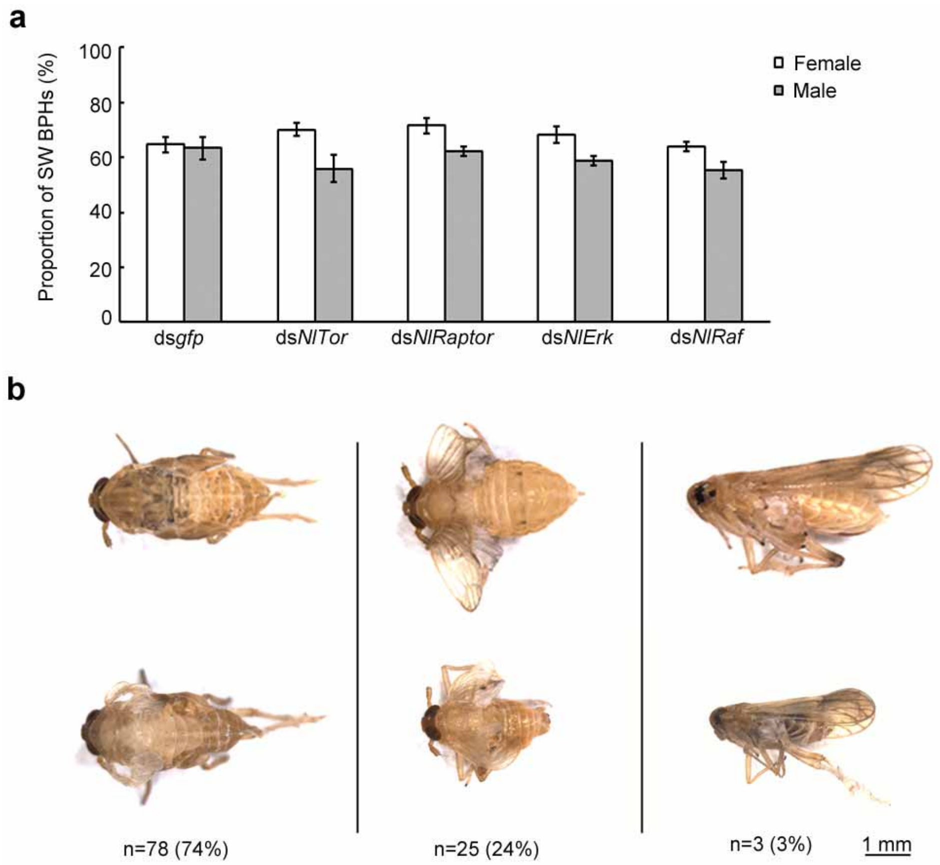

Extended Data Figure 5 | Knockdown of components of the TORC1 and the Ras/MAPK signalling cascades have no effect on wing morph switch. **a**, Third-instar nymphs were treated with dsRNAs targeting *NlTor* and *NlRaptor* genes in the TORC1 complex, and targeting *NlErk* and *NlRaf* in the Ras/MAPK signalling pathway. ds*gfp* ($n = 134$ females, 153 males), ds*NlTor* ($n = 122$ females, 130 males), ds*NlRaptor* ($n = 103$ females, 95 males), ds*NlErk* ($n = 138$ females, 148 males) and ds*NlRaf* ($n = 148$ females, 143 males). Mean ± s.e.m. from three experiments, no significant change from ds*gfp* (Student's *t*-test). **b**, Knockdown of *NlRheb*, an activator for TORC1 signalling activity. Third-instar nymphs were used for ds*NlRheb* treatment. Seventy-eight individuals (74%) failed to extricate themselves from the old cuticle, and died without completing ecdysis. Twenty-eight individuals finished nymph–adult transformation, of which twenty-five individuals (24%) were unable to stretch their wings correctly, and only three individuals (3%) showed normal morphology. Source data are provided in Supplementary Data 6.

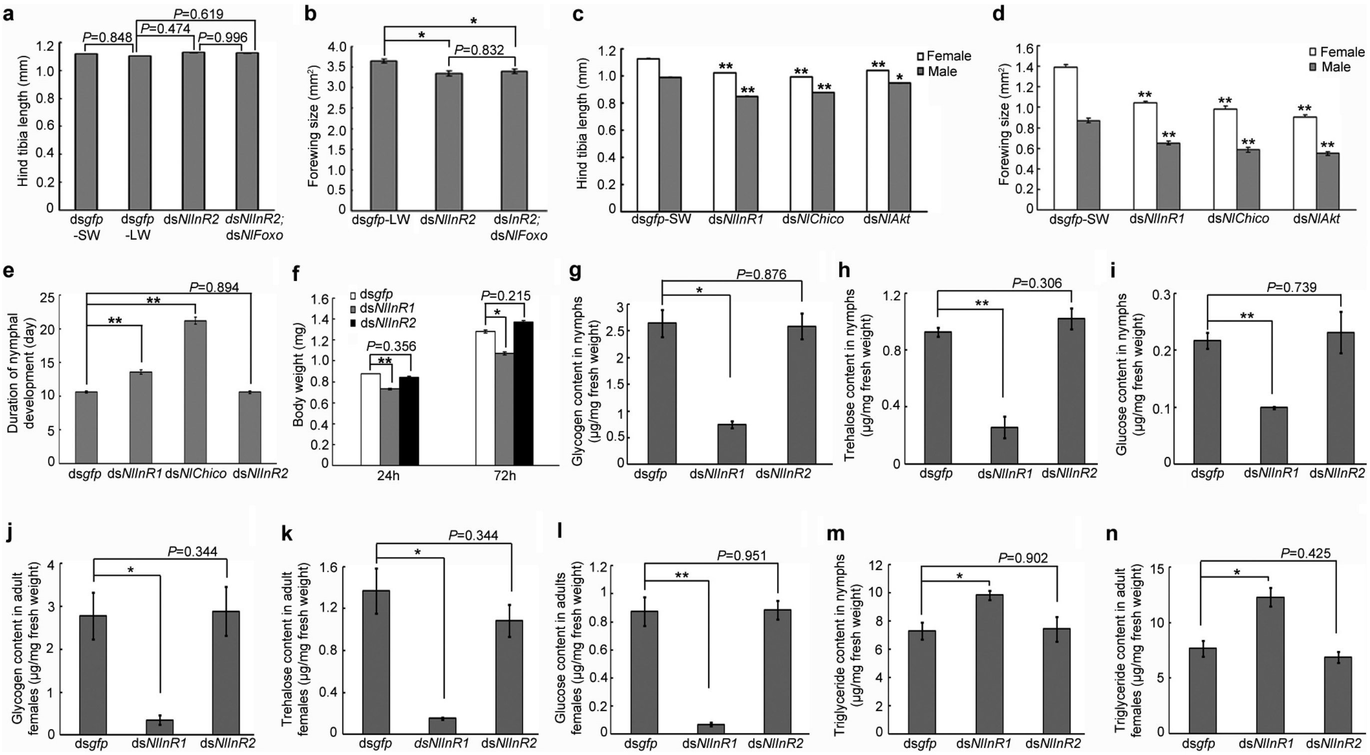

Extended Data Figure 6 | *Nl*InR2 regulates wing morph switch in a tissue-specific way. **a**–**n**, Second-instar nymphs were treated with dsRNAs targeting *gfp*, *NlInR1*, *NlInR2*, *NlChico* or *NlFoxo*, and 4th-instar nymphs were used for the ds*NlAkt* treatment. **a**, The short-winged BPHs (ds*gfp*-SW, *n* = 20) and long-winged BPHs (ds*gfp*-LW, *n* = 20) had a similar length of hind tibiae. The BPHs treated either with ds*NlInR2* (*n* = 20) or with double RNAi (ds*NlInR2*;ds*NlFoxo*, *n* = 20) had a similar length of hind tibiae as the ds*gfp*-LW (*n* = 20). **b**, The BPHs treated with ds*NlInR2* (*n* = 20) or ds*NlInR2*;ds*NlFoxo* (*n* = 20) possessed forewings of the same size or only slightly smaller than those of ds*gfp*-BPHs (ds*gfp*-LW, *n* = 20). **c**, **d**, Knockdown of *NlInR1* (*n* = 20), *NlChico* (*n* = 20) or *NlAkt* (*n* = 20) further reduced the hind tibiae length (**c**) and forewing size (**d**) compared to short-winged BPHs treated with ds*gfp* (ds*gfp*-SW, *n* = 20). **e**, Knockdown of *NlInR1* (*n* = 50) or *NlChico* (*n* = 44) but not *NlInR2* (*n* = 66) delayed nymphal development. **f**, Knockdown of *NlInR1* but not *NlInR2* resulted in body weight loss in 5th-instar nymphs. ds*gfp* (*n* = 107; 110, 24 h; 72 h), ds*NlInR1* (*n* = 117; 82, 24 h; 72 h), and ds*NlInR2* (*n* = 111; 103, 24 h; 72 h). '24 h' and '72 h' represent 24 h and 72 h after ecdysis, respectively. **g**–**l**, Knockdown of *NlInR1* but not *NlInR2* reduced levels of glycogen, trehalose and glucose both in nymphs (**g**–**i**) and adult females (**j**–**l**). **m**, **n**, Knockdown of *NlInR1* but not *NlInR2* increased levels of triglycerides in both nymphs (**m**) and adult females (**n**). **a**–**n**, Mean ± s.e.m. from three experiments. Tukey's test in **a**, **b**, and Student's *t*-test in **c**–**n**, difference from ds*gfp* (*$P < 0.05$ and **$P \leq 0.001$). Source data are provided in Supplementary Data 7.

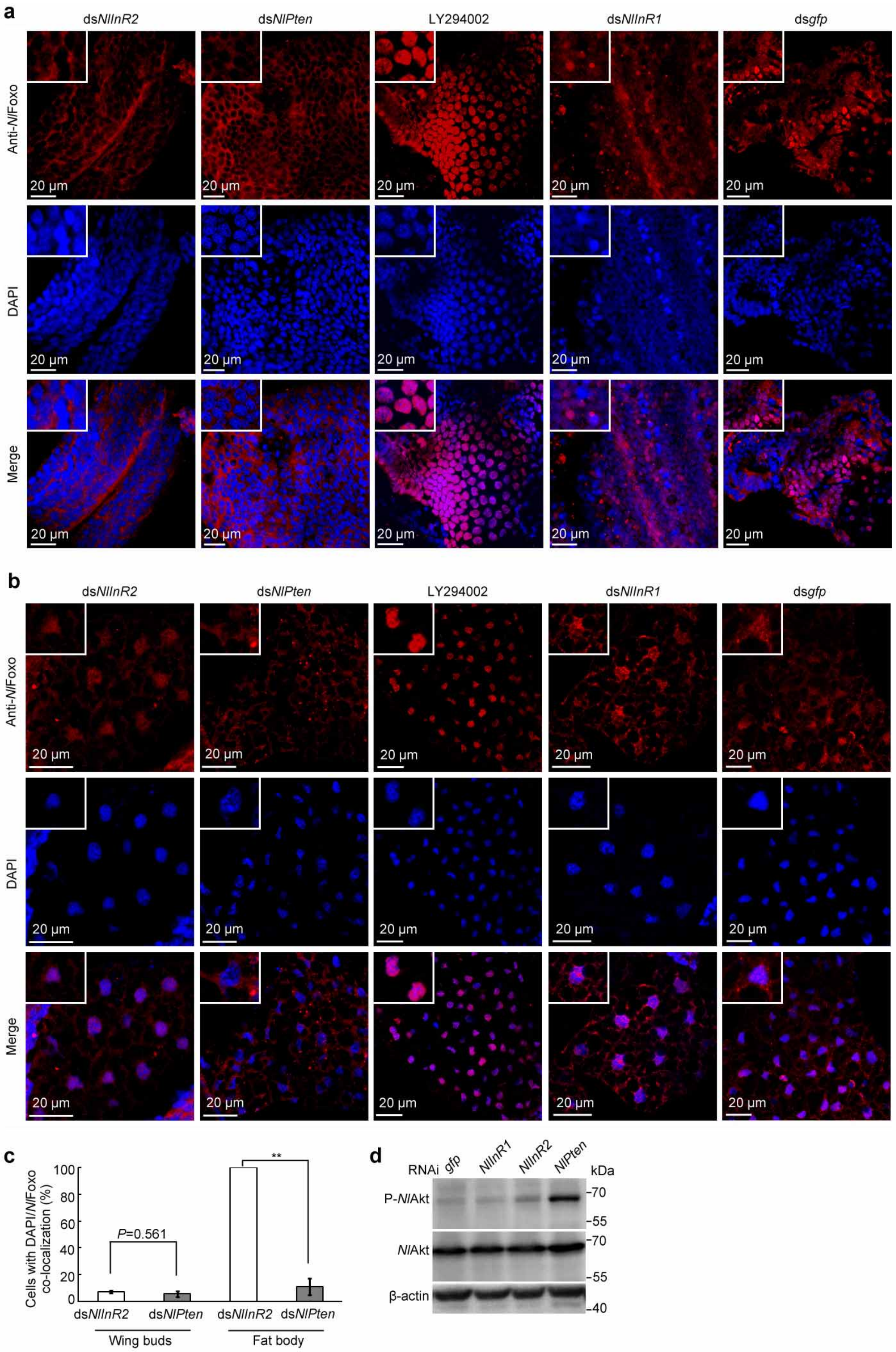

Extended Data Figure 7 | Subcellular localization of *Nl*Foxo in wing buds and fat body. **a**, **b**, Localization of *Nl*Foxo in wing buds (**a**) and fat body (**b**). Third-instar nymphs were treated with dsRNAs, and wing buds and fat body were dissected from 5th-instar nymphs (48 h after ecdysis). For LY294002 treatment, wing buds and fat body dissected from untreated 5th-instar nymphs (48 h after ecdysis) were used for immuno-staining. Red, anti-*Nl*Foxo. Blue (DAPI), cell nucleus. **c**, Proportion of cells with DAPI/Foxo co-localization in wing buds and fat body treated with ds*NlInR2* or ds*NlPten*. Error bars represent mean ± s.e.m. from cells in three images. $^{**}P \leq 0.001$ (Student's *t*-test). **d**, Knockdown of *NlInR2* did not increase P-*Nl*Akt levels in the fat body. Fat body treated with ds*gfp*, ds*NlInR1*, ds*NlInR2* or ds*NlPten* was probed with various antibodies.

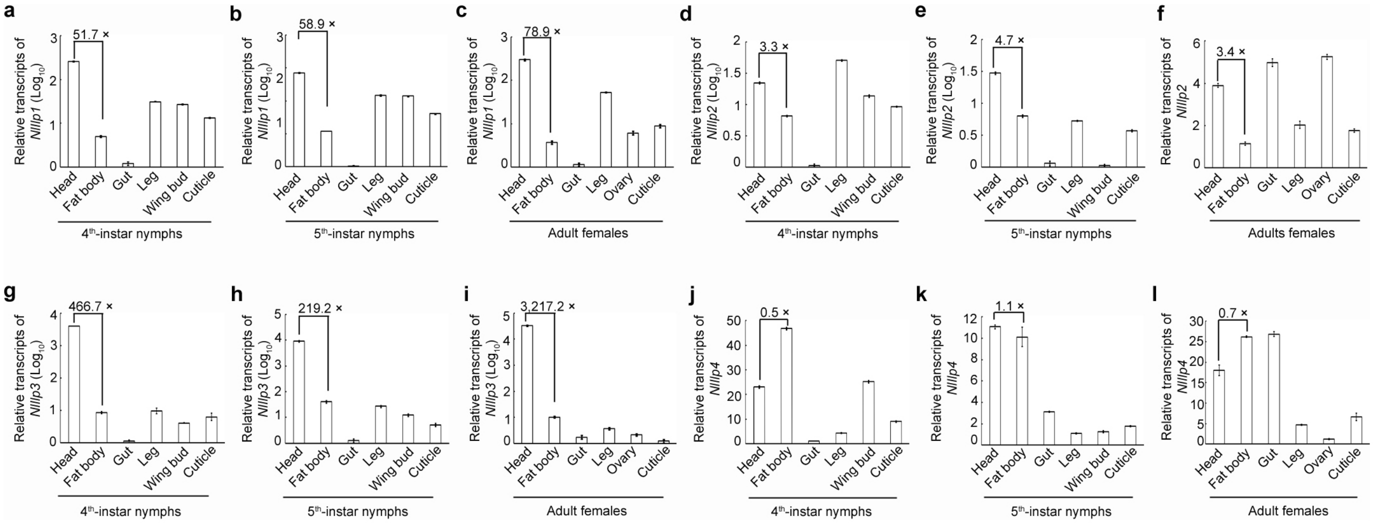

Extended Data Figure 8 | Tissue distribution of *Nl*Ilp1–4 in nymphs and adult females. **a–l**, Various tissues dissected from 4th-instar nymphs ($n = 100$), 5th-instar nymphs ($n = 60$) and adult females ($n = 30$) were exposed to qRT–PCR assays to detect *NlIlp1* (**a–c**), *NlIlp2* (**d–f**), *NlIlp3* (**g–i**) and *NlIlp4* (**j–l**) transcripts. The fold changes for transcripts in the head versus the fat body are indicated. Mean ± s.e.m. from three technical replicates.

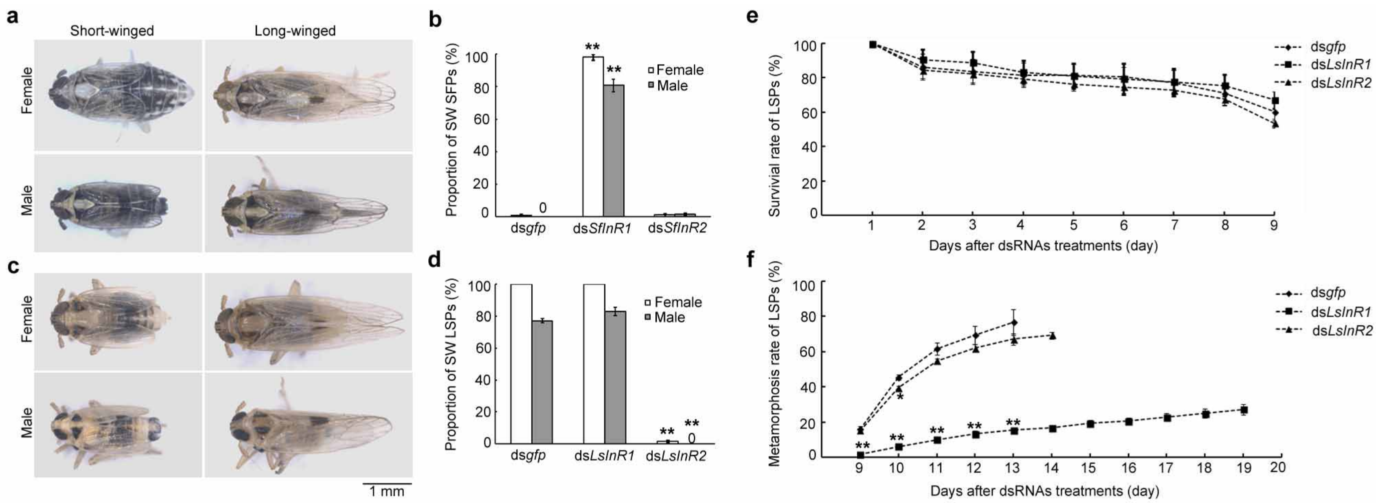

Extended Data Figure 9 | Knockdown of two insulin receptors in planthoppers, *Sogatella furcifera* and *Laodelphax striatellus*. **a**, The wing morphs of *S. furcifera* planthoppers (SFPs). **b**, Knockdown of *S. furcifera* (*Sf*)*InR1* resulted in the short-winged morph. ds*gfp* ($n = 110$ females, 89 males), ds*SfInR1* ($n = 101$ females, 135 males) and ds*SfInR2* ($n = 132$ females, 143 males). **c**, The wing morphs of *L. striatellus* planthoppers (LSPs). **d**, Knockdown of *L. striatellus* (*Ls*)*InR2* resulted in the long-winged morph. ds*gfp* ($n = 107$ females, 123 males), ds*LsInR1* ($n = 42$ females, 128 males) and ds*LsInR2* ($n = 113$ females, 107 males). **e**, Third-instar nymphs were treated with dsRNAs targeting *gfp* ($n = 200$), *LsInR1* ($n = 180$) or *LsInR2* ($n = 190$). The survival rate of LSPs was monitored every day before metamorphosis. Mean ± s.e.m. from three experiments, no significant change from ds*gfp* (Student's *t*-test). **f**, The metamorphosis rate was monitored every day at nine days after dsRNAs treatments. ds*gfp* ($n = 200$), ds*LsInR1* ($n = 180$) and ds*LsInR2* ($n = 190$). Most ds*LsInR1*-treated nymphs (>70%) died before adult eclosion, and thus yielded a significantly low metamorphosis rate. **b**–**f**, Mean ± s.e.m. from three experiments. $*P < 0.05$ and $**P \leq 0.001$ (Student's *t*-test), difference from ds*gfp*. Source data are provided in Supplementary Data 8.

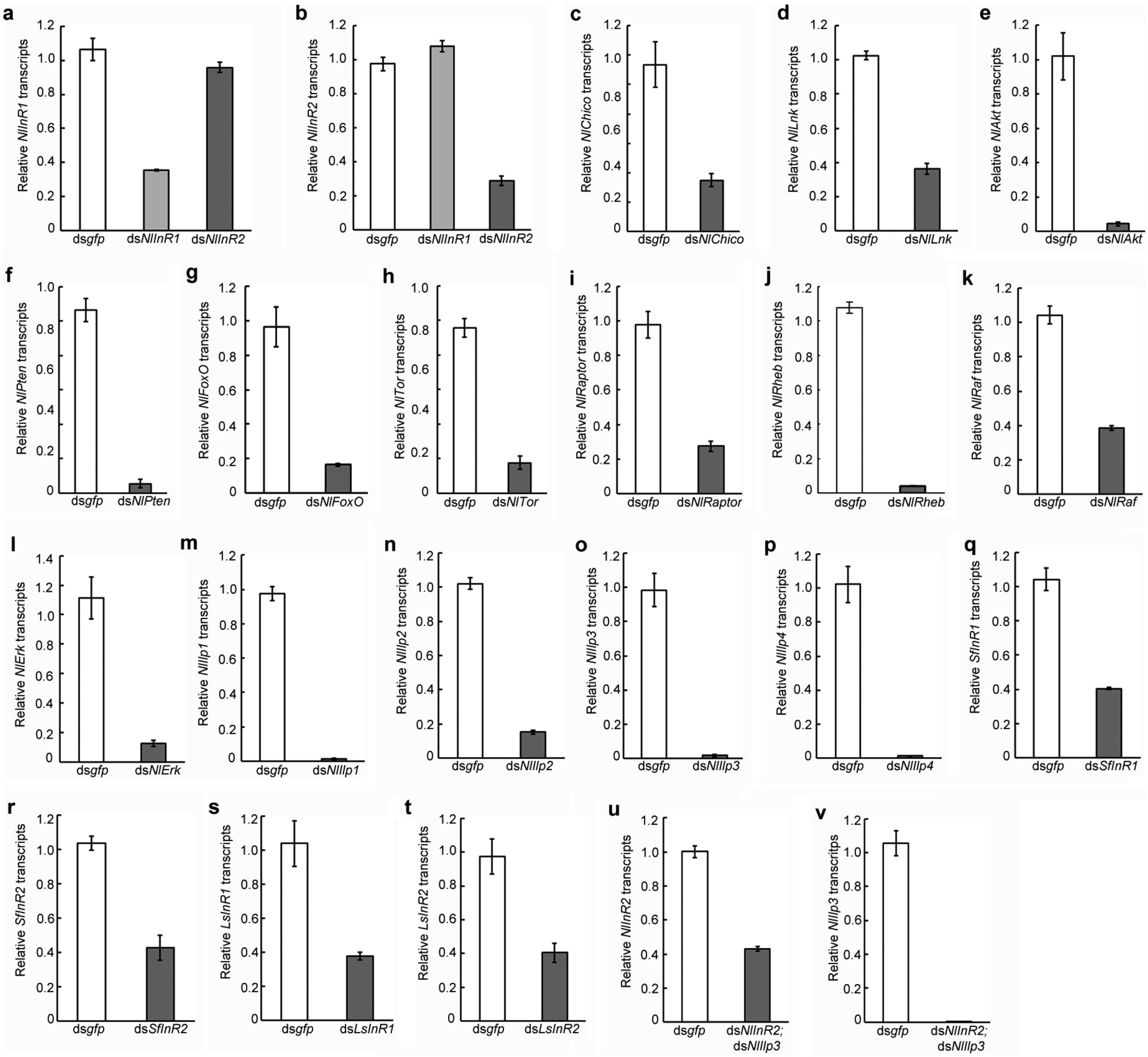

Extended Data Figure 10 | Examination of RNAi efficiency by qRT–PCR. a–v, Individual nymphs were pooled ($n = 20$) to extract total RNA after dsRNAs treatments, and cDNA was synthesized with random primers. The relative expression of each gene was normalized to the expression level of ribosomal 18S rRNA. Mean ± s.e.m. from three experiments.

doi:10.1038/nature14318

Lineage correlations of single cell division time as a probe of cell-cycle dynamics

Oded Sandler[1]*, Sivan Pearl Mizrahi[1,2]*, Noga Weiss[2], Oded Agam[2], Itamar Simon[1]§ & Nathalie Q. Balaban[2]§

Stochastic processes in cells are associated with fluctuations in mRNA[1], protein production and degradation[2,3], noisy partition of cellular components at division[4], and other cell processes. Variability within a clonal population of cells originates from such stochastic processes, which may be amplified or reduced by deterministic factors[5]. Cell-to-cell variability, such as that seen in the heterogeneous response of bacteria to antibiotics, or of cancer cells to treatment, is understood as the inevitable consequence of stochasticity. Variability in cell-cycle duration was observed long ago; however, its sources are still unknown. A central question is whether the variance of the observed distribution originates from stochastic processes, or whether it arises mostly from a deterministic process that only appears to be random. A surprising feature of cell-cycle-duration inheritance is that it seems to be lost within one generation but to be still present in the next generation, generating poor correlation between mother and daughter cells but high correlation between cousin cells[6]. This observation suggests the existence of underlying deterministic factors that determine the main part of cell-to-cell variability. We developed an experimental system that precisely measures the cell-cycle duration of thousands of mammalian cells along several generations and a mathematical framework that allows discrimination between stochastic and deterministic processes in lineages of cells. We show that the inter- and intra-generation correlations reveal complex inheritance of the cell-cycle duration. Finally, we build a deterministic nonlinear toy model for cell-cycle inheritance that reproduces the main features of our data. Our approach constitutes a general method to identify deterministic variability in lineages of cells or organisms, which may help to predict and, eventually, reduce cell-to-cell heterogeneity in various systems, such as cancer cells under treatment.

The cell division process has been extensively studied in many systems[7,8]. Models of cell-cycle durations are based on deterministic equations[7]. In order to account for cell-to-cell variability, the models typically take stochasticity into account, even in the 'deterministic growth control model'[9]. Alternatively, cell-to-cell variability may be due to a few underlying nonlinear dynamic factors, to which noise contribution is small and could, therefore, eventually be controlled. An unresolved central question is whether the observed variability originates mainly from stochasticity, or whether it stems from a deterministic process that only appears to be random, as illustrated in Fig. 1 (ref. 10). Our goal was to measure the variability in cell-cycle durations among thousands of single mammalian cells and to determine whether experiments can distinguish between stochastic processes[11] and deterministic nonlinear components[7,12,13].

To characterize the variability in cell-cycle progression at the single-cell level, we used time-lapse microscopy to monitor the total cell-cycle duration of single L1210 lymphoblasts with an accuracy of ±1%. Stably transfected lines with Fucci markers[14] also allowed us to monitor G1 and S/G2/M durations. (Fig. 2a). The cells were observed under the microscope for several days (Supplementary Video 1 and Fig. 2b, c), while maintaining constant conditions (Extended Data Fig. 1). The recorded videos were analysed by lineages to derive the total cell-cycle duration (T^{tot}), G1 duration (T^{G1}) and S/G2/M duration (T^{G2}) (Fig. 2c and Methods). This analysis resulted, for each lineage, in a series of cell-cycle durations ($T_1, T_2, T_3 \ldots$), with T_1 the cell-cycle duration of the mother, T_2 of its daughter, T_3 of its granddaughter, and so on.

In line with previous studies[15,16], we observed a strong correlation of T^{tot} between sister cells ($\rho_{\text{s-s}} = 0.71 \pm 0.07, P < 0.002$), whereas the correlation of T^{tot} between mother and daughter cells was close to zero and non-significant ($\rho_{\text{m-d}} = 0.04 \pm 0.08, P > 0.2$) (Fig. 2), and weakly positive between grandmother and granddaughter cells (Extended Data Fig. 6c). We found that T^{G1} and T^{G2} had a similar pattern of correlation to T^{tot}, namely sister cells were strongly correlated but mother–daughter cells were not (Fig. 2g). These results initially suggested that a factor inherited at birth determines the cell-cycle duration and that this factor is reset during each division, implying that the inheritance of cell-cycle duration is governed by stochastic processes[11]. When we extended our analysis to subsequent generations, we found that cousin cells were significantly correlated (Fig. 2f) ($\rho_{c\text{-}c} = 0.58 \pm 0.07; P < 0.002$). In particular, we observe that $\rho_{\text{c-c}} > |\rho_{\text{m-d}}|$, which we call the 'cousin–mother inequality', contrary to the expected behaviour $\rho_{\text{c-c}} = (\rho_{\text{m-d}})^2 \times \rho_{\text{s-s}}$ from simple inheritance rules[17]. A similar unexplained correlation in cell-cycle duration between cousins has been reported in several organisms[6,15,18].

We performed additional measurements, using different clones and microfluidic devices, in order to rule out the possibility that experimental factors were responsible for the surprisingly high correlation between cousins. In all cases, the cousin–mother inequality was observed (Extended Data Figs 2 and 3a). Additional extensive analysis of the recordings ruled out the possibility that an external experimental factor affected the microenvironment and generated artificial correlations (Fig 3a, b and Extended Data Fig. 3b, c).

We wondered how cousin cells can remain correlated when mothers and daughters are not. High correlation in cell-cycle durations between cousins is an indication of deterministic inheritance and suggests that the initial interpretation of the low mother–daughter correlation as indicating inheritance dominated by simple noise needs to be revised.

We set out to address whether the series of cell-cycle durations along a lineage ($T_1, T_2, T_3 \ldots$) is closer to a stochastic process, or whether it is mainly consistent with a deterministic process. This question has been addressed in the context of dynamical systems, which enable the detection of deterministic tendencies by evaluation of the effective number of factors that underlie the variability (Fig. 1). A small number of effective variables would be the signature of a deterministic process, and a very large number would signify a stochastic process.

The evaluation of the effective number of factors that govern the variability of a time series can be estimated using the Grassberger–Procaccia algorithm[19] (Fig. 1 and Supplementary Information). This algorithm has been applied to the analysis of time series in various systems[20,21]. The effective number of variables is estimated by the

[1]Department of Microbiology and Molecular Genetics, IMRIC, The Hebrew University Hadassah Medical School, Jerusalem 91120, Israel. [2]Racah Institute of Physics, Edmond J. Safra Campus, The Hebrew University, Jerusalem 91904, Israel.
*These authors contributed equally to this work.
§These authors jointly supervised this work.

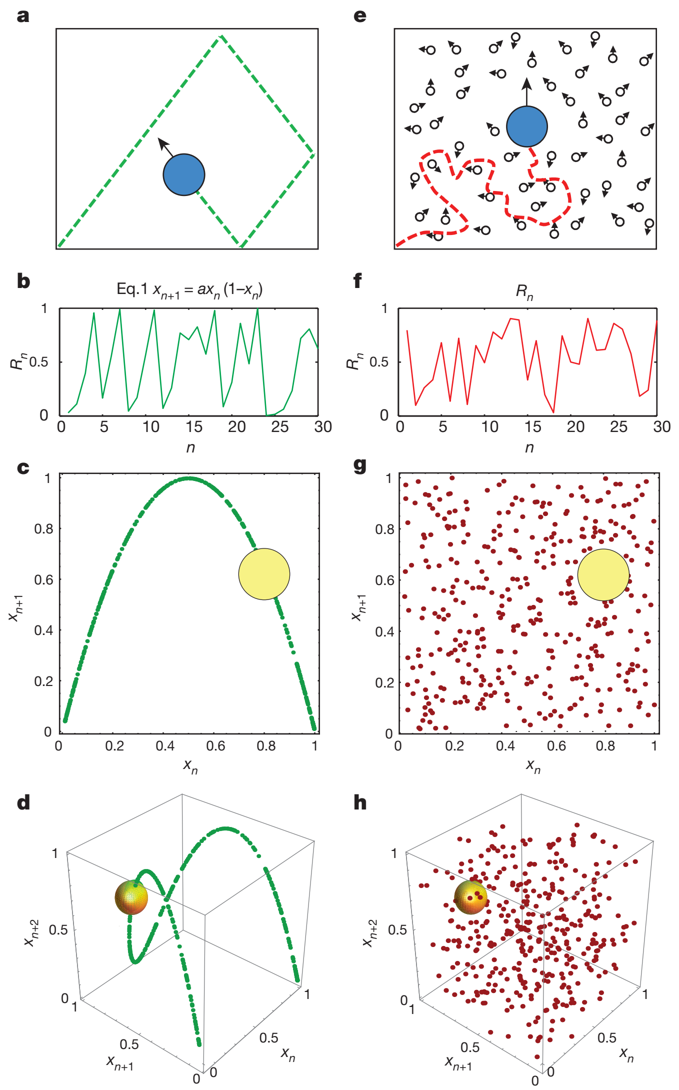

Figure 1 | Schematic illustration of stochastic versus deterministic variability. **a**, A small object's movement in an empty box. Prediction of its future location requires the knowledge of only its current location and velocity, thus the object's movement is deterministic, in contrast to the stochastic motion observed in **e** when the box is filled with a large number of colliding molecules. **b**, The logistic map (equation 1, see Supplementary Information) as an illustration of a low-dimensional deterministic process resulting in seemingly stochastic output with $a = 3.99$. **c**, Same data as in **b** plotted in embedding dimension $D_E = 2$, namely each point is associated with the coordinates (x_n, x_{n+1}), revealing its low dimensionality. **d**, Same data as in **b** plotted in embedding dimension $D_E = 3$, namely each point is associated with the coordinates (x_n, x_{n+1}, x_{n+2}). These points do not fill the 3D space but rather lie on a one-dimensional trajectory. This dimension is computed by evaluating the typical number of pairs of points inside a sphere whose radius r shrinks to zero. The number of points decreases as $r^{d_{corr}}$, where d_{corr} is the correlation dimension. **e**, Same small object as in **a** but the box is filled with a very large number of colliding molecules. Now the motion is governed by a very large number of variables thus, the object's movement is considered stochastic. **f**, Uncorrelated random numbers time series, R_n. **g**, **h**, Embedding of the random numbers time series in a higher-dimensional space. In contrast to the logistic map, here the points occupy the same dimension as the space in which they are embedded. Note that this simplified white noise example is given for illustrative purposes only and the more realistic case of coloured noise is discussed in the Supplementary Information.

'correlation dimension' which the Grassberger–Procaccia algorithm extracts from the data. Whereas the effective number of variables for simulated normally distributed random data is above 10 (the limit of the analysis) (Fig. 3c), it is found to be 1 for the logistic map series (Eq.1 in Fig. 1) (Figs 1b and 3c). The Grassberger–Procaccia algorithm is shown in Fig. 1g, h on the trivial example of white noise, but the correlation dimension can identify stochasticity also for the more general case of coloured noise, as long as the correlation time is finite (Supplementary Information). In order to further illustrate the power of the Grassberger–Procaccia algorithm on an experimental system known to be governed by stochasticity[3], we analysed the published data of constitutive fluorescent gene expression in *Escherichia coli*[22]. Similarly to the random data, the effective number of variables is found to be above 10 (Fig. 3c), as expected from a noisy process with short-range correlations (Supplementary Information).

Applying this algorithm to the series of cell-cycle durations extracted from the time-lapse recording of L1210 lymphoblasts along a lineage ($T_1, T_2, T_3\ldots$), we found that the effective number of variables is of the order of 3 (Fig. 3c and Extended Data Figs 4 and 5).

This analysis indicated that variability in cell-cycle duration is controlled by a deterministic process with a small number of dynamical factors. Note that in contrast to the typical time series on which the Grassberger–Procaccia analysis has been used, the lineage data provide an independent and more robust indication of deterministic inheritance through the cousin–mother inequality.

In order to illustrate how a deterministic process with a few factors can reproduce the cousin–mother inequality, we searched for a deterministic toy model that fulfils the following requirements, as dictated by our experimental observations: (1) deterministic factors are inherited from mother to daughter; (2) their effect on the cell-cycle duration is non-monotonic, in order to account for the low mother–daughter correlation; and (3) the nonlinear deterministic inheritance does not necessarily reach a fixed point.

A known nonlinear process affecting the cell-cycle duration and fulfilling all of the above requirements is the circadian clock. The coupling between circadian phase and cell cycle has been demonstrated in different organisms, including tissue culture cells[23], and quantitative characterizations have been carried out in Cyanobacteria[24]. We developed a discrete model of cell-cycle duration inheritance, the 'kicked cell cycle' model, the main feature of which is the deterministic influence of the circadian phase[24] at birth on the cell-cycle duration. The kicked cell cycle model predicts that correlations in cell-cycle duration between sisters ($\rho_{\text{s-s}}$) should be high, as the cell cycles of sister cells inherit the same phase of the cellular oscillator (Fig. 3d). In contrast, the correlation of cell-cycle duration between mother and daughter cells, $\rho_{\text{m-d}}$, is predicted to vary between positive and negative values, depending on the mean cell-cycle duration (Extended Data Fig. 6a). Finally, the model predicts that the cousin–mother inequality holds. Indeed, analysing the Cyanobacteria data confirmed all these predictions (Extended Data Fig. 7).

Next we applied the kicked cell cycle model to mammalian cells using a different set of parameters (Extended Data Table 1 and Fig. 4a–c), reproducing our main results. The model resolves the seemingly paradoxical cousin–mother inequality by showing that deterministic inheritance of cell-cycle duration can result in an apparent absence of correlation between mother and daughter cells (Extended Data Figs 6a and 8). Similar conclusions have been proposed in refs 6 and 25.

In agreement with the model's predictions, our measurements validate that $\rho_{\text{c-c}} > |\rho_{\text{m-d}}|$ (Fig. 4c, d). Specifically, for our data as well as for compiled correlations in cell-cycle duration reported for various mammalian cells (Extended Data Table 2), mother–daughter correlations vary between positive and slightly negative values (Fig. 4d), whereas intra-generation correlations in cell-cycle duration are positive and significant. In particular, we were able to run our analysis using cell-cycle duration measurements from a detailed study of EMT6 cells[6] and found that it fits our model's predictions (magenta dot in Fig. 4d).

The empirical data and modelling presented here reveal that deterministic factors control an important part of cell-cycle variability in mammalian cells. Our analysis shows that the oscillating term of this model results in the high correlation between cousins observed in Cyanobacteria

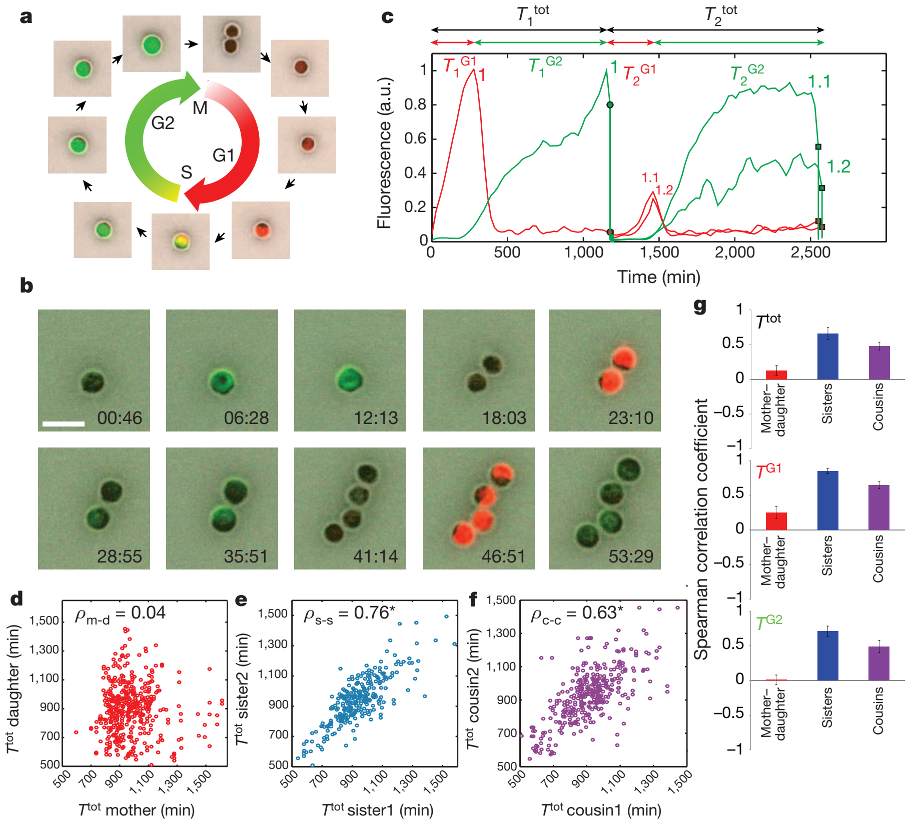

Figure 2 | Pedigree analysis of the cell-cycle duration in L1210 cells. **a**, Schematic description of the Fucci markers used for visualizing the cell-cycle progression. **b**, Time-lapse images of the dividing L1210 Fucci cells, showing overlays of phase-contrast green and red fluorescence images. Scale bar, 20 µm. **c**, Automated tracking plots of the Fucci fluorescence of a typical lineage. a.u., arbitrary units. **d**, Correlation plots in total cell-cycle duration (T^{tot}) for mother–daughter ($\rho_{m\text{-}d}$, red); **e**, sisters ($\rho_{s\text{-}s}$, blue); **f**, cousins ($\rho_{c\text{-}c}$, purple). Asterisks denote significant correlation ($P < 0.002$; Spearman); clone1, $n = 432$. **g**, Bar graphs of the measured correlations for T^{tot}, T^{G1} and T^{G2} of pairs of mother–daughter (red), sister (blue) and cousin (purple) cells; clone2, $n = 423$. Correlations were computed using one randomly chosen pair of cells per lineage. Shown are representative figures of 11 experiments.

(Extended Data Fig. 7c, $\rho_{c\text{-}c} = 0.78$; $P = 8 \times 10^{-6}$) and may reflect the reported circadian clock control over the mammalian cell cycle in cell lines[23]. Whether the circadian clock is a key parameter underlying cell-cycle variability in mammalian cells[26], via the kicked cell cycle model or other proposed models, such as size control or ageing, remains to be determined in future studies.

We extended our approach to ask if stochasticity dominates in either G1 or S/G2/M phases. We found that both T^{G1} and T^{G2} correlations follow the same pattern as T^{tot}, namely that the cousin–mother inequality is satisfied (Fig. 2g), suggesting that deterministic variability is present in both G1 and S/G2/M phases (Extended Data Fig. 8a). Furthermore, the model reproduces the surprising absence of correlation between G1 and G2 (Extended Data Fig. 8b).

The analysis of the lineage correlations, together with the ability to measure the correlation dimension in cell-cycle inheritance, as demonstrated in the present study, should enable discrimination between

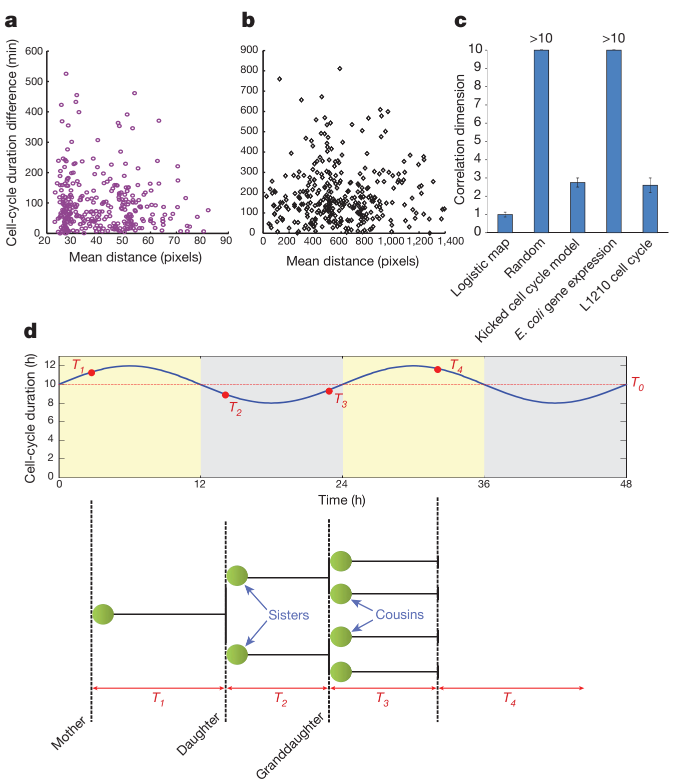

Figure 3 | Evidence for deterministic inheritance of the cell cycle duration. **a**, Physical separation (mean distance) between cousin cells versus their cell-cycle duration difference. No correlation is found ($n = 321$; ρ (Pearson) $= -0.07$; one-tailed; $P > 0.88$), suggesting that correlations between cousin cells are not due to their proximity. **b**, A scatter plot of the physical separation between a similar number of unrelated cell pairs versus their cell-cycle duration difference. No correlation is found ($n = 321$; ρ (Pearson) $= 0.04$; one-tailed; $P > 0.25$), confirming that spatial effects are not responsible for the high correlation between cousins. **c**, Correlation dimensions of several systems analysed with the Grassberger–Procaccia algorithm. A low correlation dimension indicates determinism. The logistic map is as in Fig. 1b. (Error bar is the s.d. of simulations.) Random, normally distributed random numbers. The kicked cell cycle model has the parameter range detailed in Extended Data Table 1; error bar is the s.d. of simulations with different parameters fitting our experimental data. *E. coli* gene expression, data of YFP expression in *E. coli* under a constitutive promoter from ref. 22. Note that the YFP data was sampled every 25 min (see Supplementary Information). The resulting time series was analysed with the Grassberger–Procaccia algorithm to find the correlation dimension ($n = 3,300$). L1210 cell cycle duration, the correlation dimension found when applying the Grassberger–Procaccia algorithm to experimental data. (Error bar is the s.d. between three experiments). **d**, The kicked cell cycle toy model determines the inheritance of cell-cycle durations. Top, influence of the cellular oscillator on the cell cycle. A cell born during the yellow period will have a longer cell-cycle duration, according to the oscillating term, while cells born during the grey period will divide faster. Bottom, a schematic view of the same data. Green discs represent single cells.

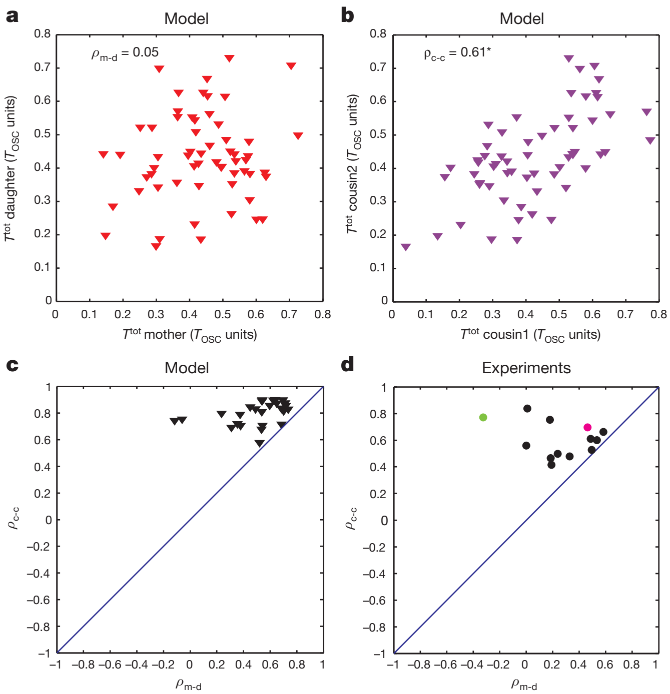

Figure 4 | The cousin–mother inequality as a probe of deterministic tendencies in the inheritance of cell-cycle duration. **a**, Mother–daughter correlation $\rho_{m\text{-}d}$, from a simulation of equations 1–4 (run on 60 lineages to simulate a typical experiment) with the parameters of Extended Data Table 1 with $k = 0.2$; $T_0 = 0.54$; see Supplementary Information for full explanations of equations and parameters). T_{osc} is the period of the underlying oscillator **b**, Cousin–cousin correlation $\rho_{c\text{-}c}$ from kicked cell-cycle simulation with parameters as in **a**, showing that cousins can be correlated despite the absence of correlation between mothers and daughters. **c**, Simulation-derived $\rho_{c\text{-}c}$ versus $\rho_{m\text{-}d}$ (Extended Data Table 1). **d**, Experimental correlations from independent experiments of L1210 displaying various mean cycle durations (black dots), EMT6 extracted from the raw data in ref. 6 (magenta dot) and raw Cyanobacteria data obtained from ref. 24 (green dot). The data points lie above the diagonal showing that cousins are more correlated than mothers–daughters, in agreement with results from the simulations (**c**).

different models. For example, the additive model proposed in ref. 17 accounts for the high sister–sister correlations, but the correlation-dimension analysis of data simulated with this model is indistinguishable from that of random noise (Extended Data Fig. 4c) and the cousin–mother inequality is not fulfilled.

The novelty of the present study, when compared to searches for chaotic dynamics in biology[27], is in the combination of correlation-dimension analysis with intra- and inter-generation correlations providing two independent indicators of deterministic inheritance. When the data are shuffled[28] (Extended Data Fig. 4b), both indicators vanish. More generally, the approach taken in this study can be applied to the identification of deterministic components controlling the inheritance along lineages of other phenotypes[29], such as expression levels, cell size and growth rate[30]. Finally, the realization of the importance of an underlying nonlinear process in the determination of cell-cycle-duration variability will pave the way for new types of models addressing cell-cycle inheritance.

Online Content Methods, along with any additional Extended Data display items and Source Data, are available in the online version of the paper; references unique to these sections appear only in the online paper.

Received 4 August 2014; accepted 13 February 2015.

Published online 11 March 2015.

1. Blake, W. J., Kærn, M., Cantor, C. R. & Collins, J. J. Noise in eukaryotic gene expression. *Nature* **422,** 633–637 (2003).
2. Sigal, A. *et al.* Variability and memory of protein levels in human cells. *Nature* **444,** 643–646 (2006).
3. Elowitz, M. B., Levine, A. J., Siggia, E. D. & Swain, P. S. Stochastic gene expression in a single cell. *Science* **297,** 1183–1186 (2002).
4. Huh, D. & Paulsson, J. Random partitioning of molecules at cell division. *Proc. Natl Acad. Sci. USA* **108,** 15004–15009 (2011).
5. Paulsson, J. Summing up the noise in gene networks. *Nature* **427,** 415–418 (2004).
6. Staudte, R. G., Guiguet, M. & d'Hooghe, M. C. Additive models for dependent cell populations. *J. Theor. Biol.* **109,** 127–146 (1984).
7. Ferrell, J. E. Jr, Tsai, T. Y. & Yang, Q. Modeling the cell cycle: why do certain circuits oscillate? *Cell* **144,** 874–885 (2011).
8. Tyson, J. J. & Novak, B. Regulation of the eukaryotic cell cycle: molecular antagonism, hysteresis, and irreversible transitions. *J. Theor. Biol.* **210,** 249–263 (2001).
9. Nurse, P. Cell-cycle control - both deterministic and probabilistic. *Nature* **286,** 9–10 (1980).
10. May, R. M. Simple mathematical models with very complicated dynamics. *Nature* **261,** 459–467 (1976).
11. Shields, R. Transition-probability and origin of variation in cell-cycle. *Nature* **267,** 704–707 (1977).
12. Grasman, J. A deterministic model of the cell-cycle. *Bull. Math. Biol.* **52,** 535–547 (1990).
13. Lloyd, D., Lloyd, A. L. & Olsen, L. F. The cell division cycle: a physiologically plausible dynamic model can exhibit chaotic solutions. *Biosystems* **27,** 17–24 (1992).
14. Sakaue-Sawano, A. *et al.* Visualizing spatiotemporal dynamics of multicellular cell-cycle progression. *Cell* **132,** 487–498 (2008).
15. Froese, G. Disbribution and interdependence of generation times of HeLa cells. *Exp. Cell Res.* **35,** 415–419 (1964).
16. Kuczek, T. & Axelrod, D. E. The importance of clonal heterogeneity and interexperiment variability in modeling the eukaryotic cell-cycle. *Math. Biosci.* **79,** 87–96 (1986).
17. Cowan, R. & Staudte, R. The bifurcating autoregression model in cell lineage studies. *Biometrics* **42,** 769–783 (1986).
18. Powell, E. O. Some features of the generation times of individual bacteria. *Biometrika* **42,** 16–44 (1955).
19. Grassberger, P. & Procaccia, I. Characterization of strange attractors. *Phys. Rev. Lett.* **50,** 346–349 (1983).
20. Theiler, J., Eubank, S., Longtin, A., Galdrikian, B. & Farmer, J. D. Testing for nonlinearity in time-series - the method of surrogate data. *Physica D* **58,** 77–94 (1992).
21. Skinner, J. E. Low-dimensional chaos in biological-systems. *Bio/Technology* **12,** 596–600 (1994).
22. Wang, P. *et al.* Robust growth of *Escherichia coli*. *Curr. Biol.* **20,** 1099–1103 (2010).
23. Nagoshi, E. *et al.* Circadian gene expression in individual fibroblasts: cell-autonomous and self-sustained oscillators pass time to daughter cells. *Cell* **119,** 693–705 (2004).
24. Yang, Q., Pando, B. F., Dong, G., Golden, S. S. & van Oudenaarden, A. Circadian gating of the cell cycle revealed in single cyanobacterial cells. *Science* **327,** 1522–1526 (2010).
25. Hejblum, G., Costagliola, D., Valleron, A. J. & Mary, J. Y. Cell-cycle models and mother daughter correlation. *J. Theor. Biol.* **131,** 255–262 (1988).
26. Altinok, A., Gonze, D., Levi, F. & Goldbeter, A. An automaton model for the cell cycle. *Interface Focus* **1,** 36–47 (2011).
27. Glass, L. & Kaplan, D. Time-series analysis of complex dynamics in physiology and medicine. *Med. Prog. Technol.* **19,** 115–128 (1993).
28. Theiler, J. On the evidence for low-dimensional chaos in an epileptic electroencephalogram. *Phys. Lett. A* **196,** 335–341 (1995).
29. Balázsi, G., van Oudenaarden, A. & Collins, J. J. Cellular decision making and biological noise: from microbes to mammals. *Cell* **144,** 910–925 (2011).
30. Tzur, A., Kafri, R., LeBleu, V. S., Lahav, G. & Kirschner, M. W. Cell growth and size homeostasis in proliferating animal cells. *Science* **325,** 167–171 (2009).

Supplementary Information is available in the online version of the paper.

Acknowledgements We thank H. Miyoshi at the Riken Tsukuba for the Fucci markers, N. Barkai, N. Shoresh, J. Theiler, S. Kadener, L. Glass, G. Asher, A. W. Murray and J. Paulsson for discussions, and M. Gorfine and R. Heller for advice on statistical analysis. We thank Q. Yang and A. van Oudenaarden for the Cyanobacteria data sets, and the authors of ref. 24 for making their published data available online. This work was supported by the ISF (grants no. 592/10 (N.Q.B.); no. 567/10(I.S.); and no. 9/09, 302/14 (O.A.)) and the ERC Starting Grant no. 281306 (I.S.), no. 260871 (N.Q.B.), the Chief Scientist Office of the Israel Ministry of Health and the Weinkselbaum family medical research fund (I.S.). I.S. thanks the USAID's ASHA Program for the upgrading of the FACS laboratory. S.P.M. is supported by the Clore Foundation.

Author Contributions O.S. constructed the Fucci cell lines; S.P.M. performed the time-lapse experiments; O.S. and S.P.M. wrote the image analysis codes; N.Q.B., I.S., S.P.M. and O.S. designed the experiments; N.Q.B., O.A. and S.P.M. developed the model and analysis; N.W. analysed the Cyanobacteria data sets; N.Q.B. and S.P.M. wrote the manuscript

Author Information Reprints and permissions information is available at www.nature.com/reprints. The authors declare no competing financial interests. Readers are welcome to comment on the online version of the paper. Correspondence and requests for materials should be addressed to N.Q.B. (nathalieqb@phys.huji.ac.il), I.S. (itamarsi@ekmd.huji.ac.il) or O.A. (agam@phys.huji.ac.il).

METHODS

Time-lapse microscopy. A polydimethylsiloxane (PDMS) square mould was filled with medium containing cells (10^4–10^5 cells per ml) and sealed with a coverslip (Supplementary Video 1). Alternatively, cells were introduced in microfluidic devices and placed under a constant flow of pre-conditioned medium. Cells were monitored using our automated microscope system. Fluorescence images were acquired with minimal excitation to minimize bleaching and photodamage. Cells exposed to one-tenth of the integrated illumination did not show measurable growth difference.

Extraction of T^{tot}, T^{G1}, T^{G2}. We used an automatic cell-tracking platform written in MATLAB (MathWorks), which was further developed to allow tracking of L1210 lineages. T^{tot} was determined from phase-contrast images acquired at ~5 min intervals. Together with the sharp division process of L1210 cells, this resulted in less than 1–2% experimental noise in T^{tot}. Some of the movies were tracked semi-automatically for supervised analysis using a plugin that we developed for ImageJ (http://rsbweb.nih.gov/ij/). T^{G1} was determined from the maximum of the mKO2 signal and T^{G2} from the subtraction of T^{G1} from T^{tot}.

Computation of correlation coefficients. Spearman correlation coefficients were computed on the experimental data. To avoid spurious dependencies, we were careful to include only one pair of cells chosen at random from each lineage. Reported values are the mean and s.d. of 100 different samples. In addition, as pointed out in ref. 18, we avoided the bias towards shorter generation times due to artificial ending of the observation time by limiting the analysis to generations for which lineages were completed. Effects of microenvironment were ruled out (Fig. 3a, b and Extended Data Fig. 3).

Construction of the L1210 Fucci cell line. L1210 (ATCC CCL219) were transfected with *mAG-hGeminin(1/110)/pcDNA3* (ref. 14). Cells were selected under 0.35 mg ml^{-1} neomycin, then, seeded on a 96-well plate by FACS to one cell per well. Next, *mKO2-hCdt1(30/120)/pcDNA3* (ref. 14) was inserted to *pcDNA3.1/Hygro* (Invitrogen) using BamhI and XbaI. A monoclonal population of L1210 cells carrying *mAG-hGeminin* was transfected with *mKO2-hCdt1(30/120)/pcDNA3.1/Hygro*. Cells were selected under 0.35 mg ml^{-1} neomycin and 0.2 mg ml^{-1} hygromycin. Finally, several doubly transfected clones were isolated and validated using FACS by verifying that each marker peaks at the correct DNA content. Two different Fucci clones (clone1 and clone2) were isolated and studied under the microscope. The wild-type L1210 was also analysed (Extended Data Fig. 2).

Fluorescence microscopy. Liebovitz's L-15 medium (Biological Industries) was supplemented with 0.2% dextrose, 100 U ml^{-1} penicillin, 100 μg ml^{-1} streptomycin,100 μM sodium pyruvate, 300 μg ml^{-1} L-glutamine and 10–20% fetal calf serum. The buffering in L-15 medium allows cell growth and pH maintenance without a CO_2 atmosphere. The Fucci reporters were monitored by microscopy using HQ480/20ex and HQ510/20em, and HQ456/11ex & HQ585/40em (Chroma, USA) for the mAG and mKO2, respectively. Excitation was performed with LEDs (Coolled, UK).

Testing for spatial effects in sisters and cousins correlations. To test whether the relatively small differences in cycle durations between cousin cells resulted from microenvironment effects due to their proximity, we analysed the correlation between distance and cycle-duration difference. For this purpose, we calculated the average distance between cousin pairs over their overlapping time points throughout the cell cycle. We did not observe a significant correlation between the cycle-duration difference and the average distance (Fig. 3a). To rule out the possibility that the absence of such correlation between cousins is due to the relatively short distances in all cousin pairs, we calculated the correlation between unrelated pairs of cells and found it insignificant also when the range of distances is increased (Fig. 3b). We selected only unrelated pairs which overlapped in time in at least 94% of the data points, which is the average overlap in cousin pairs. Among them, we randomly selected 321 pairs in order to have the same number of pairs as cousins. We did not observe a significant correlation in this case as well ($P > 0.25$). To further evaluate the spatial effect on the cycle duration on shorter scales, we scanned our movies for cousin quadruplets organized in either straight or curved lines such that the distance between the distal pair is at least twice the distance between the proximal pair (Extended Data Fig. 3b). We collected 33 such cousin quadruplets and we compared the cycle-duration differences of the proximal pairs to those of the distal pairs using a one-tailed Wilcoxon signed rank test. No significant difference was found between the two groups ($n = 33$; one-tailed Wilcoxon signed rank test, $\alpha = 0.05$; $P > 0.15$) (Extended Data Fig. 3c).

Measuring inter- and intra-generation correlations in microfluidic devices under constant flow. In order to test further that the unexpected high cousin correlations were not due to the local accumulation of cellular by-products, we repeated our experiments in microfluidic devices in which the cells are continuously washed with fresh medium. We designed and fabricated microfluidic devices, based on our previous devices[31], which consist of several layers clamped together:

Thin patterned PDMS layer with microwells: a mould was made using photolithography on silicon wafers as previously described[31] resulting in a pattern of microwells (100 μm depth and 450 μm diameter). The cured PDMS layer was separated from the wafer and exposed for 20 s to air plasma (Harrick plasma oven).

A PET transparent membrane (6-well millicell 1 μm PET. Millipore no. PIR30R48) was separated from the plastic hang and cut to the device dimensions.

Flow channel: a thick PDMS layer was patterned with a single 'snake-like' channel pattern (100 μm depth, 400 μm width).

Both patterns were created using a mould made of SU-8 photoresist (MicroChem Corp.) on silicon wafers. Photomasks were designed in Gimp and printed on transparencies at 5080 dpi (Pageworks). The patterned wafers were treated with HMDS. The PDMS (Sylgard 184, Dow Corning) was mixed according to the manufacturer's instructions. The mixture was poured onto the wafer and cured overnight at 80 °C.

The cells to be observed were trapped in the microwells of the lower patterned PDMS layer. The supernatant of exponentially growing cells, supplemented with 10% fetal calf serum, was constantly flowing in the single channel of the upper PDMS layer, such that nutrients can diffuse through the membrane to the trapped cells, without disturbing their position. This device was placed under the microscope, and single cells were tracked while being constantly exposed to the flowing medium.

Statistical methods. No statistical methods were used to predetermine sample size.

31. Gefen, O., Gabay, C., Mumcuoglu, M., Engel, G. & Balaban, N. Q. Single-cell protein induction dynamics reveals a period of vulnerability to antibiotics in persister bacteria. *Proc. Natl Acad. Sci. USA* **105,** 6145–6149 (2008).

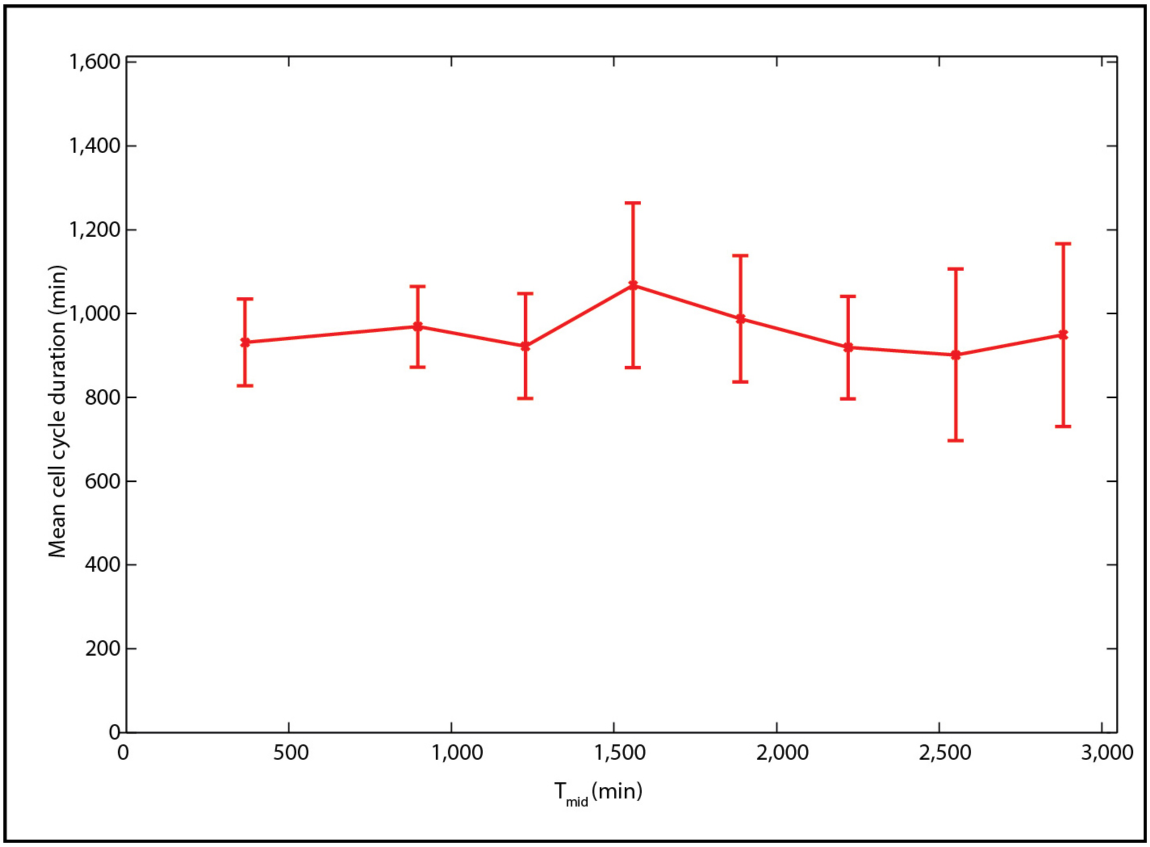

Extended Data Figure 1 | Mean cell-cycle duration during long-term time-lapse microscopy. Cycle durations were binned into eight bins according to time elapsed from the beginning of the experiment to the midpoint of the cell cycles (T_{mid}). For each bin the mean and s.d. were calculated. Both fluorescence and bright-light exposure were minimized to prevent lengthening of the cell-cycle duration. $n = 526$; error bars represent the s.d.

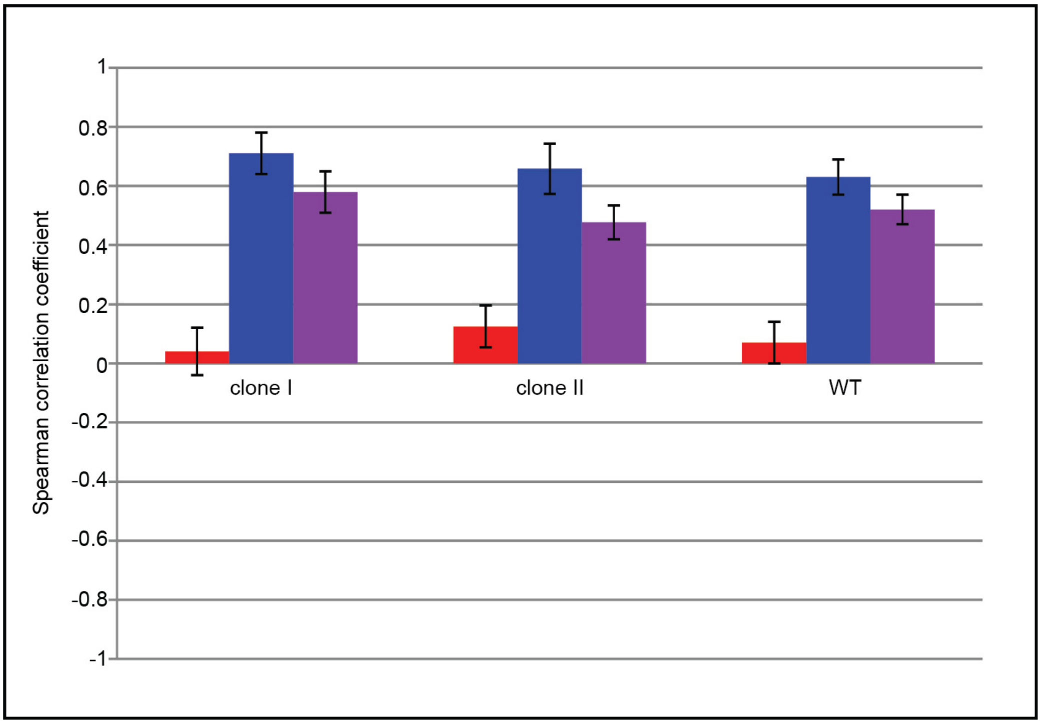

Extended Data Figure 2 | Lineage correlations in different strains and clones. Bar graphs of the measured correlations coefficients for T^{tot} of pairs of mother–daughter (red), sister (blue) and cousin (purple) cells, in different cell lines: two different clones of L1210 Fucci ($n = 423$, 432) and a wild-type (WT) L1210 ($n = 283$). The cousin–mother inequality is observed in all cases. Data are mean and s.d. of 100 independent random samples from the data set, as described in the online methods.

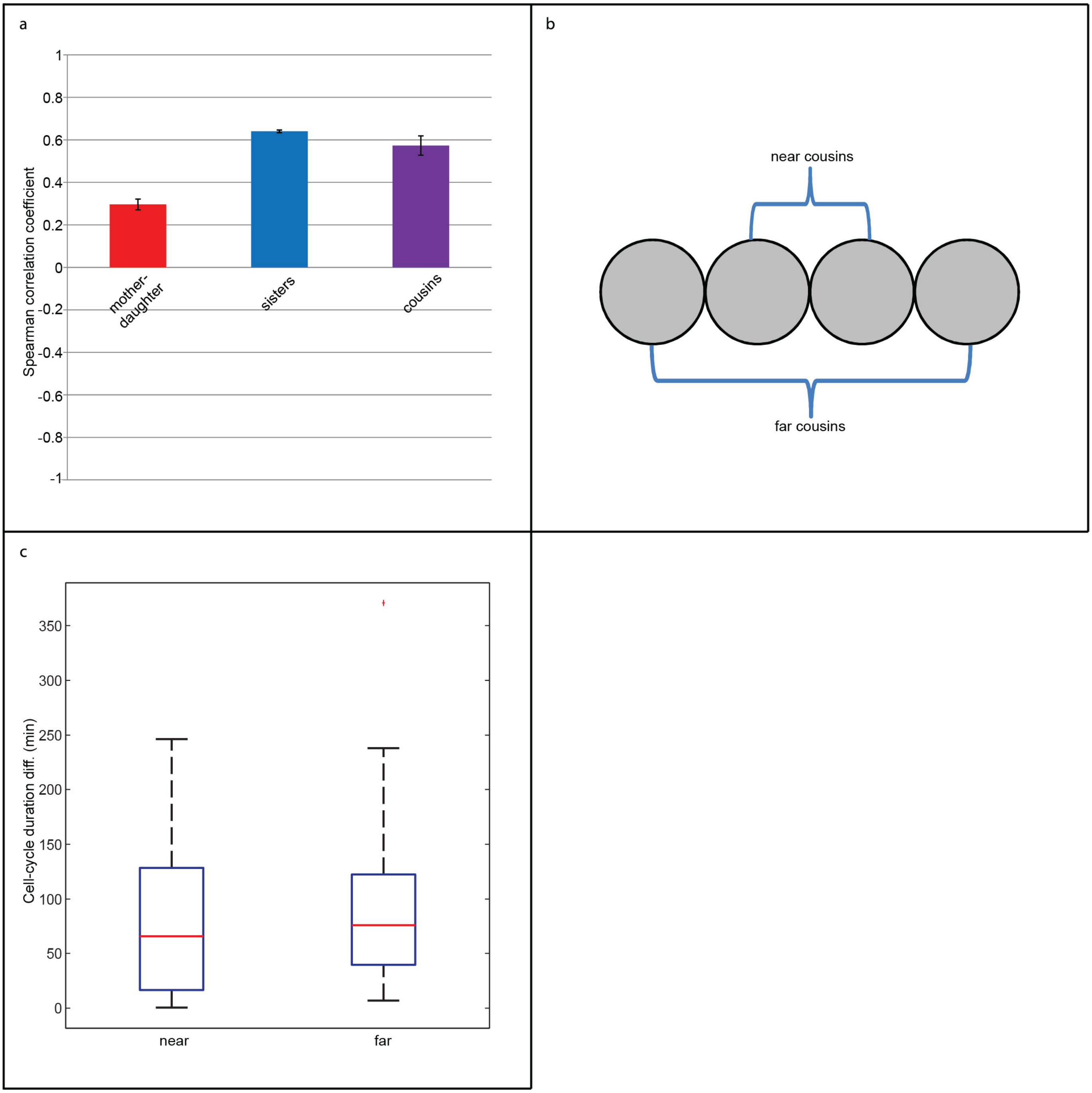

Extended Data Figure 3 | No spatial effect detected on the cell-cycle duration. **a**, Lineage correlations in microfluidic devices (clone2) (Methods). Cells are monitored under constant media flow, keeping the sample in constant conditions while washing away potential by-products of the cells' metabolism. Correlation between cousins remains higher than mother–daughter correlation, ruling out micro-environment bias ($\rho_{m\text{-}d} = 0.3 \pm 0.03$; $\rho_{s\text{-}s} = 0.64 \pm 0.01$; $\rho_{c\text{-}c} = 0.57 \pm 0.05$; $n = 381$; standard deviations represent 100 independent random samples from the data set, as described in the online methods). **b**, **c**, Cycle-duration differences within quadruplet cousins. **b**, A schematic representation of a cousin quadruplet. **c**, Cell-cycle duration differences in near and far cousin pairs. No significant difference is found. ($n = 66$; one-tailed Wilcoxon signed rank test, $\alpha = 0.05$; $P > 0.15$).

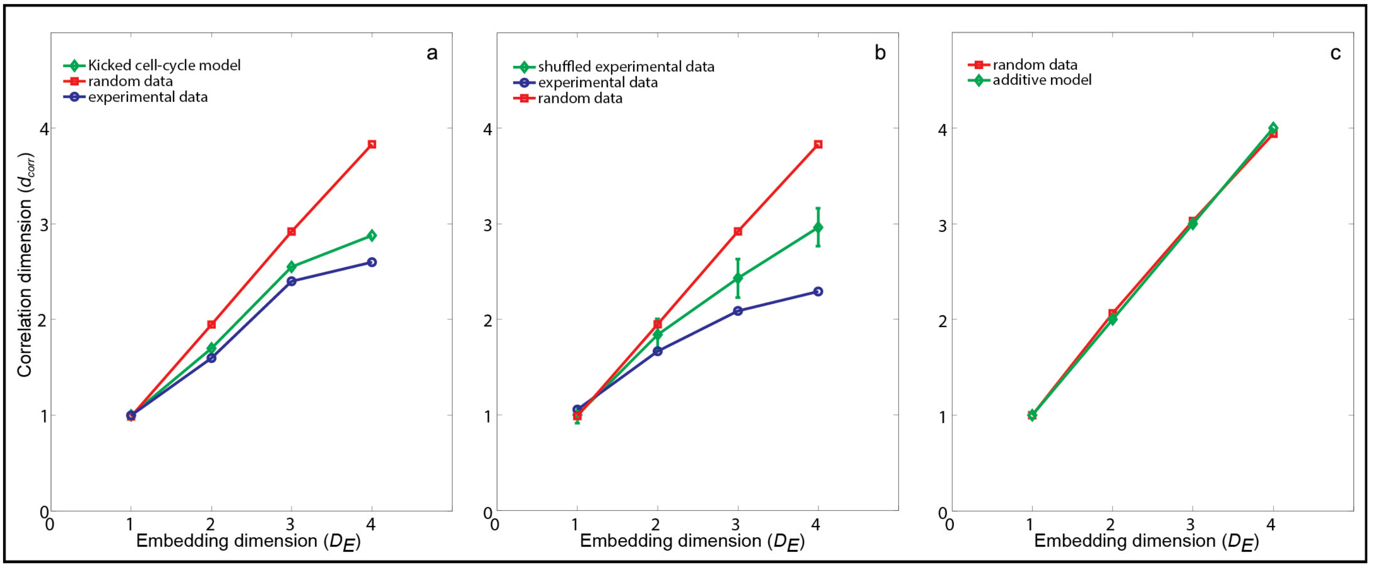

Extended Data Figure 4 | Correlation dimension. **a**, Computed dimension versus D_E for a random series (red); L1210 cell-cycle duration data (blue); and the kicked cell cycle model (equations 1–4 (see Supplementary Information); green). **b**, Correlation dimension for surrogate data obtained from random shuffling of the cell-cycle durations. The mean and s.d. of 59 randomly shuffled data are shown (green), showing that the saturation in the correlation dimension observed for the experimental data (blue) is due to a deterministic process[27]. **c**, Correlation dimension for random data (red) and data from a simulation of the additive model developed by Cowan and Staudte[17] (green).

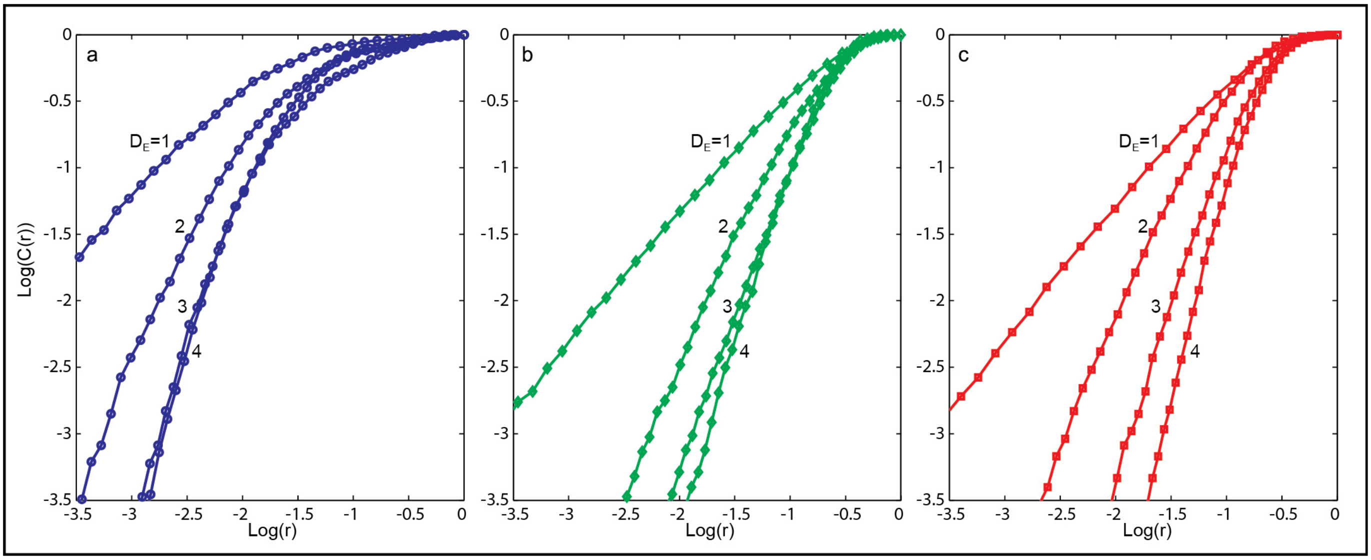

Extended Data Figure 5 | Correlation-dimension analysis. The fraction of points closer than a distance r, $C(r)$, is plotted versus r, on a log–log scale. $C(r) \rightarrow r^{d_{corr}}$ for small values of r. Therefore, the correlation dimension d_{corr} is the saturation of the slope of $\log(C(r))$ versus $\log(r)$, with increasing embedding dimension D_E. **a**, Experimental data; **b**, Simulation data of the kicked cell cycle model. Note the saturation of the slope at $D_E = 3$ and 4. **c**, Normally distributed random data with same mean and s.d. as experimental data, $n = 236$.

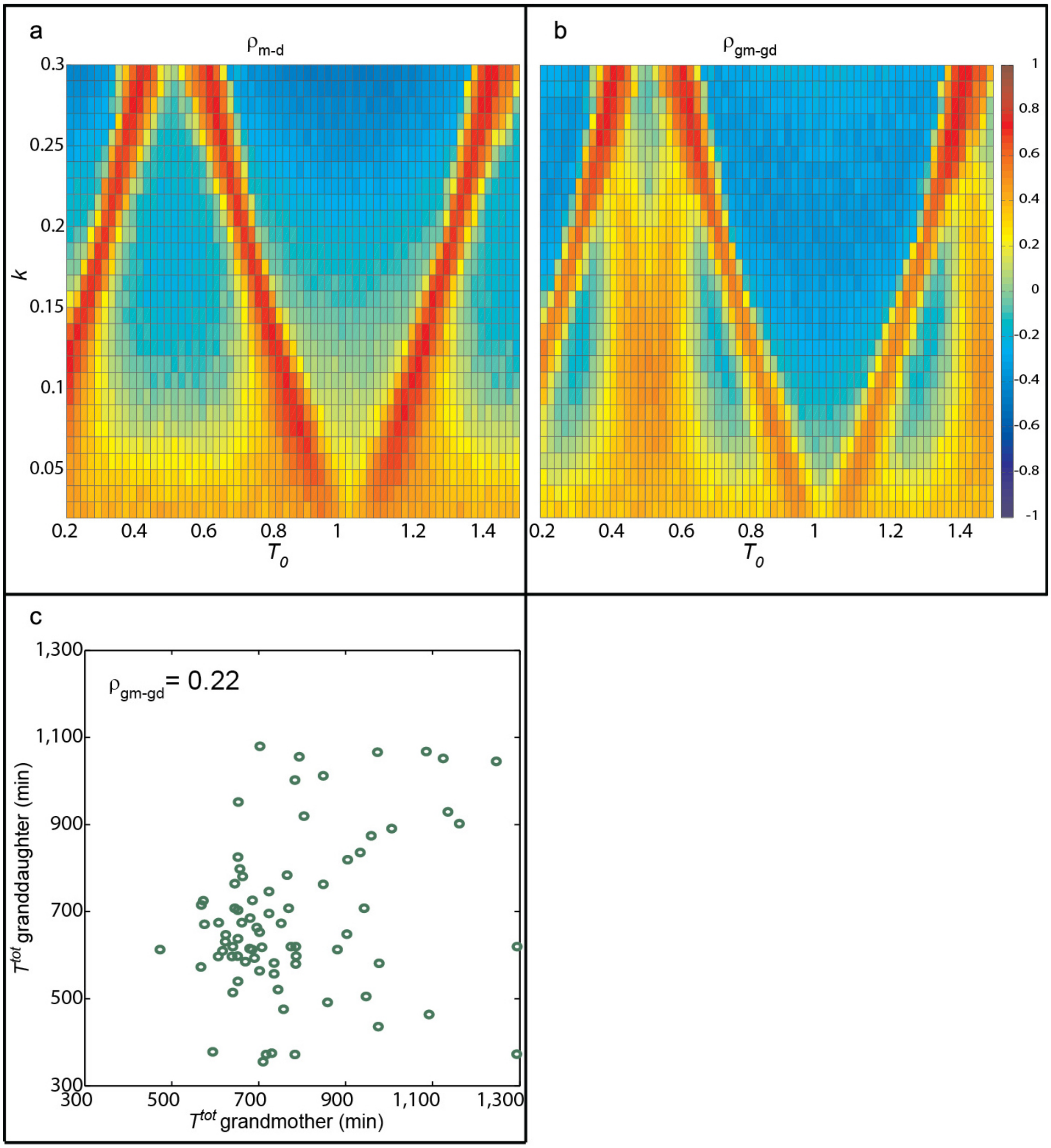

Extended Data Figure 6 | Inter-generation correlation. **a**, **b**, Simulation results of the kicked cell cycle model (equations 1–4). **a**, Pearson correlation of mother and daughter cells ($\rho_{\text{m-d}}$) is predicted to vary between negative and positive values, depending on k and T_0. **b**, Grandmother–granddaughter correlations ($\rho_{\text{gm-gd}}$) follow a similar pattern, namely correlations that are close to zero, but can vary between slightly negative and positive values, as observed experimentally. The simulations were run on 300 lineages **c**, Correlation plot of experimentally observed total cell-cycle duration T^{tot} of grandmother and granddaughter cells (clone2) s.d. of 100 independent random samples from the data set, as described in the online methods is 0.06. Spearman; $\rho_{\text{gm-gd}} = 0.22 \pm 0.06$, $n = 380$.

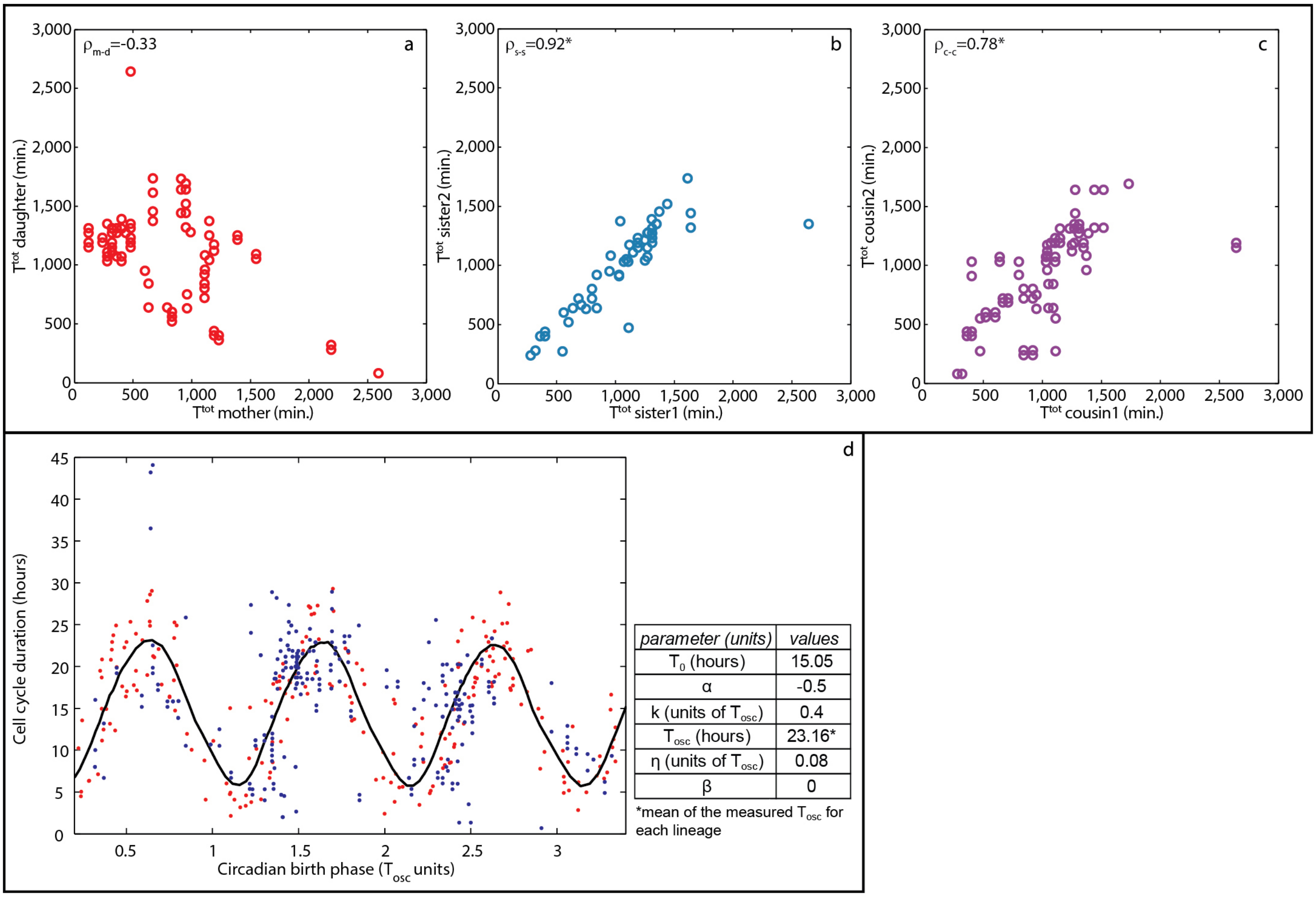

parameter (units)	values
T_0 (hours)	15.05
α	-0.5
k (units of T_{osc})	0.4
T_{osc} (hours)	23.16*
η (units of T_{osc})	0.08
β	0

Extended Data Figure 7 | Total cell-cycle duration (T^{tot}) measurements and circadian phase at birth in Cyanobacteria. Data of circadian phase and cell cycles of single *Synechococcus elongatus* cells from 29 lineages was obtained from Yang *et al.*[24] **a**, Mother–daughter correlation ($\rho_{m\text{-}d}$); **b**, Sister–sister correlation ($\rho_{s\text{-}s}$); **c**, Cousin–cousin correlation ($\rho_{c\text{-}c}$). Asterisks denote significant ($P < 0.002$) Spearman correlations. **d**, Cell-cycle duration versus circadian phase. Each dot represents a cell's circadian phase at birth and its cell-cycle duration. Experimental data (blue) and simulation (red). The black line denotes the expected trend of the model (equation 5, see Supplementary Information). Parameters used for the simulation are shown on the right.

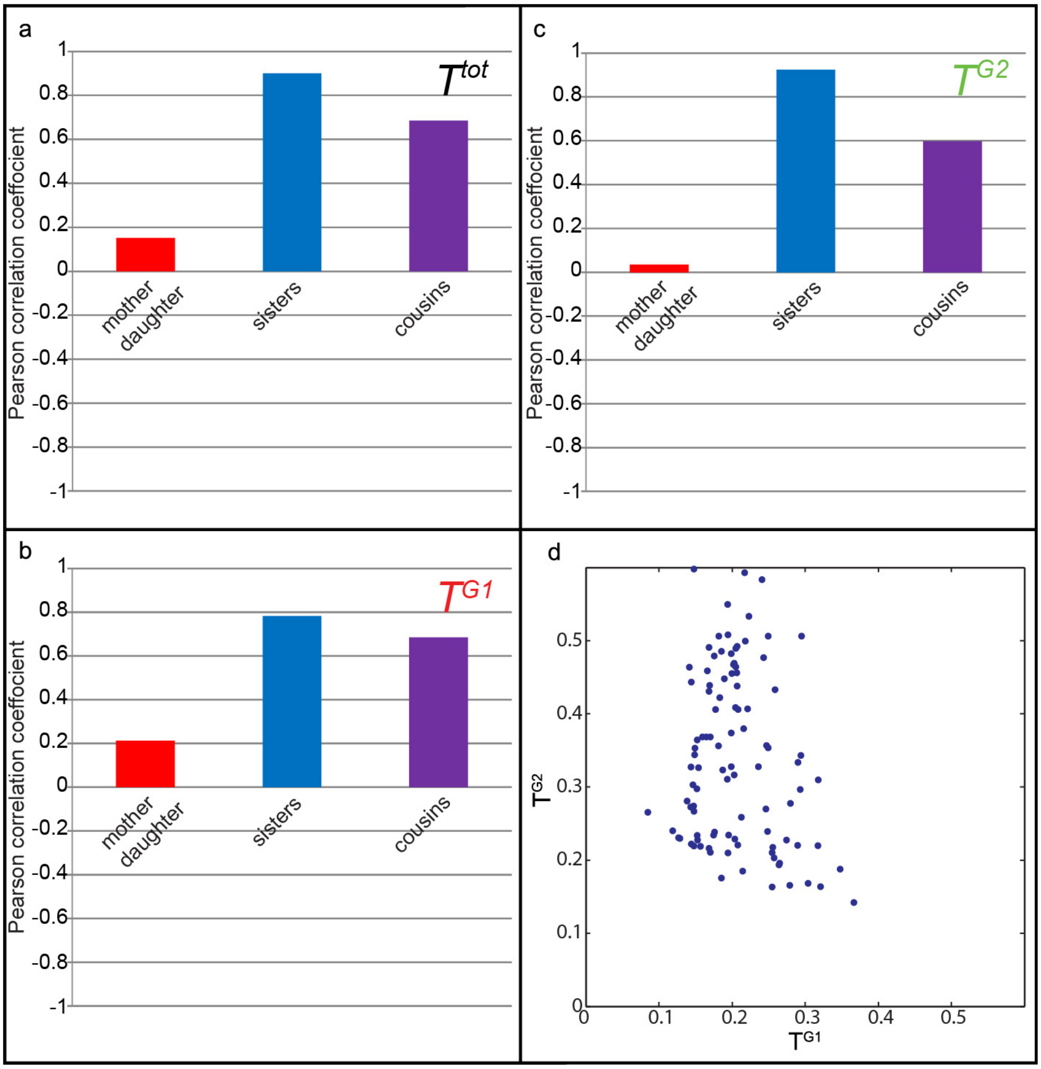

Extended Data Figure 8 | Simulation results of the kicked cell cycle model of G1 and G2 durations fit the experimental observations. a–c, Pearson correlations of simulated data of the total (T^{tot}), G1 (T^{G1}) and G2 (T^{G2}) durations between mother-daughter cells (red), sisters (blue) and cousins (purple) (equations 6–8, see Supplementary Information). Parameters as in Extended Data Table 1 ; $\beta = 0.07$. **d**, Typical plot of the simulated data for T^{G1} versus T^{G2} (in units of T_{osc}). The low correlation (-0.18; $P{=}0.07$) despite the deterministic inheritance is consistent with the experiments: the correlation coefficients from 4 independent experiments range from –0.4 to 0.17.

Extended Data Table 1 | Parameters used for the simulations presented in Fig. 3 (equations 1–4)

Parameter (units)	*Values*
T_0 (hours)	9-17
α	0.5
k (units of T_{osc})	0.02-0.3
T_{osc} (hours)	24
δ (units of T_{osc})	0.15
β	0.12

T_0, the mean cell cycle duration; α, the strength of the direct inheritance of the mother's cell cycle duration; k, the strength of the coupling to the external oscillator; T_{osc}, the period of the cellular oscillator; δ, the strength of the asymmetry between sisters; β, the relative effect of the asymmetry on cell-cycle duration.

Extended Data Table 2 | A literature compilation of correlation coefficients for mother–daughter cells and sister cells

cell type	$\rho_{m\text{-}d}$	$\rho_{s\text{-}s}$	*PMID*
HeLa	-0.79	0.95	*14195449*
HeLa	0.19	0.95	*14195449*
HeLa	0.57	0.95	*14195449*
NIH3T3 (rich medium)	-0.418	0.558	*9212596*
NIH3T3 (poor medium)	-0.241	0.357	*9212596*
human embryonic lung fibroblasts	-0.245	0.801	*6832110*
IMR-90 (young)	-0.1	0.68	*6725417*
IMR-90 (aged)	0.31	0.19	*6725417*
C3H	-0.09	NA	*562524*
NIH3T3	0.06	NA	*558988*
rat S6 sarcoma	0.194	0.56	*14281207*
GPK	0.27		*3443605*
mouse osteosarcoma (Gen1)	0.33	0.49	*6583009*
mouse osteosarcoma (Gen2)	0.28	0.54	*6583009*
EMT6 (Gen1)	0.06	0.66	*7360890*
EMT6 (Gen2)	0.47	0.88	*7360890*
EMT6 (Gen3)	0.34	0.89	*7360890*
EMT6 (Gen4)	0.59	0.69	*7360890*
EMT6 (Gen5)	0.5	0.89	*7360890*
mouse osteosarcoma	0.52	NA	*2397328*
neuroblastoma	0.61	NA	*2397328*
hepatoma HTC	0.55	0.7	*509478*
mouse L-cells	0.648	0.7	*4772368*
EMT6 (Gen1)	0.46	0.77	*6471866*
EMT6 (Gen2)	0.63	0.86	*6471866*
EMT6 (Gen3)	0.64	0.82	*6471866*
EMT6 (Gen4)	0.14	0.6	*6471866*

Note that whereas sister–sister correlations are high and positive, mother–daughter correlations vary between negative and positive values, in accordance with the kicked cell cycle model. It should be noted that the correlation coefficients are calculated in various manners. Also, spurious dependencies were not always avoided. Gen*x*, generation number *x*; NA, data not available.

doi:10.1038/nature14332

Phosphodiesterase 9A controls nitric-oxide-independent cGMP and hypertrophic heart disease

Dong I. Lee[1], Guangshuo Zhu[1], Takashi Sasaki[2], Gun-Sik Cho[1], Nazha Hamdani[3], Ronald Holewinski[1,4], Su-Hyun Jo[5], Thomas Danner[1], Manling Zhang[1], Peter P. Rainer[1], Djahida Bedja[1], Jonathan A. Kirk[1], Mark J. Ranek[1], Wolfgang R. Dostmann[6], Chulan Kwon[1], Kenneth B. Margulies[7], Jennifer E. Van Eyk[1,4], Walter J. Paulus[3], Eiki Takimoto[1] & David A. Kass[1]

Cyclic guanosine monophosphate (cGMP) is a second messenger molecule that transduces nitric-oxide- and natriuretic-peptide-coupled signalling, stimulating phosphorylation changes by protein kinase G. Enhancing cGMP synthesis or blocking its degradation by phosphodiesterase type 5A (PDE5A) protects against cardiovascular disease[1,2]. However, cGMP stimulation alone is limited by counter-adaptions including PDE upregulation[3]. Furthermore, although PDE5A regulates nitric-oxide-generated cGMP[4,5], nitric oxide signalling is often depressed by heart disease[6]. PDEs controlling natriuretic-peptide-coupled cGMP remain uncertain. Here we show that cGMP-selective PDE9A (refs 7, 8) is expressed in the mammalian heart, including humans, and is upregulated by hypertrophy and cardiac failure. PDE9A regulates natriuretic-peptide- rather than nitric-oxide-stimulated cGMP in heart myocytes and muscle, and its genetic or selective pharmacological inhibition protects against pathological responses to neurohormones, and sustained pressure-overload stress. PDE9A inhibition reverses pre-established heart disease independent of nitric oxide synthase (NOS) activity, whereas PDE5A inhibition requires active NOS. Transcription factor activation and phosphoproteome analyses of myocytes with each PDE selectively inhibited reveals substantial differential targeting, with phosphorylation changes from PDE5A inhibition being more sensitive to NOS activation. Thus, unlike PDE5A, PDE9A can regulate cGMP signalling independent of the nitric oxide pathway, and its role in stress-induced heart disease suggests potential as a therapeutic target.

The PDE super-family contains 11 sub-genes conferring different cyclic nucleotide and tissue selectivity[9]. PDE5A was the first cGMP-selective enzyme discovered, and has a major role in erectile and pulmonary vasomotor control. PDE9A was cloned 20 years later[7,8] and has the highest affinity and selectivity for cGMP with a Michaelis constant (K_m) for cGMP 1,000-fold lower than for cAMP[8]. PDE5A and PDE9A share only 28% homology[8] and PDE9A lacks amino-terminus cGMP/protein kinase G (PKG) stimulatory regulatory domains present in PDE5A[9]. PDE9A is expressed primarily in the brain, gut and kidney. To date, studies have focused on its role in cognitive function[10,11] and while mRNA is detectable in the heart and other tissues[7,8], its role outside of the brain remains largely unknown.

To test PDE9A involvement in the heart, gene and protein expression were assessed in myocardial tissue and isolated myocytes. Figure 1a shows PDE9A immunostaining in rat neonatal cardiomyocytes (RNCMs) and adult mouse myocytes, with targeted gene deletion (short interfering RNA (siRNA) or *Pde9a*$^{-/-}$ mice, Extended Data Fig. 1) as a negative control. Protein detection by immunoblot in neonatal myocytes is shown in Extended Data Fig. 2a. Basal gene expression is low but increases with agonist (for example, phenylephrine) or mechanical (*in vivo* pressure

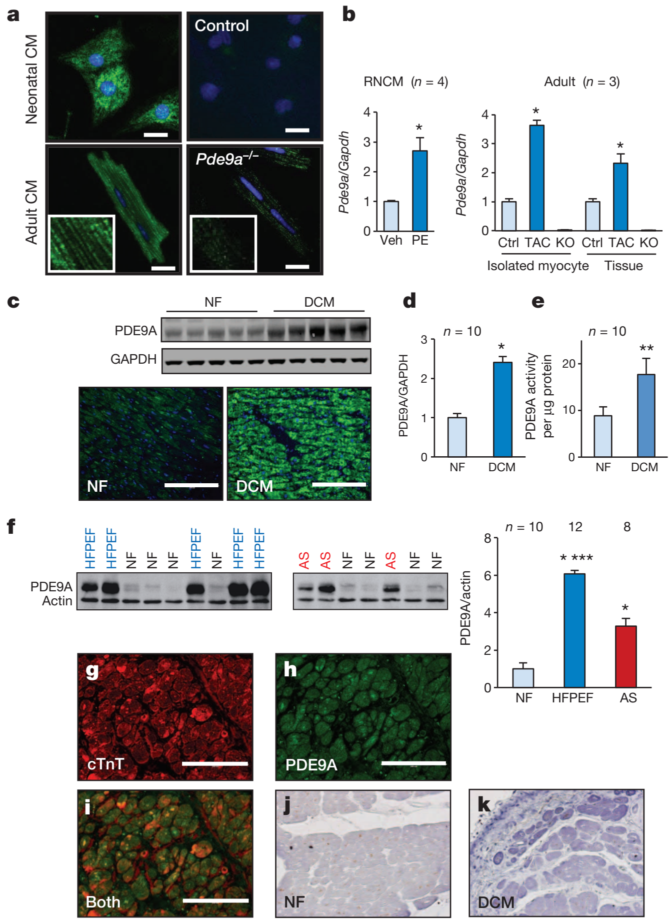

Figure 1 | PDE9A expression in heart and myocytes increases with disease. **a**, PDE9A in neonatal and adult cardiomyocytes; gene silencing as negative controls (scale bar, 20 μm). **b**, *Pde9a* gene expression in RNCMs with phenylephrine (PE) or adult myocytes/heart (mouse) after TAC. *$P < 0.01$ vs. control. Ctrl, control; KO, knockout. **c**, Immunoblot/immunostaining of PDE9A from human dilated cardiomyopathy (DCM) and non-failing (NF) myocardium (scale bar, 200 μm). **d**, **e**, PDE9A expression (**d**) and activity (**e**) in NF and DCM. **f**, PDE9A protein expression in human myocardium for NF, HFPEF and aortic stenosis (AS). *$P < 0.0001$, **$P < 0.05$ vs. non-failing; ***$P < 0.0001$ vs. AS and DCM. **g**–**i**, Co-localization of cardiac troponin T (cTnT) and PDE9A in human DCM myocardium. **j**–**k**, *In situ* hybridization of *PDE9A* in human NF and DCM myocardium. Data are mean ± s.e.m. and biological replicates are indicated.

[1]Division of Cardiology, Department of Medicine, The Johns Hopkins Medical Institutions, Baltimore, Maryland 21205, USA. [2]Advanced Medical Research Laboratories, Research Division, Mitsubishi Tanabe Pharma Corporation, Yokohama, Kanagawa 227-0033, Japan. [3]Department of Physiology, Institute for Cardiovascular Research, VU University Medical Center, Van der Boechorststraat 7, 1081 BT Amsterdam, The Netherlands. [4]Heart Institute and Advanced Clinical Biosystems Research Institute, Cedar Sinai Medical Center, 8700 Beverly Blvd, AHSP A9229 Los Angeles, California 90048, USA. [5]Department of Physiology, Institute of Bioscience and Biotechnology, BK21 plus Graduate Program, Kangwon National University College of Medicine, Chuncheon 200-701, Korea. [6]Department of Pharmacology, University of Vermont, Burlington, Vermont 05405, USA. [7]Department of Medicine, Division of Cardiovascular Medicine, Cardiovascular Institute, Perelman School of Medicine, University of Pennsylvania, Philadelphia, Pennsylvania 19104, USA.

overload) stimulation (Fig. 1b). Increased PDE9A protein expression and cGMP-esterase activity is found in left ventricular myocardium from humans with heart failure and depressed function (Fig. 1c–e, Extended Data Fig. 2b, c and Extended Data Table 1). Protein expression also increases in human left ventricular hypertrophy from aortic stenosis (pressure overload) and most notably in heart failure with preserved ejection fraction (HFPEF, Fig. 1f), a prevalent form of heart failure wherein contractile function appears normal despite symptoms[12]. Human PDE9A expression primarily localizes to myocytes based on co-localization with troponin-T (Fig. 1g–i) and *in situ* hybridization staining (Fig. 1j, k). Whereas PDE5A is expressed in fibroblasts[9], PDE9A is essentially undetectable in isolated human fibroblasts (qPCR threshold cycle = 39).

PDE9A upregulation by heart disease suggested its inhibition might blunt pathological stress responses. To test this, RNCMs and adult myocytes were stimulated with phenylephrine or endothelin-1 (ET-1), increasing protein synthesis and hypertrophic fetal gene (*Nppa*, *Nppb*) expression. Co-incubation with a selective PDE9A antagonist (PF-04449613 (PF-9613), 5 μM, Extended Data Fig. 3a for selectivity of PDE9A versus PDE5A), or *Pde9a* gene silencing/deletion (Fig. 2a, b (top)) reversed these changes. Cells lacking PDE9A were unaffected by PF-9613, confirming the drug's selectivity (Fig. 2a). Similar results were obtained with PF-04447943, another PDE9A inhibitor now used in human trials (NCT00930059, Extended Data Fig. 3b). Anti-hypertrophic effects of PDE9A inhibition required activation of PKG, as they were blocked by PKG inhibitor DT3 (Fig. 2b (bottom) and Extended Data Fig. 3c).

Both PDE5A and PDE9A regulate cGMP-PKG activity; therefore we tested if this regulation is redundant or targets different cGMP pools. Gene silencing of *Pde9a* in RNCMs had no effect on cGMP augmentation from a nitric oxide donor (diethylamine nitric oxide (DEANO), 1 μM) but enhanced cGMP (Fig. 2c) and PKG activity (Extended Data Fig. 4a) triggered by natriuretic peptide type A (ANP (also known as NPPA), 1 μM). Adult myocytes exposed to PF-9613 also augmented cGMP only with ANP stimulation (Fig. 2d; *Pde9a*$^{-/-}$ cells were negative controls). We also measured intracellular cGMP generation in adult myocytes expressing the cGMP-fluorescent sensor, FlincG[13] (Fig. 2e).

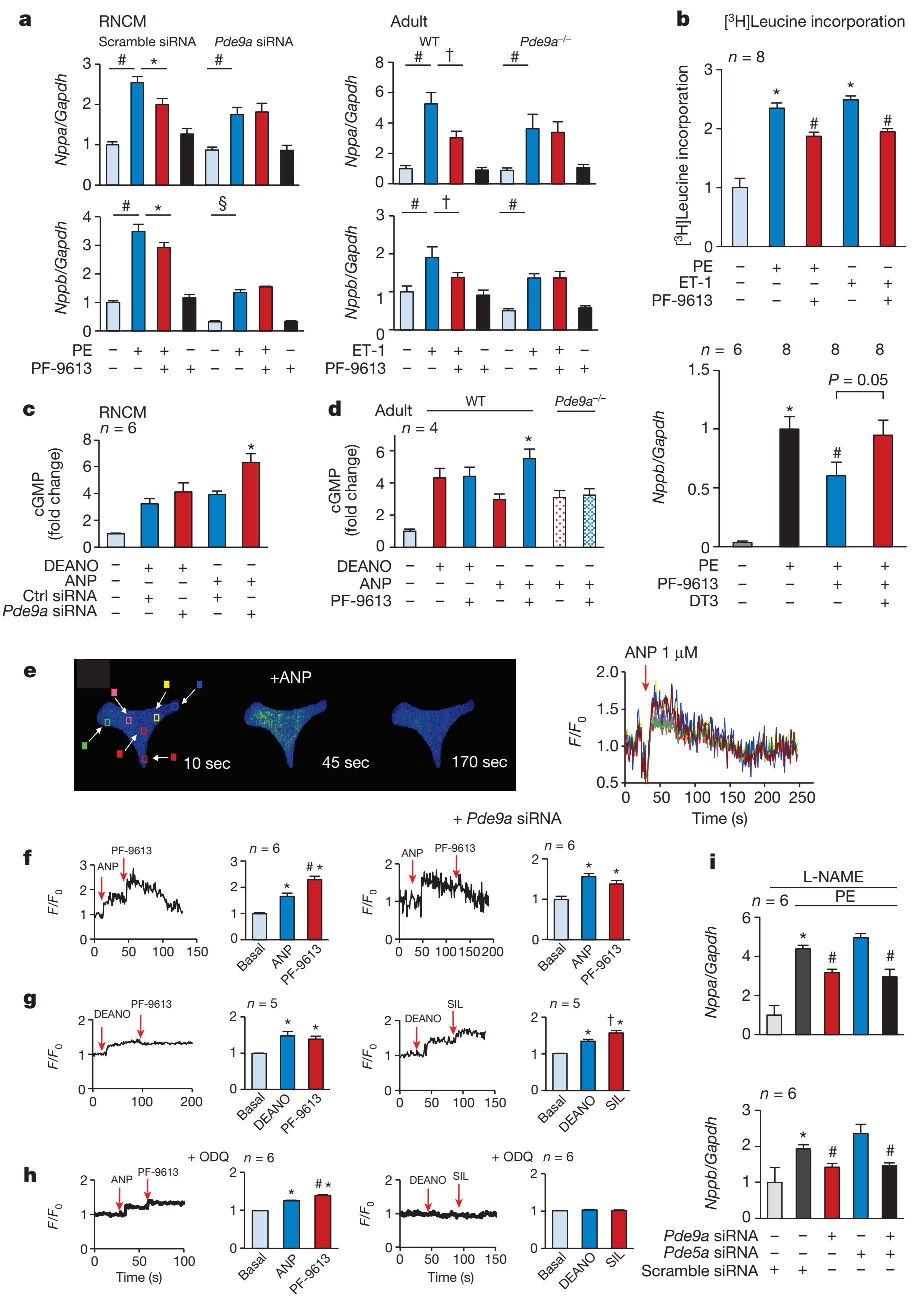

Figure 2 | PDE9A inhibition suppresses cardiac hypertrophy via natriuretic-peptide–cGMP pathway. a, Effect of PF-9613 or gene silencing on hypertrophic gene activation induced by phenylephrine (PE) or endothelin-1 (ET-1) in RNCMs ($n = 12$ per group for all but *Nppa Pde9a* siRNA $n = 8$) and adult myocytes ($n = 6$). $*P < 0.05$, $†P < 0.01$, $§P < 0.01$, $\#P < 0.001$. WT, wild type. **b**, Top, PDE9A inhibition reduces agonist-stimulated protein synthesis. $\#P < 0.01$ vs. phenylephrine/ET-1, $*P < 0.001$ vs. baseline. Bottom, PKG-inhibitor DT3 prevents anti-hypertrophic effect of PF-9613. $\#P < 0.05$, $*P < 0.001$ vs. baseline. **c**, **d**, PF-9613 or *Pde9a* siRNA augments cGMP from ANP but not DEANO simulation in neonatal and adult myocytes. All groups $P < 0.01$ vs. baseline; $*P < 0.01$ vs. ANP. **e**, Left, FlincG–cGMP fluorescence in RNCM before and after ANP stimulation (colour coded for sampled intracellular location). Right, time course normalized to baseline. **f**, Myocyte cGMP stimulated by ANP rises with PF-9613 in RNCMs but not cells with *Pde9a* silenced. **g**, PF-9613 does not alter DEANO-stimulated cGMP whereas a PDE5A inhibitor (SIL) does. **h**, ANP ± PF-9613 effects are unchanged by ODQ, whereas DEANO ± SIL are inhibited. $*P < 0.01$ vs. baseline, $†P < 0.05$ vs. DEANO, $\#P < 0.01$ vs. ANP. **i**, RNCMs exposed to L-NAME and phenylephrine ± *Pde5a* siRNA, *Pde9a* siRNA, or both. $*P < 0.05$ vs. baseline, $\#P < 0.05$ vs. phenylephrine with scrambled siRNA.
Data are mean ± s.e.m. and biological replicates are indicated.

ANP-stimulated cGMP increased more after PF-9613 in control cells, but not in those lacking PDE9A (Fig. 2f). By contrast, PF-9613 did not alter cGMP stimulated by DEANO, whereas the latter increased with PDE5A-inhibition (sildenafil (SIL), 1 μM, Fig. 2g). Neither SIL nor PDE5A-siRNA altered ANP-stimulated cGMP (Extended Data Fig. 4b, c). Pre-incubation with soluble guanylate cyclase (sGC) inhibitor ODQ (10 μM, 1H-[1,2, 4]oxadiazolo[4,3,-a]quinoxalin-1-one) had no effect on cGMP stimulated by ANP or ANP plus PF9613, but fully blocked the rise from DEANO or DEANO + SIL (Fig. 2h). Lastly, RNCMs with silenced *Pde5a*, *Pde9a*, or both were incubated with the NOS-inhibitor L-NAME (1 mM). Phenylephrine-stimulated hypertrophic genes were suppressed only if PDE9A was silenced (Fig. 2i). Thus, opposite to PDE5A, PDE9A hydrolyses cGMP coupled to natriuretic peptide but not nitric oxide stimulation.

We hypothesized that disparate cGMP targeting is related to intracellular localization and thus PDE compartmentation. Confocal immunohistochemistry confirmed this, revealing PDE5A but not PDE9A co-localization with α-actinin at the Z-disk, and PDE9A but not PDE5A co-localization with T-tubular membranes (sarcoplasmic reticulum ATPase-2a) (Extended Data Fig. 5). Interestingly, natriuretic peptide receptor type A also displays a striation pattern in myocytes[14].

To test if PDE9A contributes to maladaptive hypertrophy and heart remodelling *in vivo*, $Pde9a^{-/-}$ mice were exposed to sustained pressure overload. Their hearts developed less dilation and dysfunction, had reduced heart and lung weights, interstitial fibrosis, and myocyte hypertrophy versus TAC (transverse aortic constriction) littermate controls (Fig. 3a–d). Myocardial cGMP increased more in $Pde9a^{-/-}$ hearts (Fig. 3e), and this was accompanied by suppression of pathological genes including connective tissue growth factor, fibronectin and transient receptor potential canonical channel type 6 (Fig. 3f). The latter signals upstream of calcineurin–NFAT, transduces myofibroblast transformation and hypertrophy[15], and is directly inhibited by PKG[16,17]. Cyclic GMP can also suppress cAMP by activating PDE2[18] to blunt hypertrophy and fibrosis; however cAMP rose similarly in both groups after TAC (Extended Data Fig. 6).

The clinically relevant question is whether inhibition of PDE9A reverses pre-established hypertrophy/dysfunction, and whether this is differentiable from the protection afforded by PDE5A inhibition. To address this, C57BL/6J mice were subjected to severe TAC to rapidly induce chamber dilation, dysfunction and hypertrophy. On day 8, mice were divided into three groups: PF-9613, SIL or vehicle, and treated for an additional 4 weeks while maintaining TAC. Oral PF-9613 itself had no effect on blood pressure or heart function (Extended Data Fig. 7). To test if cGMP targeting by PDE9A differed from PDE5A *in vivo*, the experiment was repeated adding the NOS inhibitor L-NAME to the drinking water.

All groups developed marked chamber dysfunction, dilation, and hypertrophy after 1 week of TAC (pre-treatment; Fig. 4a, b). In mice that did not receive L-NAME, inhibiting either PDE reversed changes to near sham-control levels and lowered post-mortem left ventricular mass, lung weight and abnormal molecular signatures (Extended Data Fig. 8). However, in L-NAME-treated mice, only PDE9A inhibition was effective (Fig. 4a, b). Blocking either PDE increased myocardial cGMP in L-NAME^{-}-TAC but only PDE9A inhibition did so in L-NAME^{+}-TAC mice (Fig. 4c). L-NAME prevented PKG activation by SIL but not PF-9613 (Fig. 4d). *In vitro* PKG activity in PDE9A-treated myocardium was itself little altered. This parallels reported data with natriuretic peptide stimulation, but differs from increases seen with PDE5A inhibition[5].

To explore differential signalling from each PDE inhibitor further, RNCMs were infected with luciferase reporter plasmids to assess the

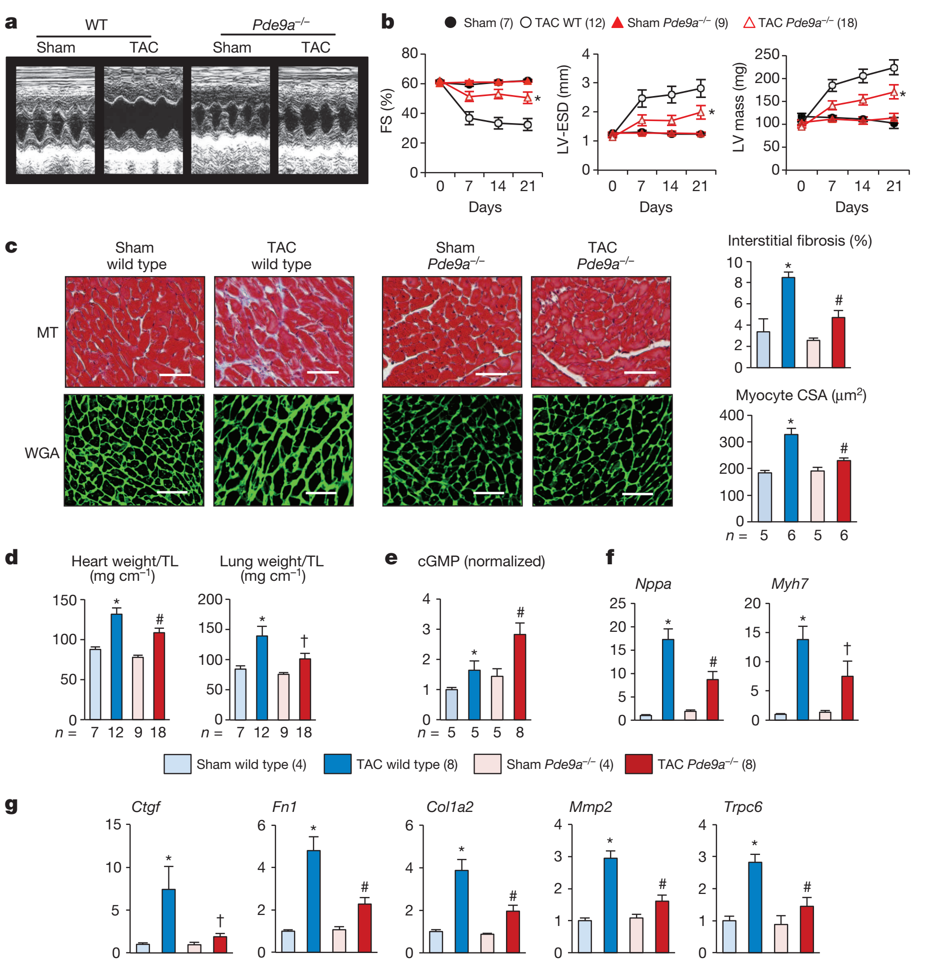

Figure 3 | Pressure-overload-induced cardiac pathobiology is suppressed in $Pde9a^{-/-}$ mice. **a**, Echocardiography of littermate control and $Pde9a^{-/-}$ left ventricle subjected to TAC. WT, wild type. **b**, Summary data for fractional shortening (FS), left ventricular end-systolic dimension (LV-ESD), and left ventricular mass. *$P < 0.01$ vs. wild-type TAC. **c**, Fibrosis and myocyte enlargement in sham and TAC wild-type and $Pde9a^{-/-}$ mice. *$P < 0.001$ vs. sham wild type, #$P < 0.001$ vs. TAC wild type. Scale bar, 50 μm. MT, Masson's trichrome; WGA, wheat germ agglutinin; CSA, cross-sectional area. **d**, Heart and lung weight normalized to tibia length (TL). *$P < 0.001$ vs. sham wild type, †$P < 0.05$, #$P < 0.001$ vs. TAC wild type. **e**, Myocardial cGMP after TAC. *$P < 0.05$ vs. sham control, #$P < 0.05$ vs. TAC wild type. **f**, **g**, *Nppa*, β-myosin heavy chain (*Myh7*), connective tissue growth factor (*Ctgf*), fibronectin (*Fn1*), collagen type-1a (*Col1a2*), metallo-proteinase 2 (*Mmp2*), and transient receptor potential canonical 6 (*Trpc6*) expression; all normalized to GAPDH. *$P < 0.001$ vs. sham wild type, †$P < 0.05$ vs. TAC wild type, #$P < 0.001$. Data are mean ± s.e.m. and biological replicates are indicated (in parentheses for **b**, **d**–**g**).

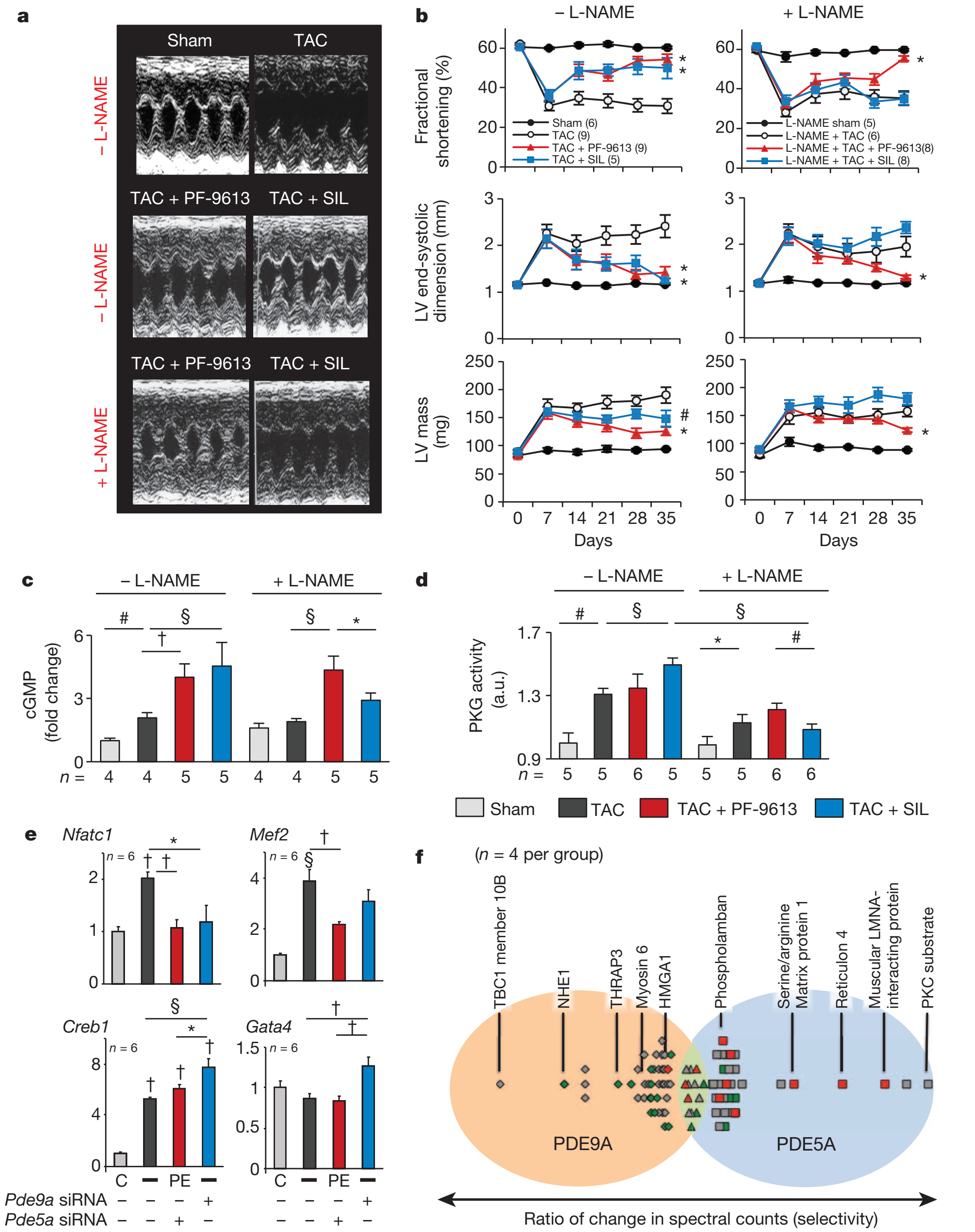

Figure 4 | Chronic PDE9A inhibition reverses pre-established hypertrophy/dysfunction in a NOS-independent manner. **a**, M-mode echocardiograms from mice ± L-NAME exposed to 5-week TAC ± PDE5A or PDE9A inhibition starting one week after TAC. **b**, PF-9613 and SIL reversed cardiac dysfunction from TAC in L-NAME$^-$ mice, but only PF-9613 was effective in L-NAME$^+$ mice. $*P < 0.01$, $\#P < 0.05$ vs. TAC. **c**, **d**, Cyclic-GMP levels (**c**) and *in vitro* PKG activity (**d**) measured in the same experiments. a.u., arbitrary units. **e**, Transcription factor activation in RNCMs stimulated by phenylephrine ± gene silencing of *Pde5a* or *Pde9a*. For **c**–**e**, $*P < 0.05$, $\dagger P < 0.01$, $\#P < 0.005$, $\S P < 0.001$ vs. control (C), or for the paired comparison identified by the horizontal bar. **f**, Differential phosphorylation of target proteins following PDE9A versus PDE5A inhibition. L-NAME co-treatment reversed PDE5A-selective changes (red) far more than PDE9A-selective changes. Data are mean ± s.e.m. and biological replicates are indicated (in parentheses for **b**).

activation of transcription factors known to regulate cardiac growth/hypertrophy and survival. NFAT, MEF2 and CREB all increased with phenylephrine stimulation. NFAT declined with PDE5 or PDE9 inhibition, consistent with results for TRPC6 (Fig. 4e and Extended Data Fig. 8) and studies showing that both natriuretic peptide and nitric oxide stimulation block this pathway[16,17]. MEF2 only declined with PDE5A-I while both GATA4 and CREB rose only with PDE9A-I (Fig. 4e). The latter two are linked to natriuretic peptide /cGMP signalling, enhanced survival and adaptive myocardial stress responses[19,20].

Lastly, we performed unbiased proteomic analysis to detect serine/threonine phosphorylation increases in myocyte proteins altered by PDE9A-I or PDE5A-I, with or without concomitant L-NAME. The majority (85%) of phosphorylated amino acid residues were modified by one or the other PDE inhibitor and the rest by both (Fig. 4f and Supplementary Table 1). Of these residues, L-NAME reduced 21% of those specific to PDE5A-I versus 5.2% to PDE9A-I (red symbols, $P < 0.02$), supporting targeting of PDE9A to non-nitric-oxide-dependent cGMP (Supplementary Table 2).

The efficacy of inhibiting a cGMP-PDE to counter myocardial responses to pathological stress requires having sufficient cGMP synthesized and PDE expressed, and pathogenic signalling suppressible by PKG. Though prior work indicated PDE5A might fulfil these criteria, its preferred targeting to NOS-dependent cGMP is a potential limitation, as this pool is often depressed in cardiovascular disease. We have now identified PDE9A-I as an alternative that, unlike PDE5A-I, remains effective even when NOS-dependent cGMP synthesis is suppressed. This non-redundant function is consistent with intracellular compartmentation[21]. The revelation that PDE9A serves as a natriuretic-peptide-cGMP-targeted PDE is important as this source of cGMP often rises in heart disease, whereas the NOS-derived pool declines. As with PDE5A, there are multiple downstream targets stemming from PDE9A regulation that collectively impact myocardial biology and disease. The current data identifies transcriptional controllers and protein substrates, setting the stage for future work.

The observation of heightened PDE9A expression in human heart failure, particularly HFPEF is exciting. Morbidity and mortality from

HFPEF is high and with still no effective therapies this remains a major unmet medical need worldwide[12]. While there is considerable enthusiasm for cGMP-PKG-targeted treatment for this disease[22], recent data from a multicentre clinical trial using PDE5A-I was disappointing[23]. Among potential reasons are a lack of PDE5A upregulation and low myocardial cGMP attributed to depressed nitric oxide signalling[24]. Our results suggest PDE9A-I as an attractive alternative. The recent success of a combined angiotensin receptor blocker and neprilysin inhibitor[25] (the latter blunting natriuretic peptide proteolysis) that is being tested in HFPEF (NCT01920711), and advances in synthetic natriuretic peptide therapies[26] offer opportunities for combined treatment. PDE9A inhibitors appear well tolerated in humans and are being studied for neurocognitive disease (https://clinicaltrials.gov/ct2/show/NCT00930059). The current results support exploring these agents as new avenues for treatment of the heart, and potentially other organs in which PDE9A and the natriuretic peptide signalling system have a role.

Online Content Methods, along with any additional Extended Data display items and Source Data, are available in the online version of the paper; references unique to these sections appear only in the online paper.

Received 26 March 2014; accepted 16 February 2015.

Published online 18 March; corrected online 25 March 2015 (see full-text HTML version for details).

1. Takimoto, E. *et al.* Chronic inhibition of cyclic GMP phosphodiesterase 5A prevents and reverses cardiac hypertrophy. *Nature Med.* **11,** 214–222 (2005).
2. Kukreja, R. C., Salloum, F. N. & Das, A. Cyclic guanosine monophosphate signaling and phosphodiesterase-5 inhibitors in cardioprotection. *J. Am. Coll. Cardiol.* **59,** 1921–1927 (2012).
3. Mullershausen, F., Russwurm, M., Koesling, D. & Friebe, A. *In vivo* reconstitution of the negative feedback in nitric oxide/cGMP signaling: role of phosphodiesterase type 5 phosphorylation. *Mol. Biol. Cell* **15,** 4023–4030 (2004).
4. Castro, L. R., Verde, I., Cooper, D. M. & Fischmeister, R. Cyclic guanosine monophosphate compartmentation in rat cardiac myocytes. *Circulation* **113,** 2221–2228 (2006).
5. Takimoto, E. *et al.* Compartmentalization of cardiac β-adrenergic inotropy modulation by phosphodiesterase type 5. *Circulation* **115,** 2159–2167 (2007).
6. Carnicer, R., Crabtree, M. J., Sivakumaran, V., Casadei, B. & Kass, D. A. Nitric oxide synthases in heart failure. *Antioxid. Redox Signal.* **18,** 1078–1099 (2013).
7. Soderling, S. H., Bayuga, S. J. & Beavo, J. A. Identification and characterization of a novel family of cyclic nucleotide phosphodiesterases. *J. Biol. Chem.* **273,** 15553–15558 (1998).
8. Fisher, D. A., Smith, J. F., Pillar, J. S., St Denis, S. H. & Cheng, J. B. Isolation and characterization of PDE9A, a novel human cGMP-specific phosphodiesterase. *J. Biol. Chem.* **273,** 15559–15564 (1998).
9. Conti, M. & Beavo, J. Biochemistry and physiology of cyclic nucleotide phosphodiesterases: essential components in cyclic nucleotide signaling. *Annu. Rev. Biochem.* **76,** 481–511 (2007).
10. Kleiman, R. J. *et al.* Phosphodiesterase 9A regulates central cGMP and modulates responses to cholinergic and monoaminergic perturbation *in vivo. J. Pharmacol. Exp. Ther.* **341,** 396–409 (2012).
11. Heckman, P. R., Wouters, C. & Prickaerts, J. Phosphodiesterase inhibitors as a target for cognition enhancement in aging and Alzheimer's disease: a translational overview. *Curr. Pharm. Des.* **21,** 317–331 (2015).
12. Sharma, K. & Kass, D. A. Heart failure with preserved ejection fraction: mechanisms, clinical features, and therapies. *Circ. Res.* **115,** 79–96 (2014).
13. Nausch, L. W., Ledoux, J., Bonev, A. D., Nelson, M. T. & Dostmann, W. R. Differential patterning of cGMP in vascular smooth muscle cells revealed by single GFP-linked biosensors. *Proc. Natl Acad. Sci. USA* **105,** 365–370 (2008).
14. Singh, G., Kuc, R. E., Maguire, J. J., Fidock, M. & Davenport, A. P. Novel snake venom ligand dendroaspis natriuretic peptide is selective for natriuretic peptide receptor-A in human heart: downregulation of natriuretic peptide receptor-A in heart failure. *Circ. Res.* **99,** 183–190 (2006).
15. Davis, J., Burr, A. R., Davis, G. F., Birnbaumer, L. & Molkentin, J. D. A. TRPC6-dependent pathway for myofibroblast transdifferentiation and wound healing *in vivo. Dev. Cell* **23,** 705–715 (2012).
16. Koitabashi, N. *et al.* Cyclic GMP/PKG-dependent inhibition of TRPC6 channel activity and expression negatively regulates cardiomyocyte NFAT activation: novel mechanism of cardiac stress modulation by PDE5 inhibition. *J. Mol. Cell. Cardiol.* **48,** 713–724 (2010).
17. Kinoshita, H. *et al.* Inhibition of TRPC6 channel activity contributes to the antihypertrophic effects of natriuretic peptides-guanylyl cyclase-A signaling in the heart. *Circ. Res.* **106,** 1849–1860 (2010).
18. Stangherlin, A. *et al.* cGMP signals modulate cAMP levels in a compartment-specific manner to regulate catecholamine-dependent signaling in cardiac myocytes. *Circ. Res.* **108,** 929–939 (2011).
19. Pilz, R. B. & Broderick, K. E. Role of cyclic GMP in gene regulation. *Front. Biosci.* **10,** 1239–1268 (2005).
20. Oka, T. *et al.* Cardiac-specific deletion of *Gata4* reveals its requirement for hypertrophy, compensation, and myocyte viability. *Circ. Res.* **98,** 837–845 (2006).
21. Maurice, D. H. *et al.* Advances in targeting cyclic nucleotide phosphodiesterases. *Nature Rev. Drug Discov.* **13,** 290–314 (2014).
22. Greene, S. J. *et al.* The cGMP signaling pathway as a therapeutic target in heart failure with preserved ejection fraction. *J. Am Heart Assoc.* **2,** e000536 (2013).
23. Redfield, M. M. *et al.* Effect of phosphodiesterase-5 inhibition on exercise capacity and clinical status in heart failure with preserved ejection fraction: a randomized clinical trial. *J. Am. Med. Assoc.* **309,** 1268–1277 (2013).
24. van Heerebeek, L. *et al.* Low myocardial protein kinase G activity in heart failure with preserved ejection fraction. *Circulation* **126,** 830–839 (2012).
25. McMurray, J. J. *et al.* Angiotensin-neprilysin inhibition versus enalapril in heart failure. *N. Engl. J. Med.* 993–1004 (2014).
26. Zakeri, R. & Burnett, J. C. Designer natriuretic peptides: a vision for the future of heart failure therapeutics. *Can. J. Physiol. Pharmacol.* **89,** 593–601 (2011).

Supplementary Information is available in the online version of the paper.

Acknowledgements We thank students R. D. Wardlow and X. Hu for their assistance with some of the assays and studies. This research was supported by: the National Institutes of Health (NIH) (HL-119012, HL-089297, HL-07227), Fondation Leducq TransAtlantic Network of Excellence, The Peter Belfer Foundation, Abraham and Virginia Weiss Professorship (D.A.K.); HL-093432 (E.T.), American Heart Association (D.I.L.) and Max Kade Fellowship of the Austrian Academy of Sciences (P.P.R). Procurement of human heart tissue was enabled by grants from the National Institutes of Health (HL089847 and HL105993) to K.B.M. N.H. and W.J.P. were supported by the European Commission FP7 project 2010 Health (MEDIA; 261409). R.H. and J.E.V.E. were supported by The Johns Hopkins Innovation Proteomics Center in Heart Failure (NHLBI-HV-10-05 (2) and HHSN268201000032C). W.R.D. was supported by NIH grant HL68891 and the Totman Trust for Biomedical Research. We thank Pfizer and in particular C. Schmidt and R. Kleiman for providing the *Pde9a*$^{-/-}$ mouse and PF-04449613, and L. Jaffe at the University of Connecticut Health Center for providing the PDE9A antibody.

Author Contributions D.I.L. and D.A.K. conceived and directed the project, designed experiments and prepared the manuscript. D.I.L. conducted most of the experiments and analysed the data. G.Z. helped with *in vivo* experiments. T.S., S.-H.J., T.D., M.Z. and P.P.R. conducted molecular biology experiments. G.-S.C. and C.K. carried out immunostaining and *in situ* hybridization analyses. N.H. and W.J.P. performed experiments for HFPEF and aortic stenosis human samples. M.J.R. and R.H. performed the experiments for phosphoproteomics and J.A.K. contributed to the data analysis. D.B. performed echocardiography and drug treatment. K.B.M. coordinated the human sample and data collection at the University of Pennsylvania, and W.R.D., J.E.V.E. and E.T. helped with data interpretation and presentation.

Author Information Reprints and permissions information is available at www.nature.com/reprints. The authors declare no competing financial interests. Readers are welcome to comment on the online version of the paper. Correspondence and requests for materials should be addressed to D.A.K. (dkass@jhmi.edu).

METHODS

Human myocardial tissue. Procurement of human myocardial tissue was performed under protocols approved by Institutional Review Boards at the University of Pennsylvania (Pennsylvania, USA), Johns Hopkins University (Maryland, USA) and VU University Medical Center, (Amsterdam, The Netherlands) and its coordinated affiliated centres[24] and consent for biopsy procedures or use of explanted tissues prospectively obtained in all cases. Explant dilated non-ischaemic failing human hearts were procured at the time of orthotopic heart transplantation at the Hospital of University of Pennsylvania. Non-failing hearts were obtained at the time of organ donation from cadaveric donors. In all cases, hearts were arrested *in situ* using ice-cold cardioplegia solution, transported on wet ice, and flash frozen in liquid nitrogen within 4 hours of explantation. All samples were full-thickness biopsies obtained from the free wall of the left ventricle. HFPEF patients were referred for cardiac catheterization and left ventricular endomyocardial biopsy because of clinical suspicion of restrictive cardiomyopathy. Left ventricular biopsies were procured using femoral artery access and a long bioptome. Diagnostic criteria and clinical characteristics of the HFPEF and aortic stenosis patients have been previously reported[24]. Control samples for these studies were obtained from explanted unused donor hearts.

***Pde9a* knockout mouse.** All protocols involving animals followed US National Institutes of Health guidelines and were approved by the animal and care use committee of the Johns Hopkins Medical Institutions. *Pde9a* global knockout (*Pde9a*$^{-/-}$) mice were developed by Pfizer Inc. The model replaced exon 12 in the catalytic domain of *Pde9a* with a *lacZ*-neomycin cassette (see Extended Data Fig. 1). Mice did not express any splice variants as they all share this sequence. *Pde9a*$^{-/-}$ mice were born in normal Mendelian ratios, and had no evident physiological or behavioural abnormalities (Supplementary Table 3). Expression of alternative cGMP-targeting PDEs, PDE1A and PDE5A were not significantly different in *Pde9a*$^{-/-}$ versus littermate control hearts (Extended Data Fig. 9).

Transverse aortic constriction and chronic drug studies. Pressure overload was performed by surgical placement of suture around the transverse aorta sized to a 27G needle, as described previously[1]. For chronic drug treatment studies, size-, age- and sex-matched (male) C57BL/6J mice (Jackson Labs) were randomized to receive vehicle, PF-9613 (30 mg kg^{-1} twice a day by oral gavage), or sildenafil (200 mg kg^{-1} per day with Bioserv soft diet). The mean free plasma concentration of PF-9613 was 77 nM, (peak of 1.5 μM at 30 min, $t_{1/2} = 1.2$ h) within the selective range, while sildenafil yielded 30 nM[1], also in the selective range. Mice were subjected to TAC or a sham operation. Mice were euthanized at 5 weeks for tissue analysis. This protocol was then repeated in mice administered L-NAME (1 mg ml^{-1} in drinking water) initiated one week before TAC, and continued for the full 5-week TAC. Tissue histology and echocardiography followed reported methods[27]. For these studies, *in vivo* analysis and post-mortem myocardial analysis were performed blinded as to experimental group. *In vivo Pde9a*$^{-/-}$ analysis included all animals studied. For the drug intervention study, which was designed to test reversal of heart disease established after one week of TAC, animals dying in the first week (before drug assignment) or who failed to develop disease after TAC (likely related to inadequate constriction) were excluded from analysis. Chronic PF-9613 had no effect on cardiac function or systemic pressures (for example, no evidence of arterial vasodilation) in shams (Extended Data Fig. 7). There was also no systemic vasodilation from drug treatment in TAC hearts (for example, systemic resistance was: vehicle, 11.5 ± 1; PF-9613, 10.6 ± 2 mm Hg per ml per min; $P > 0.5$).

PDE9A inhibitors: PF-04449613 and PF-04447943 and siRNA vectors. The structure and pharmacology of PF-04449613 and PF-04447943 have been reported[10,28]. We performed a dose-ranging study for PDE9A and PDE5A selectivity using a fluorescent polarization assay[1] (Molecular Devices) (Extended Data Fig. 3a). This identified 5 μM PF-04449613 inhibited 70% of PDE9A without altering PDE5A activity, whereas 1 μM sildenafil blocked more than 70% of PDE5A activity with no effect on PDE9A. These concentrations were used in the subsequent cell culture studies. For gene silencing, we used targeted siRNA (PDE9A, L-098890-02; PDE5A, L-093210-02; control, D-001810-10; on-target siRNA smart pool, Dharmacon) or scrambled controls, achieving 70–80% knockdown (Extended Data Fig. 1c).

Isolated myocyte hypertrophy and immunohistochemistry. Cell isolation methods for both neonatal and adult myocytes have been reported previously[27]. For adult cell studies, the isolation process itself produces variance in the absolute agonist response observed. Thus, quantitative response comparisons are best considered within a given cell type (for example, control or *Pde9a*$^{-/-}$). RNCMs were isolated from 1 to 2-day-old Sprague–Dawley rats and cultured for 2 days before study, while adult mouse myocytes were studied in primary culture for no more than 24 h. For immunohistochemistry, myocytes were plated on laminin-coated imaging dishes, fixed with 50% methanol and 50% acetone, permeabilized with 0.1% saponin in PBS, and blocked in 10% bovine serum albumin in PBS. Cells were then incubated overnight with primary antibodies at 4 °C (rabbit anti-PDE9A (using human peptide), gift of L. Jaffe, 1:100 or 1:50 dilution for wild type and knockout, respectively; rabbit anti-PDE5 (1:250, Cell Signaling); mouse anti-SERCA2 (1:250, Abcam); mouse anti-α actinin (1:500, Sigma)); then with secondary antibodies for 1 h at room temperature (Alexa Fluor 488- or Alexa Fluor 546-conjugated; Invitrogen); then imaged on an inverted epifluorescent microscope with argon–krypton laser confocal scanning (Zeiss, UltraView; Perkin Elmer Life Science Inc.).

Human heart immunostaining and *in situ* hybridization. Sectioned human heart tissues were dehydrated with PBS in buffer containing 10 mM sodium citrate, 0.05% Tween 20 at pH 6.0. Sections were blocked for 1 h at room temperature in PBS with 0.1% bovine serum albumin and 0.1% Tween-20) followed by incubation with PDE9A (1:200) or cardiac TnT antibody (1:100, Thermo).

In situ hybridization with a digoxigenin (DIG)-labelled PDE9A probe was performed as described previously[29]. We generated an anti-sense RNA probe to human *PDE9A* using a partial sequence of human *PDE9A*, flanked with forward (5′-TG TCCTAGAGAAACGCGTGG-3′) and reverse (5′-GGTGACAGGGTTGATGCT GA-3′) primers, amplified by PCR, and ligated into pGEM-T-easy vector (Promega). Anti-sense RNA probe labelled with DIG was prepared using the RNA labelling kit (Roche).

Molecular analyses. PDE and PKG activity, and cAMP and cGMP levels were determined as previously described[1]. Quantitative PCR was used to assess RNA expression using standard procedures. PCR primers were: TaqMan primers used: *Col1a2* (Mm00483888_m1), *Ctgf* (Mm01192933_g1), *Fn1* (Mm01256744_m1), *Gapdh* (Mm99999915_g1), *Myh7* (Mm00600555_m1), *Nppa* (Mm01255747_g1), *Nppb* (Mm01255770_g1), *Mmp2* (Mm00439498_m1), *Pde9a* (Mm00501049_m1), *Pde1a* (Mn00450244_m1), *Pde5a* (Mn00463177_m1), *Trpc6* (Mm01176083_m1). For SYBR primers used: rat *Nppa* (forward 5′-ATACAGTGCGGTGTCCAACACAG A-3′, reverse 5′-TGACCTCATCTT CTACCGGCATCT-3′), rat *Nppb* (forward 5′-ATGCAGAAGCTGCTGGAG CTGATA-3′, reverse 5′-CTTCTGCCCAAAG CAGCTTGAACT-3′), rat *Gapdh* (forward 5′-GACATGCCGCCTGGAGAAAC-3′, reverse 5′-AGCCCAGGATGCCCTTTAGT-3′), rat *Pde5a* (forward 5′-AACTC GTGGCAGCCGAATTCTTTG-3′, reverse 5′-TGTTCATTAGATCAGCGGGCT CCA-3′), and rat *Pde9a* (forward 5′-TACGGAAGCCCACCTTTGATGTCT-3′, reverse 5′-TTGGGTTGATGCTGAAGTCCCTGA-3′). All PCR samples were run in duplicate and normalized to GAPDH. Specificity of the SYBR green assays was confirmed by dissociation curve analysis.

Protein electrophoresis and immunoblot assays followed standard procedures, using lysis buffer (Cell Signaling) with protease inhibitor PMSF (1 mM), and run on NuPAGE 4 to 12% gel (Invitrogen). Membranes were probed for human anti-PDE9A (1:1,000), mouse anti-GAPDH or human anti-actin (1:10,000, Cell Signaling). Quantitation used fluorescence detection (Odyssey, Licor, and Odyssey Application Software 3.0). For human left ventricular biopsy tissue analysis, samples were applied at 25 μg (dry weight), and probed with primary antibody (Millipore, ABN32, dilution 1:1,000), and visualized using secondary horseradish-peroxidase-labelled, goat-anti-rabbit/mouse antibody (dilution 1:1,000; DakoCytomation) and enhanced chemiluminescence (ECL western blotting detection, Amersham Biosciences). Signals were normalized to actin (dilution 1:1,000; clone KJ43A; Sigma) stained on the same blots. Leucine incorporation assays were performed as described previously[16]

Real-time myocyte cGMP analysis. RNCMs plated on gelatin-coated 35-mm glass-bottom culture dishes (MatTek) were incubated overnight and, at 50% confluence, exposed to adenovirus expressing FlincG[13] (courtesy of W.R.D.) at a multiplicity of infection of 10, for 24–48 h at 37 °C, 5% CO2 until a 90% transfection efficiency was achieved. Since the absolute level of expressed FlincG varied among cells, each cell was used as their own control, with stimulation protocols compared within a given cell by paired analysis. Cell imaging was performed in imaging buffer (Hank's balanced salt solution (HBSS), Mediatech, Inc.) by using a 3i spinning disk confocal system on a Zeiss microscope with SlideBook 5.0 software (Intelligent Imaging Innovations, Inc.), a 63× oil dipping objective (N.A. 1.0), and iXon ENCCD DVB camera with 1-s acquisitions and 20 ms exposure time, exciting with a solid state laser at 488 nm and collecting the emission at 510 nm at 37 °C. cGMP responses are investigated upon local application (20 to 50 ml) and subsequent diffusion of DEANO (Calbiochem), ANP (Sigma), ODQ (Sigma) and specific PDE inhibitors (Pfizer). Data are analysed by using the Slidebook software.

Histology. Myocardium was fixed with 10% formaldehyde, paraffin embedded and sectioned into 4-μm slices. Masson's trichrome staining was used to visualize collagen. Quantification of fibrosis content was performed in four to six regions of each heart. For wheat germ agglutinin staining of mouse heart sections, slides were deparaffinized, rehydrated, and subjected to citrate-based heat-mediated antigen retrieval. Slides were incubated with 5 μg ml^{-1} Alexa Fluor 647-conjugated wheat germ agglutinin (Invitrogen) overnight at 4 °C and mounted using Prolong Gold mounting medium (Invitrogen)[27]. Myocyte cross sectional area was measured using an automated algorithm with NIH Image J 1.47i software. Image acquisition was performed on a Zeiss LSM510-META laser scanning microscope.

Luciferase reporter assay. RNCMs were transfected with *Nfat-luc*, *Creb1-luc*, *Gata4-luc*, *TK-luc* (Promega) or *Mef2-luc* (Addgene), using Xfect reagent (Clontech) according

to the manufacturer's protocol. After 24 h transfection, cells were stimulated with 25 μM of phenylephrine for 6 h, lysates harvested using passive lysis buffer (Promega) and luciferase activity determined using the Dual-Luciferase Reporter Assay System (Promega) and Veritas 96-well microplate luminometer (Turner Biosystems) following the manufacturer's protocol.

Phosphoproteomic analysis. Samples ($n = 4$ per group) were lysed in 8 M urea, 0.5% SDS with brief sonication and protein concentration determination by the BCA method. For each sample, 200 μg of total protein was digested with trypsin/Lys-C protease mixture (Promega) according to previously published methods[30], samples desalted on 10-mg Oasis HLB cartridges (Waters) and eluted in 300 μl of 80% acetonitrile, 5% trifluoroacetic acid and 1 M glyocolic acid, and enriched by titanium dioxide (TiO2). Enriched peptides were desalted as above but eluted in 200 μl of 80% ACN, 0.1% formic acid and dried under vacuum. Dried peptides were re-suspended in 20 μl of 0.1% FA for liquid chromatrography–tandem mass spectrometry analysis.

For each sample, 4 μl was injected in duplicate onto an EASY-nLC 1000 (mobile phase A was 0.1% FA in water and mobile phase B was 0.1% FA in ACN) connected to a Q-Exactive Plus (Thermo) equipped with a nano-electrospray ion source. All raw MS/MS data was searched using the Sorcerer 2TM-SEQUEST algorithm (Sage-N Research) using default peak extraction parameters. Post-search analysis was performed using Scaffold 4 (Proteome Software, Inc.) with protein and peptide probability thresholds set to 95% and 90%, respectively, and one peptide required for identification, and these the spectra were manually validated. Phosphosite localization was determined using Scaffold PTM version 2.1.3 and phosphosites with probabilities less than 90% were ignored. The mass spectrometry proteomics data have been deposited to the ProteomeXchange Consortium via the PRIDE partner repository with the data set identifier PXD001585.

Statistics and reproducibility. For all analyses, sample size is reported in the figure legends or figures themselves. Most *in vitro* studies were done with two to three sets of independent experiments. Comparisons of multiple groups were performed using either one-way or two-way ANOVA (as appropriate). If normality or equal variance tests failed, then a Kruskal–Wallis test was used. Two-group anlaysis used either a Student's *t*-test or a non-parametric Mann–Whitney test. Post-hoc multiple comparisons testing used either a Tukey or Dunns test. Analysis of time-dependent changes was performed by ANCOVA with repeated measures. Formal power analysis was not prospectively performed, though for variables where variance was known we could estimate sample size based on an anticipated mean effect.

27. Seo, K. *et al.* Combined TRPC3 and TRPC6 blockade by selective small-molecule or genetic deletion inhibits pathological cardiac hypertrophy. *Proc. Natl Acad. Sci. USA* **111,** 1551–1556 (2014).
28. Verhoest, P. R. *et al.* Design and discovery of 6-[(3S,4S)-4-methyl-1-(pyrimidin-2-ylmethyl)pyrrolidin-3-yl]-1-(tetrahydro-2H-pyr an-4-yl)-1,5-dihydro-4H-pyrazolo[3,4-d]pyrimidin-4-one (PF-04447943), a selective brain penetrant PDE9A inhibitor for the treatment of cognitive disorders. *J. Med. Chem.* **55,** 9045–9054 (2012).
29. Zhou, B. *et al.* Epicardial progenitors contribute to the cardiomyocyte lineage in the developing heart. *Nature* **454,** 109–113 (2008).
30. Kirk, J. A. *et al.* Cardiac resynchronization sensitizes the sarcomere to calcium by reactivating GSK-3beta. *J. Clin. Invest.* **124,** 129–139 (2014).

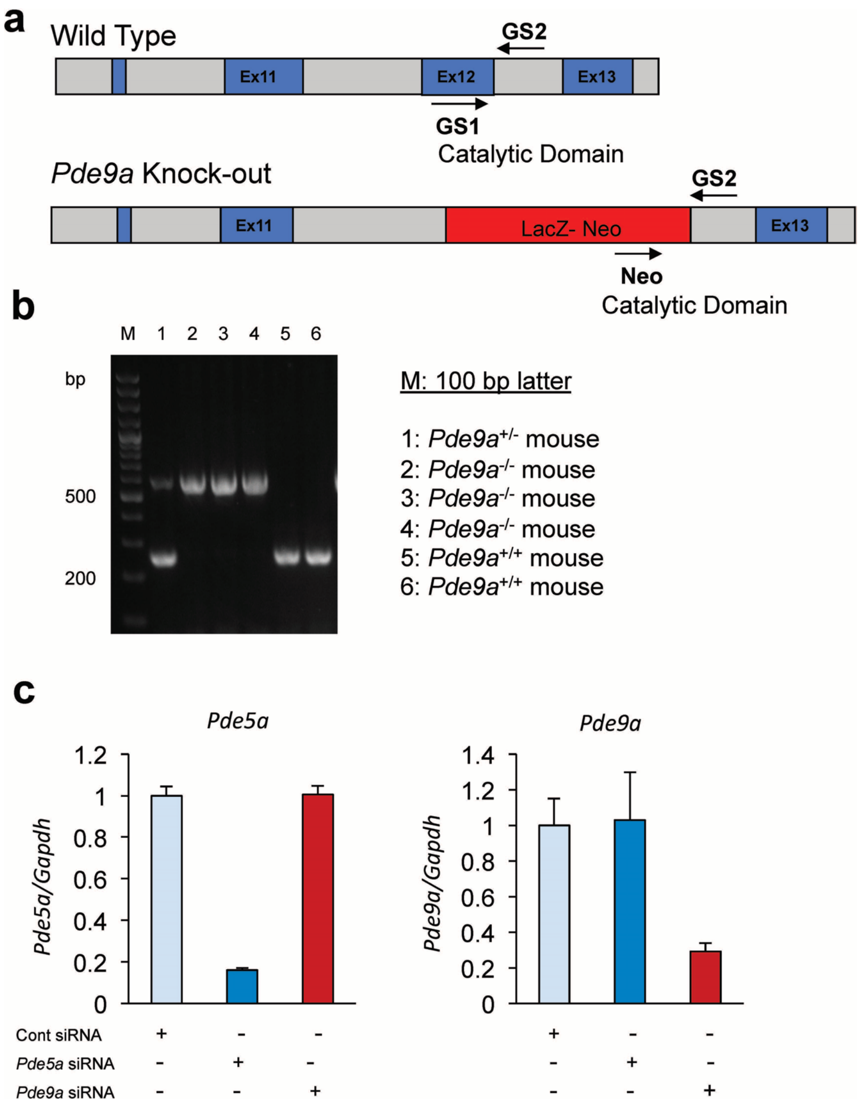

Extended Data Figure 1 | Development of *Pde9a* knockout (*Pde9a*$^{-/-}$) and specificity of *Pde5a* or *Pde9a* siRNA. **a**, *Pde9a* knockout (*Pde9a*$^{-/-}$) mice were developed by replacing the exon 12 region with *lacZ*-neomycin cassette in the catalytic domain of the carboxy terminal in the *Pde9a* gene. The genotyping was performed using specific primers designed between exons 11 and 13 including neomycin as following: *Gs1* (5′-CACAGATGATGTACAGTATGGTCTGG-3′), *Gs2* (5′-TGCAGTCATCAGGACCAAGATGTCC-3′) and *Neo* (5′-GACGAGTTCTTCTGAGGGGATCGATC-3′). **b**, The typical genotyping pattern of *Pde9a*$^{-/-}$ mice was shown on 2% agarose gel (250 bp for wild type and 500 bp for *Pde9a*$^{-/-}$ mice). **c**, Selective gene silencing using siRNAs targeting PDE5A or PDE9A. PCR confirms specificity and substantial gene knockdown achieved in cell culture ($n = 6$ per group).

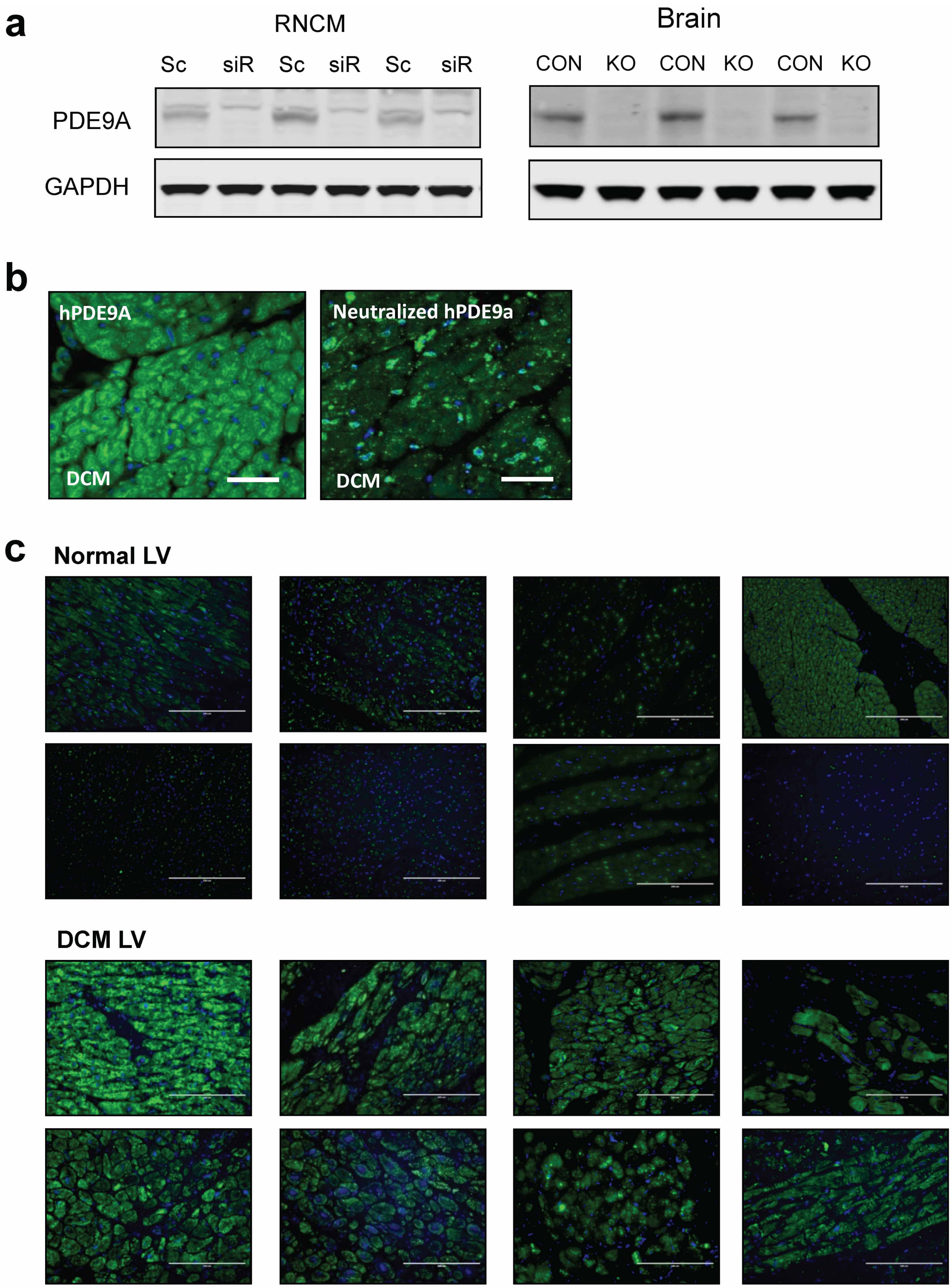

Extended Data Figure 2 | Expression of PDE9A protein in RNCM, mouse brain and human heart. **a**, Immunoblot for PDE9A in neonatal cardiomyocytes transfected with either scrambled control siRNA (Sc) or *Pde9a* siRNA (siR), confirming the suppression of protein expression by the siRNA. A control gel for comparison was derived from brain tissue using *Pde9a*$^{-/-}$ mice and littermate controls. The band identified at ~60 to 65 kDa was similar in both tissues. PDE9A bands are usually identified between 55–70 kDa depending on the splice variants expressed in a given tissue and species. **b**, Control immunohistochemistry showing that PDE9A detected by antibody can be largely quenched (inactivated) selectively by preincubation with recombinant ligand; scale bar, 50 μm. **c**, Immunostaining of PDE9A from all 8 control and DCM patients; scale bar, 200 μm. There was consistent enhanced staining in DCM patients versus controls. All images were obtained at an identical level of laser illumination and have not been altered.

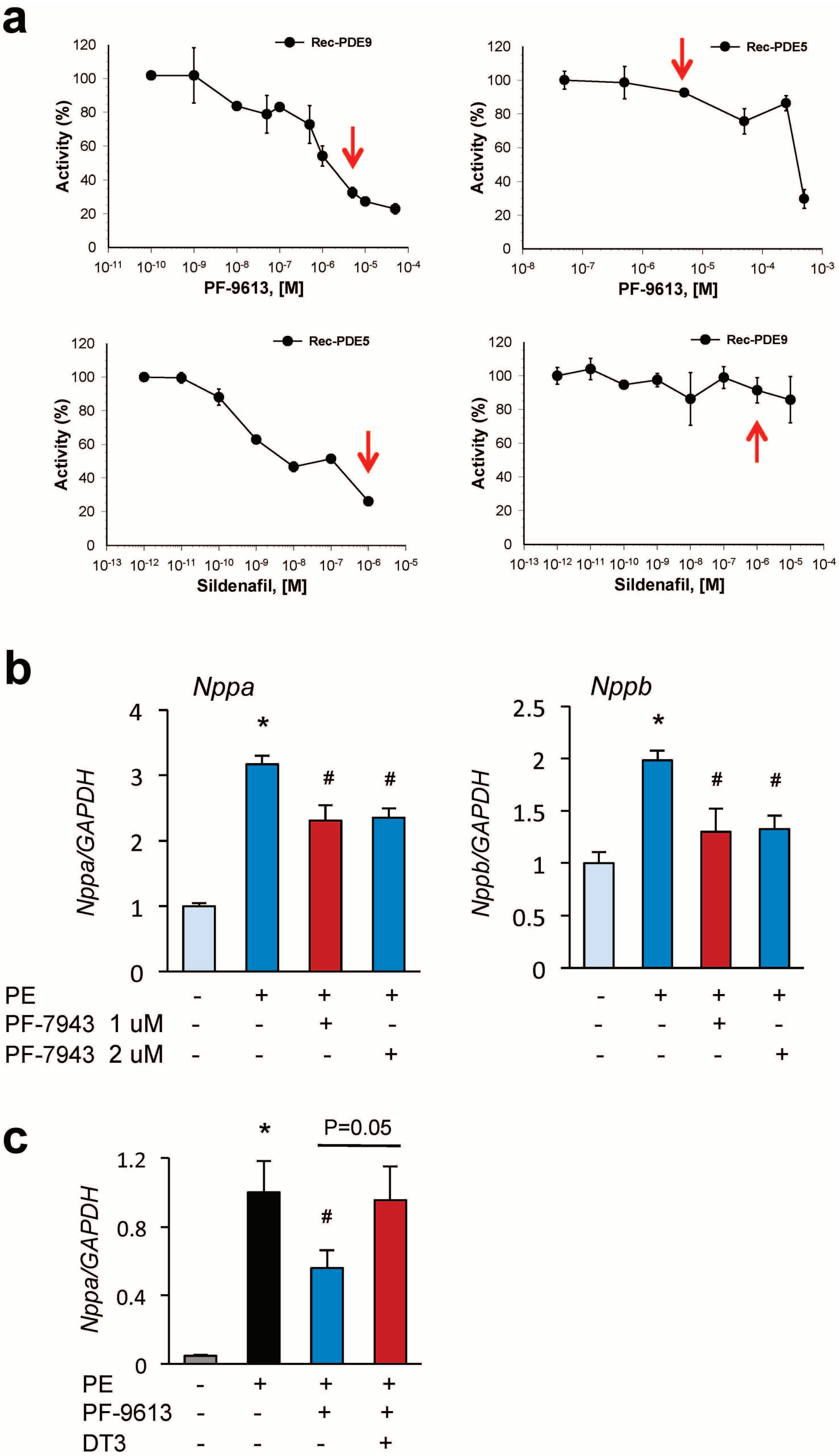

Extended Data Figure 3 | Selectivity of PDE9A inhibitors. **a**, The dose responses of recombinant PDE9A or PDE5A to a selective PDE9A inhibitor (PF-9613) and sildenafil. Data performed in triplicate at each point. A dose of 5 μM PF-9613 inhibited PDE9A effectively, but had negligible impact on PDE5A. By contrast, the PDE5A inhibitor sildenafil inhibited PDE5A by 80% at a dose of 1 μM, commonly used for cells and tissue, but had no impact on PDE9A at this dose. These doses were therefore used in our cell-based studies. **b**, Confirmation that an alternative PDE9A inhibitor (PF-04447943), currently being tested in humans, shows similar anti-hypertrophic effects as PF-9613 in cardiac myocytes ($n = 4$ per group); *$P < 0.001$ vs. baseline; #$P < 0.01$ vs. phenylephrine. **c**, Inhibition of PKG activity with DT3 reverses the suppression of phenylephrine-stimulated *Nppb* gene expression by PF-9613. This is a companion panel to Fig. 2b, bottom. $n = 6$ for basal (no drugs), $n = 8$ for other groups; *$P < 0.001$ vs. baseline; #$P < 0.01$ vs. phenylephrine. Data are mean ±s.e.m.

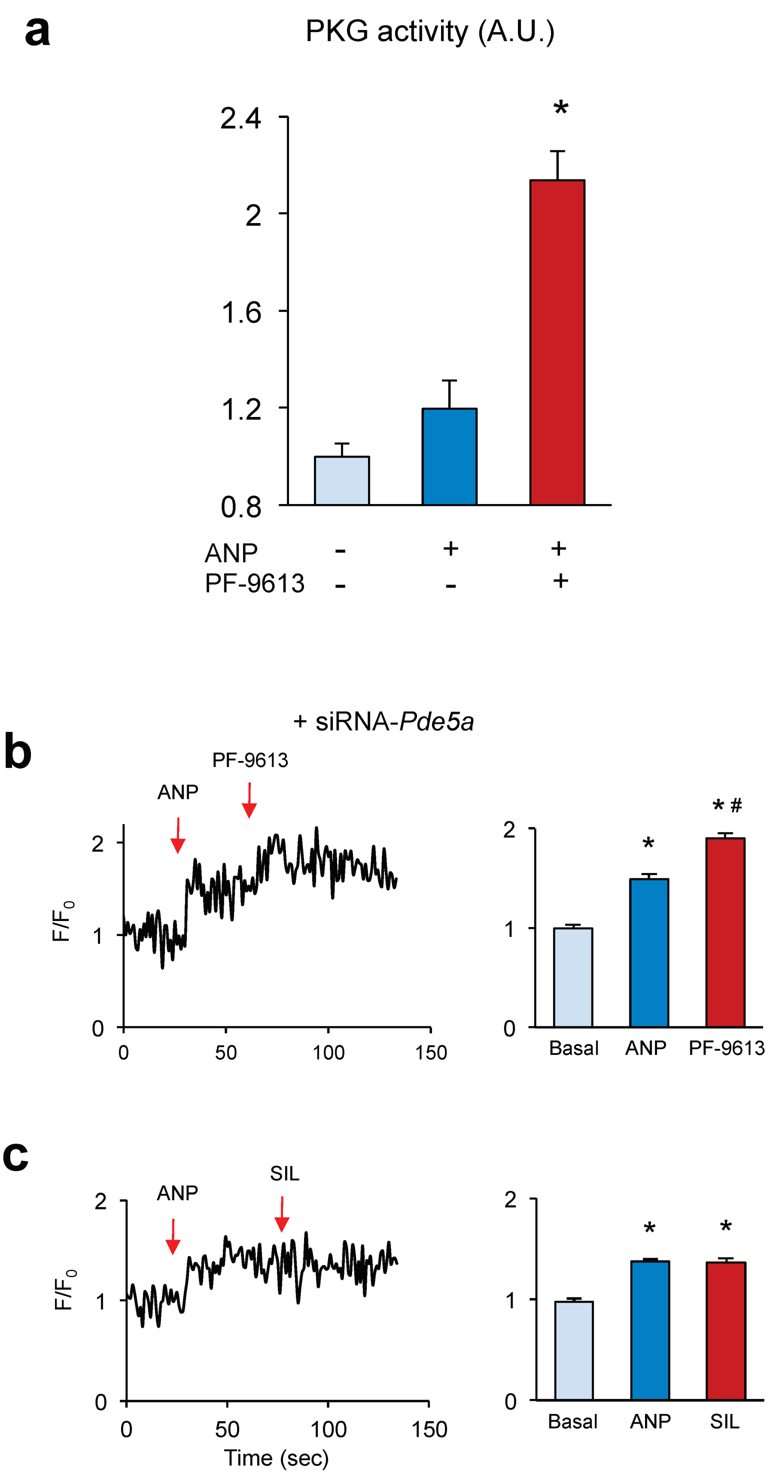

Extended Data Figure 4 | PKG activity or cGMP measurement of ANP with inhibitors in RNCM. **a**, PF-9613 significantly increases PKG activity assessed by *in vitro* assay upon stimulation with ANP; $n = 4$ per group. *$P < 0.01$ vs. other groups. **b**, PF-9613 augmentation of ANP-stimulated cGMP is not altered due to gene silencing of *Pde5a*; $n = 5$. This differs from the complete suppression of cGMP modulation by PF-9613 in myocytes with genetically silenced *Pde9a* (Fig. 1g). **c**, SIL does not enhance cGMP stimulated by ANP. This contrasts to its augmentation of nitric-oxide-donor-derived cGMP (Fig. 1h); $n = 4$. *$P < 0.01$ vs. basal state, #$P < 0.01$ vs. ANP. Data are mean ±s.e.m.

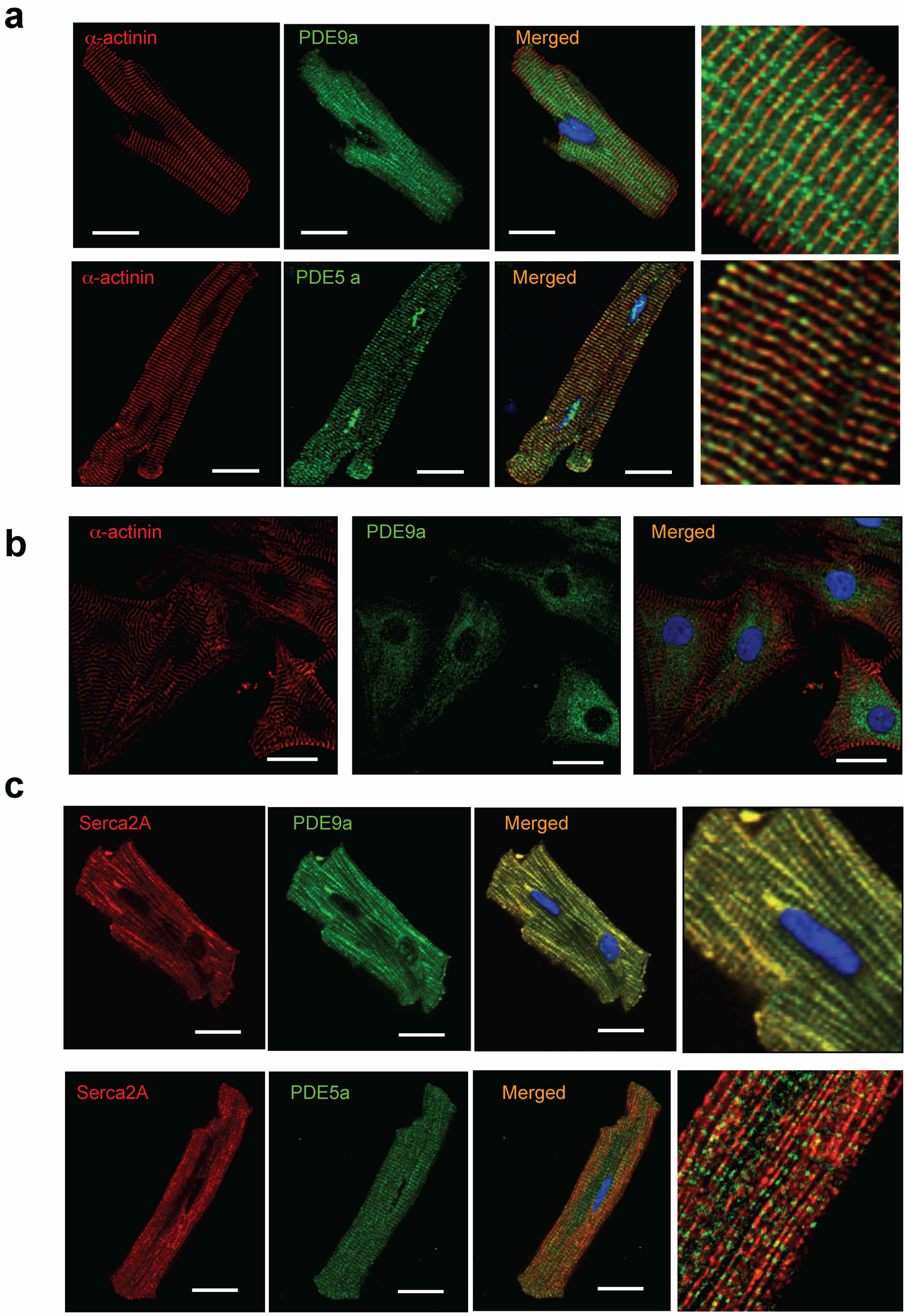

Extended Data Figure 5 | Confocal immunostaining of cardiomyocyte PDE9A and PDE5A. **a**, PDE9A does not co-localize with α-actinin at the Z-band, whereas PDE5A does. **b**, PDE9A does not co-localize with α-actinin in rat neonatal myocytes. **c**, PDE9A co-localizes with T-tubular membranes as defined by antibody staining against the sarcoplasmic reticular ATPase-2 (SERCA2a). This differed from the localization of PDE5A. Scale bars, 20 µm.

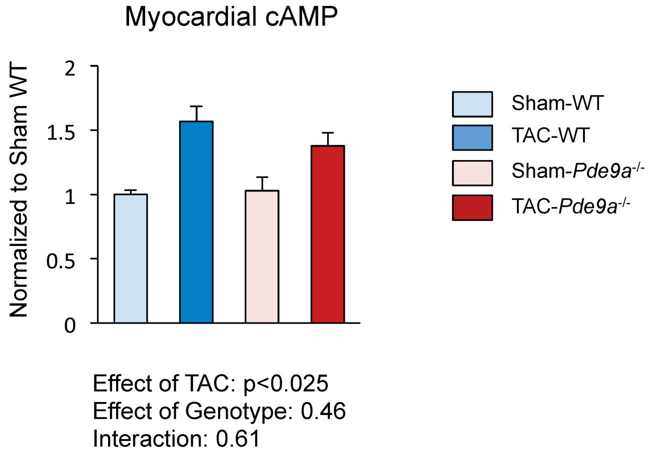

Extended Data Figure 6 | Myocardial cAMP levels in controls (sham wild type) and *Pde9a*$^{-/-}$ mice before and after TAC. The cAMP levels were increased in TAC wild type, but they were not affected by modulation of PDE9A expression. Sham wild type, $n = 4$; TAC wild type, $n = 5$; sham *Pde9a*$^{-/-}$ $n = 6$; TAC *Pde9a*$^{-/-}$ $n = 10$. Data are mean ±s.e.m.

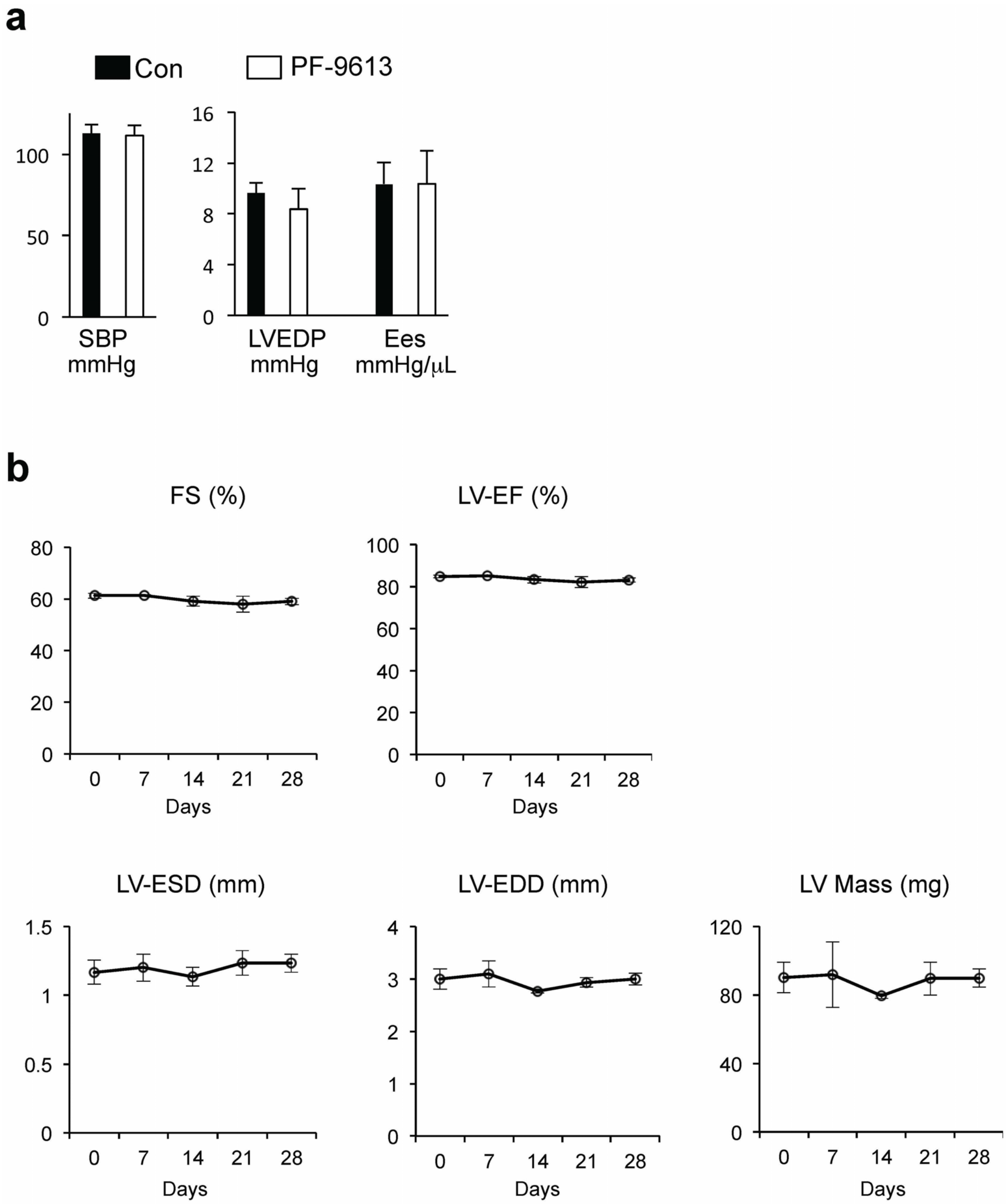

Extended Data Figure 7 | Effect of PF-9613 on blood pressure and cardiac function in mouse. a, Acute administration of PF-9613 by gavage was studied to assess effects on cardiac pressures, and contractility (end-systolic elastance; Ees). Over a 1-h observation period (peak plasma concentrations found after 30 min) there was no change in any of these parameters; $n = 3$. **b**, Chronic treatment of sham control mice with PF-9613 for 3 weeks ($n = 3$) revealed no effect on cardiac function, mass or volumes. EF, ejection fraction; FS, fractional shortening; LV-ESD, left ventricular end-systolic cross-sectional dimension; LV-EDD, left ventricular end-diastolic cross-sectional dimension. Data are mean ±s.e.m.

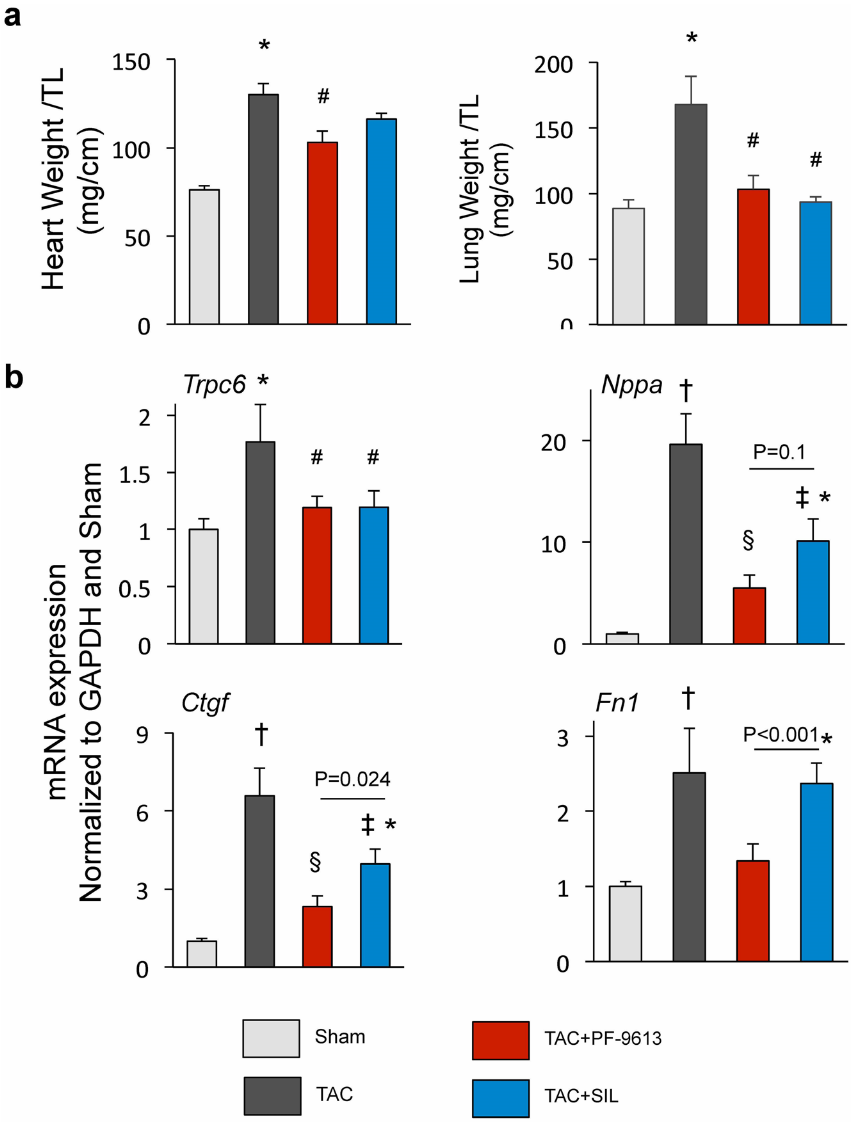

Extended Data Figure 8 | Effect of chronic PDE9A inhibition on left ventricular mass, lung weight and alteration of TAC-responsive genes. **a**, Post-mortem analysis of heart mass and lung weight (both normalized to tibia length) from mice subjected to 5 weeks of pressure overload (TAC) and co-treated with either a vehicle control, PDE9A inhibitor or PDE5A inhibitor. A sham-operation control group is also shown; sham, $n = 6$; TAC, $n = 9$; TAC + PF9613, $n = 9$; TAC + SIL, $n = 5$. **b**, Molecular analysis of TAC-responsive (increased expression) genes, including showing similar reductions from either PDE inhibitor in some (for example, *Trpc6*), a disparity between inhibitors with significant or borderline greater efficacy from PDE9A inhibition in others (for example, *Ctgf*, *Nppa*, $P < 0.02$ and $P < 0.1$, respectively between PDE5A and PDE9A inhibitor response), and substantial disparities in others (for example, *Fn1*, $P < 0.001$ between PDE5A and PDE9A inhibition). Sham, $n = 5$; TAC, $n = 5$; TAC + PF9613, $n = 6$; TAC + SIL, $n = 5$. $^*P < 0.01$ vs. sham; $^\dagger P < 0.001$ vs. sham; $\#P \leq 0.05$; $^\ddagger P < 0.01$; $\S P < 0.001$ vs. TAC. Data are mean ±s.e.m.

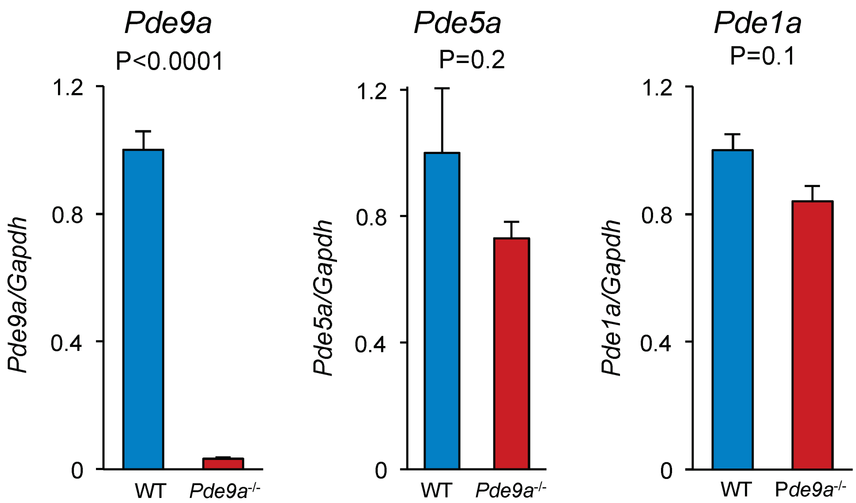

Extended Data Figure 9 | Gene expression of cGMP-hydrolyzing PDEs in *Pde9a*$^{-/-}$ and littermate controls. $n = 10$ per group. The mouse model deleted *Pde9a* gene expression (normalized to *Gapdh*), but did not impact the expression of the two other cGMP-regulating PDEs in mouse: *Pde1a* or *Pde5a*.

Extended Data Table 1 | Clinical characteristics of dilated heart failure and donor control patients

	Non-Failing Controls	Dilated HF	p
Heart Weight/Body Weight (g/kg)	4.9 ± 0.6	7.1 ± 1.0	<0.0001
Ejection Fraction (%)	53.1 ± 2.0	14.3 ± 4.2	<0.0001
Biventricular Pacing (CRT)	0	70%	0.003
History of VT/VF	0	60%	0.01
History of Diabetes	30%	30%	NS
Drugs: Amiodarone	0%	60%	0.01
Beta-blockers	0%	90%	<0.001
ACE-inhibitors	40%	20%	NS
Nitrates	0%	30%	NS

CRT, cardiac resynchronization therapy; VT, ventricular tachycardia; VF, ventricular fibrillation.

doi:10.1038/nature14107

SLC38A9 is a component of the lysosomal amino acid sensing machinery that controls mTORC1

Manuele Rebsamen[1], Lorena Pochini[2], Taras Stasyk[3], Mariana E. G. de Araújo[3], Michele Galluccio[2], Richard K. Kandasamy[1], Berend Snijder[1], Astrid Fauster[1], Elena L. Rudashevskaya[1]†, Manuela Bruckner[1], Stefania Scorzoni[1], Przemyslaw A. Filipek[3], Kilian V. M. Huber[1], Johannes W. Bigenzahn[1], Leonhard X. Heinz[1], Claudine Kraft[4], Keiryn L. Bennett[1], Cesare Indiveri[2], Lukas A. Huber[3] & Giulio Superti-Furga[1]

Cell growth and proliferation are tightly linked to nutrient availability. The mechanistic target of rapamycin complex 1 (mTORC1) integrates the presence of growth factors, energy levels, glucose and amino acids to modulate metabolic status and cellular responses[1–3]. mTORC1 is activated at the surface of lysosomes by the RAG GTPases and the Ragulator complex through a not fully understood mechanism monitoring amino acid availability in the lysosomal lumen and involving the vacuolar H^+-ATPase[4–8]. Here we describe the uncharacterized human member 9 of the solute carrier family 38 (SLC38A9) as a lysosomal membrane-resident protein competent in amino acid transport. Extensive functional proteomic analysis established SLC38A9 as an integral part of the Ragulator–RAG GTPases machinery. Gain of SLC38A9 function rendered cells resistant to amino acid withdrawal, whereas loss of SLC38A9 expression impaired amino-acid-induced mTORC1 activation. Thus SLC38A9 is a physical and functional component of the amino acid sensing machinery that controls the activation of mTOR.

Amino acids are essential for mTORC1 activity, as growth factors cannot efficiently activate mTOR in their absence[5,9]. Notwithstanding the growing number of proteins involved in the activation of mTOR at the lysosomal surface, the molecular nature of the amino acid sensing mechanisms have remained elusive[1,2,4,9–13]. Several members of the solute carrier (SLC) group belonging to families capable of transporting amino acids at the plasma membrane have been shown to regulate mTOR activity[14], raising the possibility that SLCs may also be involved in the lysosomal sensing. We hypothesized the existence of an ubiquitously expressed SLC belonging to a family competent for amino acid transport[15] with a subcellular localization compatible with lysosomal amino acid sensing. Among the list of SLCs robustly expressed in two different cell lines, we focused on member 9 of the SLC38 family as it was completely uncharacterized, showed vesicular staining[16] and had been associated to lysosomes by proteomic analysis[17] (Extended Data Fig. 1a). The SLC38 family contains eleven members, and is part of a phylogenetic cluster of amino acid transporters comprising the SLC32 and SLC36 families[18] (Extended Data Fig. 1b). SLC38A9 is predicted to encompass eleven transmembrane helices and a 120-residue cytoplasmic amino-terminal region. Treatment with peptide-*N*-glycosidase (PNGase) F showed that SLC38A9 is highly glycosylated and enabled detection of the endogenous protein (Extended Data Fig. 2a, b). Supporting a possible role in growth regulatory pathways, silencing of SLC38A9 by short hairpin RNA (shRNA) in HEK293T cells resulted in a reduction of cell size and cell proliferation (Extended Data Fig. 2c, d).

To test whether SLC38A9 would associate with the complex regulating mTORC1, we engineered HEK293 cells to express tagged SLC38A9 in an inducible fashion and verified the localization of the protein to lysosomes (Extended Data Fig. 3a–c). We purified endogenously assembled protein complexes using tandem affinity purification (TAP) coupled to one-dimensional gel-free liquid chromatography tandem mass spectrometry (LC–MS/MS). The gel-free approach was critical as upon boiling SLC38A9 formed insoluble aggregates that failed to enter sodium dodecyl sulfate–polyacrylamide gels (SDS–PAGE; Extended Data Fig. 2e, f). The analysis identified all the five members of the Ragulator/LAMTOR complex and the four RAG GTPases (known as RAGA–D or RRAGA–D) as specific interactors of SLC38A9 (Fig. 1a, Extended Data Fig. 3d). Such collective high sequence coverage of all components of the Ragulator–RAG GTPases complex strongly indicated that SLC38A9 was an additional uncharacterized member. When co-expressed in HEK293T cells, SLC38A9 co-immunoprecipitated with LAMTOR1 and overexpressed LAMTOR1 bound endogenous SLC38A9 (Fig. 1b, c). We validated complex membership entirely at the endogenous level in different cell lines. Immunoprecipitation of SLC38A9 resulted in the specific recruitment of endogenous RAGA and LAMTOR1 and, conversely, immunoprecipitated RAGA bound SLC38A9 (Fig. 1d). This association was not observed when SLC38A9 was silenced, confirming specificity. Association of endogenous SLC38A9 and RAGA was demonstrated in HeLa and K562 cells (Fig. 1e, f) and in murine NIH/3T3 fibroblasts and RAW 264.7 macrophages (Extended Data Fig. 2g, h). To further challenge specificity, we applied the identical proteomic strategy to the two highest expressed members of the SLC38 family, SLC38A1 and SLC38A2, and SLC36A1 (also known as PAT1), which has been previously associated with the Ragulator–RAG GTPase complex[19]. Despite very high bait recovery, none of the Ragulator–RAG GTPase complex members was identified among the interactors, highlighting that the association of SLC38A9 with this complex is a unique property of this family member (Extended Data Fig. 3d). Moreover, when we immunoprecipitated SLC38A9, SLC38A1, SLC38A2, SLC36A1 as well as a lysosomal member of the SLC38 family, SLC38A7 (ref. 20) and a second member of the SLC36 family, SLC36A4 (also known as PAT4), only SLC38A9 co-immunoprecipitated endogenous LAMTOR1, LAMTOR3, RAGA and RAGC, with both low and high expression levels (Fig. 1g).

Immunostaining of tagged SLC38A9 in HeLa cells revealed extensive colocalization with the late endosome/lysosome markers LAMP1, CD63 and the late endosome/multivesicular bodies lipid LBPA, but not with early endosome (EEA1) or Golgi (giantin) markers (Fig. 1h–j, Extended Data Fig. 4a, b). This supports SLC38A9 being a lysosomal component of the Ragulator–RAG GTPase complex.

Full membership to this multiprotein complex would entail physical association with any of the several detected members in reciprocal purifications. We performed affinity purification coupled to mass spectrometry analysis with LAMTOR1, 3, 4 and 5, as well as RAGA and RAGC GTPases. At the core of the interacting network obtained by combining the six independent purifications we found all the expected members of the Ragulator–RAG GTPases complex, RAPTOR as well as SLC38A9 (Fig. 2a, Extended Data Fig. 5a). The overall low sequence

[1]CeMM Research Center for Molecular Medicine of the Austrian Academy of Sciences, 1090 Vienna, Austria. [2]Department DiBEST (Biology, Ecology and Earth Sciences), University of Calabria, 87036 Arcavacata di Rende, Italy. [3]Biocenter, Division of Cell Biology, Innsbruck Medical University, 6020 Innsbruck, Austria. [4]Max F. Perutz Laboratories, University of Vienna, 1030 Vienna, Austria. †Present address: Institute of Medical Chemistry, Medical University of Vienna, 1090 Vienna, Austria.

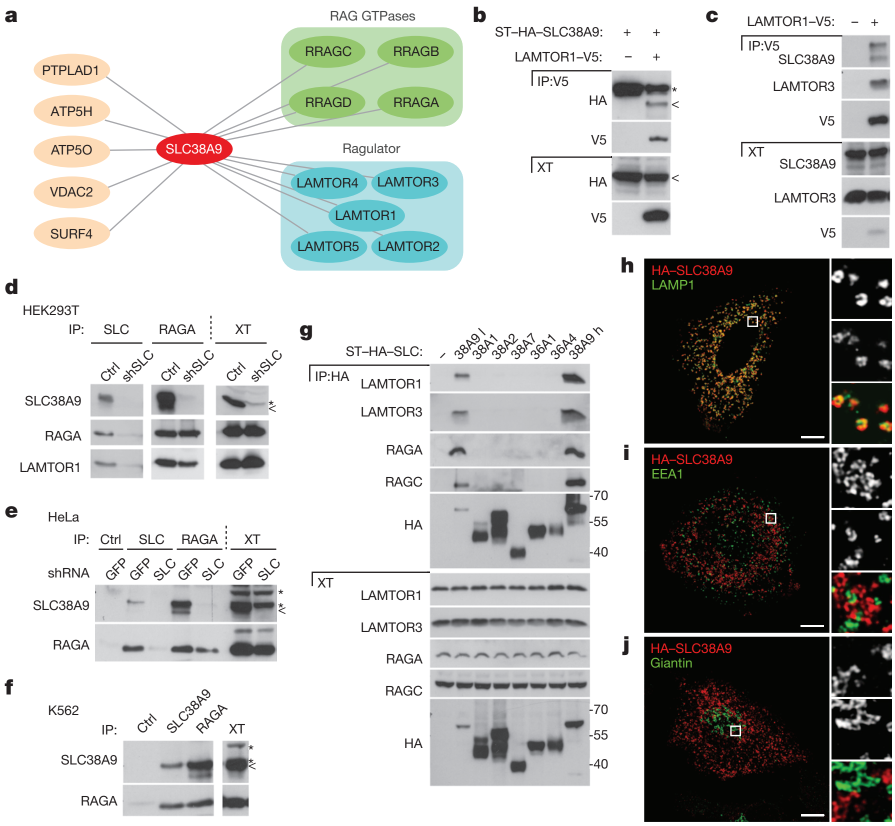

Figure 1 | SLC38A9 is a lysosomal component of the amino acid sensing machinery controlling mTORC1. **a**, Interactors of SLC38A9 identified by TAP–LC–MS/MS. Data shown are based on two independent experiments ($n = 2$), each analysed in two technical replicates. **b**–**g**, Lysates from HEK293T cells transfected with the indicated tagged constructs or empty vector (−) (**b**, **c**, **g**), control (empty vector or shGFP) or shSLC38A9-transduced HEK293T (**d**) and HeLa (**e**), or K562 (**f**) cells were subjected to immunoprecipitation. PNGase-treated immunoprecipitates (IP) and protein extracts (XT) were analysed by immunoblot with the indicated antibodies. Results are representative of two independent experiments ($n = 2$). <, ST-HA-SLC38A9; *, non-specific band. HA, haemagglutinin; ST, streptavidin; V5, V5 epitope tag. **h**–**j**, Confocal microscopy images of HeLa cells transfected with tagged SLC38A9 construct and immunostained with anti-HA and LAMP1 (**h**), EEA1 (**i**) or giantin (**j**) antibodies. Representative cells are shown. Scale bar, 10 μm.

coverage of SLC38A9 could be ascribed to inefficient proteolytic cleavage of the inaccessible transmembrane portions of the protein as it mirrored the coverage obtained when SLC38A9 was used as bait (Extended Data Fig. 5b, c). The interaction of endogenous SLC38A9 with all baits was confirmed by immunoprecipitation (Fig. 2b, c). The quality of the proteomic survey was also indicated by detection of the subunit VA0D1 of the v-ATPase complex[7] and the FLCN–FNIP2 complex[11]. Interestingly, we did not detect any other SLC member of the amino acid transporter families in any of the purifications with the members of Ragulator/GTPases complex, indicating that SLC38A9 is, at least in this cellular system, the only prominently interacting SLC.

Deletion studies indicated that the N-terminal cytoplasmic tail of SLC38A9 (amino acids 1–112), devoid of any transmembrane region, was sufficient and required to bind the Ragulator–RAG GTPases complex,

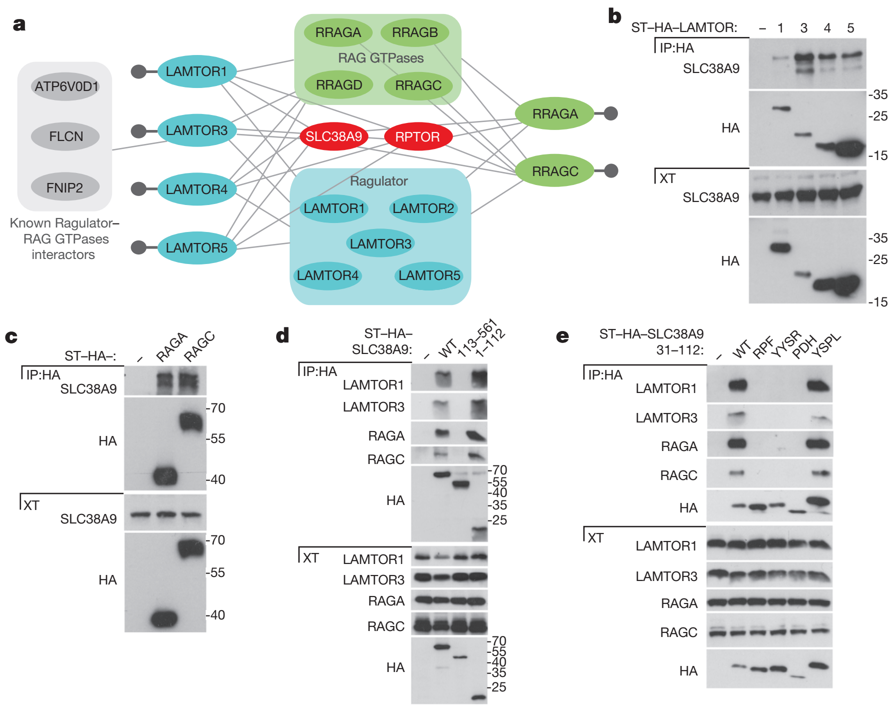

Figure 2 | SLC38A9 is an integral component of the Ragulator–RAG GTPases machinery. **a**, Interactors of LAMTOR1, LAMTOR3, LAMTOR4, LAMTOR5, RAGA and RAGC were identified by TAP–LC–MS/MS. Proteins that interacted with all the bait proteins are shown, with the addition of RAGD that was not detected in RAGC pull-down. Previously published interactors of the Ragulator–RAG GTPases complex detected are indicated. Data shown are based on two independent experiments for each condition ($n = 2$), each analysed in two technical replicates. **b**–**e**, HEK293T cells were transfected with the indicated tagged constructs or empty vector (−). Immunoprecipitates and cell extracts were treated with PNGase and analysed by immunoblot. SLC38A9 mutant constructs are labelled with the number of the encoded amino acids (**d**) or with the amino acid motif substituted to alanine (**e**). Results are representative of two independent experiments ($n = 2$). Long exp., long exposure. WT, wild type.

whereas this interaction was completely lost when the remaining eleven transmembrane-containing region (113–561), which retains lysosomal localization, was used (Fig. 2d, Extended Data Fig. 4c, d). We further mapped the minimal interacting region to amino acids 31–112 and identified four conserved motifs in this portion (Extended Data Fig. 6a, b). Mutation of any of the first three motifs completely abolished binding, while disruption of the fourth had no effect (Fig. 2e, Extended Data Fig. 6c). Importantly, none of the described mutations affected lysosomal targeting of SLC38A9 (Extended Data Fig. 4e–h). Whereas the N-terminal cytoplasmic region is evolutionarily conserved across SLC38A9 proteins, we could not detect any significant homology with the N-terminal region of any other SLC38 family member. These results defined the unique cytoplasmic portion of SLC38A9 as responsible for the interaction with the lysosomal mTOR-activating machinery.

SLC38 family members are commonly competent for the transport of glutamine[18,20] which, together with leucine and arginine, are considered the main amino acids involved in the regulation of mTORC1[9,14,21]. We monitored the transporter competence of SLC38A9 towards these amino acids in liposomes reconstituted with purified recombinant SLC38A9 (Extended Data Fig. 7a). In proteoliposomes, the cytoplasmic tail was located at the outside face of the vesicles, corresponding to the orientation observed in lysosomes (Extended Data Fig. 7b). Addition of [^{3}H]glutamine resulted in a time-dependent transport (Fig. 3a) that required intraliposomal sodium, but not addition of external sodium, and was most active at acidic pH (pH 5.5–6.5) (Extended Data Fig. 7c and e, not shown), consistent with the lysosomal localization of the natural protein. Moreover, point mutation of the putative sodium-binding site (N128A)[22] moderately affected transport (Extended Data Fig. 7d). Membrane potential artificially created by potassium gradients in the presence of valinomycin[23] both positive outside or inside did not influence the transport activity of SLC38A9 (not shown). Competition experiments showed that some polar amino acids were capable of competing efficiently for glutamine transport whereas MeAIB, an inhibitor of system A SLC38 family members, had no effect (Fig. 3b, Extended Data Fig. 7f). Direct transport assays further revealed SLC38A9 competence for [^{3}H]arginine and [^{3}H]asparagine, but not for [^{3}H]leucine or [^{3}H]histidine (Fig. 3c). The low ability of arginine to compete with glutamine transport, as previously reported also for SLC38A7 (ref. 20), may reflect differences in binding and/or transport properties for the two amino acids. The initial uptake rate calculated for 10 μM glutamine was 0.42 ± 0.10 nmol mg^{-1} of protein per minute, which is moderate when compared to other reconstituted transporters[23]. If a physiological role of SLC38A9 is to assess the intralysosomal availability of amino acids, then it is also relevant to measure its efflux-enabling activity. We monitored efflux of [^{3}H]glutamine from proteoliposomes and measured a rate of 1.7 ± 0.30 nmol mg^{-1} min^{-1} (Fig. 3d), which is higher than the uptake but overall still lower than several other amino acid transporters measured with the same approach[23]. This suggests that SLC38A9 may be a low-capacity transporter similar to SLC38A7 (ref. 20) and resembling the properties of amino acid sensors described in yeast[24] and *Drosophila*[25].

The ability of RAG GTPase heterodimers to recruit mTOR by binding Raptor is critically dependent on the nucleotide loading status and the resulting conformation of the two GTPase partners[5]. By immunoprecipitating different combinations of RAGA/B–RAGC nucleotide-binding mutant heterodimers we could recapitulate the regulated interactions with RAPTOR and LAMTOR proteins[8,11] and observed that SLC38A9 binding to RAG GTPases was markedly influenced by their

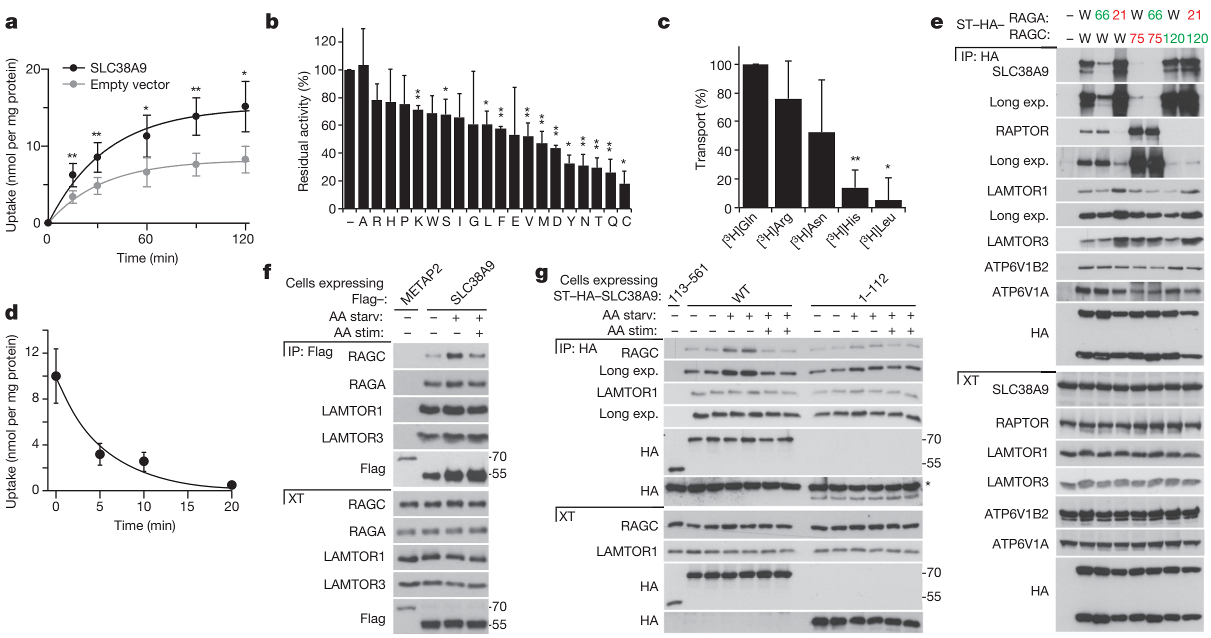

Figure 3 | SLC38A9 transports amino acids and interacts with the RAG GTPases in a nucleotide-loading and amino-acid-sensitive manner. a, Time course of [^{3}H]glutamine uptake in proteoliposomes reconstituted with purified SLC38A9 or with control empty vector. Values represent means ± s.d. from eight different experiments ($n = 8$). **b**, Inhibition by amino acids of [^{3}H]glutamine uptake in proteoliposomes. Values represent means of residual activity with respect to control (without added competitor) ± s.d. from three independent experiments ($n = 3$). **c**, Uptake of the indicated [^{3}H]-labelled amino acids by SLC38A9 in proteoliposomes. Values represent means of per cent in respect to glutamine transport measured in the same experiment ± s.d. from three independent experiments ($n = 3$). **d**, Time course of glutamine efflux from proteoliposomes reconstituted with SLC38A9. Values represent means of specific transport ± s.d. from three independent experiments ($n = 3$). **e**, HEK293T cells were transfected with the indicated combination of tagged RAG GTPases mutant constructs or empty vector (−). PNGase-treated immunoprecipitates and cell extracts were analysed by immunoblot. W, wild type; 66, Q66L; 21, T21N; 75, S75N; 120, Q120L. **f**, **g**, HEK293T cells stably expressing the indicated constructs were starved for amino acids and serum for 50 min (AA starv +) and stimulated with amino acids for 20 min (AA stim +). Immunoprecipitates and cell extracts were analysed by immunoblot. In **g** results of two biological replicates are shown. *, IgG light chain. Results are representative of two (**e**, **f**, $n = 2$) or three (**g**, $n = 3$) independent experiments. In **a**–**c** significance was estimated by Student's *t*-test (*$P < 0.01$ or **$P < 0.001$).

mutational state, even more than what was observed for the Ragulator complex (Fig. 3e, Extended Data Fig. 8). The low-affinity nucleotide-binding mutants RAGA(T21N) and RAGB(T54N) showed a strong increase in SLC38A9 recruitment, contrasting with the behaviour of RAGC(S75N) that abolished the binding of SLC38A9 to the heterodimer. GTP-bound RAGA(Q66L)/RAGB(Q99L) mutants showed also reduced SLC38A9 binding (Fig. 3e, Extended Data Fig. 8). These results indicate that the interaction of SLC38A9 with the critical GTPases moieties of the complex is highly conformation-specific. In cells stably expressing tagged SLC38A9, amino acid starvation strengthened the interaction between SLC38A9 and endogenous RAGC and, to a minor extent, RAGA, without significantly affecting LAMTOR1 and LAMTOR3 recruitment (Fig. 3f). Similarly, amino acid stimulation reduced the amount of recruited RAGC and RAGA. Altogether, the amino-acid-sensitive character of these binding properties are evocative of the ones exerted by Ragulator[8] and Folliculin[11] and point to a possible function of SLC38A9 in modulating the nucleotide status of the RAG GTPases. Amino acid sensitivity required the transmembrane region, as the recruitment of RAGC by the N-terminal region alone was not affected by amino acid availability (Fig. 3g). This is consistent with the notion that the eleven transmembrane helices-encompassing region is the moiety physically engaging amino acids and required to convey sensitivity.

Withdrawal of amino acids results in rapid inactivation of mTORC1. Cells stably expressing SLC38A9 showed sustained mTORC1 activation upon amino acid starvation, as monitored by the phosphorylation of the substrates S6 kinase and ULK1 (Fig. 4a, Extended Data Fig. 9a). This resulted in a delayed and reduced induction of autophagy upon amino acid starvation, as shown by quantification of LC3B relocalization to autophagosomes (Fig. 4b, Extended Data Fig. 9b), as well as sustained phosphorylation and delayed nuclear translocation of the transcription factor TFEB[26] (Extended Data Fig. 9c). Sustained mTOR activity triggered by SLC38A9 expression during starvation was inhibited by Torin 1 (Extended Data Fig. 9e). In contrast, the v-ATPase inhibitor concanamycin A had no effect in this setting, whereas it efficiently blocked mTORC1 activation induced by amino acid stimulation (Extended Data Fig. 9e, f). This suggests that the v-ATPase complex and SLC38A9 concur in the control of mTORC1 activity by amino acids. Most likely, the high expression levels of SLC38A9 resulted in an active signalling state that bypasses the v-ATPase input. Indeed, expression of the N-terminal region appears to be sufficient to confer prolonged mTORC1 activation, suggesting that this moiety assumes an active conformation independently of the transmembrane region (Fig. 4c, Extended Data Fig. 9d). Altogether, the data indicate that SLC38A9 is an upstream positive regulator of mTORC1 function.

Accordingly, silencing of SLC38A9 in HEK293T by shRNA resulted in a reduction of amino acid-induced mTORC1 activation (Fig. 4d). Cells left in culture for longer times manifested a weaker phenotype, possibly owing to compensatory adaptive mechanisms (not shown). We therefore silenced SLC38A9 by small interfering RNA (siRNA) and observed suppression of amino acid-induced mTORC1 activation in both HEK293T and HeLa cells with an efficiency that was comparable with knockdown of LAMTOR1 (Fig. 4f, Extended Data Fig. 10a). Depletion of SLC38A9 also impaired mTORC1 activation induced by cycloheximide, which mimics amino acid stimulation by blocking protein synthesis and thus inducing accumulation of intracellular amino acids[5] (Fig. 4e). This further suggests that SLC38A9 participates in mTORC1 activation at the lysosome rather than contributing to the import of extracellular amino acids at the plasma membrane. Moreover, SLC38A9 levels did not appear to be induced upon amino acid starvation, in contrast to several SLCs responsible for importing amino acids at the plasma membrane (Extended Data Fig. 10b, c).

Altogether, the work presented here identifies SLC38A9 as a novel integral component of the lysosomal machinery that controls mTORC1 activity in response to amino acids (Fig. 4g). SLC38A9 is the first member of the entire machinery shown to be competent for binding and transporting amino acids. As other solute carrier proteins, it should be eminently druggable[27]. We failed to observe a strong dependence on SLC38A9 in amino acid stimulation-induced mTOR lysosomal recruitment, which could be due to technical reasons or, more intriguingly, to separate, partly independent mechanisms controlling localization and activation of mTOR. Together with the adaptation observed upon prolonged SLC38A9 silencing, this suggests that additional sensing components are likely to operate in this pathway. Considering the low transport capacity and the physical association with the Ragulator–RAG

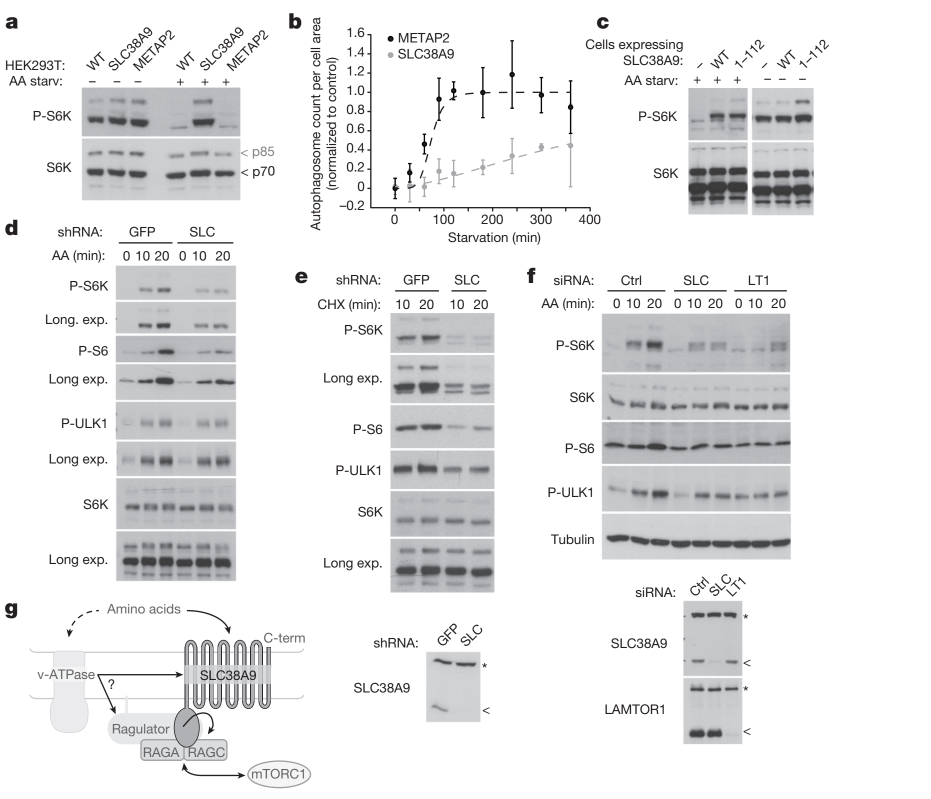

Figure 4 | SLC38A9 is a positive regulator of mTORC1 required for its activation by amino acids. **a**, Wild type, Flag–SLC38A9 or Flag–METAP2 stably expressing HEK293T cells were starved for 30 min in medium without amino acids and serum. Cell lysates were analysed by immunoblot. **b**, HEK293T cells stably expressing EGFP–LC3B and SLC38A9 or METAP2 were starved for the indicated time. LC3B-positive autophagosomes were quantified by image analysis. Data were normalized to cell size and plotted relative to the fitted METAP2 maximum. Mean ± s.d. of at least three replicate wells. **c**, HEK293T cells stably expressing the indicated untagged SLC38A9 constructs were treated and analysed as in **a**. **d**, **e**, HEK293T cells transduced with lentivirus-encoded shRNA against SLC38A9 or GFP were starved for 50 min and then stimulated with amino acids (**d**) or cycloheximide (CHX) (**e**, 25 μg ml^{-1}) for 10 or 20 min. Cell lysates were analysed by immunoblot. **f**, HEK293T were transfected with siRNA targeting SLC38A9, LAMTOR1 or non-targeting control. After 72 h, cells were treated as in **d**. In **e**, **f**, bottom panels, cell lysates were treated with PNGase; *, non-specific band. **g**, Schematic model of SLC38A9 function in amino-acid-induced mTORC1 activation. Results are representative of two (**a**–**e**, $n = 2$) or three (**f**, $n = 3$) independent experiments.

GTPase complex, it is reasonable to consider SLC38A9 a transceptor-type of SLC[24,28–30], reminiscent of yeast amino acid sensors GAP1 and ssy1p, in which amino acid engagement is used for allosteric signal transduction rather than mere transport.

Online Content Methods, along with any additional Extended Data display items and Source Data, are available in the online version of the paper; references unique to these sections appear only in the online paper.

Received 25 October 2013; accepted 20 November 2014.
Published online 7 January 2015.

1. Dibble, C. C. & Manning, B. D. Signal integration by mTORC1 coordinates nutrient input with biosynthetic output. *Nature Cell Biol.* **15,** 555–564 (2013).
2. Laplante, M. & Sabatini, D. M. mTOR signaling in growth control and disease. *Cell* **149,** 274–293 (2012).
3. Cornu, M., Albert, V. & Hall, M. N. mTOR in aging, metabolism, and cancer. *Curr. Opin. Genet. Dev.* **23,** 53–62 (2013).
4. Kim, E., Goraksha-Hicks, P., Li, L., Neufeld, T. P. & Guan, K. L. Regulation of TORC1 by Rag GTPases in nutrient response. *Nature Cell Biol.* **10,** 935–945 (2008).
5. Sancak, Y. *et al.* The Rag GTPases bind raptor and mediate amino acid signaling to mTORC1. *Science* **320,** 1496–1501 (2008).
6. Sancak, Y. *et al.* Ragulator-Rag complex targets mTORC1 to the lysosomal surface and is necessary for its activation by amino acids. *Cell* **141,** 290–303 (2010).
7. Zoncu, R. *et al.* mTORC1 senses lysosomal amino acids through an inside-out mechanism that requires the vacuolar H^+-ATPase. *Science* **334,** 678–683 (2011).
8. Bar-Peled, L., Schweitzer, L. D., Zoncu, R. & Sabatini, D. M. Ragulator is a GEF for the rag GTPases that signal amino acid levels to mTORC1. *Cell* **150,** 1196–1208 (2012).
9. Jewell, J. L., Russell, R. C. & Guan, K. L. Amino acid signalling upstream of mTOR. *Nature Rev. Mol. Cell Biol.* **14,** 133–139 (2013).
10. Bar-Peled, L. *et al.* A tumor suppressor complex with GAP activity for the Rag GTPases that signal amino acid sufficiency to mTORC1. *Science* **340,** 1100–1106 (2013).
11. Tsun, Z. Y. *et al.* The folliculin tumor suppressor is a GAP for the RagC/D GTPases that signal amino acid levels to mTORC1. *Mol. Cell* **52,** 495–505 (2013).
12. Han, J. M. *et al.* Leucyl-tRNA synthetase is an intracellular leucine sensor for the mTORC1-signaling pathway. *Cell* **149,** 410–424 (2012).
13. Panchaud, N., Peli-Gulli, M. P. & De Virgilio, C. Amino acid deprivation inhibits TORC1 through a GTPase-activating protein complex for the Rag family GTPase Gtr1. *Sci. Signal.* **6,** ra42 (2013).
14. Nicklin, P. *et al.* Bidirectional transport of amino acids regulates mTOR and autophagy. *Cell* **136,** 521–534 (2009).
15. Hediger, M. A., Clemencon, B., Burrier, R. E. & Bruford, E. A. The ABCs of membrane transporters in health and disease (SLC series): introduction. *Mol. Aspects Med.* **34,** 95–107 (2013).
16. Uhlen, M. *et al.* Towards a knowledge-based Human Protein Atlas. *Nature Biotechnol.* **28,** 1248–1250 (2010).
17. Chapel, A. *et al.* An extended proteome map of the lysosomal membrane reveals novel potential transporters. *Mol. Cell. Proteomics* **12,** 1572–1588 (2013).
18. Schiöth, H. B., Roshanbin, S., Hagglund, M. G. & Fredriksson, R. Evolutionary origin of amino acid transporter families SLC32, SLC36 and SLC38 and physiological, pathological and therapeutic aspects. *Mol. Aspects Med.* **34,** 571–585 (2013).
19. Ögmundsdóttir, M. H. *et al.* Proton-assisted amino acid transporter PAT1 complexes with Rag GTPases and activates TORC1 on late endosomal and lysosomal membranes. *PLoS ONE* **7,** e36616 (2012).
20. Hägglund, M. G. *et al.* Identification of SLC38A7 (SNAT7) protein as a glutamine transporter expressed in neurons. *J. Biol. Chem.* **286,** 20500–20511 (2011).
21. Duran, R. V. *et al.* Glutaminolysis activates Rag-mTORC1 signaling. *Mol. Cell* **47,** 349–358 (2012).
22. Zhang, Z., Gameiro, A. & Grewer, C. Highly conserved asparagine 82 controls the interaction of Na^+ with the sodium-coupled neutral amino acid transporter SNAT2. *J. Biol. Chem.* **283,** 12284–12292 (2008).
23. Oppedisano, F., Pochini, L., Broer, S. & Indiveri, C. The B degrees AT1 amino acid transporter from rat kidney reconstituted in liposomes: kinetics and inactivation by methylmercury. *Biochim. Biophys. Acta* **1808,** 2551–2558 (2011).
24. Ljungdahl, P. O. Amino-acid-induced signalling via the SPS-sensing pathway in yeast. *Biochem. Soc. Trans.* **37,** 242–247 (2009).
25. Goberdhan, D. C., Meredith, D., Boyd, C. A. & Wilson, C. PAT-related amino acid transporters regulate growth via a novel mechanism that does not require bulk transport of amino acids. *Development* **132,** 2365–2375 (2005).
26. Settembre, C. *et al.* A lysosome-to-nucleus signalling mechanism senses and regulates the lysosome via mTOR and TFEB. *EMBO J.* **31,** 1095–1108 (2012).
27. Giacomini, K. M. *et al.* Membrane transporters in drug development. *Nature Rev. Drug Discov.* **9,** 215–236 (2010).
28. Wu, B. *et al.* Competitive intra- and extracellular nutrient sensing by the transporter homologue Ssy1p. *J. Cell Biol.* **173,** 327–331 (2006).
29. Kriel, J., Haesendonckx, S., Rubio-Texeira, M., Van Zeebroeck, G. & Thevelein, J. M. From transporter to transceptor: signaling from transporters provokes re-evaluation of complex trafficking and regulatory controls. *BioEssays* **33,** 870–879 (2011).
30. Taylor, P. M. Amino acid transporters: eminences grises of nutrient signalling mechanisms? *Biochem. Soc. Trans.* **37,** 237–241 (2009).

Acknowledgements We thank D. M. Sabatini, S. Wang and Z. Tsun for discussing results before publication and generously providing Flag–SLC38A9 and Flag–METAP2 stably expressing cells, all members of the Superti-Furga laboratory for discussions, the Bennett laboratory for the proteomic analyses, F. Pauler and the Barlow laboratory for the RNA-seq analysis and M. Gstaiger for providing expression vectors. This work was supported by the Austrian Academy of Sciences, ERC grant to G.S.-F. (i-FIVE 250179), EMBO long-term and Marie Curie fellowships to M.R. (ALTF 1346-2011, IEF 301663), EMBO long-term fellowship to R.K.K. (ALTF 314-2012), Swiss NSF fellowship (P300P3_147897) to B.S., Vienna Science and Technology Fund (WWTF VRG10-001) and the Austrian Science Fund (FWF P 25522-B20) to C.K., the Italian Ministry of Instruction University and Research, PON-ricerca e competitività 2007-2013 (no. PON01_00937) to C.I., the Austrian Federal Ministry for Science and Research (GenAu projects, APP-III and BIN-III) to L.A.H., K.L.B. and G.S.-F., the Austrian Science Fund MCBO/SFB021 to L.A.H.

Author Contributions M.R. and G.S.-F. conceived the study. L.P., M.G. and C.I. designed and performed transport assays. M.R., T.S., M.E.G.d.A., E.L.R., M.B., K.L.B., L.A.H. and G.S.-F. designed and performed TAP-mass spectrometry experiments. M.R., M.E.G.d.A., B.S., A.F., M.B., S.S. and P.A.F. performed the other experiments. M.R., L.A.H. and G.S.-F. designed the other experiments. R.K.K. and B.S. performed bioinformatic data and image analysis. K.V.M.H., J.W.B., L.X.H., C.K. generated reagents and provided scientific insight. M.R. and G.S.-F. wrote the manuscript. All authors contributed to the discussion of results and participated in manuscript preparation.

Author Information The protein-protein interactions have been submitted to the IMEx (http://www.imexconsortium.org) consortium through IntAct (http://www.ebi.ac.uk/intact/) and assigned the identifier IM-23283. The SLC network has the IntAct accession number EBI-9975668 and the RAGA-RAGC-LAMTOR network is EBI-9975664. RNA-Seq data is available in ArrayExpress (http://www.ebi.ac.uk/arrayexpress) under the accession number E-MTAB-3102. Reprints and permissions information is available at www.nature.com/reprints. The authors declare competing financial interests: details are available in the online version of the paper. Readers are welcome to comment on the online version of the paper. Correspondence and requests for materials should be addressed to G.S.-F. (gsuperti@cemm.oeaw.ac.at).

METHODS

Antibodies. Antibodies used were against SLC38A9 (HPA043785 Sigma), LAMTOR1 (8975 Cell Signaling), LAMTOR3 (8169 Cell Signaling), RAGA (4357 Cell Signaling), RAGC (5466 Cell Signaling), phospho-p70 S6 Kinase (Thr389) (9234 Cell Signaling), phospho-S6 (Ser240/244) (2215 Cell Signaling), phospho-ULK1 (Ser757) (6888 Cell Signaling), raptor (2280 Cell Signaling), ATP6V1B2 (ab73404 Abcam), ATP6V1A (GTX110815 GeneTex), mouse anti-rabbit IgG (conformation-specific) (3678 Cell Signaling), LAMP1 (555798 Pharmingen and ab25630 Abcam), LAMP2 (sc-18822 Santa Cruz), CD63 (H5C6 DSHB), LBPA (Z-PLBPA Echelon, Tebu-bio), EEA1 (sc33585 Santa Cruz), giantin (ab24586 Abcam), p70 S6 kinase (sc-230 Santa Cruz), ULK1 (8054 Cell Signaling), tubulin (ab7291 Abcam), RCC1 (sc55559 Santa Cruz), HA (H6533 Sigma, 3724 Cell Signaling, MMS-101P Covance or sc-805 Santa Cruz), V5 (ab9116 Abcam), His (A7058 Sigma), Flag (F7425 Sigma). The secondary antibodies used were goat anti-mouse AlexaFluor568 (A-11004 and A-11031 Molecular probes), goat anti-rabbit AlexaFluor568 (A-11036 Molecular probes), goat anti-mouse AlexaFluor488 (A-11001 Molecular probes), goat anti-rabbit AlexaFluor488 (A-11008 Molecular probes) and horseradish peroxidase (HRP)-conjugated antibodies (Jackson ImmunoResearch).

Plasmids. Expression constructs were generated by PCR amplification from EST or from plasmids obtained from Addgene (RAGA: Plasmid 19298 (WT) and 19300 (Q66A); RAGB: 19301 (WT) and 19303 (Q99A); RAGC: 19304; EGFP–LC3B: 11645) or from the Harvard Medical School plasmid repository (SLC38A1, SLC38A2, SLC38A7, SLC36A1, SLC36A4) and subcloned by Gateway cloning (Invitrogen) into pTRACER-CV5-GW or pTO-SII-HA-GW[31] with N-terminal tagging for SLC38A9, SLC38A1, SLC38A2, SLC38A7, SLC36A1, SLC36A4, RAGA, RAGB, RAGC and LAMTOR3 (human and mouse) and C-terminal tagging for LAMTOR1, 4 and 5. Point mutations were introduced by site-directed mutagenesis (InvivoGen).

Cells. HEK293T, Raw264.7, NIH/3T3 and K562 cells were obtained from ATCC and DMSZ. HeLa were provided by M. Hentze. HEK293 Flp-In TREx cells that allow doxycycline-dependent transgene expression were from Invitrogen. Cells were kept in DMEM (Sigma) or RPMI medium (PAA Laboratories) supplemented with 10% (v/v) FBS (Invitrogen) and antibiotics ($100\,\mathrm{U\,ml^{-1}}$ penicillin and $100\,\mathrm{mg\,ml^{-1}}$ streptomycin) and checked for mycoplasma by PCR or ELISA.

Transfections, cell lysis, deglycosylation, immunoprecipitations and fractionation. Cells were transfected with Polyfect (Qiagen) and used for experiments after 24 h. For lysis, cells were resuspended in Nonidet-40 lysis buffer (1% NP-40, 50 mM HEPES pH 7.4, 250 mM NaCl, 5 mM EDTA, Halt phosphatase inhibitor cocktail (ThermoScientific), one tablet of EDTA-free protease inhibitor (Roche) per 50 ml) on ice for 5 min. Lysates were cleared by centrifugation in a microcentrifuge (13,000 r.p.m., 10 min, 4 °C). Proteins were quantified with BCA (Pierce). For immunoprecipitations, lysates were precleared on Sepharose6 beads (Sigma) (40 min with rotation, 4 °C) and then incubated either with HA-, V5- or Flag-coupled beads (3 h with rotation, 4 °C) or with primary antibody and protein G-sepharose (GE healthcare) (14 h with rotation, 4 °C). Beads were recovered and washed four times with lysis buffer before analysis by SDS–PAGE and immunoblotting. When required, a mouse anti-rabbit IgG (conformation specific) antibody was used for immunoblot and revealed with an anti-mouse HRP-conjugated antibody to avoid detection of immunoglobulin heavy chains. In case of detection of endogenous SLC38A9, samples were treated with PNGase (NEB, 250 U for 30 µl, 1 h, 37 °C) before SDS–PAGE. Nuclear-cytoplasm cell fractionation was performed as previously described[32].

Generation of stably expressing cells. HEK293T cells expressing codon-optimized Flag-tagged SLC38A9 isoform 1 (GenScript) were generated using a modified pLKO.1 lentiviral vector having a CMV promoter (pLJM60). Lentiviruses were produced by co-transfection of the lentiviral transfer vector with the ΔVPR envelope and CMV VSV-G packaging plasmids into HEK293T cells using the XTremeGene 9 transfection reagent (Roche). The media was changed 24 h post-transfection to DMEM supplemented with 30% IFS. Virus-containing supernatants were collected 48 and 72 h after washing, filtered and used for spin infection (2,200 r.p.m. for 1 h) of target HEK293T cells in presence of $8\,\mathrm{\mu g\,ml^{-1}}$ polybrene. 24 h after infection, the virus was removed and the cells selected with puromycin. HEK293T expressing codon-optimized untagged or ST-HA-tagged SLC38A9 (GenScript) full length, C-terminal (113–561) or N-terminal region (1–112) were generated using a modified pMSCV retroviral vector. Cells expressing EGFP-LC3B or TFEB-STHA were generated by infecting Flag–SLC38A9 or Flag–METAP2 stable cells using a modified pMSCV retroviral vector and blasticidin selection.

RNAi. For shRNA-mediated knockdown, shRNA-encoding pLKO.1 targeting SLC38A9 (ThermoFisher, TRCN0000151238) or GFP (ThermoFisher, RHS4459) were used. Lentiviruses were produced using second-generation packaging plasmids pMD2-VSVG and pCMV-R8.91. HEK293T cells were co-transfected with packaging plasmids and the shRNA-encoding plasmids. Cells were washed 16 h after transfection. Virus-containing supernatants were collected 24 h after washing, filtered and used for infection. After 48 h of infection, HEK293T cells were selected with puromycin ($4\,\mathrm{\mu g\,ml^{-1}}$) and used for experiments from 3 to 7 days later. For siRNA-mediated knockdown, HEK293T cells were transfected with Lipofectamine RNAiMAX (Invitrogen) with 30 nM of siRNA pool; HeLa with HiPerfect (Qiagen) with 60 nM of siRNA pool. After 48 h cells were seeded and subjected 24 h later to amino acid stimulation as described. ON-TARGETplus SMARTpool against SLC38A9 (L-007337-02, target sequences: ACACUGAAGGAUACGGUAA, GAUCCUGGACCUAUGAAUA, GAAGAGUGCUAUGUGUAUA, CAUGUCAUUCAGAGGGUUA), LAMTOR1 (L-020916-02, target sequences: UCUCCAGGAUAGCUGCUUA, GGCUUAUACAGUACCCUAA, AAGUGAGGGUAGAACCUUU, GUUUGUCACCCUCGAUAAA) and non-targeting pool (D-001810-10) were from ThermoScientific.

Proteomics. Flp-in HEK293 T-Rex cell lines inducibly expressing ST-HA-tagged SLC38A9, SLC38A1, SLC38A2, SLC36A1, RAGA, RAGC, GFP or LAMTOR complex subunits were generated as described[33]. Tandem affinity STREP-HA purifications were performed as previously described[31]. In brief, cells were stimulated with doxycycline/tetracycline for 24 h to induce expression of ST-HA-tagged bait proteins. LAMTOR3 pull-downs were done using murine protein version and performed after 9 h starvation in serum-free medium. Protein complexes were isolated by TAP using streptavidin agarose followed by elution with biotin, and a second purification step using HA–agarose beads. Proteins were eluted with 100 mM formic acid, neutralized with triethylammonium bicarbonate (TEAB) and digested with trypsin, and the peptides were analysed by LC–MS/MS.

MS data analysis and interaction data filtering. Peak list data were extracted from RAW files using ProteoWizard (release 3.0.3201, http://proteowizard.sourceforge.net/) and searched against human SwissProt database version v2013.01_20130110 (37,261 sequences and common contaminants). The search engines MASCOT (v2.3.02, MatrixScience, London, UK) and Phenyx (v2.5.14, GeneBio, Geneva, Switzerland)[34] were used. The searches were submitted to MASCOT using in-house perl scripts at precursor and fragment ions mass tolerances ± 10 p.p.m. and ± 0.6 Da, respectively. Using the high-confidence identifications from this search, precursor and fragment ion masses were recalibrated for a second-pass search on MASCOT and Phenyx with precursor and fragment ions mass tolerances ± 4 p.p.m. and ± 0.3 Da, respectively. One tryptic missed-cleavage was permitted. Carbamidomethyl cysteine and oxidized methionine were set as fixed and variable modifications, respectively. A false discovery rate of <0.25% and <0.1% were used for proteins and peptides, respectively, as described[35]. SAINT AP-MS filtering software[36] was used to filter the interactions using GFP TAP as negative control. All prey proteins with a SAINT AvgP of >0.95 were identified as high-confidence interactors. In addition, proteins with a spectral count of 1 or a CRAPome[37] frequency of >0.1 were excluded. For the LAMTOR-RAG network, we retained only those proteins that interacted with all the bait proteins (RAGD was not detected in RAGC pull-down).

Immunofluorescence. HEK293T cells were plated on fibronectin-coated glass coverslips and, after 16 h, induced with doxycycline. After 24 h, cells were washed with PBS, fixed (PBS, 4% formaldehyde) and permeabilized (PBS, 0.3% saposin, 10% FBS). Slides were incubated with anti-HA (sc-805 Santa Cruz), anti-LAMP1 (ab25630 Abcam) or anti-LAMP2 (sc-18822 Santa Cruz) antibodies (1 h, 25 °C, PBS, 0.3% saposin, 10% FBS). After three washes slides were incubated with goat anti-mouse AlexaFluor568 or anti-rabbit AlexaFlour488 antibodies (Invitrogen, 1 h, 25 °C, PBS, 0.3% saposin, 10% FBS). After DAPI staining, slides were washed three times and mounted on coverslips with ProLong Gold (Invitrogen). Images were taken with a Zeiss Laser Scanning Microscope (LSM) 700. Images were exported from lsm files to tiff files, and analysed using custom Matlab code. Nuclei and cell outlines were detected based on the DAPI and combined immunofluorescence stains respectively, and colocalization measurements were restricted to cytoplasmic regions. Colocalization was measured as the percentage of SLC38A9 (green) pixel values above background that are also above background in the LAMP1 or LAMP2 (red) channel. The SLC38A9 and LAMP1 or LAMP2 colocalization was verified to be robust to variations in the background threshold, and also shows up as significant pixel value correlations between the red and green channels.

HeLa cells were seeded to 80% confluency for transfection (Lipofectamine LTX, Invitrogen). 24 hours post transfection, cells were split into glass coverslips and incubated for another 24 hours. Cells were then washed with PBS and fixed in 4% PFA in cytoskeleton buffer (20 mM PIPES pH 6.8, 150 mM NaCl, 5 mM EGTA, 5 mM glucose and 10 mM $MgCl_2$). Permeabilization and blocking were preformed simultaneously by incubating the cells in cytoskeleton buffer supplemented with 0,025% saponin and 50 mM NH_4Cl. Cells were then incubated with primary antibodies diluted in blocking buffer for 2 hours at room temperature. Cells were then washed 6 times in cytoskeleton buffer supplemented with 50 mM NH_4Cl and incubated with the secondary antibodies diluted in blocking buffer for 45 min at room temperature. Upon washing 6 times in cytoskeleton buffer supplemented with 50 mM NH_4Cl, the coverslips were mounted using Vectashield hardening medium (vectorlabs). *Z*-stack images were taken with an SP5 Laser Scanning confocal Microscope (Leica) and a ×63x oil immersion objective (na 1.4). Original images

were deconvoluted using Huygens professional Deconvolution and Analysis Software (Scientific Volume imaging). The *Z*-stack ids files were then visualized in ImageJ (open source version), converted into a colour stack image and a representative *Z* plane was selected. The single plane images were finally converted to Adobe Photoshop CS6 format. Representative cells are shown in all figures at the same exposure and magnification.

Cell size and autophagosome measurements. HEK293T cells transduced with shRNA against SLC38A9 or GFP cells were seeded 24 h before fixation (PBS, 4% formaldehyde), permeabilized (PBS, 0.3% Saposin, 10% FBS) and stained with DAPI. Images were taken by automated microscopy using the PerkinElmer Operetta with ×20 magnification in confocal mode. Images were analysed using CellProfiler (http://www.cellprofiler.org), CellClassifier (http://www.pelkmanslab.org/?page_id=63), Population Context measurement code (https://www.pelkmanslab.org/?page_id=1150) and custom Matlab code written specifically for this study. CellProfiler was used to detect individual nuclei on each image, and iterative machine learning using CellClassifier was applied to detect properly segmented interphase nuclei. Population context measurement code was used to measure the local cell density of each individual cell, and cell size measurements were restricted to sparse cells to avoid local crowding from confounding the measurements. We used the typical nucleus diameter (that is, the diameter of a circle with the same area as that measured for each nucleus) as a robust proxy for cell size[38]. We confirmed that the cell size reduction induced by SLC38A9 shRNA treatment were present for a broad range of different local cell densities. EGFP–LC3B and SLC38A9 or METAP2 expressing cells were seeded in 96-well plates for imaging. After 24 h cells were washed with PBS and starved for amino acids and serum for the indicated time. Three by three images were acquired per well with the Operetta at ×20 magnification on living cells to minimize disruption of EGFP–LC3B-positive autophagosomes. After imaging cells were fixed, DAPI-stained and reimaged. Autophagosomes were quantified from the GFP channel using custom Matlab analysis, based on a thresholding of the integrated Laplacian of Gaussian transformation for diameters between 8 and 30 pixels. Candidate spots with a local GFP-signal enrichment of less than 42% were discarded, and remaining spots were considered autophagosomes, and normalized to the cell number and area for each condition. Each condition was measured in three replicate wells accounting for over 85,000 cells. Adjusted hill curves were fit and data were normalized to the maximum fitted value in the METAP2 control cell line.

Cell proliferation measurements. HEK293T cells transduced with shRNA against SLC38A9 or GFP were seeded and counted every 24 h using Casy (Roche).

Amino acids starvation and stimulation. HEK293T cells grown in RPMI were washed with PBS and starvation was performed by incubating the cells for 50 min in amino-acid-free RPMI without serum. Cell were then stimulated for 10 or 20 min by the addition of RPMI containing a two-time concentrated solution of amino acids. After stimulation, the final concentration of amino acids in the media was the same as in RPMI. In case of cycloheximide treatment, amino-acid-starved cells were stimulated by addition of cycloheximide diluted in amino-acid-free RPMI at a final concentration of 25 μg ml^{-1}. HeLa cells grown in RPMI were stimulated for 10 or 20 min by the addition of RPMI containing a two time concentrated solution of amino acids and insulin (1 μM final concentration, Sigma, I9278). Concanamycin A (sc202111 Santa Cruz) was used at 5 μM and torin 1 (4247, Tocris Bioscience) at 250 nM. Amino-acid-free RPMI medium powder (R8999-04A, US biological) was complemented with sodium bicarbonate and sodium phosphate, dissolved in water, adjusted to pH 7.4 and filtered. RPMI containing a two time concentrated solution of amino acids was obtained by complementing amino-acid-free RPMI medium with RPMI 1640 amino acids solution (R7131, Sigma), adjusted to pH 7.4 and filtered. L-glutamine (59202C, Sigma) was added shortly before usage.

RNA sequencing. RNA was extracted using TRI reagent (SIGMA), treated with DNase I (DNA free kit, Ambion) and RiboZero kit (Epicentre) to remove ribosomal RNA. The library was prepared using ScriptSeq kit version 1 (Epicentre, strand-specific library). Sequencing was performed on Illumina HiSeq 2000. Sequence reads in fastq format was aligned against RefSeq hg19 build (as downloaded on 2.9.2011) using TopHat and FPKM (fragments per kilobase of exon per million fragments mapped) values were calculated using Cufflinks.

qPCR. Total RNA was isolated using the RNeasy Mini Kit (Qiagen). RNA was reverse transcribed using oligo(dT) primers using RevertAid Reverse Transcriptase (Fermentas). Quantitative PCR was carried out on a RotorGene RG-600 (Qiagen) PCR machine using the SensiMix SYBR kit (Bioline). Results were quantified using the $2^{-\Delta\Delta C(t)}$ method, using GAPDH expression levels for normalization.

Primers : SLC38A9_Fw : TCCTTTGGGCAGTGGTCGAG,_Rev : ACTCCCG GCACTTGGACAAA; GAPDH_Fw : GAAGGTGAAGGTCGGAGT, Rev : GAA GATGGTGATGGGATTTC.

Cloning, expression and purification of recombinant human SLC38A9. The human SLC38A9 cDNA was optimized according to *Escherichia coli* codon usage by GenScript. In this optimized gene, the Codon Adaptation Index (CAI) was upgraded from 0.63 (wild type) to 0.87, the GC content and unfavourable peaks were optimized to prolong the half-life of the mRNA and a ribosome binding site was removed. The optimized cDNA was then sub-cloned into expression vector (pH6EX3-His$_6$-hSLC38A9)[39]. The plasmid was used to transform *E. coli* Lemo21(DE3)pLysS (NEB). Selection on LB-agar was performed as previously described[39]. 0.1 mM rhamnose was added to modulate RNA polymerase expression. After addition of 0.4 mM IPTG cells were grown at 39 °C for 2 h. Cells were treated as previously described[39]. The protein patterns of the cell lysate fractions were analysed by SDS–PAGE. The insoluble cell fraction (about 1.5 mg proteins) from cells expressing SLC38A9 or empty vector transfected cells, was washed with 100 mM Tris/HCl and resuspended in 100 mM β-mercaptoethanol, 3.5 M urea, 0.5% sarkosyl, 200 mM NaCl, 10% glycerol, 20 mM Tris/HCl pH 8.0 and centrifuged at 12,000*g* for 10 min at 4 °C. The resulting supernatant (about 1 ml) was applied onto a column (0.5 cm × 2.5 cm) filled with His select nickel affinity gel (Sigma) pre-conditioned with 8 ml of 0.1% sarkosyl, 200 mM NaCl, 10% glycerol, 10 mM Tris/HCl pH 8.0. The elution was performed with 10 ml of 0.1% $C_{12}E_8$, 150 mM NaCl, 10% glycerol, 5 mM DTE, 10 mM Tris/HCl pH 8.0 (washing buffer), 1.4 ml of the same buffer plus 10 mM imidazole; then the purified protein fraction (4–7 μg protein) was eluted by 1.4 ml of the same buffer plus 50 mM imidazole.

Reconstitution of SLC38A9 in proteoliposomes and transport measurements. The purified fractions from SLC38A9 or empty vector preparation were reconstituted by removing the detergent as previously described[40] with a batch-wise procedure from a mixture of 400 μl of protein (about 2 μg protein in 0.1% $C_{12}E_8$, β-mercaptoethanol 6 mM, 10% glycerol, 20 mM Tris/HCl pH 8.0, 150 mM NaCl, 50 mM imidazole), 80 μl of 10% $C_{12}E_8$, 100 μl of 10% egg yolk phospholipids (w/v), 20 mM HEPES/Tris pH 6.5. 600 μl of proteoliposomes were passed through a Sephadex G-75 column (0.7 cm diameter × 15 cm height) preequilibrated with 20 mM HEPES/Tris pH 6.5. Transport (uptake) measurement was started adding 10 μM [^{3}H]glutamine or other radioactive substrates as indicated (0.5 μCi nmol^{-1}) to 100 μl proteoliposomes aliquots at 25 °C. Transport was stopped by applying each sample of proteoliposomes on a Sephadex G-75 column (0.6 × 8 cm) to separate the external from the internal radioactivity. In competition experiments, the indicated amino acids (1 mM) were added together with [^{3}H]glutamine (10 μM) and transport was measured at 60 min. For efflux measurements, aliquots of the same pool of proteoliposomes passed through a Sephadex G-75 column (0.7 cm diameter × 15 cm height) preequilibrated with 20 mM HEPES/Tris pH 6.5 were incubated with external 10 μM [^{3}H]glutamine. After 120 min of loading, proteoliposomes were passed again through a Sephadex G-75 column (0.7 cm diameter × 15 cm height) preequilibrated with 20 mM HEPES/Tris pH 6.5, for removing the residual external radioactivity. The time course of [^{3}H]glutamine efflux was then measured stopping the efflux reaction at each time interval by applying proteoliposome samples on a Sephadex G-75 column (0.6 × 8 cm) to separate the external from the internal radioactivity. In both uptake and efflux assays, proteoliposomes eluted with 1 ml 50 mM NaCl were collected in scintillation cocktail for counting. The amount of reconstituted recombinant protein was estimated as previously described[39]. Time course data were interpolated by a first order rate equation from which the initial rate of transport was calculated as k x transport at equilibrium. [3,4-^{3}H(N)]L-Glutamine from PerkinElmer; [ring-2,5-^{3}H]L-histidine, [^{3}H]L-asparagine from Campro Scientific.

Orientation of SLC38A9 in proteoliposomes. After purification, His-SLC38A9 was incubated overnight at 37 °C in absence or in presence of 1 U thrombin (GE healthcare) and then assayed by immunoblotting using anti-His or anti-SLC38A9 antibody. To assess the orientation of SLC38A9, reconstituted proteoliposomes were centrifuged at 108,000*g* for 90 min, resuspended in 20 mM HEPES/Tris pH 6.5, incubated overnight at 37 °C with 1 U thrombin in the same conditions of the purified protein. After incubation proteoliposomes were dissolved by 2.5% SDS and 0.2 M Tris/HCl pH 6.8. and immunoblotting analysis was performed as described for the purified protein.

Assay of pH and intraliposomal sodium dependence of the SLC38A9 function. Reconstitution was performed in 20 mM HEPES/Tris buffer at different pH. Transport (uptake) was started by adding to proteoliposomes10 μM [^{3}H]glutamine in 20 mM HEPES/Tris buffer at the same pH of the reconstitution mixture and stopped after 30 min. To test sodium dependency, SLC38A9 was purified omitting NaCl from elution buffer. Reconstitution was performed in the absence or in the presence of 20 or 50 mM NaCl and transport (uptake) measurement was performed.

Statistical analysis. A normal distribution of data was assumed and appropriate test were applied.

31. Varjosalo, M. *et al.* Interlaboratory reproducibility of large-scale human protein-complex analysis by standardized AP-MS. *Nature Methods* **10,** 307–314 (2013).
32. Giambruno, R. *et al.* Affinity purification strategies for proteomic analysis of transcription factor complexes. *J. Proteome Res.* **12,** 4018–4027 (2013).
33. Pichlmair, A. *et al.* Viral immune modulators perturb the human molecular network by common and unique strategies. *Nature* **487,** 486–490 (2012).

34. Colinge, J., Masselot, A., Giron, M., Dessingy, T. & Magnin, J. OLAV: towards high-throughput tandem mass spectrometry data identification. *Proteomics* **3,** 1454–1463 (2003).
35. Bennett, K. L. *et al.* Proteomic analysis of human cataract aqueous humour: Comparison of one-dimensional gel LCMS with two-dimensional LCMS of unlabelled and iTRAQ(R)-labelled specimens. *J. Proteomics* **74,** 151–166 (2011).
36. Choi, H. *et al.* SAINT: probabilistic scoring of affinity purification-mass spectrometry data. *Nature Methods* **8,** 70–73 (2011).
37. Mellacheruvu, D. *et al.* The CRAPome: a contaminant repository for affinity purification-mass spectrometry data. *Nature Methods* **10,** 730–736 (2013).
38. Snijder, B. *et al.* Population context determines cell-to-cell variability in endocytosis and virus infection. *Nature* **461,** 520–523 (2009).
39. Galluccio, M. *et al.* Over-expression in *E. coli* and purification of the human OCTN1 transport protein. *Protein Expr. Purif.* **68,** 215–220 (2009).
40. Pochini, L., Scalise, M., Galluccio, M., Amelio, L. & Indiveri, C. Reconstitution in liposomes of the functionally active human OCTN1 (SLC22A4) transporter overexpressed in *Escherichia coli*. *Biochem. J.* **439,** 227–233 (2011).

a

RefSeqNT	GeneSymbol	EntrezGeneID	HEK293_FPKM	K562_FPKM	Average _FPKM	PubMed_entry
NM_001145144	SLC1A5	6510	47.08	56.21	51.65	92
NM_001013251	SLC3A2	6520	22.28	54.08	38.18	62
NM_018976	SLC38A2	54407	17.46	31.18	24.32	80
NM_001077484	SLC38A1	81539	24.41	9.34	16.87	60
NM_014331	SLC7A11	23657	9.35	7.12	8.24	148
NM_173514	SLC38A9	153129	5.81	8.83	7.32	1
NM_003045	SLC7A1	6541	9.89	2.87	6.38	81
NM_052831	SLC18B1	116843	6.10	3.68	4.89	1
NM_003038	SLC1A4	6509	1.40	7.93	4.66	36
NM_080546	SLC44A1	23446	5.85	3.10	4.48	19

b

RefSeqNT	GeneSymbol	EntrezGeneID	HEK293_FPKM	K562_FPKM
NM_001077484	SLC38A1	81539	24.41	9.34
NM_018976	SLC38A2	54407	17.46	31.18
NM_006841	SLC38A3	10991	0.05	0.00
NM_018018	SLC38A4	55089	0.01	0.00
NM_033518	SLC38A5	92745	0.03	3.22
NM_153811	SLC38A6	145389	0.99	1.90
NM_018231	SLC38A7	55238	0.92	1.49
NM_001080442	SLC38A8	146167	0.00	0.00
NM_173514	SLC38A9	153129	5.81	8.83
NM_138570	SLC38A10	124565	0.72	1.95
NM_173512	SLC38A11	151258	0.00	0.00
NM_078483	SLC36A1	206358	0.77	0.49
NM_181776	SLC36A2	153201	0.00	0.00
NM_181774	SLC36A3	285641	0.00	0.00
NM_152313	SLC36A4	120103	4.19	0.11
NM_080552	SLC32A1	140679	0.00	0.00

Extended Data Figure 1 | Expression of SLC members of amino acid transporter families. **a**, Table of SLCs belonging to amino acid transporter families robustly expressed in HEK293 and K562 cells as monitored by RNA-seq. SLC members of amino acid transporter-containing families[16] (SLC1, 6, 7, 16, 17, 18, 32, 36, 38 and 43 families) expressed (FPKM >0.5) in both cell lines were ranked according to their expression level, top ten are shown. The number of PubMed entries was obtained by querying the GeneSymbol (24 October 2013). **b**, Expression of members of the SLC32, SLC36 and SLC38 families in HEK293 and K562 cells.

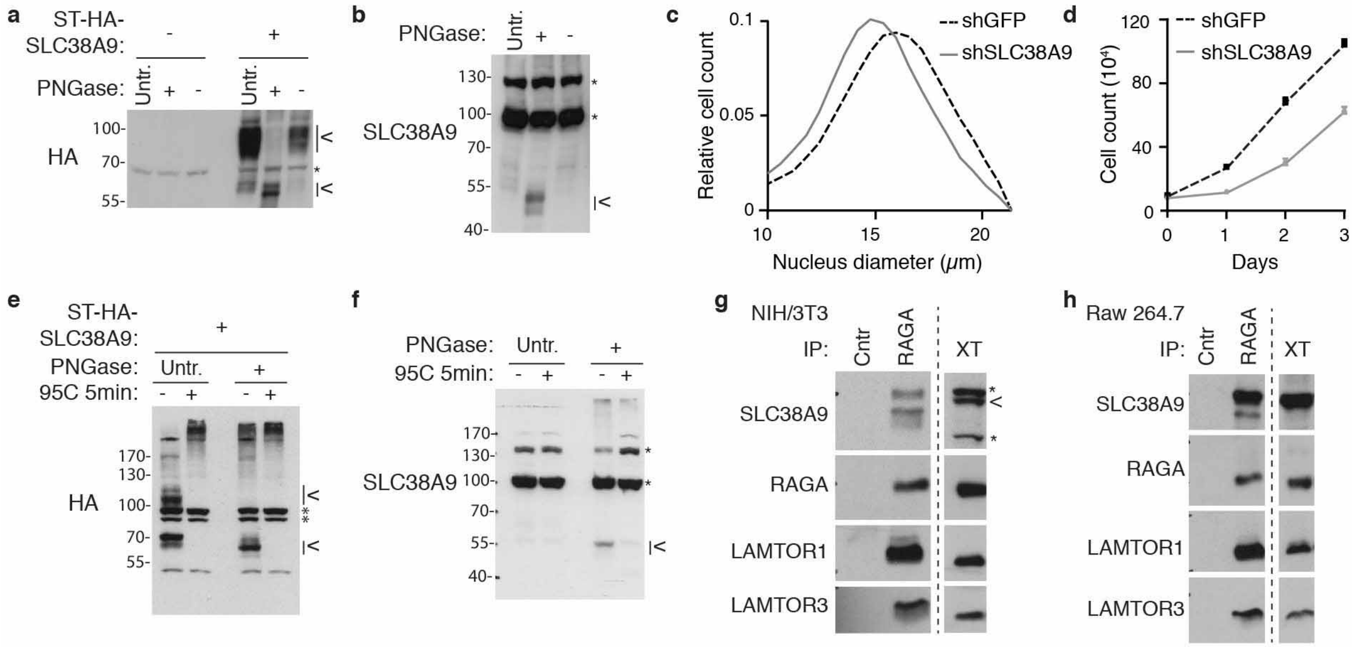

Extended Data Figure 2 | Biochemical and functional characterization of SLC38A9. **a**, **b**, Where indicated, HEK293T cells were transfected with tagged SLC38A9 constructs (+) or empty vector (−). Cell lysates were left untreated (Untr.) or incubated 1 h at 37 °C in presence or absence of PNGase and analysed by immunoblot. Results are representative of two independent experiments ($n = 2$). **c**, Cell size measurements of HEK293T cells after short hairpin (shRNA)-mediated knockdown against GFP (control, dashed black line) or SLC38A9 (grey line), measured by automated microscopy and image analysis. Sparse and interphase cells were selected using image analysis and machine learning, and nucleus diameter was used as robust proxy for cell size[38]. Smoothed distributions of 2,400 and 4,165 cells, respectively, are shown. **d**, Cell proliferation measurement of HEK293T cells transduced with lentivirus-encoded shRNA against SLC38A9 or GFP. 10^5 cells were seeded and counted every 24 h. Mean values ± s.d. from triplicates. Results are representative of two independent experiments ($n = 2$). **e**, **f**, Where indicated, HEK293T cells were transfected with tagged SLC38A9. Cell lysates were prepared and left untreated (Untr.) or incubated 1 h at 37 °C with PNGase and analysed by immunoblot, Where indicated, cell lysates were boiled for 5 min at 95 °C after PNGase treatment. **g**, **h**, Lysates from murine NIH/3T3 (**g**) or Raw 264.7 (**h**) cells were subjected to immunoprecipitation with the indicated antibodies, treated with PNGase and analysed by immunoblot. Results are representative of two independent experiments ($n = 2$). <, SLC38A9; *, non-specific band.

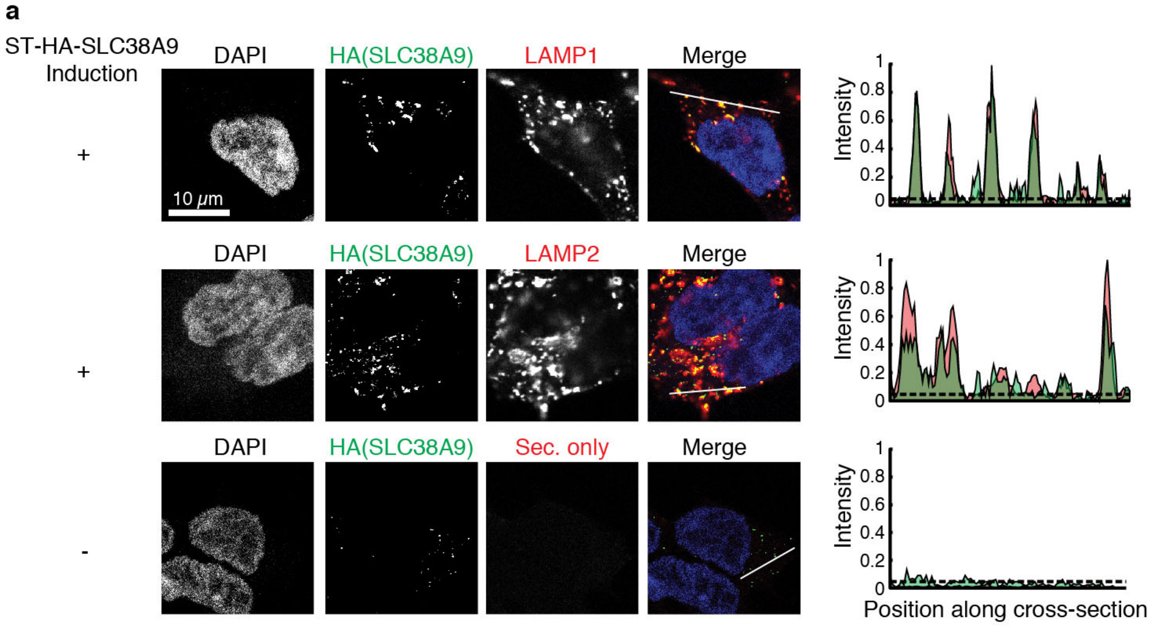

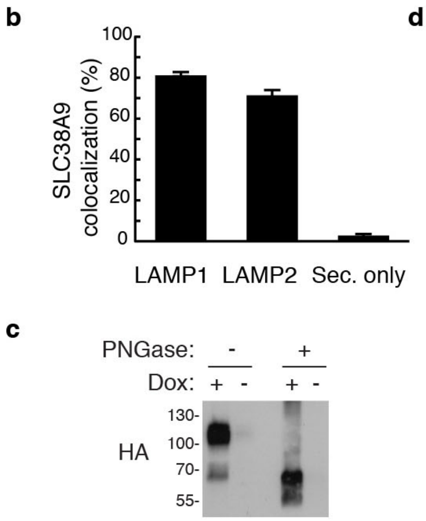

d

Interactor \ Bait	SLC38A9 Sp. c.	SLC38A9 Sq. c.	SLC38A1 Sp. c.	SLC38A1 Sq. c.	SLC38A2 Sp. c.	SLC38A2 Sq. c.	SLC36A1 Sp. c.	SLC36A1 Sq. c.
SLC38A9	36.5	30.5	0	0	0	0	0	0
SLC38A1	0	0	73.5	20.5	0	0	0	0
SLC38A2	0	0	0	0	65.5	15.0	0	0
SLC36A1	0	0	0	0	0	0	128.5	29.0
LAMTOR1	15.5	66.0	0	0	0	0	0	0
LAMTOR2	6.5	75.0	0	0	0	0	0	0
LAMTOR3	11.5	62.0	0	0	0	0	0	0
LAMTOR4	6.5	64.0	0	0	0	0	0	0
LAMTOR5	7.5	81.0	0	0	0	0	0	0
RAGA	19.5	45.0	0	0	0	0	0	0
RAGB	16.0	38.0	0	0	0	0	0	0
RAGC	23.5	45.0	0	0	0	0	0	0
RAGD	9.5	21.0	0	0	0	0	0	0

Extended Data Figure 3 | SLC38A9 proteomic analysis: bait localization and results. **a**, Single-channel and merged confocal microscopy images of DAPI stained nuclei and indirect immunofluorescence against HA-tagged SLC38A9 and endogenous lysosomal markers LAMP1 (top panel) and LAMP2 (middle panel) and the non-induced and secondary antibody only control (bottom panel) in HEK293 Flp-In TREx cells. Scale bar, 10 μm. Intensity profiles for SLC38A9 (green) and LAMP1, LAMP2 or secondary antibody control (red) along the cross-section lines indicated in the respective merged channel images are shown. **b**, Quantification of HA-SLC38A9 signal above background (dashed lines in **a**) that colocalizes with LAMP1, LAMP2 or secondary antibody only positive areas. Average and s.d. of at least two images is shown, analysing colocalization in 22, 34 and 27 cells respectively. **c**, HEK293 Flp-In TREx cells inducibly expressing SLC38A9 were treated or not with doxycycline (Dox) for 24 h. Where indicated, cell lysates were treated with PNGase and analysed by immunoblot. **d**, Tabular view summarizing the proteomic analysis of SLC38A9, SLC38A1, SLC38A2 and SLC36A1. Comparison of the SLC38A9 interactors identified by TAP–LC–MS/MS to the same analysis performed with the other transporters. Spectral counts (Sp. c., average of biological replicates) and sequence coverage (Sq. c., percentage, average of biological replicates) are indicated. Data shown are based on two independent experiments for each condition ($n = 2$), each analysed in two technical replicates.

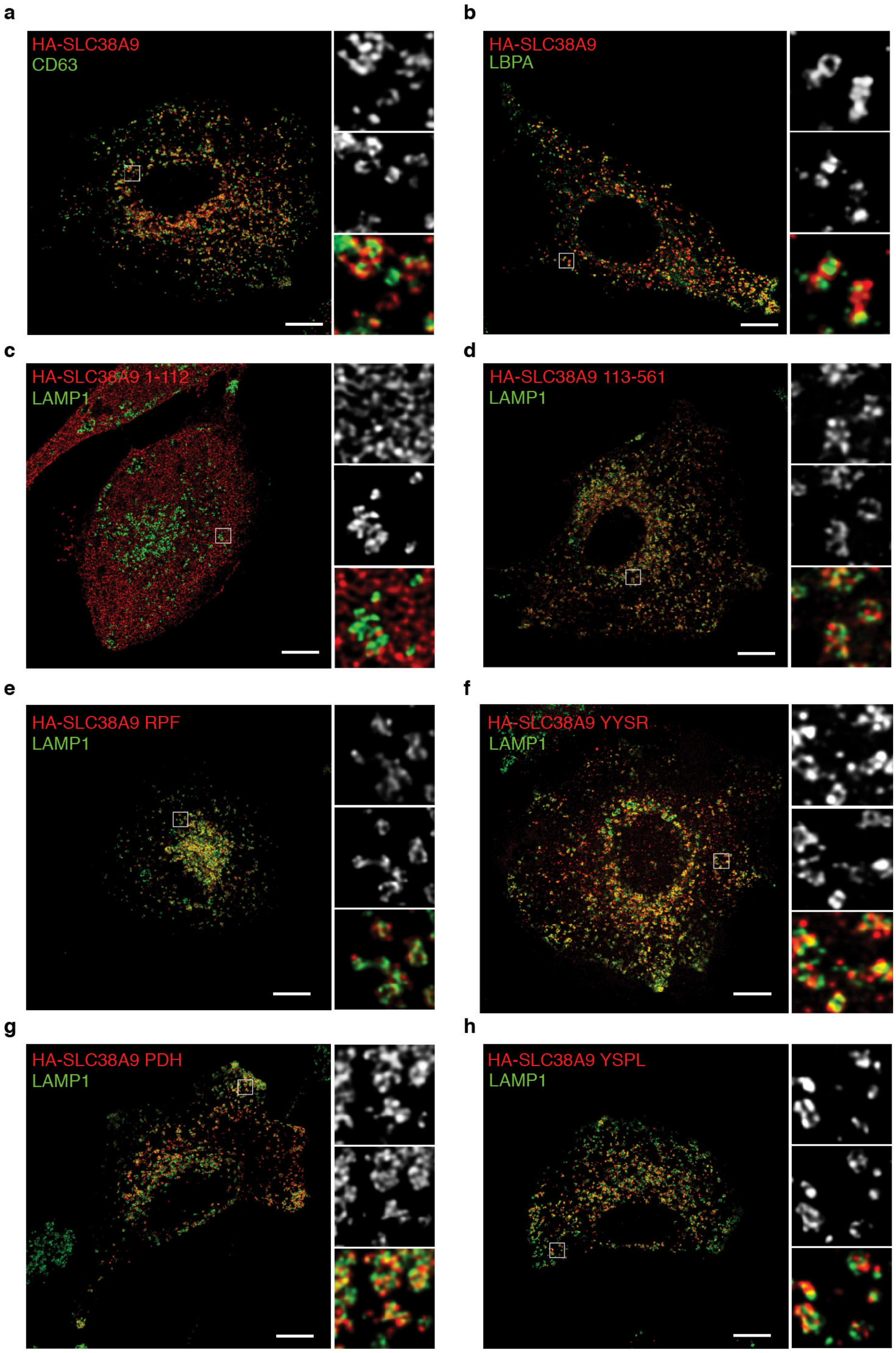

Extended Data Figure 4 | SLC38A9 localizes to the late endosome/lysosome compartment. **a–h**, HeLa cells were transfected with the indicated ST-HA tagged SLC38A9 construct. Merged and single-channel confocal microscopy images of indirect immunofluorescence of HA-tagged SLC38A9 (red) and endogenous lysosomal marker LAMP1 (green) are shown. Representative cells are shown. Scale bar, 10 μm.

a

Interactor \ Bait	LAMTOR1		LAMTOR3		LAMTOR4		LAMTOR5		RAGA		RAGC	
	Spec. count	Seq. cov.	Spec. count	Seq. cov.	Spec. count	Seq. cov.	Spec. count	Seq. cov.	Spec. count	Seq. cov.	Spec. count	Seq. cov.
SLC38A9	4.0	11.0	17.5	21.0	5.0	10.5	8.0	16.0	4.5	11.5	6.5	12.5
LAMTOR1	105.5	75.0	79.5	84.0	25.5	72.0	40.0	84.0	35.0	54.5	88.0	71.5
LAMTOR2	29.5	72.0	52.0	92.0	18.5	86.0	28.0	75.0	7.5	57.5	26.5	86.5
LAMTOR3	21.5	79.5	68.5	75.5	13.0	60.5	24.5	70.0	16.0	71.0	27.0	64.5
LAMTOR4	17.5	39.0	35.0	72.0	52.0	65.0	79.5	83.0	10.0	57.5	14.0	39.0
LAMTOR5	20.0	81.0	32.5	81.0	90.0	81.0	120.0	84.5	21.0	56.0	41.5	81.0
RAGA	31.0	42.5	67.5	64.5	21.0	39.5	25.0	47.5	145.0	56.0	82.0	51.5
RAGB	25.5	33.5	60.5	58.0	14.5	28.5	20.5	37.0	147.5	54.5	74.0	43.5
RAGC	34.5	45.5	81.5	64.5	19.0	42.0	28.5	55.5	52.5	44.5	202.5	62.0
RAGD	23.5	27.5	55.0	47.5	17.5	28.0	21.5	35.0	45.0	35.0	0	0
RAPTOR	9.0	8.0	31.5	24.5	11.5	10.0	18.5	15.5	5.0	5.0	3.0	3.0
ATP6V0D1	0	0	1.5	5.0	0	0	0	0	0	0	0	0
FNIP2	0	0	2.0	2.0	0	0	0	0	0	0	0	0
FLCN	0	0	4.5	11.0	0	0	0	0	0	0	0	0

b LAMTORs_PD - SLC38A9 Peptide Mapping

MANMNSDSRH LGTSEVDHER DPGPMNIQFE PSDLRSKRPF CIEPTNIVNV NHVIQRVSDH 60
ASAMNKRIHY YSRLTTPADK ALIAPDHVVP APEECYVYSP LGSAYKLQSY TEGYGKNTSL 120
VTIFMIWNTM MGTSILSIPW GIKQAGFTTG MCVIILMGLL TLYCCYRVVK SRTMMFSLDT 180
TSWEYPDVCR HYFGSFGQWS SLLFSLVSLI GAMIVYWVLM SNFLFNTGKF IFNFIHHIND 240
TDTILSTNNS NPVICPSAGS GGHPDNSSMI FYANDTGAQQ FEKWWDKSRT VPFYLVGLLL 300
PLLNFKSPSF FSKFNILGTV SVLYLIFLVT FKAVRLGFHL EFHWFIPTEF FVPEIRFQFP 360
QLTGVLTLAF FIHNCIITLL KNNKKQENNV RDLCIAYMLV TLTYLYIGVL VFASFPSPPL 420
SKDCIEQNFL DNFPSSDTLS FIARIFLLFQ MMTVYPLLGY LARVQLLGHI FGDIYPSIFH 480
VLILNLIIVG AGVIMACFYP NIGGIIRYSG AACGLAFVFI YPSLIYIISL HQEERLTWPK 540
LIFHVFIIIL GVANLIVQFF M

c SLC38A9_PD - SLC38A9 Peptide Mapping

MANMNSDSRH LGTSEVDHER DPGPMNIQFE PSDLRSKRPF CIEPTNIVNV NHVIQRVSDH 60
ASAMNKRIHY YSRLTTPADK ALIAPDHVVP APEECYVYSP LGSAYKLQSY TEGYGKNTSL 120
VTIFMIWNTM MGTSILSIPW GIKQAGFTTG MCVIILMGLL TLYCCYRVVK SRTMMFSLDT 180
TSWEYPDVCR HYFGSFGQWS SLLFSLVSLI GAMIVYWVLM SNFLFNTGKF IFNFIHHIND 240
TDTILSTNNS NPVICPSAGS GGHPDNSSMI FYANDTGAQQ FEKWWDKSRT VPFYLVGLLL 300
PLLNFKSPSF FSKFNILGTV SVLYLIFLVT FKAVRLGFHL EFHWFIPTEF FVPEIRFQFP 360
QLTGVLTLAF FIHNCIITLL KNNKKQENNV RDLCIAYMLV TLTYLYIGVL VFASFPSPPL 420
SKDCIEQNFL DNFPSSDTLS FIARIFLLFQ MMTVYPLLGY LARVQLLGHI FGDIYPSIFH 480
VLILNLIIVG AGVIMACFYP NIGGIIRYSG AACGLAFVFI YPSLIYIISL HQEERLTWPK 540
LIFHVFIIIL GVANLIVQFF M

Extended Data Figure 5 | SLC38A9 is an integral component of the Ragulator–RAG GTPase complex. **a**, Tabular view of spectral counts (Spec. count, average of biological replicates) and sequence coverage (Seq. cov., percentage, average of biological replicates) of the core Ragulator–RAG GTPase network and published interactors detected. Data shown are based on two independent experiments for each condition ($n = 2$), and analysed in two technical replicates. **b**, **c**, SLC38A9 peptides detected in LAMTOR1, 3, 4 and 5 (**b**) or in SLC38A9 (**c**) TAP–LC–MS/MS analysis are mapped on SLC38A9 sequence and highlighted in bold. Transmembrane helices are highlighted in light brown. Potential tryptic cleavage sites are in red.

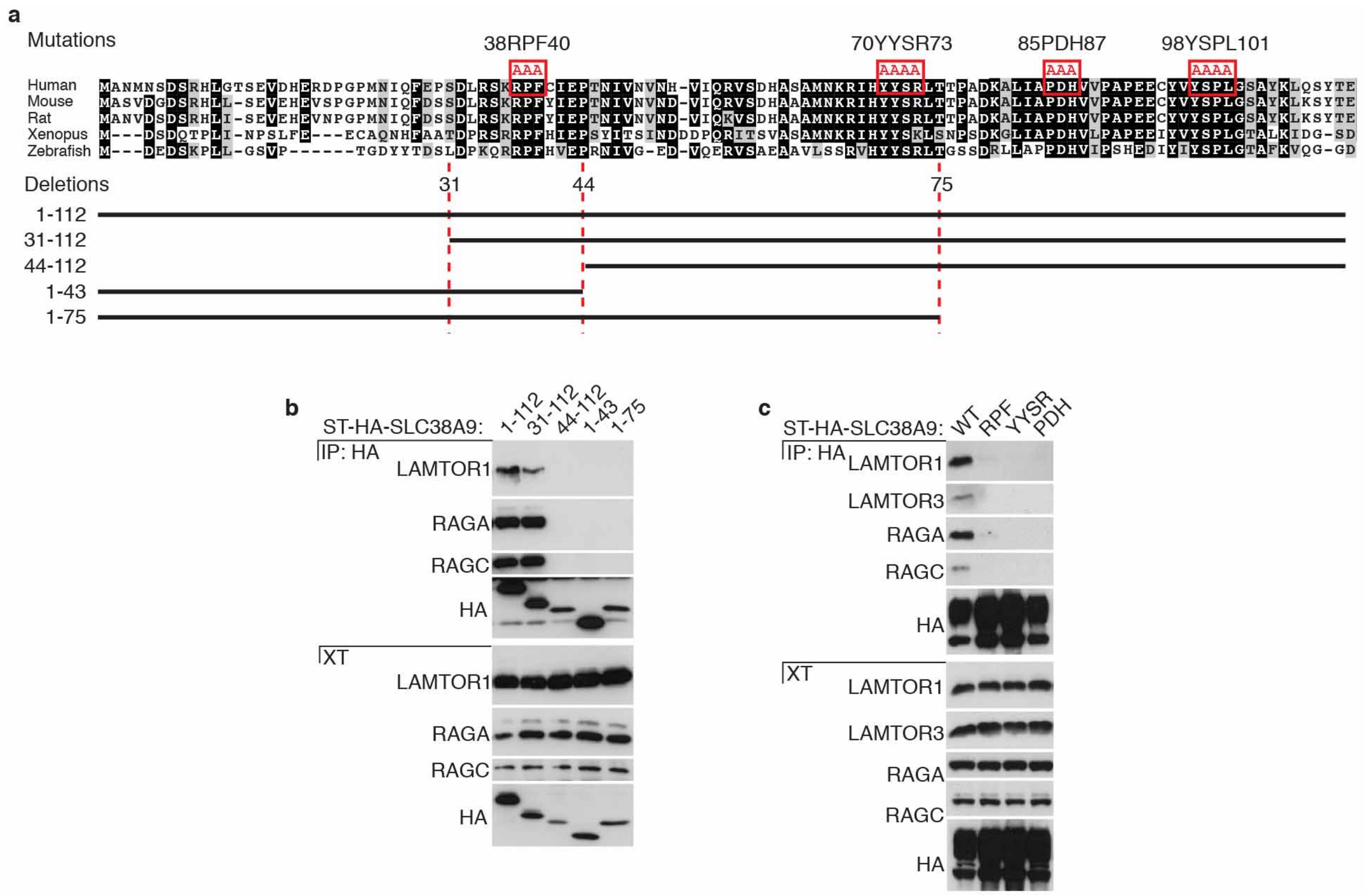

Extended Data Figure 6 | The cytoplasmic N-terminal region of SLC38A9 binds the Ragulator–RAG GTPase complex through evolutionary conserved motifs. **a**, Sequence alignment of the N-terminal cytoplasmic region (amino acids 1–112) of human, mouse, rat, *Xenopus* and zebrafish SLC38A9. Amino acids selected for deletion and motifs substituted to alanine are highlighted. Black and grey shading indicates >60% amino acid sequence identity and similarity, respectively. **b**, **c**, HEK293T cells were transfected with the indicated tagged SLC38A9 constructs. Immunoprecipitates and cell extracts were analysed by immunoblot. SLC38A9 mutant constructs are labelled with the number of the encoded amino acids (**b**) or with the amino acid motif substituted to alanine (**c**). Results are representative of two independent experiments ($n = 2$).

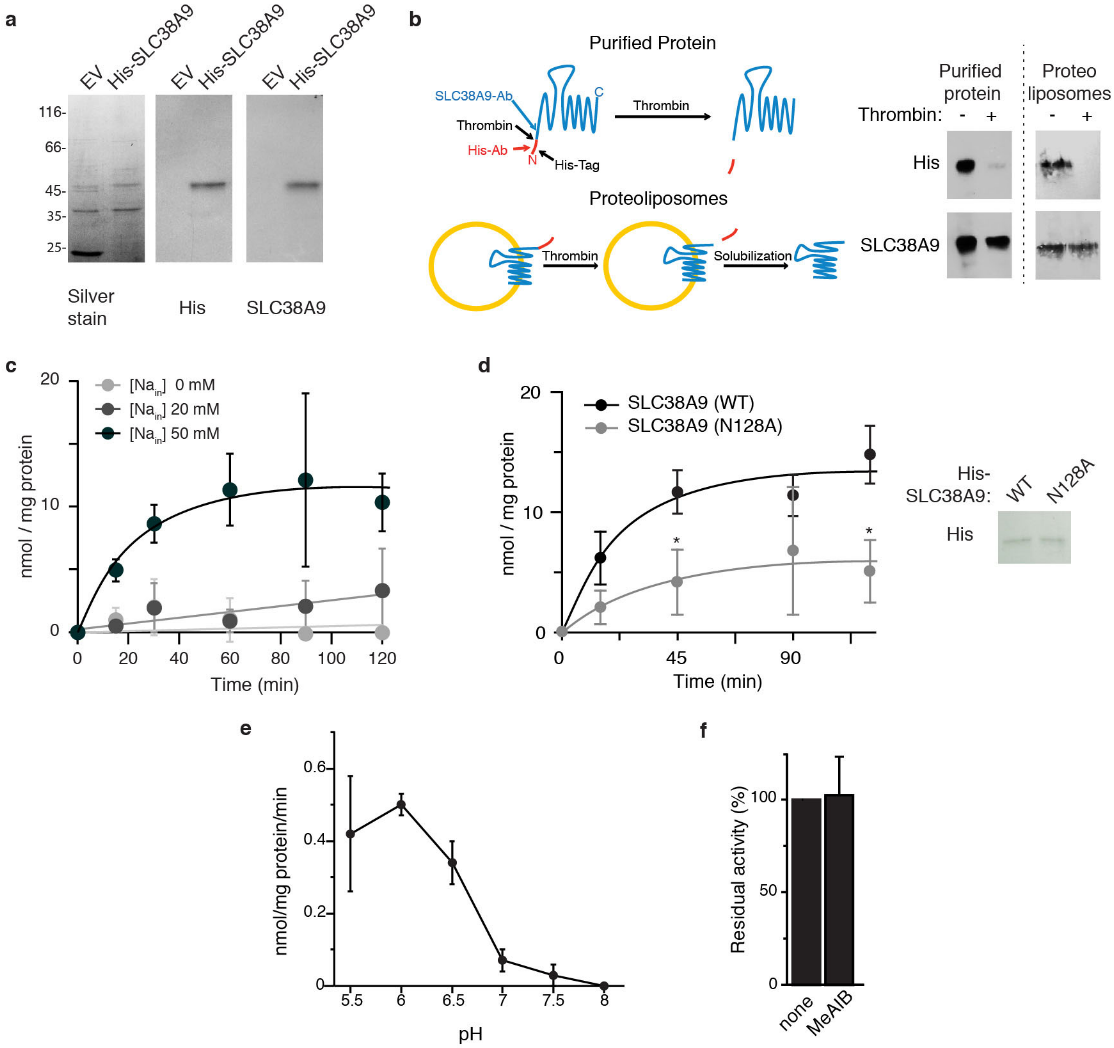

Extended Data Figure 7 | Characterization of SLC38A9-mediated amino acid transport in proteoliposomes. **a**, Purification of SLC38A9. Lanes represent empty vector control and SLC38A9 expressed in *E. coli* and purified by Ni-chelating chromatography. Immunoblot of the same fractions using anti-His or anti-SLC38A9 antibody are shown. **b**, Orientation of SLC38A9 in proteoliposomes. Purified His-SLC38A9 protein or proteoliposomes reconstituted with SLC38A9 were incubated overnight at 37 °C in presence or in absence of 1 U thrombin. Proteoliposomes were then solubilized with SDS and analysed by immunoblot. Results are representative of two independent experiments ($n = 2$). **c**, Time course of glutamine uptake by SLC38A9 in proteoliposomes reconstituted with the purified protein fraction. The uptake of 10 μM [^{3}H]glutamine was measured at different time intervals in the presence of the indicated intraliposomal sodium concentrations. Transport was calculated by subtracting the radioactivity associated to proteoliposomes reconstituted with the empty vector fraction. Values represent means of specific transport ± s.d. from three independent experiments ($n = 3$). **d**, Time course of glutamine uptake in proteoliposomes reconstituted with purified SLC38A9 wild-type or N128A mutant protein. Values represent means of specific transport ± s.d. from 3 independent experiments ($n = 3$). Significance was estimated by Student's *t*-test (*$P < 0.01$). Immunoblot analysis of purified protein reconstituted in the proteoliposomes. **e**, Effect of pH on the reconstituted SLC38A9. Reconstitution and transport assay were performed at the indicated pH. Results are means of specific transport rate ± s.d. from three different experiments ($n = 3$). **f**, Inhibition of the [^{3}H]glutamine uptake in proteoliposomes. 1 mM MeAIB (α-(methylamino)isobutyric acid) was added together with 10 μM [^{3}H]glutamine. Transport was measured at 60 min. Values represent means of percent residual activity with respect to control (without added inhibitor) ± s.d. from three independent experiments ($n = 3$).

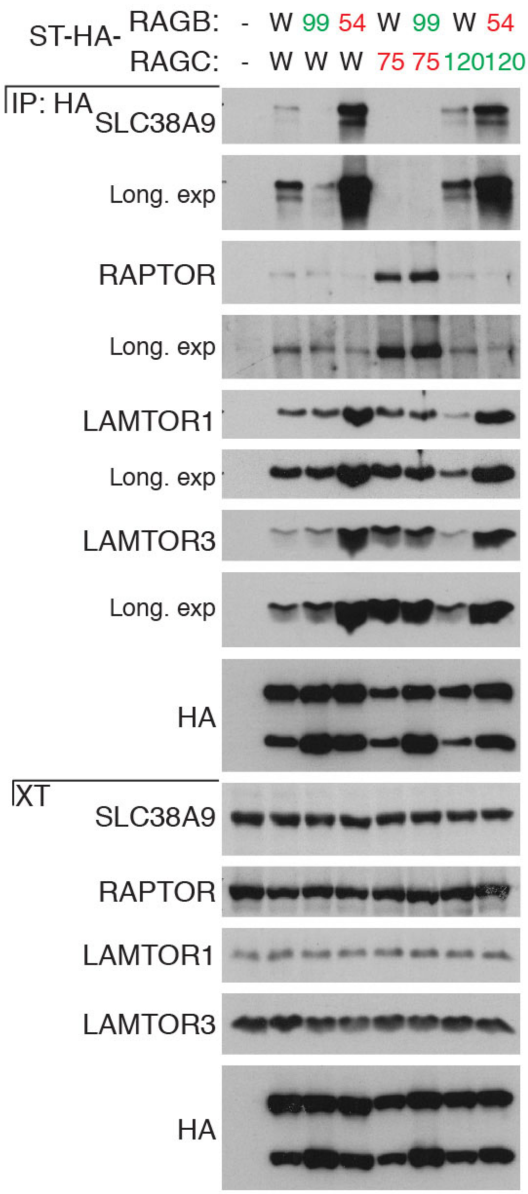

Extended Data Figure 8 | Nucleotide-loading/conformation dependent interaction of RAGB/RAGC heterodimers with SLC38A9. HEK293T cells were transfected with the indicated combination of tagged RAG GTPases mutant constructs or empty vector (−). Anti-HA immunoprecipitates and cell extracts were treated with PNGase and analysed by immunoblot. W, wild type; 75, S75N; 120, Q120L; 99, Q99L; 54, T54N. Results are representative of two independent experiments ($n = 2$).

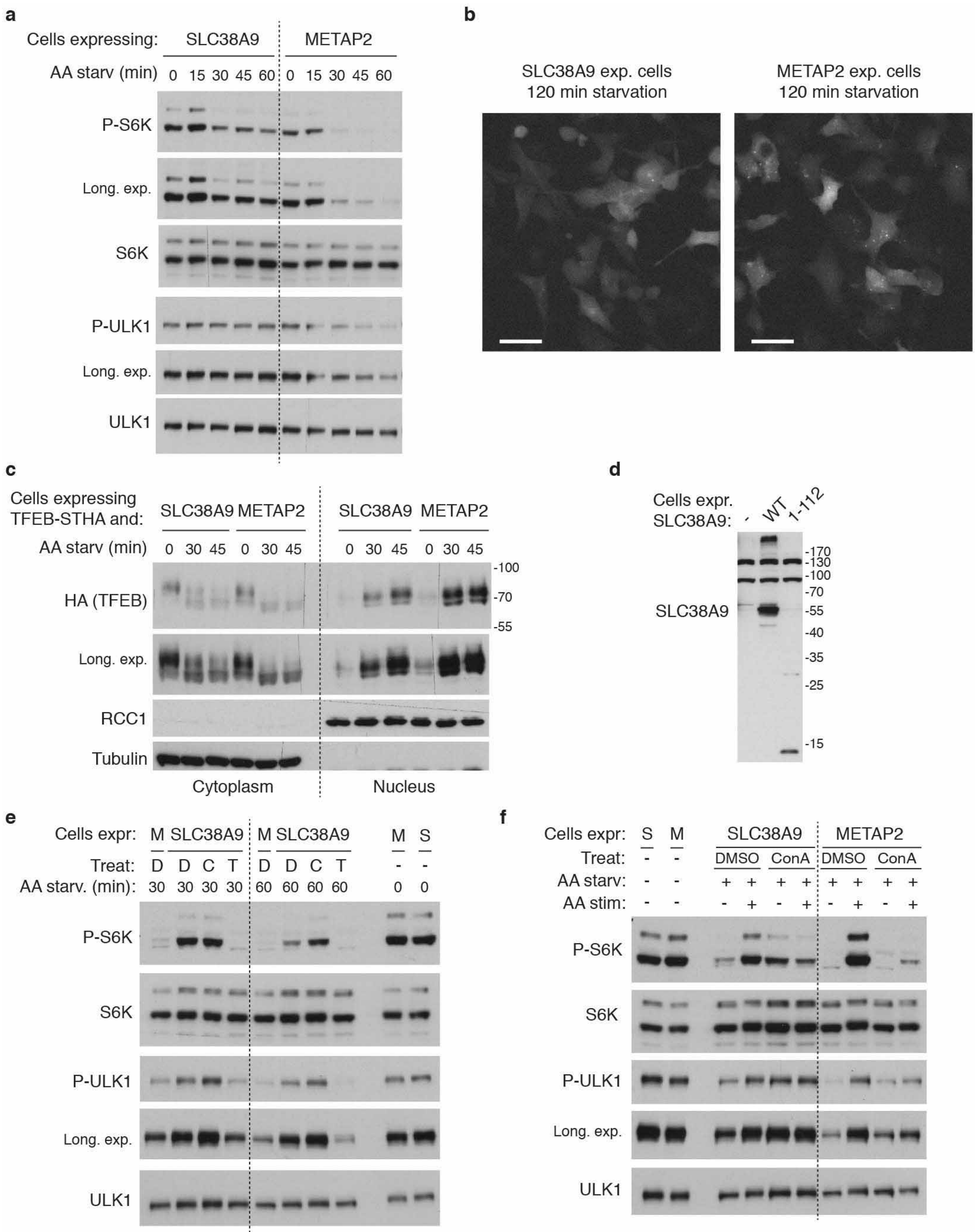

Extended Data Figure 9 | Stable expression of SLC38A9 mediates sustained mTORC1 activation upon amino acid starvation. **a**, SLC38A9 or METAP2 stably expressing HEK293T cells were starved for the indicated time in medium without amino acids and serum. Cell lysates were analysed by immunoblot. Results are representative of two independent experiments ($n = 2$). **b**, Representative images in the GFP channels of HEK293T cells stably expressing EGFP–LC3B and SLC38A9 or METAP2 starved for 120 min (related to Fig. 4b). Scale bar, 40 μm. **c**, HEK293T cells stably expressing TFEB–STHA and SLC38A9 or METAP2 were starved for the indicated time. Cytoplasmic and nuclear fraction were analysed by immunoblot. Results are representative of two independent experiments ($n = 2$). **d**, Immunoblot analysis of HEK293T cells stably expressing the indicated SLC38A9 constructs. **e**, SLC38A9 (S) or METAP2 (M) stably expressing HEK293T were starved for 50 min and then stimulated with amino acids for 20 min. Where indicated, cells were treated with concanamycin A (5 μM) or DMSO during both incubation times. Cell lysates were analysed by immunoblot with the indicated antibodies. Results are representative of two independent experiments ($n = 2$). **f**, SLC38A9 (S) or METAP2 (M) stably expressing HEK293T were treated for 30 min with DMSO (D), concanamycin A (C, 5 μM) or Torin 1 (T, 250 nM) and then starved for the indicated times in presence of the inhibitors. Cell lysates were analysed by immunoblot. Results are representative of two independent experiments ($n = 2$).

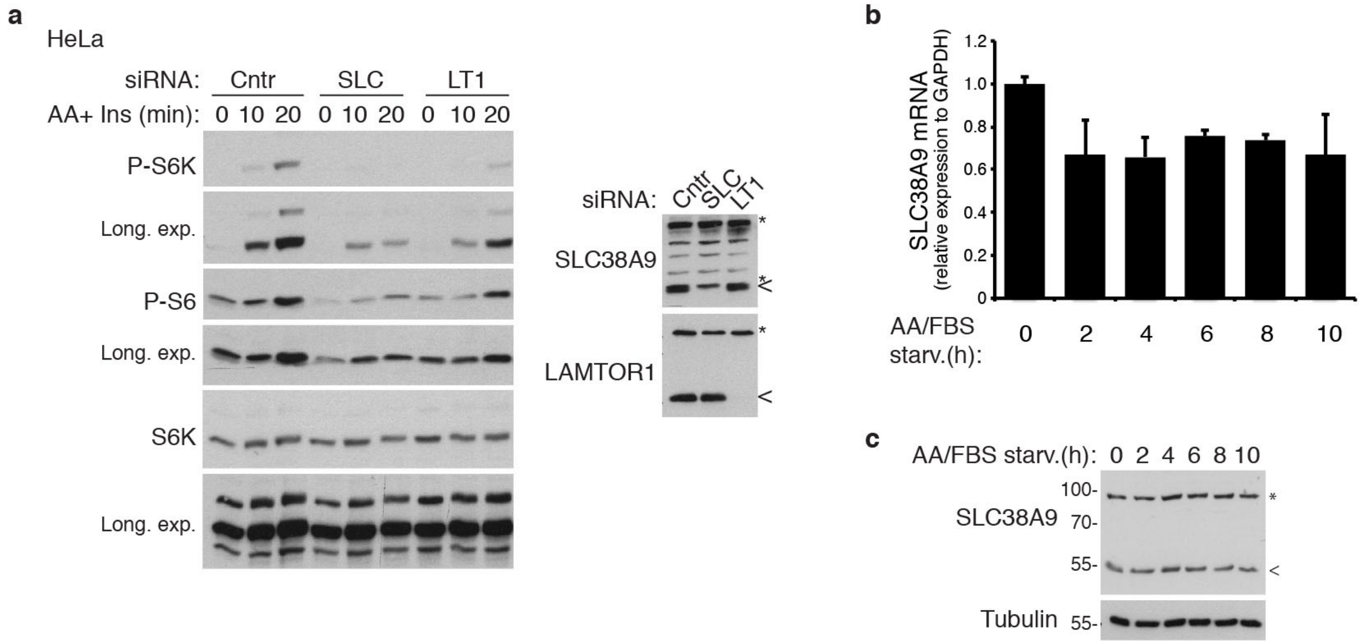

Extended Data Figure 10 | Expression of SLC38A9 is required for amino acid-induced mTORC1 activation and is not affected by starvation. a, HeLa cells were transfected with siRNA targeting SLC38A9 (SLC), LAMTOR1 (LT1) or non-targeting control (Cntr). After 72h, cells were starved for 50 min in medium without amino acids and serum and then stimulated with amino acids in presence of insulin (1 μM). Cell lysates were analysed by immunoblot. Results are representative of three independent experiments ($n = 3$). **b**, **c**, HEK293T cells were starved for the indicated times. SLC38A9 expression was analysed by quantitative PCR (**b**) and immunoblot (**c**). In **b**, mean values ± s.d. from technical triplicates are shown. Results are representative of two independent experiments ($n = 2$). <, SLC38A9; *, non-specific band.

doi:10.1038/nature14281

N^6-methyladenosine marks primary microRNAs for processing

Claudio R. Alarcón[1], Hyeseung Lee[1]*, Hani Goodarzi[1]*, Nils Halberg[1] & Sohail F. Tavazoie[1]

The first step in the biogenesis of microRNAs is the processing of primary microRNAs (pri-miRNAs) by the microprocessor complex, composed of the RNA-binding protein DGCR8 and the type III RNase DROSHA[1–4]. This initial event requires recognition of the junction between the stem and the flanking single-stranded RNA of the pri-miRNA hairpin by DGCR8 followed by recruitment of DROSHA, which cleaves the RNA duplex to yield the pre-miRNA product[5]. While the mechanisms underlying pri-miRNA processing have been determined, the mechanism by which DGCR8 recognizes and binds pri-miRNAs, as opposed to other secondary structures present in transcripts, is not understood. Here we find in mammalian cells that methyltransferase-like 3 (METTL3) methylates pri-miRNAs, marking them for recognition and processing by DGCR8. Consistent with this, METTL3 depletion reduced the binding of DGCR8 to pri-miRNAs and resulted in the global reduction of mature miRNAs and concomitant accumulation of unprocessed pri-miRNAs. *In vitro* processing reactions confirmed the sufficiency of the N^6-methyladenosine (m^6A) mark in promoting pri-miRNA processing. Finally, gain-of-function experiments revealed that METTL3 is sufficient to enhance miRNA maturation in a global and non-cell-type-specific manner. Our findings reveal that the m^6A mark acts as a key post-transcriptional modification that promotes the initiation of miRNA biogenesis.

In our search for post-transcriptional modifications that regulate miRNA processing, we conducted a systematic search for sequence motifs that are overrepresented in miRNA-containing regions using the Finding Informative Regulatory Elements (FIRE) algorithm[6], which identifies over-represented or under-represented motifs in one group of sequences versus another. We observed the overrepresentation of the GGAC motif in pri-miRNA sequences relative to shuffled sequences (Fig. 1a). This motif is consistent with a previously established recognition sequence—RGAC—for the RNA methyltransferase enzyme METTL3 (refs 7–9). In contrast to pri-miRNA sequences, this element was not enriched in pre-miRNA sequences, and was actually depleted relative to shuffled sequences (Extended Data Fig. 1a). METTL3 is the catalytic subunit of a multi-component enzyme that methylates RNA, thereby adding the m^6A mark to eukaryotic RNAs[10–13].

To determine whether the overrepresentation of the m^6A methylation motif in pri-miRNA sequences signifies increased m^6A methylated sequences, we conducted m^6A-seq[8] by immunoprecipitating nuclear RNA from the MDA-MB-231 breast cancer cell line with an anti-m^6A antibody, followed by RNA sequencing (RNA-seq) (Extended Data Fig. 10a). A search for *cis*-regulatory elements from m^6A-seq revealed a significant enrichment of the METTL3 motif relative to shuffled sequences (Fig. 1b). Furthermore, when we analysed the density of the peaks in the vicinity of miRNA loci, we found a substantial increase in the density of peaks proximal to pre-miRNA sequences, corresponding to pri-miRNA regions (Fig. 1c). We next inspected individual clusters of reads using the Integrative Genomics Viewer (IGV) software[14] and found numerous cases in which there were prominent peaks in locations that correspond to pri-miRNAs. These clusters were located in both intergenic and intragenic pri-miRNA sites that contained canonical METTL3 motifs (Fig. 1d). Thus, these results reveal that the m^6A modification is enriched within pri-miRNA sequences.

To determine whether METTL3 has a role in miRNA processing, we conducted genome-wide miRNA expression profiling of MDA-MB-231 cells expressing a control short hairpin RNA (shRNA), as well as cells

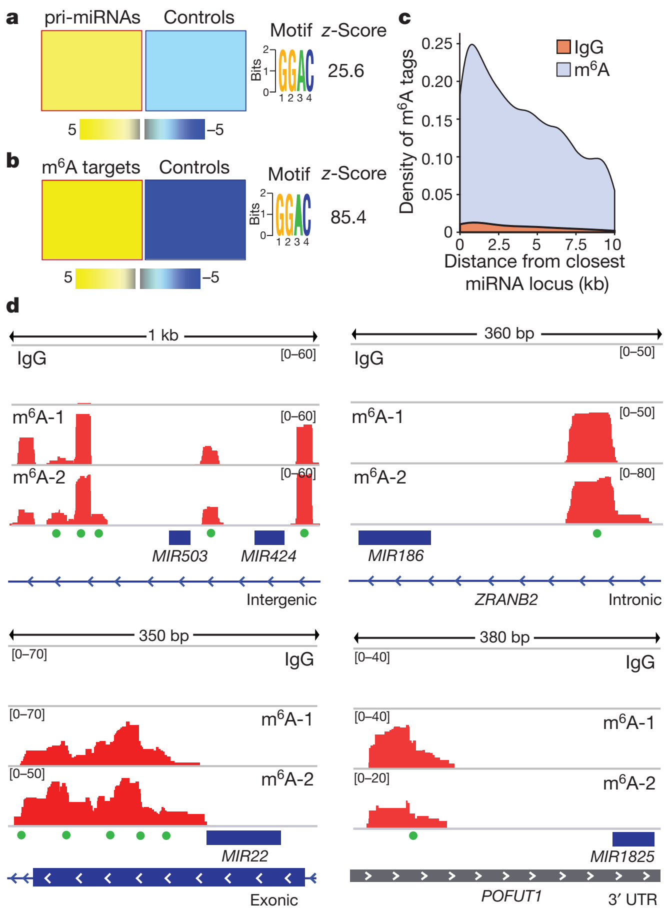

Figure 1 | The m^6A mark is present in pri-miRNA regions. **a**, Motif discovery analysis in pri-miRNA sequences using FIRE reveals overrepresentation of the METTL3 motif; yellow represents overrepresentation and blue underrepresentation. The magnitude of the over/underrepresentation is reflected in the linear-scale heat map shown at the bottom. The *z*-score is specified on the right. **b**, FIRE motif analysis of m^6A peaks compared to control sequences of the same length. The overrepresented motif and its *z*-score is depicted on the right, as in **a**. **c**, Density plot of the abundance of m^6A marks and their proximity to given miRNAs within transcripts. Peaks obtained from the immunoglobulin G (IgG) immunoprecipitation were used as controls. **d**, IGV tracks displaying examples of sequencing read clusters from two m^6A-seq replicates are shown next to the pre-miRNA genomic loci. The green dots at the bottom of the tracks depict the positions of METTL3 consensus motifs.

[1]Laboratory of Systems Cancer Biology, Rockefeller University, 1230 York Avenue, New York, New York 10065, USA.
*These authors contributed equally to this work.

expressing two independent shRNAs targeting METTL3 (Extended Data Fig. 1b, c). METTL3 depletion using independent shRNAs led to a global downregulation of mature miRNAs ($P = 2.15 \times 10^{-15}$; Fig. 2a and Extended Data Fig. 1d). Remarkably, most miRNAs (~70%) were downregulated by at least 30%. The miRNAs affected by METTL3 depletion were diverse in terms of their genomic locations, predominantly being intronic (56%), followed by intergenic (29%), exonic (12%) and in

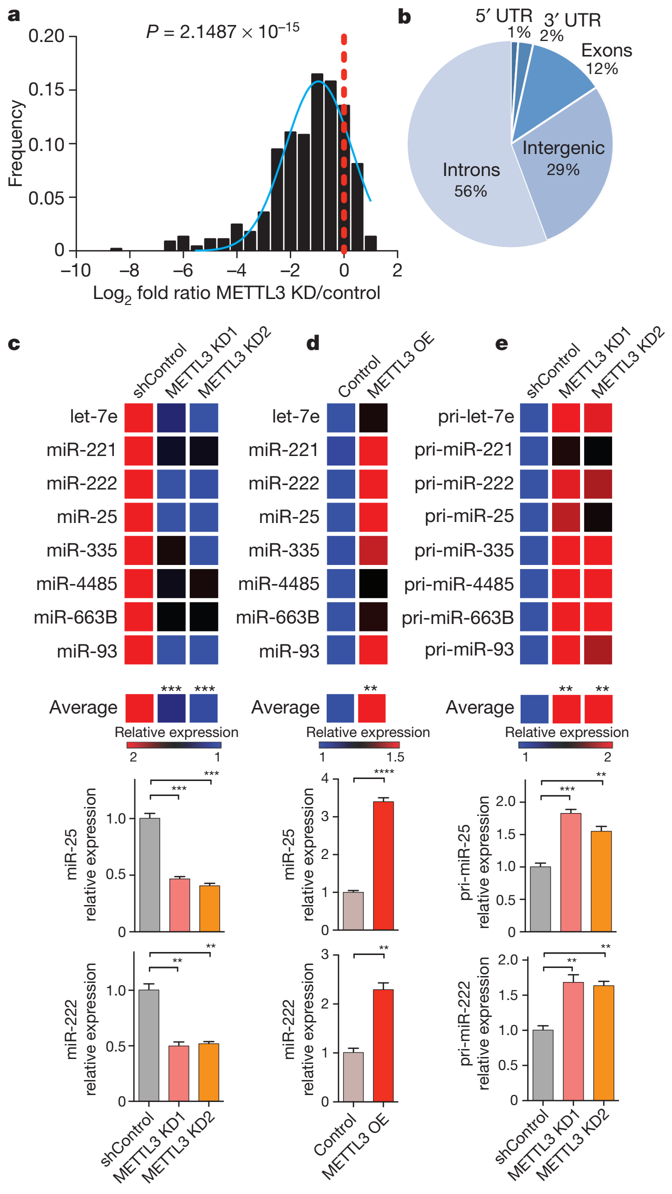

Figure 2 | METTL3 modulates the expression levels of miRNAs. **a**, Histogram depicting fold change ($\log_2$) in miRNA expression. The ratio of the average value for two independent shRNAs over the average of the two controls is shown. The *P* value of the analysis is indicated. KD, knockdown. **b**, Pie-chart representation of the genomic locations of miRNAs downregulated upon METTL3 depletion. **c**, Heat-map representation of qRT–PCR quantification of eight representative mature miRNAs that were affected by METTL3 depletion. Red represents increased expression while blue represents reduced expression. A heat map depicts their aggregate expression change upon METTL3 modulation. At the bottom, bar graphs showing specific examples. **d**, Heat-map representation of mature miRNA quantification from **c** by qRT–PCR upon METTL3 overexpression (OE). **e**, Heat map representing the quantification of pri-miRNA forms of miRNAs from **c** and **d** by qRT–PCR upon METTL3 depletion. All heat maps and bar graphs represent a linear scale. Error bars represent standard deviation (s.d.). $^{***}P < 5 \times 10^{-4}$, $^{**}P < 1 \times 10^{-3}$.

untranslated regions (UTRs; 3%), indicating that the effect of METTL3 depletion on miRNA processing was not specific to miRNAs originating from specific locations within or outside of genes (Fig. 2b). We next validated these effects by examining the expression of specific miRNAs by quantitative real-time polymerase chain reaction (qRT–PCR; Fig. 2c and Extended Data Fig. 2). Importantly, the effect of METTL3 depletion on miRNA processing was not restricted to a particular cell line and was also observed in multiple cell types (Extended Data Fig. 3). These experiments demonstrate that METTL3 is required for basal expression of the vast majority of miRNAs in both the cancerous and non-cancerous cell lines we investigated. To test whether METTL3 expression is sufficient to promote miRNA processing, we stably overexpressed METTL3 in MDA-MB-231 cells. METTL3 overexpression was sufficient to increase significantly the expression levels of mature miRNAs (Fig. 2d and Extended Data Fig. 4). We then quantified the expression levels of pri-miRNAs to determine if METTL3 depletion could impact pri-miRNA levels. As expected, we observed a clear and significant upregulation in the levels of pri-miRNAs upon METTL3 depletion (Fig. 2e and Extended Data Fig. 5a). These effects required enzymatically active METTL3, since they were abrogated upon mutation of the predicted catalytic residues[15] (Extended Data Fig. 5c, d). Neither METTL3 depletion nor its overexpression altered the expression, subcellular localization, or activity of the microprocessor complex—consistent with a direct role of METTL3 in pri-miRNA processing (Extended Data Fig. 6). Our findings reveal that pri-miRNAs are marked by the METTL3-dependent m^{6}A modification and that METTL3 expression is required for the appropriate processing of most pri-miRNAs to mature miRNAs.

To implicate directly METTL3 in the m^{6}A methylation of pri-miRNAs, we conducted high-throughput sequencing of RNA isolated by cross-linking immunoprecipitation[16] (HITS-CLIP) experiments using an antibody against endogenous METTL3 (Extended Data Fig. 10b). Consistent with our findings from m^{6}A-seq, METTL3 HITS-CLIP sequences displayed a significant enrichment of the METTL3 motif (Fig. 3a and Extended Data Fig. 7a). Despite the transient nature of the interaction between METTL3 and its targets, we observed a significant overlap in the miRNAs affected by METTL3 depletion that shared both the METTL3 footprint, as determined by HITS-CLIP, and the m^{6}A mark, as determined by m^{6}A-seq (P value $< 2.4 \times 10^{-15}$; Fig. 3b and Extended Data Fig. 7b). To investigate the evolutionary conservation of the METTL3 motif across different species, we used the PhastCons software[17] to analyse 30 miRNAs that are conserved among 100 vertebrates (http://www.targetscan.org) and also contain m^{6}A and/or METTL3 tags. This analysis showed a high degree of conservation for the METTL3 motif among vertebrates (Fig. 3c, d).

To demonstrate a direct role of the m^{6}A modification in pri-miRNA processing, we performed *in vitro* processing reactions using whole-cell extracts from HEK293T cells transfected with DGCR8 and DROSHA[18]. In this gain-of-function experiment, the extracts were used to process *in vitro* transcribed pri-miRNAs containing modified m^{6}A or unmodified bases. Consistent with our model, methylated pri-let-7e was more efficiently processed by the microprocessor to produce pre-let7e relative to its unmethylated counterpart, as detected by northern blot (Fig. 4a–c). These *in vitro* experiments suggest that m^{6}A marks in pri-miRNAs are required for efficient processing of pri-miRNAs *in vitro*. Additionally, we performed a loss-of-function experiment by testing the impact on miRNA processing of mutating select adenosines present in potential METTL3 motifs located in a pri-miRNA. To do this, we modified a previously described reporter construct[19]. In one reporter, we introduced a wild-type version of pri-let-7e. In the other reporter, the adenosines of METTL3 motifs present in the pri-let-7e region (that is, 5 out of 18 adenosines present outside the pre-miRNA sequence) were mutated (Extended Data Fig. 8a). Consistent with our findings, mutation of METTL3 motifs in pri-let-7e significantly reduced its processing to the mature form (Extended Data Fig. 8b).

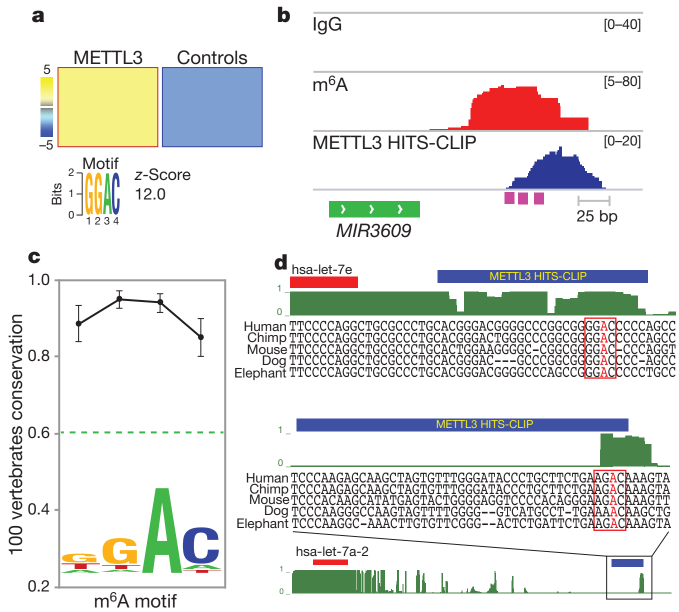

Figure 3 | METTL3 targets pri-miRNAs for m^{6}A methylation. **a**, FIRE analysis provides motif of METTL3 HITS-CLIP binding sites. The colour scale of the linear scale heat map is the same as in Fig. 1a. **b**, An example of sequencing clusters obtained from METTL3 HITS-CLIP (blue) and m^{6}A-seq (red). m^{6}A-seq was done in biological duplicate using IgG as control. METTL3 HITS-CLIP was done in biological triplicate. One example is shown for each experiment in the figure. The pink boxes at the bottom of the tracks represent conserved METTL3 motifs. **c**, Average vertebrate conservation of the METTL3 motif from a group of conserved pri-miRNAs using the PhastCons software[17]. The dotted green line depicts the average conservation of a region of 100 nucleotides that surrounds (and includes) the motifs. Error bars represent standard error of the mean (s.e.m.). **d**, Two examples of pri-miRNA genomic regions containing HITS-CLIP tags are shown. At the top, pre-miRNAs are marked in red boxes and METTL3 HITS-CLIP tags in blue boxes. The conserved METTL3 motif is framed in red with the putative methylated adenosine in red.

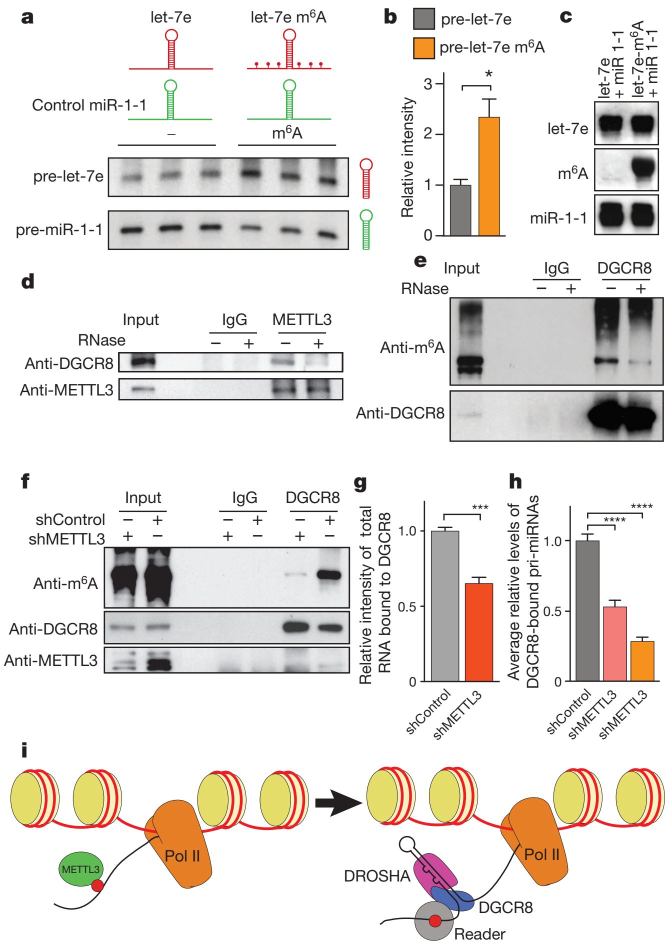

Figure 4 | m^{6}A methylation of pri-miRNAs is required for normal processing by DGCR8. **a**, *In vitro* pri-miRNA processing reactions. Pri-let-7e was transcribed with either modified m^{6}A (depicted in the schematic as red dots) or with unmodified bases. **b**, Hybridization intensities were quantified and normalized to the controls, and are shown in the bar graph. Bars represent the average normalized intensity of three biological replicates. $*P < 5 \times 10^{-2}$. **c**, Input for experiment shown in **a**. **d**, Co-immunoprecipitation of the METTL3-interacting protein DGCR8. Western blot using the indicated antibodies with IgG used as control for the immunoprecipitation. **e**, Immunoprecipitation of endogenous DGCR8. Western blot using an antibody against m^{6}A methylated RNA. **f**, Similar as **e**, but control cells or cells depleted of METTL3 were compared. **g**, Similar immunoprecipitation as **e**, however, after immunoprecipitation of DGCR8, a radiolabelled RNA linker was ligated to the RNA bound by DGCR8. Bars represent the average normalized intensity of three biological replicates. $***P < 5 \times 10^{-4}$. **h**, Similar as **g** but the pri-miRNAs bound by DGCR8 were extracted and quantified by qRT–PCR. The bar graph shows the average level of a panel of miRNAs quantified in triplicate and analysed and shown in more detail in Extended Data Fig. 9. $****P < 1 \times 10^{-4}$. **i**, Model of METTL3 regulation of miRNA biogenesis. The molecules represented in the schematic are: histones (yellow), RNA Pol II (orange), METTL3 (green), m^{6}A (red), DGCR8 (blue), DROSHA (pink) and a putative unknown reader of the m^{6}A mark (grey).

Since the m^{6}A mark is added to pri-miRNAs, and we observed an accumulation of unprocessed pri-miRNAs upon METTL3 depletion, we questioned whether METTL3 is required for the engagement of the pri-miRNA by the microprocessor. We first tested whether METTL3 and DGCR8 are part of a complex. Immunoprecipitation of METTL3 from nuclear lysates co-precipitated DGCR8; however, this interaction was mediated through RNA, as RNase treatment disrupted this association (Fig. 4d).

We next sought to determine whether DGCR8 interacts with methylated RNA *in vivo*. To do this, we exposed cells to ultraviolet light for *in vivo* crosslinking (UV-crosslinking), isolated nuclear fractions and immunoprecipitated endogenous DGCR8. After immunoprecipitation of DGCR8 and SDS–polyacrylamide gel electrophoresis (SDS–PAGE), m^{6}A immunoblotting revealed that DGCR8 indeed interacts with methylated RNA (Fig. 4e). On the basis of our observations, we predicted that a reduction in METTL3 levels should decrease the levels of methylated RNA bound by DGCR8. Indeed, depleting METTL3 significantly reduced the m^{6}A-methylated RNA bound by DGCR8 (Fig. 4f). However, the binding of DGCR8 to methylated RNA is unlikely to be direct, as we detected no preference for DGCR8 binding to methylated RNA over unmethylated RNA *in vitro* (Extended Data Fig. 8c).

Since messenger RNAs tend to form secondary structures, including short hairpins that resemble pri-miRNAs, a potential role of pri-miRNA methylation might be to confer specificity for, and facilitate the recognition of, pri-miRNA structures by DGCR8. On the basis of this hypothesis, we would expect that a reduction in the levels of methylated pri-miRNAs would reduce the total amount of RNA recognized and bound by DGCR8. To test this, we immunoprecipitated DGCR8 from control and METTL3-depleted cells and radiolabelled the total RNA bound to DGCR8. Consistent with our model, METTL3 depletion significantly reduced the amount of total RNA (Fig. 4g) as well as pri-miRNAs (Fig. 4h and Extended Data Fig. 9) bound by DGCR8. These findings suggest that the m^{6}A methylation mark allows for the effective recognition of pri-miRNAs by DGCR8 and their subsequent processing to pre-and mature miRNAs.

By using an unbiased approach, we have identified m^{6}A as a novel regulator of miRNA processing. Our findings reveal that METTL3 methylates primary inter- and intragenic miRNAs. The m6A modification facilitates the recognition of pri-miRNA sequences and marks an initiation

event in miRNA biogenesis (Fig. 4i). We propose that the m^{6}A mark on transcripts at pri-miRNA sequences initiates a global co-transcriptional program comprising the engagement and processing of primary miRNAs by the microprocessor machinery. The m^{6}A mark thus has an important role in the nucleus—allowing the microprocessor complex to recognize its specific substrates as opposed to unintended secondary structures. Additionally, altered METTL3 expression in various human malignancies may contribute to the aberrant expression of miRNAs seen in cancer.

Online Content Methods, along with any additional Extended Data display items and Source Data, are available in the online version of the paper; references unique to these sections appear only in the online paper.

Received 11 March 2014; accepted 2 February 2015.
Published online 18 March 2015.

1. Denli, A. M., Tops, B. B., Plasterk, R. H., Ketting, R. F. & Hannon, G. J. Processing of primary microRNAs by the Microprocessor complex. *Nature* **432,** 231–235 (2004).
2. Gregory, R. I. *et al.* The Microprocessor complex mediates the genesis of microRNAs. *Nature* **432,** 235–240 (2004).
3. Han, J. *et al.* The Drosha–DGCR8 complex in primary microRNA processing. *Genes Dev.* **18,** 3016–3027 (2004).
4. Landthaler, M., Yalcin, A. & Tuschl, T. The human DiGeorge syndrome critical region gene 8 and Its *D. melanogaster* homolog are required for miRNA biogenesis. *Curr. Biol.* **14,** 2162–2167 (2004).
5. Han, J. *et al.* Molecular basis for the recognition of primary microRNAs by the Drosha–DGCR8 complex. *Cell* **125,** 887–901 (2006).
6. Elemento, O., Slonim, N. & Tavazoie, S. A universal framework for regulatory element discovery across all genomes and data types. *Mol. Cell* **28,** 337–350 (2007).
7. Wei, C. M. & Moss, B. Nucleotide sequences at the N^6-methyladenosine sites of HeLa cell messenger ribonucleic acid. *Biochemistry* **16,** 1672–1676 (1977).
8. Dominissini, D. *et al.* Topology of the human and mouse m^{6}A RNA methylomes revealed by m^{6}A-seq. *Nature* **485,** 201–206 (2012).
9. Meyer, K. D. *et al.* Comprehensive analysis of mRNA methylation reveals enrichment in 3′ UTRs and near stop codons. *Cell* **149,** 1635–1646 (2012).
10. Bokar, J. A., Shambaugh, M. E., Polayes, D., Matera, A. G. & Rottman, F. M. Purification and cDNA cloning of the AdoMet-binding subunit of the human mRNA (N^6-adenosine)-methyltransferase. *RNA* **3,** 1233–1247 (1997).
11. Sibbritt, T., Patel, H. R. & Preiss, T. Mapping and significance of the mRNA methylome. *RNA* **4,** 397–422 (2013).
12. Camper, S. A., Albers, R. J., Coward, J. K. & Rottman, F. M. Effect of undermethylation on mRNA cytoplasmic appearance and half-life. *Mol. Cell. Biol.* **4,** 538–543 (1984).
13. Carroll, S. M., Narayan, P. & Rottman, F. M. N^6-methyladenosine residues in an intron-specific region of prolactin pre-mRNA. *Mol. Cell. Biol.* **10,** 4456–4465 (1990).
14. Thorvaldsdóttir, H., Robinson, J. T. & Mesirov, J. P. Integrative Genomics Viewer (IGV): high-performance genomics data visualization and exploration. *Brief. Bioinform.* **14,** 178–192 (2013).
15. Bujnicki, J. M., Feder, M., Radlinska, M. & Blumenthal, R. M. Structure prediction and phylogenetic analysis of a functionally diverse family of proteins homologous to the MT-A70 subunit of the human mRNA:m^{6}A methyltransferase. *J. Mol. Evol.* **55,** 431–444 (2002).
16. Chi, S. W., Zang, J. B., Mele, A. & Darnell, R. B. Argonaute HITS-CLIP decodes microRNA–mRNA interaction maps. *Nature* **460,** 479–486 (2009).
17. Pollard, K. S., Hubisz, M. J., Rosenbloom, K. R. & Siepel, A. Detection of nonneutral substitution rates on mammalian phylogenies. *Genome Res.* **20,** 110–121 (2010).
18. Lee, Y. & Kim, V. N. *In vitro* and *In vivo* assays for the activity of Drosha complex. *Methods Enzymol.* **427,** 87–106 (2007).
19. Auyeung, V. C., Ulitsky, I., McGeary, S. E. & Bartel, D. P. Beyond secondary structure: primary-sequence determinants license pri-miRNA hairpins for processing. *Cell* **152,** 844–858 (2013).

Acknowledgements We thank members of the Tavazoie laboratory as well as S. Kurdistani for comments on previous versions of this manuscript. We thank D. Bartel for suggestions about conservation analysis. We thank L. Fish for technical advice. We thank C. Zhao and C. Lai of the Rockefeller Genomics Resource Center for assistance with next-generation RNA-seq. We thank H. Molina of the Rockefeller Proteomics Center for his input in proteomics analysis. We thank C. Eicken of LC Sciences for assistance with microarray analysis. We thank H. Chang and P. Batista for providing targeted embryonic stem cells. C.R.A. was an Anderson Cancer Center Fellow at Rockefeller University. This work was supported by an Era of Hope Department of Defense Award to S.F.T. S.F.T. is a Department of Defense Breast Cancer Collaborative Scholars and Innovators Award recipient.

Author Contributions C.R.A. conceived the project and designed the experiments and S.F.T. supervised the project. C.R.A. performed most of the experiments, H.L. generated stable cell lines, performed qRT–PCR reactions and cloning, H.G. performed computational analyses and N.H. provided technical support. C.R.A. and S.F.T. wrote the manuscript.

Author Information RNA-seq data have been deposited in the Gene Expression Omnibus under accession number GSE60213. Reprints and permissions information is available at www.nature.com/reprints. The authors declare no competing financial interests. Readers are welcome to comment on the online version of the paper. Correspondence and requests for materials should be addressed to S.F.T. (stavazoie@rockefeller.edu).

METHODS

Tissue culture. MDA-MB-231, HeLa and human umbilical vein endothelial cells (HUVECs) were purchased from ATCC. MDA-MB-231, HEK293T and HeLa cells were propagated *in vitro* with DMEM supplemented with 10% fetal bovine serum (FBS), 1% penicillin–streptomycin, 2 mM L-glutamine, 1 mM sodium pyruvate, and 2.5 $\mu g\,ml^{-1}$ fungizone. HUVECs were cultured with Endothelial Cell Growth Media (CC-3162, Lonza). Experiments with HUVECs were conducted with cells from passage 2 to 5.

Stable overexpression and knockdowns. Generation of lentivirus-mediated knockdown and retroviral-overexpressing cells were performed as described previously[20]. For overexpression studies, human complementary DNA of *METTL3* with carboxy-terminal Flag tag was cloned into pBabe-Puro retroviral expression vector. For knockdown studies, commercially available shRNA glycerol stocks were purchased (Sigma). Two shRNAs in pLKO lentiviral expression vectors against METTL3 that showed the best knockdown efficiencies (TRCN0000034715, TRCN0000034717) and control shRNA (SHC002) were used for experiments. Owing to the loss of knockdown over time, fresh knockdown cell lines were generated after a few passages.

qRT–PCR. Mature miRNAs were quantified by either Taqman microRNA assays (Applied Biosystems) or poly-A tailing of total RNA followed by reverse-transcriptase (RT) reaction with T7 oligo dT (NEB). Quantitative miRNA expression data were acquired and analysed using a 7900HT Fast Real-Time PCR System (Applied Biosystems). Pri-miRNAs were measured using the TaqMan Pri-miRNA Assay. RNU44, GusB, GAPDH and 18S were used as endogenous controls.

Small RNA isolation. Total RNA from cells was extracted and purified using the mirVana (Applied Biosystems) or Total RNA Purification Kit (Norgen Biotek) according to the manufacturer's instructions.

m^{6}A immunoprecipitation and RNA-seq. 3×10^7 cells per sample were lysed using LB1 buffer (50 mM HEPES-KOH pH 7.5, 140 mM NaCl, 1 mM EDTA, 10% glycerol, 0.5% Triton X-100 and protease inhibitors). The nuclear fraction was then lysed with M-PER buffer (Thermo Scientific) and diluted tenfold in dilution buffer (50 mM Tris-Cl, pH 7.4, 100 mM NaCl) before the immunoprecipitation. Rabbit anti-m^{6}A antibody (Synaptic Systems) and rabbit IgG control bound to protein A Dynabeads (Invitrogen) were used for the immunoprecipitations. The immunoprecipitated RNA was eluted with N^6-methyladenosine (Sigma-Aldrich), ethanol precipitated and resuspended in water. RNA was barcoded using ScriptSeq V2 kit (Epicentre) and sent for sequencing.

m^{6}A analysis. Reads were mapped to the human genome (build hg19) using bowtie2 with "sensitive-local" option[21]. Mapped reads were converted into genomic intervals (bed format). ChIPseeqer[22] was used to detect statistically significant peaks that were present in the m^{6}A co-precipitation samples and not the IgG control. The following parameters were used: -t 10 -fold_t 2 -minlen 20. FIRE was used for non-discovery analysis, and ChIPseeqer was used for shuffled sequences.

miRNA expression profiling. Total RNA extracted from two independent stable knockdowns of METTL3 and two control cells was labelled and hybridized on miRNA microarrays by LC Sciences. The arrays have probes for all human miRNAs (1,872 precursors, 2,578 mature) available in the miRBase database (release 20). Of all the probes assayed, those corresponding to 441 miRNAs revealed a signal above background in at least two of the MDA-MB-231 cell lines. Owing to the global change in miRNA levels, normalization was done using a set of small ribosomal RNAs present on the platform for use in data normalization. This set of controls contains 6 probes against the 5S ribosomal RNAs and detects 17 RNA species altogether (NR_023363 to NR_023379).

HITS-CLIP. We performed HITS-CLIP as previously described[23] with some modifications. After UV-crosslinking (400 $mJ\,cm^{-2}$ of 254 nm ultraviolet), we isolated nuclear fractions from 3×10^7 cells per sample using LB1 buffer. The nuclear fraction was then lysed in M-PER buffer and diluted tenfold in a buffer containing 50 mM Tris-HCl pH 7.4 and 100 mM NaCl, before the immunoprecipitation. For the endogenous immunoprecipitation we used 3 μg of anti-METTL3 rabbit antibody (Bethyl) or rabbit IgG as control bound to protein A dynabeads (Invitrogen). After the immunoprecipitation a ^{32}P-labelled linker was ligated to the RNA on the beads. The samples were resolved using SDS–PAGE, transferred to nitrocellulose membrane and exposed overnight. The films were used to guide the cut of the membrane to extract the radiolabelled RNA. RNA was extracted in 200 μl of PK buffer (100 mM Tris-Cl pH 7.5, 50 mM NaCl and 10 mM EDTA) containing proteinase K (4 $mg\,ml^{-1}$), then adding 200 μl of PK buffer containing 7 M urea and lastly 400 μl of acid phenol:chloroform, each step 20 min at 37 °C at 1,000 r.p.m. shaking. The aqueous solution was then precipitated and resuspended in RNase-free water as described later. An RNA linker was ligated to the purified RNA at 16 °C overnight. The RNA was once again extracted using phenol:chloroform and precipitated as previously described. This new RNA was reverse transcribed and PCR enriched. These PCR amplicons were resolved in a TBE-Urea polyacrylamide gel and DNA between 90 and 140 bp was extracted. This DNA was further enriched with the addition of Solexa fusion primers and the product was resolved in a 2% metaphor agarose gel, from which DNA between 150–170 bp was extracted. The samples were submitted for high-throughput sequencing using an Illumina HiSeq 2000 instrument with 50 bp single-end runs.

HITS-CLIP analysis. The reads were trimmed and clipped using cutadapt (v.1.2.1) and were subsequently mapped to the human genome (build hg19) using bowtie2 (ref. 21). CIMS package[23] was used to detect CLIP clusters with crosslinking-induced mutations. FIRE was used for non-discovery analysis, and ChIPseeqer for shuffled sequences.

Density plots analysis. The distances between peaks located in introns to closest miRNAs were measured using closestBed. In R, ggplot was used to generate the density plots.

Co-immunoprecipitations. Cells were lysed with LB1 and the nuclear fraction was then lysed with M-PER buffer (Thermo Scientific) and diluted tenfold in dilution buffer. Immunoprecipitations were performed with anti-METTL3 rabbit antibody (Bethyl) or anti-DGCR8 rabbit antibody (Abcam), previously bound to magnetic Dynabeads Protein A (Life Technologies), in the presence of either RNase A or RNase inhibitor (Promega). The immunoprecipitations were washed twice with high-salt buffer (50 mM Tris-HCl pH 7.4, 300 mM NaCl) followed by two more washes with low-salt buffer (50 mM Tris-HCl pH 7.4, 50 mM NaCl). The following antibodies were used for western blot analysis: anti-METTL3 (mouse, Novus Biologicals), anti-DGCR8 (mouse, Abcam), anti-m^{6}A (mouse, Synaptic Systems). For the *in vitro* binding assay, once DGCR8 was immunopurified and still bound to the magnetic beads it was incubated with 1 μg of pri-let-7e and 200 ng of pri-miR-1-1 in the presence of RNase inhibitors for 20 min at room temperature, washed twice and eluted with 170 μl of RNA elution buffer (0.3 M sodium acetate, pH 5.5 and 2% SDS). RNA was then extracted with 200 μl of acid phenol:chloroform, precipitated and resuspended in RNase-free water as described later. An aliquot of the elution was then used for northern blot analysis.

For the radiolabelled experiments the cells were ultraviolet-crosslinked, the nuclear fraction was lysed with M-PER buffer and diluted tenfold in dilution buffer. The nuclear extracts were immunoprecipitated with anti-DGCR8 antibody or IgG as control. An RNA oligonucleotide was labelled with ^{32}P-γ-ATP (Perkin Elmer) and ligated to the co-immunoprecipitated RNA as in the HITS-CLIP protocol. The samples (triplicates) were loaded in an SDS–PAGE, transferred, and the membrane was exposed overnight or longer if needed. After the image of the radiolabelled RNA was obtained, the same membrane was immunoblotted for DGCR8 for normalization. Quantitation was achieved using ImageJ[24].

For the endogenous DGCR8-pri-miRNA binding experiments, similar to the radiolabelled experiments, the cells were ultraviolet-crosslinked and the nuclear fraction was lysed with M-PER buffer and diluted in dilution buffer. The nuclear extracts were immunoprecipitated with an anti-DGCR8 antibody or IgG as a control. The RNA was extracted by treatment with 200 μl of proteinase K (4 $mg\,ml^{-1}$) in PK buffer (100mM Tris-Cl pH 7.5, 50 mM NaCl and 10 mM EDTA) and incubation at 37 °C for 20 min with shaking. Then, 200 μl 7 M urea in PK buffer was added and incubated for 20 min more at 37 °C with shaking. After that 400 μl acid phenol:chloroform (Ambion) was added to the solution, vortexed and centrifuged at maximum speed for 5 min. The aqueous phase was precipitated with 50 μl 3 M NaOAc pH 5.2, 0.75 μl glycoblue and 1 ml of 1:1 ethanol:isopropanol at −20 °C for at least 30 min. The mix was then centrifuged at 4 °C at maximum speed for 15 min, and the pellet washed with 80% ethanol and air dried. The RNA was resuspended in 20 μl of RNase-free water and 8 μl were used to produce cDNA by ramdom hexamers (SuperScript III First-Strand Synthesis System, Life Technologies) and qRT–PCR was carried out using specific miRNA primers.

Northern blots. Non-radioactive northern blots were performed as previously described[25]. RNA was extracted with mirVana (Applied Biosystems) or Total RNA Purification Kit (Norgen Biotek). DIG-labelled LNA probes against let-7e and miR-1-1 were obtained from EXIQON. Pre-stained marker (DynaMarker) was obtained from BioDynamics Laboratory and Low Range ssRNA Ladder from NEB. Mini-protean 10% and 15% pre-cast TBE-Urea gels were purchased from Bio-RAD and TBE buffer from Invitrogen. Samples were prepared using 2× Gel Loading Buffer (Ambion) and denatured for 5 min at 95 °C. Gels were run at 200 V in 1× TBE buffer and then transferred to a nylon membrane at 80 V for 1 h in 0.5× TBE buffer. Membranes were either chemically crosslinked with EDC (0.753 g of 1-ethyl-3-(3-dimethylaminopropyl) carbodiimide in 24 ml of 125 mM solution of 1-methylimidazole pH of 8.0) for mature and pre-miRNAs (2 h at 65 °C) or ultraviolet-crosslinking for pri-miRNAs (240 mJ). The membrane was then pretreated with hybridization buffer (DIG Easy Hyb Granules, Roche) at 37 °C for at least 30 min in a hybridization oven. The probe was denatured at 95 °C for 1 min and added to the hybridization buffer (37 °C overnight). The membrane was washed twice with Low Stringent Buffer at 37 °C for 15 min, twice with High Stringent Buffer at 37 °C for 5 min and once with Washing Buffer at 37 °C for 10 min. Then the membrane was incubated in Blocking Buffer (DIG Wash and block buffer set, Roche) for 3 h

at room temperature and the anti-Digoxigenin-AP antibody (Roche) was added (1:15,000 dilution) and incubated at room temperature for an extra 30 min. The membrane was washed in DIG Washing Buffer four times for 15 min each at room temperature. Finally, the membrane was incubated in development buffer for 5 min and developed with CDP-Star (Roche) for 5 min and exposed to X-ray films.

***In vitro* pri-miRNA processing.** Pri-miRNAs were *in vitro* transcribed using the T7 based MEGAshortscript kit (Life Technologies) according to the manufacturer's indications. In cases where m^6A modifications were added *in vitro*, N^6-methyl-ATP (tri-link) was used in a ratio 4:1 to ATP in the *in vitro* transcription reaction. Pri-miRNA processing reactions were performed as previously described[18]. In brief, HEK293T cells were co-transfected with plasmids carrying DROSHA and DGCR8 (obtained from Addgene). Forty-eight hours later, cells were lysed in lysis buffer (20 mM Tris-HCl pH 8.0, 100 mM KCl and 0.2 mM EDTA) and sonicated for 1 min with 5 s pulses at 30% amplitude. The whole cell was obtained after centrifugation at 12,000 r.p.m. at 4 °C for 15 min. In the case of testing the effect of METTL3 depletion on pri-miRNA processing, cells were not transfected and the endogenous activity was measured. The *in vitro* processing reaction contained 3 µl of 64 mM $MgCl_2$ solution, 1 µg of let-7e pri-miRNA (wild type or m^6A methylated), 50 ng of control pri-miR-1-1, 0.75 µl of RNase inhibitor, 15 µl of HEK293T whole extract and RNase-free water to a final volume of 30 µl. The reactions were incubated at 37 °C for 90 min. Then 170 µl of RNA elution buffer (0.3 M sodium acetate, pH 5.5 and 2% SDS) was added to the reaction to dissociate the RNA from the proteins and terminate the reaction. RNA was then extracted with 200 µl of acid phenol:chloroform (Ambion), vortexed and centrifuged for 5 min at room temperature. After extraction the RNA was precipitated at −20 °C by adding 20 µl of sodium acetate (3 M), 1 µl of glycoblue (Life Technologies), and 800 µl of a mix of isopropanol:ethanol (1:1). The mix was then centrifuged at 4 °C at maximum speed for 15 min, and the pellet washed with 80% ethanol and air-dried. The RNA was resuspended in 30 µl of RNase-free water and 5 µl was used for northern blot analysis.

Reporter assays. Analysis of pri-miRNA processing using ectopic reporter constructs was performed as previously described[19]. We used the pri-miRNA reporter construct developed previously[19] and replaced the miRNA control pri-miR-1-1 with a mutant version in which the adenosines of the potential METTL3 motifs were mutated. Then we placed the query miRNA, either wild-type pri-let-7e or its altered version, in which the As of the putative METTL3 motifs were mutated to Ts, upstream of the pri-miR-1-1 control. We then used these two constructs to transfect HEK293T cells using Lipofectamine 2000. Forty-eight hours later the RNA was extracted and qRT–PCR was performed to test the production of mature let-7e and mature miR-1-1.

20. Tavazoie, S. F. *et al.* Endogenous human microRNAs that suppress breast cancer metastasis. *Nature* **451,** 147–152 (2008).
21. Langmead, B. & Salzberg, S. L. Fast gapped-read alignment with Bowtie 2. *Nature Methods* **9,** 357–359 (2012).
22. Giannopoulou, E. G. & Elemento, O. An integrated ChIP-seq analysis platform with customizable workflows. *BMC Bioinformatics* **12,** 277 (2011).
23. Zhang, C. & Darnell, R. B. Mapping *in vivo* protein–RNA interactions at single-nucleotide resolution from HITS-CLIP data. *Nature Biotechnol.* **29,** 607–614 (2011).
24. Schindelin, J. *et al.* Fiji: an open-source platform for biological-image analysis. *Nature Methods* **9,** 676–682 (2012).
25. Kim, S. W. *et al.* A sensitive non-radioactive northern blot method to detect small RNAs. *Nucleic Acids Res.* **38,** e98 (2010).
26. Batista, P. J. *et al.* m^6A RNA modification controls cell fate transition in mammalian embryonic stem cells. *Cell Stem Cell* **15,** 707–719 (2014).

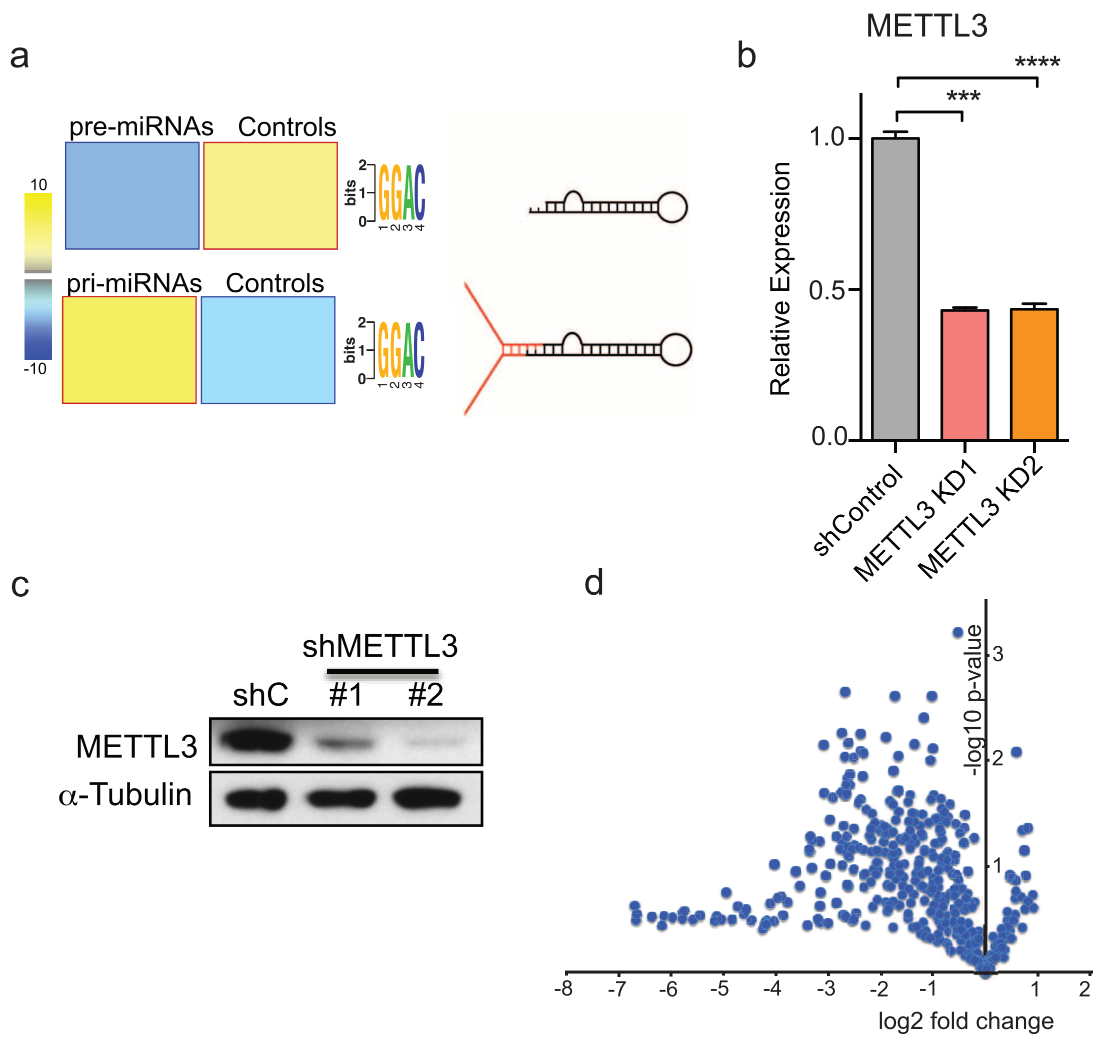

Extended Data Figure 1 | METTL3 regulates the expression levels of mature miRNAs. a, Unbiased search for *cis*-regulatory elements using the FIRE algorithm. FIRE motif discovery analysis of pre-miRNAs and pri-miRNA sequences, as well as random sequences of the same length, reveals overrepresentation of the METTL3 motif in pri-miRNAs sequences (containing pre-miRNAs plus adjacent 100 bp) but not in pre-miRNAs. Yellow represents overrepresentation, and blue depicts underrepresentation of the motif. The magnitude of the over/underrepresentation is represented by the linear-scale heat map on the left. A schematic representation of a pre-miRNA and a pri-miRNA is shown on the right. **b**, **c**, qRT–PCR (**b**) and western blot (**c**) quantifications of METTL3 upon transduction with two independent shRNAs targeting *METTL3* (METTL3 KD1 and METTL3 KD2) in MDA-MB-231 cells. Samples were normalized to *GAPDH*. Data from biological triplicates are shown. Bar graphs represent a linear scale and error bars represent s.d. $****P < 1 \times 10^{-4}$, $***P < 5 \times 10^{-4}$. **d**, A volcano plot representation of the microarray of miRNAs shown in Fig. 2a, where the *y*-axis represents the $-\log_{10}$ of the *P* value, and the *x*-axis represents the fold change ($\log_2$) between the expression levels of the miRNA from the METTL3 depletion (average of two independent shRNAs) versus the average of two control samples.

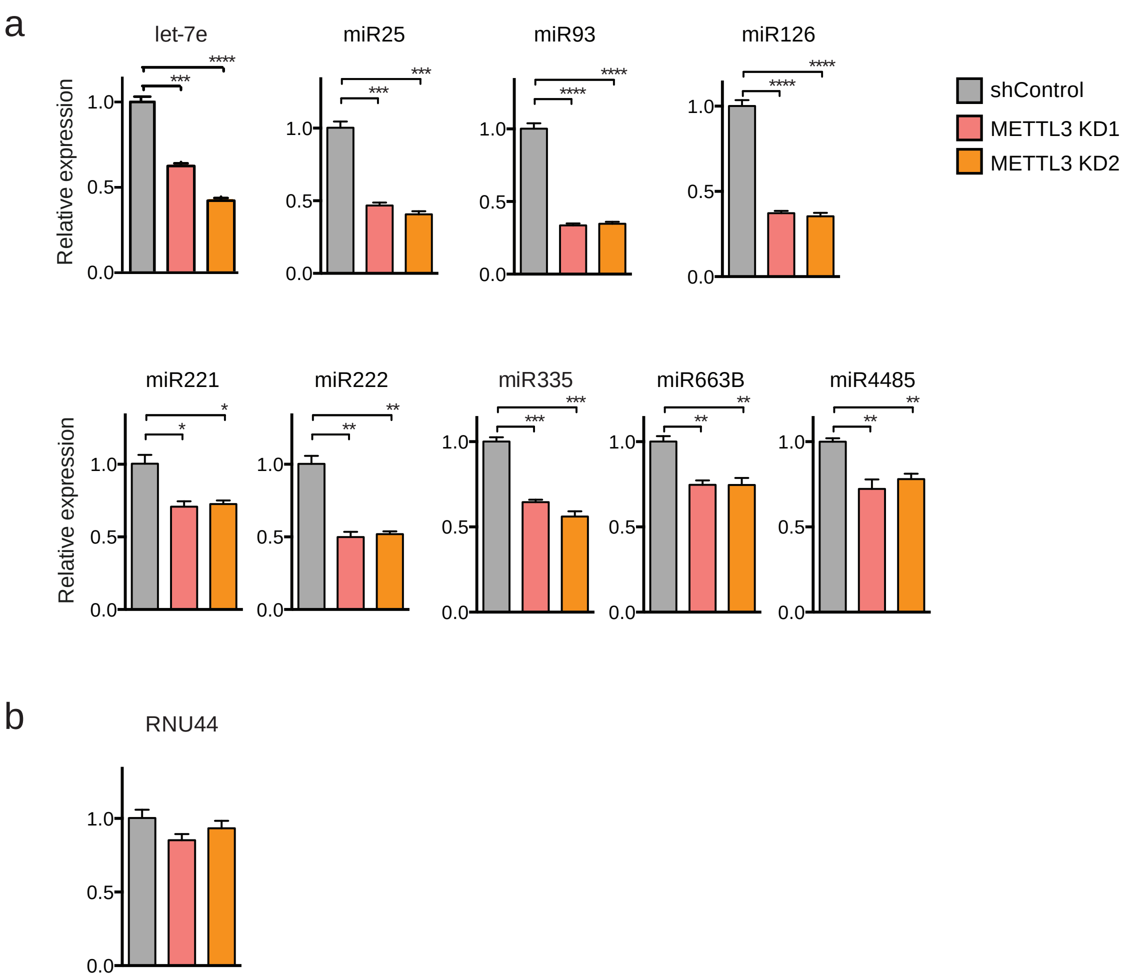

Extended Data Figure 2 | Mature miRNAs are downregulated upon METTL3 depletion in MDA-MB-231 cells. **a**, Quantification of representative miRNAs that were affected by METTL3 depletion in MDA-MB-231 cells as measured by qRT–PCR. Expression values were normalized to *SNORD44* (also known as *RNU44*). **b**, An example of a small RNA that did not display expression level changes upon METTL3 knockdown (*SNORD44*, small nucleolar RNA) normalized to 18S. All experiments were conducted in biological replicates. Bar graphs represent a linear scale and error bars represent s.e.m. $***P < 5 \times 10^{-4}$, $**P < 1 \times 10^{-3}$, $*P < 5 \times 10^{-2}$.

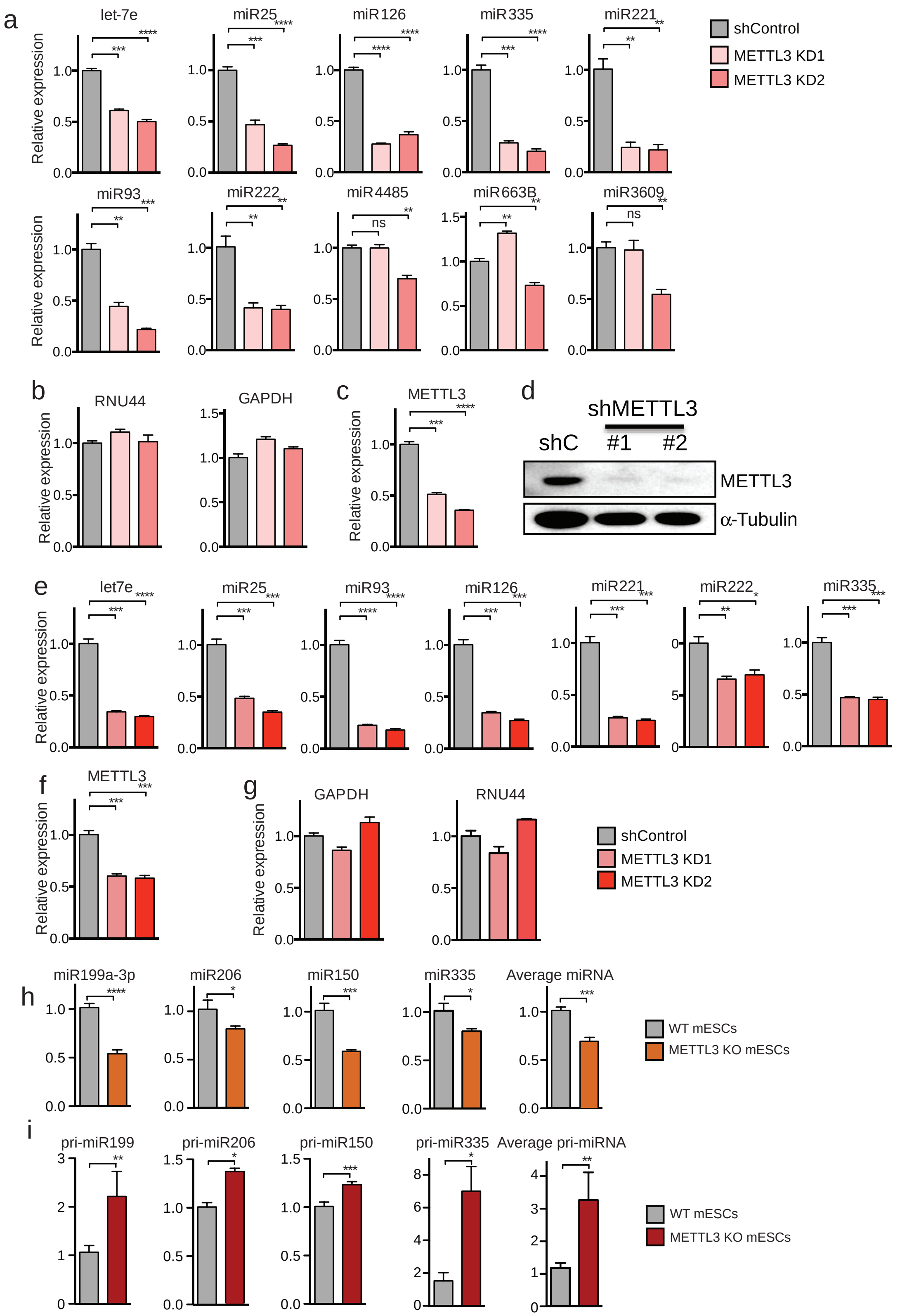

Extended Data Figure 3 | Mature miRNAs are downregulated upon METTL3 depletion in multiple mammalian cell lines. **a**, qRT–PCR quantification of examples of miRNAs that were modulated upon METTL3 depletion in HeLa cells. Samples were normalized to *RNU44*. **b**, Expression levels of genes used for normalization. All experiments were done in biological replicates. **c**, **d**, qRT–PCR (**c**) and western blot (**d**) quantifications of *METTL3* levels upon transduction with two independent shRNAs targeting *METTL3*. **e**, Expression levels of representative miRNAs that were affected by METTL3 depletion in HUVEC cells, as measured by qRT–PCR. Normalization was done by using *RNU44* as endogenous control. **f**, qRT–PCR quantification of *METTL3* upon transduction with two independent shRNAs targeting *METTL3*. **g**, Quantification of the expression levels of control genes. **h**, **i**, Examples of miRNAs affected in mouse embryonic stem cells in which *Mettl3* has been targeted using CRISPR[26], whose expression levels were measured by qRT–PCR. All experiments were done in biological replicates. Bar graphs represent a linear scale and error bars represent s.d. $***P < 5 \times 10^{-4}$, $**P < 1 \times 10^{-3}$.

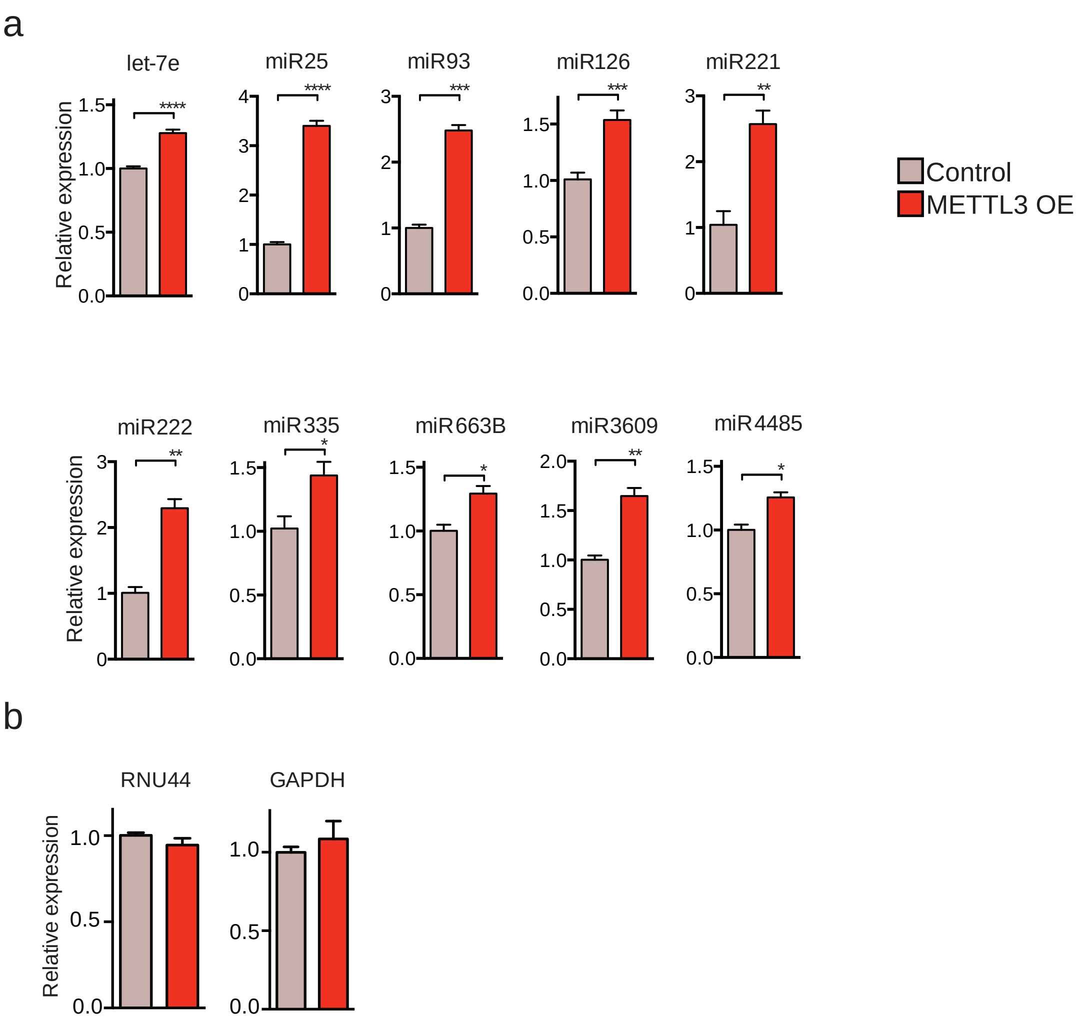

Extended Data Figure 4 | Mature miRNAs are upregulated upon METTL3 over-expression in MDA-MB-231 cells. **a**, qRT–PCR quantification of expression of representative miRNAs modulated upon METTL3 overexpression (METTL3 OE) in MDA-MB-231 cells. Samples were normalized to *RNU44*. **b**, qRT–PCR quantification of control *RNU44* and *GAPDH* genes normalized to 18S. All experiments were done in biological replicates. Bar graphs represent a linear scale and error bars represent s.d. $***P < 5 \times 10^{-4}$, $**P < 1 \times 10^{-3}$.

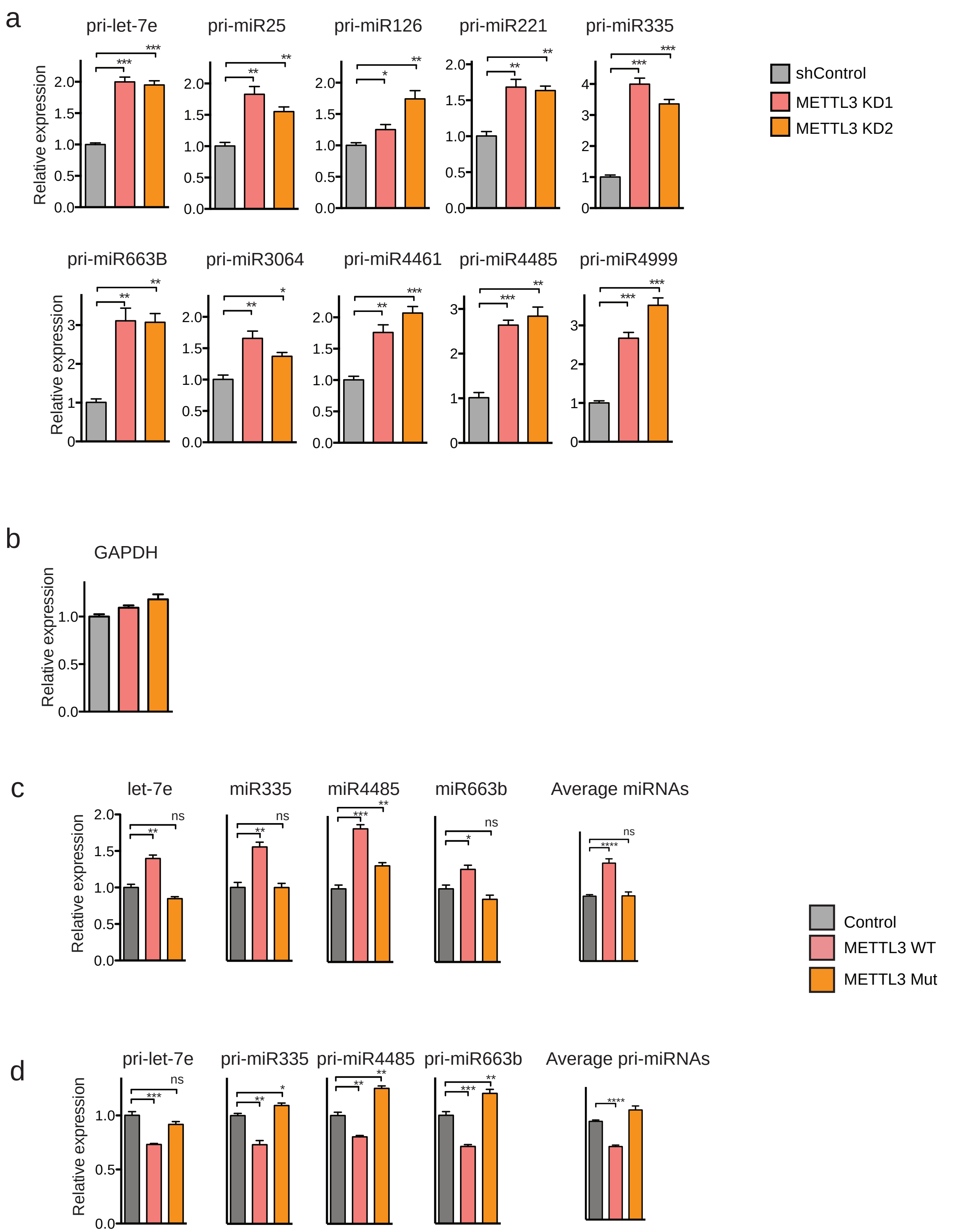

Extended Data Figure 5 | Quantification of mature and pri-miRNAs levels upon depletion and catalytic inactivation of METTL3 in MDA-MB-231 cells. **a**, qRT–PCR quantification of representative pri-miRNAs that were impacted by METTL3 depletion using two independent hairpins in MDA-MB-231 cells. Expression levels were normalized to *GAPDH*. **b**, qRT–PCR quantification of *GAPDH*, endogenous control. All experiments were done in biological replicates. **c**, **d**, Quantification of mature (**c**) and pri-miRNAs (**d**) upon stable transduction of MDA-MB-231 with either wild-type or a catalytic mutant METTL3. Mature miRNA expression was normalized to *RNU44* and pri-miRNAs to *GAPDH* expression levels. The last bar graph shows the averaged value for all individual miRNAs tested. The experiments were done in biological replicates. Bar graphs represent a linear scale and error bars represent s.d. $****P < 1 \times 10^{-4}$, $***P < 5 \times 10^{-4}$, $**P < 1 \times 10^{-3}$, $*P < 5 \times 10^{-2}$. NS, not significant.

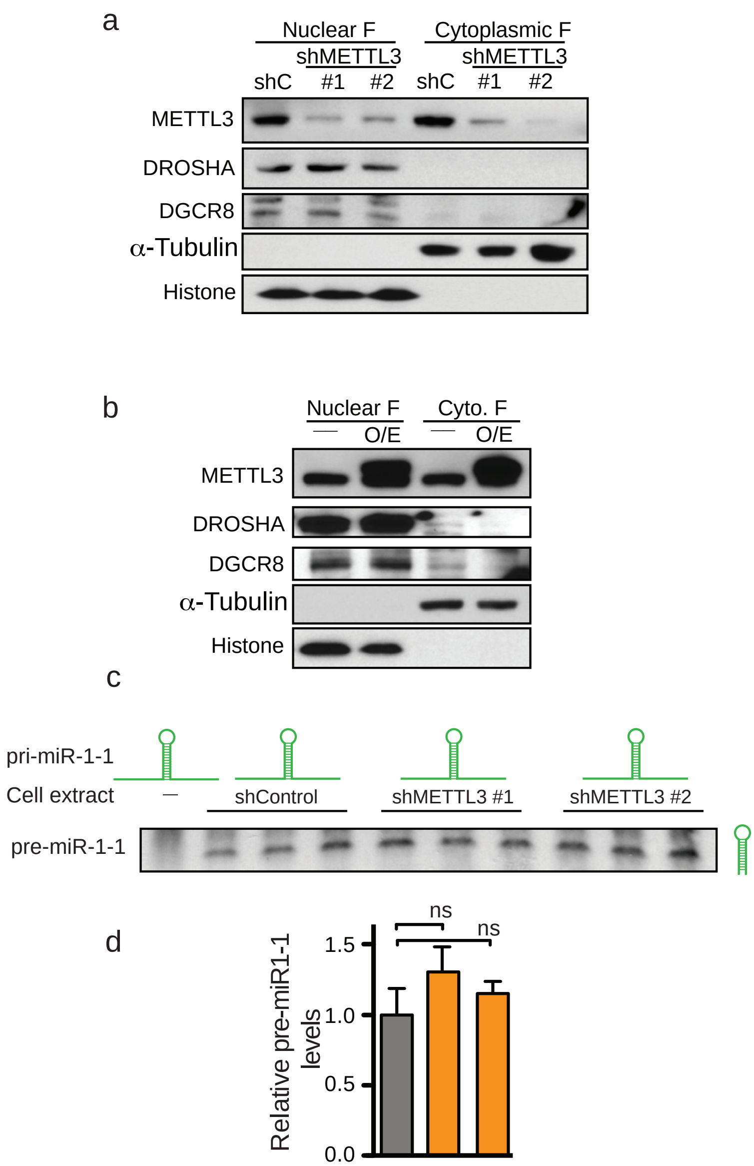

Extended Data Figure 6 | Expression and localization of the Microprocessor upon depletion or overexpression of METTL3. **a**, Western blot analysis of METTL3, DROSHA and DGCR8 obtained from nuclear and cytoplasmic fractions of cells transduced with two independent shRNAs targeting *METTL3* (shMETTL3 #1 and #2) or with an shRNA control (shC). Tubulin and histone 3 were used as loading controls as well as controls for the efficiency of the fractionation. **b**, Same as **a**, but in this case, lysate from cells overexpressing (O/E) METTL3 were compared to wild-type control cells. **c**, *In vitro* pri-miRNA processing reactions. Whole-cell extracts of control cells or cells depleted of METTL3 with two independent shRNAs were used to process *in vitro* transcribed pri-miR-1-1 to produce pre-miR-1-1 *in vitro*. Pre-miR-1-1 levels were then analysed by northern blot. **d**, Hybridization intensities of **c** were quantified, normalized by their inputs and shown in a bar graph format. Bar graphs represent a linear scale and error bars represent s.d.

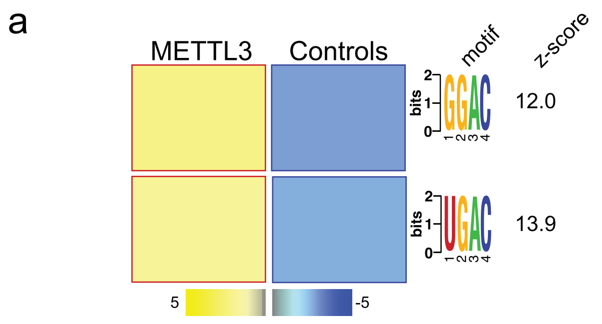

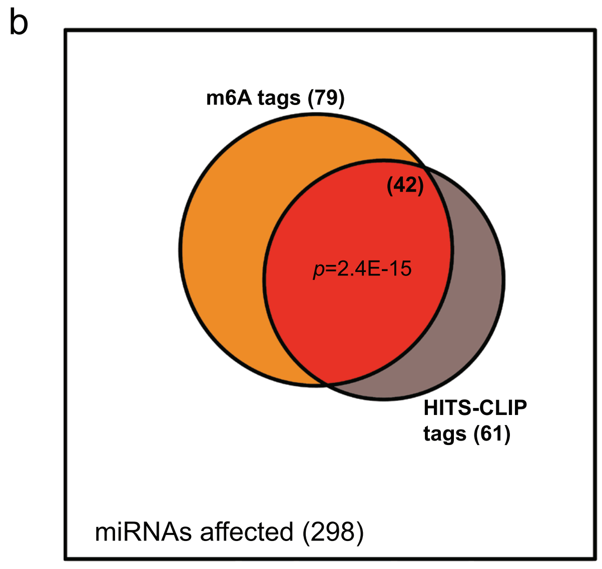

Extended Data Figure 7 | METTL3 binding and m6A co-localization in pri-miRNA regions. **a**, FIRE motif discovery analysis of the METTL3 HITS-CLIP binding sites compared to control sequences; two overrepresented versions of the METTL3 motif are shown with a *z*-score as indicated. The heat map represents a linear scale. **b**, Venn diagram representation of the overlap of miRNAs affected by METTL3 depletion and bearing the m^6A and/or the METTL3 HITS-CLIP tags within 1 kb from any particular miRNA locus. The overlap of miRNAs containing both m^6A and METTL3 HITS-CLIP tags is depicted in red. $P = 2.4 \times 10^{-15}$.

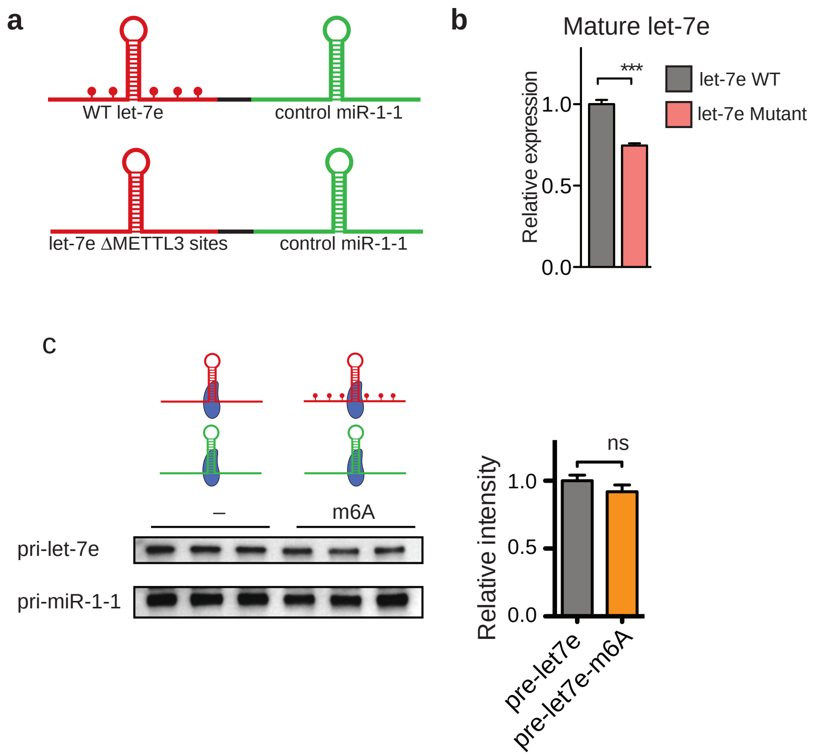

Extended Data Figure 8 | m6A facilitates processing of pri-miRNAs. **a**, Schematic representation of the reporters used to study the role of METTL3 in pri-miRNA processing. Represented in red is the pri-let-7e sequence and in green, the control pri-miR-1-1. The top reporter contains a wild-type (WT) sequence of pri-let-7e and the potential sites of methylations are depicted as red dots. The reporter on the bottom contains a mutant version of pri-let-7e in which the five putative adenines of the METTL3 motif were mutated. **b**, HEK293T cells were transfected with the reporters depicted in **a**, RNA was extracted, and mature miRNA expression was quantified by qRT–PCR. The bar graph represents the relative expression levels of mature let-7e normalized to mature miR-1-1. **c**, *In vitro* binding assays using immunopurified DGCR8. Samples containing *in vitro* transcribed pri-let-7e with N^6-methyladenosine or unmodified adenosines were incubated with magnetic-bead- bound DGCR8, washed, eluted and analysed by northern blot. All reactions contained unmodified pri-miR-1-1 as endogenous control. The top panel shows pri-let-7e and the bottom panel pri-miR-1-1. On the right side of the bar graph is depicted the average intensity of pri-let-7e normalized by pri-miR-1-1 levels. The experiment was done in biological triplicate. Bar graphs represent a linear scale and error bars represent s.d. $^{***}P < 5 \times 10^{-4}$. NS, not significant.

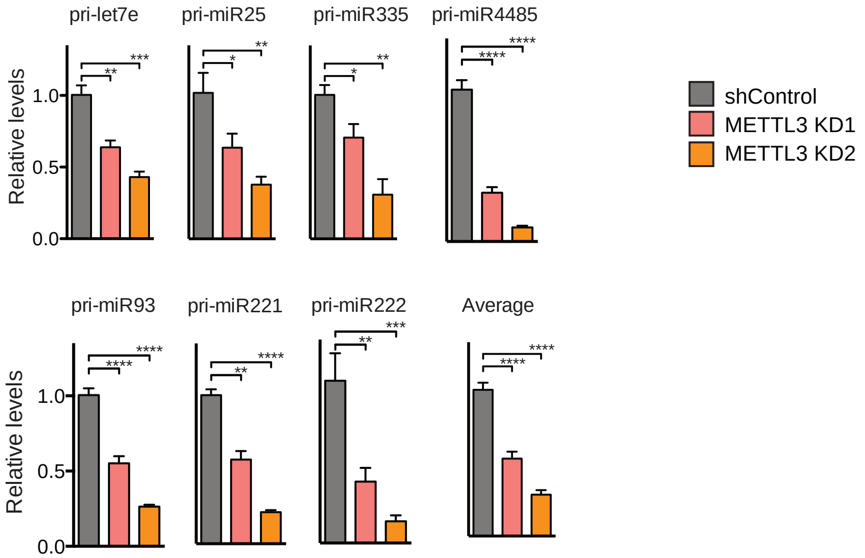

Extended Data Figure 9 | METTL3 depletion affects DGCR8 binding to endogenous pri-miRNAs. Immunoprecipitation of endogenous DGCR8 crosslinked to RNA of control cells or cells depleted of METTL3 using two independent shRNAs. After immunoprecipitation, the RNA was extracted and the expression levels of a set of pri-miRNAs were quantified by qRT–PCR. The average quantification is presented in Fig. 4h. Bar graphs represent a linear scale and error bars represent s.d. $****P < 1 \times 10^{-4}$, $***P < 1 \times 10^{-3}$, $**P < 1 \times 10^{-2}$, $*P < 5 \times 10^{-2}$.

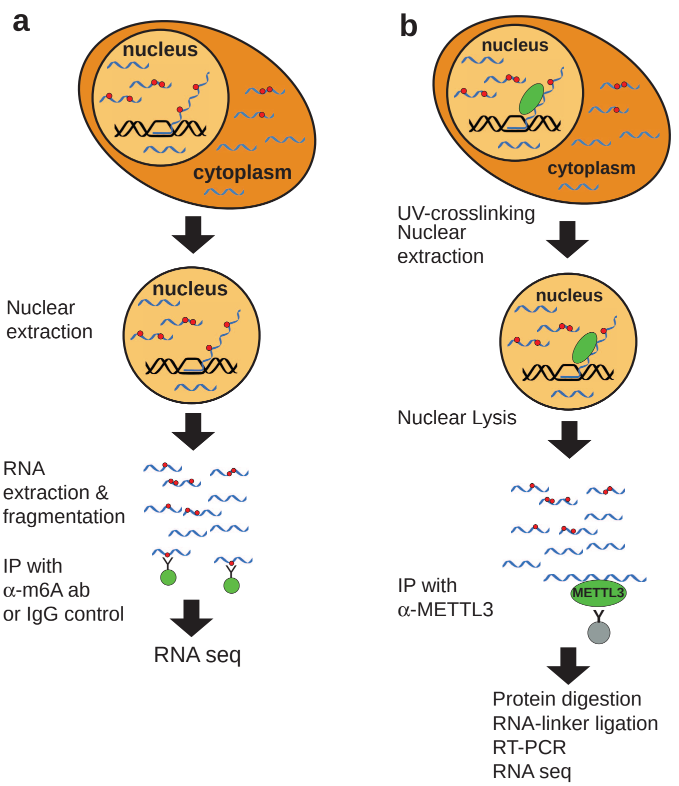

Extended Data Figure 10 | Schematic depiction of m^6A-seq and HITS-CLIP protocols. **a**, Schematic representation of the m^6A-seq protocol. **b**, Schematic representation of the HITS-CLIP protocol used. Both protocols are described in detail in Methods.

LETTER

doi:10.1038/nature14263

Structural imprints *in vivo* decode RNA regulatory mechanisms

Robert C. Spitale[1]*, Ryan A. Flynn[1]*, Qiangfeng Cliff Zhang[1]*, Pete Crisalli[2], Byron Lee[1], Jong-Wha Jung[2], Hannes Y. Kuchelmeister[2], Pedro J. Batista[1], Eduardo A. Torre[1], Eric T. Kool[2] & Howard Y. Chang[1]

Visualizing the physical basis for molecular behaviour inside living cells is a great challenge for biology. RNAs are central to biological regulation, and the ability of RNA to adopt specific structures intimately controls every step of the gene expression program[1]. However, our understanding of physiological RNA structures is limited; current *in vivo* RNA structure profiles include only two of the four nucleotides that make up RNA[2,3]. Here we present a novel biochemical approach, *in vivo* click selective 2′-hydroxyl acylation and profiling experiment (icSHAPE), which enables the first global view, to our knowledge, of RNA secondary structures in living cells for all four bases. icSHAPE of the mouse embryonic stem cell transcriptome versus purified RNA folded *in vitro* shows that the structural dynamics of RNA in the cellular environment distinguish different classes of RNAs and regulatory elements. Structural signatures at translational start sites and ribosome pause sites are conserved from *in vitro* conditions, suggesting that these RNA elements are programmed by sequence. In contrast, focal structural rearrangements *in vivo* reveal precise interfaces of RNA with RNA-binding proteins or RNA-modification sites that are consistent with atomic-resolution structural data. Such dynamic structural footprints enable accurate prediction of RNA–protein interactions and N^6-methyladenosine (m^6A) modification genome wide. These results open the door for structural genomics of RNA in living cells and reveal key physiological structures controlling gene expression.

SHAPE accurately identifies flexible (single-stranded) bases in RNA for all four nucleotides. However, current methods are potentially limited by high background rates (>70% of RNA molecules have no modification due to single-hit kinetics) and high false-positive rates due to spurious reverse transcription stops[4]. We overcome these problems by developing a new SHAPE probe that permits *in vivo* SHAPE modification and subsequent selective purification of the modified RNAs.

We designed, synthesized and tested a novel bifunctional chemical probe for *in vivo* RNA structure profiling genome wide (NAI-N_3; Fig. 1a, b and Extended Data Fig. 1). NAI-N_3 adds an azide group to NAI (2-methylnicotinic acid imidazolide), a cell-permeable SHAPE reagent[5]. By using copper-free click chemistry, a biotin moiety is selectively and efficiently added to NAI-N_3-modified RNA, providing a stringent purification handle with streptavidin-conjugated beads (Fig. 1c and Extended Data Fig. 2). NAI-N_3 generated identical profiles of reverse transcription stops to those obtained using our previously designed SHAPE reagent[5]. The fidelity of structural measurements was not affected by 'clicking' biotin onto NAI-N_3, or by molecular crowding of proteins, and NAI-N_3 showed uniform modification of all bases in denatured RNAs (Extended Data Fig. 3). We term this new chemoaffinity structure probing methodology icSHAPE; this method can also be applied to any *ex vivo* preparation of RNA, with slight modifications.

icSHAPE of ribosomal RNAs in mouse embryonic stem (ES) cells indicated that the method is quantitative and accurate, reporting the known structures of 18S and 28S ribosomal RNAs (Fig. 1d–f and Extended Data Fig. 4). Deep-sequencing results from icSHAPE showed strong correspondence with manual structure-probing gels (Pearson correlation r = 0.93, *in vivo*; Fig. 1d and Extended Data Fig. 4). rRNA is known to require the cellular environment for proper folding, and differences between *in vivo* and *in vitro* icSHAPE measurements highlighted important structural elements in the intact ribosome. We mapped our icSHAPE profiles onto the cryo-electron microscopy structure of the human 80S ribosome[6] and searched for differences between the *in vivo* and *in vitro* conditions. Conserved (mouse to human) nucleotides of high icSHAPE signal *in vivo* were unpaired in the cryo-electron microscopy structure (Fig. 1e); conversely, residues lacking icSHAPE reactivity *in vivo* were base-paired or engaged in extensive interactions that may stabilize the RNA backbone in the mature ribosome (Fig. 1f). Overall, these data

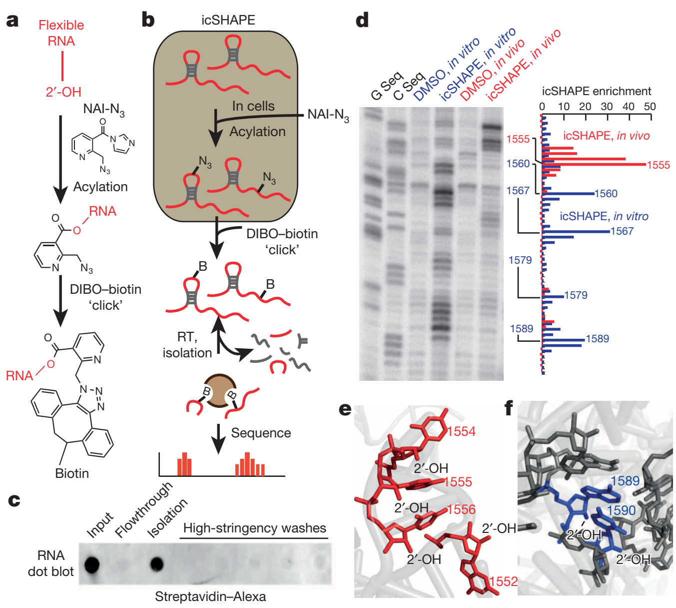

Figure 1 | icSHAPE is a novel and robust method for measuring RNA structure. **a**, Chemical scheme for the preparation of acylated RNA, which can be purified by biotin–streptavidin purification. DIBO, dibenzocyclooxtyne. **b**, Schematic of icSHAPE modification and purification steps to generate a sequencing library. RT, reverse transcription. **c**, Dot blot of biotin-modified RNA from icSHAPE through streptavidin affinity isolation. **d**, Denaturing gel electrophoresis of icSHAPE on the 18S rRNA from mouse ES cells. The corresponding icSHAPE profile, generated from deep sequencing and annotated for nucleotide position, is to the right. G Seq and C Seq indicate reverse transcription with dideoxyguanosine triphosphate or dideoxycytidine triphosphate, respectively. DMSO, dimethylsulfoxide. **e**, PyMol representation of rRNA, corresponding to regions of icSHAPE that are more reactive *in vivo* (Protein Data Bank (PDB) accession 3J3D). **f**, PyMol representation of rRNA, corresponding to regions of icSHAPE that are more reactive *in vitro*.

[1]Howard Hughes Medical Institute and Program in Epithelial Biology, Stanford University School of Medicine, Stanford, California 94305, USA. [2]Department of Chemistry, Stanford University, Stanford, California 94305, USA.
*These authors contributed equally to this work.

demonstrate that icSHAPE accurately measures RNA structures, both inside and outside of living cells.

We next used icSHAPE to measure RNA structural profiles of polyadenylated transcripts in mouse ES cells and generated ∼2.1 billion measurements for over 13,200 RNAs *in vivo* and *in vitro*, with high reproducibility (Extended Data Figs 5 and 6). The nucleotide composition in the transcriptome, mock-treated RNA and icSHAPE-treated RNAs are highly concordant, with a slight enrichment in NAI-N_3 samples for As and Us (Fig. 2a). This enrichment is expected given their bias for being located in single-stranded or loop regions[7]. icSHAPE thus affords the first complete RNA structurome of all four nucleotides *in vivo*.

icSHAPE data revealed the scale and distribution of RNA structural dynamics between *in vitro* conditions, in which folding is programmed entirely by sequence, versus *in vivo* conditions, in which folding occurs in the context of the intracellular environment[8]. Recent transcriptome-wide dimethylsulfate probing (DMS-seq), which interrogates two bases with strong bias towards adenosines (68% As and 24% Cs)[2,4], suggested that RNA structures are largely unfolded *in vivo*[2]; however, sampling only two of four nucleotides could result in an incomplete picture. We quantified RNA structural dynamics using two metrics. First, we calculated the difference in reactivity between our *in vivo* and *in vitro* icSHAPE measurements, termed the '*vivo–vitro* difference' (VTD; Fig. 2b and Methods). Adenosine residues have the largest VTD, whereas guanosine and cytidine residues are less variable between environments (Fig. 2c). These observations suggest that using probes that have a broader reactivity profile, such as NAI-N_3, will give a more complete representation of RNA structure.

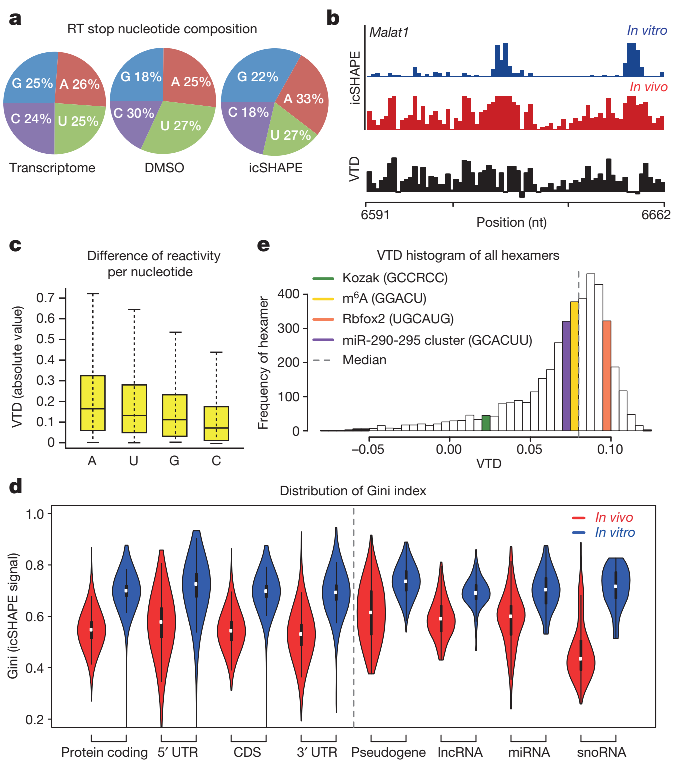

Figure 2 | icSHAPE reveals unique structural profiles for nucleobase reactivity and post-transcriptional interactions. **a**, Reverse transcription (RT) stop distribution for the transcriptome, DMSO control or icSHAPE libraries. **b**, icSHAPE data track and VTD calculation of the *Malat1* RNA (chromosome 19: 5,796,010–5,796,081). icSHAPE data are scaled from 0 (no reactivity) to 1 (maximum reactivity). nt, nucleotide. **c**, The VTD distribution for icSHAPE libraries. **d**, Gini index of icSHAPE data *in vivo* versus *in vitro*. **e**, The distribution of VTD profiles for all hexamer motifs across the transcriptome. Bin locations for several motifs for post-transcriptional regulation are highlighted.

Second, we used the Gini index[2] to quantify the distribution of icSHAPE reactivity profiles. Structured RNAs have some bases that are reactive and some not, leading to unequal distribution and a high Gini index, whereas unfolded RNAs have most bases in a uniformly reactive conformation (low Gini). We found that RNAs are less folded *in vivo*, consistent with a previous report[2], but the extent of unfolding varies in degrees that distinguish different classes of RNAs (Fig. 2d). Protein-coding messenger RNAs exhibited noticeable but partial unfolding (average Gini of 0.7 *in vitro* to 0.5 *in vivo*), with the largest variation noted at 3′ untranslated regions (UTRs) compared to coding sequences (CDSs) or 5′ UTRs. In contrast, noncoding RNAs, such as pseudogenes, long noncoding RNAs (lncRNAs) and primary microRNA (miRNA) precursors, retain substantially more of their RNA structure *in vivo* ($P < 2.2 \times 10^{-16}$, noncoding versus coding, Student's *t*-test). One exception to this rule are small nucleolar RNAs (snoRNAs), which exhibit the greatest level of increased reactivity *in vivo* among all classes of transcripts and may result from extensive rearrangements due to small nucleolar ribonucleoprotein (snoRNP) binding. Thus, most RNAs *in vivo* possess a substantial level of RNA structure beyond previous expectations based on DMS-seq[2]. Our data further suggest that RNA structural signatures *in vivo* can distinguish coding versus structural or regulatory RNAs, consistent with previous *in vitro* studies[9–12].

The dramatically different environments that RNA experiences when inside a cell compared to *in vitro* suggests that our VTD parameter could provide insight into functionally important RNA regulatory elements. To assess this possibility, we measured the VTD for all hexamer sequences (Fig. 2e and Supplementary Table 1). We observed unique VTD profiles for sequence motifs driving diverse post-transcriptional processes, including translation initiation, interaction with RNA-binding proteins (RBPs; for example, Rbfox2), RNA modification (m^6A) and miRNA seed matches[13–15] (Supplementary Tables 1 and 2). These results show that the VTD may classify RNA regulatory elements as preprogrammed or sensitive to *in vivo* remodelling. Furthermore, distinctive VTD profiles precisely at sites of post-transcriptional regulatory motifs suggest that RNA structural dynamics may be used to monitor these regulatory events in cells.

We hypothesized that translational regulatory elements may have conserved icSHAPE profiles between *in vivo* and *in vitro* conditions because the Kozak sequence, important for translation initiation[16], is among the most stable (low VTD) regions within mRNAs (Fig. 2d). RNA accessibility from −1 to −5 nucleotides upstream of the start codon has a major role in regulating translational output[10,17]. We used translation initiation[18] and pause sites[18], defined by ribosome profiling, to centre our structural reactivity analysis across the transcriptome (Fig. 3). Canonical initiation AUG sites are indeed preceded by ∼5 nucleotides of increased accessibility, and this pattern is nearly identical to *in vitro* folded RNA (Fig. 3a, b). A similar pattern of conserved upstream accessibility also precedes noncanonical start sites at upstream open reading frames (uORFs) and amino-terminal truncations (Fig. 3c). Non-start-site AUG codons are also associated with increased preceding reactivity, whereas noncanonical CUG start codons have a different profile, suggesting that RNA accessibility alone is not sufficient to dictate translational start sites (Extended Data Fig. 7). Ribosome profiling also defined ribosome pause sites as having a strong preference for glutamate or aspartate in the acceptor (A) site, where transfer RNA (tRNA) identity and the nascent peptide sequence are believed to strongly influence translation kinetics[18]. icSHAPE data at ribosome pause sites revealed a distinctive signature: loss of reactivity at the exit (E) and peptidyl-transferase (P) sites, whereas the A site is more reactive, preceded by a strong 3-nucleotide periodic reactivity pattern 5′ to the pause site for ∼12 nucleotides (Fig. 3d, e). Furthermore, a very similar pattern was observed *in vitro* under conditions that do not maintain mRNA interactions with the ribosome or tRNAs, suggesting that these structural profiles are programmed by mRNA sequence. Analysis of negative control sites—defined as sites on the same transcripts that match the codon composition, are in frame, and are at least 20 nucleotides away from

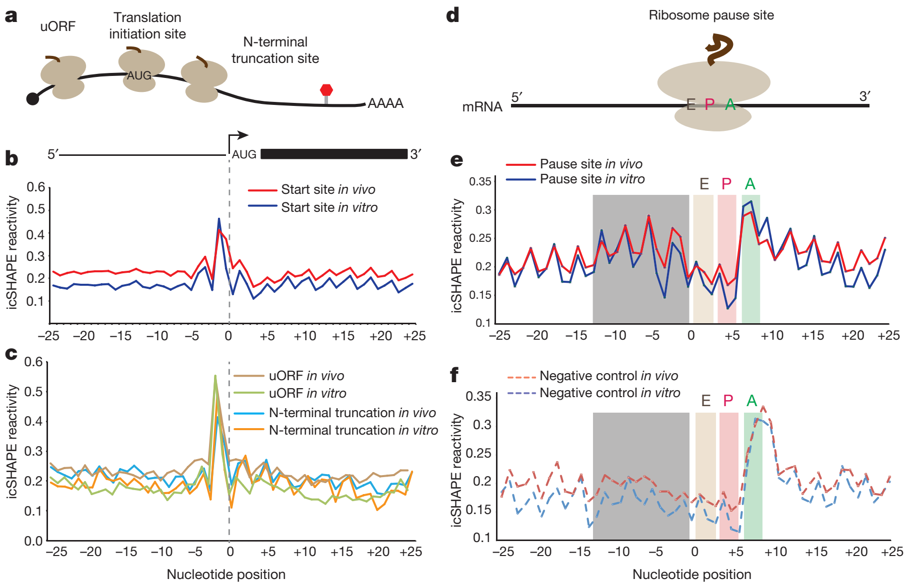

Figure 3 | icSHAPE reveals structural profiles associated with translation. **a**, Cartoon representation of ribosomes translating an mRNA. The uORF initiation site is represented by ribosome initiation upstream of the canonical start codon. The canonical start position is demarcated by 'AUG'. The N-terminal truncation is represented as a ribosome initiating to the 3′-end of the canonical start AUG. **b**, icSHAPE profile at canonical start codon position. **c**, icSHAPE profiles at uORF and N-terminal truncation sites. **d**, Cartoon representation of a paused ribosome and its corresponding A, P and E sites. **e**, The icSHAPE profile at ribosome pause sites. **f**, icSHAPE profile at negative control sites for pause sequences. Grey box highlights a region of structural difference upstream of true pause sites versus controls.

true pause sites—showed a very similar icSHAPE signature at the presumed ribosome E, P and A sites, but negative controls lacked the 5′ periodic signal (grey box in Fig. 3e, f). This observation suggests that the icSHAPE signature at ribosome pause sites is probably due to the codon bias at such sites, but sequences 5′ to the pause site may influence pausing. These results identify several physiological structural signatures of translational control elements, and suggest that they may be largely pre-programmed by the mRNA sequence.

In contrast, focal RNA structural rearrangements *in vivo* can identify sites of RBP interactions, which regulate RNA splicing, localization and stability[19] (Fig. 2d). The forkhead box (Fox) family of RBPs are important for tissue-specific control of alternative splicing, with Rbfox2 having key roles in ES cells[14,20]. High VTD at the known Rbfox2-binding motif (UGCAUG, Fig. 2e)[14,20] indicates a strong structural rearrangement *in vivo*. Alignment with the Rbfox–RNA NMR structure[21] and Rbfox2-binding sites identified by individual nucleotide crosslinking immunoprecipitation (iCLIP) in mouse ES cells[20] showed that the differential icSHAPE signal precisely matches the key RNA residues involved in Rbfox interaction (Fig. 4a, b). U1, G2 and A4 in the motif showed strong icSHAPE VTD signals. The 2′-hydroxyl groups of these three residues are flipped outward while G2 and A4 base pair upon Rbfox interaction[21], consistent with the adoption of new structural environments *in vivo* that we detected at these residues. In principle, the dynamic structural footprints of RBPs may enable comprehensive readout of RNA–RBP interactions *in vivo*. We tested this idea by implementing a support vector machine (SVM) algorithm to learn which dynamic icSHAPE signals are best able to predict sites of RNA regulation, using held out data for cross-validation of prediction accuracy (Extended Data Fig. 8 and Methods). Indeed, the combination of both *in vivo* and *in vitro* icSHAPE data increased the ability to predict true Rbfox2-binding sites compared to motif sequence or conservation alone, particularly at lower false-positive rates where accuracy is most important (area under the curve (AUC) = 0.74; Extended Data Fig. 8).

As an independent validation, we used icSHAPE data to predict the binding sites of HuR, an RBP that regulates transcript stability[15], and also performed the first HuR iCLIP, to our knowledge, in mouse ES cells. Comparing *in vivo* versus *in vitro* icSHAPE data precisely identified peaks of structural arrangement at authentic HuR-binding sites (defined by iCLIP sites), and enabled reasonably accurate prediction of HuR binding from icSHAPE data alone (AUC = 0.841; Extended Data Fig. 8 and HuR iCLIP data in Extended Data Fig. 9). Thus, icSHAPE data can distinguish true binding sites from other sequence motif instances, collectively boosting prediction accuracy.

We also identified a critical connection between RNA structure and RNA modification, a newly appreciated and pervasive mode of post-transcriptional control[13]. The most prevalent modification in mRNAs, m^6A, occurs at GGm^6ACU motifs near stop codons, and acts in part to control RNA splicing and stability[22,23]. It has been hypothesized that m^6A methylation occurs at sites that contain unpaired motifs[24], but limited structural evidence *in vivo* has been presented to support this model. Comparison of icSHAPE signals at m^6A-modified versus unmodified instances of the GGACU motif in mouse ES cells[25] revealed a specific structural signature, with stronger icSHAPE reactivity (consistent with unpaired RNA) at positions both surrounding and including the modified A (Fig. 4d and Extended Data Fig. 8). m^6A sites in different subdomains of mRNAs or in lncRNAs have nearly identical icSHAPE profiles (Extended Data Fig. 10). Evaluation of all predictive features using our SVM algorithm showed that motif conservation or motif position offers some predictive value (AUC = 0.617 or 0.824, respectively) as previously reported[24], but use of icSHAPE data (AUC = 0.846) or all features together (AUC = 0.914) improved prediction rate (Fig. 4e). These results show that icSHAPE structure profiles can be used accurately to predict post-transcriptional modifications on a transcriptome-wide scale.

The strong RNA structural signature at m^6A sites may arise from the ability of m^6A to destabilize RNA helices[26] (depicted in Fig. 4c) or the structural selectivity of the m^6A modification machinery for unpaired bases. In the former scenario, removal of m^6A should cause increased base-pairing (loss of icSHAPE signal) whereas the latter scenario predicts little change to RNA structural profile. To distinguish between these hypotheses, we determined the icSHAPE profile of mouse ES cells genetically ablated for *Mettl3* (ref. 25), a key m^6A methyltransferase that is required for ES cell differentiation. We observed that in *Mettl3*-knockout cells, canonical motif sites that lost m^6A modification also substantially lost icSHAPE signal transcriptome wide (Fig. 4d), as exemplified by key m^6A target sites in *Nanog* mRNA (Fig. 4f). These results suggest that m^6A impacts RNA structure, favouring the transition from paired to unpaired RNA. The ability to couple genetic perturbation with comprehensive, base-resolution structural maps *in vivo* is a potentially powerful approach to dissect regulators of RNA structure.

Understanding how RNA structures contribute to biological regulation opens the door to understanding a physical dimension of the transcriptome. icSHAPE bridges a gap in RNA-sequencing technologies that currently lack the ability to infer a mechanistic basis of biological function. The ability to view the structural dynamics of all four RNA bases in living cells is essential to uncover specific sequence motifs

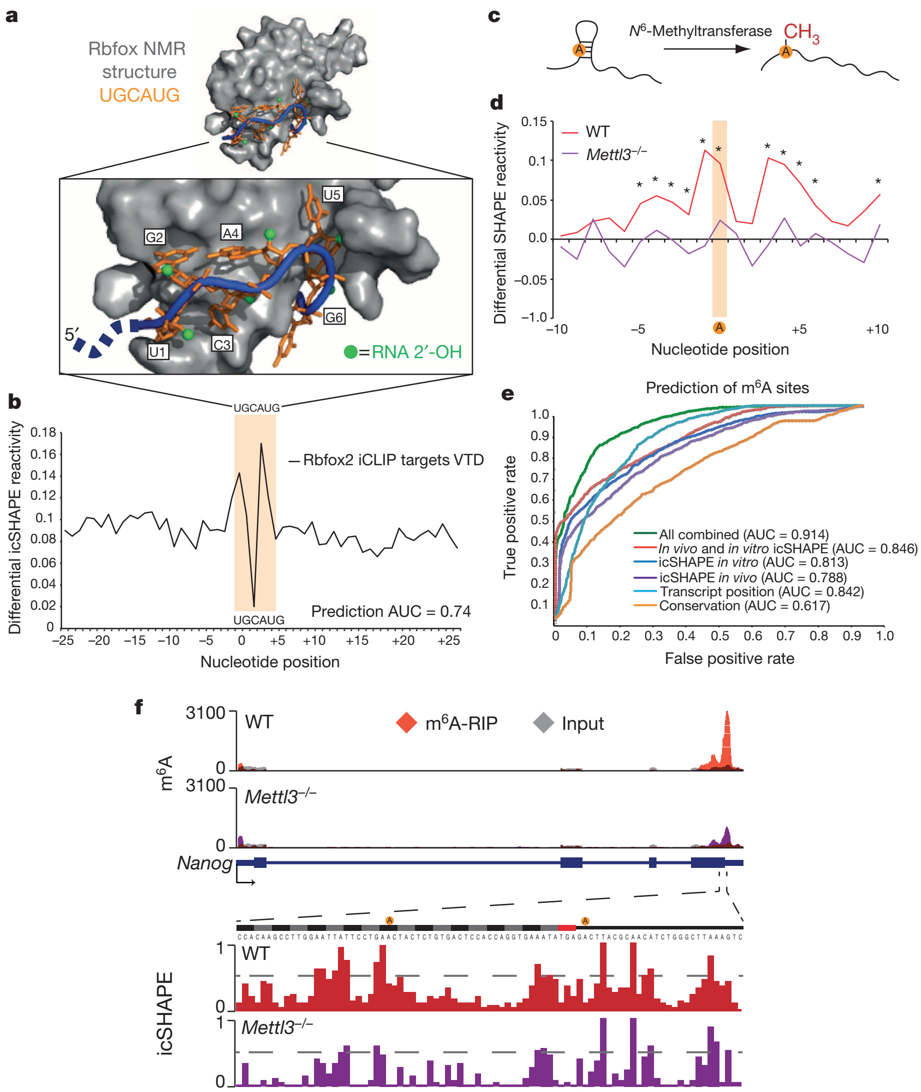

Figure 4 | icSHAPE dynamics reveal and predict post-transcriptional interactions. **a**, Structure of Rbfox1–RNA interaction, highlighting the RNA–protein interface. The RNA is shown with a blue backbone and orange bases; each 2′-hydroxyl is green (PDB accession 2ERR). **b**, The differential icSHAPE profile at Rbfox2 target mRNAs measured *in vivo* versus *in vitro* maps precisely to the Rbfox-binding sites. **c**, Model of interplay between m^6A and RNA structure. **d**, Differential icSHAPE signal for m^6A methylated versus non-methylated sites with the same underlying sequence motif, both *in vivo*. icSHAPE signals from unmodified sites are subtracted from m^6A-modified sites. $^*P < 0.05$, false discovery rate (FDR) < 0.05, positions with significant differences. Data from wild-type (WT) and *Mettl3*-knockout mouse ES cells are plotted for comparison. **e**, Receiver operating characteristic (ROC) curve for prediction of m^6A sites, incorporating icSHAPE profiles. **f**, Effect of m^6A on RNA structure of *Nanog* mRNA. Top, location of *Mettl3*-dependent m^6A sites (highlight in yellow); m^6A-RNA immunoprecipitation (m^6A-RIP) data from ref. 25. Bottom, icSHAPE profile of wild-type and *Mettl3*-knockout cells.

underlying different modes of post-transcriptional regulation[27], and has enabled the accurate identification and *de novo* prediction of *trans*-acting factor binding and chemical modification at single-nucleotide resolution. In the future, viewing the RNA structurome when cells are exposed to different stimuli or genetic perturbations should revolutionize our understanding of gene regulation in biology and medicine.

Online Content Methods, along with any additional Extended Data display items and Source Data, are available in the online version of the paper; references unique to these sections appear only in the online paper.

Received 4 August 2014; accepted 26 January 2015.
Published online 18 March 2015.

1. Wan, Y., Kertesz, M., Spitale, R. C., Segal, E. & Chang, H. Y. Understanding the transcriptome through RNA structure. *Nature Rev. Genet.* **12,** 641–655 (2011).
2. Rouskin, S., Zubradt, M., Washietl, S., Kellis, M. & Weissman, J. S. Genome-wide probing of RNA structure reveals active unfolding of mRNA structures *in vivo*. *Nature* **505,** 701–705 (2014).
3. Ding, Y. *et al. In vivo* genome-wide profiling of RNA secondary structure reveals novel regulatory features. *Nature* **505,** 696–700 (2014).
4. Lucks, J. B. *et al.* Multiplexed RNA structure characterization with selective 2′-hydroxyl acylation analyzed by primer extension sequencing (SHAPE-Seq). *Proc. Natl Acad. Sci. USA* **108,** 11063–11068 (2011).
5. Spitale, R. C. *et al.* RNA SHAPE analysis in living cells. *Nature Chem. Biol.* **9,** 18–20 (2013).
6. Anger, A. M. *et al.* Structures of the human and *Drosophila* 80S ribosome. *Nature* **497,** 80–85 (2013).
7. Weeks, K. M. & Mauger, D. M. Exploring RNA structural codes with SHAPE chemistry. *Acc. Chem. Res.* **44,** 1280–1291 (2011).
8. Schroeder, R., Grossberger, R., Pichler, A. & Waldsich, C. RNA folding *in vivo*. *Curr. Opin. Struct. Biol.* **12,** 296–300 (2002).
9. Wan, Y. *et al.* Landscape and variation of RNA secondary structure across the human transcriptome. *Nature* **505,** 706–709 (2014).
10. Wan, Y. *et al.* Genome-wide measurement of RNA folding energies. *Mol. Cell* **48,** 169–181 (2012).
11. Kertesz, M. *et al.* Genome-wide measurement of RNA secondary structure in yeast. *Nature* **467,** 103–107 (2010).
12. Vandivier, L. *et al. Arabidopsis* mRNA secondary structure correlates with protein function and domains. *Plant Signal. Behav.* **8,** e24301 (2013).
13. Jia, G., Fu, Y. & He, C. Reversible RNA adenosine methylation in biological regulation. *Trends Genet.* **29,** 108–115 (2013).
14. Jangi, M., Boutz, P. L., Paul, P. & Sharp, P. A. Rbfox2 controls autoregulation in RNA-binding protein networks. *Genes Dev.* **28,** 637–651 (2014).
15. Dai, W., Zhang, G. & Makeyev, E. V. RNA-binding protein HuR autoregulates its expression by promoting alternative polyadenylation site usage. *Nucleic Acids Res.* **40,** 787–800 (2012).
16. Kozak, M. An analysis of 5′-noncoding sequences from 699 vertebrate messenger RNAs. *Nucleic Acids Res.* **15,** 8125–8148 (1987).
17. Dvir, S. *et al.* Deciphering the rules by which 5′-UTR sequences affect protein expression in yeast. *Proc. Natl Acad. Sci. USA* **110,** E2792–E2801 (2013).
18. Ingolia, N. T., Lareau, L. F. & Weissman, J. S. Ribosome profiling of mouse embryonic stem cells reveals the complexity and dynamics of mammalian proteomes. *Cell* **147,** 789–802 (2011).
19. Lunde, B. M., Moore, C. & Varani, G. RNA-binding proteins: modular design for efficient function. *Nature Rev. Mol. Cell Biol.* **8,** 479–490 (2007).
20. Lovci, M. T. *et al.* Rbfox proteins regulate alternative mRNA splicing through evolutionarily conserved RNA bridges. *Nature Struct. Mol. Biol.* **20,** 1434–1442 (2013).
21. Auweter, S. D. *et al.* Molecular basis of RNA recognition by the human alternative splicing factor Fox-1. *EMBO J.* **25,** 163–173 (2006).
22. Meyer, K. D. *et al.* Comprehensive analysis of mRNA methylation reveals enrichment in 3′ UTRs and near stop codons. *Cell* **149,** 1635–1646 (2012).

23. Wang, X. *et al.* N^6-methyladenosine-dependent regulation of messenger RNA stability. *Nature* **505,** 117–120 (2014).
24. Schwartz, S. *et al.* High-resolution mapping reveals a conserved, widespread, dynamic mRNA methylation program in yeast meiosis. *Cell* **155,** 1409–1421 (2013).
25. Batista, P. J. *et al.* m^6A RNA modification controls cell fate transition in mammalian embryonic stem cells. *Cell Stem Cell* **15,** 707–719 (2014).
26. Kierzek, E. & Kierzek, R. The thermodynamic stability of RNA duplexes and hairpins containing N^6-alkyladenosines and 2-methylthio-N^6-alkyladenosines. *Nucleic Acids Res.* **31,** 4472–4480 (2003).
27. McGinnis, J. L. & Weeks, K. M. Ribosome RNA assembly intermediates visualized in living cells. *Biochemistry* **53,** 3237–3247 (2014).

Supplementary Information is available in the online version of the paper.

Acknowledgements We thank members of the Chang laboratory, J. Weissman and J. Doudna for comments. This work was supported by National Institutes of Health (NIH) R01HG004361 and P50HG007735, and the California Institute for Regenerative Medicine (H.Y.C.), NIH R01068122 (E.T.K.), the A.P. Giannini Foundation (R.C.S.), a Stanford Dean's Fellowship (Q.C.Z.), NIH T32AR007422 (P.J.B.), and the Stanford Medical Scientist Training Program and NIH F30CA189514 (R.A.F.). H.Y.C. is an Early Career Scientist of the Howard Hughes Medical Institute.

Author Contributions R.C.S., E.T.K. and H.Y.C. conceived the study. R.C.S., P.C., J.-W.J., H.Y.K. and E.T.K. performed chemical design and synthesis. R.C.S., R.A.F., B.L., E.A.T. and P.J.B. performed biological experiments. Q.C.Z., R.C.S., R.A.F. and H.Y.C. performed data analysis. R.C.S. and H.Y.C. wrote the paper with input from all authors.

Author Information All genomic data sets have been deposited in the Gene Expression Omnibus under accession number GSE64169. Reprints and permissions information is available at www.nature.com/reprints. The authors declare no competing financial interests. Readers are welcome to comment on the online version of the paper. Correspondence and requests for materials should be addressed to H.Y.C. (howchang@stanford.edu) or E.T.K. (kool@stanford.edu).

METHODS

Methyl 2-(azidomethyl)nicotinate. Methyl 2-methylnicotinate (1.00 g) was dissolved in 5 ml anhydrous dichloromethane. Trichloroisocyanuric acid (2.30 g) was added and the resulting suspension stirred overnight at room temperature. The reaction was diluted with dichloromethane and quenched by the addition of saturated sodium bicarbonate solution. The phases were separated and the organic phase was washed once with brine, dried over magnesium sulfate, filtered, and concentrated to afford a yellow oil. NMR data were consistent with literature reports.

The crude product of the above reaction (1.09 g) was dissolved in 12 ml anhydrous N,N-dimethylformamide and 0.77 g sodium azide was added. The reaction was stirred overnight at room temperature then quenched with saturated sodium bicarbonate solution. The aqueous layer was extracted with ethyl acetate, and the organic layer washed three times with water and three times with brine. The organic layer was dried over magnesium sulfate, filtered, and concentrated to afford 0.91 g (71%, two steps) of a yellow oil that solidified upon standing.

NMR data were as follows: ^{1}H NMR (400 MHz, $CDCl_3$): 3.94 (3H, s), 4.88 (2H, S), 7.37 (1H, m), 8.29 (1H, dd, J = 8 Hz, 1.6 Hz), 8.76 (1H, dd, J = 4.6 Hz, 1.6 Hz); ^{13}C NMR (100 MHz, $CDCl_3$): 52.8, 54.4, 122.9, 125.0, 139.1, 152.4, 156.7, 166.0. Electrospray ionization mass spectrometry (ESI-MS) (Calc M-H = 191.06): 191.98.

2-(azidomethyl)nicotinic acid. Methyl 2-(azidomethyl)nicotinate (0.50 g) was stirred vigorously in 10 ml of 1:1 MeOH:10% aqueous NaOH. After 10 min thin layer chromatography (TLC) indicated complete consumption of starting material. Twenty-five millilitres of water were added, the crude reaction mixture was washed once with ether (10 ml), then acidified to pH 4 with 10% aqueous HCl and extracted five times with 50 ml ethyl acetate. The organic layer was dried over magnesium sulfate, filtered, and concentrated to afford 0.46 g (99%) of a white solid that was pure by NMR.

NMR data were as follows: ^{1}H NMR (400 MHz, DMSO-d_6): 4.81 (2H, s), 7.50 (1H, m), 8.28 (1H, dd, J = 7.8 Hz, 1.6 Hz), 8.74 (1H, dd, J = 5 Hz, 1.6 Hz), 13.64 (1H, br. s); ^{13}C NMR (100 MHz, DMSO-d_6): 53.4, 123.4, 125.9, 139.0, 151.9, 156.0, 167.1. ESI-MS (Calc M-H = 177.04): 177.05.

2-(azidomethyl)nicotinic acid acyl imidazole. 2-(Azidomethyl)nicotinic acid (0.15 g) was dissolved in 0.21 ml anhydrous dimethylsulfoxide. A solution of 0.14 g carbonyldiimidazole in 0.21 ml anhydrous dimethylsulfoxide was added drop-wise, creating rapid gas evolution. The reaction was allowed to proceed for 1 h and the resulting solution used as a 2 M stock solution for RNA SHAPE experiments. For NMR data collection, an analytical sample was prepared in dichloromethane as described earlier. The reaction was stirred overnight and the solvent removed in vacuum. The product was then isolated by flash column chromatography on silica (ethyl acetate).

NMR data were as follows: ^{1}H NMR (400 MHz, DMSO-d_6): 4.62 (2H, s), 7.16 (1H, dd, J = 1.7 Hz, 0.8 Hz), 7.60 (1H, dd, J = 7.9 Hz, 4.9 Hz), 7.66 (1H, m), 8.15 (2H, m), 8.84 (1H, dd, J = 4.9 Hz, 1.7 Hz); ^{13}C NMR (100 MHz, DMSO-d_6): 52.8, 117.9, 123.0, 127.3, 130.9, 137.7, 138.5, 151.9, 154.6, 164.7.

***In vitro* transcription and acylation of RNA.** RNA was transcribed from amplified inserts using T7 Megascript kit from Ambion, following the manufacturer's protocol. In a typical *in vitro* modification protocol, RNA was heated in metal-free water for 2 min at 95 °C. The RNA was then flash-cooled on ice. The RNA 3× SHAPE buffer (333 mM HEPES, pH 8.0, 20 mM $MgCl_2$, 333 mM NaCl) was added and the RNA was allowed to equilibrate at 37 °C for 10 min. To this mixture, 1 µl of 10× electrophile stock in DMSO (+) or DMSO (−) was added. The reaction was permitted to continue until the desired time. Reactions were cleaned up using RNeasy columns (Qiagen) following the manufacturer's protocol and eluted RNase-free water.

***In vitro* manual SHAPE analysis.** ^{32}P-end-labelled DNA primer (reverse primer above) was annealed to 3 µg of total RNA by incubating at 95 °C for 2 min followed by a step-down cooling (2° per s) to 4 °C. To the reaction first-strand buffer, dithiothreitol (DTT) and dNTPs were added. The reaction was pre-incubated at 52 °C for 1 min, then Superscript III (2 U µl^{-1} final concentration) was added. Extensions were performed for 10 min. To the reaction, 1 µ of 4 M NaOH was added and allowed to react for 5 min at 95 °C. Ten microlitres of Gel Loading Buffer II (GLBII, Ambion) was then added, and cDNA extensions were resolved on 8% denaturing (7 M urea) polyacrylamide gels (29:1 acrylamide:bisacrylamide, 1× TBE). All (−) lanes are those from DMSO control-treated cells. In addition, all sequencing lanes are from DMSO control-treated cells. cDNA extensions were visualized by phosphorimaging (STORM, Molecular Dynamics). cDNA bands were integrated with SAFA[28]. SHAPE reactivities were normalized to a scale spanning 0 to 1.5, where 1.0 is defined as the mean intensity of highly reactive nucleotides[29]. RNA secondary structures were predicted using mFOLD software[30].

Characterization of manual SHAPE-enriched reverse transcription stops. *Copper-free click chemistry of acylated RNA.* In a typical reaction, acylated RNA (1 pmol) was reacted with 100 equivalents of DIBO-biotin (Life Technologies) for 2 h, at 37 °C, in 1× PBS. Reactions were extracted once with acid phenol:chloroform (pH 4.5 ± 0.2) and twice with chloroform. RNA was precipitated with 40 µl of 3 M sodium acetate buffer (pH 5.2) and 1 µl of glycogen (20 µg µl^{-1}). Pellets were washed twice with 70% ethanol and resuspended in 10 µl RNase-free water.

Enrichment of NAI-N_3-modified RNA. The following protocol was used for manual enrichment protocols used to optimize capture conditions. To 1 pmol of precipitated and biotinylated RNA (in 900 µl of binding buffer: 50 mM Tris-HCl pH 7.0 and 1 mM EDTA) was added 50 µl (slurry) of DYNAL MyOneC1 beads (Life Technologies). The reaction mixture was then incubated for 1 h at room temperature. The beads were then collected on a magnetic plate and the solution decanted. The beads were then resuspended and washed four times with Biotin Wash Buffer (10 mM Tris-HCl, pH 7.0, 1 mM EDTA, 4 M NaCl, 0.2% Tween). The beads were then washed three times with RNase-free water. To elute the purified RNA, streptavidin-conjugated beads were incubated in 1× proteinase K buffer with 20 U of proteinase K (Life Technologies), 1 mM D-biotin (Sigma-Aldrich), and 20 U of SUPERaseIn (Life Technologies). The reaction was permitted to run for 30 min at 37 °C. Beads were then collected by magnet and the supernatant removed and set on ice. This was repeated twice more and elutions were pooled. Reactions were extracted once with acid phenol:chloroform (pH 4.5 ± 0.2) and twice with chloroform. RNA was precipitated with 40 µl of 3 M sodium acetate buffer (pH 5.2) and 1 µl of glycogen (20 µg µl^{-1}). Pellets were washed twice with 70% ethanol and resuspended in 10 µl RNase-free water.

Dot blot analysis of enriched NAI-N_3-modified RNA. Hybond N+ membranes (GE) were pre-incubated in 1× PBS. Precipitated RNA was dissolved in 100 µl of 1× PBS. RNA was added to the Hybond membrane and crosslinked using 254 nm ultraviolet light. The Hybond membrane was washed three times with 1× PBS. To the membrane was added NorthernLights Streptavidin NL493 (in PBS-Tween-20) for visualization. After incubation, the membrane was washed three times in 1× PBS-Tween-20. The membrane was dried and imaged by phosphorimaging (STORM, Molecular Dynamics).

Tissue culture and *in vivo* SHAPE modification. Mouse ES cells (v6.5 line) were grown on gelatinized dishes in serum and LIF. Unmodified total RNA was extracted by removing media, washing once in room temperature 1× PBS, and adding 2 ml (10 cm dish) or 7 ml (15 cm dish) of TRIzol directly to the cells. Subsequent RNA clean up was performed using the miRNeasy mini- or midi-column and protocol (Qiagen) as recommended by the manufacturer. *In vivo* modification of cellular RNAs was performed as described previously[5]. Briefly, cells were rinsed once on the plate in room temperature 1× PBS, decanted, scraped in 1× PBS, and collected into a 15 ml tube. Cells were pelleted at room temperature and resuspended in 450 µl of 1× PBS. Fifty microlitres of 10× electrophile stock in DMSO (+) or DMSO (−) was added drop-wise, immediately mixed by inversion, and incubated at 37 °C on end-over-end rotation for 20 min. Reactions were pelleted for 1 min at 4 °C at 10,000 r.p.m. and resuspended in 500 µl of 1× PBS. Samples were then transferred to 15 ml tubes with 2–7 ml of pre-aliquoted TRIzol and RNA was extracted as described earlier.

Methods to ensure titrated hit kinetics of RNA modification. We titrated NAI-N_3 for single-hit kinetics that are comparable to those routinely used in chemical probing of RNA structure. For example, we obtained nearly identical secondary structure for 5S rRNA as previously reported with a single-hit regime[5]. After NAI-N_3 modification and biotin pulldown, we retrieved approximately 10–20% of the input RNA as modified RNA, consistent with the expected Poisson distribution of single-hit modification.

icSHAPE deep-sequencing library preparation. *RNA preparation.* DMSO (mock) or NAI-N_3 (experimental) modified total RNA was used as input for the deep-sequencing library preparation. Before library preparation, input RNA should be modified (or mock-treated) under *in vitro* or *in vivo* conditions as described earlier. For 'total RNA' libraries, no additional processing was needed. For 'poly-A selected' samples, 200 µg of total RNA was used per poly-A purist column (Ambion), which should yield ~2 µg of enriched RNA. Poly-A selection was performed a total of two times using the same poly-dT beads ('double poly-A selection'). The NAI-N_3 sample may have lower yields after purification so additional starting material could be required.

NAI-N_3 biotinylation and RNA fragmentation. All RNA samples (NAI-N_3 and DMSO treated) are processed through a copper-free 'click' reaction. RNA is brought to 97 µl in 1× PBS and 1 µl of SUPERaseIn and 2 µl of 185 mM DIBO-biotin are added. Samples were mixed by brief vortexing and then incubated at 37 °C for 2 h in a Thermomixer (Eppendorf). Reactions were stopped by adding 350 µl of Buffer RLT (Qiagen) and then 900 µl of 100% ethanol (EtOH). Each RNA sample was processed by passing over a RNeasy Mini column (Qiagen), two 500 µl washes with Buffer RPE (Qiagen), one no-buffer spin to dry the column, and finally two 50 µl elutions in RNase-free water (final 100 µl). Samples were then frozen for 5 min on dry ice and concentrated to 9 µl using a lyophilizer (Labconco). Concentrated RNA samples (9 µl) were then moved to 0.5 ml PCR tubes for fragmentation. Samples were heated to 95 °C for 90 s and then 1 µl of 10× RNA Fragmentation Reagent

(Ambion) was added and samples were placed back at 95 °C for 70–90 s. Reactions were quenched by adding 1 μl of RNA Fragmentation Stop Solution (Ambion) and moved to ice. RNA was cleaned up by adding 35 μl of Buffer RLT and 100 μl of 100% EtOH and purified using RNeasy Mini columns as described earlier. Samples are then concentrated with a lyophilizer to 5 μl.

RNA end repair, RNA ligation, and RNA size selection. To resolve the 3′-end phosphate generated by the fragmentation process, T4 PNK is used. To each 5 μl sample 2 μl of 5× PNK buffer (350 mM Tris-HCl pH 6.5, 50 mM $MgCl_2$, 25 mM DTT), 1 μl SUPERaseIn, and 2 μl of T4 PNK (NEB) is added, mixed by flicking, and incubated at 37 °C for 1 h. After end-repair samples are moved directly to 3′-end ligation by adding 1 μl of 50 μM 3′ Adaptor, 1 μl of 10× T4 RNL2tr buffer (NEB), 1.5 μl of T4 RNL2tr K227Q (NEB), 1 μl of 100 mM DTT, and 8 μl of 50% PEG8000. Mix samples by flicking and incubate at 16 °C overnight.

Ligation. Note that NAI-N_3 samples must use 3′-Adaptor-3′ddc (/5rApp/AGATCGGAAGAGCGGTTCAG/3ddC/) while DMSO samples must use 3′-Adaptor-3′Biotin (/5rApp/AGATCGGAAGAGCGGTTCAG/3Bio/). The 'click' chemistry will label only the NAI-N_3-modified RNAs in the NAI-N_3 pool of transcripts with a biotin moiety, thus allowing the selective purification of structurally informative molecules. The DMSO samples are not capable of 'click' chemistry and every molecule in this pool is desired for sequencing so addition of a biotin moiety must happen in an unbiased fashion. Thus, DMSO samples have a 3′-biotin modification added specifically to their 3′ Adaptor to allow for downstream processing in parallel of the DMSO and NAI-N_3 samples.

After the overnight ligation, 30 μl of water, 185 μl of Buffer RLT and 400 μl of 100% EtOH is added to each sample and purified using RNeasy Mini columns as described earlier. Samples are concentrated to 5 μl using a lyophilizer and 5 μl of GLBII is added and stored on ice. To size select the RNA samples a mini 6% TBE PAGE gel with 7 M urea is cast and pre-run to 50 W for 8 min. Samples are loaded without prior heating and the PAGE gel is imaged using a 1:10,000 dilution of SybrGold (Life Technologies). RNA is visualized on a BlueBox (Clare Chemical) and fragmented RNA ranging between 20–120 nucleotides (40–140 nucleotides with the 3′ Adaptor ligated) are excised with a scalpel. Gel slices are crushed through a 0.75 ml tube nested in a 2 ml tube by centrifugation and 300 μl of Crush Soak Buffer (500 mM NaCl, 1 mM EDTA) is added with 3 μl of SUPERaseIn. RNA is eluted overnight at 4 °C on rotation.

Reverse transcription, streptavidin capture, cDNA elution and cDNA size selection. RNA samples are purified away from residual PAGE using 0.45 μm Spin-X columns (Corning) and the 300 μl elutions are transferred to siliconized 1.5 ml tubes (Fisher Scientific, used in all subsequent steps). RNA is precipitated by adding 30 μl of 3 M sodium acetate buffer (pH 5.2), 0.8 μl of GlycoBlue (Ambion) and 1 ml of 100% EtOH. Samples are frozen for 1 h on dry ice, spun at maximum speed (15,000 r.p.m.) for 1 h at 4 °C, washed with 800 μl of ice-cold 80% EtOH, decanted, air-dried and then resuspended in a 0.5 ml PCR tube with 11.5 μl of water. To the RNA samples add 1 μl of 10 μM RT primer (/5phos/DDDNNAACCNNNNAGATCGGAAGAGCGTCGTGAT/iSp18/GGATCC/iSp18/TACTGAACCGC, /5phos/ = 5′ phosphate, D = A/T/G, /iSp18/ = 18carbon PEG spacer) and 1 μl of 10 mM dNTPs. Heat the samples to 70 °C for 5 min and then cool slowly to 25 °C (2° per s) and hold at 25 °C for 1 min. After primer annealing add 0.5 μl of SUPERaseIn, 1 μl 100 mM DTT, 4 μl of 5× First Strand Buffer and 1 μl of SuperScript III (Life Technologies). cDNA extension occurs for 3 min at 25 °C, 7 min at 42 °C, and finally at 52 °C for 15 min. After cDNA extension do not raise samples above 37 °C to avoid denaturing conditions.

MyOneC1 streptavidin beads for cDNA capture and NAI-N_3-modified RNA enrichment are prepared (40 μl slurry per sample) by washing three times in 1 ml of Biotin Bind Buffer (100 mM Tris-HCl pH 7.0, 10 mM EDTA, 1 M NaCl) and resuspending the beads in 40 μl Biotin Bind Buffer and 1 μl SUPERaseIn per reaction. After the reverse transcription reaction completes, 40 μl of pre-washed beads are added to each sample, mixed by flicking, and incubated at room temperature for 45 min. After streptavidin capture, samples are washed at room temperature serially with four times 100 μl of Biotin Wash Buffer, two times 100 μl 1× PBS and finally moved to 1.5 ml tubes. cDNA is eluted by adding 1 μl RNaseA/T1 cocktail (Ambion), 1 μl RNaseH (Enzymatics), 12.5 μl 50 mM D-biotin, 5 μl 10× Elution Buffer (500 mM HEPES, 750 mM NaCl, 30 mM $MgCl_2$, 1.25% Sarkosyl, 0.25% Na-deoxycholate, 50 mM DTT), 30.5 μl water and incubating at 37 °C for 30 min in a Thermomixer at 800 r.p.m. Samples are mixed with 1 μl 100% DMSO, heated to 95 °C for 3 min, placed on a magnet, and the 50 μl cDNA elution moved to a new tube. The elution is repeated once (total of two times and final of 100 μl). cDNA is processed by adding 1 ml of Buffer PNI and purifying over a MiniElute columns (Qiagen), following the manufacturer's protocol, and eluting twice in 15 μl of Buffer EB (final 30 μl). cDNAs are concentrated using a lyophilizer to 5 μl and an equal volume of GLBII is added. Size selection of cDNAs is performed as was done for the RNA size selection. 6% PAGE gel pre-running is critical to achieve denaturing conditions as well as heating the samples to 95 °C for 3 min before PAGE separation. cDNAs are selected for insert sizes of ~20–120 nucleotides (~85–205 nucletodies with RT primer extension) and, depending on the input material amount, the libraries may be invisible at this step. Gel slices are crushed as above, 300 μl of Crush Soak Buffer is added and cDNAs are eluted at 50 °C overnight on rotation.

cDNA circularization, library qPCR, library size selection and sequencing PCR. Purification of eluted cDNA is performed as described earlier for RNA elution. After cDNA precipitation, samples are resuspended in 16 μl of water, 2 μl of 10× CircLigaseII Buffer, 1 μl of CircLigaseII (Epicentre) and moved to 0.5 ml PCR tubes. cDNA circularization takes place at 60 °C for 120 min in a PCR machine. Circularized cDNA is purified by adding 200 μl of Buffer PNI and processing as described earlier using MiniElute columns, eluting the cDNA twice in 14 μl (final ~27 μl). Samples are initially amplified in a 60 μl qPCR reaction (27 μl cDNA, 30 μl 2× Phusion HF Master Mix, 0.75 μl of 10 μM P3_short primer (CTGAACCGCTCTTCCGATCT), 0.75 μl of 10 μM P5_short primer (ACACGACGCTCTTCCGATCT), 0.72 μl of 25× SybrGold). The qPCR machine is programmed as follows: 98 °C for 1 min, 98 °C for 15 s, 62 °C for 30 s, 72 °C for 45 s. After qPCR amplification, samples are purified with 600 μl of Buffer PNI and MiniElute columns as described earlier. Library DNA is eluted twice in 15 μl (total 30 μl) and concentrated using a lyophilizer to less than 5 μl. A second 6% TBE 7 M urea PAGE gel selection is performed as described earlier to remove any PCR dimer products and all short qPCR primers. Gel slices are crushed as described earlier and eluted overnight at 50 °C on rotation. Purification of library DNA is performed as described earlier, post-PAGE gel elution and after precipitation, resuspended in 19 μl of water. A final library PCR amplification is performed for three cycles in 40 μl reactions (19 μl library DNA, 0.5 μl of 10 μM P3_solexa primer (CAAGCAGAAGACGGCATACGAGATCGGTCTCGGCATTCCTGCTGAACCGCTCTTCCGATCT), 0.5 μl of 10 μM P5_solexa primer (AATGATACGGCGACCACCGAGATCTACACTCTTTCCCTACACGACGCTCTTCCGATCT)) and cleaned up using Agencourt AMPure XP beads (Beckman) according to the manufacturer's protocol and we eluted the library in 20 μl of water. Final library material was quantified on the BioAnalyzer High Sensitivity DNA chip (Agilent) and then sent for deep sequencing on the Illumina HiSeq2500 machine for 1× 100 bp cycle run.

iCLIP and data analysis. The iCLIP method was performed as described before with the specific modifications below[31]. v6.5 mouse ES cells were grown as described earlier and UV-C crosslinked to a total of 0.3 J cm^{-2}. Whole-cell lysates were generated in CLIP lysis buffer (50 mM HEPES, 200 mM NaCl, 1 mM EDTA, 10% glycerol, 0.1% NP-40, 0.2% Triton X-100, 0.5% N-lauroylsarcosine) and briefly sonicated using a probe-tip Branson sonicator to solubilize chromatin. Each iCLIP experiment was normalized for total protein amount, typically 2 mg, and partially digested with RNaseA (Affymetrix) for 10 min at 37 °C and quenched on ice. Immunoprecipitations of HuR were carried out with Protien G Dynabeads (Life Technologies) and anti-HuR antibody (3A2, Santa Cruz) for 3 h at 4 °C on rotation. Samples were washed sequentially in 1 ml for 5 min each at 4 °C: 2× high stringency buffer (15 mM Tris-HCl pH 7.5, 5 mM EDTA, 2.5 mM EGTA, 1% Triton X-100, 1% Na-deoxycholate, 120 mM NaCl, 25 mM KCl), 1× high salt buffer (15 mM Tris-HCl pH 7.5, 5 mM EDTA, 2.5 mM EGTA, 1% Triton X-100, 1% Na-deoxycholate, 1 M NaCl), 1× NT2 buffer (50 mM Tris-HCl pH 7.5, 150 mM NaCl, 1 mM $MgCl_2$, 0.05% NP-40). 3′-End RNA dephosphorylation, 3′-end ssRNA ligation, 5′ labelling, SDS–PAGE separation and transfer, autoradiograph, RNP isolation, Proteinase K treatment, and overnight RNA precipitation took place as previously described[31]. The 3′-ssRNA ligation adaptor was modified to contain a 3′-biotin moiety as a blocking agent. The iCLIP library preparation was performed as described previously[31]. Final library material was quantified on the BioAnalyzer High Sensitivity DNA chip (Agilent) and then sent for deep sequencing on the Illumina HiSeq2500 machine for 1× 75 bp cycle run. iCLIP data analysis was performed as previously described[31].

RNA structure analysis. *Sequencing, reads mapping and data quality control.* We generated four replicates for each library (DMSO PolyA, NAI PolyA *in vivo* and *in vitro*). We performed single-end sequencing on Illumina's HiSeq sequencer and obtained approximately 200 million to 600 million raw reads for each replicates, totalling 3.9 billion reads. We collapsed these reads to remove PCR duplicates (only reads that have identical sequences including barcode region are regarded as duplicates). Collapsed reads were then subjected to barcode removal and primer and linker trimming by using Trimmomatic[32]. We mapped trimmed reads to the mouse transcriptome of the Ensembl annotation (build GRCm38.74)[33] by using Bowtie2 (ref. 34). For reads that can be mapped to multiple locations of the transcriptome, we evenly distribute them to up to ten random hits. Finally, we obtained 2.1 billion mapped reads in total. We define the '−1 positions' of each sequencing read as the first 5′-end nucleotide mapped. This represents the reverse transcription stop, which corresponds to the position adjacent to modified nucleotides in the NAI-N_3 libraries, and intrinsic modified (or fragmentation) positions in the DMSO libraries. We defined reverse transcription stop coverage as the number of times a base is mapped as a reverse transcription stop.

We calculated the expression level of all transcripts in the mouse transcriptome in terms of reads per kilobase per million mapped reads (RPKM). The correlations of transcript expression value (RPKM > 0.1) in different replicates are very high (in the range of 0.96 to 1.00). We constructed the background base density profile for each transcript as the sequencing depth of each base in the DMSO libraries. We also calculated the correlation of reverse transcription stops for each transcript in different replicates. As shown in Extended Data Fig. 5, the correlation is high for most transcripts if we limit the analysis to transcripts of average reverse transcription stop coverage higher than 2 and regions of background base density higher than 200. So for each library (DMSO poly-A, NAI poly-A *in vivo* and *in vitro*) we combine all four replicates into one for the following analyses.

Reactivity score calculation and construction of structural profile. We performed a 5–5% normalization for each transcript; that is, the mean of the reverse transcription stops of the second top 5% bases, excluding the 32 bases at the beginning and 32 bases at the end of the transcript, will be normalized to 1, and all reverse transcription stops will be normalized proportionally.

We defined reactivity score (R) as the subtraction of background reverse transcription stops (DMSO libraries) from reverse transcription stops of the modified NAI-N_3 libraries, and then adjusted by the background base density:

$$R = (\mathrm{RT\_stop}_{\mathrm{NAI\text{-}N3}} - \alpha\mathrm{RT\_stop}_{\mathrm{DMSO}})/\mathrm{background\_base\_density}_{\mathrm{DMSO}}$$

The score is then scaled into the range of [0, 1], after removing the outliers by 90% Winsorization (the top 5th percentile is set to 1 and the bottom 5th percentile is set to 0. We trained the parameter α on the ribosomal RNA structures, and set it to 0.25 to maximize the correlation of reactively score R determined by deep sequencing and reactivity score measured in low-throughput gel shift experiments.

For each transcript, we defined its structural profile as the vector of base-resolution reactivity scores from the beginning to the end. The valid structural profile of a transcript is limited to regions of reverse transcription stop coverage higher than 2 and background base density higher than 200. Finally, we obtained valid structural profiles for, respectively, 19,347 and 13,281 transcripts from *in vivo* and *in vitro* polyA-selected RNA libraries, among which the majority are mRNAs (Extended Data Fig. 6).

Metagene analysis of translation, pause, m^{6}A and protein-binding sites. We calculated metagene structure profile around different functional sits by averaging all valid reactivity score R: (1) 10 nucleotides upstream and downstream of the RNA methylation m^{6}A site, as determined by our laboratory previously[25]; (2) 25 nucleotides upstream and downstream of the translation pause site, as determined in the same ribosome profiling experiment; (3) 25 nucleotides upstream and downstream of the RNA methylation m^{6}A site; (4) 25 nucleotides upstream and downstream of the binding sites of RNA-binding proteins Rbfox2 (ref. 35) and HuR (Extended Data Figs 8 and 9; see later for details).

In the analysis of differential profiles of icSHAPE reactivity scores around m^{6}A and negative control sites, we retrieved a set of target m^{6}A sites that have icSHAPE reactivity scores in both wild-type and *Mettl3*-knockout cells, and defined a set of a similar number of non-methylated m^{6}A sites with the same sequence motifs (GG ACU). For both wild-type and knockout cells, we calculated the profiles of average reactivity scores in target sites and negative controls and subtracted the latter from the former scores to define the differential icSHAPE profiles.

We calculated *in vivo* and *in vitro* metagene structure profile separately. For each transcript functional site and its flanking regions, we demand a stringent R score for thousands of transcripts being compared. We generated roughly the same number of negative controls for each set of functional sites. And whenever a sequence motif exists for a functional site, we use that motif in generating the negative control. For example, the same sequence motif GGACU is used to scan the transcriptome and negative controls are randomly selected from the hits, excluding regions that are close to a true m^{6}A site.

The HuR iCLIP experiments are performed and clusters of binding sites are determined with the pipeline as described previously[31]. Threshold 9 (at least 9 unique reverse transcription stops are each genomic coordinate) is used to filter for the true binding sites. The highest peak and its flanking 50 nucleotides in each cluster were retrieved and used to call sequence motifs by using HOMER, with random sequences of 50 nucleotides from the same set of transcripts as background. The motifs are used as the anchor point in calculating metagene profiles and also used to generate negative controls, using the same protocol as the m^{6}A negative control generation described earlier.

VTD analysis. We defined and calculated the VTD profile of a transcript by subtracting its valid *in vitro* structural profile from the *in vivo* one. We calculate the average VTD profiles for all 4,096 possible hexamers in our structurome. The overall VTD score of each hexamer is defined as the average score across the six bases of the hexamer.

We retrieved sequence motifs of important functional sites, including Kozak sequences (GCCRCC), m^{6}A sites (GGACU), miR-290 family hexamers seed matches (GCACUU, complementary to the seeds) and Rbfox2-binding sites (UGCAUG), and highlighted their VTD scores on the VTD histogram of all hexamers. For sites with ambiguity, for example, m^{6}A sites, we took the average of all hexamers that contain GGACU.

We also compiled a resource (Supplementary Tables 1 and 2) of VTD scores for all RNA protein-binding motifs studied by RNAcompete experiments[36], and all mouse microRNA hexamers seed matches from miRBase[37]. In addition to the VTD scores, for every motif or seed match, we asked three questions by using a permutation test: (1) is the absolute value of the motif (or seed match) VTD significantly less than a random hexamer, that is, represents a stable region; (2) is the motif (or seed match) VTD significantly smaller than a random hexamer, that is, represents a region that is more structured *in vivo*; and (3) is the motif (or seed match) VTD significantly bigger than a random hexamer, that is, represents a region that is more structured *in vitro*.

Structure-based prediction of m^{6}A sites and protein-binding sites. We constructed a set of SVM models[38] for the prediction of m^{6}A sites and protein-binding sites using structural profiles, genomic locations, conservations and their combinations.

The structural profile is limited to the range from the -10 to the $+10$ position of the m^{6}A site or the motifs of the protein-binding sites. We used *in vivo* and *in vitro* reactivity scores separately and jointly in making predictions. We also retrieved a set of genomic features for the prediction of m^{6}A sites and protein-binding sites, including whether the site is in the 5′ UTR, CDS or 3′ UTR, whether it is at the last exon, whether it is at the largest exon, the distance to start codon, the distance to stop codon, the distance to 5′ of the splicing junction, and so on. In addition, we retrieved the UCSC 60-way phastCons conservation score[39] for nucleotides in the range from the -10 to the $+10$ position of the m^{6}A site or the motifs of the protein-binding sites.

We used the same set of positive and negative controls and the best predictor is selected by using a parameter-searching tool that is included with the LIBSVM package (http://www.csie.ntu.edu.tw/~cjlin/libsvm/). We used a fivefold cross-validation and calculated the AUC of the ROC curve to evaluate the performance of the predictors (Extended Data Fig. 8).

Source code. Source code used for the icSHAPE analysis is freely available at https://github.com/qczhang/icSHAPE.

28. Das, R., Laederach, A., Pearlman, S. M., Herschlag, D. & Altman, R. B. SAFA: semi-automated footprinting analysis software for high-throughput quantification of nucleic acid footprinting experiments. *RNA* **11,** 344–354 (2005).
29. Gherghe, C. *et al.* Definition of a high-affinity Gag recognition structure mediating packaging of a retroviral RNA genome. *Proc. Natl Acad. Sci. USA* **107,** 19248–19253 (2010).
30. Zuker, M. Mfold web server for nucleic acid folding and hybridization prediction. *Nucleic Acids Res.* **31,** 3406–3415 (2003).
31. Flynn, R. A. *et al.* Dissecting noncoding and pathogen RNA-protein interactomes. *RNA* **21,** 135–143 (2015).
32. Bolger, A. M., Lohse, M. & Usadel, B. Trimmomatic: a flexible trimmer for Illumina sequence data. *Bioinformatics* **30,** 2114–2120 (2014).
33. Flicek, P. *et al.* Ensembl 2014. *Nucleic Acids Res.* **42,** D749–D755 (2014).
34. Langmead, B., Trapnell, C., Pop, M. & Salzberg, S. L. Ultrafast and memory-efficient alignment of short DNA sequences to the human genome. *Genome Biol.* **10,** R25 (2009).
35. Jangi, M., Boutz, P. L., Paul, P. & Sharp, P. A. Rbfox2 controls autoregulation in RNA-binding protein networks. *Genes Dev.* **28,** 637–651 (2014).
36. Ray, D. *et al.* A compendium of RNA-binding motifs for decoding gene regulation. *Nature* **499,** 172–177 (2013).
37. Kozomara, A. & Griffiths-Jones, S. miRBase: annotating high confidence microRNAs using deep sequencing data. *Nucleic Acids Res.* **42,** D68–D73 (2014).
38. Cortes, C. & Vapnik, V. Support–vector networks. *Mach. Learn.* **20,** 273–297 (1995).
39. Siepel, A. *et al.* Evolutionarily conserved elements in vertebrate, insect, worm, and yeast genomes. *Genome Res.* **15,** 1034–1050 (2005).

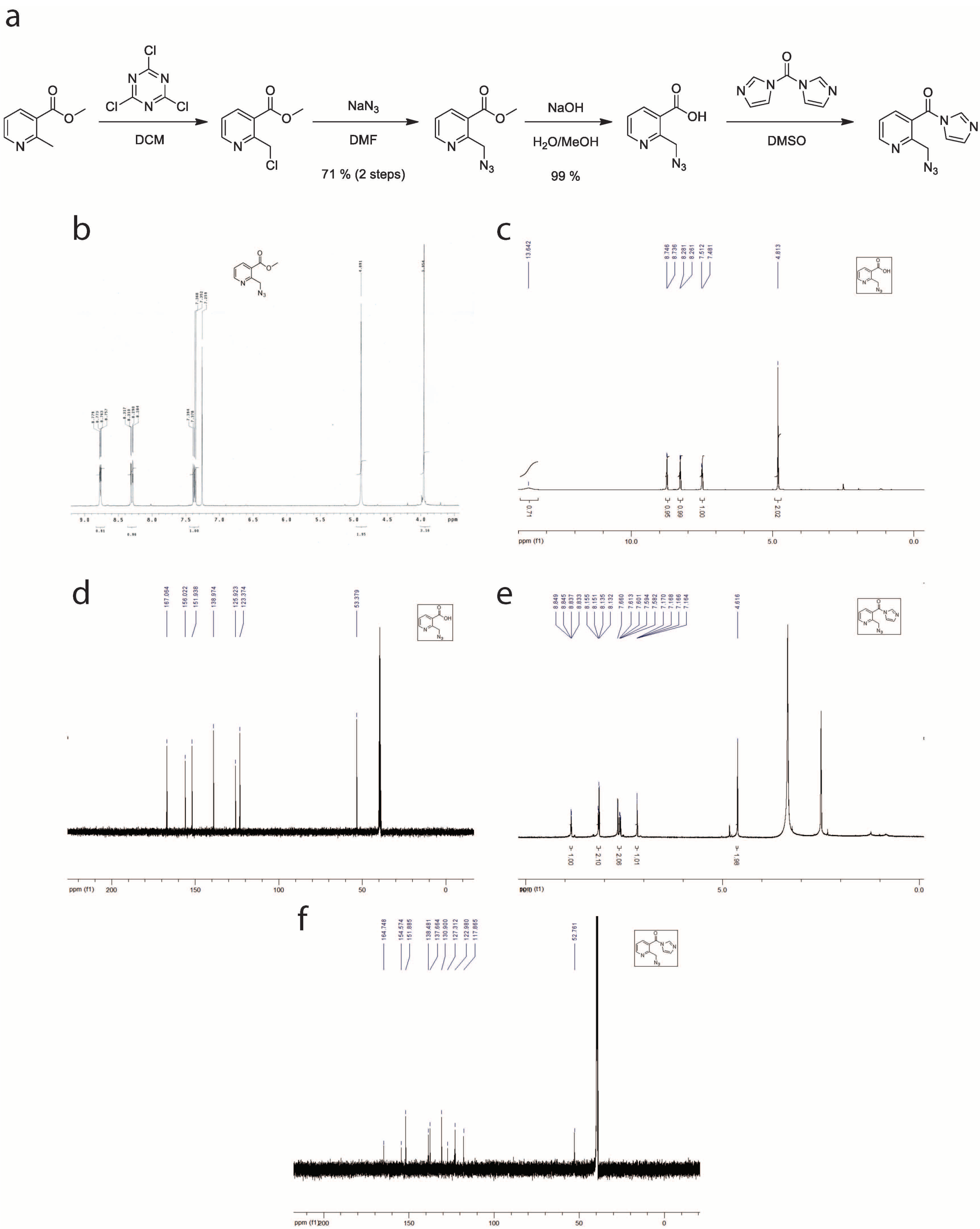

Extended Data Figure 1 | Chemical synthesis of NAI-N_3. **a**, Synthetic scheme for NAI-N_3. **b**, [1]HMR of methyl 2-(azidomethyl)nicotinate. **c**, [1]HNMR of 2-(azidomethyl)nicotinic acid. **d**, [13]CNMR of 2-(azidomethyl)nicotinic acid. **e**, [1]HNMR of 2-(azidomethyl)nicotinic acid acyl imidazole. **f**, [13]CNMR of 2-(azidomethyl)nicotinic acid acyl imidazole.

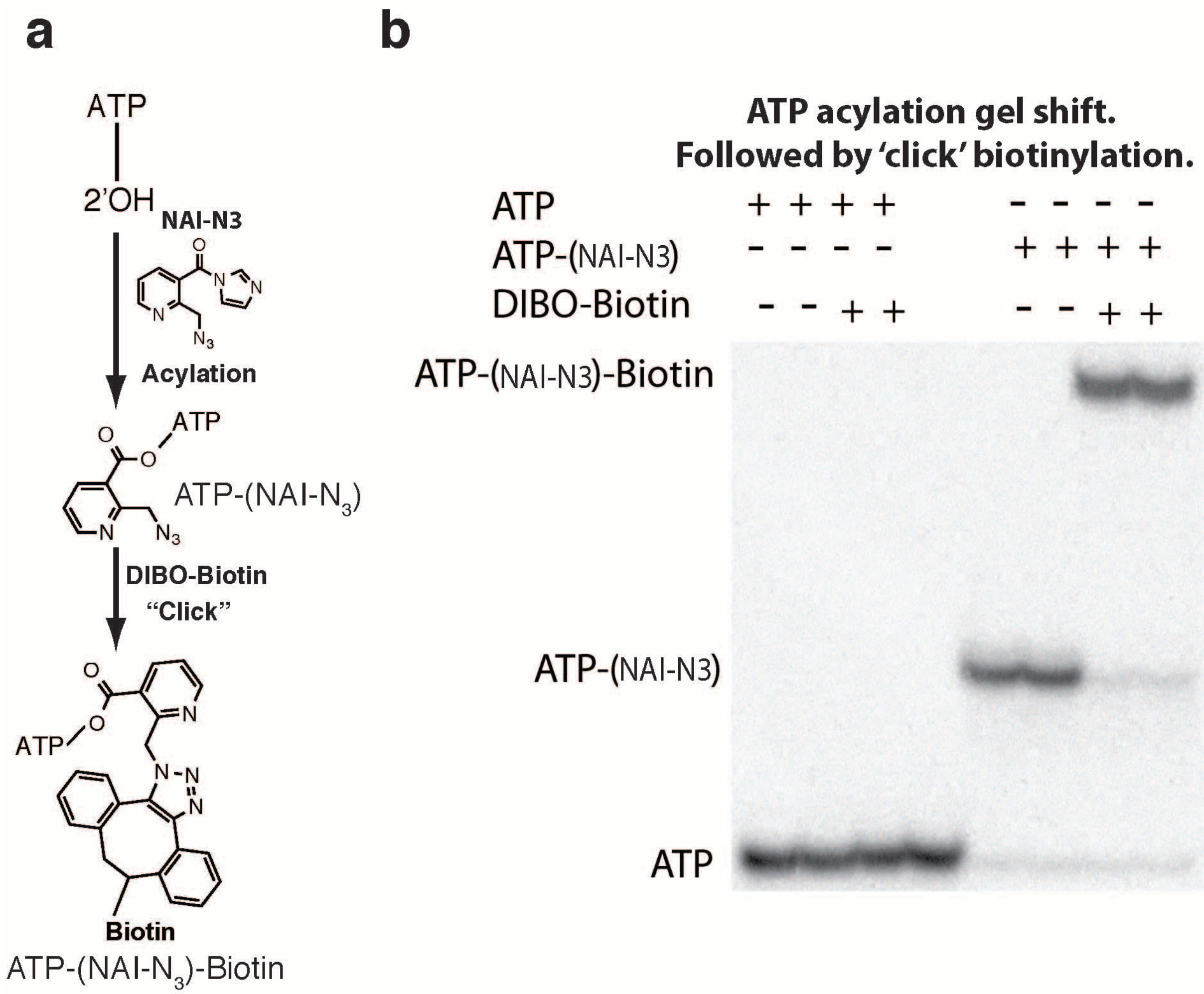

Extended Data Figure 2 | NAI-N_3 is a novel RNA acylation reagent that enables RNA purification. **a**, Chemical schematic of RNA acylation and copper-free 'click' chemistry using NAI-N_3 and dibenzocyclooxtyne (DIBO)–biotin conjugate. **b**, ATP acylation gel shift showing ATP acylation and copper-free 'click' chemistry using NAI-N_3 and DIBO–biotin conjugate.

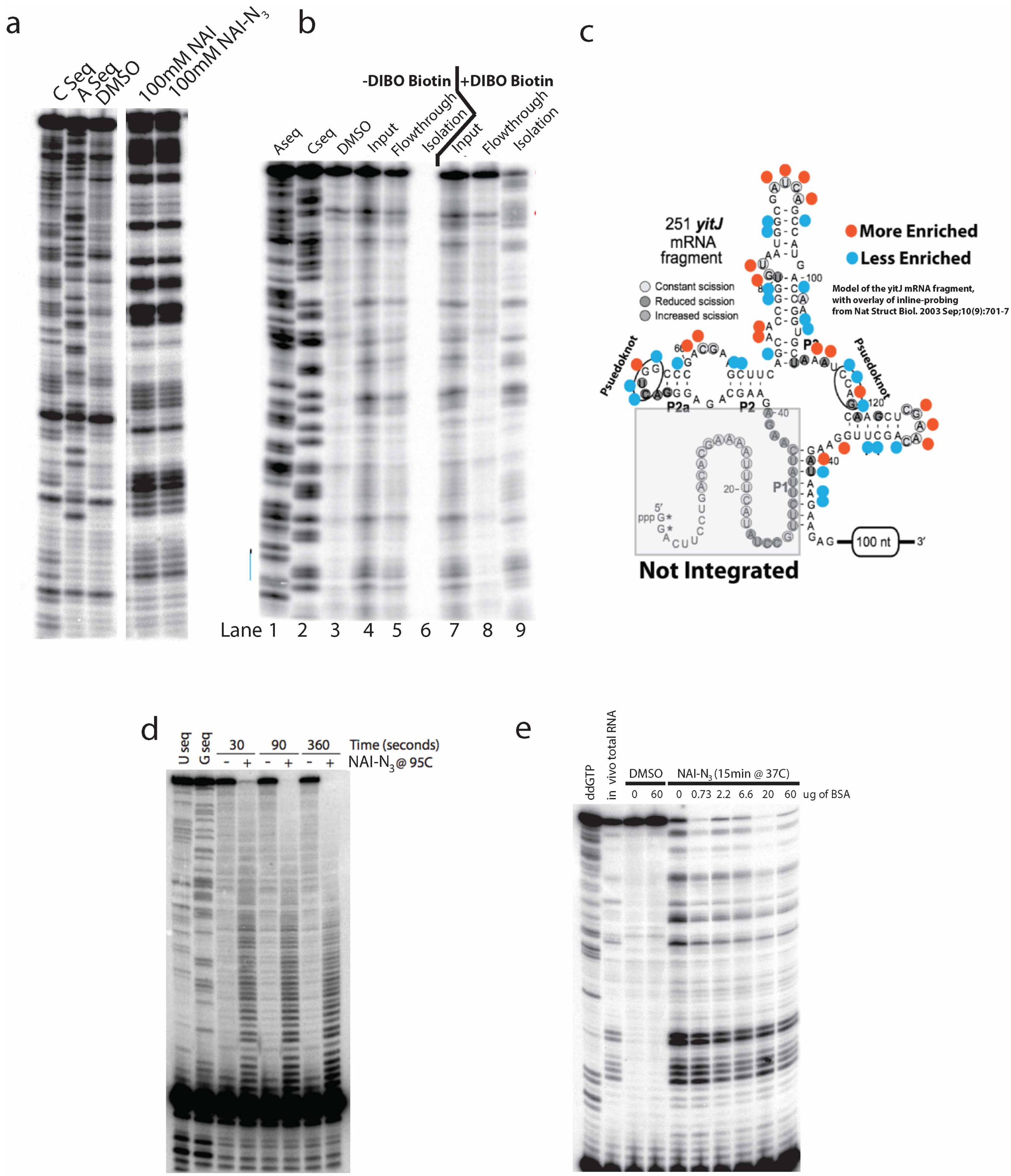

Extended Data Figure 3 | NAI-N$_3$ is a novel RNA acylation reagent that accurately reads out RNA structure. **a**, Comparative denaturing gel of NAI and NAI-N$_3$ RNA acylation. **b**, Denaturing gel analysis of cDNAs that originate from the biotin-purification protocol (Extended Data Fig. 1). **c**, Secondary structure of the SAM-I Riboswitch with enriched residues highlighted in orange and depleted residues highlighted in blue. **d**, Denaturing gel analysis of denatured RNA probed with NAI-N$_3$ shows even coverage of 2′-hydroxyl reactivity when RNA is unfolded. **e**, Protein titration with bovine serum albumin (BSA), demonstrating no difference in the SHAPE pattern as a function of protein concentration.

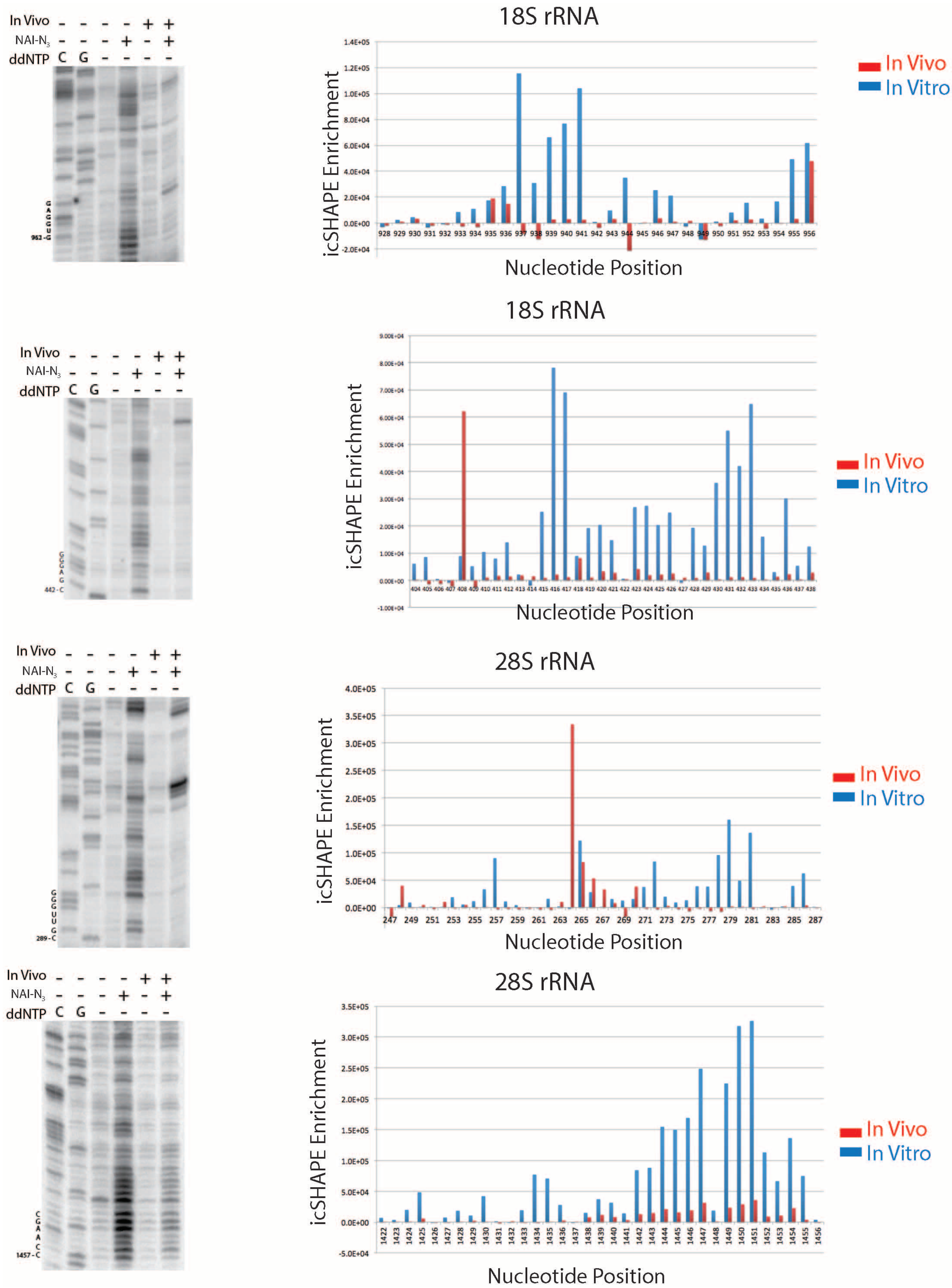

Extended Data Figure 4 | icSHAPE is capable of reproducing RNA acylation profiles obtained by manual RNA modification experiments. icSHAPE profiles (right) of rRNA, and compared to those obtained by manual SHAPE (left).

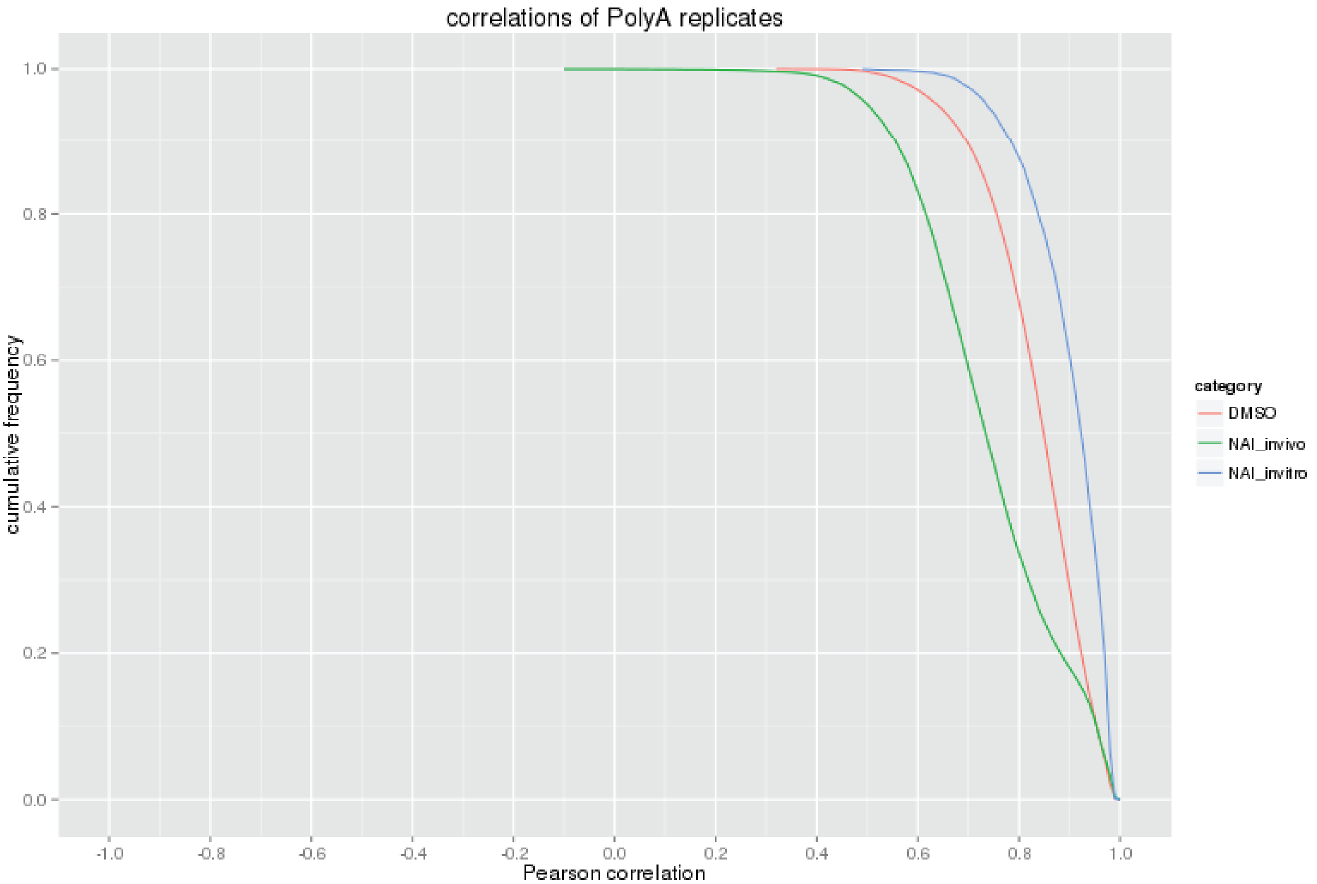

Extended Data Figure 5 | Reverse transcription stops measured by icSHAPE are very well correlated in different library replicates.

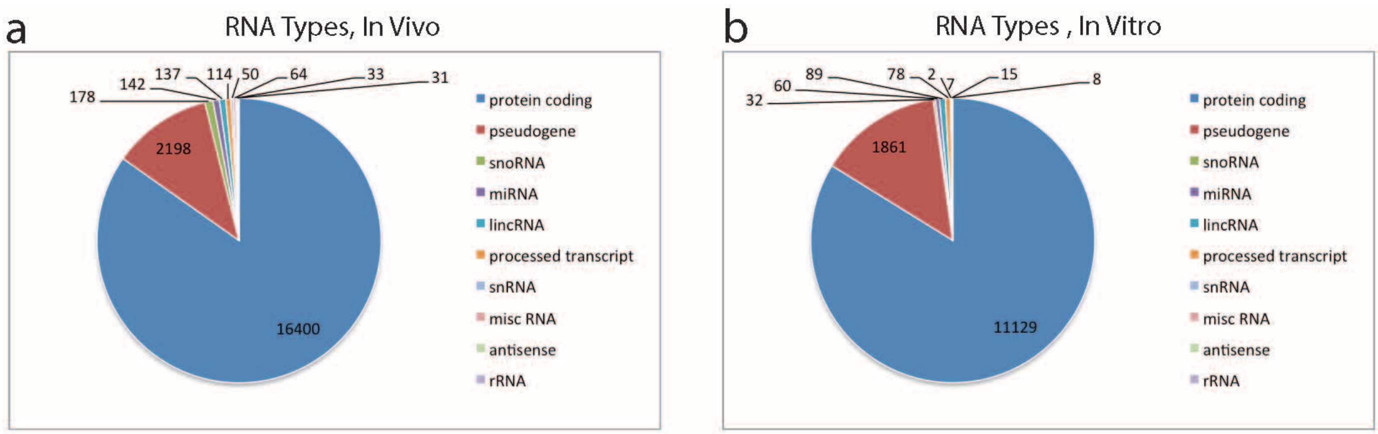

Extended Data Figure 6 | icSHAPE is capable of measuring the RNA structure profiles of thousands of RNAs simultaneously. **a**, The RNAs represented in polyA-selected RNA, *in vivo*. **b**, The RNAs represented in polyA-selected RNA, *in vitro*.

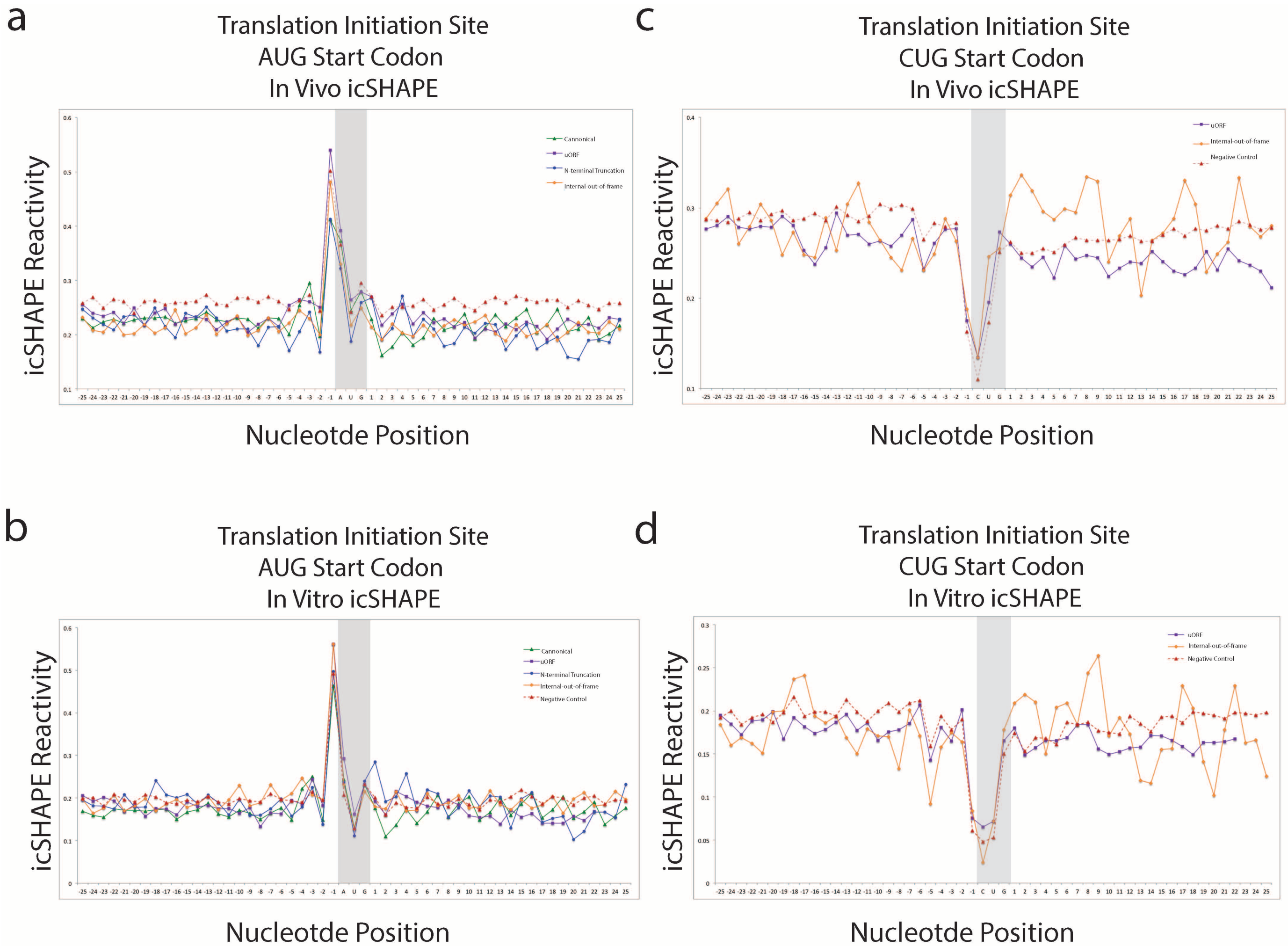

Extended Data Figure 7 | Non-AUG start codons are associated with preceding reactivity, and non-AUG start codons have a different profile, suggesting that RNA accessibility alone is not sufficient to drive translation. **a**, icSHAPE profile at AUG start codons, *in vivo*. **b**, icSHAPE profile at AUG start codons, *in vitro*. **c**, icSHAPE profile at CUG start codons, *in vivo*. **d**, icSHAPE profile at CUG start codons, *in vitro*.

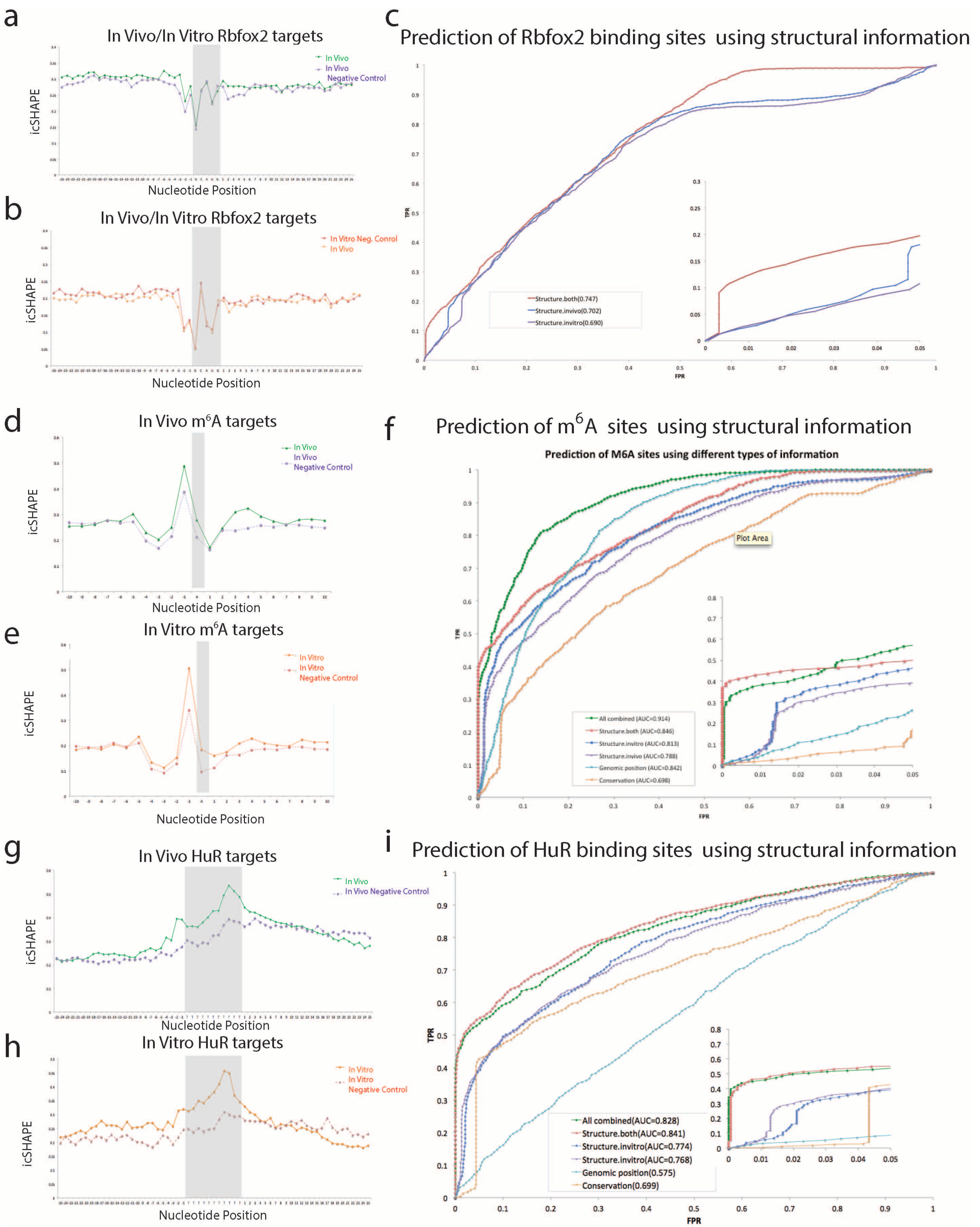

Extended Data Figure 8 | icSHAPE can be used to predict post-transcriptional regulatory elements. **a**, icSHAPE profile at Rbfox2 targets, *in vivo*. **b**, icSHAPE profile at Rbfox2 targets, *in vitro*. **c**, ROC curve of Rbfox2 RNA–protein interactions, predicted using icSHAPE profiles. **d**, icSHAPE profile at m^6A targets, *in vivo*. The negative control is the set of motif instances that are not m^6A modified. **e**, icSHAPE profile at m^6A targets, *in vitro*. **f**, ROC curve of m^6A RNA modification sites, predicted using icSHAPE profiles. **g**, icSHAPE profile at HuR targets, *in vivo*. **h**, icSHAPE profile at HuR targets, *in vitro*. **i**, ROC curve of HuR RNA–protein interactions, predicted using icSHAPE profiles.

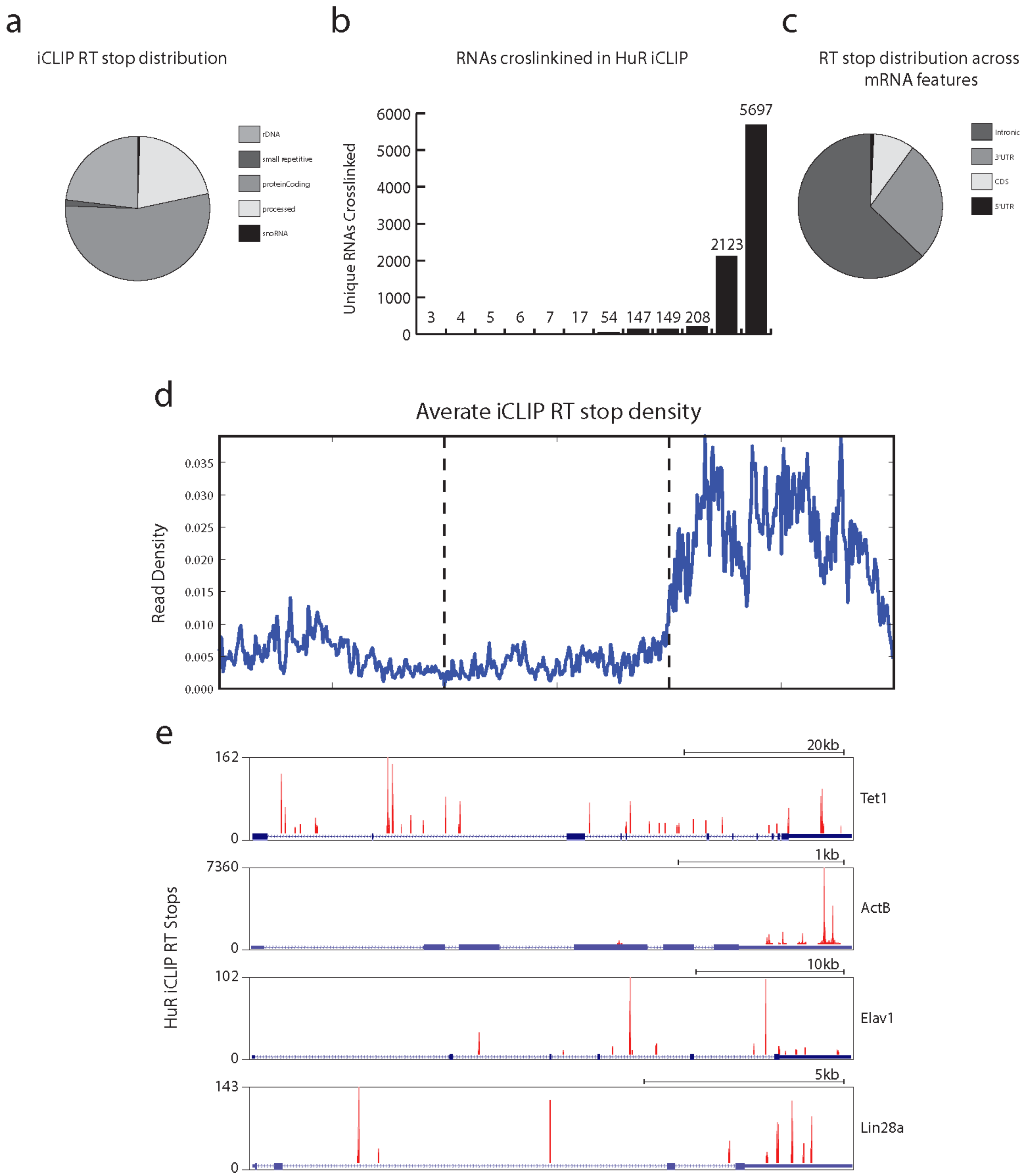

Extended Data Figure 9 | iCLIP analysis of HuR in mouse ES cells. a, Global binding preference of the RBP HuR in mouse ES cells as represented by reverse transcription (RT) stops across the mouse transcriptome (mm9). HuR mainly binds protein-coding, processed and ribosomal RNAs. **b**, Number of unique RNA transcripts bound by HuR. **c**, HuR reverse transcription stops distributed across protein-coding transcript functional domains. HuR prefers intronic and 3′ UTR regions. **d**, Metagene analysis of all HuR binding sites. Each mRNA region (5′ UTR, CDS or 3′ UTR) was scaled to a standard width and reverse transcription stop density across all bound protein-coding genes and was plotted, revealing a clear enrichment for 3′ UTR regions in mature protein-coding transcripts. **e**, Individual mRNA binding events of HuR to genes important for mouse ES cell biology, including *Tet1*, β-actin, *Elav1* (encoding HuR itself) and *Lin28a*. Discrete binding sites are observed focused in 3′ UTR and intronic regions.

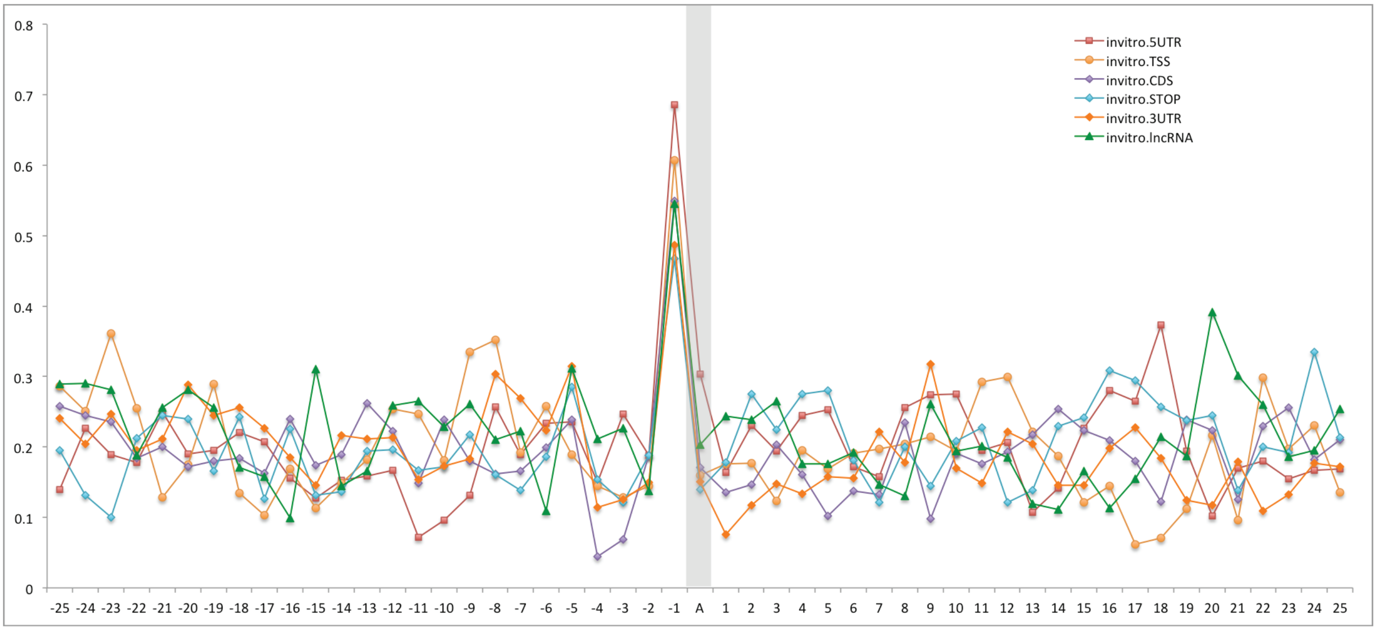

Extended Data Figure 10 | m^{6}A-associated RNA structure features are preserved, independent of their position along the RNA transcript.

doi:10.1038/nature14280

hiCLIP reveals the *in vivo* atlas of mRNA secondary structures recognized by Staufen 1

Yoichiro Sugimoto[1], Alessandra Vigilante[3,4]*, Elodie Darbo[3]*, Alexandra Zirra[2], Cristina Militti[2], Andrea D'Ambrogio[1,2], Nicholas M. Luscombe[3,4,5] & Jernej Ule[1,2]

The structure of messenger RNA is important for post-transcriptional regulation, mainly because it affects binding of *trans*-acting factors[1]. However, little is known about the *in vivo* structure of full-length mRNAs. Here we present hiCLIP, a biochemical technique for transcriptome-wide identification of RNA secondary structures interacting with RNA-binding proteins (RBPs). Using this technique to investigate RNA structures bound by Staufen 1 (STAU1) in human cells, we uncover a dominance of intra-molecular RNA duplexes, a depletion of duplexes from coding regions of highly translated mRNAs, an unexpected prevalence of long-range duplexes in 3′ untranslated regions (UTRs), and a decreased incidence of single nucleotide polymorphisms in duplex-forming regions. We also discover a duplex spanning 858 nucleotides in the 3′ UTR of the X-box binding protein 1 (*XBP1*) mRNA that regulates its cytoplasmic splicing and stability. Our study reveals the fundamental role of mRNA secondary structures in gene expression and introduces hiCLIP as a widely applicable method for discovering new, especially long-range, RNA duplexes.

RNA secondary structure is emerging as a key determinant of post-transcriptional regulation[1–7]. However, identifying the base-paired duplexes forming these structures remains challenging on a transcriptomic scale. The recently reported method CLASH (crosslinking, ligation, and sequencing of hybrids) detects RNA duplexes complexed with RBPs[8]; but several challenges arise from the direct ligation of the two RNA strands forming the duplex[9] (Supplementary Note). To this end, we developed hiCLIP (RNA hybrid and individual-nucleotide resolution ultraviolet crosslinking and immunoprecipitation). Like CLASH, hiCLIP identifies duplexes by ligating the two RNA strands in the duplex and sequencing the resulting hybrids. However, hiCLIP incorporates an adaptor between the two RNA strands to gain greater control over the ligation reaction and to define duplexes accurately through unambiguous identification of the two arms of hybrid reads (Extended Data Fig. 1a–c). Using hiCLIP, we studied RNA duplexes directly bound by STAU1, a double-stranded RBP that is important for mRNA localization[10], stability[11,12] and translation[13]. Despite several investigations into its target RNAs[11–18], characteristics of secondary structures bound *in vivo* remain poorly understood.

We performed hiCLIP from cytoplasmic extracts of Flp-In T-REx 293 cells. To recover a broad spectrum of RNAs and to ensure that only directly bound duplexes are identified, we used two different RNase concentrations and stringent purification conditions (Fig. 1a and Extended Data Fig. 2a). We obtained 35,358 hybrid reads whose arms could be mapped to non-contiguous segments of RNA transcripts (Extended Data Fig. 1a–c and Supplementary Table 1). Hybrid reads comprised approximately 2% of all reads. The remaining non-hybrid reads (1.2 million reads including control library; Supplementary Table 1) were equivalent to traditional iCLIP reads and defined STAU1 crosslink sites[19] (Extended Data Fig. 1a, step 6). In contrast, hybrid reads comprised just 0.06% of control experiments omitting the second ligation reaction (Fig. 1b). Despite different RNase concentrations between replicates, there was good correlation in the numbers of reads mapping to each mRNA transcript ($r = 0.876$; Extended Data Fig. 2b).

Of the 35,358 hybrid reads, 50% mapped to mRNAs, 21% to ribosomal RNAs (rRNAs) and the remainder to other RNA species (Fig. 1c). We defined putative STAU1-binding duplexes as the longest predicted double-stranded region when computationally annealing the two arms of hybrid reads (Extended Data Fig. 1d). We assessed the validity of these duplexes first by examining whether hiCLIP identifies the best-characterized STAU1-bound duplex in the 3′ UTR of the ADP-ribosylation factor 1 (*ARF1)* transcript[12,14]. Both hybrid reads and STAU1 crosslink sites overlapped with the known duplex, and also revealed additional duplexes in *ARF1* 3′ UTR (Extended Data Fig. 2c–e).

We also tested the thermodynamic stability of duplexes on a transcriptomic level by comparing the minimum free energy of hybridization between the two arms of hybrid reads with those of randomly repositioned sequences within the same transcript region. Hybrid reads showed lower energies across all types of RNAs (Fig. 1d and Extended Data Fig. 3a–d). Furthermore, a comparison with the PARS (parallel analysis of RNA structure)[4] scores confirmed that hiCLIP duplexes in mRNAs are enriched for double-stranded bases compared with neighbouring regions (Extended Data Fig. 3e).

STAU1 interacts with the ribosome in an RNA-dependent manner[13,20]. Therefore we compared the distribution of hybrid reads from rRNAs with the human 18S and 28S rRNA structures resolved by cryo-electron microscopy (cryo-EM)[21]. 78% and 72% of hiCLIP duplexes mapping to the 18S and 28S rRNAs, respectively, agreed with cryo-EM-resolved secondary structures (Extended Data Fig. 4), giving a maximum false discovery rate of 28%. In fact, we propose that many of the non-overlapping hybrid reads are candidate novel duplexes that were missed by cryo-EM; for instance, 8% of hybrid reads in 18S rRNA map to a putative duplex connecting distal regions of the molecule (Fig. 1e). The sequences underlying this newly identified duplex are conserved between yeast and human (Extended Data Fig. 4), suggesting their functional relevance. Thus hiCLIP appears to reveal previously undetected secondary structures or tertiary RNA–RNA contacts that are formed *in vivo*.

As a final validation, we assessed whether hiCLIP duplexes overlap with STAU1 crosslink sites defined by non-hybrid 'iCLIP-like' reads. These crosslink sites were enriched up to 70 nucleotides upstream of hiCLIP duplexes (Extended Data Fig. 3f). Moreover, crosslink sites were more likely to be single-stranded (Extended Data Fig. 3g), suggesting STAU1 crosslinks to single-stranded RNA regions located 5′ of the duplexes. The likely reason for this is that bases within the duplexes are inaccessible for protein–RNA crosslinking.

Having examined the validity of the hiCLIP data, we investigated general properties of STAU1-bound duplexes in mRNAs and long non-coding RNAs (Extended Data Fig. 5a). A total of 96% of hybrid reads originated from two regions of the same RNA species. Of 4,693 hiCLIP duplexes

[1]MRC Laboratory of Molecular Biology, Francis Crick Avenue, Cambridge Biomedical Campus, Cambridge CB2 0QH, UK. [2]Department of Molecular Neuroscience, UCL Institute of Neurology, Queen Square, London WC1N 3BG, UK. [3]Cancer Research UK London Research Institute, 44 Lincoln's Inn Fields, London WC2A 3LY, UK. [4]UCL Genetics Institute, Department of Genetics, Evolution and Environment, University College London, Gower Street, London WC1E 6BT, UK. [5]Okinawa Institute of Science & Technology, 1919-1 Tancha, Onna-son, Kunigami-gun, Okinawa 904-0495, Japan.
*These authors contributed equally to this work.

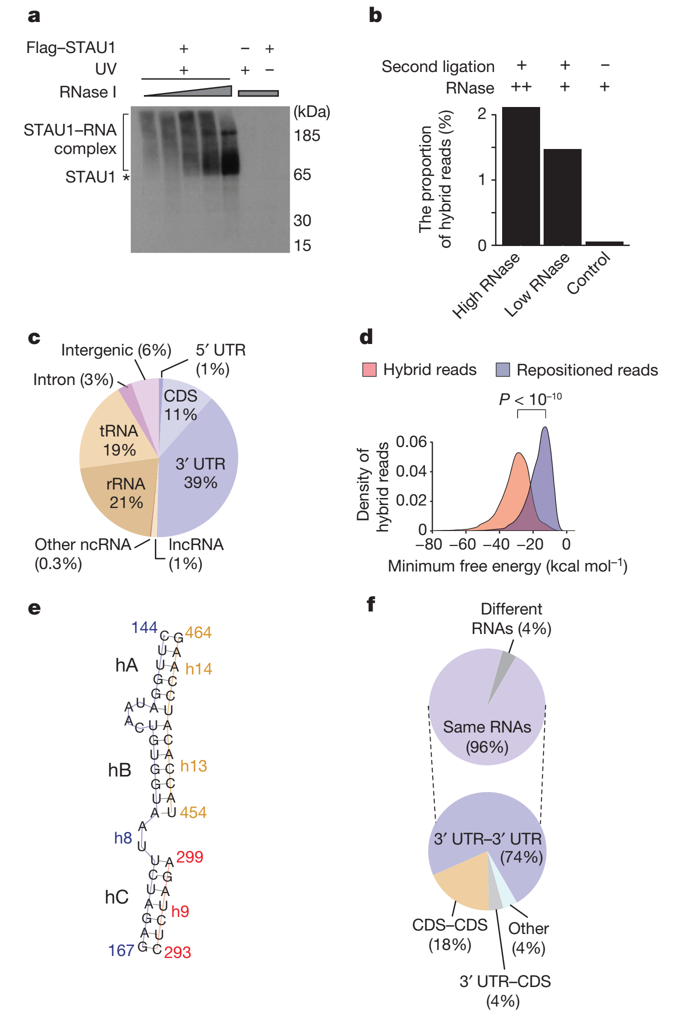

Figure 1 | hiCLIP identifies RNA duplexes bound by STAU1. **a**, Autoradiography analysis of the STAU1–RNA complex at different RNase I concentrations or in the absence of crosslinking or STAU1 induction. The star shows the migration of STAU1 when not crosslinked to RNA. **b**, The proportion of uniquely annotated hybrid reads in the hiCLIP libraries at high and low RNase conditions and from the control in which the second ligation (step 5 in Extended Data Fig. 1a) was omitted. **c**, Mapping summary of the arms of hybrid reads. **d**, Probability density distributions of minimum free energies of hybridization between the two arms of hybrid reads from mRNAs and long non-coding RNAs, or randomly repositioned sequences. Distributions were compared using the Mann–Whitney U-test ($n = 6{,}120$ for both). **e**, Alignment of three newly identified duplexes (hA, hB and hC) that connect distal regions of the human 18S rRNA. The nucleotide position and the nearest annotated helix from the cryo-electron microscopy structure of the rRNA (Extended Data Fig. 4b) are marked in a different colour for each region. **f**, Top, proportion of hybrid reads that map to same or different RNA species. Bottom, for hybrid reads mapping to same mRNA species, proportion in CDS, 3′ UTR, or other (that is, 5′ UTR or spanning across two regions).

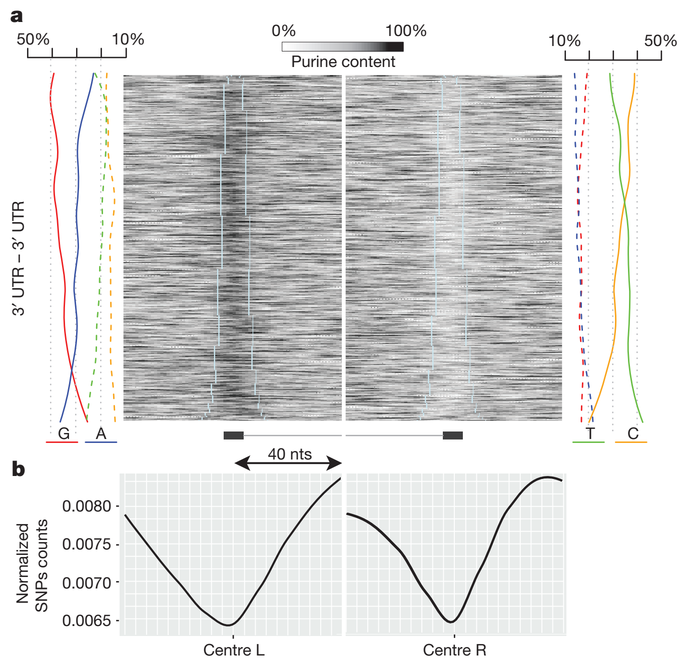

Figure 2 | Properties of STAU1-target RNA duplexes. **a**, Heat map of purine content around the two arms of 2,291 duplexes in 3′ UTRs (only duplexes with distance >80 nucleotides between the two arms are shown in order to allow analysis of loop sequence). Duplexes are oriented so that the arm with the higher purine content is on the left-hand side of the plot. Line graphs on both sides show the nucleotide content of each arm. **b**, Metaprofile of the normalized occurrences of SNPs in the regions around the two arms of the 2,291 duplexes.

across 2,964 mRNAs, 3,530 were found in 3′ UTRs, 894 in coding sequences (CDS), and the rest were in 5′ UTRs or spanned two regions of the same mRNA (Fig. 1f). Only 4% of hybrid reads corresponded to intermolecular duplexes between transcripts of different genes (Fig. 1f and Extended Data Fig. 1a-c). In agreement with previous studies[11,22], the proportion of long non-coding RNAs was higher among these intermolecular hybrids (Extended Data Fig. 5a). Alu repeat elements (Alus) were previously reported as common intermolecular STAU1 binding sites[11]; however, we found minor enrichment of Alu sequences around the STAU1 cross-link sites. Nevertheless, we detected STAU1-binding to Alus when performing iCLIP on whole-cell extracts, indicating these interactions may occur in the nucleus[23] (Extended Data Fig. 6a). We concluded that STAU1 rarely binds duplexes formed by different transcripts in the cytoplasm of 293 cells, and therefore we focused our further analyses on duplexes that have both arms in the same RNA.

Despite efforts to characterize STAU1-bound duplexes[13,15–17], it is still not known whether Staufen proteins recognize duplexes of specific length or sequence. 90% of duplexes were between 5 to 14 nucleotides in length, with a median length of 8 nucleotides (Extended Data Fig. 5b). We observed a prevalence of G-tracts interspersed by A, or C-tracts interspersed by U (Extended Data Fig. 5c); that is, each duplex arm generally contained stretches of purines or pyrimidines, but not both (Fig. 2a). Short duplexes displayed higher GC content and long duplexes showed higher AU content, consistent with the greater stability of GC base pairs (Fig. 2a). The same sequence characteristics were present at hiCLIP duplexes in the CDS, as well as in control duplexes predicted by the RNAfold software[24] in 3′ UTRs that did not contain any hiCLIP duplexes (Extended Data Fig. 5d–f). This suggests that STAU1 lacks precise sequence specificity, and instead the asymmetric positioning of purine/pyrimidine tracts is a general property of RNA duplexes in human mRNAs. As evidence of selection pressure to retain STAU1-bound duplexes, we found decreased occurrence of single nucleotide polymorphisms (SNPs) in hiCLIP duplexes compared with neighbouring 3′ UTR regions (Fig. 2b and Extended Data Fig. 6b, c and Supplementary Table 2), whereas there was no similar depletion in control duplexes (Extended Data Fig. 6d).

Most previous studies of RNA secondary structures were limited to analyses of stem loops; that is, duplexes with short intervening loops (Extended Data Fig. 1e and Supplementary Note). An important feature of hiCLIP is the ability to detect duplexes regardless of loop length: 57% of hiCLIP duplexes in 3′ UTRs had loop lengths of over 100 nucleotides and 20% over 500 nucleotides (Fig. 3a, b). Moreover, hiCLIP duplexes in 3′ UTRs had significantly longer loops compared with those in the CDS (Fig. 3b). Many long-range hiCLIP duplexes connected the start and end of the 3′ UTR or of the CDS, so that the stop codon is brought

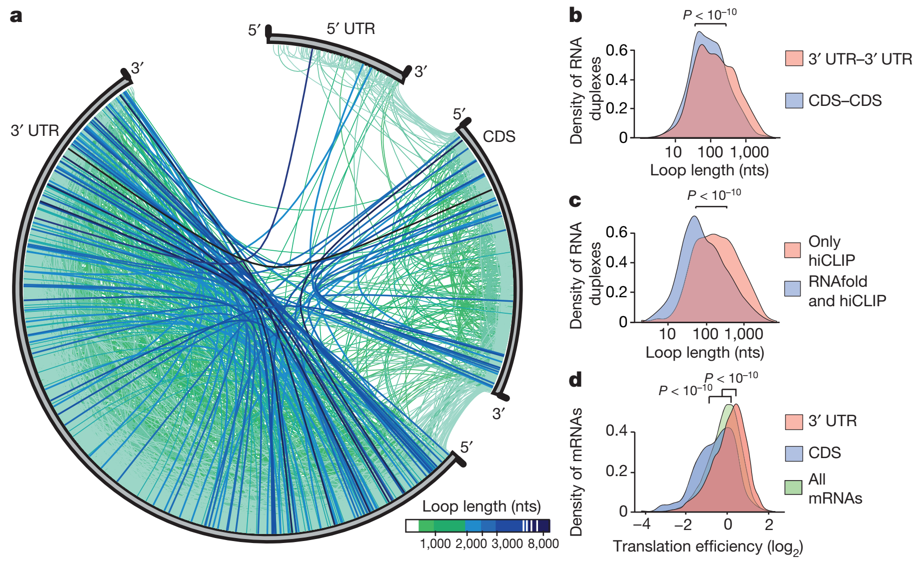

Figure 3 | Insights into the secondary structures of mRNAs. **a**, Circos plot illustrating the position of two arms of all duplexes within a standardized mRNA. The mRNA is shown at the circumference of the plot, divided into the 5′ UTR, CDS and 3′ UTR. The left and right arms are positioned relative to the start and end of each segment. The lines connecting the two arms are coloured according to the loop length. **b**, Probability density distributions of loop lengths among hiCLIP duplexes in the CDS and 3′ UTRs. Counts of RNA duplexes were weighted by the number of hybrid reads that identified them. Distributions were compared using the Mann–Whitney *U*-test ($n = 953$ reads from 894 unique duplexes for CDS and $n = 4,447$ reads from 3,530 unique duplexes for 3′ UTR). **c**, Probability density distribution of loop lengths among hiCLIP duplexes in 3′ UTRs that were or were not predicted by RNAfold[24]. Distributions were compared using the Mann–Whitney *U*-test ($n = 1,348$ and 2,182, respectively). **d**, Probability density distributions of translational efficiencies among mRNAs with hybrid reads in the CDS or 3′ UTR, compared with all mRNAs. mRNA counts were weighted by the number of hybrid reads that identified them. Translational efficiencies were compared using the Mann–Whitney *U*-test ($n = 8,199$ from 81,99 mRNAs for all, 885 from 696 mRNAs for CDS, and 4,064 from 1,986 mRNAs for 3′ UTR).

into the vicinity of the start codon or the poly(A) tail (Fig. 3a). As these regions generally bind proteins controlling mRNA translation or stability[25], it is possible that long-range duplexes may affect interactions between these factors.

To evaluate if hiCLIP duplexes could be computationally predicted, we used RNAfold to identify secondary structures in 3′ UTRs by their minimum free energy[24]. The software predicted just 1,348 of 3,530 hiCLIP duplexes; the remaining 2,182 duplexes generally contain much longer loops with lengths up to 8 kb (Fig. 3c). This indicates that current computational and experimental methods that rely on thermodynamic-based folding algorithms miss many duplexes with long loops (Supplementary Note).

Of the 2,964 distinct mRNAs with hiCLIP duplexes, 70% contain at least one duplex in the 3′ UTR, 23% in the CDS, but only 6% contain duplexes both in CDS and 3′ UTR (Extended Data Fig. 7a). We used ribosome profiling to assess how the position of duplexes in these different classes of transcripts relates to their translational efficiencies (Extended Data Fig. 7b, c). Transcripts with hiCLIP duplexes in the CDS were poorly translated compared with all mRNAs, whereas those with 3′ UTR duplexes were highly translated (Fig. 3d). In agreement with previous studies[4,5,26], the absence of hiCLIP duplexes from the CDS of highly translated mRNAs indicates that translating ribosomes unwind RNA structures.

Next, we examined the effect of STAU1 on mRNA stability and translational efficiency by analysis of STAU1 knockdown cells with or without inducible expression of short interfering RNA (siRNA)-resistant STAU1 (Extended Data Fig. 7d, e). Transcripts with 3′ UTR duplexes displayed an overall increase in abundance upon STAU1 depletion, but no change

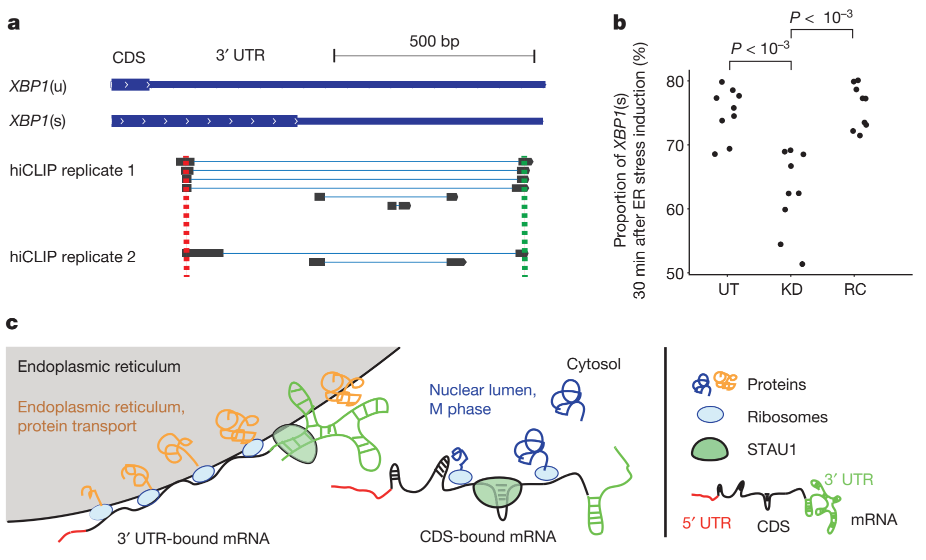

Figure 4 | STAU1 regulates cytoplasmic splicing of *XBP1* mRNA. **a**, Schematic representation of the unspliced *XBP1*(u) and spliced *XBP1*(s) mRNA, shown together with hybrid reads that identify RNA duplexes. **b**, Proportion of *XBP1*(s) out of total *XBP1* mRNA 30 min after endoplasmic reticulum (ER) stress induction in untreated (UT), STAU1 knockdown (KD), and rescued (RC) cells. The proportions of *XBP1*(s) in different conditions were compared using the two-tailed Welch's *t*-test ($n = 9$ from 3 independent experiments). **c**, Schematic diagram summarizing the functional analyses of STAU1-target mRNAs. 3′ UTR-bound mRNAs tend to be highly translated and encode membrane proteins that are translated at the endoplasmic reticulum (in grey). CDS-bound mRNAs tend to be translated at a low level and encode proteins that function in the cell cycle M phase. Loops formed by RNA duplexes in the 3′ UTR tend to be longer than in the CDS.

in translational efficiency (Extended Data Fig. 7f). This is consistent with the reported function of 3′ UTR-bound STAU1 in mRNA decay[12]. mRNAs with CDS duplexes displayed the opposite trend, with no change in abundance but increased translational efficiency upon STAU1 depletion (Extended Data Fig. 7f). These results contrast with the reported enhancing effect of STAU1 on translation of structured CDS[13]; the reason for the discrepancy is unclear, though it might be because the RNA immunoprecipitation in tandem (RIPiT-seq) method used in the previous study may co-purify ribosomes or other proteins. This might also explain why CDS reads are enriched in STAU1 RIPiT-seq, whereas 3′ UTR reads are enriched in STAU1 hiCLIP (Fig. 1f).

The mRNA encoding XBP1 (also known as endoplasmic reticulum to nucleus signalling 1; ERN1), a central player in ER stress response[27], was one of the mRNAs with substantially increased abundance upon STAU1 knockdown (Extended Data Fig. 7f). hiCLIP identified a duplex spanning 858 nucleotides in the *XBP1* 3′ UTR, which is required for efficient splicing of the *XBP1* transcript during endoplasmic reticulum stress (Fig. 4a, b and Extended Data Fig. 8a–d). We produced three reporter constructs to examine the effect of this long-range duplex on the stability of the *XBP1* transcript; one containing the *XBP1* 3′ UTR with the original sequence, one with an AA dinucleotide insertion to disrupt the duplex, and one with an additional insertion of a complementary TT dinucleotide to restore the duplex structure (Extended Data Fig. 8a). We observed that the AA insertion decreased mRNA stability, whereas the complementary TT mutation restored it back to original levels (Extended Data Fig. 8e).

To examine further the functions of proteins encoded by STAU-bound transcripts, we evaluated the enrichment of Gene Ontology terms. Transcripts with duplexes in their 3′ UTRs were enriched for protein trafficking annotations; this suggests that many such transcripts are translated at the rough endoplasmic reticulum (Fig. 4c, Extended Data Figs 9 and 10, and Supplementary Table 2), in agreement with the known localization of STAU1 to this compartment[28,29]. In contrast, transcripts with hiCLIP duplexes in the CDS were enriched for annotations relating to nuclear localization and mitosis (Extended Data Fig. 9). This suggests that STAU1 represses translation of mRNAs encoding mitotic proteins, which is consistent with a recent report that STAU1 degradation is required during mitosis for efficient cell cycle progression[30].

Our study reveals the unexpected prevalence of long-range duplexes in 3′ UTRs with importance for mRNA stability, whereas duplexes in the CDS have shorter loops and are mainly found in poorly translated mRNAs. Depletion of SNPs from the long-range duplexes suggests that some disease-causing mutations in 3′ UTRs could be explained by their effects on the structure of full-length mRNAs. In conclusion, hiCLIP identifies RNA duplexes that form *in vivo* and thereby opens a new avenue for transcriptome-wide studies of RNA structures.

Online Content Methods, along with any additional Extended Data display items and Source Data, are available in the online version of the paper; references unique to these sections appear only in the online paper.

Received 6 September 2014; accepted 2 February 2015.
Published online 18 March 2015.

1. Wan, Y., Kertesz, M., Spitale, R. C., Segal, E. & Chang, H. Y. Understanding the transcriptome through RNA structure. *Nature Rev. Genet.* **12,** 641–655 (2011).
2. Ding, Y. *et al. In vivo* genome-wide profiling of RNA secondary structure reveals novel regulatory features. *Nature* **505,** 696–700 (2014).
3. Rouskin, S., Zubradt, M., Washietl, S., Kellis, M. & Weissman, J. S. Genome-wide probing of RNA structure reveals active unfolding of mRNA structures *in vivo*. *Nature* **505,** 701–705 (2014).
4. Wan, Y. *et al.* Landscape and variation of RNA secondary structure across the human transcriptome. *Nature* **505,** 706–709 (2014).
5. Li, F. *et al.* Global analysis of RNA secondary structure in two metazoans. *Cell Rep.* **1,** 69–82 (2012).
6. Goodarzi, H. *et al.* Metastasis-suppressor transcript destabilization through TARBP2 binding of mRNA hairpins. *Nature* **513,** 256–260 (2014).
7. Lovci, M. T. *et al.* Rbfox proteins regulate alternative mRNA splicing through evolutionarily conserved RNA bridges. *Nature Struct. Mol. Biol.* **20,** 1434–1442 (2013).
8. Kudla, G., Granneman, S., Hahn, D., Beggs, J. D. & Tollervey, D. Cross-linking, ligation, and sequencing of hybrids reveals RNA–RNA interactions in yeast. *Proc. Natl Acad. Sci. USA* **108,** 10010–10015 (2011).
9. Grosswendt, S. *et al.* Unambiguous identification of miRNA:target site interactions by different types of ligation reactions. *Mol. Cell* **54,** 1042–1054 (2014).
10. Heraud-Farlow, J. E. & Kiebler, M. A. The multifunctional Staufen proteins: conserved roles from neurogenesis to synaptic plasticity. *Trends Neurosci.* **37,** 470–479 (2014).
11. Gong, C. & Maquat, L. E. lncRNAs transactivate STAU1-mediated mRNA decay by duplexing with 3′ UTRs via Alu elements. *Nature* **470,** 284–288 (2011).
12. Kim, Y. K., Furic, L., Desgroseillers, L. & Maquat, L. E. Mammalian Staufen1 recruits Upf1 to specific mRNA 3′ UTRs so as to elicit mRNA decay. *Cell* **120,** 195–208 (2005).
13. Ricci, E. P. *et al.* Staufen1 senses overall transcript secondary structure to regulate translation. *Nature Struct. Mol. Biol.* **21,** 26–35 (2014).
14. Kim, Y. K. *et al.* Staufen1 regulates diverse classes of mammalian transcripts. *EMBO J.* **26,** 2670–2681 (2007).
15. Heraud-Farlow, J. E. *et al.* Staufen2 regulates neuronal target RNAs. *Cell Rep.* **5,** 1511–1518 (2013).
16. Laver, J. D. *et al.* Genome-wide analysis of Staufen-associated mRNAs identifies secondary structures that confer target specificity. *Nucleic Acids Res.* **41,** 9438–9460 (2013).
17. de Lucas, S., Oliveros, J. C., Chagoyen, M. & Ortin, J. Functional signature for the recognition of specific target mRNAs by human Staufen1 protein. *Nucleic Acids Res.* **42,** 4516–4526 (2014).
18. LeGendre, J. B. *et al.* RNA targets and specificity of Staufen, a double-stranded RNA-binding protein in *Caenorhabditis elegans*. *J. Biol. Chem.* **288,** 2532–2545 (2013).
19. König, J. *et al.* iCLIP reveals the function of hnRNP particles in splicing at individual nucleotide resolution. *Nature Struct. Mol. Biol.* **17,** 909–915 (2010).
20. Luo, M., Duchaine, T. F. & DesGroseillers, L. Molecular mapping of the determinants involved in human Staufen-ribosome association. *Biochem. J.* **365,** 817–824 (2002).
21. Anger, A. M. *et al.* Structures of the human and *Drosophila* 80S ribosome. *Nature* **497,** 80–85 (2013).
22. Kretz, M. *et al.* Control of somatic tissue differentiation by the long non-coding RNA TINCR. *Nature* **493,** 231–235 (2013).
23. Elbarbary, R. A., Li, W., Tian, B. & Maquat, L. E. STAU1 binding 3′ UTR IRAlus complements nuclear retention to protect cells from PKR-mediated translational shutdown. *Genes Dev.* **27,** 1495–1510 (2013).
24. Lorenz, R. *et al.* ViennaRNA Package 2.0. *Algorithms Mol. Biol.* **6,** 26 (2011).
25. Roy, B. & Jacobson, A. The intimate relationships of mRNA decay and translation. *Trends Genet.* **29,** 691–699 (2013).
26. Qu, X. *et al.* The ribosome uses two active mechanisms to unwind messenger RNA during translation. *Nature* **475,** 118–121 (2011).
27. Walter, P. & Ron, D. The unfolded protein response: from stress pathway to homeostatic regulation. *Science* **334,** 1081–1086 (2011).
28. Marión, R. M., Fortes, P., Beloso, A., Dotti, C. & Ortin, J. A human sequence homologue of Staufen is an RNA-binding protein that is associated with polysomes and localizes to the rough endoplasmic reticulum. *Mol. Cell. Biol.* **19,** 2212–2219 (1999).
29. Wickham, L., Duchaine, T., Luo, M., Nabi, I. R. & DesGroseillers, L. Mammalian Staufen is a double-stranded-RNA- and tubulin-binding protein which localizes to the rough endoplasmic reticulum. *Mol. Cell. Biol.* **19,** 2220–2230 (1999).
30. Boulay, K. *et al.* Cell cycle-dependent regulation of the RNA-binding protein Staufen1. *Nucleic Acids Res.* **42,** 7867–7883 (2014).

Supplementary Information is available in the online version of the paper.

Acknowledgements We wish to thank S. Granneman and C. Sibley for discussions on the development of hiCLIP protocol; K. Zarnack, N. Haberman, C. Ravarani and B. Lang for assistance with bioinformatic analyses; D. Daujotyte and P. Lukavsky for sharing the STAU1 plasmid and helping in setting up the project; L. Maquat for sharing the ARF1 SBS plasmid; the genomic team at the Cancer Research UK Cambridge Institute for Illumina HiSeq sequencing, and M. Babu Mohan and Ule group members for support and comments on the manuscript. This work was supported by funding from Human Frontier Science Program (RGP0024/2008-C), European Research Council (206726-CLIP and 617837-Translate) and Medical Research Council (U105185858) to J.U., Cancer Research UK and UCL to N.M.L., a Wellcome Trust Joint Investigator Award to N.M.L. and J.U. (103760/Z/14/Z), the Nakajima Foundation fellowship and MRC Centenary Early Career Award to Y.S.

Author Contributions Y.S. and J.U. developed the hiCLIP protocol and designed the project; Y.S. performed the hiCLIP, mRNA-seq, ribosome profiling experiments; Y.S., A.V., E.D. and N.M.L. designed and performed bioinformatic analyses; A.D., C.M. and A.Z. performed the reporter assays. Y.S., A.D., N.M.L. and J.U. wrote the manuscript. All authors contributed to the analysis and interpretation of the data.

Author Information The sequence data and scripts are publicly available from ArrayExpress (E-MTAB-2937, E-MTAB-2940, E-MTAB-2941) and (https://github.com/jernejule/STAU1_hiCLIP). Reprints and permissions information is available at www.nature.com/reprints. The authors declare no competing financial interests. Readers are welcome to comment on the online version of the paper. Correspondence and requests for materials should be addressed to J.U. (j.ule@ucl.ac.uk) or N.M.L. (nicholas.luscombe@ucl.ac.uk).

METHODS

Analysis pipeline. We developed a computational pipeline for data analysis, which is freely accessible from (https://github.com/jernejule/STAU1_hiCLIP). The pipeline is implemented as a package of codes that enables the user to reproduce most plots and results using the sequencing data as input. All sequencing data are available from ArrayExpress (iCLIP and hiCLIP: E-MTAB-2937, mRNA-seq: E-MTAB-2940, ribosome profiling: E-MTAB-2941).

Plasmids. We produced two Flp-In T-REx 293 cell lines; one expressing Flag–STAU1 (used for hiCLIP), and the other expressing siRNA-resistant Flag–STAU1 (used for all functional assays). For the Flag–STAU1, the sequence of 3 × FLAG tag was added to the 3′ end of the STAU1 coding sequence from NM_017454.2, and inserted into the pcDNA5/FRT/TO plasmid (Life Technologies, V6520-20). For the siRNA-resistant FLAG-STAU1, a region of STAU1 CDS (ggactagtaataaagaggatgagtt) was silently mutated to gCacAagCaaCaaGgaAgaCgaAtt (capital letters show the positions of mutations). These mutations were introduced using the si_pr1 (ACGATGCTGC TGCCAAAGCGT), si_pr2 (aaTtcGtcTtcCttGttGctTgtGccattttcatccccagagccagg), si_pr3 (gCacAagCaaCaaGgaAgaCgaAttcaggatgccttatctaagtcatc), si_pr4 (ACGGG GGAGGGGCAAACAAC) primers.

To generate the plasmids used for formaldehyde crosslinking and RNA co-immunoprecipitation assay, reporter constructs were inserted into pcDNA3 FLuc, where the CDS of firefly luciferase (FLuc) was inserted into the pcDNA3 plasmid (Life Technologies). The plasmid containing ARF1 STAU1 binding site (SBS) was a gift from Professor Maquat[14]. The ARF1 SBS was PCR amplified from this plasmid using C_pr1 (ATTTTTTGGATCCACGCGACCCCCCTCCCTC) and C_pr2 (ATT TTTTCTCGAGGTGCCCATGGGCCTACATCC), and cloned into pcDNA3 FLuc (pcDNA3 FLuc ARF1 SBS). pcDNA3 FLuc ARF1 SBSΔ was generated from pcDNA3 FLuc ARF1 SBS using D_pr1 (GTGCGGCTCGTGGTGTCGTGGTTT GGTCACCG) and D_pr2 (CGGTGACCAAACCACGACACCACGAGCCGCAC). The 3′ UTR of XBP1 was PCR amplified from the total RNA of Flp-In T-REx 293 cells using C_pr3 (ATTTTTTGGATCCTGACCACATATATACCAAGCCCC) and C_pr4 (ATTTTTTCTCGAGGCATTGTACCTTTTAATTGCATGGG), and cloned into pcDNA3 FLuc (pcDNA3 FLuc XBP1). pcDNA3 FLuc XBP1Δ were generated from pcDNA3 FLuc XBP1 using D_pr3 (CTAATGTGGTAGTGAAAA TCCTCAGCCCCTCAGAG) and D_pr4 (CTCTGAGGGGCTGAGGATTTTCA CTACCACATTAG).

To generate the plasmids used for functional studies of the long-range duplex in the 3′ UTR of *XBP1* mRNA, the 3′ UTR of XBP1 was PCR amplified from the total RNA of Flp-In T-REx 293 cells using fX_pr1 (CCGCTCGAGTTCGTT TTG ACCACATATATACCAAG) and fX_pr2 (ATAGTTTAGCGGCCGCGATGCT GCATTGTACCTTTTAATTGC), and cloned into psiCHeck2 (Promega, C8021). The XBP1 mut and comp reporter (Fig. 4b) were generated from the XBP1 wt construct using fX_pr3 (GCTAGTGTAGCTTCTGAAAGGTGaaCTTTCTCCA TTTATTTAAAACTACCC) and fX_pr4 (GGGTAGTTTTAAATAAATGGAG AAAGttCACCTTTCAGAAGCTACACTAGC) –, and from the XBP1 mut construct using fX_pr5 (CTAATGTGGTAGTGAAAATCGAGGAAGttCACCTCT CAGCCCCTCAGAGAA) and fX_pr6 (TTCTCTGAGGGGCTGAGAGGTGaa CTTCCTCGATTTTCACTACCACATTAG). All cloning was performed with the Phusion High-Fidelity PCR master mix with HF Buffer (NEB, M0531L) according to the manufacturer's protocol (PCR template plasmid < 250 ng).

Antibodies used for western blotting. Anti-GAPDH (14C10) antibody (NEB, 2118) and anti-Staufen 1 antibody (Proteintech, 14225-1-AP) were used for the western blotting analysis.

Cell culture. Flp-In 293 T-REx cells (Life Technologies, R780-07) were cultured in DMEM with 10% FBS, 3 μg ml^{-1} Blasticidin S HCl (Life Technologies, A11139-03), 50 μg ml^{-1} Zeocin (Life Technologies, R250-01). To produce cell lines, the pcDNA5/FRT/TO plasmid with FLAG-STAU or siRNA-resistant FLAG-STAU1 was co-transfected with pOG44 plasmid into Flp-In 293 T-REx cells. Cells stably expressing these proteins were selected by culturing in DMEM containing 10% FBS, 3 μg ml^{-1} Blasticidine S HCl, 200 μg ml^{-1} Hygromycine (InvivoGen, ant-hm-5). Absence of mycoplasma contamination was confirmed using the LookOut Mycoplasma PCR Detection Kit (Sigma, MP0035).

Knockdown and rescue of STAU1. We performed all knockdown experiments with siRNA-resistant Flag–STAU1 Flp-In 293 T-REx cell line under three conditions: untransfected controls (UT), knockdown with an siRNA against STAU1 (KD), and a rescue comprising knockdown combined with inducible expression of siRNA-resistant STAU1 (Extended Data Fig. 7d). 120 pmol of stealth STAU1 siRNA (Life Technology, STAU1HSS110293) was transfected to cells growing on 6-well dishes with 4.5 μl of RNAiMAX (Life Technologies, 13778-150) using the manufacturer's reverse-transfection protocol. 24 h after transfection, the medium was replaced with DMEM with 10% FBS and 48 h after the transfection, the cells were collected for the analysis. For untreated control (UT), cells were only treated with RNAiMAX. For rescue experiment (RC), 24 h after transfection of 120 pmol of Stealth STAU1 siRNA, the medium was replaced with DMEM with 10% FBS and 100 ng ml^{-1} of doxycycline (DOX) to induce expression of siRNA-resistant STAU1, and cells were collected 48 h after transfection.

hiCLIP (preparation of adaptors). Adaptor A (/5Phos/rArGrArUrCrGrGrArA rGrArGrCrGrGrUrUrCrArG/3ddC/; 5Phos indicates 5′ phosphate, rN indicates the nucleotide is ribonucleotides, and 3ddC indicates 3′-dideoxycytidine) and Adaptor B (/5Phos/rCrUrGrUrArGrGrCrArCrCrArUrArCrArArUrG/3Phos/; 3Phos indicates 3′-phosphate) were ordered as HPLC-purified RNA (Integrated DNA Technologies). They were pre-adenylated using 5′ DNA Adenylation Kit (NEB: E2610) and purified by PAGE with the following protocol: 200 μl of pre-adenylation mix (10 μl 100 μM non-adenylated adaptor A or B, 20 μl 10 × 5′ DNA adenylation reaction buffer, 20 μl 1 mM ATP, 20 μl Mth RNA ligase, and 130 μl water) was prepared and incubated at 65 °C for 1 h. 20 μl of TE buffer and 400 μl acid-phenol:chloroform, pH 4.5 (acid-PCI, Life Technologies, AM9722) was added and the mixture was transferred to a 2 ml Phase Lock Gel Heavy tube (VWR, 713-2536). The tube was inverted at least 10 times to mix fully and the phases were separated by 5 min centrifugation at 15,871*g* at room temperature. The aqueous layer was transferred to a new tube and the isolated RNA was precipitated by mixing 1.5 μl of linear acrylamide (Life Technologies, AM9510), 40 μl of 3 M sodium acetate pH 5.5, and 1 ml 100% ethanol, and incubated overnight at −20 °C. The reaction was centrifuged at 21,800*g* for 15 min at 4 °C. The supernatant was removed and the pellet was washed with 500 μl of 80% ethanol. The pellet was resuspended in 5 μl water. The pre-adenylated linkers were purified by 15% TBE-Urea PAGE (Life Technologies) and gel excision. To extract the adaptors from the gel, 400 μl TE buffer with 1 μl of RNasin (Promega, N2615) was added to excised gel piece, which was crushed into small pieces with a Squisher-Single (Zymo Research, H1001-50). The crushed gel in TE buffer was incubated at 37 °C for 1 h at 1,100 r.p.m. shaking using the Thermomixer Comfort (Eppendorf, 5355 000.011) or Compact (Eppendorf, 5350 000.013), then placed on dry ice for 2 min, and incubated again at 37 °C for 1 h with 1,100 r.p.m. shaking. Adaptors were purified using acid-PCI extraction and ethanol precipitation as described above. The adenylated adaptors were used in hiCLIP experiments (and called adaptor A and Adaptor B respectively).

hiCLIP (UV crosslinking). STAU1 was induced in Flag–STAU1 Flp-In 293 T-REx cell line by adding 250 ng ml^{-1} of doxycycline to the medium cells growing on a 15-cm dish. After 16 h incubation at 37 °C at 5% CO_2, cells were washed once by ice-cold PBS, and 10 ml ice-cold PBS was added. Cells were subjected to 150 mJ cm^{-2} of UV-C (254 nm) irradiations with Stratlinker 2400 on ice, and scraped off. The cells from 5 dishes were transferred to a 50 ml tube and used for single hiCLIP experiment. The cells were pelleted by centrifugation at 514*g* for 5 min at 4 °C, and the supernatant was removed. The pellets were snap-frozen on dry ice and stored at −80 °C until use.

hiCLIP (preparation of antibody-coupled beads). Dynabeads covalently coupled to the M2-Flag antibody were prepared using the Dynabeads Antibody Coupling Kit (Life Technologies, 14311D) following the manufacturer's protocol (30 μg of antibody per 1 mg of beads). 100 μl antibody-coupled beads were used for a single immunopreciptation experiment. Before immunoprecipitation, beads were washed once with CLIP lysis buffer (50 mM Tris-HCl, pH 7.4, 100 mM NaCl, 1% NP-40, 0.5% sodium deoxycholate), and twice with high salt wash (50 mM Tris-HCl, pH 7.4, 1 M NaCl, 1 mM EDTA, 1% Igepal CA-630 (Sigma, I8896), 0.1% SDS, 0.5% sodium deoxycholate). Beads were left in PGB cell lysis buffer (20 mM Tris-HCL (pH 7.4), 140 mM NaCl, 5 mM $MgCl_2$, 1% Triton-X 100) until cell lysate was prepared.

hiCLIP (preparation of the cell lysate and partial RNA digestion). Frozen cell pellet in a 50 ml tube was resuspended in 30 ml of PGB Cell Lysis Buffer Complete (PGB Cell Lysis Buffer supplemented with 1:1,000 1 M DTT, 1:1,000 anti-RNase (Life Technologies, AM2690), 4:1,000 protease inhibitor cocktail Set III, EDTA-Free (MERCK, 539134), 0.1 μl per ml TURBO DNase (Life Technologies, AM2238)). The lysate was homogenized by passing twice through a syringe with a 21G needle and cleared by centrifugation at 14,000*g* for 5 min at 4 °C. The supernatant was collected and centrifuged again at 14,000*g* for 15 min at 4 °C. The supernatant was collected and 20 ml of PGB Cell Lysis Buffer Complete was added and filtered through a 0.45 μm syringe filter. Unprotected RNA was digested by adding 0.4 U ml^{-1} (high RNase condition) or 0.2 U ml^{-1} (low RNase, second round ligation-minus control and STAU1 induction-minus condition) of RNase I (Life Technologies, AM2294) to the lysate, and the lysate was incubated for 5 min at 37 °C. After incubation, the tube was transferred to ice for a minimum of 5 min. In order to stop RNase I activity, 20 μl of SUPERaseIn (Life Technologies, AM2694) was added.

hiCLIP (immunoprecipitation). PGB cell lysis buffer was removed from the beads. The beads were resuspended in 1 ml of PGB cell lysis buffer and added to the cell lysate. The bead/lysate mix was incubated for ~2–3 h at 4 °C while rotating. The beads were collected by centrifugation at 805*g* for 5 min at 4 °C and the supernatant removed. Then 500 μl of PGB cell lysis buffer was added and the beads were resuspended and transferred to a 1.5 ml tube. The supernatant was discarded using a magnetic stand and the beads were washed twice with PGB cell lysis buffer (the second wash was rotated for at least 1 min in the cold room). To remove completely the residual DNA, the beads were resuspended in 1 ml of PGB lysis buffer (containing 1 μl of

RNasin, 2 μl of TURBO DNase, 1 μl of SUPERaseIn) and incubated at 37 °C for 3 min at 1,100 r.p.m. shaking. The supernatant was discarded and the beads were washed twice with PGB cell lysis buffer (the second wash was rotated for at least 1 min in the cold room). The beads were further washed twice with PNK buffer (20 mM Tris-HCl, pH 7.4, 10 mM $MgCl_2$, 0.2% Tween-20) and resuspended in 1 ml PNK buffer.

hiCLIP (3′ end RNA dephosphorylation and first round of adaptor ligation). 5× PNK pH 6.5 buffer (350 mM Tris-HCl (pH 6.5), 50 mM $MgCl_2$, 25 mM DTT) was prepared. The supernatant was discarded and the beads were resuspended in 20 μl of the PNK mix (4 μl 5× PNK pH 6.5 buffer, 0.5 μl T4 PNK (NEB, M0201), 0.5 μl RNasin, 0.5 μl SUPERaseIn, 14.5 μl water) and incubated at 37 °C for 20 min with 1,100 r.p.m. shaking. The beads were washed once with PNK buffer and twice with PGB cell lysis buffer (the last wash was rotated for at least 5 min in the cold room). Beads were further washed three times with PNK buffer.

We ligated the RNA duplexes bound to STAU1 to an equimolar concentration of RNA adaptors A and B. Assuming that ligation efficiency is 100%, this should lead to 50% of duplexes with adaptor A ligated to one arm, and adaptor B to the other arm, which is necessary for the production of hybrid reads by hiCLIP (Extended Data Fig. 1a). A 4× ligation buffer was prepared (200 mM Tris-HCl, pH 7.8, 40 mM $MgCl_2$, 40 mM DTT). The supernatant was removed and the beads were resuspended in 20 μl of the first round ligation mix (6 μl water, 4 μl 4× ligation buffer, 1 μl T4 RNA ligase 2, truncated K227Q (NEB, M0351), 0.5 μl RNasin, 0.5 μl SUPERaseIn, 2 μl adaptor A (10 μM), 2 μl adaptor B (10 μM), 4 μl PEG400 (Sigma, 81170)). T4 RNA ligase 2, truncated K227Q was chosen to selectively ligate pre-adenylated adaptor to RNA. The mixture was incubated overnight at 16 °C at 1,100 r.p.m. shaking. 500 μl PNK buffer was added and the supernatant was removed. The beads were washed twice with 1 ml PGB cell lysis buffer (both of wash was rotated 5 min at 4 °C). The beads were further washed twice with 1 ml PNK buffer. Beads resuspended in 1 ml PNK buffer were transferred to a new tube after the first wash.

hiCLIP (5′ end phosphorylation of RNA, removal of adaptor B's phosphate blocking, and second round of RNA ligation). 5′ end phosphorylation of RNA and removal of adaptor B's phosphate blocking were simultaneously performed. The supernatant was removed and 20 μl of PNK mix (1 μl T4 PNK, 2 μl 10 mM ATP, 2 μl 10× PNK buffer (NEB), 0.25 μl RNasin, 0.25 μl SUPERaseIn, 14.5 μl water) was added. The reaction was incubated at 37 °C for 30 min at 1,100 r.p.m. shaking. The beads were washed once with 1 ml PNK buffer, twice with 1 ml PGB cell lysis buffer (the wash was rotated for at least 5 min in cold room), and once with 1 ml PNK buffer.

The supernatant was removed and 20 μl of ligation mix (10 μl 10 mM ATP, 72.5 μl water, 10 μl 10× T4 RNA ligase 1 buffer (NEB, B0216S that does not contain ATP), 5 μl T4 RNA ligase 1 (ssRNA Ligase) (NEB, M0204), 2 μl RNasin, 0.5 μl SUPERaseIn) was added. The reaction was incubated overnight at 16 °C at 1,100 r.p.m. shaking. After incubation, 800 μl of ice-cold PNK buffer was immediately added, the supernatant was removed, and the tube was transferred to ice. The beads were washed once with high salt wash and twice with PNK buffer.

hiCLIP (denaturation of crosslinked protein–RNA complexes). We denatured proteins with urea to ensure that no additional proteins could interact with STAU1 during purification. The protocol for purifying protein–RNA complexes with urea denaturation was adapted from Kiel *et al.*[31]. In our preliminary experiments, we found that this UREA denaturation step was required to remove other RNA-binding proteins that tightly interact with STAU1 and are co-purified under standard iCLIP conditions[32]. Thus, we included these stringent purification conditions in the hiCLIP protocol to ensure that only RNAs directly interacting with STAU1 *in vivo* were isolated. The supernatant was removed from immunoprecipitated beads and 80 μl of 1.25× urea cracking buffer (66.6 mM Tris-HCl, pH 7.4, 8 M urea, 1.33% SDS) was added. The reaction was incubated for 3 min at 65 °C at 1,100 r.p.m. shaking. The supernatant was collected and 920 μl of ice-cold Tween 20 IP buffer with 1 μl of anti-RNase, 10 μl of protease inhibitor cocktail set III, EDTA-free and 1 μl of SUPERaseIn was added. The supernatant was further cleared using a magnetic stand in order to remove any remaining beads.

hiCLIP (preparation of antibody-attached beads). 100 μl of Dynabeads Protein G (Life Technologies, 10004D) were used per experiment. The beads were washed twice with CLIP lysis buffer. The beads were resuspended in 100 μl CLIP lysis buffer with 10 μg M2-Flag antibody per experiment and incubated at room temperature for 1–2 h with rotation. The beads were washed twice with CLIP lysis buffer, once with Tween 20 IP Buffer (50 mM Tris-HCl, pH 7.4, 150 mM NaCl, 0.5% Tween 20, 0.1 mM EDTA)[31].

hiCLIP (stringent purification and radiolabelling of protein–RNA complexes). The supernatant of denatured protein–RNA complexes was added to 100 μl of antibody-attached beads and incubated at 4 °C for 2 h with rotating. The beads were washed twice with high salt wash and twice with PNK buffer and left in the final wash. In order to visualize protein crosslinked RNA complexes, the 5′ end of the RNA was radiolabelled. 200 μl (20%) of beads resuspended in 1 ml PNK buffer was transferred to a new tube and the supernatant was removed. The beads were mixed with hot PNK mix (0.2 μl PNK, 0.4 μl [$\gamma-^{32}$P]ATP, 0.4 μl 10× PNK buffer, 3 μl water) and incubated at 37 °C for 5 min at 1,100 r.p.m. shaking. The supernatant was removed and 20 μl of 1× NuPAGE LDS sample buffer (Life Technologies, NP0007) with NuPAGE sample reducing agent (Life Techonologies, NP0004) was added to the beads. The supernatant of the remaining non-radiactive beads (80%) was removed and the radioactively labelled beads (20%) resuspended in 20 μl of NuPAGE buffer were added to the non-radioactive beads.

hiCLIP (SDS–PAGE and transfer of protein–RNA complexes to nitrocellulose). The supernatant in NuPAGE buffer was incubated at 70 °C for 5 min at 1,100 r.p.m. shaking. The tube was placed on a magnetic stand to remove the beads, and the supernatant was loaded on the SDS–PAGE gel. The SDS–PAGE was performed using 4–12% NuPAGE Bis-Tris gel (Life Technologies, NP0321BOX) following the manufacturer's protocol with MOPS running buffer (Life Technologies, NP0001), NuPAGE Antioxidant (Life Technologies, NP0005) was added to the buffer in the upper chamber, and PAGE was performed for 45 min at 180 V. 5 μl of PAGE ruler plus (Thermo Scientific, SM1811) was used as protein size marker.

After the run, the dye front of the gel was removed and discarded since this part contained free radioactive ATP. The protein–RNA complexes from the gel were transferred to a Protran BA85 Nitrocellulose Membrane (Whatman) using the Novex wet transfer apparatus following the manufacturer's protocol (Life Technologies; transfer for 1 h at 30 V using NuPAGE transfer buffer (Life Technologies, NP0006-1, supplemented with 10% methanol). The membrane was wrapped with Saran wrap and exposed to a Carestream Kodak BioMax XAR Film (SIGMA, Z358487) at −80 °C for 1 h and overnight.

hiCLIP (purification condition test). To optimize the ideal RNase concentration, purification condition test (Fig. 1a) was performed using the hiCLIP protocol with the following modifications. One third of cells grown on a 15 cm dish were used for each immunoprecipitation experiment. The cells were resuspended in 1 ml of PGB cell lysis buffer complete. The lysate was cleared with centrifugation. Unprotected RNA was digested by adding 0.05, 0.1, 0.2, 0.4, 2 U ml^{-1} (from low to high RNase condition) RNase I to lysate, or in case of UV-C crosslinking minus control and STAU1 induction-minus control, 0.4 U ml^{-1} of RNase I. For this optimization, the steps '3′ end RNA dephosphorylation and first round of adaptor ligation' and '5′ end phosphorylation of RNA, removal of adaptor B's phosphate blocking, and second round of RNA ligation' were skipped to determine the exact molecular weight of the protein that was crosslinked to RNA.

hiCLIP (RNA isolation). We observed a slower migration of the band after the adaptor ligation (compare Fig. 1a and Extended Data Fig. 2a), showing the linker ligation to crosslinked RNA increases the apparent molecular weight of the protein–RNA complex. The region of the membrane containing the radioactively labelled crosslinked protein–RNA complex was excised using autoradiograph as a mask, and the nitrocellulose piece was transferred to a 1.5 ml tube. 10 μl proteinase K (Roche, 03115828001) in 200 μl PK buffer (100 mM Tris-HCl, pH 7.4, 50 mM NaCl, 10 mM EDTA) was added to the piece of membrane and incubated at 37 °C for 20 min at 1,100 r.p.m. shaking. 200 μl of PK buffer with 7 M urea was added and incubated at 37 °C for 20 min at 1,100 r.p.m. shaking. The supernatant was collected and added together with 400 μl acid-PCI to a 2 ml Phase Lock Gel Heavy tube. The tube was inverted at least 10 times and the phases were separated by centrifugation at 15,871*g* for 5 min at room temperature. The aqueous layer was transferred to a new tube and isolated RNA was precipitated by mixing 1 μl linear acrylamide, 40 μl 3 M sodium acetate pH 5.5, and 1 ml 100% ethanol, incubated overnight at −20 °C and centrifuged at 21,800*g* for 15 min at 4 °C. The supernatant was removed and the pellet was washed with 500 μl of 80% ethanol. The pellet was resuspended in 6.25 μl of water.

hiCLIP (Reverse transcription and purification of cDNAs). The RNA duplexes that contain adaptor A ligated to one arm, and adaptor B to the other arm, are the template for producing hybrid reads by hiCLIP (Extended Data Fig. 1a). Most cDNAs usually truncate at the position of protein–RNA crosslink site. Our analysis reveals that crosslink generally occurs 5′ of the duplex (Extended Data Fig. 3f). Thus, we expect that the duplexes containing the crosslink site in the arm ligated to the Adaptor B will be well suited for producing hybrid reads, which will contain both arms of the duplex.

The RT mix 1 (1 μl primer Rt#clip (0.5 μM; Rt15clip (/5Phos/NNTATTNNNNAGATCGGAAGAGCGTCGTGGATCCTGAACCGC) for the high RNase condition, Rt1clip (/5Phos/NNAACCNNNNAGATCGGAAGAGCGTCGTGGATCCTGAACCGC) for the low RNase condition, Rt5clip (/5Phos/NNCGCCNNNNAGATCGGAAGAGCGTCGTGGATCCTGAACCGC) for the second round ligation minus control, and Rt12clip (/5Phos/NNGTGGNNNNAGATCGGAAGAGCGTCGTGGATCCTGAACCGC) for FLAG-STAU1 minus induction control) and 1 μl dNTP mix (10 mM each)) was added to the resuspended pellet. The primers were annealed to the linkers by incubating at 70 °C for 5 min and 25 °C for 1 min. RT mix 2 (4 μl 5× RT buffer (Life Technologies), 1 μl 0.1 M DTT, 0.5 μl Superscript III RT (200 U μl^{-1}; Life Technologies, 18080-044), 0.5 μl RNasin, 5.75 μl water) was

added and reverse transcription reaction was performed by using the program of 25 °C for 5 min, 42 °C for 20 min, 50 °C for 40 min, 80 °C for 5 min, 16 °C for hold. The RNA template was hydrolyzed by adding 2.2 µl of 1 M NaOH and incubated at 98 °C for 20 min. The reaction was neutralized by adding 25 µl of 1M HEPES-NaOH and 352.8 µl of TE buffer. The cDNA was ethanol precipitated as described above.

The pellet was resuspended in 6 µl of water and 6 µl of 2× Novex TBE-urea sample buffer (Life Technologies, LC6876) was added. The cDNA was denatured by incubating at 80 °C for min and immediately run on 6% TBE-urea gel (Life Technology, EC6865BOX). The region of the gel corresponding to 100–300 nucleotides of cDNAs were cut out and transferred to a 1.5 ml tube. In order to extract cDNAs, 400 µl TE buffer was added to the gel piece and the gel was crushed into small pieces with a Squisher-Single. The crushed gel was incubated at 37 °C for 1 h at 1,100 r.p.m. shaking, then placed on dry ice for 2 min, and incubated again at 37 °C for 1 h at 1,100 r.p.m. shaking. The extracted cDNA was ethanol precipitated as described above.

hiCLIP (circulization and linearization of cDNAs). The pellet was resuspended in 8 µl ligation mix (6.5 µl water, 0.8 µl 10× CircLigase buffer II (Epicentre), 0.4 µl 50 mM $MnCl_2$, 0.3 µl CircLigase II (Epicentre, CL9025K)) and incubated for 1 h at 60 °C. 30 µl oligo annealing mix (26 µl water, 3 µl 10× FastDigest buffer (Thermo Scientific), 1 µl 10 µM Cut_oligo (GTTCAGGATCCACGACGCTCTTCAAAA)) was added. The oligo was annealed to cDNAs with the program of (95 °C for 2 min; successive cycles of 20 s, starting from 95 °C and decreasing the temperature by 1 °C each cycle down to 25 °C; and 25 °C hold). 2 µl FastDigest BamHI (Thermo Scientific, FD0055) was added and incubated for 30 min at 37 °C, and then the enzyme was inactivated by incubating at 80 °C for 10 min. cDNA was ethanol precipitated as described above.

hiCLIP (PCR amplification of cDNA library). The pellet was resuspended in 11 µl of water. The PCR mix (5 µl cDNA, 2.5 µl primer mix containing P5Solexa (AATGATACGGCGACCACCGAGATCTACACTCTTTCCCTACACGACGC TCTTCCGATCT) and P3Solexa (CAAGCAGAAGACGGCATACGAGATCGG TCTCGGCATTCCTGCTGAACCGCTCTTCCGATCT) at 10 µM each, 50 µl Accuprime Supermix 1 enzyme (Life Technologies, 12342-010), 42.5 µl water) was prepared. PCR was performed by following program (94 °C for 2 min; 24 cycles of 94 °C for 15 s, 65 °C for 30 s and 68 °C for 30 s; 68 °C for 3 min, and 25 °C hold).

Ribosome profiling and mRNA-seq (preparation of cell lysate). The published protocols were adjusted[33–36]. The siRNA-resistant Flag–STAU1 Flp-In 293 T-REx cell line was grown on a 15 cm dish, and knockdown or rescue was performed as described above by adjusting the volume accordingly. The medium of cells was replaced with DMEM with 10% FBS and 100 µg ml^{-1} of cycloheximide (SIGMA, C4859) and incubated at 37 °C for 1 min at 5% CO_2. The medium was removed and the dish was moved to ice. The cells were washed once with 10 ml of ice cold PBS with 100 µg ml^{-1} of cycloheximide. PBS was removed and 1 ml of PGB cell lysis buffer with 1 µl of 100 mg ml^{-1} cycloheximide, 10 µl of 100 mM DTT and 12.5 µl of TURBO DNase was added. Cells were scraped off on ice, pipetted up and down, and collected in 1.5 ml tubes. The lysate was homogenized by passing syringe 26G needle twice. The lysate was centrifuged twice at 20,000*g* for 10 min at 4 °C, and 700 µl of the supernatant was collected for ribosome profiling experiment, 250 µl for mRNA-seq and 50 µl for western blotting. For mRNA-seq samples, 250 µl of lysate was directly added to 750 µl of TRIzol LS (Life Technologies, 10296-028), incubated at room temperature for 5 min and stored at −80 °C till use.

Ribosome profiling (generation of ribosome footprints). 17.5 µl of RNase I was added to 750 µl of the cell lysate and incubated at 23 °C for 45 min at 800 r.p.m. shaking. RNase digestion was stopped by adding 35 µl of SUPERaseIn. 600 µl of the lysate was immediately loaded to a pre-cooled centrifuge tube (Beckman, 349622), then 900 µl of 1 M ice-cold sucrose cushion buffer (1 M sucrose cushion, 20 mM Tris-HCl (pH 7.4), 140 mM NaCl, 5 mM $MgCl_2$ and 1 ml of this buffer was supplemented with 1 µl SUPERaseIn, 10 µl 100 mM DTT, 1 µl 100 mg ml^{-1} cycloheximide) was added under the cell lysate by placing the tips to the bottom of the tube. The cushion was centrifuged at 70,000 r.p.m. for 4 h at 4 °C with TLA-100.3 rotor (Beckman). The supernatant was discarded and the RNA was extracted using TRIzol reagent (Life Technologies, 15596-026) following the manufacturer's protocol except that the sample was incubated overnight at −80 °C before centrifugation.

mRNA-seq (poly(A) RNA selection and fragmentation). mRNAs were purified from 250 µl of the cell lysate using TRIzol LS following the manufacturer's protocol except that the sample was incubated overnight at −80 °C before centrifugation. Poly(A) RNA was purified using Dynabeads mRNA DIRECT Kit (Life Technologies, 61011) following the manufacturer's protocol after resuspending RNA pellet to 1 ml of Lysis/Binding Buffer of the kit. RNA was eluted in 20 µl of 10 mM Tris-HCl (pH 8.0).

Then 20 µl of 2× Alkaline fragmentation solution (2 mM EDTA, 10 mM Na_2CO_3, 90 mM $NaHCO_3$ (pH 9.3)) was added to the eluted RNA and incubated for 20 min at 95 °C. Fragmentation was stopped by adding 560 µl ice-cold stop/precipitation solution (final 300 mM NaOAc pH 5.5 and 1 µl of GlycoBlue (Life Technologies, AM9516) per reaction). 600 µl of room-temperature isopropanol was added and incubated at −20 °C overnight. The RNA was precipitated by centrifuging at 21,800*g* for 30 min at 4 °C. The supernatant was discarded and the pellet was washed twice with 500 µl of 75% ethanol and dried at room temperature for 3 min.

Ribosome profiling and mRNA-seq (size selection of fragmented RNAs). For ribosome footprints, 26–34 nucleotides of RNA were purified using 15% TBE-urea gel (Life Technologies) as was described by Ingolia *et al.*[36], while 50–80 nucleotides of RNA were purified using 10% TBE-urea gel (Life Technologies) for mRNA-seq. The RNA was extracted from the gel using the same protocol as hiCLIP cDNA extraction except that 1 µl of RNasin Plus (Promega, N2615) was added to TE buffer and extracted RNA was subjected to acid-PCI extraction before ethanol precipitation.

Ribosome profiling and mRNA-seq (3′ end dephosphorylation and adaptor ligation). The RNA pellet was resuspended in 20 µl of H_2O and mixed with PNK master mix (10 µl 5× PNK pH 6.5 buffer (custom buffer, described above), 1.25 µl PNK (10 U μl^{-1}), 1 µl RNasin, 17.75 µl H_2O). The reaction was incubated for 20 min at 3 °C and RNA was purified by acid-PCI extraction and ethanol precipitation as described above.

The RNA was resuspended in 4.5 µl of water and mixed with ligation master mix (4 µl 4× ligation buffer (custom buffer described above), 1 µl T4 RNA ligase, 0.5 µl RNasin, 1 µl of 100 µM L3-App (/5rApp/AGATCGGAAGAGCGGTTC AG/ddC/; 5rApp indicates 5′ adenylation), 4 µl PEG400, 5 µl water). The reaction was incubated overnight at 16 °C and purified by PCI (UltraPure Phenol:Chloroform: Isoamyl Alcohol (pH 8.05) (Life Technologies; 15593-031); Acid-PCI was used for RNA extraction, while this PCI was used for DNA–RNA hybrid and DNA extraction in this study) extraction and EtOH precipitation as described above. The adaptor ligated RNA fragments corresponding the size of 47–54 nucleotides for the ribosome profile, while 71–101 nucleotides for mRNA-seq were PAGE purified as described above using 10% TBE urea gel.

Ribosome profiling and mRNA-seq (reverse transcription, circularization and linearization of cDNAs, PCR amplification of cDNA library). Reverse transcription and size selection, circularization and linearization of cDNAs, PCR amplification of cDNA library were performed using the same protocol as hiCLIP except the following modifications. 0.5 µl of 100 µM primer Rt#clip (Rt13clip (/5Phos/NNT CCGNNNAGATCGGAAGAGCGTCGTGGATCCTGAACCGC) for the replicate 1 of UT, KD, and RC conditions, and Rt9clip (/5Phos/NNGCCANNNAGATC GGAAGAGCGTCGTGGATCCTGAACCGC) for the replicate 2 of UT, KD, and RC conditions) was used instead of 0.5 µM for reverse transcription. At cDNA size selection from gel, the sizes of purified cDNAs were 78–88 nucleotides for ribosome profiling, and 102–132 nucleotides for mRNA-seq. 68 µl oligo annealing mix and 4 µl FastDigest BamHI were used for linearization. 10–15 cycles of PCR amplifications were used.

High-throughput DNA sequencing. The hiCLIP library was sequenced using MiSeq Reagent Kit v2 (300 cycle) (Illumina, MS-102-2002) and Illumina MiSeq for 196 cycles. Ribosome profiling and mRNA-Seq library was sequenced using Illumina HiSeq for 50 cycles.

iCLIP. STAU1 iCLIP was performed according to the denaturing iCLIP[32] protocol as described previously.

Formaldehyde crosslinking and RNA co-immunoprecipitation assay. 48 h before the immunoprecipitation experiment, 1 µg of plasmid mix (ARF1 WT, ARF1 Δ, XBP1 WT, XBP1 Δ, PRKCSH WT and PRKCSH Δ; equal amount of wt and Δ was mixed) was co-transfected to siRNA-resistant Flag–STAU1 Flp-In 293 T-REx cell line grown in a 10 cm dish with 10 µl of TurboFect Transfection Reagent (Thermo Scientific, R0531) following the manufacturer's protocol. PRKCSH WT and Δ did not express, and thus were not reported in this manuscript. 24 h before the immunoprecipitation experiment, Flag tagged STAU1 was induced by adding 250 ng ml^{-1} of doxycycline. Cells were crosslinked using 1% formaldehydes for 10 min and quenched by glycine as described in Niranjanakumari *et al.*[37]. Whole cell pellet from a 10 cm dish was used for a single immunoprecipitation experiment. Later parts of the protocol were modified in the following way. 100 µl of protein G Dynabeads were washed twice with CLIP lysis buffer. Beads were resuspended in 100 µl CLIP lysis buffer with 10 µg M2 anti-Flag antibody and incubated for 1–2 h at room temperature. The beads were washed three times with CLIP lysis buffer. The previously prepared cell pellet was resuspended in 100 µl 6 M urea cracking buffer and sonicated using a Bioruptor (low amplitude, 5× of 30 s on and 30 s off). 1 ml of T20 IP buffer (with 10 µl of protease inhibitors, 1 µl of anti-RNase) was added to dilute urea. Lysate was centrifuged two times at 21,800*g* for 20 min at 4 °C and the supernatant was collected each time. 35 µl of cleared lysate was used for total RNA extraction by mixing with 205 µl of ChIP elution buffer (100 mM Tris-HCL (pH 7.4), 10 mM EDTA, 1% SDS, 200 mM NaCl) and crosslinks were reversed as described below.

The cleared cell lysate was mixed with previously prepared beads and incubated for 2 h at 4 °C with rotation. The beads were washed twice with high salt buffer (second

wash was rotated at 4 °C for 1 min). Beads were further washed twice with PNK buffer and resuspended in 240 μl of ChIP elution buffer. Crosslinking was reversed by adding 10 μl of proteinase K and the mixture was incubated at 42 °C for 1 h, then at 70 °C for 45 min. RNA was purified by acid-PCI extraction and ethanol precipitation. To remove residual DNA, RNA was resuspended in 50 μl of TURBO DNase buffer and subjected to DNase digestion and DNase removal using TURBO DNA-free Kit (Life Technologies, AM1907).

Reverse transcription and PCR experiment were performed with SuperScript III One-Step RT–PCR System with Platinum Taq DNA Polymerase (Life Technologies, 12574-026) following the manufacturer's protocol. 2 μl of RNA prepared above was used for each reaction and following program was used (55 °C for 30 min, 94 °C for 2 min, 40 cycles of (94 °C for 15 s, 55 °C for 30 s, and 68 °C for 30 s), and 68 °C for 5 min). Primers fC_pr1 (GGGCGGAAAGTCCAAATTGT) and fC_pr4 (GATGC ACACGGTGACCAAAC) and primers fC_pr1 and fC_pr5 (GGTGATCATTCTCTG AGGGGC) were used for ARF1 and XBP1, respectively. The forward primer annealed to the CDS of FLuc and the reverse primer annealed downstream of the deletion site. Thus, these primer sets only amplified RNAs from the reporter and not endogenous mRNAs, and simultaneously amplified RNAs from wt and Δ constructs, maintaining their ratios. The PCR product was analysed by QIAxcel system and QIAxcel DNA Screening Kit (Qiagen, 929004).

Induction of ER stress and XBP1 splicing assay. Knockdown and rescue were performed as described above. The siRNA-resistant FLAG-STAU1 Flp-In 293 T-REx cell line was grown in 6-well plates, and treated with thapsigargin (Sigma, T9033) by replacing medium with pre-warmed DMEM supplemented with (10% FBS, 300 nM thapsigargin, 100 ng μl^{-1} doxycycline (for RC experiment only)). In order to achieve equal thermal transfer for all samples, plates were always placed directly on incubator shelves. The cells were further incubated for 30 min at 5% CO_2 to induce ER stress. RNA was purified using RNeasy plus mini kit (Qiagen, 74136). To avoid any systematic error of experimental handling, we performed three independent experiments by varying the order of each condition. In experiment 1, we induced ER stress and lysed cells by the order of UT, KD and RC conditions, experiment 2 using KD, RC and UT, and experiment 3 using RC, UT, KD.

In order to monitor the cytoplasmic splicing of XBP1, RT–PCR and the analysis were performed using the SuperScript III One-Step RT–PCR System with Platinum Taq DNA Polymerase, X_pr1 (TTACGAGAGAAAACTCATGGC) and X_pr2 (GGGTC CAAGTTGTCCAGAATGC) primers[38], and QIAxcel system as described above except that 100 μg of template RNA and 35 cycles of PCR program were used. QIAxcel electropherograms are available at (http://figshare.com/s/d09b7b6e929a11 e48bf206ec4bbcf141).

Reporter assay of *XBP1* mRNA level. The plasmids (XBP1 wt, XBP1 mut, and XBP1 com) were transfected into siRNA-resistant FLAG-STAU1 Flp-In T-REx 293 cell line using Lipofectamine3000 (Life Technologies, L3000015) according to the manufacturer's instructions. After 24 h, RNA was extracted with TRIzol (Life Technologies, 15596018) and Direct-zol RNA MiniPrep (Zymo Research, R2052), and reverse-transcribed with RevertAid (Fermentas, #EP0441). Renilla (the 3′ UTR of XBP1 was appended) and Firefly (reference) Luciferases were quantified by qPCR on an Applied Biosystems 7900HT using the ΔΔCt method with default parameters and the PCR conditions for Fast SYBR Green PCR Master Mix (Life Technologies, 4385612). The oligos Fluc_pr1 (CCACTGTCTAAGGAGGTGGG) and Fluc_pr2 (GGTAATCAGAATGGCGCTGG), and Rluc_pr1 (GCTCATATC GCCTCCTGGAT) and Rluc pr2 (CGTGGCCCACAAAGATGATT) were used to amplify the CDS of Firefly and Renilla, respectively.

Data analysis. Data analysis was performed using R-2.15.1[39] and Python-2.7.1 (http://www.python.org). The following R (ggplot2 (0.9.3)[40], plyr (1.8)[41], reshape2 (1.2.2)[42]) and Bioconductor packages (BSgenome.Hsapiens.UCSC.hg19 (1.3.17)[43], GenomicRanges (1.8.13)[44], ShortRead (1.14.4)[45]) were used throughout. latticeExtra_ 0.6-24, RColorBrewer_1.0-5, Rsamtools_1.8.6, lattice_0.20-10, Biostrings_2.24.1, IRanges_1.14.4 and BiocGenerics_0.2.0 were included in these packages. Other packages used for individual analyses are described in the appropriate sections.

Sequence processing and mapping of reads (hiCLIP, overview). We used a sequential mapping approach to identify the source RNA. Reads were first mapped to rRNAs and tRNAs (Phase 1). Any remaining unmapped reads were then mapped to the mitochondrial genome and pre-rRNA (Phase 2). The remaining reads were then mapped to representative transcripts for all genes present in ENSEMBL (Phase 3). Finally, the remaining unmapped reads were mapped to the genome (Phase 4). Mapped read counts after each phase are summarized in Supplementary Table 1, and details are described below.

Sequence processing and mapping of reads (hiCLIP, pre-processing of sequence reads, identifying hybrid and non-hybrid reads). The FASTX-Toolkit (http://hannonlab.cshl.edu/fastx_toolkit/index.html) was used for the basic processing of sequence reads. FASTQ files were converted to FASTA format. Reads were de-multiplexed using the experimental barcode located at positions 3–6 and the random barcode at the positions 1–2 and 7–9.

Hybrid and non-hybrid reads were selected as follows. Our initial analysis showed that 20–30% of reads contained adaptor B directly followed by adaptor A. This may have resulted from the imperfect 3′ end phosphorylation of adaptor B (from the manufacturer's website). Thus, we first trimmed adaptor B-adaptor A sequences in the 3′ end of reads using Cutadapt (http://journal.embnet.org/index.php/embnetjournal/article/view/200; cutadapt -a CTGTAGGCACCATACAAT GAGATCGGAAGAGCGGTTCAG -e 0.06 -n 10 -m 186), and the trimmed reads were stored for later analysis. The 60–70% of reads lacking adaptor B–adaptor A sequences were trimmed to remove the adaptor A sequence (cutadapt -a AGATC GGAAGAGCGGTTCAG -e 0.06 -n 10 -O 10 -m 186) and the trimmed reads were used for further analysis. To ensure that we analysed cDNAs that were fully sequenced, we accepted only those reads in which at least part of the adaptor A sequence was present before trimming.

After trimming, reads containing one adaptor B sequence and at least 17 nucleotides each of the left and right arms were considered to be hybrids. This leaves a minimum read length of 53 nucleotides for hybrids (minimum 17 nucleotides for the left arm, 19 nucleotides for adaptor B, and minimum 17 nucleotides for the right arm). The left and right arms were separated and mapped independently. Reads longer than 53 nucleotides lacking adaptor B sequences were considered to be non-hybrid reads. One mismatch was allowed for the search of adaptor B sequence. The analysis was performed with the python_Levenshtein-0.10.2 package (https://github.com/miohtama/python-Levenshtein).

Sequence processing and mapping of reads (hiCLIP, phase 1: mapping to rRNAs and tRNAs). The processed reads were first mapped to a library of mature rRNAs and tRNAs allowing multiple hits (rRNA: RefSeq id, NR_023363.1, NR_003285.2, NR_003287.2, and NR_003286.2, tRNA: downloaded from Genomic tRNA Database: (http://gtrnadb.ucsc.edu). tRNAs named as Homo_sapiens were selected and CCA was added to the 3′ end of the sequence.). Mapping was performed using Bowtie (v0.12.7 9(ref. 46); bowtie -f -p 8 -v 2 -k 1–best–sam–un).

Sequence processing and mapping of reads (hiCLIP, phase 2: mapping to mtDNA and pre-rRNA). Unmapped reads in Phase 1 were aligned against the mitochondrial genome and pre-rRNA allowing multiple hits (Mitochondrial genome: RefSeq id AF347015.1 and pre-rRNA: RefSeq id NR_046235.1; bowtie -f -p 8 -v 2 -k 1–best–sam–un). Reads mapped in this step were removed from further analyses.

Sequence processing and mapping of reads (hiCLIP, phase 3: mapping to representative transcripts). The remaining unmapped reads were aligned to a data set containing annotated transcript sequences for all genes present in ENSEMBL 67 (http://may2012.archive.ENSEMBL.org/index.html). For genes with multiple transcript isoforms, we selected the longest "protein_coding" transcript as the representative isoform. If all isoforms were non-coding, then the longest non-coding isoform was selected as the representative. Transcript sequences and coordinates were obtained from version hg19 of BSgenome.Hsapiens.UCSC.hg19 (1.3.17)[43]. Mapping was performed using Bowtie (options -f -p 8 -v 2 -m 1–best–strata–sam –un). Only uniquely mapping reads were considered for further analysis.

Sequence processing and mapping of reads (hiCLIP, phase 4: mapping to the genome). To identify reads from introns and un-annotated transcripts, the remaining unmapped reads were aligned to the human genome (hg19: indexed file downloaded from http://bowtie-bio.sourceforge.net/index.shtml) using Bowtie (options -f -p 8 -v 2 -m 1–best–strata –sam). Only uniquely mapped reads were considered for further analysis.

Sequence processing and mapping of reads (hiCLIP, reads uniquely mapped to rRNAs). The complete secondary structures of the 18S, 28S and 5.8S rRNAs were previously determined using cryo-EM data[21]. To compare the positions of hiCLIP duplexes with the secondary structures, we identified hybrid reads with both arms uniquely mapping to rRNAs in phase 1 above (bowtie -f -p 8 -m 1 -v 2–best –sam). The random barcodes were not considered.

Sequence processing and mapping of reads (ribosome profiling and mRNA-seq). Sequence reads from the ribosome profiling and mRNA-seq experiments were processed and analysed in a similar way to above with following changes. Between the de-multiplexing and the barcode trimming steps, we performed the phase 1 and phase 2 mapping procedures (bowtie -f -p 8 -v 2–trim5 9–trim3 15–un). Sequence reads were trimmed to 35 nucleotides (26 nucleotides of sequence reads + 9 nucleotides of experimental and random barcode). The random barcodes were separated and stored, and the experimental barcodes were trimmed. Phase 3 mapping was performed (bowtie -f -p 8 -v 2 -m 1–best–strata–sam). After mapping, the positions of the ribosome profiling and mRNA-seq reads were defined by using the twelfth nucleotide of the read as an estimate of the ribosome A site (Extended Data Fig. 6).

Annotation of reads. The reads mapped in Phase 1 were annotated as rRNA or tRNA. Those mapped in Phase 3 and 4 were annotated as mRNA, long non-coding RNA (lncRNA), miRNA or other ncRNA in the following manner. Transcripts annotated as protein_coding in ENSEMBL were categorized as mRNA. Reads mapping to the boundary of regions (for example, across CDS–3′ UTR junction) were

annotated according to the position of the 5′ end nucleotide. miRNAs were annotated as defined in ENSEMBL. Transcripts annotated as (processed_transcript, antisense, lincRNA, sense_intronic, sense_overlapping, 3prime_overlapping_ncrna, pseudogene, transcribed_processed_pseudogene, unprocessed_pseudogene, transcribed_unprocessed_pseudogene) in ENSEMBL and those longer than 200 nucleotides were defined as lncRNAs. Any remaining unannotated transcripts were classified as 'other ncRNAs'. Reads mapping to the anti-sense of annotated transcripts were classed as intergenic. In the main text, hybrid reads with both arms mapped in Phase 3 were referred to as "mRNA and long non-coding RNA reads", as the vast majority of reads mapped to these RNAs in phase 3.

Reads mapping in sense to protein-coding transcripts were further annotated as intronic, 5′ UTR, CDS, or 3′ UTR. To enable unique annotation of each read, we defined a single annotation for each fragment of the protein-coding genes by creating collapsed annotation. Transcripts annotated as protein_coding and sharing gene id were collected from ENSEMBL 67. Exons were collapsed and regions of the gene that did not overlap with any exon were annotated as introns. Regions of collapsed exons 5′ to the first start codon in each gene were annotated as 5′ UTR, and those 3′ to the last stop codon in each gene were annotated as 3′ UTR, and remaining exonic regions were annotated as CDS. The collapsed annotation was created by modifying functions from Quantify RNA-seq data version 0.01 (https://r-forge.r-project.org/scm/viewvc.php/?root=qrnaseq).

Generation of randomly repositioned control sequences. We generated randomly repositioned control sequences by randomly re-positioning each arm of the hybrid reads within the same segments of the gene using 'sample' function in R (for example, if the read mapped to the 3′ UTR of gene A, the control was generated by randomly picking a read of the same length within the 3′ UTR of gene A).

Calculation of folding free energies of hybrid reads. The folding free energies of hybrid reads and randomly repositioned sequences were calculated using the RNAhybrid program[47] (options -s 3utr_human -m 1000 -n 1000 -c). The software calculates the minimum free energy of hybridization between two distinct RNA molecules but not of intra-molecular base-pairing. The Mann–Whitney *U*-test and the *P* value were calculated using 'wilcox.test' function in R.

Probability density distribution plots. The plots in Fig. 1d and 3b–d were drawn using Kernel density estimate with 'geom_density' function from ggplot2 package[40] in R.

Selection and processing of hybrid reads used to evaluate the general properties of STAU1-bound RNA duplexes. After analysis of RNA duplexes in rRNAs, we focused all further analyses on the hybrid reads that were mapped in phase 3 (that is, mainly mRNAs and ncRNAs). We removed PCR duplicates by keeping only one copy of identical reads containing the same random barcode[19]. N in random barcode was treated as a wild card.

Enrichment analysis of STAU1 crosslink sites around the hiCLIP-identified duplexes. For analysis in Extended Data Fig. 3f, the STAU1 crosslink sites were defined by the start sites of non-hybrid reads. Crosslink sites around the two arms of duplexes identified in all transcripts except rRNAs, tRNAs and mtRNAs were compared to those around random transcript positions. Only intra-molecular duplexes were examined. Crosslink sites were not weighted by the cDNA counts.

Identification of intra-molecular RNA duplexes. For all remaining analyses (described in the remaining sections of methods and shown in Figs 3b–g and 4), we used only intra-molecular duplexes. 'Intra-molecular' duplexes are those in which both arms of hybrid reads mapped to the same RNA species (Extended Data Fig. 1b). 2,964 mRNAs were found to contain at least one intra-molecular duplex. We are aware that it is possible that these duplexes are formed by hybridization of two separate molecules of the same RNA species. We removed PCR duplicates as described above, merged the data for hybrid reads obtained from the high RNase and low RNase conditions, and then retained only hybrid reads where both arms uniquely mapped to the same mRNA (Extended Data Fig. 1b). The longest duplex formed by the pair of the arms from a hybrid read was searched by computationally annealing the two arms using the RNAhybrid program[47] (options -s 3utr_human -m 1000 -n 1000 -c) and the longest base-paired region was defined as the duplex (Extended Data Fig. 1d). If more than two candidate duplex regions tied for length, the one reported first by the RNAhybrid program was chosen. If the right arm of a hybrid read was mapped to the 5′ side of the left arm, the left arm and the right arm were swapped. If the left and right arm of a hybrid read overlapped, the reads were discarded. The resulting hybrid reads were visually examined with the IGV browser (2.1.20)[48,49].

Identification of non-redundant intra-molecular RNA duplexes. Some RNA duplexes were identified by more than one hybrid read. In order to extract the non-redundant set of RNA duplexes, we defined the duplexes identified by at least 2 hybrid reads (step 1), and those duplexes identified by single hybrid reads (step 2). Subsequently, the two subsets of the duplexes were merged, and used as the non-redundant set of RNA duplexes. The terminology of this section was described before (http://www.bioconductor.org/help/course-materials/2010/BioC2010/Workflow.pdf).

Step 1. The reads from the left and right arm were pre-filtered separately. If different reads mapped to the same position in transcripts (equal start and end), then they were collapsed (counted as one). The coverage of reads from the left arm of hybrid reads was calculated using the 'coverage' function of GenomicRanges[44], and the regions covered by more than 1 reads were considered as islands (depth ≥ 2). If the width of an island was less than 9, the island was discarded. Then, hybrid reads with the left arm overlapping with an island were selected, and then the coverage of the right arms was calculated as described above. If the right arm of those hybrid reads formed an island with depth ≥ 2 and width ≥ 9, the two islands formed by the left and right arms were defined as a pair of islands. If the right arm formed more than 1 island with depth ≥ 2 and width ≥ 9, the island with the higher depth was selected. If two islands had the same depth, then the one closer to the left island was selected. If the width of the islands were shorter than 17 nucleotides, the width of the islands was extended to 17 nucleotides. The pair of the islands was treated as the pair of arms from a hybrid read, and the duplex was identified as described above. If more than two candidate duplex regions tied for the length, the one reported first was chosen. The number of hybrid reads overlapping both islands were also calculated and later used to weight the data. This subset of the duplexes were named as confident duplexes, and used to examine the robustness of genome-wide results obtained with only the confident duplexes (Extended Data Fig. 10).

Step 2. We then defined the duplexes identified by a single hybrid read in the following manner. From the hybrid reads where both arms were mapped to the same RNAs, those that did not overlap with the pairs of islands defined above were selected. The duplexes identified by the selected hybrid reads were defined as described above. In a few occasions, two hybrid reads identify the same duplex, but do not pass the filtering of confident duplexes described above because the overlap was shorter than 9 nucleotides. Therefore, if identical duplexes were identified by more than 1 hybrid read in this step, we collapsed them as a single duplex.

Subsequently, the set of the RNA duplexes defined by the step 1 and 2 were merged, and the merged data set was defined as the non-redundant set of intra-molecular RNA duplexes.

Generation of randomly repositioned control duplexes. We generated 20 sets of control duplexes by randomizing the positions of the two arms in the transcript region that contained the original hiCLIP duplex. For example, if an arm of the duplex mapped to a 3′ UTR, it was re-positioned within the 3′ UTR of the same transcript, such that the length of the arm was preserved after repositioning.

The STAU1 sequence specificity analysis. We extended the hiCLIP and control duplexes by 10 nucleotides up and downstream (or less if the region between the two arm was shorter than 20 nucleotides). The nucleotide contents were analysed in the duplexes and in the whole 3′ UTR. The statistical significance of differences in nucleotide content between the hiCLIP duplexes, control duplexes and the whole 3′ UTRs was computed using a binomial test.

To find overrepresented motifs, we used the RSATools suite[50] (option –noov -1str). The statistical score ($-\log$(binomial *P* values) corrected for multiple testing) of each tetramer in the extended duplexes was computed by comparing the occurrence of motifs to a background model computed from whole 3′ UTRs. The background model consisted of a second order Markov model using the frequencies of di-nucleotides in the 3′ UTRs. The significance threshold was determined by running the same analysis on the control duplexes and using the maximal statistical score found in the analysis (that is, $\max(-\log_{10}(\text{corrected binomial } P \text{ value})) = 86.6$).

The occurrences of each tetramer were mapped using the dna-pattern program in RSATools. Overlapping tetramers were assembled to create matrices using the matrix-from-pattern program in RSATools. The generated matrices were used to scan the duplexes and the control regions using matrix-scan-quick in RSATools with a minimum site weight of 5.2, which corresponds to a *P* value of 10^{-3} (matrix-distrib, RSATools).

We calculated the purine and pyrimidine content of each duplex arm using a 9 nucleotide sliding window across a 40 nucleotide region up and downstream of the duplex. The two arms of the duplexes are shown in an orientation in which the arm with the higher purine content is on the right (Fig. 2a). The duplexes were then ordered by increasing arm length. The heat maps were drawn using the gplots R package and the heatmap.2 function.

To check if the results observed for STAU1 targeted duplexes were specific, we picked randomly 1,000 non-STAU1 target mRNAs and predicted duplex-formation using the RNAfold software with default parameters[24] on their 3′ UTRs. Among more than 10,000 predicted duplexes, we selected a subset of 3,000 duplexes having the same arm length distribution as the one observed in the hiCLIP duplexes. The heat map was drawn as described above.

Sequence analyses were reproduced on the subset of STAU1-target mRNAs containing the duplexes that were identified by more than one hybrid read to ensure robustness of results (Extended Data Fig. 10a, b).

Enrichment analysis of Alu elements at the STAU1 crosslink sites. The enrichment of Alu elements was examined around the STAU1 crosslink sites from the cytoplasmic

or total fraction, or from hnRNP C crosslink sites. For this purpose, the enrichment of Alu elements in the non-hybrid reads of STAU1 hiCLIP and in the sequence reads of STAU1 iCLIP and hnRNP C iCLIP were examined. For hnRNP C iCLIP, data from the previous study was used[19]. The sequence reads of these data sets were trimmed to the length of 26 nucleotides and analysed using the Repeat Enrichment Estimator server[51].

Analysis of single nucleotide polymorphisms (SNPs). We used the genomic coordinates of hiCLIP duplexes according to ENSEMBL 67 (http://may2012.archive.ENSEMBL.org/index.html) and obtained the list of human SNPs and their genomic coordinates from dbSNP build 138 (http://ftp.ncbi.nih.gov/snp). We used BEDTools[52] to determine SNPs that overlap with duplexes (option intersect). We calculated the frequencies of SNPs in duplexes by dividing the number of SNPs by the number of nucleotides in each duplex. We calculated the background SNP frequency by dividing the number of SNPs in all 3′ UTRs that are STAU1 targets by the total number of nucleotides in these 3′ UTRs. We conducted a simple binomial exact test. The metaprofiles were calculated for the 2,291 3′ UTR–3′ UTR duplexes with loops >80 nucleotides by plotting the normalized count of SNPs over each arm extended by 40 nucleotides from the centre of the left and right arms in each direction. Plots were drawn using the ggplot2 R package and the geom_smooth function. This analysis was reproduced on the subset of STAU1-target mRNAs containing the duplexes that were identified by more than one hybrid read to ensure robustness of results (Extended Data Fig. 10c).

Calculating the length of the loop of hiCLIP duplexes. The loop lengths of hiCLIP duplexes were defined as the distance from the 3′ boundary of the left arm to the 5′ boundary of the right arm (Extended Data Fig. 1e). For the comparison shown in Fig. 3b, the counts of RNA duplexes were weighted by the number of hybrid reads that identified them. Same comparison was reproduced on the subset of STAU1-target mRNAs containing the duplexes that were identified by more than one hybrid read to ensure robustness of results (Extended Data Fig. 10d).

Visualizing RNA duplexes in mRNAs with a Circos plot. Circos plots were produced using the Circos[53] software. The script and settings are for available from https://github.com/jernejule/STAU1_hiCLIP (options -conf data/HiCLIP_mRNA_norm.conf –pdf).

Computational prediction of the secondary structure of mRNA 3′ UTRs. RNA secondary structures in mRNA 3′ UTRs were computationally predicted using the RNAfold program with default parameters[24]. Predicted duplexes were extracted using the forgi 0.1 package (http://www.tbi.univie.ac.at/~pkerp/forgi/). hiCLIP duplexes were considered predictable if hybrid read overlapped partially or completely with the predicted duplexes.

mRNA abundance and translational efficiency estimation from mRNA-Seq and ribosome profiling reads. Only reads mapping to mRNAs were considered. For the mRNA abundance analysis all mRNA-seq reads were used. Translational efficiency was studied for mRNAs with CDS longer than 100 nucleotides and excluding those with HGNC symbol starting with HIST, since histone mRNAs are poorly polyadenylated[54]; mRNA-seq and ribosome profiling reads were mapped to trimmed CDS regions (trimmed 30 nucleotides from 5′ and 3′ ends because these regions accumulate ribosomes during translation initiation and termination; Extended Data Fig. 6b). The number of reads mapped on each mRNA or trimmed CDS was calculated and a set of mRNAs with sufficient read depth were analysed (>30 reads in all 6 replicate experiments). Total library sizes were normalized using DESeq (1.8.3)[55] with locfit_1.5-8 and Biobase_2.16.0 and the count of each mRNA was further normalized by a multiplying normalization factor (1,000,000 / mean value of the total library size of the 6 DESeq normalized libraries).

The translational efficiency of each mRNA was calculated by dividing the number of ribosome profiling reads mapping to the trimmed CDS by the number of mRNA-seq reads mapping to the trimmed CDS after library normalization. mRNA abundance was defined by dividing normalized count of the mRNA-seq by the length of the mRNA and multiplying by 1,000 (RPKN: read per kilobase per normalized library). The mRNA abundance and translational efficiency of each condition (UT, KD and RC) was defined as the average of these counts from duplicate experiments. The fold change of translational efficiency or mRNA abundance between conditions was calculated using these values.

Analysis of the relationship between translational efficiency and RNA structures in CDS or 3′ UTR. Since highly expressed mRNAs are expected to have more depth of data, we weighted the translational efficiency of these mRNAs by the number of hybrid reads in the genes (that is, if mRNA A had 2 hybrid reads, translational efficiency of mRNA A was calculated twice). The weighted translational efficiency was compared with translational efficiency of all mRNAs that passed our filter by the Mann–Whitney *U*-test.

Analysis of the effect of STAU1 depletion on mRNA abundance and translational efficiency. To examine off-target effects of the siRNA, the list of mRNAs was ranked by fold change of mRNA level between untransfected (UT) and knockdown (KD) condition and analysed by SylArray[56] using 'use all available words' option. Top 3 significantly enriched motifs were reported to demonstrate that the primary changes in mRNA stability result from off-target effects of the siRNA (Extended Data Fig. 7e). Therefore, to avoid these off-target effects, all comparisons of ribosome profiling and mRNA-seq were performed between knockdown (KD) and rescue (RC) conditions.

Gene Ontology analysis. We calculated the enrichment of annotated Gene Ontology terms in hiCLIP duplex containing mRNAs using the David GO tool[57]. We used the lists of genes for which mRNAs contained duplexes in the 3′ UTR or in the CDS. The list of genes from the whole genome was used as the background. Enrichments with an FDR cut-off of 0.01 were considered statistically significant. Results were visualized using the ReviGO tool[58]. This analysis was reproduced on the subset of STAU1-target mRNAs containing the duplexes that were identified by more than one hybrid read to ensure robustness of results (Extended Data Fig. 10e).

31. Kiel, J. A., Emmrich, K., Meyer, H. E. & Kunau, W. H. Ubiquitination of the peroxisomal targeting signal type 1 receptor, Pex5p, suggests the presence of a quality control mechanism during peroxisomal matrix protein import. *J. Biol. Chem.* **280,** 1921–1930 (2005).
32. Huppertz, I. *et al.* iCLIP: protein–RNA interactions at nucleotide resolution. *Methods* **65,** 274–287 (2014).
33. Ingolia, N. T., Ghaemmaghami, S., Newman, J. R. & Weissman, J. S. Genome-wide analysis *in vivo* of translation with nucleotide resolution using ribosome profiling. *Science* **324,** 218–223 (2009).
34. Guo, H., Ingolia, N. T., Weissman, J. S. & Bartel, D. P. Mammalian microRNAs predominantly act to decrease target mRNA levels. *Nature* **466,** 835–840 (2010).
35. Ingolia, N. T., Lareau, L. F. & Weissman, J. S. Ribosome profiling of mouse embryonic stem cells reveals the complexity and dynamics of mammalian proteomes. *Cell* **147,** 789–802 (2011).
36. Ingolia, N. T., Brar, G. A., Rouskin, S., McGeachy, A. M. & Weissman, J. S. The ribosome profiling strategy for monitoring translation in vivo by deep sequencing of ribosome-protected mRNA fragments. *Nature Protocols* **7,** 1534–1550 (2012).
37. Niranjanakumari, S., Lasda, E., Brazas, R. & Garcia-Blanco, M. A. Reversible cross-linking combined with immunoprecipitation to study RNA–protein interactions in vivo. *Methods* **26,** 182–190 (2002).
38. Li, H., Korennykh, A. V., Behrman, S. L. & Walter, P. Mammalian endoplasmic reticulum stress sensor IRE1 signals by dynamic clustering. *Proc. Natl Acad. Sci. USA* **107,** 16113–16118 (2010).
39. R Core Team. A language and environment for statistical computing. (2012).
40. Wickham, H. *ggplot2: Elegant Graphics For Data Analysis* (Springer, 2009).
41. Wickham, H. The Split-Apply-Combine Strategy for Data Analysis. *J. Stat. Softw.* **40,** 1–29 (2011).
42. Wickham, H. Reshaping data with the reshape package. *J. Stat. Softw.* **21,** 1–20 (2007).
43. The Bioconductor Dev Team. BSgenome.Hsapiens.UCSC.hg19: Homo sapiens (human) full genome (UCSC version hg19).
44. Aboyoun, P., Pages, H. & Lawrence, M. GenomicRanges: Representation and manipulation of genomic intervals. *PloS Computational Biol.* **9,** e1003118.
45. Morgan, M. *et al.* ShortRead: a bioconductor package for input, quality assessment and exploration of high-throughput sequence data. *Bioinformatics* **25,** 2607–2608 (2009).
46. Langmead, B., Trapnell, C., Pop, M. & Salzberg, S. L. Ultrafast and memory-efficient alignment of short DNA sequences to the human genome. *Genome Biol.* **10,** R25 (2009).
47. Rehmsmeier, M., Steffen, P., Hochsmann, M. & Giegerich, R. Fast and effective prediction of microRNA/target duplexes. *RNA* **10,** 1507–1517 (2004).
48. Robinson, J. T. *et al.* Integrative genomics viewer. *Nature Biotechnol.* **29,** 24–26 (2011).
49. Thorvaldsdóttir, H., Robinson, J. T. & Mesirov, J. P. Integrative Genomics Viewer (IGV): high-performance genomics data visualization and exploration. *Brief. Bioinform.* **14,** 178–192 (2013).
50. van Helden, J. Regulatory sequence analysis tools. *Nucleic Acids Res.* **31,** 3593–3596 (2003).
51. Day, D. S., Luquette, L. J., Park, P. J. & Kharchenko, P. V. Estimating enrichment of repetitive elements from high-throughput sequence data. *Genome Biol.* **11,** R69 (2010).
52. Quinlan, A. R. & Hall, I. M. BEDTools: a flexible suite of utilities for comparing genomic features. *Bioinformatics* **26,** 841–842 (2010).
53. Krzywinski, M. *et al.* Circos: an information aesthetic for comparative genomics. *Genome Res.* **19,** 1639–1645 (2009).
54. Cho, J. *et al.* LIN28A is a suppressor of ER-associated translation in embryonic stem cells. *Cell* **151,** 765–777 (2012).
55. Anders, S. & Huber, W. Differential expression analysis for sequence count data. *Genome Biol.* **11,** R106 (2010).
56. Bartonicek, N. & Enright, A. J. SylArray: a web server for automated detection of miRNA effects from expression data. *Bioinformatics* **26,** 2900–2901 (2010).
57. Huang da. W., Sherman, B. T. & Lempicki, R. A. Systematic and integrative analysis of large gene lists using DAVID bioinformatics resources. *Nature Protocols* **4,** 44–57 (2009).
58. Supek, F., Bosnjak, M., Skunca, N. & Smuc, T. REVIGO summarizes and visualizes long lists of gene ontology terms. *PLoS ONE* **6,** e21800 (2011).
59. Zarnack, K. *et al.* Direct competition between hnRNP C and U2AF65 protects the transcriptome from the exonization of *Alu* elements. *Cell* **152,** 453–466 (2013).

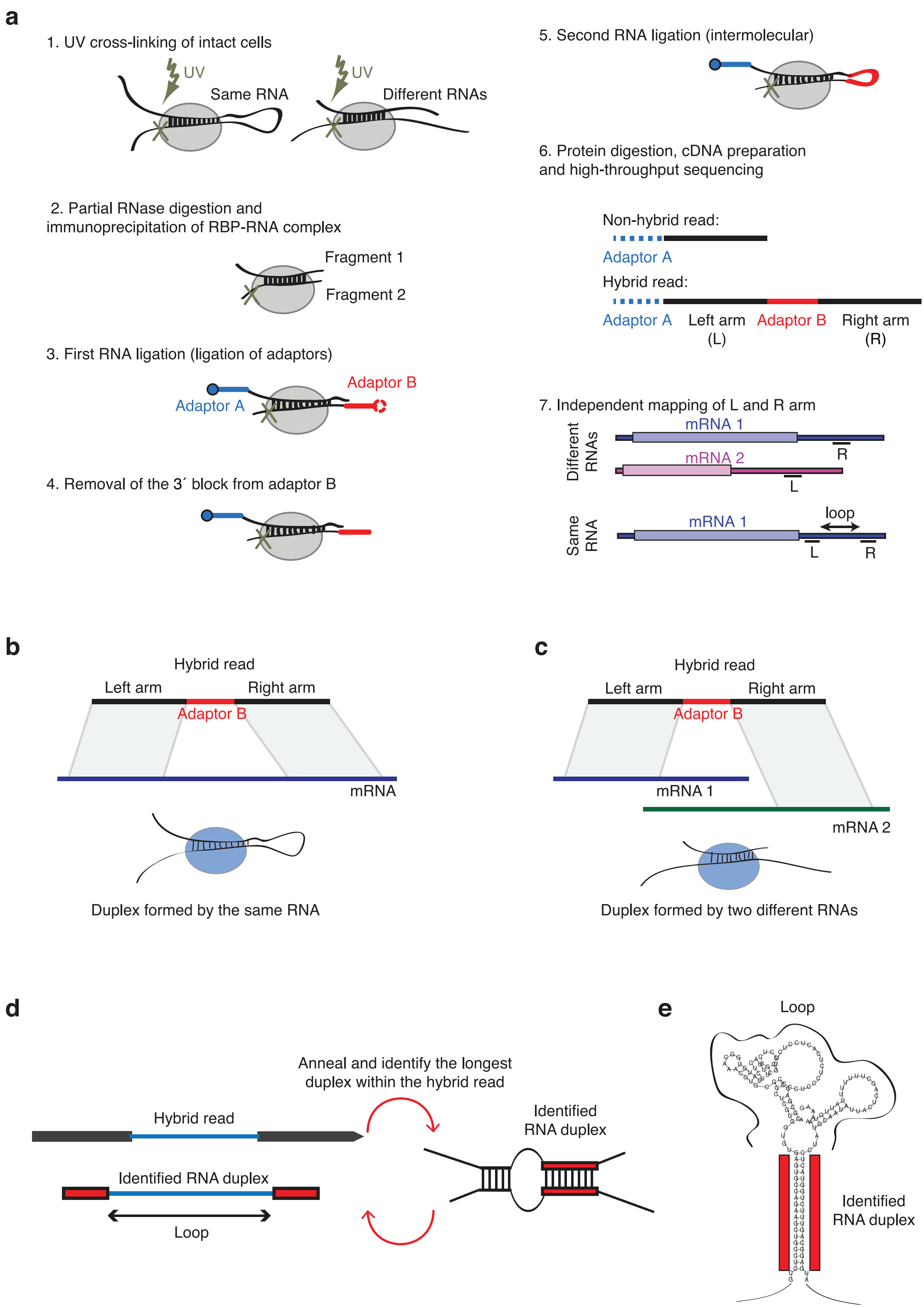

Extended Data Figure 1 | Diagrams illustrating the mapping of hybrid reads, duplex assignment and use of terms. **a**, Schematic overview of the hiCLIP protocol. (1) Cells are irradiated with UV-C light. (2) After cell lysis, the unprotected sections of RNAs are digested by RNase I, and the RBP is co-immunoprecipitated with the crosslinked RNA duplex. (3) Two designated adaptors are ligated to both strands of the RNA duplex. Adaptor A (cloning adaptor) has a permanent 3′ block, while adaptor B (linker adaptor) has a removable 3′ block. (4) 3′ block of adaptor B is removed. (5) The two strands of the RNA duplex are ligated via adaptor B. (6) The RNA hybrid products are converted into a cDNA library and sequenced as in iCLIP protocol[19]. The resulting data comprise hybrid and non-hybrid reads. (7) Hybrid reads are selected and adaptors are trimmed to define the sequences of left (L) and right (R) arms, which are mapped independently to the transcriptome. **b**, **c**, The left arm of hybrid read locates upstream of adaptor B, and the right arm locates downstream of adaptor B. Each arm is mapped independently to transcriptome. If both arms locate into the same gene, then the duplex is considered to be formed by the same RNA. If the arms locate to different genes, then the duplex is formed by two different RNAs. **d**, A diagram describing how a hybrid read is used to identify an RNA duplex. **e**, A diagram describing how the loop (intervening sequence) is defined for each RNA duplex.

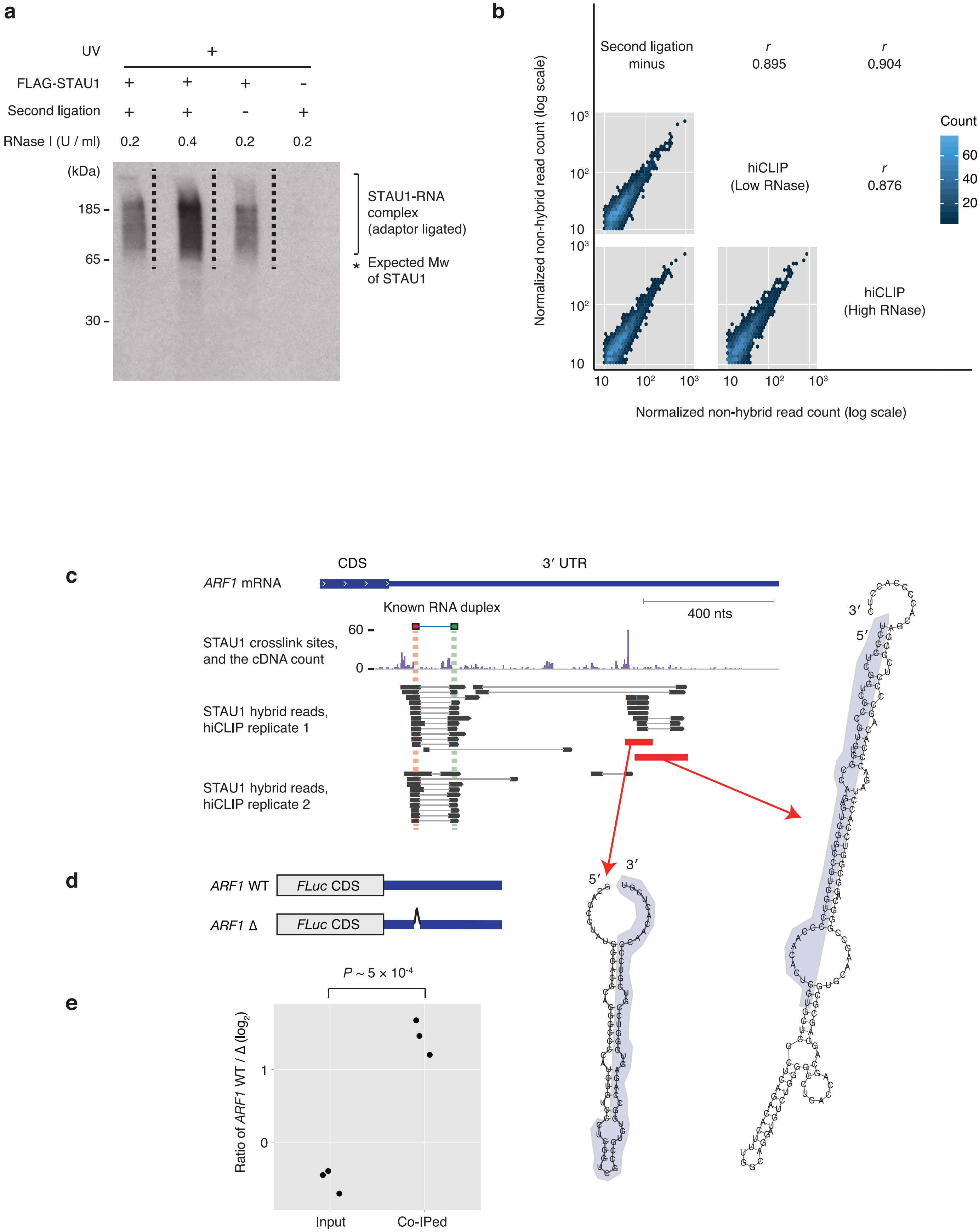
a
UV
+
FLAG-STAU1
+ + + -
Second ligation
+ + - +
RNase I (U / ml)
0.2 0.4 0.2 0.2
(kDa)
185 –
65 –
30 –
STAU1-RNA complex (adaptor ligated)
* Expected Mw of STAU1
b
Second ligation minus
r 0.895
r 0.904
hiCLIP (Low RNase)
r 0.876
hiCLIP (High RNase)
Count
60
40
20
Normalized non-hybrid read count (log scale)
10 10² 10³
c
CDS
3′ UTR
ARF1 mRNA
Known RNA duplex
400 nts
60 –
0 –
STAU1 crosslink sites, and the cDNA count
STAU1 hybrid reads, hiCLIP replicate 1
STAU1 hybrid reads, hiCLIP replicate 2
5′
3′
d
ARF1 WT
FLuc CDS
ARF1 Δ
FLuc CDS
e
P ~ 5 × 10⁻⁴
Ratio of ARF1 WT / Δ (log₂)
1
0
Input
Co-IPed

Extended Data Figure 2 | Autoradiography analysis of the STAU1–RNA complex, and analysis of hybrid reads in a known STAU1 mRNA target, *ARF1*. **a**, Autoradiograph of STAU1–RNA complex that was isolated for the hiCLIP experiment. hiCLIP experiments were performed with high and low RNase conditions, and the two controls omitted either the second intermolecular ligation or STAU1 induction. After adaptor ligation, STAU1 crosslinked RNA was radiolabelled and the complex was analysed by denaturing gel electrophoresis and membrane transfer. The size of the band is slightly higher compared to that in Fig. 1a, presumably due to the efficient adaptor ligation that adds to the size of the RNAs (the experiment shown in Fig. 1a didn't include adaptor ligation). **b**, Correlation analysis of the non-hybrid read count on each RNA between the replicates of the hiCLIP experiments. **c**, Schematic representations of *ARF1* mRNA and the known STAU1-target RNA duplex, along with the position of STAU1 hybrid reads and crosslink sites identified by non-hybrid reads. The left and right arms of hybrid reads are depicted as black boxes, and lines connect arms originating from the same hybrid read. The previously studied STAU1-target RNA duplex[12,14] is indicated by green and red boxes. In addition to the known duplex, hybrid reads also identified additional duplexes in the *ARF1* 3′ UTR. Interestingly, two newly identified duplexes are part of overlapping secondary structures, both of which represent the minimum free energy of folding for the local sequence, as predicted by RNAfold[24] (shown on the right). This suggests that some regions of the *ARF1* 3′ UTR may adopt alternative conformations. The overlapping region of the two structures is shaded in blue. **d**, The constructs of reporters (*ARF1* WT and Δ) used for the validation of the STAU1 binding to the known STAU1-target RNA duplex by formaldehyde crosslinking and co-immunoprecipitation experiment are shown. The reporter has firefly luciferase (*FLuc*) CDS and *ARF1* 3′ UTR. **e**, The ratio of *ARF1* WT and Δ in total cell lysate fraction (input) or STAU1 co-immunopreciptated fraction (Co-IPed) were analysed by RT–PCR using forward primer annealed to CDS of FLuc and reverse primer annealed to downstream of the deletion site. The ratios ($\log_2$) of two populations were compared by the two-tailed Welch's t-test ($n = 3$). The corresponding Qiaxcel electropherograms are available at: (http://figshare.com/s/5f83e88e929b11e4b77106ec4b8d1f61).

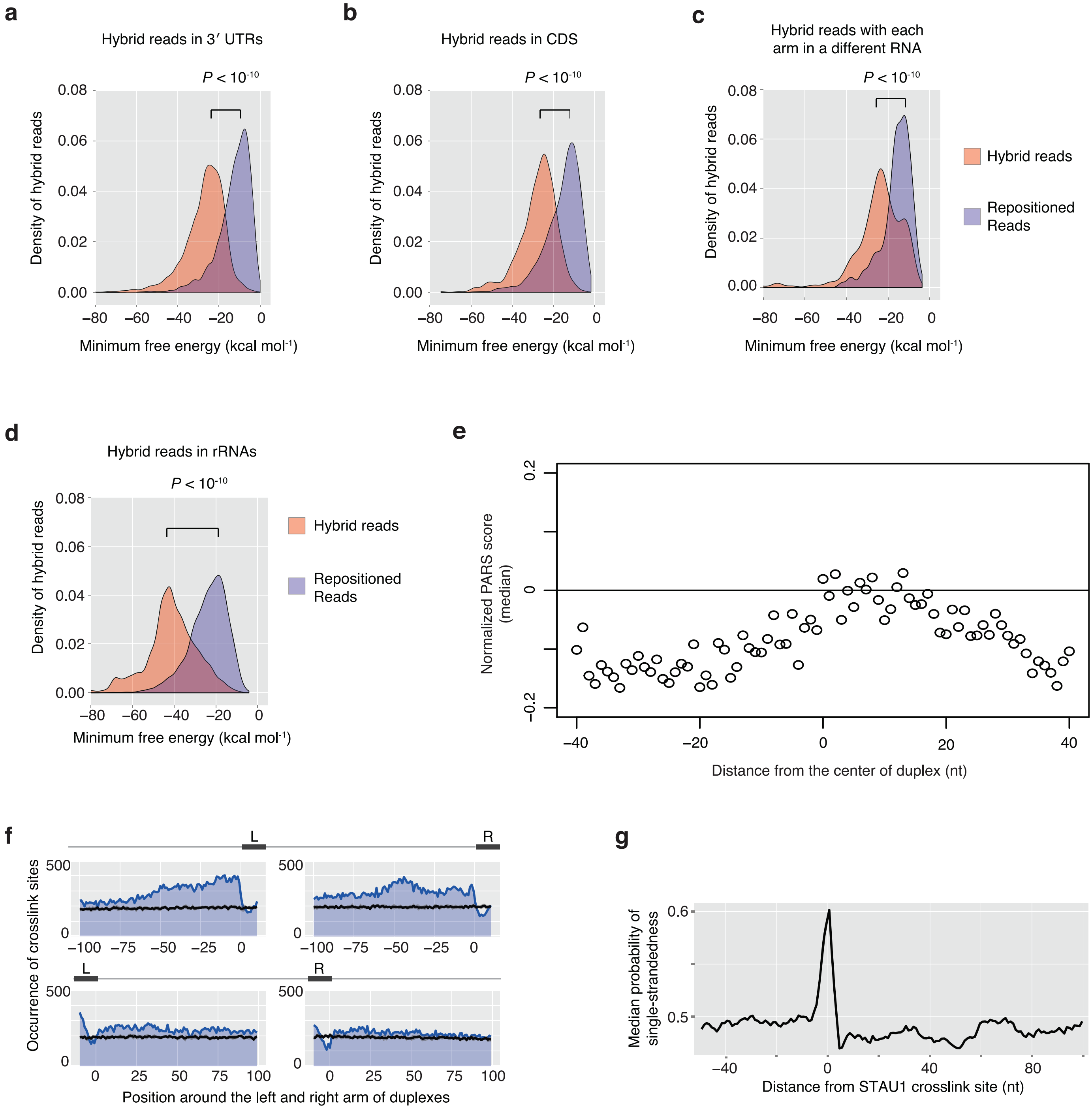

Extended Data Figure 3 | Hybrid reads identify RNA duplexes. **a**, Analysis of hybrid reads in 3′ UTRs (taking into account only those where left and right arm originated from same gene) demonstrates significantly smaller minimum free energies of hybridization between the two arms of hybrid reads compared to randomly repositioned sequences as calculated by RNAhybrid[47]. The probability density distribution of the minimum free energies is plotted, and the distributions for hybrid reads and randomly repositioned sequences were compared using the Mann–Whitney U-test ($n = 4{,}492$ for both hybrid reads and random RNAs). **b**, Similar to **a**, but for hybrid reads in CDS ($n = 958$). **c**, Similar to **a**, but for intermolecular hybrid reads (that is, hybrid reads whose left and right arm originated from different genes; $n = 257$). **d**, Similar to **a**, but for hybrid reads in rRNAs ($n = 3{,}502$). **e**, Median normalized PARS scores were calculated around centre of all mRNA duplexes. PARS scores were obtained from Wan *et al.*[4], and positions with 0 values were removed. PARS score represents a ratio between reads starts after cutting with dsRNase (positive) / ssRNase (negative). Assuming that the double-stranded RNase fully digests each duplex, it is expected that the positive values in PARS-seq will be highest at the last nucleotide of each duplex. This might explain why maximum PARS values occur at the positions closer to the 3′ end of duplexes. **f**, Metaprofiles of the distribution of STAU1 crosslink sites, identified by the start sites of non-hybrid hiCLIP reads (blue), or the randomly repositioned sites (black, mean value of 10 randomizations; grey, standard deviation of the 10 randomizations) around the positions of hiCLIP duplexes. **g**, Distribution of median probability of RNA bases to be single-stranded from position −50 to +100 nucleotides around the STAU1 crosslink sites.

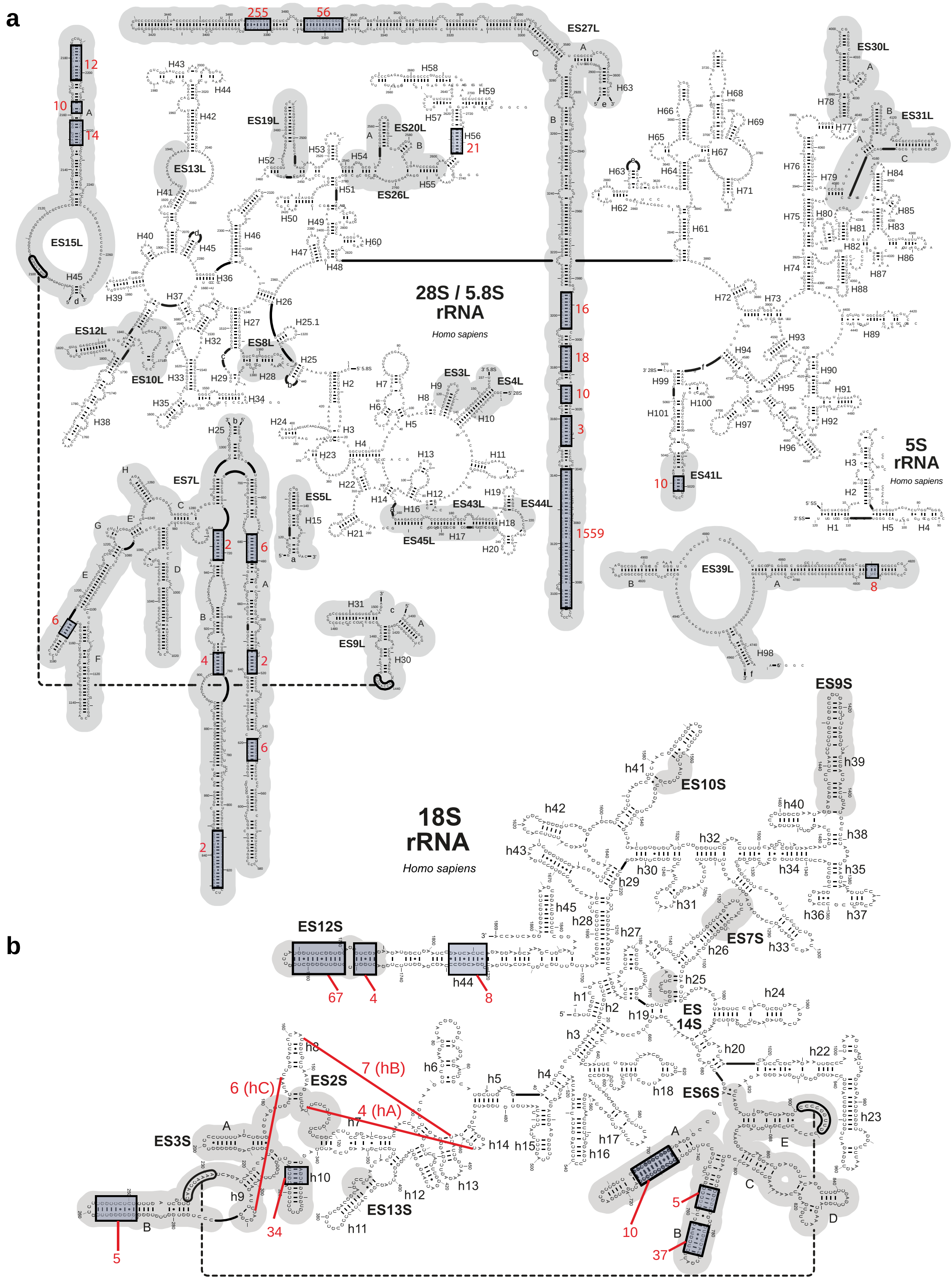

Extended Data Figure 4 | Analysis of duplexes identified by hiCLIP in the secondary structure of human ribosomal RNAs. a, The position of duplexes identified by hybrid reads in the 28S rRNA secondary structure. 2,962 hybrids mapped to 28S rRNA. We first removed the duplexes with only one read, obtaining a final list of 2,816 hybrid reads uniquely mapped to 28S rRNA, and 2,020 of these reads (72%) identified duplexes that were previously determined with CryoEM structure. These duplexes are marked by blue rectangles, and the number of reads that identify each duplex is marked. 756 hybrid reads (27%) map to different double stranded regions of the 28S rRNA while the remaining 40 hybrid reads (1%) map to single strand regions of the rRNA 28S known structure. The metazoan-specific rRNA expansion segments are indicated by grey shadowing. **b**, Similar to **a**, but the position of duplexes identified by hybrid reads in the 18S rRNA secondary structure. 218 hybrid reads uniquely mapped to 18S rRNA, and 170 of these reads identified duplexes that were previously determined with CryoEM structure. Red lines mark the putative newly identified duplexes that are not part of the CryoEM structure, but are complementary and are identified by hybrid reads. The numbers next to the lines shows the number of hybrid reads that identify each of these putative duplexes, and the three newly identified duplexes (helices) that are aligned in Fig. 1e are marked as hA, hB and hC. Complementarity of the novel duplex is conserved from yeast to human as seen at: (http://figshare.com/s/47473d24929c11e493f106ec4bbcf141). The rRNA secondary structure is reprinted by permission from Macmillan Publishers Ltd: Nature copyright (2013)[21].

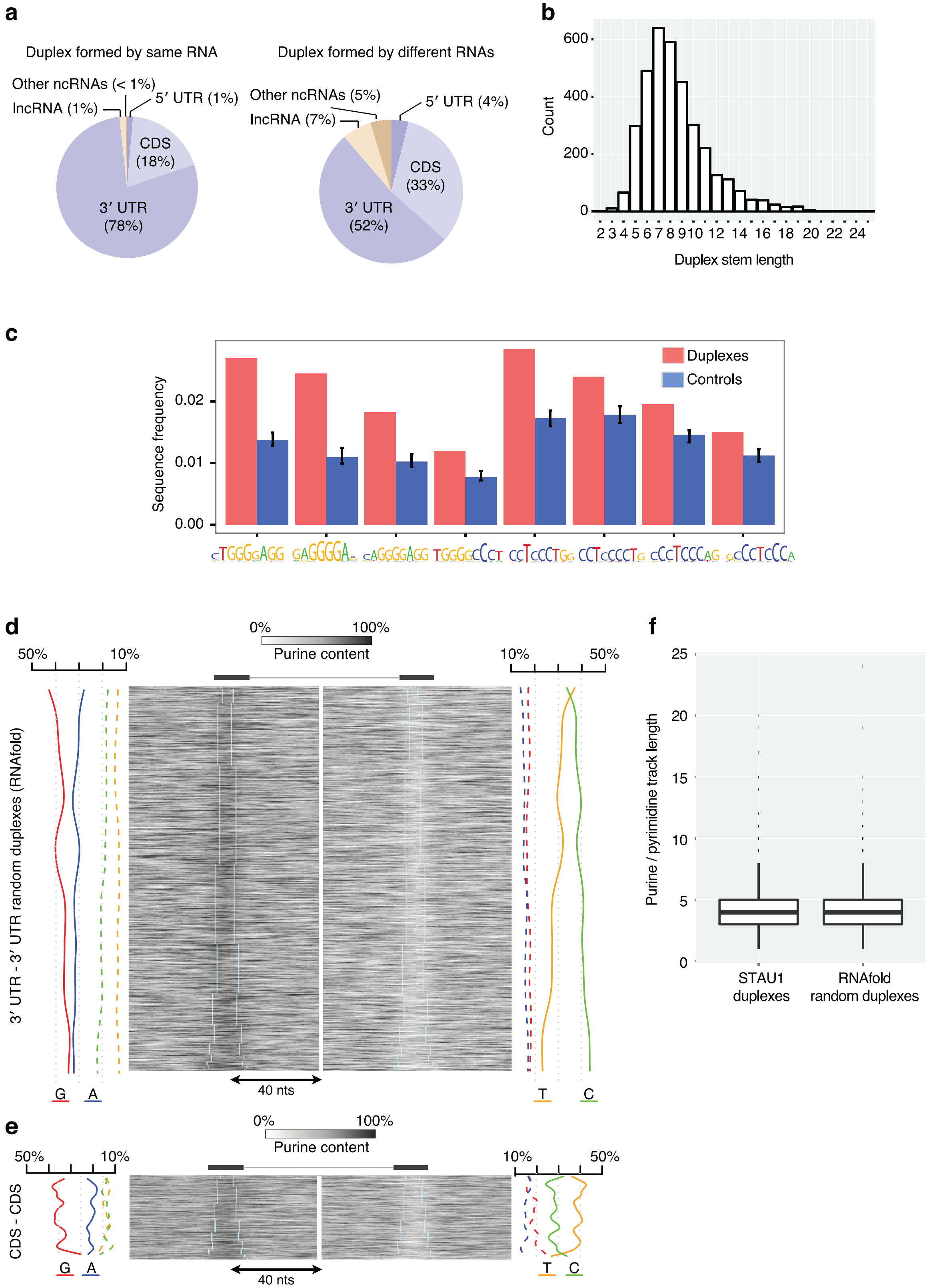

Extended Data Figure 5 | Analysis of RNA types, stem lengths, and sequence motifs at STAU1-target RNA duplexes. **a**, Relative proportions of RNA types that were identified by hybrid reads, where each arm maps to the same (left) or different RNAs (right). **b**, Distribution of duplex stem lengths for 3′ UTR duplexes. **c**, Sequence motifs enriched at STAU1-target 3′ UTR duplexes when compared to surrounding regions of same 3′ UTRs (controls). **d**, Purine content is plotted within each arm of randomly selected 2,291 3′ UTR duplexes that were detected using RNAfold[24] in mRNAs that don't contain any STAU1-target hiCLIP duplex in their 3′ UTR, and surrounding sequence up to 40 nucleotides on each side. **e**, Purine content is plotted within each arm of 494 CDS–CDS STAU1-target duplexes and surrounding sequence up to 40 nucleotides on each side. **f**, Boxplots showing the frequencies of consecutive purine tracks in the 3′ UTR STAU1-target duplexes (boxplot on the left) and in the randomly selected 3′ UTR duplexes that were detected using RNAfold in mRNAs that don't contain any STAU1-target hiCLIP duplex in their 3′ UTR (boxplot on the right).

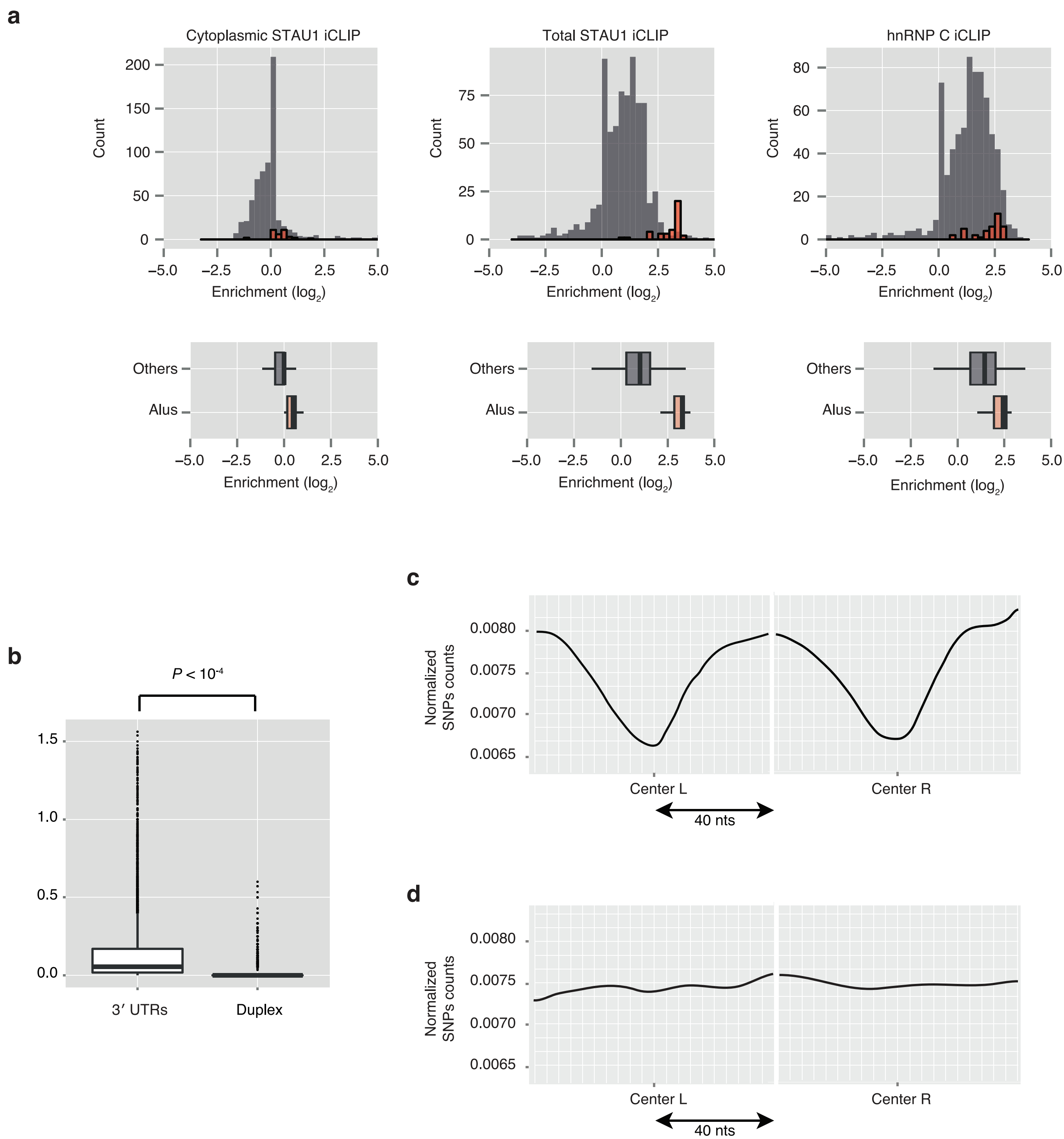

Extended Data Figure 6 | Analysis of repeat elements and SNPs at STAU1-target RNA duplexes. **a**, Enrichment analysis of repeat elements. The Repeat Enrichment Estimator software[51] was used to calculate the enrichment of repeat elements in the cytoplasmic STAU1 iCLIP reads (that is, hiCLIP non-hybrid reads), STAU1 iCLIP reads from the total cellular fraction and hnRNP C iCLIP reads with normalized relative to mRNA-Seq reads. The enrichment was calculated by comparing the proportion enrichment of repeat elements in the cytoplasmic STAU1 iCLIP (that is, hiCLIP non-hybrid reads), STAU1 iCLIP from the total cellular fraction, and hnRNP C iCLIP reads with normalized relative to mRNA-Seq reads using Repeat Enrichment Estimator software[51]. For comparison, we show same analysis of hnRNP C, which is known to bind *Alu* sequences[59]. The enrichment was estimated for all repeat element families (for example, AluJb, AluJo, LTR1, and LTR10A) defined by the Repeat Enrichment Estimator. The panels show the enrichment distribution of different types of repeat element in histogram (top) or box plot (bottom) format; all families of Alu repeat elements are plotted in red, and all remaining repeat elements are plotted in grey. **b**, Box plots showing the SNPs frequency in all the 3′ UTRs of the targets (box plot on the left) and inside the duplexes in the 3′ UTRs. A binomial test has been performed to test the statistical significance of the depletion of SNPs inside the duplexes, compared to the total 3′ UTRs ($P < 10^{-4}$). **c**, Normalized count profile of SNPs occurrence in the long-range 3′ UTR–3′ UTR hiCLIP duplexes; those that have a loop longer than 500 nucleotides. **d**, Normalized count profile of SNPs occurrence in random control 3′ UTR–3′ UTR duplexes with a loop of at least 80 nucleotides that are identified by RNAfold[24] but not by STAU1 hiCLIP.

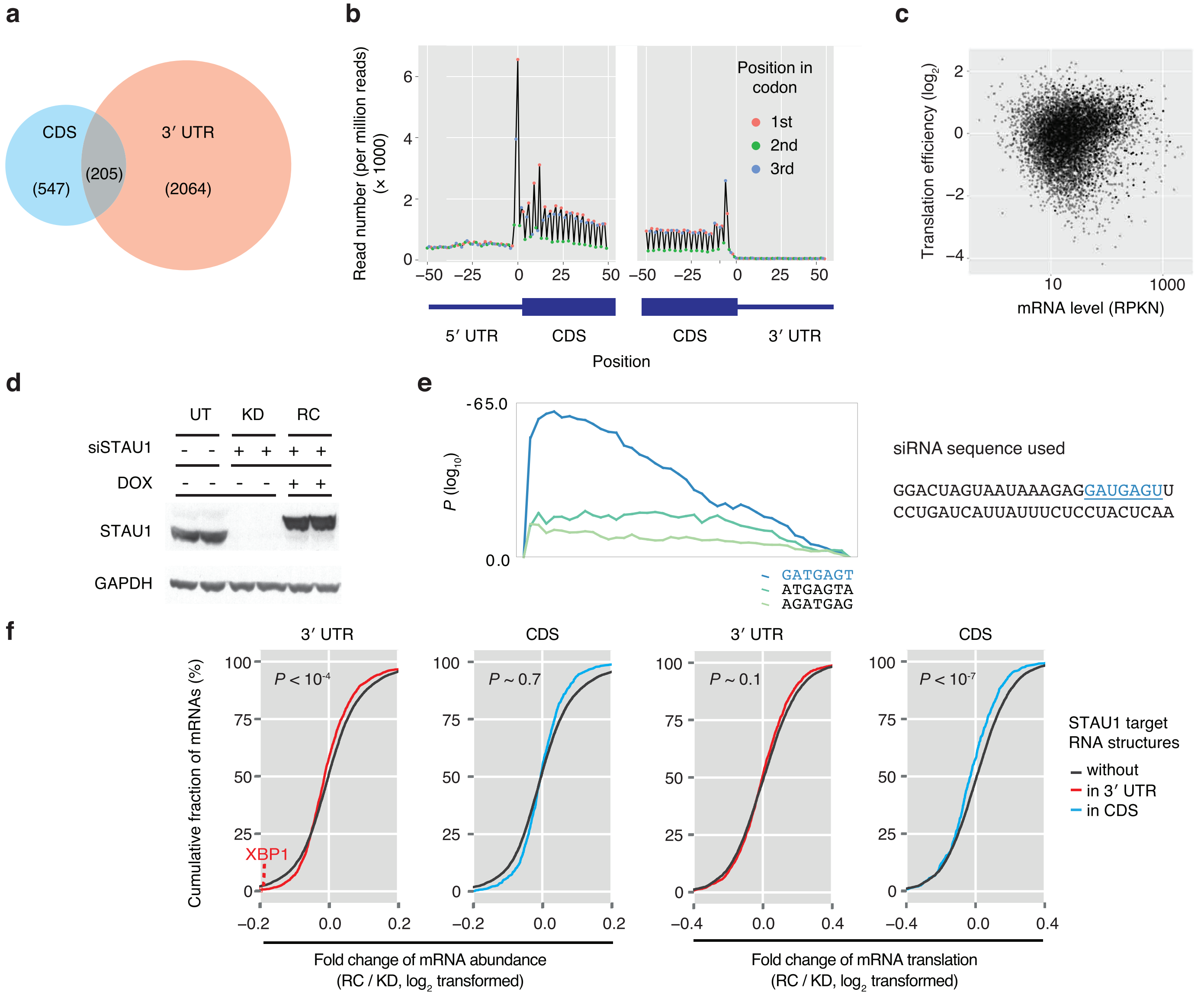

Extended Data Figure 7 | Analysis of mRNA abundance and translational efficiency with mRNA-seq and ribosome profiling. **a**, Venn diagram shows that few mRNAs contain hiCLIP duplexes both in their 3′ UTR and CDS. **b**, Metagene analysis of ribosome profiling reads. The position +12 from the 5′ end of the sequence reads was used as the definition of the read positions. The number of reads mapped around start codon or stop codon is shown. The colour of dots corresponds to the positions in each codon. The sharp peak at start codon shows our definition of read position well approximated the position of ribosome A site, and trinucleotide periodicity of peak confirms that the reads captured the codon dependent positioning of ribosome. **c**, Translational efficiency was independent of the mRNA level (RPKN: read per kilo base per normalized library). All mRNAs that passed our filter are plotted (see Methods, for details). **d**, Western blotting analysis for untreated (UT), STAU1 knockdown (KD) and rescue condition (RC; knockdown with inducible expression of siRNA-resistant STAU1 in knockdown cells) for the cell sample used for ribosome profiling and mRNA-seq library generation. Duplicate experiments were performed for each condition. **e**, In order to examine the potential off-target effects of siRNA treatment, we analysed sequence motifs enriched in mRNAs downregulated in KD condition compared to UT using SylArray[56]. The plot shows the incremental hypergeometric P value of the 3 most significantly enriched 7mer motifs in the gene list sorted by the downregulation level (the leftmost gene is the most downregulated). The most significantly enriched motif corresponded to the seed sequence of siRNA, indicating that most changes in mRNA abundance between UT and KD corresponded to off-target effects. Therefore, we focused our analyses on the comparison between RC and KD, which had no significant enrichment of such motifs by the SylArray analysis. **f**, The cumulative fraction of mRNAs relative to their fold change of mRNA abundance or translation efficiency between STAU1 rescue (RC) and knockdown (KD) cells is plotted. The p-values were calculated by the Mann–Whitney U-test (n = 2,269, 752, and 12,122 for the RNAs containing the duplexes in their 3′ UTR or CDS or other mRNAs for the analysis of mRNA abundance and n = 1,986, 694, and 8,199 for the mRNAs containing the duplexes in their 3′ UTR or CDS or other mRNAs for the analysis of translational efficiency).

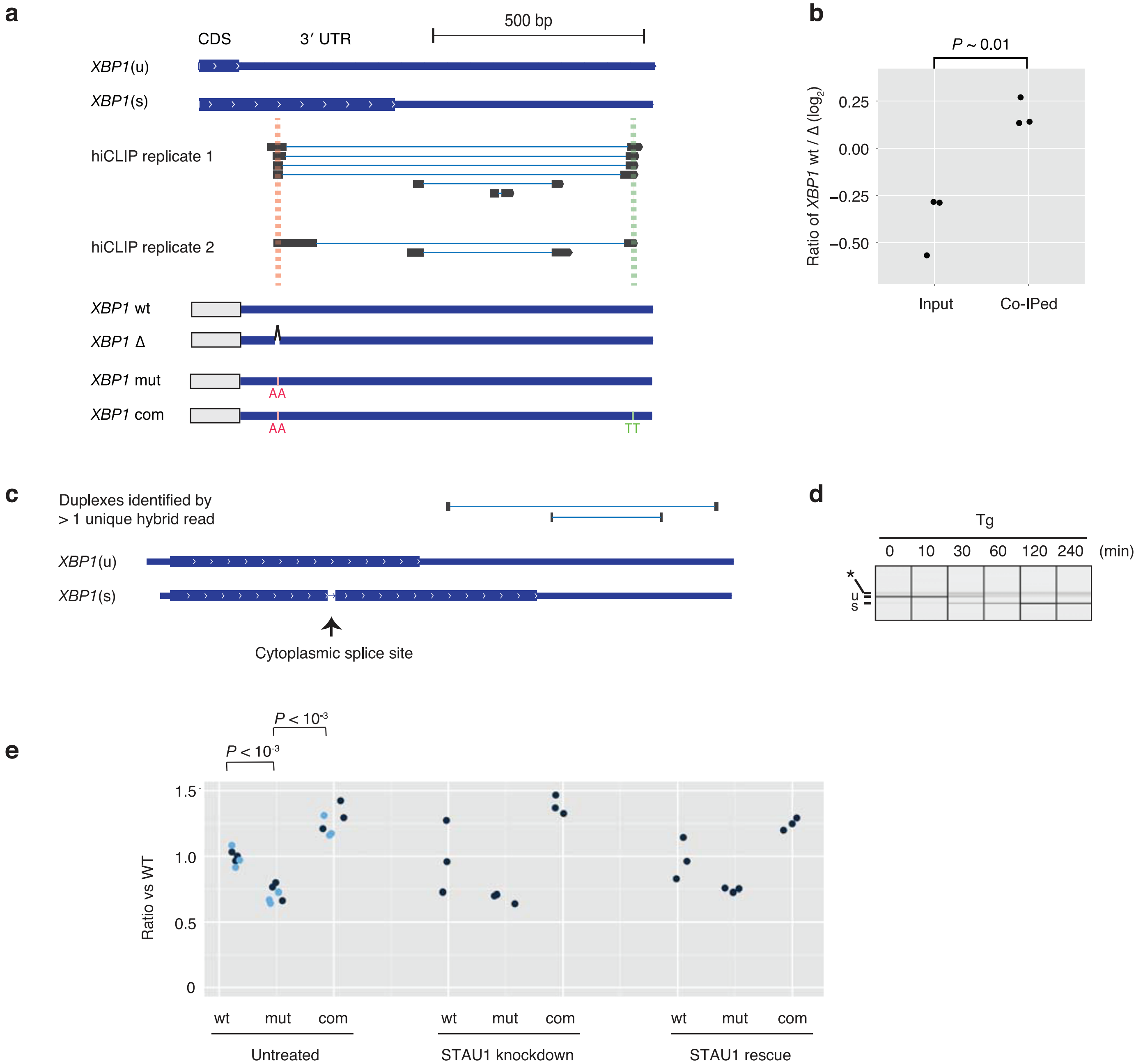

Extended Data Figure 8 | STAU1 regulates the cytoplasmic splicing of *XBP1* mRNA. **a**, Schematic represents the unspliced (*XBP1*(u)) and spliced (*XBP1*(s)) mRNAs, together with hybrid reads that identified a long-range STAU1-target RNA structure. The constructs of reporters (*XBP1* wt and Δ) used for the validation by formaldehyde crosslinking, co-immunoprecipitation or reporter assay experiment are shown at the bottom. **b**, STAU1 interacts with *XBP1* mRNA via the long-range RNA structure. The ratio of *XBP1* wt and Δ in total cell lysate fraction (Input) or STAU1 co-immunoprecipitated fraction (Co-IPed) were analysed by RT–PCR. The ratios ($\log_2$) of two populations were compared by the two-tailed Welch's t-test ($n = 3$). The corresponding Qiaxcel electropherograms are available at: (http://figshare.com/s/f0e32272929b11e4a56606ec4b8d1f61). **c**, Overview of *XBP1*(u) and *XBP1*(s) mRNAs. The position of cytoplasmic splicing site is indicated by an arrow. The longer RNA duplex overlaps with the region translated in *XBP1*(s). **d**, Thapsigargin induces endoplasmic reticulum stress and cytoplasmic splicing of *XBP1* mRNA. After the induction of endoplasmic reticulum stress by thapsigargin, cells were lysed, and the alternative region of *XBP1*(s) and *XBP1*(u) mRNAs was amplified by PCR. The PCR products of *XBP1*(s) and *XBP1*(u) mRNAs were examined by the electropherogram (the expected sizes of PCR products from *XBP1*(s) and *XBP1*(u) mRNAs are indicated as s and u respectively, while a hybrid PCR product is indicated by *)[38]. We confirmed that after 30 min of the endoplasmic reticulum stress induction, *XBP1* mRNA was actively spliced. **e**, Real-time PCR analysis of reporter mRNA levels containing wt, mut or com *XBP1* 3′ UTR (as marked in **a**). Analysis is done in untreated cells (UT), in cells treated with siRNA against STAU1 (KD), or in cells where siRNA-resistant STAU1 is induced with doxycycline to rescue expression of STAU1 in spite of knockdown (RC). Differences in expression were compared by the two-tailed Student's t-test. The two independent experiments are marked by black and blue colour, and each dot represents replicates performed on separate wells of cells as part of the same experiment. Disruption of duplex destabilizes the mRNA, and compensatory mutation restores the stability slightly above the wt level. This may be because the duplex in the 'com' reporter is longer by 2 nucleotides compared to 'wt'. The mechanism whereby the long-range duplex impacts mRNA stability remains to be determined.

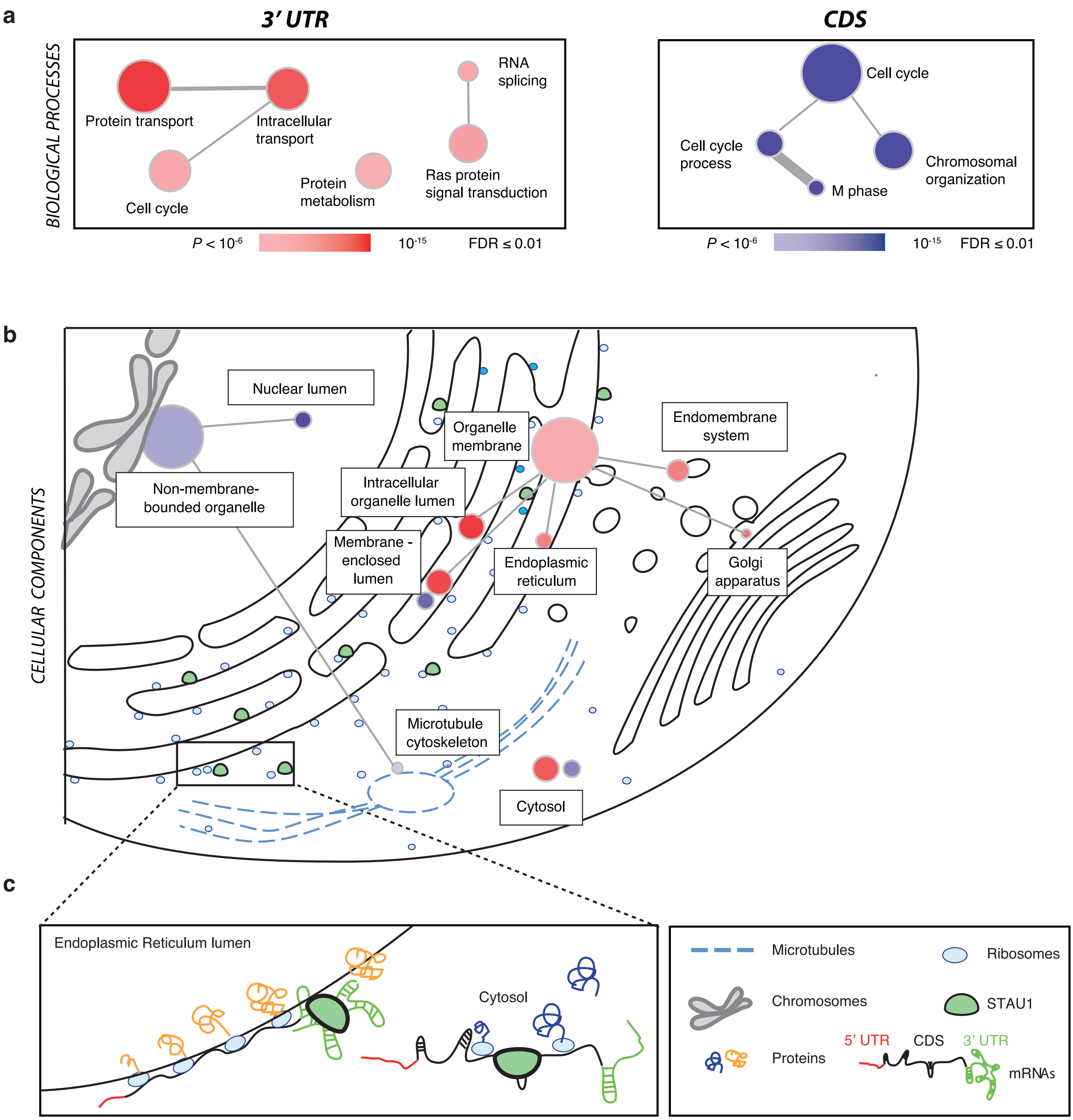

Extended Data Figure 9 | Gene Ontology analysis and schematic of STAU1 function in 293 cells. Gene ontology analysis of the genes bound by STAU1 in the 3′ UTR (red) and in the CDS (purple), using the DAVID Gene Ontology Tool[57] and visualized using ReviGO[58]. Node colour indicates the P value (threshold: P value $<10^{-6}$, FDR <0.01), and node size indicates the frequency of the GO term in the GOA database. Each gene is mapped only to the most specific terms that are applicable to it (in each ontology). Highly similar GO terms are linked by edges in the graph, with the edge width depicting the degree of similarity. **a**, Diagram summarizing the enriched Biological Processes GO terms. 3′ UTR-bound mRNAs tend to encode proteins that function in intracellular transport (in red), whereas CDS-bound mRNAs tend to encode proteins that function in the cell cycle M phase (in blue). **b**, Diagram summarizing the enriched Cellular Components GO terms in the context of their location in the cell. 3′ UTR-bound mRNAs tend to encode membrane proteins that are translated at the endoplasmic reticulum (in red), whereas CDS-bound mRNAs tend to encode nuclear proteins (in blue). **c**, Schematic diagram of the functional analyses of CDS and 3′ UTR-bound mRNAs. 3′ UTR-bound mRNAs tend to be highly translated and encode membrane proteins that are translated at the endoplasmic reticulum (in grey). CDS-bound mRNAs tend to be lowly translated and encode nuclear proteins that function in the cell cycle M phase. Loops formed by RNA duplexes in the 3′ UTR tend to be longer than in the CDS, and 3′ UTRs have higher density of bound duplexes.

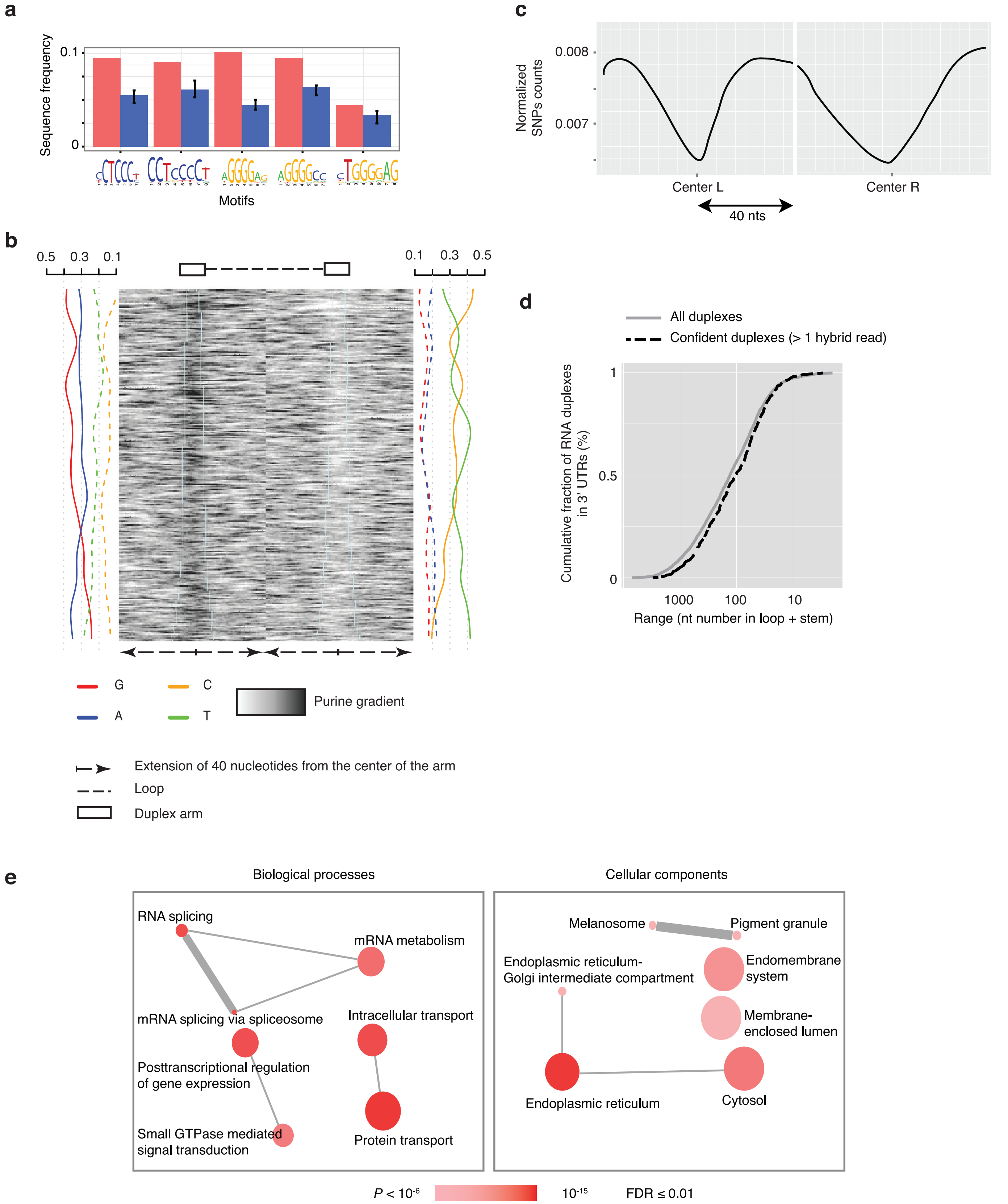

Extended Data Figure 10 | Analysis of confident duplexes that were identified by >1 hybrid read. **a**, Sequence motifs enriched at confident STAU1-target RNA duplexes (those identified by >1 unique hybrid read). **b**, Visualization of purine content at confident duplexes (as in Fig. 2a). **c**, Normalized count profile of SNPs occurrence in confident 3′ UTR–3′ UTR duplexes with a loop of at least 80 nucleotides. **d**, Comparison of range (the length of loop plus duplex) distribution among all duplexes and confident duplexes located in 3′ UTRs. **e**, Gene Ontology analysis of mRNAs containing confident STAU1 duplexes in 3′UTRs (as in Extended Data Fig. 9).

CAREERS

POSTDOCS Efforts to assess and change the post-PhD position **go.nature.com/wmymzy**

@NATUREJOBS Follow us on Twitter for the latest news and features **go.nature.com/e492gf**

NATUREJOBS For the latest career listings and advice **www.naturejobs.com**

CENTRE FOR GENOMIC REGULATION

One of the core facilities at Spain's Centre for Genomic Regulation provides proteomics services.

CORE FACILITIES

Shared support

Centralized laboratories offer an alternative for researchers with a predilection for the latest technology.

BY JULIE GOULD

Stefan Green always wanted to pursue biology, and fell in love with microbiology as a graduate student. As he advanced through his graduate education and postdoctoral fellowships, he reckoned that everything would come together because he had ticked all the right boxes. Following the pathway of his parents, both of whom are biologists, he earned a master's in environmental engineering and a PhD in microbiology and plant protection, completed two postdocs and has a long list of publications and posters. But — not surprisingly in today's discouraging research-career environment — his drive for a tenure-track position stalled in 2010. He could not get an academic tenure-track position despite his stellar CV. "I did two postdocs. I taught microbial ecology for a semester," he recalls. "But after several interviews for permanent positions, I wasn't having any luck."

Green gave up the academic-research battle and found a different way to keep his hand in science. During one of his postdocs, Green had tried to find ways to characterize microbial communities without using modern sequencing techniques because the financial and labour costs of the technology was out of the reach of his lab. From this experience, he discovered that he enjoys and has a knack for working with instrumentation. Today, he is director of the DNA-services laboratory at the University of Illinois at Chicago.

Green enjoys step-by-step, logical thinking and finds that it is one of the main components of his work there. "I like tinkering with methods and technology, so working at a core facility suits me," he says. "I can be a fertilizer for research without worrying about the bigger picture" — the grant and publication competition that academic scientists face daily.

Core labs, or core facilities, as they are often called, are centralized technology-based laboratories that maintain and support sophisticated equipment for use by their host institution's researchers and often by external customers, too. Some provide training on the technology; most also offer computational and statistical services, all under one roof. For scientists who do not want to leave the lab, a position at a core facility offers a more stable alternative to the fast-disappearing academic tenure track.

Researchers who would like to become a core director need a doctorate that is related to the core lab's discipline — molecular biology, say, for work in a sequencing core — and a passion for and experience with the technology they want to work with. The experience can come through specialized training or development of a new method or technology as part of their research. Alternatively, those without a doctorate can start as technicians and work their way up.

Green's core lab is the largest and most complex of the 20 cores, centres and labs that comprise the university's Research Resources Center. Outfitted with the next-generation DNA-sequencing equipment, it has seven full-time staff scientists, a PhD student and an undergraduate student. Green relishes the challenge of managing the lab: he must determine what technology and equipment to buy; learn how to operate and maintain it; run the business, including marketing, advertising and training; and keep abreast of the research needs of his clients. "Every project and problem is different. You think you know a lot, but you quickly realize that you don't," he says. "For me, that is both frustrating and rewarding."

UPS AND DOWNS

The need for more-sophisticated lab equipment is rising even as research grants are shrinking, so core labs have sprung up across all disciplines. Some research institutions, such as the University of Illinois, host many — in transgenic production, animal imaging and more. The ▸

European Molecular Biology Laboratory in Heidelberg, Germany, has seven — genomics, proteomics and flow cytometry among them.

Positions at core labs are quite different from those in a research laboratory. The labs are essentially service centres for the local research community, so their value lies in providing broad access to sophisticated and expensive equipment. Their existence means that individual principal investigators (PIs) do not need to spend huge amounts of money to buy the hardware themselves — and then learn how to use it, train their lab staff on it, budget for costly repairs and risk it being unusable when it breaks. "What they really represent is the natural evolution of the way we work in science," says Patrick Descombes, head of the Functional Genomics Core at the Nestlé Institute of Health Sciences in Lausanne, Switzerland. He says that such communal centres are a logical outgrowth of science's increasing dependence on technology and the trend towards more collaboration.

Mónica Morales, head of Core Facilities and Internal Scientific Services at the Centre for Genomic Regulation in Barcelona, Spain, says that by providing a level playing field, core labs help to democratize science. "You don't have to be a well-funded PI to get access to the latest in cutting-edge instrumentation and expertise," she says.

Core labs must focus on serving their users, who generally pay to use the equipment, or get results from it. As such, it is crucial for would-be core-lab scientists to remember that the facilities operate largely as businesses, and that customer-service and project-management skills are paramount. "It's a non-profit business in a university," says Yuriy Alekseyev, director of the Microarray Resource at Boston University in Massachusetts. Running within a budget, managing difficult customers and marketing available services are all parts of the operation of a technology-driven laboratory. James Hadfield, head of the genomics core at the Cancer Research UK Cambridge Institute, says that he seeks applicants who are comfortable with the service aspect: "We're looking for people who understand the importance of customer interaction," he says.

As part of the service remit, core-lab directors also must be savvy about the market, both for the technology and the researchers who use it. "A person working in a core has to be able to look ahead and see what's coming next, what they've got to invest in," says Hadfield. To get an insight into what is new and hot, Morales says that she talks to clients and vendors and studies publications, online resources and conference presentations in her discipline. Core-lab directors would also do well to build up networks in the research-and-development and marketing teams at major technology companies.

Stefan Green swapped academic work for providing research services.

STEFAN GREEN

DUE CREDIT

How to gain authorship

Core scientists should receive appropriate credit for their work on clients' research. That can range from a note in a publication's acknowledgements — when a researcher is simply using the core lab's services — to co-authorship when a core scientist is heavily involved in planning the experiments.

One way to get co-authorship is to become a faculty member at your host institution. Another is to be a co-principal investigator on core-lab client research, says Gerd Prehna, associate director of the Center for Structural Biology at the University of Illinois at Chicago. Last year, he co-authored a paper on the predatory behaviour of bacteria (G. Prehna, B. E. Ramirez and A. L. Lovering *PLoS ONE* **9,** e115390; 2014). "I did all the experimental work here at this core: everything was done in house. It's a nice example of what we do," he says. "I was able to line up the research and my core-facility duties, making it mutually beneficial."

If an internal customer wants a series of studies on a certain piece of equipment, Prehna draws up a collaboration agreement. "Instead of looking at my hours of usage," he says, "I will train their students and become a co-author." **J.G.**

MINIMAL OVERSIGHT

They might not get to do much independent research (see 'How to gain authorship'), but core-lab scientists face a good deal less financial pressure than academic researchers because most labs are supported by their host universities or institutions. And despite the subsidy, most operate independently with minimal oversight or administration. Funding models differ: in some cases, the universities cover only the equipment-purchase costs, and customers pay to use the technology and for the staff's time. In others, universities subsidize user fees too. Some universities do not subsidize at all: the core is run completely independently.

Core labs are not immune to the difficult research-funding environment, however. A 2013 survey of core-lab directors from 135 institutions worldwide found that although more than half had seen their client base grow over the past year, the increase was 13% less than the previous year. Less funding for research has meant less financial support for core labs, says Alicia Cravens, marketing director at iLab Solutions, a provider of core-facility management software in Cambridge, Massachusetts, which conducted the survey. Many are now trying to become independent, adopting a more efficient, business-based model and learning how to market services and draw customers, she adds.

Still, core labs are not tied as tightly to the vagaries of research funding as academic labs. They can support themselves because the need for their products and services is high and will continue to rise, predicts Vladimir Benes, who heads EMBL's genomics core. "The demand is there," he says.

A testament to the rising demand is the emergence of online marketplaces for core facilities and services, says Dan Knox, co-founder and chief operating officer of Science Exchange, which connects core labs with scientists (analogous to platforms such as Etsy). "The market for core-lab services is growing rapidly, so I think their economic future is very good," Knox says. The company's external customers have grown in number in the past two years and include drug makers, biotechnology companies, government agencies, non-profit organizations and charities, academic researchers, independent researchers and other core labs. "We've had researchers from every continent, including Antarctica, order experiments," he says.

That increase in demand has opened up the variety of research that core scientists can get involved with, and this is one reason that core scientists say that they find their work compelling. "The craziest projects walk through the door," says Green. One of the more challenging projects he worked on involved mapping the methylation sites of the DNA of a virus. "I've learnt that so many fields require sequencing, from dentistry to epidemiology," he says. "It's a very nice way to interact with many different aspects of science that you never knew existed." ■

Julie Gould *is editor of Naturejobs in London.*

ASYMMETRICAL WARFARE

So you want to be a star?

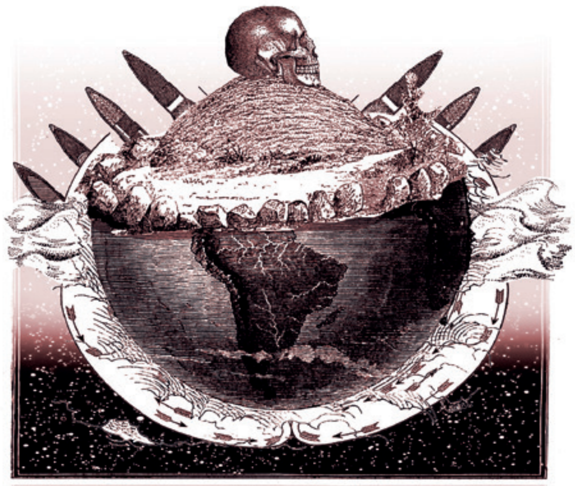

ILLUSTRATION BY JACEY

BY S. R. ALGERNON

Time: Contact + 0.2 nano Galactic Years
The battle is joined! Our first volley neutralized their coastal cities and orbital grid. A lesser race would have capitulated, knowing itself to be outmatched, but Earth fired back with chemical rockets and atomics. We lost one orbiter and six surface reconnaissance craft. This race shows every sign of predatory genetic stock. Their progeny will make fine additions to the Galactic Legion.

How I wish I could be in their place right now, to see the cosmic battlefield with young eyes.

Time: Contact + 0.45 nano Galactic Years
The Earth drones and missiles held us off for a surprisingly long time, but we have encircled their bases. I have ordered our subcommanders to use beam and blade only, so that we may preserve the fallen. This race is young — perhaps too young to face conquest — but in their hearts they are ready. Natural selection will take them the rest of the way.

Time: Contact + 0.68 nano Galactic Years
I have seen with my own eyes the first of the fallen Earth commanders. The body repulses me and casts a pall on the entire campaign. Despite the prominence of star insignias on most of their vessels, the Earthers are not star-shaped. They are, in fact, biologically identical to the ones who live out in the open, whom we had assumed to be a slave race. I beg you, General, not to tell the Council. They will declare this conquest an abomination and force me from the planet in disgrace.

I am well aware of the Council's ruling that only stellate races have standing to compete, but the Council has never faced these bipeds in battle. They deserve to be lifted onto the Celestial Arena. They are ready for the stars.

I hold out hope that the people of Earth are somehow a degenerate stellate race, and that living on dry land has led their appendages to droop downward. Their future generations will vindicate me.

Time: Contact + 0.8 nano Galactic Years
Fighting has largely ceased. I have conveyed the best of our fallen to the coastlines of Earth. Of our hundred field commanders and strike force leaders, twelve fell in battle. The Earthers mutilated the bodies with projectile weapons — clearly a violation of civilized combat, but they are a young race and deserve some latitude. I have in all cases managed to preserve at least one intact arm or remnant of the central disk. Renewal has begun.

My teams have been scrupulous in preserving the appendages and torso of each fallen Earth commander. We have laid out thousands of bodies along the coastline. The Council will not be so quick to call this conquest an abomination when the harvest comes in.

Time: Contact + 1.0 nano Galactic Years
Something has gone wrong. The fallen of Earth have shown no signs of renewal. It is becoming difficult to prevent their remains from putrefying. We have frozen many of them, while our xenobiologists argue over how best to spur regeneration.

These Earthers are stubborn even in death.

Time: Contact + 1.25 nano Galactic Years
Today brought a hopeful sign. We faced sustained attack from a band of surviving Earth soldiers. They fought with skill and ferocity that exceeded their fallen comrades. I met the leader personally on the field of battle and asked it where it wanted its body to be placed. Surely it would know the optimal location for renewal on its own world.

It told me to go to Hell. I asked for coordinates but did not receive a coherent reply.

I split the body cleanly along the midline, to give it two chances at renewal. Afterward, I let some of the survivors take the body, to see what they did with it. The results have been enlightening. Apparently, Earthers are planted in dry ground, like seeds. We should have suspected as much from a terrestrial species. The survivors fired projectiles into the air and played musical instruments. Could sound be the key to their regeneration? I will try acoustic stimulation with the remaining bodies.

➲ NATURE.COM
Follow Futures:
@NatureFutures
go.nature.com/mtoodm

Time: Contact + 1.65 nano Galactic Years
None of my experiments has succeeded. What if Earthers simply do not renew? How could evolution permit such a disaster? Without regeneration, the ones who fought most bravely would excise themselves from the gene pool, resulting in a timid prey species. The Earthers are not timid.

The Council was right. This is an abomination. The Earthers have led themselves to extinction, and the Council will blame me.

And yet, there is hope. Clearly the Earthers have endured for millions of years. They must renew, even if I cannot yet determine how.

Time: Contact + 2.45 nano Galactic Years
The formal campaign is over, yet a continued insurgency drains our resources. The Earthers attack at night. They befoul our regeneration beds. They drag the bodies onto the beaches and burn them. They disrupt planetside operations at every opportunity. Our orbiters have detected energy spikes from remote mountain regions. I believe new weapons are being brought to bear.

I understand the Earthers now. I have, it seems, waged war on a prey species, one bred by nature to wait in the shadows. What I mistook for fighting spirit must simply have been this planet's way of weeding out the stubborn and foolhardy. A new generation, more cunning and cautious than the last, rises from the husks of their cities.

I shall stay and fight them, to speed their evolution. It is the least I can do to atone for my mistakes.

If I fall, General, and if you find my body, find a place for me along Earth's coastline and keep the Earthers away somehow while I renew. In my next incarnation, I wish to call this world my home. ■

S. R. Algernon *studied fiction writing and biology, among other things, at the University of North Carolina at Chapel Hill. He currently lives in Singapore.*

nature OUTLOOK

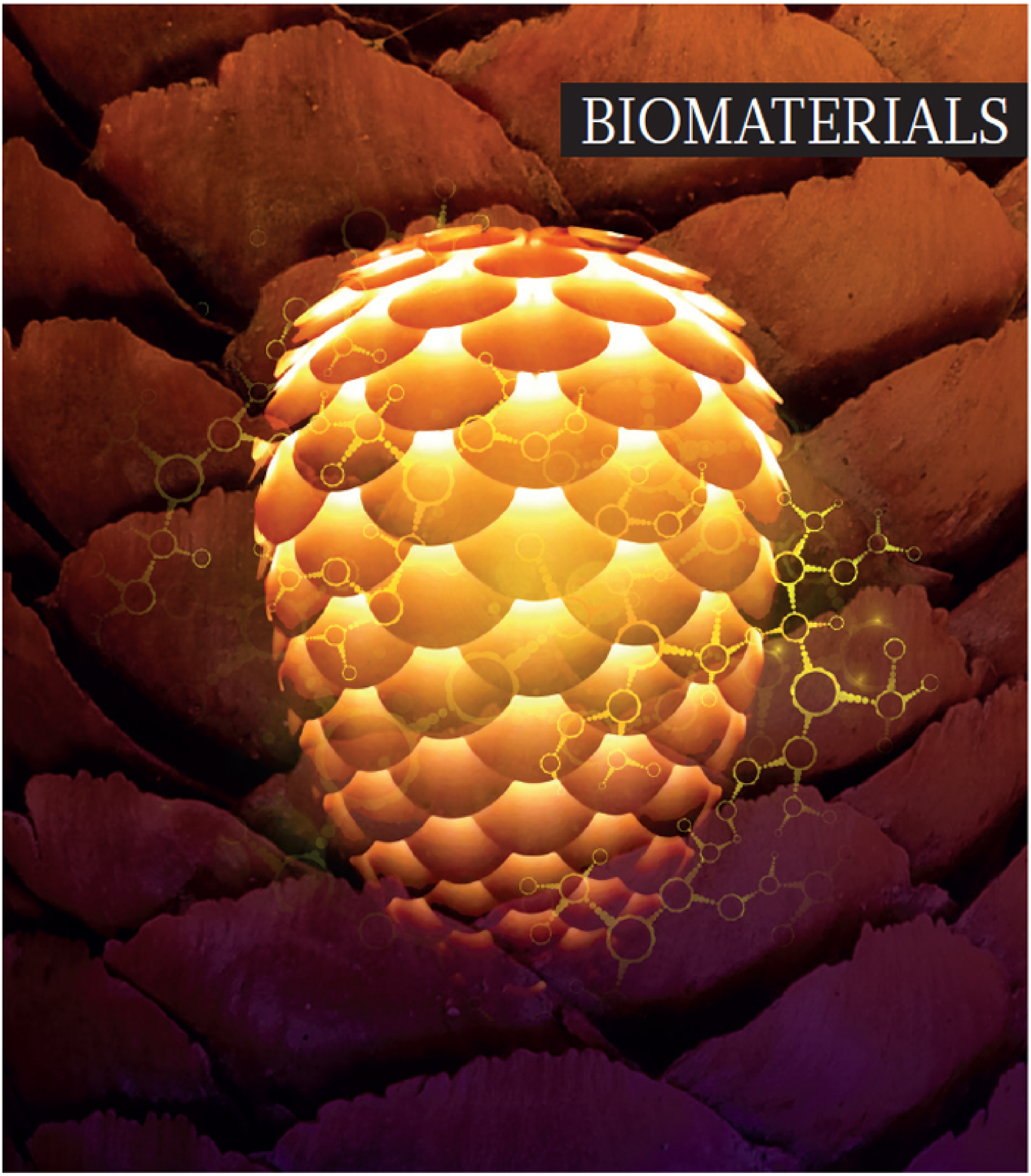

Produced with support from:

KISCO

Inspired by the natural world

natureOUTLOOK

BIOMATERIALS

26 March 2015 / Vol 519 / Issue No 7544

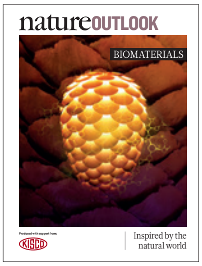

Cover art: Paul Price

Editorial
Herb Brody,
Michelle Grayson,
Kathryn Miller

Art & Design
Wesley Fernandes,
Mohamed Ashour,
Andrea Duffy

Production
Karl Smart,
Ian Pope

Sponsorship
Yuki Fujiwara,
Yvette Smith

Marketing
Hannah Phipps

Project Manager
Anastasia Panoutsou

Art Director
Kelly Buckheit Krause

Publisher
Richard Hughes

Chief Magazine Editor
Rosie Mestel

Editor-in-Chief
Philip Campbell

Millions of years of evolution have made the biological world into a supremely effective materials-development laboratory. This Outlook examines the ways in which substances found in the natural world are inspiring imitations that might eventually endow humans with superhuman powers (see page S2).

We begin the exploration with a close look at a familiar creature: the spider (S4). The silk that these arthropods use to spin webs is extraordinarily tough. Indeed, the scene from *Spider-Man 2* in which a New York City subway train is stopped by a spiderweb is not far removed from the realms of reality. Scientists are learning how to fabricate synthetic versions of these fibres.

Other researchers are studying plants and animals for ideas on how to design coatings and textures that imbue surfaces with special properties, such as the extreme stickiness of gecko feet (S7). In the sea, the adhesive that mussels use to cling to slippery rocks is leading to the development of polymeric glues that could repair wounds (S12). Hard natural materials such as bone and fish scales have intricate structures that could potentially lead to flexible, protective armour (S14). And what better inspiration for improving clothes than the tissues that shield plants and animals from the elements and provide them with adaptive camouflage (S10)?

Biomaterials are essential in developing organ-on-a-chip technology (S16). And they have a promising niche in improved drug-delivery systems that would go a long way to solving one of medicine's biggest problems: that patients rarely follow their prescribed course of treatment (S19).

We are pleased to acknowledge that this Outlook was produced with the support of KISCO Ltd. in association with Spiber Inc. As always, *Nature* retains sole responsibility for all editorial content.

Herb Brody
Supplements Editor

CONTENTS

RELATED RESEARCH

The latest papers on materials science published in *Nature*-affiliated journals.

Nature Outlooks are sponsored supplements that aim to stimulate interest and debate around a subject of interest to the sponsor, while satisfying the editorial values of *Nature* and our readers' expectations. The boundaries of sponsor involvement are clearly delineated in the Nature Outlook Editorial guidelines available at go.nature.com/e4dwzw

CITING THE OUTLOOK
Cite as a supplement to *Nature*, for example, Nature **Vol. XXX**, No. XXXX Suppl., Sxx–Sxx (2015).

VISIT THE OUTLOOK ONLINE
The *Nature Outlook Biomaterials* supplement can be found at http://www.nature.com/nature/outlook/biomaterials
It features all newly commissioned content as well as a selection of relevant previously published material.

All featured articles will be freely available for 6 months.

SUBSCRIPTIONS AND CUSTOMER SERVICES
For UK/Europe (excluding Japan): Nature Publishing Group, Subscriptions, Brunel Road, Basingstoke, Hants, RG21 6XS, UK. Tel: +44 (0) 1256 329242. Subscriptions and customer services for Americas – including Canada, Latin America and the Caribbean: Nature Publishing Group, 75 Varick St, 9th floor, New York, NY 10013-1917, USA. Tel: +1 866 363 7860 (US/Canada) or +1 212 726 9223 (outside US/Canada). Japan/China/Korea: Nature Publishing Group — Asia-Pacific, Chiyoda Building 5-6th Floor, 2-37 Ichigaya Tamachi, Shinjuku-ku, Tokyo, 162-0843, Japan. Tel: +81 3 3267 8751.

CUSTOMER SERVICES
Feedback@nature.com

LEARNING FROM NATURE'S BEST

Materials researchers are taking cues from specific plants and animals that make substances that could endow humans with superhero powers. By **Julie Gould.**

1 SUPER STRONG

See page S4

The inspiration

Spiders can make up to seven different types of silk. The strongest is dragline silk, which is used for building webs[1].

Fact
Darwin's bark spider (Caerostris darwini) can spin silk threads[2] that can measure up to **25 m.**

The structure

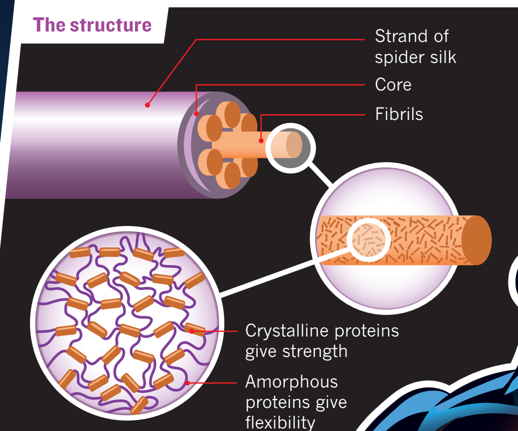

Spider dragline silk is made of fibrils comprising proteins that are made of crystalline structures that provide strength and amorphous, formless, regions that provide flexibility.

The application

Infusing metal into spider silk increases its toughness tenfold[3]. The resulting thread could be used in artificial tendons.

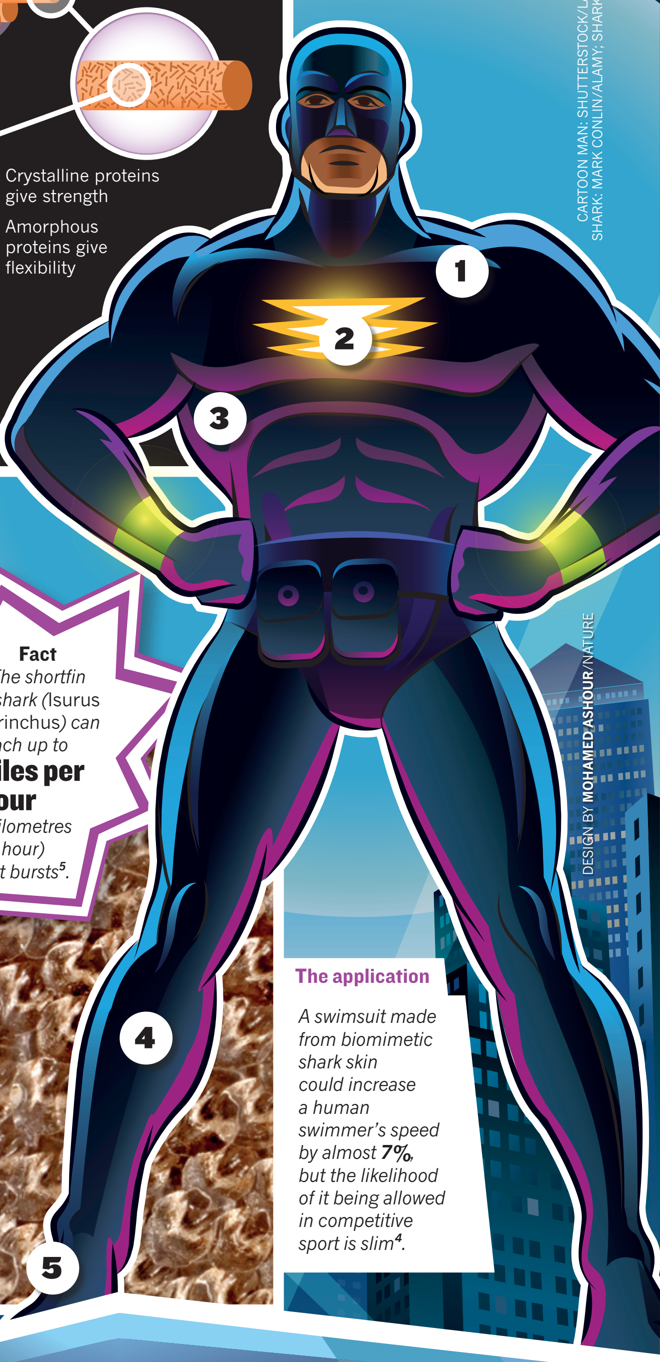

2 SUPER FAST

See page S10

The inspiration

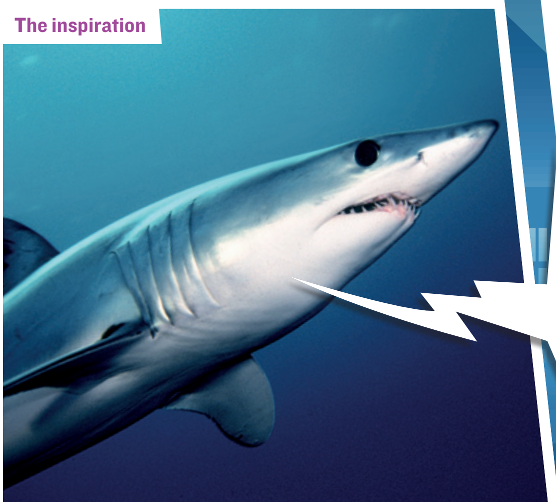

Shark skin is made up of tooth-like V-shaped scales called dermal denticles that ***align parallel*** *to the direction of local water flow to reduce drag[4].*

The structure

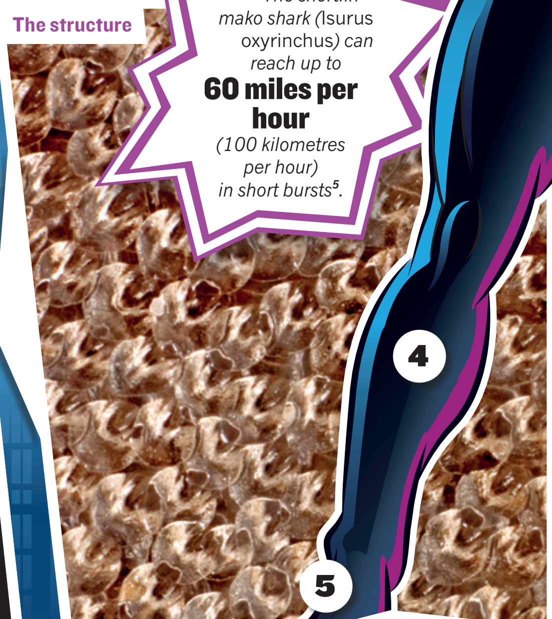

Fact
The shortfin mako shark (Isurus oxyrinchus) can reach up to **60 miles per hour** *(100 kilometres per hour) in short bursts[5].*

The application

A swimsuit made from biomimetic shark skin could increase a human swimmer's speed by almost ***7%****, but the likelihood of it being allowed in competitive sport is slim[4].*

References: 1. Römer, L. & Scheibel, T. *Prion* **2,** 154–161 (2008); 2. Gregorič, M. *et al. PLoS ONE* **6,** e26847 (2011); 3. Lee, S. M. *et al. Science* **324,** 488–492 (2009); 4. Wen, L. *et al. J. Experim. Biol.* **217,** 1656–1666 (2014); 5. Ebert, D. A. *et al. Sharks of the World: A Fully Illustrated Guide* 230 (Dolby, 2013);

CARTOON MAN: SHUTTERSTOCK/LANA STEM; SPIDERWEB: THINKSTOCK; SHARK: MARK CONLIN/ALAMY; SHARK SCALES: PASCAL GOETGHELUCK/SPL

DESIGN BY MOHAMED ASHOUR/NATURE

3 SUPER DRY See page S10

The inspiration

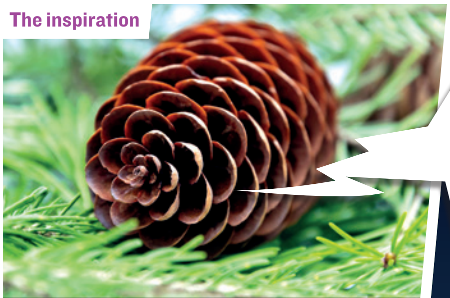

The scales of a pine cone are made up of two different layers, each reacting differently to changes in humidity. One layer elongates in damp conditions and the other works to resist this, causing the scales to bend. It is similar to the way a thermostat's bimetallic strip bends in response to changing temperature[6].

The structure

Fact
The cones of the knobcone pine (Pinus attenuata) only open their scales to drop seeds in the extreme heat of a **wildfire.**

The application

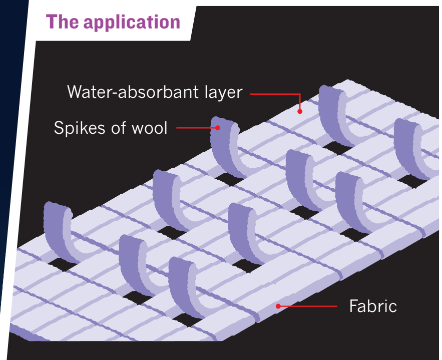

Researchers have developed smart materials with woollen spikes that are sensitive to relative humidity. The wool spikes open when the wearer sweats and close when the layer dries out.

4 SUPER CLEAN See page S7

The inspiration

The leaves of the lotus plant (Nelumbo spp.) have evolved an intricate structure consisting of papillae covered in a dense coating of wax tubules. Trapped air reduces the liquid-to-surface contact area, so water ***rolls off the surface*** *and collects dust particles on its way[7].*

The structure

Fact
By 2019, the global nanocoatings market is forecast to reach a value of US$14.2 billion.

The application

Synthetic materials with a hierarchical surface, such as those that mimic the lotus leaf, have ***gaps filled with a lubricant*** *so that the material is stain- as well as water-resistant[8].*

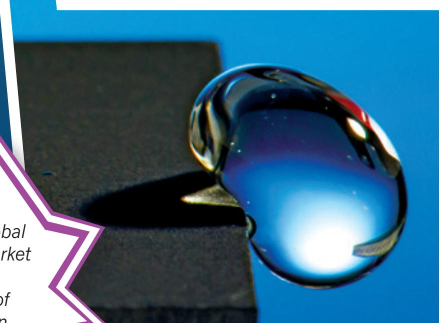

5 SUPER STICKY See page S7

The inspiration

Geckos (Hemidactylus spp.) can climb glass walls and hang from ceilings without a visible method of sticking to them. Researchers found that geckos can adhere to gravity-defying surfaces because of the electrostatic interaction between the molecules in their feet and the molecules on a surface[9].

The structure

Fact
Geckos' feet are so sticky that, in theory, they could support the weight of a **130 kg** *person hanging from the ceiling[10].*

The application

Hand pads, each covered in tiles with tiny silicon rubber hairs that ***mimic geckos' feet****, mean humans can scale walls like lizards. The more force applied to the pads, the stickier they become[11].*

PINE CONE: THINKSTOCK; CONE CLOSE-UP: JULIAN VINCENT, UNIV. OXFORD; LOTUS LEAF: BLICKWINKEL/ALAMY; LOTUS CLOSE-UP: EYE OF SCIENCE/SPL; DROPLET: J. ADAM FENSTER / UNIV. ROCHESTER; GECKO: BOSTON GLOBE/ GETTY IMAGES; GECKO CLOSE-UP: MATT REINBOLD; CLIMBING MAN: ERIC EASON, STANFORD UNIV.

6. Dawson, C. *et al. Nature* **390,** 668 (1997); 7. Ensikat, H. J. *et al. J. Nanotech.* **2,** 152–161 (2011); 8. Shillingford, C. *et al. Nanotechnology* **25,** 014019 (2014); 9. Autumn, K. *et al. Proc. Natl Acad. Sci. USA* **99,** 12252–12256 (2002); 10. Autumn, K. & Peattie, A. M. *Integr. Comp. Biol.* **42,** 1081–1090 (2002); 11. Hawkes, E. W. *et al. Roy. Soc. Interface* http://dx.doi.org/10.1098/rsif.2014.06

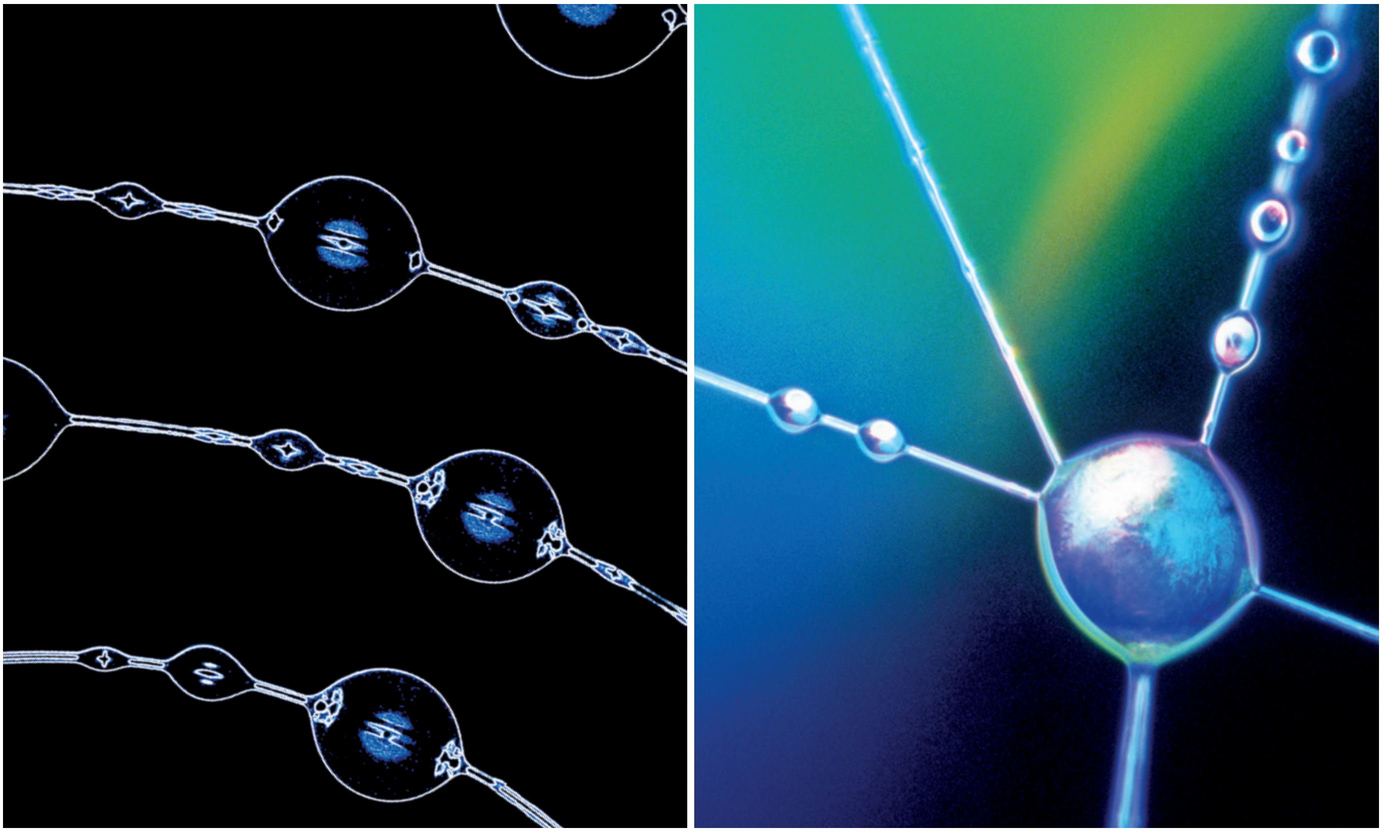

A synthetic mimic (left) of natural spider silk (right) incorporates polymer drops that can be used as a drug-delivery system.

SPIDERS

Web of intrigue

The sturdy, stretchy, sticky silks spun by spiders have inspired engineers to design pioneering medical devices such as artificial tendons and corneas.

BY KATHERINE BOURZAC

A Madagascan bark spider releases a silk dragline into the air. The wind carries the thin threads to the other side of a river, where they land on foliage on the opposite bank 25 metres away. The spider (*Caerostris darwini*) then stretches the bridgeline to establish tension, reinforces it, and draws on a palette of other silks, stretchier or stickier as needed, to fashion a web to capture the bugs flying over the water[1].

C. darwini's bridging silk is the world's toughest known biomaterial — it is even tougher than steel (see 'The toughest thread'). But *C. darwini's* versatility in producing different kinds of silk is not unique. Many spiders can spin several silks: stiff, structural strands to stabilize their webs; gooey, stretchy spirals to capture flying insects; adhesive pads to anchor their homes in place; and extraordinarily robust draglines from which to hang.

The remarkable mechanical properties of these natural fibres have attracted the attention of materials scientists. Researchers are looking to arachnids and other silk makers for ideas about how to make new structural materials for bridges and vehicles, dirt-resistant adhesives for climbing robots and sturdy polymers for biomedical devices. Many silks bring together properties that are not readily present in man-made materials — the extreme toughness and elasticity seen in spider threads is one example. Silk proteins can be moulded like plastic or perform optical functions like silicon. Yet because they're organic, biological materials, silks are environmentally friendly and biocompatible. Silk proteins can be fashioned into films that can be implanted in the body, releasing drugs as they dissolve. This combination of features is unavailable in polyester or collagen or anything else, says David Kaplan, an early proponent of high-tech biomedical silk at Tufts University in Medford, Massachusetts. "There's clearly a need for new biomaterials," he says. For Kaplan and others, silk is the best way to meet that need.

NATURE.COM
Read about spider genomes at:
go.nature.com/jwvsc4

COMMON THREAD

Silk evolved independently in many invertebrates, including spiders, honeybees and silkworms. Individual spiders can make as many as six different kinds of silk proteins (and two glue proteins), each of which has evolved over the creatures' 400 million years of natural history. Each spider species uses its own variations of these proteins to make many different types of thread.

"We think that a primordial spider had one kind of silk, and then there were multiple events when the gene duplicated and evolved," says Cheryl Hayashi, a spider specialist at the University of California, Riverside. The species that are more closely related to these ancestors, such as tarantulas and trapdoor spiders, make silks of simple designs — messy tangles to trap walking insects, for example, using fewer types

of silk. Other spiders evolved to make more complex spiralling orb webs, in which different regions are composed of different kinds of silk — some optimized for capturing prey, others for structural support of large web designs.

This evolutionary bounty has happy implications for engineers looking to put spider silk into human service. If a design calls for a fibre with a particular ratio of strength to stretchiness, "it's probably already been invented" by one of the tens of thousands of types of spider, says Hayashi.

Most research has centred on taking advantage of the toughness of spider silk — in materials science, toughness is a measure of how much energy it takes to break something. Materials such as spider silk are both strong and elastic. A large insect that flies into a spiderweb at top speed stretches the superfine fibres in the web but does not break them.

The toughest silks are found in spider draglines, which researchers are studying intensely. Spiders use draglines to dangle safely, to make the frames of their webs, and for situations in which resistance to breakage is paramount. In a scene from the 2004 movie *Spider-Man 2*, the eponymous superhero stops a runaway New York City subway train with his webbing, which is not too far of a stretch from reality. In 2012, physics graduate students at the University of Leicester, UK, calculated that dragline silk spun by the Darwin's bark spider would be able to perform a feat just as shown in the film.

If it could be manufactured, the Darwin's bark spider's dragline silk would be valuable for use in applications in which a lightweight, yet very strong, material is crucial: helmets for fighter pilots, artificial tendons and ligaments, or Spider-Man-like climbing ropes. But spiders are, from a practical, manufacturing point of view, useless. Spiders become cannibals when kept in captivity, and so must be caught from the wild. To obtain natural spider silk, a researcher must anaesthetize a spider, attach the end of one of its fibres to a variable-speed motor from an electric drill, then gently pull the thread out of one of the spider's glands. Depending on the species of spider, this technique can yield up to 100 metres of silk. This painstaking process is easier than picking apart the threads from spiderwebs, but it is not scalable. So researchers have been working on how to generate spider silks without spiders. The process presents two initial challenges: first, where to find the proteins; and second, how to assemble the proteins into a useful fibre.

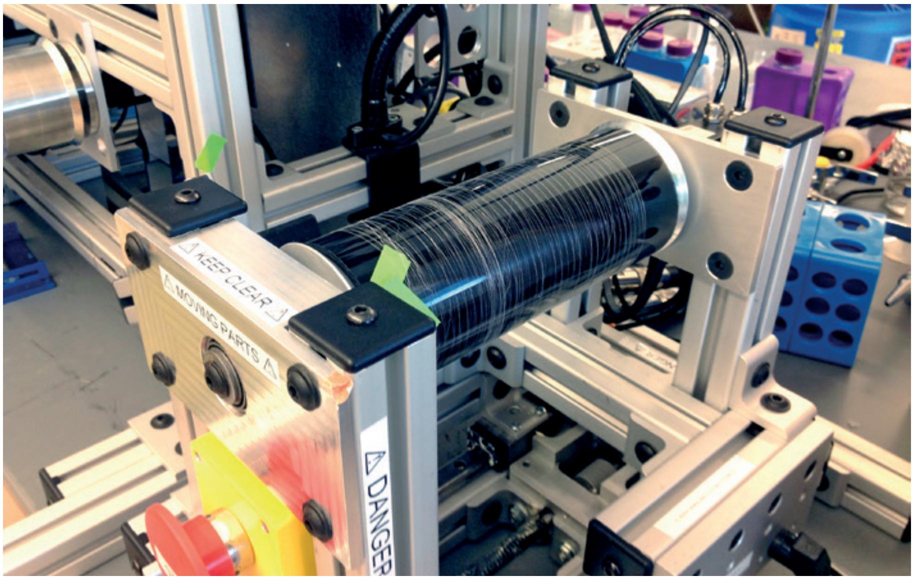

RANDOLPH V. LEWIS

Artificial silk is spun from genetically engineered spider-silk proteins at Utah State University in Logan.

FIBRE FOCUS

To realize the dream of artificial spider silk as an engineering material, researchers have started with genes. Randolph Lewis, a bioengineer at Utah State University in Logan, sequenced[2] the first spider-silk protein gene in 1990. Lewis chose the dragline of *Nephila clavipes*, a species indigenous to the Americas that is also known as the golden silk orbweaver. Since then, Lewis and others have succeeded in expressing this protein in many production systems, including the bacterium *Escherichia coli*, alfalfa and goats, which express the molecule in their milk. Lewis has started a company called Araknitek to develop and license these proteins.

There are other companies developing spider-silk proteins. AMSilk, which is based near Munich, Germany, manufactures synthetic spider-silk proteins for use in cosmetics and shampoos; Spiber Technologies, based in Stockholm, is selling meshes and films for growing cell cultures consisting of laboratory-made spider silk. Another almost identically named company — Spiber Inc. in Tsuruoka, Japan — has spun off from Keio University. Many commercially minded companies are developing films or fibres of artificial spider silk for use in medical devices and textiles.

"Our best fibres have about half to two-thirds the tensile strength of spider silk."

But no one has figured out how to produce spools of silk as tough as the original. "Our best fibres have about half to two-thirds the tensile strength of spider silk," says Lewis. One problem is that engineered spider-silk protein molecules are not as large as the originals. A general rule of fibre-spinning, whether the materials are proteins or plastics, is that the larger the molecules, the stronger the fibre. But this trend bumps up against an axiom of bioengineering: the bigger the protein, the more difficult it is to produce in a genetically modified organism. Natural dragline proteins have molecular masses of 250 to 500 kilodaltons; genetically modified organisms made in the laboratory produce silk proteins of only about 60 to 80 kilodaltons. Lewis says that he is continuing to work on producing proteins two to three times that size, much closer to natural spider-silk proteins, in genetically modified organisms. "The tensile strength is going to improve," he says.

Even with the right proteins, humans are at a disadvantage in putting them together because we still do not fully understand how spiders do it. Artificial silk fibre-spinning techniques are based on the methods used to make polymer fibres such as Kevlar. These techniques work well for the artificial polymers they were designed for but not as well for proteins. The proteins are pushed out of the tip of a fine needle, washed in baths of water or alcohol, then stretched and dried — a process very different from the method spiders use. Scientists know that spiders pull silks out of dedicated glands, some of which contain more than one kind of protein. The silk emerges from the gland as a highly concentrated liquid solution of fibres that solidifies as it is pulled out. This process has not yet been mimicked, and researchers are only beginning to understand the details of anatomy and physiology that make silk possible.

Anna Rising, a biochemist at the Swedish University of Agricultural Sciences in Uppsala, is turning to spiders for clues on fibre spinning. To learn more about how to make tough silk fibres, she and a student performed an intricate study[3] that they hope will lead to insights that can be applied to industrial silk-making. They placed microelectrodes along a living spider's silk glands, from the bag-like reservoir down the narrowing tube to its opening. These sensors revealed that "there's quite an impressive pH gradient and an increase in CO_2" along the length of the gland, she says. Rising is now working on replicating these gradients, which she says probably help to control the crystallization of the silk proteins as they are spun.

Rising has also found that, while inside the gland, the head of one silk protein attaches to the tail of the next in such a way that groups of them line up in a row[4]. As the proteins are assembled inside the gland, they pre-align. The better aligned the proteins are in a fibre, the stronger it is. This might also be mimicked in synthetic fibres. Swedish company Spiber is working to commercialize Rising's ideas, producing recombinant silk proteins in *E. coli* with the goal of making replacement tendons and ligaments for clinical use.

Hayashi hopes more insights will come from watching the silk gland develop, as young spiders mature into adults. She is studying *Latrodectus hesperus*, commonly called the black widow spider. This species has seven types of silk glands, each of which it draws on to make a unique silk fibre.

Although many researchers have been inspired by the mechanical toughness of spider draglines, others see broader potential in spider silks. Todd Blackledge, an entomologist at the University of Akron in Ohio, was the first to characterize the silk of Darwin's bark spider. He says that focusing on just one spider or one kind of silk would be like working only with inbred white laboratory rats. He is looking at silks made by other spiders, and is working with Akron materials scientist Ali Dhinojwala to study what makes some spiderwebs sticky. The pair have found that, for many silks, stickiness comes not only from chemistry but also from architecture.

One common arachnid adhesive technique is to make a patch of tightly packed, parallel silk threads to secure the dragline at one end. Spiders do this so that they may safely dangle. The adhesive patch is made of parallel threads of a coil-shaped silk protein called pyriform silk; fibres made from this protein are highly elastic, like a rubber band. The pyriform silk is coated with a sticky protein solution. Removal of this kind of dense adhesive patch requires pulling hundreds of elastic silk strands past their breaking point. Dhinojwala, a polymer chemist, mimicked this in a polymer adhesive patch. He showed that a patch of polymer threads with the right elasticity is sticky like the spider patches and hopes to develop artificial patches for use in surgical repair of tendons.

BEYOND SPIDERS

Whereas some researchers have been untangling the challenges of spider silks, others have been taking advantage of the properties of silks made by an animal that is easier to work with. The silkworm, *Bombyx mori*, has long been domesticated for the production of lustrous textiles.

Silkworm fibre is not as tough as spiders' silks and is in many ways simpler. The insects do only one thing with their silks: build cocoons for shelter during metamorphosis. And their silk has just one structural component, called fibroin. Kaplan sees the potential of fibroin — and it is not necessarily in the form of fibres.

THE TOUGHEST THREAD

Seemingly delicate spiderwebs are constructed from incredibly robust silk fibres that surpass artficial materials in toughness (the amount of energy they can absorb before breaking).

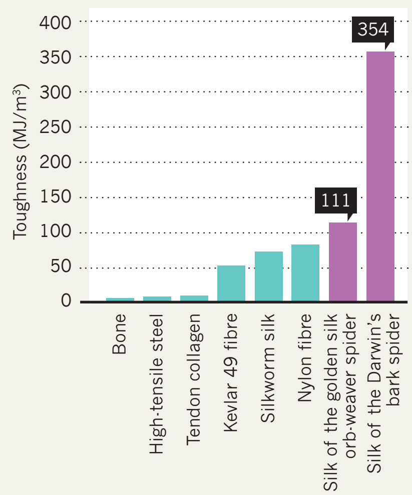

SOURCES: AGNARSSON, I., KUNTNER, M. & BLACKLEDGE, T.A. *PLOS ONE* **5**, E11234 (2010); OMENETTO, F. G. & KAPLAN D. L. *SCIENCE* **329**, 528–531 (2010).

Silkworm fibroin is readily available and easy to work with, says Fiorenzo Omenetto, a Tufts biomedical engineer with expertise in photonic materials. To compete with commodity materials such as plastics and silicon for applications in electronics and medical devices, scale is key. Omenetto orders huge boxes of silkworm cocoons, then processes them according to a recipe originally developed by Kaplan. The cocoons are cut open and the pupae removed. Then the cocoons are put into a hot bath to wash the silk fibres clean of the gluey glycoprotein sericin, before being processed to dissolve and purify the fibroin protein.

> ***"Silk is the best stuff on Earth. There's nothing like it."***

The thick, water-based solution that results can be mixed with drugs or other biomolecules or nanoparticles, then moulded into films or other structures. By controlling the conditions during the drying step, researchers can direct the crystallization of fibroin into forms that will dissolve on a desired timescale inside the body.

Kaplan and Omenetto have made silk films to house biodegradable electronic devices that monitor heart function and then dissolve[5]. They have also made drug-releasing implants, artificial corneas, silk orthopaedic hardware strong enough to screw into bone and then degrade over time, and squishy scaffolds for growing neurons from the brain's cerebral cortex.

Medical applications are paving the way for technological uses of silk, says Kaplan. Silk thread is already used extensively in medical settings, where it is the most commonly used suture material. And some silk biomedical devices made by Kaplan and other researchers are on the market or in clinical trials for soft-tissue reconstructive surgery. Furthermore, Orthox in Oxfordshire, UK, is testing silk devices for knee repair. Many of the researchers working on producing spider silk would like to use it in similar applications, such as repairing ligaments, where its extra toughness would be an additional bonus.

Tara Sutherland, a bioengineer at the Commonwealth Scientific and Industrial Research Organization in Canberra, Australia, is looking to silks that are less well known than those from spiders and silkworms. Sutherland's analysis[6] has uncovered 23 groups of independently evolved types of silk in 100,000 different insect species. In common with Kaplan, Sutherland has medical applications in mind. She zeroed in on one insect from thousands of options: the honeybee. Honeybees use silk to provide thermal insulation and structural support for their hives.

Sutherland approached the problem of picking the right silk from a bioinformatics point of view, not an evolutionary one. She wanted to make the most of what biopolymers offer. Unlike plastics and other materials, proteins can sense and respond to the environment. Sutherland wants to make tissue-engineering scaffolds that release cell-attracting signals on cue, or silk bandages that release antibiotics when they sense an infection. She has funding from the clothing firm Nike and NASA, among others.

Seeking a silk that would be easy to modify to add smart features, her analysis pointed to the type produced by honeybees. These proteins are smaller than those found in spider silks and so are easier to genetically engineer. Sutherland's analysis showed that huge stretches of the genetic sequence could be altered without interfering with the proteins' toughness and biodegradability. That gives her more room to engineer in new functions, such as attracting cells to help rebuild tissue. Sutherland is now developing bioactive bandages and other medical devices that use these silks.

For Sutherland and others, the fibres produced by silk makers in the wild are endlessly fascinating and full of design ideas. "Silk is the best stuff on Earth," says Kaplan. "There's nothing like it." ■

Katherine Bourzac *is a freelance science writer in San Francisco, California.*

1. Gregorič, M., Agnarsson, I., Blackledge, T. A. & Kuntner, M. *PLoS ONE* **6,** e26847 (2011).
2. Xu, M. & Lewis, R. V. *Proc. Natl Acad. Sci. USA* **87,** 7120–7124 (1990).
3. Andersson, M. *et al. PLoS Biol.* **12,** e1001921 (2014).
4. Kronqvist, N. *et al. Nature Commun.* **5,** 3254 (2014).
5. Tao, H. *et al. Proc. Natl Acad. Sci. USA* **111,** 17385–17389 (2014).
6. Sutherland, T. D., Young, J. H., Weisman, S., Hayashi, C. Y. & Merritt, D. J. *Annu. Rev. Entomol.* **55,** 171–188 (2010).

MITCH DIAMOND/GETTY

Ivy produces one of nature's strongest adhesives; by studying the plant's attributes, researchers are developing advanced surgical glue.

SYNTHETIC COATINGS

Super surfaces

Characteristics adapted from lizards, ivy and other natural materials could help to engineer everyday objects with remarkable properties.

BY NEIL SAVAGE

For millennia, people looked at birds and wished for the gift of flight — and finally the Wright Brothers made it so. Similarly, some scientists have gazed at geckos walking up walls and wondered whether humans could do the same. Now they can. In June 2014, a 100-kilogram man wearing a heavy pack climbed up a vertical sheet of glass using only a pair of hand-held paddles made from an advanced material inspired by geckos.

The synthetic gecko skin on the paddles has plenty of company in the world of materials science. Researchers are increasingly looking towards plants and animals for ideas on how to design coatings and textures that imbue surfaces with special properties. The adhesive that ivy uses to cling to walls, for example, has inspired a material that might help damaged tissues to regenerate. Molecules taken from mussel adhesives could provide a way to target cancer cells. And the veins on nasturtium leaves have led to the development of a synthetic surface that could prevent rain from freezing on aeroplane wings or keep grimy fingerprints off smartphone screens. The trick is to take ideas sparked by nature — some of them long in development, others brand new — and make them practical and durable.

THE LIZARD'S SECRET

Biologists had long believed that the secret to geckos' residue-free, sticky feet was a series of microscopic fibres called setae. Setae, which cover the pads of the lizards' feet, were thought to increase the contact area between each foot pad and the surface it is trying to climb, thereby allowing the attraction between atoms (known as van der Waals forces) to overcome other forces, such as gravity. But researchers who tried to duplicate the effect using artificial setae were not successful.

That is because the setae are not the whole story. "These fibrils are interesting, but they're not enabling," says Al Crosby, a polymer scientist and engineer at the University of Massachusetts Amherst, who helped to develop the Geckskin that the US Defense Advanced Research Projects Agency used in its June 2014 demonstration. A piece of Geckskin measuring 10 x 10 centimetres can hold about 318 kg. Whereas other researchers had focused on surface features of the gecko's foot, Crosby and his colleagues turned their attention to underlying questions of how the foot behaved when it came into contact with a wall.

The researchers made mathematical models of the forces at play — principally the van der Waals forces created by the contact between the gecko's foot and whatever it touched, and

the gravitational tug on the lizard's body. The models led the team to examine how the gecko's anatomy interacted with those forces.

In particular, the gecko has an unusual tendon in its foot. In most animals, including humans, tendons connect muscle to bone. The gecko tendon, however, is attached at one end directly to the skin of its foot pad, and at the other end to a muscle. When the gecko puts its toes down, sinuses in the foot pad swell with blood, pressing the skin against the surface. At the same time, the tendon pulls on the skin, causing an unusual level of stiffness in the direction in which force is being applied. The combination of the softness of the skin and the stiffness provided by the tendon allows the gecko to drape and conform its skin to the surface and hold it in place. This distributes the force of gravity over a larger area. As a result, the van der Waals attraction between the gecko's feet and the surface it is climbing is greater than the opposing force of gravity. When the gecko wants to take a step, it curls its foot. That action releases tension on the tendon and diminishes the stiffness, letting the animal peel its foot away from the surface.

Geckskin mimics geckos' feet by using a soft, rubber-like material such as polyurethane for the pad, combined with a stiff fabric such as Kevlar or carbon fibre to provide the stiffness of the tendon. And the material forgoes the setae. "It's not a requirement that we do things exactly the way nature did," says Duncan Irschick, a biologist and Crosby's colleague in developing Geckskin. "We just sort of took inspiration from the gecko and went further."

CLIMBERS AND CREEPERS

Unlike the gecko, ivy's adhesive seems more conventionally glue-like. Ivy produces a sticky, yellowish liquid that lets it cling to walls and which dries into a material that can withstand forces equivalent to two million times its own weight. "It's one of the strongest adhesives in nature," says Mingjun Zhang, a biomedical engineer at Ohio State University in Columbus, who hopes that he can apply what he is learning about the plant's properties to new surgical adhesives.

Zhang found that the yellow fluid was a mix of water, polysaccharides and organic particles about 70 nanometres in diameter. These tiny particles reduce the viscosity of the liquid, which helps it to spread across the surface that the ivy wants to cling to, and thus maximizes contact. The nanoparticles also form a molecular bond with the polymer in the adhesive. This renders the final product strong and elastic, not hard and brittle the way some glues become when they dry. Zhang thinks that the material uses sacrificial bonds, in which molecules break apart and rejoin; such bonds give bones and mother-of-pearl their strength because they allow a hard material to dissipate the energy of an impact without shattering. The ivy nanoparticles also prevent cracks from spreading, making the material particularly tough. Zhang has subsequently found[1] other nanoparticles in the fluid secreted by mussels, an adhesive that famously allows the crustaceans to remain on wet rocks despite the force of waves pushing and pulling them — something that is beyond the capacity of most artificial glues (see page S12). Other researchers have found similar structures in adhesives produced by starfish and barnacles.

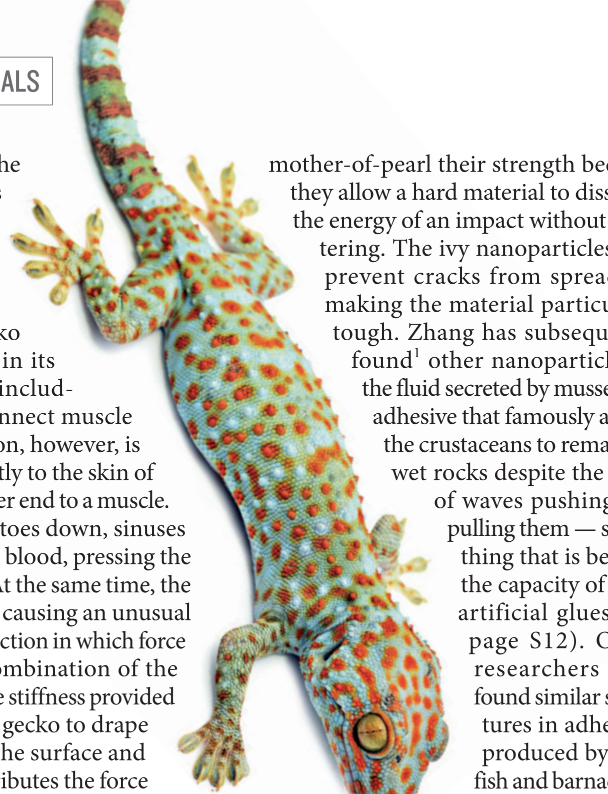

The anatomy of geckos such as the tokay (above) helps them to hold on to walls.

THAWATS/THINKSTOCK

Some scientists say that for nanoparticles to fulfil their technological promise they will need to be better understood. "It would be interesting to know more information about specific amino acids and protein structures as well as the underlying adhesion mechanism," says Chao Zhong, a professor of bio-inspired engineering at ShanghaiTech University in China. Phillip Messersmith, a materials scientist and bioengineer at the University of California, Berkeley, stresses that the research is still at an early stage and the results are inconclusive. "I do not think I have seen convincing evidence that the nanoparticles within the ivy adhesive are responsible for adhesion," he says.

But if they are, the combination of toughness, adhesion and biologically based components would make ivy nanoparticles attractive for a variety of uses, says Zhang, who is trying to develop ways to repair damaged tissues using ivy adhesive. In theory, a bandage made with ivy adhesive could provide an environment that would encourage new cells to grow, allowing an organ such as the heart to heal itself. It might also be seeded with stem cells to help the process along. In tests in a Petri dish, Zhang has shown that the adhesive helps cells to grow and attach to a surface. "It's not a simple mechanical bond," he says. "It's a biomaterial to help create a biological environment for wound healing." Zhang is starting animal studies on this application, although he says that it may be quite some time before it is ready for use in humans.

A different kind of coating based on ivy nanoparticles might be ready sooner. Zhang proposes using them in sunscreen, replacing the titanium oxide or zinc oxide now used. Zhang has found that the sizes of the ivy nanoparticles do not vary as much as the sizes of their metal counterparts, which means that they scatter light more uniformly. So a liquid laced with ivy nanoparticles would appear clearer than conventional sunscreens, and block a wider range of ultraviolet wavelengths[2]. Zhang is also trying to take what he has learned about ivy's mechanisms and apply it to other materials. He is synthesizing nanoparticles with different chemical compositions and trying them in different polymer matrices. That should lead to a variety of adhesives for different situations, he says; perhaps one would be very strong, whereas another would be more elastic. "I'm trying to go beyond what nature does."

Many other researchers are also taking inspiration from nature and pushing it in new directions. Messersmith studies mussel adhesive, which is ideal for securing objects underwater. But he hopes to use engineered versions of mussel adhesive in different environments, possibly even in a space probe. "If you were to simply mimic a natural material, you would get something that would work and perform well only under the conditions in which that natural material has evolved," says Messersmith. "Nature never evolved materials to have to survive interplanetary travel."

Messersmith has focused on a key component of mussel adhesives: the amino acid L-3,4-dihydroxyphenylalanine (DOPA). It turns out that DOPA makes a useful coating that helps attachments — such as antibodies — to stick to the surface. "In paint terminology, it's essentially a primer," he says. Messersmith's proprietary DOPA coating method involves dissolving DOPA in water, making sure the solution has the same acidity as the ocean, and then immersing the object to be coated. Advanced Hydro of Austin, Texas, licenses Messersmith's coating technique to make filters for wastewater treatment and desalination plants. Advanced Hydro coats its filters with DOPA, then attaches molecules of polyethylene glycol to make the filters resistant to fouling, improving their efficiency and reducing maintenance costs.

At the Materials Research Society's meeting in December 2014 in Boston, Massachusetts, Messersmith described the latest application of the technique. He put a coating of polydopamine, a molecular cousin of DOPA, on gold nanorods, which allowed him to add an antibody that targets cancer cells. The antibodies carry the nanorods to the cancer. The rods would then be heated with near-infrared light, killing the tumour. He reported using the method to kill cancer cells in a culture.

"We just sort of took inspiration from the gecko and went further."

Messersmith is looking beyond DOPA to sticky chemicals known as polyphenols, found in cacao, green tea and red wine[3]. Such compounds have similar chemical properties to DOPA and can be more cheaply extracted, he says. "These molecules, because they're found in tissue, have biological properties one could exploit in the

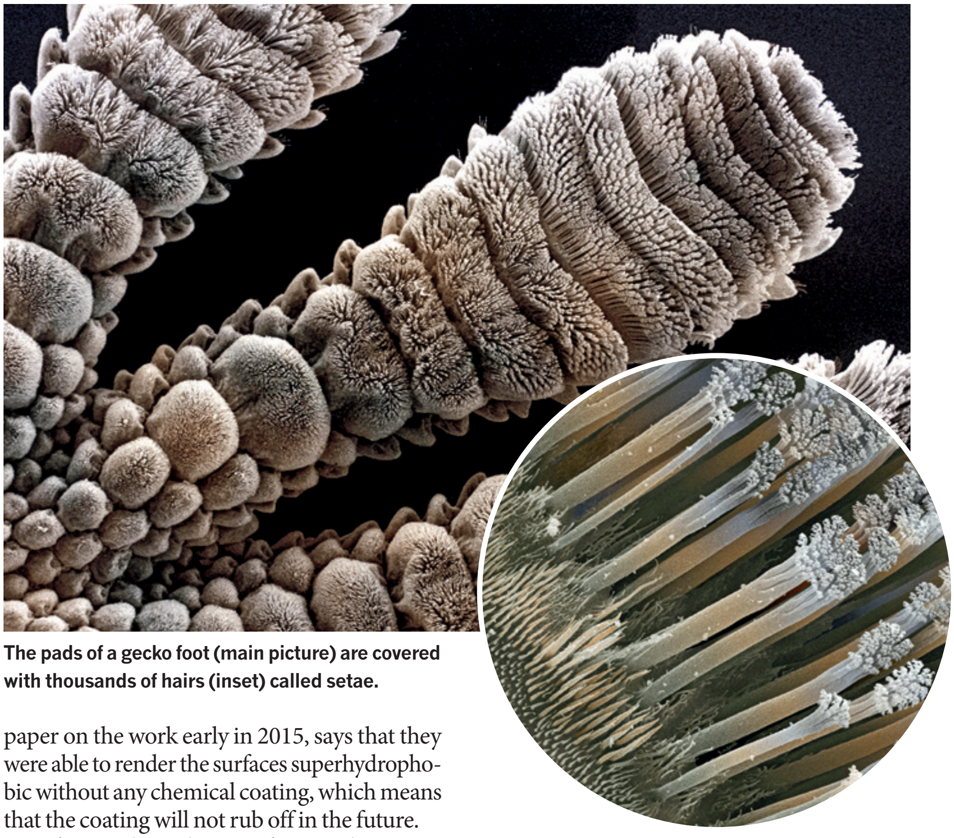
BOTH IMAGES: POWER AND SYRED/SPL

The pads of a gecko foot (main picture) are covered with thousands of hairs (inset) called setae.

form of a coating," he explains. Specifically, he adds, their antioxidant and antibacterial properties would make such coatings useful for medical instruments or food-preparation surfaces.

DROP ZONE

Although getting things to stick to surfaces is useful, there is also value in making surfaces more slippery — for instance to keep them clean or dry or to reduce drag. Mechanical engineer Kripa Varanasi develops nano-engineered surfaces to be hydrophobic so that water runs off. Varanasi found inspiration in a nasturtium plant in his office at the Massachusetts Institute of Technology in Cambridge. "I was one day struck by the fact that the veins were on the top of the leaf, not the bottom," he says.

Until then, plant scientists thought that nature's most water-repellent — also called superhydrophobic — surface belonged to the lotus leaf. Lotus leaves are coated with wax, which chemically repels the water. The wax is arranged in microscopic bumps; the roughness means that there is less contact between the water and the leaf, so a droplet stays rounder and rolls off more easily. Such a surface is also self-cleaning, because the water carries away contaminants; this makes the lotus effect popular among researchers developing surfaces that need to resist moisture or bacterial build-up. But Varanasi wondered whether the nasturtium had veins on the top of its leaves to do the same job as the lotus leaf's waxy bumps.

Varanasi had a reason for studying his office plant. He wanted to see whether he could increase the speed at which water bounces off a surface — specifically, he wanted it to bounce off so quickly that it would not have time to freeze on a plane's wing or to start the process of rusting a metal part. Reduced contact time could also decrease drag for wind turbines in the rain, making them more efficient. Normally when a drop hits a superhydrophobic surface, it briefly flattens out, then recoils into a ball shape and bounces off. On a surface using the lotus effect, Varanasi measured the recoil time at 12.4 microseconds. Then he took pieces of aluminium and milled thin ridges into them, 100 micrometres (μm) high and 200 μm wide, to mimic the nasturtium's veins. Drops that hit the ridges broke into smaller bits, and recoiled in 7.8 microseconds. Those few microseconds can mean the difference between freezing and not[4].

Varanasi guesses that plants may have evolved superhydrophobic properties because droplets that bounce away quickly have less opportunity to deposit bacteria or viruses. He says that butterflies, which need to resist the effects of rain, have even more complicated vein structures on their wings, and he is exploring those to see what effects he can mimic.

Two laser specialists at the University of Rochester in New York have used a laser to mill ridges into pieces of brass, platinum and titanium, and got a similar bouncing effect. Chunlei Guo, one of the physicists who published a paper on the work early in 2015, says that they were able to render the surfaces superhydrophobic without any chemical coating, which means that the coating will not rub off in the future.

In fact, making these surfaces and coatings strong enough to stand up to the wear and tear of use is a challenge for scientists trying to take their ideas out of the laboratory and into manufacturing. "We have to find a way to make this material robust," says Ajay Malshe, a professor of materials and manufacturing processes at the University of Arkansas in Fayetteville. "In biology there's always a constant self-healing process going on, whereas we don't have that" in materials engineered for oil pipelines or plane wings.

Water-repellent surfaces are one challenge for researchers, but surfaces that repel oil (superoleophobic), which would be valuable in arenas from energy to consumer electronics, are even harder to realize, says Bharat Bhushan, a mechanical engineer whose laboratory at Ohio State University analyses the microscopic structures on the surfaces of living things. Because oil has a lower surface tension than water, it is more prone to spreading across a surface, so applying a repellent lotus-like effect requires different chemistries and surface structures. Bhushan makes a surface superoleophobic by covering it with a series of tiny pillars, 14 μm in diameter and 30 μm tall, and coating the surface with a fluorine compound (such compounds are well known for their anti-stick properties; Teflon is a prime example). The set-up traps air pockets beneath any oil near the surface, so the oil cannot stick. Bhushan says that Sony, which makes touch screens for mobile phones, has enquired about using the technique to prevent smudging on its screens. Treating the inside of an oil pipeline in this way could let oil flow more smoothly, reducing the need for higher pressures that push the oil along but can promote leaks.

Bhushan is also tackling the problem of biofouling[5], where bacteria and other organisms form hard-to-remove colonies on a surface. The US Navy estimates that it spends US$56 million a year dealing with biofouling, from cleaning hulls to the extra fuel used to counteract drag. Bhushan covers a surface with pillars of different heights and spacings. Because of the spacing, an individual bacterium is either isolated on top of the pillars or falls into the gaps between, and is unable to link up with its fellows to form a film. "If you have a structured surface, bacteria cannot spread very easily," Bhushan says.

Evolution has produced an endless variety of materials and techniques that might be exploited, so there is no danger of running out of ideas. When faced with an engineering puzzle, Varanasi says he always starts by asking a simple question: "In that situation, what would an insect or what would some other kind of living thing do?" ■

Neil Savage *is a freelance science and technology writer in Lowell, Massachusetts.*

1. Zhang, M. Liu, M. Bewick, S. & Suo, Z. *J. Biomed Nanotechnol.* **5,** 294–299 (2009).
2. Huang, Y. *et al. J. Nanobiotechnol.* http://dx.doi.org/10.1186/1477-3155-11-3 (2013).
3. Sileika, T. S.,Barrett, D. G., Zhang, R., Lau, K. H. & Messersmith, P. B. *Angew. Chem. Int. Ed. Engl.* **52,** 10766–10770 (2013).
4. Bird, J. C., Dhiman, R., Kwon, H.-M. & Varanasi, K. K. *Nature* **503,** 385–388 (2013).
5. Bixler, G. D., Theiss, A., Bhushan, B. & Lee, S. C. J. *Colloid Interface Sci.* **419,** 114–133 (2014).

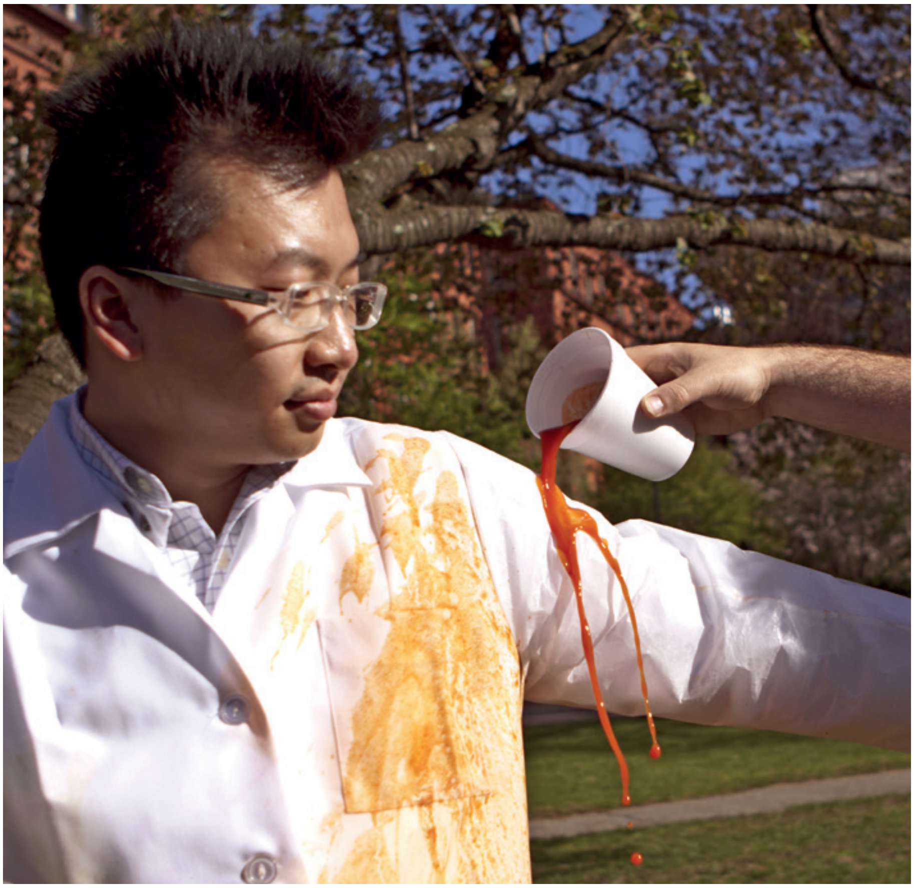

ELIZA R. GRINNELL, HARVARD SEAS

The water-repellent fabric used to make the sleeves of this lab coat was inspired by a carnivorous plant.

TEXTILES

Fabrics of life

Bioinspired fibres and coatings that can repel water, oil and other liquids form the basis of cutting-edge cloth.

BY ELIE DOLGIN

Philseok Kim fills a syringe full of reddish-brown oil and dribbles it onto a swatch of polyester cloth. The viscous fluid beads into a droplet and gradually slides into the bin below, leaving the fabric as clean and stain-free as the day it was milled. Kim then squirts on a splash of red-tinted water, a stand-in for human blood. "It just rolls off," he says.

Kim is a chemist and a founder of SLIPS Technologies, a company in Cambridge, Massachusetts, that derives its name from an innovative approach to creating super-slick coatings: 'slippery liquid-infused porous surfaces'. SLIPS can make a substrate friction-free, simply by locking a thin film of lubricating liquid onto any material. Modelled on the insect-trapping mechanism of the *Nepenthes* pitcher plant, SLIPS could one day become state-of-the-art in repellent surfaces — replacing designs now on the market that themselves were modelled on another plant, the *Nelumbo* lotus flower, the leaves of which wick away water.

According to Scott Healey, vice-president of business development at SLIPS Technologies, the company's platform has a range of potential applications in the energy, automotive, environmental and manufacturing sectors. But it is in cutting-edge textiles that the technology could be first put to use. "We have interest from several textile and apparel companies," says Healey. "The market is coming to us right now."

In October 2014, the company inked its first partnership, with BASF, a German chemical manufacturer headquartered in Ludwigshafen, to produce SLIPS-coated thermoplastics for footwear and other functions. Other companies have expressed interest in co-developing sportswear, specialized garments for construction, tactical suits for the military and medical gowns for hospitals — all enhanced with the SLIPS surfaces. "They have ideas, we have technology, and we're trying to blend those together," Healey says.

SLIPS Technologies, which Kim co-founded with Joanna Aizenberg, a materials scientist at the nearby Wyss Institute for Biologically Inspired Engineering at Harvard University, is part of a new wave of commercial and academic efforts to apply the lessons learned from nature to the textile industry. This strategy has a history dating back at least a century — from the production of rayon (then known as viscose) in the late nineteenth century and acrylic in the 1940s, developed as artificial mimics of silk and wool, to the invention of Velcro, which was modelled on the sticky fruit of the cocklebur plant.

But today the approach has moved well beyond synthetic fibres and fabric fasteners. From breathable clothes to camouflage systems, textile designers are taking inspiration from evolution to help them solve their problems. "People are borrowing and finding great ideas all over the place," says Matt Powell, a sportswear-industry analyst at NPD Group, a market-research firm based in Port Washington, New York. "The technology advances are just staggering."

CREATIVE COATING

Aizenberg and her colleagues first described SLIPS in 2011, showing that the bioinspired technology could repel blood, oil and other complex fluids under a range of harsh conditions and temperatures[1]. That study looked only at solid surfaces; the next challenge was to see how SLIPS fared on fabrics such as cotton and polyester.

Choosing which textiles to test required a unique kind of field research. Cicely Shillingford, one of the lead scientists on the project, sifted through the racks of brand-named athletics gear at a department store. She peered through a magnifying glass to find the densest weave of polyester, which helps to boost the repellency, and settled on a pair of Nike running shorts.

Shillingford and Noah MacCallum, who at the time were students visiting from the University of Waterloo in Ontario, Canada, put the SLIPS-treated running shorts and six other SLIPS-enabled fabrics through a battery of tests. They twisted and rubbed the samples to see how the coating would stand up to physical damage. They analysed the repellency using two assays defined by the American Association of Textile Chemists and Colorists, and they examined breathability using a standard water-vapour transmission test[2]. "Pretty much on every score, except for breathability, we had much better results than anything that other [repellent] fabrics would have," says Aizenberg.

Because SLIPS relies on impregnating materials with lubricant, "it's a direct trade-off between breathability and repellency", explains Shillingford. The technology could be used today in clothes for which breathability is not paramount, such as those worn by construction workers to protect them from exposure to dangerous chemicals. But for active wear in which moisture

MAIN IMAGE: IAN SHAW/ALAMY; INSET: PAUL D. STEWART/SPL

release is important, some scientists have turned to a different botanical artefact.

MMT Textiles was established in 2009 to commercialize a type of fabric that mimics the structure of pine cones by opening and closing depending on the humidity in the microclimate of the garment. Ordinarily, when a fabric gets wet, the fibres swell as they absorb moisture. London-based MMT Textiles' fibres behave differently: they incorporate two synthetic polymers that are stuck together in a single fibre. One polymer is hydrophobic, which means that it resists water, whereas the other is hygroscopic and absorbs moisture. The tension between these two layers causes the fabric to curl and shrink in response to water vapour — in the same way that a bimetallic strip bends in response to temperature changes. Under dry conditions, the MMT Textiles fabrics open up like a pine cone, which reduces airflow and increases the fabric's insulation properties. Under wet or sweaty ones, "the yarns become tighter, which improves the air permeability of the garment," explains Veronika Kapsali, a biomimetic-fashion researcher at Northumbria University in Newcastle, UK, and technical director of MMT Textiles.

Like SLIPS Technologies, MMT Textiles is partnering with several international apparel companies to develop sportswear, denim, bedding and other materials. Kapsali expects to have a product on the market by early 2016. Switzerland's Schoeller Textiles, based in Sevelen, also has a pine-cone-inspired technology, called c_change. This fabric opens and closes depending on temperature, and thus releases, when necessary, warm and moist air from the interior of the clothing. Several high-end lines of outerwear, including one tailored for professional yacht racing, already incorporate breathable c_change designs.

WHEN APPEARANCE IS DECEPTIVE

The responsive features of biomimetic textiles, such as those that improve repellency and breathability, might go unnoticed by the naked eye. But for other biologically inspired designs, changes in the appearance of the fabric are the desired goal.

Some companies have taken inspiration from the South American blue morpho butterfly (genus *Morpho*) and are creating structurally coloured fibres with no dyes or pigments. The butterfly's iridescent colouring is not from a pigment but is produced when tiny scales on its wings reflect the light. The companies mimic this effect by laminating dozens of ultra-thin layers of polyester or nylon, and the thickness of the layers, their patterning and the different refractive indices of the materials give rise to a variety of colours. The technology's proponents claim these colours will never fade, and that the manufacturing is environmentally friendly because no chemical colouring is involved. "The ability to colour things just by light refraction is going to be really cool," says Michael Ellison, a polymer-fibre physicist who studies biomimetic materials at Clemson University, South Carolina.

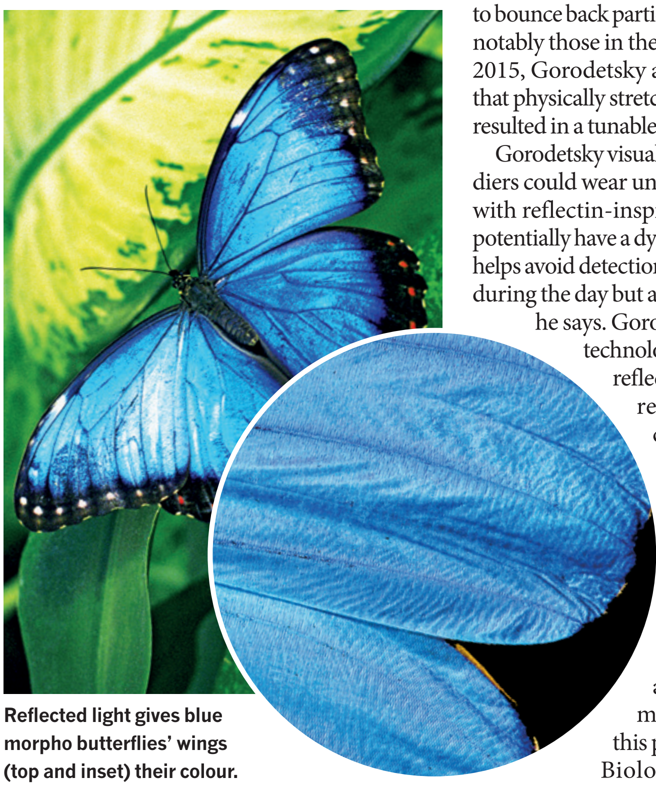

Reflected light gives blue morpho butterflies' wings (top and inset) their colour.

The US military is also expressing a growing interest in colour-changing fabrics. These focus on cephalopods — marine invertebrates such as squid and octopus that naturally alter their skin patterns in response to different visual backgrounds — to develop more-effective camouflage techniques. In 2014, researchers at the University of Illinois at Urbana–Champaign, funded by the US Office of Naval Research, reported the construction of cephalopod-inspired flexible sheets that can 'read' surrounding patterns and adapt to match the environment[3]. The artificial skin emulates the mottled patterns of cuttlefish, with their small-scale light and dark patches. A combination of sensors and colour-changing materials enables the sheets to match the backdrop. The prototype is small and only works in black and white, but its designers say the material can be scaled up and adapted to encompass the full colour spectrum.

> ***"You could have a dynamic camo patterning that helps avoid detection in visible light."***

The influence of cephalopods extends beyond the visible spectrum. Alon Gorodetsky, a materials scientist at the University of California, Irvine, is drawing inspiration from these animals to fabricate materials for infrared stealth applications. He is working with a protein called reflectin, which is normally found in the skin of squid. Using various chemical, mechanical and electrical stimuli, he has found a way to fine-tune the optical properties of coatings based on reflectin to bounce back particular wavelengths of light — notably those in the near infrared. In February 2015, Gorodetsky and his colleagues showed that physically stretching films of these proteins resulted in a tunable shift in reflectance[4].

Gorodetsky visualises a scenario in which soldiers could wear uniforms coated or patterned with reflectin-inspired materials. "You could potentially have a dynamic camo patterning that helps avoid detection not only in the visible light during the day but also in the infrared at night," he says. Gorodetsky is also adapting the technology to create fabrics that can reflect longer-wavelength infrared. "This thermocomfort cloth would let a person dynamically regulate how their body emits thermal radiation," he says. In December 2014, Gorodetsky received a US$2.4 million grant from the Advanced Research Projects Agency-Energy, an arm of the US Department of Energy, to explore this possibility.

Biologically inspired materials might also lead to swifter swimmers. Swimwear companies such as Speedo have claimed to make shark-skin-like fabrics, but George Lauder, an ichthyologist at Harvard University, has demonstrated that the Speedo suits that were banned after the 2008 Olympics do not contain the microscopic shark scales, called denticles, that reduce drag[5]. Using a three-dimensional (3D) printer, Lauder last year constructed true artificial skin of the shortfin mako shark (*Isurus oxyrinchus*) and showed that it not only limits drag but also increases thrust[6].

Unfortunately, current manufacturing limitations preclude the production of true shark-skin-like swimwear or dive suits. "You can't 3D print this at scale with the surface structure that we want," said Lauder from his Harvard office, with a sample of the flexible, scaly, artificial shark skin in his hand. So for now, the research continues. Lauder is even teaming up with Aizenberg, his Harvard colleague, to see whether SLIPS coatings applied to his artificial shark skin can create a superfast and water-repellent material. Pitcher plants and mako sharks might never meet in nature. But the insights they bring to the lab could inspire the next biomimetic fabric. ■

Elie Dolgin *is a science writer in Somerville, Massachusetts.*

1. Wong, T. S. *et al. Nature* **477,** 443–447 (2011).
2. Shillingford, C., MacCallum, N., Wong, T. S., Kim, P. & Aizenberg, J. *Nanotechnology* **25,** 014019 (2014).
3. Yu, C. *et al. Proc. Natl Acad. Sci. USA.* **111,** 12998–13003 (2014).
4. Phan, L. *et al. J. Mater. Chem. C* http://dx.doi.org/10.1039/C5TC00125K (2015).
5. Oeffner, J. & Lauder, G. V. *J. Exp. Biol.* **215,** 785–795 (2012).
6. Wen, L., Weaver, J. C. & Lauder, G. V. *J. Exp. Biol.* **217,** 1656–1666 (2014).

JONATHAN WILKER

Mussels' adhesive threads are inspiring scientists to create glues that can form bonds underwater.

POLYMERS

Secrets from the deep sea

The mechanism used by mussels to stick to slippery rocks is the idea behind glue that could mend broken bones.

BY ANDREW R. SCOTT

Fifteen years ago, while being thrown about by heavy seas during a scuba dive off the California coast, Jonathan Wilker was impressed by the mussels sticking firm and untroubled to the rocks surounding him. Wilker, a chemist and materials engineer, wondered how the molluscs managed to hold on. In particular, he thought about how the mussels could form a strong adhesive bond under water, given that most artificial glues require completely dry surfaces before application. The thought inspired him to embark on a long journey into the world of marine polymers that has become the foundation of his chemical research.

Wilker is not alone in his quest. Many other scientists have been inspired by natural polymers leading to a global effort to create a range of materials such as glues, structural components and smart, responsive materials for medicine and industry.

The lessons that Wilker learned from the Californian mussels have helped his research group at Purdue University in West Lafayette, Indiana, to get completely submerged surfaces to bond. Although a few synthetic underwater adhesives already exist, Wilker says that preliminary tests suggest his group have made much stronger ones. Some of the biomimetic polymer glues the researchers have developed are now ready for production and commercialization. One of Wilker's particular interests is in using glues to repair wounds. When giving presentations about the medical potential of his work he often asks, "Wouldn't it be better if we could just glue you back together and if we could put sutures out of business?" Speaking from his office, he says that he hopes to find a bonding material that could fix a broken bone and is stronger than the bone itself. That explains the noise drifting into his office from a saw cutting through bones in another room. Pausing to close the door, he apologizes for the "kind of gross" sound and then continues enthusiastically about the possibilities for his wet-setting glues that incorporate ideas culled from mussels and oysters.

MUSSEL-PROTEIN MIMICRY

The secret to mussel glues is their unusual protein molecules. Specifically, many of the tyrosine amino acids have been converted into 3,4-dihydroxyphenylalanine (DOPA) groups by adding extra hydroxyl (OH) groups to the tyrosine six-carbon rings that protrude from the protein chain. This modification allows crosslinks to form between the protein chains that allow the glue to set. Wilker's laboratory found that naturally occurring iron also seems to be involved, creating an organic–inorganic glue that is not yet fully understood.

Why not extract mussel or oyster glues directly from the animals? Wilker says that is not feasible: each animal makes only tiny amounts of adhesive and so large-scale harvesting is not possible. Wilker's solution to this problem uses a synthetic polymer based on a polystyrene that has been modified in the laboratory to mimic the long chains of mussel proteins, with DOPA-like groups attached to duplicate the wet-setting crosslinking abilities of the mussel glues. The resulting polymers are then combined with simpler chemicals such as iron, which is found in natural mussel glues, to create a range of adhesive options[1].

"We now have adhesives that, under some circumstances, are stronger than superglue," says Wilker. Medical applications will require rigorous safety and biocompatibility testing. In a promising first step, experiments in late 2014 have found no toxicity to growing cells. The glues are now being trialled for bonding soft tissues and broken bones in the laboratory. Domestic and industrial applications such as adhesives for buildings, vehicles or even false fingernails could be approved more quickly than those for clinical uses; with this in mind, Wilker applied for a patent for the new polymeric adhesives, which was issued in 2014. "We just need to hook up with the right industrial partner now," says Wilker, adding that he is currently sending samples of his glues to a variety of companies for testing. If the results are

FRANS LANTING, MINT IMAGES/SPL

as positive as Wilker hopes, artificial versions of mussel glue may soon make their way into industry and eventually medicine.

THE SENSITIVITY OF SEA CUCUMBERS

But it is not only mussels and oysters that have piqued the interest of materials scientists. Sea cucumbers have evolved different protective features that researchers are trying to exploit. When threatened by predators, some species of the ocean-floor dwelling, soft-bodied animals can voluntarily stiffen in less than a second so that they become less appealing to prey. Sea cucumbers are able to make the reversible transformation because they possess a natural material that contains fibrils of the protein collagen mixed with a soft matrix. Regulatory protein molecules in the matrix can change the number of cross-links between the collagen fibrils so that the creature is able to switch rapidly between its soft and stiff states.

Jeffrey Capadona and colleagues realized that such variable flexibility might be exactly what they needed to make better microelectrodes for brain implants. Capadona is a biomaterials scientist and neural engineer at Case Western Reserve University and at the US Department of Veterans Affairs Medical Center, both in Cleveland, Ohio. His research is mainly focused on implants that receive signals from the brain and which could also carry signals back into the brain or to other parts of the body. A key long-term aim of clinical researchers, including some at Case Western, is to restore motor function in people with paralysis and perhaps even to improve cognitive functions. Alzheimer's and multiple sclerosis are examples of possible diseases that might be targeted in this way.

When conventional, stiff electrodes are implanted into the brain they can damage the tissues and cause inflammation. A flexible and biocompatible material would solve that problem, but it would be difficult to insert. "We needed something that was stiff to get it in but then softened once it was in," says Capadona. The sea-cucumber system suggested a model for a substrate that could surround a thin metal electrode and bring the necessary changes in rigidity to the combined structure.

"We looked to nature for a unique design to inspire ours."

Capadona and his colleagues developed a system of natural cellulose fibrils they call 'whiskers', which they combined with a synthetic polymer called polyvinyl acetate[2]. When dry, the material is rigid — the hydrogen bonds in the cross-links hold the cellulose in a semi-crystalline state — but when embedded in the brain it absorbs water and swells to become flexible. Capadona explains that fine control over the changes in stiffness and degree of swelling is crucial, rather than just a simple issue of changing between soft and stiff states. "This is why we looked to nature for a unique design to inspire ours," he says.

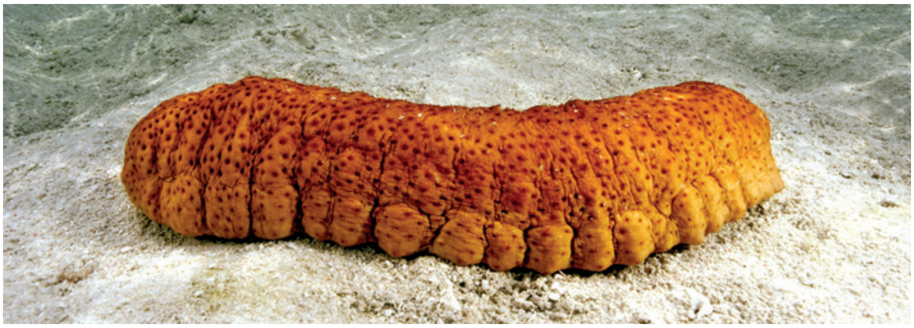

Studying sea cucumbers is helping researchers to develop advanced brain electrodes.

Tests of electrodes embedded in this material are being conducted on rats, with a goal of soon moving to trials on non-human primates — and then eventually to humans. "It has proved to be one of the most successful approaches for minimizing tissue damage and inflammation," says Capadona of his most recent results, reporting negligible inflammation or loss of neurons[3]. So far, however, the only tests have been short term, involving rats under anaesthesia. Capadona says that his group must now undertake longer term studies.

Although he is focused mainly on developing functional electrodes for brain–computer interfaces, Capadona also envisages less sophisticated medical uses for the technology. Catheters and stents, for example, need to be rigid for insertion but flexibile once in place. His polymer-containing composite materials have even attracted some interest from toy manufacturers. He is not sure what applications toy designers might have in mind, but, he says, "It's fun to speculate."

STRONG AND SMART HYDROGELS

Much of the research into biomimetic polymers involves hydrogels — materials comprising networks of polymer chains that can absorb or release water as conditions change. Applications range from the mundane, such as high-absorbency diapers, to pioneering medical uses to help wounds to heal and biomedical implants to be accepted by the body. Fariba Dehghani, a bioengineer at the University of Sydney in Australia, has developed a biomimetic hydrogel based on natural gelatin and a mixture of synthetic polymers that could be used to regenerate bone[4]. In experiments *in vitro*, the hydrogel provides a home in which to grow bone cells that could be used to help repair fractures or rebuild limbs. The results of compression and strain tests have led Dehghani to claim that her material can withstand significant forces and should be assessed for bone-regeneration applications.

In addition to providing the substrate in which cells can live and grow, a key feature of many natural biological polymers is their ability to respond to a wide range of stimuli. In efforts to replicate this ability, some researchers are developing hydrogels that can mimic living tissues by swelling and then shrinking in response to chemical triggers and to changes in conditions such as temperature, pH, electric and magnetic fields and light levels. Bioengineer Shyni Varghese of the Bio-Inspired Materials and Stem Cell Engineering Laboratory at the University of California, San Diego, says that in response to any of these stimuli, a hydrogel could be used to achieve multiple useful actions such as releasing a drug, opening and closing implanted valves and stents or sealing wounds.

"Nature has truly been an inspiration in designing stimuli-responsive hydrogels with dynamic functions and features," says Varghese, who co-authored a review of current and potential applications[5]. He emphasizes that most of the advances are still at the proof-of-concept phase, but as an example of the technology already on the market he cites a class of temperature-responsive polymers known as poloxamers, which are moving into drug-delivery uses[6]. Varghese points to self-regulated insulin-delivery devices and hydrogel sealants for stomach perforations as applications that are moving out of the lab and into clinical use.

Conducting extensive real-world trials and gaining safety approvals are significant scientific challenges faced by many researchers on the path from laboratory to commercialization, but Wilker points out that having the correct technology is only part of the story. "You have to have the right personnel, the right landscape for competition and the right investors who put in enough money on a reasonable timeframe," he says. For Wilker and other researchers, the pieces are all coming together to make widespread use of biomimetics a reality. Years after his rough-but-inspiring scuba dive, Wilker hopes to take a dive into the turbulent waters of the marketplace very soon. ■

Andrew R. Scott *is a science writer based in Perth, UK.*

1. Meredith, H. J., Jenkins, C. L. & Wilker, J. *J. Adv. Funct. Mater.* **24,** 3259–3267 (2014).
2. Jorfi, M., Skousen, J. L., Weder, C. & Capadona, J. R. *J. Neural. Eng.* **12,** 011001 (2015).
3. Nguyen, J. K. *et al. J. Neural Eng.* **11,** 056014 (2014).
4. Fathi, A. *et al. Eur. Polym. J.* **59,** 161–170 (2014).
5. Lim, L. H., Hwang, Y., Kar, M. & Varghese, S. *Biomater. Sci.* **2,** 603–618 (2014).
6. Shubhra, Q. T. H., Tóth, J., Gyenis, J. & Feczkó, T. *Polym. Rev.* **54,** 112–138 (2014).

DANITA DELIMONT/GETTY

The strong yet flexible shell of the armadillo is helping biomedical scientists to devise super-materials.

STRUCTURE

Artificial armour

Researchers are borrowing tricks from armadillo shells and mother-of-pearl to create replacements for human bone and to develop a new generation of protective clothing.

BY KATHARINE SANDERSON

Would you put such trust in your bones to hold you up and move you around if you knew they were made from jelly and chalk? Hydroxyapatite is the inorganic, mineral component — a brittle, white, calcium-based, chalky material. Collagen, the organic, carbon-based part of bone, "is very similar to gelatine", says André Studart, a materials scientist at the Swiss Federal Institute of Technology in Zürich.

Yet from these weak raw materials, nature produces a strong, flexible, self-healing structure. Living cells guide the growth of a complex, rigid frame that houses blood vessels and supports the entire body. Trying to better understand this complex structure and how it works has kept teams of scientists busy for many years. And bone is not the only natural structure worth investigating. Nacre, also known as mother-of-pearl, is extraordinarily fracture-resistant. Dentin in the teeth is similar to bone, and is comprised mostly of calcium minerals, water and organics in an intricate structure that, beneath the enamel layer, is strong enough to worry steak or crack nutshells. Armour plates seen on fish and armadillos are models of materials that are flexible, puncture-proof and water-resistant. Research reported in February 2015 suggests that limpets' teeth, endowed with nanometre-scale fibres intertwined with minerals, may be the strongest material that nature has crafted[1].

The hope: if scientists could learn some of the tricks used to make these types of materials, perhaps people, too, could make self-healing, super-strong items from cheap and abundant ingredients, or biological implants that work as well as the body parts they want to replace. Humans, of course, need not be limited to particular substances found in living things. Perhaps the tricks nature has perfected over millions of years might be applied to graphene, Kevlar, titanium or glass, to create even more advanced materials.

Researchers are making steady progress towards recreating what has been honed over thousands of years of evolution. It is now possible to make artificial nacre, although a fully synthetic bone replacement is still a distant goal. Borrowing tricks from bone has enabled the manufacture of shatterproof glass, however. Materials scientists are working with the military to develop armour based on some of the principles that fish use to protect themselves. But evolution has had one luxury that humans lack: "Nature doesn't have the time restraints we have," says materials scientist Eduardo Saiz from Imperial College London.

TWISTED TALES

The first part of the challenge is to understand how these materials are built. Bone, nacre and other tough, natural materials have complex structures at the atomic and molecular level, at the nanometre scale, which in turn influences their micrometre-scale structure — and so on up to a whole shin bone or left molar. Working out what all these intricacies are at each scale requires a wide range of state-of-the art techniques, including atomic force microscopy, X-ray analysis and tomography (which looks at materials slice by slice) says Christine Ortiz, a materials scientist from Massachusetts Institute of Technology in Cambridge. She hopes to borrow tricks from these materials — but that will only be possible by properly understanding them at each level of the structural hierarchy.

In bone, this hierarchy is well understood. It begins with long molecules of collagen: three chains twist into nanometre-sized helices, which then come together to form fibrils about one millimetre thick. The fibrils weave together to make filaments that are around ten times as thick, leaving just enough room for the hydroxyapatite to fill the holes, adding stiffness. The thicker filaments organize into a flat, foil-like structure and roll up to form tubes, called osteons, that allow blood vessels to run through bone's interior. Many osteons together make a fully formed piece of bone.

The cells alter the chemistry around the collagen fibres to dictate what kind of structure, or what level of mineralization, occurs at each site. Studart's aim is to mimic this level of intricacy, but that is a long way off. "We're far from being able to reach the organization of building blocks we have in nature," he says. "We lack a deep understanding of what the cell really does."

Nevertheless, researchers are starting to borrow ideas from this hierarchical complexity to try and create their own super-materials. Studart, for one, is seeking other ways to control how materials organize themselves, in a crude version of what happens in bone. "I take the engineering approach," he says — which in his case, has led to magnets. He and his team add small amounts of strongly magnetic nano-sized particles to composite materials made from tiny flakes and rods of alumina, polyurethane and other polymers with varying elastic properties, all of which are swimming in a solvent. Application of a weak magnetic field causes the magnetic nanoparticles to drag the fibres in specific directions to create an organized structure — much like collagen fibrils in bone. Once the flakes and rods are in position, they can be frozen in place by evaporating the solvent. Studart has used this method to make composite materials that are tough and durable and have some memory of their shape when deformed.

But the alignment of molecules to provide a material with stability is only one small part of what occurs in the natural world. Another trick is to use the same building blocks to make materials with different physical properties. Think of tendons attached to a bone: many of the same starting materials, particularly collagen, combine in different quantities and with different structures to have opposite functions in a joint. At the bone end, they are calcified and very hard. At the tendon end, the collagen is much less calcified, and forms soft, flexible tissue. Studart is trying to work out how to make materials with a compositional gradient in the laboratory[2] and has made onewith elasticity that varies by five orders of magnitude. That is a large improvement on natural bone–tendon connections, where the elasticity spans a mere two orders of magnitude. In nature, the range in physical properties alters depending on how much hydroxyapatite reinforces collagen fibrils. Studart, similarly, gets his wide range of elasticity by reinforcing polyurethane with differently sized particles of tougher aluminium oxide or a synthetic clay.

It will be a while before artificial materials replace worn out vertebrae or tendons. Capturing the intricacies of bone and nacre in one step is "very complicated", says Saiz. He pins some hope on the advent of three-dimensional (3D) printing, which can, in theory, print any structure when supplied with a range of materials. But he notes that machines capable of printing structures with nanometre-scale features are not currently available.

SMALL DETAILS MATTER

The nanoscale structure of bone, nacre and teeth consists of flake-like mineral pieces, arranged like bricks in a wall, with the organic component making up the mortar. In nature, specialized proteins inside bone cells are responsible for getting the mineral molecules to form in the right places in that wall-like pattern — a process called biomineralization. This bottom-up way of building is difficult to recreate in the lab, says François Barthelat, a materials engineer from McGill University in Montreal, Canada, not only because of the physical challenge of manipulating nanoscale bricks, but also because the nature of the forces on the surface of the materials radically changes at such a small scale.

PHIL DEGGINGER/ALAMY

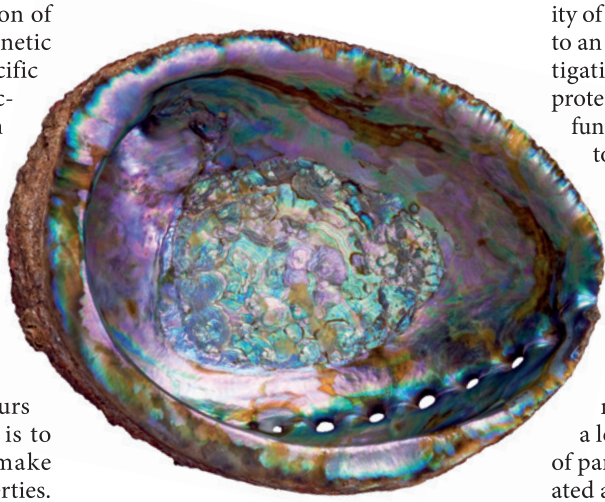

The microstructure of nacre has inspired researchers to develop low-cost, strong materials.

Some materials scientists, including Saiz, think that to make a synthetic mimic of bone it is essential to recreate all the features at each level in the structural hierarchy: nano, micro and macro. But others believe it might be possible to skip the tiniest level of the hierarchy. "You don't have to work at the nanoscale to get good properties," says Barthelat. Instead of building up a wall nanobrick-by-nanobrick, Barthelet approached the problem from another angle. His team etched into glass a 3D brick wall pattern similar to that in bone, but with the bricks about 200 micrometres wide rather than nanometres[3]. The team used a laser that could penetrate the glass and etch not only on the surface, but inside the glass sheet as well. Even these micrometre patterns have an effect. "It totally changes the way the material works," Barthelat says of this bio-inspired technique. The resulting glass was 200 times tougher than non-etched glass, and could even be bent out of shape. The reason, Barthelet says, is that patterns etched into the glass are conduits for the destructive energy carried in a propagating crack, and give that energy a route of escape out of the material without shattering it. He hopes that using his approach, artificial materials such as glass or ceramics could be made tougher or more durable than they currently are, and perhaps even superior to natural materials.

"We're far from being able to reach the organization of building blocks we have in nature."

FISH OUT OF WATER

To truly make the most of these super-strong natural materials means mimicking not only their structures, but also the way they are used. Take fish scales, which offer tough armour for the animal even as it is flexing, flipping and squirming. Intrigued by this ability of fish skin to offer such good protection to an uneven surface, Ortiz has been investigating how the structure of such natural protective surfaces is related to the way they function, and in doing so she is finding ways to make some remarkably effective protective clothing for humans.

Her team examined how scales of different species of fish provided armour against bite attacks. They found that fish have scales arranged in many layers, with scales of different sizes, each layer having its own unique deformation mechanism, mechanical properties and ability to bear a load. They made scaled-up 3D models of parts of the fishy armour. They also created a computational model that they used to design custom armour for a human body, which would offer protection to vulnerable joints parts, including shoulders, knees and elbows, as well as the flatter areas such as the torso. Actual armour made for use in the field is some way off. Ortiz has a patent on the shape of such armour, but she says that the patent and the computer design are just the first steps to actually making the armour with all its intricacies.

The artificial structural materials made so far are not yet as sophisticated as bone, fish scales or nacre — but perhaps they don't need to be. Graphene, a form of carbon consisting of single-atom sheets of molecules laid out in a honeycomb pattern, is the strongest material ever measured — and so once graphene production has been mastered, crafting intricate 3D arrangements from it might turn it into the toughest, strongest, most flexible material by a factor of hundreds. By combining natural building processes with synthetic materials, lightweight, sensitive, responsive, self-healing and tough structures will be the future of super-materials. "We should surpass nature," says Studart. The difficult part is to first understand nature. ■

Katharine Sanderson *is a freelance journalist based in the UK.*

1. Barber, A. H., Lu, D. & Pugno, L. M. *R. Soc. Interface* http://dx.doi.org/10.1098/rsif.2014.1326 (2015).
2. Libanori, R. *et al. Nature Commun.* **3,** 1265 (2012).
3. Mirkhalaf, M., Khayer Dastjerdi, A. & Barthelat, F. *Nature Commun.* **5,** 3166 (2014).

PAUL PRICE

ARTIFICIAL ORGANS

Honey, I shrunk the lungs

Miniature versions of hearts, lungs and other organs are heralding a bright future for drug research and discovery.

BY MICHAEL EISENSTEIN

In 1537, the Swiss German scientist Paracelsus conceived a method for creating a miniature person who "will look somewhat like a man, but transparent, without a body". However, his protocol for generating what he dubbed a homunculus was an unsavoury blend of alchemy and inter-species breeding.

Now scientists are having another attempt at the homunculus concept — but this time they are using advanced biomaterials, engineering techniques and physiological insights to coax cells to grow into simplified, but functional, miniature versions of hearts, lungs and other human organs. Set on microchip-like devices, several of these organs can be connected by artificial circulatory systems to yield 'human-on-a-chip' devices that usually measure no more than a few centimetres in length.

The goal is to 're-humanize' biomedical research. For generations, scientists have worked mainly with cells grown in single layers on flat, artificial surfaces — typically hard plastics such as polycarbonate that bear no resemblance to living material — in pools of synthetic cell-culture media comprising cocktails of only the most essential ions, nutrients and growth factors.

A DIFFERENT APPROACH

In contrast, the bioengineered homunculi that researchers such as Donald Ingber, founding director of Harvard University's Wyss Institute for Biologically Inspired Engineering in Boston, Massachusetts, and his colleagues are devising aim to recreate the physical structures, forces and interactions that affect cells within living organs and tissues. The resulting experimental models are more realistic than conventional cell culture, more relevant than laboratory animals, but still small enough to fit under a microscope. They promise to eliminate a lot of the false starts and dead ends in the challenging and expensive world of drug discovery and testing (see 'Conceptual view of a human-on-a-chip').

The current system of drug development, which requires multiple rounds of animal testing, can lead to problems because humans often metabolize chemical compounds very differently from rodents and other test animals. For example, troglitazone was initially approved in the mid-1990s for treating diabetes in the United States, Japan and the United Kingdom, but was withdrawn in 2000 after causing liver failure in hundreds of patients — including 63 deaths. The toxicity did not show up in earlier rat experiments.

Actual human tissues can be used to complement animal testing, but tissue slices are short-lived and hard to come by. Researchers can also extract primary cells, such as liver hepatocytes, from the relevant human organs but these gradually lose their functional identity when cultured on flat plastic. Even more daunting is the fact that it is difficult to recreate in cultures the complex interplay between communities of multiple cell types that enable an organ to function, says John Wikswo, a physicist and biomedical engineer at Vanderbilt University

in Nashville, Tennessee. "Heterogeneity is a big deal," he says.

Advances in biomaterials now enable scientists to begin mimicking this organization by taking advantage of how cells naturally arrange themselves within nests of protein fibres known as the extracellular matrix. These fibres not only provide a physical scaffold, but also interact with receptors on the surface of the cells to trigger essential signals that regulate cell growth and development. Although the natural structure of the extracellular matrix is difficult to replicate, simply coating plasticware with a carpet of extracellular matrix proteins can give cultured cells a comfortable surface to latch on to and help to restore some of their capacity for self-organization.

FORCES OF NATURE

Sangeeta Bhatia's biomedical engineering team at the Massachusetts Institute of Technology (MIT) in Cambridge developed a greatly improved liver culture model[1] by depositing human hepatocytes onto islands of the extracellular matrix protein collagen. These were then surrounded by other cell types, such as skin fibroblasts, which interact with these hepatocyte islands to help maintain liver-specific metabolic function and gene-activity profiles that would otherwise be lost. "We can basically create a miniature human liver on a dish," says Bhatia. This has enabled her team to study liver diseases caused by human-specific pathogens that are extremely challenging to model in animals, such as hepatitis and malaria.

These culture systems still lack the multi-layered three-dimensionality of real organs, a feature that can greatly affect the behaviour of cells within a tissue. Researchers are therefore attempting to make the systems more realistic by endowing them with more volume using specialized materials and even cell-printing processes to construct solid volumes of organized, cultured cells. Various water-based hydrogel polymers can be coaxed from a liquid to a solid state by changing the pH or by using lasers, allowing scientists to entrap defined cell populations within solid matrices. Bhatia's inVERT technique[2] uses moulds to generate three-dimensional (3D) patterns of hydrogel-encased cells, which can then be overlaid with additional layers of cells — sequentially assembling different cell types into highly designed, customized tissue communities in a manner similar to the way in which a printmaker adds layer after layer of stencilled colours to produce a complete artwork.

These 3D systems may be more physiologically accurate than conventional Petri cultures, but they still fail to recapitulate many core organ functions because they are static. Within the dynamic environment of the body, physical forces create pressure and tension on environment-sensing cell-surface proteins. In a process known as mechanotransduction, those physical forces generate biochemical signals that can trigger dramatic changes in cellular organization and behaviour. The most universal of these is the shear force generated by blood flow; the endothelial cells that line blood vessels form a chaotic sprawl in static culture, but reorganize and align when subjected to directional fluid flow. The bioreactor systems that scientists have long used to replicate such flow are costly and bulky. As an alternative, techniques and tools developed for silicon-chip construction are being adapted to create scaled-down bioreactors based on microfluidics — glass-and-polymer-based devices in which tiny pumps, valves and channels direct liquids similarly to how a microchip moves electrons.

"We can basically create a miniature human liver on a dish."

Organ-on-a-chip systems can also harness other biologically relevant forces, which is especially evident in the work of researchers such as Ingber. To mimic the conditions of the lung within a microfluidic device, Ingber's team cultivated epithelial cells derived from human alveoli and endothelial cells derived from blood vessels on either side of a porous polymer membrane. The cells on one side were exposed to air; those on the other side to flowing liquid. By periodically applying a vacuum to adjacent cavities in the chip, the scientists could cause these membrane-bound cell sheets to stretch and relax, mirroring the rhythmic strain of breathing. This artificial lung reacted in a human-like way when exposed to bacteria and to inflammation-causing nanoparticles, and allowed Ingber's team to explore the mechanisms underlying fluid accumulation within the lungs of people with pulmonary oedema[3]. By selectively applying physical forces in culture models, his group has also been able to re-enact the real-world function of a host of other organ systems using just a handful of cell types. "All we do is change the physical microenvironment and we observe behaviours that nobody else sees," he says. "We saw the same thing in models of the gut with peristalsis and the kidney with liquid flow, and we were surprised by the level of fidelity and robustness."

COMMUNITY ORGANIZERS

Researchers say that the greatest promise for this kind of technology will come when organs-on-a-chip are integrated into simplified simulations of the body. This might yield significant benefits in drug testing, where the full effects of a compound are often not clear until processing in the liver or excretion from the kidney is accounted for.

Michael Shuler, a biomedical engineer at Cornell University in Ithaca, New York, was among the pioneers in this field. Shuler's team analyses the toxicity of various chemicals using what Shuler calls a microscale cell-culture analogue device, which steadily pumps cell-culture media between culture compartments representing different mammalian organ systems. As an initial test, the team used the household chemical naphthalene (the active ingredient in mothballs) in a multi-organ device containing lung, liver and fat tissue. The study revealed how naphthalene is converted by the liver into metabolites that cause cell damage and death in the lung — even though naphthalene itself is relatively harmless to this organ. "If we removed the liver component we no longer observed this cell death in the lung tissue," says Shuler. Other multi-organ systems followed, evolving from two-dimensional (2D) cultures on porous membranes to more complex aggregates within 3D hydrogels and other matrices.

At the Wyss, Ingber and his colleagues are in the process of linking up large numbers of their miniaturized organs; in February 2014, they reached a key milestone of building an automated system that could keep a ten-organ chip alive and functional for longer than a week. Ingber, Shuler and others have also shown that simpler multi- or single-organ constructs can be sustained for up to a month — sufficient for analysing toxicity caused by long-term exposure to a chemical or product.

But linking multiple organs is not as simple as connecting biological Lego. Some of the biggest challenges involve scaling *in vitro* systems to match human physiology[4], such as maintaining proper fluid volume relative to tissue volume. Microfluidic systems that stream small quantities of culture media through narrow channels containing 3D cell structures can mirror real life better than large-volume culture systems, but these systems must still

FRANK E. BLOCK, III; VIRGINIA PENSABENE, DMITRY MARKOV & JOHN P. WIKSWO

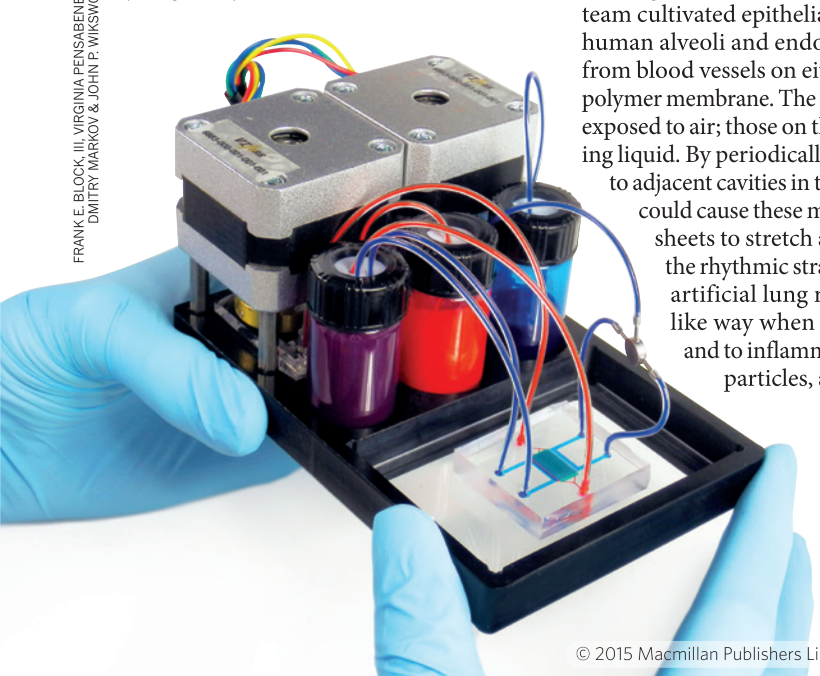

A mock-up of a neurovascular unit-on-a-chip being developed at Vanderbilt University.

CONCEPTUAL VIEW OF A HUMAN ON A CHIP

Researchers are using advanced biomaterials and other technologies to coax cells to grow into simplified, but functional, miniature organs that can be interconnected into a simulation of the human body.

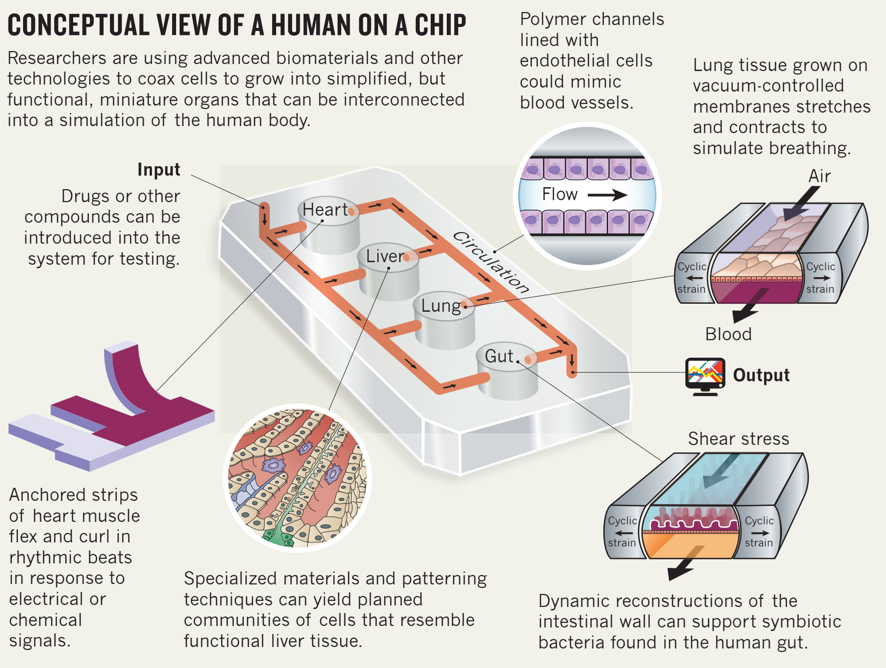

be carefully designed. "If you get the volumes wrong, suddenly the liver and the kidney are each swimming in oceans of media and they don't know that the other organ exists," says Wikswo. Relative size also matters: building a miniature human body-on-a-chip does not merely involve shrinking every organ 1,000-fold. Organ size is determined by diverse factors, including an organism's mass, surface area and fluid volume. For simplicity's sake, many researchers are looking to scale organs on a functional basis to preserve their relative physiological output, with tissue compartments sized such that the simulated lung draws in the appropriate amount of oxygen with each breath, and the liver metabolizes biomolecules at a proportional rate. "I essentially treat each organ as a chemical reactor," says Shuler.

Substrate materials also remain a challenge. Most organ- and body-on-a-chip devices are constructed from polydimethylsiloxane (PDMS), a polymer that is cheap, transparent, non-toxic and easily developed into prototypes. But PDMS also absorbs small molecules — including, unfortunately, many drugs — so the hunt is on for more suitable polymers. One alternative would be to connect various organ compartments using bioengineered blood vessels that line the chip's polymer channels. In autumn 2014, Bhatia collaborated with Christopher Chen of Boston University in Massachusetts, Gordana Vunjak-Novakovic of Columbia University in New York and Karen Hirschi of Yale School of Medicine in New Haven, Connecticut, to develop such a multi-organ chip, in which heart and liver compartments are joined by living capillaries. Uwe Marx of the Technical University of Berlin says that this will add a crucial dimension of realism. "The cells in these vessels are also transmitting information between the tissues," he says. "The blood-vessel system is about a lot more than just providing nourishment for organs."

It still remains unclear exactly what should be pumped through these vessels; although every tissue in our body is supported by a common fluid — blood — the search is still underway for a blood surrogate that many different cultured cell types find universally agreeable. "We may end up using the same fluid throughout the chip, but locally supplementing each compartment with distinct growth factors," says Bhatia. "That's kind of how the body operates." If lung tissue requires a biomolecule that adversely affects liver or other cell types, for example, it could be possible to limit its area of effect by storing it in a hydrogel repository that slowly releases the factor into media entering the lung compartment.

SIMPLE, BUT NOT TOO SIMPLE

Ingber emphasizes that his primary goal is to mirror function, not structure. "We start at the simplest embodiment and see what it can do," he says. "If it's missing something, we add complexity one step at a time, and if not we've just learned that we don't need that."

However, he also emphasizes that his group is pursuing the lofty goal of constructing a representation of the human body with the greatest possible functionality, in partnership with Wyss colleague Kevin Parker. It would have a beating heart, churning guts and breathing lungs, all supported by an automated system. This may be more sophisticated than many research groups require. Wikswo's group, in contrast, is looking into simpler arrangements. "The ultimate way to exploit these systems," he says, "will be to get small, cheap gadgets in the hands of any biologist who needs them."

Many labs in this space have created spin-off companies to develop their platforms; Marx co-founded the Berlin-based TissUse in 2010, which now offers two-tissue chips for drug and toxicology testing. Ingber and Shuler have also launched start-ups. In parallel, the US National Institutes of Health and the Defense Advanced Research Programs Agency have committed nearly US$150 million to a cross-agency programme funding development of single-organ and body-on-a-chip devices. The US Food and Drug Administration has been actively involved as well, exploring how these systems might fit into their regulatory processes.

There is general agreement that by offering a true window into the body's inner workings, these compact, transparent organ-on-a-chip systems could transform drug testing. It is possible to incorporate sensors that track metabolism using glucose levels and pH, or precisely measure the strain of contracting muscle or the flow of blood in real time. This could, for example, show whether a drug has the potential to alter a patient's heart rate or interfere with liver function. Wikswo is collaborating with Vanderbilt chemist John McLean to directly integrate molecular analysis using mass spectrometry, quantifying thousands of biomolecules within tiny volumes at ten-minute intervals. Simulated organs can even be removed for closer histological examination, and then replaced without disrupting experiments.

> ***"I essentially treat each organ as a chemical reactor."***

"The goal now is to learn and understand the questions that could not be solved with animals or with any other single organ or single tissue culture solution so far," says Marx. Beyond sparing myriad lab animals, these devices could also greatly streamline human trials — for example, evaluating preclinical candidates so that only the best proceed to phase I. "You can test five to ten related drugs on microhuman chips and then send one of those forward," says Wikswo. "Then if something interesting — good or bad — happens during phase I, you can wheel these devices back out to figure out what's happening."

The broad hope, Wikswo says, is that biomedical research will benefit from a shift based on static cultures to dynamic platforms that generate steady streams of physiological data. "We want it reliable enough that it works for the experiment, small enough that you can fit 20 of them in an incubator and cheap enough that you can throw it out afterward." ■

Michael Eisenstein *is a freelance science writer in Philadelphia, Pennsylvania.*

1. Khetani, S. R. & Bhatia, S. N. *Nature Biotechnol.* **26,** 120–126 (2008).
2. Stevens, K. R. *et al. Nature Commun.* **4,** 1847 (2013).
3. Huh, D. *et al. Science Transl. Med.* **4,** 159ra147 (2012).
4. Wikswo, J. P. *et al. Lab Chip.* 13, 3496–3511 (2013).

PERSPECTIVE

LANGER: BACHRACH

Giovanni Traverso (left) and Robert Langer.

Special delivery for the gut

Wanted: biomaterials for a risky journey. **Giovanni Traverso** and **Robert Langer** explain the gastrointestinal frontier.

"Drugs don't work if people don't take them." That succinct analysis by former US surgeon general C. Everett Koop points the way towards the huge contribution that biomaterials technology can make to health care.

The failure of patients to follow instructions for taking medication is a major barrier to effective clinical care. In developed nations, adherence to long-term therapies is only 50%, and it is much lower in developing countries and in people who take multiple drugs with complex dose regimens[1]. Medication non-adherence is estimated to cost more than US$100 billion in avoidable hospitalizations every year in the United States. Technologies that would enable extended drug release — lasting for up to several months — through the gastrointestinal (GI) tract could therefore radically improve delivery of medical therapies. This may be especially useful for patients in areas afflicted by war, regions with poor access to health care, patients suffering from psychiatric illness or dementia, and paediatric populations.

There is good reason to suppose that the gut could host long-acting medication — known as depot formulations — for weeks or even months without significant adverse effects. We know this, for example, from observation of patients with bezoars — indigestible masses trapped in the GI tract that typically pose no problem until they grow quite large[2]. Patients also are generally able to tolerate intra-gastric balloons for several months[3] in their quest to lose weight.

IN DEVELOPED NATIONS, ADHERENCE TO LONG-TERM THERAPIES IS ONLY 50%.

POTENTIAL CHALLENGES

But translating this possibility into a reality poses a big challenge. To begin with, the gut's typical healthy transit time (from mouth to anus) is about 30 hours. This transit would have to be extended significantly for a drug to achieve weekly or monthly dosing. Furthermore, the GI environment has tremendous variability: pH in different sections ranges from 1 (extremely acidic) to 7 (neutral). Natural variability in the timing and content of meals results in frequent changes in lipid abundance. Then there are the high bacterial loads, 100% humidity, 37 °C temperature and a huge variety of proteases, lipases and other enzymes that work against biomaterial integrity and long-term drug stability. Thus it is imperative to prolong this transit time, which in turn requires developing materials that can withstand extreme conditions while delivering the drug continuously and without compromising safety.

There are two basic engineering approaches to extend transit time. One is to slow a drug's passage through the GI system by using devices that increase friction with the gut's mucosal walls[4]. The other is to prolong retention by loading drugs into devices that are larger than the points in the gut that limit passage of materials beyond a certain size: the pyloric sphincter at the exit of the stomach and the anus[5]. Also crucial to the successful development of such technologies are ways to ensure that drugs survive the harsh GI environment.

Significant efforts have been made using a range of materials, including bioadhesives[4] and swellable polymers[6]. But so far, systems are able to provide extended release times only on the order of hours. It will take a multidisciplinary effort to realize systems that can be safely retained in the GI tract for weeks or months, that deliver drugs continuously and with predictable kinetics during that time.

One big issue is safety. Any drug-delivery system that is intended to work in the gastric environment requires mechanisms that enable it to be automatically disassembled in the event of accidental passage through the pylorus, or if the drug being delivered causes an adverse reaction. Such designs require expertise in physiology, polymer chemistry, chemical engineering and mechanical engineering — plus the ability to design a system for testing in a large animal model.

PROLONGED RELEASE

The clinical applications could be vast. Non-adherence is of particular concern in the treatment of infectious diseases, where it can increase spread of infectious agents as well as rates of multi-drug resistance[7]. Other potential applications include extended-release GI systems for antibodies, DNA and RNA, now available only by injection. Similar technologies could also enable long-term delivery of chemicals that stimulate or inhibit growth of specific bacterial species in the GI tract; such agents are likely to be of significant interest as we learn more about the role of the microbiome in human disease.

We challenge the drug-delivery and medical-device community to unify their efforts in engineering and biomaterials to develop extended drug-release systems that can be orally delivered, as a novel approach to the prevalent and costly problem of medication non-adherence. To achieve this goal, safe, extended GI retention of delivery systems will have to be demonstrated in large animal models to maximize the chances for success in the translation to humans. Extended-release systems that retain their properties in the GI environment and pass without obstruction once they have released their therapeutic payload could revolutionize current clinical-care models and maximize effective treatment for a wide range of diseases in a variety of clinical settings. ■

Giovanni Traverso *is a gastroenterologist and biomedical engineer at the Massachusetts General Hospital and Harvard Medical School in Boston.* **Robert Langer** *is a chemical engineer at the Koch Institute for Integrative Cancer Research at the Massachusetts Institute of Technology in Cambridge.*
e-mails: ctraverso@partners.org; rlanger@mit.edu

1. Sabaté, E. (ed.) *Adherence to long-term therapies: evidence for action*. (WHO, 2003).
2. Fallon, S. C., Slater, B. J., Larimer, E. L., Brandt, M. L. & Lopez, M. E. *J. Pediatr. Surg.* **48,** 830–834 (2013).
3. Kethu, S. R. *et al. Gastrointest. Endosc.* **76,** 1–7 (2012).
4. Lam, P. L. & Gambari, R. *J. Control Release* **178,** 25–45 (2014).
5. Cargill, R. *et al. Pharm. Res.* **5,** 533–536 (1988).
6. Gordi, T., Hou, E., Kasichayanula, S. & Berner, B. *Clin. Ther.* **30,** 909–916 (2008).
7. Ereqat, S., Spigelman, M., Bar-Gal, G. K., Ramlawi, A. & Abdeen, Z. *Lancet Infect. Dis.* **11,** 662 (2011).

nature INDEX 2015

ASIA-PACIFIC

natureindex.com

nature publishing group npg

COVER ART: ALISDAIR MACDONALD

nature INDEX 2015

ASIA-PACIFIC

NATURE, VOL. 519, NO. 7544 (26 MARCH 2015)

The Asia-Pacific region accounts for more than a quarter of the publications in the Nature Index, and some individual countries are scientific heavy-hitters. China trails only the United States in the total number of science papers published in 2014. Japan, South Korea, Australia, India, Singapore and Taiwan are among the world's top-20. Most of these top performers in the region are adopting policies that should ensure they retain their high standing in the research world. But how will their science policies and budget plans determine the quantity and quality of research in the years to come?

China, for example, has been increasing research spending over the past decade and the financial input has already yielded results. For example, the Chinese Academy of Science (CAS) leads the Nature Index in three of the four publishing categories: earth and environmental sciences; chemistry; and physical sciences. In chemistry, CAS published three times more than the second-placed French National Centre for Scientific Research (CNRS).

But other countries in the region have more uncertain futures. In Japan, for example, commentators warn that significant government funding and policy reforms are needed to keep the country at the top end of science and technology.

Likewise, many scientists in India hoped for more favourable science and technology policies after the election of Prime Minister Narendra Modi. They were disappointed when the increase in research spending in his first budget did not even keep up with inflation. It remains to be seen if Modi's election platform will translate into results.

For some countries in this index, success comes through specialized forms of research. For instance, almost half of South Korea's published articles are in physical sciences. In India, about half of the articles explore topics in chemistry. New Zealand, on the other hand, publishes across a much broader range of topics.

As well as looking at the countries individually, this index examines the interaction among them. In particular, we analyse data on collaborations both within and outside the Asia-Pacific. The results show that scientists in the Asia-Pacific team up more often with researchers in other parts of the world than with those in their home region.

The revealing Nature Index dataset provides many ways to examine and explore science and technology in the Asia-Pacific. It's a resource that depicts the existing landscape of science and technology research, and also foreshadows changes that might lie ahead.

Mike May
Guest Editor

Herb Brody
Supplements Editor

CONTENTS

EDITORIAL: Herb Brody, Michelle Grayson, Mike May, Rebecca Dargie, Victoria Kitchener. **EDITORIAL SUPPORT:** Nobuko Miyairi, Larissa Kogleck. **ART & DESIGN:** Wesley Fernandes, Alisdair Macdonald, Kate Duncan, Chris Gilloch. **WEB & DATA:** Bob Edenbach, Olivier Lechevalier, Yuxin Wang, Naomi Nakahara, Masamichi Wada, Jyoti Miglani, Akiko Murakami, Takeshi Ouchi, Maxime Fontaine, Jennie Pao, Jörn Ishikawa. **PRODUCTION:** Sue Gray, Karl Smart, Ian Pope, Robert Sullivan, Chandler Gibbons. **MARKETING:** Hannah Phipps. **SALES:** Yuki Fujiwara, Janet Cen. **PROJECT MANAGER:** Anastasia Panoutsou. **ART DIRECTOR:** Kelly Buckheit Krause. **PUBLISHING:** Nick Campbell, Richard Hughes, David Swinbanks.

NATURE INDEX 2015 ASIA-PACIFIC
The Nature Index 2015 Asia-Pacific, a supplement to *Nature*, is produced by Nature Publishing Group, a division of Macmillan Publishers Ltd. This publication is based on data from the Nature Index, a website maintained by Nature Publishing Group and made freely available at natureindex.com.

Nature Editorial Offices
The Macmillan Building
4 Crinan Street,
London N1 9XW, UK
Tel: +44 (0)20 7833 4000
Fax: +44 (0)20 7843 4596/7

CUSTOMER SERVICES
To advertise with the Nature Index, please visit natureindex.com/support
feedback@nature.com

THE ASIA-PACIFIC IMPACT

The Nature Index 2015 Asia–Pacific reveals strong overall results from the traditional science leaders in this region. In addition, some smaller countries excel in specific areas.

THE REGION'S TOP-10 PRODUCERS

China leads the Asia-Pacific in weighted fractional count (WFC) — second only to the United States globally — and many countries in the region focus on chemistry and physical sciences.

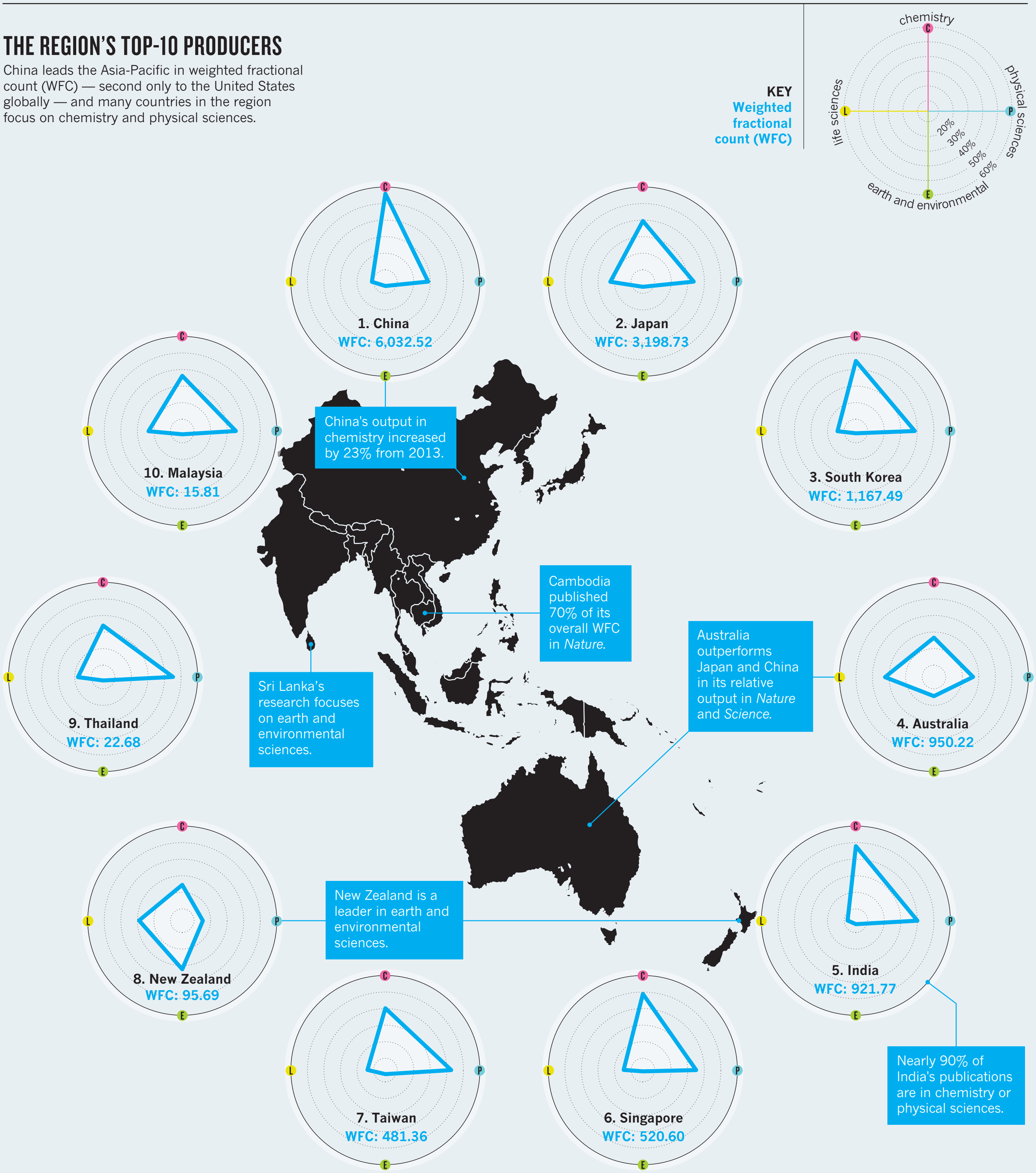

SUBJECT SHIFTS

Compared to the global balance of articles by category, scientists in the Asia-Pacific region publish less in the life sciences and more in chemistry.

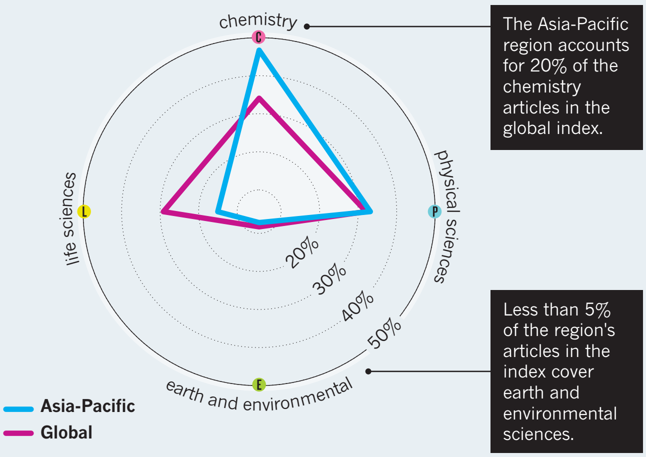

ASIA-PACIFIC VS. THE WORLD

Scientists in the Asia-Pacific region account for about a quarter of the global WFC.

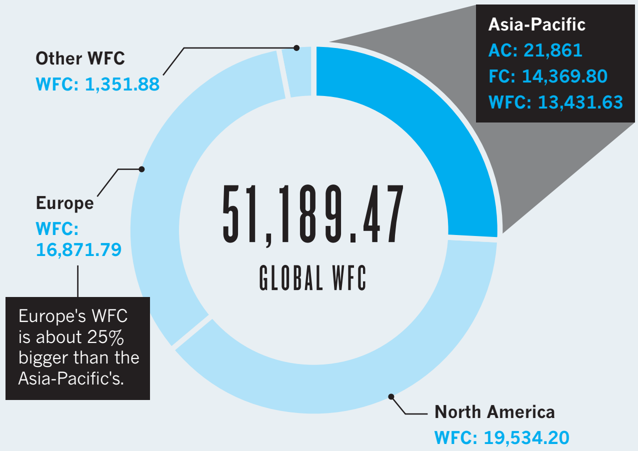

STRENGTHS BY SUBJECT

Based on WFC, China leads three of the four categories, and dominates chemistry with 53%.

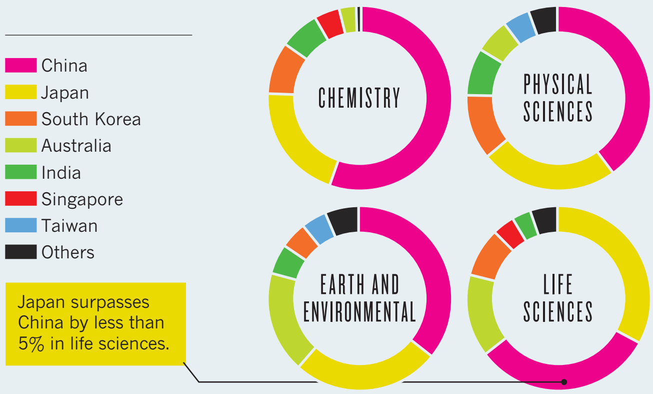

THE FRUITS OF INVESTMENT

Countries with higher gross domestic expenditure on R&D (GERD) publish more articles.

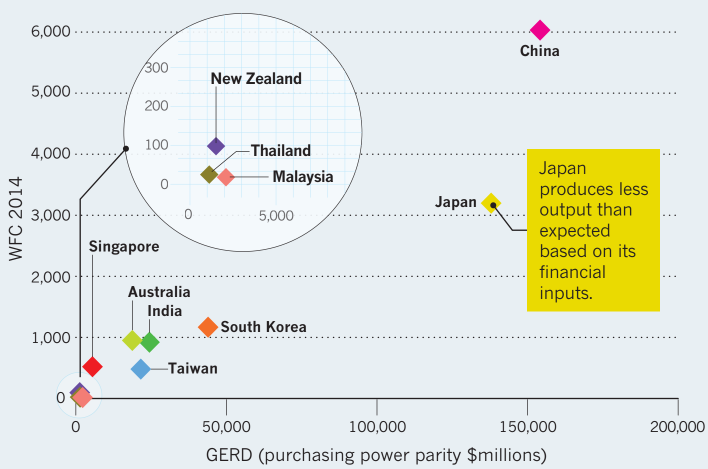

COOPERATION FROM AFAR

For nearly every country, collaborations outside the Asia-Pacific region far exceed those with scientists from within the region.

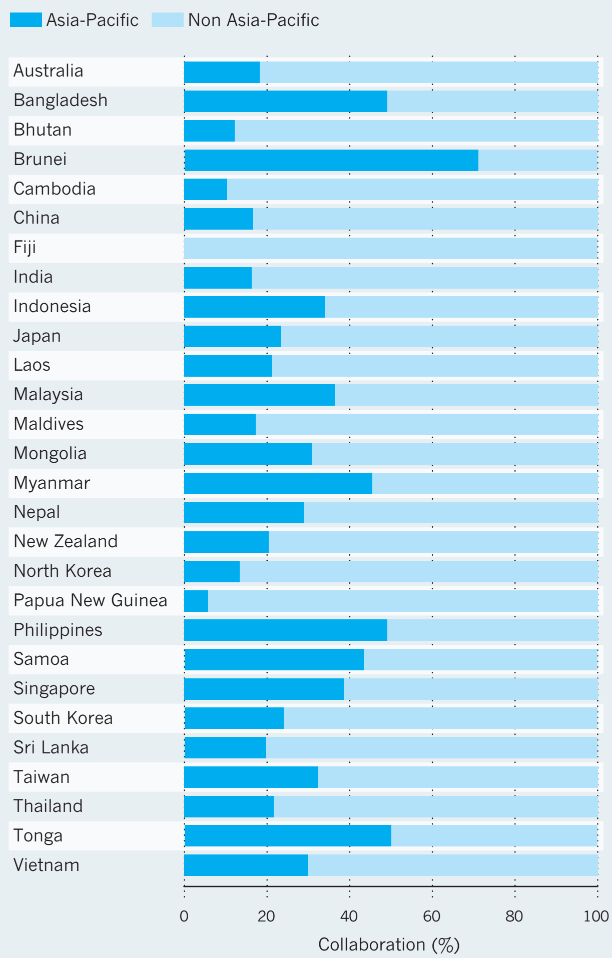

China

Increased investment levels continue to signal China's intention of becoming a global research leader and structural reform has been implemented to encourage collaboration on the country's acute needs — such as clean energy.

ARTICLE COUNT (AC): 8,632
FRACTIONAL COUNT (FC): 6,323.43
WEIGHTED FRACTIONAL COUNT (WFC): 6,032.51

As 2015 dawned, Chinese scientists sent images around the world of exotic marine life found while exploring the bottom of the ocean in the country's first manned deep-sea submarine. Jiaolong, the record-breaking submersible, capable of reaching depths of more than 7,000 meters, is a source of great pride. "Jiaolong marks a milestone as one of the major advances in China's marine technology," says physical oceanographer, Wu Lixin, of the Ocean University of China in Qingdao. Soon after Jiaolong's journey, the Chinese Academy of Sciences (CAS) and The European Space Agency put out a call for mission proposals for their joint robotic space mission, scheduled to launch in 2021. Both these adventurous forays are examples of a concentrated investment in Chinese science that began around the turn of the century.

Since then China has been accelerating science investment levels to match the spending commitments of other developed countries. The country's research and development spending has increased by an average 23% a year over the past decade, with a goal of reaching 2.5% of its gross domestic product (GDP) by 2020, up from 1% in 2000.

China's leaders have long-term plans to reap the practical benefits of research. A 15-year plan announced in 2006 committed the country to developing strategies for indigenous innovation and set targets of turning China into a technology powerhouse by 2020 and a global leader by 2050. Goals outlined include limiting China's reliance on imported technology to 30%, and for the country to rank in the world's top five for invention patents and most cited scientific academic papers. China's recent leap into inner space and efforts to reach outer space show just how far the country has already come.

"RESEARCHERS INCREASINGLY SEE SCIENCE AS A MEANS TO IMPROVE SOCIETY"

IMPROVED PUBLICATIONS

The OECD Science, Technology and Industry Outlook 2014 biennial report predicted that if China continues on its high-spending trajectory, the country will overtake the United States in R&D spending by the end of the decade (it surpassed Japan in 2008 and the European Union in 2013). The outcomes of this investment are evident not only in technological achievement, but also in academic research. In the 2014 Nature Index, China ranks second in publishing output — only behind the United States, but it out-published China by nearly three times. CAS, however, leads the world as the top publishing institution, beating second-place Harvard University by 1.5 times.

To further improve China's research output, Beijing has announced comprehensive structural reform to science policy. These changes aim to encourage richer collaboration and make the funding process more transparent. In October 2014, the government unveiled a radical overhaul of spending, which included establishing a new agency to unify the planning and assessment of scientific projects. A centralized platform for distributing grants will be introduced to replace the large, fragmented system currently overseen by 30 different departments.

In addition, the government is going back to basics on research funding. While China's total expenditure on research and development has increased rapidly, the portion of that devoted to basic research has remained less than 5% — insignificant compared to the 10–25% in many developed countries.

At the 12th National People's Congress in 2014, Premier Li Keqiang said that basic research spending would increase by 12.5% — to US$6.6 billion —and would be directed

CHINA ANALYSIS

Top ten institutions
The Chinese Academy of Sciences' contribution to Nature Index (NI) was nearly five times larger — based on its WFC — than China's second largest contributor.

RANK	INSTITUTION	WFC 2014	AC 2014
1	Chinese Academy of Sciences (CAS)	1,303.86	3,114.00
2	Peking University (PKU)	291.45	932.00
3	Tsinghua University (TH)	205.48	605.00
4	Nanjing University (NJU)	201.91	469.00
5	University of Science & Technology of China (USTC)	190.96	536.00
6	Zhejiang University (ZJU)	188.39	349.00
7	Fudan University	162.89	343.00
8	Shanghai Jiao Tong University (SJTU)	106.78	281.00
9	Lanzhou University (LZU)	106.27	174.00
10	Jilin University (JLU)	101.87	184.00

Top five collaborators
Most NI articles with Chinese authors (70%) include no international collaborators. The USA accounts for almost half the contribution to papers with non-Chinese authors.

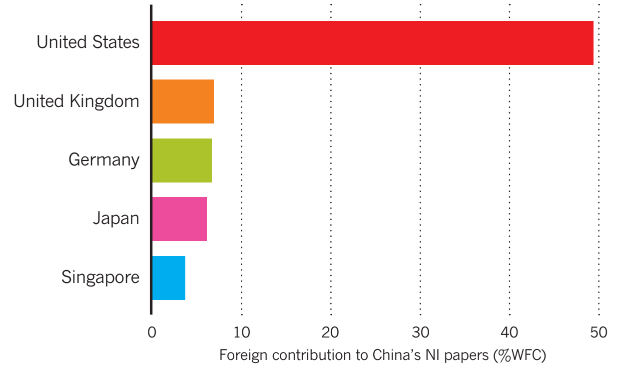

towards areas such as pollution, supercomputers and neurodegenerative disease. The recent drive to revitalize Chinese science follows decades of low spending that left China lagging. China's catch-up period may now be coming to an end: "In the next 15 years, Chinese science will switch to the period of performing original research and finally take over the leading position," predicts Lei Jiang of the CAS Institute of Chemistry, one of the nation's most influential scientists. Notably, 60.3% of China's publications in the 2014 Nature Index are in chemistry.

There are clear signs of a concerted push for more indigenous innovation in China taking place across the board, from basic research funding to industrial reform. The changes to China's central government funding framework should encourage scientists to put their creativity to more effective use, says Chen Liwei, a nanotechnologist at the Suzhou Institute of Nanotech and Nanobionics. "Chinese scientists are increasingly seeing the purpose of science as not just about the number of publications, but improving our society," he says.

CLEAN-AIR CHALLENGES

In fact, science could work to alleviate social problems in China. The country remains largely dependent on foreign energy, importing more than half its crude oil from overseas. Developing new cleaner energy sources and moving away from smog-producing coal-fired power stations is key to the country's future economic stability, meeting carbon targets and tackling air pollution. Sixteen of the world's 20 most polluted cities are in China. Beijing battled unusually thick smog in January 2013, a problem often seen in the two years since. However, less than 4% of China's 2014 scientific publications were in environmental science.

Government events and programmes have brought to light the concern over such environmental problems. At the Asia-Pacific Economic Cooperation summit in Beijing last November, for instance, President Barack Obama and President Xi Jinping announced an agreement to stem the greenhouse gas emission levels of their two countries. As a result, Chinese scientists are looking for applied research solutions to help meet their leader's goals: to get 20% of its energy from non-fossil-fuel sources by 2030 — up from less than 12% in 2011 — and for its overall carbon dioxide emissions to start decreasing in the same year.

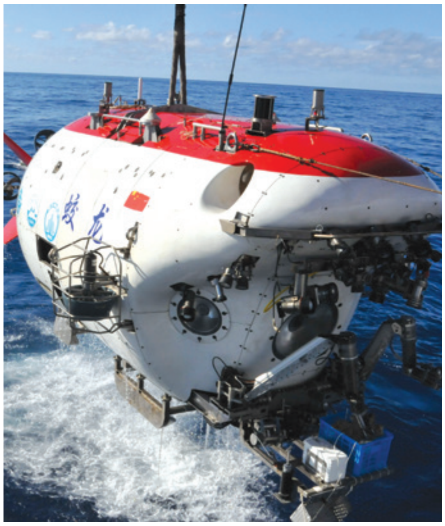

The deep-sea submersible Jiaolong returns from hydrothermal vents in the south China sea.

ZHANG XUDONG/XINHUA PRESS/CORBIS

To combat air pollution, China's nuclear research community has been told to bring forward its deadline to build the first working experimental nuclear reactor to be fuelled with thorium rather than uranium. The $350 million project based at the Shanghai Institute of Nuclear and Applied Physics started in 2014, and the government is pushing to see a finished product by 2024 — 15 years earlier than originally planned. It's a daunting challenge. Gu Zhongmao, an official at the China Institute of Atomic Energy, has pointed out that so-called fourth-generation reactors remain troubled by technological issues that he says could take decades to resolve.

COMMERCIAL IMPACT

Some of the highest impact science is going on in the private sector. BGI-Shenzhen, the world's largest genomics research centre, having sequenced more than 57,000 human genomes, last year bought its biggest competitor, US-based Complete Genomics — a company that developed a custom-built genome sequencing platform, plus software that can be used to study disease treatment and prevention.

According to George Baeder, director of China Global Insight, there has been a marked increase in Chinese participation in the pharmaceuticals market. He says: "At a recent JP Morgan healthcare conference in San Francisco, by far the most impressive thing was the number of Chinese companies that clearly have aspirations in innovative medicine and bringing those to a global market." China is already the world's third-biggest pharmaceuticals market and sales have been growing by 25% each year since 2009.

At the research level, scientists are working more collaboratively to become leaders in key areas of pharmacological research. China has the world's second highest number of obese citizens — exceeded only by the United States. For the past year, Liu Feng, director of the Metabolic Syndrome Research Center in Changsha, has been working with partner institutes across the country to tackle the problem. Last year, Liu's team identified a key regulator that promotes the activation of brown and beige fat, which are more easily burned off by the body to produce heat. The finding could lead to better weight-loss solutions.

The combination of academic and industrial research, plus commercial successes, sets China up for further opportunities. It takes more than a few commercial successes to become a global leader in applied science and technology, but reforms underway could be just what it takes to put China at the front end of innovation. ■

CHINA ANALYSIS

Chinese Academy of Sciences

Peking University

Tsinghua University

Nanjing University

University of Science & Technology of China

Institutional subject spread

All of China's top five institutions are strong in chemistry and physical sciences — in all cases accounting for more than 90% of the NI WFC.

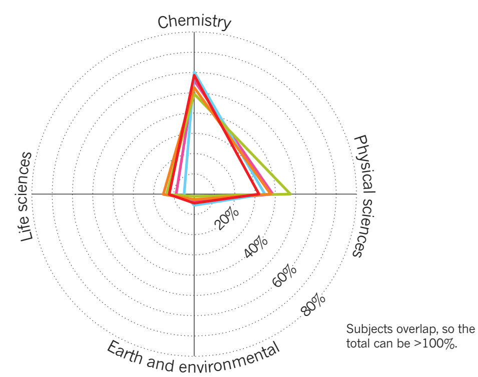

Subjects overlap, so the total can be >100%.

***Nature* and *Science* ratio**

The percentages of China's NI publications in these top journals all lag behind the global average.

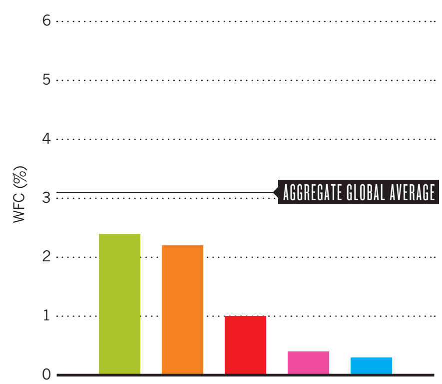

Japan

Reforms are underway to make best use of tight research budgets, but it remains unclear if changes will address Japan's many challenges or further destabilize the deeply unsettled science powerhouse.

ARTICLE COUNT (AC): 4,973
FRACTIONAL COUNT (FC): 3,428.46
WEIGHTED FRACTIONAL COUNT (WFC): 3,198.73

Over the past year, Japan's scientific activities have been notable for many reasons, from widely publicized misconduct in stem-cell research to breakthroughs in efficient blue light-emitting diodes that won the 2014 Nobel Prize for Physics. As a backdrop, the government is implementing drastic structural reforms of the research environment, including organizational changes aimed to improve project management.

In 2012, Prime Minister Shinzō Abe took power, and hoped to use advances in science and technology innovation to revive the stagnant economy. His aims are laid out in the government's sustainable growth plan, the Japan Revitalization Strategy, under which activity is already going ahead. Under this plan for example, the government is accelerating the push to turn breakthroughs into new industries.

Innovation, though, can only take place with structural reforms, such as improving government oversight of national science programmes. Such reforms "are essential to make the most of the limited budgets," says Atsushi Sunami, professor of science policy at the National Graduate Institute for Policy Studies (GRIPS) in Tokyo. Many scientists hope that Abe will revamp the research structure, but wonder if it will solve deep problems in Japan's scientific foundation.

Despite the push for innovation, Japan's economic outlook remains bleak and the main research budget for 2015, which accounts for a third of the total science and technology allocation, fell 3.9% from the previous year to about US$10 billion. Every year the government has also been cutting another form of support called management expenses grants, a basic subsidy to operate universities and research institutes. To compensate for the reductions in those grants, the University of Tokyo secures much of its revenue from external funds. In 2013, for example, it obtained more than US$580 million, about 30% of revenue, from external sources.

"YOUNG PEOPLE DON'T KNOW HOW TO FOSTER ORIGINALITY TO BECOME FULLY-FLEDGED SCIENTISTS"

To get the maximum impact from the curtailed budgets, Japan's government strengthened the authority of the Council for Science, Technology and Innovation (CSTI), which is an advisory body chaired by the prime minister. For 2015, the CSTI selected 153 projects under five themes: clean energy, improved life expectancy, next-generation infrastructure, the creation of new industries with regional resources, and reconstruction in northern Japan after the huge 2011 earthquake. Many of these projects are coordinated beyond the boundary of government ministries, which have been criticized for inconsistent support and duplication of projects.

Fifty of CSTI's projects are categorized in the SIP (Strategic Innovation Promotion Programme), which provides about US$425 million over five years to support 10 non-medical programmes. In the best-funded SIP activity, retired University of Tokyo geologist Tetsuro Urabe will lead a US$51 million effort to find better ways to exploit ocean resources, such as rare metals, for commercial applications. Half of the 10 SIP programme directors come from Toyota and other large manufacturers. Yuko Ito, an expert on policy at the National Institute of Science and Technology Policy (NISTEP), says, "Large companies are looking to research and development partners abroad." Ito suggests that SIP will also explore domestic universities and that programme directors could even require academics to put a case forward for potential commercial applications of basic science to obtain research grants.

The CSTI also created a US$450 million programme called ImPACT that takes chances on

JAPAN ANALYSIS

Top ten institutions

The University of Tokyo published nearly 60% more — on the Nature Index (NI) — than second place Kyoto University, based on WFC

RANK	INSTITUTION	WFC 2014	AC 2014
1	The University of Tokyo (UTokyo)	453.45	1,242.00
2	Kyoto University	286.13	714.00
3	Osaka University	218.62	553.00
4	Tohoku University	177.99	423.00
5	RIKEN	144.14	495.00
6	Tokyo Institute of Technology	127.21	329.00
7	Nagoya University	125.28	431.00
8	National Institute for Material Science (NIMS)	100.08	239.00
9	Hokkaido University (HU)	100.03	234.00
10	Kyushu University	98.30	274.00

Top five collaborators

About 35% of Japan's NI publications include non-Japanese authors, and roughly a third of them come from the United States, but about 10% are Chinese.

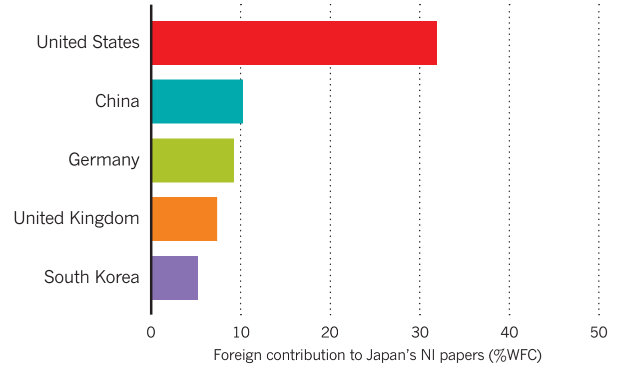

risky research that could bring high-impact results. Under ImPACT, 12 projects are underway, including the development of super-green IT devices using spintronics, a next-generation technology to use both the charge and the spin of electrons for energy-efficient information storing and processing, by reducing power consumption to a hundredth of existing memories.

Japan already contributes significant efforts to related disciplines. In the 2014 Nature Index, for example, 75% of Japan's articles come from chemistry and physical sciences.

A NEW MEDICAL RESEARCH SYSTEM

Japan's rapidly ageing population — 24.1% of its people were 65 or older in 2012, and the figure is expected to grow to 39.9% in 2060 — is driving the country's urgency for R&D on drugs and other therapies. Such development, it is hoped, would have a major economic benefit. In 2013, Japan's import of drugs exceeded its exports by about US$15 billion, and its trade deficit for medical equipment was about US$6 billion in 2012. To reduce this imbalance, the Japanese government set an ambitious goal of doubling the exports of medical equipment by 2020.

The government is consolidating the management and funding for medical research into the newly established Japan Agency for Medical Research and Development (AMED). Headed by Makoto Suematsu, currently dean of Keio University's School of Medicine in Tokyo, AMED will take over projects managed by three different ministries. It will have a 2015 budget of about US$1.1 billion, to be distributed between nine areas identified for their contribution to the economy and the healthy longevity of citizens. Among the focus areas will be cancer and neural diseases, plus innovative technologies. Currently, about a quarter of Japan's Nature Index publications are in life sciences.

"There will be a lot of difficulties in running the new organization, but we expect the system will stimulate the activities of academia and companies and bring results to patients at the earliest possible time," says Yutaka Hishiyama,

THE ASAHI SHIMBUN/GETTY IMAGES

Techniques, such as this 3D-printed organ model along with work on engineered tissues, drive Japan's reputation for medical capabilities.

deputy director general of the Office of the Healthcare Policy, which will oversee AMED.

The government's biggest push involves regenerative medicine. Efforts will be centered on induced pluripotent stem (iPS) cells, which can achieve embryonic-like status by being reprogrammed with specific genes, a technique that Shinya Yamanaka of Kyoto University won the Nobel Prize in Physiology or Medicine 2012 for developing. In September 2014, a team led by stem-cell biologist Masayo Takahashi at RIKEN succeeded in the first attempt to implant tissue derived from iPS cells into a patient with visual impairment, but results remain uncertain.

GETTING MORE COMPETITIVE

Leaders of Japanese science have legitimate concern that the country is stagnating. "We fear that both the quality and quantity of research have kept deteriorating since around 2002," says Ito. Between 1999 and 2011 the number of papers published by scientists in Germany, the United Kingdom and the United States increased by more than 20%. But during this same period, Japan's count increased by a mere 3%, according to National Institute of Science and Technology Policy (NISTEP). The quality of the Japanese papers also appears to be slipping. Japan ranked fifth in the most-cited papers in 1999–2001, but its position had fallen to eighth a decade later.

Government initiatives could improve Japan's competitiveness. For example, the science ministry plans to allocate Management Expenses Grants to universities based on performance, measured by such indicators as the number of papers published and external grants received.

MOVING TOO FAST?

Excessive pressure to produce results too quickly, however, might undermine the country's scientific foundation, says Michinari Hamaguchi, president of Nagoya University — home of six out of the 13 Japan-born scientists who have won a Nobel Prize in the 21st century. He says that his university's strength lies in its tradition of open discussion and curiosity-driven research. He says, "But nowadays, the atmosphere in Japan's academia doesn't allow such free discussion. Japanese culture is demanding conclusions quickly and shutting out different opinions."

Mitiko Go, former president of Ochanomizu University in Tokyo, says that large-scale funding schemes are thwarting the creative thinking of young people. "Faculty staffers with sufficient funding are too busy producing papers in high-impact journals, which are the indicator for their evaluation," she says. "And young people are like factory workers. They don't know how to foster originality and become a full-fledged scientist."

Careers in academia are losing their allure. The number of graduate students in the science and engineering doctoral courses at national universities has been falling — down 24.3% from 2000. The number of tenure positions fell 9.8% from 2005 to 2012. Scientists say people are shying away from academia because of working conditions. "Some post-docs cannot marry, or even get a credit card," Sunami says. Post-docs in the US, for example, do not suffer from this kind of constraint. "Can the government-led innovation policies prevent this from worsening? We don't have clear answers yet," Sunami says. "But whatever we do we cannot afford to fail." ■

JAPAN ANALYSIS

Institutional subject spread
The NI WFC publications from the leading institutions cover several areas, but with little research in earth and environmental sciences.

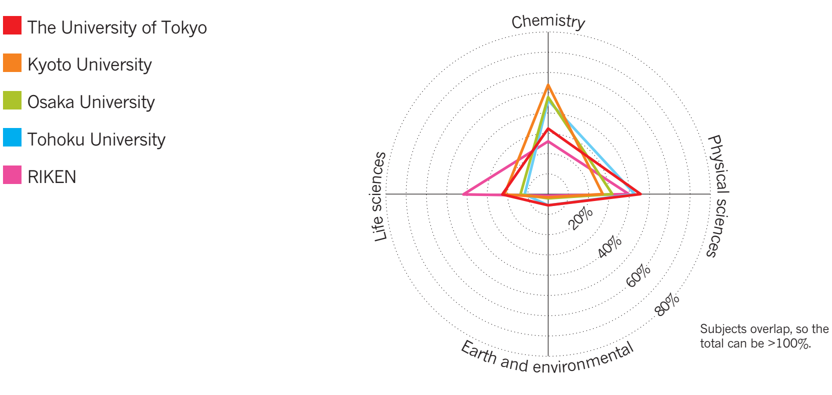

***Nature* and *Science* ratio**
Only RIKEN surpassed the global average for NI publications in these leading journals.

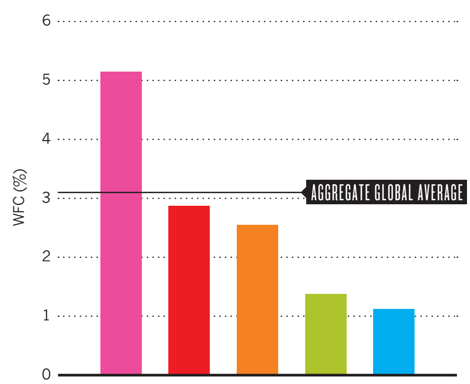

South Korea

Working to build a 'creative economy', the country has boosted its significant science spending with researchers particularly focusing on nanotechnology, nuclear fusion and stem-cell research.

ARTICLE COUNT (AC): 1,966
FRACTIONAL COUNT (FC): 1,232.24
WEIGHTED FRACTIONAL COUNT (WFC): 1,167.49

South Korea is often called the world's most innovative country. Last year, for example, it beat Sweden and the United States to claim first place in Bloomberg's 2014 Global Innovation Index. If its endeavours are measured by financial commitment, South Korea is shining. The Organization for Economic Cooperation and Development's (OECD's) Science, Technology and Industry Outlook 2014 shows the country spent 4.4% of its GDP on R&D in 2012, leading the world. The Battelle Institute's estimates have South Korea's total R&D spending at about US$63 billion in 2014. The lion's share of these funds goes into industrial work led by giants, such as Hyundai and Samsung. But South Korean researchers also are making increasingly important contributions in basic and applied research, in fields ranging from nanotechnology to nuclear fusion and from stem cells to space science, and boosting efforts to transfer their advances to industry.

An educated workforce is key to achieving scientific and technological success, and this is Korea's greatest strength, according to Sung-Mo Kang, president of the Korea Advanced Institute of Science and Technology (KAIST) in Daejeon. He points out that more than 65% of young people graduate from college — compared to only about 40% of the entire US population.

However, observers inside and outside South Korea advise that getting the most from this well-educated workforce will require more ambitious basic research programmes; Korean scientists historically have published relatively few papers in leading scientific journals. "Today, Korea faces a new challenge in the field of basic research: the country has attained a goal in terms of growth, but it needs to improve its quality of research," researchers from Chungnam National University and the National Research Foundation of Korea noted in a 2014 paper. "Korean researchers need to demonstrate excellence, a far more critical issue than the number of papers published." In 2014, for example, only 0.6% — compared to a global average of 3.1% — of its papers were published in *Nature* or *Science*.

"SOUTH KOREAN SCIENCE HAS MOSTLY BEEN A FAST FOLLOWER RATHER THAN A FIRST MOVER."

TAKING IT FROM THE TOP

Enhancing basic science capabilities and goals is a key part of the national initiatives that President Park Geun-hye prioritized when she was elected in 2013 and outlined a vision of a "creative economy". This effort is supposed to push the country's strengths in R&D — especially in information and communications technologies (ICT) — towards industrial application and help generate innovative products and services. To promote this, the Park government merged three agencies to establish the Ministry of Science, ICT and Future Planning, a new ministry designed to ease coordination within the government and overcome bureaucratic barriers. However, Sean Connell, an expert on South Korean research and development, who analysed the quest for a creative economy on behalf of the Washington-based Korea Economic Institute of America, says the restructuring was the third such reorganization of governance for South Korean science, technology and innovation in a decade and that its effectiveness is yet to be seen.

Supporting such reorganization and deriving results requires funding. To this end, in February 2014, President Park announced plans to increase Korea's R&D investments to represent 5% of its GDP by 2017, to further support the establishment of a creative economy. In recent years, the government has boosted its own R&D spending by an impressive average of 11% a year. This year's federal R&D expenditures are pegged at US$19 billion, up 5.9% from 2014. Within these expanding budgets, spending on basic research also will rise, to 40% of the total by 2017.

SOUTH KOREA ANALYSIS

Top ten institutions
South Korea's leading institutions publish — in the Nature Index (NI) WFC — less than those in China and Japan, but with more of a balance across the top ten.

RANK	INSTITUTION	WFC 2014	AC 2014
1	Seoul National University (SNU)	160.24	434.00
2	Korea Advanced Institute of Science & Technology (KAIST)	116.33	222.00
3	Yonsei University	71.00	200.00
4	Pohang University of Science & Technology (POSTECH)	70.33	150.00
5	Korea University (KU)	61.21	210.00
6	Sungkyunkwan University (SKKU)	58.83	240.00
7	Hanyang University (HYU)	48.74	127.00
8	Ulsan National Institute of Science &Technology (UNIST)	38.28	87.00
9	Kyung Hee University (KHU)	30.98	122.00
10	Institute for Basic Science (IBS)	29.08	116.00

Top five collaborators
Of the roughly 40% of South Korea's NI WFC papers with international authors, Japan and China rank in the top five, but far below the rate of collaboration with US scientists.

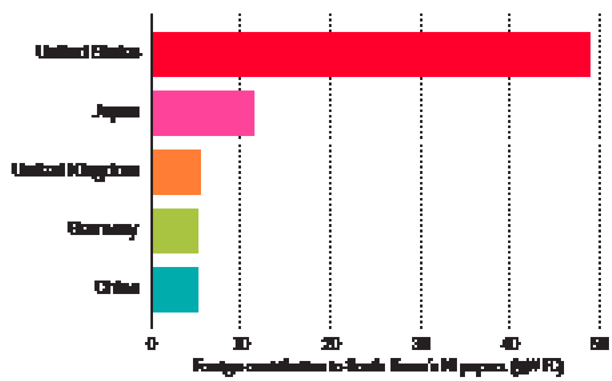

One project exemplifying the push into basic research is the Institute for Basic Science (IBS), which was launched in 2012. IBS focuses on big and sometimes risky research, historically not a particular strength of Korean science. Now 24 IBS research centres are up and running. In 2014, the government also pushed forward with plans to build a rare-ion accelerator — managed by IBS and funded at around US$2.1 billion through 2021 — for work in nuclear physics, materials science and biomedicine.

STRENGTHS IN SCIENCE

Short of domestic energy sources, South Korea is playing a significant role in nuclear-fusion research, especially as a major player in the International Thermonuclear Experimental Reactor (ITER) project. In 2014, researchers celebrated the 10,000th plasma-generation experiment of its Korea Superconducting Tokamak Advanced Research device, which began operating in 2008. Researchers also began conceptual designs for a fusion demonstration reactor (K-DEMO) in 2012 and hope an upgraded version of the reactor will go into operation around 2037. If this ambition is realized, K-DEMO will be the first nuclear-fusion device to contribute to a power grid.

Nanotechnology is a focus and the government has invested several billion US dollars in nanotechnology since 2001. Research into the discipline receives big industrial support. Results in 2014 ranged from developing graphene for flexible electronics to gelatin-based nanoparticles for delivering drugs to the brain. Unsurprisingly, nearly half of South Korea's published articles are in physical sciences.

In space science, 2013 marked the first success for a South Korean launch vehicle putting a satellite into Earth orbit. Aiming to move from Earth monitoring to Moon monitoring, the Korea Aerospace Research Institute is leading an effort to build a lunar orbiter and lunar module, for take-off in 2020.

In life sciences, South Korea's fame and notoriety has been in stem-cell research — both for genuine advances, such as the first cloned dog,

EPA/ALAMY

Researchers at KAIST interact though this transwall, a two-sided touchscreen, which could be used in classrooms or laboratories.

and for a fraudulent claim a decade ago to have isolated the first human embryonic stem-cell line using somatic cell nuclear transfer (SCNT, in which a nucleus is removed from an egg and replaced with a donor nucleus). Both projects came from the lab of Woo Suk Hwang, formerly of Seoul National University, who now runs a startup that clones pet dogs.

In the wake of the Hwang scandal in 2009, the government stopped funding embryonic stem-cell research, a moratorium that has now ended. The government is again encouraging such work — much of it led by CHA University in Seoul. In 2011 South Korea became the first country to award medical approval to stem cell-based therapies for solid tissues, giving a go-ahead for treating myocardial infarction with a patient's own mesenchymal stem cells. Among laboratory advances in 2014, CHA researchers, working with US scientists and using SCNT, generated human embryonic stem cells using skin cells from two adult males, a promising step in regenerative medicine.

Strengthening research in a less visible field, in December 2014 the government announced it was necessary by 2023 for the nation to invest US$18.1 billion for developing clean energy technologies. Of that total, the government would provide US$10.9 billion and industry would come up with the remainder.

In an ambitious move to boost the scope and quality of university research, in 2014 President Park introduced a Korea Research Fellowship programme, which aims to bring 300 top scientists from around the world to the country's universities. The programme joins a wave of new centres targeting promising areas of research reflecting societal challenges. For example, in 2014, Seoul National University opened an agricultural sciences campus in Pyeongchang and launched a Big Data Institute to conduct interdisciplinary research across a very broad range of fields, while KAIST began to work with partners to create a medical campus in Sejong City.

KAIST president, Kang, also highlights the institute's rapid approach to implementing an "Education 3.0" initiative, with a "flipped classroom" approach, which eschews traditional big-lecture classes, integrates online and classroom education, and offers the potential for more engaging and effective learning. "Students watch video lectures provided by professors prior to class, and go to class to meet their professors and classmates for in-depth discussions, problem solving, group assignments and Q&A sessions," explains Kang. While leading universities worldwide dabble with the approach, KAIST plans to deliver no less than 30% of all its classes this way by 2017, with 65 newly-designed classrooms.

Such initiatives exemplify a push to broaden and strengthen research efforts, says Heeyoon Lee, a KAIST professor of organic chemistry. "With the rapid expansion of output in Korea, the country is looking into two areas for expansion of its research strength," Lee adds. One is creating new fields in basic research, he says. "Korean science has mostly been a fast follower rather than a first mover and pioneer. Korea is now looking to see many first movers." Secondly, Lee says, "Korean science has focused mostly on pure academic research fields and thus provided little or remote impact on industries." Achieving these goals will go hand in hand with a successful implementation of Park's creative economy. ■

SOUTH KOREA ANALYSIS

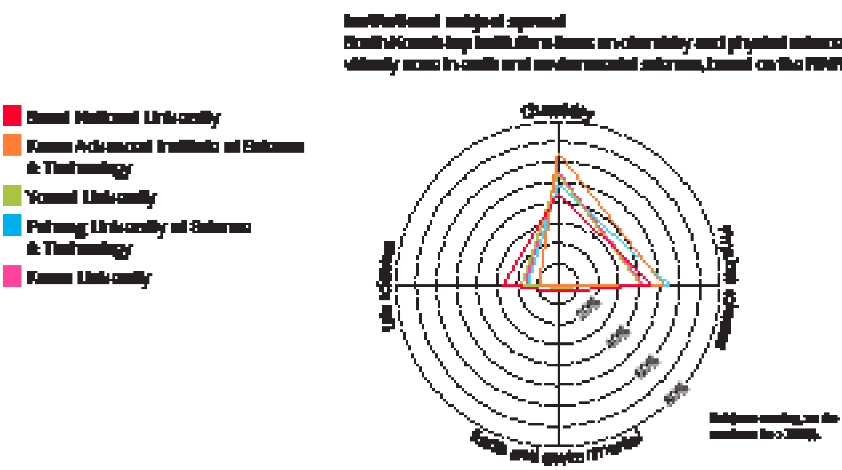

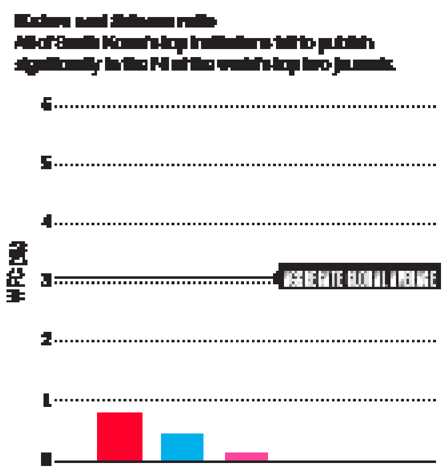

Australia

Amid sweeping funding cuts and an often hostile political environment, the country's science leaders look outward for multi-disciplinary collaboration and prepare to take the long-term strategic view.

ARTICLE COUNT (AC): 2,496
FRACTIONAL COUNT (FC): 1,144.32
WEIGHTED FRACTIONAL COUNT (WFC): 950.22

In 2014, Australia's science leaders focused on promoting research in realms outside academia, encouraging commercial development of breakthrough discoveries from interdisciplinary research and increasing international collaboration in big science.

The bigger-picture approach is a necessary reaction to significant funding cuts, and a political apathy to the importance of scientific research, according to Andrew Holmes, president of the Australian Academy of Sciences and a University of Melbourne chemist. "We have to react by being smarter in the way that we work and also more convincing in persuading the political masters how effective science can be in creating wealth and raising our standard of living," he says. Holmes calls it the "foresight aspect" of how science is practiced and says the strategy has not been used much in the past in Australia.

CONTINUING BEYOND THE CUTS

In the short term, any Australian science and technology strategy must deal with dwindling federal funds. In 2014, Australian government spending on research and development dropped to its lowest level since 1984 — just 2.2% of the federal budget, down from a high of 2.8% in the mid-1990s, according to analysis by The Sydney Morning Herald. In effect, R&D investment has grown at less than half the rate of total government expenditure — having punitive ramifications given that government funding still supports more than two-thirds of all Australian researchers.

Among the cuts announced, nearly US$82 million of promised grant money will be taken from the major funding body, the Australian Research Council (ARC), over the coming four years. It means that by 2016–17 the ARC funds available for researchers will have dropped nearly 5%. Research dollars were also taken from the Commonwealth Scientific and Industrial Organisation (CSIRO), the Australian Nuclear Science and Technology Organisation (ANSTO) and the Defence Science and Technology Organisation (DSTO). At the end of 2014, there was continuing uncertainty about a US$123 million provision for some of the country's major science infrastructure, including the Australian Synchrotron, because this funding lies in controversial budget provisions that were still being blocked by Australia's upper house.

"WE HAVE TO REACT BY BEING SMARTER IN THE WAY THAT WE WORK"

In the case of the CSIRO, an approximate US$91 million reduction in funding over four years — a 4% cut in the budget over 2014–2015 alone — is forecast to spell the end of 489 jobs by mid-2015. The cuts have already cost the CSIRO a funded position for chemist, San Thang, who is considered a strong future candidate for a Nobel Prize for his work as the co-inventor of the RAFT polymer process (reversible addition-fragmentation chain transfer). The CSIRO has historically been a strong performer in the Australian research community. Among other achievements, it was responsible for the development of Wi-Fi, and it was one of the global top-50 institutions for earth and environmental science publication in the 2014 Nature Index. Nonetheless, recent reports suggest funding cuts at the organization have forced researchers to take on cleaning labs and writing media releases.

ONGOING ADVANCES

Despite the funding crisis, Australia ranked fourth in overall publishing output in 2014 for the Asia-Pacific region. With an emphasis on chemistry, life sciences and physical sciences, Australia was once again ranked twelfth in the 2014 Nature Global Index, albeit with an increase in its weighted fractional count of 9.2% over its achievement in 2013.

Six of the country's research-intensive universities earned spots on the 2014 Nature Index's

AUSTRALIA ANALYSIS

Top ten institutions
Among Australia's top ten institutions on the Nature Index (NI), those in the middle — third through sixth — finish very close, based on WFC.

RANK	INSTITUTION	WFC 2014	AC 2014
1	The University of Queensland (UQ)	108.83	392.00
2	Monash University	102.98	381.00
3	The University of New South Wales (UNSW)	88.12	277.00
4	Australian National University (ANU)	87.16	498.00
5	The University of Melbourne	82.47	474.00
6	The University of Sydney (USYD)	79.89	491.00
7	The University of Adelaide	38.73	180.00
8	The University of Western Australia (UWA)	37.45	294.00
9	Commonwealth Scientific & Industrial Research Organisation	33.01	237.00
10	Macquarie University	19.71	154.00

Top five collaborators
Australian scientists collaborate internationally on more than 60% of their articles in the NI WFC, and spread that more evenly that others in the region.

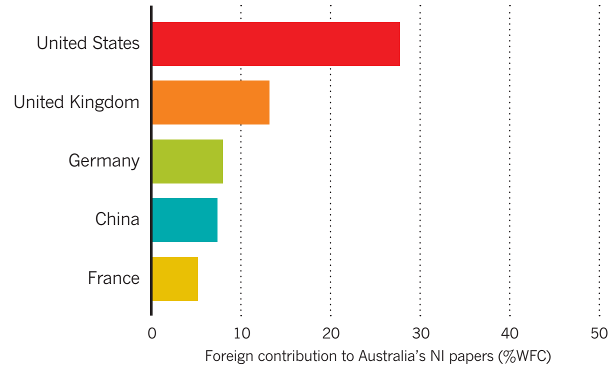

Top 200. Leading them was the University of Queensland, where Timothy Barnett from the School of Chemistry and Molecular Biosciences was one of the stars. Work by Barnett and his team reshaped understanding of how group A *Streptococcus* bacteria infects the body, effectively hiding from the immune system and growing within cells. The new comprehension of the bacteria's behaviour is an important step towards better treatment for an infection linked to more than 500,000 deaths globally each year.

Australia continues to perform well in life sciences — placing third in this category in the 2014 Asia-Pacific Index — despite funding austerity. Medical researchers in particular were buoyed by the government's proposed establishment of a Medical Research Future Fund worth approximately US$16 billion. The fund would distribute around US$820 million per year for medical research beginning in 2022 which would double the country's medical research funding. Researchers welcomed the proposal, but its funding source — a charge for patients for each visit to a physician — meant that the legislation was still under debate at the end of 2014.

In the physical sciences, Australians provide strong ongoing performances, exemplified by the quantum computation being led by the team at the University of New South Wales (UNSW) Centre of Excellence for Quantum Computation and Communication. Two separate papers from the centre were published simultaneously in *Nature Nanotechnology* in October 2014. They demonstrated two versions of silicon qubits, the building block for quantum computers, each able to process quantum data at above 99% accuracy, vastly exceeding levels for earlier silicon prototypes and within the realm of effective error correction. Quantum computing — using the spin of individual electrons to encode information — has potential to enable calculations of a scope and speed dwarfing anything today. The UNSW team leads the world in of solid-state quantum computing using silicon, which has cost advantages and is already widely used in commercial electronics.

Funding cuts at CSIRO fuel protests.

CSIRO STAFF ASSOCIATION

Government cuts to renewable energy and climate-change research are beginning to bite, but Australia continues to publish strongly in earth and environmental sciences — also placing third in this category in the 2014 Asia-Pacific Index. Highlights include publication by the Australian National University (ANU) of extensive modelling of environmental conditions from the past and into the future. In one crucial study, ANU researchers, in collaboration with French and Chinese investigators, showed that recent rises in ocean levels are not within the scope of past natural fluctuations. In 2015 and beyond, marine investigations facilitated by the CSIRO's new US$98.4 million research ship, the RV *Investigator,* will add to the country's earth and environmental sciences capabilities.

TOMORROW'S TEAMWORK

Looking ahead, the nation's leaders of science are hoping to fortify against future cuts. Among those leading the push for a more coherent national strategy, has been Australia's chief scientist, Ian Chubb. "You've got to invest in the long term," says Chubb, a neuroscientist. He consulted widely with the science community, government and business and is looking to develop a strategy that will help persuade the broader community of the high value of research and help it to attract younger Australians as a career choice.

Part of that strategy is greater collaboration, says Chubb, across disciplines and borders. There is growing enthusiasm about the potential of interdisciplinary research among Australian scientists and two major interdisciplinary centres were launched in 2014. At the University of Sydney, the Charles Perkins Centre opened with much fanfare in July and began bringing together mixed-discipline teams — from architects to cardiologists to economists — to work together on solutions for the country's rapidly growing chronic health problems, including obesity, cardiovascular disease and diabetes. Later in the year, the University of Adelaide, Macquarie University and RMIT University jointly established the Centre for Nanoscale Biophotonics, with the remit of convening researchers from medicine, engineering, biology and other areas to work together on better methods to observe and affect life on the nanoscale.

On a larger scale, Chubb is advocating the formation of an Asian Research Zone to foster greater collaboration in the region. He wants a genuine partnership between Asia-Pacific countries, a Southern Hemisphere version of the European Research Area. The starting point, he says, is to consider a multilateral approach to the science needed to overcome the region's challenges. He points to the risk of pandemics : "They are probably a subset of what the planet needs to confront," Chubb says.

Chubb has already taken the ambition to the new Commonwealth Science Council, intended to be the government's chief strategy advisor on science and technology. Chaired by the Prime Minister and with members including the Ministers for Industry and Science, Health, and Education as well as business representatives and researchers, the council's endorsement could turn the Asian Research Zone to national policy. Such a policy will forge closer links between Australia and its regional neighbours such as China and Japan, enabling the sharing of science infrastructure and research talent. Given domestic deficiencies, the appetite for international science partnerships is only likely to grow in 2015. ■

AUSTRALIA ANALYSIS

Institutional subject spread
The University of Queensland — Australia's leading institution on the NI WFC — publishes more than half of its articles in life sciences.

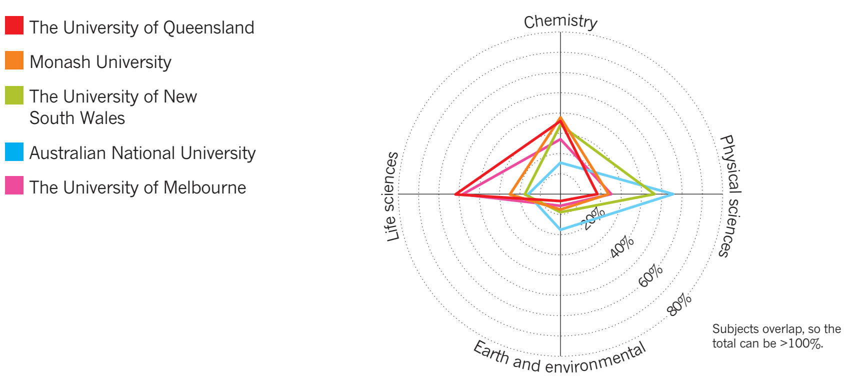

***Nature* and *Science* ratio**
The University of Queensland hits nearly twice the global average on this NI metric.

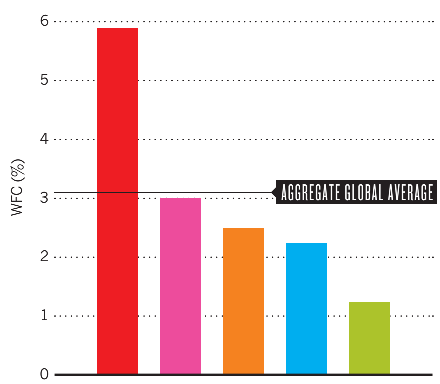

India

Space-travel success inspires the growing science and technology community, but financial difficulties create obstacles and industry is being called upon to take up more of the financial burden.

ARTICLE COUNT (AC): 1,483
FRACTIONAL COUNT (FC): 1,029.92
WEIGHTED FRACTIONAL COUNT (WFC): 921.77

On 24 September 2014, India's Mangalyaan probe started to orbit Mars, making it only the third country (after the Soviet Union and the United States) to reach the red planet. This milestone, along with the election of prime minister Narendra Modi on a platform that promised to promote and support scientific endeavour, seemed to bode well for technical advancements in India, but back on the ground much remains to be done.

Commentators point to a need to streamline lengthy and complex funding processes, clarify government rules and regulations, and increase the number of trained personnel in the science and technology industry. In July 2014, Modi's first budget delivered allocated research funding increases that lagged behind inflation—not a good start.

Anurag Chaurasia, a biotechnologist at the Indian Council of Agricultural Research, agrees with the need for infrastructure reform, but notes that positive steps have been taken despite funding constraints.

OUTSIDE INVESTMENTS

Despite government promises of improved financial support, India's science centres must often supplement funding from a range of other sources. For example, the TTK Centre for Rehabilitation Research and Device Development relies on grants from various organizations, including about US$600,000 over five years from the TTK Group, an Indian business conglomerate. These types of funding negate the vagaries of government grants, says mechanical engineer Sujatha Srinivasan, at the Indian Institute of Technology (IIT), Madras, and an instructor at the centre. "With [India's Department of Science and Technology and the Department of Biotechnology], it is a go/no-go scenario," Srinivasan says. "There is very little feedback." In contrast, she says, foundations follow a more rigorous grant process.

"IT'S A CHALLENGE TO DELIVER THE ADVANTAGE OF DEVELOPMENT TO THE POPULATION"

Funding support from the TTK Group, however, does come through a circuitous government route, the Companies Act of 2013. Under a clause in this act successful companies are compelled to contribute 2% of their net profits toward addressing social problems in India. According to government data, there are at least five million people in India whose physical movement is impaired, and so the grant fulfils the criteria for bringing about change.

Indeed, government policy appears designed to procure even more funding from industry. India spends less than 0.88% of its GDP on science research compared with 2.76% for the United States and 4.04% for South Korea, according to the science and technology minister Harsh Vardhan in response to a question tabled in parliament. Vardhan also pointed out that only a third of India's funding is contributed by the private sector, a lower proportion than in many emerging countries.

CREATING CONNECTIONS

Even now some industry participants in India do contribute significantly to the research community. At the Indian Institute of Science (IISc) in Bengaluru, for instance, Kris Gopalakrishnan, a co-founder of the Indian IT company Infosys, is funding a brain research centre. To complement the centre, three chairs in computational brain research have been set up at IIT Madras. The first occupant is Partha Mitra of Cold Spring Harbor Laboratory in New York, whose group is attempting to map neuroanatomical circuitry in the mouse brain.

Mitra will set up collaborations between IIT, Cold Spring Harbor and IISc. In return, he gets substantial computing power from the Indian institutes for his data analysis. "I think it's kind of overdue to build up computational brain research in India," says Mitra, who will

INDIA ANALYSIS

Top ten institutions
Even among India's leaders on the Nature Index (NI) WFC, the volume of publishing never gets very high and falls off fast.

RANK	INSTITUTION	WFC 2014	AC 2014
1	Indian Institutes of Technology (IITs)	168.17	287.00
2	Council of Scientific & Industrial Research (CSIR)	128.64	196.00
3	Indian Institute of Science (IISC)	93.72	149.00
4	Indian Institute of Science Education & Research (IISER)	75.88	106.00
5	Indian Association for the Cultivation of Science (IACS)	49.95	70.00
6	Tata Institute of Fundamental Research (TIFR)	29.63	199.00
7	Jawaharlal Nehru Centre for Advanced Scientific Research	24.13	43.00
8	Harish-Chandra Research Institute (HRI)	19.47	40.00
9	University of Hyderabad (UoH)	19.04	28.00
10	Saha Institute of Nuclear Physics (SINP)	15.45	100.00

Top five collaborators
Among India's NI articles that include international collaboration (about 40%), few include scientists in other Asia-Pacific countries.

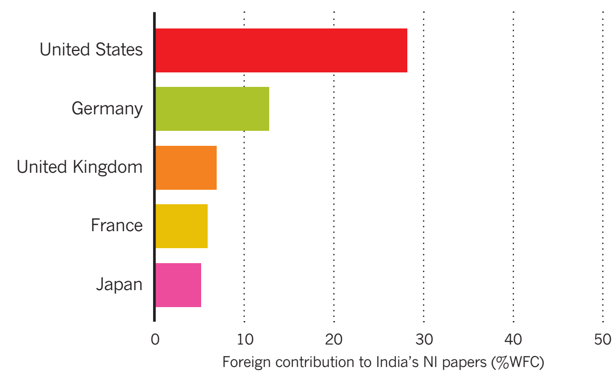

act as visiting faculty and help students build networks.

Other science projects also depend on teamwork. The International Centre for Theoretical Sciences (ICTS) in Bengaluru, which emerged in 2007 from the theoretical physics department at the Tata Institute for Fundamental Research, focuses on collaborations. ICTS was modelled on the Kavli Institute for Theoretical Physics in Santa Barbara and the Institute for Advanced Study in Princeton, New Jersey, the revered home of Einstein and other luminaries. "ICTS is a centre where the international community congregates, interacts and collaborates with Indian scientists and students, to everyone's benefit," says its director Spenta Wadia, a physicist.

ICTS is also a nodal centre, along with others, for the proposed Laser Interferometer Gravitational-Wave Observatory India, an Indo-US collaboration to detect gravitational waves. So far, several of its key contributions help scientists solve physics problems, such as proofs of filtering techniques used in weather and climate prediction. Physical sciences already make up a focus of India's research, accounting for 40.5% of its articles in the 2014 Nature Index.

Developing an interdisciplinary institute requires a community. "Bengaluru provides the ecosystem," says Wadia, who had to lobby the government hard, and prepare a white paper explaining why ICTS should be set up here. The city (which until October 31, 2014 was officially known as Bangalore) is also home to the Jawaharlal Nehru Centre for Advanced Scientific Research, the National Centre for Biological Sciences, the Raman Research Institute and the Indian Space Research Organisation.

Although the ICTS has government support for building its infrastructure and facilities, like the TTK centre, it supplements this with grants from outside. For example, the French aircraft manufacturer, Airbus, funded a chair in the mathematics of complex systems (shared with the TIFR Centre for Applicable Mathematics).

JOERG BOETHLING/ALAMY

Transgenic cotton must be optimized to be resistant to crop-destroying pests in India.

"These grants — over and above government grants — are absolutely critical to fulfilling the mission of ICTS," says Wadia. "They also give you flexibility in what you do."

MAKING SCIENCE SOCIAL

Beyond just moving ahead in the lab, India needs to get results to the people. As Chaurasia says, "It is a challenge to deliver the advantages of scientific and technological development to the majority of the population, which is living below the poverty line." In particular, Chaurasia points out challenges in feeding India, which ranks 55th out of 76 countries on the United Nation's Global Hunger Index. The primary agricultural challenge facing India, Chaurasia says is "to develop climate-resilient, green, high-yielding, sustainable agricultural technologies that are affordable for rural areas." This is not one of India's strengths, because only 8.4% of its publications in the 2014 Nature Index address any kind of life science.

To achieve that, however, Chaurasia believes that the country must explore more of today's advanced options for farming, though past attempts have not been successful. In the early 2000s, for example, a pilot project of planting Bt cotton, which includes a gene for an insect toxin that comes from the bacterium *Bacillus thuringiensis* (Bt), was ineffective in resisting bollworms because the cotton was a hybrid from Western countries in which the toxin was not concentrated highly enough. The lesson learned, says Chaurasia, is that India must "develop indigenous transgenic crops — genetically modified organisms — especially after the failure of the Indian government-led Bt-transgenic programmes." Developing transgenic hybrids optimized for India, though, will probably require the nation's industry taking up the challenge.

Chaurasia believes that the government must take a bigger part and "enhance all-round investment in agriculture without surrendering to private interests." In particular, private interests from outside India, such as US-based Monsanto, received some of the blame for past failures with transgenic crops. Chaurasia also calls for other changes, including "attracting the best talents for agricultural research by reinventing the education system."

AMBITIOUS IDEAS

The progression of India's science and technology depends on finding routes for scientists to do world-class research. In virtually all cases, that requires funding from research institutes. Optical physicist, Pavan Kumar, at the Indian Institutes of Science and Research in Pune, says that the institute provides reasonable funding to researchers. For instance, a start-up grant can be in the order of US$200,000. Consequently, says Kumar, "You can think about ambitious problems that a starting principal investigator might be hesitant to think about." Even with existing funding issues, India placed 13th for global publishing output in the 2014 Nature Index.

Research like Kumar's easily branches between basic and applied. Such connections could be the key to better funding. At IIT, for example, Srinivasan is carving a niche between basic and industrial research, but she points out that her work may not lend itself to publication. Still, she says, "Everybody need not do the same thing. I have enough academic freedom to contribute in my own way." ■

INDIA ANALYSIS

Institutional subject spread

Scientists at most of India's leading research centres focus on chemistry in papers in the NI WFC.

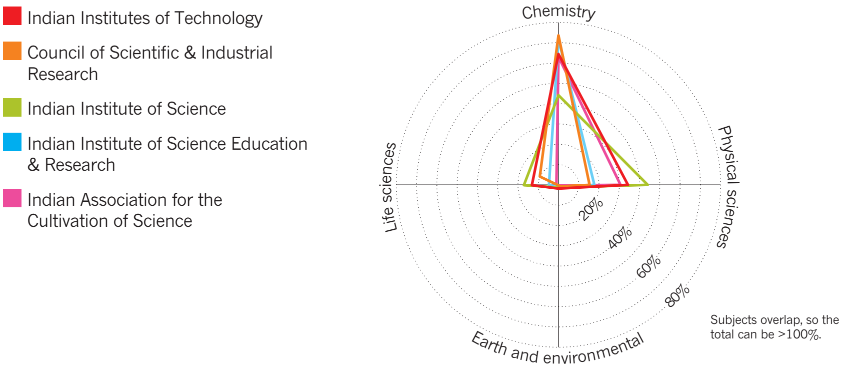

***Nature* and *Science* ratio**

Although other NI metrics show the low volume of articles from India, this one highlights the lack of quality.

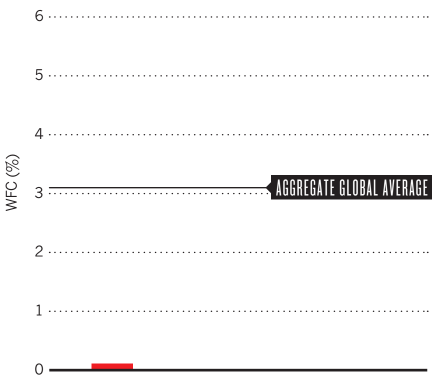

Asian Tigers, Pacific Panthers

Even Asia-Pacific's smaller players — notably Singapore, Taiwan and New Zealand — work to improve their scientific and technical capabilities, while several tiny nations in the region are beginning to shine.

SINGAPORE

ARTICLE COUNT (AC): **873**
FRACTIONAL COUNT (FC): **521.40**
WEIGHTED FRACTIONAL COUNT (WFC): **520.60**

Singapore's reputation for science and technology has long belied its small size. The island nation has a population of just 5.5 million people, but boasts one of the world's highest numbers of scientists and engineering researchers per capita. As the country celebrates its 50th birthday this year, Singapore can proudly point to its global standing in the fields of electronics, petrochemicals and, of late, pharmaceuticals.

More than 30 of the top global drug companies have a presence in Singapore, collectively spending approximately US$500 million per year on research and development. Amgen, the world's largest biotechnology company, is constructing its first Asian manufacturing facility in Singapore while Novartis, the Swiss pharma giant, is building a new biological drugs production plant that should be operational by 2017. Novartis already has a few production plants in Singapore, as well as the company's Asia-Pacific headquarters, the Novartis Institute for Tropical Diseases.

Singapore has achieved its scientific prominence, in part, by forging international partnerships to bolster its research credentials. In May 2014, for example, the National Research Foundation of Singapore signed an agreement with the French National Research Agency to jointly fund three-year basic research projects in materials science and nanotechnology. Scientists involved in each collaborative Franco-Singaporean project will receive up to US$590,000, with equal funds provided by each country. In July 2014, Singapore also joined the Human Frontier Science Program, which funds international collaborations in the life sciences.

"SINGAPORE HAS THIS BIODIVERSITY THAT HASN'T BEEN MAPPED"

Individual research institutions in Singapore have also forged alliances with top-tier universities in Europe, the United States and elsewhere. This spirit of collaboration is spreading into industry.

Last year, for example, the government-backed Agency for Science, Technology and Research (A*STAR) and the Swiss food giant Nestlé agreed to work together to study how natural processes, such as fermentation, can transform raw ingredients into foods that are more digestible or have extended shelf-lives. Meanwhile, the National University of Singapore (NUS) partnered with California-based Agilent Technologies to develop the first database of lipid, or fat, levels among healthy people of different racial and ethnic backgrounds. In 2014, A*STAR also entered a five-year research arrangement with GE Healthcare to build new medical scanning technologies that improve on computed tomography and magnetic resonance imaging.

Many of Singapore's scientists and engineers are native to the country, but it continues to attract top researchers from around the world. Academics are often drawn to Singapore's international atmosphere and the funding opportunities for a range of long-term support options. One recent recruit was James Best, a leader in the fields of diabetes and kidney research. Best left his post at the University of Melbourne in Australia last year to serve as dean of the Lee Kong Chian School of Medicine at Nanyang Technological University (NTU) in Singapore. Best praises Singapore's "optimistic and positive culture," which he says places exceptional emphasis on education, as well as the country's high level of research investment.

To foster talent, focused research centres are being established across the country. In October 2014, for instance, NTU opened the Photonics Institute to explore research involving light technologies, such as those found in fibre-optic cables, lasers and consumer electronics.

SINGAPORE ANALYSIS

Top ten institutions
Only Singapore's top three institutions in the Nature Index (NI) make a significant contribution to publishing in science and technology, based on their WFCs.

RANK	INSTITUTION	WFC 2014	AC 2014
1	Nanyang Technological University (NTU)	199.86	371.00
2	National University of Singapore (NUS)	190.30	465.00
3	Agency for Science, Technology & Research (A*STAR)	100.33	284.00
4	Singapore University of Technology & Design (SUTD)	8.50	24.00
5	National Research Foundation (NRF)	4.57	35.00
6	National University Health System (NUHS)	1.40	18.00
7	National Cancer Centre Singapore	1.11	7.00
8	National Neuroscience Institute (NNI)	0.85	4.00
9	Defence Science and Technology Agency (DSTA)	0.58	3.00
10	Singapore General Hospital	0.55	7.00

Top five collaborators
About 40% of Singapore's NI articles include international collaborators, and China runs a close second to the United States.

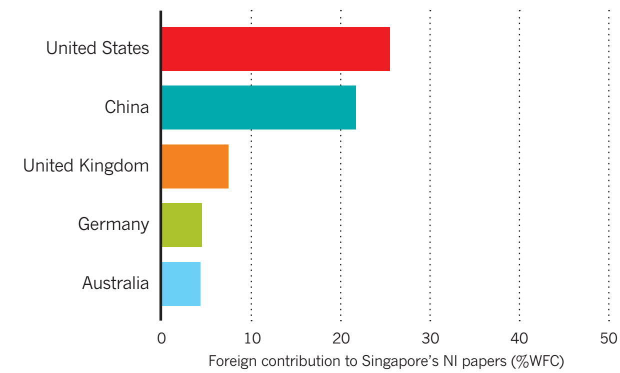

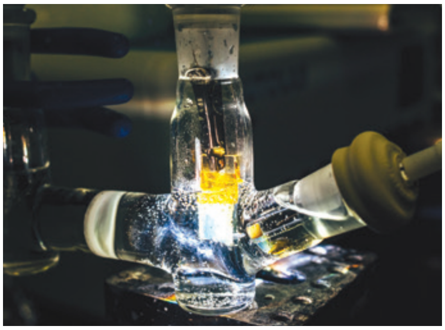
NTU SINGAPORE

Researchers at NTU Singapore study light technologies, such as this artificial leaf.

A month earlier, NTU had joined forces with A*STAR and the National Healthcare Group to launch the Rehabilitation Research Institute of Singapore, which aims to make advances in areas such as stroke recovery, clinical robotics and biomechanics.

Meanwhile, as part of an effort to understand health issues unique to Asian populations, the NUS Yong Loo Lin School of Medicine recently opened the doors of its new Centre for Translational Medicine. The centre will focus on two areas of research that particularly affect Singapore and the region, including diseases such as liver cancer that are more common in Asian populations. It will also investigate why Asian people respond to drug therapies differently than people in the West. In line with the "translational" part of the centre's remit, basic life scientists work "right next to clinicians in the same building," says Barry Halliwell, deputy president for research and technology at NUS.

In February 2015, the NUS Lee Kong Chian Natural History Museum also unveiled its Animal and Plants of Singapore project, which tracks research and observations about the country's flora and fauna, especially in the face of climate change.

"Until recently most of Singapore's research into life sciences has been in the biomedical arena," Halliwell says. "But we're now more conscious of the fact that Singapore has all this biodiversity around us that really hasn't been mapped."

In addition, all the buildings, infrastructure, land and environment of Singapore are being mapped through the country's Smart Nation Initiative, a major new government investment in information technology.

One of the first projects of this programme involves building a sophisticated three-dimensional model of Singapore for researchers to run large-scale simulations of cell phone-coverage patterns, evacuation measures and other engineering issues that instruct the work of city planners.

TAIWAN

ARTICLE COUNT (AC): 887
FRACTIONAL COUNT (FC): 520.18
WEIGHTED FRACTIONAL COUNT (WFC): 481.36

Among the Asian Tigers — the economically emergent nations of the Pacific Rim — Taiwan has been a strong contender in engineering, computer science, materials and condensed matter physics. Almost 90% of its publications in the 2014 Nature Index were in chemistry or physical sciences. That bedrock will be strengthened in the coming year with the opening of the Taiwan Photon Source, a physics research facility that will accelerate electrons to energies exceeding three gigaelectronvolts, making it one of the world's brightest x-ray sources.

The new research centre complements the older Taiwan Light Source, which opened more than 20 years ago at the National Synchrotron Radiation Research Center (NSRRC) in Hsinchu City with only half the energy capacity. "The Taiwan Photon Source will provide one of the best medium energy storage rings in the world, which will be very useful for imaging, diffraction and spectroscopy research," says Shih-Lin Chang, a physicist who directed the Hsinchu facility from 2010 to 2014.

Taiwan is also scaling up its efforts in climate sciences with the country's first petabyte-scale database for assessing conditions related to atmosphere, hydrology, ocean currents and tectonics. (1 petabyte is 10^{15} bytes, or 1,000 gigabytes.) The new Earth Science Observation Knowledgebase (ESOK) holds more than 10 million satellite images, shock-wave records and other measurements from an array of national academic sources. With the ability to access 18,000 data points per second, ESOK will serve scientists as they model the impact of climate change and natural disasters.

Taiwan's National Space Organisation last year also unveiled a new satellite component that should help the country create its own space technology. In the past, Taiwanese satellites have relied on foreign equipment, which is tightly regulated by export controls. The new component helps satellites to receive signals from global positioning systems and to transmit photos with improved resolution. Officials expect the component will be installed on the Formosa-7 satellite, which is set to be launched in 2018.

In the biological sciences, Taiwan is creating major new research facilities. Last year, the government built a new marine biology and ecology research centre on Dongsha Island — a tiny coral atoll 450 kilometres southwest of the main island of Taiwan. With a focus on environmental protection and sustainable development, the new centre boasts wave- and water-quality monitoring devices, marine biology laboratories and research vessels.

Meanwhile, Academia Sinica, the country's national academy with more than 900 researchers, is building a National Biotechnology Research Park, set to open in Taipei's Nankang District in 2016. The park will expand the country's capacity for translational medicine — the conversion of basic scientific discoveries into health benefits — as well as provide a home for startup drug companies.

Not all new infrastructure projects have gone according to plan. In recent years, Taiwan

TAIWAN ANALYSIS

Top ten institutions
NTU and Academia Sinica account for nearly 50% of the NI articles published by the top ten institutions.

RANK	INSTITUTION	WFC 2014	AC 2014
1	National Taiwan University (NTU)	106.54	294.00
2	Academia Sinica	81.86	482.00
3	National Tsing Hua University (NTHU)	65.28	171.00
4	National Chiao Tung University (NCTU)	46.60	99.00
5	National Cheng Kung University (NCKU)	19.28	60.00
6	National Taiwan Normal University	17.80	45.00
7	National Central University (NCU)	15.60	112.00
8	National Sun Yat-Sen University (NSYSU)	12.78	29.00
9	National Chung Hsing University (NCHU)	10.49	21.00
10	National Synchrotron Radiation Research Center (NSRRC)	10.22	35.00

Top five collaborators
About half of Taiwan's NI publications include international collaborators, and about 20% of them come from China and Japan.

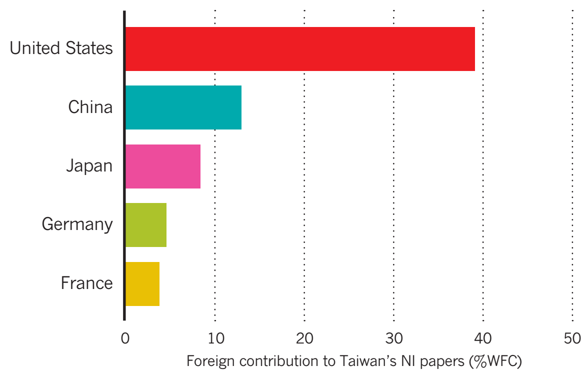

had been bolstering its capacity in oceanographic research. But tragedy struck in October 2014 when the country's RV *Ocean Researcher V* — a 73-metre, 2,700-tonne research vessel — sank in rough seas in the Penghu Passage between Taiwan and China. The shipwreck, less than two years after the boat's maiden voyage, killed two scientists and scuppered more than a dozen research projects. Liang-Saw Wen, deputy director of the Taiwan Ocean Research Institute in Kaohsiung, admits to "facing very severe setbacks."

Taiwan's government pledged to restore and strengthen its oceanic research capacity with the construction of a new large vessel and the purchase of other smaller ones. "Hopefully, we will be back in business in full stride soon," says Wen.

NEW ZEALAND

ARTICLE COUNT (AC): 275
FRACTIONAL COUNT (FC): 102.96
WEIGHTED FRACTIONAL COUNT (WFC): 95.69

New Zealand is well known for its sheep and spectacular scenery, and those national assets undoubtedly influence the country's research agenda. Case in point: researchers at the government-funded New Zealand Agricultural Greenhouse Gas Research Centre in Palmerston North are leading global efforts to develop a vaccine that can reduce methane emissions from livestock. But the country is hoping to add high-value research in health, housing and new technologies to its national output. For now, about a third of its publications are in life sciences, according to the 2014 Nature Index.

Last year, the government launched its National Science Challenges initiative, which will contribute more than US$23 million per year to 11 scientific areas of particular national relevance. These include studies of resilience to natural disasters, nutritional interventions, biosecurity and explorations of Antarctica's


OTAGO DAILY TIMES

At New Zealand's Dodd-Walls Centre, many scientists study photonics, such as the rare earth ion-doped crystals being used here to detect ultrasound.

impact on New Zealand's climate. Notably, the National Science Challenges will provide the money to interdisciplinary, multi-institutional teams for ten years — much longer than the typical three- to five-year grant cycle.

The National Science Challenges programme is in addition to new investments in the country's Centres of Research Excellence (CoRE), which, since 2002, have built New Zealand's research capacity in targeted scientific areas. The newest CoREs, funded from 2015 to 2020, focus on medical technologies, human disease, advanced materials, photonics, complex networks and brain research.

"WE AIM TO MELD THIS STRENGTH INTO A COHERENT RENOWNED WHOLE"

Each centre serves as a collaborative hub for research and training. "We have numerous world-recognized individuals," says David Hutchinson, director of the Dodd-Walls Centre for Photonic and Quantum Technologies, a new CoRE at the University of Otago in Dunedin. "The CoRE aims to take this strength and meld it into a coherent, world renowned whole."

To turn basic scientific discoveries into commercial products, the New Zealand government launched a programme in 2013 to help build new start-up companies from emergent technologies. The Callaghan Innovation (named after physicist Sir Paul Callaghan, who died in 2012), has forged partnership arrangements with more than 20 research organizations across New Zealand. In 2014, the programme created a number of incubators to nurture fledgling firms. "We support New Zealand businesses developing or commercializing high value products and services," says Mary Quin, Callaghan Innovation's chief executive. "This includes providing access to the specialist research, engineering and commercial expertise, and research funding they need to gain a technical edge on the competition."

The country's largest newspaper, the *New Zealand Herald*, named Quin, a materials scientist, as the New Zealander of the Year for 2014. But perhaps no scientist is as well known to the New Zealand public as the country's Chief Science Adviser, Peter Gluckman. In his five years in the post, Gluckman, a paediatrician who studied developmental endocrinology and neuroscience at the University of Auckland before entering government in 2009, has been a key voice informing debate around issues as varied as childhood obesity, fluoride treatment of water, and climate change.

In March 2014, Gluckman authored a policy document in *Nature* outlining ten principles for building public trust and government influence. Months later, he hosted the first global conference on science advice to governments. The meeting — held in Auckland in August — brought together about 200 participants from more than 40 countries that shared practices and perspectives in the provision of advice in the scientific arena. Gluckman is leading efforts to build a more formal network of science advice practitioners.

NEW ZEALAND ANALYSIS

Top ten institutions
Compared to the leaders in the Asia-Pacific, New Zealand scientists publish very few NI papers.

RANK	INSTITUTION	WFC 2014	AC 2014
1	University of Otago	27.79	79.00
2	The University of Auckland	20.97	132.00
3	Victoria University of Wellington	12.47	62.00
4	GNS Science	7.93	30.00
5	University of Canterbury (UC)	7.47	101.00
6	Massey University	5.16	39.00
7	National Institute of Water & Atmospheric Research (NIWA)	4.25	28.00
8	University of Waikato	2.24	13.00
9	AgResearch	1.43	5.00
10	Lincoln University	1.23	3.00

Top five collaborators
About 65% of New Zealand's NI articles include collaborators from other countries, and the only top source in the region is neighbouring Australia.

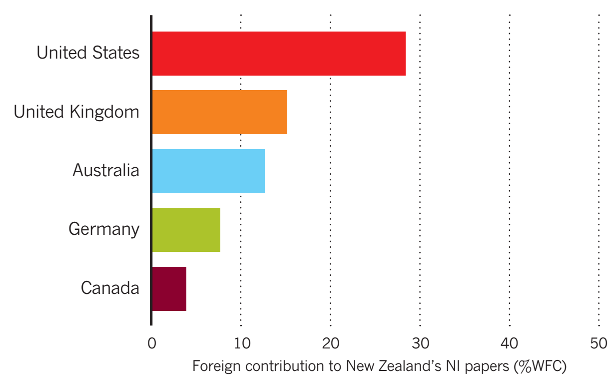


REUTERS/CORBIS

Farmers expect better yields from new forms of rice, such as those developed at Vietnam's Agricultural Genetics Institute.

OTHER COUNTRIES

Vietnam had much to be proud of in 2014. The country's Agricultural Genetics Institute received international accolades for developing hardier varieties of rice and soybeans; researchers at the Vietnam Academy of Science and Technology created steel from red mud; and Vietnam became the second Asian country to develop, test and produce an anti-diarrhoeal vaccine for children. Also in 2014, Vietnam celebrated its first Science and Technology Day. This new national holiday will be held annually on 18 May to honour scientific achievements in the country and to raise awareness of the social, physical and natural sciences.

Bangladesh is making huge strides in research and technology. Through its Vision 2021 development programme, the country is starting to focus on telecommunications, transportation and aquatic research. But the most significant achievements continue to be made in the health sciences — in particular by researchers at the International Centre for Diarrhoeal Disease Research, Bangladesh (ICDDR,B) in Dhaka. Last year, for example, scientists from the 50-year-old ICDDR,B published two papers in *Nature* describing how gut microbes affect healthy growth in children and recovery from cholera in adults. "Our ultimate goal is to improve the health conditions of the children who are suffering from infectious diseases and malnutrition," says Rashidul Haque, head of the parasitology laboratory at ICDDR,B.

Many of the countries in the Asia-Pacific region often serve as test sites for clinical trials involving diseases endemic there. Last year, Sanofi Pasteur, the French vaccine giant, published the first ever phase-3 clinical trials for a vaccine candidate for dengue fever, a mosquito-borne illness with no proven vaccines or antiviral drugs. That trial took place in five countries: Indonesia, Malaysia, Philippines, Thailand and Vietnam. Maria Rosario Capeding, who led the study, from the Research Institute for Tropical Medicine in the Philippines, says these sites were chosen for their "exemplary capabilities and the efficiency of the clinical trial teams in this region." In 2015, the first in-human clinical trial of an experimental leprosy vaccine will also be conducted in the Philippines.

"IT WILL FIND SOUND SOLUTIONS ACCEPTABLE TO LOCAL CULTURE"

Many current and former US territories in the South Pacific are beefing up their biomedical research capacity. Last year, the Republic of Palau became the latest nation to open a training laboratory under the Pacific Short-Term Education Program for Underrepresented Persons (STEP-UP). The hope is that STEP-UP will "increase the pipeline of underrepresented or disadvantaged individuals engaging in health and biomedical research," says programme director, George Hui, a malaria vaccine researcher at the University of Hawaii. "It will find solutions that would be scientifically sound and acceptable to the local culture and community practices."

Since 2010, the programme has helped establish similar facilities at the American Samoa Community College, the Northern Marianas College, the College of the Marshall Islands and the College of Micronesia.

Also in the South Pacific, the tiny island chain of Kiribati is making a big contribution to conservation research. In July 2014, President Anote Tong pledged to ban all commercial fishing in the country's Phoenix Islands Protected Area. "Its closure will make a major contribution to the conservation and rejuvenation of fish stocks and to global food security," Tong told delegates of the 2014 Our Ocean conference. The 40 million hectare reserve will remain open to scientists hoping to study tuna, sharks and other tropical fish species.

Outside conservation and ecology, however, few of the island nations that dot Oceania have a significant influence on the global science enterprise. Individually, each country is too small. But collectively, they could have a much bigger impact and a new cooperative agreement is helping foster the necessary international scientific teamwork. At the Pacific Islands Leaders Forum held in Palau in July 2014, more than a dozen countries agreed on a new Framework for Pacific Regionalism, committing to advance integration on a range of issues, including intellectual property rights and scientific projects. Among other goals, the framework promises to spur joint agricultural research on crops endemic to the Pacific rim.

In Southeast Asia, ten countries are also joining forces in 2015 to formally launch the integrated ASEAN Economic Community. The new single market — which encompasses Indonesia, Malaysia, the Philippines, Singapore, Brunei, Vietnam, Laos, Myanmar, Thailand and Cambodia — will advance scientific cooperation in the fields of food science, biotechnology, meteorology, microelectronics and space technology, among other disciplines. Scientists, engineers and doctors will be able to move more freely between countries. Laboratory testing and customs procedures will be harmonized. An Asian power grid will be built that draws on biofuels and other alternative energy sources.

Research innovation is becoming an increasingly global phenomenon. And, as it does, traditional national borders could become less significant — good news for the smaller players in the Asia-Pacific region, and positive for scientific enterprise as a whole. ■

A guide to the Nature Index

A description of the terminology and methodology used in this supplement, and a guide to the functionality available free online at natureindex.com.

The Nature Index is a database of author affiliations and institutional relationships, used to track contributions to articles published in a group of highly selective science journals that have been chosen by an independent group of active researchers.

Data in the Nature Index are updated monthly, with the most recent 12 months of data made available under a Creative Commons license at natureindex.com.

The Nature Index provides absolute counts of high-quality publication productivity at the institutional and national level, and as such is one indicator of high-quality research output across the globe.

The database is compiled by Nature Publishing Group (NPG) in collaboration with sister company Digital Science.

The current journals tracked by the Nature Index will be reviewed again in 2015, and from 2016, coverage will be extended to include the clinical sciences.

NATUREINDEX.COM

A global indicator of high-quality research

Users of natureindex.com can search for specific institutions or countries and generate their own reports, ordered by article count (AC), fractional count (FC) or weighted fractional count (WFC).

Each query will return a profile page that lists the country or institution's recent research outputs, from which it is possible to drill down for more information. For example, articles can be displayed by journal, and then by article title. As in the supplement, research outputs are organized by subject area. The profile page also lists the institution or country's top collaborators, as well as its relationship with other research organizations.

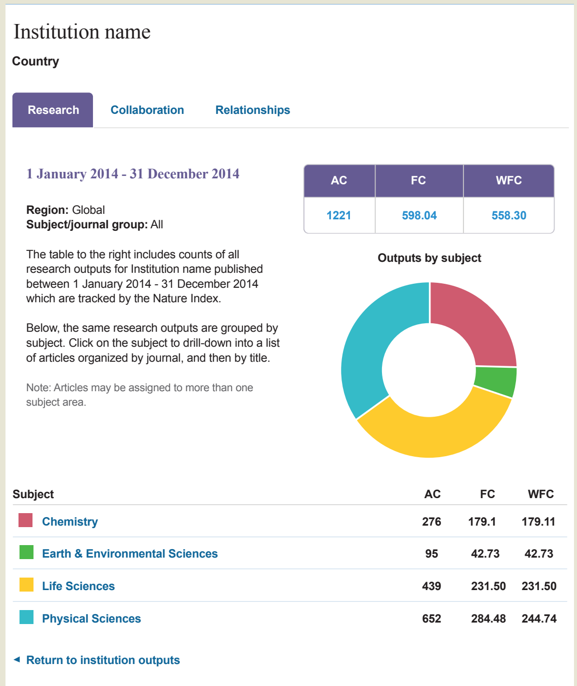

NATURE INDEX METRICS

There are three measures provided by the Nature Index to track affiliation data. The simplest is the article count (AC). A country or institution is given an AC of 1 for each article that has at least one author from that country or institution. This is the case whether an article has one or a hundred authors, and it means that the same article can contribute to the AC of multiple countries or institutions.

To get a better sense of a country or institution's contribution to an article, and to remove the issue of double-counting of articles, the Nature Index uses the fractional count (FC). FC takes into account the relative contribution of each author to an article.

The total FC available per paper is 1, and this is shared between all authors under the assumption that each contributed equally. For instance, a paper with 10 authors means that each author receives an FC of 0.1. For authors who have worked with joint affiliations, the individual FC is then split equally between each affiliation.

The third measure used is the weighted fractional count (WFC), which applies a weighting to the FC in order to adjust for the over-representation of papers from astronomy and astrophysics.

The four journals in these disciplines publish about 50% of all papers in international journals in this field — approximately five-times the equivalent figures for other fields. Therefore, although the data for astronomy and astrophysics are compiled in exactly the same way as for all other disciplines, articles from these journals are assigned one-fifth the weight of other articles (i.e., the FC is multiplied by 0.2 to derive the WFC).

The total FC or WFC for an institution is derived by summing the FC or WFC for individual authors.

The process is similar for countries, although complicated by the fact that some institutions have overseas labs that will be counted towards the host country totals. What's more, there is great variability in the way authors present their affiliations. Every effort is made to count affiliations consistently, and with the background of reasonable assumptions.

For more information on how the affiliation information is processed and counted, please see the frequently asked questions at natureindex.com.

THE SUPPLEMENT

Nature Index 2015 Asia-Pacific is based on a snapshot of data from natureindex.com, covering articles published between 1 January and 31 December, 2014.

Most analyses within the supplement use the WFC as the primary metric, as it provides a more even basis for comparison, and in determining the relative contribution of each country/institution. ■

Nature Index tables

Asia–Pacific's leading institutions for high–quality science, ordered by weighted fractional count (WFC) for 2014. Also shown are the total number of articles, and the change in WFC from 2013. Articles are from the 68 natural science journals that comprise the Nature Index (see A guide to the Nature Index, page S75).

TOP INSTITUTIONAL CONTRIBUTORS

2014	INSTITUTION	COUNTRY	WFC	ARTICLE COUNT	2013 WFC	2013–2014 CHANGE IN WFC
1	Chinese Academy of Sciences (CAS)	China	1,303.86	3,114	1,207.39	8%
2	The University of Tokyo (UTokyo)	Japan	453.45	1,242	472.87	−4.1%
3	Peking University (PKU)	China	291.45	932	275.46	5.8%
4	Kyoto University	Japan	286.13	714	313.51	−8.7%
5	Osaka University	Japan	218.62	553	219.88	−0.6%
6	Tsinghua University (TH)	China	205.48	605	194.93	5.4%
7	Nanjing University (NJU)	China	201.91	469	196.00	3%
8	Nanyang Technological University (NTU)	Singapore	199.86	371	187.38	6.7%
9	University of Science and Technology of China (USTC)	China	190.96	536	175.73	8.7%
10	National University of Singapore (NUS)	Singapore	190.30	465	191.72	−0.7%
11	Zhejiang University (ZJU)	China	188.39	349	150.42	25.2%
12	Tohoku University	Japan	177.99	423	189.01	−5.8%
13	Indian Institutes of Technology (IITs)	India	168.17	287	128.43	30.9%
14	Fudan University	China	162.89	343	129.22	26.1%
15	Seoul National University (SNU)	South Korea	160.24	424	158.13	1.3%
16	RIKEN	Japan	144.14	495	165.95	−13.1%
17	Council of Scientific and Industrial Research (CSIR)	India	128.64	196	115.24	11.6%
18	Tokyo Institute of Technology	Japan	127.21	329	105.59	20.5%
19	Nagoya University	Japan	125.28	431	132.97	−5.8%
20	Korea Advanced Institute of Science and Technology (KAIST)	South Korea	116.33	222	103.03	12.9%
21	The University of Queensland (UQ)	Australia	108.83	392	94.78	14.8%
22	Shanghai Jiao Tong University (SJTU)	China	106.78	281	96.01	11.2%
23	National Taiwan University (NTU)	Taiwan	106.54	294	101.28	5.2%
24	Lanzhou University (LZU)	China	106.27	174	69.71	52.4%
25	Monash University	Australia	102.98	381	94.47	9%
26	Jilin University (JLU)	China	101.87	184	97.72	4.2%
27	Agency for Science, Technology and Research (A*STAR)	Singapore	100.33	284	81.62	22.9%
28	National Institute for Material Science (NIMS)	Japan	100.08	239	81.79	22.4%
29	Hokkaido University (HU)	Japan	100.03	234	105.93	−5.6%
30	Kyushu University	Japan	98.30	274	84.51	16.3%
31	Indian Institute of Science (IISC)	India	93.72	149	83.64	12%
32	Xiamen University (XMU)	China	93.35	205	76.02	22.8%
33	Nankai University	China	91.74	220	113.52	−19.2%
34	Wuhan University (WHU)	China	90.63	152	98.80	−8.3%
35	Sichuan University (SCU)	China	89.40	165	76.82	16.4%
36	The University of New South Wales (UNSW)	Australia	88.12	277	69.81	26.2%
37	University of Chinese Academy of Sciences (UCAS)	China	88.02	514	71.24	23.5%
38	Sun Yat–sen University (SYSU)	China	87.84	189	79.43	10.6%
39	Australian National University (ANU)	Australia	87.16	498	93.53	−6.8%
40	Soochow University	China	86.09	156	65.31	31.8%
41	The University of Melbourne	Australia	82.47	474	89.33	−7.7%

2014	INSTITUTION	COUNTRY	WFC	ARTICLE COUNT	2013 WFC	2013–2014 CHANGE IN WFC
42	Academia Sinica	Taiwan	81.86	482	80.06	2.2%
43	East China Normal University (ECNU)	China	80.63	144	65.56	23%
44	The University of Sydney (USYD)	Australia	79.89	491	95.13	–16%
45	Indian Institute of Science Education and Research (IISER)	India	75.88	106	58.72	29.2%
46	Hong Kong University of Science and Technology (HKUST)	China	73.59	133	54.60	34.8%
47	Hunan University (HNU)	China	73.19	103	54.57	34.1%
48	The University of Hong Kong (HKU)	China	71.71	183	71.38	0.5%
49	Yonsei University	South Korea	71.00	200	61.62	15.2%
50	Pohang University of Science and Technology (POSTECH)	South Korea	70.33	150	70	0.5%
51	National Institute of Advanced Industrial Science and Technology (AIST)	Japan	69.79	185	79.53	–12.2%
52	Xi'an Jiaotong University (XJTU)	China	67.97	166	42.98	58.1%
53	East China University of Science and Technology (ECUST)	China	67.48	119	56.75	18.9%
54	National Tsing Hua University (NTHU)	Taiwan	65.28	171	66.23	–1.4%
55	Shandong University (SDU)	China	62.07	154	39.18	58.4%
56	Korea University (KU)	South Korea	61.21	210	72.01	–15%
57	Sungkyunkwan University (SKKU)	South Korea	58.83	240	50.72	16%
58	Huazhong University of Science & Technology (HUST)	China	56.97	150	43.62	30.6%
59	University of Tsukuba	Japan	53.68	224	50.15	7.1%
60	Southeast University (SEU)	China	52.19	108	30.94	68.6%
61	Dalian University of Technology (DUT)	China	50.61	94	61.42	–17.6%
62	Indian Association for the Cultivation of Science (IACS)	India	49.95	70	51.20	–2.4%
63	Hanyang University (HYU)	South Korea	49.74	127	37.06	34.2%
64	Beijing Normal University (BNU)	China	49.63	142	39.60	25.3%
65	Northeast Normal University (NENU)	China	47.53	66	30.73	54.7%
66	National Chiao Tung University (NCTU)	Taiwan	46.60	99	64.35	–27.6%
67	Tongji University	China	44.86	105	40.83	9.9%
68	Keio University	Japan	44.60	117	58.33	–23.6%
69	South China University of Technology (SCUT)	China	44.59	89	30.74	45.1%
70	Tianjin University (TJU)	China	43.42	145	33.98	27.8%
71	National Institutes of Natural Sciences (NINS)	Japan	40.35	361	46.63	–13.5%
72	The University of Adelaide	Australia	38.73	180	26.69	45.1%
73	Ulsan National Institute of Science and Technology (UNIST)	South Korea	38.28	87	28.42	34.7%
74	The University of Western Australia (UWA)	Australia	37.45	294	44.55	–16%
75	The Chinese University of Hong Kong (CUHK)	China	35.59	107	39.39	–9.6%
76	Fuzhou University	China	34.71	54	26.76	29.7%
77	Chiba University	Japan	34.56	96	36.84	–6.2%
78	The Commonwealth Scientific and Industrial Research Organisation (CSIRO)	Australia	33.01	237	48.86	–32.4%
79	Chinese Academy of Medical Sciences & Peking Union Medical College (CAMS & PUMC)	China	31.37	92	24.72	26.9%
80	City University of Hong Kong	China	31.28	76	36.51	–14.3%
81	Kyung Hee University (KHU)	South Korea	30.98	122	36.22	–14.5%
82	Beijing Institute of Technology (BIT)	China	30.10	63	20.11	49.7%
83	Shanghai University	China	29.81	67	16.49	80.8%
84	Harbin Institute of Technology (HIT)	China	29.73	59	36.22	–17.9%
85	Tata Institute of Fundamental Research (TIFR)	India	29.63	199	54.74	–45.9%
86	Institute for Basic Science (IBS)	South Korea	29.03	116	14.51	100.1%
87	University of Science and Technology Beijing (USTB)	China	28.85	53	25.79	11.9%
88	Ewha Womans University	South Korea	28.67	83	26.13	9.7%
89	Beijing University of Chemical Technology (BUCT)	China	28.34	48	23.45	20.8%
90	Hiroshima University (HU)	Japan	28.15	120	44.45	–36.7%
91	University of Otago	New Zealand	27.79	79	27.20	2.2%
92	Tokyo University of Science (TUS)	Japan	25.48	75	24.75	3%
93	Northwest University (NWU)	China	25.39	39	12.04	110.9%
94	Samsung Electronics Co., Ltd	South Korea	24.96	73	43.55	–42.7%

2014	INSTITUTION	COUNTRY	WFC	ARTICLE COUNT	2013 WFC	2013–2014 CHANGE IN WFC
95	Gwangju Institute of Science and Technology (GIST)	South Korea	24.83	50	20.10	23.5%
96	Jawaharlal Nehru Centre for Advanced Scientific Research (JNCASR)	India	24.13	43	28.77	–16.1%
97	Kanazawa University (KU)	Japan	23.98	49	31.25	–23.3%
98	Okayama University	Japan	23.71	128	26.73	–11.3%
99	Korea Institute of Science and Technology (KIST)	South Korea	23.62	89	25.82	–8.5%
100	Japan Agency for Marine–Earth Science and Technology (JAMSTEC)	Japan	23.60	78	31.54	–25.2%
101	Zhengzhou University	China	23.53	51	13.77	70.9%
102	Osaka Prefecture University (OPU)	Japan	23.42	57	22.41	4.5%
103	Kumamoto University	Japan	22.67	57	18.27	24.1%
104	Beihang University (BUAA)	China	22.50	75	17.71	27%
105	High Energy Accelerator Research Organization (KEK)	Japan	22.34	180	24.05	–7.1%
106	Kobe University	Japan	22.21	136	23.51	–5.5%
107	Southwest University (SWU)	China	21.67	36	16.11	34.5%
108	Waseda University	Japan	21.58	134	25.74	–16.1%
109	Central China Normal University (CCNU)	China	21.08	57	15.93	32.3%
110	The University of Auckland	New Zealand	20.97	132	26.71	–21.5%
111	Nanjing Tech University (NanjingTech)	China	20.74	45	11.92	74%
112	Macquarie University	Australia	19.71	154	19.97	–1.3%
113	Central South University (CSU)	China	19.66	58	10.15	93.6%
114	Harish–Chandra Research Institute (HRI)	India	19.47	40	14.10	38%
115	University of Tasmania (UTAS)	Australia	19.42	106	17.99	7.9%
116	Curtin University	Australia	19.29	194	21.85	–11.7%
117	National Cheng Kung University (NCKU)	Taiwan	19.28	60	33.56	–42.5%
118	University of Hyderabad (UoH)	India	19.04	28	19.10	–0.3%
119	Yokohama City University (YCU)	Japan	18.76	46	10.75	74.5%
120	NTT Group	Japan	18.73	32	28.40	–34%
121	Chongqing University (CQU)	China	18.69	32	12.90	45%
122	Nanjing Normal University (NNU)	China	18.67	46	7.75	140.9%
123	Nara Institute of Science and Technology (NAIST)	Japan	18.64	47	21.24	–12.2%
124	University of Electronic Science and Technology of China (UESTC)	China	18.42	49	11.98	53.7%
125	The Hong Kong Polytechnic University (PolyU)	China	18.40	49	25.94	–29.1%
126	The Graduate University for Advanced Studies (Sokendai)	Japan	18.21	139	19.17	–5%
127	Pusan National University	South Korea	18.20	76	18.26	–0.3%
128	Kangwon National University	South Korea	17.91	72	10.23	75%
129	Shandong Normal University (SDNU)	China	17.88	22	12.73	40.5%
130	National Taiwan Normal University	Taiwan	17.80	45	15.76	12.9%
131	RMIT University	Australia	17.49	42	12.86	36%
132	China University of Geosciences (CUG)	China	17.01	38	14.52	17.2%
133	China Agricultural University (CAU)	China	16.22	43	14.65	10.7%
134	James Cook University (JCU)	Australia	15.98	52	12.98	23%
135	Yunnan University	China	15.77	33	11.39	38.4%
136	National Central University (NCU)	Taiwan	15.60	112	18.56	–15.9%
137	South China Normal University (SCNU)	China	15.59	34	6.87	126.9%
138	Tokyo University of Agriculture and Technology	Japan	15.53	39	22.66	–31.5%
139	Chung–Ang University (CAU)	South Korea	15.47	41	12.71	21.7%
140	Saha Institute of Nuclear Physics (SINP)	India	15.45	100	15.30	1%
141	Wuhan University of Technology (WUT)	China	15.24	28	8.59	77.5%
142	State Oceanic Administration (SOA)	China	15.18	34	5.93	155.9%
143	Henan Normal University	China	14.96	35	12.42	20.4%
144	Kyungpook National University (KNU)	South Korea	14.83	119	13.71	8.2%
145	The University of Wollongong (UOW)	Australia	14.76	57	23.02	–35.9%
146	S. N. Bose National Centre for Basic Sciences (SNBNCBS)	India	14.73	34	10.33	42.6%
147	Ocean University of China (OUC)	China	14.69	38	13.03	12.7%

2014	INSTITUTION	COUNTRY	WFC	ARTICLE COUNT	2013 WFC	2013–2014 CHANGE IN WFC
148	Griffith University	Australia	14.60	69	10	46%
149	Shanxi University	China	14.50	26	10.82	34.1%
150	Ajou University	South Korea	14.46	40	10.58	36.7%
151	Osaka City University	Japan	14.40	56	15.55	–7.4%
152	Toyota Group	Japan	14.14	25	9.42	50.2%
153	Tokyo Metropolitan University	Japan	14.09	108	15.57	–9.5%
154	Huazhong Agricultural University (HZAU)	China	14.05	28	10.57	32.9%
155	China University of Petroleum (UPC)	China	14.00	36	7.15	95.9%
156	Xiangtan University	China	13.83	27	12.87	7.5%
157	Changzhou University	China	13.81	21	5.93	133.1%
158	Northwestern Polytechnical University (NPU)	China	13.80	28	12.90	7%
159	The Walter and Eliza Hall Institute of Medical Research (WEHI)	Australia	13.72	53	12.09	13.5%
160	Nagasaki University	Japan	13.67	31	5.75	137.8%
161	Northeastern University	China	13.66	21	2.10	550%
162	Beijing Genomics Institute (BGI)	China	13.64	59	15.34	–11.1%
163	Swinburne University of Technology	Australia	13.54	201	19.56	–30.8%
164	Gyeongsang National University	South Korea	13.37	45	10.82	23.6%
165	Sogang University	South Korea	13.36	28	27.88	–52.1%
166	Beijing University of Technology (BJUT)	China	13.27	29	7.67	73%
167	Shanghai Normal University (SHNU)	China	13.20	24	3.75	251.8%
168	Japan Atomic Energy Agency (JAEA)	Japan	13.14	66	13.76	–4.5%
169	Shaanxi Normal University (SXU)	China	13.08	23	11.80	10.8%
170	National Sun Yat-Sen University (NSYSU)	Taiwan	12.78	29	25.98	–50.8%
171	Ehime University	Japan	12.74	70	15.11	–15.7%
172	Tokyo Medical and Dental University (TMDU)	Japan	12.68	56	16.00	–20.8%
173	Second Military Medical University (SMMU)	China	12.62	41	16.99	–25.7%
174	Nagoya Institute of Technology (NITech)	Japan	12.61	19	20.96	–39.8%
175	Nanjing University of Aeronautics and Astronautics (NUAA)	China	12.61	25	6.58	91.5%
176	South University of Science and Technology of China (SUSTC)	China	12.52	31	2.24	458.3%
177	Victoria University of Wellington	New Zealand	12.47	62	24.91	–50%
178	Korea Institute for Advanced Study (KIAS)	South Korea	12.31	45	15.89	–22.5%
179	Kinki University	Japan	12.23	34	9.21	32.9%
180	China Meteorological Administration (CMA)	China	12.19	35	9.93	22.8%
181	Anhui Normal University	China	12.00	14	5.96	101.4%
182	Hong Kong Baptist University (HKBU)	China	11.99	30	12.77	–6.1%
183	University of Toyama	Japan	11.81	28	14.18	–16.7%
184	Physical Research Laboratory (PRL)	India	11.69	41	8.80	32.9%
185	Shizuoka University	Japan	11.68	32	13.95	–16.3%
186	Nanjing Medical University (NJMU)	China	11.64	49	7.27	60%
187	University of Hyogo	Japan	11.62	40	5.32	118.6%
188	Henan University (HENU)	China	11.35	18	12.53	–9.4%
189	Japan Synchrotron Radiation Research Institute (JASRI)	Japan	11.34	68	14.15	–19.8%
190	Zhejiang University of Technology	China	11.10	22	8.03	38.2%
191	Wenzhou University	China	11.06	19	8.05	37.4%
192	Inha University	South Korea	11.04	34	11.21	–1.5%
193	China Pharmaceutical University (CPU)	China	10.87	24	3.88	180.1%
194	University of Delhi (DU)	India	10.83	79	7.71	40.6%
195	QIMR Berghofer Medical Research Institute	Australia	10.83	63	4.28	153.1%
196	Chonnam National University (CNU)	South Korea	10.83	103	5.85	85.2%
197	National Institute of Biological Sciences, Beijing (NIBS)	China	10.79	31	11.73	–8%
198	Niigata University	Japan	10.77	60	12.75	–15.5%
199	Banaras Hindu University (BHU)	India	10.76	21	10.47	2.8%
200	Yamagata University	Japan	10.72	34	7.76	38.3%

TOP INSTITUTIONAL CONTRIBUTORS: LIFE SCIENCES

2014	INSTITUTION	COUNTRY	WFC	ARTICLE COUNT	2013 WFC	2013–2014 CHANGE IN WFC
1	Chinese Academy of Sciences (CAS)	China	155.22	420	147.94	4.9%
2	The University of Tokyo (UTokyo)	Japan	99.33	262	112.59	–11.8%
3	Kyoto University	Japan	62.04	160	70.86	–12.5%
4	RIKEN	Japan	59.26	201	70.06	–15.4%
5	The University of Queensland (UQ)	Australia	55.69	182	42.16	32.1%
6	Osaka University	Japan	49.95	153	59.94	–16.7%
7	Peking University (PKU)	China	46.51	160	41.55	11.9%
8	Seoul National University (SNU)	South Korea	43.02	119	34.35	25.3%
9	The University of Melbourne	Australia	39.47	183	44.21	–10.7%
10	Monash University	Australia	36.93	120	30.11	22.6%
11	National University of Singapore (NUS)	Singapore	33.45	160	36.72	–8.9%
12	Agency for Science, Technology and Research (A*STAR)	Singapore	30.72	112	30.25	1.6%
13	Nagoya University	Japan	29.84	80	28.69	4%
14	Tsinghua University (TH)	China	27.87	107	27.63	0.9%
15	Shanghai Jiao Tong University (SJTU)	China	27.48	91	20.50	34%
16	Hokkaido University (HU)	Japan	25.94	76	27.86	–6.9%
17	Kyushu University	Japan	24.54	73	25.57	–4%
18	The University of Sydney (USYD)	Australia	24.51	83	28.98	–15.4%
19	Academia Sinica	Taiwan	24.13	60	25.71	–6.1%
20	Zhejiang University (ZJU)	China	23.06	73	16.53	39.5%
21	Sun Yat–sen University (SYSU)	China	21.37	60	11.21	90.5%
22	Tohoku University	Japan	20.12	69	24.25	–17%
23	Chinese Academy of Medical Sciences & Peking Union Medical College (CAMS & PUMC)	China	18.89	67	13.43	40.6%
24	Shandong University (SDU)	China	18.28	40	6.63	175.7%
25	University of Science and Technology of China (USTC)	China	17.30	44	19.07	–9.3%
26	Fudan University	China	17.15	88	21.72	–21%
27	Indian Institute of Science (IISC)	India	16.59	24	9.25	79.3%
28	The University of New South Wales (UNSW)	Australia	16.38	74	20.83	–21.3%
29	Australian National University (ANU)	Australia	15.28	65	17.31	–11.7%
30	Keio University	Japan	15.07	56	19.98	–24.6%
31	University of Chinese Academy of Sciences (UCAS)	China	14.75	91	8.39	75.9%
32	The University of Adelaide	Australia	14.42	51	10.30	40%
33	Nanyang Technological University (NTU)	Singapore	13.93	55	11.57	20.4%
34	The Walter and Eliza Hall Institute of Medical Research (WEHI)	Australia	13.72	53	12.09	13.5%
35	National Institutes of Natural Sciences (NINS)	Japan	13.68	50	15.72	–13%
36	Wuhan University (WHU)	China	12.94	29	15.08	–14.2%
37	Yonsei University	South Korea	12.92	44	11.53	12%
38	Council of Scientific and Industrial Research (CSIR)	India	12.92	26	14.80	–12.7%
39	Beijing Genomics Institute (BGI)	China	12.73	58	15.19	–16.2%
40	The University of Hong Kong (HKU)	China	12.49	46	10.28	21.5%
41	National Taiwan University (NTU)	Taiwan	12.02	38	14.53	–17.3%
42	The University of Western Australia (UWA)	Australia	11.63	78	8.20	41.8%
43	University of Tsukuba	Japan	11.48	37	10.02	14.6%
44	James Cook University (JCU)	Australia	11.45	35	11.30	1.4%
45	Nanjing University (NJU)	China	11.10	27	9.20	20.7%
46	University of Otago	New Zealand	10.99	41	14.46	–24%
47	Pohang University of Science and Technology (POSTECH)	South Korea	10.86	32	6.45	68.4%
48	Huazhong University of Science & Technology (HUST)	China	10.71	42	8.71	22.8%
49	Korea Advanced Institute of Science and Technology (KAIST)	South Korea	10.70	33	17.10	–37.4%
50	Korea University (KU)	South Korea	10.21	38	13.43	–24%

TOP INSTITUTIONAL CONTRIBUTORS: CHEMISTRY

2014	INSTITUTION	COUNTRY	WFC	ARTICLE COUNT	2013 WFC	2013–2014 CHANGE IN WFC
1	Chinese Academy of Sciences (CAS)	China	768.72	1,395	679.89	13.1%
2	Peking University (PKU)	China	151.32	366	142.68	6.1%
3	Kyoto University	Japan	151.26	237	157.12	–3.7%
4	Nanyang Technological University (NTU)	Singapore	143.06	217	123.90	15.5%
5	The University of Tokyo (UTokyo)	Japan	142.72	227	159.48	–10.5%
6	Zhejiang University (ZJU)	China	125.25	178	86.42	44.9%
7	Nanjing University (NJU)	China	120.27	206	117.34	2.5%
8	Fudan University	China	114.38	186	80.10	42.8%
9	University of Science and Technology of China (USTC)	China	107.51	223	93.78	14.6%
10	Indian Institutes of Technology (IITs)	India	106.58	141	74.77	42.6%
11	Osaka University	Japan	105.69	171	106.33	–0.6%
12	Tsinghua University (TH)	China	101.79	201	92.06	10.6%
13	National University of Singapore (NUS)	Singapore	93.39	177	83.81	11.4%
14	Council of Scientific and Industrial Research (CSIR)	India	90.40	117	79.46	13.8%
15	Lanzhou University (LZU)	China	84.31	118	50.35	67.5%
16	Tohoku University	Japan	81.32	138	62.89	29.3%
17	Jilin University (JLU)	China	77.57	128	73.88	5%
18	Korea Advanced Institute of Science and Technology (KAIST)	South Korea	73.01	132	56.93	28.2%
19	Xiamen University (XMU)	China	71.62	138	59.87	19.6%
20	Sichuan University (SCU)	China	70.75	98	68.45	3.4%
21	Seoul National University (SNU)	South Korea	68.64	111	70.70	–2.9%
22	Nankai University	China	66.08	160	86.00	–23.2%
23	Hunan University (HNU)	China	64.94	85	51.90	25.1%
24	East China University of Science and Technology (ECUST)	China	63.17	105	53.04	19.1%
25	Tokyo Institute of Technology	Japan	60.60	104	63.19	–4.1%
26	Wuhan University (WHU)	China	59.68	90	63.22	–5.6%
27	Indian Institute of Science Education and Research (IISER)	India	58.13	70	44.18	31.6%
28	Soochow University	China	57.60	94	34.75	65.7%
29	Nagoya University	Japan	56.84	107	66.82	–14.9%
30	University of Chinese Academy of Sciences (UCAS)	China	54.75	270	47.89	14.3%
31	Sun Yat–sen University (SYSU)	China	54.67	94	52.10	4.9%
32	East China Normal University (ECNU)	China	52.72	82	41.54	26.9%
33	Shanghai Jiao Tong University (SJTU)	China	50.11	85	45.14	11%
34	Hokkaido University (HU)	Japan	48.56	87	53.72	–9.6%
35	Kyushu University	Japan	43.50	87	38.45	13.1%
36	National Institute for Material Science (NIMS)	Japan	42.64	97	46.34	–8%
37	Agency for Science, Technology and Research (A*STAR)	Singapore	41.91	112	28.20	48.6%
38	Northeast Normal University (NENU)	China	41.59	53	25.65	62.1%
39	Indian Institute of Science (IISC)	India	40.82	54	37.78	8%
40	Dalian University of Technology (DUT)	China	39.58	74	47.16	–16.1%
41	Monash University	Australia	38.91	101	39.02	–0.3%
42	The University of Queensland (UQ)	Australia	38.86	74	23.99	62%
43	RIKEN	Japan	38.43	101	44.57	–13.8%
44	National Tsing Hua University (NTHU)	Taiwan	38.20	67	32.04	19.2%
45	South China University of Technology (SCUT)	China	38.20	71	28.75	32.9%
46	National Taiwan University (NTU)	Taiwan	37.80	70	43.58	–13.2%
47	Yonsei University	South Korea	37.51	79	28.87	29.9%
48	The University of Hong Kong (HKU)	China	36.29	59	39.04	–7%
49	Sungkyunkwan University (SKKU)	South Korea	36.04	80	23.97	50.4%
50	Indian Association for the Cultivation of Science (IACS)	India	35.76	41	38.48	–7.1%

TOP INSTITUTIONAL CONTRIBUTORS: PHYSICAL SCIENCES

2014	INSTITUTION	COUNTRY	WFC	ARTICLE COUNT	2013 WFC	2013–2014 CHANGE IN WFC
1	Chinese Academy of Sciences (CAS)	China	412.10	1,367.00	406.86	1.3%
2	The University of Tokyo (UTokyo)	Japan	202.87	729.00	193.50	4.8%
3	Peking University (PKU)	China	111.85	449.00	105.09	6.4%
4	Tsinghua University (TH)	China	98.15	357.00	87.94	11.6%
5	National University of Singapore (NUS)	Singapore	80.80	171.00	88.74	–8.9%
6	Kyoto University	Japan	77.14	328.00	91.02	–15.3%
7	Tohoku University	Japan	75.61	209.00	96.92	–22%
8	University of Science and Technology of China (USTC)	China	74.12	296.00	71.40	3.8%
9	Nanyang Technological University (NTU)	Singapore	72.88	141.00	71.87	1.4%
10	Seoul National University (SNU)	South Korea	72.26	237.00	66.08	9.4%
11	Nanjing University (NJU)	China	68.04	228.00	64.94	4.8%
12	Osaka University	Japan	67.57	243.00	62.61	7.9%
13	National Institute for Material Science (NIMS)	Japan	67.51	165.00	43.97	53.5%
14	Korea Advanced Institute of Science and Technology (KAIST)	South Korea	58.91	103.00	49.76	18.4%
15	RIKEN	Japan	57.25	228.00	60.42	–5.3%
16	Fudan University	China	57.22	116.00	39.64	44.4%
17	Indian Institutes of Technology (IITs)	India	56.10	132.00	48.41	15.9%
18	National Taiwan University (NTU)	Taiwan	54.67	177.00	46.59	17.3%
19	Tokyo Institute of Technology	Japan	53.49	194.00	35.67	50%
20	Zhejiang University (ZJU)	China	48.69	124.00	64.83	–24.9%
21	Australian National University (ANU)	Australia	48.32	361.00	49.56	–2.5%
22	Indian Institute of Science (IISC)	India	40.55	76.00	35.96	12.8%
23	The University of New South Wales (UNSW)	Australia	40.47	127.00	24.51	65.1%
24	Xi'an Jiaotong University (XJTU)	China	39.97	92.00	32.80	21.9%
25	Nagoya University	Japan	38.73	246.00	35.21	10%
26	Pohang University of Science and Technology (POSTECH)	South Korea	37.32	74.00	33.24	12.3%
27	Agency for Science, Technology and Research (A*STAR)	Singapore	35.01	83.00	31.35	11.7%
28	Shanghai Jiao Tong University (SJTU)	China	34.63	119.00	34.28	1%
29	National Institute of Advanced Industrial Science and Technology (AIST)	Japan	33.43	77.00	42.83	–22%
30	National Tsing Hua University (NTHU)	Taiwan	33.41	115.00	35.70	–6.4%
31	Hong Kong University of Science and Technology (HKUST)	China	33.38	60	22.12	50.9%
32	Sungkyunkwan University (SKKU)	South Korea	30.92	153.00	29.13	6.2%
33	Soochow University	China	29.57	58.00	27.31	8.3%
34	Jilin University (JLU)	China	29.43	60	29.09	1.2%
35	Yonsei University	South Korea	28.17	100	29.67	–5.1%
36	Academia Sinica	Taiwan	26.20	355.00	27.42	–4.5%
37	National Chiao Tung University (NCTU)	Taiwan	25.95	65.00	41.37	–37.3%
38	Huazhong University of Science & Technology (HUST)	China	25.67	69.00	25.42	1%
39	Kyushu University	Japan	25.53	107.00	25.36	0.6%
40	The University of Sydney (USYD)	Australia	25.28	346.00	27.87	–9.3%
41	Korea University (KU)	South Korea	25.01	126.00	29.15	–14.2%
42	Southeast University (SEU)	China	24.87	57.00	20.09	23.8%
43	Hanyang University (HYU)	South Korea	24.40	68.00	24.03	1.6%
44	Monash University	Australia	24.36	151.00	24.94	–2.3%
45	Tata Institute of Fundamental Research (TIFR)	India	22.20	179.00	41.05	–45.9%
46	The University of Hong Kong (HKU)	China	21.86	75.00	25.81	–15.3%
47	Nankai University	China	21.67	53.00	23.56	–8.1%
48	East China Normal University (ECNU)	China	21.32	47.00	16.97	25.6%
49	Ulsan National Institute of Science and Technology (UNIST)	South Korea	20.75	46.00	10.75	93.1%
50	Hokkaido University (HU)	Japan	20.65	54.00	23.26	–11.2%

TOP INSTITUTIONAL CONTRIBUTORS: EARTH AND ENVIRONMENT

2014	INSTITUTION	COUNTRY	WFC	ARTICLE COUNT	2013 WFC	2013–2014 CHANGE IN WFC
1	Chinese Academy of Sciences (CAS)	China	66.45	156	68.50	–3%
2	The University of Tokyo (UTokyo)	Japan	33.29	69	32.72	1.7%
3	Japan Agency for Marine–Earth Science and Technology (JAMSTEC)	Japan	19.15	58	25.16	–23.9%
4	Australian National University (ANU)	Australia	15.98	47	15.45	3.4%
5	The Commonwealth Scientific and Industrial Research Organisation (CSIRO)	Australia	14.46	44	14.47	–0.1%
6	State Oceanic Administration (SOA)	China	13.53	29	5.18	161.3%
7	Nanjing University (NJU)	China	12.41	29	9.33	33%
8	China Meteorological Administration (CMA)	China	12.00	33	9.76	23%
9	Tohoku University	Japan	10.88	25	12.23	–11%
10	Hokkaido University (HU)	Japan	10.56	25	9.50	11.2%
11	China University of Geosciences (CUG)	China	9.68	24	9.40	2.9%
12	China Earthquake Administration	China	9.17	25	9.50	–3.5%
13	Peking University (PKU)	China	8.97	27	5.61	59.9%
14	Academia Sinica	Taiwan	8.86	25	4.39	101.9%
15	Monash University	Australia	8.35	29	5.91	41.2%
16	National Taiwan University (NTU)	Taiwan	8.22	24	6.30	30.4%
17	University of Tasmania (UTAS)	Australia	8.13	40	4.89	66.4%
18	Kyushu University	Japan	7.98	18	2.72	193.4%
19	The University of New South Wales (UNSW)	Australia	7.91	30	10.91	–27.5%
20	The University of Western Australia (UWA)	Australia	7.67	36	7.85	–2.2%
21	Nagoya University	Japan	7.53	17	5.32	41.5%
22	Tokyo Institute of Technology	Japan	7.32	16	4.07	79.6%
23	Beijing Normal University (BNU)	China	7.22	25	5.76	25.2%
24	Curtin University	Australia	7.12	29	8.19	–13.1%
25	University of Science and Technology of China (USTC)	China	7.05	19	6.52	8.1%
26	Ministry of Earth Sciences (MoES)	India	7.03	13	7.79	–9.8%
27	Ocean University of China (OUC)	China	6.67	17	9.35	–28.6%
28	GNS Science	New Zealand	6.67	18	2.65	151.6%
29	Japan Meteorological Agency	Japan	6.59	20	12.08	–45.4%
30	Council of Scientific and Industrial Research (CSIR)	India	6.44	14	8.42	–23.5%
31	The University of Adelaide	Australia	5.91	10	2.61	126.4%
32	Xiamen University (XMU)	China	5.58	15	1.80	210%
33	The University of Melbourne	Australia	5.42	31	5.38	0.6%
34	Indian Space Research Organisation (ISRO)	India	5.35	7	4.43	20.6%
35	Lanzhou University (LZU)	China	5.16	13	5.18	–0.3%
36	Seoul National University (SNU)	South Korea	5.15	15	8.10	–36.4%
37	University of Chinese Academy of Sciences (UCAS)	China	5.05	27	2.96	70.8%
38	University of Otago	New Zealand	4.89	14	2.98	64.3%
39	National Institute of Advanced Industrial Science and Technology (AIST)	Japan	4.79	13	3.81	25.6%
40	Ehime University	Japan	4.68	14	3.15	48.5%
41	Wuhan University (WHU)	China	4.65	9	5.93	–21.5%
42	James Cook University (JCU)	Australia	4.57	13	5.04	–9.2%
43	Hong Kong University of Science and Technology (HKUST)	China	4.46	5	4.54	–1.7%
44	The University of Auckland	New Zealand	4.41	14	2.90	52%
45	Research Organization of Information and Systems (ROIS)	Japan	4.34	13	4.55	–4.4%
46	Nanjing University of Information Science & Technology (NUIST)	China	4.07	19	6.30	–35.3%
47	Kyoto University	Japan	3.96	11	9.02	–56.1%
48	Korea Institute of Ocean Science and Technology (KIOST)	South Korea	3.73	8	3.48	7.3%
49	Osaka University	Japan	3.65	8	0.65	462.3%
50	National Research Institute for Earth Science and Disaster Prevention (NIED)	Japan	3.63	10	2.27	60.2%

TOP INSTITUTIONAL CONTRIBUTORS IN *NATURE* AND *SCIENCE*

2014	INSTITUTION	COUNTRY	WFC	ARTICLE COUNT	2013 WFC	2013–2014 CHANGE IN WFC
1	The University of Tokyo (UTokyo)	Japan	13.21	44	15.55	–15.1%
2	Chinese Academy of Sciences (CAS)	China	13.11	58	18.71	–29.9%
3	Kyoto University	Japan	7.44	25	7.48	–0.5%
4	RIKEN	Japan	7.33	32	9.62	–23.8%
5	Peking University (PKU)	China	6.48	28	4.10	58%
6	The University of Queensland (UQ)	Australia	6.44	38	2.42	166%
7	Tsinghua University (TH)	China	4.90	20	5.43	–9.8%
8	National University of Singapore (NUS)	Singapore	3.99	18	2.17	83.6%
9	Nagoya University	Japan	3.62	17	1.35	167.4%
10	Beijing Genomics Institute (BGI)	China	2.84	14	1.78	59.1%
11	Osaka University	Japan	2.74	19	4.69	–41.6%
12	Monash University	Australia	2.55	15	4.82	–47.1%
13	The University of Melbourne	Australia	2.50	24	3.30	–24.3%
14	Zhejiang University (ZJU)	China	2.19	8	1.70	28.9%
15	National Institute of Biological Sciences, Beijing (NIBS)	China	2.11	4	1.12	87.3%
16	The University of Sydney (USYD)	Australia	2.01	17	0.70	189.5%
17	Tohoku University	Japan	1.98	12	2.31	–14.4%
18	Australian National University (ANU)	Australia	1.94	20	2.04	–5.1%
19	The University of Adelaide	Australia	1.93	11	0.38	400.8%
20	National Institute for Material Science (NIMS)	Japan	1.73	7	0.54	219.5%
21	Agency for Science, Technology and Research (A*STAR)	Singapore	1.36	6	2.81	–51.7%
22	James Cook University (JCU)	Australia	1.35	7	1.13	19.4%
23	University of Tasmania (UTAS)	Australia	1.33	9	0.78	71.3%
24	National Institutes of Natural Sciences (NINS)	Japan	1.31	11	1.12	17.1%
25	Academia Sinica	Taiwan	1.28	11	0.73	74.4%
26	Seoul National University (SNU)	South Korea	1.23	8	1.97	–37.6%
27	University of Chinese Academy of Sciences (UCAS)	China	1.20	7	0.50	138.5%
28	The University of Western Australia (UWA)	Australia	1.18	13	0.72	63.6%
29	Ocean University of China (OUC)	China	1.17	3	0.17	600%
30	The University of New South Wales (UNSW)	Australia	1.09	11	1.86	–41.4%
31	The Commonwealth Scientific and Industrial Research Organisation (CSIRO)	Australia	1.07	15	2.88	–62.9%
32	Sungkyunkwan University (SKKU)	South Korea	1.04	6	0.51	102.9%
33	National Tsing Hua University (NTHU)	Taiwan	1.00	1	1.28	–22.1%
34	Hokkaido University (HU)	Japan	0.98	10	0.27	268.7%
35	Huazhong University of Science & Technology (HUST)	China	0.92	1	0.05	1733.3%
36	The Walter and Eliza Hall Institute of Medical Research (WEHI)	Australia	0.89	3	0.85	4.9%
37	National Institute of Water and Atmospheric Research (NIWA)	New Zealand	0.87	3	0	–
38	Yanshan University	China	0.82	1	0.73	11.6%
39	University of Science and Technology of China (USTC)	China	0.82	7	1.69	–51.6%
40	Tokyo Institute of Technology	Japan	0.81	7	1.28	–36.6%
41	Harbin Institute of Technology (HIT)	China	0.80	1	0.07	1020.0%
42	The University of Wollongong (UOW)	Australia	0.80	5	0	–
43	Japan Aerospace Exploration Agency (JAXA)	Japan	0.75	5	0.30	149.5%
44	Massey University	New Zealand	0.71	3	0	–
45	Ibaraki University	Japan	0.70	3	0.34	103.7%
46	Nara Institute of Science and Technology (NAIST)	Japan	0.68	2	0.37	82.7%
47	Kinki University	Japan	0.67	1	0	–
48	China National Genebank (CNGB)	China	0.64	7	0	–
49	Second Military Medical University (SMMU)	China	0.64	3	0	–
50	Korea Institute of Geoscience and Mineral Resources (KIGAM)	South Korea	0.63	2	0	–

Weighted fractional count (WFC) for each institution is shown to two decimal places only. When two or more institutions have the same WFC, their positions are determined by the thousandth place (or beyond).

These results are based on the most recent data available as of 6 February 2015. Owing to continual refinements of the data, the figures in the database are liable to change and might differ to those printed in the supplements.



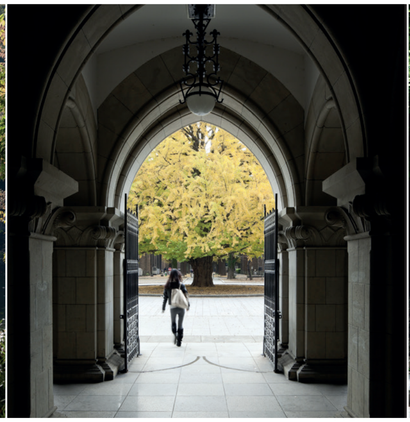


THE UNIVERSITY OF TOKYO
RESEARCH WITHOUT LIMITS

The University of Tokyo is harnessing the collective, cross-disciplinary intellect of the world's most talented scientists to foster innovation and ground-breaking insight with the potential to move civilization forward. Housed in world-class interdisciplinary and international research institutes, researchers at the university are pushing the boundaries of science, from Big Data to the Big Bang.

In 2011, President Junichi Hamada launched Institutes for Advanced Study to provide special support to the best of these institutes, with the aim of creating a top-tier international research hub. Two research institutes have made the grade so far: the Kavli Institute for the Physics and Mathematics of the Universe (Kavli IPMU), and the Integrated Research System for Sustainability Science (IR3S).

"These institutes have been evaluated as world-class centres of research by government organizations and the global research community, as well as having ongoing external funding and an international research environment," says the director and university executive vice president, Yoichiro Matsumoto.

IR3S is a global pioneer in sustainability science and the university's first interdisciplinary research project. The programme takes a holistic, integrated approach to understanding and addressing complex, long-term environmental issues such as climate change and biodiversity loss, drawing on expertise from across diverse disciplines and regions.

Researchers at the Kavli IPMU, under the proactive directorship of Hitoshi Murayama, are combining mathematics with particle physics, astrophysics and cosmology to unravel the mysteries of the Universe. The interdisciplinary research program encompasses fields from supernovae, observational cosmology and astroparticle physics, to alternative gravity theories, dark matter and the string theory of quantum gravity, as well as a number of international collaborative experimental and observational projects.

SEARCHING THE UNIVERSE FOR ANSWERS

Now in its eighth year, the Kavli IPMU continues from strength to strength. "This year, Mikhail Kapranov, a world-renowned mathematician from Yale University in the United States, will assume a full professorship at the Kavli IPMU," says Murayama. "His visionary leadership in categorical geometry will further enhance our research capabilities, and his acceptance of the position demonstrates that we continue to attract the best scientists from around the world."

This accumulation of the world's greatest minds and the promise of generous long-term funding on a timeframe of a decade or more — a rare luxury in modern research — permits some audacious thinking. "We currently have an ambitious project to launch a satellite called LiteBIRD (short for 'light satellite for the studies of B-mode polarization and inflation from cosmic background radiation detection') to look at what came before the Big Bang," explains Murayama. "The aim is to observe direct evidence of 'inflation' — the primordial event that stretched the Universe from smaller than the size of an atom to the macroscopic Universe we see today."

Examples of the exemplary research undertaken at the institute abound, but of particular note is the ground-breaking work

THE UNIVERSITY OF TOKYO

LEARN MORE
Visit: www.u-tokyo.ac.jp/en
www.facebook.com/UTokyo.News.en
www.twitter.com/UTokyo_News_en
www.youtube.com/user/UtokyoPR
Phone: +81-3-3811-3393

on the direct observation of dark matter by the Xenon detector for weakly interacting MASSive particles (XMASS) experiment at the University of Tokyo's Kamioka Observatory. The XMASS collaboration's most recent investigation involved searching for direct observational evidence of the particles that theory has suggested might produce 'warm' dark matter.

Cosmological observations and theories of the Big Bang and the evolution of the Universe indicate that more than 80 per cent of the mass in the Universe is in a form that does not interact with light and is therefore invisible, or 'dark'. Although yet to be detected or observed, physicists believe that weakly interacting massive particles (WIMPs) are the most likely manifestation of dark matter, but exactly which particle constitutes a WIMP and whether dark matter is predominantly 'hot' (due to particles travelling at close to the speed of light) or 'cold' (much slower particles) remains the subject of debate. Both the cold and hot dark matter theories have their inconsistencies with cosmological observations, but somewhere in between is warm dark matter, which theory predicts would produce hybrid structures closer to those observed.

The liquid xenon detector developed by the XMASS collaboration is designed to measure the signature of dark matter particles. One of the candidate particles for warm dark matter is the bosonic super-WIMP — a boson with a superweak interaction. Although interactions between dark matter and normal matter are predicted to be rare, calculations show that such bosons are absorbed by xenon atoms and deposit energy equivalent to their rest mass, making their detection theoretically possible. Yet an experiment that used 165 days of data for 41 kilogrammes of liquid xenon, achieving unprecedented levels of sensitivity, revealed no trace of such particles. The result provides a crucial constraint in the search for dark matter, proving that the bosonic super-WIMP cannot be a significant constituent of dark matter and giving parameter ranges for future experiments.

BIG DATA AND PERSONALIZED MEDICINE

The University of Tokyo's pursuit of research excellence crosses many disciplines. Another research centre rapidly earning a prominent international reputation as a world leader is the Medical Genomics Research Initiative directed by Shoji Tsuji. The initiative targets the molecular bases for diseases and the exploitation of genomic information to guide treatment — goals that have only become possible with the explosion in genome science over the past decade and the development of technologies that make clinical sequencing viable.

Ever since the first complete sequencing of the human genome just over a decade ago, medical researchers have been searching and analysing the genomic database for the origins of diseases and the clues to potential treatments and cures. That first sequencing challenge took many years and a collaboration of hundreds of researchers and institutes from around the world to produce a common human genome. Since that historical achievement, the technologies used for genome sequencing have become almost unrecognizable with machines now able to turn out the entire protein-coding excerpt of the genome — the exome — for a patient in a matter of hours. Acquisition of the exome is no longer the problem; establishing what can be done with the vast volumes of data being produced is now the next frontier in medical science.

The initiative's Medical Genome Center established in 2011 has a robotics-driven laboratory for exome analysis with a capacity of 384 exomes per month. That equates to about four terabytes of data, which needs to be structured, annotated and stored in a way that makes it searchable and useful for both medical research and clinical care. This is Big Data, an area where the University of Tokyo has taken a lead role in collaboration with Japan's National Institute of Informatics.

"By analysing a patient's exome, it will be possible to identify genetic variations that lead to differences in drug responses and side effects, as well as variants causing or indicating a susceptibility to certain diseases," says Tsuji. "This leads to the possibility of 'personal genome-based medicine,' where prevention and treatment are optimized for each patient based on their own genome."

Most genomic studies of disease, such as genome-wide association studies, involve searching for a small number of common genetic variants with links to disease. Such genetic associations have limited utility in personalized treatment and are more indicative of population-scale markers for susceptibility. At the other end of the scale are the ultra-rare variants that are implicated in rare, complex and typically heritable diseases. Tsuji is targeting the overlapping zone as the most promising source of data for improving treatments. "We need to focus on common diseases associated with multiple rare genetic variants," he notes. "These have real clinical utility as well as scientific validity."

An example is Tsuji's research on multiple system atrophy (MSA), an intractable neurodegenerative disease affecting many aspects of the nervous system. Widely regarded as non-genetic, whole genome sequencing and analysis by Tsuji's laboratory has revealed the involvement of genetic components. Functionally deleterious mutations on the *COQ2* gene are strongly associated with MSA, and the corresponding enzyme is essential to catalyse the biosynthesis of coenzyme Q_{10}, which presumably leads to reduced biosynthesis of coenzyme Q_{10} and contributes to the development of MSA. Supplementation of coenzyme Q_{10} may therefore be efficacious in the treatment of MSA — an example of disease-modifying therapy.

"We now have a clear roadmap to genome-based personal medicine," says Tsuji. "Through research on the molecular bases of diseases and more effective and targeted use of genomic data, we expect very soon to be on the cusp of another revolution in medicine."

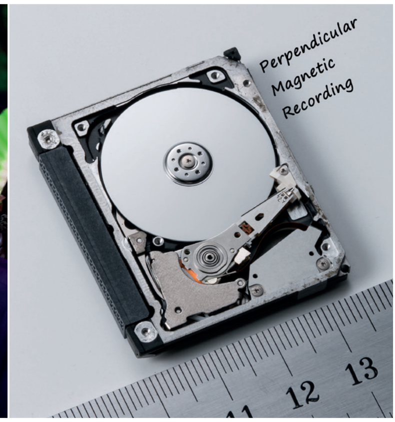

TOHOKU UNIVERSITY

INNOVATIVE MINDS IN SPIN-CENTRED SCIENCE

Tohoku University was established as Japan's third national university in 1907. As a world-leading university, it has contributed continuously to extending fundamental knowledge in a wide range of fields. It has an illustrious record of progress in science, technology and innovation, especially in the fields of materials science and engineering.

Some standout achievements from the university's numerous technological advances include Hidetsugu Yagi and Shintaro Uda's world-famous directional antenna, Jun-ichi Nishizawa's optical devices, which underpin modern optical communication systems, and Kotaro Honda's KS and NKS steels — the strongest magnets of their times.

Honda's legacy has been influential. He is regarded as the father of magnetism studies at Tohoku University because his achievements sparked the vigorous pursuit of research into magnetism at the university. Subsequent discoveries and cutting-edge inventions have placed Tohoku University on the world map of magnetism research. One of Honda's motto was "Industry is the *dojo* (testing ground) of learning". His passion for overcoming societal challenges through technological innovation has inspired researchers, students and graduates of Tohoku University.

A particularly notable example of a recent innovative technological contribution to society is Shun-ichi Iwasaki's perpendicular magnetic recording (PMR) technology. Originally proposed in 1976, PMR technology was first implemented in commercial hard disk drives in 2005. Within a mere five years, annual production of PMR-based hard disks was estimated to be 620 million units and PMR technology had almost completely replaced conventional hard disk drives. Current PMR technology can amass zettabytes of data on a global scale, making it indispensable for our information-based society. It has proven to be a giant stride in data storage.

SPIN-CENTRED SCIENCE AT TOHOKU UNIVERSITY

Based on its strong magnetism research and recent advances in nanotechnology, Tohoku University researchers have made a series of seminal contributions to an emerging research field known as spintronics. As its name suggests, this field is associated with electron spin. Specifically, it seeks to integrate the charge and spin of electrons, which have traditionally been considered independently. In fact, not just spintronics, but also broader spin-related studies are currently generating much excitement; they have the potential to revolutionize aspects of the traditional textbook presentation of physics and realize high-performance devices that are both incredibly compact and energy efficient. Researchers at Tohoku University have coined the new term 'spin-centred science' to describe their broad study of spin-related science and technology.

Tohoku University is the epicentre of spin-centred science in Japan with roughly four in five spintronics scientists in Japan currently based at the university. Its global reputation is also attracting prominent researchers from overseas. Tohoku University has strong collaborative relations with world-class institutes including the University of Chicago, Harvard University and the University of California, Santa Barbara in addition to global companies. Tohoku University's attractiveness for spin-centred scientists is evidenced by the

TOHOKU
UNIVERSITY

LEARN MORE

Visit: www.tohoku.ac.jp/en
Facebook.com/TohokuUniversityPR
Twitter.com/TohokuUniPR
Phone: +81-22-217-4816

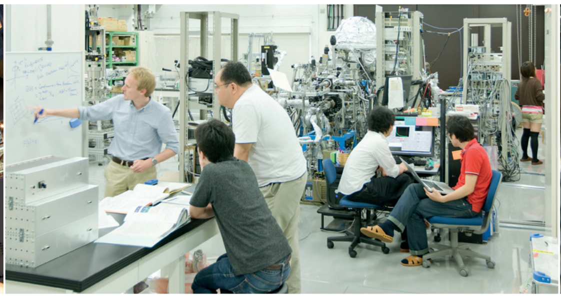

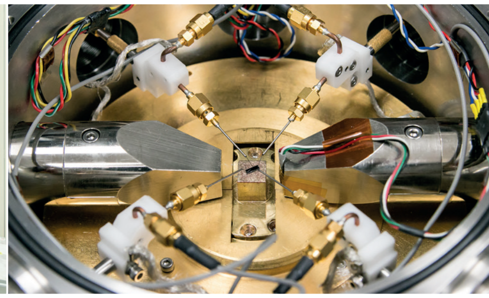

recent relocation of high-profile spintronics researcher Gerrit Bauer from the Netherlands. "As an applied theoretical physicist, I need inspiration from experiments," explains Bauer. "With such a large number of leading experimental groups in spintronics, Tohoku University provides an ideal environment to explore the boundaries between abstract theory, real experiments, and potential applications."

LEADING RESEARCHERS

Spin-centred science at Tohoku University covers a whole spectrum of research activities from fundamental science to technological applications.

On the fundamental science side, Eiji Saitoh's recent discoveries of two new phenomena — the inverse spin-Hall effect and the spin Seebeck effect — are particularly noteworthy. The discovery of the inverse spin-Hall effect, in which a spin current is

> "Spin-centred science can potentially realize extremely low-energy-consuming massive brain-type computers with artificial intelligence and high performance."

converted into an electric charge current, has led to a reliable way to measure spin current. The spin Seebeck effect, which involves the thermal generation of a spin voltage, has been applied in a new thermoelectric conversion mechanism that allows a voltage to be harvested from heat. This effect has been exploited in spin-thermoelectric coating technology. "In the same way that electromagnetic theory launched a technological revolution, spin science will provide fundamental laws for a completely new system of technology." Saitoh predicts. "In particular, it will provide new principles for power generation and computer technologies."

On the more applied side, Hideo Ohno, a pioneer of magnetic semiconductors, has made a breakthrough in the information and communication technology field, for which he was awarded a Thomson Reuters Citation Laureate in 2011. He is also renowned for leading the development of non-volatile integrated circuits that both perform calculations and store information in a single system. These integrated circuits perform considerably better and consume less energy than conventional integrated circuits; moreover, they do not consume any energy when in standby mode. Ohno has developed a magnetic tunnel junction with ferromagnetic electrodes, which realizes a high thermal stability at reduced dimensions and low-current magnetization switching while maintaining a high tunnel magnetoresistance ratio. This is a significant contribution towards the realization of non-volatile very large scale integration technology. "Spin-centred science can potentially realize extremely low-energy-consuming massive brain-type computers with artificial intelligence and high performance," Ohno says.

Masashi Sahashi is trying to create green information technology devices based on spin-centred science and existing technology. Sahashi was appointed as programme manager of one of the 12 programmes of the Impulsing Paradigm Change through Disruptive Technologies (ImPACT) Program, which is overseen by the Japanese Cabinet Office with the goal of enhancing Japan's capacity to innovate. One possible outcome from Sahashi's ambitious technology programme is the development of mobile devices that can function for over a month without being charged. "I hope to use spin-centred technology to greatly reduce electricity consumption and alleviate the need to frequently charge mobile devices," says Sahashi.

As well as spearheading research into spintronics, Tohoku University is also pursuing education in the field. In April 2015, the university, in collaboration with leading overseas universities including Johannes Gutenberg-Universität Mainz in Germany, will launch an international graduate programme on spintronics. Tohoku University is perfectly positioned to continue advancing this field and contribute to the new scientific paradigm of charge and spin. The revolution in spin-centred science will transform society by enabling high-performance artificial intelligence and accelerating the Internet of Things.

A DIVERSE UNIVERSITY

In addition to science and technological innovation, Tohoku University seeks to address unconventional problems by funnelling expertise from different disciplines, including the social sciences and humanities. As society becomes increasingly complex, any attempt to understand and solve societal challenges must consider the human dimension. Tohoku University's interdisciplinary projects for improving society include big data, energy, and sensing and genomic health care.

One area in which the university has a particularly strong sense of mission is disaster science. As the largest university in the area affected by the 2011 Great East Japan Earthquake, Tohoku University has taken a leading role in restoration and disaster-mitigation efforts. In 2012, it founded the International Research Institute of Disaster Science (IRIDeS), which brings together researchers with natural science, engineering, medicine, social science and humanities backgrounds to explore multidisciplinary, holistic approaches to disasters and related issues.

Tohoku University and the IRIDeS act as a vital hub for regional, national, and international support and collaboration for disaster and risk reduction. As such, they presented their experience and lessons at the third United Nations' World Conference on Disaster Risk Reduction, which was held in Sendai on 14–18 March 2015.

Tohoku University will continue to be innovative in creating global excellence and promoting the well-being of our society by attracting diverse talents from around the world. The university will also continue to develop as a globally open, intellectually flourishing community of aspiring students and dynamic academics.

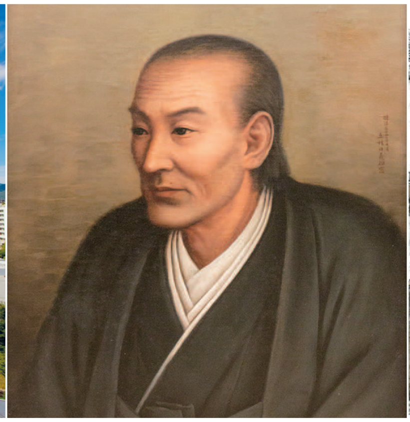

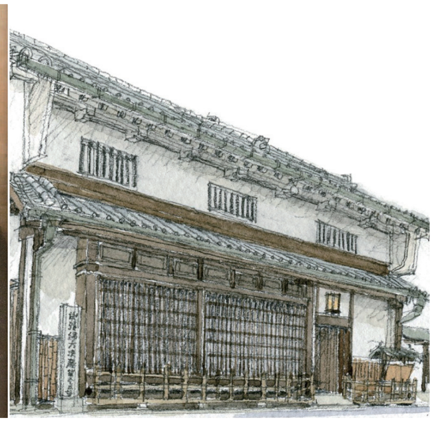

OSAKA UNIVERSITY

TAKING THE OSAKA SPIRIT TO THE WORLD

From humble beginnings in Japan's burgeoning medical heartland, Osaka University has risen to become one of Japan's top three universities. Underlying this success has been a unique culture of selfless commitment that has produced some of Japan's most visionary leaders. Toshio Hirano, the president of Osaka University, has taken up the challenge of bringing this 'Osaka spirit' to the world.

As early as the 1600s, Osaka served as a national hub for medicinal ingredients, and from it sprang a vibrant pharmaceutical industry centred on the district of Doshomachi. It was near this area that, in 1838, the legendary school which would later emerge as Osaka University was founded.

"The school, called Tekijuku, was created by one of Japan's great educators, Koan Ogata," says Hirano. "It was a private school, or *juku* in Japanese, devoted to the study of European texts on medicine and the life sciences. The school's name comes from Koan's pseudonym, *Tekitekisai*, which roughly translates as 'be true to yourself when choosing your path while accepting things as they are.' Tekijuku grew to become a centre of unparalleled scholarship in Osaka, which at that time was already a bustling hub of economic activity."

At this remarkable academy, young people from various backgrounds and hometowns gathered to study in a rigorous academic environment of friendly competition, guided by the selfless sense of commitment advocated by Ogata. It was at Tekijuku that many of Japan's formative leaders of the early Meiji era were educated.

"Tekijuku was a place where future leaders could rise above fixed social standings to engage in solving the societal issues of the day," explains Hirano. "It is from this outstanding ideal that we draw our inspiration for the 'World Tekijuku' initiative — a modern, international recreation of Koan's Tekijuku. We hope that this initiative will attract the most talented students and researchers from around the world to solve the global issues of our time through excellence in collaborative research and education."

THE WORLD TEKIJUKU INITIATIVE

The founding principle of Osaka University's World Tekijuku initiative is 'the creation of harmonious diversity through scholarship,' says Hirano. "The world has a diversity of languages, peoples, customs, cultures and religions. This diversity has the potential to foster revolutionary innovations and a prosperous society. It is our greatest asset. Yet diversity can also lead to the erection of barriers and even to war. In the global era of the twenty-first century, a new and important role of the university as an institution is to use cooperative scholarship to promote the harmonization of this diversity."

In this way, the World Tekijuku initiative aims to promote mutual understanding and respect through the universal language of scholarship in a manner that makes it possible to harness the many benefits of global diversity.

First among the raft of programmes supporting the World Tekijuku initiative is the International Joint Research Promotion Program, which facilitates the establishment of international cooperative laboratories with pioneering researchers from around the world.

大阪大学
OSAKA UNIVERSITY

LEARN MORE
Visit: www.osaka-u.ac.jp/en
Email: ki-kousyagaku-kouhou@office.osaka-u.ac.jp
Address: 1-1 Yamadaoka, Suita, Osaka, 565-0871 Japan
Phone: +81-6-6877-5111

"We invite principal researchers from overseas to be part of these joint laboratories at Osaka University," says Hirano, who is himself an internationally respected immunologist and a recipient of the Crafoord Prize for his discovery of interleukin 6 — an important mediator of inflammation. "At the same time, we cover travel expenses for students and faculty going abroad to study as part of these joint laboratories. Throughout the duration of each research project, we support the collaboration by providing funding for assistants and young researchers, as well as for post-doctoral researchers. This ensures that we maintain research momentum, even when the principal researchers are absent from Osaka."

> **"The founding principle of Osaka University's World Tekijuku initiative is 'the creation of harmonious diversity through scholarship,' says Hirano."**

With 22 joint laboratories established in just two years of launching the initiative, the International Joint Research Promotion Program is already significantly impacting the university's global recognition. "With this initiative, we will enhance the density of our international collaborative research. We are already well on the way to reaching our goal of 100 joint laboratories by 2023," notes Hirano.

Supporting this flagship programme is the university's renewed focus on increasing the number of international students on campus as well as helping more local students to complete major portions of their studies in other countries. "We are strengthening the international competitiveness of our university in eight key disciplines for which we are already ranked in the world's top 100 — immunology, chemistry, materials science, physics, biology and biochemistry, molecular biology and genetics, microbiology, and multidisciplinary studies," says Hirano. "On top of this, we are actively promoting new interdisciplinary fields such as innovative research for drug development, cognitive neuroscience robotics, photon science and technology, and even global history."

A GLOBAL UNIVERSITY

A major goal of the university is to double the number of inbound and outbound students over the next decade. Yet many aspects of the conventional Japanese university system make achieving this goal challenging.

"The traditional summer vacation at Osaka University, like virtually all universities in Japan, is August to September," says Hirano. "This makes it difficult for students from other countries, particularly the USA and European countries, to attend our summer programmes. Very few universities in Japan have altered their academic calendars to help accommodate more international students, but that is what we are planning right now."

Osaka University is in the process of transitioning to an academic calendar that matches the trimester schedule and summer schooling common in the USA, with a spring term from April to June, an autumn term from September to November and a winter term from December to February. "This initiative will allow us to offer summer programmes at a time more in line with international standards, enhancing our summer programmes and enriching our international exchange participation. The change will also benefit our academic staff, who will be able to attend more international conferences and academic meetings, many of which are held in the July to August summer break."

The university has also implemented a cross-appointment system that allows researchers at other universities around the world to be on the payroll of Osaka University while maintaining their status at their home institution. "We strongly believe that this system is important to be able to welcome renowned world-class researchers to Osaka University to carry out concentrated studies with our researchers," says Hirano. "In this we are leaping ahead of most Japanese universities. We currently have 21 international researchers contracted under this programme with active personnel exchange, and we expect to double or triple this exchange in the coming year."

Professor Toshio Hirano, the president of Osaka University.

Taking aim at the long-term challenge of becoming one of the world's top ten universities by its centenary in 2031, Hirano's World Tekijuku initiative is set to propel Osaka University into the global era as one of the many pillars of the international research community. To catalyse this revolution, the university will host the Association of Pacific Rim Universities (APRU) annual presidents meeting in June 2015. The meeting will provide Hirano with an opportunity to convey his aspirations for harmonious diversity to his peers across the region.

"In a world undergoing rapid globalization, which is unprecedented in the whole of human history, we need to be aware of the potential for the negative aspects of diversity to intensify global strife," says Hirano. "As a university, we should become a centre of scholarship that acts like a beacon for the harmonization of diversity for the common good. And in the spirit of this harmonious diversity, we should be guided by the selfless sense of commitment embodied by the famous words of our spiritual founder, Koan Ogata: 'For people, for society, and for the pursuit of truth.'"

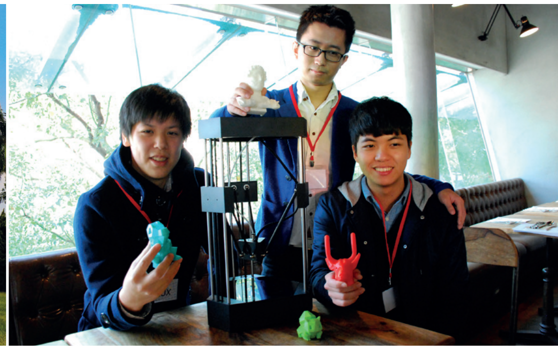

NATIONAL TAIWAN UNIVERSITY

PIONEER OF EDUCATION INNOVATION

"And the winner is … PaGamO!" With that declaration, the PaGamO team leader, Professor Ping-Cheng Yeh from National Taiwan University (NTU), leapt onto the stage to claim the prize (above left). The team was overall winner in the Wharton-QS Stars Awards 2014 (Reimagine Education) — the 'Oscars' of innovation in higher education. Entries were received from 427 universities and enterprises in 43 countries for 21 awards, making the awards a veritable 'who's who' of higher education.

PaGamO is the first online social game to provide a platform that permits large groups of students to compete against each other. Placed on a virtual map, students engage in problem-based battles.

This highly interactive platform makes it easy to add new problems in any subject or language. For example, it has been used to teach probability on the Coursera website. Students of all levels use it. A Fortune 500 company even uses it for corporate training.

OPENING UP HIGHER EDUCATION

NTU was the first university to provide Massive Open Online Courses (MOOCs) in Chinese on Coursera, joining other world-class universities in offering high-quality university courses. With inspiring lecture videos and creative assignments, these courses have redefined online learning. To date, NTU has provided 21 courses on Coursera, which have received over 7 million views. Its MOOCs are among the most popular Chinese ones on Coursera. NTU firmly believes that open-access learning is a powerful socioeconomic equalizer — transforming what was a limited opportunity for a privileged few into something that anyone can freely access.

The NTU OpenCourseWare (OCW) programme began in 2010 and now offers over 160 college-level courses online, which have received about 17 million views. Its material is licensed under Creative Commons, so that it can be freely accessed and reused. Out of over 300 websites on the Open Education Consortium (OEC), NTU's OCW site was selected Outstanding Site of 2014 by OEC. NTU will continue to work with other universities to improve and promote online courses.

FLIPPING THE CLASSROOM

Many Asian students are under extreme pressure to do well in exams. Some enthusiastic teachers and professors in Taiwan are trying to change this by 'flipping' their classrooms. This involves encouraging students to learn by watching online video lectures in their own time and doing homework in the classroom, where teachers and students discuss and solve questions. The Center for Teaching and Learning Development (CTLD) of NTU was the first to promote flipped teaching in Taiwan. NTU held the first nationwide workshop on flipped teaching in 2014, where teachers learned how others had effectively flipped their classrooms. The workshop has been generalized for primary and high school teachers in Taiwan. NTU's promotion of flipped teaching has resulted in more and more teachers joining the revolution and developing their own approaches. Taiwan is now one of the most successful Asian countries in promoting flipped teaching at all educational levels.

NEXT GENERATION OF INNOVATION

The CTLD of NTU is the largest teaching centre in Asia, with over ten years of experience. In March 2015, the CTLD launched Innovative Teaching — a new course produced by Yeh. It will be the first MOOC on education innovation on Coursera and is expected to transform tens of thousands of teachers into true innovators. NTU will continue to strive to be a major driving force in next-generation education innovation.

INCUBATING ENTREPRENEURIAL TALENT

NTU promotes both educational excellence and entrepreneurship. Embracing top professionals from around the world, NTU remains firmly committed to research and education in its quest for excellence, while striving to improve society. It considers itself a bastion of scholarship, a catalyst for economic development and a contributor to the sustained development of humanity, while aiming to join the ranks of world-class universities.

Entrepreneurship lies at the heart of NTU's philosophy. In its Creativity and Entrepreneurship Program, students from different fields meet on a cross-disciplinary platform in which ideas and teamwork flourish. For example, a team of five NTU students developed a prototype FLUX 3D printer (above right) that will make 3D printing technology a reality in households. This exemplifies NTU's strength in creative entrepreneurship.

The NTU Garage programme nurtures promising start-up teams by providing mentorship and meeting spaces. It also invites leading alumni and Silicon Valley venture capitalists to give consultation and equip budding teams with relevant resources. By providing these resources, NTU has reduced the learning curve of start-up teams and launched them into the start-up scene.

臺灣大學
National Taiwan University

LEARN MORE

Visit: www.ntu.edu.tw



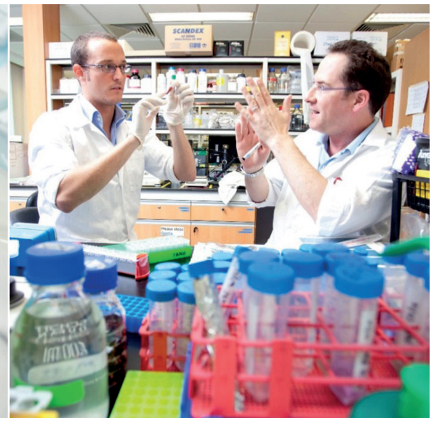

NATIONAL UNIVERSITY OF SINGAPORE

A LEADER IN RESEARCH IN ASIA AND BEYOND

NUS
National University of Singapore

nus.edu.sg

Founded in 1905 as a modest medical school, the National University of Singapore (NUS) has since developed into a research-intensive institution that is consistently ranked among the world's top universities.

With leading researchers and state-of-the-art facilities, NUS aspires to produce world-class research based on a broad definition of research excellence. The university consists of 26 university-level research institutes and centres along with 16 faculties and schools that together form a dynamic network for education and research. NUS hosts three of Singapore's five Research Centres of Excellence — those specializing in quantum technologies, cancer science and mechanobiology — and is a partner in another Research Centre of Excellence, which draws on NUS's strengths in the life sciences and sustainability research.

As a global university based at the heart of Asia, NUS brings Asian perspectives and expertise to bear on issues relevant to the region and beyond. A rigorous academic culture and an enterprising spirit drive high-impact research and innovation at Singapore's flagship university.

HIGH-IMPACT RESEARCH

At NUS, researchers push the boundaries of discovery, with a focus on developing practical applications that benefit society. Recent highlights include a regulatory protein loop involved in bone marrow cancer that may offer a therapeutic target for cancer treatment, a seven-atom-thick sandwich for improved photovoltaic devices and the discovery of bacteria that can degrade the environmentally toxic compound polychlorinated biphenyl (PCB).

Researchers at the Cancer Science Institute of Singapore at NUS discovered that STAT3, a molecule with the potential to cause cancer, associates with and regulates the expression of PRL-3, which has been implicated in various types of cancers. A reduction in STAT3 levels led to a corresponding decrease in the levels of PRL-3 and diminished the malignant properties of leukaemic cells. The scientists concluded that disrupting this regulatory loop may offer an attractive therapeutic strategy against acute myeloid leukaemia, an aggressive blood cancer that causes dysfunctional blood cells to accumulate in the body. Furthermore, PRL-3 is a potential biomarker that could be used in personalized therapy for patients with acute myeloid leukaemia.

In the field of materials science, researchers at the Graphene Research Centre at NUS have made a breakthrough by developing a heterostructure consisting of boron nitride, semiconducting transition metal dichalcogenides, graphene and gold nanoparticles. When used to form seven-atom-thick photovoltaic cells, these 'hi-tech sandwiches' outperform current technologies for photovoltaic devices and can be painted onto any surface where they act like solar panels.

Another group of NUS researchers at the Graphene Research Centre and the Graduate School for Integrative Sciences and Engineering has found that the interface and chemical bonding between graphene and diamond are restructured at high temperatures. The water molecules trapped between the two materials attain a distinct supercritical phase above 400 degrees Celsius and exhibit different behaviours from normal

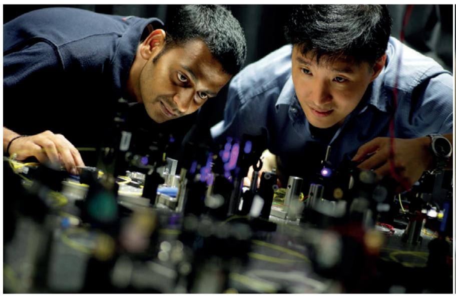

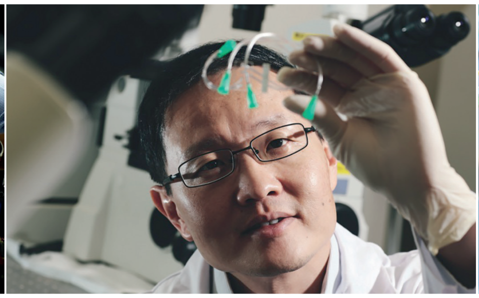

water. This superheated water can corrode diamond and can be used for degrading organic waste in an environmentally friendly manner as well as applied to laser-assisted etching of semiconductor or dielectric films.

An NUS team of bioengineers has developed the world's first microfluidic device for efficient, rapid separation and detection of nonspherical bioparticles. The method developed by the team can complete diagnosis in under an hour — a vast improvement over the 24–48 hours required for bacterial detection using conventional methods. The device can also efficiently separate red blood cells from blood samples by exploiting the nonspherical shape of red blood cells. This facilitates rapid detection of diagnostic biomarkers in blood samples. Outperforming conventional designs, the device can potentially be used for rapid medical diagnostics and treatment.

Another team of researchers from the NUS Department of Civil and Environmental Engineering has discovered three powerful bacteria from the genus *Dehalococcoides* that can degrade PCBs. The team also developed an effective method of culturing these PCB dechlorinators in large quantities to enhance their degradation efficiency. Using these advances, it is now possible to design and engineer methods for ridding the environment of harmful PCBs more effectively.

BUILDING COLLABORATIVE INSTITUTIONS

To further its research mission, NUS continues to develop its infrastructure and pursue ventures with key partners. For example, NUS has established the Centre for Aerospace Engineering, which carries out cutting-edge research with its industry partners, DSO National Laboratories, SIA Engineering Company and ST Aerospace. In another initiative, the Singapore Centre for Nutritional Sciences, Metabolic Diseases and Human Development was launched as a partnership between the Yong Loo Lin School of Medicine at NUS and the Singapore Institute for Clinical Sciences of the Agency for Science, Technology and Research. And the Keppel-NUS Corporate Laboratory — a collaboration between NUS, the Keppel Corporation and the National Research Foundation of Singapore — was set up to meet the emerging challenges of the offshore industry.

> **"At NUS, researchers push the boundaries of discovery, with a focus on developing practical applications that benefit society."**

Recognizing that new breakthroughs are more likely to result from cross-disciplinary initiatives than through traditional forms of inquiry along divided paths, NUS has established several Integrative Research Clusters focusing on six major research themes: finance and risk management, biomedical science and translational medicine, ageing, integrative sustainability solutions, Asian studies and materials science. These clusters provide novel infrastructure for fostering synergy among specific knowledge domains, enabling researchers to tackle complex, multidisciplinary issues. NUS's cross-disciplinary approach is also evident in its educational programmes, such as the NUS Graduate School for Integrative Sciences and Engineering, which encourages its students to transcend traditional subject boundaries.

ALLIANCES AT HOME AND ABROAD

NUS fosters further research and education in Singapore and overseas through key alliances in both the East and West. For example, phase two of the Duke-NUS Graduate Medical School partnership is currently underway to provide leading-edge medical education and conduct patient-oriented research. And Yale-NUS College, which began its first classes in August 2013, ushers in a new model of liberal arts and science education for a complex, globalized world.

University Town at NUS is home to the national-level Campus for Research Excellence and Technological Enterprise (CREATE), an initiative of the National Research Foundation of Singapore, where researchers from different centres and disciplines work closely together to translate cutting-edge research into practical applications. CREATE houses 15 interdisciplinary groups from 10 renowned universities: Massachusetts Institute of Technology, ETH Zurich, Technical University of Munich, Technion – Israel Institute of Technology, The Hebrew University of Jerusalem, Ben-Gurion University of the Negev, Peking University, Shanghai Jiao Tong University, University of Cambridge and University of California, Berkeley.

NUS takes advantage of the close proximity of its main campus to several of Singapore's key science and technology hubs to build partnerships with industrial and government entities. Additional collaborations are facilitated by NUS Enterprise, a university-level cluster dedicated to promoting entrepreneurship and building on the university's intellectual property in various fields. Further afield, NUS is the first non-Chinese university to establish a research institute in the Suzhou Industrial Park, one of the most developed industrial zones in China. NUS has also signed an agreement concerning the Sino-Singapore Tianjin Eco-City and will use the socially harmonious, environmentally friendly and resource-efficient city to study the benefits and challenges of developing green buildings.

As an Asian thought leader, NUS actively develops global initiatives. NUS President Tan Chorh Chuan was appointed chair of the Global University Leaders Forum (GULF) by the World Economic Forum for a two-year term commencing in 2014. He has also recently been appointed a member of the Global Learning Council, a new consortium of education and technology research leaders created by Carnegie Mellon University.

In its global approach to transformative education and cutting-edge research, NUS strives to provide real-world solutions for emerging problems and improve society.




CHIBA UNIVERSITY

ALWAYS AIMING HIGHER

Having established an enviable record in scientific research, Chiba University is lifting its sights even higher as it looks to the future.

Chiba University was founded as a national university in Japan in 1949 when Chiba Normal School, established in 1874, merged with Chiba Medical College and several other educational institutions. Currently composed of 9 faculties and 11 graduate schools, Chiba University is one of Japan's largest national universities having about 11,000 undergraduate students, 3,500 graduate students and 3,000 faculty members on four campuses located near Tokyo. The main campus at Nishi-Chiba occupies an area of almost 400,000 square metres (100 acres) and is conveniently located between Tokyo Station (about 40 minutes by train) and Narita International Airport. The 800-bed University Hospital, a core hospital for the region, is adjacent to the School of Medicine on the Inohana campus.

Guided by its motto "Always aim higher," Chiba University strives to nurture globally minded students who have broad outlooks. The university values academic diversity and actively conducts leading-edge fundamental and applied research. Chiba University's high standing in research is evidenced by the fact that it is ranked tenth among Japan's national universities in Nature Index 2014.

Among the many research accomplishments of Chiba University, its continuing achievements in basic and clinical medicine stand out, particularly in the field of immunology. Toshinori Nakayama's group conducts basic research in areas related to immunology and contributes to the development of new therapies for treating refractory immune disorders (including allergies, autoimmune diseases, cancer and cardiovascular disease) that involve regulation of the immune system. His group has combined forces with the School of Medicine, the Faculty of Pharmaceutical Sciences, the School of Nursing, Chiba University Hospital and the Medical Mycology Research Center in order to establish a hub for developing next-generation therapeutics.

In the physical sciences, Takashige Omatsu's group is seeking to use vortex light beams to control the chirality of substances. With a view to establishing a key centre for material science, his group is collaborating with groups specializing in molecular chirality, biostructural science and molecular electronics.

Also in the physical sciences, the International Center for Hadron Astrophysics uses a large-scale neutrino detector (IceCube) at the South Pole to observe high-energy cosmic neutrinos. The first detection of neutrinos with peta (10^{15}) electron volt energies — the most energetic neutrinos ever observed — by IceCube researchers at Chiba University, led by Shigeru Yoshida, has opened a new window for exploring the Universe. This achievement by the International IceCube collaboration, prompted by the initial detection of the Chiba group, was specified as the Breakthrough of the Year 2013 by the Institute of Physics magazine *Physics World*.

The Center for Frontier Medical Engineering plays a leading role in the research and development of innovative biomeasurement technologies, contributing to the development of high-precision diagnostic systems and minimally invasive treatment.

The Center for Environment, Health and Field Sciences at the Kashiwa-no-ha campus engages in research and development of production systems (plant factories) aimed at producing high-value-added plants containing health functional and medicinal constituents. A group led by Kazuki Saito (identified as a Highly Cited Researcher by Thomson Reuters in 2014) of the Faculty of Pharmaceutical Sciences researches functional foods and ingredients and performs gene editing and metabolic studies of medicinal plants.

The Center for Environmental Remote Sensing focuses on research and development of ground and atmospheric telemetric technologies using satellites and aircraft, and studies the use of observation data in environmental protection, meteorological forecasting and agricultural monitoring in Asia.

Chiba University has been selected as one of the nation's Top Global Universities for its role in leading the globalization of Japanese society. Aspiring to become a globally acknowledged university for both education and research, Chiba University actively promotes joint research and researcher exchanges with other countries. Placing particular emphasis on collaboration within Asia, it has, for example, jointly established the International Cooperative Research Center (ICRC) with Shanghai Jiao Tong University (China). It also plans to establish an overseas campus in Thailand in the next decade.

All this is evidence that Chiba University is living up to its motto of "Always aiming higher" as it looks to what lies ahead.

CHIBA UNIVERSITY

LEARN MORE
Address: 1-33 Yayoi-cho, Inage-ku, Chiba-shi, Chiba 263-8522, JAPAN
Visit: www.chiba-u.ac.jp/e/
E-mail: kokusai@office.chiba-u.jp




NAGOYA UNIVERSITY

NAGOYA IN THE SPOTLIGHT

Strategically located between Tokyo and Japan's western population centres of Kyoto and Osaka, Nagoya has played a largely unsung but vital role in the country's political and economic development for centuries. With the award of two more Nobel prizes to Nagoya University researchers in 2014, the spotlight has now firmly turned on Nagoya and its flagship university as a fertile hotbed for ground-breaking innovation and research.

With the sprawling metropolis and commercial hub of Tokyo to its east and the tradition-steeped Kyoto and vibrant urbanity of Osaka to its west, the city of Nagoya has not always attracted the attention it deserves. The greater Nagoya region and surrounding Aichi prefecture is the largest manufacturing base in Japan, has the largest international shipping port in the country and is the third largest population centre with over 8 million residents.

Nagoya is also the headquarters of Toyota Motor Corporation and boasts a long history of industrial and agricultural development. But the 'engine room' of Japan is much more than just an industrial powerhouse. In centuries past, it was home to three of Japan's most influential warlords — Nobunaga Oda, Hideyoshi Toyotomi and Ieyasu Tokugawa — who were successively responsible for the unification of feudal Japan and putting it on the path to becoming the modern country it is today. Nagoya Castle, around which the city was built, symbolizes this proud history.

IMPERIAL PEDIGREE

With roots dating back to 1871, Nagoya University was formally instituted as the seventh and last of Japan's renowned imperial universities in 1939. Originally established as a school and hospital for the practice of Western medicine, the school developed as a comprehensive medical college, before the addition of a school of science on its inauguration as Nagoya Imperial University. By the early 1950s, the university had a full complement of disciplines with associated graduate schools. In the 1990s, many independent graduate schools were established and the institution's focus shifted to postgraduate studies.

Today, Nagoya University boasts 9 undergraduate schools, 14 graduate schools, more than 30 research institutes and centres, and it is recognized as one of the Japan's core comprehensive universities. Whilst it is the smallest of the National Seven Universities, with just under 10,000 undergraduate students and over 6,000 graduate students — including a generous complement of almost 2,000 international students — the university now has 6 Nobel laureates to its name, making it more than a match for its imperial peers.

NOBEL RECOGNITION

The award of the 2014 Nobel Prize in physics to Nagoya University's Isamu Akasaki and Hiroshi Amano reinforced the university's reputation for being one of Japan's leading Nobel-generating institutions. Prior to this pair of awards, four other researchers affiliated with Nagoya University had been recognized with Nobel prizes.

In 2001, Ryoji Noyori was awarded the Nobel Prize in chemistry for his discovery of a method for selectively synthesizing right- and left-handed versions of organic molecules. Many molecules in nature occur in two mirror-image or 'chiral' forms, and the two chiral versions often have markedly different biological activities. In 1966, Noyori discovered a molecular catalysis technique that allowed the asymmetric synthesis of one chiral form; this

NAGOYA UNIVERSITY

LEARN MORE

Visit: http://en.nagoya-u.ac.jp
http://www.aip.nagoya-u.ac.jp/ru/english/index.html
http://www.aip.nagoya-u.ac.jp/public/nu_research_en
E-mail: nuinfo@adm.nagoya-u.ac.jp

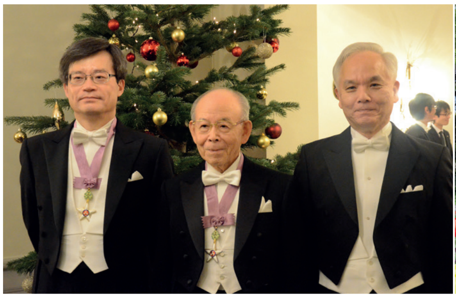

technique is now a fundamental part of many industrial processes and drug development. Then, in 1968, he was appointed associate professor at Nagoya University and led a new organic chemistry laboratory under the guidance of one of Japan's great mentor chemists, Yoshimasa Hirata. Noyori is a special professor of Nagoya University and president of Japan's flagship research organization, RIKEN.

In 2008, three alumni of Nagoya University became Nobel laureates. Osamu Shimomura was awarded the Nobel Prize in chemistry for his discovery in the 1960s of 'green fluorescent protein', which is now routinely used to observe the activity of proteins in biological studies across nearly all fields of medical and biological research. Like Noyori, Shimomura was also mentored by Hirata at Nagoya University, where he received his doctorate in 1960.

The two other recipients in that year, Makoto Kobayashi and Toshihide Maskawa, were jointly awarded the Nobel Prize in physics for their discovery in 1972 of the origin of a 'broken-symmetry' phenomenon in physics, which predicted the existence of three new families of subatomic particles known as quarks — a theory that has since been confirmed in high-energy particle accelerator experiments around the world. Maskawa and Kobayashi both earned their doctorate degrees at Nagoya under the mentorship of Shoichi Sakata and now head Nagoya University's Kobayashi–Maskawa Institute for the Origin of Particles and the Universe.

A message from Nagoya University President Michinari Hamaguchi

In December last year, I attended the Nobel Prize ceremony for two of our most esteemed alumni, Isamu Akasaki and Hiroshi Amano, who, along with the US-based Shuji Nakamura, were jointly awarded the physics prize for their invention of the blue light-emitting diode (LED). Akasaki spoke eloquently of his half-century dedication to the development of the gallium nitride system that made the blue LED possible and of the fortitude needed for such an endeavour. Amano spoke also of the challenges they faced in the research and gave a particularly stirring message emphasizing that the ultimate aspiration of all researchers should be to contribute to society. Nakamura, an engineer who furthered the work of Akasaki and Amano in making gallium nitride LEDs a practical reality, also spoke of the significant challenges he faced in his research. I think all aspiring researchers should hear the message of these prodigious minds regarding the keywords 'fortitude', 'contribution' and 'challenge'.

With so many Nobel laureates linked to Nagoya University, many are now asking how our university continues to produce researchers of this calibre. I believe the main reason is our university's emphasis on strong and constructive mentor–pupil relationships. Hirata mentored Noyori and Shimomura, Sakata mentored Kobayashi and Maskawa, and Akasaki was the mentor of Amano. Mentors have bird's-eye perspectives, deep knowledge, and leadership skills. When a mentor's strength is matched with a younger researcher's fresh enthusiasm and there is a strong relationship of mutual trust, innovation will soon follow. This mutual trust fosters free and vigorous debate and frank argument, which supports the independence of young researchers. At Nagoya University, young researchers are able to concentrate on their study with passion under their mentors' insightful guidance and persevere through many challenges. As we have demonstrated, this is a recipe for Nobel success.

A GLOBAL PERSPECTIVE

On becoming president of Nagoya University in 2009, I immediately began planning its 'globalization'. I see this as absolutely essential as a way to add a contemporary set of values to Nagoya's proud heritage. I want our students not just to study the concept of a close global community, but to live 'internationalism' as an actual experience.

At the annual entrance ceremony, I always encourage our new students to strive to become independent and to study in other countries. The number of students from our university who go out and study abroad has now increased every year for the past five years, and it has now reached 550 students. My goal is to make that 1,000 students–about 10 per cent of our undergraduate population.

As part of our globalization strategy, we are now making more than 500 degree courses available in English under the national government's Global 30 programme. These courses have been remarkably popular, with enrolments increasing more than seven-fold over the past four years.

President Hamaguchi: constructive student–mentor relationships are vital.

We have also established satellite campuses across Asia and now offer double degrees in collaboration with universities in Europe, the USA and Australia. Under this programme, doctoral students who study in the partner university for more than a year are able to acquire their doctorate degree from both universities.

As a result of these initiatives, Nagoya University has achieved top-tier status in the Japanese government's Top Global University Project, guaranteeing financial support for globalization for the next nine years.

With our global outlook and a spirit of 'fortitude', 'contribution' and 'challenge', I believe Nagoya University is poised to make even greater achievements in the future.

NAGOYA UNIVERSITY

A NOBEL NOD FOR LIGHTING THE WORLD

The 2014 Nobel Prize in Physics was jointly awarded to Nagoya University's Isamu Akasaki and Hiroshi Amano, and Shuji Nakamura from the University of California, Santa Barbara, for the invention of the blue light-emitting diode — a technology that has already initiated a global lighting revolution and has the potential to bring light to hundreds of millions of homes across the developing world.

"The importance of the blue light-emitting diode (LED) should not be underestimated," says Nagoya University President Michinari Hamaguchi. "Visible-light LEDs have been around since the 1960s, but with colours that are unsuitable for general lighting. The blue LED is indispensable for obtaining a 'white' spectrum amenable for room lighting and electronic displays. Without the blue LED, computer displays and smartphones would not be as they are today, and the emerging revolution in LED room lighting would never occur."

The white light now achievable with LED lighting is created by pairing a blue LED with a yellow phosphor. This is significant because white LEDs are six times more efficient at converting electrical energy into light than conventional incandescent lamps, and their lifetimes are ten times longer. This technology will thus greatly improve global energy efficiency for lighting. "In Japan, for example, it is expected that the use of LEDs will reduce the total electricity demand by 7% within a few years — that's the energy equivalent of ten or so nuclear power plants," says Hamaguchi.

As LEDs can work at low voltages, the blue LED is also expected bring light to 1.5 billion people in Africa and central Asia who currently lack reliable mains power. "The blue LED is one of the main technologies that will dramatically change human society in the 21st century and is the biggest revolution in lighting since Edison's light bulb," Hamaguchi notes.

INNOVATION SPRINGS FROM HERCULEAN EFFORT

"The invention of the blue LED came about through the superhuman-like devotion of Drs Akasaki and Amano to this research," beams Hamaguchi. Although Amano succeeded in growing the gallium nitride crystal that underlies the blue LED technology by the age of 24, he persevered through more than 1,500 subsequent failures before a working device presented itself. Through all this, his mentor, Akasaki, continued to provide support and direction, allowing Amano to devote himself to his study. "It was the process by which the young Amano became a genius," Hamaguchi observes.

Under the guiding hand of Akasaki, many people across Nagoya University were brought in to help deal with the various difficulties that arose through the course of the study. The peerless work of Akasaki and Amano was also assisted in no small way by a strong and fruitful university–industry collaboration with Toyoda Gosei Company. In many respects it was this collaboration that made the achievement possible. Toyoda Gosei partnered with Nagoya University from a very early stage in the blue LED research, and the collaboration produced

Leading lights: Nobel laureates Isamu Akasaki and Hiroshi Amano.

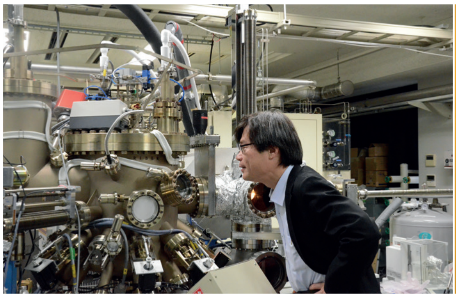

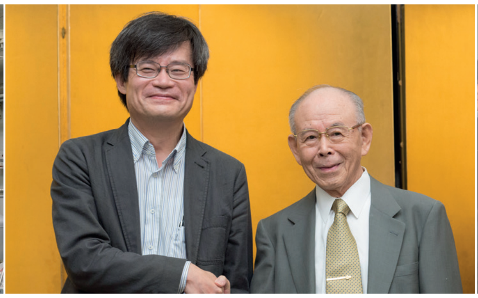

hundreds of patents and practical uses. “In the initial stages, research funding was difficult to secure since the research was not expected to bear fruit for some time,” notes Hamaguchi. “I believe the deep trust and support of Toyoda Gosei was instrumental in navigating these difficulties — it was an ideal collaboration.”

RECOGNITION FOR A TRULY WORLD-CHANGING INVENTION

The Royal Swedish Academy of Sciences awarded the 2014 Nobel Prize in physics to Akasaki, Amano and Nakamura for an invention that they believe fulfils the spirit of Alfred Nobel’s reward — an invention of great benefit to humankind. Such accolades are typically not conferred until many decades after the original discovery, once the full potential of the achievement has become apparent. Yet in inventing the blue LED, the Nobel laureates have developed a new way of creating white light, leading to longer-lasting and more efficient alternatives to older light sources with immediate and far-reaching applications. According to the Academy, “The invention of the efficient blue LED is just 20 years old, but it has already permitted the creation of white light in an entirely new manner to the benefit of us all.”

THE BLUE LED CHALLENGE

Since the discovery of fire, humans have been experimenting with light in the search for better light sources, from the first flame torches, to candles and oil lamps, Edison’s incandescent light bulb and more recently fluorescent and high-intensity discharge lamps. LEDs represent an extremely simple and efficient technology for generating light, but getting them into our homes as a replacement for older technologies involved many challenges worthy of Nobel recognition.

When the first visible-light LED was created in the 1960s by Nick Holonyak Jr., few thought much of the invention. It was expensive to produce, and since it emitted only red light, it was limited to use as a replacement for incandescent indicator lamps on electronic switch boards. Holonyak’s work, which many believe also warrants a Nobel Prize, built on a technology first invented in the early 1900s.

At its simplest, an LED is a semiconducting material that produces light when a suitable voltage is applied across it. The semiconducting material is ‘doped’ on one side with impurities, resulting in one side having a deficiency of electrons (called ‘holes’) and the other side having an excess of electrons. When current flows across this junction between the ‘p-type’ and ‘n-type’ sides of the semiconductor, the holes and electrons recombine and emit light. The colour or wavelength of the light is determined by the ‘bandgap’ energy of the semiconductor. Holonyak’s red LED, for example, uses gallium arsenide phosphide as its semiconductor. Gallium arsenide produces infrared light, but the addition of phosphorus to the semiconductor alloy increases the bandgap and hence reduces the wavelength of light emitted, pushing it into the long-wavelength end of the visible spectrum — red.

Since Holonyak’s invention, there has been a steady stream of new semiconductor compositions with different bandgaps. These devices all emit at a specific wavelength, whether it be green, yellow or red. The ambient light we are used to, however, is a complex spectrum of colours that together create a cool or warm white illumination — something that is impossible to achieve using non-blue LEDs alone.

To make LEDs suitable as a general white light source that could be used in homes, offices and electronic displays, a native blue emission was needed, paired with a phosphor to shift and broaden the emission spectrum to produce a ‘colour’ recognizable as white.

MOUNTING OBSTACLES

Not only must the semiconductor compound forming the basis for a blue LED have a large bandgap suitable for blue emission, it also needs to be a direct (rather than indirect) bandgap in order to generate blue light, and must be able to be produced as a high-quality single crystal with controllable conduction properties.

Relatively early in the quest for a blue LED, gallium nitride (GaN) was recognized as having the right bandgap as well as the potential to satisfy all the other requirements. Yet despite intensive and persistent efforts by many researchers around the world, producing high-quality single crystals of gallium nitride

Young researchers are indispensable for innovation, says Amano.

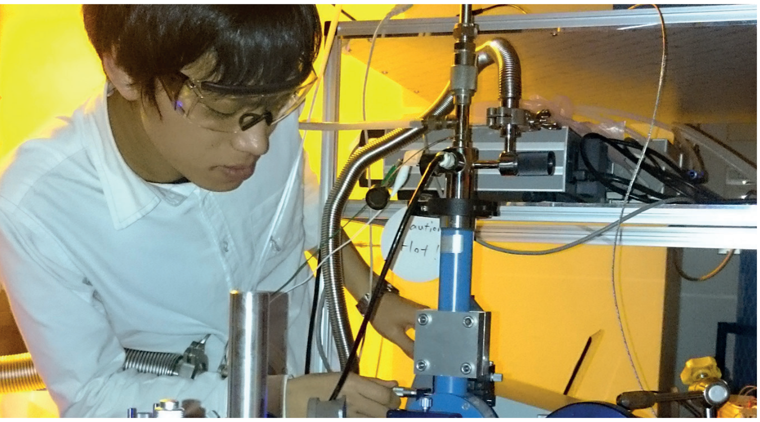

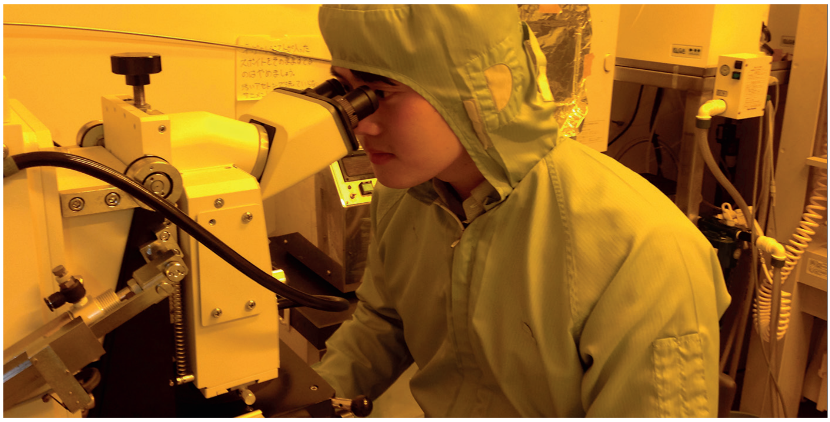

or any other suitable direct-bandgap semiconductor proved elusive. Furthermore, it was found to be impossible to produce p-type materials and to control the electrical conductivity of such semiconductors.

One way around this conundrum was to select zinc selenide, which can be lattice-matched to a gallium arsenide substrate. On the other hand, no lattice-matched substrates were known for GaN, and few researchers considered GaN to be the best candidate for blue LEDs.

INSPIRATION MATCHED BY PERSEVERANCE

Based on his experience with advanced semiconductor growth techniques such as hydride vapour-phase epitaxy and molecular beam epitaxy, Isamu Akasaki found that metal organic vapour-phase epitaxy (MOVPE) was the best for growing crystalline GaN. It was at Nagoya University that Hiroshi Amano, under the supervision of Akasaki, eventually succeeded in growing high-quality GaN single crystals on a thin aluminium nitride buffer layer using a homemade MOVPE system. The resulting crystals were completely transparent and had vastly superior crystal quality and electrical and luminescent properties relative to GaN crystals grown without a buffer layer. This breakthrough in 1985 was the first major milestone on the road to blue LEDs.

The next step was to fabricate a p–n junction. Where many groups around the world tried and failed, Akasaki, Amano and their laboratory colleagues persevered and eventually succeeded in doping GaN, not with zinc as previously used, but magnesium. This required the discovery of a suitable dopant precursor, bis-cyclopentadienyl magnesium, that would allow doping while maintaining high crystal quality. This led to the fabrication in 1989 of the world's first GaN p–n junction, resulting in a blue LED with encouraging electrical characteristics. The team then improved the efficiency of the blue LED by developing a way to control the conductivity in n-type GaN, which was again challenging. They eventually discovered the necessary conductivity control could be realized by using silicon hydride and a silicon dopant.

An inside perspective — a message from Nobel laureate Hiroshi Amano

I am of course humbled and gratified that our study on the blue LED was recognized through a Nobel Prize. From a young age, I have always desired to contribute to human society, and I became interested in the study of blue LEDs as a student. I thought that the LED had the potential to change the world. It proved to be much harder to make a blue LED than I had ever imagined. Winning a Nobel Prize is the result of the efforts of many people in this field in Japan, and I am delighted that the world values this discovery. I hope this invention will give the many children around the world who lack the luxury of reliable power the opportunity to study and read books at night.

The achievement for which the Nobel Prize was awarded represents a period of about six years in my research career, when I was a graduate student from the age of 24 to around 29. I think this shows that even the achievements of a young graduate have the potential to produce Nobel-worthy breakthroughs. I would like all young researchers to take heart that such achievements are possible.

A driving force in my study was a desire to create something that will benefit people. That desire is still strong. The blue LED has already seen tremendous and widespread adoption, but I think many aspects still need to be studied and improved. Energy conversion efficiency, in particular, which is now around 60 per cent, should be improved to close to 100 per cent . I want to create an LED system that freely allows emission of any colour at 100 per cent efficiency. The white LED is also too expensive to be used in some of the most needed applications. I have a goal of cutting the cost of white LEDs to one-fifth of their current cost by 2020, while at the same time raising energy efficiency.

Our gallium nitride system also has many potential uses beyond LEDs. Here I challenge our students to devise new applications that contribute to society. Japan faces unique energy supply challenges; we need to find ways to reduce energy consumption and improve energy efficiency.

I regard myself as an average person. That even I could be awarded a Nobel Prize should spur young researchers to work harder. When we encountered a major problem in our study, it was young minds that resolved it. I feel that young researchers are indispensable for innovation. There are many people in the world that are more talented than me; if they were each to wrestle toward some seemingly unattainable target, significant technological advances would be made every day.

Hiroshi Amano: "Even the achievements of a young graduate have the potential to produce Nobel-worthy breakthroughs."

NAGOYA UNIVERSITY

BRINGING A GLOBAL FOCUS TO NAGOYA RESEARCH

As a top-tier recipient of funding under two high-profile government programmes — the Top Global University Project and the Program for Promoting the Enhancement of Research Universities — Nagoya University is strengthening its global presence and networks, and reengineering the way that research opportunities are identified and coordinated.

The world's universities have instigated an explosion in the number and quality of inter-university networks and exchange programmes. This rapidly increasing global connectivity has been a boon for both students and researchers, multiplying the opportunities available to budding researchers and enhancing the richness and diversity of research itself. For the universities themselves, however, particularly government-funded ones, the era of globalization has resulted in fierce competition for global talent and even continuing relevance. "How the university organization can survive, and how we, as a higher education institute, should continue to foster the human resources of the next generation, are monumental issues that have been presented to us," says Nagoya University president Michinari Hamaguchi.

In a bid to help Japanese universities make the leap into the global arena, the national government — through the Ministry of Education, Culture, Sport, Science and Technology (MEXT) and the Japan Society for the Promotion of Science (JSPS) — established the Top Global University Project in 2014.

This government initiative aims to strengthen the international competitiveness of Japan's higher education sector by supporting universities that are taking substantial steps toward internationalization and reform, and specifically universities that are conducting world-class research and playing a lead role in promoting the globalization of Japanese universities.

Nagoya University was awarded the highest level of funding available under the scheme for its plan to become a 'hub university of Asia, contributing to a sustainable society in the 21st century'. In accepting the university's plan — one of only 13 accepted across the country for 'top-type' funding — the JSPS recognizes Nagoya University as a world-class institution with the potential to be ranked among the top 100 universities globally.

AN ASIAN LEADER

At the heart of Nagoya University's globalization plans is the establishment of satellite university offices throughout Asia, supported by transnational doctoral programmes for leading professionals. "We have already set up Asian satellite campuses in Mongolia, Vietnam and Cambodia," notes Hamaguchi. "In the coming fiscal year, we will also expand into Laos, Uzbekistan and other Asian countries"

Operated and managed by Nagoya University, these satellite offices foster close cooperative ties between the partner institutions and specific schools at Nagoya University, including the graduate schools of law, bioagricultural sciences, international development, and medicine, and the Center for Asian Legal Exchange and the Research and Education Center for Japanese Law.

The satellite offices will each accept up to two doctoral students from each graduate school per year, drawn from a pool of applicants with work experience as an executive in government or public administration, as well as a strong command of English and an active professional role in policy formulation and implementation in their home country.

Over the course of their doctoral studies, students will enjoy intensive courses delivered in English by Nagoya University academics. In addition to these teleconference-based lectures, the students have the opportunity to visit the main Nagoya University campus in Japan at least once a year. On acceptance of their final dissertation in English, students will be conferred a doctoral degree from Nagoya University.

GLOBAL LINKAGE

"In addition to the Asian Hub programme, we have established a double-degree system modelled on the systems in Europe and the USA," says Hamaguchi. "The first of these is a joint supervision programme in medicine with the University of Freiburg in Germany and the University of Adelaide in Australia. Under this programme, PhD students who study in the partner university for more than a year are able to acquire a doctorate degree from both universities. This programme will become a full joint degree programme in the near future, and the president of the University of Freiburg for one has given his commitment to push forward with a broader range of fields."

The university also recently secured important interchange agreements with the University of Edinburgh in Scotland and St John's College at the University of Cambridge in the UK — the first such agreement made between a Japanese university and St John's in the college's 500-year history.

PROMOTING INTERNATIONAL STUDENT EXCHANGE

To offer all of its Japanese undergraduate students the opportunity to study internationally by 2023, Nagoya University is increasing the number of study-abroad preparatory courses including Nagoya University Take-off Initiative training course, for which students can receive degree credit. The course is a valuable stepping stone to mid- and long-term study by Japanese students in other countries, and encompasses a self-funded study-abroad savings system as well as an introduction to student safety and medical care networks, in collaboration with Bangkok Hospital.

At the same time, the university is aiming to raise the number of international students studying at the Nagoya campus to 3,000 by 2020 in recognition of the need to develop Nagoya University as a multicultural community. This initiative includes hiring more foreign faculty, revising curricula in accordance with international standards, offering more classes in English, and increasing the number of Japanese-language programmes. Supporting this are major initiative such as the Global 30 International programmes, which are specifically tailored to international undergraduate and post-graduate students, and the Nagoya University Program for Academic Exchange, which allows students at partner universities around the world to visit Nagoya for a short-term exchange of up to 12 months.

RESTORING THE BALANCE

Part and parcel of a global perspective is the adoption of international standards for equality. For more than a decade, Nagoya University has recognized the low proportion of women in academic and research support roles across the university sector in Japan and the need to increase their representation across the board, not just to promote equality but to tap into a pool of under-utilized creativity and talent. The university has various policies in place to promote female participation in research and research support to a level comparable to that in the USA and Europe.

A specific initiative aimed at placing more women in university administration roles has resulted in a steady increase in the ratio of female staff over the past few years. Nagoya University has also recently signed on to a government partnership programme for the support of female researchers, which provides additional financial support to the university to equalize the research potential of women over the course of their research careers. This initiative aims to minimize the disruption of maternity leave to the career path of female researchers, putting them on an even footing with their male colleagues and actively promoting their appointment to higher positions while enhancing their research potential.

Nagoya aims to have 3,000 international students at the Nagoya campus by 2020.

STRENGTHENING BONDS

With the globalization of culture, information and people comes a shift not only in the values and expectations of young researchers but also in the role of universities themselves. "The young researchers of today tend to regard themselves as time-limited employees of academic institutions and forcibly seek breakthrough results in ever-shorter periods of time," explains Hamaguchi. "Such expectations have the potential to undermine the strong mentor–student relationship nurtured by our university and weaken our students' independence."

To counter this trend and form stronger and longer-lasting ties with its students, Nagoya University has been reinventing the relationship between young researchers and the university through the Young Leaders Cultivation (YLC) programme. Nurturing and retaining young faculty is fundamental to the growth and success of any university. The young

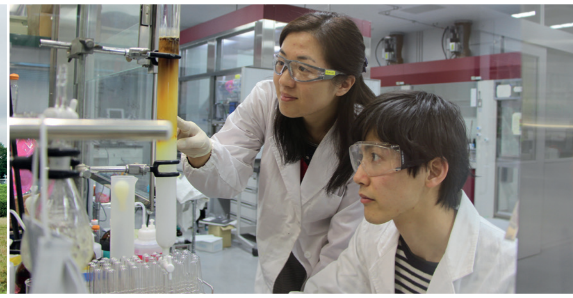

leaders programme provides a planned and consistent framework for recruiting and supporting these valuable human resources. Faculty members recruited under the YLC programme — 40 so far — are affiliated with the Institute for Advanced Research and are put on a tenure track to become an independent researcher.

> "Having been selected as one of the top four universities nationally to receive support under the research universities enhancement program, Nagoya University is eligible for the largest pool of funding available under that scheme."

THE STRATEGY OF INNOVATION

Having been selected as one of the top four universities nationally to receive support under the research universities enhancement program, Nagoya University is eligible for the largest pool of funding available under that scheme.

One of the most important initiatives under the programme is the establishment of an 'Innovation Room' where domestic and international research trends are studied with the aim of identifying research areas in which Nagoya University can become a world leader. This strategic think tank is composed of professors from all research departments under the direction of the university vice president.

Out of this innovation strategy comes the establishment of collaborative international research units and new research units in novel or undeveloped fields, with the goal of eventually turning these research nuclei into world-class research institutes.

"As a result of this systematic reinforcement of our research system, the university has been awarded record competitive external funding for 2015," beams Hamaguchi. "For the 2013 academic year, we also secured the highest number of Grants-in-Aid for Scientific Research per researcher in the country. Through these initiatives Nagoya University will continue to be recognized as a university that cultivates courageous intellectuals endowed with the power to open up new possibilities and contribute to the advancement of science."

Several such research units have already been created, including two collaborative international research programmes and four new research units on emerging topics.

The International Research Unit for Elementary Particle Physics, led by Toru Iijima, is an ambitious project aimed at searching for new physics beyond the standard model with a focus on 'heavy flavour' particles such as the tau lepton, and top, bottom and charm quarks. They are pursuing this goal in collaboration with researchers from the Jozef Stefan Institute in Slovenia.

Taking advantage of Nagoya University's strength of research on neural circuits using small-brained animals, Ikue Mori's International Research Unit for Reconstruction of Neural Function will explore Mori's 'local domain' element as a new concept in neuroscience. Research by this unit aims to visualize and manipulate the functions and activities of local neural domains with the goal of redefining the brain's information processing mechanisms in collaboration with researchers from the University of California, San Francisco.

Newly established research units on emergent topics include Yoshihiko Okamoto's research unit on novel functional materials utilizing 'free' orbital effects as a potentially new type of electronics, Tomohiro Nishitani's research unit on a versatile and innovative high-performance electron beam using a semiconductor photocathode and compact electron gun, Hiroki Gotoh's unit on the evolution of gene networks as the developmental basis for the evolution of novel traits, and Kei Zaitsu's real-time *in vivo* 'omics' laboratory, which aims to establish technology for the comprehensive real-time analysis of biological components in living systems.

More information about Nagoya University's research activities and achievements can be found at NU Research (http://www.aip.nagoya-u.ac.jp/public/nu_research_en/).

BRINGING IT ALL TOGETHER

With the support of the research enhancement programme, the university has also embarked on a major restructure of its own research support systems. Under the new system, research administrators are centrally aggregated as an Office for Academic Research and Industry–Academia–Government Collaboration, where they are able to consolidate their shared research information and provide strategic support for fund raising and management of large-scale projects. Furthermore, the number of university research administrators has been significantly increased, and all are now provided training in international themes and their key support area, as well as being provided a career path toward professionalization of the research administrator role.

THE FUTURE IS GLOBAL

Universities around the world are facing significant challenges. Alongside globalization and generational change, with all its diversity and complexity, is a renewed emphasis by governments and the community on the tangible contributions to society expected of universities amid a climate of global economic instability and budgetary pressure. It is an evolving environment that will shape the future of higher education and research.

"On becoming the president of Nagoya University," says Michinari Hamaguchi, "I advocated a 'Hamaguchi plan' to globalize our institution. Why? Because I wanted to uphold our strong reputation by taking our university from being one of the top research institutions in Japan, to one of the best in the world."